NUCLEIC ACIDS-BASED CANCER THERANOSTICS

EDITED BY: Fu Wang, Guo Chen, Dongkyoo Park, Patrick Baril and Manfred Ogris

PUBLISHED IN: Frontiers in Medicine

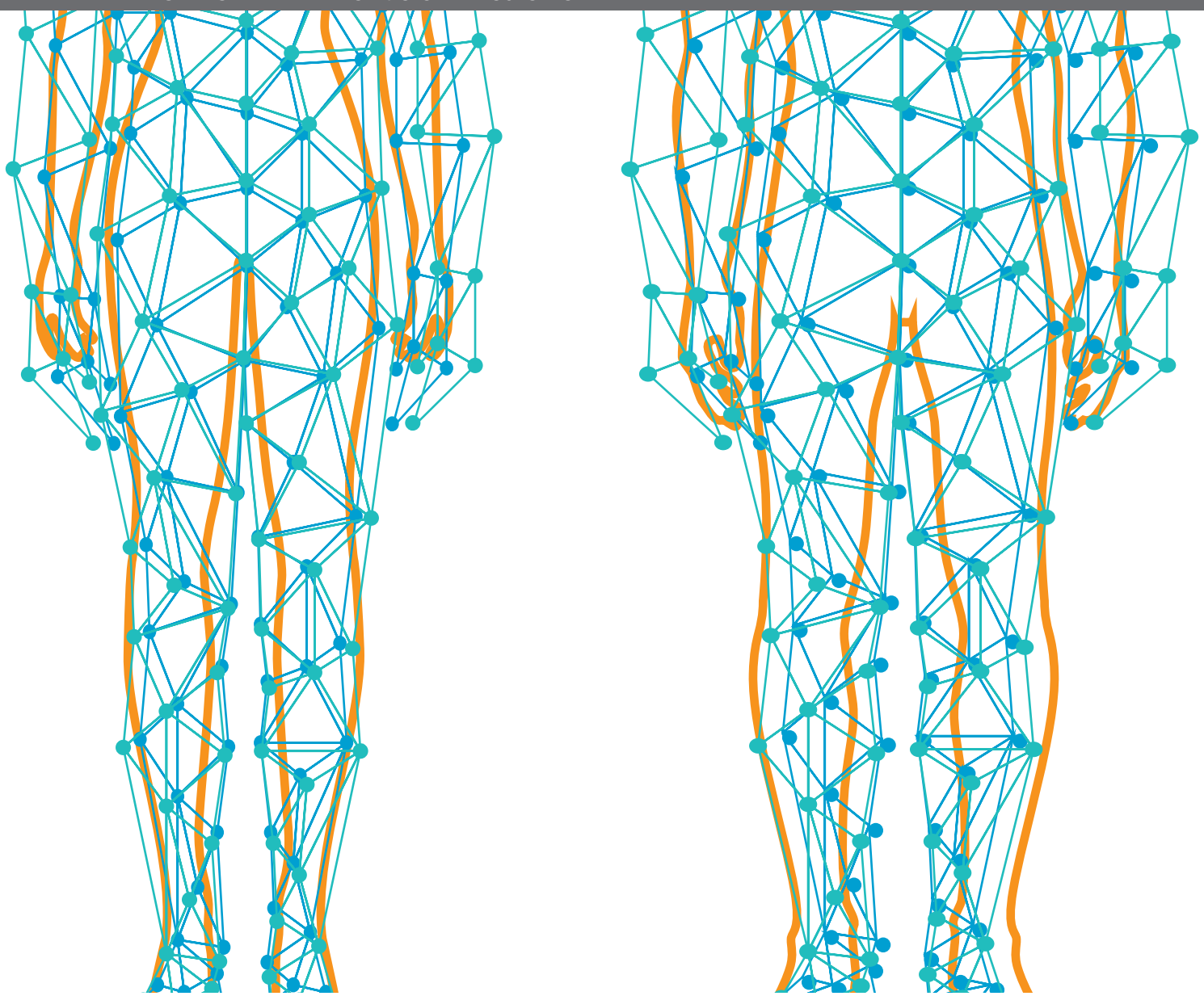

frontiers Research Topics



frontiers

Frontiers eBook Copyright Statement

The copyright in the text of individual articles in this eBook is the property of their respective authors or their respective institutions or funders. The copyright in graphics and images within each article may be subject to copyright of other parties. In both cases this is subject to a license granted to Frontiers.

The compilation of articles constituting this eBook is the property of Frontiers.

Each article within this eBook, and the eBook itself, are published under the most recent version of the Creative Commons CC-BY licence. The version current at the date of publication of this eBook is CC-BY 4.0. If the CC-BY licence is updated, the licence granted by Frontiers is automatically updated to the new version.

When exercising any right under the CC-BY licence, Frontiers must be attributed as the original publisher of the article or eBook, as applicable.

Authors have the responsibility of ensuring that any graphics or other materials which are the property of others may be included in the CC-BY licence, but this should be checked before relying on the CC-BY licence to reproduce those materials. Any copyright notices relating to those materials must be complied with.

Copyright and source acknowledgement notices may not be removed and must be displayed in any copy, derivative work or partial copy which includes the elements in question.

All copyright, and all rights therein, are protected by national and international copyright laws. The above represents a summary only. For further information please read Frontiers' Conditions for Website Use and Copyright Statement, and the applicable CC-BY licence.

ISSN 1664-8714
ISBN 978-2-88974-372-8
DOI 10.3389/978-2-88974-372-8

About Frontiers

Frontiers is more than just an open-access publisher of scholarly articles: it is a pioneering approach to the world of academia, radically improving the way scholarly research is managed. The grand vision of Frontiers is a world where all people have an equal opportunity to seek, share and generate knowledge. Frontiers provides immediate and permanent online open access to all its publications, but this alone is not enough to realize our grand goals.

Frontiers Journal Series

The Frontiers Journal Series is a multi-tier and interdisciplinary set of open-access, online journals, promising a paradigm shift from the current review, selection and dissemination processes in academic publishing. All Frontiers journals are driven by researchers for researchers; therefore, they constitute a service to the scholarly community. At the same time, the Frontiers Journal Series operates on a revolutionary invention, the tiered publishing system, initially addressing specific communities of scholars, and gradually climbing up to broader public understanding, thus serving the interests of the lay society, too.

Dedication to Quality

Each Frontiers article is a landmark of the highest quality, thanks to genuinely collaborative interactions between authors and review editors, who include some of the world's best academicians. Research must be certified by peers before entering a stream of knowledge that may eventually reach the public - and shape society; therefore, Frontiers only applies the most rigorous and unbiased reviews.
Frontiers revolutionizes research publishing by freely delivering the most outstanding research, evaluated with no bias from both the academic and social point of view. By applying the most advanced information technologies, Frontiers is catapulting scholarly publishing into a new generation.

What are Frontiers Research Topics?

Frontiers Research Topics are very popular trademarks of the Frontiers Journals Series: they are collections of at least ten articles, all centered on a particular subject. With their unique mix of varied contributions from Original Research to Review Articles, Frontiers Research Topics unify the most influential researchers, the latest key findings and historical advances in a hot research area! Find out more on how to host your own Frontiers Research Topic or contribute to one as an author by contacting the Frontiers Editorial Office: frontiersin.org/about/contact

NUCLEIC ACIDS-BASED CANCER THERANOSTICS

Topic Editors:
Fu Wang, Xi'an Jiaotong University, China
Guo Chen, Jinan University, China
Dongkyoo Park, Emory University, United States
Patrick Baril, Université d'Orléans, France
Manfred Ogris, University of Vienna, Austria

Citation: Wang, F., Chen, G., Park, D., Baril, P., Ogris, M., eds. (2022). Nucleic Acids-Based Cancer Theranostics. Lausanne: Frontiers Media SA. doi: 10.3389/978-2-88974-372-8

Table of Contents

06 ***Expression Pattern and Prognostic Value of Key Regulators for m6A RNA Modification in Hepatocellular Carcinoma***
Lele Zhang, Yiting Qiao, Jiacheng Huang, Dalong Wan, Lin Zhou, Shengzhang Lin and Shusen Zheng

19 ***A Novel miRNA Restores the Chemosensitivity of AML Cells Through Targeting FosB***
Huiwen Wang, Huien Zhan, Xinya Jiang, Lilian Jin, Tianming Zhao, Shurong Xie, Wei Liu, Yan Jia, Hui Liang and Hui Zeng

28 ***Design, Bioanalytical, and Biomedical Applications of Aptamer-Based Hydrogels***
Ya Di, Ping Wang, Chunyan Li, Shufeng Xu, Qi Tian, Tong Wu, Yaling Tian and Liming Gao

43 ***Bibliometric Analysis of ATAC-Seq and Its Use in Cancer Biology via Nucleic Acid Detection***
Yu Zhao, Xianwen Zhang, Zhenhua Song, Danian Wei, Hong Wang, Wei Chen, Guodong Sun, Weiying Ma and Kebing Chen

54 ***DNA Repair-Based Gene Expression Signature and Distinct Molecular Subtypes for Prediction of Clinical Outcomes in Lung Adenocarcinoma***
Bin Hu, Di Liu, Yinqiang Liu and Zhixi Li

67 ***Long Non-coding RNAs in Cancer: Implications for Diagnosis, Prognosis, and Therapy***
Yuchen Qian, Lei Shi and Zhong Luo

75 ***DGCR8/miR-106 Axis Enhances Radiosensitivity of Head and Neck Squamous Cell Carcinomas by Downregulating RUNX3***
Chunlin Zhang, Hangqi Chen, Zeyi Deng, Dan Long, Li Xu and Zhaohui Liu

86 ***Development and Multi-Data Set Verification of an RNA Binding Protein Signature for Prognosis Prediction in Glioma***
Chunpeng Sheng, Zhihua Chen, Jianwei Lei, Jianming Zhu and Shuxin Song

99 ***Visualization and Analysis in the Field of Pan-Cancer Studies and Its Application in Breast Cancer Treatment***
Xianwen Zhang, Han Lai, Fan Zhang, Yixi Wang, Li Zhang, Ni Yang, Chunrong Wang, Zheng Liang, Jieping Zeng and Jinrong Yang

109 ***Comprehensive Analysis Identifies Potential Ferroptosis-Associated mRNA Therapeutic Targets in Ovarian Cancer***
Jiyan Zhang, Jie Xi, Ping Huang and Saitian Zeng

123 ***C3AR1 mRNA as a Potential Therapeutic Target Associates With Clinical Outcomes and Tumor Microenvironment in Osteosarcoma***
Tiannan Zou, Weibing Liu, Zeyu Wang, Jiayu Chen, Sheng Lu, Kun Huang and Weichao Li

137 ***Diagnostic and Prognostic Value of Circulating CircRNAs in Cancer***
Mina Wang, Feiyu Xie, Jiaran Lin, Yihan Zhao, Qian Zhang, Zehuan Liao and Peng Wei

151 ***Mutant Allele Frequency-Based Intra-Tumoral Genetic Heterogeneity Related to the Tumor Shrinkage Mode After Neoadjuvant Chemotherapy in Breast Cancer Patients***
Chun-hui Zheng, Zhao-yun Liu, Chen-xi Yuan, Xiao-yun Dong, Hai-mei Li, Jin-jin Wang, Zhao-peng Zhang, Hong-Ying Liu, Xiao-yan Ding, Wendy Wu, Rui-ru Wang and Yong-sheng Wang

160 ***Three Immune-Related Prognostic mRNAs as Therapeutic Targets for Pancreatic Cancer***
Cangang Zhang, Yueji Zou, Yanan Zhu, Yi Liu, Hui Feng, Fan Niu, Pengcheng He and Haibo Liu

173 ***A Ferroptosis-Related Signature Robustly Predicts Clinical Outcomes and Associates With Immune Microenvironment for Thyroid Cancer***
Mingqin Ge, Jie Niu, Ping Hu, Aihua Tong, Yan Dai, Fangjiang Xu and Fuyuan Li

186 ***Targeting Antisense lncRNA PRKAG2-AS1, as a Therapeutic Target, Suppresses Malignant Behaviors of Hepatocellular Carcinoma Cells***
Yanjiao Ou, Yong Deng, Hong Wang, Qingyi Zhang, Huan Luo and Peng Hu

199 ***Long Non-coding RNA LINC00847 Induced by E2F1 Accelerates Non-small Cell Lung Cancer Progression Through Targeting miR-147a/IFITM1 Axis***
Huan Li, Yao-kai Chen, Qiu Wan, An-qi Shi, Min Wang, Ping He and Li-xin Tang

212 ***hsa-miR-33-5p as a Therapeutic Target Promotes Apoptosis of Breast Cancer Cells* via *Selenoprotein T***
Wei Zhuang, Jianhui Liu and Wenjin Li

222 ***LncRNA PITPNA-AS1 as a Potential Diagnostic Marker and Therapeutic Target Promotes Hepatocellular Carcinoma Progression via Modulating miR-448/ROCK1 Axis***
Qing-fang Wang, Qing-lin Wang and Ming-bo Cao

235 ***Exosomal Circular RNA RNA-seq Profiling and the Carcinogenic Role of Exosomal circ-CYP24A1 in Cutaneous Squamous Cell Carcinoma***
Zheng Zhang, Hao Guo, Wenjia Yang and Jiuhong Li

249 ***Multi-Omics Integrative Analysis Uncovers Molecular Subtypes and mRNAs as Therapeutic Targets for Liver Cancer***
Yi Shen, Wei Xiong, Qi Gu, Qin Zhang, Jia Yue, Changsong Liu and Duan Wang

262 ***Long Non-coding RNA EBLN3P Regulates UHMK1 Expression by Sponging miR-323a-3p and Promotes Colorectal Cancer Progression***
Xiang-hao Xu, Wen Song, Jun-hua Li, Ze-qi Huang, Ya-fang Liu, Qiang Bao and Zhi-wen Shen

275 ***MicroRNA-1-3p Suppresses Malignant Phenotypes of Ameloblastoma Through Down-Regulating Lysosomal Associated Membrane Protein 2-Mediated Autophagy***
Xing Niu, Biying Huang, Xue Qiao, Jinwen Liu, Lijie Chen and Ming Zhong

288 ***Long Non-coding RNA SNHG12, a New Therapeutic Target, Regulates miR-199a-5p/Klotho to Promote the Growth and Metastasis of Intrahepatic Cholangiocarcinoma Cells***
Hong-Guo Yang, Tian-peng Wang, Sheng-an Hu, Chao-zhou Hu, Cheng-hang Jiang and Qiang He

299 ***FABP5, a Novel Immune-Related mRNA Prognostic Marker and a Target of Immunotherapy for Multiple Myeloma***
Haipeng Jia, Xiaofen Zhang, Xinxin Liu, Ruifang Qiao, Yan Liu, Sulong Lv, Hongbo Zhu, Jie Wang, Qiuhong Kong, Hong Zhang and Zhirong Zhang

312 ***A Novel RNA-Binding Protein Signature to Predict Clinical Outcomes and Guide Clinical Therapy in Gastric Cancer***
Zhigang Qiu, Haitao Jiang, Kun Ju and Xichun Liu

325 ***m^{6}A RNA Methylation Regulator YTHDF1 Correlated With Immune Microenvironment Predicts Clinical Outcomes and Therapeutic Efficacy in Breast Cancer***
Ying Hu, Qinwen Pan, Minghao Wang, Xiang Ai, Yuzhao Yan, Yuan Tian, Yuting Jing, Peng Tang and Jun Jiang

339 ***Isoflurane Suppresses Proliferation, Migration, and Invasion and Facilitates Apoptosis in Colorectal Cancer Cells Through Targeting miR-216***
Zhe Cai, Liangyuan Suo and Zeqing Huang

350 ***Molecular Characteristics, Clinical Implication, and Cancer Immunity Interactions of Pyroptosis-Related Genes in Breast Cancer***
Dandan Xu, Zhipeng Ji and Ling Qiang

frontiers in Medicine

ORIGINAL RESEARCH
published: 16 September 2020
doi: 10.3389/fmed.2020.00556

Expression Pattern and Prognostic Value of Key Regulators for m6A RNA Modification in Hepatocellular Carcinoma

Lele Zhang[1,2,3,4,5†], *Yiting Qiao*[1,3,4,5†], *Jiacheng Huang*[1,2,3,4,5], *Dalong Wan*[1], *Lin Zhou*[1,3,4,5], *Shengzhang Lin*[2,6*] and *Shusen Zheng*[1,3,4,5,6*]

[1] The First Affiliated Hospital, Zhejiang University School of Medicine, Division of Hepatobiliary and Pancreatic Surgery, Department of Surgery, Hangzhou, China, [2] School of Medicine, Zhejiang University, Hangzhou, China, [3] NHC Key Laboratory of Combined Multi-organ Transplantation, Hangzhou, China, [4] Key Laboratory of the Diagnosis and Treatment of Organ Transplantation, Research Unit of Collaborative Diagnosis and Treatment for Hepatobiliary and Pancreatic Cancer, Chinese Academy of Medical Sciences (2019RU019), Hangzhou, China, [5] Key Laboratory of Organ Transplantation, Hangzhou, China, [6] Shulan (Hangzhou) Hospital Affiliated to Zhejiang Shuren University Shulan International Medical College, Hangzhou, China

OPEN ACCESS

Edited by:
Guo Chen,
Jinan University, China

Reviewed by:
Liang Xu,
National University of Singapore, Singapore
Naidi Yang,
Nanjing Tech University, China

***Correspondence:**
Shengzhang Lin
1311046@zju.edu.cn
Shusen Zheng
shusenzheng@zju.edu.cn

[†] These authors share first authorship

Specialty section:
This article was submitted to Precision Medicine, a section of the journal Frontiers in Medicine

Received: 09 July 2020
Accepted: 04 August 2020
Published: 16 September 2020

Citation:
Zhang L, Qiao Y, Huang J, Wan D, Zhou L, Lin S and Zheng S (2020) Expression Pattern and Prognostic Value of Key Regulators for m6A RNA Modification in Hepatocellular Carcinoma. Front. Med. 7:556. doi: 10.3389/fmed.2020.00556

As the most prevalent type of mRNA modification in mammals, N6-methyladenosine (m6A) is involved in various biological processes. Accumulating studies have indicated that the deregulation of m6A RNA modification is linked to cancer and other diseases. However, its implications in hepatocellular carcinoma (HCC) remain poorly characterized. Herein, we sought to investigate the expression pattern of 13 key regulators for m6A RNA modification and to evaluate their prognostic value in HCC. First, we systematically analyzed data from The Cancer Genome Atlas (TCGA) database pertaining to patient clinical information and mRNA gene expression data. We found that 11 out of 13 key regulators for m6A RNA modification showed significantly higher expression levels in HCC. Subsequently, we identified two subgroups (clusters 1 and 2) *via* consensus clustering based on the expression of 13 m6A RNA methylation regulators. Cluster 2 had a worse prognosis and was also significantly correlated with higher histological grade and pathological stage when compared with cluster 1. Moreover, cluster 2 was remarkedly enriched for cancer-related pathways. We further constructed a robust risk signature of five regulators for m6A RNA modification. Further analysis indicated that this risk signature could be an independent prognostic factor for HCC, and the prognostic relevance of this five-gene risk signature was successfully validated using the Gene Expression Omnibus (GEO) dataset. Finally, we established a novel prognostic nomogram on the basis of age, gender, histological grade, pathological stage, and risk score to precisely predict the prognosis of patients with HCC. In summary, we herein uncovered the vital role of regulators for m6A RNA modification in HCC and developed a risk signature as a promising prognostic marker in HCC patients.

Keywords: m6A, hepatocellular carcinoma, bioinformatics, prognostic signature, nomogram

INTRODUCTION

Hepatocellular carcinoma (HCC) remains among the most prevalent and deadly types of cancer worldwide, with more than 700,000 deaths documented annually (1). Epidemiological studies have shown that hepatitis virus infection, alcohol abuse, and aflatoxin contamination are primary risk factors for HCC (2). Due to the lack of apparent symptoms at the early stages of HCC, the majority of patients diagnosed with this cancer are first identified in an advanced stage where the complication of intrahepatic and/or extrahepatic metastasis has taken place (3). Even though the prognosis for HCC patients has improved due to recent advances in various treatment approaches, including surgical tumor resection, targeted drug therapy, transarterial chemoembolization, and liver transplantation, the 5-year survival rate remains dismal due to the high rate of metastasis and recurrence (4). At present, the tumor, lymph node, and metastasis (TNM) staging system is still the most widely adopted prognostic indicator for monitoring the progress of HCC. However, HCC is highly heterogeneous; therefore, patients with the same TNM stage often present remarkable differences in survival outcomes and treatment responses. Therefore, to improve the unsatisfactory outcomes of patients with HCC, it is important to identify novel and reliable molecular signatures for prognostic prediction.

Methylation at the position N6 of adenosine, also known as N6-methyladenosine (m6A) modification, is evolutionarily conserved and widely present in most eukaryotic species (yeast, plants, and mammals) and viral mRNA (5, 6). The process of m6A modification is reversible and dynamic and is controlled by methyltransferases ("writers"), demethylases ("erasers"), and methyl-binding proteins ("readers") (7). Methyltransferases, such as METTL3, RBM15, KIAA1429, METTL14, WTAP, and ZC3H13 are responsible for the methylation modification of RNA (8). Demethylases, including ALKBH5 and FTO, mediate the process of demethylation of RNA (9, 10). Methyl-binding proteins, including YTHDF1, HNRNPC, YTHDC1, YTHDF2, and YTHDC2, can recognize m6A-modified sites and preferentially bind to such sites to regulate downstream signals (11). RNA m6A modification is involved in many vital cellular processes, such as gene expression, alternative splicing, degradation, translation of mRNA, and RNA–protein interaction (12).

The poor prognosis of cancer patients is due to the unique malignant biological characteristics of the cancer, including epithelial–mesenchymal transition (EMT), cancer stem cell formation, signaling transduction, tumor angiogenesis, and cancer metabolism. Several studies have shown that aberrant m6A RNA modification plays key roles in these biological processes closely associated with the HCC progression by regulating mRNA stability or protein translation (13–15). For example, METTL3- and YTHDF1-dependent m6A modification could promote EMT by enhancing the translation of Snail mRNA in liver cancer (16). In hypoxic environment, the expression of ALKBH5 was stimulated in a HIF-dependent manner in breast cancer. Overexpression of ALKBH5 decreased m6A modification and stabilizes NANOG mRNA, thus resulting in higher stemness (17). Considering that hypoxia also plays an important role in the progression of HCC, m6A may also promote the formation of cancer stem cells through a similar approach. As research continues, m6A modification has been shown to participate in the many signaling pathways, including but not limited to the MYC/CEBPA, Wnt/PI3K-Akt, AFF4/NF-κB/MYC, YAP, and TGF-β signaling pathways, to promote cancerous growth as well as angiogenesis (18, 19). In addition, m6A modification can modulate cancer metabolism through downregulating the translation of ATG5/7, the key signal node for autophagy, as well as upregulating the translation of 6PGD, the central player of pentose phosphate pathway (20, 21). To summarize, deregulation of m6A modification profoundly promoted the malignancy of cancer. This explains why m6A RNA modification has prognostic impacts on patients with HCC.

In this study, transcriptome data from The Cancer Genome Atlas (TCGA) datasets were used to assess the expression of 13 key regulators for m6A RNA modification in HCC. Additionally, HCC patients were categorized into two clusters according to the expression pattern of regulators for m6A RNA modification by consensus clustering, and two clusters exhibited significantly different clinical outcomes. Furthermore, a risk signature prognostic prediction model was established and showed a favorable predictive value for HCC patients. More importantly, the prognostic relevance of this risk signature was successfully validated in the Gene Expression Omnibus (GEO) database.

MATERIALS AND METHODS

Data Collection

RNA-sequencing transcriptomic data and corresponding clinical information for patients with HCC were obtained from TCGA (https://portal.gdc.cancer.gov/; until February 21, 2020). A total of 374 HCC cases and 50 normal adjacent tumor tissues were included for further analysis.

Thirteen currently known genes, including YTHDF1, YTHDF2, YTHDC1, YTHDC2, METTL3, METTL14, ALKBH5, FTO, HNRNPC, KIAA1429, RBM15, WTAP, and ZC3H13, are recognized as m6A methylation regulators. The expression data of these 13 genes were extracted for subsequent analysis from the HCC cohort of the TCGA database. For external validation, we used an independent cohort (GSE54236) containing 78 HCC samples with corresponding gene expression data and the survival information, which were obtained from the GEO (http://www.ncbi.nlm.nih.gov/geo).

Bioinformatics Analysis

Differentially expressed genes encoding m6A RNA methylation regulators between HCC and normal tissues were screened using the Wilcoxon test method in R (version R 3.6.3, https://www.r-project.org/). Significance criteria were as follows: false discovery rate (FDR) < 0.05 and absolute log2 fold change (FC) > 1. Subsequently, a vioplot was used to exhibit the expression of these m6A-related genes in 374 HCC patients and 50 normal adjacent samples. Spearman correlation analyses were

conducted using R to identify the association between m6A RNA methylation regulators.

To assess the link between m6A RNA methylation regulators expression and HCC prognosis, HCC cohort was clustered into two different subgroups using the "ConsensusClusterPlus" R package. Principal component analysis (PCA) was then carried out using the "ggplot2" and "limma" package to verify the results of the classification. A survival curve was plotted to compare survival between subgroups based on the Kaplan–Meier analysis log-rank test. The difference in clinical parameters between the two clusters was determined using the Chi-square test. In order to conduct functional annotation of the genes with different expression in two subgroups, we performed Gene ontology (GO) and Kyoto Encyclopedia of Genes and Genomes (KEGG) analyses.

Univariate Cox regression analyses were utilized to assess the relationship between m6A-related genes and overall survival (OS). Subsequently, to avoid overfitting, we performed least absolute shrinkage and selection operator (LASSO) Cox regression to eliminate the highly correlated genes with the "glment" package. Ultimately, a five-m6A-regulatory-gene risk signature was identified. To generate a risk score, we multiplied

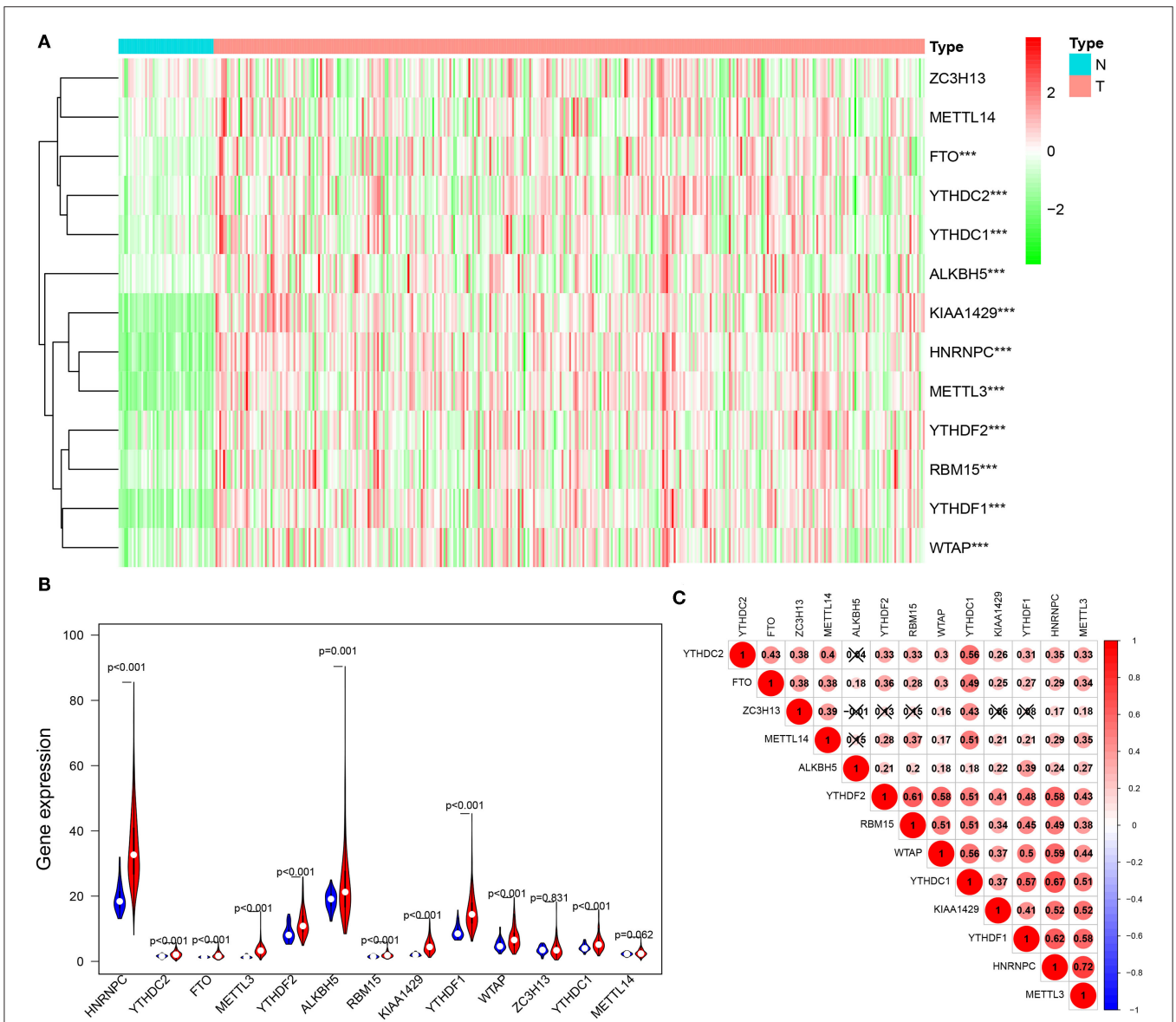

FIGURE 1 | Expression of m6A modification regulators in HCC. **(A)** The heatmap visualizes the expression levels of m6A RNA modification regulators in each sample. "N" represents normal samples and "T" represents tumor samples. Green represents low expression and red represent high expression. **(B)** The violplot shows the differentially m6A RNA modification regulators in HCC. Blue represents normal sample and red represents HCC sample. White spot represents the median value of expression. **(C)** Spearman correlation analysis of the 13 m6A RNA modification regulators in HCC. ***$p < 0.001$.

the gene expression and its coefficient obtained from the LASSO Cox regression. Median risk scores were then used to separate HCC patients into low- and high-risk groups. Kaplan–Meier analysis was performed using "survival" package. Receiver operating characteristic (ROC) curves were used to examine the accuracy of the model for prognostic prediction. The differences in clinicopathological variables between low- and high-risk groups were assessed *via* Chi-square text and visualized *via* a heatmap. In addition, univariate and multivariate Cox regression analyses were used as a means of assessing whether the risk score was an independent prognostic indicator.

To validate the prognostic value of this five-m6A-regulatory-gene risk signature, we used GSE54236 datasets as the validation cohort. Patient risk scores were calculated using the same formula as above. We applied the same cutoff criteria to classify the patients into low- and high-risk groups. Subsequently, Kaplan–Meier survival analysis and ROC curve analysis were performed to assess the prognostic value.

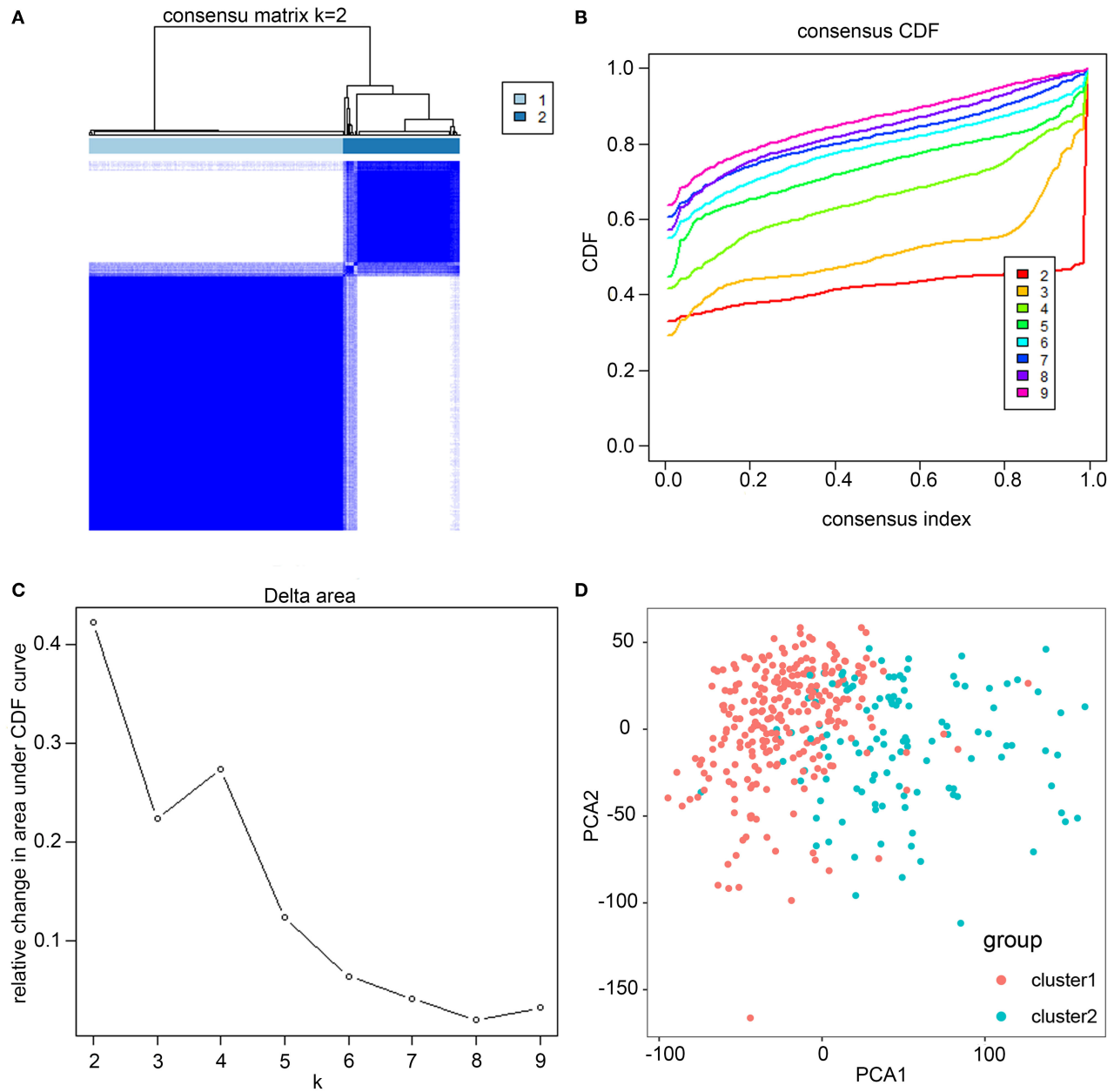

FIGURE 2 | Consistent cluster analysis of HCC. **(A)** The correlation between subgroups when cluster numbers $k = 2$. **(B)** Cumulative distribution function (CDF) is displayed for $k = 2$–9. **(C)** The relative change in area under the CDF curve for $k = 2$–9. **(D)** Principal component analysis of the RNA-seq data. Red dots represent cluster 1 and cyan dots represent cluster 2.

Finally, clinical factors (gender, age, histologic grade, and pathological stage) and risk score were utilized to develop a prognostic nomogram to predict 1-, 3-, and 5-year survival of patients with HCC *via* "rms" package.

All R packages mentioned above were obtained from http://www.bioconductor.org.

Statistical Analysis

R software (version 3.6.3) was utilized for all statistical analyses, and $p < 0.05$ was the significance threshold.

RESULTS

Identification of Differentially Expressed m6A RNA Modification Regulators in HCC

We conducted a differential expression analysis of 13 m6A regulatory genes in HCC ($n = 375$) and adjacent tissues ($n = 50$). Heatmap clearly revealed that most of these m6A-related genes were differentially expressed between HCC and control tissues (**Figure 1A**). Specifically, the expression levels of HNRNPC, YTHDF2, FTO, METTL3, YTHDF2, ALKBH5, RBM15, KIAA1429, YTHDF1, WTAP, and YTHDC1 (all $p < 0.001$) were remarkably higher in tumor samples than those in normal tissues. There was no significant difference for ZC3H13 ($p = 0.831$) and METTL14 ($p = 0.062$) (**Figure 1B**). Moreover, a correlation analysis was performed to further understand the intrinsic association between 13 m6A RNA modification regulators. **Figure 1C** shows that the correlation between METTL13 and HNRNPC is the most significant. The HNRNPC expression level is most likely to be positively correlated with METTL13.

Use of Consensus Clustering Based on m6A RNA Modification Regulators to Identify Two HCC Patient Clusters With Distinct Clinical Outcomes

To further investigate the clinical relevance of 13 m6A RNA modification regulators, we clustered HCC patients into subgroups according to their gene expression patterns.

Based on similarities in m6A RNA modification regulators, $k = 2$ gave the optimum clustering and the HCC cohort could be divided into two distinct and non-overlapping clusters (**Figures 2A–C**). In order to verify the result of the clustering, we further analyzed these two clusters by PCA. The PCA plot showed significant distinction between cluster 1 and cluster 2 (**Figure 2D**). We then assessed whether there were significant differences in OS and clinical parameters between these two clusters. As a result, a significantly better OS was observed in cluster 1, compared to that in cluster 2 ($p < 0.01$) (**Figure 3B**). Moreover, the expression level of most m6A RNA modification regulators of cluster 2 was higher than that of cluster 1 (**Figure 3A**). Compared with cluster 1, cluster 2 was significantly associated with female gender ($p < 0.05$), higher histologic grade ($p < 0.001$), and higher pathological stage ($p < 0.05$). No significant difference was observed for age (**Figure 3A**). Thus, the results of consensus clustering suggested a close association between the expression pattern of m6A RNA modification regulators and HCC malignancy.

In order to further interpret the clustering results from the perspective of fundamental biological processes, we performed GO and KEGG analyses on genes that are differentially expressed between cluster 1 and cluster 2. According to the results of the GO analysis, upregulated genes were primarily enriched in malignancy-related biological processes, such as "humoral

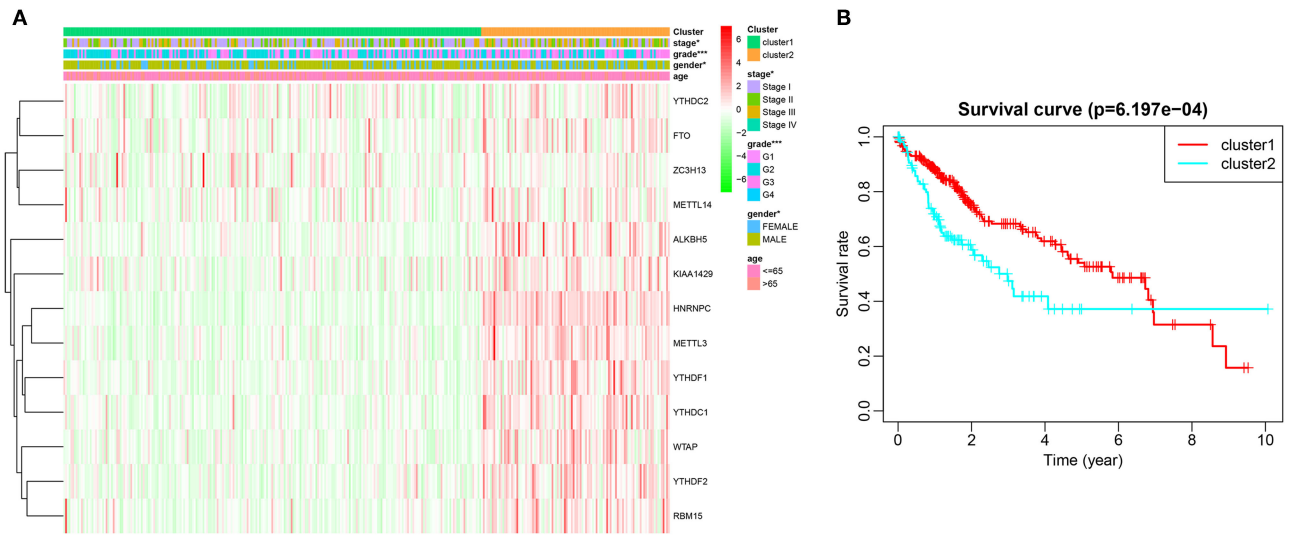

FIGURE 3 | Difference in clinicopathological features and overall survival between cluster 1 and cluster 2. **(A)** Heatmap and clinicopathological characteristics of these two clusters. Green represents low expression and red represent high expression. **(B)** Comparison of overall survival (OS) between cluster 1 and cluster 2. *$p < 0.05$, ***$p < 0.001$.

immune response mediated by circulating immunoglobulin," "B cell mediated immunity," "immunoglobulin mediated immune response," "complement activation, classical pathway," and "protein activation cascade" (**Figures 4A,B**). The results of the KEGG analysis showed that these upregulated genes were significantly enriched in "cell cycle," "herpes simplex virus 1 infection," and "extracellular matrix (ECM)–receptor interaction" (**Figures 4C,D**).

Establishment of a Prognostic Risk Model Based on the Expression Level of m6A Regulator Genes

Considering the strong association between m6A RNA methylation regulators and the prognosis of HCC patients, we applied a univariate Cox regression analysis on the expression levels of 13 key regulators. The results showed that nine out of 13 regulators were significantly correlated with OS ($p < 0.05$) (**Figure 5A**). Among these nine regulators, YTHDF1, YTHDF2, METTL3, KIAA1429, HNRNPC, WTAP, YTHDC1, and RBM15 were considered as risky genes, with HR > 1; meanwhile only ZC3H13 was considered as a protective gene, with HR < 1. Subsequently, LASSO Cox regression analysis was used to identify the m6A RNA modification regulators with the strongest prognostic power (**Figures 5B,C**). Ultimately, five optimal genes (YTHDF1, YTDFH2, METTL3, KIAA1429, and ZC3H13) were selected for the establishment of the risk model for HCC, and the corresponding coefficients from the LASSO algorithm (**Figure 5D**). The formula for calculating the risk score was as follows: risk score = (0.084 * expression value of YTHDF2) + (0.025 * expression value of YTHDF1) + (0.101 * expression value of METTL3) + (0.046 * expression value of KIAA1429) – (0.107 * expression value of ZC3H13).

To explore the prognostic role of this five-gene signature model, HCC patients were separated into low- and high-risk groups based on the median risk score. Survival analysis

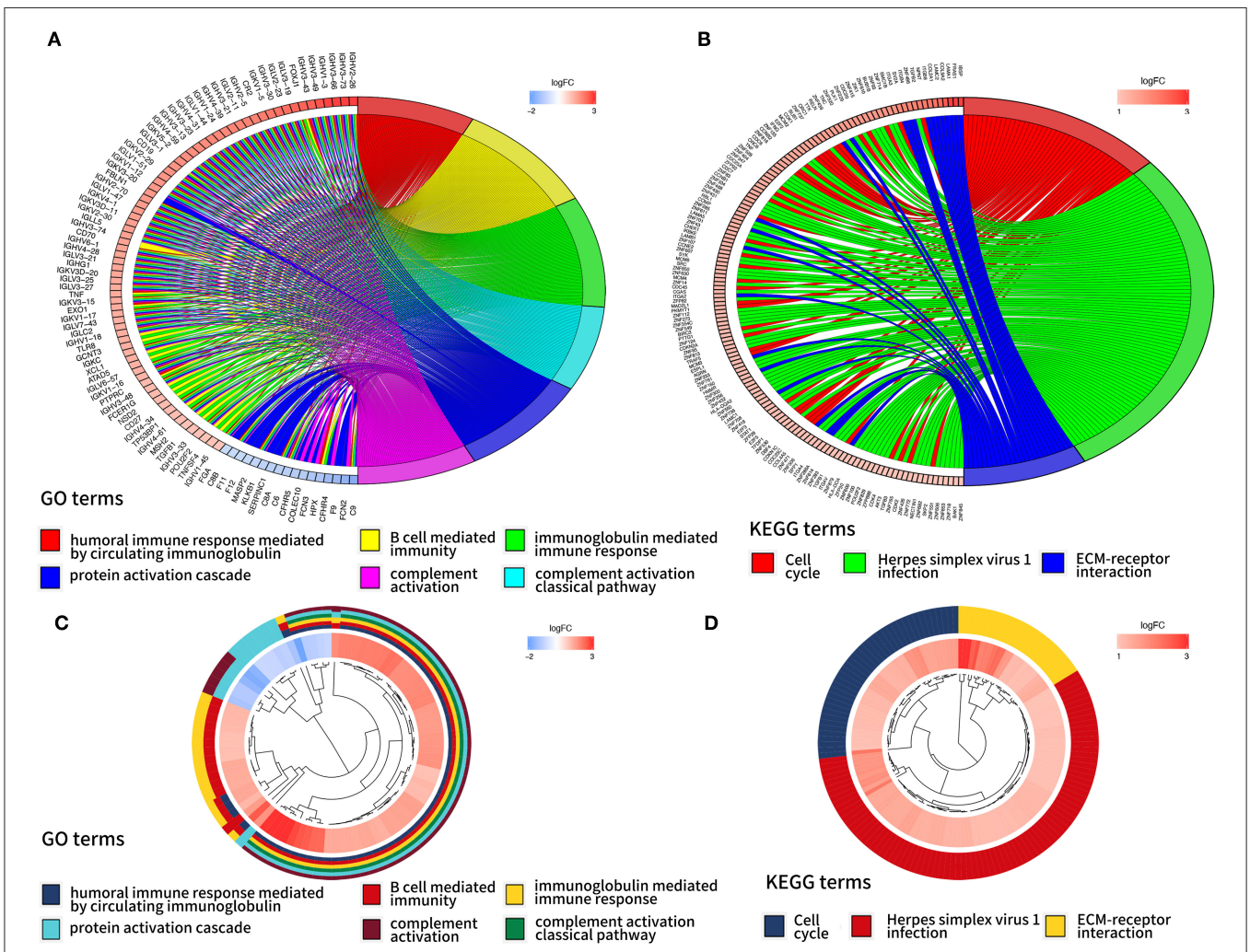

FIGURE 4 | Gene ontology (GO) and Kyoto Encyclopedia of Genes and Genomes (KEEG) analyses of differentially expressed genes between two clusters. Function annotation on higher expressed genes in cluster 2 using GO terms **(A,B)** and KEGG pathway **(C,D)**.

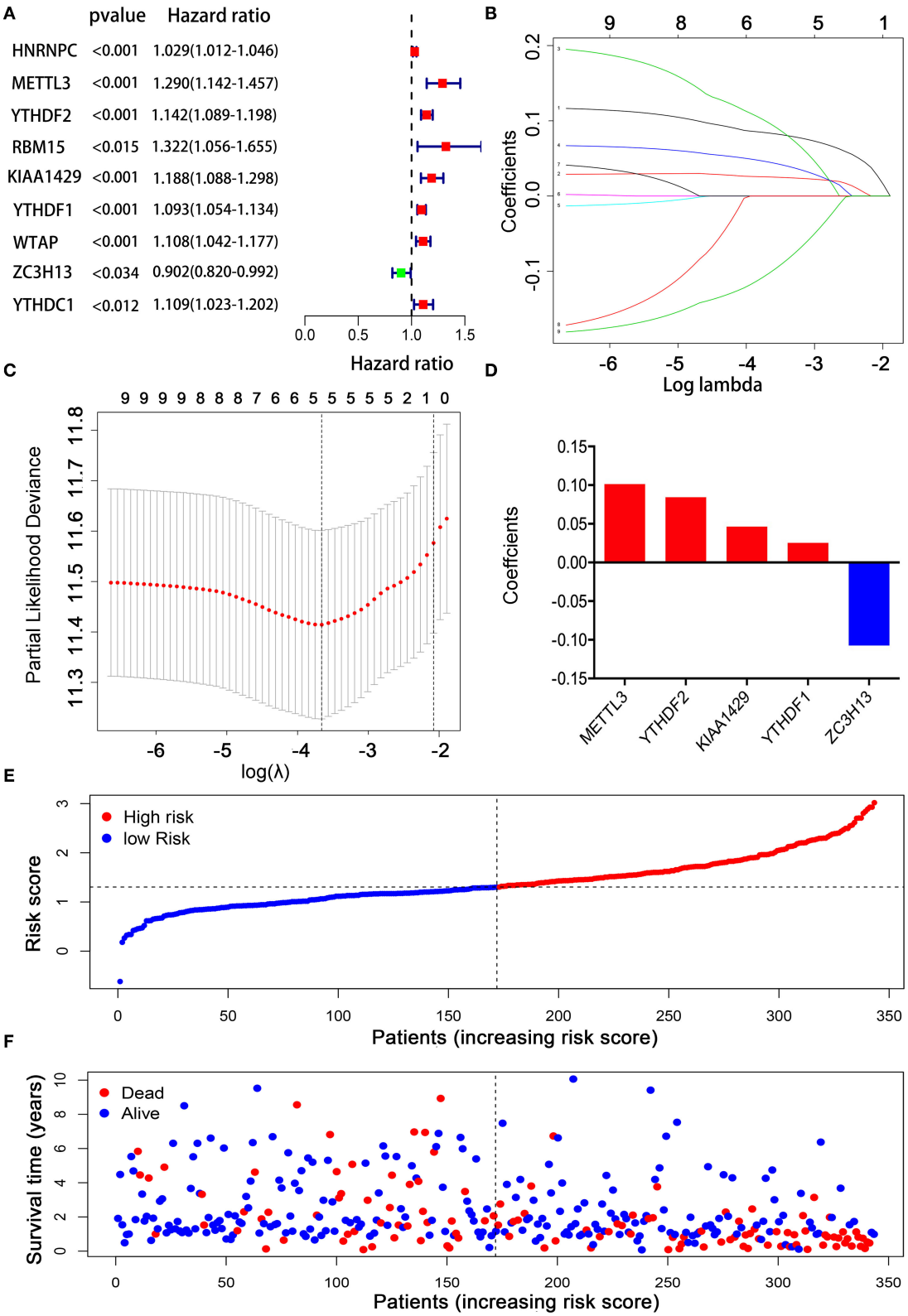

FIGURE 5 | Establishment of the prognostic risk model based on m6A RNA modification regulator genes. **(A)** Univariate Cox regression analysis of the m6A RNA methylation regulators. **(B–D)** The process of constructing the signature using absolute shrinkage and selection operator (LASSO) Cox regression. **(E)** The distributions of risk scores in the prognostic model. **(F)** The distributions of survival status in the prognostic model.

demonstrated a worse OS in patients with a high-risk score relative to patients with a low-risk score (**Figure 6A**, p = 1.118e−04). The 5-year OS rate was 43.4% in the high-risk group and 57.4% in the low-risk group. We then performed a ROC curve analysis and assessed the area under this curve (AUC) of 0.782, 0.723, and 0.617 for the 1-, 3-, and 5-year OS, respectively, which showed good predictive power for survival outcomes (**Figure 6B**). Moreover, the risk score distribution of patients with HCC was plotted, as shown in **Figure 5E**. A dot pot was used to display the survival status of each patient (**Figure 5F**). The expression of five prognostic genes in the high- and low-risk groups was displayed in a heatmap (**Figure 7A**). Clinical relevance was simultaneously plotted above the heatmap. When comparing the clinical parameters between the low- and high-risk groups, significant differences were observed in terms of stage ($p < 0.01$) and grade ($p < 0.001$).

Validation of the Prognostic Signature Using the GEO Database

To evaluate the prognostic value of the five-gene signature for survival prediction in other datasets, we used the GEO microarray data (GSE54236) for validation (22). A total of 78 HCC patients in the GSE54236 cohort were divided into high-risk (n = 42) and low-risk (n = 36) groups according to the cutoff value of the TCGA cohort. Same as the results in the TCGA cohort, the survival analysis demonstrated that HCC patients in the low-risk group had markedly better OS compared to high-risk patients (**Figure 6C**, p = 5.811e−4). The AUCs for 1-, 2-, and 3-year OS were 0.689, 0.705, and 0.696, respectively, indicating that this prognostic model could predict OS of HCC patients with a good accuracy (**Figure 6D**). Since there was no patient survival beyond 5 years, the 5-year ROC curve was not plotted.

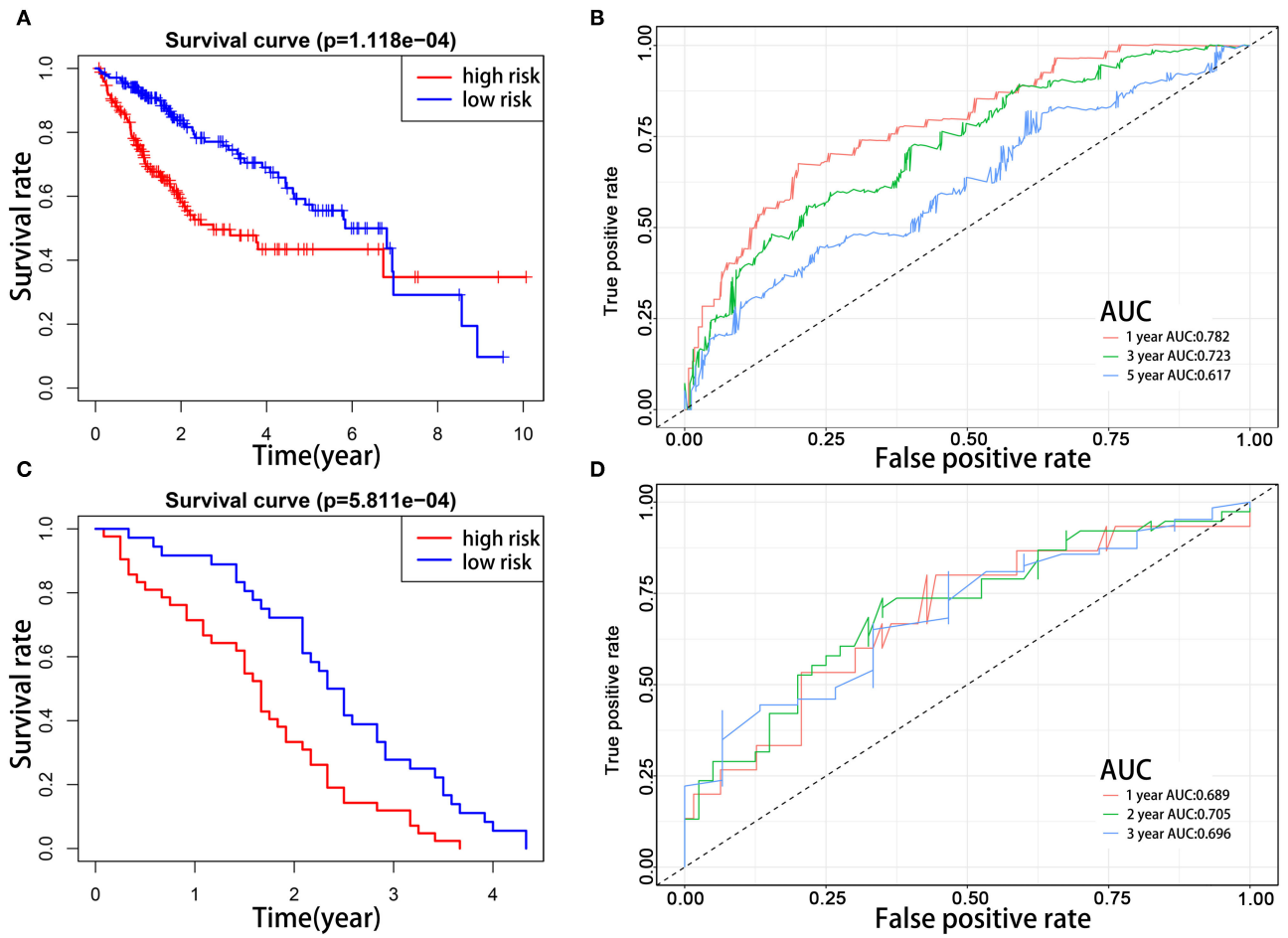

FIGURE 6 | Kaplan–Meier survival analyses of prognostic model. Patients in two datasets were assigned to low-risk (blue) and high-risk (red) groups using median risk score as the cutoff. **(A,B)** In the TCGA cohort, the survival probability of the low-risk group is higher than the high-risk group (p = 1.118e−4). The 1-, 3-, and 5-year AUCs were 0.782, 0.723, and 0.617, respectively. **(C,D)** The prognostic model was validated in the GEO cohort. The survival probabilities were higher for the low-risk group than the high-risk group (p = 5.811e−04). The 1-, 2-, and 3-year AUCs were 0.689, 0.705, and 0.696, respectively.

The Five-Gene Risk Signature Independently Predicts the Prognostic of HCC Patients

After excluding cases with incomplete clinical information, 339 cases were eligible for Cox regression analysis. Univariate analysis revealed that the five-gene risk score and stage were significantly related to the OS of patients with HCC (**Figure 7B**, $p < 0.001$). In order to evaluate whether the five-gene risk signature was independent from other clinicopathologic characteristics as a prognostic factor for HCC, we additionally conducted multivariate Cox regression analyses, which demonstrated that both risk score and stage were independently correlated with OS for patients with HCC (**Figure 7C**, $p < 0.001$). These results demonstrated that the five-gene risk signature was able to predict prognosis independently of gender, age, histological grade and pathological stage, indicating that this five-gene risk signature could serve as an independent prognostic factor for HCC.

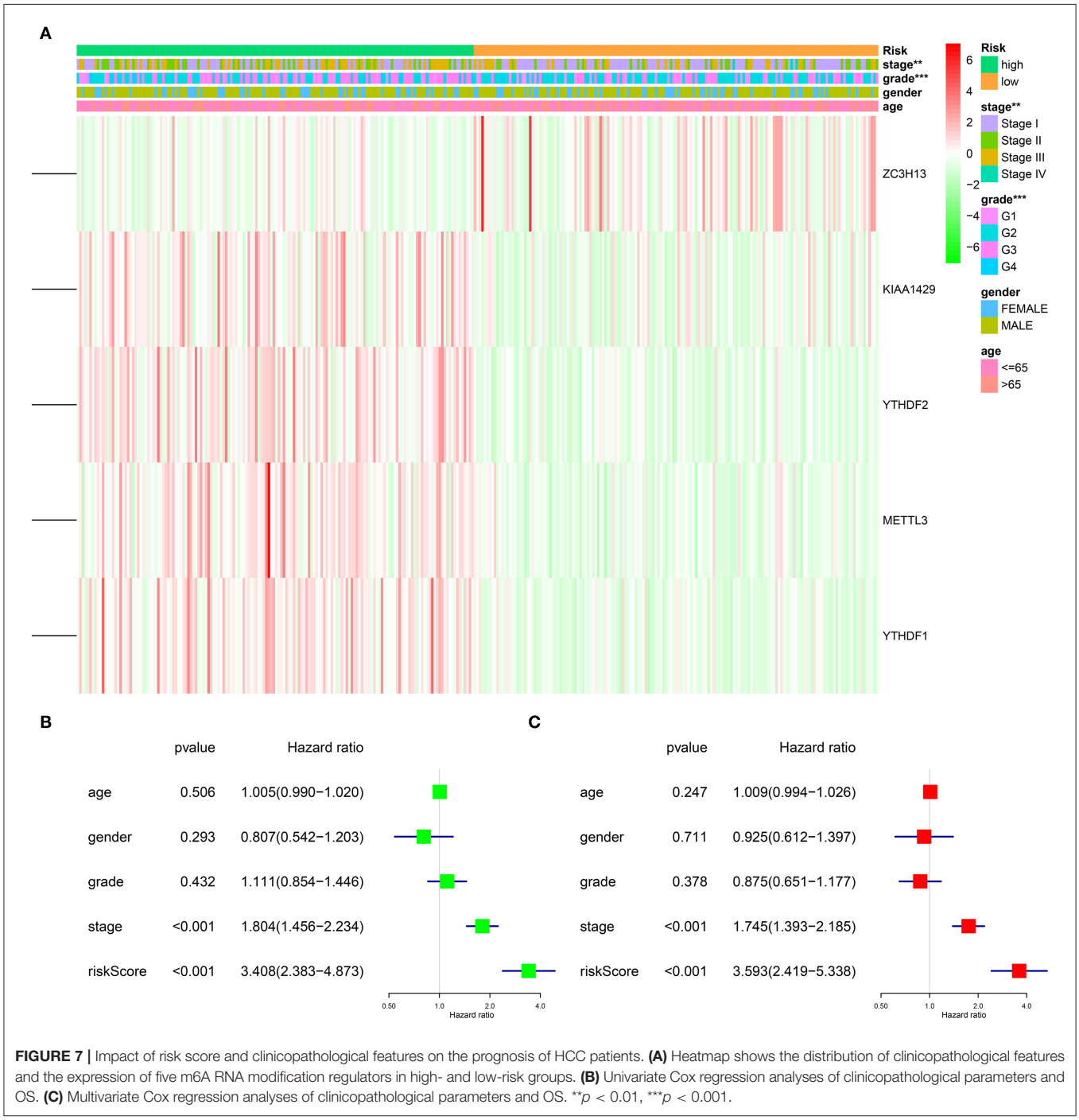

FIGURE 7 | Impact of risk score and clinicopathological features on the prognosis of HCC patients. **(A)** Heatmap shows the distribution of clinicopathological features and the expression of five m6A RNA modification regulators in high- and low-risk groups. **(B)** Univariate Cox regression analyses of clinicopathological parameters and OS. **(C)** Multivariate Cox regression analyses of clinicopathological parameters and OS. $^{**}p < 0.01$, $^{***}p < 0.001$.

Establishment of a Prognostic Nomogram for HCC

To provide a quantitative method to predict the survival of individuals, we established a novel prognostic nomogram on the basis of age, gender, histological grade, pathological stage, and risk score (**Figure 8**). The results showed that the nomogram could systematically predict the 1-, 3-, and 5-year OS of patients with HCC.

DISCUSSION

Globally, HCC is the most prevalent type of liver malignancy, which ranks as the fourth of cancer mortality (1). However, there is currently no effective therapy, and the OS of patients with HCC is still far from satisfactory. Therefore, it is urgent to elucidate the underlying molecular mechanisms contributing to tumorigenesis in HCC. RNA m6A modification, as a new dimension of gene expression control, has aroused strong interest among the academic community in recent years. However, the study of m6A modification in the cancer field is still in its initial stage. Due to the wide application of RNA-seq and microarray techniques, risk scoring systems based on multiple-gene signature are increasingly frequently applied to predict prognosis for human cancers (23–25). In the present study, we established a prognostic signature using five m6A RNA modification regulators. Encouragingly, the risk score was able to independently predict the prognosis of HCC patients. Therefore, the risk signature in this study can help clinicians perform individualized survival predictions more accurately.

As shown in our prognostic model, ZC3H13 was the only m6A-related gene positively associated with HCC patient prognosis, indicating that ZC3H13 might exert a suppressive effect on HCC. ZC3H13 encodes a CCCH-type zinc finger protein, which plays an important role in the modulation of RNA m6A modification in the nucleus (26, 27). To date, even though a few studies have reported the correlation between ZC3H13 and human tumors, its biological function still needs further investigation. According to published studies, ZC3H13 exhibited heterogeneous roles in various types of human cancer. For example, Zhu et al. found that ZC3H13 inhibits colorectal cancer (CRC) proliferation and invasion *via* inactivating Ras-ERK signaling pathway, suggesting that ZC3H13 acts as a tumor suppressor in CRC (28). Similarly, Kim et al. demonstrated that ZC3H13 is often mutated in CRC, suggesting that ZC3H13 might function as a tumor suppressor (26). On the contrary, Gewurz et al. revealed that ZC3H13 acts as a key upstream regulator of the NFκB activation pathway. Since hyperactivation of the NFκB promotes tumor proliferation and invasion, ZC3H13 might function as an oncogene (29). Therefore, the specific role of ZC3H13 in HCC remains elusive, which requires in-depth research.

Our prognostic model showed that the expression of the remaining four genes (YTHDF1, YTHDF2, METTL3, and KIAA1429) was adversely associated with the prognosis of patients with HCC. Chen et al. reported that METTL3 is significantly upregulated in HCC. Overexpression of METTL3

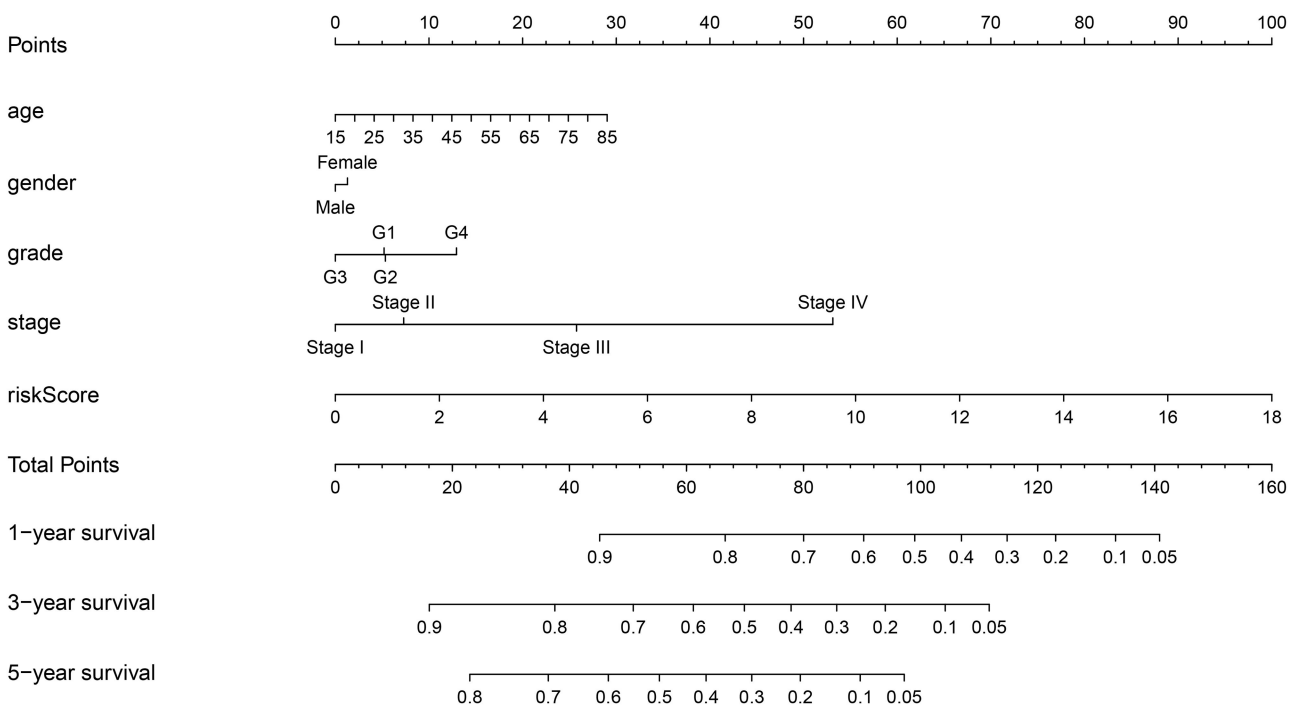

FIGURE 8 | Establishment of prognostic nomogram by combining clinicopathologic characteristics and risk score.

in HCC is linked to poor prognosis. In addition, knockdown of METTL3 impairs HCC oncogenicity and lung metastasis, indicating that METTL3 might act as an oncogene in HCC. Mechanistically, METTL3 promotes the progression of HCC through post-transcriptional silencing SOCS2 (a tumor suppressor gene) in a YTHDF2-dependent manner (15). Vice versa, Lin et al. revealed that the suppression of METTL3 attenuated EMT through downregulating the translation of Snail (16). In agreement with the oncogenic functions of METTL3 in HCC, similar observations have recently been reported in several other types of cancer, namely, AML (30), GMB (31), bladder cancer (32), gastric cancer (33), and breast cancer (34).

KIAA1429, a relatively new component of the m6A "writer" complex, has also been reported to be upregulated in HCC (35). Clinically, overexpression of KIAA1429 is linked to a worse prognosis for HCC patients. Mechanistically, KIAA1429 promotes HCC progression by inhibiting ID2 *via* upregulating its m6A level (35). Similarly, Lan et al. also showed that KIAA1429 is highly expressed in HCC and correlated with poor prognosis of HCC patients. Their study demonstrated that silencing KIAA1429 inhibited proliferation and metastasis of cancer cells (36). Mechanistically, KIAA1429 could induce m6A modification of GATA3 pre-mRNA, resulting in the degradation of GATA3 pre-mRNA, thus contributing to HCC progression. Interestingly, Qian et al. reported that KIAA1429 could exert oncogenic functions in breast cancer through positive regulating CDK1 in an m6A-independent manner (37). These studies suggest that KIAA1429 is an oncogenic protein that functions through multiple signaling pathways.

YTHDF1 and YTHDF2 are both members of the YTH domain family, which also includes YTHDF3, YTHDC1, and YTHDC2. YTHDF1 is an m6A "reader," which recognizes and binds to m^6A-modified mRNA, thus improving the translation efficiency of their target RNAs (38). In a recent study, YTHDF1 was reported to be upregulated in HCC, and its overexpression is highly related to unfavorable prognosis (39), which is consistent with the observations of Zhao et al. (40). Additionally, it has been reported that YTHDF1 is highly expressed in CRC and serves as an oncogene in CRC *via* promoting CRC cell oncogenesis and stem cell-like activity through the Wnt/β-catenin pathway (41, 42).

According to current research, the major function of YTHDF2 is to regulate mRNA degradation (43). Yang et al. found that YTHDF2 is upregulated in HCC, and miR145 is a negative posttranscriptional regulator of YTHDF2. Also, miR145 downregulates the expression of YTHDF2 through elevating m6A levels *via* binding to the 3′ UTR of YTHDF2 mRNA (14). On the contrary, Hou et al. revealed that YTHDF2 was downregulated in HCC. YTHDF2 deficiency robustly facilitated HCC growth and metastasis, suggesting that YTHDF2 is a tumor suppressor in HCC. Mechanistically, Hou et al. showed that YTHDF2 inhibited cancer progression by promoting the decay of IL11 and SERPINE2 mRNAs (44). Therefore, the specific role of YTHDF2 in HCC remains controversial. These contradictory findings may be due to the high heterogeneity of HCC. Further studies are required to address these conflicting observations.

Some studies have reported that deregulation of m6A regulators is associated with the drug resistance in tumors. Therefore, it is critical to know the expression of m6A regulators in cancer patients in order to choose individualized chemotherapeutic regimens. METTL3 is known to promote the resistance of pancreatic cancer cells against chemotherapy and radiotherapy. Knockdown of METTL3 can significantly increase the sensitivity of pancreatic cancer cells to 5-fluorouracil (5-FU), cisplatin, gemcitabine, and radiotherapy (45). Similarly, METTL3 is overexpressed in gliomas and is involved in the maintenance of its radio-resistance (31). In colorectal cancer, knockout of YTHDF1 can suppress the proliferation of cancer cells and enhance their sensitivity to chemotherapy drugs such as 5-FU and oxaliplatin (42). FTO is highly expressed in cervical squamous cell carcinoma (CSCC) tissues. By activating β-catenin and excision repair pathways, FTO enhances the chemo-radiotherapy resistance of CSCC (46). In tyrosine kinase inhibitor (TKI)-resistant leukemia cells, decreased m6A levels by FTO upregulation results in the overexpression of survival and proliferation-related genes. Vice versa, knockdown of FTO rendered resistant leukemia cells remarkably sensitive to TKI treatments (47). These studies highlight the significance of m6A in chemo-radiotherapy resistance and suggest its potential value as a treatment target. At present, there are no studies investigating the role of m6A in drug resistance in HCC. Nevertheless, given that METTL3 and YTHDF1 are significantly associated with prognosis of HCC patients, elucidating the mechanisms of m6A in HCC chemoresistance is of great importance for the treatment of drug resistance in HCC.

Previous studies have shown that m6A plays an important role in tumor initiation, progression, metastasis, and other malignant biological behaviors. Therefore, the development of specific inhibitors of m6A regulators has great scientific significance and clinical value. Rhein is the first FTO inhibitor that exerts its inhibitory effect by competitive binding to the FTO active site (48). However, rhein has the problem of low specificity due to its cross-activity with ALKB family demethylases (49). Meclofenamic acid (MA) is a highly selective FTO inhibitor that can bind to FTO and stabilize FTO without affecting the demethylase activity of ALKBH5 (50). In addition to natural products, Huang et al. developed two FTO inhibitors, namely, FB23 and FB23-2, by structure-based rational design. *In vitro* and *in vivo* experimental evidence demonstrated that FB23-2 exhibits a potent ability to suppress the progression of AML (51). More recently, based on structure-based virtual screening and a series of *in vivo* and *in vitro* experiments, Peng et al. discovered that entacapone, which was previously approved for the treatment of Parkinson's disease by the Food and Drug Administration (FDA), can be used as a specific inhibitor of FTO. Entacapone inhibits FTO activity through competitive binding with m6A-modified RNA substrates. After treatment with entacapone, the diet-induced obese mice showed a significant decrease in body weight and blood glucose levels (52). Science entacapone is already an FDA-approved drug, and it could be readily generalizable to other clinical indications that are related to FTO, such as cancer and obesity. For the time being, other than

FTO, there are no known inhibitors for m6A regulatory. More effective and specific inhibitors for targeting m6A regulatory are urgently needed. The development of such inhibitors will not only deepen the understanding about the mechanism of m6A in carcinogenesis but also provide more tools for designing novel therapies.

Nevertheless, we acknowledge that several limitations in this study deserve mention. First, since our data are drawn from the TCGA and GEO databases, further experimental evidence is needed to verify our findings. Second, the sample size varied significantly between the normal and tumor groups, which may affect the reliability of the results. Finally, as the main patients are Americans and Italians, selection bias inevitably occurred. As a result, the findings in our study might not be generalizable to all populations.

In summary, we demonstrated that the gene expression signature of m6A modification regulators possesses great potential for HCC prognosis prediction. Our study offers additional evidence for further research regarding m6A RNA modification in HCC. However, further experimental and clinical exploration are necessary to confirm these findings.

DATA AVAILABILITY STATEMENT

All datasets presented in this study are included in the article/supplementary material.

AUTHOR CONTRIBUTIONS

SL, SZ, and LZha designed the study. LZha and YQ collected the data. JH, LZho, and DW performed the bioinformatics analysis. LZha and YQ wrote the manuscript. SL and SZ were responsible for the supervision of the work. All authors contributed to the article and approved the submitted version.

FUNDING

Funding was provided by the Innovative Research Groups of the National Natural Science Foundation of China (No. 81721091), the National S&T Major Project (No. 2017ZX10203205), the Zhejiang International Science and Technology Cooperation Project (No. 2016C04003), the Research Unit Project of the Chinese Academy of Medical Sciences (2019-I2M-5-030), and the Major Program of the National Natural Science Foundation of China (No. 91542205).

REFERENCES

1. Bray F, Ferlay J, Soerjomataram I, Siegel RL, Torre LA, Jemal A. Global cancer statistics 2018: GLOBOCAN estimates of incidence and mortality worldwide for 36 cancers in 185 countries. *CA Cancer J Clin*. (2018) 68:394–424. doi: 10.3322/caac.21492
2. El-Serag HB, Rudolph KL. Hepatocellular carcinoma: epidemiology and molecular carcinogenesis. *Gastroenterology*. (2007) 132:2557–76. doi: 10.1053/j.gastro.2007.04.061
3. Frenette C, Gish RG. Hepatocellular carcinoma: molecular and genomic guideline for the clinician. *Clin Liver Dis*. (2011) 15:307–21, vii-x. doi: 10.1016/j.cld.2011.03.010
4. Roessler S, Jia HL, Budhu A, Forgues M, Ye QH, Lee JS, et al. A unique metastasis gene signature enables prediction of tumor relapse in early-stage hepatocellular carcinoma patients. *Cancer Res*. (2010) 70:10202–12. doi: 10.1158/0008-5472.CAN-10-2607
5. Krug RM, Morgan MA, Shatkin AJ. Influenza viral mRNA contains internal N6-methyladenosine and 5'-terminal 7-methylguanosine in cap structures. *J Virol*. (1976) 20:45–53. doi: 10.1128/JVI.20.1.45-53.1976
6. Horowitz S, Horowitz A, Nilsen TW, Munns TW, Rottman FM. Mapping of N6-methyladenosine residues in bovine prolactin mRNA. *Proc Natl Acad Sci USA*. (1984) 81:5667–71. doi: 10.1073/pnas.81.18.5667
7. Yang Y, Hsu PJ, Chen YS, Yang YG. Dynamic transcriptomic m(6)A decoration: writers, erasers, readers and functions in RNA metabolism. *Cell Res*. (2018) 28:616–24. doi: 10.1038/s41422-018-0040-8
8. Tuncel G, Kalkan R. Importance of m N(6)-methyladenosine. (m(6)A) RNA modification in cancer. *Med Oncol*. (2019) 36:36. doi: 10.1007/s12032-019-1260-6
9. Jia G, Fu Y, Zhao X, Dai Q, Zheng G, Yang Y, et al. N6-methyladenosine in nuclear RNA is a major substrate of the obesity-associated FTO. *Nat Chem Biol*. (2011) 7:885–7. doi: 10.1038/nchembio.687
10. Zheng G, Dahl JA, Niu Y, Fedorcsak P, Huang CM, Li CJ, et al. ALKBH5 is a mammalian RNA demethylase that impacts RNA metabolism and mouse fertility. *Mol Cell*. (2013) 49:18–29. doi: 10.1016/j.molcel.2012.10.015
11. Zhang C, Fu J, Zhou Y. A review in research progress concerning m6A methylation and immunoregulation. *Front Immunol*. (2019) 10:922. doi: 10.3389/fimmu.2019.00922
12. Sun T, Wu R, Ming L. The role of m6A RNA methylation in cancer. *Biomed Pharmacother*. (2019) 112:108613. doi: 10.1016/j.biopha.2019.108613
13. Ma JZ, Yang F, Zhou CC, Liu F, Yuan JH, Wang F, et al. METTL14 suppresses the metastatic potential of hepatocellular carcinoma by modulating N(6) -methyladenosine-dependent primary MicroRNA processing. *Hepatology*. (2017) 65:529–43. doi: 10.1002/hep.28885
14. Yang Z, Li J, Feng G, Gao S, Wang Y, Zhang S, et al. MicroRNA-145 modulates N(6)-methyladenosine levels by targeting the 3'-untranslated mRNA region of the N(6)-methyladenosine binding YTH domain family 2 protein. *J Biol Chem*. (2017) 292:3614–23. doi: 10.1074/jbc.M116.749689
15. Chen M, Wei L, Law CT, Tsang FH, Shen J, Cheng CL, et al. RNA N6-methyladenosine methyltransferase-like 3 promotes liver cancer progression through YTHDF2-dependent posttranscriptional silencing of SOCS2. *Hepatology*. (2018) 67:2254–70. doi: 10.1002/hep.29683
16. Lin X, Chai G, Wu Y, Li J, Chen F, Liu J, et al. RNA m(6)A methylation regulates the epithelial mesenchymal transition of cancer cells and translation of Snail. *Nat Commun*. (2019) 10:2065. doi: 10.1038/s41467-019-09865-9
17. Zhang C, Samanta D, Lu H, Bullen JW, Zhang H, Chen I, et al. Hypoxia induces the breast cancer stem cell phenotype by HIF-dependent and ALKBH5-mediated m(6)A-demethylation of NANOG mRNA. *Proc Natl Acad Sci USA*. (2016) 113:E2047–56. doi: 10.1073/pnas.1602883113
18. Panneerdoss S, Eedunuri VK, Yadav P, Timilsina S, Rajamanickam S, Viswanadhapalli S, et al. Cross-talk among writers, readers, and erasers of m(6)A regulates cancer growth and progression. *Sci Adv*. (2018) 4:eaar8263. doi: 10.1126/sciadv.aar8263
19. Chen M, Wong CM. The emerging roles of N6-methyladenosine (m6A) deregulation in liver carcinogenesis. *Mol Cancer*. (2020) 19:44. doi: 10.1186/s12943-020-01172-y
20. Sheng H, Li Z, Su S, Sun W, Zhang X, Li L, et al. YTH domain family 2 promotes lung cancer cell growth by facilitating 6-phosphogluconate dehydrogenase mRNA translation. *Carcinogenesis*. (2020) 41:541–50. doi: 10.1093/carcin/bgz152
21. Wang X, Wu R, Liu Y, Zhao Y, Bi Z, Yao Y, et al. m(6)A mRNA methylation controls autophagy and adipogenesis by targeting Atg5 and Atg7. *Autophagy*. (2020) 16:1221–35. doi: 10.1080/15548627.2019.1659617
22. Villa E, Critelli R, Lei B, Marzocchi G, Camma C, Giannelli G, et al. Neoangiogenesis-related genes are hallmarks of fast-growing hepatocellular

carcinomas and worst survival. Results from a prospective study. *Gut*. (2016) 65:861–9. doi: 10.1136/gutjnl-2014-308483
23. Chen HY, Yu SL, Chen CH, Chang GC, Chen CY, Yuan A, et al. A five-gene signature and clinical outcome in non-small-cell lung cancer. *N Engl J Med*. (2007) 356:11–20. doi: 10.1056/NEJMoa060096
24. Zhang JX, Song W, Chen ZH, Wei JH, Liao YJ, Lei J, et al. Prognostic and predictive value of a microRNA signature in stage II colon cancer: a microRNA expression analysis. *Lancet Oncol*. (2013) 14:1295–306. doi: 10.1016/S1470-2045(13)70491-1
25. Wang Y, Zhang Q, Gao Z, Xin S, Zhao Y, Zhang K, et al. A novel 4-gene signature for overall survival prediction in lung adenocarcinoma patients with lymph node metastasis. *Cancer Cell Int*. (2019) 19:100. doi: 10.1186/s12935-019-0822-1
26. Kim YR, Chung NG, Kang MR, Yoo NJ, Lee SH. Novel somatic frameshift mutations of genes related to cell cycle and DNA damage response in gastric and colorectal cancers with microsatellite instability. *Tumori*. (2010) 96:1004–9.
27. Wen J, Lv R, Ma H, Shen H, He C, Wang J, et al. Zc3h13 regulates nuclear RNA m(6)A methylation and mouse embryonic stem cell self-renewal. *Mol Cell*. (2018) 69:1028–38 e1026. doi: 10.1016/j.molcel.2018.02.015
28. Zhu D, Zhou J, Zhao J, Jiang G, Zhang X, Zhang Y, et al. ZC3H13 suppresses colorectal cancer proliferation and invasion *via* inactivating Ras-ERK signaling. *J Cell Physiol*. (2019) 234:8899–907. doi: 10.1002/jcp.27551
29. Gewurz BE, Towfic F, Mar JC, Shinners NP, Takasaki K, Zhao B, et al. Genome-wide siRNA screen for mediators of NF-kappaB activation. *Proc Natl Acad Sci USA*. (2012) 109:2467–72. doi: 10.1073/pnas.1120542109
30. Vu LP, Pickering BF, Cheng Y, Zaccara S, Nguyen D, Minuesa G, et al. The N(6)-methyladenosine (m(6)A)-forming enzyme METTL3 controls myeloid differentiation of normal hematopoietic and leukemia cells. *Nat Med*. (2017) 23:1369–76. doi: 10.1038/nm.4416
31. Visvanathan A, Patil V, Arora A, Hegde AS, Arivazhagan A, Santosh V, et al. Essential role of METTL3-mediated m(6)A modification in glioma stem-like cells maintenance and radioresistance. *Oncogene*. (2018) 37:522–33. doi: 10.1038/onc.2017.351
32. Cheng M, Sheng L, Gao Q, Xiong Q, Zhang H, Wu M, et al. The m(6)A methyltransferase METTL3 promotes bladder cancer progression *via* AFF4/NF-kappaB/MYC signaling network. *Oncogene*. (2019) 38:3667–80. doi: 10.1038/s41388-019-0683-z
33. Liu T, Yang S, Sui J, Xu SY, Cheng YP, Shen B, et al. Dysregulated N6-methyladenosine methylation writer METTL3 contributes to the proliferation and migration of gastric cancer. *J Cell Physiol*. (2020) 235:548–62. doi: 10.1002/jcp.28994
34. Cai X, Wang X, Cao C, Gao Y, Zhang S, Yang Z, et al. HBXIP-elevated methyltransferase METTL3 promotes the progression of breast cancer *via* inhibiting tumor suppressor let-7g. *Cancer Lett*. (2018) 415:11–9. doi: 10.1016/j.canlet.2017.11.018
35. Cheng X, Li M, Rao X, Zhang W, Li X, Wang L, et al. KIAA1429 regulates the migration and invasion of hepatocellular carcinoma by altering m6A modification of ID2 mRNA. *Onco Targets Ther*. (2019) 12:3421–8. doi: 10.2147/OTT.S180954
36. Lan T, Li H, Zhang D, Xu L, Liu H, Hao X, et al. KIAA1429 contributes to liver cancer progression through N6-methyladenosine-dependent post-transcriptional modification of GATA3. *Mol Cancer*. (2019) 18:186. doi: 10.1186/s12943-019-1106-z
37. Qian JY, Gao J, Sun X, Cao MD, Shi L, Xia TS, et al. KIAA1429 acts as an oncogenic factor in breast cancer by regulating CDK1 in an N6-methyladenosine-independent manner. *Oncogene*. (2019) 38:6123–41. doi: 10.1038/s41388-019-0861-z
38. Wang X, Zhao BS, Roundtree IA, Lu Z, Han D, Ma H, et al. N(6)-methyladenosine Modulates Messenger RNA Translation Efficiency. *Cell*. (2015) 161:1388–99. doi: 10.1016/j.cell.2015.05.014
39. Zhou Y, Yin Z, Hou B, Yu M, Chen R, Jin H, et al. Expression profiles and prognostic significance of RNA N6-methyladenosine-related genes in patients with hepatocellular carcinoma: evidence from independent datasets. *Cancer Manag Res*. (2019) 11:3921–31. doi: 10.2147/CMAR.S191565
40. Zhao X, Chen Y, Mao Q, Jiang X, Jiang W, Chen J, et al. Overexpression of YTHDF1 is associated with poor prognosis in patients with hepatocellular carcinoma. *Cancer Biomark*. (2018) 21:859–68. doi: 10.3233/CBM-170791
41. Bai Y, Yang C, Wu R, Huang L, Song S, Li W, et al. YTHDF1 regulates tumorigenicity and cancer stem cell-like activity in human colorectal carcinoma. *Front Oncol*. (2019) 9:332. doi: 10.3389/fonc.2019.00332
42. Nishizawa Y, Konno M, Asai A, Koseki J, Kawamoto K, Miyoshi N, et al. Oncogene c-Myc promotes epitranscriptome m(6)A reader YTHDF1 expression in colorectal cancer. *Oncotarget*. (2018) 9:7476–86. doi: 10.18632/oncotarget.23554
43. Du H, Zhao Y, He J, Zhang Y, Xi H, Liu M, et al. YTHDF2 destabilizes m(6)A-containing RNA through direct recruitment of the CCR4-NOT deadenylase complex. *Nat Commun*. (2016) 7:12626. doi: 10.1038/ncomms12626
44. Hou J, Zhang H, Liu J, Zhao Z, Wang J, Lu Z, et al. YTHDF2 reduction fuels inflammation and vascular abnormalization in hepatocellular carcinoma. *Mol Cancer*. (2019) 18:163. doi: 10.1186/s12943-019-1082-3
45. Taketo K, Konno M, Asai A, Koseki J, Toratani M, Satoh T, et al. The epitranscriptome m6A writer METTL3 promotes chemo- and radioresistance in pancreatic cancer cells. *Int J Oncol*. (2018) 52:621–9. doi: 10.3892/ijo.2017.4219
46. Zhou S, Bai ZL, Xia D, Zhao ZJ, Zhao R, Wang YY, et al. FTO regulates the chemo-radiotherapy resistance of cervical squamous cell carcinoma (CSCC) by targeting beta-catenin through mRNA demethylation. *Mol Carcinog*. (2018) 57:590–7. doi: 10.1002/mc.22782
47. Yan F, Al-Kali A, Zhang Z, Liu J, Pang J, Zhao N, et al. A dynamic N(6)-methyladenosine methylome regulates intrinsic and acquired resistance to tyrosine kinase inhibitors. *Cell Res*. (2018) 28:1062–76. doi: 10.1038/s41422-018-0097-4
48. Chen B, Ye F, Yu L, Jia G, Huang X, Zhang X, et al. Development of cell-active N6-methyladenosine RNA demethylase FTO inhibitor. *J Am Chem Soc*. (2012) 134:17963–71. doi: 10.1021/ja3064149
49. Li Q, Huang Y, Liu X, Gan J, Chen H, Yang CG. Rhein inhibits AlkB repair enzymes and sensitizes cells to methylated DNA damage. *J Biol Chem*. (2016) 291:11083–93. doi: 10.1074/jbc.M115.711895
50. Huang Y, Yan J, Li Q, Li J, Gong S, Zhou H, et al. Meclofenamic acid selectively inhibits FTO demethylation of m6A over ALKBH5. *Nucleic Acids Res*. (2015) 43:373–84. doi: 10.1093/nar/gku1276
51. Huang Y, Su R, Sheng Y, Dong L, Dong Z, Xu H, et al. Small-molecule targeting of oncogenic FTO demethylase in acute myeloid leukemia. *Cancer Cell*. (2019) 35:677–91 e610. doi: 10.1016/j.ccell.2019.03.006
52. Peng S, Xiao W, Ju D, Sun B, Hou N, Liu Q, et al. Identification of entacapone as a chemical inhibitor of FTO mediating metabolic regulation through FOXO1. *Sci Transl Med*. (2019) 11:eaau7116. doi: 10.1126/scitranslmed.aau7116

Conflict of Interest: The authors declare that the research was conducted in the absence of any commercial or financial relationships that could be construed as a potential conflict of interest.

Copyright © 2020 Zhang, Qiao, Huang, Wan, Zhou, Lin and Zheng. This is an open-access article distributed under the terms of the Creative Commons Attribution License (CC BY). The use, distribution or reproduction in other forums is permitted, provided the original author(s) and the copyright owner(s) are credited and that the original publication in this journal is cited, in accordance with accepted academic practice. No use, distribution or reproduction is permitted which does not comply with these terms.

frontiers in Medicine

ORIGINAL RESEARCH
published: 06 October 2020
doi: 10.3389/fmed.2020.582923

A Novel miRNA Restores the Chemosensitivity of AML Cells Through Targeting FosB

Huiwen Wang[1†], *Huien Zhan*[2†], *Xinya Jiang*[1], *Lilian Jin*[2], *Tianming Zhao*[2], *Shurong Xie*[2], *Wei Liu*[1], *Yan Jia*[1], *Hui Liang*[1] *and Hui Zeng*[2*]

[1] Department of Hematology, Xiangya Hospital, Central South University, Changsha, China, [2] Department of Hematology, The First Affiliated Hospital of Jinan University, Guangzhou, China

The heterogeneous nature of acute myeloid leukemia (AML) and its poor prognosis necessitate therapeutic improvement. Current advances in AML research yield important insights regarding both AML genetics and epigenetics. MicroRNAs (miRNAs) play important roles in cell proliferation, differentiation, and survival and may be useful for AML diagnosis and prognosis. In this study, a novel miRNA, hsa-miR-12462, was identified in bone marrow (BM) samples from AML patients at diagnosis by small RNA sequencing. A significant higher level of hsa-miR-12462 was found in patients who achieve complete remission (AML-CR) after induction therapy compared with those who suffer relapse/refractory (AML-RR). FosB was predicted to be the target of hsa-miR-12462 through RNA sequencing, bioinformatics analysis, and protein–protein interaction (PPI) network analysis and then verified by luciferase activity assay. T-5224, the inhibitor of FosB, was administered to AML cell lines, which could inhibit cell proliferation, promote apoptosis, and restore the sensitivity of AML cells to cytarabine (Ara-C). In summary, a higher level of hsa-miR-12462 in AML cells is associated with increased sensitivity to Ara-C *via* targeting FosB.

Keywords: acute myeloid leukemia, FosB, chemosensitivity, miRNA, targeting therapy

OPEN ACCESS

Edited by:
Fu Wang,
Xidian University, China

Reviewed by:
Wenjuan Yu,
Zhejiang University, China
Zhipeng Meng,
University of Miami, United States

***Correspondence:**
Hui Zeng
androps2011@hotmail.com

[†]These authors have contributed equally to this work

Specialty section:
This article was submitted to Precision Medicine, a section of the journal Frontiers in Medicine

Received: *13 July 2020*
Accepted: *26 August 2020*
Published: *06 October 2020*

Citation:
Wang H, Zhan H, Jiang X, Jin L, Zhao T, Xie S, Liu W, Jia Y, Liang H and Zeng H (2020) A Novel miRNA Restores the Chemosensitivity of AML Cells Through Targeting FosB. Front. Med. 7:582923. doi: 10.3389/fmed.2020.582923

INTRODUCTION

Acute myeloid leukemia (AML) is a highly heterogeneous hematologic malignancy characterized by unlimited clonal proliferation of myeloid blasts. In the United States, almost 20,000 new patients suffer from AML and up to 11,000 patients die from the disease per year (1). The standard treatment is induction therapy followed by consolidation in the manner of chemotherapy or hematopoietic stem cell transplantation (HSCT), aiming to eradicate the residual disease (2). Since the 1970s, the mainstay of induction therapy consisting of cytarabine (Ara-C) with anthracycline has been established and rendered relatively favorable complete remission (CR) rates. However, high recurrence rate and drug resistance remain a Gordian knot to further improve the patients' survival. Therefore, exploring elaborate mechanisms and exploiting novel agents are consistently emphasized. From 2017 to 2018, at least eight new drugs have been approved by Food and Drug Administration (FDA) for the treatment of AML. The dramatic emergence in epigenetic knowledge is somewhat responsible for part of these advances. For example, hypomethylating agents (decitabine and azacitidine) have been widely applied for elderly patients, and a novel histone deacetylase inhibitor chidamide has also been approved by China SFDA in the near past. Thus, focusing on epigenetic alternations might be promising in targeting therapy of AML.

MicroRNAs (miRNAs) are a class of endogenous small non-coding RNAs, each with a single strand of 22 nucleotides approximately (3). By binding to partially complementary sites of the 3′-untranslated regions (3′-UTRs) of specific target mRNA, miRNAs regulate the gene expression at the posttranscriptional level *via* degrading mRNA or inhibiting their translation (4). The aberrant expression of miRNAs was proved to be closely related to the occurrence and development of tumor, including proliferation, differentiation, and apoptosis (5), which enabled clinicians to predict the disease status and prognosis (6).

The activator protein (AP-1) is a ubiquitously expressed dimeric transcription factor complex comprising proteins belonging to the Jun, Fos, activating transcription factor (ATF), or MAF BZIP transcription factor (MAF) protein families (7). As a pivotal role, AP-1 modulates the transcription of multiple cytokines and growth factors and is implicated in the proliferation, survival, differentiation, and transformation of cells (8). Regarding hematologic malignancies, abnormalities of AP-1 components exist in AML (9), chronic myelogenous leukemia (CML) (10), Hodgkin's disease (HD) (11), as well as anaplastic large cell lymphoma (ALCL) (12). Staber et al. (9) claimed that the expression of c-Jun and c-Fos in the transcriptional level was enhanced in relapsed AML over untreated patients, indicating that the AP-1 family is associated with poor prognosis, while the mechanism of other AP-1 components, such as FosB, has not been investigated in AML. In pancreatic cancer, miR-144-3p plays an important role in migration and invasion by targeting FosB (13). Thus, it is intriguing whether the interaction between miRNA and FosB participates in regulating the phenotypes of AML.

In our research, a novel miRNA, hsa-miR-12462, was determined by small RNA sequencing and stood out from the rest in the AML-CR group. Our latest study has verified that overexpression of hsa-miR-12462 inhibits the growth of AML cells and enhances Ara-C sensitivity (14). Next, we aimed to explore the potential target of hsa-miR-12462 and its contribution in maintaining indefinite proliferation and intractable drug sensitivity as to AML cell lines.

MATERIALS AND METHODS

Patient Enrollment

A total of 128 bone marrow (BM) specimens from AML patients aged 15–71 years old were collected at the outpatient and inpatient departments from January 2016 to November 2019. All specimens were collected before chemotherapy and grouped into cohort groups based on curative effect: (1) those achieving a CR with conventional induction chemotherapy and remaining in CR $\geq$6 months (AML-CR cohort); and (2) those not achieving CR after two courses of standard induction chemotherapy (refractory) or relapsed in <6 months after CR (relapsed) (AML-RR cohort). All specimens were collected after chemotherapy and divided into two cohorts based on curative effect, referring to the AML-RR cohort and the AML-CR cohort. The group criteria are consistent with the above. All BM samples were collected into sterile tubes containing anticoagulant (heparin sodium). Mononuclear cells (MNCs) were enriched by density centrifugation with Ficoll-Paque (Sigma, St. Louis, MO, USA) and stored at −80°C. The study protocols were approved by the Medical Institutional Ethics Committee of the Xiangya Hospital of Central South University. Written informed consent was obtained from all participants. Diagnosis of AML was carried out according to the 2016 WHO criteria.

Cell Culture and Lentivirus Transfection

Three human AML cell lines and two normal tissue cell strains were used in this study. All cell lines were obtained from the Cell Resource Center (Xiangya Medical College, Central South University, Hunan, China). U937, THP-1, and HL-60 cell lines were cultured in RPMI-1640 medium (Hyclone, USA) supplemented with 10% fetal bovine serum (Solarbio, Beijing, China) and 1% antibiotic solution of penicillin and streptomycin (Hyclone, USA). 293T and human umbilical vein endothelial cells (HUV-EC-C) cell lines were cultured in Dulbecco's modified Eagle's medium with high glucose (DMEM) (General Electric, USA) containing 10% fetal bovine serum (Solarbio, Beijing, China). Cells were incubated in a humidified atmosphere containing 5% CO_2 at 37°C. To overexpress hsa-miR-12462, U937, THP-1, and HL-60 were infected with lentivirus (lentivirus vector: pGC-FU-3FLAG-SV40-EGFP-IRES-puromycin; promoter: Ubiqutin) containing the open reading frame of hsa-miR-12462 [multiplicity of infection (MOI): [30]]. After 12 h of infection, we replaced the media for the cell lines and continued to culture for another 72 h. Then, the transfection efficiency was observed under a fluorescence microscope.

Dual Luciferase Reporter Assay

293T cells were inoculated at a density of 50% into a 96-well plate and transfected with luciferase reporter plasmids after 16 h when reaching a confluency of 70%. Each sample set was placed in three multiple wells. First, four groups were designed: blank group (transfection reagent + cells), plasmid group, plasmid + hsa-miR-12462 NC group, and plasmid + hsa-miR-12462 mimic group. After co-transfection for 18–48 h, Firefly luciferase and Renilla luciferase activity were detected by the dual luciferase reporting analysis system. Each sample had two values: RLU1-Firefly luciferase reaction intensity and RLU2-inner Renilla luciferase reaction intensity, and the ratio of the two groups was calculated, namely, RLU1/RLU2.

Quantitative RT-PCR for microRNA and mRNA Expression

Total RNA (500 ng) was isolated from 1×10^6 cells using Trizol reagent (Promega, USA). For hsa-miR-12462, Bulge-LoopTM miRNA RT primer was obtained from RiboBio Corporation (Guangzhou, China). miDETECT A Track miRNA qRT-PCR Starter Kit (RiboBio, China) was applied according to the manufacturer's instructions. For FosB, All-in-One First-Strand cDNA Synthesis Kit (GeneCopoeia, Rockville, USA) was applied to synthesize cDNA, and qPCR assay was carried out using Hieff qPCR SYBR® Green Master Mix kit (Yeasen Biotech, Shanghai, China) with an Applied Biosystems Prism machine using ABI StepOnePlus (Applied Biosystems, Foster City, CA,

USA). The primers of FosB were designed by GeneCopoeia Inc., China. The relative expression level of hsa-miR-12462 and FosB was normalized to U6 and glyceraldehyde 3-phosphate dehydrogenase (GAPDH), respectively, and calculated using the 2-ΔΔCT method.

Western Blotting

Equal amounts of protein were separated by 10% sodium dodecyl sulfate–polyacrylamide gel electrophoresis (SDS-PAGE) and then transferred electrophoretically to polyvinylidene fluoride (PVDF) membranes (Millipore, Billerica, MA, USA). The membranes were incubated with TBST containing 5% bovine serum albumin (BSA) (Bio Sharp Sigma A-4612) for an hour at room temperature and then with primary antibodies overnight at 4°C. After incubation with secondary antibodies, the protein bands were detected with a ChemiDoc TMMP imaging system (Bio-Rad Laboratories. Inc., Hercules, CA, USA).

Cytotoxicity Assay

To evaluate the cell response to different drugs, cell proliferation was determined by the Cell Counting Kit-8 (7sea biotech, China) assay after treatment. In brief, HL-60 and THP-1 cells (5×10^4/ml) were seeded in 96-well culture plates and incubated with T-5224 (Selleck, USA) (concentration gradient is set to 0, 10, 20, 40, 60, and 80 μM) or united Ara-C (SinoPharm YiXin, China) (concentration gradient is set to 0.625, 1.25, 2.5, 5, 10, and 20 μM) treatment for a period of time (24, 48, and 72 h). After certain times, 10 μl of CCK8 solution was added to each well for a 3-h culture at 37°C. Absorbance was measured by a spectrophotometer (Bio Tek Instruments, USA) at a wavelength of 450 and 630 nm. The calculation formula of relative cell vitality (%) is: (experimental well - blank well)/(control well - blank well) × 100%.

Apoptosis Assessment

A total of 5×10^6 cells were inoculated in six-well culture plates and treated with T-5224 at final concentrations of 0, 40, and 80 μM, respectively. After 24 h incubation, cells were collected and treated with Annexin V-7-AAD kit (Multi Sciences, China) and subjected to flow cytometry (Becton Dickinson, USA) to analyze apoptosis.

Small RNA Sequencing

Total RNA was qualified and quantified using a NanoDrop and an Agilent 2100 Bioanalyzer. Total RNA was purified by electrophoretic separation on a 15% urea denaturing PAGE gel, and regions corresponding to the 18–30-nt small RNA bands in the marker lane were excised and recovered. Then, the 18–30-nt small RNAs were ligated to a 5′-adaptor and a 3′-adaptor, which were subsequently transcribed into cDNA by SuperScript II Reverse Transcriptase (Invitrogen, USA), and then several rounds of PCR amplification with PCR Primer Cocktail and PCR Mix were performed to enrich the cDNA fragments. The PCR products were selected by agarose gel electrophoresis with target fragments of 100–120 bp and then purified with a QIAquick Gel Extraction Kit (QIAGEN, Valencia, CA). The final PCR ligation

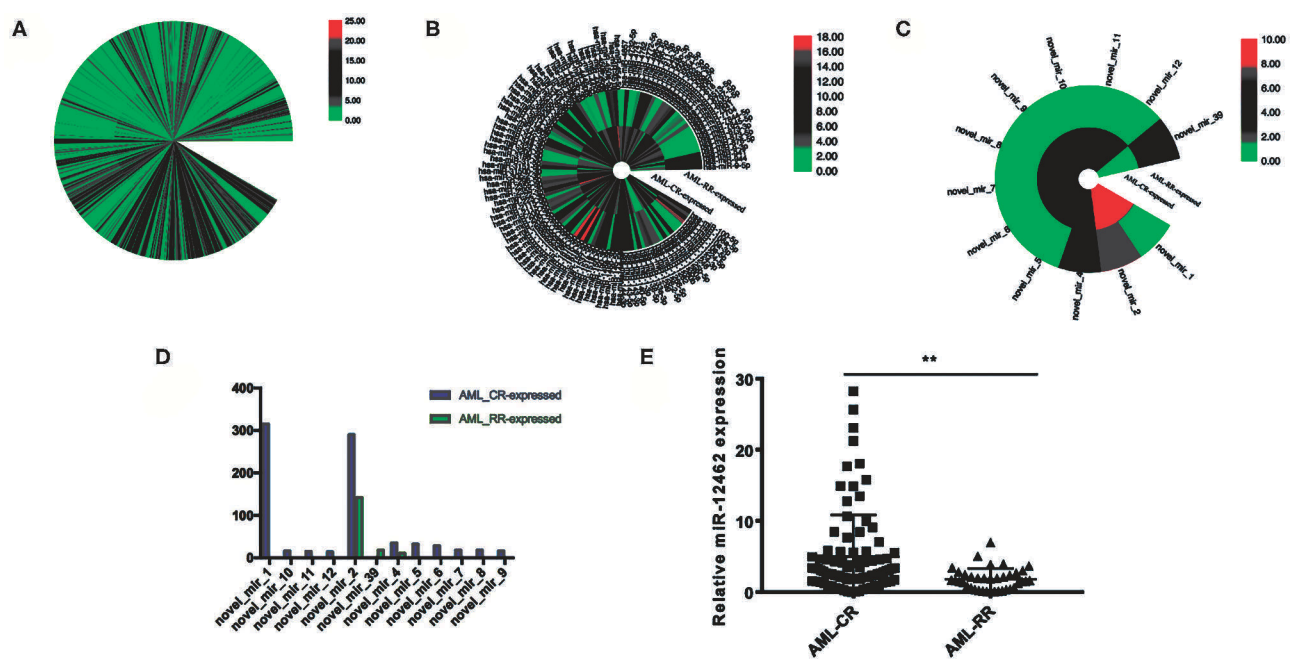

FIGURE 1 | Identification of hsa-miR-12462 and its expression characteristics in acute myeloid leukemia (AML). **(A)** 1,099 differentially expressed miRNAs between patients who achieve complete remission (AML-CR) and patients who suffer relapse/refractory (AML-RR). **(B)** Two hundred fifty-one differentially expressed miRNAs showing over 2-fold significance between AML-CR cohort and AML-RR cohort. **(C)** Twelve unreported miRNAs among the 251 miRNAs. **(D)** novel_mir_1, which we named as hsa-miR-12462, showed the most significant difference. **(E)** Quantitative PCR analysis to compare the endogenous levels of hsa-miR-12462 in AML-CR and AML-RR patients (*p*-value: AML-CR vs. AML-RR < 0.01). $^{**}p < 0.01$.

products were sequenced using the BGISEQ-500 platform (BGI-Shenzhen, China). Gene expression levels were measured in RPKM using Cufflinks.

RNA Sequencing

RNA sample quality was analyzed, and cDNA libraries were synthesized and sequenced using BGI technology. In brief, an Agilent 2100 Bioanalyzer (Agilent) was used to assess the quality of the RNA samples and generate the cDNA libraries. Each library was sequenced on a HiSeq4000 (Illumina) using single reads. Gene expression levels were measured in RPKM using Cufflinks.

Statistics

Data were analyzed using SPSS 13.0 (SPSS, Chicago, IL, USA) and reported as mean ± standard deviation (SD). Differences among the two groups were tested by Student's *t*-test or one-way ANOVA, as appropriate. $P < 0.05$ were considered significant. Diagrams were drawn using GraphPad Prism 7 software.

RESULTS

The Expression of Hsa-miR-12462 Is Increased in AML Cases With Complete Remission (AML-CR) Over Cases With Relapsed/Refractory (AML-RR)

To unveil the alternations between different curative efficacy, we collected 128 BM specimens composing of AML-CR ($n = 90$) and AML-RR ($n = 38$) and analyzed them by small RNA sequencing analysis. A total of 1,099 miRNAs displayed differences between the two cohorts (**Figure 1A**), and 251 miRNAs showed significant alternation >2-fold (**Figure 1B**). Among them, 12 miRNAs were unveiled for the first time (**Figure 1C**), and the most conspicuous one, hsa-miR-12462, demonstrated 315-fold increase in the

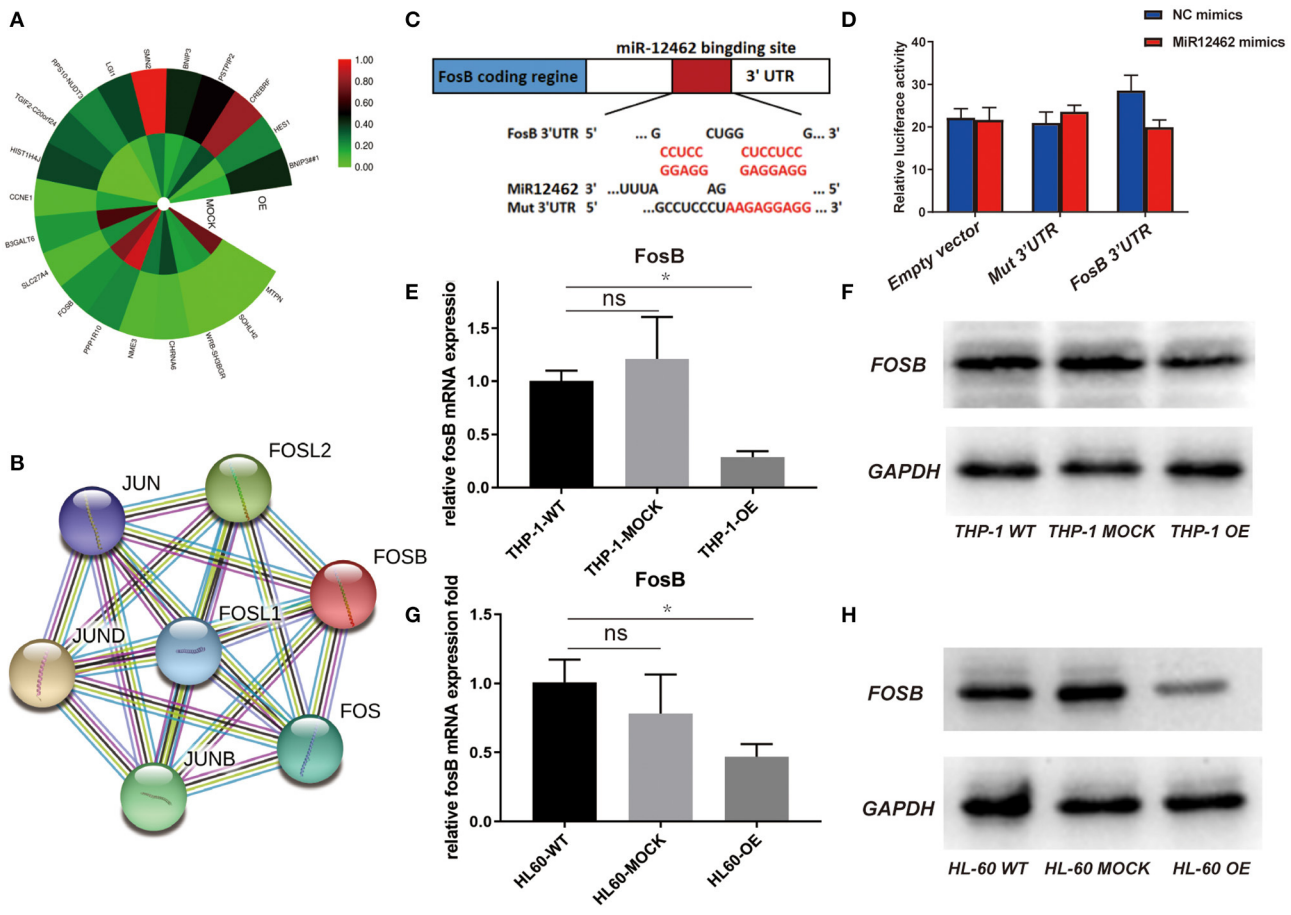

FIGURE 2 | Direct regulation of hsa-miR-12462 on FosB expression. **(A)** RNA sequencing analysis to predict the target gene of hsa-miR-12462. OE represents hsa-miR-12462 overexpressed U937 cells, and MOCK represents mock-infected U937 cells. **(B)** Protein–protein interaction (PPI) network analysis to predict proteins interacted with FosB. **(C)** Online search program TargetScan to match the potential hsa-miR-12462 binding sites in FosB gene sequence. **(D)** Dual luciferase activity was assayed in hsa-miR-12462-mimic transfected and hsa-miR-12462 NC transfected 293T cells. Statistical analysis by Student's *t*-test. Data are mean ± SEM of three independent experiments (*$p < 0.05$). **(E,F)** Expression level of FosB in hsa-miR-12462-OE THP-1 cells, wild-type (WT) THP-1 cells, and MOCK THP-1 cells by quantitative PCR **(E)** and Western blotting **(F)** (*p*-value: THP-1 OE vs. THP-1 WT < 0.05). **(G,H)** Expression level of FosB in hsa-miR-12462-OE HL-60 cells, WT HL-60 cells, and MOCK HL-60 cells by quantitative PCR **(G)** and Western blotting **(H)** (*p*-value: HL-60 OE vs. HL-60 WT < 0.01). *$p < 0.05$, **$p < 0.01$.

AML-CR cohort greater than that in the AML-RR cohort (**Figure 1D**), as we previously verified (14). As to the tissue distribution of hsa-miR-12462 in mice, its level in skeletal muscle was significantly higher than that in lung, BM, kidney, heart, spleen, intestine, and stomach (14), while its expression in human and importance to mechanism need to be studied. In AML cell lines, its expression in HL-60 cells was higher than that in THP-1 cells (**Supplementary Figure 1A**). Next, 128 specimens were used to verify the differential expression of hsa-miR-12462 *via* quantitative RT-PCR. As anticipated, hsa-miR-12462 was confirmed to be upregulated in AML-CR patients vs. AML-RR patients (**Figure 1E**).

FosB Is a Direct Target of Hsa-miR-12462

To elucidate the detailed mechanisms of the suppressive effects of hsa-miR-12462 on phenotype changes, RNA sequencing (**Figure 2A**) together with protein–protein interaction (PPI) network analysis (**Figure 2B**) was performed in both hsa-miR-12462 overexpressed (OE) U937 cells and mock-infected (MOCK) U937 cells. We analyzed 307 differentially expressed genes in the hsa-miR-12462-OE group and discovered that the AP-1 transcription factor components including FosB were mostly involved. To clarify the interaction between hsa-miR-12462 and FosB, we firstly predicted the potential binding site for hsa-miR-12462 within the 3′-UTR region of FosB using the online search program TargetScan (**Figure 2C**). To prove the direct regulation of FosB by hsa-miR-12462, a mutant FosB at the putative binding sequence in a 3′-UTR element and a wild type (WT) were cloned into a dual luciferase reporter and then transiently transfected into 293T cells. Indeed, FosB mutation inhibited the hsa-miR-12462-mediated downregulation of luciferase activity (**Figure 2D**), indicating FosB was regulated by hsa-miR-12462 as a direct target.

To further corroborate these findings, we tested the expression of FosB both in THP-1 and HL-60 cell lines with different hsa-miR-12462 expressions (OE, WT, and MOCK).

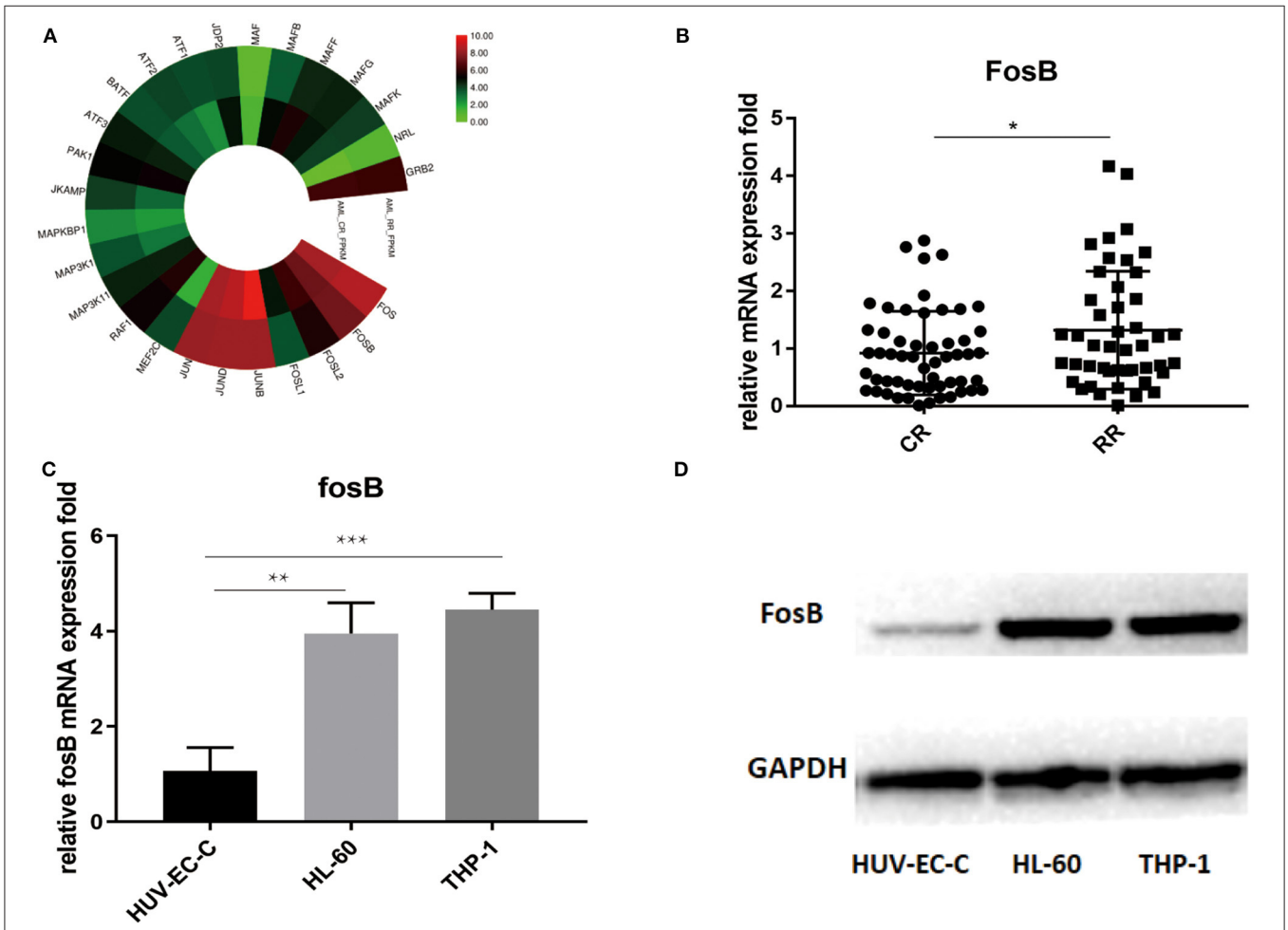

FIGURE 3 | FosB is augmented in acute myeloid leukemia (AML) especially in AML-RR patients. **(A)** RNA sequencing analysis revealed the enhanced expression of activator protein (AP-1)-associated pathways in AML-RR vs. AML-CR. **(B)** Difference of FosB mRNA expression between AML-RR and AML-CR by quantitative PCR (*p*-value: CR vs. RR < 0.05). **(C)** FosB mRNA expression in normal human cell line (HUV-EC-C) and AML cell lines (HL-60 and THP-1) by quantitative PCR (*p*-value: HL-60 vs. HUV-EC-C < 0.01, THP-1 vs. HUV-EC-C < 0.001). **(D)** FosB protein level in normal human cell line (HUV-EC-C) and AML cell lines (HL-60 and THP-1) by Western blotting. $^{*}p < 0.05$, $^{**}p < 0.01$, $^{***}p < 0.001$.

Overexpression of hsa-miR-12462 induced a statistically significant downregulation of FosB expression when compared with WT and MOCK groups, both at the mRNA (**Figures 2E,G**) and protein level (**Figures 2F,H**). Taken together, hsa-miR-12462 could suppress the expression of FosB in AML by direct interaction.

The Expression of FosB Is Augmented in the AML-RR Group

As a key component of AP-1, FosB regulates gene networks associated with oncogenic transformation, reflecting in the proliferative and invasive modulation of solid tumor (15). Considering that the role of FosB to AML is still elusive, we aimed to depict more details on its specific expression and mechanism. RNA sequencing analysis revealed the distinctions on gene expression between AML-CR ($n = 90$) and AML-RR ($n = 38$). The results demonstrated that the expression of AP-1 components including FosB was augmented in the AML-RR group (**Figure 3A**, **Supplementary Figure 1B**). Next, the alternation of FosB was validated by quantitative RT-PCR among 128 patient samples. The results were in accordance with the RNA sequencing analysis, showing an apparent increase in the AML-RR cohort (**Figure 3B**). To identify whether the expression of FosB is AML-specific or widespread in normal tissues, we compared HUV-EC-C and AML cell lines (THP-1 and HL-60) of the FosB expression differences. FosB was more predominantly expressed in the AML than normal human cell lines, both at the mRNA (**Figure 3C**) and protein level (**Figure 3D**). Thus, we concluded that FosB was augmented in AML and more prominent in AML-RR vs. AML-CR patients and deduced that FosB might play an important role in modulating drug sensitivity and could be a potential therapeutic target.

T-5224 Could Regulate the Proliferation, Apoptosis, and Drug Sensitivity in Acute Myeloid Leukemia Cells

To delineate the concrete role of FosB in AML, we next depleted the function of FosB by pharmacological inhibition. T-5224 is a non-peptidic small molecule designed as an AP-1-specific inhibitor. It can inhibit the binding of heterodimer AP-1 formed

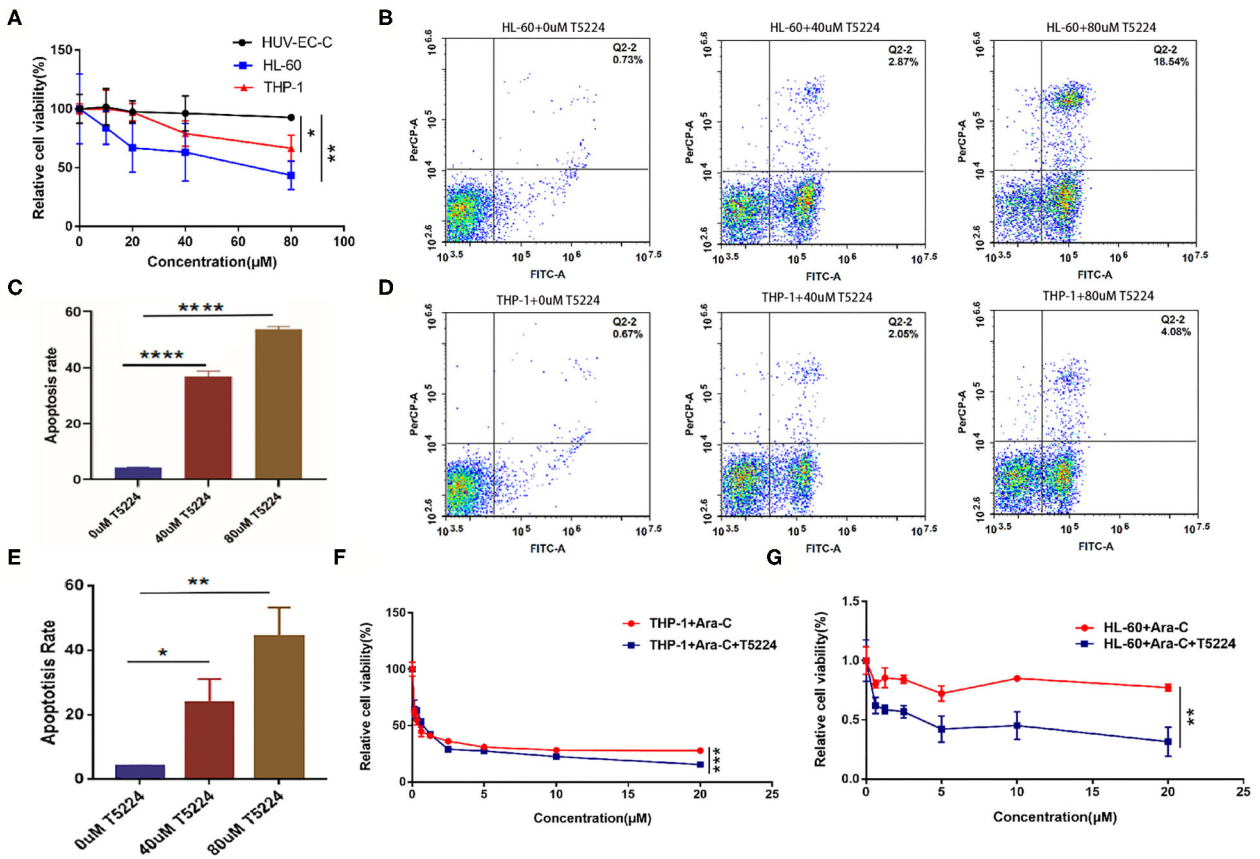

FIGURE 4 | The function of T-5224 on the proliferation, apoptosis, and drug sensitivity in acute myeloid leukemia (AML) cell lines. **(A)** Cell proliferation of HUV-EC-C, HL-60, and THP-1 cells after T-5224 exposure for 24 h (*p*-value: THP-1 vs. HUV-EC-C < 0.05, HL-60 vs. HUV-EC-C < 0.01). **(B,C)** Flow cytometry analysis **(B)** and relative apoptosis rate **(C)** of HL-60 cell lines after being treated with different concentrations of T5224 for 24 h (*p*-value: HL-60 + 0 μM T-5224 vs. HL-60 + 40 μM T-5224 < 0.0001; HL-60 + 0 μM T-5224 vs. HL-60 + 80 μM T-5224 < 0.0001). **(D,E)** Flow cytometry analysis **(D)** and relative apoptosis rate **(E)** of THP-1 cell lines after being treated with different concentrations of T5224 for 24 h (*p*-value: THP-1 + 0 μM T-5224 vs. THP-1 + 40 μM T-5224 < 0.05, THP-1 + 0 μM T-5224 vs. THP-1 + 80 μM T-5224 < 0.01). **(F,G)** Cell viability of THP-1 cells **(F)** and HL-60 cells **(G)** after cotreatment with Ara-C ± T-5224 (*p*-value: THP-1 + Ara-C vs. THP-1 + Ara-C + T-5224 < 0.001, HL-60 + Ara-C vs. HL-60 + Ara-C + T-5224 < 0.01). *$p < 0.05$, **$p < 0.01$, ***$p < 0.001$, ****$p < 0.0001$.

by FosB and Jun protein to AP-1 binding site in the promoter region, thus inhibiting the activation of AP-1 signaling pathway (16). HL-60, THP-1, and HUV-EC-C cells were inoculated with T-5224 at a concentration gradient and were detected with CCK8 assay after 24 h. Cell proliferation was significantly suppressed in AML cell lines while almost unaffected in HUV-EC-C cells (**Figure 4A**). Moreover, coincident with what we discovered above that miR-12462 reduced the expression of FosB in AML, T-5224 exerted little influence on viability in hsa-miR-12462-OE cells (**Supplementary Figure 1C**). Furthermore, we aimed to elaborate the effect of T-5224 on apoptosis. After 24 h exposure of T-5224, the percentage of apoptotic cells elevated, accompanied by progressively increased concentration (**Figures 4B–E**).

Ara-C is widely administrated in clinical practice as an indispensable component of induction and consolidation therapy. We treated AML cells with Ara-C ± T-5224 (40 μM) to illustrate the collaboration between Ara-C and T-5224. The results showed that Ara-C combined with T-5224 exhibited a stronger inhibitory effect on cell proliferation than monotherapy (**Figures 4F,G**). These findings indicated FosB might be related to the sensitivity of AML cells to chemical drugs.

DISCUSSION

Over the past decade, the fields of applied and functional miRNA research have been explored and miRNAs have been implicated across a spectrum of diseases as biomarkers, therapeutics, or vital regulators (17). As to AML, miRNAs may counteract with oncogenes or tumor suppressors to modulate the development and differentiation of hematopoietic cells, thereby contributing to AML formation (18). Our small RNA sequencing analysis revealed the miRNA profiling signatures between AML-CR and AML-RR patients. We chose hsa-miR-12462, which presents the most obvious difference, as we verified before. In clinical BM samples, the expression profile of has-miR-12462 corresponded with our previous findings, showing significant increase in AML-CR patients vs. AML-RR patients. Next, we combined RNA sequencing, PPI network analysis, and bioinformatics method (TargetScan) to predict target genes. The results indicated that the key components of AP-1 complex were involved, and FosB might be the most likely target of hsa-miR-12462. Dual luciferase reporter assay was used for validation. Consistent with our expectations, overexpression of

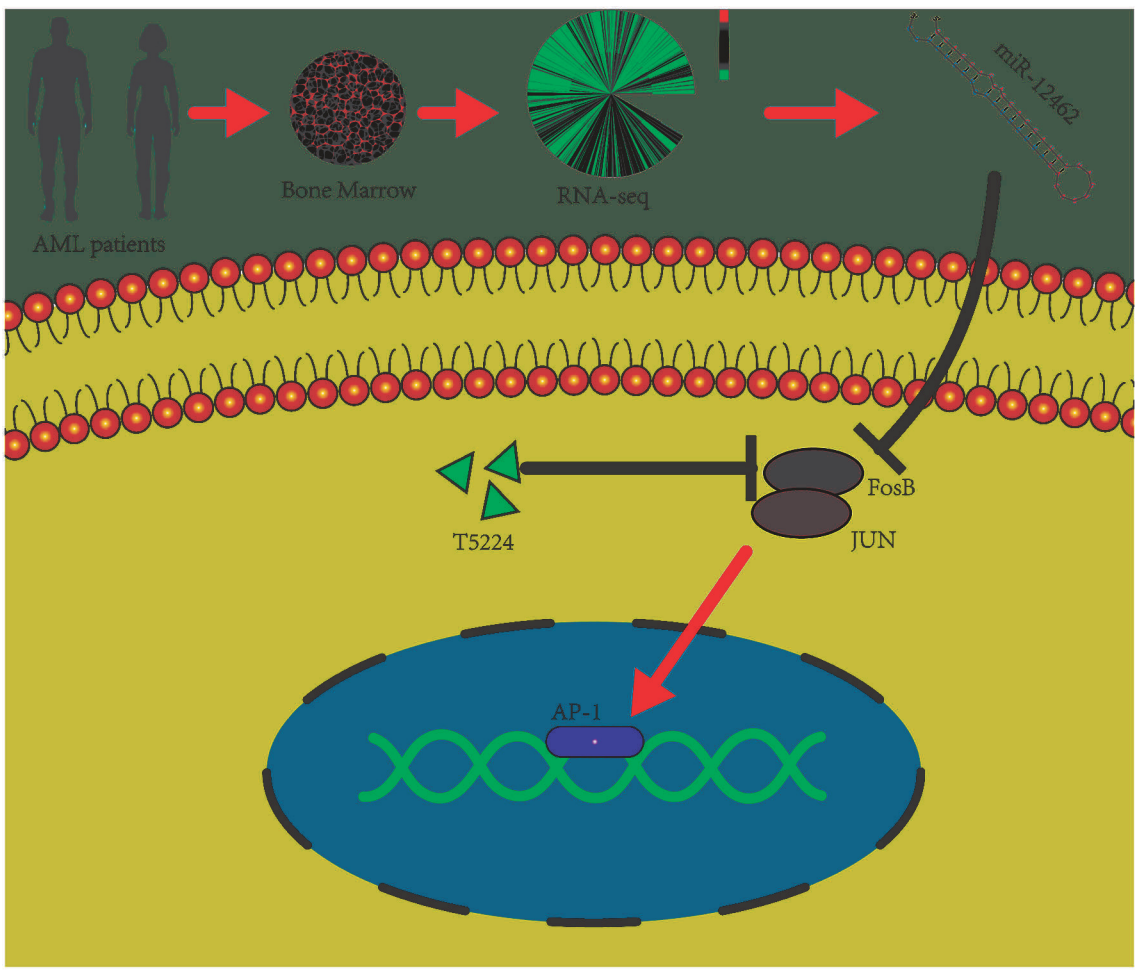

FIGURE 5 | Schematic diagram of the potential roles of hsa-miR-12462 in modulating acute myeloid leukemia (AML) cell proliferation and drug sensitivity by targeting FosB.

hsa-miR-12462 suppressed the level of FosB in both mRNA and protein aspects.

AP-1 has been implicated in lots of biological processes including cell proliferation, death, differentiation, and oncogenic transformation (19, 20). In our experiment, RNA sequencing analysis suggested that compared with the AML-CR group, the AML-RR group showed high expression of AP-1 components including FosB. It was in accordance with the quantitative RT-PCR results in clinical samples. The expression of FosB in AML cell lines (HL-60 and THP-1) significantly elevated compared with that in normal human cell line (HUV-EC-C). In addition, through comparing the results of proliferation and apoptosis of AML cell lines after intervention with an inhibitor of FosB, T-5224, it was demonstrated that FosB may play a pivotal role in modulating cell viability as well as death in AML and is related to sensitivity to Ara-C.

In conclusion, the expression of hsa-miR-12462 was augmented significantly in AML-CR patients. Upregulation of hsa-miR-12462 influenced the proliferation and apoptosis of AML cell lines through negatively targeting FosB. Combining T-5224 and Ara-C had better cytotoxic impact than monotherapy. The findings provide new evidences about the underlying molecular mechanisms of hsa-miR-12462 and FosB (**Figure 5**), which deserves exploration in more detail through *in vivo* studies.

DATA AVAILABILITY STATEMENT

The dataset presented in this study can be found in Gene Expression Omnibus (GEO) repository. The accession number of the repository is GSE156654.

ETHICS STATEMENT

The studies involving human participants were reviewed and approved by the Medical Institutional Ethics Committee of the Xiangya Hospital of Central South University. Written informed consent to participate in this study was provided by the participants' legal guardian/next of kin.

AUTHOR CONTRIBUTIONS

HZe designed the project and approved the final version. HW, HZh, LJ, TZ, SX, YJ, WL, and HL performed the experiments. HW and HZh analyzed the data. HW, XJ, and HZh wrote the manuscript. All authors contributed to the article and approved the submitted version.

FUNDING

This work was supported by the National Natural Science Foundation of China (Grant Nos. 81770184 and 81970143).

ACKNOWLEDGMENTS

The authors are very grateful to the participants who volunteered to enroll in the study.

SUPPLEMENTARY MATERIAL

The Supplementary Material for this article can be found online at: https://www.frontiersin.org/articles/10.3389/fmed.2020.582923/full#supplementary-material

Supplementary Figure 1 | (A) The expression of hsa-miR-12462 in HL-60 and THP-1 cell lines. **(B)** The expression of FosB is augmented in AML-RR group. **(C)** The exposure of T-5224 shows no influence on viability in hsa-miR-12462-OE HL-60 cells.

REFERENCES

1. Siegel RL, Miller KD, Jemal A. Cancer statistics, 2020. *CA Cancer J Clin.* (2020) 70:7–30. doi: 10.3322/caac.21590
2. de Kouchkovsky I, Abdul-Hay M. Acute myeloid leukemia: a comprehensive review and 2016 update. *Blood Cancer J.* (2016) 6:e441. doi: 10.1038/bcj.2016.50
3. Li J, Tan S, Kooger R, Zhang C, Zhang Y. MicroRNAs as novel biological targets for detection and regulation. *Chem Soc Rev.* (2014) 43:506–17. doi: 10.1039/C3CS60312A
4. Bartel DP. MicroRNAs: target recognition and regulatory functions. *Cell.* (2009) 136:215–33. doi: 10.1016/j.cell.2009.01.002
5. Mitra R, Adams CM, Jiang W, Greenawalt E, Eischen CM. Pan-cancer analysis reveals cooperativity of both strands of microRNA that regulate tumorigenesis and patient survival. *Nat Commun.* (2020) 11:968. doi: 10.1038/s41467-020-14713-2
6. Liu Y, Cheng Z, Pang Y, Cui L, Qian L, Zhae H, et al. Role of microRNAs, circRNAs and long noncoding RNAs in acute myeloid leukemia. *J Hematol Oncol.* (2019) 12:51. doi: 10.1186/s13045-019-0734-5
7. Shaulian E, Karin M. AP-1 as a regulator of cell life and death. *Nat Cell Biol.* (2002) 4:E131–6. doi: 10.1038/ncb0502-e131
8. Eferl R, Wagner EF. AP-1: a double-edged sword in tumorigenesis. *Nat Rev Cancer.* (2003) 3:859–68. doi: 10.1038/nrc1209
9. Staber PB, Linkesch W, Zauner D, Beham-Schmid C, Guelly C, Schauer S, et al. Common alterations in gene expression and increased proliferation in recurrent acute myeloid leukemia. *Oncogene.* (2004) 23:894–904. doi: 10.1038/sj.onc.1207192
10. Yang MY, Liu TC, Chang JG, Lin PM, Lin SF. JunB gene expression is inactivated by methylation in chronic myeloid leukemia. *Blood.* (2003) 101:3205–11. doi: 10.1182/blood-2002-05-1598
11. Leventaki V, Drakos E, Karanikou M, Psatha K, Lin P, Schlette E, et al. c-JUN N-terminal kinase (JNK) is activated and contributes to tumor cell proliferation in classical Hodgkin lymphoma. *Hum Pathol.* (2014) 45:565–72. doi: 10.1016/j.humpath.2013.10.024
12. Mathas S, Hinz M, Anagnostopoulos I, Krappmann D, Lietz A, Jundt F, et al. Aberrantly expressed c-Jun and JunB are a hallmark of Hodgkin lymphoma cells, stimulate proliferation and synergize with NF-kappa B. *EMBO J.* (2002) 21:4104–13. doi: 10.1093/emboj/cdf389
13. Liu S, Luan J, Ding Y. miR-144-3p targets FosB proto-oncogene, AP-1 transcription factor subunit (FOSB) to suppress proliferation, migration, and invasion of PANC-1 pancreatic cancer cells. *Oncol Res.* (2018) 26:683–90. doi: 10.3727/096504017X14982585511252

14. Jia Y, Liu W, Zhan HE, Yi PE, Liang H, Zheng QL, et al. Roles of hsa-miR-12462 and SLC9A1 in acute myeloid leukemia. *J Hematol Oncol.* (2020) 13:101. doi: 10.1186/s13045-020-00935-w
15. Kim DS, Lee WK, Park JY. Association of FOSB exon 4 unmethylation with poor prognosis in patients with late-stage non-small cell lung cancer. *Oncol Rep.* (2020) 43:655–61. doi: 10.3892/or.2019.7431
16. Aikawa Y, Morimoto K, Yamamoto T, Chaki H, Hashiramoto A, Narita H, et al. Treatment of arthritis with a selective inhibitor of c-Fos/activator protein-1. *Nat Biotechnol.* (2008) 26:817–23. doi: 10.1038/nbt1412
17. Witwer KW, Halushka MK. Toward the promise of microRNAs - enhancing reproducibility and rigor in microRNA research. *RNA Biol.* (2016) 13:1103–16. doi: 10.1080/15476286.2016.1236172
18. He C, Luo B, Jiang N, Liang Y, He Y, Zeng J, et al. OncomiR or antioncomiR: role of miRNAs in acute myeloid leukemia. *Leuk Lymphoma.* (2019) 60:284–94. doi: 10.1080/10428194.2018.1480769
19. Renaud SJ, Kubota K, Rumi MA, Soares MJ. The FOS transcription factor family differentially controls trophoblast migration and invasion. *J Biol Chem.* (2014) 289:5025–39. doi: 10.1074/jbc.M113.523746
20. Milde-Langosch K. The Fos family of transcription factors and their role in tumourigenesis. *Eur J Cancer.* (2005) 41:2449–61. doi: 10.1016/j.ejca.2005.08.008

Conflict of Interest: The authors declare that the research was conducted in the absence of any commercial or financial relationships that could be construed as a potential conflict of interest.

Copyright © 2020 Wang, Zhan, Jiang, Jin, Zhao, Xie, Liu, Jia, Liang and Zeng. This is an open-access article distributed under the terms of the Creative Commons Attribution License (CC BY). The use, distribution or reproduction in other forums is permitted, provided the original author(s) and the copyright owner(s) are credited and that the original publication in this journal is cited, in accordance with accepted academic practice. No use, distribution or reproduction is permitted which does not comply with these terms.

frontiers in Medicine

REVIEW
published: 22 October 2020
doi: 10.3389/fmed.2020.00456

Design, Bioanalytical, and Biomedical Applications of Aptamer-Based Hydrogels

Ya Di[1], Ping Wang[2], Chunyan Li[2], Shufeng Xu[1], Qi Tian[1], Tong Wu[1], Yaling Tian[1] and Liming Gao[1]*

[1] Department of Respiratory Medicine, The First Hospital of Qinhuangdao, Qinhuangdao, China, [2] Department of Respiratory Medicine, Chinese People's Liberation Army General Hospital, Beijing, China

Aptamers are special types of single-stranded DNA generated by a process called systematic evolution of ligands by exponential enrichment (SELEX). Due to significant advances in the chemical synthesis and biotechnological production, aptamers have gained considerable attention as versatile building blocks for the next generation of soft materials. Hydrogels are high water-retainable materials with a three-dimensional (3D) polymeric network. Aptamers, as a vital element, have greatly expanded the applications of hydrogels. Due to their biocompatibility, selective binding, and molecular recognition, aptamer-based hydrogels can be utilized for bioanalytical and biomedical applications. In this review, we focus on the latest strategies of aptamer-based hydrogels in bioanalytical and biomedical applications. We begin this review with an overview of the underlying design principles for the construction of aptamer-based hydrogels. Next, we will discuss some bioanalytical and biomedical applications of aptamer-based hydrogel including biosensing, target capture and release, logic devices, gene and cancer therapy. Finally, the recent progress of aptamer-based hydrogels is discussed, along with challenges and future perspectives.

Keywords: aptamer-based hydrogels, aptamer, hydrogels, bioanalysis, biomedicine

OPEN ACCESS

Edited by:
Fu Wang,
Xidian University, China

Reviewed by:
Jianxun Ding,
Changchun Institute of Applied Chemistry (CAS), China
Thean Hock Tang,
Universiti Sains Malaysia (USM), Malaysia

***Correspondence:**
Shufeng Xu
shufengxu1965@sina.com

Specialty section:
This article was submitted to Precision Medicine, a section of the journal Frontiers in Medicine

Received: *12 June 2020*
Accepted: *09 July 2020*
Published: *22 October 2020*

Citation:
Di Y, Wang P, Li C, Xu S, Tian Q, Wu T, Tian Y and Gao L (2020) Design, Bioanalytical, and Biomedical Applications of Aptamer-Based Hydrogels. Front. Med. 7:456. doi: 10.3389/fmed.2020.00456

INTRODUCTION

Hydrogels are a kind of high water-retainable material (containing up to 99 wt% water) with a three-dimensional (3D) polymeric network which is similar to natural tissue. Due to the hydrophilic residues in the backbone of polymers, an immense amount of water molecules are retained within their structures (1). In addition, an extremely large surface area with good porosity has abundant interior space for biomolecules to be retained within the system through Coulombic attraction (2), while maintaining their biological activities. Moreover, the polymers or polymer monomers are easily dissolved in water before crosslinking, while after crosslinking, they are in a gel state with a defined shape. Due to their excellent properties, hydrogels have attracted much attention over the past years as the elaborate scaffolds in drug delivery carriers (3), tissue engineering, sensors (4) and cancer therapy (5). Hydrophilic polymer networks of hydrogels are formed through the crosslinking of monomers or polymer chains via covalent

bonds and/or non-covalent interactions including hydrogen bonding, electrostatic interactions, host-guest complexation and their combinations (6–11). Plus, hydrogels can be made from a very large range of building blocks including polymers, peptides (12–15), and surfactants (16), with different types, degrees of cross-linking, and properties leading to the nanoscopic structures, size range, physical properties, and functions of hydrogel (17). Great attention has been paid to explore the strategy to control the functionalities of hydrogels. For example, many of the stimuli-responsive hydrogels have been constructed by using polymers modified with specific functional units that can rapidly respond to external stimuli. A variety of physical and chemical changes of the hydrogel, including volume change and sol-gel transition, are particularly sensitive to specific external stimuli due to their component materials (18–21). These stimuli-responsive hydrogels have gained immense consideration because of their potential in drug delivery systems (22–26), sensors (27–32), cancer therapy (33–37), cell culture substrates (38–40), and tissue engineering (38, 41–44). Beyond these stimulants, many specific biomolecules, such as antibodies, nucleic acids (or DNA), and enzymes, that can rapidly respond to target analytes are used for functional materials to modify polymers in order to construct target-responsive hydrogels (45, 46).

Aptamers are used to construct polymer networks as the stimuli-responsive element in aptamer-based hydrogels, and due to their unique characteristics they have gained great attention among the development of hydrogels which are responsive to specific target analytes (45, 47). Nucleic acid aptamers are single-stranded DNA(ssDNA) or RNA molecules, commonly containing 12–80 nucleotides (48, 49), generated by the systematic evolution of ligands by exponential enrichment (SELEX) (50) from a random ssDNA or RNA library (usually $10^{15}\sim10^{16}$ different sequences) by means of three main steps including selection, separation, and amplification. Aptamer DNA hybridization and aptamer-target recognition both have very high specificity. Aptamers also possess high recognition ability toward specific molecular targets including ions (51, 52), small molecules (53, 54), proteins (55, 56), and cells (57, 58), because aptamers fold into a unique secondary or tertiary structure to bind to a target of interest, depending on van der Waals forces, hydrogen bonds, or electrostatic interactions (48, 59–62). Since they were discovered in the 1990s by Tuerk and Gold (63) and Ellington and Szostak (50), aptamers have become smart, specific, and high-affinity probes in bioanalytical, diagnostic, and therapeutic applications. Moreover, compared to other antibodies, aptamers are often called chemical antibodies due to their unique properties: (1) Aptamers are structurally stable with little immunogenicity and are chemically synthesized using standard solid state phosphoramidite reactions, which minimizes the batch-to-batch variation and improves the reproducibility of hydrogel systems. (2) aptamers are highly selective and have an affinity to targets, and low-dissociation constant values (K_{ds}, 1×10^{-12}-1×10^{-9} M) (64), so that aptamers can specifically recognize and undergo changes of their substrates even at very low concentrations. (3) The molecular weight of an aptamer is between 5 and 20 kDa, which is smaller than antibodies (ca.150 kDa), leading to better tumor uptake kinetics (6). (4) Aptamers are stable in a wide range of temperature, solvents, and pH. (5) Aptamers can be synthesized by chemical or enzymatic procedures or by a combination of these two methods without any animal-based synthesis. (6) Aptamers are easily modified with other functional moieties and have the capability of directional amplification by polymerase chain reaction (PCR). These excellent characters of aptamers make aptamer-based hydrogels even more versatile, and are excellent components in hydrogel engineering: (1) Aptamers can chemically conjugate with polymers such as acrydite and carboxymethylcellulose to construct the hydrogel (65, 66). (2) Aptamers can be integrated onto the surface of particles by chemical or physical methods and mixed with a pre-gel solution to form particle/hydrogel composites (67, 68). (3) Aptamers can recognize both target molecules and trigger complementary sequences (69–72). Especially to trap or introduce drugs (73–75), nanoparticles (76–78) into aptamer-based hydrogels have greatly expanded the applications in biosensing, target capture and release, cell adhesion and targeted therapy.

In this review, we focus on the latest strategies of aptamer-based hydrogels in bioanalytical and biomedical applications (**Scheme 1**). We begin this review with an overview of the underlying design principles for the construction of aptamer-based hydrogels. Next, we will discuss some bioanalytical and biomedical applications of aptamer-based hydrogels including biosensing, target capture and release, logic devices, gene and cancer therapy. Finally, recent progress of aptamer-based hydrogels is discussed along with challenges and future perspectives.

DESIGN AND PRINCIPLE OF APTAMER-BASED HYDROGELS

Aptamer as Cross-Linkers

Aptamer-based hydrogels have been prepared based on different design principles. The selected design and preparation methods have a strong impact on the characteristic features of hydrogels and thus determine their respective biomedical applications. Using DNA aptamers as crosslinkers in hydrogels allows the hydrogels to be prepared to recognize the targets. In the absence of the target, the aptamer acts only as a conventional DNA crosslinker, but when the target is present, the aptamer preferentially forms a complex with the target and induces the change of the structure of the hydrogel. Such hydrogels utilize both the smart and programmable features of the DNA components as well as short aptamer sequences acting as supramolecular cross-linking agents (79–81). The first DNA-based polymer hydrogels were reported by Nagahara and Matsuda in which the short DNA sequences were grafted to a poly(acrylamide) polymer chain, and two pathways achieved gelation: (1) two DNA strands grafted to the polymer backbone were hybridized by other DNA sequences to induce the formation of gelation. (2) DNA strands attached to the polymer chain hybridized directly to form gelation without any external

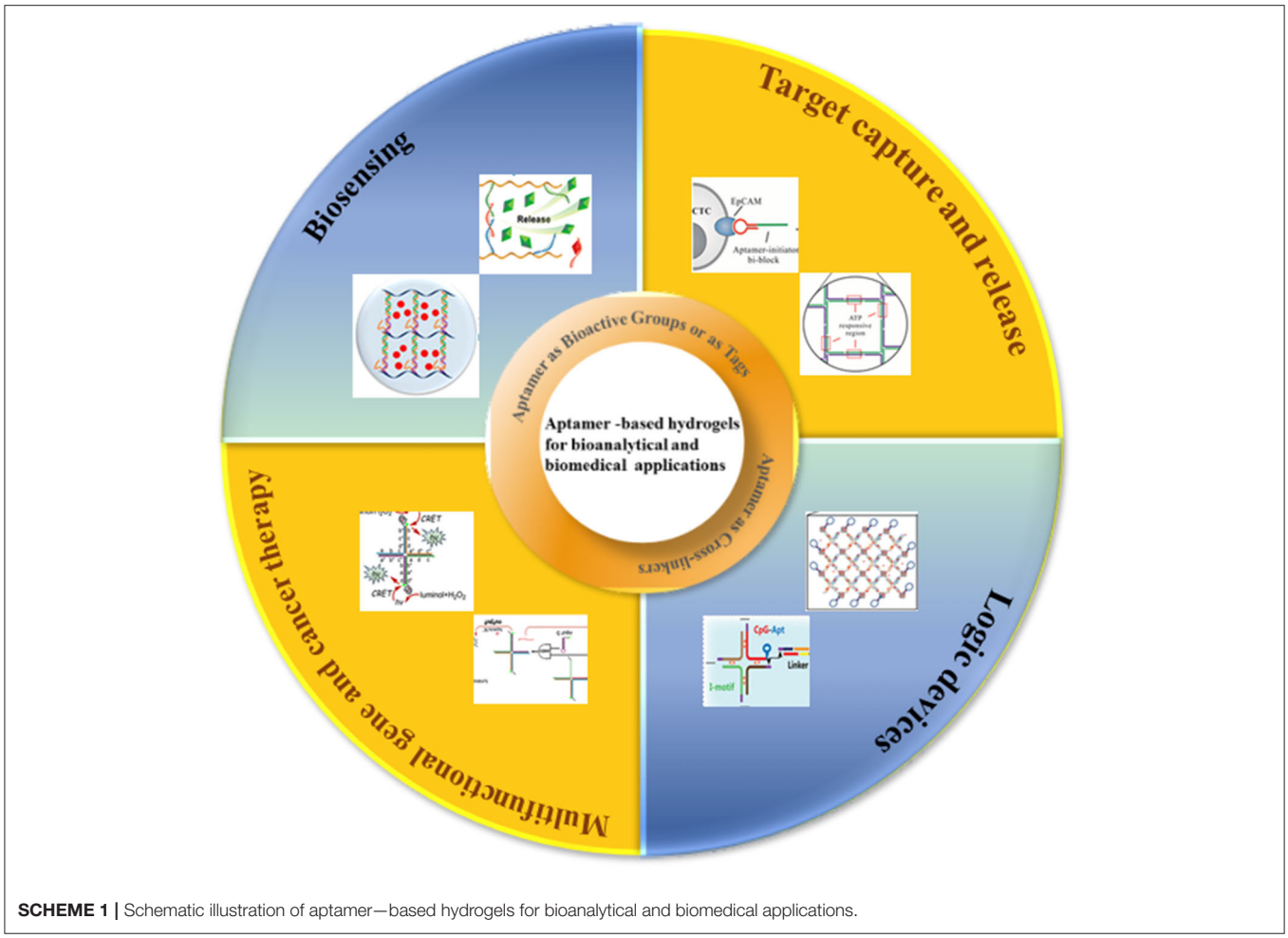

SCHEME 1 | Schematic illustration of aptamer—based hydrogels for bioanalytical and biomedical applications.

cross-linking agents (82). Based on this principle, a series of aptamer-based hydrogels have been prepared responding to target molecules (**Figure 1A**a) (85, 86). Aptamers can also be used as crosslinkers in pure DNA hydrogels. A typical example is that a pure DNA hydrogel was constructed using a Y-shaped DNA and a thrombin aptamer linker through DNA self-assembly (**Figure 1A**b) (87). The aptamers for ochratoxin A, ATP and adenine were used as DNA linkers to construct pure DNA hydrogels that were sensitive to targets (88–90).

Aptamer as Bioactive Groups or as Tags for Functionalization

As we know, DNA segments as functional, bioactive elements rather than structural components were incorporated into hydrogels, and have also been explored for various bioanalytical and biomedical applications (84, 91–93). The presence of aptamer DNA as a bioactive group in these hydrogels typically does not change the mechanical properties and brings their high specificity toward a wide range of biological target molecules. Liu et al. (94) put forward a new strategy for fabricating a protein-scaffolded DNA nanohydrogel. By further incorporating therapeutic agents and tumor-targeting MUC1 aptamer, these SA-scaffolded DNA nanohydrogels can specifically target cancer cells and selectively release the preloaded therapeutic agents via a structure switching. A thrombin-binding aptamer was incorporated into the gel which can bind to adenosine, AMP, and ATP as shown in **Figure 1B**. DNA-functionalized gold nanoparticles or liposomes to DNA-functionalized hydrogels, when thrombin was added, a stable G-quadruplex structure emerged in the aptamer structure, which looked like a molecular switch between tight and relaxed states (95). X-shaped DNA, a DNA linker, and an aptamer were used to create a DNA hydrogel through the one-pot and the aptamer was only used as a functional unit for the target protein capture (96). A DNA nanohydrogel was developed to efficiently take up cells due to the recognition of an aptamer in the nanohydrogel (97). Moreover, an outstanding advantage of aptamer-functionalized hydrogels, as we know, would overcome the shortcomings of aptamers in bioanalytical and biomedical applications. Compared to antibodies, aptamers with high target-specific binding affinity values, were easily tailored for different targets. However, the drawback is their low cellular uptake for their high negative charge density and the limitation of stability in DNA degrading enzymes which are typically present in cells.

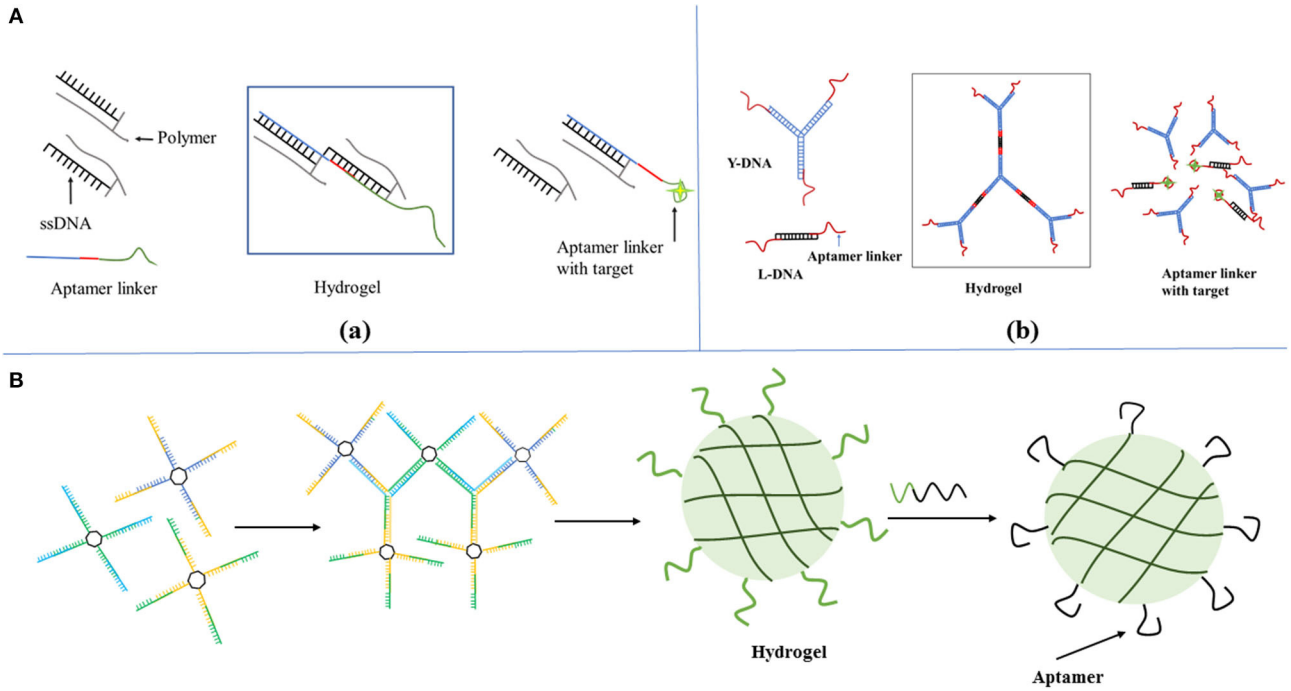

FIGURE 1 | Schematic representation of the design strategy for formation and dissolution of aptamer-based hydrogel based on aptamers as **(A)** crosslinkers in (a) DNA functional polymer hydrogels [Reprinted with permission from Wang et al. (83). Copyright (2008) American Chemical Society] and (b) pure DNA hydrogels [Reprinted with permission from Previtera et al. (82). Copyright (2013) American Chemical Society]. **(B)** Bioactive groups or as tags for functionalization [Reprinted with permission from Lai et al. (84). Copyright (2019) American Chemical Society].

APTAMER-FUNCTIONALIZED HYDROGELS FOR BIOANALYTICAL AND BIOMEDICAL APPLICATIONS

Aptamer-Based Hydrogels for Biosensing

Biosensors, as the powerful tools in monitoring biological or biochemical processes, have been applicated in various fields including medicine, disease diagnosis, food safety, and the environment (92). Nucleic acid aptamers are systematically engineered functional nucleic acids that demonstrate a very high affinity and specificity for targets including ions, metabolites, drugs, proteins, and even whole cells (98). Compared with antibodies, aptamers have been thought the ideal candidates as molecular recognition units to develop biosensors. Combined with DNA nanostructures possessing desirable advantages, aptamer-based biosensors hold great promise for the detection of a variety of targets. However, aptamers cannot freely penetrate the cell membrane and some nucleic acid probes are unstable in both intercellular and intracellular environments so that aptamer-based biosensors are usually compromised in intracellular environments (78, 99). Due to the protection of hydrogel nets, aptamer-based hydrogels have gained great attention in biosensing detection for their biocompatibility, chemical stability, and selective binding. Based on the designable conformational changes of aptamers, aptamer-based hydrogels can be combined with a variety of signaling mechanisms including fluorescence, electrochemistry, colorimetry, electroluminescence, and surface plasmon resonance, to construct rapid and sensitive biosensors to detect inorganic ions, organic small molecules, proteins, cells, and tissues. Usually, DNA-functionalized polymers have been simply crosslinked by the hybridization of aptamers with their complementary sequences to construct a hydrogel network structure. Because the binding affinities of aptamers to their target analytes are much stronger than that of simple hybridization, the network structure may deform or disintegrate when the specific target analytes are presented. The deformation of the aptamer-based hydrogel network can be easily detected with naked eyes or various colorimetric or fluorescence agents including, silver, gold nanoparticles, iodine, fluorescent dyes, and quantum dots (83, 100–107). The constructed hydrogel biosensor may achieve visual detection easily.

To detect biological molecules is vital for understanding their physiological and pathological functions. Since aptamers are easily modified and engineered, a large number of aptamer-based sensing hydrogel systems have been developed for the efficient detection of a wide range of biomolecules. Based on the use of DNA aptamers that cross-link with linear polyacrylamide chains, the first reported in this field was an aptamer-based hydrogel based on a gel-sol transition for detecting adenosine (85). In this design, when two oligonucleotide (DNA1, DNA2)-conjugated polyacrylamide chains (P1, P2) were mixed, a

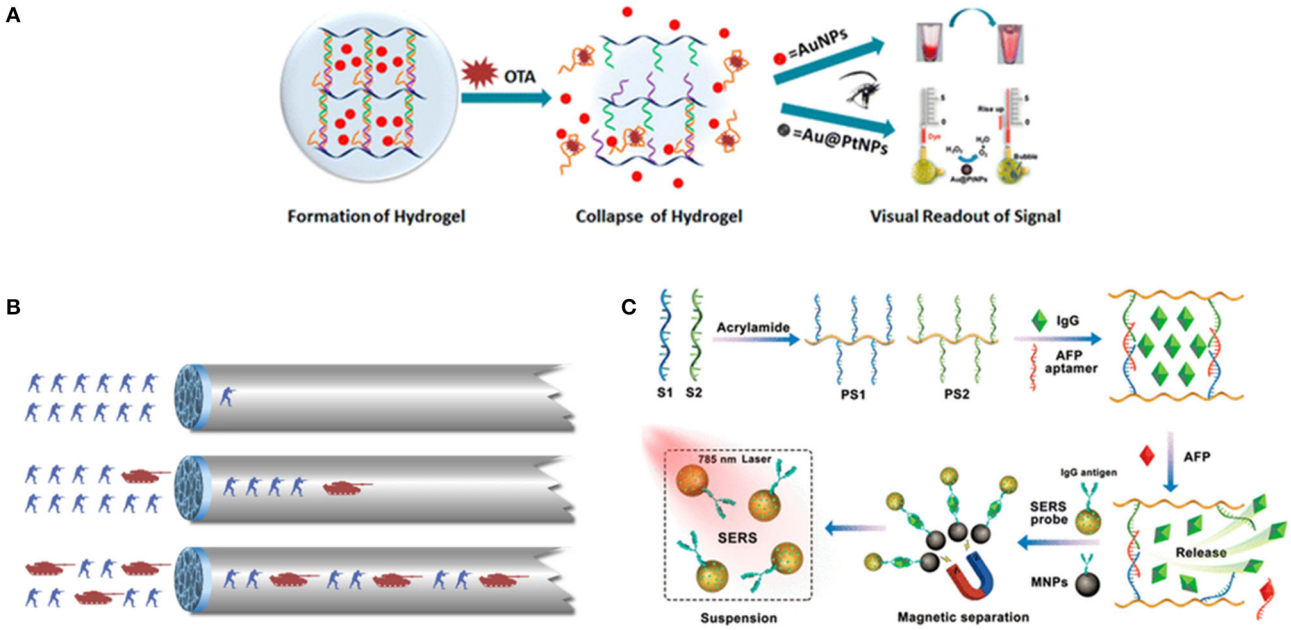

FIGURE 2 | (A) Scheme of DNA-induced formation and adenosine-induced dissolution of hydrogel. Reprinted with permission from Wang et al. (83). Copyright (2008) American Chemical Society. **(B)** The scheme of a target-responsive hydrogel film in capillary tube for visual quantitative detection. [Reprinted with permission from Li et al. (110). Copyright (2019)]. **(C)** Preparation of aptamer functionalized hydrogels for the sensitive detection of α-fetoprotein using SERS method, Reprinted with permission from Guo et al. (103). Copyright (2020) American Chemical Society.

transparent and fluid state was obtained. Subsequently, upon the cross-linking of the oligonucleotides DNA3 was added, so that the above fluid system could undergo a sol-gel transition. The linker strand DNA3 contained three functional domains, that is, the complementary domains with DNA1, DNA2, and aptamer sequence domain. When target adenosine molecules were presented in system, aptamers competitively bound to adenosine molecules, leading to the breakdown of the hydrogel and target-responsive payload release. In order to achieve visual detection, gold nanoparticles were used as the indicator to add into the gel to monitor the process of gel-sol transition because of their unique optical properties. In the presence of adenosine, the upper buffer solution turned from colorless to red, indicating that the AuNPs had been released into the solution. The method was generally representative to use a target molecule as a trigger for the dissociation of the aptamer-based hydrogels to develop a biosensing system with high selectivity and visuality. In a similar work, a detection of food toxin, toxin A, was developed by applying this approach. The linear polyacrylamide polymers functionalized with short DNA strands were hybridized by OTA aptamer strands to construct the hydrogel network structure, and gold nanoparticles were still entrapped within the hydrogel using optical agent (108) (**Figure 2A**). An aptamer-functionalized DNA hydrogel was also prepared though DNA hybridization and incorporated inorganic nanomaterials including gold nanoparticles (AuNPs) and quantum dots (QDs) as signal indicators. The pure DNA hydrogel was directly constructed using Y-shaped DNA, linker DNA, and aptamer sequence with two different recognition sites for thrombin and the complementary sequence. Upon adding thrombin, it competitively bonded with aptamer, leading to the collapse and dissolution of the DNA hydrogel. The released negatively charged AuNPs would meet positively charged polyethyleneimine (PEI)-functionalized QDs and a fluorescence quenching strategy based on the Förster resonance energy transfer (FRET) was developed for the sensitive detection of thrombin in complex matrices (87). It is obvious that great progress has been made in this research area, however, regarding AuNPs, quantum dots etc. as visual indicators, there are several issues that need to be considered. For example, AuNPs exhibited an intense background color in the process of gel dissolution. As a result, this detecting method is not sensitive enough.

More recently, a thrombin-binding aptamer was incorporated into hydrogel. When thrombin was presented, a stable G-quadruplex structure in the aptamer structure emerged which changed the form of hydrogel by the molecular switch between tight and relaxed states (109). Li et al. (110) reported a gel film in a capillary tube based on the thermally reversible principle which transformed the analyte-induced small changes inside the DNA hydrogel into visual signals. In the analysis process, the permeability of the DNA hydrogel film will increase because of the small structural changes in the gel induced by the interaction between target molecules and the aptamer linkers, thereby changing the flow velocity of the sample solution in the capillary tube (**Figure 2B**). The duration time

of the target solution flowing through the capillary tube with a specified length was used to characterize the concentration of different solutions. The ultra-trace aptamer DNA hydrogel (0.01 ml) detected cocaine directly with a low detection limitation (1.17 nM) and excellent selectivity as (**Figure 1B**). A novel SERS biosensing platform was constructed by combining the target-responsive DNA hydrogel for the sensitive detection of α-fetoprotein (AFP) (83). The aptamer as a linker strand in DNA hydrogel specifically recognized AFP and accurately controlled the release of immunoglobulin G (IgG) encapsulated in hydrogel. In the presence of AFP, the hydrogels were disentangled and the IgG was released. Interestingly, the released IgG was captured by SERS probes and bio-functional magnetic beads through the formation of sandwich-like structures to decrease the detecting signals, which significantly improved the detecting sensitivity (**Figure 2C**).

Furthermore, the exploration and introduction of new functional nanomaterials to produce aptamer-based hydrogel biosensing systems which are highly sensitive are also being developed. Aptamer-incorporated graphene oxide (GO) hydrogel without synthetic polymers was developed for the detection of antibiotics. GO hydrogels were readily prepared by physically mixing GO solution with adenosine. The fast gelation of the GO dispersion in the presence of adenosine would attribute to the strong hydrogen bonding and electrostatic interactions between the adenosine and the GO nanosheets. Aptamer chains flatly lay on the surfaces of GO sheets as a result of the strong π-π stacking interactions between the hexagonal cells of graphene and the ring structure of nucleobases in ssDNA, which had been elucidated as an effective driving force for assembling GO sheets into hydrogels (111, 112). Tan et al. (113) reported a fluorescence biosensor based on GO hydrogel incorporated with aptamers, which could selectively bind to tetracyclines. After GO hydrogels were formed, the fluorescence signal of fluorescence labeled aptamers was quenched for fluorescence resonance energy transfer (FRET). When hydrogel was exposed to the tetracycline, the fluorescence recovered. Using the quenching/recovering of fluorescence, this biosensor of GO hydrogel provided a quantitative analysis of tetracycline with high sensitivity at much lower concentration.

APTAMER-BASED HYDROGELS FOR TARGET CAPTURE AND RELEASE

Capture and Release of Circulating Tumor Cells (CTCs)

Circulating tumor cells (CTCs) are the collective term for the tumor cells that escape from the primary tumor sites and travel through the circulatory system into the peripheral blood stream, at which point then, the metastases can be ultimately formed in resident organs. Therefore, detection of CTCs at early stages of tumors will increase diagnostic accuracy and therapeutic efficacy. However, CTCs are a very small population. In general, there are <10 CTCs/mL whereas there are approximately 5×10^9 normal cells present in the same volume of blood sample (65, 114, 115). Therefore, a variety of materials have been recently investigated for sensitive catch and release of CTCs. Aptamer-based hydrogels as an emerging biomaterial, have recently attracted great attention in the fields of medical devices for cell catch and separation. For example, aptamer-based hydrogels were reported for *in situ* identification of live CTCs by cloaking/decloaking of CTCs (93). In this design as shown in **Figure 3A**, an aptamer DNA strand that specifically recognized epithelial cell adhesion molecule (EpCAM) on the CTCs surface triggered a hybridization chain reaction (HCR) via toehold-initiated branch migration. And an ATP aptamer was incorporated in the clamped HCR to decloak the DNA hydrogel on cell surface in order to achieve the phase transition from hydrogel to solution. The encapsulated AuNPs were exploited as the indicators of hydrogel formation via generating a red color at this state. Moreover, this method allowed to identify a low number of CTCs in whole blood by DNA hydrogel cloaking with high sensitivity and specificity for diagnosis. More significantly, controlled and defined chemical stimuli was used for the decloaking of CTCs without damages for subsequent culture and live cell analysis. Ye et al. (117) proposed an aptamer-trigger-clamped hybridization chain reaction (atcHCR) method for the capture of CTCs by porous 3D DNA hydrogels. The 3D environment of the DNA networks minimizes cell damage, and the CTCs can subsequently be released for live-cell analysis. In their work, initiator DNAs with aptamer-toehold biblocks specifically bind to the epithelial cell adhesion molecule (EpCAM) on the surface of CTCs triggering the atcHCR and the formation of a DNA hydrogel. The DNA hydrogel cloaks the CTCs, which would facilitate quantification with minimal cell damage. 10 MCF-7 cells in a 2-μl blood as sample were used to quantitively identify the decloaking of tumor cells via gentle chemical stimulus (ATP) which is used to release living tumor cells for subsequent cell culture and live-cell analysis. The whole experiment only was about 2.5 d including downstream cell culture and analysis. Aptamer-DNA hydrogels would open new powerful and effective routes for capturing rare live CTCs and their quantification in whole blood so that it can provide a new approach for cancer diagnostics and therapeutics. An aptamer-functionalized hydrogel was also reported that could catch CTCs with a density over 1,000 cells/mm^2. When the hydrogel was coated by restriction endonucleases, the bound cells were released from the hydrogel coating because of the endonuclease-mediated sequence-specific hydrolysis of the aptamer sequences. The release efficiency reached 99%. Importantly, 98% of the released cells maintained viability (118). Polyvalent aptamer-functionalized hydrogel could also induce cell attachment on the hydrogel in dynamic flow. The cell density on the hydrogel was increased from 40 cells/mm^2 to nearly 700 cells/mm^2 when the shear stress was decreased from 0.05 to 0.005 Pa. After the attachment onto the hydrogel surface, approximately 95% of the cells could be triggered to detach within 20 min by using an oligonucleotide complementary sequence that displaced polyvalent aptamer strands from the hydrogel surface (119).

Capture and Release of Protein

To develop the efficient systems for the protection and sustained release of encapsulated molecules would be beneficial in

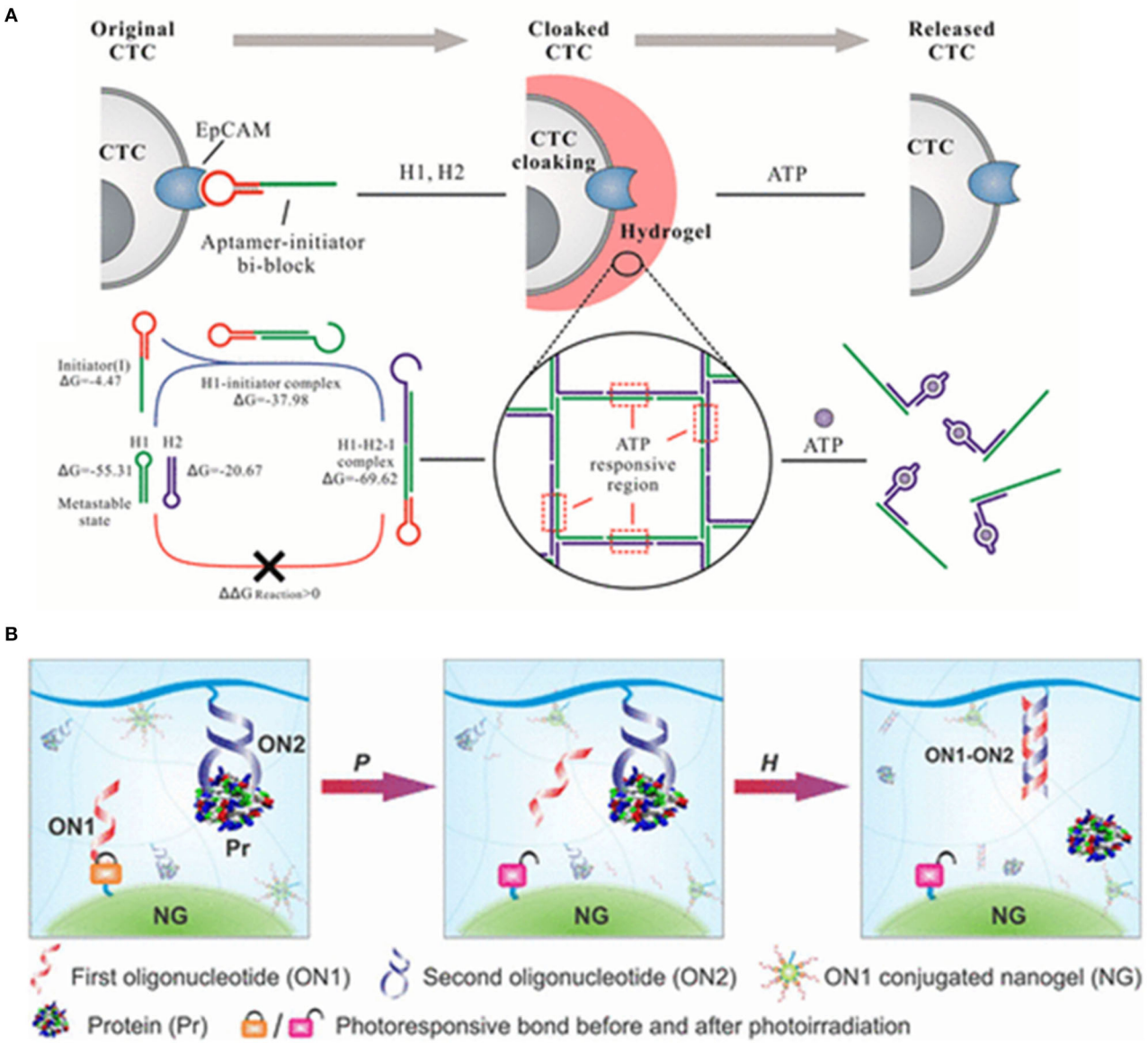

FIGURE 3 | (A) DNA hydrogel with aptamer-toehold-based recognition, cloaking, and decloaking of circulating tumor cells for live cell analysis, reprinted with permission from Tan et al. (113). Copyright (2017) American Chemical Society. **(B)** Programmable self-assembly of protein-scaffolded dna nanohydrogels for tumor-targeted imaging and therapy, reprinted with permission from Pasparakis et al. (116). Copyright (2019) American Chemical Society.

improving how we treat disease and study complex biochemical processes. Exogenous signaling molecules as biochemical cues promoted mesenchymal stem cells (MSCs) survival, presumably because MSCs themselves can release a variety of potent signaling molecules. Zhao et al. (120) examined whether the release of exogenous signaling molecules from hydrogels can promote the survival of MSC spheroids. They thought that aptamer-functionalized fibrin hydrogel (aFn) could release exogenous VEGF and PDGF-BB in a sustained manner. PDGF-BB-loaded aFn could double the survival rate of MSC spheroids in comparison with VEGF-loaded aFn during the 1-week test *in vivo*. Therefore, aptamer-based hydrogels have been considered as the new and promising materials which could be used for encapsulating a variety of biomacromolecules because they are responsive to environmental changes and multiple stimulus could trigger conformational or chemical changes of elastic network in hydrogels resulting in deswelling or degrading of hydrogels. Aptamer-based hydrogels have been utilized as smart systems with sensitivities toward various non-invasive stimuli. However, several factors, including the pore size of the polymer network, the diffusion rate of the entrapped target molecule, and the affinity between the aptamer and target molecule

usually influence the functionality and efficiency of aptamer-based hydrogels as capture-release systems (85, 116, 121–123). Moreover, biochemical signals or biomarkers stimuli are subtle or presented at subnanomolar concentrations. Therefore, a sensitive signal trigger is usually necessary to control the release of preloaded effectors in aptamer-based hydrogels (124–127). Recently, Lai et al. (128) developed new responsive hydrogels for controlled protein release by multistep molecular recognition events. Two oligonucleotides were integrated into the system as pendant motifs. The first oligonucleotide was used to covalently construct a hydrogel nanoparticle via a photolabile linker; and the other aptamer which could form a protein-DNA complex, was covalently conjugated to the bulk hydrogel network. When the hydrogel system was exposed to an external light signal, the nanogel was activated and dissociated. Subsequently, the freed oligonucleotide would hybridize with aptamer strands to induce the dissociation of the protein-DNA complex to release the bound protein (**Figure 3B**).

Capture and Release of Pollutants

An aptamer-based hydrogel was developed for water remediation with both high selectivity and multiple adsorbing abilities for several pollutants. In water remediation techniques, the contradiction between selectivity and multiple adsorptions limited this approach for environmental crisis previously (129). Aptamers in hydrogel were used to accommodate the molecular structure of pollutants in the scavenger and afforded the perfect selectivity. Meanwhile, Janus nanoparticles with an antibacterial function, in which aptamers were on the anisotropic surfaces to handle different kinds of pollutants. The final hydrogel scavenger was prepared by entrapping aptamer-functionalized Janus nanoparticles into a porous cellulose hydrogel. An aptamer column for the removal of trace pharmaceuticals in drinking water was reported (130). 5′-Aminomodified DNA aptamer bound to CNBr-Sepharose as sorbent was packed into gel as a column to simultaneously test cocaine and diclofenac in drinking water. The removal of pharmaceuticals was as high as 88–95%. The aptamer column was reusable and achieved a high removal efficiency from 4°C to 30°C in normal cation ion concentrations (5–100 mg L^{-1}) for multiple pollutants without cross effects and secondary pollution.

Aptamer-Based Hydrogels for Logic Devices

Nucleic acid molecules can be rationally designed, synthesized, and further integrated into Boolean operations, which provided an unprecedented potential to develop the basic components of molecular computing devices, because nucleic acid have high-capacity and low-maintenance digital information storage due to their predictable structures, high throughput synthesis and sequencing techniques (131, 132). Nucleic acid-based logic devices were first introduced in 1994 by Adleman and Lipton to solve the directed Hamiltonian path problem and the "SAT" question in computer science with single-stranded DNA sequences and enzymes (133, 134). Since then, science has seen the emergence of new logic systems for mimicking mathematical functions, diagnosing disease and even imitating biological systems (135–142). In recent years, logic gate systems based on aptamer-based hydrogels have attracted remarkable attention due to their intelligent responses to the external stimuli and convert input signals into a certain output signal.

Comparing this to silicon-based computation, although many challenges in designing computation devices, aptamer-based hydrogels logic circuits are still developing with great rapidity, due to their stability, biocompatibility, and predictable structure (143–146). Yin et al. (147) exploited a hydrogel structure based on hybridization behavior between crosslinker strands with aptamer sequences of ATP and cocaine molecules onto polymer chains. As detecting signals output, the BSA-modified gold nanoparticles were trapped in the hydrogel. The hydrogel served as an "AND" logic gate, when both cocaine and ATP presented, it was dissolved and led to the release of entrapped AuNPs And, the "OR" logic gate was reached if either cocaine or ATP presented, which led to the collapse of the hydrogel and release of the AuNPs. A novel colorimetric logic system based on an aptamer-crosslinked colloidal crystal hydrogel was also reported (148). When the Hg^{2+} and Ag^{+} responsive aptamers was incorporated into hydrogels, the reversible binding between the specific target ion (Hg^{2+} and Ag^{+}) could induce the conformational change of the aptamers and thus make shrinkage of the hydrogels with different stimuli. The visualization of the logic output signals was realized, the aptamer-crosslinked hydrogel displayed a shrinking response and color change corresponding to a logical "OR" and "AND" gate when the stimuli of Hg^{2+} and Ag^{+} at a concentration of 0.1 μM was input.

Bi et al. (149) reported a DNA four-way junction (DNA-4WJ) which is target-catalytically formed through cascade assembly of four DNA hairpins on the basis of DNA TM-SDR. A concatenated logic circuit composed of one YES gate and three AND gates with an automatic reset function by using four DNA hairpins as inputs was fabricated and the formed DNA-4WJs serving as building units to construct DNA nanohydrogels (∼120 nm). By incorporating aptamers, bioimaging agents, and drug loading sites into the building unit aptamer-based DNA nanohydrogels were synthesized with high loading capacity, target ability and good biocompatibility (**Figure 4**).

For traditional silicon circuitry, logic devices of aptamer-based hydrogels showed more powerful functions in medical diagnosis (150, 151), *in situ* analysis (151), and artificial intelligence. However, this is still in its infancy. Most of the reported works are conceptional, with isolated logic functions and limited applications. The breakthrough and development of novel design and construction might promote the development of logic devices of aptamer-based hydrogels.

Aptamer-Based Hydrogels for Multifunctional Gene and Cancer Therapy

Gene therapy is a promising approach for the treatment of inherited diseases, such as cancers, hemophilia, and viral infections. It depends mainly on the research and development of the delivery vectors for gene. To achieve the safety and efficiency of gene delivery vectors, there remain many technical barriers

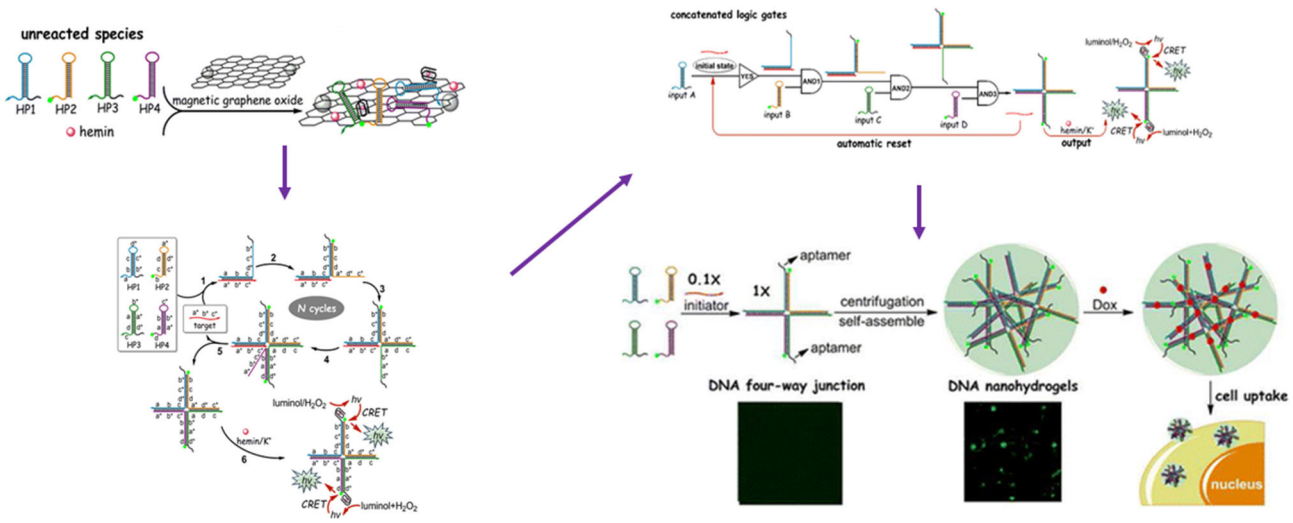

FIGURE 4 | Schematic Illustration of the four-input concatenated logic gates based on target-catalyzed DNA four-way junctions. Reprinted with permission from Ramezani and Dietz (143). Copyright (2015) American Chemical Society.

to explore the potential of gene therapy. To date, gene therapy vectors mainly include viral vectors and non-viral vectors. Viral vectors are widely used for efficient gene transfer, but they are usually high-risk for immunogenicity and mutagenicity. In several clinical cases, their use has resulted in patient death. Compared with viral vectors, non-viral vectors are safer and more desirable. Therefore, the development of safe non-viral vectors is highly desirable (97, 149, 152, 153).

Recently, a variety of non-viral vectors, including liposomes (154), micelles (155), inorganic nanoparticles (156, 157), DNA nanostructures (73), and polymeric nano-hydrogel (158), have been explored as delivery vector for gene therapy. Among these, aptamer-based hydrogels are used as strong delivery vector candidates owing to their high payload capacity, as well as their biocompatibility, flexibility, and mechanical stability (78, 159, 160) as **Table 1** shown. Tan (97) created a self-assembly process using three kinds of building units, Y-shaped monomer A with three sticky ends (YMA), Y-shaped monomer B with one sticky end (YMB), and DNA linker (LK) with two sticky ends, to hybridize a DNA nanohydrogel. By incorporating aptamers, disulfide linkages, and therapeutic genes into different building units, the aptamer-based DNA nanohydrogels (Y-gel-Apt) were formatted for targeted and stimuli-responsive gene therapy. And, a new intelligent DNA nano system integrating targeting, immunostimulant, and chemotherapy was also prepared based on unmethylated cytosine-phosphate-guanine oligonucleotides (CpG ODNs) DNA nanohydrogels (CpG-MUC1-hydrogel) (163). The cross-shaped DNAs (C-DNAs) assembled from pH-responsive I-motif sequences and targeted MUC1 aptamer-immunoadjuvant CpG-fused sequences (CpG-MUC1) were integrated into DNA nanohydrogels. DOX was successively intercalated into the base pairs of CpG-MUC1-hydrogel to form the CpG-MUC1-hydrogel/Dox that would controllably release DOX and CpGs at acidic conditions (**Figure 5A**). Moreover, a new class of physically cross-linked nanogel based on DNA, protein, and biotin as a nanocarrier using for the targeted cancer therapy was reported (162). The specific molecular recognition interaction between biotin and streptavidin was used to explore the cross-linking of a nanogel. The selective uptake of a doxorubicin-loaded nanogel by aptamer-receptor-positive cell lines (CCRF-CEM and HeLa) resulted in the specific interaction between the aptamer DNA decorated on the surface of the nanogel with the PTK7 receptor overexpressed on CCRF-CEM and HeLa cell lines (**Figure 5B**).

During clinical treatment, the side effects and accuracy of drug molecules in intravenous chemotherapy are the main topic of discussion for treatment. To design multifunctional therapeutic delivery nanoplatforms would overcome these limitations. A protein-scaffolded aptamer DNA nanohydrogel was fabricated by three types of streptavidin (SA)-based DNAtetrad accompanying with the further incorporation of therapeutic agents and tumor-targeting MUC1 aptamer. In an ATP-rich intracellular environment, this aptamer DNA nanohydrogel specifically targeted cancer cells and selectively released the preloaded therapeutic agents via a structure switching to attain the image and treatment of cancer cells (94). Furthermore, a novel class of physically cross-linked nanogels solely made of DNA, protein, and biotin were designed and the biotin–streptavidin molecular recognition interaction was used for the physical cross-linking of DNA nanostructures. Biotin-modified ssDNAs were assembled to form 5′-biotin-tethered X-shaped branched DNA acting as a tetravalent host and then streptavidin-modified aptamer DNAs interacted with them to form the aptamer-based hydrogels which allowed the loading of doxorubicin inside

TABLE 1 | A list of aptamer-based hydrogels for multifunctional gene and cancer therapy.

Hydrogel materials	Aptamer function	Agents	Therapy application	References
DNA	Bioactive Groups	Dox	On-demand drug release upon H2O2	(161)
DNA	Bioactive Groups	mRNA, MMP-9	GSH induce release of therapeutic genes	(97)
DNA	Bioactive Groups	Dox	Protonation triggering the release of the encapsulated drug	(162)
Polyacrylamide	Bioactive Groups	Dox	Near-infrared light-responsive drug delivery	(124)
DNA	Bioactive Groups	DOX, CpGs	pH induces transition of I-motif sequences	(163)
Polyacrylamide	Cross-linkers	Dox	Target protein nucleolin leads the gel to dissolve as a result of reducing the cross-linking density by competitive target-aptamer binding.	(164)
DNA, PLL-g-Dex	Cross-linkers	protein drugs	Complementary sequences (CSs) of aptamer induce release of protein	(165–167)
Carboxymethyl chitosan	Cross-linkers	Dox	ATP triggering sol–gel transition and DOX release	(166)

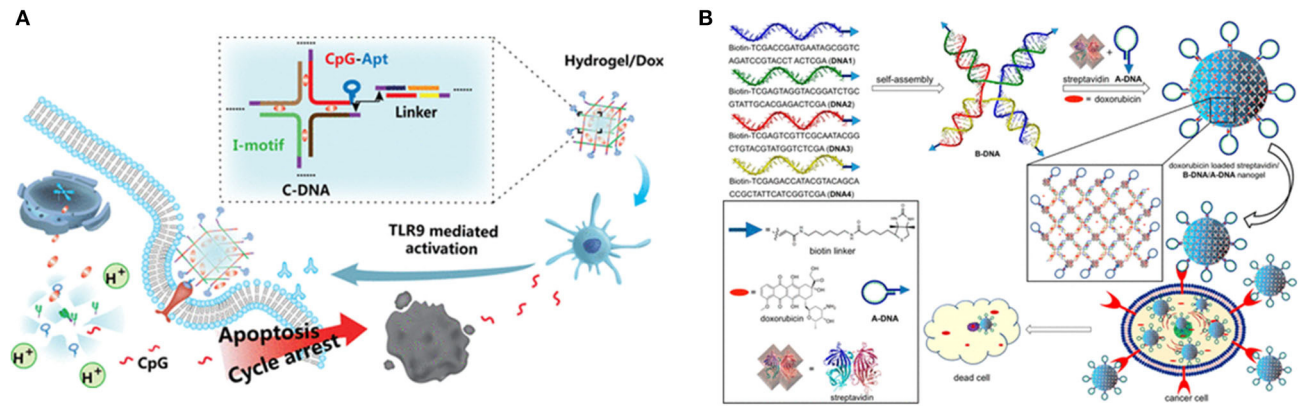

FIGURE 5 | (A) Schematic diagram of the synthesis and action procedure of CpG-MUC1-hydrogel/Dox. Reprinted with permission from Ding et al. (168). Copyright (2019) American Chemical Society. **(B)** Doxorubicin-loaded nanogels using for delivery of doxorubicin. Reprinted with permission from Mazloumi Tabrizi et al. (154). Copyright (2019) American Chemical Society.

the gel network and delivered in the cancerous environment. The aptamer-functionalized and doxorubicin-loaded nanogels exhibited selective uptake into target cell lines (162). In the clinical treatment of tumors, the delivery of drugs or genes, nanogels nanocarriers need long term circulation in the blood, enhanced permeability and retention effect (EPR effect), enrichment, infiltration, uptake, and release of the drug or gene. Aptamer-based hydrogels as intelligent nanocarriers demonstrated excellent biocompatibility and high selectivity for target cancer cells (156, 169).

CONCLUSIONS AND PERSPECTIVES

In summary, the recent progress in preparing aptamer-based hydrogels has made these kinds of materials accessible for encouraging applications in bioanalytical and biomedical fields. Aptamer DNA as the unique building blocks have prompted the development in sensitive biosensors, drug delivery systems, and cellular scaffolds for regenerative therapies. In this review, we divided aptamer-based hydrogels into two categories according to the gelation mechanism: aptamer as cross-linkers, bioactive groups or as tags for Functionalization. Various synthetic strategies and applications have been detailed. It is worth noting that the aptamer technology enables the design of DNA hydrogels that can detect almost any type of analyte with high selectivity and sensitivity. New aptamers are easy to generate which would lead to continue to growth of addressable targets. Despite the tremendous progress in the development of aptamer-based hydrogels, several challenges remained: (1) Aptamer-based hydrogels, as DNA hydrogels have low storage modulus and consequent thixotropic property, in which the strength is much lower than of most conventional polymers. It is crucial to regulate the mechanical properties for biological applications (78). (2) Mechanism studies on synthesis and responsiveness of aptamer-based hydrogels are needed to promote the development of hydrogels in biosensing, controlled release, and tissue engineering. Although the release profile of some stimuli-responsive hydrogels has been investigated, theoretically kinetic studies are rarely reported to reveal the release characteristics of aptamer-based hydrogels. Deeper kinetic studies will promote the design of aptamer-based hydrogels for biological applications. (3) There are still some problems in large scale applications of aptamer-based hydrogels because of their high cost and difficulty of preparation. To develop more techniques and novel synthetic methods to obtain more aptamer DNA should be mainly considered in order to

reduce the cost. Furthermore, to explore new materials to hybrid with aptamer to construct multiple hydrogels is also a solution for cost concern.

AUTHOR CONTRIBUTIONS

YD: conceptualization and writing-original draft preparation. PW: conceptualization. CL: investigation. QT and TW: investigation and writing-original draft preparation. YT and LG: supervision. SX: writing-reviewing and Editing. All authors read and approved the final manuscript.

FUNDING

This research was supported by the Key Research and Development Program of Qin Huang Dao (201602A110).

REFERENCES

1. Ganji F, Vasheghani Farahani S, Vasheghani Faraahani E. Theoretical description of hydrogel swelling: a review. *Iran Polym J.* (2010) 19:375–98.
2. Li P, Poon YF, Li W, Zhu HY, Yeap SH, Cao Y, et al. A polycationic antimicrobial and biocompatible hydrogel with microbe membrane suctioning ability. *Nat Mater.* (2011) 10:149–56. doi: 10.1038/nmat2915
3. Annabi N, Tamayol A, Uquillas JA, Akbari M, Bertassoni LE, Cha C, et al. 25th anniversary article: rational design and applications of hydrogels in regenerative medicine. *Adv Mater.* (2014) 26:85–124. doi: 10.1002/adma.201303233
4. Liu S, Li L. Ultrastretchable and self-healing double-network hydrogel for 3d printing and strain sensor. *ACS Appl Mater Interfaces.* (2017) 9:26429–37. doi: 10.1021/acsami.7b07445
5. Willner I. Stimuli-controlled hydrogels and their applications. *Acc Chem Res.* (2017) 50:657–8. doi: 10.1021/acs.accounts.7b00142
6. Loebel C, Rodell CB, Chen MH, Burdick JA. Shear-thinning and self-healing hydrogels as injectable therapeutics and for 3D-printing. *Nat Protoc.* (2017) 12:1521–41. doi: 10.1038/nprot.2017.053
7. Liu X, Chen X, Chua MX, Li Z, Loh XJ, Wu Y-L. Cancer therapy: injectable supramolecular hydrogels as delivery agents of bcl-2 conversion gene for the effective shrinkage of therapeutic resistance tumors. Adv. *Healthc Mater.* (2017) 6. doi: 10.1002/adhm.201770053
8. Huang F, Scherman OA. Supramolecular polymers. *Chem Soc Rev.* (2012) 41:5879–80. doi: 10.1039/c2cs90071h
9. Voorhaar L, Diaz MM, Leroux F, Rogers S, Abakumov AM, Van Tendeloo G, et al. Supramolecular thermoplastics and thermoplastic elastomer materials with self-healing ability based on oligomeric charged triblock copolymers. *NPG Asia Mate.* (2017) 9:e385. doi: 10.1038/am.2017.63
10. Song P, Xu Z, Lu Y, Guo Q. Bio-Inspired hydrogen-bond cross-link strategy toward strong and tough polymeric materials. *Macromolecules.* (2015) 48:3957–64. doi: 10.1021/acs.macromol.5b00673
11. Zhang X, Qu W, Li D, Shi K, Li R, Han Y, et al. Functional polymer-based nerve guide conduits to promote peripheral nerve regeneration. *Adv Mater Interfaces.* (2020) 7:2000225. doi: 10.1002/admi.202000225
12. Leach DG, Dharmaraj N, Piotrowski SL, Lopez-Silva TL, Lei YL, Sikora AG, et al. STINGel: controlled release of a cyclic dinucleotide for enhanced cancer immunotherapy. *Biomaterials.* (2018) 163:67–75. doi: 10.1016/j.biomaterials.2018.01.035
13. Asai D, Kanamoto T, Takenaga M, Nakashima H. *In situ* depot formation of anti-HIV fusion-inhibitor peptide in recombinant protein polymer hydrogel. *Acta Biomater.* (2017) 64:116–25. doi: 10.1016/j.actbio.2017.10.024
14. Wu C, Liu J, Liu B, He S, Dai G, Xu B, et al. NIR light-responsive short peptide/2D NbSe2 nanosheets composite hydrogel with controlled-release capacity. *J Mater Chem B.* (2019) 7:3134–42. doi: 10.1039/C8TB03326A
15. Badeau BA, Comerford MP, Arakawa CK, Shadish JA, DeForest CA. Engineered modular biomaterial logic gates for environmentally triggered therapeutic delivery. *Nat Chem.* (2018) 10:251–8. doi: 10.1038/nchem.2917
16. Chu Z, Dreiss CA, Feng Y. Smart wormlike micelles. *Chem Soc Rev.* (2013) 42:7174–203. doi: 10.1039/c3cs35490c
17. Qiu H, Guo H, Li D, Hou Y, Kuang T, Ding J. Intravesical hydrogels as drug reservoirs. *Trends Biotechnol.* (2020) 38:579–83. doi: 10.1016/j.tibtech.2019.12.012
18. Klouda L. Thermoresponsive hydrogels in biomedical applications: a seven-year update. *Eur J Pharm Biopharma.* (2015) 97:338–49. doi: 10.1016/j.ejpb.2015.05.017
19. Pang X, Xie D, Ge X, Li Y, Zhen X, Yu X. Switchable sol-gel transition controlled by ultrasound and body temperature. *Supramol Chem.* (2016) 28:335–8. doi: 10.1080/10610278.2015.1102262
20. Xiong X, Wu C, Zhou C, Zhu G, Chen Z, Tan W. Responsive DNA-based hydrogels and their applications. *Macromol Rapid Commun.* (2013) 34:1271–83. doi: 10.1002/marc.201300411
21. Liu J. Oligonucleotide-functionalized hydrogels as stimuli responsive materials and biosensors. *Soft Matter.* (2011) 7:6757–67. doi: 10.1039/c1sm05284e
22. Deng G, Wong W-T, Huang M, Wu R, Lai W-F. Chapter 8—self-healing properties of hydrogels based on natural polymers. In: Chen Y, editor. *Hydrogels Based on Natural Polymers*. Hong Kong: Elsevier (2020). p. 223–45.
23. Cascone S, Lamberti G. Hydrogel-based commercial products for biomedical applications: a review. *Int J Pharma.* (2020) 573:118803. doi: 10.1016/j.ijpharm.2019.118803
24. Ornell KJ, Lozada D, Phan NV, Coburn JM. Controlling methacryloyl substitution of chondroitin sulfate: injectable hydrogels with tunable long-term drug release profiles. *J Mater Chem B.* (2019) 7:2151–61. doi: 10.1039/C8TB03020K
25. Pourreza N, Ghomi M. Hydrogel based aptasensor for thrombin sensing by Resonance Rayleigh Scattering. *Anal Chim Acta.* (2019) 1079:180–91. doi: 10.1016/j.aca.2019.06.049
26. Palmese LL, Thapa RK, Sullivan MO, Kiick KL. Hybrid hydrogels for biomedical applications. *Curr Opin Chem Eng.* (2019) 24:143–57. doi: 10.1016/j.coche.2019.02.010
27. Guo Z, Gu H, He Y, Zhang Y, Xu W, Zhang J, et al. Dual dynamic bonds enable biocompatible and tough hydrogels with fast self-recoverable, self-healable and injectable properties. *Chem Eng J.* (2020) 388:124282. doi: 10.1016/j.cej.2020.124282
28. Shao X, Feng Y, Zhu L, Zhang Y, Luo Y, Mei X, et al. Three dimensional DNA nanotracks: a novel method for ultrasensitive and visible mercury (II) detection. *Sensors Actuat B: Chem.* (2020) 303:126988. doi: 10.1016/j.snb.2019.126988
29. Liu X, Liu J, Lin S, Zhao X. Hydrogel machines. *Mater Today.* (2020) 36:102–24. doi: 10.1016/j.mattod.2019.12.026
30. Uygun M, Doganci E, Tasdelen MA, Gurek AG. One-pot photoinduced synthesis of dansyl containing acrylamide hydrogels and their chemosensing properties. *J Appl Polym Sci.* (2019) 136:47096. doi: 10.1002/app.47096
31. Torres L, Daristotle JL, Ayyub OB, Bellato Meinhardt BM, Garimella H, Margaronis A, et al. Structurally colored protease responsive nanoparticle hydrogels with degradation-directed assembly. *Nanoscale.* (2019) 11:17904–12. doi: 10.1039/C9NR04624K
32. Chen J, Xu L, Yang M, Chen X, Chen X, Hong W. Highly stretchable photonic crystal hydrogels for a sensitive mechanochromic sensor and direct ink writing. *Chem Mater.* (2019) 31:8918–26. doi: 10.1021/acs.chemmater.9b02961
33. Xu K, Lee F, Gao SJ, Chung JE, Yano H, Kurisawa M. Injectable hyaluronic acid-tyramine hydrogels incorporating interferon-α2a for liver cancer therapy. *J Control Release.* (2013)166:203–10. doi: 10.1016/j.jconrel.2013.01.008
34. Dosio F, Arpicco S, Stella B, Fattal E. Hyaluronic acid for anticancer drug and nucleic acid delivery. *Adv Drug Deliv Rev.* (2016) 97:204–36. doi: 10.1016/j.addr.2015.11.011
35. Tripodo G, Trapani A, Torre ML, Giammona G, Trapani G, Mandracchia D. Hyaluronic acid and its derivatives in drug delivery and imaging:

recent advances and challenges. *Eur J Pharm Biopharm.* (2015) 97:400–16. doi: 10.1016/j.ejpb.2015.03.032
36. Weiden J, Tel J, Figdor CG. Synthetic immune niches for cancer immunotherapy. *Nat Rev Immunol.* (2018) 18:212–9. doi: 10.1038/nri.2017.89
37. Talebian S, Foroughi J, Wade SJ, Vine KL, Dolatshahi-Pirouz A, Mehrali M, et al. Biopolymers for antitumor implantable drug delivery systems: recent advances and future outlook. *Adv Mater.* (2018) 30:1706665. doi: 10.1002/adma.201706665
38. Schmidt S, Zeiser M, Hellweg T, Duschl C, Fery A, Möhwald H. Adhesion and mechanical properties of pnipam microgel films and their potential use as switchable cell culture substrates. *Adv Funct Mater.* (2010) 20:3235–43. doi: 10.1002/adfm.201000730
39. Xia Y, Wu H, Tang D, Gao S, Chen B, Zeng Z, et al. Graphene oxide nanosheet-composited poly(n-isopropylacrylamide) hydrogel for cell sheet recovery. *Macromol Res.* (2019) 27:679–85. doi: 10.1007/s13233-019-7099-z
40. Liu J, Shang J, Chen Y, Tian Y, Yang Q, Chen M, et al. A surface-engineered NIR light-responsive actuator for controllable modulation of collective cell migration. *J Mater Chem B.* (2019) 7:5528–34. doi: 10.1039/C9TB01038F
41. Afewerki S, Sheikhi A, Kannan S, Ahadian S, Khademhosseini A. Gelatin-polysaccharide composite scaffolds for 3D cell culture and tissue engineering: towards natural therapeutics. *Bioeng Transl Med.* (2019) 4:96–115. doi: 10.1002/btm2.10124
42. Hosseini V, Maroufi NF, Saghati S, Asadi N, Darabi M, Ahmad SNS, et al. Current progress in hepatic tissue regeneration by tissue engineering. *J Transl Med.* (2019) 17:383. doi: 10.1186/s12967-019-02137-6
43. Caballero Aguilar LM, Silva SM, Moulton SE. Growth factor delivery: defining the next generation platforms for tissue engineering. *J Control Release.* (2019) 306:40–58. doi: 10.1016/j.jconrel.2019.05.028
44. Zhu T, Cui Y, Zhang M, Zhao D, Liu G, Ding J. Engineered three-dimensional scaffolds for enhanced bone regeneration in osteonecrosis. *Bioact Mater.* (2020) 5:584–601. doi: 10.1016/j.bioactmat.2020.04.008
45. Zhu Z, Wu C, Liu H, Zou Y, Zhang X, Kang H, et al. An aptamer cross-linked hydrogel as a colorimetric platform for visual detection. *Angew Chem Int Ed.* (2010) 49:1052–6. doi: 10.1002/anie.200905570
46. Kim J, Singh N, Lyon LA. Label-free biosensing with hydrogel microlenses. *Angew Chem Int Ed.* (2006) 45:1446–9. doi: 10.1002/anie.200503102
47. Liu J, Liu H, Kang H, Donovan M, Zhu Z, Tan W. Aptamer-incorporated hydrogels for visual detection, controlled drug release, and targeted cancer therapy. *Anal Bioanal Chem.* (2012) 402:187–94. doi: 10.1007/s00216-011-5414-4
48. Ostrovidov S, Salehi S, Costantini M, Suthiwanich K, Ebrahimi M, Sadeghian RB, et al. 3D bioprinting in skeletal muscle tissue engineering. *Small.* (2019). 15:1805530. doi: 10.1002/smll.201805530
49. Liang K, Bae KH, Kurisawa M. Recent advances in the design of injectable hydrogels for stem cell-based therapy. *J Mater Chem B.* (2019) 7:3775–91. doi: 10.1039/C9TB00485H
50. Ellington AD, Szostak JW. *In vitro* selection of RNA molecules that bind specific ligands. *Nature.* (1990) 346:818–22. doi: 10.1038/346818a0
51. Li M, Sato Y, Nishizawa S, Seino T, Nakamura K, Teramae N. 2-aminopurine-modified abasic-site-containing duplex dna for highly selective detection of theophylline. *J Am Chem Soc.* (2009). 131:2448–9. doi: 10.1021/ja8095625
52. Zheng D, Zou R, Lou X. Label-free fluorescent detection of ions, proteins, and small molecules using structure-switching aptamers, sybr gold, and exonuclease I. *Anal Chem.* (2012) 84:3554–60. doi: 10.1021/ac300690r
53. Shamsipur M, Fsrzin L, Amouzadeh Tabrizi M, Shanesaz M. CdTe amplification nanoplatforms capped with thioglycolic acid for electrochemical aptasensing of ultra-traces of ATP. *Mater Sci Eng C.* (2016) 69:1354–60. doi: 10.1016/j.msec.2016.08.038
54. Zhang S, Wang L, Liu M, Qiu Y, Wang M, Liu X, et al. A novel, label-free fluorescent aptasensor for cocaine detection based on a G-quadruplex and ruthenium polypyridyl complex molecular light switch. *Anal Methods.* (2016) 8:3740–6. doi: 10.1039/C6AY00231E
55. Amouzadeh Tabrizi M, Shamsipur M, Farzin L. A high sensitive electrochemical aptasensor for the determination of VEGF165 in serum of lung cancer patient. *Biosens Bioelectron.* (2015) 74:764–9. doi: 10.1016/j.bios.2015.07.032
56. Shamsipur M, Farzin L, Tabrizi MA. Ultrasensitive aptamer-based on-off assay for lysozyme using a glassy carbon electrode modified with gold nanoparticles and electrochemically reduced graphene oxide. *Microchim Acta.* (2016) 183:2733–43. doi: 10.1007/s00604-016-1920-6
57. Mir TA, Yoon J-H, Gurudatt NG, Won M-S, Shim Y-B. Ultrasensitive cytosensing based on an aptamer modified nanobiosensor with a bioconjugate: detection of human non-small-cell lung cancer cells. *Biosens Bioelectron.* (2015) 74:594–600. doi: 10.1016/j.bios.2015.07.012
58. Wang T, Liu J, gu X, Li D, Wang J, Wang E. Label-free electrochemical aptasensor constructed by layer-by-layer technology for sensitive and selective detection of cancer cells. *Anal Chim Acta.* (2015) 882:32–7. doi: 10.1016/j.aca.2015.05.008
59. Trachman RJ, Ferré-D'Amaré AR. Tracking RNA with light: selection, structure, and design of fluorescence turn-on RNA aptamers. *Q Rev Biophy.* (2019) 52:e8. doi: 10.1017/S0033583519000064
60. Munzar JD, Ng A, Juncker D. Duplexed aptamers: history, design, theory, and application to biosensing. *Chem Soc Rev.* (2019) 48:1390–419. doi: 10.1039/C8CS00880A
61. Samanta D, Ebrahimi SB, Mirkin CA. Nucleic-acid structures as intracellular probes for live cells. *Adv Mater.* (2019) 32:1901743. doi: 10.1002/adma.201901743
62. Agnew HD, Coppock MB, Idso MN, Lai BT, Liang J, McCarthy-Torrens AM, et al. Protein-catalyzed capture agents. *Chem Rev.* (2019) 119:9950–70. doi: 10.1021/acs.chemrev.8b00660
63. Tuerk C, Gold L. Systematic evolution of ligands by exponential enrichment: RNA ligands to bacteriophage T4 DNA polymerase. *Science.* (1990) 249:505–10. doi: 10.1126/science.2200121
64. Cho EJ, Lee J-W, Ellington AD. Applications of aptamers as sensors. *Annu Rev Anal Chem.* (2009) 2:241–64. doi: 10.1146/annurev.anchem.1.031207.112851
65. Gačanin J, Synatschke CV, Weil T. Biomedical applications of DNA-based hydrogels. *Adv Funct Mater.* (2020) 30:1906253. doi: 10.1002/adfm.201906253
66. Battig MR, Huang Y, Chen N, Wang Y. Aptamer-functionalized superporous hydrogels for sequestration and release of growth factors regulated via molecular recognition. *Biomaterials.* (2014) 35:8040–8. doi: 10.1016/j.biomaterials.2014.06.001
67. Battig MR, Soontornworajit B, Wang Y. Programmable release of multiple protein drugs from aptamer-functionalized hydrogels via nucleic acid hybridization. *J Am Chem Soc.* (2012) 134:12410–3. doi: 10.1021/ja305238a
68. Bae KH, Wang L-S, Kurisawa M. Injectable biodegradable hydrogels: progress and challenges. *J Mater Chem B.* (2013) 1:5371–88. doi: 10.1039/c3tb20940g
69. Rusconi CP, Scardino E, Layzer J, Pitoc GA, Ortel TL, Monroe D, et al. RNA aptamers as reversible antagonists of coagulation factor IXa. *Nature.* (2002) 419:90–4. doi: 10.1038/nature00963
70. Rusconi CP, Roberts JD, Pitoc GA, Nimjee SM, White RR, Quick G, et al. Antidote-mediated control of an anticoagulant aptamer *in vivo*. *Nat Biotechnol.* (2004) 22:1423–8. doi: 10.1038/nbt1023
71. Liu J, Lu Y. Non-base pairing dna provides a new dimension for controlling aptamer-linked nanoparticles and sensors. *J Am Chem Soc.* (2007) 129:8634–43. doi: 10.1021/ja072075+
72. Yang CJ, Jockusch S, Vicens M, Turro NJ, Tan W. Light-switching excimer probes for rapid protein monitoring in complex biological fluids. *Proc Natl Acad Sci USA.* (2005) 102:17278. doi: 10.1073/pnas.0508821102
73. Wu C, Han D, Chen T, Peng L, Zhu G, You M, et al. Building a multifunctional aptamer-based dna nanoassembly for targeted cancer therapy. *J Am Chem Soc.* (2013) 135:18644–50. doi: 10.1021/ja4094617
74. Xiang D, Shigdar S, Qiao G, Wang T, Kouzani AZ, Zhou S-F, et al. Nucleic acid aptamer-guided cancer therapeutics and diagnostics: the next generation of cancer medicine. *Theranostics.* (2015) 5:23–42. doi: 10.7150/thno.10202
75. Hu Q, Li H, Wang L, Gu H, Fan C. DNA nanotechnology-enabled drug delivery systems. *Chem Rev.* (2019) 119:6459–506. doi: 10.1021/acs.chemrev.7b00663
76. Liang H, Zhang X-B, Lv Y, Gong L, Wang R, Zhu X, et al. Functional DNA-containing nanomaterials: cellular applications in biosensing, imaging,

and targeted therapy. *Acc Chem Res.* (2014) 47:1891–901. doi: 10.1021/ar500078f
77. Li F, Lyu D, Liu S, Guo W. DNA Hydrogels and microgels for biosensing and biomedical applications. *Adv Mater.* (2020) 32:1806538. doi: 10.1002/adma.201806538
78. Zhou L, Jiao X, Liu S, Hao M, Cheng S, Zhang P, et al. Functional DNA-based hydrogel intelligent materials for biomedical applications. *J Mater Chem B.* (2020) 8:1991–2009. doi: 10.1039/C9TB02716E
79. Li C, Faulkner-Jones A, Dun AR, Jin J, Chen P, Xing Y, et al. Rapid Formation of a supramolecular polypeptide–dna hydrogel for in situ three-dimensional multilayer bioprinting. *Angew Chem Int Ed.* (2015) 54:3957–61. doi: 10.1002/anie.201411383
80. Kahn JS, Hu Y, Willner I. Stimuli-responsive dna-based hydrogels: from basic principles to applications. *Acc Chem Res.* (2017) 50:680–90. doi: 10.1021/acs.accounts.6b00542
81. Lu C-H, Guo W, Hu Y, Qi X-J, Willner I. Multitriggered shape-memory acrylamide–DNA hydrogels. *J Am Chem Soc.* (2015) 137:15723–31. doi: 10.1021/jacs.5b06510
82. Previtera ML, Chippada U, Schloss RS, Yurke B, Langrana NA. Mechanical properties of DNA-crosslinked polyacrylamide hydrogels with increasing crosslinker density. *Biores Open Access.* (2012) 1:256–9. doi: 10.1089/biores.2012.9906
83. Wang Q, Hu Y, Jiang N, Wang J, Yu M, Zhuang X. Preparation of aptamer responsive DNA functionalized hydrogels for the sensitive detection of α-fetoprotein using SERS method. *Bioconjug Chem.* (2020) 31:813–20. doi: 10.1021/acs.bioconjchem.9b00874
84. Lai J, Li S, Shi X, Coyne J, Zhao N, Dong F, et al. Displacement and hybridization reactions in aptamer-functionalized hydrogels for biomimetic protein release and signal transduction. *Chem Sci.* (2017) 8:7306–11. doi: 10.1039/C7SC03023A
85. Yang H, Liu H, Kang H, Tan W. Engineering target-responsive hydrogels based on aptamer–target interactions. *J Am Chem Soc.* (2008) 130:6320–1. doi: 10.1021/ja801339w
86. Zhou L, Chen C, Ren J, Qu X. Towards intelligent bioreactor systems: triggering the release and mixing of compounds based on DNA-functionalized hybrid hydrogel. *Chem Commun.* (2014) 50:10255–7. doi: 10.1039/C4CC04791E
87. Zhang L, Lei J, Liu L, Li C, Ju H. Self-assembled DNA hydrogel as switchable material for aptamer-based fluorescent detection of protein. *Anal Chem.* (2013) 85:11077–82. doi: 10.1021/ac4027725
88. Zhou L, Sun N, Xu L, Chen X, Cheng H, Wang J, et al. Dual signal amplification by an "on-command" pure DNA hydrogel encapsulating HRP for colorimetric detection of ochratoxin A. *RSC Adv.* (2016) 6:114500–4. doi: 10.1039/C6RA23462C
89. Muckley ES, Naguib M, Wang H-W, Vlcek L, Osti NC, Sacci RL, et al. Multimodality of structural, electrical, and gravimetric responses of intercalated mxenes to water. *ACS Nano.* (2017) 11:11118–26. doi: 10.1021/acsnano.7b05264
90. Simon AJ, Walls-Smith LT, Plaxco KW. Exploiting the conformational-selection mechanism to control the response kinetics of a "smart" DNA hydrogel. *Analyst.* (2018) 143:2531–8. doi: 10.1039/C8AN00337H
91. Wang X, Wang X. Aptamer-functionalized hydrogel diffraction gratings for the human thrombin detection. *Chem Commun.* (2013) 49:5957–9. doi: 10.1039/c3cc41827h
92. Soontornworajit B, Zhou J, Zhang Z, Wang Y. Aptamer-functionalized in situ injectable hydrogel for controlled protein release. *Biomacromolecules.* (2010) 11:2724–30. doi: 10.1021/bm100774t
93. Song P, Ye D, Zuo X, Li J, Wang J, Liu H, et al. DNA hydrogel with aptamer-toehold-based recognition, cloaking, and decloaking of circulating tumor cells for live cell analysis. *Nano Lett.* (2017) 17:5193–8. doi: 10.1021/acs.nanolett.7b01006
94. Li N, Wang X-Y, Xiang M-H, Liu J-W, Yu R-Q, Jiang J-H. Programmable self-assembly of protein-scaffolded dna nanohydrogels for tumor-targeted imaging and therapy. *Anal Chem.* (2019) 91:2610–4. doi: 10.1021/acs.analchem.8b05706
95. El-Hamed F, Dave N, Liu J. Stimuli-responsive releasing of gold nanoparticles and liposomes from aptamer-functionalized hydrogels. *Nanotechnology.* (2011) 22:494011. doi: 10.1088/0957-4484/22/49/494011
96. Liu C, Han J, Pei Y, Du J. Aptamer functionalized dna hydrogel for wise-stage controlled protein release. *Appl Sci.* (2018) 8:1941. doi: 10.3390/app8101941
97. Li J, Zheng C, Cansiz S, Wu C, Xu J, Cui C, et al. Self-assembly of DNA nanohydrogels with controllable size and stimuli-responsive property for targeted gene regulation therapy. *J Am Chem Soc.* (2015) 137:1412–5. doi: 10.1021/ja512293f
98. Srinivas RL, Chapin SC, Doyle PS. Aptamer-functionalized microgel particles for protein detection. *Anal Chem.* (2011) 83:9138–45. doi: 10.1021/ac202335u
99. Meng HM, Liu H, Kuai H, Peng R, Mo L, Zhang XB. Aptamer-integrated DNA nanostructures for biosensing, bioimaging and cancer therapy. *Chem Soc Rev.* (2016) 45:2583–602. doi: 10.1039/C5CS00645G
100. Li J, Mo L, Lu C-H, Fu T, Yang H-H, Tan W. Functional nucleic acid-based hydrogels for bioanalytical and biomedical applications. *Chem Soc Rev.* (2016) 45:1410–31. doi: 10.1039/C5CS00586H
101. Baruah U, Chowdhury D. Functionalized graphene oxide quantum dot–PVA hydrogel: a colorimetric sensor for Fe2+, Co2+and Cu2+ions. *Nanotechnology.* (2016) 27:145501. doi: 10.1088/0957-4484/27/14/145501
102. Tian T, Wei X, Jia S, Zhang R, Li J, Zhu Z, et al. Integration of target responsive hydrogel with cascaded enzymatic reactions and microfluidic paper-based analytic devices (μPADs) for point-of-care testing (POCT). *Biosens Bioelectron.* (2016) 77:537–42. doi: 10.1016/j.bios.2015.09.049
103. Guo W, Orbach R, Mironi-Harpaz I, Seliktar D, Willner I. Fluorescent DNA hydrogels composed of nucleic acid-stabilized silver nanoclusters. *Small.* (2013) 9:3748–52. doi: 10.1002/smll.201300055
104. Wang J, Wang X, Tang H, He S, Gao Z, Niu R, et al. A ratiometric magnesium sensor using DNAzyme-templated CdTe quantum dots and Cy5. *Sensors Actuat B: Chem.* (2018) 272:146–50. doi: 10.1016/j.snb.2018.05.162
105. Wang J, Gao Z, He S, Jin P, Ma D, Gao Y, et al. A universal growth strategy of DNA-programmed quantum dots on graphene oxide surface. *Nanotechnology.* (2020) 31:24LT02. doi: 10.1088/1361-6528/ab7c42
106. Wang J, Zhai J, Han S. Non-injection one-pot preparation strategy for multiple families of magic-sized CdTe quantum dots with bright bandgap photoemission. *Chem Eng J.* (2013) 215–216:23–8. doi: 10.1016/j.cej.2012.10.092
107. Zheng Y, Wang X, He S, Gao Z, Di Y, Lu K, et al. Aptamer-DNA concatamer-quantum dots based electrochemical biosensing strategy for green and ultrasensitive detection of tumor cells via mercury-free anodic stripping voltammetry. *Biosens Bioelectron.* (2019) 126:261–8. doi: 10.1016/j.bios.2018.09.076
108. Liu R, Huang Y, Ma Y, Jia S, Gao M, Li J, et al. Design and synthesis of target-responsive aptamer-cross-linked hydrogel for visual quantitative detection of ochratoxin A. *ACS Appl Mater Interfaces.* (2015) 7:6982–90. doi: 10.1021/acsami.5b01120
109. Deshpande SR, Hammink R, Nelissen FHT, Rowan AE, Heus HA. Biomimetic stress sensitive hydrogel controlled by DNA nanoswitches. *Biomacromolecules.* (2017) 18:3310–7. doi: 10.1021/acs.biomac.7b00964
110. Li Y, Ma Y, Jiao X, Li T, Lv Z, Yang CJ, et al. Control of capillary behavior through target-responsive hydrogel permeability alteration for sensitive visual quantitative detection. *Nat Commun.* (2019) 10:1036. doi: 10.1038/s41467-019-08952-1
111. Xu Y, Wu Q, Sun Y, Bai H, Shi G. Three-dimensional self-assembly of graphene oxide and DNA into multifunctional hydrogels. *ACS Nano.* (2010) 4:7358–62. doi: 10.1021/nn1027104
112. Zhu Y, Cai Y, Xu L, Zheng L, Wang L, Qi B, et al. Building an aptamer/graphene oxide fret biosensor for one-step detection of bisphenol A. *ACS Appl Mater Interfaces.* (2015) 7:7492–6. doi: 10.1021/acsami.5b00199
113. Tan B, Zhao H, Du L, Gan X, Quan X. A versatile fluorescent biosensor based on target-responsive graphene oxide hydrogel for antibiotic detection. *Biosens Bioelectron.* (2016) 83:267–73. doi: 10.1016/j.bios.2016.04.065
114. De Mattos-Arruda L, Tabernero J, Seoane J, Cortes J. Circulating tumour cells in early breast cancer. *Lancet Oncol.* (2012) 13:e370. doi: 10.1016/S1470-2045(12)70316-9
115. Ji X, Wang J, Niu S, Ding C. Size-controlled DNA-cross-linked hydrogel coated silica nanoparticles served as a ratiometric fluorescent probe for the

detection of adenosine triphosphate in living cells. *Chem Commun.* (2019) 55:5243–6. doi: 10.1039/C9CC01832H
116. Pasparakis G, Manouras T, Vamvakaki M, Argitis P. Harnessing photochemical internalization with dual degradable nanoparticles for combinatorial photo–chemotherapy. *Nat Commun.* (2014) 5:3623. doi: 10.1038/ncomms4623
117. Ye D, Li M, Zhai T, Song P, Song L, Wang H, et al. Encapsulation and release of living tumor cells using hydrogels with the hybridization chain reaction. *Nat Protoc.* (2020) 15:2163–85. doi: 10.1038/s41596-020-0326-4
118. Li S, Chen N, Zhang Z, Wang Y. Endonuclease-responsive aptamer-functionalized hydrogel coating for sequential catch and release of cancer cells. *Biomaterials.* (2013) 34:460–9. doi: 10.1016/j.biomaterials.2012.09.040
119. Gaddes ER, Gydush G, Li S, Chen N, Dong C, Wang Y. Aptamer-based polyvalent ligands for regulated cell attachment on the hydrogel surface. *Biomacromolecules.* (2015) 16:1382–9. doi: 10.1021/acs.biomac.5b00165
120. Zhao N, Coyne J, Abune L, Shi P, Lian XL, Zhang G, et al. Exogenous signaling molecules released from aptamer-functionalized hydrogels promote the survival of mesenchymal stem cell spheroids. *ACS Appl Mater Interfaces.* (2020) 12:24599–610. doi: 10.1021/acsami.0c05681
121. Tomatsu I, Peng K, Kros A. Photoresponsive hydrogels for biomedical applications. *Adv Drug Deliv Rev.* (2011) 63:1257–66. doi: 10.1016/j.addr.2011.06.009
122. Fomina N, Sankaranarayanan J, Almutairi A. Photochemical mechanisms of light-triggered release from nanocarriers. *Adv Drug Deliv Rev.* (2012) 64:1005–20. doi: 10.1016/j.addr.2012.02.006
123. Yan B, Boyer J-C, Habault D, Branda NR, Zhao Y. Near infrared light triggered release of biomacromolecules from hydrogels loaded with upconversion nanoparticles. *J Am Chem Soc.* (2012) 134:16558–61. doi: 10.1021/ja308876j
124. Kang H, Trondoli AC, Zhu G, Chen Y, Chang Y-J, Liu H, et al. Near-infrared light-responsive core–shell nanogels for targeted drug delivery. *ACS Nano.* (2011) 5:5094–9. doi: 10.1021/nn201171r
125. Vermonden T, Censi R, Hennink WE. Hydrogels for protein delivery. *Chem Rev.* (2012) 112:2853–88. doi: 10.1021/cr200157d
126. Hu Y, Guo W, Kahn JS, Aleman-Garcia MA, Willner I. A shape-memory DNA-based hydrogel exhibiting two internal memories. *Angew Chem Int Ed.* (2016) 55:4210–4. doi: 10.1002/anie.201511201
127. Huang F, Liao W-C, Sohn YS, Nechushtai R, Lu C-H, Willner I. Light-responsive and pH-responsive DNA microcapsules for controlled release of loads. *J Am Chem Soc.* (2016) 138:8936–45. doi: 10.1021/jacs.6b04773
128. Lai J, Jiang P, Gaddes ER, Zhao N, Abune L, Wang Y. Aptamer-functionalized hydrogel for self-programmed protein release via sequential photoreaction and hybridization. *Chem Mater.* (2017) 29:5850–7. doi: 10.1021/acs.chemmater.7b00875
129. Wang J, Shen H, Hu X, Li Y, Li Z, Xu J, et al. A targeted "capture" and "removal" scavenger toward multiple pollutants for water remediation based on molecular recognition. *Adv Sci.* (2016) 3:1500289. doi: 10.1002/advs.201500289
130. Hu X, Mu L, Zhou Q, Wen J, Pawliszyn J. ssDNA aptamer-based column for simultaneous removal of nanogram per liter level of illicit and analgesic pharmaceuticals in drinking water. *Environ Sci Technol.* (2011) 45:4890–5. doi: 10.1021/es104241z
131. Church GM, Gao Y, Kosuri S. Next-generation digital information storage in DNA. *Science.* (2012) 337:1628. doi: 10.1126/science.1226355
132. Goldman N, Bertone P, Chen S, Dessimoz C, LeProust EM, Sipos B, et al. Towards practical, high-capacity, low-maintenance information storage in synthesized DNA. *Nature.* (2013) 494:77–80. doi: 10.1038/nature11875
133. Adleman LM. Molecular computation of solutions to combinatorial proteins. *Science.* (1994) 266:1021. doi: 10.1126/science.7973651
134. Lipton RJ. DNA solution of hard computational problems. *Science.* (1995) 268:542. doi: 10.1126/science.7725098
135. Stojanovic MN, Stefanovic D. A deoxyribozyme-based molecular automaton. *Nat Biotechnol.* (2003) 21:1069–74. doi: 10.1038/nbt862
136. Seelig G, Soloveichik D, Zhang DY, Winfree E. Enzyme-free nucleic acid logic circuits. *Science.* (2006) 314:1585. doi: 10.1126/science.1132493
137. Zhang DY, Turberfield AJ, Yurke B, Winfree E. Engineering entropy-driven reactions and networks catalyzed by DNA. *Science.* (2007) 318:1121. doi: 10.1126/science.1148532
138. Qian L, Winfree E. Scaling up digital circuit computation with DNA strand displacement cascades. *Science.* (2011) 332:1196. doi: 10.1126/science.1200520
139. Qian L, Winfree E, Bruck J. Neural network computation with DNA strand displacement cascades. *Nature.* (2011) 475:368–72. doi: 10.1038/nature10262
140. Xie Z, Wroblewska L, Prochazka L, Weiss R, Benenson Y. Multi-input RNAi-based logic circuit for identification of specific cancer cells. *Science.* (2011) 333:1307. doi: 10.1126/science.1205527
141. Douglas SM, Bachelet I, Church GM. A Logic-gated nanorobot for targeted transport of molecular payloads. *Science.* (2012) 335:831. doi: 10.1126/science.1214081
142. Siuti P, Yazbek J, Lu TK. Synthetic circuits integrating logic and memory in living cells. *Nat Biotechnol.* (2013) 31:448–52. doi: 10.1038/nbt.2510
143. Ramezani H, Dietz H. Building machines with DNA molecules. *Nat Rev Genet.* (2020) 21:5–26. doi: 10.1038/s41576-019-0175-6
144. Harroun SG, Prévost-Tremblay C, Lauzon D, Desrosiers A, Wang X, Pedro L, et al. Programmable DNA switches and their applications. *Nanoscale.* (2018) 10:4607–41. doi: 10.1039/C7NR07348H
145. Morihiro K, Ankenbruck N, Lukasak B, Deiters A. Small molecule release and activation through dna computing. *J Am Chem Soc.* (2017) 139:13909–15. doi: 10.1021/jacs.7b07831
146. Yang S, Yang C, Huang D, Song L, Chen J, Yang Q. Recent progress in fluorescence signal design for dna-based logic circuits. *Chem Eur J.* (2019) 25:5389–405. doi: 10.1002/chem.201804420
147. Yin B-C, Ye B-C, Wang H, Zhu Z, Tan W. Colorimetric logic gates based on aptamer-crosslinked hydrogels. *Chem Commun.* (2012) 48:1248–50. doi: 10.1039/C1CC15639J
148. Ye B, Wang H, Ding H, Zhao Y, Pu Y, Gu Z. Colorimetric logic response based on aptamer functionalized colloidal crystal hydrogels. *Nanoscale.* (2015) 7:7565–8. doi: 10.1039/C5NR00586H
149. Bi S, Xiu B, Ye J, Dong Y. Target-catalyzed dna four-way junctions for cret imaging of microrna, concatenated logic operations, and self-assembly of dna nanohydrogels for targeted drug delivery. *ACS Appl Mater Interfaces.* (2015) 7:23310–9. doi: 10.1021/acsami.5b07827
150. Liu Y-L, Wu H-P, Zhou Q, Song Q-X, Rui J-Z, Guan X-X, et al. Controllable extension of hairpin-structured flaps to allow low-background cascade invasive reaction for a sensitive DNA logic sensor for mutation detection. *Chem Sci.* (2018) 9:1666–73. doi: 10.1039/C7SC04210H
151. Guo S, Huang H, Deng X, Chen Y, Jiang Z, Xie M, et al. Programmable DNA-responsive microchip for the capture and release of circulating tumor cells by nucleic acid hybridization. *Nano Res.* (2018) 11:2592–604. doi: 10.1007/s12274-017-1885-8
152. Li Y, Ding J, Xu X, Shi R, Saw PE, Wang J, et al. Dual hypoxia-targeting rnai nanomedicine for precision cancer therapy. *Nano Lett.* (2020) 20:4857–63. doi: 10.1021/acs.nanolett.0c00757
153. Wang J, Li Z, Wang Z, Yu Y, Li D, Li B, et al. Nanomaterials for combinational radio–immuno oncotherapy. *Adv Funct Mater.* (2020) 30:10676. doi: 10.1002/adfm.201910676
154. Mazloumi Tabrizi M, Hosseini SA, Akbarzadeh A. *Liposome & Nanotechnology*. (2017).
155. Chen T, Wu CS, Jimenez E, Zhu Z, Dajac JG, You M, et al. DNA micelle flares for intracellular mRNA imaging and gene therapy. *Angew Chem Int Ed.* (2013) 52:2012–6. doi: 10.1002/anie.201209440
156. Sun Q, Sun X, Ma X, Zhou Z, Jin E, Zhang B, et al. Integration of nanoassembly functions for an effective delivery cascade for cancer drugs. *Adv Mater.* (2014) 26:7615–21. doi: 10.1002/adma.201401554
157. Antonelli A, Sfara C, Manuali E, Bruce IJ, Magnani M. Encapsulation of superparamagnetic nanoparticles into red blood cells as new carriers of MRI contrast agents. *Nanomedicine.* (2011) 6:211–23. doi: 10.2217/nnm.10.163
158. Dunn SS, Tian S, Blake S, Wang J, Galloway AL, Murphy A, et al. Reductively responsive siRNA-conjugated hydrogel nanoparticles for gene silencing. *J Am Chem Soc.* (2012) 134:7423–30. doi: 10.1021/ja300174v
159. Gruber A, Navarro L, Klinger D. Reactive precursor particles as synthetic platform for the generation of functional nanoparticles, nanogels, and microgels. *Adv Mater Interfaces.* (2020) 7:1901676. doi: 10.1002/admi.201901676

160. Stickdorn J, Nuhn L. Reactive-ester derived polymer nanogels for cancer immunotherapy. *Eur Polym J.* (2020) 124:109481. doi: 10.1016/j.eurpolymj.2020.109481
161. Li F, Tang J, Geng J, Luo D, Yang D. Polymeric DNA hydrogel: design, synthesis and applications. *Prog Polym Sci.* (2019) 98:101163. doi: 10.1016/j.progpolymsci.2019.101163
162. Thelu HVP, Atchimnaidu S, Perumal D, Harikrishnan KS, Vijayan S, Varghese R. Self-assembly of an aptamer-decorated, dna–protein hybrid nanogel: a biocompatible nanocarrier for targeted cancer therapy. *ACS Appl Bio Mater.* (2019) 2:5227–34. doi: 10.1021/acsabm.9b00323
163. Wei H, Zhao Z, Wang Y, Zou J, Lin Q, Duan Y. One-Step self-assembly of multifunctional DNA nanohydrogels: an enhanced and harmless strategy for guiding combined antitumor therapy. *ACS Appl Mater Interfaces.* (2019) 11:46479–89. doi: 10.1021/acsami.9b15874
164. Zhang L, Abdullah R, Hu X, Bai H, Fan H, He L, et al. Engineering of bioinspired, size-controllable, self-degradable cancer-targeting dna nanoflowers via the incorporation of an artificial sandwich base. *J Am Chem Soc.* (2019) 141:4282–90. doi: 10.1021/jacs.8b10795
165. Wang Z, Xia J, Cai F, Zhang F, Yang M, Bi S, et al. Aptamer-functionalized hydrogel as effective anti-cancer drugs delivery agents. *Colloids Surf B: Biointerfaces.* (2015) 134:40–6. doi: 10.1016/j.colsurfb.2015.06.031
166. Zhang Z, Han J, Pei Y, Fan R, Du J. Chaperone copolymer-assisted aptamer-patterned DNA hydrogels for triggering spatiotemporal release of protein. *ACS Appl Bio Mater.* (2018) 1:1206–14. doi: 10.1021/acsabm.8b00450
167. Zhao M, Zhang Y, Yuan S, Xu X, Wu Z, Wu Z, et al. ATP responsive DNA nanogels grown on biocompatible branches for anticancer drug delivery. *Soft Matter.* (2019) 15:3655–8. doi: 10.1039/C9SM00480G
168. Ding L, Li J, Wu C, Yan F, Li X, Zhang S. A self-assembled RNA-triple helix hydrogel drug delivery system targeting triple-negative breast cancer. *J Mater Chem B.* (2020) 8:3527–33. doi: 10.1039/C9TB01610D
169. Wang Y, Yan M, Xu L, Zhao W, Wang X, Dong S, et al. Aptamer-functionalized DNA microgels: a strategy towards selective anticancer therapeutic systems. *J Mater Chem B.* (2016) 4:5446–54. doi: 10.1039/C6TB01224H

Conflict of Interest: The authors declare that the research was conducted in the absence of any commercial or financial relationships that could be construed as a potential conflict of interest.

Copyright © 2020 Di, Wang, Li, Xu, Tian, Wu, Tian and Gao. This is an open-access article distributed under the terms of the Creative Commons Attribution License (CC BY). The use, distribution or reproduction in other forums is permitted, provided the original author(s) and the copyright owner(s) are credited and that the original publication in this journal is cited, in accordance with accepted academic practice. No use, distribution or reproduction is permitted which does not comply with these terms.

frontiers in Medicine

SYSTEMATIC REVIEW
published: 03 November 2020
doi: 10.3389/fmed.2020.584728

Bibliometric Analysis of ATAC-Seq and Its Use in Cancer Biology via Nucleic Acid Detection

Yu Zhao[1†], Xianwen Zhang[2†], Zhenhua Song[3], Danian Wei[3], Hong Wang[4,5], Wei Chen[6], Guodong Sun[7], Weiying Ma[8*] and Kebing Chen[9*]*

[1] Department of Hematology, The Third Affiliated Hospital of Southern Medical University, Guangzhou, China, [2] School of Basic Medical Sciences, Chengdu University of Traditional Chinese Medicine, Chengdu, China, [3] Guangdong Provincial Key Laboratory of Bone and Joint Degeneration Disease, Department of Treatment Center for Traumatic Injuries, The Third Affiliated Hospital of Southern Medical University (Academy of Orthopedics of Guangdong Province), Guangzhou, China, [4] Guangdong Provincial Key Laboratory of Bone and Joint Degeneration Disease, The Third Affiliated Hospital of Southern Medical University, Guangzhou, China, [5] Academy of Orthopedics of Guangdong Province, Guangzhou, China, [6] Guangdong Provincial Key Laboratory of Bone and Joint Degeneration Disease, Department of Musculoskeletal Oncology, The Third Affiliated Hospital of Southern Medical University (Academy of Orthopedics of Guangdong Province), Guangzhou, China, [7] Department of Orthopedics, The First Affiliated Hospital of Jinan University, Guangzhou, China, [8] Department of Anesthesiology, Sun Yat-sen Memorial Hospital, Guangzhou, China, [9] Guangdong Provincial Key Laboratory of Bone and Joint Degeneration Disease, Department of Spine Surgery, The Third Affiliated Hospital of Southern Medical University (Academy of Orthopedics of Guangdong Province), Guangzhou, China

OPEN ACCESS

Edited by:
Guo Chen,
Jinan University, China

Reviewed by:
Ting Wang,
Huazhong University of Science and Technology, China
Youwei Sun,
Emory University, United States
Zhongqiu Xie,
University of Virginia, United States

***Correspondence:**
Guodong Sun
sgd96@jnu.edu.cn
Weiying Ma
mawy5@mail.sysu.edu.cn
Kebing Chen
chenkb@smu.edu.cn

[†] These authors have contributed equally to this work

Specialty section:
This article was submitted to Precision Medicine, a section of the journal Frontiers in Medicine

Received: 17 July 2020
Accepted: 24 September 2020
Published: 03 November 2020

Citation:
Zhao Y, Zhang X, Song Z, Wei D, Wang H, Chen W, Sun G, Ma W and Chen K (2020) Bibliometric Analysis of ATAC-Seq and Its Use in Cancer Biology via Nucleic Acid Detection. Front. Med. 7:584728. doi: 10.3389/fmed.2020.584728

Assay for transposase-accessible chromatin using sequencing (ATAC-seq) is associated with significant progress in biological research and has attracted increasing attention. However, the impact of ATAC-seq on cancer biology has not been objectively analyzed. We categorized 440 ATAC-seq publications according to the publication date, type, field, and country. R 3.6.2 was used to analyze the distribution of research fields. VOSviewer was used for country co-authorship and author co-authorship analyses, and GraphPad Prism 8 was used for correlation analyses of the factors that may affect the number of articles published in different countries. We found that ATAC-seq plays roles in carcinogenesis, anticancer immunity, targeted therapy, and metastasis risk predictions and is most frequently used in studies of leukemia among all types of cancer. We found a significantly strong correlation between the top 10 countries in terms of the number of publications and the gross expenditure on research and development (R&D), the number of universities, and the number of researchers. At present, ATAC-seq technology is undergoing a period of rapid development, making it inseparable from the emphasis and investment in scientific research by many countries. Collectively, ATAC-seq has advantages in the study of the cancer mechanisms because it can detect nucleic acids and thus has good application prospects in the field of cancer, especially in leukemia studies. As a country's economic strength increases and the emphasis on scientific research deepens, ATAC-seq will definitely play a more significant role in the field of cancer biology.

Keywords: ATAC-seq, open chromatin, bibliometric analysis, cancer biology, leukemia

INTRODUCTION

Cancer has shown annual increases in incidence in recent years and is currently a major life-threatening disease (1). Thus, exploring the genetic background leading to the occurrence and development of cancer and finding targeted therapeutic drugs for cancer are essential tasks for reducing the morbidity and mortality of cancer. Research on the cancer genome facilitates to analyses of the occurrence and development of cancer (2) and plays an essential role in the diagnosis and treatment of cancer.

Assay for transposase-accessible chromatin using sequencing (ATAC-seq) is a method that uses Tn5 transposase to integrate its adaptor load into an accessible chromatin region to explore chromatin accessibility (3). ATAC-seq, which was first invented in 2013 by Chang and Greenleaf, requires only a small number of cells or amount of tissues to perform experiments and can simultaneously reveal the interactions among of the chromatin genome location, DNA binding protein, and transcription binding site (4). In 2015, ATAC-seq was applied to map chromatin accessibility in primary CD4+ T cells isolated from standard blood draws from healthy volunteers and cancer patients and during T-cell activation (5). In 2016, Ackermann et al. integrated ATAC-seq with RNA-seq to identify human alpha cell and beta cell signature genes (6). ATAC-seq was then used to compare the chromatin accessibility landscapes of adult mouse dentate granule neurons *in vivo* before and after synchronous neuronal activation, which suggests how transient neuronal activation leads to dynamic changes in gene expression (7). Scientists were also concerned about mitochondrial sequencing reads in ATAC-seq samples, which had limited open chromatin; thus, CRISPR technology was used to reduce the mitochondrial reads, which could reduce the cost of ATAC-seq (8). For systematic ATAC-seq data analysis, Wei et al. developed esATAC, which covers the elementary steps for full a full analysis procedure (9). Gontarz et al. compared the sensitivity and specificity of six different accessibility analysis strategies for ATAC-seq data (10). In addition to chromosomal DNA, scientists can now use ATAC-seq to identify thousands of extrachromosomal circular DNA present in normal and tumor cells (11).

ATAC-seq has led to significant progress in biological research and has attracted increasing attention. To date, scientists have used ATAC-seq in cancer research and have obtained some encouraging results. Zhang et al. applied ATAC-seq and RNA-seq to reveal that CHD1 loss resulted in global changes in chromatin with associated transcriptomic change and it was also a factor underlying antiandrogen resistance in prostate cancer (12). Liu et al. used ATAC-seq to reveal that CASZ1 regulates skeletal muscle genes by chromatin accessibility. The loss of CASZ1 activity impairs embryonal rhabdomyosarcoma differentiation and contributes to tumorigenesis (13). ATAC-seq analysis demonstrated that hypoxia treatment significantly reduced chromatin accessibility at RAR/RXR binding sites, while acetate supplementation restored chromatin accessibility and promoted tumor cell differentiation (14). However, an objective analysis of the current status of ATAC-seq research in the field of cancer biology has not been performed.

The present study investigated the use of ATAC-seq in cancer biology by detecting nucleic acids via a bibliometric analysis, with a particular focus on whether ATAC-seq can be used to identify the pathogenesis of leukemia. We aim to provide a new perspective on the study of the pathogenesis of cancer, especially leukemia, so that scientists can better use ATAC-seq for the prevention, diagnosis, and treatment of cancer.

MATERIALS AND METHODS

Source Database

Our research was performed using Scopus (http://www.scopus.com/), the world's most extensive database of abstracts and citations as well as the world's largest collection of abstracts, references, and indexes of scientific and medical literature (15). The PubMed (http://www.ncbi.nlm.nih.gov/pubmed) database that provides free searches of articles in biomedical sciences (16) was used further to determine the online publication date of the searched items.

Search Design and Data Collection

The following search words were used in Scopus: TITLE-ABS-KEY ("ATAC-seq"). The database search was initially performed on April 30, 2020, and then to add items from the second quarter of 2020, it was again performed on July 12, 2020. We checked the total articles by PubMed, excluded the items from July 2020, and obtained a total of 488 articles. The online publication dates of these articles were from 2013 to the second quarter of 2020. By limiting the language to English and excluding unpublished articles, erratum, and book chapters, a total of 440 items were retained. All the results were exported together with the author, title, year, source, country, keywords, and other information. The results were exported in CSV format for further analysis.

Data Analysis

The filtered database file was imported into Microsoft Excel Version 2016 for analysis, and it included the following information: author, title, year of publication, source journal, affiliation, citations, DOI, and keywords. We classified the research fields of these articles by reading the title, abstract, and full text if necessary. Items in the field of cancer biology were screened out and exported in CSV format into Microsoft Excel 2013 for further analysis. GraphPad Prism 8, R 3.6.2, and VOSviewer 1.6.15.0 were used to create charts.

Visualization Maps

All the articles were classified by article type, and GraphPad Prism 8 was used to generate percentage graphs. We counted the number of articles published in each quarter from 2013 to the second quarter of 2020 and used GraphPad Prism 8 to make a histogram. We calculated the number of articles from the top 10 countries by corresponding author and searched for the GDP, number of universities, and number of researchers of these countries. GraphPad Prism 8 was used to perform correlation analyses.

The R 3.6.2 drawing language and operating environment is an excellent tool for statistical analysis (17). We classified

the research fields of the included articles into cancer biology, technologies, immunity, neurology, metabolism, and cell differentiation, including interdisciplinary studies in different research fields. The research fields of the 440 included articles were analyzed, and upset graphs were drawn using R 3.6.2.

VOSviewer is a visualization tool that enables researchers to create knowledge maps, evaluate the latest research progress, and identify hotspots in a research field (18). Co-authorship, co-citation, and co-occurrence analyses are the most frequently used methods. In our research, we used country co-authorship and author co-authorship analyses. Country co-authorship analyses provide information about collaborative relationships among authors in various countries. The cooperation preferences of authors from different countries can be used to improve cooperation with foreign authors. Author co-authorship analysis reveals collaborative relationships among authors, which can help researchers understand the relationships among researchers in a field and identify potential collaborators. Bibliographic database files were imported into VOSviewer 1.6.15.0 to build network visualization maps of the researchers and countries.

Statistical Analysis

Correlation analyses of the factors affecting the number of included articles from a country were performed using GraphPad Prism 8. The series of data were analyzed by linear regression and plotted on a graph. The *p*-values were observed, and a significant correlation existed when $p < 0.05$.

RESULTS

Publication Type and Date of ATAC-Seq-Related Articles

We searched for titles, abstracts, and keywords in the Scopus database using "ATAC-seq" as the search term and retrieved 488 articles. We chose a cutoff date of June 30, 2020. By limiting the language to English, 485 items were retained. By excluding unpublished articles, erratum, and book chapters, a total of 440 items were screened for analysis (**Figure 1A**). None of the included 440 articles have been retracted. Regarding the publication types of the 440 articles, research articles accounted for 95.5% (420 studies), which was the majority. Reviews accounted for 3.4% (15 studies), which was the second largest group. The remaining publication types were short surveys (0.5%, 2 studies), notes (0.5%, 2 studies), and conference papers (0.2%, 1 study) (**Figure 1B**).

The number of articles on ATAC-seq-related research published according to the quarter of the year is shown in **Figure 1C**. In the fourth quarter of 2013, the first article appeared because ATAC-seq was developed at that time. No articles appeared in 2014, which was probably because scientists were still considering this technology and performing experiments with it during that period. A total of 15 articles appeared in 2015. In the third quarter of 2017, 23 articles appeared, which is higher than the number of articles in the other three quarters of the same year and close to the average number of articles published in each quarter of 2018. The overall trend was that the number of ATAC-seq-related articles increased annually. The total number of articles for the whole year was highest in 2019, with a total of 143 articles published. This trend continued in the first half year of 2020, with 47 articles published in the first quarter and 56 articles published in the second quarter. Although the emergence of SARS-CoV-2 had a significant impact on social life during that time (19), scientists did not stop using ATAC-seq for scientific research. The number of articles related to ATAC-seq is increasing dramatically, which indicates that this technology has broad application prospects.

Distribution of Research Fields of ATAC-Seq-Related Articles

The accessibility of chromatin is a prerequisite for the interaction between cis-regulatory elements and trans-acting factors (20). ATAC-seq utilizes the advantage that T5 transposase can insert into the open region of chromatin and can be used to draw an open chromosome map (21). ATAC-seq can provide information from gene transcription to prove that the differential expression of transcription is caused by certain regulatory factors of transcription initiation. It is possible to observe epigenetic modifications of certain transcription factor-affected regions, which is essential in fields such as embryonic development (22).

By reading the title, abstract, keywords, and full text of the included articles, we classified the research fields of these articles into cancer biology, technologies, immunity, neurology, metabolism, and cell differentiation, including interdisciplinary approaches in these research fields. To describe the distribution of articles in different fields, we used R 3.6.2 to draw an upset graph.

As shown in **Figure 2**, a matrix layout was used to represent the common set between different research fields. The left bar indicates the total number of ATAC-seq articles in different research fields. The top bar indicates the number of articles that cross between ATAC-seq research fields. The largest number of articles that included ATAC-seq was in the field of cell differentiation at 120 articles, followed by technologies and cancer biology at 72 and 38 articles, respectively. There were 73 articles in total that included ATAC-seq in the field of cancer biology, including articles that overlap with other fields, and they accounted for 16.6% of the total number of articles. These findings indicate that ATAC-seq has a wide range of application fields and has good prospects for use in the field of cancer biology.

Characteristics of ATAC-Seq-Related Articles in Cancer Biology

By reading ATAC-seq-related articles on cancer biology, we found that the application of ATAC-seq in cancer research is as follows: First, ATAC-seq can be used to explore the mechanism of cancer development by studying transcription factors. Second, ATAC-seq can be used to analyze immune cells and explore cancer immunotherapy (23). Third, ATAC-seq can be used to predict the risk of tumor metastasis by detecting metastasis-related open chromatin (24). Finally, ATAC-seq can be used to explore the target of cancer treatment by studying drugs as inhibitors of transcription factors (25). The highest number of articles that used ATAC-seq was found for

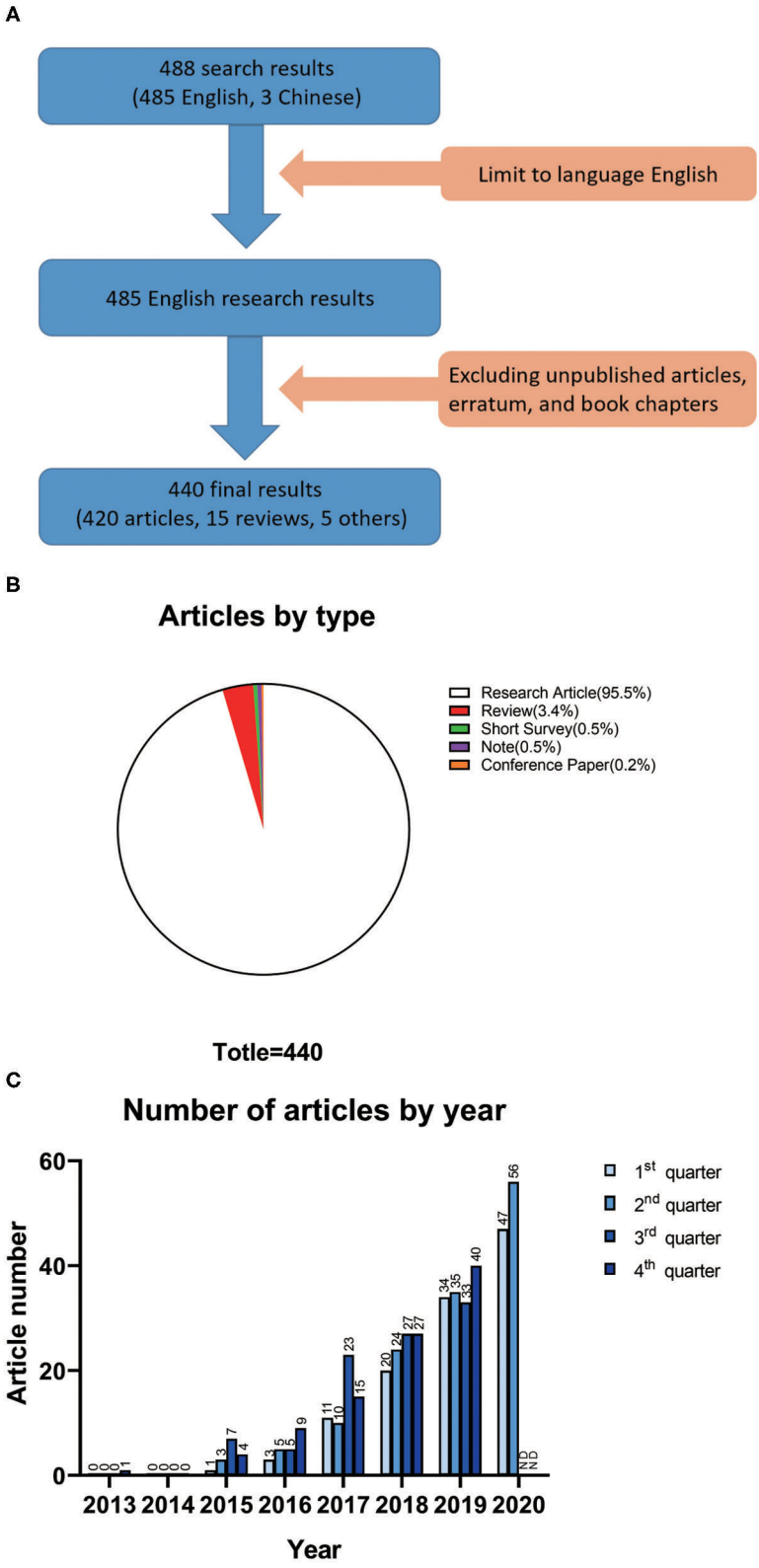

FIGURE 1 | (A) Details of the data filtration process. A language filter was applied to the original search on Scopus so that only English results were exported. Then, a document-type filter was performed. **(B)** Article types of all 440 results for ATAC-seq studies. **(C)** Number of articles on ATAC-seq based on the quarter of the year.

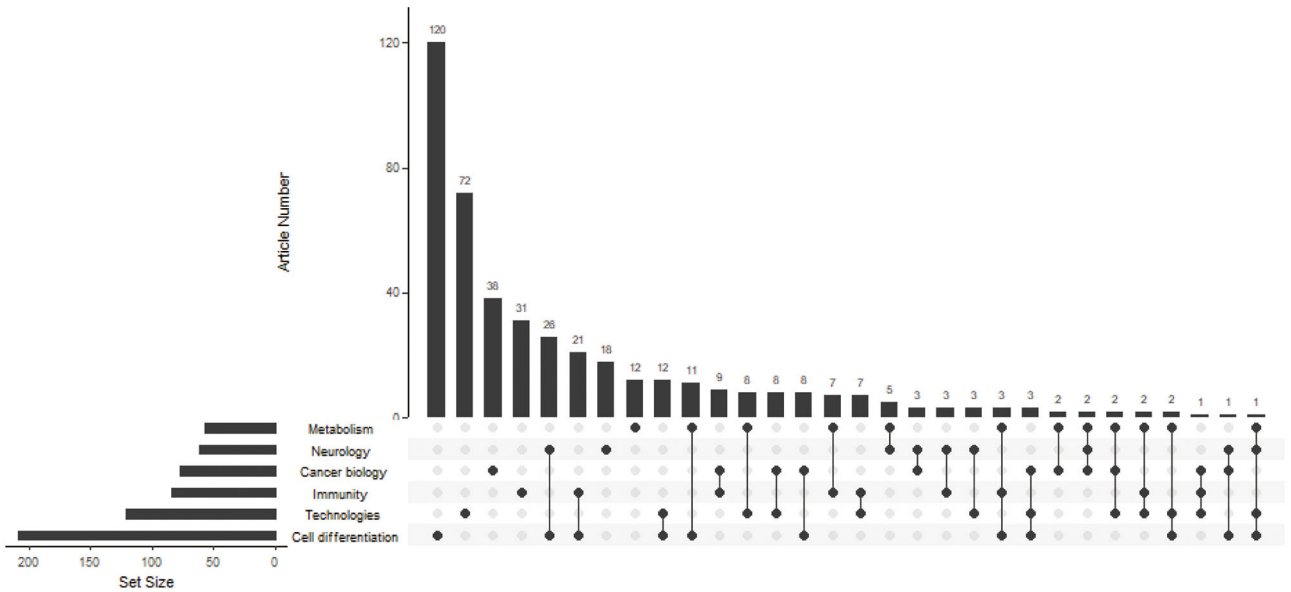

FIGURE 2 | Matrix layout for the number of ATAC-seq-related articles in different research fields. Dark circles in the matrix indicate sets that are part of the intersection. The left bar indicates the total number of ATAC-seq-related articles in different research fields. The top bar indicates the number of articles that cross between ATAC-seq research fields.

the mechanism of cancer, with 51 articles (**Figure 3A**). Of the included articles, seven on anticancer immunity used ATAC-seq (**Figure 3A**), indicating that ATAC-seq also has optimistic prospects in this field. Eleven and four of the included articles on targeted cancer therapy and tumor metastasis used ATAC-seq, respectively (**Figure 3A**).

We have listed several types of cancer with the most applications of ATAC-seq (**Figure 3B**). The type of cancer with the highest number of included articles that used ATAC-seq was leukemia, accounting for 20 articles. Leukemia is a malignant disease of the blood system. ATAC-seq has applications in the pathogenesis (26), targeted therapy (27), and immunotherapy (28) of leukemia. The type of cancer with the second highest number of included articles that used ATAC-seq was digestive system tumors at 14 articles, including gastric cancer (25), pancreatic cancer (29), liver cancer (30), and colorectal cancer (31). Of the included articles, 6, 3, and 2 were on breast cancer, ovarian cancer, and sarcoma, respectively. These results show that ATAC-seq can be applied in various tumor types, of which leukemia research is the most prevalent.

Co-authorship Analysis in the Unit of Countries

We used VOSviewer to analyze co-authorship between different countries and produced country co-authorship visualization maps. Country co-authorship maps can help researchers to understand existing partnerships and identify potential partners. **Figure 4A** shows the country co-authorship maps of the 440 ATAC-seq-related articles. Among them, countries with more than five published articles were screened out, and 18 countries met the threshold. The closely related topics were grouped into clusters of the same color. The higher the number of published articles is, the larger the size of the circle. The larger the scale of cooperation is, the thicker the connection line. The country with the most published articles is the United States, accounting for 297 articles. Researchers in the United States presented early developments in the field of ATAC-seq; thus, the United States exhibits a distinct advantage (32). The number of ATAC-seq-related articles published in the United States is the highest, which is more than the total number of articles published by other countries. The next highest is 76 articles published in China. The United Kingdom and Germany are both in Europe and presented 49 and 40 articles related to ATAC-seq published in these countries, respectively. They were followed by Israel, Japan, Sweden, France, Canada, Australia, and Spain. Some articles have authors from different countries; therefore, the total number of articles in the top 10 countries of published articles adds up to more than 440 articles. The cooperation between the United States and other countries is very close, with a total link strength of 135, followed by that of the United Kingdom, with a total link strength of 56. The color of each country is based on its average publication year. For example, the average publication year in the United States is in early 2018, and the color is blue-green. This finding does not mean that the United States published the most articles in 2018. Rather, the United States published articles from 2013 to 2020 and the average publication year is 2018. From this result, we can also see the leading position of the United States in ATAC-seq-related research. As shown in the figure, the color of China is yellow, and the average publication year is in early 2019, indicating that Chinese scientists are currently using ATAC-seq for more active research. The different

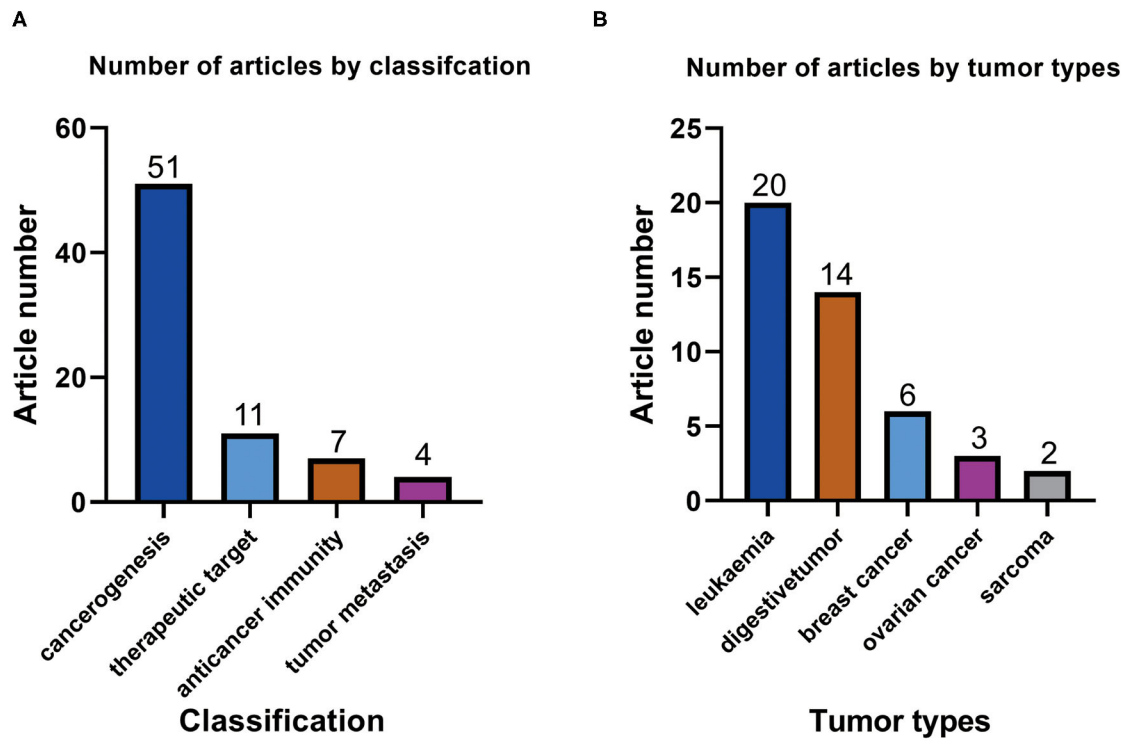

FIGURE 3 | (A) Number of ATAC-seq-related articles with different classifications in the field of cancer biology. **(B)** Numbers of ATAC-seq-related articles on different tumor types.

average publication years among the countries reflect the uneven scientific research level.

Figure 4B shows the country co-authorship maps of 73 ATAC-seq-related articles in cancer biology. Articles using ATAC-seq in cancer biology accounted for 16.6% of the total number of articles. We selected the countries with more than two articles, and 12 countries met the requirements. The country with the most published articles is also the United States, accounting for 50 articles, followed by China with 17 articles. The numbers of articles published by the United Kingdom and Germany are 7 and 6, thus ranking third and fourth, respectively. The national ranking of the number of articles on cancer biology is consistent with the national ranking of the total number of articles. The cooperation between the United States and other countries is very close, and the total link strength is 23, followed by China and Germany, with total link strengths of 10. The average publication year in the United States is in early 2018, while the average publication year in China is in early 2019. This finding indicates that the national distribution characteristics of ATAC-seq-related articles on cancer biology are consistent with the national distribution characteristics of total ATAC-seq-related articles.

Analysis of Author and Co-authorship

Figure 5A shows the author co-authorship network visualization map of the 440 ATAC-seq-related articles. In this visualization, one circle represents one author, the size of the circle represents the number of publications of an author, the line represents the cooperation relationship of the authors, the thickness of a line represents the scale of collaboration among authors, and the color represents the average publication year. In the figure, authors with more than five published articles are selected, including 32 authors with a close cooperative relationship. Chang and Greenleaf are the authors with the most published articles at 19 and 18, respectively. They are both from the Stanford University School of Medicine and invented ATAC-seq. The two authors published several articles on ATAC-seq from 2015 to 2020 and used ATAC-seq to map CD4+ T cells (5), study the effect of leukemia-related adhesion protein mutations on the differentiation of human hematopoietic progenitor (33), and study the activation of cutaneous T cell lymphoma regulating DNA landscape and dynamics (34). Buenrostro published nine articles. He first worked at the Stanford University School of Medicine and then at Harvard Medical School and works in close cooperation with Chang and Greenleaf. Chang's total strength of contact with other authors is 45, and Greenleaf's total strength of contact with other authors is 39. The average publication year of Chang and Greenleaf is early 2017. These authors, as the inventors of ATAC-seq, played a leading role in the subsequent ATAC-seq-related research.

Figure 5B shows the author co-authorship network visualization map of 73 ATAC-seq-related articles on cancer biology. In the figure, authors with more than three published

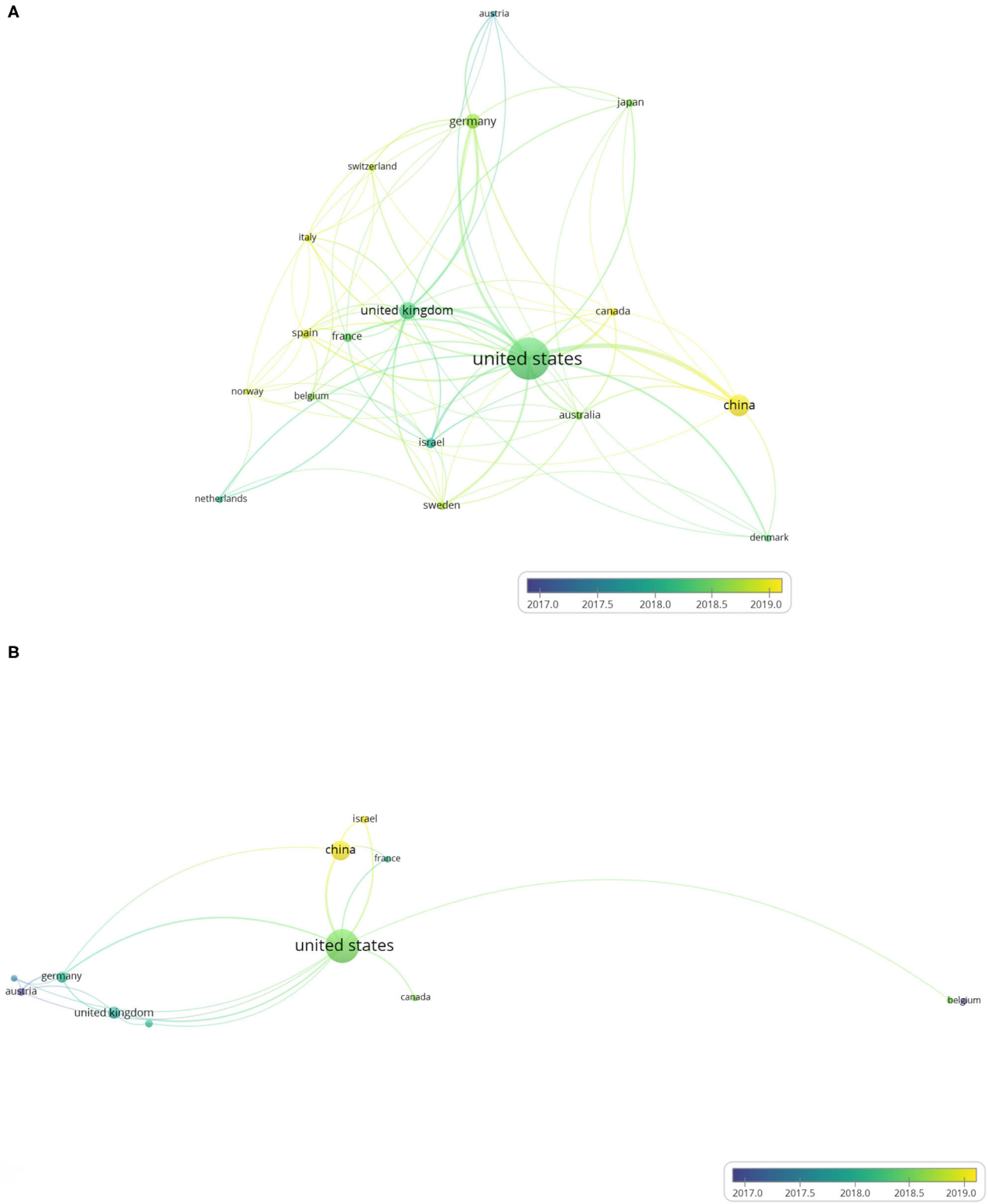

FIGURE 4 | Country co-authorship overlay visualization map. The size of each circle indicates the number of articles produced by that country. The distance between any two circles indicates the relatedness of their co-authorship link, and the thickness of the connecting line indicates the strength of the link. The color of each circle indicates the average publication year of the author, according to the color gradient in the lower right corner. **(A)** Country co-authorship overlay visualization map of the 384 ATAC-seq-related articles. **(B)** Country co-authorship overlay visualization map of 58 ATAC-seq-related articles on cancer biology.

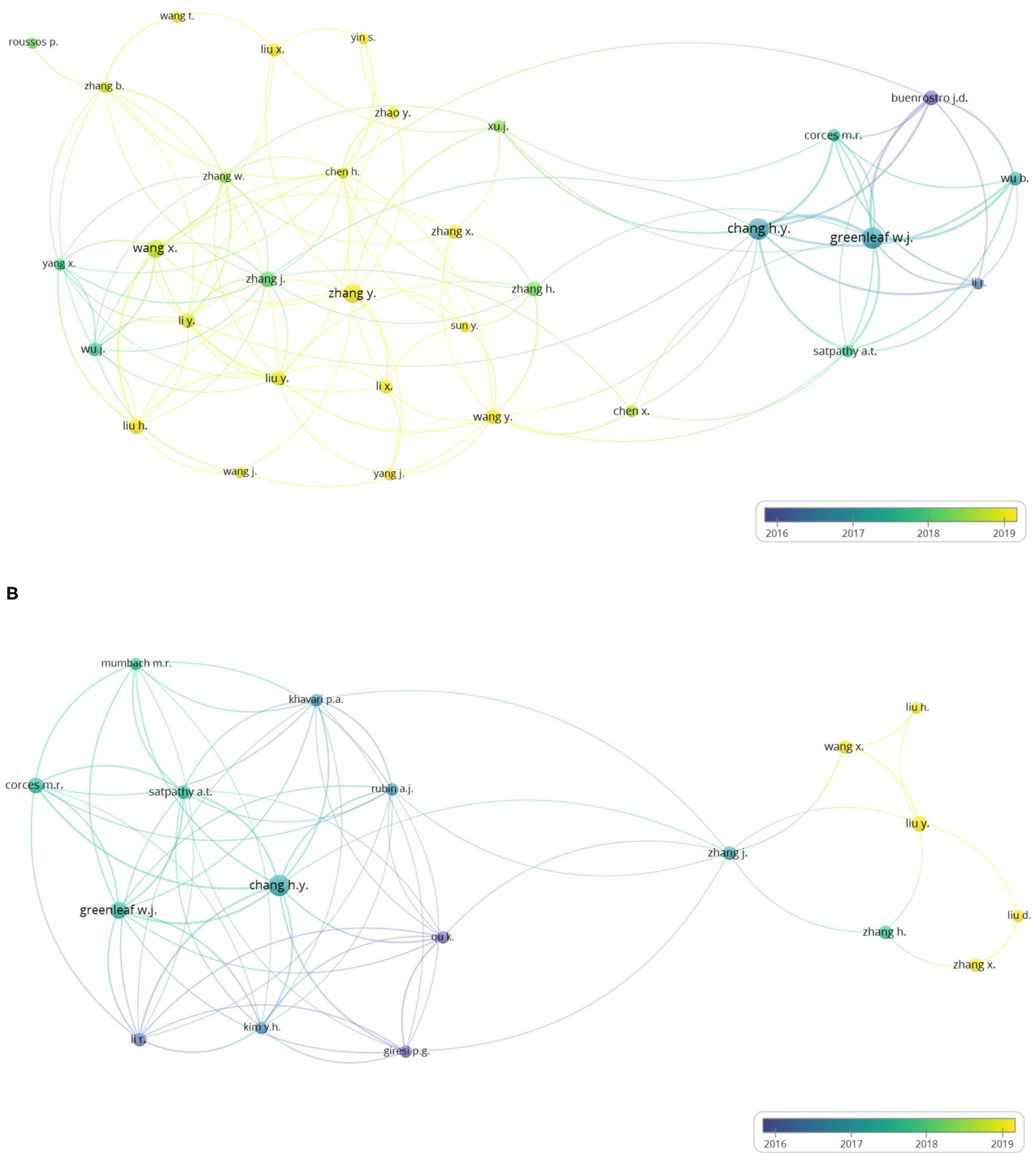

FIGURE 5 | Author co-authorship overlay visualization map. The last names of the authors are listed. The size of each circle indicates the number of articles published by the author. The distance between any two circles indicates the relatedness of their co-authorship link, and the thickness of the connecting line indicates the strength of the link. The color of each circle indicates the average publication year of the author, according to the color gradient in the lower right corner. **(A)** Author co-authorship overlay visualization map of the 384 ATAC-seq-related articles. **(B)** Author co-authorship overlay visualization map of 58 ATAC-seq-related articles on cancer biology.

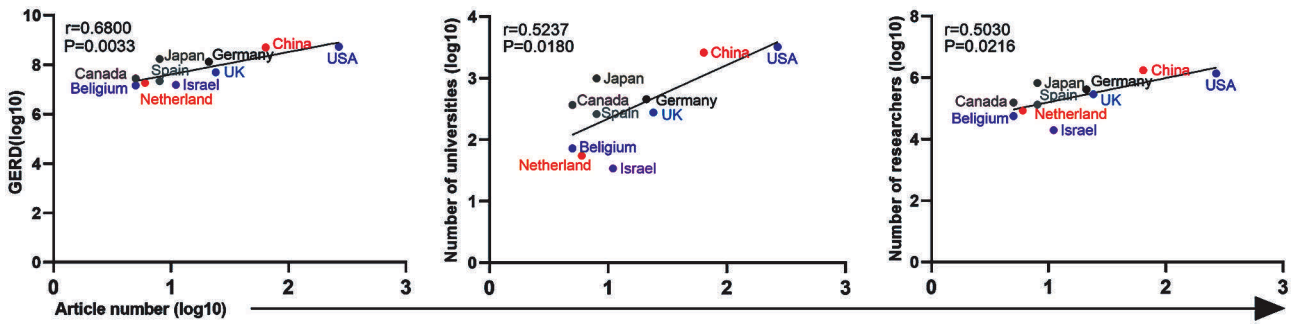

FIGURE 6 | Correlation analysis among the GERD, number of universities, number of researchers, and article number of different countries. The horizontal axis represents the log10 value of the number of articles published by the top 10 countries (the corresponding author's country). The vertical axis represents the country's GERD (log10), number of universities (log10), and number of researchers (log10).

articles are selected. Eighteen of the total 635 total authors meet the threshold. Chang and Greenleaf are also the top two authors in this map, with the most published articles at nine and six articles, respectively. The average publication year was also in early 2017. Thus, the inventors of ATAC-seq quickly applied this technology in the field of cancer biology after its invention, and other scientists also applied it to carry out cancer research.

Analysis of Factors That May Affect the Number of Articles

For the 440 ATAC-seq-related articles, we correlated the number of articles published by the top 10 countries by the corresponding authors according to the national GDP, the number of universities, the number of researchers, the GERD (gross expenditure on research and development), the average salary of researchers, and the number of college students. As shown in **Figure 6**, the number of articles (log10) is linearly related to the GERD (log10), $r = 0.6800$, $P = 0.0033$; the number of universities (log10), $r = 0.5237$, $P = 0.0180$; and the number of researchers (log10), $r = 0.5030$, $P = 0.0216$. There was no correlation with GDP, average researcher salary, or number of college students. The distribution of ATAC-seq articles in the field of cancer biology among countries is not related to the above factors, which is possibly because the number of articles is relatively small.

The United States ranks first in the number of articles, and its GERD, universities, and researchers are also far ahead of those of other countries. China, which published the second highest number of articles of ATAC-seq-related articles, ranks second in terms of GERD, universities, and researchers. Israel ranked fifth in the number of ATAC-seq-related articles. Although its GDP is not high, Israel ranks high in research investment, and the numbers of universities and researchers, reflecting its emphasis on scientific research. From these results, we can see that the national investment in scientific research is closely related to the publication of ATAC-seq-related articles.

DISCUSSION

This study provides new insights into cancer biology by detecting nucleic acids. The primary use of ATAC-seq in cancer biology demonstrated herein is to explore the pathogenesis of cancer from the perspective of epigenetics.

ATAC-seq has a wide range of applications, as shown in **Figure 2**. We focus on the field of cancer biology. We found that scientists used ATAC-seq for cancer research quickly after its invention. Scientists have known for a long time that the dysregulation of epigenetics can lead to the occurrence of cancer and that the use of epigenetic drugs for chromatin regulatory factors has clinical application prospects (35). By sequencing open chromatin, ATAC-seq can be used to study carcinogenesis. Transcription factors can affect the epigenetic modification of genes, thereby regulating gene expression, leading to the occurrence of cancer (13). People with specific gene mutations must avoid exposure to some environmental factors to reduce their risk of cancer. In addition, the monitoring frequency of these individuals should be increased for the early detection of cancer. The immune system can regulate the tumor microenvironment through the participation of immune cells (36). By analyzing immune cells, ATAC-seq can be used to explore cancer immunotherapy (23). Immunotherapy, such as PD-1 (37) and CART-T (38), has already been used in cancer patients. Tumor metastasis is the leading cause of death in cancer patients (39). ATAC-seq can be used to detect open chromatin in metastatic tissue, thus predicting the risk of tumor metastasis (24). Targeted therapy for cancer has made a leap from the macroworld to the microworld, which improved the efficiency of chemotherapy. By studying drugs as inhibitors of transcription factors, scientists use ATAC-seq to explore the target of cancer treatment (40). Thus, ATAC-seq can play a role in the prevention, diagnosis, and treatment of cancer.

ATAC-seq can be applied in the study of various types of cancer, especially leukemia. Leukemia is a malignant clonal disease that originates from hematopoietic stem and progenitor cells, and its occurrence is due to a combination of genetic and environmental effects (33). Cytogenetics and molecular genetics have important significance for the prognosis of leukemia. Taking

acute myeloid leukemia as an example, patients with CEBPA mutations have a good prognosis while patients with FLT3-ITD mutations have a poor prognosis (41). The D152V mutation of the transcription factor c-Myb impairs the ability of c-Myb to contribute to chromatin opening at specific sites, which causes the early differentiation and out-of-control proliferation of hematopoietic cells and therefore induces leukemia (42). As a "pioneer factor," the combination of the Ikaros protein with specific chromatin sites can increase chromatin accessibility, thereby starting the T cell differentiation process and inhibiting the growth of T cell leukemia cells (43). Mutations in cohesive proteins cause changes in chromatin accessibility, block the differentiation of hematopoietic progenitor cells, and induce leukemia (33). ATAC-seq can detect changes in chromatin accessibility by detecting nucleic acids; from the perspective of epigenetics, ATAC-seq can also be used to explore the pathogenesis of leukemia and provide new clues for the diagnosis and treatment of leukemia.

ATAC-seq is an innovative epigenetics research technology, although its high experimental cost limits its application to a certain extent. Compared to the national GDP, a country's emphasis on scientific research investment and scientific research, including more scientists and more universities conducting scientific research, is more critical for the development of ATAC-seq. There is no doubt that economic growth can promote the progress of science and technology (44). Nevertheless, a country's investment in scientific research is more likely to encourage the development of science and technology. As the economic strength of certain countries increases, the number of ATAC-seq-related articles published will probably increase accordingly.

In conclusion, our results demonstrate that ATAC-seq can be used to explore the pathogenesis of cancer from the perspective of epigenetics by detecting nucleic acids, especially in leukemia research. As a country's economic strength increases and its emphasis on scientific research deepens, ATAC-seq will almost certainly play a larger role in cancer biological research.

DATA AVAILABILITY STATEMENT

The raw data supporting the conclusions of this article will be made available by the authors, without undue reservation.

AUTHOR CONTRIBUTIONS

YZ and XZ preformed the bibliometric analysis and wrote the manuscript. ZS, DW, HW, and WC designed the research and contributed to writing the manuscript. GS, WM, and KC designed the research, organized the calculations, and contributed to writing the manuscript. All authors contributed to the article and approved the submitted version.

FUNDING

This work was supported by the National Natural Science Foundation of China (Grant Nos. 81201434 and 82072513, KC), the Natural Science Foundation of Guangdong Province (Grant No. S2012040007947, KC), and the Science and Technology Program of Guangzhou (2021-02-08-06-3028-0001, KC).

SUPPLEMENTARY MATERIAL

The Supplementary Material for this article can be found online at: https://www.frontiersin.org/articles/10.3389/fmed.2020.584728/full#supplementary-material

REFERENCES

1. Torre LA, Siegel RL, Ward EM, Jemal A. Global cancer incidence and mortality rates and trends–an update. *Cancer Epidemiol Biomarkers Prev.* (2016) 25:16–27. doi: 10.1158/1055-9965.EPI-15-0578
2. Graham TA, Sottoriva A. Measuring cancer evolution from the genome. *J Pathol.* (2017) 241:183–91. doi: 10.1002/path.4821
3. Buenrostro JD, Wu B, Chang HY, Greenleaf WJ. ATAC-seq: a method for assaying chromatin accessibility genome-wide. *Curr Protoc Mol Biol.* (2015) 109:21.29.1–21.29.9. doi: 10.1002/0471142727.mb2129s109
4. Buenrostro JD, Giresi PG, Zaba LC, Chang HY, Greenleaf WJ. Transposition of native chromatin for fast and sensitive epigenomic profiling of open chromatin, DNA-binding proteins and nucleosome position. *Nat Methods.* (2013) 10:1213–8. doi: 10.1038/nmeth.2688
5. Qu K, Zaba LC, Giresi PG, Li R, Longmire M, Kim YH, et al. Individuality and variation of personal regulomes in primary human T cells. *Cell Syst.* (2015) 1:51–61. doi: 10.1016/j.cels.2015.06.003
6. Ackermann AM, Wang Z, Schug J, Naji A, Kaestner KH. Integration of ATAC-seq and RNA-seq identifies human alpha cell and beta cell signature genes. *Mol Metab.* (2016) 5:233–44. doi: 10.1016/j.molmet.2016.01.002
7. Su Y, Shin J, Zhong C, Wang S, Roychowdhury P, Lim J, et al. Neuronal activity modifies the chromatin accessibility landscape in the adult brain. *Nat Neurosci.* (2017) 20:476–83. doi: 10.1038/nn.4494
8. Montefiori L, Hernandez L, Zhang Z, Gilad Y, Ober C, Crawford G, et al. Reducing mitochondrial reads in ATAC-seq using CRISPR/Cas9. *Sci Rep.* (2017) 7:2451. doi: 10.1038/s41598-017-02547-w
9. Wei Z, Zhang W, Fang H, Li Y, Wang X. esATAC: an easy-to-use systematic pipeline for ATAC-seq data analysis. *Bioinformatics.* (2018) 34:2664–5. doi: 10.1093/bioinformatics/bty141
10. Gontarz P, Fu S, Xing X, Liu S, Miao B, Bazylianska V, et al. Comparison of differential accessibility analysis strategies for ATAC-seq data. *Sci Rep.* (2020) 10:10150. doi: 10.1038/s41598-020-66998-4
11. Kumar P, Kiran S, Saha S, Su Z, Paulsen T, Chatrath A, et al. ATAC-seq identifies thousands of extrachromosomal circular DNA in cancer and cell lines. *Sci Adv.* (2020) 6:eaba2489. doi: 10.1126/sciadv.aba2489
12. Zhang Z, Zhou C, Li X, Barnes SD, Deng S, Hoover E, et al. Loss of CHD1 promotes heterogeneous mechanisms of resistance to AR-targeted therapy via chromatin dysregulation. *Cancer Cell.* (2020) 37:584–98.e11. doi: 10.1016/j.ccell.2020.03.001
13. Liu Z, Zhang X, Lei H, Lam N, Carter S, Yockey O, et al. CASZ1 induces skeletal muscle and rhabdomyosarcoma differentiation through a feed-forward loop with MYOD and MYOG. *Nat Commun.* (2020) 11:911. doi: 10.1038/s41467-020-14684-4
14. Li Y, Gruber JJ, Litzenburger UM, Zhou Y, Miao YR, LaGory EL, et al. Acetate supplementation restores chromatin accessibility and promotes tumor cell differentiation under hypoxia. *Cell Death Dis.* (2020) 11:102. doi: 10.1038/s41419-020-2303-9

15. Romero L, Portillo-Salido E. Trends in sigma-1 receptor research: a 25-year bibliometric analysis. *Front Pharmacol.* (2019) 10:564. doi: 10.3389/fphar.2019.00564
16. Falagas ME, Pitsouni EI, Malietzis GA, Pappas G. Comparison of PubMed, Scopus, Web of Science, and Google Scholar: strengths and weaknesses. *FASEB J.* (2008) 22:338–42. doi: 10.1096/fj.07-9492LSF
17. Conway JR, Lex A, Gehlenborg N. UpSetR: an R package for the visualization of intersecting sets and their properties. *Bioinformatics.* (2017) 33:2938–40. doi: 10.1093/bioinformatics/btx364
18. Chen C. Searching for intellectual turning points: progressive knowledge domain visualization. *Proc Natl Acad Sci USA.* (2004) 101(Suppl. 1):5303–10. doi: 10.1073/pnas.0307513100
19. Huang C, Wang Y, Li X, Ren L, Zhao J, Hu Y, et al. Clinical features of patients infected with 2019 novel coronavirus in Wuhan, China. *Lancet.* (2020) 395:497–506. doi: 10.1016/S0140-6736(20)30183-5
20. Corces MR, Granja JM, Shams S, Louie BH, Seoane JA, Zhou W, et al. The chromatin accessibility landscape of primary human cancers. *Science.* (2018) 362:eaav1898. doi: 10.1126/science.aav1898
21. Kumasaka N, Knights AJ, Gaffney DJ. Fine-mapping cellular QTLs with RASQUAL and ATAC-seq. *Nat Genet.* (2016) 48:206–13. doi: 10.1038/ng.3467
22. Wu J, Xu J, Liu B, Yao G, Wang P, Lin Z, et al. Chromatin analysis in human early development reveals epigenetic transition during ZGA. *Nature.* (2018) 557:256–60. doi: 10.1038/s41586-018-0080-8
23. Joshi S, Liu KX, Zulcic M, Singh AR, Skola D, Glass CK, et al. Macrophage Syk-PI3Kgamma inhibits antitumor immunity: SRX3207, a novel dual Syk-PI3K inhibitory chemotype relieves tumor immunosuppression. *Mol Cancer Ther.* (2020) 19:755–64. doi: 10.1158/1535-7163.MCT-19-0947
24. Cai WL, Greer CB, Chen JF, Arnal-Estapé A, Cao J, Yan Q, et al. Specific chromatin landscapes and transcription factors couple breast cancer subtype with metastatic relapse to lung or brain. *BMC Med Genomics.* (2020) 13:33. doi: 10.1186/s12920-020-0695-0
25. Zhou S, Zhang S, Wang L, Huang S, Yuan Y, Yang J, et al. BET protein inhibitor JQ1 downregulates chromatin accessibility and suppresses metastasis of gastric cancer via inactivating RUNX2/NID1 signaling. *Oncogenesis.* (2020) 9:33. doi: 10.1038/s41389-020-0218-z
26. Broux M, Prieto C, Demeyer S, Vanden Bempt M, Alberti-Servera L, et al. Suz12 inactivation cooperates with JAK3 mutant signaling in the development of T-cell acute lymphoblastic leukemia. *Blood.* (2019) 134:1323–36. doi: 10.1182/blood.2019000015
27. Wang X, Fan H, Xu C, Jiang G, Wang H, Zhang J, et al. KDM3B suppresses APL progression by restricting chromatin accessibility and facilitating the ATRA-mediated degradation of PML/RARalpha. *Cancer Cell Int.* (2019) 19:256. doi: 10.1186/s12935-019-0979-7
28. Satpathy AT, Saligrama N, Buenrostro JD, Wei Y, Wu B, Rubin AJ, et al. Transcript-indexed ATAC-seq for precision immune profiling. *Nat Med.* (2018) 24:580–90. doi: 10.1038/s41591-018-0008-8
29. Cheng Q, Ouyang X, Zhang R, Zhu L, Song X. Senescence-associated genes and non-coding RNAs function in pancreatic cancer progression. *RNA Biol.* (2020) 1–14. doi: 10.1080/15476286.2020.1719752
30. Dechassa ML, Tryndyak V, de Conti A, Xiao W, Beland FA, Pogribny IP. Identification of chromatin-accessible domains in non-alcoholic steatohepatitis-derived hepatocellular carcinoma. *Mol Carcinog.* (2018) 57:978–87. doi: 10.1002/mc.22818
31. Zhou B, Guo R. Genomic and regulatory characteristics of significant transcription factors in colorectal cancer metastasis. *Sci Rep.* (2018) 8:17836. doi: 10.1038/s41598-018-36168-8
32. Corces MR, Trevino AE, Hamilton EG, Greenside PG, Sinnott-Armstrong NA, Vesuna S, et al. An improved ATAC-seq protocol reduces background and enables interrogation of frozen tissues. *Nat Methods.* (2017) 14:959–62. doi: 10.1038/nmeth.4396
33. Mazumdar C, Shen Y, Xavy S, Zhao F, Reinisch A, Li R, et al. Leukemia-associated cohesin mutants dominantly enforce stem cell programs and impair human hematopoietic progenitor differentiation. *Cell Stem Cell.* (2015) 17:675–88. doi: 10.1016/j.stem.2015.09.017
34. Qu K, Zaba LC, Satpathy AT, Giresi PG, Li R, Jin Y, et al. Chromatin accessibility landscape of cutaneous t cell lymphoma and dynamic response to HDAC inhibitors. *Cancer Cell.* (2017) 32:27–41.e4. doi: 10.1016/j.ccell.2017.05.008
35. Kwong YL. Pathogenesis and treatment of leukemia: an Asian perspective. *Expert Opin Ther Targets.* (2012) 16(Suppl. 1):S37–43. doi: 10.1517/14728222.2011.621418
36. Hinshaw DC, Shevde LA. The tumor microenvironment innately modulates cancer progression. *Cancer Res.* (2019) 79:4557–66. doi: 10.1158/0008-5472.CAN-18-3962
37. Xu-Monette ZY, Zhou J, Young KH. PD-1 expression and clinical PD-1 blockade in B-cell lymphomas. *Blood.* (2018) 131:68–83. doi: 10.1182/blood-2017-07-740993
38. Feins S, Kong W, Williams EF, Milone MC, Fraietta JA. An introduction to chimeric antigen receptor (CAR) T-cell immunotherapy for human cancer. *Am J Hematol.* (2019) 94:S3–9. doi: 10.1002/ajh.25418
39. Wan L, Pantel K, Kang Y. Tumor metastasis: moving new biological insights into the clinic. *Nat Med.* (2013) 19:1450–64. doi: 10.1038/nm.3391
40. Naoum GE, Morkos M, Kim B, Arafat W. Novel targeted therapies and immunotherapy for advanced thyroid cancers. *Mol Cancer.* (2018) 17:51. doi: 10.1186/s12943-018-0786-0
41. Heidrich K, Thiede C, Schäfer-Eckart K, Schmitz N, Aulitzky WE, Krämer A, et al. Allogeneic hematopoietic cell transplantation in intermediate risk acute myeloid leukemia negative for FLT3-ITD, NPM1- or biallelic CEBPA mutations. *Ann Oncol.* (2017) 28:2793–8. doi: 10.1093/annonc/mdx500
42. Fuglerud BM, Lemma RB, Wanichawan P, Sundaram AYM, Eskeland R, Gabrielsen OS. A c-Myb mutant causes deregulated differentiation due to impaired histone binding and abrogated pioneer factor function. *Nucleic Acids Res.* (2017) 45:7681–96. doi: 10.1093/nar/gkx364
43. Ding Y, Zhang B, Payne JL, Song C, Ge Z, Gowda C, et al. Ikaros tumor suppressor function includes induction of active enhancers and super-enhancers along with pioneering activity. *Leukemia.* (2019) 33:2720–31. doi: 10.1038/s41375-019-0474-0
44. Mormina M. Science, technology and innovation as social goods for development: rethinking research capacity building from sen's capabilities approach. *Sci Eng Ethics.* (2019) 25:671–92. doi: 10.1007/s11948-018-0037-1

Conflict of Interest: The authors declare that the research was conducted in the absence of any commercial or financial relationships that could be construed as a potential conflict of interest.

The handling editor declared a shared affiliation with one of the authors, GS, at time of review.

Copyright © 2020 Zhao, Zhang, Song, Wei, Wang, Chen, Sun, Ma and Chen. This is an open-access article distributed under the terms of the Creative Commons Attribution License (CC BY). The use, distribution or reproduction in other forums is permitted, provided the original author(s) and the copyright owner(s) are credited and that the original publication in this journal is cited, in accordance with accepted academic practice. No use, distribution or reproduction is permitted which does not comply with these terms.

frontiers in Medicine

ORIGINAL RESEARCH
published: 27 November 2020
doi: 10.3389/fmed.2020.615981

DNA Repair-Based Gene Expression Signature and Distinct Molecular Subtypes for Prediction of Clinical Outcomes in Lung Adenocarcinoma

Bin Hu[1†], *Di Liu*[2†], *Yinqiang Liu*[3*] *and Zhixi Li*[4*]

[1] Department of Thoracic Surgery, Sichuan Cancer Hospital & Institute, Sichuan Cancer Center, The Affiliated Cancer Hospital, School of Medicine, University of Electronic Science and Technology of China, Chengdu, China, [2] Department of Thoracic Surgery, Guizhou Provincial People's Hospital, Guiyang, China, [3] Department of Thoracic Surgery, The First Affiliated Hospital of Kunming Medical University, Kunming, China, [4] Lung Cancer Center, West China Hospital of Sichuan University, Chengdu, China

OPEN ACCESS

Edited by:
Fu Wang,
Xidian University, China

Reviewed by:
Chaoyun Pan,
Sun Yat-sen University, China
Xing Niu,
ShengJing Hospital of China Medical University, China

***Correspondence:**
Zhixi Li
lizhixi_scu@163.com
Yinqiang Liu
yinqiangliu@aliyun.com

[†]These authors have contributed equally to this work

Specialty section:
This article was submitted to Precision Medicine, a section of the journal Frontiers in Medicine

Received: 10 October 2020
Accepted: 03 November 2020
Published: 27 November 2020

Citation:
Hu B, Liu D, Liu Y and Li Z (2020) DNA Repair-Based Gene Expression Signature and Distinct Molecular Subtypes for Prediction of Clinical Outcomes in Lung Adenocarcinoma. Front. Med. 7:615981. doi: 10.3389/fmed.2020.615981

Objective: To conduct a robust prognostic gene expression signature and characterize molecular subtypes with distinct clinical characteristics for lung adenocarcinoma (LUAD).

Methods: Based on DNA repair genes from the GSEA database, a prognostic signature was conducted in the TCGA-LUAD training set via univariate and multivariate cox regression analysis. Its prediction power was validated by overall survival analysis, relative operating characteristic (ROC) curves and stratification analysis in the GSE72094 verification set. Involved pathways in the high- and low-risk groups were analyzed by GSEA. A nomogram was built based on the signature and clinical features and its performance was assessed by calibration plots. LUAD samples were clustered via the ConsensusClusterPlus package. The differences in clinical outcomes, single nucleotide polymorphism (SNP) and sensitivity to chemotherapy drugs between molecular subtypes were analyzed.

Results: A 13-DNA repair gene-signature was constructed for LUAD prognosis. Following validation, it can robustly and independently predict patients' clinical outcomes. The GSEA results exhibited the differences in pathways between high- and low- risk groups. A nomogram combining the signature and stage could accurately predict 1-, 3-, and 5-year survival probability. Two distinct molecular subtypes were characterized based on DNA repair genes. Patients in the Cluster 2 exhibited a worse prognosis and were more sensitive to common chemotherapy than those in the Cluster 1.

Conclusion: This study proposed a 13-DNA repair gene-signature as a prognostic factor for LUAD patients, which can independently predict clinical outcomes by complement of the stage. Moreover, we characterized two LUAD subtypes with distinct clinical outcomes, somatic gene mutations, and drug sensitivity in cancer based on DNA repair genes.

Keywords: lung adenocarcinoma, DNA repair, risk score, nomogram, molecular subtype, clinical outcomes

INTRODUCTION

Lung cancer is one of the leading causes of cancer-related death globally (1). Non-small-cell lung cancer (NSCLC) occupies 85% of lung cancer (1). Among all cases of NSCLC, 50% are LUAD (2). Even with surgical resection at an early stage, patients with LUAD exhibit poor clinical outcomes and high recurrence risk (3). In comparison to other subtypes, LUAD has distinct molecular biological characteristics (4). Despite advances in targeted therapy, chemotherapy is still the standard treatment of LUAD. However, the incidence of chemotherapy resistance is relatively high, which can cause relapse and therapy failure, thereby ultimately lowering patients' survival time (5). High-throughput sequencing technology has accelerated the advancement of precision medicine (6). How to effectively classify the patients with same disease into different states is of importance to achieve precision medicine, depending on the genome characteristics of an individual patient. Many gene expression-related models have been conducted for prediction and stratification of LUAD patients' prognosis. Unfortunately, none of them is applied to routine clinical practice, partly due to small sample size, immoderate data fitting, as well as deficient evidence (7).

In the various activities of life, DNA damage is inevitable in organisms. The outcome of this damage depends on the degree of DNA damage and the cell's ability to repair DNA damage (8). If the damage is not repaired in time and correctly, it may lead to abnormal cell function. DNA repair is a process of correcting mismatched bases between two single strands of DNA, removing damaged bases or sugar bases on the DNA strands, and restoring the normal structure of DNA (9). DNA repair is an important link for the body to maintain the integrity and stability of the DNA structure and ensure the continuation of life and the stability of species. There are many pathways or systems to repair DNA damage in cells. Common DNA repair pathways or systems include direct repair, excision repair, recombination repair, and damage spanning repair (10). One kind of DNA damage can be repaired through multiple pathways, and one DNA repair pathway can also participate in the repair process of DNA damage at the same time. Damage to DNA bases can lead to changes in genetic code, which can produce abnormal RNA and proteins through transcription and translation, causing cell function decline, apoptosis, and even malignant transformation (11). DNA damage can lead to the activation of proto-oncogenes and the inactivation of tumor suppressor genes. The unbalanced expression of proto-oncogene and tumor suppressor gene is an important mechanism of cell malignancy (12). Studies have confirmed that DNA repair is involved in chemotherapy resistance (13), metastasis (14), and prognosis (15) of LUAD. Hence, it is of clinical significance to characterize prognostic signatures and molecular characteristics of LUAD based on these DNA repair-related gene expression profiles.

In this study, we conducted a novel prognostic gene expression signature and characterized two molecular subtypes with distinct clinical features on the basis of DNA repair-associated genes for LUAD.

TABLE 1 | The clinical features of LUAD samples in the training and validation sets.

Characteristics	Training set (n = 522)	Validation set (n = 398)
Age		
<65	247	107
≥65	275	291
Gender		
Female	282	222
Male	240	176
Stage		
Stage I-II	110	321
Stage III-IV	412	72
Unknown	0	5

MATERIALS AND METHODS

Selection of DNA Repair-Related Genes

One hundred and fifty DNA repair-related genes (**Supplementary table 1**) were retrieved from the defined gene sets of "hallmark DNA repair" pathway by the Gene Set Enrichment Analysis (GSEA) database (https://www.gsea-msigdb.org/gsea/index.jsp) (16).

LUAD Datasets

RNA-sequencing (RNA-seq) data and clinical features of 598 LUAD samples were downloaded from The Cancer Genome Atlas (TCGA) database (https://portal.gdc.cancer.gov/) on July 13, 2020. The raw data were normalized and log2 converted. Totally, 522 LUAD patients possessed complete clinical information (stage, age, gender, and overall survival time). The TCGA-LUAD dataset was applied as the training set. Somatic gene mutations for 567 LUAD samples were also obtained from TCGA portal. GSE72094 dataset containing microarray expression profile and corresponding clinical information from 398 LUAD patients was retrieved from the Gene Expression Omnibus (GEO) database (https://www.ncbi.nlm.nih.gov/geo/) (17), which was used as the validation set. **Table 1** describes the clinical features of LUAD samples in the training and validation sets, respectively.

Construction of a Prognostic Risk Score Based on DNA Repair-Related Genes

Firstly, we screened out prognosis-related DNA repair genes with $p < 0.05$ via univariate cox regression survival analysis in the training set. Following multivariate cox regression analysis, genes

Abbreviations: LUAD, lung adenocarcinoma; ROC, relative operating characteristic; SNP, single nucleotide polymorphism; NSCLC, non-small-cell lung cancer; LUAD, lung adenocarcinoma; GSEA, Gene Set Enrichment Analysis; RNA-seq, RNA-sequencing; TCGA, The Cancer Genome Atlas; GEO, Gene Expression Omnibus; AUCs, area under the curves; OS, overall survival; HR, hazard ratio; CI, confidence interval; FDR, false discovery rate; CMap, Connectivity Map; MoA, mechanism of action; DEGs, differentially expressed genes; FC, fold change; IC50, half maximal inhibitory concentration; GDSC, Genomics of Drug Sensitivity in Cancer.

independently associated with prognosis of LUAD were selected for construction of a prognostic risk score. The risk score of each sample was calculated on the basis of the regression coefficients and expression levels of selected genes, as follows: risk score $= \sum_{i=1}^{N} (Expi^{*}Coei)$ (where N refers to the number of selected DNA repair genes; Expi indicates the expression levels of gene i in each LUAD sample and Coei is the regression coefficient of gene i). The cutoff value was determined according to the median value of the risk scores among all samples. Then, all patients were separated into high- and low-risk groups. The expression patterns of selected genes between the two groups were visualized into a heat map via the pheatmap package in R. Kaplan-Meier survival curves were depicted for prediction of the clinical outcomes in the two groups via the survival package in R. The differences in survival were evaluated via the log-rank test. The ROC curves were built and the area under the curves (AUCs) for 1-, 3-, and 5-year overall survival (OS) were calculated utilizing the survivalROC package in R.

Subgroup Kaplan-Meier Survival Analysis

LUAD samples in the training and validation sets were stratified into different subgroups based on age ($\geq$65 and <65) and gender (female and male). Then, cancer samples in each subgroup were clustered into high- and low- risk groups. The differences on prognosis between the two groups were assessed via Kaplan-Meier OS analysis, followed by log-rank test.

Univariate and Multivariate Cox Regression Analysis

The relationships between age, gender, stage, and risk score and LUAD patients' prognosis were calculated using univariate cox regression analysis. To assess which clinical factors could independently predict the clinical outcomes of LUAD patients, we presented multivariate cox regression survival analysis. Hazard ratio (HR), 95% confidence interval (CI) and p-value were calculated, respectively.

GSEA

The differences in signaling pathways between the two groups were presented by adoption of the gene sets from The Molecular Signatures Database, with the cutoff values of the number of permutations = 1,000, and a false discovery rate (FDR) <0.25.

Development of a Predictive Nomogram

The two independent prognostic factors including risk score and stage were incorporated into the nomogram model for predicting the 1-, 3-, and 5-year survival probability. The calibration plots were depicted to evaluate the relationship between actual and nomogram-predicted survival utilizing the rms package in R.

Molecular Subtypes of LUAD Classification Based on DNA Repair Genes

On the basis of DNA repair-related genes, LUAD samples in the training and validation sets were clustered into k (2 to 9) groups using the ConsensusClusterPlus package in R (17). The optimal k value was determined to obtain a stable cluster. The PCA package in R was utilized to observe gene expression arrays in the LUAD groups. The differences on clinical outcomes between the two clusters were assessed via Kaplan-Meier survival analysis.

Connectivity Map (CMap) Mechanism of Action (MoA) Analysis

Differential expression analysis between high- and low-risk groups was carried out via the limma package (18). Differentially expressed genes (DEGs) were determined under the criteria of |log fold change (FC)| >1 and adjusted p-value <0.01. The lists of up- and down-regulated genes were uploaded into the CMap database (build 02, https://portals.broadinstitute.org/cmap/index.jsp) (19). The connectivity between the expression of these DEGs and small molecules-induced gene expression profiles was measured. Small molecules negatively associated with the indicated genes were screened out according to negative connectivity scores and $p < 0.05$.

Chemotherapy Drug Sensitivity Analysis

The half maximal inhibitory concentration (IC50) of six chemotherapy drugs (Cisplatin, Paclitaxel, Docetaxel, Gemcitabine, Vinorelbine and Etoposide) in each LUAD sample from TCGA database was estimated via Genomics of Drug Sensitivity in Cancer (GDSC; http://www.cancerrxgene.org/) (20) utilizing the pRRophetic package in R (21). The differences in drug sensitivity of samples between two clusters were analyzed by Wilcoxon test.

Statistical Analysis

All statistical analyses were presented via R 3.6.3 (https://www.r-project.org/).

RESULTS

Development and Validation of a Prognostic Model for LUAD Patients Based on 13 DNA Repair-Related Genes

As tested by the univariate cox regression OS analysis, 32 DNA repair-related genes had distinct associations with OS of LUAD in the training set (all p-value < 0.05; **Table 2**). Among them, 27 genes were risk factors for LUAD prognosis [hazard ratio (HR) > 1]. Based on the multivariate cox regression OS analysis, 13 genes were independently related to prognosis of LUAD. Based on the regression coefficients and expression levels of these 13 DNA repair-related genes in each sample, the risk score was calculated as follows: 0.155162493 * expression (ADA) + (−0.172491643) * expression (BCAM) + 0.283098385 * expression (CANT1) + 0.282699006 * expression (ERCC8) + (−0.250057666) * expression (HCLS1) + 0.270360541 * expression (NCBP2) + (−0.289483144) * expression (NME1) + 0.20066966 * expression (NME4) + 0.276521771 * expression (POLA2) + (−0.491115581) * expression (RFC5) + 0.285872813 * expression (SSRP1) + (−0.582522672) * expression (STX3) + 0.300334712 * expression (TYMS). Among them, eight genes were risk factors (HR > 1) and five were protective factors (HR < 1) for LUAD prognosis. Based on the median value of the risk score, LUAD patients were separated into the high- and low-risk groups (**Figure 1A**). As the risk score increased, the number

TABLE 2 | Thirty two DNA repair-related genes associated with prognosis in TCGA-LUAD cohort.

Gene symbol	Hazard ratio	Low 95%	High 95%	*P*-value
ADA	1.276466	1.097591	1.484492	0.001531
BCAM	0.900808	0.815995	0.994436	0.038401
CANT1	1.405956	1.114076	1.774305	0.004106
CDA	1.093281	1.019235	1.172708	0.012688
DUT	1.604697	1.189018	2.165696	0.001990
ERCC1	1.377498	1.064050	1.783282	0.015047
ERCC8	1.378663	1.031678	1.842350	0.029947
FEN1	1.374169	1.151363	1.640091	0.000429
GTF2A2	1.321664	1.021947	1.709282	0.033552
HCLS1	0.824927	0.719482	0.945826	0.005813
HPRT1	1.241742	1.008485	1.528950	0.041395
LIG1	1.270208	1.018105	1.584735	0.034097
NCBP2	1.395600	1.016886	1.915356	0.039053
NME1	1.193964	1.001807	1.422979	0.047688
NME4	1.278442	1.064148	1.535891	0.008686
PNP	1.239829	1.015621	1.513533	0.034663
POLA2	1.478941	1.158915	1.887338	0.001658
POLD1	1.236396	1.003002	1.524100	0.046807
PRIM1	1.251763	1.058700	1.480034	0.008605
RAD51	1.326782	1.142959	1.540169	0.000202
REV3L	0.762314	0.599641	0.969116	0.026683
RFC2	1.247070	1.004926	1.547561	0.045008
RFC3	1.252040	1.036454	1.512468	0.019736
RFC4	1.260330	1.080214	1.470479	0.003276
RFC5	1.248384	1.001078	1.556784	0.048892
RRM2B	0.790524	0.645450	0.968205	0.023067
SAC3D1	1.239607	1.022339	1.503049	0.028913
SSRP1	1.376528	1.043073	1.816583	0.023950
STX3	0.648227	0.486480	0.863754	0.003076
TYMS	1.355027	1.169523	1.569955	5.24E-05
UMPS	1.425316	1.076630	1.886930	0.013295
ZWINT	1.246273	1.090559	1.424221	0.001225

of patients under death status gradually increased (**Figure 1B**). There were distinct differences in the expression levels of the 13 genes between high- and low-risk groups (**Figure 1C**). LUAD patients in the high-risk group exhibited lower OS time in comparison to those in the low-risk group ($p = 7.008e\text{-}10$; **Figure 1D**). The sensitivity as well as specificity of the risk score was assessed via the ROC curve. The AUCs of the ROC curves for 1-, 3-, and 5- year OS were 0.712, 0.719, and 0.635, respectively (**Figure 1E**). We further validated the prognostic values of the risk score on the basis of 13 DNA repair-related genes in an independent GSE72094 validation set ($n = 398$). With the same calculation formular of the risk score, LUAD patients in the validation set were divided into high- and low- risk groups according to the median value of the risk scores in each sample (**Figure 1F**). Consistent with the training set, the number of LUAD patients with dead status was gradually augmented with the increase of the risk score (**Figure 1G**). The differences in the expression patterns of 13 DNA repair genes were shown in **Figure 1H**. As expected, LUAD patients in the high-risk group exhibited shorten OS time in comparison to those in the low-risk group ($p = 9.014e\text{-}06$; **Figure 1I**). The AUCs of the ROC curves for 1-, 3-, and 5- year OS were 0.673, 0.642 and 0.656, indicating the relatively high sensitivity and accuracy of the prediction model (**Figure 1J**).

The Risk Score Based on 13 DNA Repair Genes Is an Independent Prognostic Factor for LUAD

The prognostic characteristics of the risk score were analyzed via stratification analysis. For the training set, both in the ≥65 (**Figure 2A**) and <65 (**Figure 2B**) subgroups, patients with high risk scores exhibited a worsen prognosis in comparison to those with low risk scores (both $p < 0.001$). Regardless of whether it was a female (**Figure 2C**) or a male (**Figure 2D**) patient, high-risk score implied shorter survival time compared to low-risk

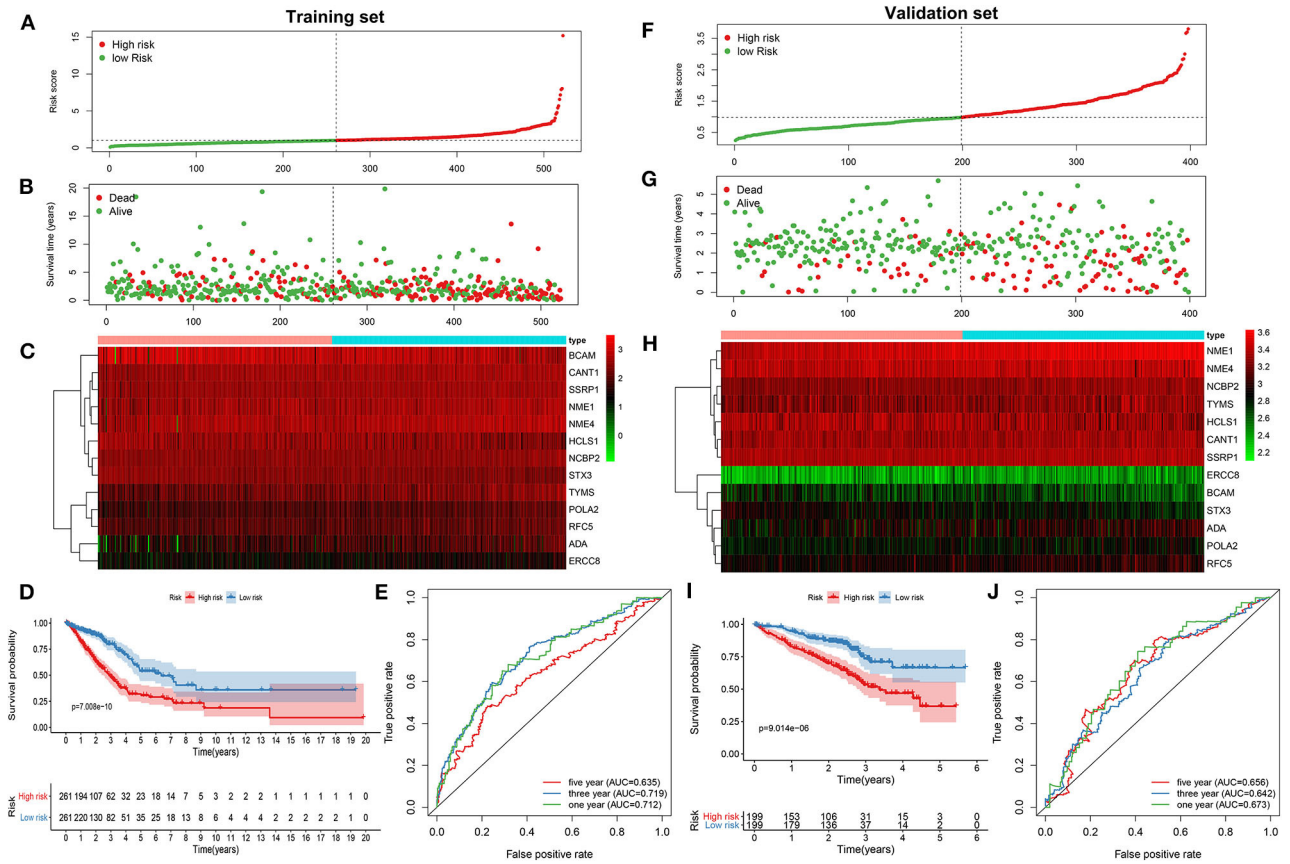

FIGURE 1 | Construction and verification of a prognostic model for LUAD patients according to 13 DNA repair-related genes. In the training set, **(A)** the distribution of the risk scores among all LUAD samples. According to the median value (dotted line), LUAD samples were divided into high- (red dot) and low- risk (green dot) groups. **(B)** The distribution of survival status of all LUAD samples. Red dot is indicative of dead status and green dot indicates alive status. **(C)** Heat map depicting the expression patterns in the 13 DNA repair genes between high- and low- risk groups. **(D)** Kaplan-Meier survival curve demonstrating the OS differences between high- and low- risk groups. **(E)** The ROC curves for 1-, 3-, and 5-year OS. In the validation set, **(F)** the distribution of the risk scores among all LUAD samples. **(G)** The distribution of survival status of all patients. **(H)** Hierarchical clustering heat map depicting the expression differences in the 13 DNA repair genes between high- and low- risk groups. **(I)** Kaplan-Meier survival curve showing the OS differences between the two groups. **(J)** The ROC curves for 1-, 3-, and 5-year OS.

score (both $p < 0.001$). Patients both at stage I-II (**Figure 2E**; $p < 0.001$) and III-IV (**Figure 2F**; $p = 0.008$) in the high-risk group had poorer prognosis compared to those in the low-risk group. Above results were confirmed in the validation set. Both ≥65 (**Figure 2G**; $p < 0.001$) and <65 (**Figure 2H**; $p = 0.003$) patients with high risk score indicated shorten OS time than those with low risk score. High risk score was indicative of shorten OS time than low risk score both for female (**Figure 2I**; $p < 0.001$) and male patients (**Figure 2J**; $p = 0.008$). Also, for patients both at stage I-II (**Figure 2K**; $p < 0.001$) and stage III-IV (**Figure 2L**; $p = 0.012$), high risk score usually implied an unfavorable prognosis. We further evaluated the independence of the risk score in predicting the prognosis of LUAD patients. In the training set, the univariate cox regression analysis results demonstrated that age [$p = 0.038$ and HR (95%CI) = 1.014 (1.001–1.028)], stage [$p = 0.038$ and HR (95%CI) = 1.014 (1.001–1.028)] and risk score [$p < 0.001$ and HR (95%CI) = 1.429 (1.332–1.534)] were distinctly associated with LUAD patients' prognosis (**Figure 2M**). According to the multivariate cox regression analysis results, stage [$p < 0.001$ and HR (95%CI) = 1.531 (1.325–1.769)] and risk score [$p < 0.001$ and HR (95%CI) = 1.355 (1.259–1.458)] were both independent prognostic factors for LUAD (**Figure 2N**). The independency of the risk score for prediction of LUAD prognosis was confirmed in the validation set (**Figures 2O,P**). Collectively, the risk score was an independent prognostic factor for LUAD.

Differences in Signaling Pathways Between High- and Low- Risk Groups

The differences in signaling pathways between high- and low-risk groups were analyzed via GSEA. For the training set, base excision repair, cell cycle, DNA replication, mismatch repair, oocyte meiosis, P53 signaling pathway and spliceosome were distinctly enriched in the high-risk group (**Figure 3A**). At the same time, ABC transporters and vascular smooth muscle contraction were significantly enriched in the low-risk group (**Figure 3B**). The similar enrichment results for high- (**Figure 3C**) and low- risk groups (**Figure 3D**) were confirmed in the validation set.

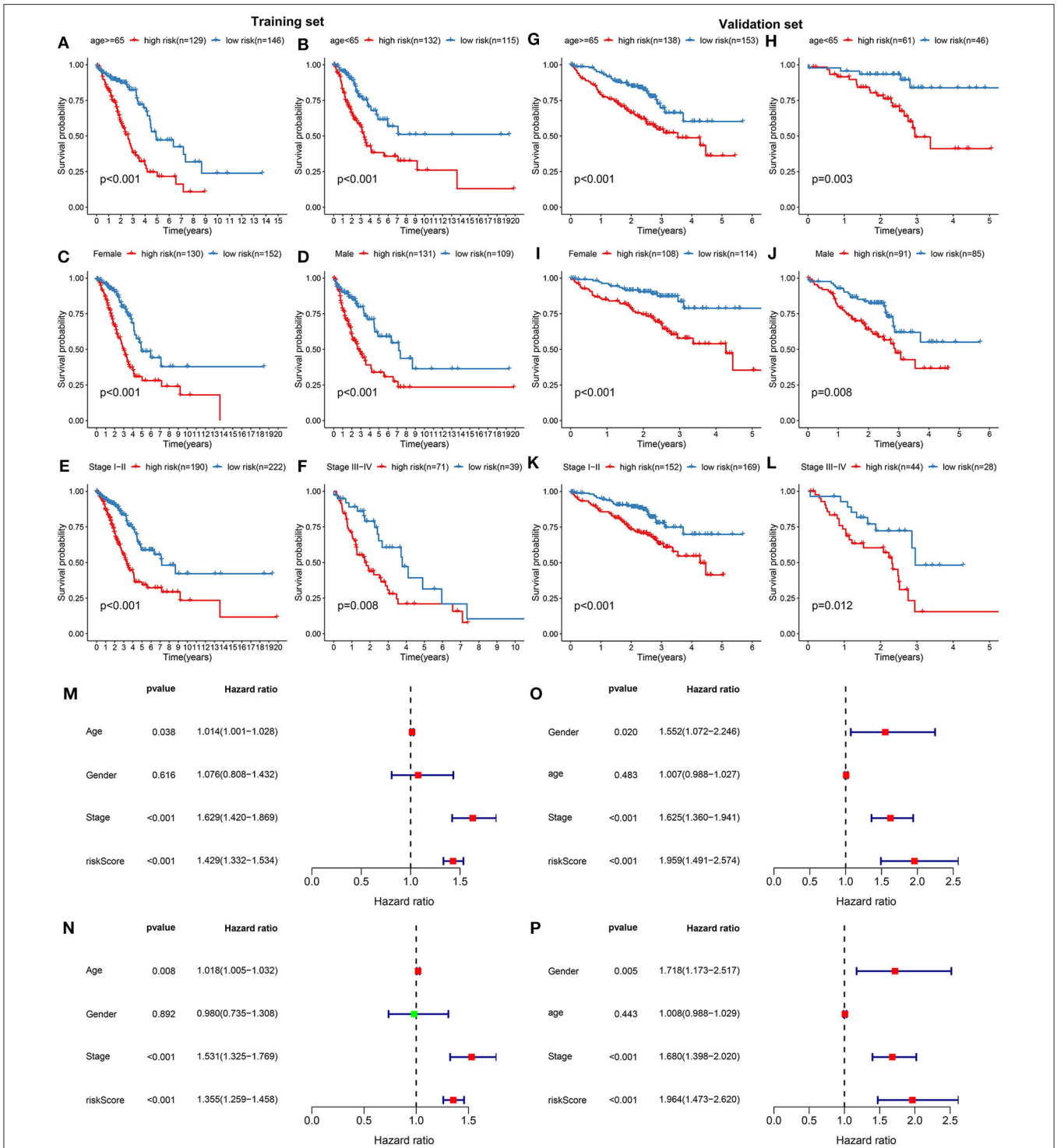

FIGURE 2 | Validation the independency of the risk score based on 13 DNA repair genes for prediction of LUAD prognosis. In the training set, Kaplan-Meier curves depicted the differences on prognosis between high- and low- risk groups in different LUAD subgroups, including **(A)** ≥65, **(B)** <65, **(C)** female, **(D)** male, **(E)** stage I-II, and **(F)** stage III-IV. In the validation set, the differences on prognosis between high- and low- risk groups were confirmed in **(G)** ≥65, **(H)** <65, **(I)** female, **(J)** male, **(K)** stage I-II, and **(L)** stage III-IV subgroups. Univariate and multivariate cox regression survival analysis validated whether age, gender, stage, and risk score could independently predict the clinical outcomes of LUAD patients in the training **(M,N)** and validation sets **(O,P)**.

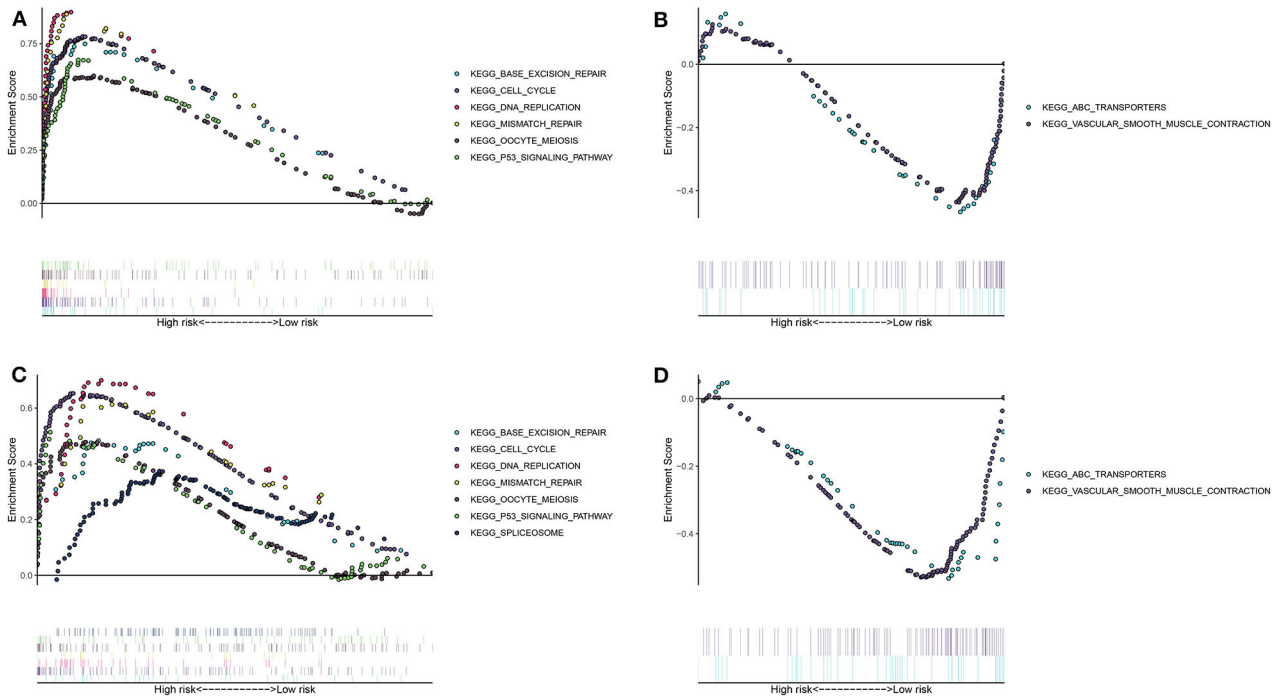

FIGURE 3 | Unveiling the differences in involved signaling pathways between high- and low- risk groups. **(A,B)** Involved signaling pathways in the high- and low-risk groups in the training set. **(C,D)** Involved signaling pathways in the high- and low-risk groups in the validation set.

Development and Verification of a Personalized Prognostic Prediction Nomogram for LUAD

Two independent prognostic factors including stage and risk score were utilized for constructing the nomogram for prediction of the 1-, 3-, and 5-year survival probability in the training set (**Figure 4A**). Its feasibility in clinical practice was confirmed in the validation set (**Figure 4B**). As shown in the calibration plots, the nomogram could stably predict 1- (**Figure 4C**), 3- (**Figure 4D**), and 5-year (**Figure 4E**) OS in the training set. By confirmed in the validation set, 1- (**Figure 4F**), and 3-year (**Figure 4G**) OS was robustly predicted by the nomogram for LUAD patients. Taken together, the nomogram could possess the high clinical applicability for prediction of the survival probability of LUAD patients.

Characterization of Two LUAD Molecular Subtypes With Distinct Clinical Outcomes Based on DNA Repair-Associated Genes

Utilizing the ConsensusClusterPlus package, LUAD samples were clustered into different groups. When $k = 2$, two molecular subtypes were stably classified both in the training (**Figures 5A–C**) and validation sets (**Figures 5D–F**). PCA results demonstrated that there was a distinct difference in the expression profiles of DNA repair genes between the two molecular subtypes in the training set (**Figure 5G**). As shown in Kaplan-Meier OS curve, LUAD patients in the cluster 2 exhibited shorten OS time than those in the cluster 1 ($p = 0.002$; **Figure 5H**). Consistent with the training set, LUAD samples in the validation set were stably divided into two groups based on the expression profiles of DNA repair genes (**Figure 5I**). Moreover, patients in the cluster 2 had distinctly poorer prognosis in comparison to those in the cluster 1 ($p = 1.909e\text{-}05$; **Figure 5J**). Taken together, we characterized two LUAD molecular subtypes with distinct clinical outcomes according to DNA repair-associated genes.

MoA Analysis via CMap Database

One hundred and nine DEGs were identified between high- and low-risk groups, with the threshold of $|\log FC| > 1$ and adjusted p-value < 0.01, as shown in **Figure 6A** and **Supplementary Table 2**. The up- and down-regulated genes were imported into the CMap database. The results showed that 78 small molecules were predicted to target these DEGs. Moreover, 58 kinds of mode of drug actions were distinctly enriched by MoA analysis results (**Figure 6B**).

Differences in Somatic Mutations Between Two LUAD Clusters

Among 567 LUAD samples from TCGA database, 459 (80.95%) occurred somatic mutations. Twenty frequently mutated genes were defined. Among them, TP53 (42%), TTN (40%), MUC16 (35%), CSMD3 (33%) and RYR2 (32%) were the five most frequently mutated genes (**Figure 7**). The most frequently mutation type was missense. Furthermore, the samples in the cluster 2 exhibited higher mutation levels in comparison to those in the cluster 1.

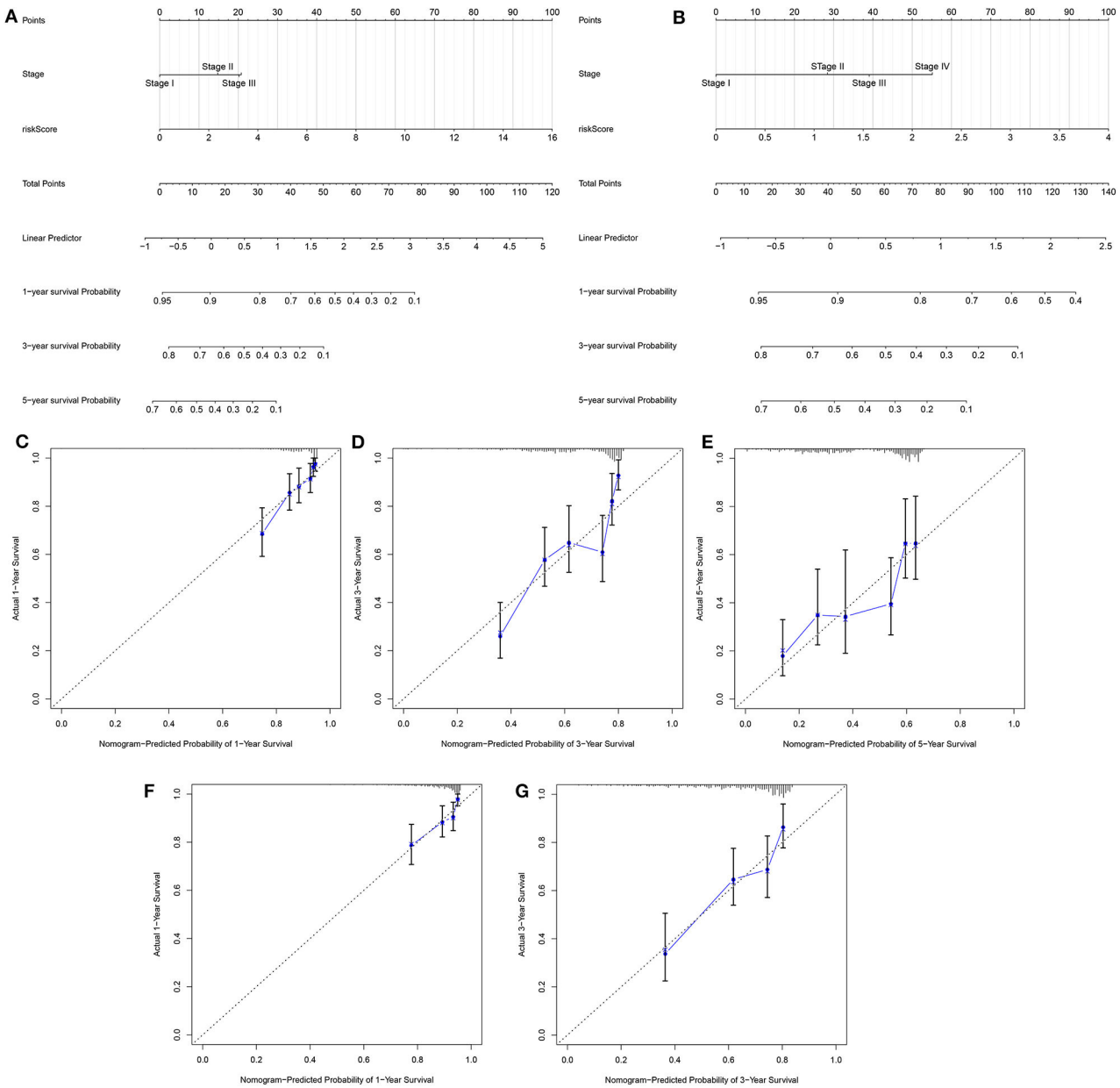

FIGURE 4 | Development and verification of a nomogram for prediction of LUAD patients' 1-, 3-, and 5-year OS time. The nomogram including stage and risk score for prediction of 1-, 3-, and 5-year survival probability was conducted and verified in the **(A)** training set as well as **(B)** validation set. **(C–E)** Calibration plots showed the association between actual and the nomogram-predicted probability of 1-, 3-, and 5-year survival in the training set. **(F,G)** The association between actual and the nomogram-predicted probability of 1- and 3-year survival was confirmed in the validation set.

Evaluation of the Sensitivity of Chemotherapy Drugs to Two LUAD Clusters

We evaluated the differences in the sensitivity of chemotherapy drugs between the Two LUAD clusters using the GDSC database. The estimated IC50 values of Cisplatin (**Figure 8A**), Paclitaxel (**Figure 8B**), Docetaxel (**Figure 8C**), Gemcitabine (**Figure 8D**), Vinorelbine (**Figure 8E**) and Etoposide (**Figure 8F**) were all significantly higher in samples in the cluster 1 in comparison to those in the cluster 2 (all $p < 0.05$). These findings suggested that LUAD patients in the cluster 2 could show sensitivity to these six chemotherapy drugs.

DISCUSSION

In this study, we constructed a robust 13-DNA repair gene-signature for LUAD patients' prognosis, which could assist the stage system to predict the clinical outcomes, thereby providing

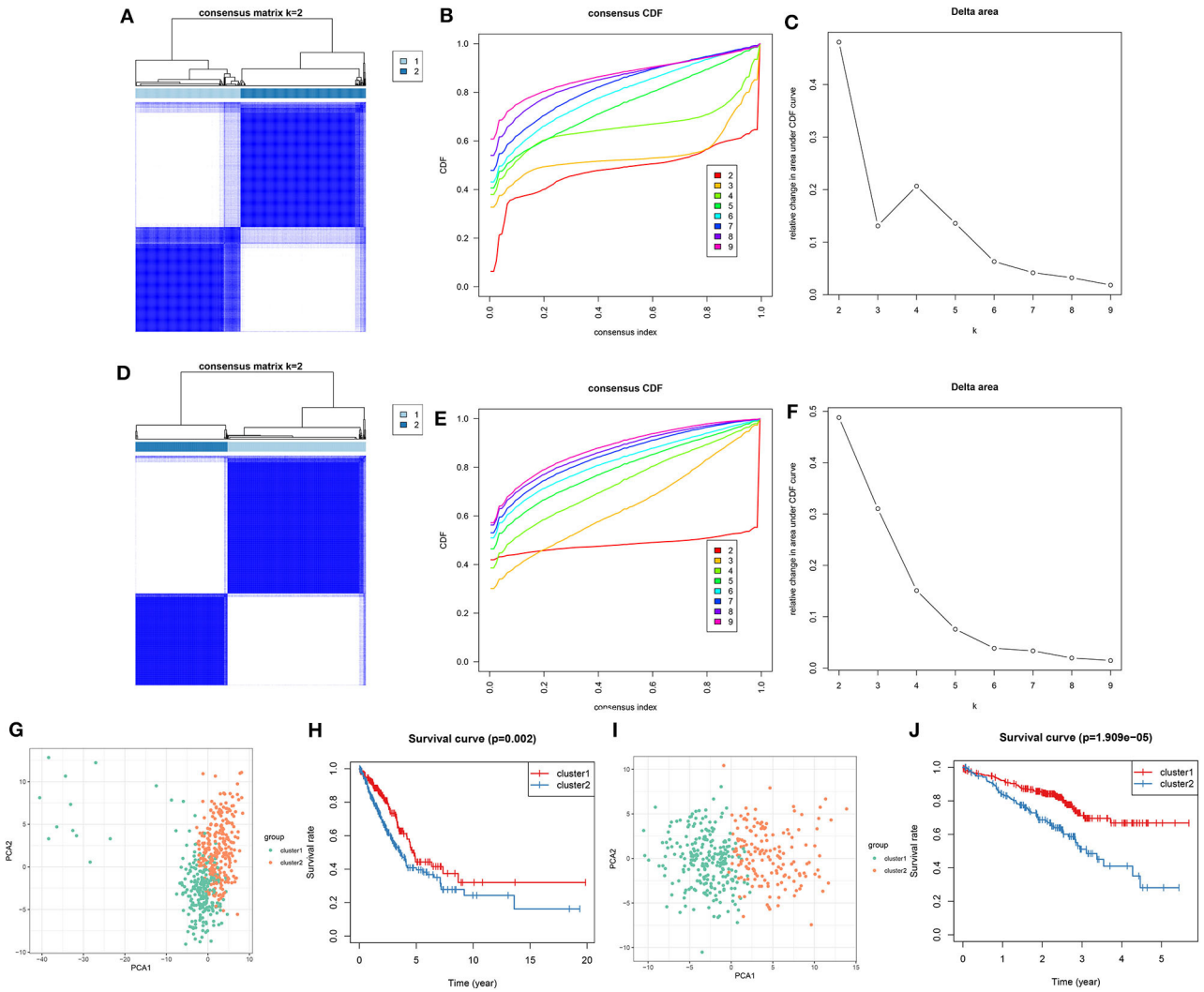

FIGURE 5 | Consensus clustering of DNA repair-associated genes clustered LUAD samples into two clusters with distinct clinical outcomes. In the training set, **(A)** the heat map showing the consensus matrix when $k = 2$. **(B)** Consensus clustering cumulative distribution function (CDF) under $k = 2$–9. **(C)** Relative change in area under CDF curve. In the validation set, **(D)** the heat map depicting the correlation between cluster 1 and 2. **(E)** Consensus clustering CDF under $k = 2$–9. **(F)** Relative change in area under CDF curve. **(G)** PCA of the expression profile of DNA repair genes from cluster 1 and 2 in the training dataset. **(H)** Kaplan-Meier OS curve between cluster 1 and 2 in the training set. **(I)** PCA of the expression profile of DNA repair genes from cluster 1 and 2 in the validation dataset. **(J)** Kaplan-Meier OS curve between cluster 1 and 2 in the validation dataset.

more suitable treatments. Furthermore, two molecular subtypes with distinct clinical features were built on the basis of the expression profiles of DNA repair genes, which could be applied to tailor therapeutic strategies for LUAD patients.

It has been confirmed that DNA repair is widely involved in chemosensitivity, prognosis and metastasis of LUAD (22). A thorough understanding of the expression profile of DNA repair-associated genes in LUAD specimens may provide new ideas for improvement of patients' clinical outcomes. Totally, 150 DNA repair genes were obtained from the GSEA database. Via the univariate and multivariate cox regression analysis, we constructed a 13-gene signature. Patients with high risk score were indicative of poorer OS time than those with low-risk score. The AUCs of the ROCs for 1-, 3-, and 5-year OS time confirmed its well-predictive performance, which were confirmed in the validation set. Furthermore, its predictive accuracy and independency were verified by stratification analysis and multivariate cox regression analysis. As previous research, the prognostic potential of DNA repair genes has been found in gastric cancer (23). A 7-DNA repair gene-signature can predict hepatocellular carcinoma patients' prognosis (24). We further probed into involved signaling pathways for high- and low-risk groups. As a result, different pathways were enriched in the high- and low-risk groups. Several LUAD-related pathways including base excision repair (25), cell cycle (26), DNA replication (27), mismatch repair (28), oocyte meiosis

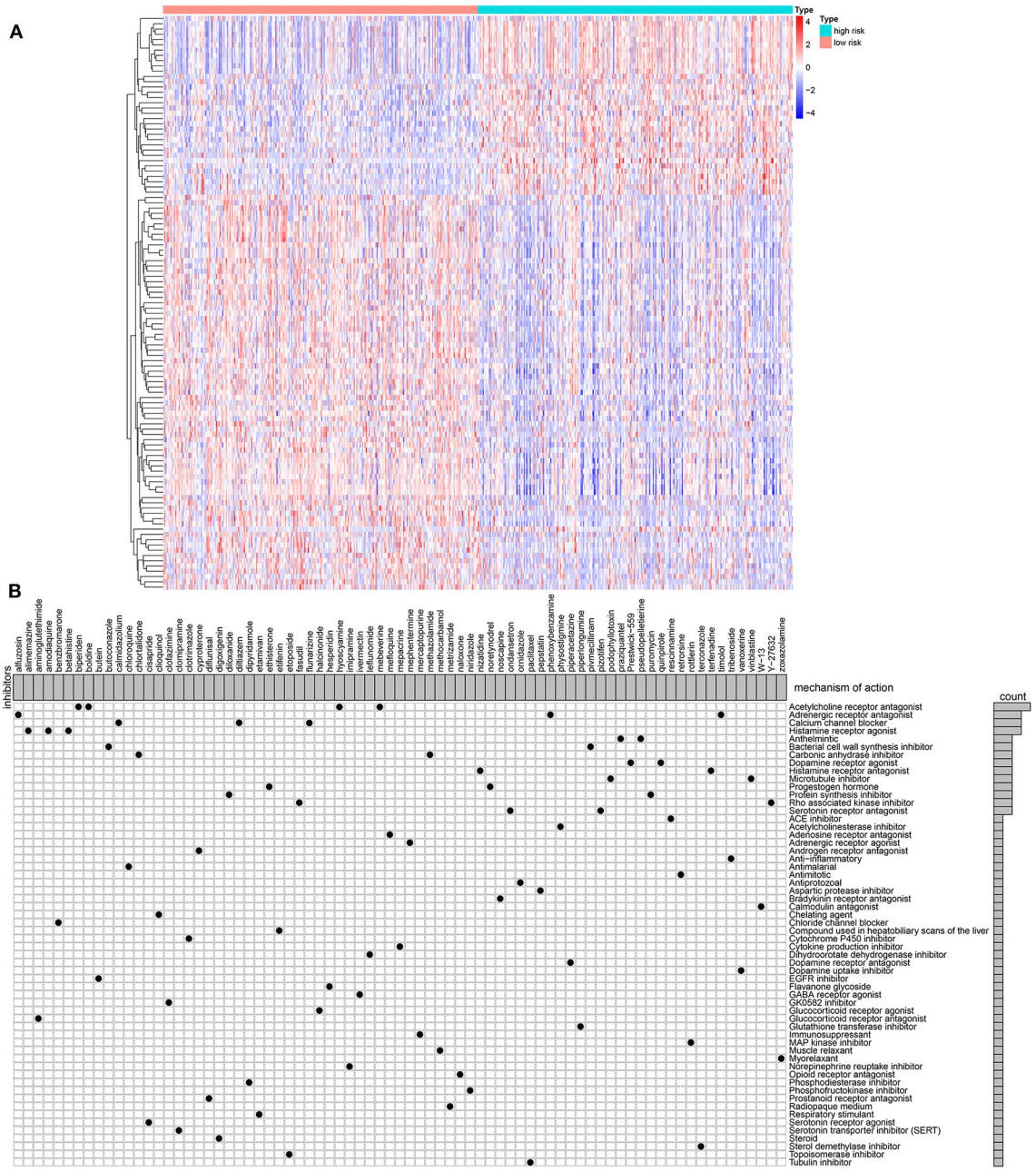

FIGURE 6 | MoA analysis results via CMap database. **(A)** Heat map showing all DEGs between high- and low-risk groups. **(B)** Shared mechanism diagram of each compound in CMap.

(29), P53 signaling pathway (30) and spliceosome (31) were distinctly enriched in the high-risk group. Moreover, ABC transporters (32) and vascular smooth muscle contraction (33) were significantly enriched in the low-risk group, suggesting that DNA repair genes for high- and low-risk groups participated in distinct pathways. Precision medicine largely depends on the identification of individual genomic characteristics of different LUAD patients. By combining the signature and stage, we established a nomogram for prediction of 1-, 3-, and 5-year OS. The model can accurately classify patients' prognostic risk. Based on DEGs between high- and low-risk groups, we screened 77 small molecule drugs and 58 drug mechanisms for LUAD, which should be validated by in-depth analysis.

The prediction of the therapy response is one of the main goals of precision medicine, depending largely on an unknown subset of biological characteristics. Characterization of the molecular characteristics for a specific patient is essential to alleviate heterogeneity and tailor treatment (34). By analyzing the LUAD samples from the TCGA-LUAD training set and an independent GSE72094 verification set, we characterized two LUAD molecular

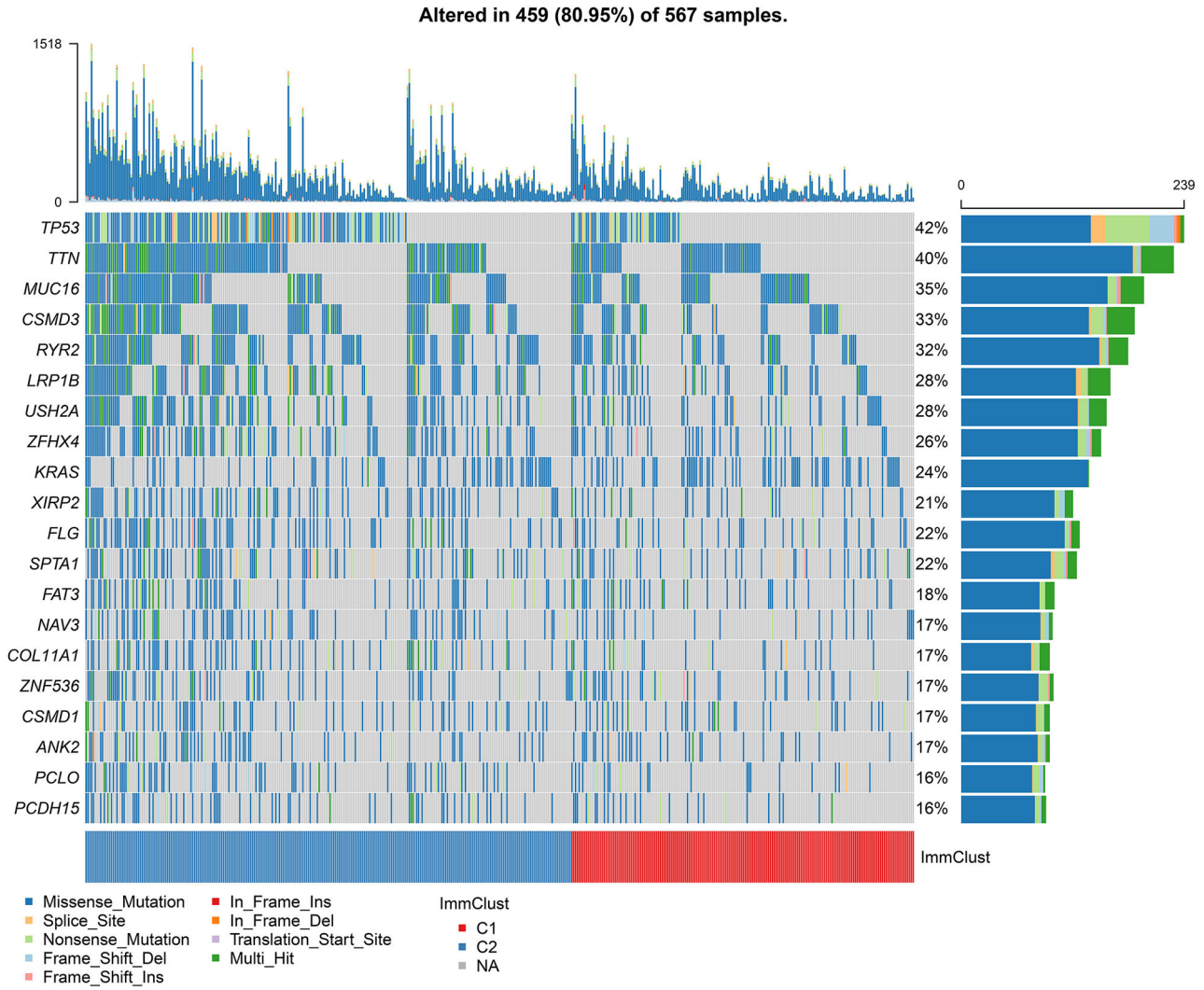

FIGURE 7 | Differences in somatic mutations between two LUAD clusters from TCGA database. The 20 genes are ordered according to the frequencies of mutation. The bottom of the panel exhibits the mutation types as well as sample clusters. The right of the panel displays the mutation frequencies of the genes.

subtypes based on DNA repair-related gene expression profiles. Kaplan-Meier OS analysis results demonstrated that LUAD patients in the cluster 2 exhibited worsen clinical outcomes than those in the cluster 1. Chemotherapy is the first choice for LUAD patients in the advanced stage, but its response rate is very low (35). Chemoresistance contributes to the short survival time of LUAD patients following initial chemotherapy (32). It has been estimated that chemotherapy can only reduce the deaths of lung cancer patients by 4% following 5 years in comparison to the untreated group (36). Hence, it is of importance to identify a specific molecular subtype of LUAD that could be sensitive to chemotherapy. In this study, patients in the cluster 2 may be more sensitive to six chemotherapy drugs (Cisplatin, Paclitaxel, Docetaxel, Gemcitabine, Vinorelbine, and Etoposide) compared to those in the cluster 1, which should be validated in future clinical trials.

However, there are several limitations in our study. Firstly, the signature and molecular subtypes were constructed by a retrospective study. In future studies, their predictive power will be verified in large-scale prospective research. Secondly, due to lack of SNP data in other databases, the differences in SNP between the two molecular subtypes were verified in independent datasets. Taken together, the signature and molecular subtypes that we constructed could be used to improve the current risk stratification of LUAD.

CONCLUSION

Collectively, this study constructed a 13-DNA repair gene-signature for LUAD prognosis. Following validation, this signature can accurately and independently predict patients' clinical outcomes. A nomogram combining the signature and stage was established as an individual clinical prediction tool. According to DNA repair gene expression profiles, two molecular subtypes were characterized, with distinct clinical outcomes, somatic gene mutations as well as sensitivity to

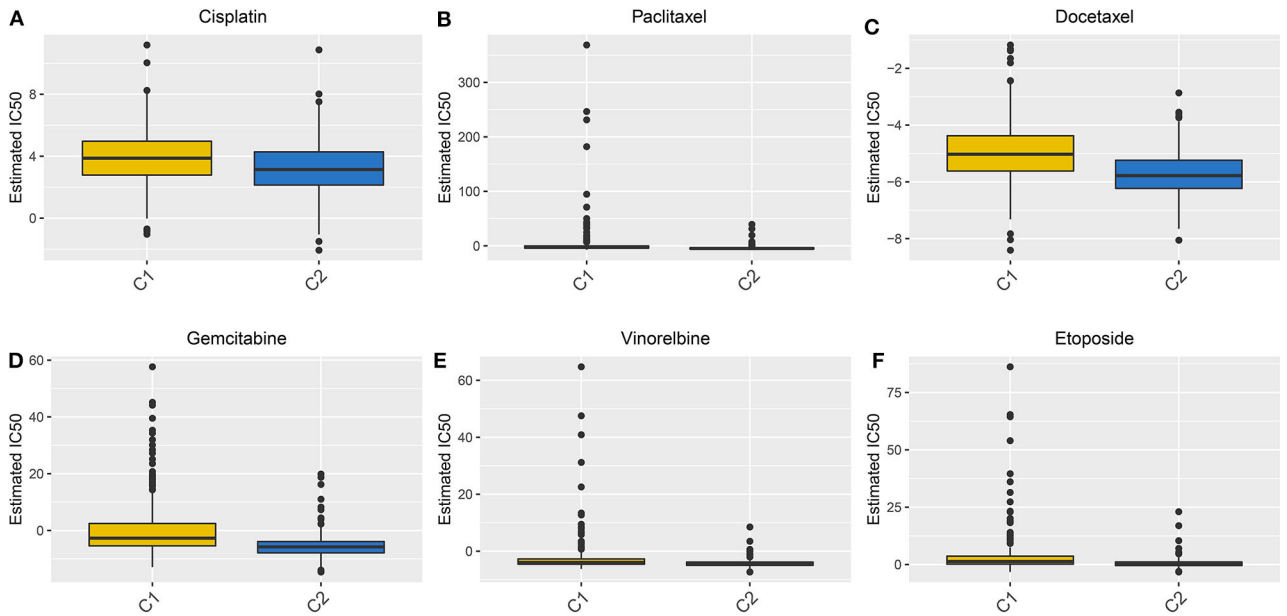

FIGURE 8 | Box plots showing the differences in estimated IC50 values of six chemotherapy drugs between the two LUAD clusters. **(A)** Cisplatin. **(B)** Paclitaxel. **(C)** Docetaxel. **(D)** Gemcitabine. **(E)** Vinorelbine. **(F)** Etoposide. Each dot is indicative of the estimated IC50 value in each LUAD sample. The higher the sensitivity to the drug, the lower the IC50 value.

chemotherapy drugs, which may be used to guide clinical treatment decisions.

DATA AVAILABILITY STATEMENT

The original contributions presented in the study are included in the article/**Supplementary Materials**, further inquiries can be directed to the corresponding author.

AUTHOR CONTRIBUTIONS

ZL conceived and designed the study. YL and BH conducted most of the experiments and data analysis, and wrote the manuscript. DL participated in collecting data and helped to draft the manuscript. All authors reviewed and approved the manuscript. All authors contributed to the article and approved the submitted version.

FUNDING

This work was funded by Sichuan Science and Technology Program (CN) (2019JDRC0068, 2019YFG0517); Research Project of Sichuan Provincial Health Commission (19PJ254); Yunnan Province Health and Family Planning Commission Medical Reserve Talents Plan (H-2017-013); and 2018CSCO-Qilu Cancer Research Fund Project (Y-Q201802-011).

SUPPLEMENTARY MATERIAL

The Supplementary Material for this article can be found online at: https://www.frontiersin.org/articles/10.3389/fmed.2020.615981/full#supplementary-material

Supplementary Table 1 | A total of 150 DNA repair-related genes.

Supplementary Table 2 | 109 DEGs between high- and low-risk groups with the threshold of |logFC| >1 and adjusted *p*-value <0.01.

REFERENCES

1. Zhu X, Chen L, Liu L, Niu X. EMT-mediated acquired EGFR-TKI resistance in NSCLC: mechanisms and strategies. *Front Oncol.* (2019) 9:1044. doi: 10.3389/fonc.2019.01044
2. Yun X, Zhang K, Wang J, Pangeni RP, Yang L, Bonner M, et al. Targeting USP22 suppresses tumorigenicity and enhances cisplatin sensitivity through ALDH1A3 downregulation in cancer-initiating cells from lung adenocarcinoma. *Mol Cancer Res.* (2018) 16:1161–71. doi: 10.1158/1541-7786.MCR-18-0042
3. Moreno Leon L, Gautier M, Allan R, Ilié M, Nottet N, Pons N, et al. The nuclear hypoxia-regulated NLUCAT1 long non-coding RNA contributes to an aggressive phenotype in lung adenocarcinoma through regulation of oxidative stress. *Oncogene.* (2019) 38:7146–65. doi: 10.1038/s41388-019-0935-y
4. Denisenko TV, Budkevich IN, Zhivotovsky B. Cell death-based treatment of lung adenocarcinoma. *Cell Death Dis.* (2018) 9:117. doi: 10.1038/s41419-017-0063-y
5. Zhang Y, Du H, Li Y, Yuan Y, Chen B, Sun S. Elevated TRIM23 expression predicts cisplatin resistance in lung adenocarcinoma. *Cancer Sci.* (2020) 111:637–46. doi: 10.1111/cas.14226

6. Guan NN, Zhao Y, Wang CC, Li JQ, Chen X, Piao X. Anticancer drug response prediction in cell lines using weighted graph regularized matrix factorization. *Mol Ther Nucleic Acids.* (2019) 17:164–74. doi: 10.1016/j.omtn.2019.05.017
7. Zhang M, Zhu K, Pu H, Wang Z, Zhao H, Zhang J, et al. An immune-related signature predicts survival in patients with lung adenocarcinoma. *Front Oncol.* (2019) 9:1314. doi: 10.3389/fonc.2019.01314
8. Chatterjee N, Walker GC. Mechanisms of DNA damage, repair, and mutagenesis. *Environ Mol Mutagen.* (2017) 58:235–63. doi: 10.1002/em.22087
9. Chang HHY, Pannunzio NR, Adachi N, Lieber MR. Non-homologous DNA end joining and alternative pathways to double-strand break repair. *Nat Rev Mol Cell Biol.* (2017) 18:495–506. doi: 10.1038/nrm.2017.48
10. Sancar A, Lindsey-Boltz LA, Unsal-Kaçmaz K, Linn S. Molecular mechanisms of mammalian DNA repair and the DNA damage checkpoints. *Annu Rev Biochem.* (2004) 73:39–85. doi: 10.1146/annurev.biochem.73.011303.073723
11. Gavande NS, VanderVere-Carozza PS, Hinshaw HD, Jalal SI, Sears CR, Pawelczak KS, et al. DNA repair targeted therapy: the past or future of cancer treatment? *Pharmacol Ther.* (2016) 160:65–83. doi: 10.1016/j.pharmthera.2016.02.003
12. Stover EH, Konstantinopoulos PA, Matulonis UA, Swisher EM. Biomarkers of response and resistance to DNA repair targeted therapies. *Clin Cancer Res.* (2016) 22:5651–60. doi: 10.1158/1078-0432.CCR-16-0247
13. Lu GS, Li M, Xu CX, Wang D. APE1 stimulates EGFR-TKI resistance by activating Akt signaling through a redox-dependent mechanism in lung adenocarcinoma. *Cell Death Dis.* (2018) 9:1111. doi: 10.1038/s41419-018-1162-0
14. Choi EB, Yang AY, Kim SC, Lee J, Choi JK, Choi C, et al. PARP1 enhances lung adenocarcinoma metastasis by novel mechanisms independent of DNA repair. *Oncogene.* (2016) 35:4569–79. doi: 10.1038/onc.2016.3
15. Dong Y, Zhang D, Cai M, Luo Z, Zhu Y, Gong L, et al. SPOP regulates the DNA damage response and lung adenocarcinoma cell response to radiation. *Am J Cancer Res.* (2019) 9:1469–83.
16. Subramanian A, Tamayo P, Mootha VK, Mukherjee S, Ebert BL, Gillette MA, et al. Gene set enrichment analysis: a knowledge-based approach for interpreting genome-wide expression profiles. *Proc Natl Acad Sci USA.* (2005) 102:15545–50. doi: 10.1073/pnas.0506580102
17. Schabath MB, Welsh EA, Fulp WJ, Chen L, Teer JK, Thompson ZJ, et al. Differential association of STK11 and TP53 with KRAS mutation-associated gene expression, proliferation and immune surveillance in lung adenocarcinoma. *Oncogene.* (2016) 35:3209–16. doi: 10.1038/onc.2015.375
18. Ritchie ME, Phipson B, Wu D, Hu Y, Law CW, Shi W, et al. limma powers differential expression analyses for RNA-sequencing and microarray studies. *Nucleic Acids Res.* (2015) 43:e47. doi: 10.1093/nar/gkv007
19. Musa A, Ghoraie LS, Zhang SD, Glazko G, Yli-Harja O, Dehmer M, et al. A review of connectivity map and computational approaches in pharmacogenomics. *Brief Bioinform.* (2018) 19:506–23. doi: 10.1093/bib/bbx023
20. Yang W, Soares J, Greninger P, Edelman EJ, Lightfoot H, Forbes S, et al. Genomics of drug sensitivity in cancer (GDSC): a resource for therapeutic biomarker discovery in cancer cells. *Nucleic Acids Res.* (2013) 41:D955–61. doi: 10.1093/nar/gks1111
21. Geeleher P, Cox N, Huang RS. pRRophetic: an R package for prediction of clinical chemotherapeutic response from tumor gene expression levels. *PLoS ONE.* (2014) 9:e107468. doi: 10.1371/journal.pone.0107468
22. Wang C, Gu Y, Zhang E, Zhang K, Qin N, Dai J, et al. A cancer-testis non-coding RNA LIN28B-AS1 activates driver gene LIN28B by interacting with IGF2BP1 in lung adenocarcinoma. *Oncogene.* (2019) 38:1611–24. doi: 10.1038/s41388-018-0548-x
23. Jinjia C, Xiaoyu W, Hui S, Wenhua L, Zhe Z, Xiaodong Z, et al. The use of DNA repair genes as prognostic indicators of gastric cancer. *J Cancer.* (2019) 10:4866–75. doi: 10.7150/jca.31062
24. Li N, Zhao L, Guo C, Liu C, Liu Y. Identification of a novel DNA repair-related prognostic signature predicting survival of patients with hepatocellular carcinoma. *Cancer Manag Res.* (2019) 11:7473–84. doi: 10.2147/CMAR.S204864
25. Parry EM, Gable DL, Stanley SE, Khalil SE, Antonescu V, Florea L, et al. Germline mutations in DNA repair genes in lung adenocarcinoma. *J Thorac Oncol.* (2017) 12:1673–8. doi: 10.1016/j.jtho.2017.08.011
26. Luo J, Liu K, Yao Y, Sun Q, Zheng X, Zhu B, et al. DMBX1 promotes tumor proliferation and regulates cell cycle progression via repressing OTX2-mediated transcription of p21 in lung adenocarcinoma cell. *Cancer Lett.* (2019) 453:45–56. doi: 10.1016/j.canlet.2019.03.045
27. You J, Wang X, Wang J, Yuan B, Zhang Y. DDX59 promotes DNA replication in lung adenocarcinoma. *Cell Death Discov.* (2017) 3:16095. doi: 10.1038/cddiscovery.2016.95
28. Basse V, Schick U, Guéguen P, Le Maréchal C, Quintin-Roué I, Descourt R, et al. A mismatch repair-deficient hepatoid adenocarcinoma of the lung responding to anti-PD-L1 durvalumab therapy despite no PD-L1 expression. *J Thorac Oncol.* (2018) 13:e120–2. doi: 10.1016/j.jtho.2018.03.004
29. Yu B, Li T, Chen J, Wang FQ, Fu JH, Liu SM, et al. Identification of activated pathways in lung adenocarcinoma based on network strategy. *J Cancer Res Ther.* (2020) 16:793–9. doi: 10.4103/0973-1482.199458
30. Yin N, Liu Y, Khoor A, Wang X, Thompson EA, Leitges M, et al. Protein kinase Cι and Wnt/β-catenin signaling: alternative pathways to Kras/Trp53-driven lung adenocarcinoma. *Cancer Cell.* (2019) 36:156–167.e157. doi: 10.1016/j.ccell.2019.07.002
31. Kim S, Park C, Jun Y, Lee S, Jung Y, Kim J. Integrative profiling of alternative splicing induced by *U2AF1 S34F* mutation in lung adenocarcinoma reveals a mechanistic link to mitotic stress. *Mol Cells.* (2018) 41:733–41. doi: 10.14348/molcells.2018.0176
32. Zhan J, Wang P, Li S, Song J, He H, Wang Y, et al. HOXB13 networking with ABCG1/EZH2/Slug mediates metastasis and confers resistance to cisplatin in lung adenocarcinoma patients. *Theranostics.* (2019) 9:2084–99. doi: 10.7150/thno.29463
33. Wu X, Zhang W, Hu Y, Yi X. Bioinformatics approach reveals systematic mechanism underlying lung adenocarcinoma. *Tumori.* (2015) 101:281–6. doi: 10.5301/tj.5000278
34. Koras K, Juraeva D, Kreis J, Mazur J, Staub E, Szczurek E. Feature selection strategies for drug sensitivity prediction. *Sci Rep.* (2020) 10:9377. doi: 10.1038/s41598-020-65927-9
35. Seidl C, Panzitt K, Bertsch A, Brcic L, Schein S, Mack M, et al. MicroRNA-182-5p regulates hedgehog signaling pathway and chemosensitivity of cisplatin-resistant lung adenocarcinoma cells via targeting GLI2. *Cancer Lett.* (2020) 469:266–76. doi: 10.1016/j.canlet.2019.10.044
36. Pignon JP, Tribodet H, Scagliotti GV, Douillard JY, Shepherd FA, Stephens RJ, et al. Lung adjuvant cisplatin evaluation: a pooled analysis by the LACE collaborative group. *J Clin Oncol.* (2008) 26:3552–9. doi: 10.1200/JCO.2007.13.9030

Conflict of Interest: The authors declare that the research was conducted in the absence of any commercial or financial relationships that could be construed as a potential conflict of interest.

Copyright © 2020 Hu, Liu, Liu and Li. This is an open-access article distributed under the terms of the Creative Commons Attribution License (CC BY). The use, distribution or reproduction in other forums is permitted, provided the original author(s) and the copyright owner(s) are credited and that the original publication in this journal is cited, in accordance with accepted academic practice. No use, distribution or reproduction is permitted which does not comply with these terms.

frontiers in Medicine

MINI REVIEW
published: 30 November 2020
doi: 10.3389/fmed.2020.612393

Long Non-coding RNAs in Cancer: Implications for Diagnosis, Prognosis, and Therapy

Yuchen Qian, Lei Shi and Zhong Luo**

School of Life Sciences, Chongqing University, Chongqing, China

Long non-coding RNAs (lncRNAs) are major components of cellular transcripts that are arising as important players in various biological pathways. They have received extensive attention in recent years, regarded to be involved in both developmental processes and various diseases. Due to their specific expression and functional diversity in a variety of cancers, lncRNAs have promising applications in cancer diagnosis, prognosis and therapy. Studies have shown that lncRNAs with high specificity and accuracy have the potential to become biomarkers in cancers. LncRNAs can be noninvasively extracted from body fluids, tissues and cells, and can be used as independent or auxiliary biomarkers to improve the accuracy of diagnosis or prognosis. Currently, the most well-recognized lncRNA is PCA3, which has been approved for use in the diagnosis of prostate cancer. Moreover, the underlying mechanisms of lncRNAs were explored as therapeutic targets, which have been investigated in clinical trials of several cancers. In this review, we presented a compilation of recent publications, clinical trials and patents, addressing the potential of lncRNAs that could be considered as biomarkers or therapeutic targets, with the hopes of providing promised implications for future cancer therapy.

Keywords: long non-coding RNAs, cancer, biomarker, diagnosis, prognosis, therapy

OPEN ACCESS

Edited by:
Guo Chen,
Jinan University, China

Reviewed by:
Zhaojun Qiu,
The Ohio State University, United States
Lijuan Du,
University of Maryland, United States

****Correspondence:***
Lei Shi
shil@cqu.edu.cn
Zhong Luo
luozhong918@cqu.edu.cn

Specialty section:
This article was submitted to Precision Medicine, a section of the journal Frontiers in Medicine

Received: *30 September 2020*
Accepted: *09 November 2020*
Published: *30 November 2020*

Citation:
Qian Y, Shi L and Luo Z (2020) Long Non-coding RNAs in Cancer: Implications for Diagnosis, Prognosis, and Therapy. Front. Med. 7:612393. doi: 10.3389/fmed.2020.612393

INTRODUCTION

Cancer is a life-threating disease with rising morbidity and mortality (1). Despite tremendous progress made in recent years, there are still a number of issues in cancer treatment that need improvements, such as delayed diagnosis and poor prognosis (2). Most tumor biomarkers or therapeutic targets currently in clinical use are proteins. However, only 2% of human genome is translated into proteins. Therefore, we may need to focus more on non-coding regions, where more cancer mutations occur than in coding regions (2, 3). In recent years, long non-coding RNAs (lncRNAs), which occupy the majority of non-coding RNAs (ncRNAs), are hotspots in cancer research. Due to the large number of lncRNAs, with an estimate of 102,000, lncRNA-based research holds great promise in cancer treatment (3, 4).

LncRNAs are non-coding transcripts with more than 200 nucleotides in length, and most of them remain in the nucleus after transcription (5, 6). Due to their low expression levels, lncRNAs were initially considered to be transcription noise. With better understanding, lncRNAs are found to be involved in transcriptional and post-transcriptional regulation, through interactions with DNA, RNA or proteins (6). LncRNAs promote or inhibit the formation of transcription loops, and recruit or block regulators, regulating gene transcription (7–9). Besides, lncRNAs also regulate

mRNA splicing and act as precursors to other ncRNAs, such as microRNAs (miRNAs) (10). LncRNAs function as oncogenes or tumor suppressors, taking part in various signaling pathways (11). Of note, by analyzing the expression of lncRNAs in peripheral blood, urine sediments or tissue samples, a series of lncRNAs were identified with great promise as auxiliary or independent biomarkers in cancer diagnosis and prognosis (12).

There are currently few biomarkers or therapeutic agents targeting lncRNAs. Prostate cancer antigen 3 (PCA3), an early diagnostic biomarker for prostate cancer (PCa), is the first and only approved lncRNA for clinical use at this time (13). There are also some lncRNAs undergoing clinical trials or having been patented, which we will discuss in more details below. Moreover, other research of lncRNA-based drug discoveries, including UBE3A-ATS in Angelman syndrome, SCN1ANAT in Dravet syndrome and SMN-AS1 in spinal muscular atrophy, also illustrate the potential of lncRNAs (14–17).

In this review, we discuss the mechanisms by which lncRNAs function. A thorough understanding of these mechanisms is critical for the development of anti-tumor drugs. We next summarize a collection of recent publications, clinical trials, and patents and also discuss the potential of lncRNAs that could be considered as biomarkers or therapeutic targets in cancer diagnosis, prognosis and treatment.

MECHANISMS OF LncRNAs

Understanding how lncRNAs work is critical to know how they cause diseases such as cancers, and therefore to their potential applications in cancer treatment. Based on current studies, lncRNAs are implicated in many intracellular molecular interaction networks. The levels of their expression are regulated by many factors, and they are also involved in complex networks as regulatory factors. The myriad mechanisms behind these complex regulations can be summarized in four ways, including signal, scaffold, decoy, and guide (**Figure 1**) (5, 18, 19).

(i) Some lncRNAs are expressed at different levels in various cell states. Thus, they can be turned into signals, serving as indicators to reflect development or disease status (18, 20). For example, Xist, which is typically transcribed by the inactive X chromosome, can be used to indicate X chromosome inactivation (21, 22).

(ii) LncRNAs can bind proteins and act as scaffolds to assist in the assembly of regulatory complexes (23). In this way, HOTAIR interacts with polycomb repressive complex 2 (PRC2) to recruit EZH2 to promote H3K27 trimethylation or LSD1 to demethylate H3K4me2 (23, 24).

(iii) As decoys, lncRNAs regulate gene expression by preventing the binding of transcription regulators (19, 25). For example, p53-dependent PANDA inhibits proptosis by directly sequestering of NF-YA (26). In addition, as competing endogenous RNAs (ceRNAs), lncRNAs also bind miRNAs and prevent RNA degradation (27). This is common in cancers. H19 acts as ceRNAs both for miR-17-5P in thyroid cancer and for miR-152 in breast cancer (27, 28).

(iv) LncRNAs can also guide the transcription factors to specific sites (29). In this way, MEG3 guides PRC2 and forms a complex with DNA (30). It is noteworthy that each type is not mutually exclusive, and an individual lncRNA may have one or more of these functions (20).

LncRNAs IN CANCER DIAGNOSIS

Some lncRNAs are highly tissue specific and abnormally expressed in cancer, which can be extracted noninvasively from the circulation (31, 32). These features render them potential candidates for cancer diagnosis (**Table 1**). The one most well-recognized is PCA3, a biomarker for early diagnosis of prostate cancer (PCa) (67). As mentioned above, it has been approved in clinical use (13). The diagnosis of PCa currently relies on the elevation of serum prostate-specific antigen (PSA) (12). However, its specificity in discriminating benign and malignant tumors is low, which may lead to over-diagnosis in low-risk patients (68). PSA is a good predictor when its level is above 10 ng/ml. However, in the gray area of PSA, some auxiliary indicators are still needed to improve diagnostic accuracy (12).

Urine PCA3 diagnosis is not only highly sensitive (58–82%) but also has excellent specificity (59–76%) (33). PCA3 is up-regulated 60 to 100-folds in more than 95% of PCa specimens (18, 33). It is noteworthy that PCA3-based assays are still effective when cancer cells make up <10% of the examined sample (33). PCA3 silence leads to an increase in the expression of E-cadherin, Claudin-3, and Keratin-18, while a decrease of Vimentin. The association between PCA3 and these traditional protein biomarkers provides more support for its application as diagnostic marker (34).

MALAT1 can be used as an auxiliary biomarker to improve the accuracy of early diagnosis, especially in the gray area of PSA. Its diagnostic accuracy is higher than the previous index, free/total PSA ratio (12, 69). In fact, one of the MALAT1 assay has been patented in PCa diagnosis (CN104498495).

H19 is another lncRNA with high diagnostic sensitivity and specificity. In breast cancer, patient plasma H19 levels were elevated, with an sensitivity of 0.81 (AUC, area under the curve), higher than traditional diagnostic biomarkers (42). H19 is related to many important miRNAs in the network of cancer-related functions (70). It is a precursor of miR-675 which has downstream targets like c-CbI, CbI-b and Igf1r (71, 72). H19/miR-675 also causes the activation of EGRF and c-Met, which leads to the sustained activation of Akt and Erk (43). Besides, H19 acts as a ceRNA for Let-7 to maintain the activation of breast cancer stem cells (73). The potential of miRNAs like miR-675 and Let-7 as biomarkers has been reported in cancers, which implicate the diagnostic

Abbreviations: LncRNA, Long Non-coding RNA; ncRNA, Non-coding RNA; miRNA, MicroRNA; PCA3, Prostate Cancer Antigen 3; PCa, Prostate Cancer; ceRNA, Competing Endogenous RNA; PSA, Prostate-specific Antigen; AUC, Area Under the Curve; EGRF, Epidermal Growth Factor Receptor; GC, Gastric Cancer; SNPs, Single Nucleotide Polymorphisms; CRC, Colorectal Cancer; OS, Overall Survival; TCC, Bladder Transitional Cell Carcinoma; EMT, Epithelial to Mesenchymal Transition; HCC, Hepatocellular Carcinoma.

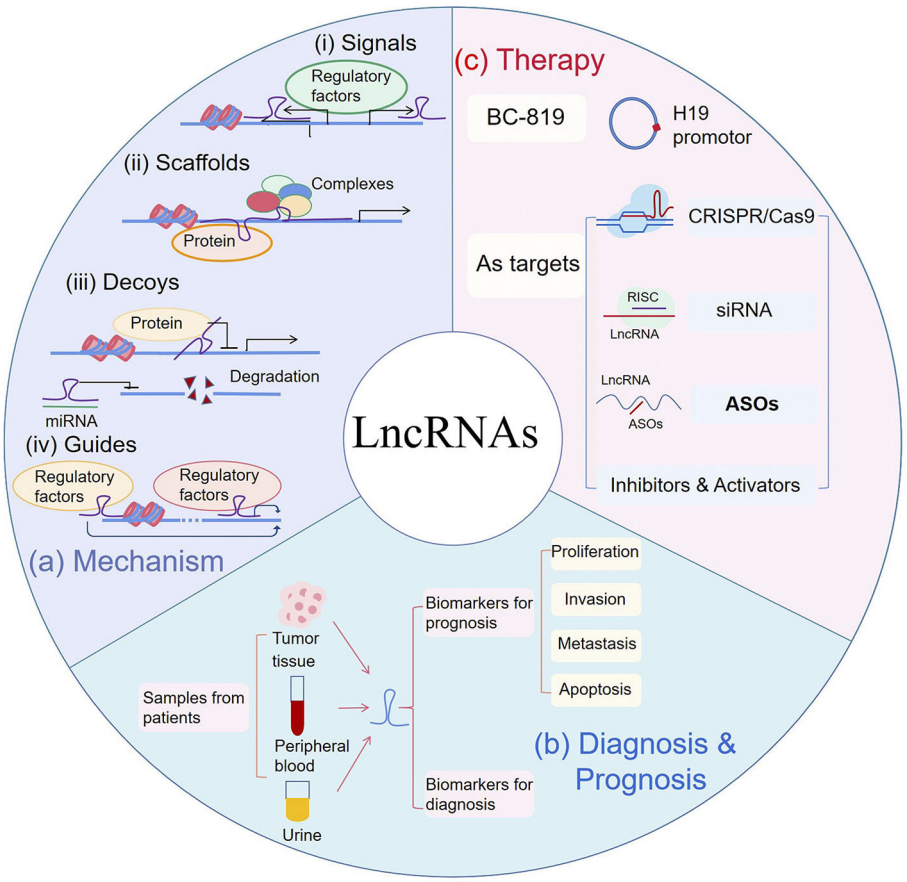

FIGURE 1 | (a) Mechanism: (i) LncRNAs can serve as signals to reflect the activity of pathways or developmental status. (ii) LncRNAs act as scaffolds by recruiting proteins to regulate gene expression. (iii) LncRNAs can be used as decoys to block activities of proteins and can also bind to microRNA (miRNA) to inhibit miRNA-induced degradation. (iv) As guides, lncRNAs recruit transcription regulators to specific sites. **(b)** Diagnosis & Prognosis: As biomarkers for cancer diagnosis and prognosis, lncRNAs can be extracted from tumor tissues, peripheral blood and urine samples of patients. In prognosis, they are correlated to patient's proliferation, metastasis, invasion or survival. **(c)** Therapy: BC-819, fused with H19 promotor and Diphtheria toxin gene, was used in phase 2 clinical trial. Gene editing such as CRISPR/Cas9, small interfering RNA (siRNA) and antisense oligonucleotides (ASOs), were used to silence targeted lncRNAs. RISC RNA-induced silencing complex.

potential of H19 (74). In gastric cancer (GC), H19 had a high diagnostic ability with an AUC of 0.838. A patent has been filed for gastric cancer diagnosis with HOTAIR and MALAT1 (CN105586399A), showing possible applications. Notably, single nucleotide polymorphisms (SNPs) of H19 are used to predict the risk of cancer, such as rs2839698 and rs2107425 genotypes are found to be related to decreased risk of bladder cancer (75).

LncRNAs are usually aberrantly expressed and can be extracted noninvasively from the circulation (32). Although some lncRNAs overlap in various cancer, ∼60% of these abnormally expressed lncRNAs are cancer type-specific (31). Recently, the diagnostic potential of some lncRNAs has been implicated by clinical trials (76). One report have shown that UCA1 was sensitive for bladder cancer, especially in patients with superficial G2-G3 (77). Another clinical trial is underway to explore the possible application of CCAT1 in CRC (NCT04269746). Moreover, lncRNAs can not only be used as an independent biomarkers, but also can be combined with other lncRNAs or proteins to improve the sensitivity and accuracy of diagnosis (76).

LncRNAs IN CANCER PROGNOSIS

The expression of lncRNAs in cancer correlates with overall survival (OS), metastasis, tumor stage or grade, thus can potentially serve as markers for prognosis (**Table 1**).

HOTAIR is transcribed from HOXC locus located at 12q13.13 (78). It has been proved to be poor prognostic indicators of various cancers. Bladder transitional cell carcinoma (TCC) patients with high HOTAIR have lower overall survival, and positively associated with histological grade (41).

An analysis of a large cohort containing 300 samples showed that the increased expression level of HOTAIR in GC tissues was correlated with peritoneal diffusion (55). In addition, in diffuse GC, tissues with a high HOTAIR level showed more

TABLE 1 | LncRNAs as diagnostic or prognostic biomarkers.

Cancer[a]	LncRNAs	Expression	Applications	References[b]
Prostate	PCA3	Up	Diagnosis	(33–35), Approved
	MALAT1	Up	Diagnosis	(36), CN104498495
	LincRNA-p21	Up	Diagnosis	(37)
Bladder	PTENP1	Down	Diagnosis	(38)
	UCA1	Up	Diagnosis	(39)
	SPRY4-IT1	Up	Diagnosis	(40)
	HOTAIR	Up	Prognosis	(41)
Breast	H19	Up	Diagnosis	(42, 43)
	MALAT1	Up/Down[c]	Prognosis	(44, 45)
Colorectal	CCAT1	Up	Diagnosis	(46), NCT04269746, US20110097271A1
	CCAT2	Up	Prognosis	(47, 48)
	MALAT1	Up	Prognosis	(49)
	MEG3	Down	Prognosis	(50)
	HOTAIR	Up	Prognosis	(51, 52)
Gastric	HOTAIR	Up	Diagnosis	(53, 54), CN105586399A
	HOTAIR	Up	Prognosis	(55–57)
	MALAT1	Up	Diagnosis	(58), CN105586399A
	MALAT1	Up	Prognosis	(59)
Liver	MALAT1	Up	Prognosis	(60–62)
	H19	Up	Diagnosis	(42), CN105132559
Esophageal	CCAT2	Up	Prognosis	(48)
	PCAT1	Up	Prognosis	(63)
Glioma	CASC2	Down	Diagnosis	(64), CN103993088A
	CRNDE	Up	Prognosis	(65), CN103966339A
Thyroid	HOTAIR	Up	Diagnosis	(66), NCT03469544

[a] *The cancer types to which the indicated tissue corresponds.*
[b] *The accession numbers of clinical trials or patents were list as follows.*
[c] *The expression of MALAT1 in breast cancer is still controversial as described in the text.*

venous infiltration and poorer overall survival (56). Besides, HOTAIR is involved in tumorigenicity in pancreatic cancer and can also cause CRC proliferation and metastasis mediated by PCR2 complex (51, 52).

MALAT1, located on chromosome 11q13.1, is dysregulated in many cancers (49). A cohort analysis of 169 patients showed that patients with high MALAT1 expression levels had a worse prognosis than the normal group (79). Moreover, upregulated MALAT1 is closely related to hepatocellular carcinoma (HCC) progression, and can be an independent biomarker for recurrence after liver transplantation (80). However, the roles of MALAT1 in breast cancer are still controversial. In previous reports, MALAT1 acts as a ceRNA for miR-1/CDC42 axis to enhance cell migration and invasion (44). On the contrary, Kim et al. reported that MALAT1 acted as a metastasis suppressor by preventing the binding of transcription factor TEAD and its co-activator YAP (45). In addition, MALAT1 knockout leads to different phenotypes in various cell lines and models, and there is no clear explanation for this variation. Therefore, further investigation is required before MALAT1 could be use as a potential prognositic biomarker (81, 82).

CCAT2 showed extensive effects during proliferation and metastasis in a variety of cancers (47). In fact, patients with high CCAT2 had a lower overall survival and almost twice the risk of death (48).

LncRNAs IN CANCER THERAPY

The aberrant expression of lncRNAs and their involvement in diverse cellular processes make them possible targets for cancer therapy. Clinical studies have demonstrated the importance of studying the mechanisms of lncRNA. BC-819, a plasmid containing the promoter of H19 and coding sequence of diphtheria toxin, has been applied in clinical trials of bladder, pancreatic and ovarian cancer (83, 84). The H19 promoter allows diphtheria toxin to be specifically expressed in tumor tissues. Thus, BC-819 can effectively ablate tumors, reduce tumor growth, prolong recurrence time, and has low local toxicity (83–85). We can also learn about the prospect of lncRNAs from patent applications (86). For example, an inhibitor of LINC01212 is used to treat melanoma (US2016271163). What's more, lncMyoD, acts directly as functional element on IMP1 and IMP2 for sarcoma therapy (WO2015020960). Furthermore, although lncRNAs are considered with no protein-coding ability, some special lncRNAs can be translated into micropeptides (87). In fact, some patents utilized these polypeptides for antibodie

design in cancer diagnosis and treatment, such as lncRNA-6585 and its antibody in cervical cancers (CN109337903A).

LncRNAs and their loci can be targeted for the design and synthesis of specific nucleic acid sequences in therapy, such as CRISPR/Cas9 design, small interfering RNA (siRNA) and antisense oligonucleotides (ASOs). However, unlike mRNA, most lncRNAs are located in the nucleus and have high-level structure (88, 89). Oligonucleotide drugs must enter cells and bind to their target RNA to function, which raises challenges for drug delivery and intrinsic affinity (90). To address these issues, a common approach is to modify the sequence of oligonucleotides, and the development of nanomedicine to improve drug delivery.

(i) CRISPR/Cas9 silencing of NEAT1 or MALAT1 was reported to inhibit metastasis of cancer cells (91). A patent used CRISPR/Cas9 to silence UCA1 inhibited the growth of cancer cells (CN106399306B). However, due to the overlap of loci, CRISPR/Cas9 cannot be applied to the silencing of all lncRNAs. In a genome-wide study including 15,929 lncRNA loci, only 38% were successfully silenced as expected, while the remaining had a severe negative impact on the expression of neighboring genes (91).

(ii) Both of siRNA and ASOs can effectively and specifically silence the expression of target genes, making them essential tools for research and clinical uses. Despite some challenges, the progress of siRNAs as therapy drugs has evolved from pre-design to clinical trials (92). Recently, a siRNA targeting DDX11-AS1 has been patented in liver cancer (CN108546702A). Compare to siRNA, ASOs enter the nucleus more efficiently and bind to precursor RNAs near the intron and exon junction, affecting the alternative splicing process (93).

(iii) Methods for affinity and delivery improvement: Affinity of oligonucleotides can be improved by constructing aptamers (94). They can also be modified to reduce nuclease degradation and increase their internal affinity (95, 96). For delivery, one effective approach is to construct drug carriers, such as in the form of gold nanoparticles (97).

DISCUSSION

In recent years, many studies have been devoted to lncRNAs in cancer progression and treatment. Due to their highly specific expression and diverse functions, lncRNAs hold great promise for cancer diagnosis, prognosis and therapy. To the best of our knowledge, however, the sole lncRNA that has been approved in clinical use is PCA3 in the diagnosis of PCa. Although multiple lncRNAs have been extensively investigated in clinical trials or have been patented, their applications still have a long way to go. Here we review potential lncRNAs that could be considered as biomarkers or therapeutic targets and discuss some of the issues that deserve special consideration.

First, the actual mechanisms by which lncRNA act are not fully understood. Indeed, the developing of oligonucleotide drug Genasense can be served as an informative case. Due to the lack of in-depth understanding of the mechanism, the development of Genasense failed, revealing the importance of understanding the mechanism in drug development (93). Second, the low conservation of lncRNAs, some of which are expressed only in primates, makes it difficult to establish universal experimental models (98). For the majority of lncRNAs, we have yet to establish a suitable animal model, which is essential for understanding the functions better. Third, although some experiments have been conducted on the applications of lncRNAs, they are not very reliable due to the small sample size. Moreover, for therapeutic targets, it is important to study whether the dysregulated expression of lncRNAs is the cause or a result of cancer.

Although there are many challenges, the prospects and clinical significance of lncRNAs cannot be overlooked in the long run. A distinctive feature of lncRNAs is their high specificity in tumor tissues and cells, making it possible for them to be specific and accurate biomarkers (99). In addition, abnormally expressed lncRNAs can be extracted non-invasively, showing great potential to be more economical and less harmful. Compared to protein-based anti-tumor drugs, lncRNA are more refined and less toxic, and the low expression of lncRNA means that only a small amount of inhibitors are needed to make a difference (16). Besides, bioinformatics and computational tools provide new opportunities for lncRNA biomarker development (100). However, due to the lack of experimental evidence and no further clinical validation, we do not discuss it here. Although there are currently no lncRNA-based oncology drugs, drugs targeting lncRNAs in other diseases will provide useful clinical insights.

In conclusion, the intensive study of lncRNAs has brought new hope for the diagnosis and treatment of cancer. Although limitations exist, such as mechanisms, conservative, and animal models, the successful application of PCA3 is a great source of inspiration and impetus for clinical research on lncRNAs. A comprehensive understanding of lncRNA's expression, structure, and mechanisms will help to open up a new intervention, identifying novel and sensitive biomarkers and therapeutic targets.

AUTHOR CONTRIBUTIONS

YQ and LS participated in the design of the study, prepared table, figure, and wrote the manuscript. LS and ZL conceived the study and wrote the manuscript. All authors contributed to the article and approved the submitted version.

FUNDING

This work was supported by the Fundamental Research Funds for the Central Universities (2019CDYGYB024), the National Natural Science Foundation of China (31300726), and Chongqing Primary and Middle School Innovation Talent Training Project (CY200118).

REFERENCES

1. Bray F, Ferlay J, Soerjomataram I, Siegel RL, Torre LA, Jemal A. Global cancer statistics 2018: GLOBOCAN estimates of incidence and mortality worldwide for 36 cancers in 185 countries. *CA Cancer J Clin.* (2018) 68:394–424. doi: 10.3322/caac.21492
2. Chandra Gupta S, Nandan Tripathi Y. Potential of long non-coding RNAs in cancer patients, from biomarkers to therapeutic targets. *Int J Cancer.* (2017) 140:1955–67. doi: 10.1002/ijc.30546
3. Cuykendall TN, Rubin MA, Khurana E. Non-coding genetic variation in cancer. *Curr Opin Syst Biol.* (2017) 1:9–15. doi: 10.1016/j.coisb.2016.12.017
4. Zhao Y, Li H, Fang S, Kang Y, Wu W, Hao Y, et al. NONCODE 2016: an informative and valuable data source of long non-coding RNAs. *Nucleic Acids Res.* (2016) 44:D203–8. doi: 10.1093/nar/gkv1252
5. Wang KC, Chang HY. Molecular mechanisms of long noncoding RNAs. *Mol Cell.* (2011) 43:904–14. doi: 10.1016/j.molcel.2011.08.018
6. Quinn JJ, Chang HY. Unique features of long non-coding RNA biogenesis and function. *Nat Rev Genet.* (2016) 17:47–62. doi: 10.1038/nrg.2015.10
7. Li W, Notani D, Ma Q, Tanasa B, Nunez E, Chen AY, et al. Functional roles of enhancer RNAs for oestrogen-dependent transcriptional activation. *Nature.* (2013) 498:516–20. doi: 10.1038/nature12210
8. Lai F, Orom UA, Cesaroni M, Beringer M, Taatjes DJ, Blobel GA, et al. Activating RNAs associate with mediator to enhance chromatin architecture and transcription. *Nature.* (2013) 494:497–501. doi: 10.1038/nature11884
9. Khalil AM, Guttman M, Huarte M, Garber M, Raj A, Rivea Morales D, et al. Many human large intergenic noncoding RNAs associate with chromatin-modifying complexes and affect gene expression. *Proc Natl Acad Sci USA.* (2009) 106:11667–72. doi: 10.1073/pnas.0904715106
10. Jarroux J, Morillon A, Pinskaya M. History, discovery, and classification of lncRNAs. *Adv Exp Med Biol.* (2017) 1008:1–46. doi: 10.1007/978-981-10-5203-3_1
11. Huarte M. The emerging role of lncRNAs in cancer. *Nat Med.* (2015) 21:1253–61. doi: 10.1038/nm.3981
12. Smolle MA, Bauernhofer T, Pummer K, Calin GA, Pichler M. Current insights into long non-coding RNAs (LncRNAs) in prostate cancer. *Int J Mol Sci.* (2017) 18:473. doi: 10.3390/ijms18020473
13. Groskopf J, Aubin SM, Deras IL, Blase A, Bodrug S, Clark C, et al. APTIMA PCA3 molecular urine test: development of a method to aid in the diagnosis of prostate cancer. *Clin Chem.* (2006) 52:1089–95. doi: 10.1373/clinchem.2005.063289
14. Meng L, Ward AJ, Chun S, Bennett CF, Beaudet AL, Rigo F. Towards a therapy for Angelman syndrome by targeting a long non-coding RNA. *Nature.* (2015) 518:409–12. doi: 10.1038/nature13975
15. Hsiao J, Yuan TY, Tsai MS, Lu CY, Lin YC, Lee ML, et al. Upregulation of haploinsufficient gene expression in the brain by targeting a long non-coding RNA improves seizure phenotype in a model of dravet syndrome. *EBioMedicine.* (2016) 9:257–77. doi: 10.1016/j.ebiom.2016.05.011
16. d'Ydewalle C, Ramos DM, Pyles NJ, Ng SY, Gorz M, Pilato CM, et al. The antisense transcript SMN-AS1 regulates SMN expression and is a novel therapeutic target for spinal muscular atrophy. *Neuron.* (2017) 93:66–79. doi: 10.1016/j.neuron.2016.11.033
17. Woo CJ, Maier VK, Davey R, Brennan J, Li G, Brothers J, et al. Gene activation of SMN by selective disruption of lncRNA-mediated recruitment of PRC2 for the treatment of spinal muscular atrophy. *Proc Natl Acad Sci USA.* (2017) 114:E1509–18. doi: 10.1073/pnas.1616521114
18. Schmitz SU, Grote P, Herrmann BG. Mechanisms of long noncoding RNA function in development and disease. *Cell Mol Life Sci.* (2016) 73:2491–509. doi: 10.1007/s00018-016-2174-5
19. Balas MM, Johnson AM. Exploring the mechanisms behind long noncoding RNAs and cancer. *Noncoding RNA Res.* (2018) 3:108–17. doi: 10.1016/j.ncrna.2018.03.001
20. Kazemzadeh M, Safaralizadeh R, Orang AV. LncRNAs: emerging players in gene regulation and disease pathogenesis. *J Genet.* (2015) 94:771–84. doi: 10.1007/s12041-015-0561-6
21. Pontier DB, Gribnau J. Xist regulation and function explored. *Hum Genet.* (2011) 130:223–36. doi: 10.1007/s00439-011-1008-7
22. Zylicz JJ, Bousard A, Zumer K, Dossin F, Mohammad E, da Rocha ST, et al. The implication of early chromatin changes in X chromosome inactivation. *Cell.* (2019) 176:182–97.e23. doi: 10.1016/j.cell.2018.11.041
23. Zappulla DC, Cech TR. Yeast telomerase RNA: a flexible scaffold for protein subunits. *Proc Natl Acad Sci USA.* (2004) 101:10024–9. doi: 10.1073/pnas.0403641101
24. Rinn JL, Kertesz M, Wang JK, Squazzo SL, Xu X, Brugmann SA, et al. Functional demarcation of active and silent chromatin domains in human HOX loci by noncoding RNAs. *Cell.* (2007) 129:1311–23. doi: 10.1016/j.cell.2007.05.022
25. Rinn JL, Chang HY. Genome regulation by long noncoding RNAs. *Annu Rev Biochem.* (2012) 81:145–66. doi: 10.1146/annurev-biochem-051410-092902
26. Puvvula PK, Desetty RD, Pineau P, Marchio A, Moon A, Dejean A, et al. Long noncoding RNA PANDA and scaffold-attachment-factor SAFA control senescence entry and exit. *Nat Commun.* (2014) 5:5323. doi: 10.1038/ncomms6323
27. Li Z, Li Y, Li Y, Ren K, Li X, Han X, et al. Long non-coding RNA H19 promotes the proliferation and invasion of breast cancer through upregulating DNMT1 expression by sponging miR-152. *J Biochem Mol Toxicol.* (2017) 31:e21933. doi: 10.1002/jbt.21933
28. Liu L, Yang J, Zhu X, Li D, Lv Z, Zhang X. Long noncoding RNA H19 competitively binds miR-17-5p to regulate YES1 expression in thyroid cancer. *FEBS J.* (2016) 283:2326–39. doi: 10.1111/febs.13741
29. Hung T, Chang HY. Long noncoding RNA in genome regulation: prospects and mechanisms. *RNA Biol.* (2010) 7:582–5. doi: 10.4161/rna.7.5.13216
30. Mondal T, Subhash S, Vaid R, Enroth S, Uday S, Reinius B, et al. MEG3 long noncoding RNA regulates the TGF-beta pathway genes through formation of RNA-DNA triplex structures. *Nat Commun.* (2015) 6:7743. doi: 10.1038/ncomms8743
31. Yan X, Hu Z, Feng Y, Hu X, Yuan J, Zhao SD, et al. Comprehensive genomic characterization of long non-coding RNAs across human cancers. *Cancer Cell.* (2015) 28:529–40. doi: 10.1016/j.ccell.2015.09.006
32. Schmitt AM, Chang HY. Long noncoding RNAs in cancer pathways. *Cancer Cell.* (2016) 29:452–63. doi: 10.1016/j.ccell.2016.03.010
33. Hessels D, Klein Gunnewiek JM, van Oort I, Karthaus HF, van Leenders GJ, van Balken B, et al. DD3(PCA3)-based molecular urine analysis for the diagnosis of prostate cancer. *Eur Urol.* (2003) 44:8–15. discussion: 15–6. doi: 10.1016/S0302-2838(03)00201-X
34. Lemos AE, Ferreira LB, Batoreu NM, de Freitas PP, Bonamino MH, Gimba ER. PCA3 long noncoding RNA modulates the expression of key cancer-related genes in LNCaP prostate cancer cells. *Tumour Biol.* (2016) 37:11339–48. doi: 10.1007/s13277-016-5012-3
35. Salameh A, Lee AK, Cardo-Vila M, Nunes DN, Efstathiou E, Staquicini FI, et al. PRUNE2 is a human prostate cancer suppressor regulated by the intronic long noncoding RNA PCA3. *Proc Natl Acad Sci USA.* (2015) 112:8403–8. doi: 10.1073/pnas.1507882112
36. Ren S, Wang F, Shen J, Sun Y, Xu W, Lu J, et al. Long non-coding RNA metastasis associated in lung adenocarcinoma transcript 1 derived miniRNA as a novel plasma-based biomarker for diagnosing prostate cancer. *Eur J Cancer.* (2013) 49:2949–59. doi: 10.1016/j.ejca.2013.04.026
37. Luo J, Wang K, Yeh S, Sun Y, Liang L, Xiao Y, et al. LncRNA-p21 alters the antiandrogen enzalutamide-induced prostate cancer neuroendocrine differentiation via modulating the EZH2/STAT3 signaling. *Nat Commun.* (2019) 10:2571. doi: 10.1038/s41467-019-09784-9
38. Zheng R, Du M, Wang X, Xu W, Liang J, Wang W, et al. Exosome-transmitted long non-coding RNA PTENP1 suppresses bladder cancer progression. *Mol Cancer.* (2018) 17:143. doi: 10.1186/s12943-018-0880-3
39. Xue M, Pang H, Li X, Li H, Pan J, Chen W. Long non-coding RNA urothelial cancer-associated 1 promotes bladder cancer cell migration and invasion by way of the hsa-miR-145-ZEB1/2-FSCN1 pathway. *Cancer Sci.* (2016) 107:18–27. doi: 10.1111/cas.12844
40. Liu D, Li Y, Luo G, Xiao X, Tao D, Wu X, et al. LncRNA SPRY4-IT1 sponges miR-101-3p to promote proliferation and metastasis of bladder cancer cells through up-regulating EZH2. *Cancer Lett.* (2017) 388:281–91. doi: 10.1016/j.canlet.2016.12.005
41. Sun X, Du P, Yuan W, Du Z, Yu M, Yu X, et al. Long non-coding RNA HOTAIR regulates cyclin J via inhibition of microRNA-205 expression in bladder cancer. *Cell Death Dis.* (2015) 6:e1907. doi: 10.1038/cddis.2015.269

42. Zhang K, Luo Z, Zhang Y, Zhang L, Wu L, Liu L, et al. Circulating lncRNA H19 in plasma as a novel biomarker for breast cancer. *Cancer Biomark.* (2016) 17:187–94. doi: 10.3233/CBM-160630
43. Zhan H, Tu S, Zhang F, Shao A, Lin J. MicroRNAs and long non-coding RNAs in c-Met-regulated cancers. *Front Cell Dev Biol.* (2020) 8:145. doi: 10.3389/fcell.2020.00145
44. Chou J, Wang B, Zheng T, Li X, Zheng L, Hu J, et al. MALAT1 induced migration and invasion of human breast cancer cells by competitively binding miR-1 with cdc42. *Biochem Biophys Res Commun.* (2016) 472:262–9. doi: 10.1016/j.bbrc.2016.02.102
45. Kim J, Piao HL, Kim BJ, Yao F, Han Z, Wang Y, et al. Long noncoding RNA MALAT1 suppresses breast cancer metastasis. *Nat Genet.* (2018) 50:1705–15. doi: 10.1038/s41588-018-0252-3
46. Younger ST, L J. Rinn: 'Lnc'-ing enhancers to MYC regulation. *Cell Res.* (2014) 24:643–4. doi: 10.1038/cr.2014.54
47. Ling H, Spizzo R, Atlasi Y, Nicoloso M, Shimizu M, Redis RS, et al. CCAT2, a novel noncoding RNA mapping to 8q24, underlies metastatic progression and chromosomal instability in colon cancer. *Genome Res.* (2013) 23:1446–61. doi: 10.1101/gr.152942.112
48. Zhang X, Xu Y, He C, Guo X, Zhang J, He C, et al. Elevated expression of CCAT2 is associated with poor prognosis in esophageal squamous cell carcinoma. *J Surg Oncol.* (2015) 111:834–9. doi: 10.1002/jso.23888
49. Xu C, Yang M, Tian J, Wang X, Li Z. MALAT-1: a long non-coding RNA and its important 3' end functional motif in colorectal cancer metastasis. *Int J Oncol.* (2011) 39:169–75. doi: 10.3892/ijo.2011.1007
50. Zhang X, Zhou Y, Mehta KR, Danila DC, Scolavino S, Johnson SR, et al. A pituitary-derived MEG3 isoform functions as a growth suppressor in tumor cells. *J Clin Endocrinol Metab.* (2003) 88:5119–26. doi: 10.1210/jc.2003-030222
51. Kogo R, Shimamura T, Mimori K, Kawahara K, Imoto S, Sudo T, et al. Long noncoding RNA HOTAIR regulates polycomb-dependent chromatin modification and is associated with poor prognosis in colorectal cancers. *Cancer Res.* (2011) 71:6320–6. doi: 10.1158/0008-5472.CAN-11-1021
52. Kim K, Jutooru I, Chadalapaka G, Johnson G, Frank J, Burghardt R, et al. HOTAIR is a negative prognostic factor and exhibits pro-oncogenic activity in pancreatic cancer. *Oncogene.* (2013) 32:1616–25. doi: 10.1038/onc.2012.193
53. Zhang J, Qiu WQ, Zhu H, Liu H, Sun JH, Chen Y, et al. HOTAIR contributes to the carcinogenesis of gastric cancer via modulating cellular and exosomal miRNAs level. *Cell Death Dis.* (2020) 11:780. doi: 10.1038/s41419-020-02946-4
54. Elsayed ET, Salem PE, Darwish AM, Fayed HM. Plasma long non-coding RNA HOTAIR as a potential biomarker for gastric cancer. *Int J Biol Markers.* (2018) 33:1724600818760244. doi: 10.1177/1724600818760244
55. Okugawa Y, Toiyama Y, Hur K, Toden S, Saigusa S, Tanaka K, et al. Metastasis-associated long non-coding RNA drives gastric cancer development and promotes peritoneal metastasis. *Carcinogenesis.* (2014) 35:2731–9. doi: 10.1093/carcin/bgu200
56. Endo H, Shiroki T, Nakagawa T, Yokoyama M, Tamai K, Yamanami H, et al. Enhanced expression of long non-coding RNA HOTAIR is associated with the development of gastric cancer. *PLoS ONE.* (2013) 8:e77070. doi: 10.1371/journal.pone.0077070
57. Sun W, Yang Y, Xu C, Xie Y, Guo J. Roles of long noncoding RNAs in gastric cancer and their clinical applications. *J Cancer Res Clin Oncol.* (2016) 142:2231–7. doi: 10.1007/s00432-016-2183-7
58. Li L, Geng Y, Feng R, Zhu Q, Miao B, Cao J, et al. The human RNA surveillance factor UPF1 modulates gastric cancer progression by targeting long non-coding RNA MALAT1. *Cell Physiol Biochem.* (2017) 42:2194–206. doi: 10.1159/000479994
59. Xia H, Chen Q, Chen Y, Ge X, Leng W, Tang Q, et al. The lncRNA MALAT1 is a novel biomarker for gastric cancer metastasis. *Oncotarget.* (2016) 7:56209–18. doi: 10.18632/oncotarget.10941
60. Abbastabar M, Sarfi M, Golestani A, Khalili E. lncRNA involvement in hepatocellular carcinoma metastasis and prognosis. *EXCLI J.* (2018) 17:900–13. doi: 10.17179/excli2018-1541
61. Liu D, Zhu Y, Pang J, Weng X, Feng X, Guo Y. Knockdown of long non-coding RNA MALAT1 inhibits growth and motility of human hepatoma cells via modulation of miR-195. *J Cell Biochem.* (2018) 119:1368–80. doi: 10.1002/jcb.26297
62. Li C, Miao R, Liu S, Wan Y, Zhang S, Deng Y, et al. Down-regulation of miR-146b-5p by long noncoding RNA MALAT1 in hepatocellular carcinoma promotes cancer growth and metastasis. *Oncotarget.* (2017) 8:28683–95. doi: 10.18632/oncotarget.15640
63. Shi WH, Wu QQ, Li SQ, Yang TX, Liu ZH, Tong YS, et al. Upregulation of the long noncoding RNA PCAT-1 correlates with advanced clinical stage and poor prognosis in esophageal squamous carcinoma. *Tumour Biol.* (2015) 36:2501–7. doi: 10.1007/s13277-014-2863-3
64. Wang P, Liu YH, Yao YL, Li Z, Li ZQ, Ma J, et al. Long non-coding RNA CASC2 suppresses malignancy in human gliomas by miR-21. *Cell Signal.* (2015) 27:275–82. doi: 10.1016/j.cellsig.2014.11.011
65. Wang Y, Wang Y, Li J, Zhang Y, Yin H, Han B. CRNDE, a long-noncoding RNA, promotes glioma cell growth and invasion through mTOR signaling. *Cancer Lett.* (2015) 367:122–8. doi: 10.1016/j.canlet.2015.03.027
66. Di W, Li Q, Shen W, Guo H, Zhao S. The long non-coding RNA HOTAIR promotes thyroid cancer cell growth, invasion and migration through the miR-1-CCND2 axis. *Am J Cancer Res.* (2017) 7:1298–1309.
67. Xu YH, Deng JL, Wang G, Zhu YS. Long non-coding RNAs in prostate cancer: functional roles and clinical implications. *Cancer Lett.* (2019) 464:37–55. doi: 10.1016/j.canlet.2019.08.010
68. Leyten GH, Hessels D, Jannink SA, Smit FP, de Jong H, Cornel EB, et al. Prospective multicentre evaluation of PCA3 and TMPRSS2-ERG gene fusions as diagnostic and prognostic urinary biomarkers for prostate cancer. *Eur Urol.* (2014) 65:534–42. doi: 10.1016/j.eururo.2012.11.014
69. Wang F, Ren S, Chen R, Lu J, Shi X, Zhu Y, et al. Development and prospective multicenter evaluation of the long noncoding RNA MALAT-1 as a diagnostic urinary biomarker for prostate cancer. *Oncotarget.* (2014) 5:11091–02. doi: 10.18632/oncotarget.2691
70. Ghafouri-Fard S, Esmaeili M, Taheri M. H19 lncRNA: roles in tumorigenesis. *Biomed Pharmacother.* (2020) 123:109774. doi: 10.1016/j.biopha.2019.109774
71. Vennin C, Spruyt N, Dahmani F, Julien S, Bertucci F, Finetti P, et al. H19 non coding RNA-derived miR-675 enhances tumorigenesis and metastasis of breast cancer cells by downregulating c-Cbl and Cbl-b. *Oncotarget.* (2015) 6:29209–23. doi: 10.18632/oncotarget.4976
72. Keniry A, Oxley D, Monnier P, Kyba M, Dandolo L, Smits G, et al. The H19 lincRNA is a developmental reservoir of miR-675 that suppresses growth and Igf1r. *Nat Cell Biol.* (2012) 14:659–65. doi: 10.1038/ncb2521
73. Peng F, Li TT, Wang KL, Xiao GQ, Wang JH, Zhao HD, et al. H19/let-7/LIN28 reciprocal negative regulatory circuit promotes breast cancer stem cell maintenance. *Cell Death Dis.* (2017) 8:e2569. doi: 10.1038/cddis.2016.438
74. Chirshev E, Oberg KC, Ioffe YJ, Unternaehrer JJ. Let-7 as biomarker, prognostic indicator, and therapy for precision medicine in cancer. *Clin Transl Med.* (2019) 8:24. doi: 10.1186/s40169-019-0240-y
75. Verhaegh GW, Verkleij L, Vermeulen SH, den Heijer M, Witjes JA, Kiemeney LA. Polymorphisms in the H19 gene and the risk of bladder cancer. *Eur Urol.* (2008) 54:1118–26. doi: 10.1016/j.eururo.2008.01.060
76. Yu X, Li Z, Zheng H, Chan MT, Wu WK. NEAT1: a novel cancer-related long non-coding RNA. *Cell Prolif.* (2017) 50:e12329. doi: 10.1111/cpr.12329
77. Wang XS, Zhang Z, Wang HC, Cai JL, Xu QW, Li MQ, et al. Rapid identification of UCA1 as a very sensitive and specific unique marker for human bladder carcinoma. *Clin Cancer Res.* (2006) 12:4851–8. doi: 10.1158/1078-0432.CCR-06-0134
78. Hajjari M, Salavaty A. HOTAIR: an oncogenic long non-coding RNA in different cancers. *Cancer Biol Med.* (2015) 12:1–9. doi: 10.7497/j.issn.2095-3941.2015.0006
79. Zheng HT, Shi DB, Wang YW, Li XX, Xu Y, Tripathi P, et al. High expression of lncRNA MALAT1 suggests a biomarker of poor prognosis in colorectal cancer. *Int J Clin Exp Pathol.* (2014) 7:3174–81.
80. Lai MC, Yang Z, Zhou L, Zhu QQ, Xie HY, Zhang F, et al. Long non-coding RNA MALAT-1 overexpression predicts tumor recurrence of hepatocellular carcinoma after liver transplantation. *Med Oncol.* (2012) 29:1810–6. doi: 10.1007/s12032-011-0004-z

81. Arun G, Spector DL. MALAT1 long non-coding RNA and breast cancer. *RNA Biol.* (2019) 16:860–3. doi: 10.1080/15476286.2019.1592072
82. Gutschner T, Hammerle M, Diederichs S. MALAT1 – a paradigm for long noncoding RNA function in cancer. *J Mol Med.* (2013) 91:791–801. doi: 10.1007/s00109-013-1028-y
83. Smaldone MC, Davies BJ. BC-819, a plasmid comprising the H19 gene regulatory sequences and diphtheria toxin A, for the potential targeted therapy of cancers. *Curr Opin Mol Ther.* (2010) 12:607–16.
84. Hanna N, Ohana P, Konikoff FM, Leichtmann G, Hubert A, Appelbaum L, et al. Phase 1/2a, dose-escalation, safety, pharmacokinetic and preliminary efficacy study of intratumoral administration of BC-819 in patients with unresectable pancreatic cancer. *Cancer Gene Ther.* (2012) 19:374–81. doi: 10.1038/cgt.2012.10
85. Gofrit ON, Benjamin S, Halachmi S, Leibovitch I, Dotan Z, Lamm DL, et al. DNA based therapy with diphtheria toxin-A BC-819: a phase 2b marker lesion trial in patients with intermediate risk nonmuscle invasive bladder cancer. *J Urol.* (2014) 191:1697–702. doi: 10.1016/j.juro.2013.12.011
86. Zhang Y, Tang L. The application of lncRNAs in cancer treatment and diagnosis. *Recent Pat Anticancer Drug Discov.* (2018) 13:292–301. doi: 10.2174/1574892813666180226121819
87. Anderson DM, Anderson KM, Chang CL, Makarewich CA, Nelson BR, McAnally JR, et al. A micropeptide encoded by a putative long noncoding RNA regulates muscle performance. *Cell.* (2015) 160:595–606. doi: 10.1016/j.cell.2015.01.009
88. Lennox KA, Behlke MA. Cellular localization of long non-coding RNAs affects silencing by RNAi more than by antisense oligonucleotides. *Nucleic Acids Res.* (2016) 44:863–77. doi: 10.1093/nar/gkv1206
89. Cabili MN, Dunagin MC, McClanahan PD, Biaesch A, Padovan-Merhar O, Regev A, et al. Localization and abundance analysis of human lncRNAs at single-cell and single-molecule resolution. *Genome Biol.* (2015) 16:20. doi: 10.1186/s13059-015-0586-4
90. Bennett CF, Swayze EE. RNA targeting therapeutics: molecular mechanisms of antisense oligonucleotides as a therapeutic platform. *Annu Rev Pharmacol Toxicol.* (2010) 50:259–93. doi: 10.1146/annurev.pharmtox.010909.105654
91. Goyal A, Myacheva K, Gross M, Klingenberg M, Duran Arque B, Diederichs S. Challenges of CRISPR/Cas9 applications for long non-coding RNA genes. *Nucleic Acids Res.* (2017) 45:e12. doi: 10.1093/nar/gkw883
92. Ozcan G, Ozpolat B, Coleman RL, Sood AK, Lopez-Berestein G. Preclinical and clinical development of siRNA-based therapeutics. *Adv Drug Deliv Rev.* (2015) 87:108–9. doi: 10.1016/j.addr.2015.01.007
93. Matsui M, Corey DR. Non-coding RNAs as drug targets. *Nat Rev Drug Discov.* (2017) 16:167–79. doi: 10.1038/nrd.2016.117
94. Renganathan A, Felley-Bosco E. Long noncoding RNAs in cancer and therapeutic potential. *Adv Exp Med Biol.* (2017) 1008:199–222. doi: 10.1007/978-981-10-5203-3_7
95. Nulf CJ, Corey D. Intracellular inhibition of hepatitis C virus (HCV) internal ribosomal entry site (IRES)-dependent translation by peptide nucleic acids (PNAs) and locked nucleic acids (LNAs). *Nucleic Acids Res.* (2004) 32:3792–8. doi: 10.1093/nar/gkh706
96. Nielsen PE, Egholm M, Berg RH, Buchardt O. Sequence-selective recognition of DNA by strand displacement with a thymine-substituted polyamide. *Science.* (1991) 254:1497–500. doi: 10.1126/science.1962210
97. Gong N, Teng X, Li J, Liang XJ. Antisense oligonucleotide-conjugated nanostructure-targeting lncRNA MALAT1 inhibits cancer metastasis. *ACS Appl Mater Interfaces.* (2019) 11:37–42. doi: 10.1021/acsami.8b18288
98. Boon RA, Jae N, Holdt L, Dimmeler S. Long noncoding RNAs: from clinical genetics to therapeutic targets? *J Am Coll Cardiol.* (2016) 67:1214–26. doi: 10.1016/j.jacc.2015.12.051
99. Bhan A, Soleimani M, Mandal SS. Long noncoding RNA and cancer: a new paradigm. *Cancer Res.* (2017) 77:3965–81. doi: 10.1158/0008-5472.CAN-16-2634
100. Huang R, Zhou L, Chi Y, Wu H, Shi L. LncRNA profile study reveals a seven-lncRNA signature predicts the prognosis of patients with colorectal cancer. *Biomark Res.* (2020) 8:8. doi: 10.1186/s40364-020-00187-3

Conflict of Interest: The authors declare that the research was conducted in the absence of any commercial or financial relationships that could be construed as a potential conflict of interest.

Copyright © 2020 Qian, Shi and Luo. This is an open-access article distributed under the terms of the Creative Commons Attribution License (CC BY). The use, distribution or reproduction in other forums is permitted, provided the original author(s) and the copyright owner(s) are credited and that the original publication in this journal is cited, in accordance with accepted academic practice. No use, distribution or reproduction is permitted which does not comply with these terms.

frontiers in Medicine

ORIGINAL RESEARCH
published: 15 December 2020
doi: 10.3389/fmed.2020.582097

DGCR8/miR-106 Axis Enhances Radiosensitivity of Head and Neck Squamous Cell Carcinomas by Downregulating RUNX3

Chunlin Zhang[1], *Hangqi Chen*[1], *Zeyi Deng*[2], *Dan Long*[1], *Li Xu*[1] *and Zhaohui Liu*[1]*

[1] Department of Otorhinolaryngology, Head and Neck Surgery, Affiliated Hospital of Zunyi Medical University, Zunyi, China, [2] Department of Otorhinolaryngology, Head and Neck Surgery, Zhujiang Hospital, Southern Medical University, Guangzhou, China

Purpose: Head and neck squamous cell carcinoma (HNSCC) is the sixth most prevalent malignant tumor worldwide, and the radiotherapy effect is strongly associated with human papillomavirus (HPV) infection. Therefore, the aim of our study was to analyze the mechanism of HPV E7 and its effects on radiosensitivity in HNSCC cells.

Methods: The mRNA expression of DiGeorge syndrome critical region gene 8 (DGCR8), has-miR-106a, and Runt-related transcription factor 3 (RUNX3) was examined by quantitative real-time PCR (RT-qPCR). The protein expression of DGCR8, E7, RUNX3, caspase-3/cleaved caspase-3, poly(ADP-ribose) polymerase (PARP)/cleaved PARP, and γH2AX was measured by Western blot. The expression level of DGCR8 was measured by immunofluorescence assay. Starbase database (http://starbase.sysu.edu.cn/) was used to analyze the correlation between has-miR-106a-5p and DGCR8. TargetScan database (http://www.targetscan.org/vert_72/) was adopted to calculate the prediction of binding sites. Radiosensitivity was evaluated through clone formation assays and Cell Counting Kit-8 (CCK-8) assays.

Results: In our study, we found that the mRNA and protein expression levels of HPV E7 and DGCR8 in HPV-positive HNSCC cells were higher than those in HPV-negative cells. The expression of DGCR8 was increased in FaDu and UM-SCC-4 with E7 overexpression, while the expression of DGCR8 was decreased in UM-SCC-47 and UPCI-SCC-090 with E7 silence. The miR-106a expression was increased after DGCR8 overexpression in FaDu and UM-SCC-4. However, the miR-106a expression was decreased in UM-SCC-47 and UPCI-SCC-090 with E7 silence. In radiation conditions, clone formation assays found that less clones formed in FaDu and UM-SCC-4 cells subsequent to silencing DGCR8 or miR-106a than that in the control group, and more clones were formed in UM-SCC-47 and UPCI-SCC-090 cells overexpressing DGCR8 or miR-106a than that in the control group. Luciferase reporter gene assays verified that miR-106a targeted the 3′ untranslated region (UTR) of RUNX3 mRNA. MiR-106a overexpression resulted in a decrease in RUNX3 expression, and miR-106a silence

OPEN ACCESS

Edited by:
Guo Chen,
Jinan University, China

Reviewed by:
Zhongqiu Xie,
University of Virginia, United States
Chaoyun Pan,
Sun Yat-sen University, China

***Correspondence:**
Zhaohui Liu
rzent@163.com

Specialty section:
This article was submitted to Precision Medicine, a section of the journal Frontiers in Medicine

Received: *10 July 2020*
Accepted: *02 November 2020*
Published: *15 December 2020*

Citation:
Zhang C, Chen H, Deng Z, Long D, Xu L and Liu Z (2020) DGCR8/miR-106 Axis Enhances Radiosensitivity of Head and Neck Squamous Cell Carcinomas by Downregulating RUNX3. Front. Med. 7:582097. doi: 10.3389/fmed.2020.582097

increased RUNX3 expression. Rescue experiments conducted with miR-106a inhibitor restored radiation resistance and reduced DNA damage in radiation condition.

Conclusions: Our study indicated that HPV E7 activated DGCR8/miR-106a/RUNX3 axis to enhance radiation sensitivity and provided directions for targeted therapeutic interventions.

Keywords: head and neck cancer, HPV, DGCCR8, miR-106a, RUNX3, radiotherapy

BACKGROUND

Head and neck cell carcinoma is one of the most common malignancies, and its incidence rate ranks sixth among all cancers (1). Over 600,000 new cases are diagnosed as head and neck cell carcinoma every year worldwide, and the incidence is increasing year by year (2). Ten percent of the cases are in the oropharynx approximately. Head and neck squamous cell carcinoma (HNSCC) is the most common kind of head and neck cancer (3). Due to the lack of indicators for early diagnosis, HNSCC cannot be easily detected and ∼60% of patients with HNSCC are already at an advanced stage at the time of treatment (4). Smoking and alcohol are the principal risk factors for HNSCC worldwide (5). Currently, surgery, radiotherapy, and chemotherapy make a great progress, but the overall survival rate of patients has not been improved. The 5-year survival rate is <50% (6).

Human papillomavirus (HPV) E6/E7 oncoproteins represent potentially ideal targets for therapeutics (7) based on a previous study, but the possible mechanism was not in-depth. Currently, it is believed that HPV infection is a relevant causative factor in the development of HNSCC. The expression of HPV E6/E7 causes tumorigenesis and degrades the expression products of the tumor suppressor genes p53 and retinoblastoma protein (pRb) (8). HPV E7 represses Rb activity and reversely activates multiple transcription factors related to the tumor process (9). HPV-negative and HPV-positive patients have different responses to treatment and prognosis (10, 11). It is shown that HPV E6/E7 enhances the sensitivity of radiotherapy in HNSCC.

Recently, some studies have found that HPV E7 affects miRNA expression profiles *via* DiGeorge syndrome critical region gene 8 (DGCR8) (12, 13). In the nucleus, miRNAs are transcribed into pri-miRNAs and are processed to pre-miRNAs by Drosha and DGCR8 (14). DGCR8 is a factor of the microprocessor complex and has been shown to be necessary for miRNA maturation (15). High-risk HPV does not have its own miRNA but alters miRNA level in host cells. The effects of HPV E6/E7 on the maintenance of cell invasion and proliferation or drug resistance and radiosensitivity through miRNAs have not been demonstrated clearly.

Runt-related transcription factor 3 (RUNX3) is a member of the runt domain-containing family of transcription factors (16–18). It is involved in the control of cellular proliferation and differentiation. Samarakkody et al. (19) and Tay et al. (20) demonstrated that RUNX3 participated in DNA damage repair, which radiation mainly caused. In addition, RUNX3 is an proto-oncogene in head and neck cancer (21). RUNX3 expression is a useful marker and therapeutic target to predict malignant behaviors and radiotherapy in HNSCC.

Similar to a previous study, we found that HPV-positive HNSCC cells were more sensitive to radiotherapy. In our study, we proved that HPV E7 could promote the content of DGCR8, a protein that affected miRNA maturation, the transcription of hsa-miR-106a, and thus disinhibited RUNX3 expression in HNSCC. Thereby, it can enhance the sensitivity of radiotherapy, which potentially provides directions for targeted therapeutic interventions.

METHODS

Cell Cultures and Transfection

HPV-negative HNSCC cell lines FaDu, UM-SCC-4, and HPV-positive cell line UM-SCC-47, UPCI-SCC-090, were purchased from American Type Culture Collection (ATCC). FaDu and UM-SCC-47 were cultured in Dulbecco's modified Eagle's medium (DMEM) (Gibco, Carlsbad, CA) with 10% fetal bovine serum (FBS). UM-SCC-4 was cultured in DMEM/F12 medium (Gibco, Carlsbad, CA) with 10% FBS. UPCI-SCC-090 was cultured in Minimum Essential Medium (MEM) (Gibco, Carlsbad, CA) with 10% FBS. All cells were cultured in an incubator at 37°C with 5% CO_2. Cells were allowed to acclimate for 24 h before any treatment in all experiments. SiRNAs were purchased from RiboBio (Guangzhou, China), and overexpression/luciferase reporter plasmids were purchased from GeneChem (Shanghai, China). Cells were transiently transfected with corresponding siRNAs or overexpression/luciferase reporter plasmids using Lipofectamine 3000 Transfection Reagent (Invitrogen, United States) according to the manufacturer's instructions. After transfection for 48 h, the cells were collected for further analysis.

Abbreviations: HPV, Human Papillomavirus; DGCR8, Microprocessor complex subunit DGCR8; RUNX3, Runt-related transcription factor 3; PARP, Poly (ADP-Ribose) Polymerase 1; CCK-8, Cell Counting Kit-8; UTR, Untranslated region; pRb, Retinoblastoma protein; ATCC, American Type Culture Collection; DMEM, Dulbecco's Modified Eagle's Medium; MEM, Minimum Essential Medium; RIPA, Radio Immunoprecipitation Assay; PMSF, Phenylmethanesulfonyl fluoride; SDS-PAGE, Sodium dodecyl sulfate polyacrylamide gel electrophoresis; BSA, Bovine Serum Albumin; GAPDH, Glyceraldehyde-3-Phosphate Dehydrogenase; ECL, Electrochemiluminescence; PBS, Phosphate buffer saline; DAPI, 4′,6-diamidino-2-phenylindole; TCGA, The Cancer Genome Atlas.

TABLE 1 | The primer sequences for RT-qPCR.

Gene	Primer
HPV E7	Forward: CAGAGGAGGAGGATGAAATAGATG Reverse: CACAACCGAAGCGTAGAGTC
DGCR8	Forward: GTGCATGCTTGTCCCTTTGG Reverse: TGCCAACATACCTCGTAGGG
Hsa-miR-106a	Forward: GAAAAGTGCTTACAGTGCAG Reverse: GTCCAGTTTTTTTTTTTTTTTCTACCT
GAPDH	Forward: CGCTCTCTGCTCCTCCTGTTC Reverse: ATCCGTTGACTCCGACCTTCAC
U6	Forward: CTCGCT TCGGCAGCA Reverse: AACGCT TCACGAATT TGC

GAPDH, glyceraldehyde-3-phosphate dehydrogenase; HPV, human papillomavirus; RT-qPCR, quantitative real-time PCR.

Western Blot

Cells were lysed with radioimmunoprecipitation assay (RIPA) buffer with phenylmethylsulfonyl fluoride (PMSF) and phosphatase inhibitor (KeyGene Biotech, China). Proteins (30 μg) were segregated by sodium dodecyl sulfate–polyacrylamide gel electrophoresis (SDS–PAGE) and then electrophoretically transferred the protein onto a polyvinylidene difluoride (PVDF) membrane. After blocking with 5% bovine serum albumin (BSA) for 2 h, the PVDF membranes were incubated with specific primary antibodies in recommended dilution ratio at 4°C overnight. The primary antibodies used in this study included anti-glyceraldehyde-3-phosphate dehydrogenase (GAPDH) antibody (1:5,000, 60004-1-lg, Proteintech, China), anti-DGCR8 antibody (1:1,000, 10996-1-AP, Proteintech, China), and rabbit anti-RUNX3 antibody (1:1,000, ab135248, Abcam). Subsequently, the PVDF membranes were incubated with secondary antibodies (BOSTER, China) for 2 h. The protein strips were visualized and detected using a chemiluminescence reagent [enhanced chemiluminescence (ECL)] kit (Beyotime, China).

Quantitative Real-Time PCR

Total RNA was extracted using TRIzol reagent (Invitrogen, Carlsbad, CA), and the reverse-transcription reactions were using PrimeScript RT Master Mix (Takara, Japan). Real-time PCR was using TB Green Fast qPCR Mix (Takara, Japan) according to the instructions. LineGene 9600 Plus Real Time PCR system (Bioer, China) was adopted, and GAPDH was used as a reference. The $2^{-\Delta\Delta Ct}$ method was used to determine the relative quantitation of gene expression. The primer sequences were listed in **Table 1**.

Immunofluorescent Staining Assay

Cells plated in 24-well plates were fixed with 4% paraformaldehyde in phosphate buffered saline (PBS) for 10 min, permeabilized in 0.5% Triton X-100 for 20 min, washed twice in PBS, and then blocked with 3% BSA (KeyGene Biotech, China) in PBS. After 1 h, the cells were incubated with anti-DGCR8 antibody (1:500, 10996-1-AP, Proteintech, China) at 4°C overnight, then with Alexa Fluor 488 secondary antibody (1:200, SA00013-2, Proteintech, China) for 1 h at 37°C. The nuclei were stained with 5 μg/ml 4′,6-diamidino-2-phenylindole (DAPI) (KeyGene Biotech, China) for 5 min and viewed with a fluorescence microscope (Olympus, Japan).

Colony Formation Assay

Cells were seeded in 6-well plates and cultured for 14 days upon 4 Gy radiation. The cells were fixed using cold methanol for 20 min and stained with 0.1% crystal violet for 10 min. The number of colonies was used to evaluate the clone formation ability.

Dual Luciferase Reporter Gene Assay

The wide type (WT) according to the binding site between hsa-miR-106a and RUNX3 and the mutant type (MUT) were, respectively, inserted into the psiCHECK2 (Promega, USA). Subsequently, WT or MUT reporter vectors were co-transfected with hsa-miR-106s mimics or inhibitor. The luciferase activity was measured using dual luciferase reporter gene assay kit (Beyotime, China). Renilla luciferase was used as an internal reference.

Statistical Analysis

SPSS 21.0 (IBM, United States) was adopted for statistical analysis. Data were shown as mean ± standard derivation (mean ± SD). Student *t*-test was used to analyze differences between two groups, and the *p*-value was acquired from two-tailed tests. A $p < 0.05$ was considered statistically significant. All experiments were repeated in triplicate.

RESULTS

Human Papillomavirus E7 Upregulates DGCR8 Expression in Head and Neck Squamous Cell Carcinoma Cells

According to previous studies, we had proved that FaDu and UM-SCC-4 were HPV-negative cell lines and do not express HPV E7 proteins, while UM-SCC-090 and UM-SCC-47 were HPV-positive cell lines expressing E7 proteins (22). The mRNA (**Figure 1A**) and protein (**Figure 1B**) expressions of E7 in HPV-positive cell lines were higher than those of HPV-negative cell lines. Besides, the content of DGCR8 was also much higher in HPV-positive cell lines than that in HPV-negative cell lines (**Figures 1A,B**). Previous studies had revealed that DGCR8 expression was related to E7. The expression of DGCR8 was measured in HPV-negative cell lines with E7 overexpression and HPV-positive cell lines with E7 silencing. As shown in **Figures 1C,D**, DGCR8 expression was downregulated as E7 silencing, while the opposite result was obtained after E7 overexpression. We confirmed the above results by using immunofluorescence analysis (**Figure 1E**). Results presented above suggested that HPV E7 upregulated DGCR8 expression in HNSCC cells.

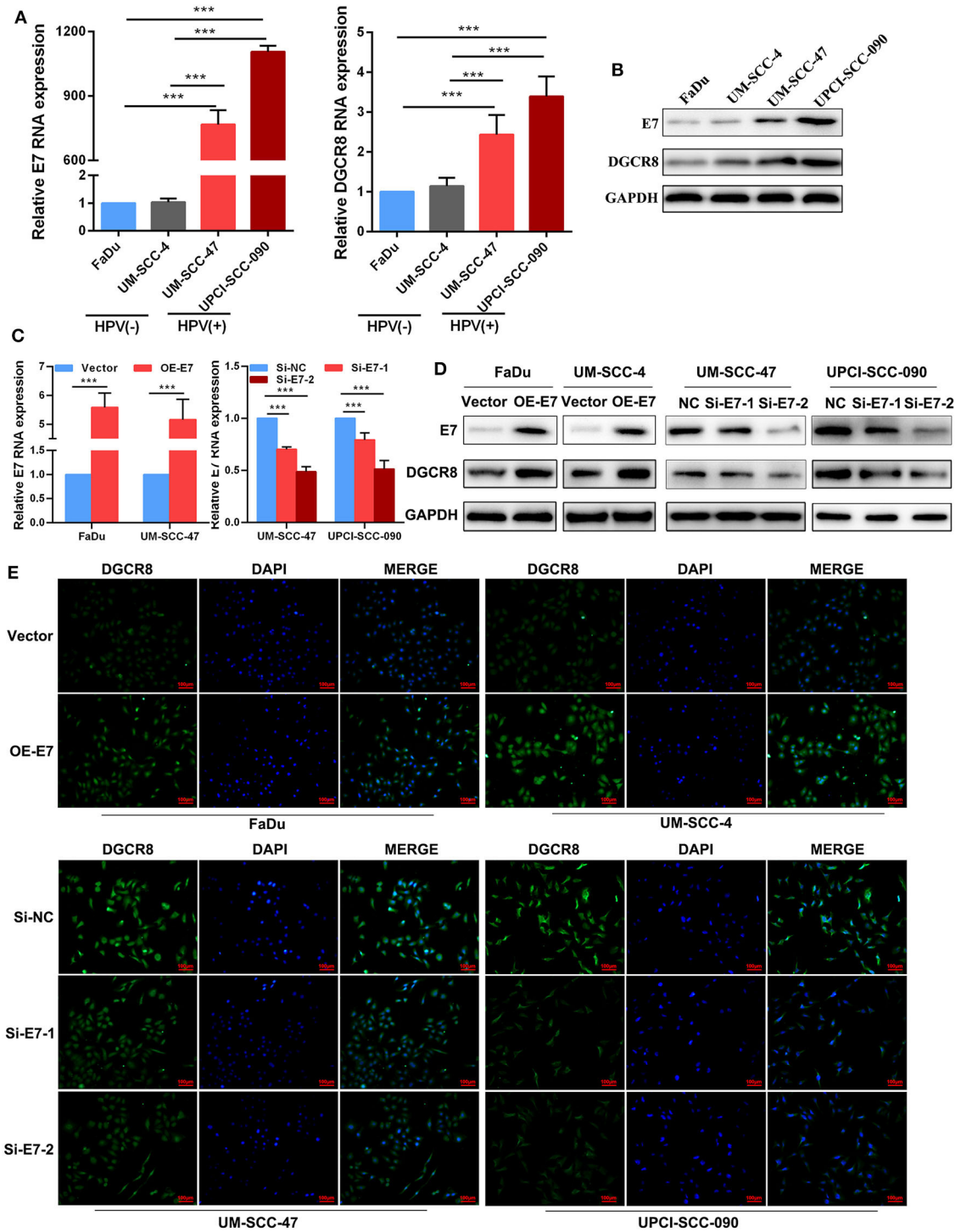

FIGURE 1 | Human papillomavirus (HPV) E7 upregulates DGCR8 expression in head and neck squamous cell carcinoma (HNSCC) cells. **(A)** The mRNA expressions of HPV E7 and DGCR8 in FaDu, UM-SCC-4, UM-SCC-47, and UPCI-SCC-090. **(B)** The protein expressions of HPV E7 and DGCR8 in FaDu, UM-SCC-4, UM-SCC-47, and UPCI-SCC-090. **(C)** The mRNA expression of HPV E7 in FaDu and UM-SCC-4 with E7 overexpression and UM-SCC-47 and UPCI-SCC-090 with E7 silencing. **(D)** The protein expressions of HPV E7 and DGCR8 in FaDu and UM-SCC-4 with E7 overexpression and UM-SCC-47 and UPCI-SCC-090 with E7 silencing. **(E)** HPV E7 upregulated DGCR8 expression in HPV-negative/positive cell lines by immunofluorescence. ***$p < 0.001$.

DGCR8 Promotes Hsa-miR-106a Transcription and Enhances Radiation Sensitivity

The correlation between DGCR8 and hsa-miR-106a was analyzed according to HNSCC from The Cancer Genome Atlas (TCGA) database. A strong positive correlation was apparent between DGCR8 and hsa-miR-106a (**Figure 2A**). We had known that the content of DGCR8 was less in HPV-negative cell lines than that in HPV-positive cell lines (**Figures 1A,B**). RT-qPCR was adopted to measure the expression of DGCR8 after transfection pcDNA3.1-DGCR8 in HPV-negative cells and siRNA-DGCR8 in HPV-positive cells (**Figure 2B**). DGCR8 overexpression promoted the transcription of hsa-miR-106a in FaDu and UM-SCC-4, while DGCR8 silencing obtained an opposite trend in UM-SCC-4 and UM-SCC-090 (**Figure 2C**). To investigate the effect of DGCR8 on radiation sensitivity, clone formation assay was used to evaluate the sensitivity of radiation after DGCR8 overexpression in HPV-negative cells and silencing in HPV-positive cells upon radiation. As shown in **Figures 2F,G**, high expression of DGCR8 increased the sensitivity of cells to radiation and low expression of DGCR8 decreased the sensitivity of cells to radiation. However, DGCR8 rarely affected cell proliferation in non-radiation conditions (**Figures 2D,E**). Based on the study results described above, DGCR8 promoted hsa-miR-106a transcription and enhanced radiation sensitivity in HNSCC cells.

Hsa-miR-106a Inhibits the Expression of RUNX3 and Enhances Radiation Sensitivity

miRNAs cannot directly involve protein translation, and its effect on radiation sensitivity must be targeted to regulate mRNA transcription. It has been reported that RUNX3 is involved in the process of DNA damage repair (19, 20), and one of the most important factors affecting radiation sensitivity is the repair of DNA damage. In order to further explore whether hsa-miR-106a is one of the key steps for DGCR8 to promote radiation sensitivity, we found that hsa-miR-106a targeted and regulated RUNX3, which was the key gene of DNA damage repaired by bioinformatics analysis (**Figure 3A**). The transfection efficiency was as expected in FaDu, UM-SCC-4, UM-SCC-47, and UPCI-SCC-090 (**Figure 3D**). PsiCHECK2, a luciferase reporter vector, was constructed with the 3′ untranslated region (UTR) sequence of RUNX3 and co-transfected mimics or inhibitor of hsa-miR-106a to explore the regulation of hsa-miR-106a on RUNX3. As shown in **Figure 3B**, hsa-miR-106a overexpression downregulated the relative luciferase rate, while hsa-miR-106a silencing upregulated the relative luciferase rate in Fadu and UM-SCC-47 with RUNX3-WT plasmid co-transfection. The relative luciferase rate was rarely changed in the RUNX3-MUT group. E7 overexpression downregulated the relative luciferase rate compared with vector group in FaDu and UM-SCC-47 cells (**Figure 3B**). It indicated that hsa-miR-106a could inhibit the transcription of RUNX3 by targeting its 3′ UTR and HPV E7 affected the regulation of hsa-miR-106a on RUNX3. In addition, it could negatively regulate the gene expression in the mRNA and protein levels of RUNX3 (**Figures 3C,E**). A clone formation assay was performed to investigate the impact of hsa-miR-106a on radiation sensitivity in HNSCC cells. In 2Gy radiation condition, the number of clone formation in hsa-miR-106a overexpression group was much more than that of the negative control (NC) group in FaDu and UM-SCC-4; however, the number of clone formation in the inhibitor group was less than that of the NC group in UM-SCC-47 and UPCI-SCC-090 (**Figure 3F**). However, miR-106a rarely increased the clone formation number in non-radiation conditions. The results above suggested that hsa-miR-106a inhibited the transcription of RUNX3 by targeting its 3′ UTR and enhanced radiation sensitivity.

Human Papillomavirus E7/DGCR8 Inhibits the Expression of RUNX3 and Affects Radiation Sensitivity by Promoting the Expression of hsa-miR-106a

Previously, we had confirmed the relationship in DGCR8/hsa-miR-106a and hsa-miR-106a/RUNX3, as well as the effects on radiation or non-radiation sensitivity. Here, we assumed that HPV E7/DGCR8 inhibited the expression of RUNX3 and enhanced radiation sensitivity by promoting the expression of hsa-miR-106a. Rescue experiments were performed to examine whether radiation sensitivity promoted by HPV E7/DGCR8 were achieved by downregulation of hsa-miR-106a. As shown in **Figures 4A,B**, the content of RUNX3 decreased after DGCR8 overexpression, while the expression of RUNX3 increased with hsa-miR-106a inhibitor transfection. In addition, the expression of RUNX3 was rescued after hsa-miR-106 silencing upon DGCR8 overexpression in FaDu (**Figures 4A,B**). The clone formation assay was used to measure sensitivity on radiation. The number of clone formation was increased after hsa-miR-106a rescue upon radiation, while the number of clone formation changed little in non-radiation condition, indicating has-miR-106a could increase radiosensitivity (**Figure 4D**). Cell Counting Kit-8 (CCK-8) assay was used to measure cell viability. The results indicated that cell viability increased after hsa-miR-106a rescue upon radiation and supported the results presented above (**Figure 4C**). The protein expressions of apoptosis-related caspase-3, poly(ADP-ribose) polymerase (PARP), and DNA damage-related γH2AX were measured by Western blot. Cleaved caspase-3, cleaved PARP, and γH2AX decreased after hsa-miR-106a silencing upon DGCR8 overexpression (**Figure 4E**). It indicated that hsa-miR-106a promoted DNA damage and apoptosis induced by radiation in FaDu under radiation condition. However, neither DGCR8 nor miR-106a had effects on DNA damage and apoptosis caused by radiation. The above experiments indicated that DGCR8 inhibited the expression of RUNX3 and affected radiation sensitivity by promoting the expression of hsa-miR-106a.

In **Figures 5A,B**, E7 overexpression evaluated DGCR8 expression in FaDu and decreased RUNX3 content. Knockdown of miR-106a promoted RUNX3 expression in FaDu. The clone formation assay was used to measure the content of E7 and miR-106a on radiosensitivity. The number of clone formation was increased after miR-106a knockdown upon radiation, while the number of clone formation rarely changed in non-radiation condition, indicating has-miR-106a could increase

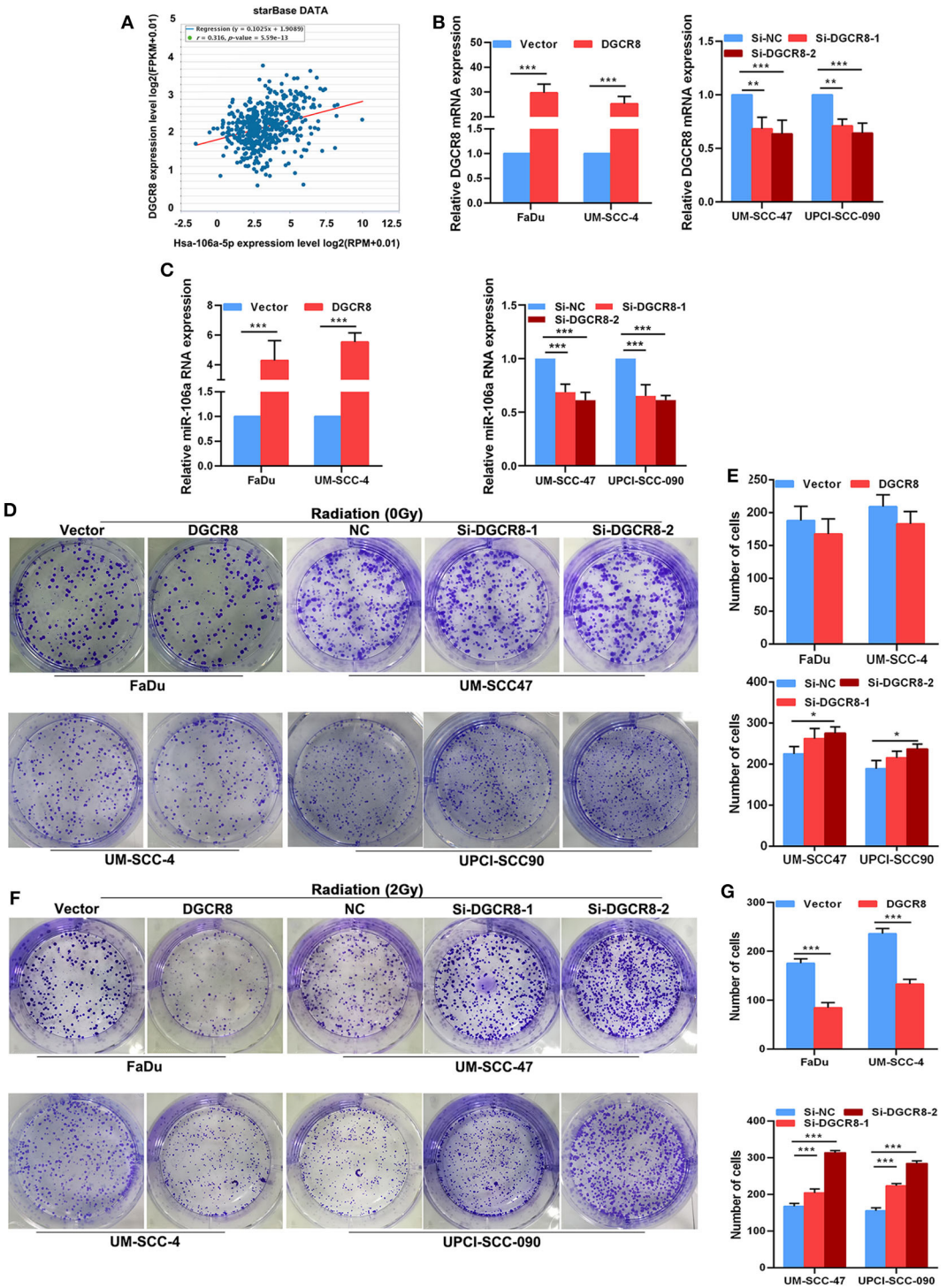

FIGURE 2 | DGCR8 promotes hsa-miR-106a transcription and enhances radiation sensitivity. **(A)** Correlation between DGCR8 and hsa-miR-106a based on TCGA-HNSC cohort. **(B)** The mRNA expression of DGCR8 in the human papillomavirus (HPV)-positive and HPV-negative cells. **(C)** Expression level of hsa-miR-106a was measured in HPV-negative cells with DGCR8 overexpression and HPV-positive cells with DGCR8 silencing. **(D,E)** The effect of DGCR8 on cell proliferation was detected by clonogenic survival upon DGCR8 overexpression in HPV-negative cells and DGCR8 silencing in HPV-positive cells. **(F,G)** The sensitivity of the cells to radiation was detected by clonogenic survival upon DGCR8 overexpression in HPV-negative cells and DGCR8 silencing in HPV-positive cells. $^{*}p < 0.05$, $^{**}p < 0.01$, $^{***}p < 0.001$.

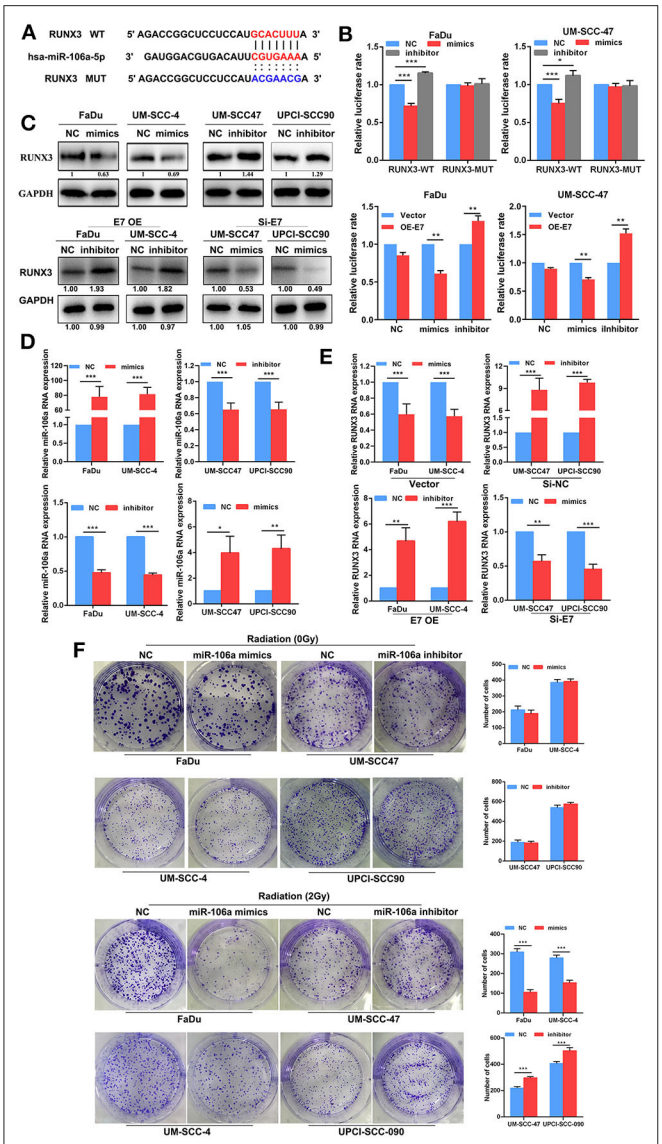

FIGURE 3 | Hsa-miR-106a inhibits the expression of RUNX3 and enhances radiation sensitivity. **(A)** Alignment of the predicted miRNA binding sites in the 3′ untranslated region (UTR) of the RUNX3 mRNA. **(B)** Luciferase reporter gene demonstrated that hsa-miR-106a directly targeted the 3′ UTR of RUNX3. **(C)** The protein expression of RUNX3 in FaDu, UM-SCCC-4, UM-SCC47, and UPCI-SCC90. **(D)** Hsa-miR-106a transfection efficiency was measured by RT-qPCR. **(E)** The mRNA expression of RUNX3 in human papillomavirus (HPV)-negative cells with hsa-miR-106a overexpression and HPV-positive cells with hsa-miR-106a silencing. **(F)** The sensitivity of the cells to radiation was detected by clonogenic survival with the condition of hsa-miR-106a overexpression in HPV-negative cells and hsa-miR-106a silencing in HPV-positive cells. $^{*}p < 0.05$, $^{**}p < 0.01$, $^{***}p < 0.001$.

radiosensitivity (**Figure 5E**). HPV E7 and miR-106a could not affect cell viability in non-radiation condition. However, knockdown of miR-106a increased cell viability, while E7 overexpression decreased it in radiation condition (**Figure 5C**). Cleaved caspase-3, cleaved PARP, and γH2AX decreased after hsa-miR-106a silencing upon E7 overexpression (**Figure 5D**). It indicated that HPV E7 inhibited the expression of RUNX3 and affected radiation sensitivity by promoting the expression of hsa-miR-106a.

Diagram of the Human Papillomavirus E7/DGCR8/hsa-miR-106a Axis Enhances Radiation Sensitivity

According to previous studies, we have known that HPV-positive HNSCC is more sensitive to radiation. Through the detection of HNSCC tumor tissue and the analysis of TCGA database, we found that DGCR8, a protein that affected the maturation of miRNA, promoted the transcription of hsa-miR-106a and had a strong correlation. In addition, hsa-miR-106a targeted binding to 3′ UTR region of RUNX3, a key protein for DNA damage repair and inhibited its transcription (**Figure 6**). In an overview, HPV E7/DGCR8/hsa-miR-106a axis enhanced radiation sensitivity. It is expected to be an effective treatment for radiation-insensitive HNSCC patients by targeting DGCR8 or hsa-miR-106a.

DISCUSSION

Previous studies have already shown that the radiation sensitivity of HNSCC is closely related to HPV E7. To further explore the underlying mechanism between E7 expression and radiation sensitivity, we found that DGCR8, a protein impacting the process of miRNA maturation, promoted hsa-miR-106a transcription in HNSCC cell lines. Besides, hsa-miR-106a targeted binding to 3′ UTR region of RUNX3 to inhibit its transcription and radiation resistance in HNSCC. In conclusion, HPV E7/DGCR8/hsa-miR-106a axis enhanced radiation sensitivity in HNSCC.

HPV is a major agent of HNSCC according to epidemiological data (23). In the present meta-analysis, the average incidence rate of HPV-associated HNSCC is 42.62% (24). Lajer et al. (25) found that HPV-positive HNSCC had a distinct miRNA profile compared with HPV-negative HNSCC. DGCR8 regulates multiple signaling pathways through miRNA-regulated genes (26). In our study, we found that the content of DGCR8 in HPV-positive HNSCC cells was much higher than that of HPV-negative cells (**Figure 1**). Besides, there was a strong correlation between DGCR8 and hsa-miR-106a (**Figure 2**). As we have known in previous studies (22), HPV-positive HNSCC cells were highly sensitive to radiation, and HPV-positive cells were rich in DGCR8 and hsa-miR-106a. Ardenne and Reitnauer (27) demonstrated that hsa-miR-106a suppressed proliferation and induced apoptosis. Application of miR-106a mimics induced cerebrovascular endothelial cell death under oxygen-glucose deprivation conditions (28). Therefore, DGCR8 promoting hsa-miR-106a transcription might be one of the important reasons for enhancing radiation sensitivity.

Based on current research, miRNAs are deemed to regulate more than 60% of human protein coding genes (29). It does not participate in protein translation but affects the content of many proteins. Non-small-cell lung cancer patients with a high RUNX3 level exhibited a significantly higher

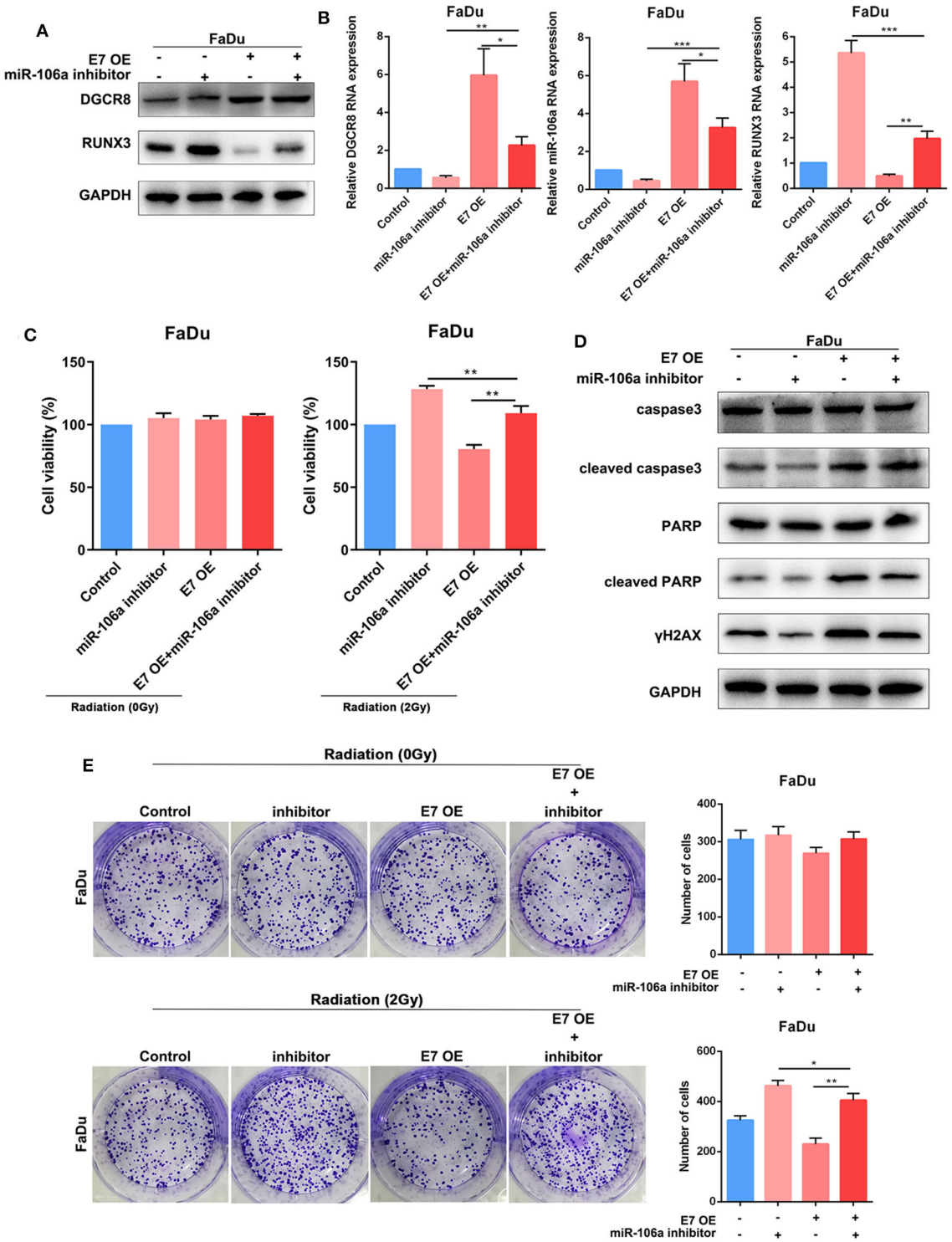

FIGURE 4 | DGCR8 inhibits the expression of RUNX3 and affects radiation sensitivity by promoting the expression of hsa-miR-106a. **(A)** Western blot showing rescue of RUNX3 expression level in FaDu. **(B)** Quantitative real-time PCR (RT-qPCR) was performed to detect DGCR8, miR-106a, and RUNX3 expression level in FaDu. **(C)** Cell Counting Kit-8 (CCK-8) showing rescue of cell viability in FaDu in radiation or non-radiation condition. **(D)** The clone formation assay showing rescue of radiation sensitivity in FaDu. **(E)** The protein expressions of apoptosis-related caspase-3, PARP, and DNA damage-related γH2AX were measured by Western blot. $^{*}p < 0.05$, $^{**}p < 0.01$, $^{***}p < 0.001$.

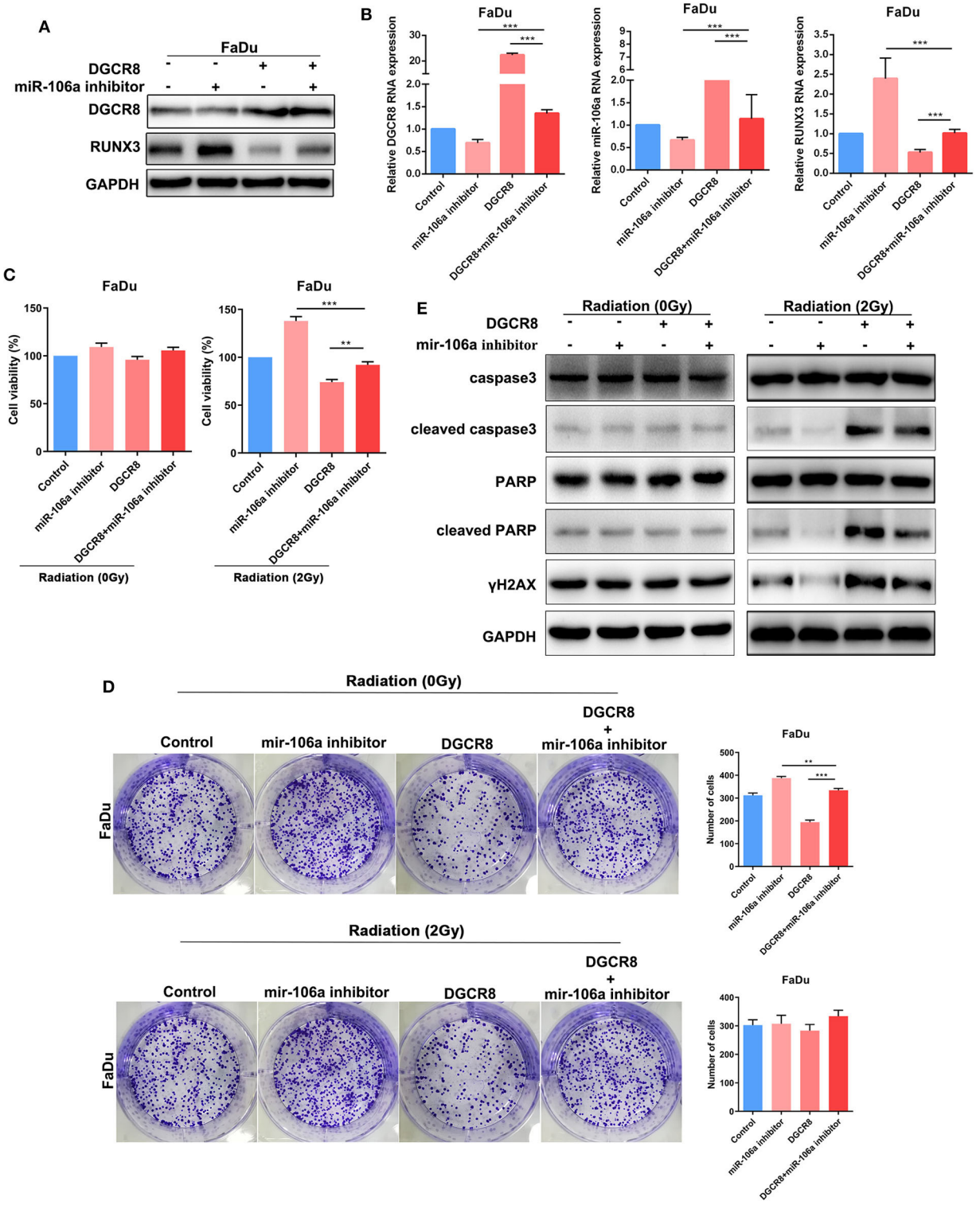

FIGURE 5 | Human papillomavirus (HPV) E7 inhibits the expression of RUNX3 and affects radiation sensitivity by promoting the expression of hsa-miR-106a. **(A)** Western blot showing rescue of RUNX3 expression level in FaDu. **(B)** Quantitative real-time PCR (RT-qPCR) was performed to detect DGCR8, miR-106a, and RUNX3 expression levels in FaDu. **(C)** Cell Counting Kit-8 (CCK-8) showing rescue of cell viability in FaDu in radiation or non-radiation condition. **(D)** The protein expressions of apoptosis-related caspase-3, PARP, and DNA damage-related γH2AX were measured by Western blot. **(E)** The clone formation assay showing rescue of radiation sensitivity in FaDu. $^{**}p < 0.01$, $^{***}p < 0.001$.

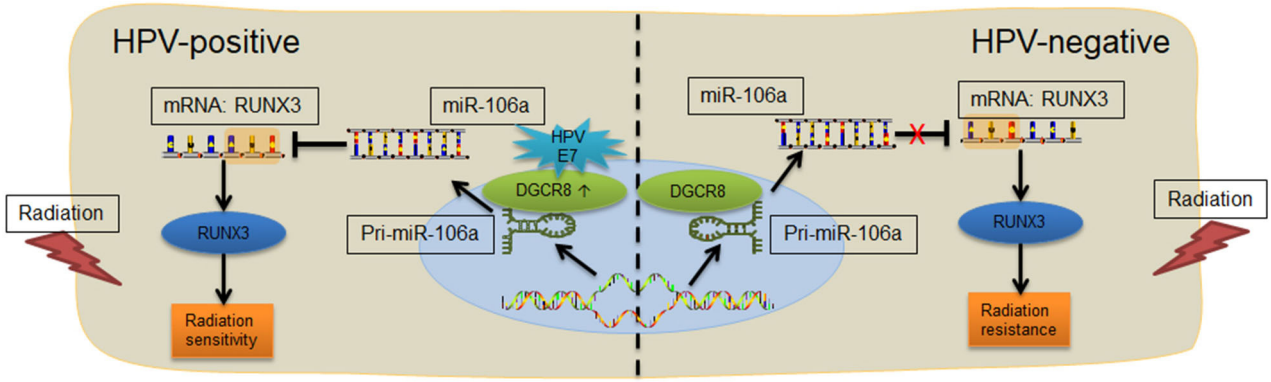

FIGURE 6 | Diagram of the E7/DGCR8/hsa-miR-106a axis enhances radiation sensitivity. Human papillomavirus (HPV)-positive head and neck squamous cell carcinoma (HNSCC) with high DGCR8 expression promoted the expression of miR-106a. The miR-106a suppressed RUNX3 mRNA expression *via* binding to the 3′ untranslated region (UTR) of RUNX3 and enhanced radiation sensitivity.

apoptosis index than that with a low level of RUNX3 (30). It participated in cell growth and apoptosis. Exogenous RUNX3 expression decreased cell proliferation and increased gemcitabine sensitivity in endogenous RUNX3-negative cell lines (31). In our study, we demonstrated that the expression of RUNX3 was negatively regulated by has-miR-106a in HNSCC cell lines (**Figures 3A–C**). In addition, RUNX3 silencing increased the sensitivity of HNSCC cells to radiation (**Figure 3F**). It was a key suppressor protein regulated by HPV E7/DGCR8/miR-106a axis to increase radiation sensitivity in HNSCC. Therefore, blocked RUNX3 might enhance the efficacy of radiation and reverse radioresistance in HNSCC patients.

Overall, the expression of DGCR8 in HPV-negative cells was lower than that in HPV-positive cells in HNSCC cells. It inhibited has-miR-106a transcription and disinhibition of RUNX3 expression. RUNX3 was a key protein to cause radioresistance. This might be one of the important reasons why HPV-negative HNSCC was not sensitive to radiotherapy. We can target to increase the content of has-miR-106a or reduce the content of RUNX3 to improve radiotherapy sensitivity of radioresistant patients.

CONCLUSIONS

Our study indicated that HPV E7 activated DGCR8/miR-106a/RUNX3 axis to enhance radiosensitivity. It may enhance the efficacy of radiation and reverse radioresistance in HNSCC patients and provides directions for targeted therapeutic interventions.

DATA AVAILABILITY STATEMENT

Publicly available datasets were analyzed in this study. This data can be found at: https://www.cancer.gov/about-nci/organization/ccg/research/structural-genomics/tcga.

AUTHOR CONTRIBUTIONS

ZL and CZ designed the study. All authors contributed to data analysis, drafting and revising the article, gave final approval of the version to be published, and agree to be accountable for all aspects of the work.

FUNDING

This work was supported by the National Natural Science Foundation of China (81760493 to CZ and 81860482 to ZL), funds from the Education Department of Guizhou Province for Young Scientific and Technological Talents (QKH NO. 2017-201), research funds from the Guizhou Provincial Health and Family Planning Commission (gzwjkj2016-1-038), and the Ph.D. Start-up Fund of Zunyi Medical University.

REFERENCES

1. Ferlay J, Shin HR, Forman D, Forman D, Mathers C, Parkin DM. Estimates of worldwide burden of cancer in 2008: GLOBOCAN 2008. *Int J Cancer.* (2010) 127:2893–917. doi: 10.1002/ijc.25516
2. Siegel RL, Miller KD, Jemal A. Cancer statistics, 2019. *CA: Cancer J Clin.* (2019) 69:7–34. doi: 10.3322/caac.21551
3. Gubanova E, Brown B, Ivanov SV, Helleday T, Mills GB, Yarbrough WG, et al. Downregulation of SMG-1 in HPV-positive head and neck squamous cell carcinoma due to promoter hypermethylation correlates with improved survival. *Clin Cancer Res.* (2012) 18:1257–67. doi: 10.1158/1078-0432.CCR-11-2058
4. Catsburg C, Gunter MJ, Chen C, Cote ML, Kabat GC, Nassir R, et al. Insulin, estrogen, inflammatory markers, and risk of benign proliferative breast disease. *Cancer Res.* (2014) 74:3248–58. doi: 10.1158/0008-5472.CAN-13-3514
5. Rettig EM, D'Souza G. Epidemiology of head and neck cancer. *Surg Oncol Clin N Am.* (2015) 24:379–96. doi: 10.1016/j.soc.2015.03.001
6. Canning M, Guo G, Yu M, Myint C, Groves MW, Byrd JK, et al. Heterogeneity of the head and neck squamous cell carcinoma immune

landscape and its impact on immunotherapy. *Front Cell Dev Biol.* (2019) 7:52. doi: 10.3389/fcell.2019.00052
7. Zeng Q, Peng S, Monie A, Yang M, Pang X, Hung CF, et al. Control of cervicovaginal HPV-16 E7-expressing tumors by the combination of therapeutic HPV vaccination and vascular disrupting agents. *Hum Gene Ther.* (2011) 22:809–19. doi: 10.1089/hum.2010.071
8. Squarzanti DF, Sorrentino R, Landini MM, Chiesa A, Pinato S, Rocchio F, et al. Human papillomavirus type 16 E6 and E7 oncoproteins interact with the nuclear p53-binding protein 1 in an *in vitro* reconstructed 3D epithelium: new insights for the virus-induced DNA damage response. *Virol J.* (2018) 15:176. doi: 10.1186/s12985-018-1086-4
9. Deng W, Tsao SW, Guan XY, Cheung AL. Pericentromeric regions are refractory to prompt repair after replication stress-induced breakage in HPV16 E6E7-expressing epithelial cells. *PloS ONE.* (2012) 7:e48576. doi: 10.1371/journal.pone.0048576
10. Oh JE, Kim JO, Shin JY, Zhang, XH, Won HS, Chun SH, et al. Molecular genetic characterization of p53 mutated oropharyngeal squamous cell carcinoma cells transformed with human papillomavirus E6 and E7 oncogenes. *Int J Oncol.* (2013) 43:383–93. doi: 10.3892/ijo.2013.1953
11. Poropatich K, Paunesku T, Zander A, Wray B, Schipma M, Dalal P, et al. Elemental Zn and its binding protein zinc-α2-glycoprotein are elevated in HPV-positive oropharyngeal squamous cell carcinoma. *Sci Rep.* (2019) 9:16965. doi: 10.1038/s41598-019-53268-1
12. Wu Y, Chen H, Chen Y, Qu L, Zhang E, Wang Z, et al. HPV shapes tumor transcriptome by globally modifying the pool of RNA binding protein-binding motif. *Aging.* (2019) 11:2430–46. doi: 10.18632/aging.101927
13. Liu F, Zhang S, Zhao Z, Mao X, Huang J, Wu Z, et al. MicroRNA-27b up-regulated by human papillomavirus 16 E7 promotes proliferation and suppresses apoptosis by targeting polo-like kinase2 in cervical cancer. *Oncotarget.* (2016) 7:19666–79. doi: 10.18632/oncotarget.7531
14. Kogure A, Kosaka N, Ochiya T. Cross-talk between cancer cells and their neighbors via miRNA in extracellular vesicles: an emerging player in cancer metastasis. *J Biomed Sci.* (2019) 26:7. doi: 10.1186/s12929-019-0500-6
15. Gregory RI, Yan KP, Amuthan G, Chendrimada T, Doratotaj B, Cooch N, et al. The Microprocessor complex mediates the genesis of microRNAs. *Nature.* (2004) 432:235–40. doi: 10.1038/nature03120
16. Liu Y, Zou J, Li B, Wang Y, Wang D, Hao Y, et al. RUNX3 modulates hypoxia-induced endothelial-to-mesenchymal transition of human cardiac microvascular endothelial cells. *Int J Mol Med.* (2017) 40:65–74. doi: 10.3892/ijmm.2017.2998
17. Calin GA, Sevignani C, Dumitru CD, Hyslop T, Noch E, Yendamuri S, et al. Human microRNA genes are frequently located at fragile sites and genomic regions involved in cancers. *Proc Natl Acad Sci USA.* (2004) 101:2999–3004. doi: 10.1073/pnas.0307323101
18. Martinez I, Gardiner AS, Board KF, Monzon FA, Edwards RP, Khan SA. Human papillomavirus type 16 reduces the expression of microRNA-218 in cervical carcinoma cells. *Oncogene.* (2008) 27:2575–82. doi: 10.1038/sj.onc.1210919
19. Samarakkody AS, Shin NY, Cantor AB. Role of RUNX family transcription factors in DNA damage response. *Mol Cells.* (2020) 43:99–106. doi: 10.14348/molcells.2019.0304
20. Tay LS, Krishnan V, Sankar H, Chong YL, Chuang LSH, Tan TZ, et al. RUNX Poly(ADP-Ribosyl)ation and BLM interaction facilitate the fanconi anemia pathway of DNA repair. *Cell Rep.* (2018) 24:1747–55. doi: 10.1016/j.celrep.2018.07.038
21. Tsunematsu T, Kudo Y, Iizuka S, Ogawa I, Fujita T, Kurihara H, et al. RUNX3 has an oncogenic role in head and neck cancer. *PLoS ONE.* (2009) 4:e5892. doi: 10.1371/journal.pone.0005892
22. Zhang C, Mi J, Deng Y, Deng Z, Long D, Liu Z. DNMT1 enhances the radiosensitivity of HPV-positive head and neck squamous cell carcinomas via downregulating SMG1. *OncoTargets Ther.* (2020) 13:4201–11. doi: 10.2147/OTT.S227395
23. Kobayashi K, Hisamatsu K, Suzui N, Hara A, Tomita H. A review of HPV-related head and neck cancer. (2018) 7:241. doi: 10.3390/jcm7090241
24. Gotz C, Bischof C, Wolff KD, Kolk A. Detection of HPV infection in head and neck cancers: promise and pitfalls in the last ten years: a meta-analysis. *Mol Clin Oncol.* (2019) 10:17–28. doi: 10.3892/mco.2018.1749
25. Lajer CB, Garnaes E, Friis-Hansen L, Norrild B, Therkildsen MH, Glud M, et al. The role of miRNAs in human papilloma virus (HPV)-associated cancers: bridging between HPV-related head and neck cancer and cervical cancer. *Br J Cancer.* (2012) 106:1526–34. doi: 10.1038/bjc.2012.109
26. Zou Y, Chen Z, Jennings BL, Zhao G, Gu Q, Bhattacharya A, et al. Deletion of DGCR8 in VSMCs of adult mice results in loss of vascular reactivity, reduced blood pressure and neointima formation. *Sci Rep.* (2018) 8:1468. doi: 10.1038/s41598-018-19660-z
27. Ardenne M, Reitnauer PG. Demonstration of tumor inhibiting properties of a strongly immunostimulating low-molecular weight substance. Comparative studies with ifosfamide on the immuno-labile DS carcinosarcoma. Stimulation of the autoimmune activity for approx. 20 days by BA 1, a N-(2-cyanoethylene)-urea. Novel prophylactic possibilities. *Arzneimittel-Forschung.* (1975) 25:1369–79.
28. Huang R, Hu Z, Feng Y, Yu L, Li X. The transcription factor IRF6 Co-represses PPARgamma-mediated cytoprotection in ischemic cerebrovascular endothelial cells. *Sci Rep.* (2017) 7:2150. doi: 10.1038/s41598-017-02095-3
29. Friedman RC, Farh KK, Burge CB, Bartel DP. Most mammalian mRNAs are conserved targets of microRNAs. *Genome Res.* (2009) 19:92–105. doi: 10.1101/gr.082701.108
30. Chen X, Deng Y, Shi Y, Zhu W, Cai Y, Xu C, et al. Loss of expression rather than cytoplasmic mislocalization of RUNX3 predicts worse outcome in non-small cell lung cancer. *Oncol Lett.* (2018) 15:5043–55. doi: 10.3892/ol.2018.7993
31. Horiguchi S, Shiraha H, Nagahara T, Kataoka J, Iwamuro M, Matsubara M, et al. Loss of runt-related transcription factor 3 induces gemcitabine resistance in pancreatic cancer. *Mol Oncol.* (2013) 7:840–9. doi: 10.1016/j.molonc.2013.04.004

Conflict of Interest: The authors declare that the research was conducted in the absence of any commercial or financial relationships that could be construed as a potential conflict of interest.

Copyright © 2020 Zhang, Chen, Deng, Long, Xu and Liu. This is an open-access article distributed under the terms of the Creative Commons Attribution License (CC BY). The use, distribution or reproduction in other forums is permitted, provided the original author(s) and the copyright owner(s) are credited and that the original publication in this journal is cited, in accordance with accepted academic practice. No use, distribution or reproduction is permitted which does not comply with these terms.

frontiers in Medicine

ORIGINAL RESEARCH
published: 09 February 2021
doi: 10.3389/fmed.2021.637803

Development and Multi-Data Set Verification of an RNA Binding Protein Signature for Prognosis Prediction in Glioma

*Chunpeng Sheng, Zhihua Chen, Jianwei Lei, Jianming Zhu and Shuxin Song**

Department of Neurosurgery, The Second Affiliated Hospital of Nanchang University, Nanchang, China

Objective: Increasing evidence emphasizes the clinical implications of RNA binding proteins (RBPs) in cancers. This study aimed to develop a RBP signature for predicting prognosis in glioma.

Methods: Two glioma datasets as training ($n = 693$) and validation ($n = 325$) sets were retrieved from the CGGA database. In the training set, univariate Cox regression analysis was conducted to screen prognosis-related RBPs based on differentially expressed RBPs between WHO grade II and IV. A ten-RBP signature was then established. The predictive efficacy was evaluated by ROCs. The applicability was verified in the validation set. The pathways involving the risk scores were analyzed by ssGSEA. scRNA-seq was utilized for evaluating their expression in different glioma cell types. Moreover, their expression was externally validated between glioma and control samples.

Results: Based on 39 prognosis-related RBPs, a ten RBP signature was constructed. High risk score distinctly indicated a poorer prognosis than low risk score. AUCs were separately 0.838 and 0.822 in the training and validation sets, suggesting its well performance for prognosis prediction. Following adjustment of other clinicopathological characteristics, the signature was an independent risk factor. Various cancer-related pathways were significantly activated in samples with high risk score. The scRNA-seq identified that risk RBPs were mainly expressed in glioma malignant cells. Their high expression was also found in glioma than control samples.

Conclusion: This study developed a novel RBP signature for robustly predicting prognosis of glioma following multi-data set verification. These RBPs may affect the progression of glioma.

Keywords: RNA binding proteins, signature, glioma, prognosis, single cell RNA sequencing

OPEN ACCESS

Edited by:
Fu Wang,
Xi'an Jiaotong University, China

Reviewed by:
Jingang Huang,
Sun Yat-sen Memorial Hospital, China
Chaoyun Pan,
Sun Yat-Sen University, China

****Correspondence:***
Shuxin Song
shuxinsong@tom.com

Specialty section:
This article was submitted to Precision Medicine, a section of the journal Frontiers in Medicine

Received: *04 December 2020*
Accepted: *11 January 2021*
Published: *09 February 2021*

Citation:
Sheng C, Chen Z, Lei J, Zhu J and Song S (2021) Development and Multi-Data Set Verification of an RNA Binding Protein Signature for Prognosis Prediction in Glioma. Front. Med. 8:637803. doi: 10.3389/fmed.2021.637803

INTRODUCTION

Glioma is the most frequently diagnosed primary brain malignancy, accounting for 70% of all brain malignancies (1). In line with the 2016 World Health Organization (WHO) classification, glioblastoma (GBM) is the most common histology type, which corresponds to WHO grade IV, with a median survival of <2 years and a 5-year survival rate of 5% (2).

The incidence of lower grade gliomas (LGG) WHO grade II is relatively lower and patients with grade II exhibit better clinical outcomes and more sensitive to therapies (3). At present, the diagnosis of glioma primarily depends on histopathology, imaging as well as molecular diagnosis (4–6). Nevertheless, because of complicacy and heterogeneity, traditionally diagnostic and therapeutic techniques exert side effects for the clinical outcomes of patients. To prolong the survival time of patients, it is of clinical importance for discovering novel accurate molecular biomarkers for prognosis prediction in glioma.

RBPs play major participants of the life cycle of mRNAs (7). One thousand five hundred forty-two RBP genes have been discovered in the human genome, corresponding to over 7.5% of protein-encoding genes (8). Totally, ∼50% of RBPs exert post-transcriptional mediated effects on gene expression (8). Abnormally expressed RBPs have been considered as drivers for cancers. They may be involved in regulating the progression and spread of cancers (9). Increasing evidence highlights the critical roles of RBPs in the malignant biological behaviors in gliomas (10). For example, RBP SRSF1 could regulate the cell cycle through stabilizing NEAT1 for glioma (11). RBP PCBP2 may modulate glioma growth via regulation of FHL3 (12). RBP SRSF3 regulates RNA alternative splicing, thereby inducing glioblastoma occurrence via influencing key biological processes (13). Nevertheless, their roles still require to be explored in depth via further functional studies. Recent studies suggest that several RBPs exhibit significant associations with clinical outcomes of glioma patients, such as SNRPN and IGF2BP3 (14). Hence, targeting RBPs appears to be promising strategies for the development of novel treatment against cancers. Moreover, it is of significance to understand the prognostic implications of RBPs in glioma. Herein, our findings developed a RBP signature for predicting the clinical outcomes of glioma patients. After validation, this signature exhibited a robust predictive efficacy.

MATERIALS AND METHODS

Glioma Data Acquirement and Preprocessing

Two glioma datasets ($n = 693$ or 325) containing mRNA sequencing and corresponding clinical information were retrieved from the Chinese Glioma Genome Atlas (CGGA). A dataset ($n = 693$) was used as the training set and another ($n = 325$) was utilized as the validation set. The batch effects were presented after integration of the two datasets.

Differential Expression Analysis

The mRNA expression profiles of RBPs were extracted from the training and validation sets. Differentially expressed RBPs were defined by comparing WHO grade II and IV samples via the edgeR package in R (15). The criteria were set as follows: $|\log$ fold change (FC)$| \geq 0.58$ and false discovery rate (FDR) > 0.5. Differentially expressed RBPs were visualized into volcano and heatmap plots.

Univariate and Multivariate Cox Proportional Hazard Model

Univariate cox regression analysis was conducted for differentially expressed RBPs in the training set. RBPs with hazard ratio > 1 and $p < 0.001$ were risk factors and those with hazard ratio < 1 and $p < 0.001$ were protective factors. RBPs with $p < 0.001$ were chosen for multivariable cox regression. Totally, ten RBPs were filtered out for building up the predictive model. The risk score for each sample was calculated by combining the coefficient and the expression level of RBP. Afterwards, the patients were separated into high- and low-risk groups in line with the median values of the risk scores. Kaplan-Meier curves were constructed and the differences in survival time between groups were compared by log-rank test. Using the heatmap package in R, the ten RBPs were displayed between the two groups. Relative operating characteristic curves (ROCs) were built for assessment of the predictive efficacy of the signature. Univariate and multivariate cox regression analysis was utilized to evaluate the associations between risk score as well as other clinical features and prognosis among glioma samples.

Functional Enrichment Analysis

Kyoto Encyclopedia of Genes and Genomes (KEGG) and Gene Ontology (GO) enrichment analyses were conducted for prognosis-related RBPs via the clusterProfiler package in R (16). Terms with adjusted $p < 0.05$ were statistically significant.

Single Sample Gene Set Enrichment Analysis (ssGSEA)

Hallmark gene sets were obtained from the Molecular Signatures Database v7.2. ssGSEA was utilized to analyze the associations between risk scores and signaling pathways via the Gene Set Variation Analysis (GSVA) in R package (17). GSVA score in each pathway was calculated for a specific sample. The difference in a specific alteration in a pathway was compared between high and low risk groups via Wilcoxon rank-sum test.

Construction and Evaluation of a Nomogram

Based on the coefficients of the ten RBPs from the multivariate Cox regression analysis, the score was determined for each RBP. The total point was obtained by adding all scores of the RBPs. Through the function conversion relationship between the total point and the 1-, 2-, and 3-year survival probability, the predicted probability of the individual outcome event was calculated. The nomogram was conducted via the forestplot package in R. Calibration curve was drawn for internal verification utilizing the rms package. The predicted 5-year survival was compared with the actual survival time.

Abbreviations: RBPs, RNA binding proteins; WHO, World Health Organization; LGG, lower grade gliomas; CGGA, Chinese Glioma Genome Atlas; FC, fold change; FDR, false discovery rate; ROCs, relative operating characteristic curves; KEGG, Kyoto Encyclopedia of Genes and Genomes; GO, Gene Ontology; ssGSEA, single sample Gene Set Enrichment Analysis; GSVA, Gene Set Variation Analysis; scRNA-seq, single cell RNA-sequencing; GEO, Gene Expression Omnibus; t-SNE, t-distributed stochastic neighbor embedding; GEPIA, Gene Expression Profiling Interactive Analysis; AUC, area under the curve.

Single Cell RNA-Sequencing (scRNA-seq) Data

Three single cell RNA-seq datasets for glioma including GSE131928 Smart-seq2 (18), GSE131928 10X Genomics, GSE102130 datasets were retrieved from the Gene Expression Omnibus (GEO; https://www.ncbi.nlm.nih.gov/gds/). Following quality control, normalization and linear scaling analyses, cell cluster was presented via the Seurat package in R (19). Cell types were visualized by the t-distributed stochastic neighbor embedding (t-SNE). The expression levels of the ten RBPs were visualized in each cell type.

Spearson Correlation Analysis

The expression levels of IGF2BP3, RDM1, NSUN7, EXO1, APOBEC3F, FBXO17, FAM46A, ANG, ADARB2, and EIF4E1B were compared between glioma WHO grade II and IV samples. At the mRNA levels, Spearson correlation analysis was presented between these RBPs among the whole datasets.

Gene Expression Profiling Interactive Analysis (GEPIA)

Using the GEPIA database; (http://gepia2.cancer-pku.cn/#index), the expression of RBPs was compared between tumor ($n = 163$) and normal ($n = 207$) specimens in the GBM dataset from TCGA and GTE_X database. The cutoffs were set as $|\log2FC| > 1$ and $p < 0.01$.

Reverse Transcription Quantitative Polymerase Chain Reaction (RT-qPCR)

Ten pairs of glioma and normal tissue specimens were collected from The Second Affiliated Hospital of Nanchang university. All patients provided written informed content. This study was approved by the Ethics Committee of The Second Affiliated Hospital of Nanchang university (2020018). Total RNA was extracted from tissues utilizing TRIzol (Beyotime, Shanghai), which was reverse transcribed into cDNA. RT-qPCR was presented by the miScript SYBR Green PCR Kit (Applied Biosystems, USA). **Table 1** listed the sequence information of primers. GAPDH was utilized as a control. The expression levels were calculated with the $2-\Delta\Delta Ct$ method. Using GraphPad Prism 7.0, the differences between tumor and normal groups were determined using student's *t*-test. $P < 0.05$ indicated statistically significant.

TABLE 1 | The primer sequences for RT-qPCR.

Gene name	Primer sequence (5′-3′)
ANG	CTGGGCGTTTTGTTGTTGGTC (forward) GGTTTGGCATCATAGTGCTGG (reverse)
EXO1	TGAGGAAGTATAAAGGGCAGGT (forward) AGTTTTTCAGCACAAGCAATAGC (reverse)
FBXO17	CTGACCCGGTCCTTCAGTG (forward) CTCCCGTACTGCTCAAAAGATAC (reverse)
IGF2BP3	TATATCGGAAACCTCAGCGAGA (forward) GGACCGAGTGCTCAACTTCT (reverse)
NSUN7	GGACTCCGTTTATGTCATGGC (forward) CTCAGACTCGGACAAGGACC (reverse)

RESULTS

Screening Prognosis-Related RBPs for Glioma

In this study, we compared the differences in expression of 1,487 RBPs between glioma WHO grade II and IV samples in the training set. With the criteria of $|\log FC| \geq 0.58$ and FDR > 0.5, 40 RBPs were abnormally expressed between glioma II and IV samples (**Supplementary Table 1**). Among them, 23 RBPs were up-regulated whereas 17 RBPs were down-regulated in glioma grade IV compared to II (**Figure 1A**). Heat maps visualized the expression patterns of these RBPs between glioma II and IV samples (**Figure 1B**). We explored prognosis-related RBPs in glioma via univariate cox regression analysis. Our data suggested that 39 RBPs were significantly associated with prognosis of glioma (**Figure 1C**). Among them, 22 RBPs were risk factors for glioma and 17 RBPs were protective factors for glioma. To further probe the biological functions of these prognosis-related RBPs, we carried out KEGG and GO enrichment analysis. Our data suggested that RNA transport, mRNA surveillance and RNA degradation pathways were distinctly enriched, as shown in **Figure 1D**. GO enrichment analysis results revealed that these RBPs were involved in mediating various key biological processes such as mRNA metabolic process, RNA splicing, mRNA processing, RNA transport and localization (**Figures 1E,F**). These data demonstrated that the prognosis-related RBPs we selected could be involved in the progression of glioma.

Establishment of an RBP Signature for Prognosis Prediction in Glioma

Based on prognosis-related RBPs, in the training set, a ten-RBP signature was established for glioma via multivariate cox regression analysis (**Figure 2A**). The risk score for each glioma was determined as follows: 0.772546974482237 * the expression levels of IGF2BP3 + (-0.529440079138294) * the expression levels of RDM1 + 0.959791181375875 * the expression levels of NSUN7 + 1.28748170838841 * the expression levels of EXO1 + (−0.92777652353892) * the expression levels of APOBEC3F + 0.746260894529048 * the expression levels of FBXO17 + (−0.545584467299167) * FAM46A + 0.999495382483528 * the expression levels of ANG + 0.682420092015883 * the expression levels of ADARB2 + (−0.565975323034877) * the expression levels of EIF4E1B. Among them, IGF2BP3 (HR: 2.165, 95%CI: 1.547–3.030, $p < 0.001$), NSUN7 (HR: 2.611, 95%CI: 1.226–5.561, $p = 0.013$), EXO1 (HR: 3.624, 95%CI: 1.978–3.030, $p < 0.001$), FBXO17 (HR: 2.109, 95%CI: 1.161–3.831, $p = 0.014$), ANG (HR: 2.717, 95%CI: 1.454–5.078, $p = 0.002$) and ADARB2 (HR: 1.979, 95%CI: 1.308–2.992, $p = 0.001$) were negatively correlated with survival time for glioma patients. APOBEC3F (HR: 0.395, 95%CI: 0.201–0.778, $p = 0.007$) and EIF4E1B (HR:

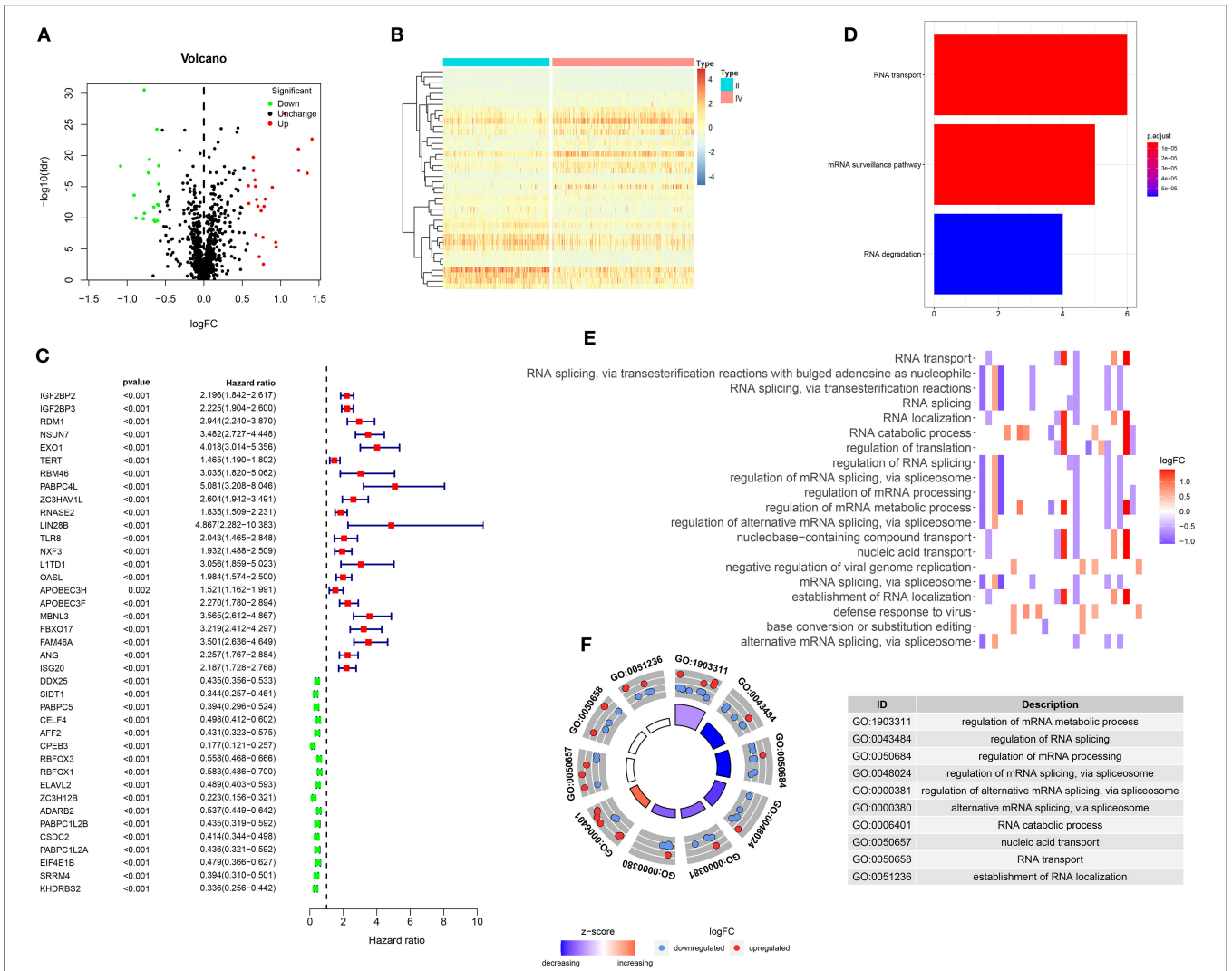

FIGURE 1 | Screening prognosis-related RBPs for glioma. **(A)** Volcano plots for up-regulated (red) and down-regulated (green) RBPs in glioma WHO grade IV compared to grade II samples. **(B)** Hierarchical clustering analysis for differentially expressed RBPs between glioma WHO II and IV samples. **(C)** Univariate cox regression analysis for screening 39 glioma prognosis-related RBPs. **(D)** The signal pathways involved in these RBPs. **(E,F)** Key biological processes enriched by these RBPs.

0.568 95%CI: 0.342–0.943, $p = 0.029$) were positively associated with clinical outcomes in glioma patients. On the grounds of the median risk score, these patients were separated into high and low risk groups (**Figure 2B**). In comparison to the low-risk group, the number of dead patients was higher in the high-risk group (**Figure 2C**). There were distinct differences in expression levels of these ten RBPs between the two subgroups (**Figure 2D**). The patients in the high-risk group exhibited an unfavorable prognosis compared to those in the low-risk group ($p < 0.0001$; **Figure 2E**). The area under the curve (AUC) was 0.838, demonstrating that the signature possessed the well performance for prognosis prediction in glioma patients (**Figure 2F**). Based on the univariate cox regression analysis, PRS type (HR: 2.003, 95%CI: 1.359–2.953, $p < 0.001$), grade (HR: 3.008, 95%CI: 2.297–3.938, $p < 0.001$), age (HR: 3.797, 95%CI: 2.444–5.900, $p < 0.001$), chemotherapy status (HR: 1.911, 95%CI: 1.151–3.174, $p = 0.012$) and risk score (HR: 1.294, 95%CI: 1.229–1.363, $p < 0.001$) were risk factors for glioma (**Figure 2G**). We further assessed whether the signature could independently predict the clinical outcomes of glioma patients. Our multivariate cox regression analysis revealed the independency of the predictive efficacy of the signature (HR: 1.217, 95%CI: 1.143–1.295, $p < 0.001$; **Figure 2H**). Grade (HR: 2.702, 95%CI: 1.948–3.749, $p < 0.001$) and age (HR: 1.975, 95%CI: 1.249–3.123, $p = 0.004$) were both independently predictive of the clinical outcomes of glioma patients. Collectively, this signature could be robustly and accurately predictive of the clinical outcomes for glioma patients.

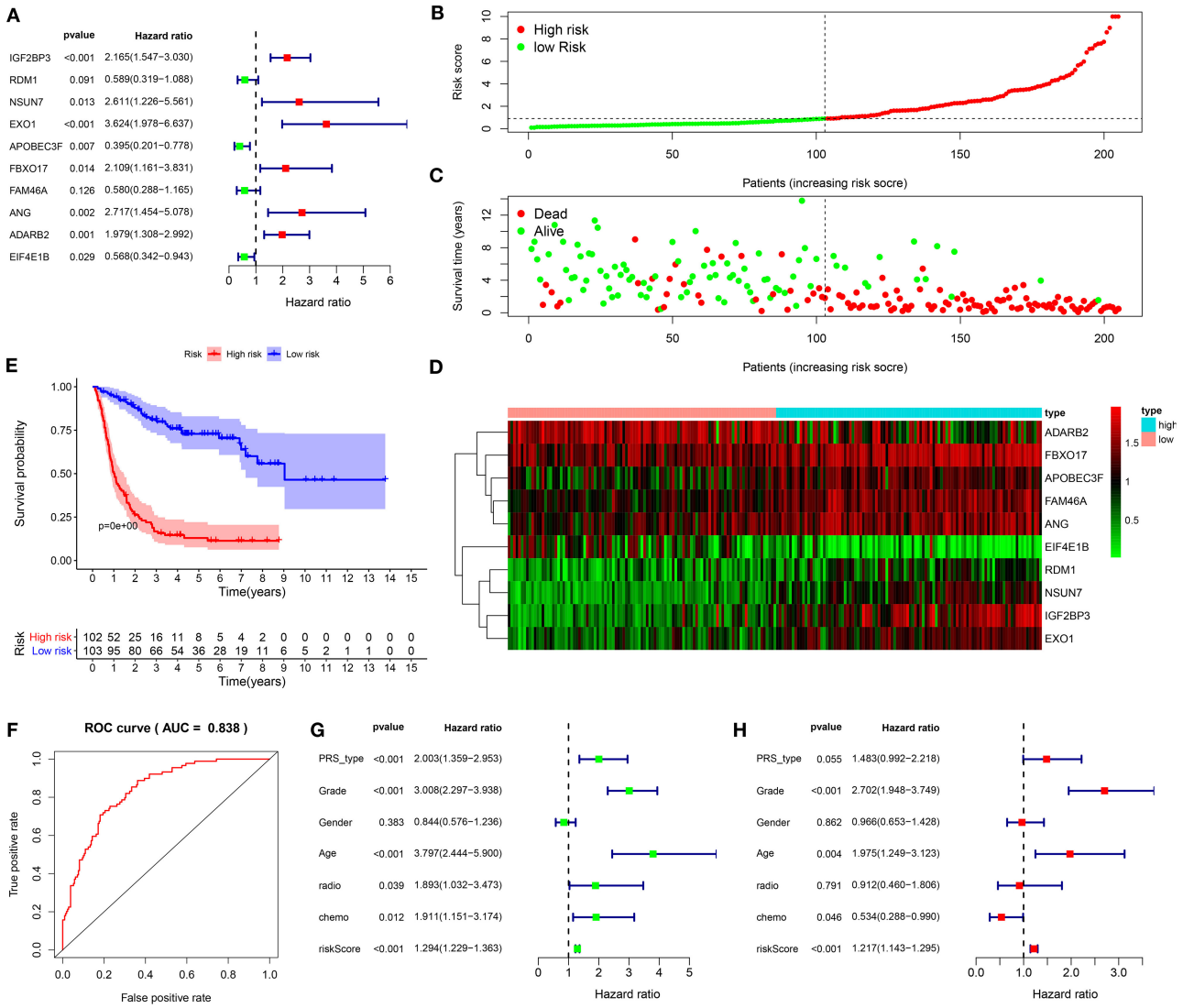

FIGURE 2 | Establishment of a ten-RBP signature for predicting the prognosis of glioma in the training set. **(A)** Multivariate cox regression analysis for the predictive values of the ten RBPs in glioma. **(B)** The ranking of the risk scores among glioma patients. **(C)** Survival status in high and low risk groups. **(D)** Heat map for the expression levels of the RBPs between high and low risk groups. **(E)** Kaplan-Meier curves for high and low risk glioma patients. **(F)** Construction of a ROC curve for assessment of the predictive efficacy of the signature. **(G)** Univariate and **(H)** multivariate cox regression analysis for the association between risk score as well as clinical features and prognosis in glioma.

Validation of the RBP Signature for Predicting Prognosis of Glioma

We further verified the applicability of the signature for predicting prognosis of glioma in the validation set. Following the same method, patients were divided into high and low risk groups in accordance with the median value (**Figure 3A**). In the high-risk group, the number of dead patients was much higher than in the low-risk group (**Figure 3B**). In **Figure 3C**, these ten RBPs were abnormally expressed between the two subgroups. Patients in the high-risk group exhibited shorter survival time than those in the low-risk group ($p < 0.0001$; **Figure 3D**). The high predictive value was confirmed by the ROC curve (AUC = 0.822; **Figure 3E**). PRS type (HR: 2.541, 95%CI: 1.879–3.436, $p < 0.001$), grade (HR: 2.868, 95%CI: 2.360–3.486, $p < 0.001$), age (HR: 2.166, 95%CI: 1.386–3.386, $p < 0.001$), chemotherapy (HR: 1.574, 95%CI: 1.155–2.145, $p < 0.004$), and risk score (HR: 1.298, 95%CI: 1.248–1.351, $p < 0.001$) had negative correlations with prognosis of glioma patients (**Figure 3F**). Following the multivariate cox regression analysis, risk score (HR: 1.214, 95%CI: 1.156–1.274, $p < 0.001$), PRS type (HR: 1.958, 95%CI: 1.413–2.715, $p < 0.001$), and grade (HR: 2.430, 95%CI: 1.943–3.040, $p < 0.001$) were independent risk factors for glioma (**Figure 3G**).

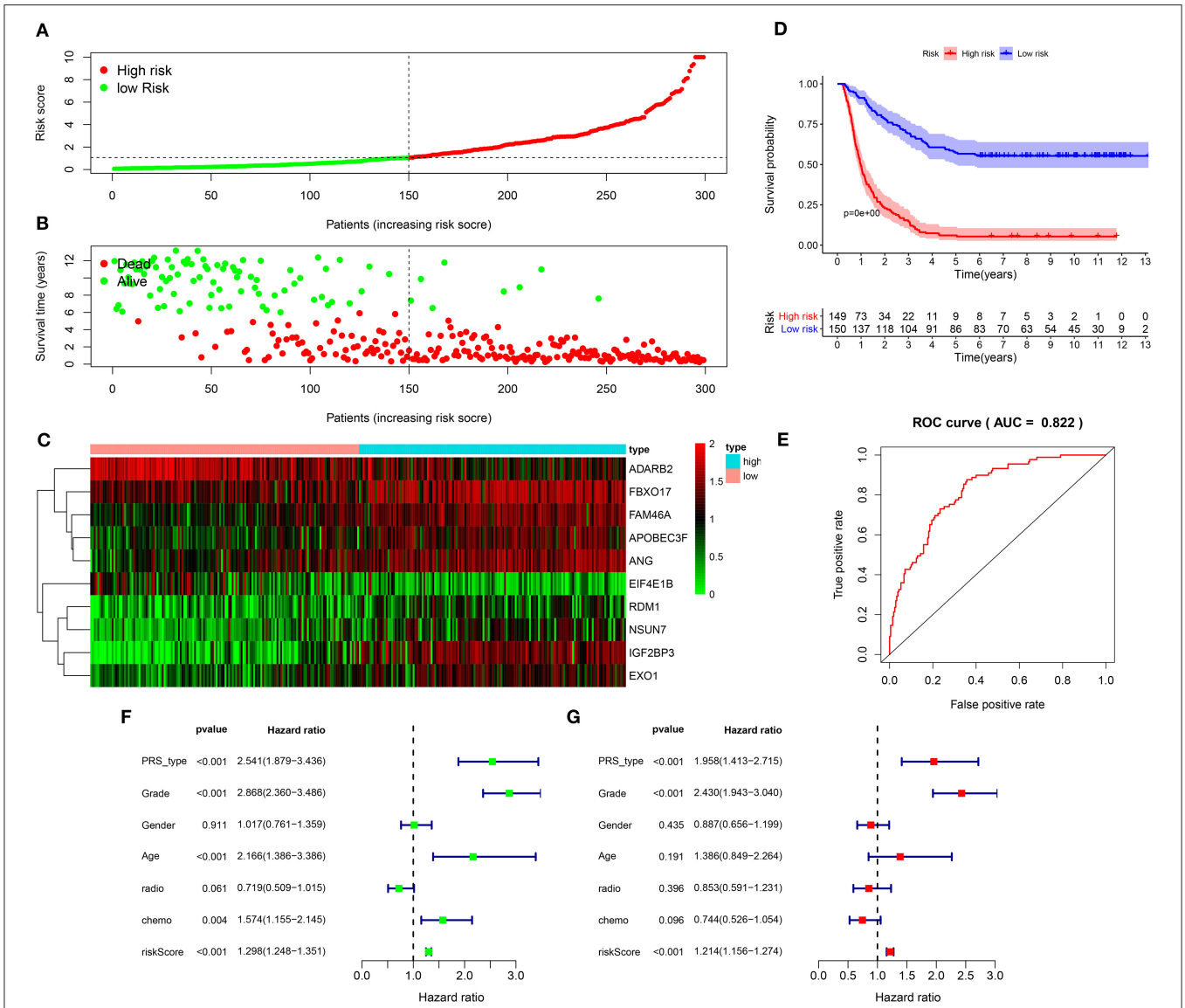

FIGURE 3 | Validation of the RBP signature for predicting prognosis of glioma in the validation set. **(A)** The ranking of the risk scores and **(B)** survival status distribution in high and low risk glioma samples. **(C)** Heat map visualizing the expression levels of the RBPs in high and low risk groups. **(D)** Kaplan-Meier curves for high and low risk patients. **(E)** A ROC curve for evaluating the predictive efficacy of the signature. **(F)** Univariate and **(G)** multivariate cox regression analysis for the associations between risk score as well as clinical characteristics and prognosis in glioma.

ssGSEA Determines Signaling Pathways Involved in the Ten-RBP Signature

GSVA score of a specific alteration in a pathway was calculated in each glioma sample. Our data suggested that the high-risk scores were significantly associated with hypoxia, TNFα signaling pathway via NF-κB, inflammatory response, mitotic spindle, PI3K-Akt-mTOR signaling pathway, Notch signaling pathway, interferon α response, interferon γ response and glycolysis (all $p < 0.0001$; **Figure 4**). No difference in WNT β-Catenin signaling was found between high and low risk score groups. Above findings revealed that cancer-related pathways were activated in the glioma samples with high risk scores.

Construction and Evaluation of a Nomogram for Prognosis Prediction of Glioma

To personally calculate the survival rate of specific patient with glioma, a nomogram was established based on the ten RBPs in the training set. According to the influence levels of each RBP in the model on the clinical outcomes, each score of the RBP was assigned, and the total score was determined. The 1-, 2-, and 3-year survival probability of an individual patient was predicted based on the total scores (**Figure 5A**). We further evaluated the predictive efficacy of the nomogram in the validation set (**Figure 5B**). Calibration curves were depicted

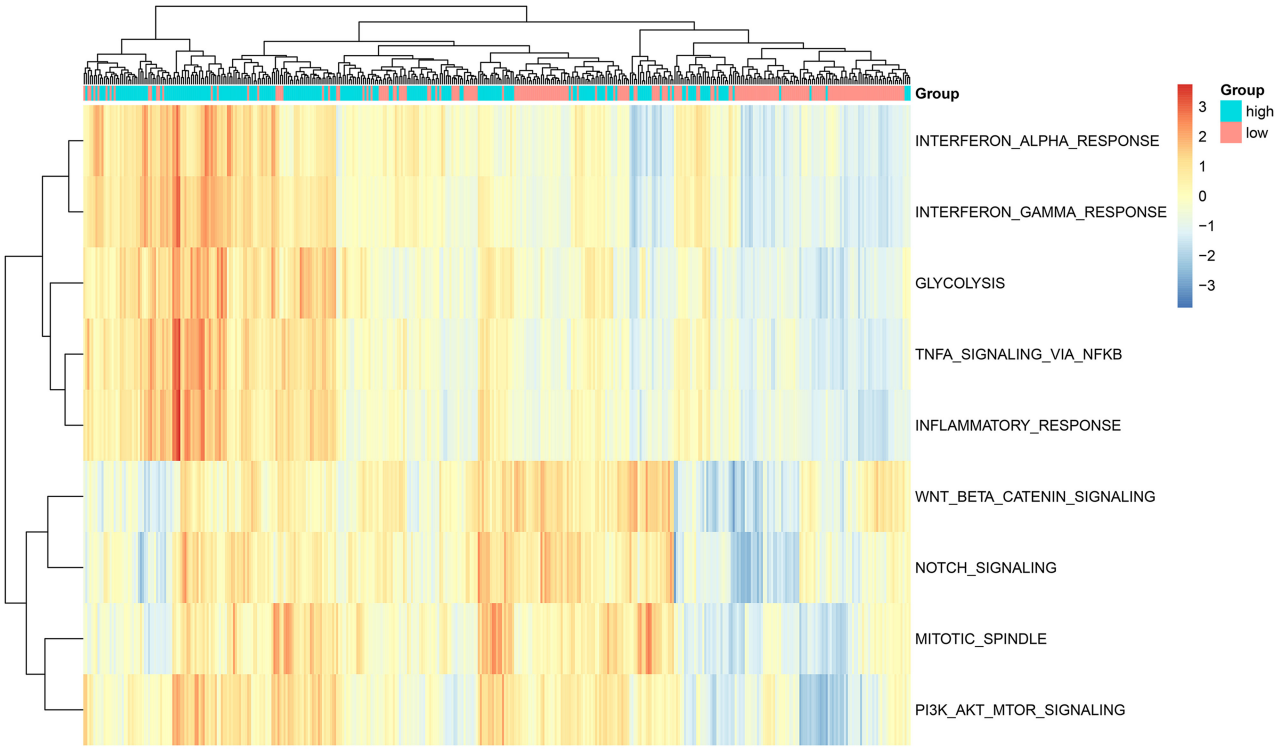

FIGURE 4 | ssGSEA determines the relationships between the ten-RBP signature and signaling pathways for glioma patients.

to compare the nomogram-predicted 5-year survival probability and actual survival time. Both in the training (**Figure 5C**) and validation (**Figure 5D**) sets, the nomogram exhibited the well performance for prediction of the 5-year survival time for glioma patients. Thus, the nomogram could be used for accurately assessing the survival probability for glioma patients.

Single Cell RNA-seq Reveals the Expression of the Risk RBP Signatures in Glioma

We deeply analyzed the expression levels of the risk RBP signatures in a single glioma cell in the three datasets. In the GSE131928 Smart-seq2 dataset, seven cell types were clustered, including AC-like malignant, CD8Tex, MES-like malignant, mon/macrophages, NPC-like malignant, OPC-like malignant and oligodendrocyte (**Figure 6A**). Consistent with our multivariate Cox regression analysis results, IGF2BP3, NSUN7, EXO1, and FBXO17 were highly expressed in AC-, MES-, NPC-, and OPC-like malignant cells (**Figures 6B–F**). Furthermore, heat map visualized the expression patterns of EXO1 (**Figure 6G**), FBXO17 (**Figure 6H**), IGF2BP3 (**Figure 6I**), and NSUN7 (**Figure 6J**) in different cell types in the three datasets. Higher expression levels of the four RBPs were detected in the AC-, MES-, NPC- and OPC-like malignant cells, which could be related to poor prognosis for glioma patients.

The Risk RBP Signatures Are Highly Expressed in Glioma Grade IV Than II

We further compared the expression levels of the ten RBP signatures in glioma grade II and IV samples. The data showed that ADARB2 and EIF4E1B had lower expression levels in glioma grade IV than II samples (both $p < 0.001$; **Figure 7A**). Most risk signatures exhibited higher expression levels of IGF2BP3, RDM1, NSUN7, EXO1, APOBEC3F, FBXO17, FAM46A, and ANG in grade IV than II. These results demonstrated that these risk signatures could affect the progression of glioma. Our study assessed whether these signatures could interact to promote tumor progression. The correlation analysis showed that, at the mRNA levels, there were obvious positive correlations between most of risk signatures (**Figure 7B**), such as RDM1 and EXO1 ($r = 0.53$), ANG and FAM46A ($r = 0.51$), APOBEC3F and FBXO17 ($r = 0.54$), APOBEC3F and ANG ($r = 0.7$).

The Risk RBP Signatures Are Highly Expressed in Glioma Than Controls

The expression of risk RBP signatures was compared in glioma ($n = 163$) and control samples ($n = 207$) in TCGA-GTEx database. The results showed that ANG (**Figure 8A**), EXO1 (**Figure 8B**), FBXO17 (**Figure 8C**), IGF2BP3 (**Figure 8D**), and NSUN7 (**Figure 8E**) displayed distinctly higher expression levels in glioma compared to controls ($p < 0.05$). Furthermore, we validated their expression in 10 pairs of glioma and normal

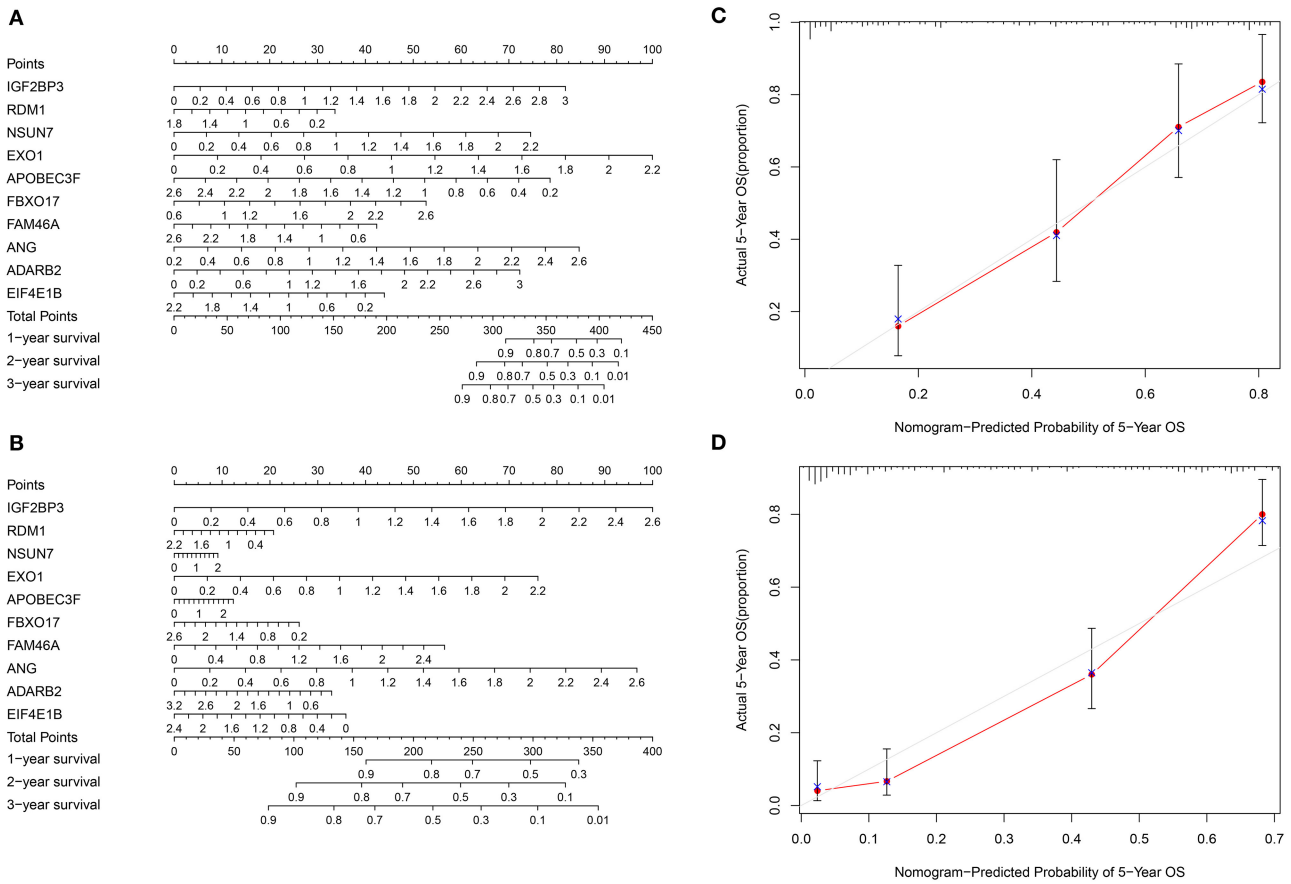

FIGURE 5 | Construction and evaluation of a nomogram for prognosis prediction of glioma. **(A)** A nomogram combining the ten RBPs for predicting the 1-, 2- and 3-year survival time of glioma patients in the training set. **(B)** Evaluation of the nomogram in the validation set. **(C,D)** Calibration curves for assessment of the 5-year survival probability of the nomogram in the **(C)** training and **(D)** validation sets.

tissue specimens by RT-qPCR. Our data confirmed the up-regulation of ANG (**Figure 9A**), EXO1 (**Figure 9B**), FBXO17 (**Figure 9C**), IGF2BP3 (**Figure 9D**), and NSUN7 (**Figure 9E**) in glioma than normal samples (all $p < 0.0001$). These findings revealed that these risk signatures could participate in the progression of glioma.

DISCUSSION

Recent research demonstrates that several RBPs have closely correlations with the malignant behaviors of glioma (14). Nevertheless, the functions of most of the RBPs in glioma tumorigenesis remain unclear (20). In this study, based on prognosis-related RBPs, we established a ten-RBP signature for prognosis prediction in glioma. Following multi-dataset verification, this signature could robustly predict clinical outcomes for glioma patients.

Herein, 40 RBPs were differentially expressed between glioma WHO grade IV and II. Among them, 39 RBPs were correlated to prognosis of glioma, which might be involved in the malignancies of glioma. Hence, we probed the biological functions involving these RBPs. Our data suggested that these RBPs could post-transcriptionally mediate gene expression via the interaction with targeted RNAs, such as RNA transport, degradation, splicing and localization. Based on them, we developed a ten-RBP signature for glioma. The signature could be utilized for robustly predicting the prognosis of patients. Both in the training and validation sets, high risk score was predictive of poorer prognosis. AUCs were 0.838 and 0.822 in the two sets, respectively, suggesting the well performance. Following adjustment with other clinical features, the signature was an independent prognostic factor. As previous studies, several RBP signatures have been constructed for other cancers. For example, Li et al. built up a nine-RBP gene signature for lung squamous cell carcinoma prognosis (21). A six-RBP model constructed by Wu et al. demonstrated a well performance for predicting the clinical outcomes of bladder cancer (22). However, so far, there is still a lack of RBP-related signature for glioma. Our research fills this gap at some extents.

Our findings revealed that high-risk scores were markedly associated with various cancer-related pathways, like hypoxia, TNFα signaling pathway via NF-κB, inflammatory response,

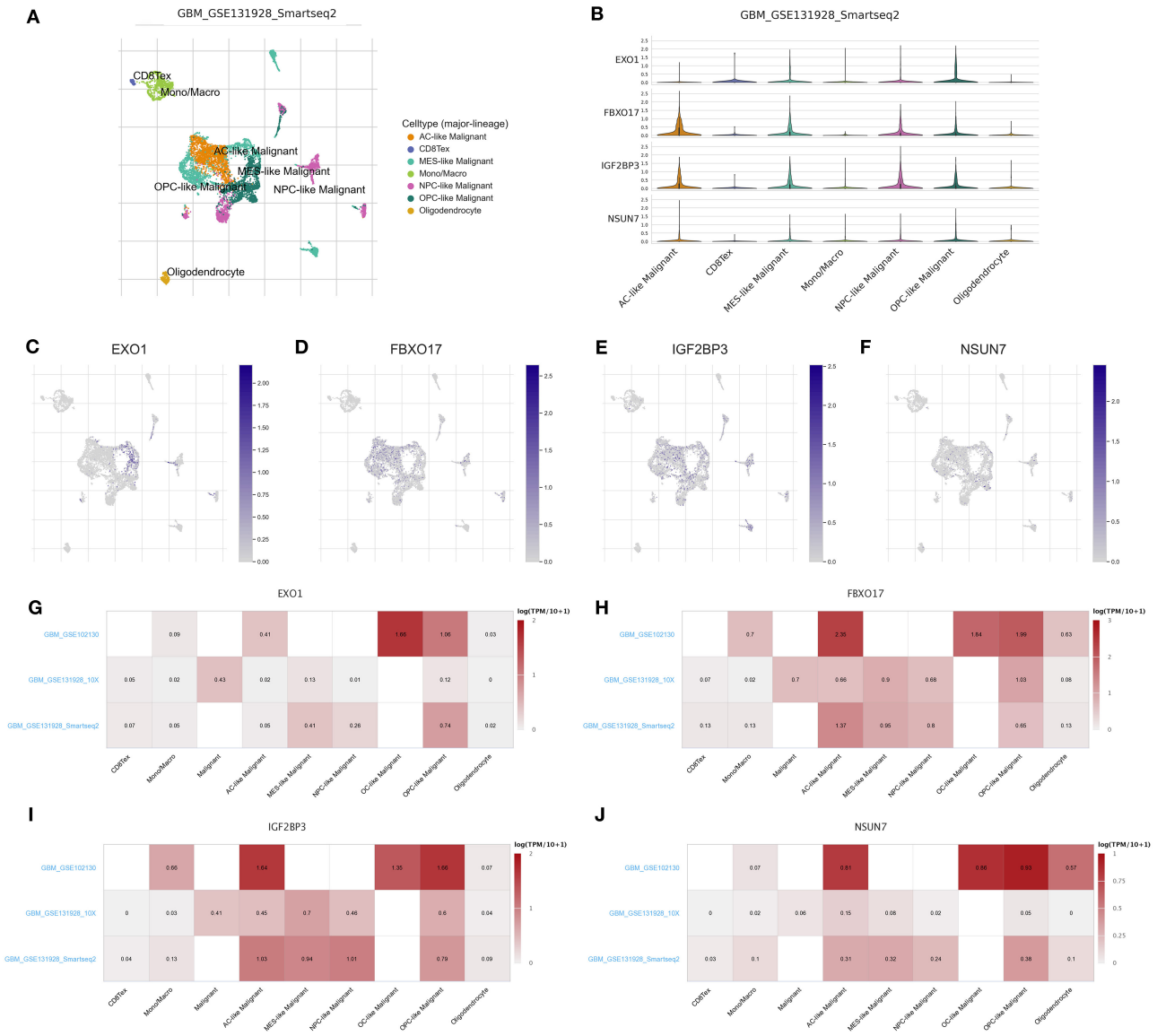

FIGURE 6 | scRNA-seq reveals the expression of the RBP signatures in glioma. **(A)** t-SNE visualizing the seven cell clusters in glioma in the GSE131928 dataset. **(B)** Violin plots for the expression patterns in different cell clusters for IGF2BP3, NSUN7, EXO1, and FBXO17 in the GSE131928 dataset. The expression distributions of **(C)** EXO1, **(D)** FBXO17, **(E)** IGF2BP3, and **(F)** NSUN7 in different cell types in the GSE131928 dataset. Heat maps visualizing the expression patterns of **(G)** EXO1, **(H)** FBXO17, **(I)** IGF2BP3, and **(J)** NSUN7 in different cell types in the GSE131928, GSE131928 and GSE102130 datasets.

mitotic spindle, PI3K-Akt-mTOR, Notch, interferon α response, interferon γ response and glycolysis pathways, indicating that cancer-related pathways were activated in glioma samples with high-risk scores. These RBPs could affect glioma progression via mediating above pathways. Previously, RBP ZEB1 facilitated hypoxia-mediated epithelial-mesenchymal transition in glioma cells (23). RBP MOV10 that bound to circ-DICER1 induced the proliferation, migration as well as tube formation in glioma cells via activation of PI3K/Akt pathway (24). RBP Musashi1 modulated the proliferative capacities of glioma cells via Notch and PI3K/Akt pathways. Hence, activation of cancer-related pathways could be related to poor prognosis in high-risk score patients. To improve the clinical application potential of RBPs, we constructed a nomogram combining the ten RBPs for assessment of the 1-, 2-, and 3-year survival probability. This nomogram was validated in the validation set, indicating the high application values. After evaluation of calibration curves, the nomogram-predicted 5-year survival was highly consistent with the actual survival, suggesting that the nomogram possessed the potential as a scoring tool for predicting the clinical outcomes of patients.

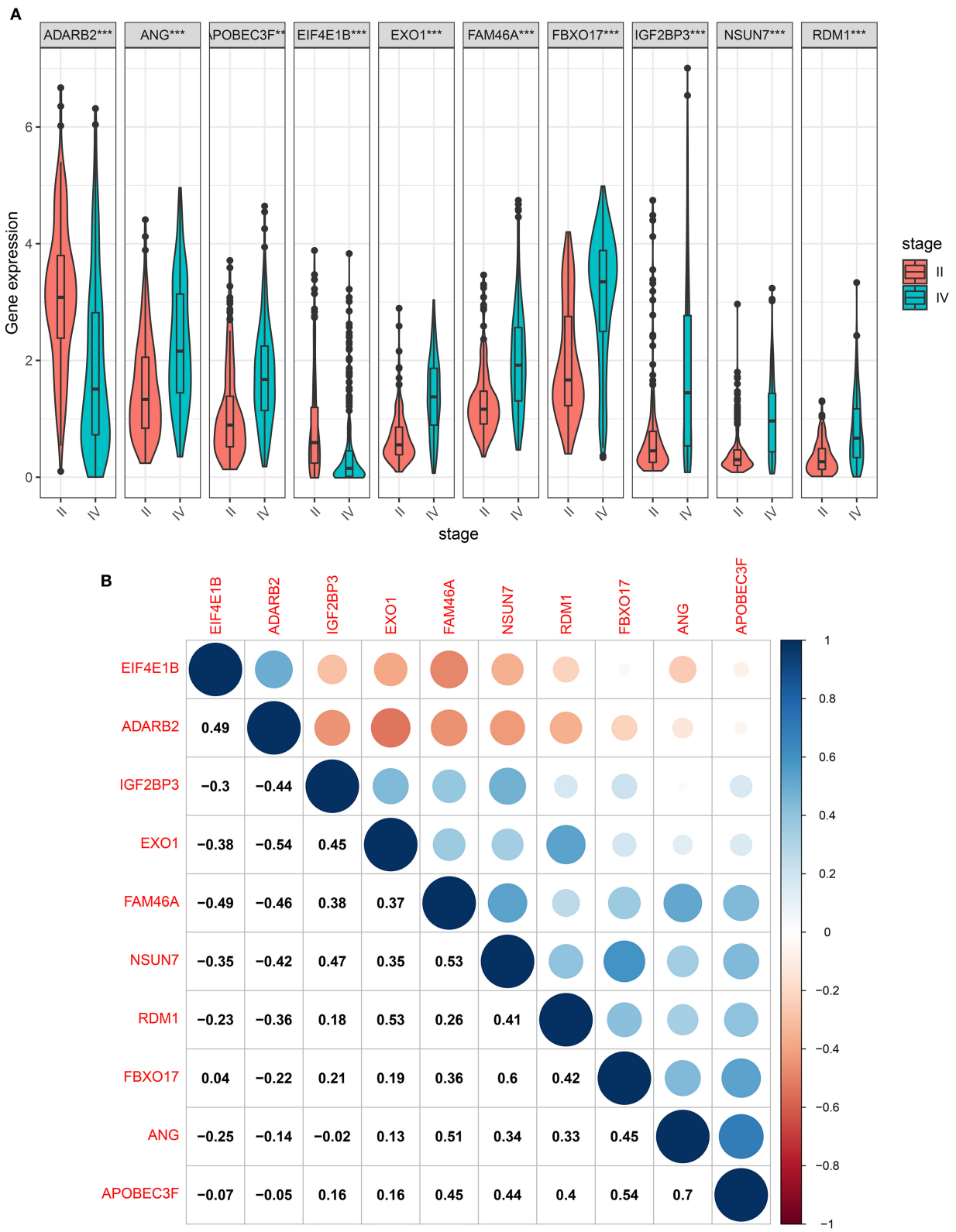

FIGURE 7 | The risk RBP signatures are highly expressed in glioma grade IV than II. **(A)** Box plots showing the expression levels of the ten RBP signatures in glioma grade IV and II samples. ***$p < 0.001$. **(B)** The correlation between the ten RBP signatures at the mRNA levels. Blue: negative correlation; red: positive correlation. The size of the circle is proportional to the correlation coefficient.

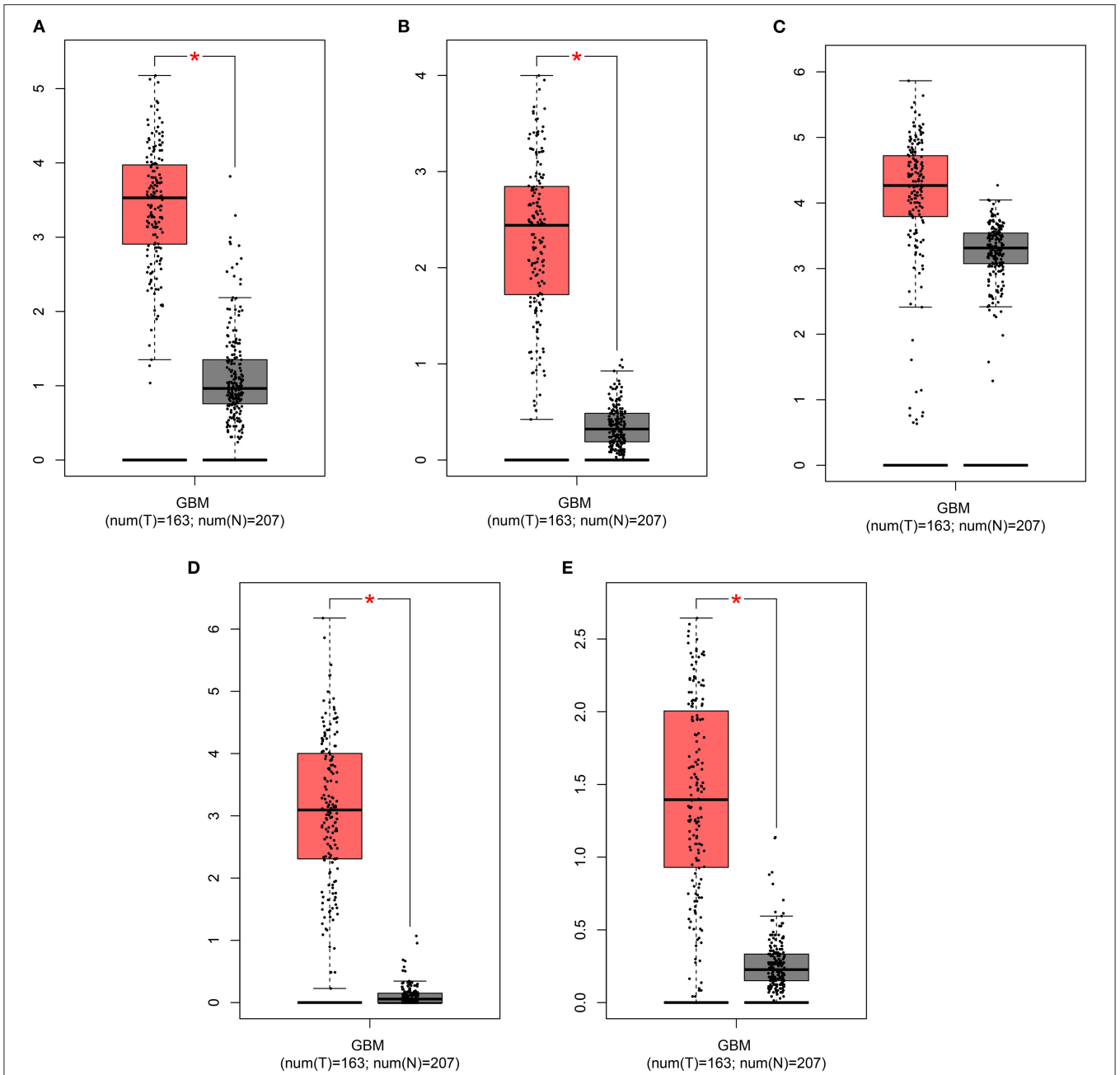

FIGURE 8 | GEPIA displays the highly expressed risk RBP signatures in glioma than controls. Box plots depicting the expression of **(A)** ANG, **(B)** EXO1, **(C)** FBXO17, **(D)** IGF2BP3, and **(E)** NSUN7 in glioma and control samples. *$p < 0.01$.

We further explored why the high-risk scores indicated poor clinical outcomes. ScRNA-seq technology is widely used in basic scientific research and clinical research (25). Single cells have a place in many fields and are of great significance for the early diagnosis, tracking and individualized treatment of cancer (26, 27). The information displayed by traditional sequencing methods is also average information at the multi-cell level, while sequencing at the single-cell level can completely reflect the transcriptome status of different cells in the same cell group (28). Due to the high heterogeneity and complexity of glioma, the survival time of patients in the same pathological stage is completely different. It is of significance to present scRNA-seq analysis for glioma. Herein, we detected the expression of the risk RBP signatures in different glioma cell types. Our data suggested that IGF2BP3, NSUN7, EXO1, and FBXO17 were highly expressed in AC-, MES-, NPC-, and OPC-like

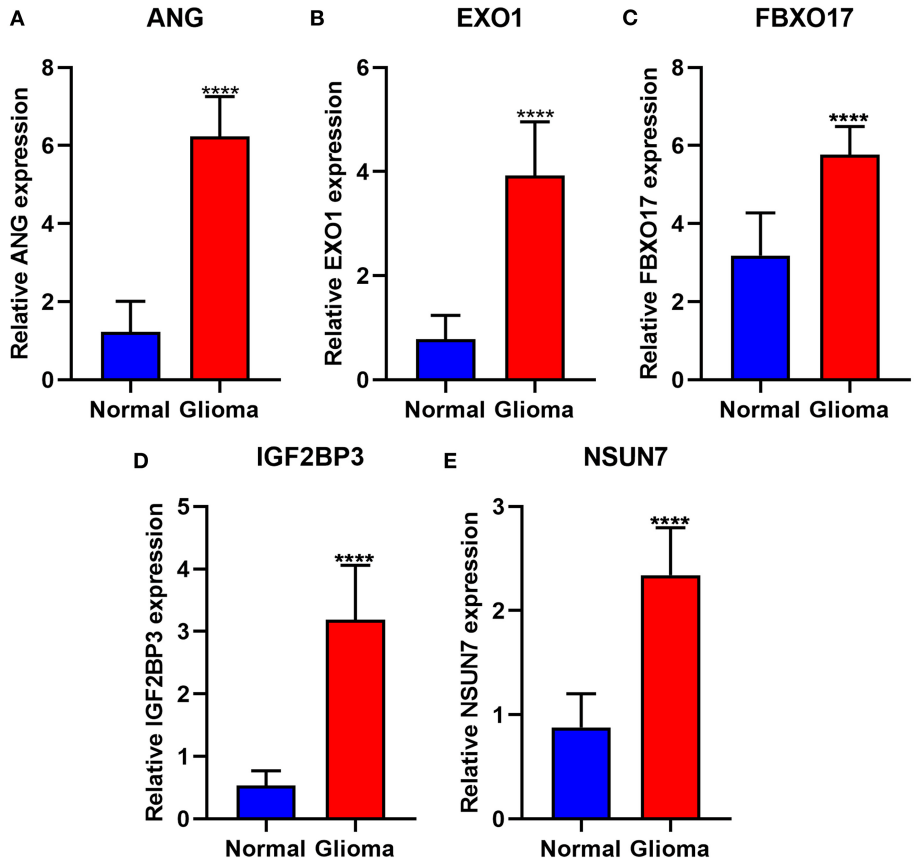

FIGURE 9 | Validation of the highly expressed risk RBP signatures in glioma and normal samples via RT-qPCR. **(A)** ANG, **(B)** EXO1, **(C)** FBXO17, **(D)** IGF2BP3, and **(E)** NSUN7. ****$p < 0.0001$.

malignant cells, which could be related to poor prognosis for glioma patients. Furthermore, the four RBPs exhibited higher expression in WHO grade IV than II, indicating that they were associated with the malignancy of glioma. After validation by RT-qPCR, IGF2BP3, NSUN7, EXO1, and FBXO17 had higher expression levels in glioma than controls. As previous studies, IGF2BP3 facilitated viability and migration for glioma cells (29). NSUN7 is a risk factor for lower-grade glioma patients (30). EXO1 is associated with shorter survival time and hyposensitivity to temozolomide treatment in glioma (31). High FBXO17 expression could independently predict the clinical outcomes for high-grade glioma (32). Combining our results and previous research, these risk RBPs could accelerate the malignant behaviors of glioma.

In this study, a ten-RBP signature was constructed for glioma prognosis. This signature could independently predict the prognosis of patients with high accuracy and sensitivity. Combining RNA-seq and scRNA-seq analysis, we found that the four risk RBPs could contribute to the malignant behaviors of glioma. Their roles should be investigated by basic experiments and larger cohorts.

CONCLUSION

The 10-RBP gene signature exhibited a predictive efficacy for glioma prognosis under multi-data set verification. This signature may possess a promising application for clinical decision-making as well as individualized therapy.

DATA AVAILABILITY STATEMENT

The original contributions presented in the study are included in the article/**Supplementary Material**, further inquiries can be directed to the corresponding author/s.

ETHICS STATEMENT

The studies involving human participants were reviewed and approved by the Ethics Committee of The Second Affiliated Hospital of Nanchang university (2020018). The patients/participants provided their written informed consent to participate in this study.

AUTHOR CONTRIBUTIONS

SS conceived and designed the study. CS and ZC conducted most of the experiments and data analysis, and wrote the manuscript. JL and JZ participated in collecting data and helped to draft the manuscript. All authors contributed to the article and approved the submitted version.

SUPPLEMENTARY MATERIAL

The Supplementary Material for this article can be found online at: https://www.frontiersin.org/articles/10.3389/fmed.2021.637803/full#supplementary-material

Supplementary Table 1 | A list of 40 differentially expressed RBPs between glioma WHO grade II and IV samples.

REFERENCES

1. Malta TM, de Souza CF, Sabedot TS, Silva TC, Mosella MS, Kalkanis SN, et al. Glioma CpG island methylator phenotype (G-CIMP): biological and clinical implications. *Neuro Oncol*. (2018) 20:608–20. doi: 10.1093/neuonc/nox183
2. Wang Z, Gao L, Guo X, Feng C, Lian W, Deng K, et al. Development and validation of a nomogram with an autophagy-related gene signature for predicting survival in patients with glioblastoma. *Aging*. (2019) 11:12246–69. doi: 10.18632/aging.102566
3. Wang Z, Tang W, Yuan J, Qiang B, Han W, Peng X. Integrated analysis of RNA-binding proteins in glioma. *Cancers*. (2020) 12:892. doi: 10.3390/cancers12040892
4. Braunstein S, Raleigh D, Bindra R, Mueller S, Haas-Kogan D. Pediatric high-grade glioma: current molecular landscape and therapeutic approaches. *J Neurooncol*. (2017) 134:541–9. doi: 10.1007/s11060-017-2393-0
5. Bush NA, Chang SM, Berger MS. Current and future strategies for treatment of glioma. *Neurosurg Rev*. (2017) 40:1–14. doi: 10.1007/s10143-016-0709-8
6. Booth TC, Williams M, Luis A, Cardoso J, Ashkan K, Shuaib H. Machine learning and glioma imaging biomarkers. *Clin Radiol*. (2020) 75:20–32. doi: 10.1016/j.crad.2019.07.001
7. Coppin L, Leclerc J, Vincent A, Porchet N, Pigny P. Messenger RNA life-cycle in cancer cells: emerging role of conventional and non-conventional RNA-binding proteins? *Int J Mol Sci*. (2018) 19:650. doi: 10.3390/ijms19030650
8. Gerstberger S, Hafner M, Tuschl T. A census of human RNA-binding proteins. *Nat Rev Genet*. (2014) 15:829–45. doi: 10.1038/nrg3813
9. Mohibi S, Chen X, Zhang J. Cancer the'RBP'eutics-RNA-binding proteins as therapeutic targets for cancer. *Pharmacol Ther*. (2019) 203:107390. doi: 10.1016/j.pharmthera.2019.07.001
10. Cao S, Zheng J, Liu X, Liu Y, Ruan X, Ma J, et al. FXR1 promotes the malignant biological behavior of glioma cells via stabilizing MIR17HG. *J Exp Clin Cancer Res*. (2019) 38:37. doi: 10.1186/s13046-018-0991-0
11. Zhou X, Li X, Yu L, Wang R, Hua D, Shi C, et al. The RNA-binding protein SRSF1 is a key cell cycle regulator via stabilizing NEAT1 in glioma. *Int J Biochem Cell Biol*. (2019) 113:75–86. doi: 10.1016/j.biocel.2019.06.003
12. Han W, Xin Z, Zhao Z, Bao W, Lin X, Yin B, et al. RNA-binding protein PCBP2 modulates glioma growth by regulating FHL3. *J Clin Invest*. (2013) 123:2103–18. doi: 10.1172/JCI61820
13. Song X, Wan X, Huang T, Zeng C, Sastry N, Wu B, et al. SRSF3-regulated RNA alternative splicing promotes glioblastoma tumorigenicity by affecting multiple cellular processes. *Cancer Res*. (2019) 79:5288–301. doi: 10.1158/0008-5472.CAN-19-1504
14. Wang J, Qi J, Hou X. Systematically dissecting the function of RNA-binding proteins during glioma progression. *Front Genet*. (2019) 10:1394. doi: 10.3389/fgene.2019.01394
15. Robinson MD, McCarthy DJ, Smyth GK. edgeR: a Bioconductor package for differential expression analysis of digital gene expression data. *Bioinformatics*. (2010) 26:139–40. doi: 10.1093/bioinformatics/btp616
16. Yu G, Wang LG, Han Y, He QY. clusterProfiler: an R package for comparing biological themes among gene clusters. *Omics*. (2012) 16:284–7. doi: 10.1089/omi.2011.0118
17. Hänzelmann S, Castelo R, Guinney J. GSVA: gene set variation analysis for microarray and RNA-seq data. *BMC Bioinformat*. (2013) 14:7. doi: 10.1186/1471-2105-14-7
18. Hakes AE, Brand AH. Tailless/TLX reverts intermediate neural progenitors to stem cells driving tumourigenesis via repression of asense/ASCL1. *Elife*. (2020) 9:e53377. doi: 10.7554/eLife.53377.sa2
19. Butler A, Hoffman P, Smibert P, Papalexi E, Satija R. Integrating single-cell transcriptomic data across different conditions, technologies, and species. *Nat Biotechnol*. (2018) 36:411–20. doi: 10.1038/nbt.4096
20. Velasco MX, Kosti A, Guardia GDA, Santos MC, Tegge A, Qiao M, et al. Antagonism between the RNA-binding protein Musashi1 and miR-137 and its potential impact on neurogenesis and glioblastoma development. *RNA*. (2019) 25:768–82. doi: 10.1261/rna.069211.118
21. Li W, Li X, Gao LN, You CG. Integrated analysis of the functions and prognostic values of RNA binding proteins in lung squamous cell carcinoma. *Front Genet*. (2020) 11:185. doi: 10.3389/fgene.2020.00185
22. Wu Y, Liu Y, He A, Guan B, He S, Zhang C, et al. Identification of the six-RNA-binding protein signature for prognosis prediction in bladder cancer. *Front Genet*. (2020) 11:992. doi: 10.3389/fgene.2020.00992
23. Zhang S, Wang W, Liu G, Xie S, Li Q, Li Y, et al. Long non-coding RNA HOTTIP promotes hypoxia-induced epithelial-mesenchymal transition of malignant glioma by regulating the miR-101/ZEB1 axis. *Biomed Pharmacother*. (2017) 95:711–20. doi: 10.1016/j.biopha.2017.08.133
24. He Q, Zhao L, Liu X, Zheng J, Liu Y, Liu L, et al. MOV10 binding circ-DICER1 regulates the angiogenesis of glioma via miR-103a-3p/miR-382-5p mediated ZIC4 expression change. *J Exp Clin Cancer Res*. (2019) 38:9. doi: 10.1186/s13046-018-0990-1
25. Ziegenhain C, Vieth B, Parekh S, Reinius B, Guillaumet-Adkins A, Smets M, et al. Comparative analysis of single-cell RNA sequencing methods. *Mol Cell*. (2017) 65:631–43.e634. doi: 10.1016/j.molcel.2017.01.023
26. Peng J, Sun BF, Chen CY, Zhou JY, Chen YS, Chen H, et al. Single-cell RNA-seq highlights intra-tumoral heterogeneity and malignant progression in pancreatic ductal adenocarcinoma. *Cell Res*. (2019) 29:725–38. doi: 10.1038/s41422-019-0195-y
27. Maynard A, McCoach CE, Rotow JK, Harris L, Haderk F, Kerr DL, et al. Therapy-induced evolution of human lung cancer revealed by single-cell RNA sequencing. *Cell*. (2020) 182:1232–51.e1222. doi: 10.1016/j.cell.2020.07.017
28. Huang X, Liu S, Wu L, Jiang M, Hou Y. High throughput single cell RNA sequencing, bioinformatics analysis and applications. *Adv Exp Med Biol*. (2018) 1068:33–43. doi: 10.1007/978-981-13-0502-3_4
29. Jin P, Huang Y, Zhu P, Zou Y, Shao T, Wang O. CircRNA circHIPK3 serves as a prognostic marker to promote glioma progression by regulating miR-654/IGF2BP3 signaling. *Biochem Biophys Res Commun*. (2018) 503:1570–4. doi: 10.1016/j.bbrc.2018.07.081
30. Sato K, Tahata K, Akimoto K. Five genes associated with survival in patients with lower-grade gliomas were identified by information-theoretical analysis. *Anticancer Res*. (2020) 40:2777–85. doi: 10.21873/anticanres.14250
31. Wang Q, He Z, Chen Y. Comprehensive analysis reveals a 4-gene signature in predicting response to temozolomide in low-grade glioma patients. *Cancer Control*. (2019) 26:1073274819855118. doi: 10.1177/1073274819855118
32. Du D, Yuan J, Ma W, Ning J, Weinstein JN, Yuan X, et al. Clinical significance of FBXO17 gene expression in high-grade glioma. *BMC Cancer*. (2018) 18:773. doi: 10.1186/s12885-018-4680-3

Conflict of Interest: The authors declare that the research was conducted in the absence of any commercial or financial relationships that could be construed as a potential conflict of interest.

Copyright © 2021 Sheng, Chen, Lei, Zhu and Song. This is an open-access article distributed under the terms of the Creative Commons Attribution License (CC BY). The use, distribution or reproduction in other forums is permitted, provided the original author(s) and the copyright owner(s) are credited and that the original publication in this journal is cited, in accordance with accepted academic practice. No use, distribution or reproduction is permitted which does not comply with these terms.

frontiers in Medicine

SYSTEMATIC REVIEW
published: 17 February 2021
doi: 10.3389/fmed.2021.635035

Visualization and Analysis in the Field of Pan-Cancer Studies and Its Application in Breast Cancer Treatment

Xianwen Zhang[1†], Han Lai[2†], Fan Zhang[3†], Yixi Wang[4], Li Zhang[1], Ni Yang[1], Chunrong Wang[1], Zheng Liang[1], Jieping Zeng[5*] and Jinrong Yang[1*]*

[1] School of Basic Medical Sciences, Chengdu University of Traditional Chinese Medicine, Chengdu, China, [2] School of Foreign Languages, Chengdu University of Traditional Chinese Medicine, Chengdu, China, [3] Department of General Surgery, The 5th Affiliated Hospital, Guangzhou Medical University, Guangzhou, China, [4] Guangdong Provincial Key Laboratory of Stomatology, Guanghua School of Stomatology, Hospital of Stomatology, Sun Yat-sen University, Guangzhou, China, [5] Department of Ophthalmology, Affiliated Hospital of Chengdu University of Traditional Chinese Medicine (Sichuan Provincial Hospital of Traditional Chinese Medicine), Chengdu, China

OPEN ACCESS

Edited by:
Guo Chen,
Jinan University, China

Reviewed by:
Xue Gao,
University of Chicago, United States
Ting Wang,
Huazhong University of Science and Technology, China

***Correspondence:**
Zheng Liang
proteinliang@163.com
Jieping Zeng
zengjieping2000@126.com
Jinrong Yang
yangjinrong@cdutcm.edu.cn

[†] These authors have contributed equally to this work

Specialty section:
This article was submitted to Precision Medicine, a section of the journal Frontiers in Medicine

Received: 29 November 2020
Accepted: 26 January 2021
Published: 17 February 2021

Citation:
Zhang X, Lai H, Zhang F, Wang Y, Zhang L, Yang N, Wang C, Liang Z, Zeng J and Yang J (2021) Visualization and Analysis in the Field of Pan-Cancer Studies and Its Application in Breast Cancer Treatment. Front. Med. 8:635035. doi: 10.3389/fmed.2021.635035

Although all cancers are molecularly distinct, many share common driver mutations. Pan-cancer analysis, utilizes next-generation sequencing (NGS), pan-cancer model systems, and pan-cancer projects such as The Cancer Genome Atlas (TCGA), to assess frequently mutated genes and other genomic abnormalities that are common among many cancer types, regardless of the tumor origin, providing new directions for tumor biology research. However, there is currently no study that has objectively analyzed the results of pan-cancer studies on cancer biology. For this study, 999 articles on pan-cancer published from 2006 to 2020 were obtained from the Scopus database, and bibliometric methods were used to analyze citations, international cooperation, co-authorship and keyword co-occurrence clusters. Furthermore, we also focused on and summarized the application of pan-cancer in breast cancer. Our result shows that the pan-cancer studies were first published in 2006 and entered a period of rapid development after 2013. So far, 86 countries have carried out international cooperation in sharing research. Researchers form the United States and Canada have published the most articles and have made the most extensive contribution to this field, respectively. Through author keyword analysis of the 999 articles, TCGA, biomarkers, NGS, immunotherapy, DNA methylation, prognosis, and several other keywords appear frequently, and these terms are hot spots in pan-cancer studies. There are four subtypes of breast cancer (luminalA, luminalB, HER2, and basal-like) according to pan-cancer analysis of breast cancer. Meanwhile, it was found that breast cancer has genetic similarity to pan-gynecological cancers, such as ovarian cancer, which indicates related etiology and possibly similar treatments. Collectively, with the emergence of new detection methods, new cancer databases, and the involvement of more researchers, pan-cancer analyses will play a greater role in cancer biology research.

Keywords: pan-cancer, TCGA, bibliometrics, Scopus, VOSviewer

INTRODUCTION

The projected incidence of cancer was estimated to be more than 4,000,000 in China in 2020, with much larger numbers worldwide. Despite impressive progress made recently in cancer research (1, 2), there is an unmet need for effective treatments. Therefore, a more comprehensive understanding of the molecular characteristics and gene mutations of tumors is imperative (3). Generally, cancer is classified (4) according to the tissue where it occurs, such as in breast cancer, gastric cancer, or liver cancer. Most studies on the molecular, pathological, and clinical characteristics of tumors are based on the classification of tumor type. With reference to the guidelines followed by the oncology department of most cancer centers, principles of medicine or surgery for tumors are based on the origin (tissues and organ) (5). This framework has been established for a long time, but molecular analysis suggests that it could be problematic (6, 7): the tumors from different organs may have many common characteristics, whereas tumors from the same organ may have many differences. To investigate cancer study by molecular characteristics, medical researchers launched the Pan-Cancer Initiative (8) at a conference in Santa Cruz, California in 2012.

Pan-cancer analysis utilizes next-generation sequencing (NGS), pan-cancer model systems, and pan-cancer projects, such as The Cancer Genome Atlas (TCGA), to assess frequently mutated genes and other genomic abnormalities common that are common among many cancer types, regardless of the tumor origin (9). Currently, data for pan-cancer studies are obtained primarily from TCGA (10–12), which stores the sequences of all genes that encode proteins from more than 30 cancers that are represented by up to 500 tumors each. The results of pan-cancer analysis show that some cancers originating from different organs have molecular similarities, whereas some cancers originating from the same tissue may have very different genomic profiles (13, 14). Thus, researchers have begun classifying tumors into subtypes on the basis of pan-cancer data (15–17). For example, different subtypes of breast ductal carcinoma (luminalA, luminalB, HER2, and basal-like) can be identified by different biomarkers that manifest as different clinical characteristics (18), which should influence the treatment regimen patients should follow. Although increasing research on pan-cancer is gaining influence, there is no systematic analysis of its current hot spots, future trends, shortcomings, or impact on tumor biology.

With the aim of exploring the characteristics and advantages of pan-cancer research as well as promoting and guiding the involvement of researchers in pan-cancer research, this study evaluated the field of pan-cancer using visualization and bibliometrics analyzes. Bibliometric methods were used on 999 studies on pan-cancer published from 2006 to 2020, which were obtained from the Scopus database, to analyze the citations, international cooperation, co-authorship, and keyword co-occurrence clusters. Using breast cancer as an example, we explore how pan-cancer analysis can be used to identify new biomarkers and develop treatment options on the basis of the molecular subtypes. Collectively, this study provides interesting data to promote cancer biology research through exploring advancements in pan-cancer studies.

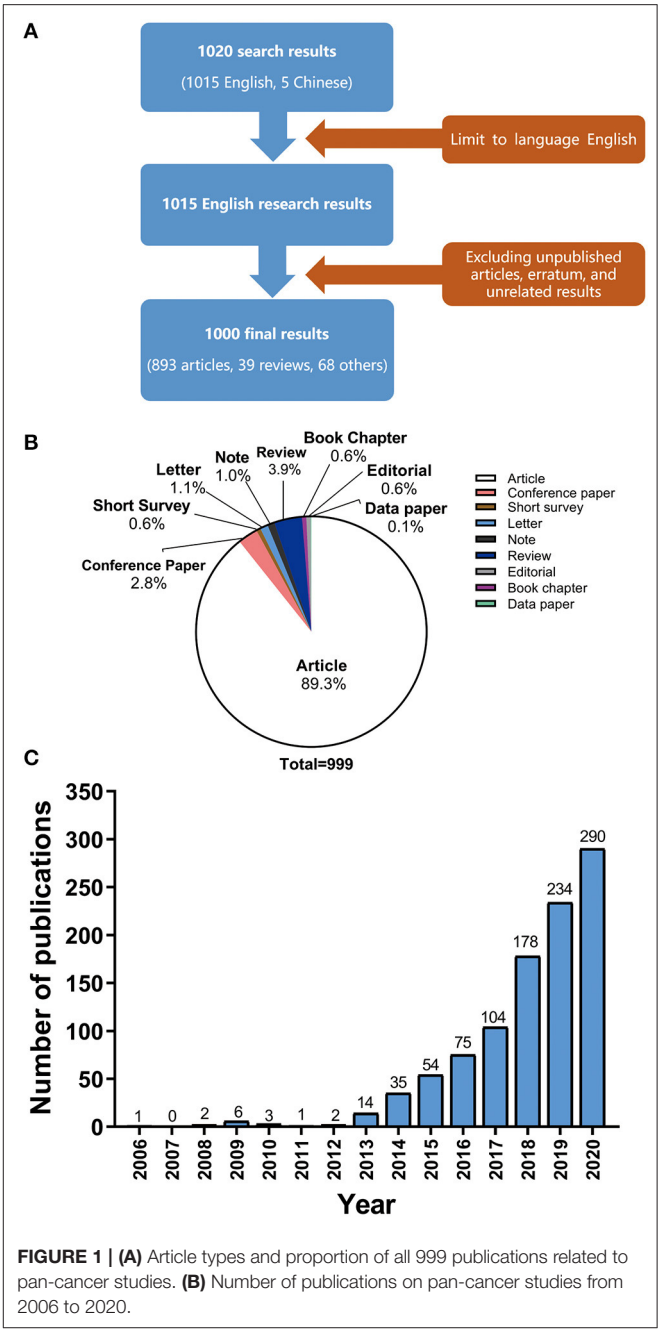

FIGURE 1 | (A) Article types and proportion of all 999 publications related to pan-cancer studies. **(B)** Number of publications on pan-cancer studies from 2006 to 2020.

METHODS

Source Database

This study used Scopus (https://www.scopus.com/), which is one of the most comprehensive databases for bibliometric analysis. Scopus is the world's largest database of abstracts and citations of peer-reviewed literature (scientific journals, books, and conference proceedings). The database includes different

TABLE 1 | The top 10 journals in the number of pan-cancer publications.

Rank	Journal	NA	NC	CA	IF	Publisher
1	Nature Communications	51	1,445	28.3	12.121	Nature Research
2	Scientific Reports	41	677	16.5	3.998	Nature Publishing Group
3	Oncotarget	30	471	15.7	0	Impact Journals LLC
4	Cancers	21	36	1.7	6.126	MDPI AG
5	Nucleic acids research	20	599	29.9	11.501	Oxford University Press
6	Nature Genetics	19	4,310	226.8	27.603	Nature Publishing Group
7	Bioinformatics	19	273	15.2	5.610	BioMed Central Ltd.
8	BMC Genomics	18	207	12.2	3.594	BioMed Central Ltd.
9	PLoS ONE	17	874	58.3	2.740	Public Library of Science
10	Cell Reports	15	109	7.8	8.109	Elsevier

Rank, rank by NA; NA, number of articles; NC, number of citations; CA, Citations per article; IF, 2019 impact factor.

types of literature and relevant information that are critical to our study.

Search Design

The title, abstract, and keywords related to pan-cancer of various types of studies were searched. Scopus was used as the only database. We designed the search query string as: (TITLE-ABS-KEY ("pan-cancer") and limited the language to English. The search was conducted on October 20, 2020, so any updates to the database since then may reflect differences in the data reported herein. The search query returned 1,015 studies. Statistical analyzes of the country of publication, number of annual publications, type of publication, and t total citations were performed.

Data Collection and Filtration

All queries using the above string and output were searched on Scopus with as much relevant information as possible included in CSV file. As shown in **Figure 1A**, unpublished articles, erratum, and unrelated results were excluded first. Then the two authors manually screened each title, abstract, and set of keywords to determine if any were significantly correlated with pan-cancer. For uncertain articles, we read the full text to determine whether to include them. Overall, 999 results (**Figure 1A**) were retained after independent screening, effective comparison, and discussion by two authors.

Data Analysis

GraphPad Prism 8.0.2 software was used to conduct statistical analysis on the article type, number of articles and citations, and to draw pie charts and histograms from the results. VOSviewer, which is a scientific knowledge mapping software tool, uses "network data" (mainly literature knowledge units) for relationship building and visual analysis to perform scientific knowledge mapping and to show the structure, evolution, cooperation and other relationships (19). Co-authorship, co-citation, and keyword co-occurrence analyses were performed via VOSviewer1.6.13 after the CVS file containing the 999 publications was imported. In our study, various analytical results were presented in the form of network visualization maps through co-occurrence analysis of the national cooperation, author co-authorship, co-citation and author keywords.

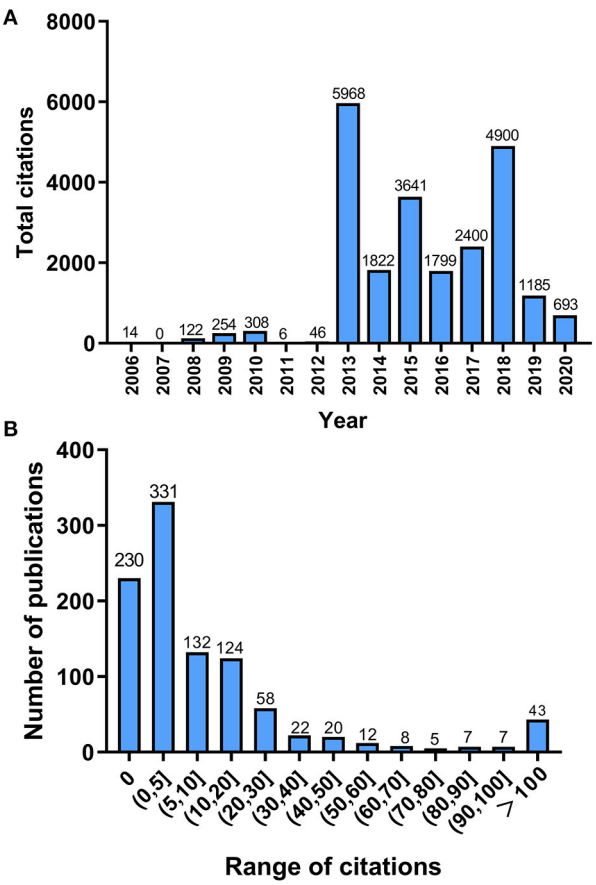

FIGURE 2 | (A) Total annual citations of all 999 pan-cancer studies from 2006 to 2020. **(B)** Citation distributions of the 999 publications included. The range of citations (from 10 to 100) is divided into equally wide intervals, except those articles that received more than 100 citations and <10 citations.

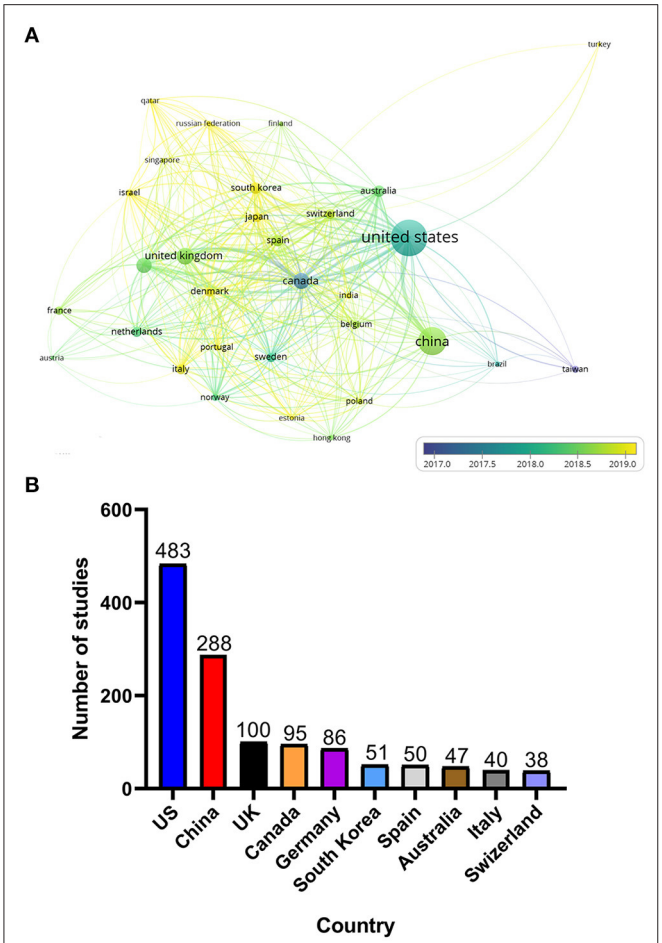

FIGURE 3 | (A) Country co-authorship overlay visualization map. The size of each circle indicates the number of articles of that country. The distance between any two circles indicates the relatedness of their co-authorship link, and the thickness of the connecting line indicates the strength of the link. The color of each circle indicates the average years of publication of the articles from each country, according to the color gradient in the lower right corner. **(B)** Top 10 countries in terms of number of publications on pan-cancer studies.

Research Ethics

All data in the study were collected from the Internet, and a bibliometric analysis was conducted. No animal or human subjects were involved in the study; thus, the approval of the ethics committee and the consent procedure were not required.

RESULTS

Analysis of the Types of Study and Citations

Of these 999 different studies (**Figure 1B**), articles made up the largest portion, accounting for 89.3% (893 studies). Reviews accounted for 3.9% (39 studies), second only to articles. Other types of documents made up the remaining 6.8%, including the short surveys (0.6%, 6 studies), letters (1.1%, 11 studies), conference papers (2.8%, 28 studies), editorials (0.6%, 6 studies), notes (1%, 10 studies), book chapters (0.6%, 6 studies), and data paper (0.1%, 1 studies). It is worth noting that the publications of pan-cancer studies are mainly research articles. The data paper, which is a new type of document, is a peer-reviewed document that describes a dataset.

The annual number of published articles of pan-cancer studies is shown in **Figure 1C**. Since 2013, the number of publications on pan-cancer research has been increasing each year. **Table 1** shows the top 10 journals with the highest number of pan-cancer publications. Some journals have high impact factors, such as Nature Communications (51 articles), Nucleic Acids Research (20 articles), and Nature Genetics (19 articles). A substantial number of articles were categorized as having high impact factors, which indicates that research on pan-cancer is a popular topic at present.

However, the total number of citations decreased significantly each year compared to the number of publications in previous years (**Figure 2A**). We theorized that the total number of papers published increased, whereas in the total number of citations decreased, because older research has been accumulating citations since it was published, whereas newer research has had less time to accumulate citations. The range of citations from 10 to 100 could be divided into equal intervals, except for those articles that received more than 100 citations and <10 citations. The number of studies in each interval is counted (**Figure 2B**). There were 331 articles cited in the range of (0, 5), which is relatively the largest number; and despite the number of highly cited articles being small, research in this field is growing rapidly.

Analysis of Country and International Cooperation

The 999 studies included spanned 86 countries. However, when setting the minimum number of publications and citations per country to five, only 34 countries met the threshold. **Figure 3A** shows the different degrees of cooperation of 34 countries and the average publication date of each country's studies. **Figure 3B** shows the number of articles published by the top 10 countries for pan-cancer studies. Some research publications were carried out by researchers from two or more countries, so we counted the number of publications from those countries separately. The United States contributed more publications than did any other country, accounting for almost half of all pan-cancer publications. Canada was one of the first countries to begin pan-cancer research and has established collaboration with researchers from many other countries. In addition, researchers from China, Britain, Germany and South Korea have become increasingly active in recent years, which has revitalized the development of pan-cancer research.

Co-Authorship Analysis and Author Co-Citation Analysis

According to VOSviewer analysis, a total of 5,558 authors were involved in the articles analyzed here, but only 95 authors met the minimum publication and citation thresholds when set to four. During the analysis, we found many similar or identical abbreviations of names, for which we manually

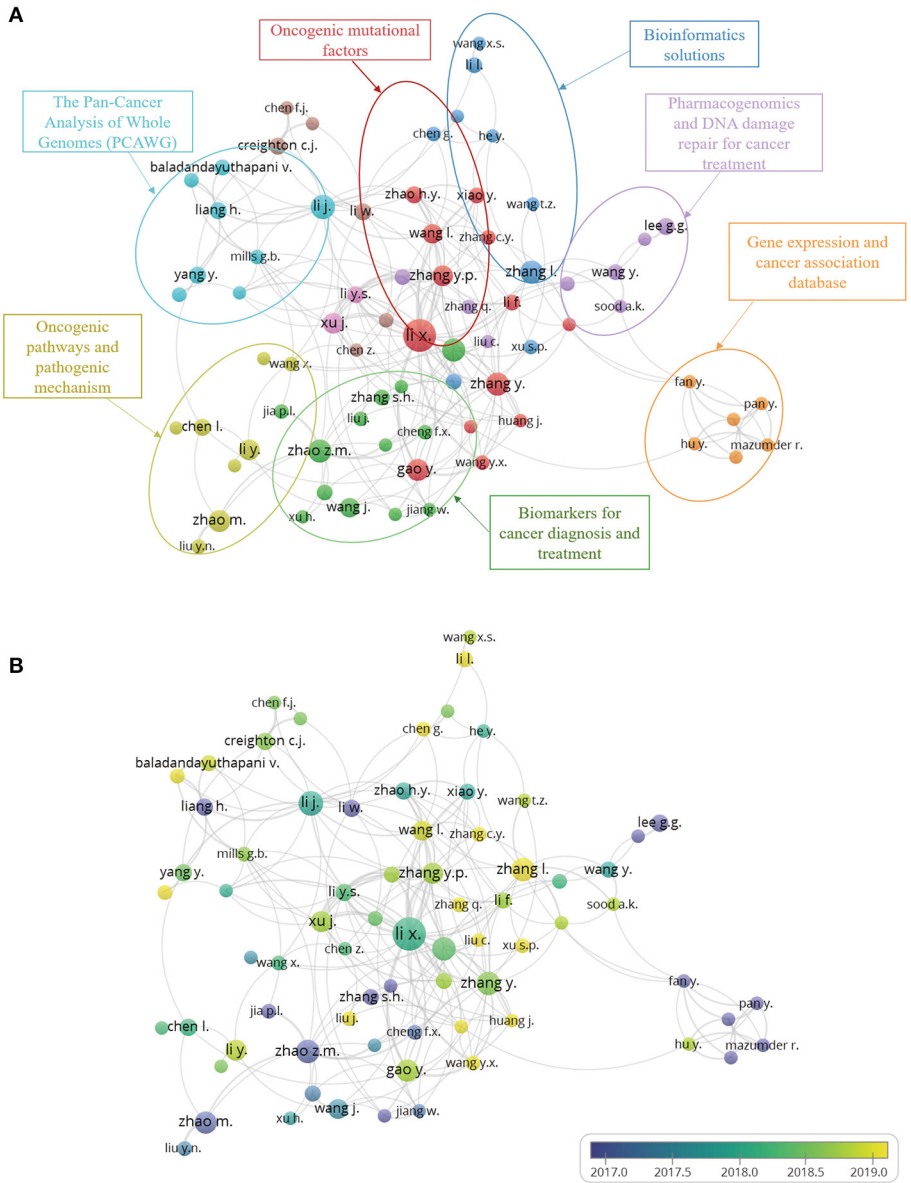

FIGURE 4 | (A) Author co-authorship network visualization map. The same color represents a close relationship between the authors of clusters. The main research categories of each cluster were marked. **(B)** Author co-authorship overlay visualization map. The colors of different authors are based on the average year they published their articles.

supplemented most of the names by referring to the original text. The number of publications and collaborations among authors can be seen from the overlay visualization map of the author co-authorship analysis (**Figure 4A**). The same color represents a closely related cluster of authors; the size of the circle represents the number of publications; and the thickness of the line represents the closeness of cooperation between the authors. Meanwhile, by analyzing the articles in each cluster, we manually and subjectively identified and labeled the main areas of research for each cluster. The orientations of pan-cancer studies include the following: (1) mechanism of tumor by oncogenic mutational factors; (2) oncogenic pathways and pathogenic mechanism; (3) different cancer biomarkers for cancer diagnosis and treatment; (4) pan-cancer analysis of whole genomes (PCAWG) and bioinformatics solutions; (5) Pharmacogenomics and DNA damage repair for cancer treatment; and (6) gene expression and cancer association database. **Figure 4B** depicts the co-authorship overlay visualization map, in which the colors of different authors are based on the average year of their publications. Mazumder R, Zhao ZM, Lee GG, et al. are represented by purple, which indicates indicating that they began their research in this field at an earlier date. Newer

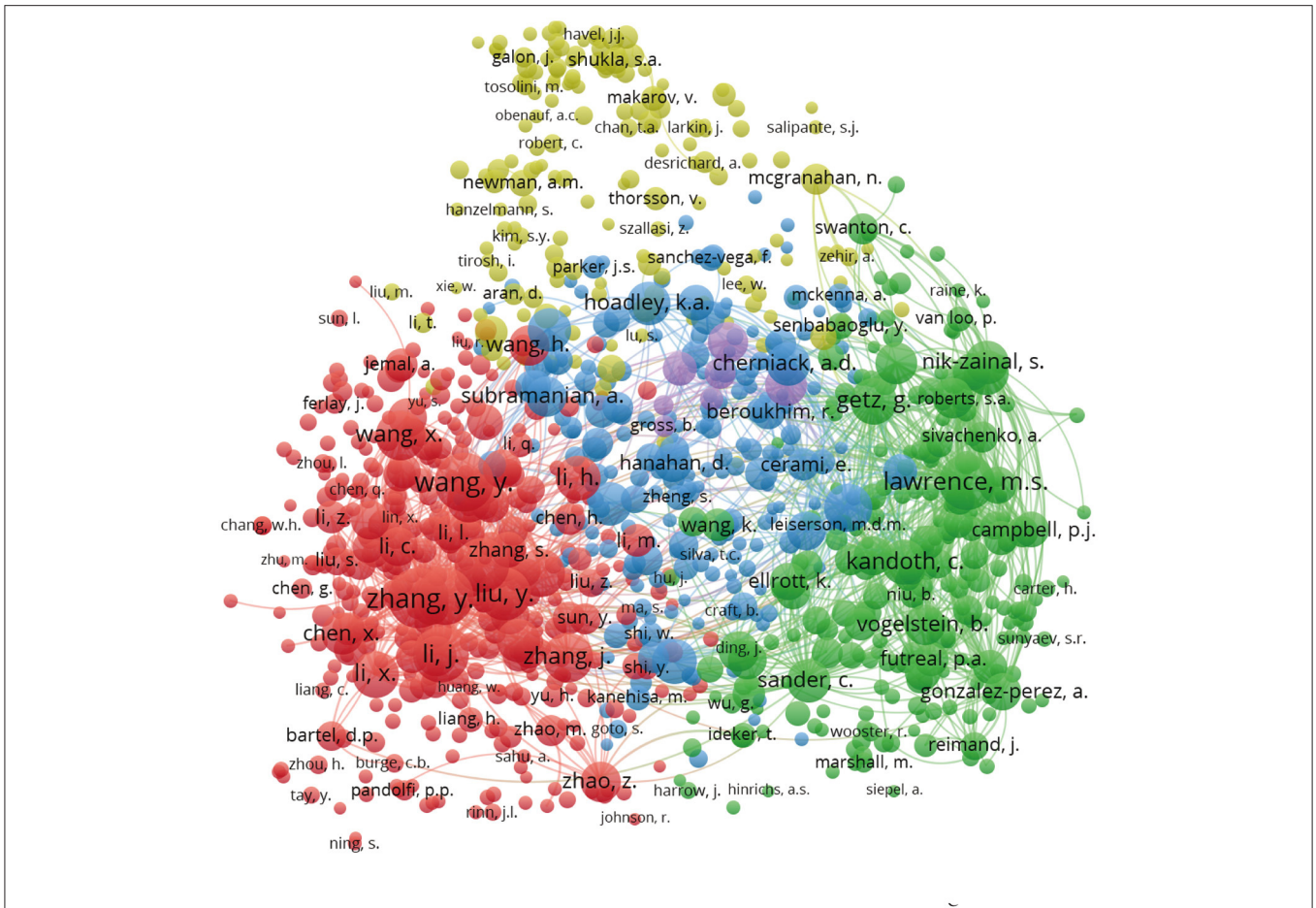

FIGURE 5 | Author co-citation network visualization map. The area of circles indicated the total citations of each author. Different colors of the circles represented clusters divided by co-citations. Authors in the same color are based on the close relationship connected groups.

researchers, like Zhang L., Huang J., and others, are shown in yellow.

For author co-citation analysis (20, 21), when the articles of two authors were cited by a third author in the same publication, the two authors were said to have a co-citation relationship. The higher the co-citation frequency between two authors, the closer their academic relationship. In the author co-citation analysis, the threshold was set at a minimum of 20 citations, and 988 of the 5,558 authors met the threshold. The size of each circle represents the number of times the author has been cited, so a larger circle indicates a higher number of citations. As shown in **Figure 5**, the author co-citation analysis network visualization map is divided into five colors (red, green, yellow, purple, and blue). Authors that have published on the same topic are represented by the same color, and authors with the same color are based on the connected groups. The figure visually demonstrates the impact of authors who have conducted pan-cancer research, thus, this map reveals the leading researchers in this field. **Table 2** shows the top 10 articles that have been cited in pan-cancer studies. Most of the highly cited articles in the table are research articles with high impact factors.

Analysis of Keyword Co-Occurrence Clusters

An analysis of the keyword co-occurrence clusters (20) reveals the internal composition and structure of the academic field through a co-occurrence relationship based on keywords. The results can also be used to reveal the development trends of specialized disciplines. When the minimum number of occurrences of a keyword was set to 566 of the total 1,787 keywords met the threshold. The overlay visualization drawn in proportion to events (**Figure 6**) shows what content of pan-cancer studies is most popular. Meanwhile, author keywords are marked in different colors according to the average year of their publishing activities. Bibliometric analysis of the keywords can provide a simple description of the research hot spots. Owing to the non-unity of single and plural keywords and the synonyms in some publications, we altered some of the author keywords in CSV file, such as unifying "pan cancer" and "pan-cancer analysis" as "pan-cancer," and unifying "the cancer genome atlas" as "TCGA," so that these terms would be represented accurately in the data analysis. Keywords such as "targeted therapy," "cancer genomics" and "epigenetics" appeared more frequently in the early stage. However, in recent years, terms such

TABLE 2 | The top 10 articles cited in pan-cancer studies.

Rank	Journal	Article title	Authors	CA	IF	Article type	Publication year
1	Nature Genetics	The cancer genome atlas pan-cancer analysis project	Weinstein JN, Collisson EA, Mills GB, et al.	2,359	27.603	Research article	2013
2	Nature	Mutational landscape and significance across 12 major cancer types	Kandoth C, McLellan MD, Vandin F, et al.	2,087	42.778	Research article	2013
3	Nature Genetics	Pan-cancer patterns of somatic copy number alteration	Zack TI, Schumacher SE, Carter SL, et al.	855	27.603	Research article	2013
4	Nature Medicine	The prognostic landscape of genes and infiltrating immune cells across human cancers	Gentles AJ, Newman AM, Liu CL, et al.	790	36.130	Research article	2015
5	Cell	Oncogenic signaling pathways in the cancer genome atlas	Sanchez-Vega F, Mina M, Armenia J, et al.	402	38.637	Research article	2018
6	Nature Genetics	Pan-cancer network analysis identifies combinations of rare somatic mutations across pathways and protein complexes	Leiserson MDM, Vandin F, Wu H-T, et al.	369	27.603	Research article	2015
7	Cell Reports	Pan-cancer immunogenomic analyses reveal genotype-immunophenotype relationships and predictors of response to checkpoint blockade	Charoentong P, Finotello F, Angelova M, et al.	344	8.109	Research article	2017
8	Wspolczesna Onkologia	The Cancer Genome Atlas (TCGA): an immeasurable source of knowledge	Tomczak K, Czerwińska P, Wiznerowicz M.	322	0.215	Review	2015
9	Cell	An integrated TCGA pan-cancer clinical data resource to drive high-quality survival outcome analytics	Liu Jianfang, Lichtenberg T, Hoadley KA, et al.	313	38.637	Research article	2018
10	Cell	Cell-of-origin patterns dominate the molecular classification of 10,000 tumors from 33 types of cancer	Hoadley KA, Yau C, Hinoue T, et al.	304	38.637	Research article	2018

Rank, rank by CA; CA, Citations per article; IF, 2019 impact factor.

as "prognosis," "immunotherapy," "methylation," "glioma" were more frequently used, which indicates that the research focus in the field has shifted from observing the molecular characteristics of major tumors to identifying molecular signatures for patient treatment and prognosis. Keywords, such as TCGA, biomarker, NGS, immunotherapy, DNA methylation, and prognosis, appear frequently in all author keywords, so these terms are presumed to be the hot spots of pan-cancer research.

DISCUSSION

Cancer has been recognized as a genetic disease, and the goal of the Pan-Cancer Initiative is to identify and analyze the genetic changes that contribute to the commonality and differences among the genotypes and phenotypes that determine tumor lineage (8, 21). By conducting extensive pan-cancer research, researchers can explore the potential genomes of cancer mutations, including germline mutation (genetics) and somatic mutation (acquisition), to identify biomarkers that aid in cancer diagnosis (22). Furthermore, as common molecular signatures and action signal pathways, are discovered, in the etiology and optimal therapeutics of that work for one tumor can be applied to another, tumor on the basis of its molecular subtype, which will help lead to various innovative cancer treatment methods. Tumors with low incidence, such as pediatric malignancies, benefit substantially (23).

Since the Pan-Cancer Initiative was launched in 2012, pan-cancer studies have entered a period of rapid development (**Figure 1C**). A growing number of researchers from various countries have initiated pan-cancer research. The fact that 2,400 authors have published more than one publication and that the predominance of articles are recent research (**Figure 1B**) indicates that pan-cancer research is gaining popularity among researchers. It is estimated that there will be more than 300 articles published on pan-cancer studies in 2020. Molecular analysis techniques of tumors, such as NGS, RNA-seq and DNA methylation arrays, have gradually matured and become affordable (24–26), which has supported further development of pan-cancer research. As shown in **Figure 3**, the United States, Canada and other developed countries with advanced technology and closer cooperation have carried out research over longer time periods, so they are leaders in this field. The number of pan-cancer research publications in China ranks second worldwide. Because of China's large population, high number of cancer cases, and high mortality rate, the Chinese have invested in research that could lead to the detection, diagnosis, and treatment of cancers. Meanwhile, the rapid growth of China's GDP has also provided support for China's pan-cancer studies. According to the keyword co-occurrence classification and timeline in **Figure 4**, we found that the previous study mainly used the TCGA database to distinguish similarities and differences between tumors of different types of tissue, whereas the current research direction is to explore mutated tumor biomarkers through tumor gene and cell molecular detection comparisons. The molecular characterization of many different tumors may help to identify biomarkers and corresponding

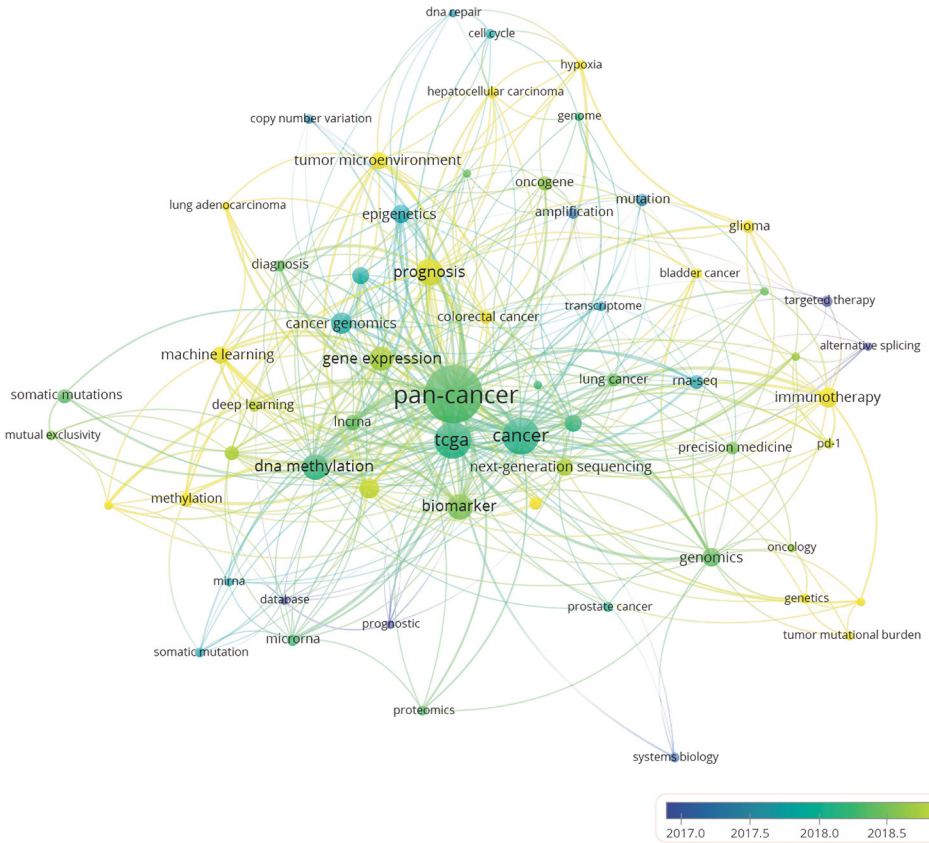

FIGURE 6 | Author keyword overlay visualization map. The size of each circle indicates the frequency of occurrences of the author keyword. According to the color label in the lower right corner, the color of each circle indicates the average year when the keyword appeared in articles. The distance between any two circles is indicative of their co-occurrence link, and the thickness of the connecting line indicates the strength of the link.

immunotherapies that can be used to treat different cancers of the same molecular characterization in patients with other types of cancer. In the future, when the pan-cancer analysis data of most tumor have expanded, we predict that the focus of research on cancer will shift to specific molecular subtypes and previously unstudied tissues with the aim of developing tumor treatments, prognosis, prevention, and detection markers. By using NGS and TCGA, pan-cancer studies have made significant contributions to our understanding of DNA and RNA variants across many cancer types (27). However, most current pan-cancer studies are based on the 33 tumors that are registered in the TCGA database. Therefore, it is necessary to include new tumor types, integrate data from similar databases, and attract more researchers to conduct pan-cancer studies.

There are numerous pan-cancer studies on various tumors, especially breast tumors. Breast cancer is currently one of the most common cancers (28). The classification of breast cancer subtypes is based on molecular characteristics, genomic characteristics, clinical data, and histomorphology (29). A study published in Nature (18) analyzed 510 tumors from 507 patients by using genomic DNA copy number array, DNA methylation, exome sequencing, mRNAseq, microRNAseq, and antiphasing protein array and revealed four subtypes of breast cancer (luminalA, luminalB, HER2, and basal-like). At present, there are over-treatment and under-treatment for different subtypes of breast cancer, and primary routine surgery is no longer the best choice for all patients (30–32). On the basis of a standardized uPA/PAI-1 biomarker ELISA, almost half of node-negative breast cancer patients (negative) could be spared chemotherapy (33). According to different clinical tumor subtypes, treatment methods include endocrine therapy, anti-HER2 targeting and chemotherapy (34). Through a comprehensive analysis of all 33 TCGA tumor types, it was found that invasive breast cancer (BRCA) and highly malignant serous ovarian cystadenocarcinoma (OV), endometrial carcinoma (UCEC), cervical squamous cell carcinoma, cervical adenocarcinoma (CESC), and uterine carcinosarcoma (UCS) are similar at the molecular level (35). Except for OV, pan-gynecologic tumor types have similar miRNA profiles (36), which indicates that pan-gynecologic tumors have relative specificity (37). This also suggests that the diagnosis and treatment strategies for BRCA may be applied to other gynecologic cancers with high cure rates. Furthermore, the development of pan-cancer studies on breast

cancer will also may lead to the diagnosis and treatment of rare gynecological cancers.

Collectively, through bibliometric analysis and visualization of 999 publications, our study analyzed the research hot spots, advantages, and disadvantages in the field of pan-cancer research, with the aim of providing references for future researchers who intend to conduct pan-cancer studies. Our results reveal that pan-cancer analysis and gene sequencing of the biomarkers and genes of different cancer types, especially in breast cancer research, can lead to molecular characterizations and subsequent identification of similar etiologies for which the therapeutics of one tumor type can be applied to other tumor types of a similar genomic profile. Thus, with the emergence of new sequencing methods and cancer databases, pan-cancer analysis will play an increasingly significant role in cancer biology research.

DATA AVAILABILITY STATEMENT

The original contributions presented in the study are included in the article/**Supplementary Material**, further inquiries can be directed to the corresponding authors.

AUTHOR CONTRIBUTIONS

XZ, HL, and YW did bibliometric analysis and wrote the manuscript. LZ, NY, and CW extracted the data and used VOSviewer to draw the map. FZ, ZL, JZ, and JY designed the research, organized the calculations, and contributed to manuscript writing and rivision. All authors have read and approved the final manuscript.

FUNDING

This work was supported by the National Natural Science Foundation of China (NO. 81973911, JZ, www.nsfc.gov.cn), Grants from the State Administration of Traditional Medicine of China (2017124, JY), Grants from Education Department of Sichuan Province (NO. 3192018079, ZL).

SUPPLEMENTARY MATERIAL

The Supplementary Material for this article can be found online at: https://www.frontiersin.org/articles/10.3389/fmed.2021.635035/full#supplementary-material

REFERENCES

1. Gotwals P, Cameron S, Cipolletta D, Cremasco V, Crystal A, Hewes B, et al. Prospects for combining targeted and conventional cancer therapy with immunotherapy. *Nat Rev Cancer*. (2017) 17:286–301. doi: 10.1038/nrc.2017.17
2. Mun EJ, Babiker HM5, Weinberg U, Kirson ED, Von Hoff DD. Tumor-treating fields: a fourth modality in cancer treatment. *Clin Cancer Res*. (2018) 24:266–75. doi: 10.1158/1078-0432.CCR-17-1117
3. Taking pan-cancer analysis global. *Nat Genet*. (2013) 45:1263. doi: 10.1038/ng.2825
4. McDermott U, Settleman J. Personalized cancer therapy with selective kinase inhibitors: an emerging paradigm in medical oncology. *J Clin Oncol*. (2009) 27:5650–9. doi: 10.1200/JCO.2009.22.9054
5. Hanahan D, Weinberg RA. Hallmarks of cancer: the next generation. *Cell*. (2011) 144:646–74. doi: 10.1016/j.cell.2011.02.013
6. Saghafinia S, Mina M, Riggi N, Hanahan D, Ciriello G. Pan-cancer landscape of aberrant DNA methylation across human tumors. *Cell Rep*. (2018) 25:1066–80.e8. doi: 10.1016/j.celrep.2018.09.082
7. Yang X, Gao L, Zhang S. Comparative pan-cancer DNA methylation analysis reveals cancer common and specific patterns. *Brief Bioinform*. (2017) 18:761–73. doi: 10.1093/bib/bbw063
8. Weinstein JN, Collisson EA, Mills GB, Shaw KR, Ozenberger BA, Ellrott K, et al. The cancer genome atlas pan-cancer analysis project. *Nat Genet*. (2013) 45:1113–20. doi: 10.1038/ng.2764
9. Han L, Yuan Y, Zheng S, Yang Y, Li J, Edgerton ME, et al. The Pan-Cancer analysis of pseudogene expression reveals biologically and clinically relevant tumour subtypes. *Nat Commun*. (2014) 5:3963. doi: 10.1038/ncomms4963
10. Tomczak K, Czerwińska P, Wiznerowicz M. The cancer genome atlas (TCGA): an immeasurable source of knowledge. *Contemp Oncol*. (2015) 19:A68–77. doi: 10.5114/wo.2014.47136
11. Kandoth C, McLellan MD, Vandin F, Ye K, Niu B, Lu C, et al. Mutational landscape and significance across 12 major cancer types. *Nature*. (2013) 502:333–9. doi: 10.1038/nature12634
12. Akbani R, Ng PK, Werner HM, Shahmoradgoli M, Zhang F, Ju Z, et al. A pan-cancer proteomic perspective on the cancer genome atlas. *Nat Commun*. (2014) 5:3887. doi: 10.1038/ncomms4887
13. Priestley P, Baber J, Lolkema MP, Steeghs N, de Bruijn E, Shale C, et al. Pan-cancer whole-genome analyses of metastatic solid tumours. *Nature*. (2019) 575:210–6. doi: 10.1038/s41586-019-1689-y
14. Schneider G, Schmidt-Supprian M, Rad R, Saur D. Tissue-specific tumorigenesis: context matters. *Nat Rev Cancer*. (2017) 17:239–53. doi: 10.1038/nrc.2017.5
15. Donna MM, Matthew NB, Kyle C, Huyen HD, Jennifer AD, Gerald F, et al. The Cancer Genome Atlas Network. Comprehensive molecular characterization of human colon and rectal cancer. *Nature*. (2012) 487:330–7. doi: 10.1038/nature11252
16. Wang Y, Xu X, Maglic D, Dill MT, Mojumdar K, Ng PK, et al. Comprehensive molecular characterization of the hippo signaling pathway in cancer. *Cell Rep*. (2018) 25:1304–17.e5. doi: 10.1016/j.celrep.2018.10.001
17. Ciriello G, Gatza ML, Beck AH, Wilkerson MD, Rhie SK, Pastore A, et al. Comprehensive molecular portraits of invasive lobular breast cancer. *Cell*. (2015) 163:506–19. doi: 10.1016/j.cell.2015.09.033
18. Daniel CK, Robert SF, Michael DM, Heather S, Joelle KV, Joshua FM, et al. The Cancer Genome Atlas Network. Comprehensive molecular portraits of human breast tumours. *Nature*. (2012) 490:61–70. doi: 10.1038/nature11412
19. van Eck NJ, Waltman L. Software survey: VOSviewer, a computer program for bibliometric mapping. *Scientometrics*. (2010) 84:523–38. doi: 10.1007/s11192-009-0146-3
20. Romero L, Portillo-Salido E. Trends in sigma-1 receptor research: a 25-year bibliometric analysis. *Front Pharmacol*. (2019) 10:564. doi: 10.3389/fphar.2019.00564
21. Rupaimoole R, Slack FJ. MicroRNA therapeutics: towards a new era for the management of cancer and other diseases. *Nat Revi Drug Discov*. (2017) 16:203–22. doi: 10.1038/nrd.2016.246
22. Wang HL, Liu PF, Yue J, Jiang WH, Cui YL, Ren H, et al. Somatic gene mutation signatures predict cancer type and prognosis in multiple cancers with pan-cancer 1000 gene panel. *Cancer Lett*. (2020) 470:181–90. doi: 10.1016/j.canlet.2019.11.022
23. Okamura R, Boichard A, Kato S, Sicklick JK, Bazhenova L, Kurzrock R. Analysis of NTRK alterations in pan-cancer adult and pediatric malignancies: implications for NTRK-targeted therapeutics. *JCO Precision Oncol*. (2018) 2018:1–20. doi: 10.1200/PO.18.00183
24. Slatko BE, Gardner AF, Ausubel FM. Overview of next-generation sequencing technologies. *Curr Protoc Mol Biol*. (2018) 122:e59. doi: 10.1002/cpmb.59

25. Vieth B, Parekh S, Ziegenhain C, Enard W, Hellmann I. A systematic evaluation of single cell RNA-seq analysis pipelines. *Nat Commun*. (2019) 10:4667. doi: 10.1038/s41467-019-12266-7
26. Tang Q, Cheng J, Cao X, Surowy H, Burwinkel B. Blood-based DNA methylation as biomarker for breast cancer: a systematic review. *Clin Epigenetics*. (2016) 8:115. doi: 10.1186/s13148-016-0282-6
27. Lai Z, Markovets A, Ahdesmaki M, Chapman B, Hofmann O, McEwen R, et al. VarDict: a novel and versatile variant caller for next-generation sequencing in cancer research. *Nucleic Acids Res*. (2016) 44:e108. doi: 10.1093/nar/gkw227
28. Anastasiadi Z, Lianos GD, Ignatiadou E, Harissis HV, Mitsis M. Breast cancer in young women: an overview. *Updat Surg*. (2017) 69:313–7. doi: 10.1007/s13304-017-0424-1
29. Mueller C, Haymond A, Davis JB, Williams A, Espina V. Protein biomarkers for subtyping breast cancer and implications for future research. *Expert Rev Proteomics*. (2018) 15:131–52. doi: 10.1080/14789450.2018.1421071
30. Senkus E, Łacko A. Over-treatment in metastatic breast cancer. *Breast*. (2017) 31:309–17. doi: 10.1016/j.breast.2016.06.024
31. Van Leeuwen BL, Rosenkranz KM, Feng LL, Bedrosian I, Hartmann K, Hunt KK, et al. The effect of under-treatment of breast cancer in women 80 years of age and older. *Crit Rev Oncol Hematol*. (2011) 79:315–20. doi: 10.1016/j.critrevonc.2010.05.010
32. Peart O. Breast intervention and breast cancer treatment options. *Radiol Technol*. (2015) 86:535M—58. doi: 10.1016/j.ccell.2018.03.014
33. Harbeck N, Schmitt M, Meisner C, Friedel C, Untch M, Schmidt M, et al. Ten-year analysis of the prospective multicentre Chemo-N0 trial validates American Society of Clinical Oncology (ASCO)-recommended biomarkers uPA and PAI-1 for therapy decision making in node-negative breast cancer patients. *Eur J Cancer*. (2013) 49:1825–35. doi: 10.1016/j.ejca.2013.01.007
34. Harbeck N, Gnant M. Breast cancer. *Lancet*. (2017) 389:1134–50. doi: 10.1016/S0140-6736(16)31891-8
35. Berger AC, Korkut A, Kanchi RS, Hegde AM, Lenoir W, Liu W, et al. A Comprehensive pan-cancer molecular study of gynecologic and breast cancers. *Cancer Cell*. (2018) 33:690–705.e9.
36. Deb B, Uddin A, Chakraborty S. miRNAs and ovarian cancer: an overview. *J cell Physiol*. (2018) 233:3846–54. doi: 10.1002/jcp.26095
37. Wang M, Fan W, Ye M, Tian C, Zhao L, Wang J, et al. Molecular profiles and tumor mutational burden analysis in Chinese patients with gynecologic cancers. *Sci Rep*. (2018) 8:8990. doi: 10.1038/s41598-018-25583-6

Conflict of Interest: The authors declare that the research was conducted in the absence of any commercial or financial relationships that could be construed as a potential conflict of interest.

Copyright © 2021 Zhang, Lai, Zhang, Wang, Zhang, Yang, Wang, Liang, Zeng and Yang. This is an open-access article distributed under the terms of the Creative Commons Attribution License (CC BY). The use, distribution or reproduction in other forums is permitted, provided the original author(s) and the copyright owner(s) are credited and that the original publication in this journal is cited, in accordance with accepted academic practice. No use, distribution or reproduction is permitted which does not comply with these terms.

frontiers in Medicine

ORIGINAL RESEARCH
published: 05 March 2021
doi: 10.3389/fmed.2021.644053

Comprehensive Analysis Identifies Potential Ferroptosis-Associated mRNA Therapeutic Targets in Ovarian Cancer

Jiyan Zhang[1], *Jie Xi*[2], *Ping Huang*[2] *and Saitian Zeng*[2]*

[1] *Department of Gynecologic Oncology, Cangzhou Central Hospital, Cangzhou, China,* [2] *Department I of Obstetrics and Gynecology, Cangzhou Central Hospital, Cangzhou, China*

Objective: This study aimed to explore ferroptosis-related mRNAs as potential therapeutic targets for ovarian cancer treatment.

Methods: Molecular subtypes were classified based on ferroptosis-related mRNAs via ConsensusClusterPlus package. The differences in prognosis, stromal score, immune score, immune function, and immune checkpoints were assessed between subtypes. Small molecular drugs were predicted via the CMap database. The sensitivity to chemotherapy drugs was estimated through the GDSC. A LASSO Cox regression model was conducted via the glmnet package, followed by a nomogram model.

Results: Based on ferroptosis mRNA expression profile, two molecular subtypes (C1 and C2) were classified, with distinct clinical outcomes. C1 subtype exhibited higher stromal score, immune cell score (T helper, Treg, neutrophil) and immune function (APC co-inhibition, parainflammation and Type II IFN response). Higher mRNA expression levels of immune checkpoints (like PDCD1) were found in C1 than C2. Potential small molecular drugs (PI3K and mTOR inhibitors) were found for treatment of ovarian cancer. C1 was more sensitive to eight chemotherapy drugs (A.443654, AZD.0530, AZD6482, AZD7762, AZD8055, BAY.61.3606, Bicalutamide, and CGP.60474). A 15-ferroptosis-related mRNA signature was developed, which could robustly and independently predict the outcomes. Moreover, a nomogram was established combining the signature and age, which could intuitively and accurately predict the 5-year overall survival probability.

Conclusion: Our study characterized two ferroptosis-related subtypes with distinct prognosis and tumor immune features, which could assist clinicians make decisions and individual therapy. Moreover, 15 ferroptosis-related mRNAs were identified, which could become potential therapeutic targets for ovarian cancer.

Keywords: ovarian carcinoma, ferroptosis, mRNA, therapeutic targets, prognosis, tumor microenvironment

OPEN ACCESS

Edited by:
Fu Wang,
Xi'an Jiaotong University, China

Reviewed by:
Chaoyun Pan,
Sun Yat-Sen University, China
Jing He,
Guangzhou Medical University, China

***Correspondence:**
Saitian Zeng
saitianzeng@163.com

Specialty section:
This article was submitted to Precision Medicine, a section of the journal Frontiers in Medicine

Received: *19 December 2020*
Accepted: *02 February 2021*
Published: *05 March 2021*

Citation:
Zhang J, Xi J, Huang P and Zeng S (2021) Comprehensive Analysis Identifies Potential Ferroptosis-Associated mRNA Therapeutic Targets in Ovarian Cancer. Front. Med. 8:644053. doi: 10.3389/fmed.2021.644053

INTRODUCTION

Ovarian carcinoma is a highly lethal gynecological malignancy globally (1). Because early symptoms are rare, ovarian cancer is usually diagnosed as advanced, partly leading to unfavorable clinical outcomes, with a 5-year overall survival (OS) of 45% (2). So far, ovarian cancer is mainly classified according to histology, grade, and stage. Nevertheless, molecular features of genome, transcription, translation, and post-translational modifications contribute to the heterogeneity of ovarian cancer (3). Characterization of specific molecular subtypes may assist clinicians make decisions and individual therapy.

It is of importance to discover and intervene risk factors via effective cancer prevention during cancer progression (4). Currently, various driver genes have been found. Recent findings demonstrate that ferroptosis, a novel cell death type with an iron-dependent mechanism, may participate in cancer progression (5). Activation of ferroptosis remarkably suppresses the proliferative capacity of ovarian cancer cells (6), indicating that inducing ferroptosis is a promising therapeutic strategy for ovarian cancer. The mechanism of ferroptosis is still largely unknown. Recent research has found that ferroptosis can be activated by TAZ-ANGPTL4-NOX2 axis for ovarian cancer, which provides a ferroptosis-inducing therapeutic implication (2). Immunotherapy such as immune checkpoint inhibitors has been applied in the treatment of ovarian cancer (7). It is clinical importance to probe which factors affect the outcomes of immunotherapy. Increasing evidence highlights the critical roles of ferroptosis on immune evasion (8). In turn, CD8 + T cells induce tumor ferroptosis in immunotherapy (9). Targeting ferroptosis combined with immunotherapy may be an underlying therapeutic strategy. Nevertheless, the roles and prognostic values of ferroptosis mRNAs remain to be illustrated in ovarian cancer.

Accordingly, this study established tumor subtypes for ovarian cancer on the basis of ferroptosis mRNAs. Furthermore, 15 ferroptosis-related mRNAs were identified as potential therapeutic targets for ovarian cancer.

MATERIALS AND METHODS

Patients and Specimens

The mRNA expression data and matched clinical information were retrieved from The Cancer Genome Atlas (TCGA; https://portal.gdc.cancer.gov/) database on November 23, 2020. Following removing samples with incomplete follow-up information, 379 samples were retained, as the training cohort. A microarray ovarian carcinoma dataset (accession: GSE26193) was obtained from the Gene Expression Omnibus (GEO; https://www.ncbi.nlm.nih.gov/geo/) database on the GPL570 platform. If a gene ID corresponded to multiple probes, the expression value was averaged. The GSE26193 dataset was utilized as the validation cohort.

Abbreviations: OS, overall survival; TCGA, The Cancer Genome Atlas; GEO, Gene Expression Omnibus; CDF, cumulative distribution function; PCA, principal components analysis; ESTIMATE, Estimation of stromal and immune cells in malignant tumors using expression data; CMap, Connectivity map; DEGs, differentially expressed genes; MoA, mode-of-action; ssGSEA, single sample gene set enrichment analysis; GDSC, Genomics of Drug Sensitivity in Cancer; IC50, half maximal inhibitory concentration; LASSO, least absolute shrinkage and selection operation; GEPIA, Gene Expression Profiling Interactive Analysis; ROCs, receiver operating characteristic curves; HR, hazard ratio; CI, confidence interval.

Consensus Clustering

Consensus clustering, an unsupervised clustering method, classifies samples based on the mRNA expression profiles. Herein, ovarian carcinoma samples were clustered on the basis of the expression levels of ferroptosis-related mRNAs (**Supplementary Table 1**) using the ConsensusClusterPlus package in R (version 1.54.0) (10). Re-sampling was used to sample 80% of the samples. After multiple sampling, the optimal k value was identified when the number of clusters $k = 2, 3, 4, \cdots\cdots 9$. The optimal k value was determined when the cumulative distribution function (CDF) index was up to the approximate maximum. The classification was verified by principal components analysis (PCA) based on the mRNA expression profiles of ovarian cancer.

Estimation of Stromal and Immune Cells in Malignant Tumors Using Expression Data (ESTIMATE)

Tumor microenvironment is composed of tumor cells, stromal cells, immune cells, and the like. The ESTIMATE (version 2.0.0) package in R was applied for evaluation of the stromal score, immune score, and tumor purity in each ovarian cancer tissue sample.

Connectivity Map (CMap)

Differentially expressed genes (DEGs) were filtered between two tumor subtypes through the limma package with the threshold values of false discovery rate < 0.05 and $|\text{fold change}| \geq 1.5$. The two lists of up- and down-regulated genes were input into the CMap (http://portals.broadinstitute.org/cmap/) database (11). Potential small molecule drugs were predicted based on the enrichment values as well as permutation p-values. Moreover, underlying mechanisms of action were probed via the CMap mode-of-action (MoA) analysis.

Single Sample Gene Set Enrichment Analysis (ssGSEA)

The ssGSEA method was utilized to quantify the enrichment scores of immune cells (aDCs, B cells, CD8+ T cells, DCs, iDCs, macrophages, mast cells, neutrophils, NK cells, pDCs, T helper cells, Tfh, Th1 cells, Th2 cells, TIL and Treg), and immune functions (APC co-inhibition, APC co-stimulation, CCR, check-point cytolytic activity, HLA, inflammation-promoting, MHC class I, parainflammation, T cell co-inhibition, T cell co-stimulation, type I IFN response and type II IFN response) for each ovarian cancer specimen (12).

Drug Sensitivity Prediction

The sensitivity to chemotherapy drugs was estimated through the Genomics of Drug Sensitivity in Cancer (GDSC; https://www.cancerrxgene.org/) database

(13). The half maximal inhibitory concentration (IC50) was estimated using the pRRophetic package in R (14).

Construction of a Ferroptosis-Related Signature

Univariate Cox regression analysis was applied to screen prognosis-related ferroptosis mRNAs with $p < 0.05$ through the survival package in R (version 2.41–3). The key mRNAs that affected clinical outcomes of patients were then screened by the least absolute shrinkage and selection operation (LASSO) Cox regression model, which was achieved by the glmnet package (version 3.0–1) (15). The regression coefficient was calculated for each variable via the multivariate Cox regression analysis. The risk score was determined for each ovarian cancer patient by combining the regression coefficients and expression levels of the key mRNAs. The cutoff point was determined according to the median value of risk scores. Afterwards, patients in the training and validation cohorts were separated into high- and low-risk groups. The survival differences were evaluated between the two groups.

Nomogram

A nomogram model was established by combining variables that could independently predict the survival of ovarian cancer. The predictive efficacy of the model for prediction of 5-year overall survival probability was assessed through calibration plots via the rms package in R.

Gene Expression Profiling Interactive Analysis (GEPIA)

The expression levels of 15 ferroptosis-related mRNAs in the signature were analyzed in ovarian cancer ($n = 426$) and normal specimens ($n = 88$) from match TCGA normal and GTEx data via the GEPIA website (http://gepia2.cancer-pku.cn/#index).

Immunohistochemistry

Immunohistochemistry images of 15 ferroptosis-related proteins in ovarian cancer tissues from the signature model were downloaded from the Human Protein Atlas (https://www.proteinatlas.org/).

RT-qPCR

Twenty pairs of ovarian cancer and adjacent normal tissues were collected from the Department of Obstetrics and Gynecology of Cangzhou Central Hospital (China). None of the patients received any treatment before surgery. Each patient signed a written informed consent. This study was approved by the Ethics Committee of Cangzhou Central Hospital (2019045). Total RNA from tissues was extracted by TRIzol reagent (Beyotime, Beijing, China), which was reverse-transcribed into cDNA. RT-PCR for mRNAs was carried out through SYBR Premix Ex Taq reagent kit (Invitrogen, USA) on the ABI StepOne RT-PCR System. The mRNA expression was normalized against GAPDH. Primer sequences were listed in **Table 1**.

TABLE 1 | Primer sequences for RT-qPCR.

Target genes	Primer sequences (5′-3′)
CDKN1B	AACGTGCGAGTGTCTAACGG (forward) CCCTCTAGGGGTTTGTGATTCT (reverse)
FAS	TCTGGTTCTTACGTCTGTTGC (forward) CTGTGCAGTCCCTAGCTTTCC (reverse)
FOS	CCGGGGATAGCCTCTCTTACT (forward) CCAGGTCCGTGCAGAAGTC (reverse)
FOXO1	TCGTCATAATCTGTCCCTACACA (forward) CGGCTTCGGCTCTTAGCAAA (reverse)
GABARAPL1	ATGAAGTTCCAGTACAAGGAGGA (forward) GCTTTTGGAGCCTTCTCTACAAT (reverse)
HDAC1	CTACTACGACGGGGATGTTGG (forward) GAGTCATGCGGATTCGGTGAG (reverse)
NFKB1	AACAGAGAGGATTTCGTTTCCG (forward) TTTGACCTGAGGGTAAGACTTCT (reverse)
PEX3	CCAAGCACGACGACAATATCA (forward) TCAGTGTTGGAAGCATGGACA (reverse)
PPP1R15A	ATGATGGCATGTATGGTGAGC (forward) AACCTTGCAGTGTCCTTATCAG (reverse)
SIRT2	TGCGGAACTTATTCTCCCAGA (forward) GAGAGCGAAAGTCGGGGAT (reverse)
CXCR4	ACTACACCGAGGAAATGGGCT (forward) CCCACAATGCCAGTTAAGAAGA (reverse)
IFNG	TCGGTAACTGACTTGAATGTCCA (forward) TCGCTTCCCTGTTTTAGCTGC (reverse)
IL24	TTGCCTGGGTTTTACCCTGC (forward) AAGGCTTCCCACAGTTTCTGG (reverse)
MTMR14	GGAGTTCTCCCGGACTCAGTA (forward) AACAGTAGTCTCGGCCAAACA (reverse)
RB1	CTCTCGTCAGGCTTGAGTTTG (forward) GACATCTCATCTAGGTCAACTGC (reverse)
GAPDH	ACAACTTTGGTATCGTGGAAGG (forward) GCCATCACGCCACAGTTTC (reverse)

Statistical Analysis

Statistical analyses were conducted through R language (version 3.6.2) or SPSS (version 19.0). Differences between two groups were analyzed via the Wilcoxon test or student's *t*-test. Kaplan-Meier curves were utilized for measurement of survival rates for OS and disease-free survival (DFS), and differences in survival rates were presented via the log-rank test. The predictive efficacy of signature was estimated by time-dependent receiver operating characteristic curves (ROCs). The area under the curves (AUCs) was calculated. Univariate and multivariate cox regression analyses were employed to probe whether clinical features (age, FIGO stage, and grade) and signature were associated with prognosis of ovarian cancer. Hazard ratio (HR) and 95% confidence interval (CI) of each variable were estimated using the survminer package.

RESULTS

Two Molecular Subtypes of Ferroptosis-Related mRNAs in Ovarian Cancer

This study classified molecular subtypes based on the expression profiles of ferroptosis-related mRNAs in ovarian cancer via the ConsensusClusterPlus package in the TCGA ovarian cancer dataset. When $k = 2$, the classification was reliable and stable (**Figures 1A–D**). The patients were divided into C1 and C2. The PCA confirmed that C1 was significantly different from C2 (**Figure 1E**). Patients in C2 exhibited the prolonged survival time than those in C1 ($p = 4.502e-02$; **Figure 1E**). Thus, ferroptosis-based signatures characterized two tumor subtypes with distinct clinical outcomes for ovarian cancer.

Association Between Two Subtypes and Tumor Immune Microenvironment

Recently, it has been demonstrated the crosstalk between ferroptosis and tumor immune microenvironment in cancers (16). Therefore, we analyzed the associations between two subtypes and tumor immune microenvironment. The stromal score, immune score and tumor purity of each ovarian cancer sample were calculated via the ESTIMATE. We found that there was a significant correlation in stromal score between C1 and C2 ($p = 0.003$; **Figure 2A**). C2 had a distinctly higher stromal score than C1. However, no significant differences in immune score and tumor purity were found between two subtypes. Furthermore, we assessed whether subtypes were in relation to immune cells and immune functions in ovarian cancer. The data showed that C1 exhibited significantly higher infiltration levels of DCs, macrophages, mast cells, neutrophils, T helper cells, and Treg than C2 (**Figure 2B**). Moreover, the relationships between subtypes and immune functions were assessed in depth. APC co-inhibition, parainflammation, and type II IFN response exhibited higher levels in C1 compared to C2. Taken together, two subtypes had a relationship with tumor immune microenvironment in ovarian cancer.

Association Between Subtypes and Immune Checkpoints in Ovarian Cancer

The immune checkpoint inhibitors have been used in ovarian cancer (7). Herein, we found that C1 had significantly higher CD274, PDCD1LG2, PDCD1, LAG3, TIGIT, CTLA4, and HAVCR2 compared to C2, indicating that patients in C1 could be sensitive to the immune checkpoint inhibitors (**Figure 3A**).

Analysis of Small Drugs and Mechanism of Action Between Subtypes

Four thousand two hundred seventy-five up- and 264 down-regulated genes were screened between two subtypes. Based on them, CMap analysis was utilized to identify candidate small molecular drugs for ovarian cancer. For example, mTOR (LY-294002 and sirolimus) and PI3K inhibitors (wortmannin) were predicted for the treatment of ovarian cancer (**Figure 3B**).

Sensitivity of Chemotherapy Drugs Between Subtypes

Radical surgery in combination with adjuvant chemotherapy is the basic approach regarding ovarian cancer. Thus, it is of significance for predicting the sensitivity to chemotherapy, which may assist clinicians to employ the optimal strategy. The estimated IC50 levels of A.443654 ($p = 2.67e-07$), AZD.0530 ($p = 1.08e-07$), AZD6482 ($p = 2.16e-24$), AZD7762 ($p = 0.001$), AZD8055 ($p = 0.02$), BAY.61.3606 ($p = 7.54e-19$), Bicalutamide ($p = 3.05e-08$), and CGP.60474 ($p = 6.82e-17$) were distinctly lowered in C1 compared to C2 (**Figures 4A–H**), indicating that C1 subtype was more sensitive to these chemotherapeutic drugs.

Establishment of a Ferroptosis-Related Signature for Prognosis Prediction

Twenty-five ferroptosis mRNAs were distinctly related to prognosis of ovarian cancer (**Supplementary Table 2**). After screening the key mRNAs, a LASSO Cox regression model was then constructed (**Figures 5A,B**). The risk score for each patient was calculated, as follows: 0.0461419186912939 * CDKN1B +−0.110510609535903 * CXCR4 + 0.0795555188969791 * FAS + 0.0239651512531641 * FOS + 0.0864413738704437 * FOXO1 + 0.0399109420909256 * GABARAPL1 + 0.0910556896121155 * HDAC1 +−0.147263024908922 * IFNG + (−0.190901967548489) * IL24 + 0.0821435843345801 * MTMR14 + 0.00734788035781478 * NFKB1 + 0.00606909390683674 * PEX3 + 0.0456165637799593 * PPP1R15A + 0.0822296594101889 * RB1 + 0.0733586200221587 * SIRT2. Ovarian cancer patients were separated into high and low risk groups. Our results showed that patients with high risk exhibited shorter OS ($p = 1.452e-07$; **Figure 5C**) and DFS time ($p = 6.479e-05$; **Figure 5D**) than those with low risk. The predictive efficacy of this signature was verified by ROCs. The AUCs for OS (**Figure 5E**) and DFS (**Figure 5F**) were 0.712 and 0.648, suggesting that the signature possessed the accurate and robust performance for prediction of prognosis.

Evaluation of the Stability and Reliability of the Signature for Prediction of Prognosis in Ovarian Cancer

Univariate cox regression analysis results showed that the risk score was significantly associated with poor prognosis ($p = 5.279e-11$, HR: 1.146, CI: 1.100–1.193) for ovarian cancer patients (**Figure 6A**). Furthermore, age was a risk score for ovarian cancer prognosis ($p = 0.001$, HR: 1.020, CI: 1.008–1.033). To verify the efficacy of these factors on prediction of prognosis, multivariate cox regression analysis was carried out. Our data suggested that the risk score ($p = 1.460e-10$, HR: 1.142, CI: 1.097–1.189) and age ($p = 0.002$, HR: 1.020, CI: 1. 007–1.032) were independent risk factors for ovarian cancer (**Figure 6B**). To further verify the generalizability of this signature, the predictive performance was externally validated in the GSE26193 dataset. Consistent with the training set, the signature was markedly associated with OS ($p = 5.102e-07$; **Figure 6C**) and DFS ($p = 2.704e-06$; **Figure 6D**). ROCs confirmed the stability and reliability of the signature for

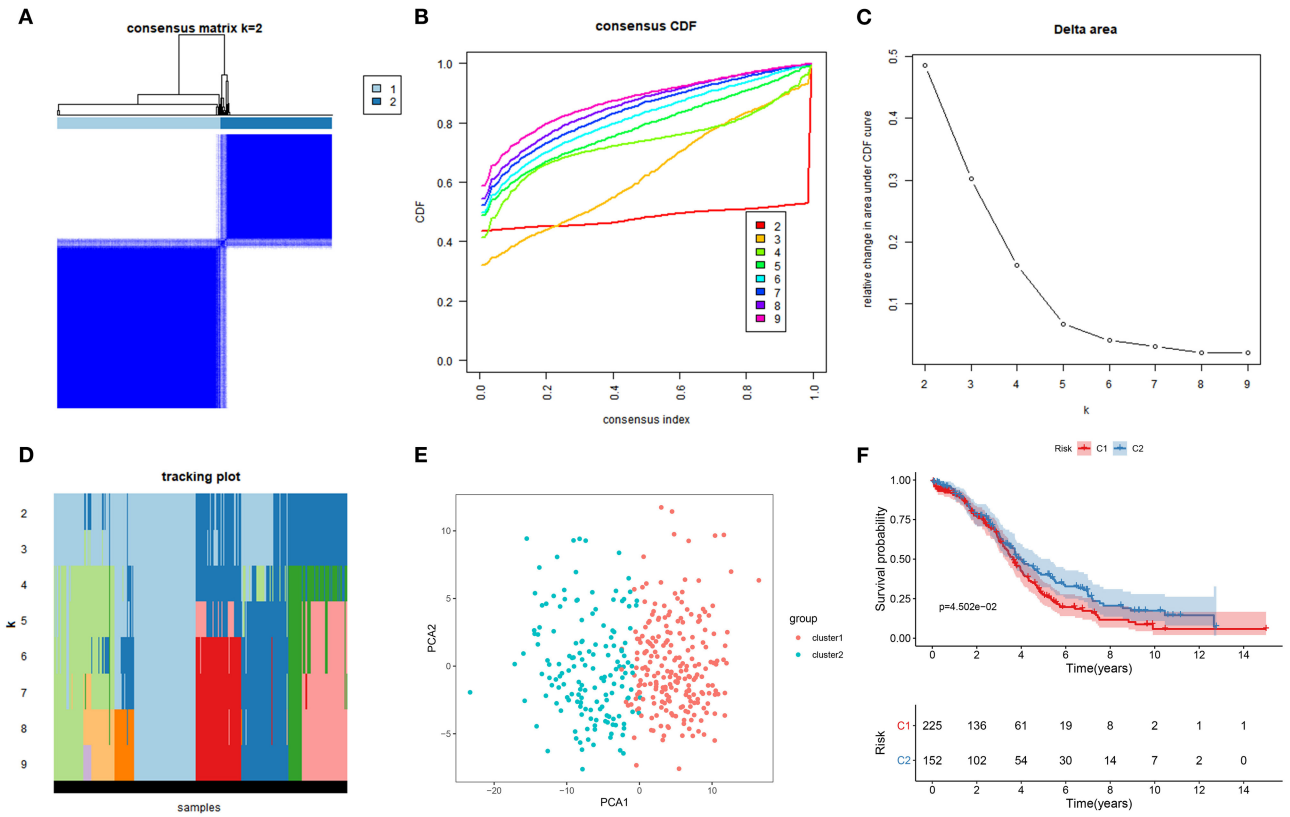

FIGURE 1 | Characterization of two molecular subtypes based on ferroptosis-related mRNAs in ovarian cancer. **(A)** Consensus matrix when $k = 2$. Both the rows and columns of the matrix represent samples. From white to dark blue, the value of the consistency matrix is from 0 to 1. **(B)** Consensus CDF, **(C)** Delta area, and **(D)** tracking plot for validation of the clustering results. **(E)** PCA plots for validation of the stability and reliability of the classification. **(F)** Kaplan-Meier OS curves for ovarian cancer patients between C1 and C2 subtypes.

prediction of OS (AUC = 0.748; **Figure 6E**) and DFS (AUC = 0.729; **Figure 6F**). Hence, this signature could be a stable and reliable risk factor for ovarian cancer.

Construction of a Nomogram Model Based on the Risk Score and Age

Through combining the two independent risk factors (signature and age), we established a nomogram model for predicting the clinical outcomes of ovarian cancer. The risk score made the most contribution to the prediction of 5-year OS time (**Figure 7A**). The prediction efficacy of the nomogram was assessed by calibration plots. The data showed that the 5-year OS predicted by the nomogram was close to the actual survival time (**Figure 7B**). It was indicative of the superior predictive capacity of the nomogram.

15 Ferroptosis-Related mRNAs as Potential Therapeutic Targets for Ovarian Cancer

The expression of the 15 mRNAs from the signature was analyzed in TCGA ovarian cancer cohort. We found that CDKN1B, FAS, FOS, FOXO1, GABARAPL1, HDAC1, NFKB1, PEX3, PPP1R15A, and SIRT2 were all significantly lowly expressed in ovarian cancer than normal specimens (**Figures 8A–J**). Moreover, CXCR4, IFNG, IL24, MTMR14, and RB1 all exhibited higher expression in ovarian cancer compared to normal specimens (**Figures 8K–O**). These data indicated that these ferroptosis-related mRNAs were associated with ovarian cancer progression.

Expression of Gene Products From the 15-mRNA Model in Ovarian Cancer

We analyzed the expression of gene products in the 15-mRNA signature in ovarian cancer tissues. Among them, CXCR4 was not contained in the database. The immunohistochemistry images of CDKN1B, FAS, FOS, FOXO1, GABARAPL1, HDAC1, NFKB1, PEX3, PPP1R15A, SIRT2, IFNG, IL24, MTMR14, and RB1 in ovarian cancer tissues were shown in **Figures 9A–N**. This study found that the expression intensity of CDKN1B, GABARAPL1 and IFNG was moderate and the quantity was low. The expression intensity and quantity of FAS and FOXO1 were both low. For FOS, NFKB1, PPP1R15A, and IL24, the intensity was weak, but the quantity was low to high. HDAC1, PEX3, MTMR14, and RB1 had the moderate intensity and high quantity in ovarian cancer. SIRT2 expression was not detected in ovarian cancer. CDKN1B, FOS, FOXO1, HDAC1, and RB1 were mainly

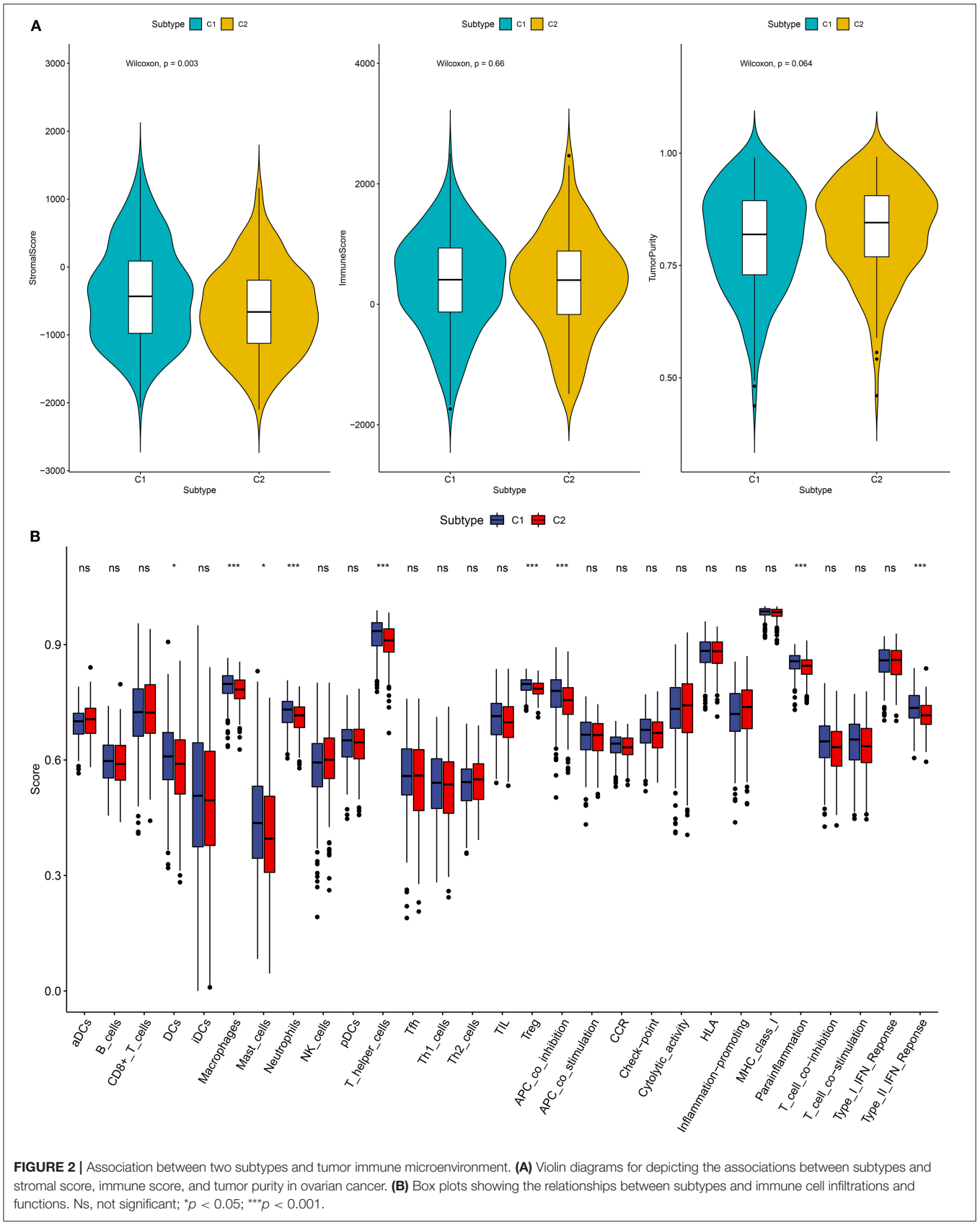

FIGURE 2 | Association between two subtypes and tumor immune microenvironment. **(A)** Violin diagrams for depicting the associations between subtypes and stromal score, immune score, and tumor purity in ovarian cancer. **(B)** Box plots showing the relationships between subtypes and immune cell infiltrations and functions. Ns, not significant; $^{*}p < 0.05$; $^{***}p < 0.001$.

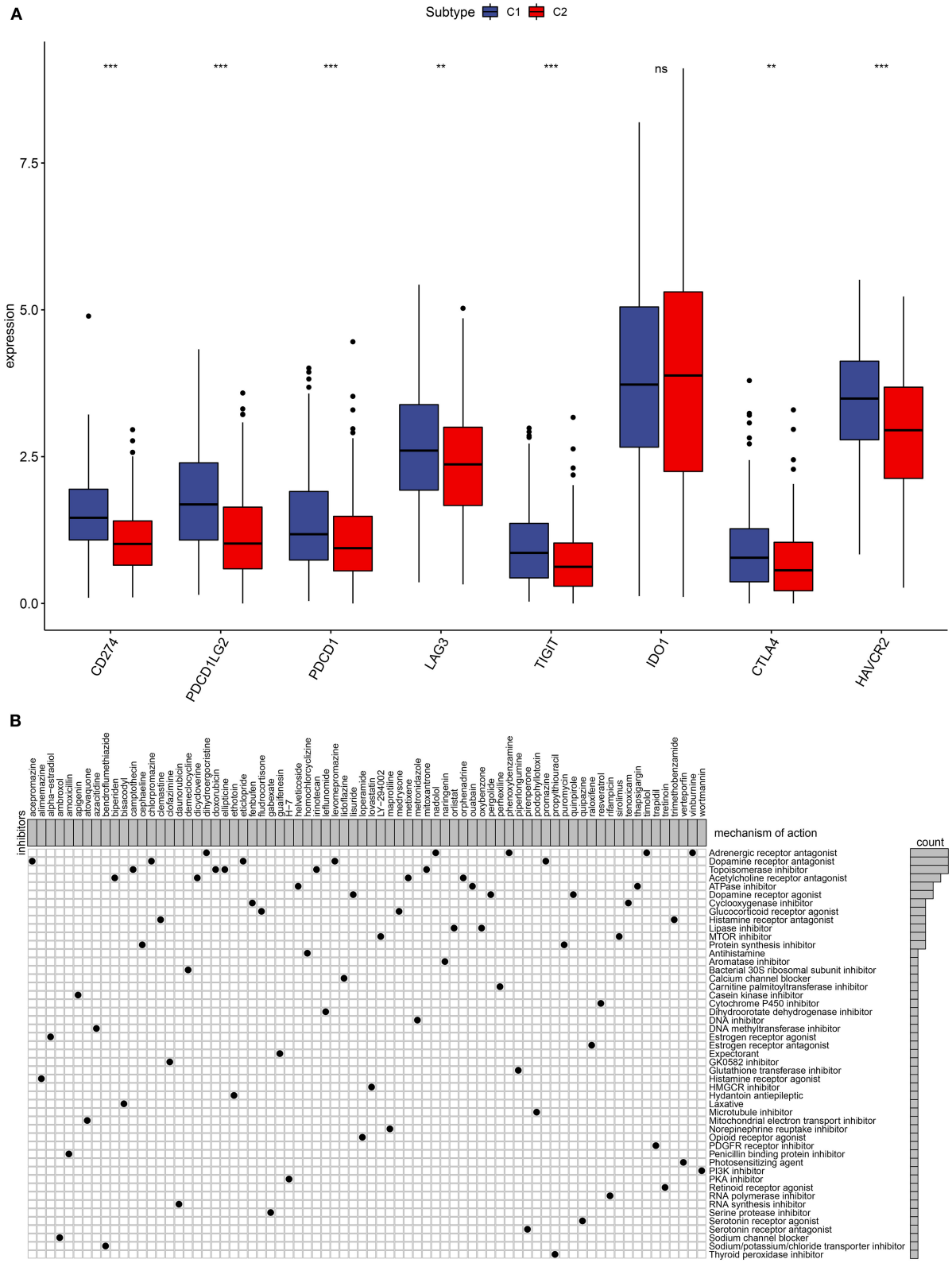

FIGURE 3 | Immune checkpoints and small molecular drugs in ovarian cancer. **(A)** Box plots for the associations between subtypes and immune checkpoints in ovarian cancer. Ns, not significant; $^{**}p < 0.01$; $^{***}p < 0.001$. **(B)** Heatmap showing small inhibitors (perturbagen) and their shared mechanisms of action (rows) from the CMap database.

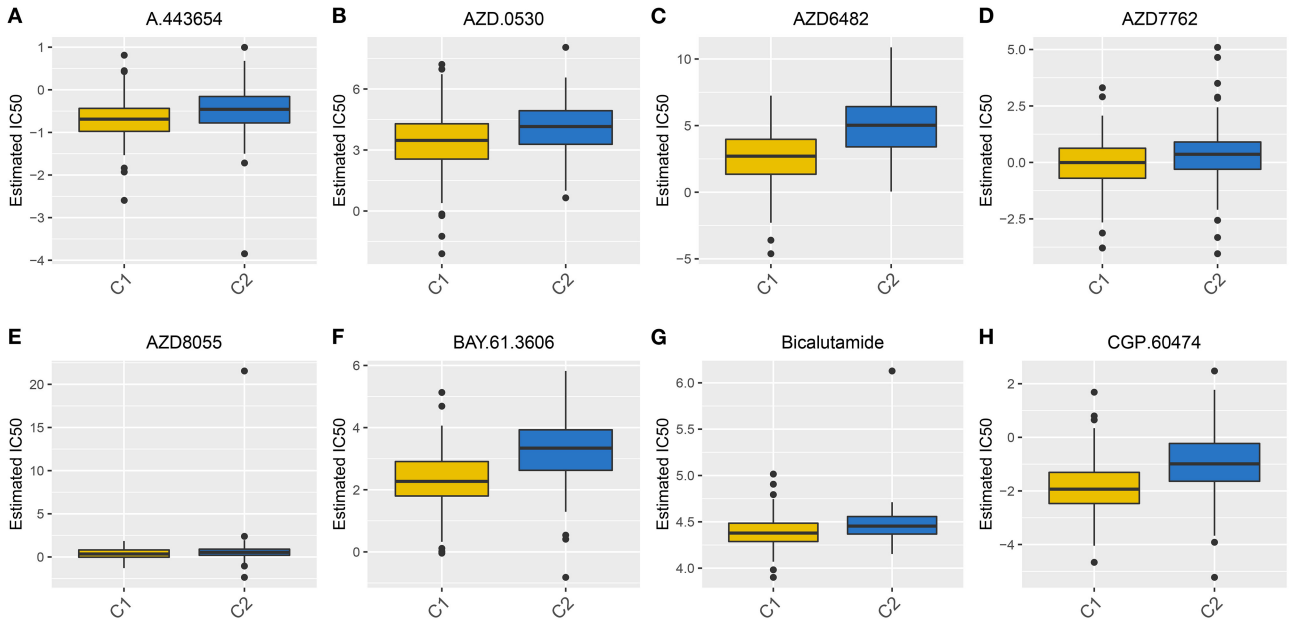

FIGURE 4 | Box plots for the estimated IC50 of chemotherapy drugs between two subtypes. **(A)** A.443654. **(B)** AZD.0530. **(C)** AZD6482. **(D)** AZD7762. **(E)** AZD8055. **(F)** BAY.61.3606. **(G)** Bicalutamide. **(H)** CGP.60474.

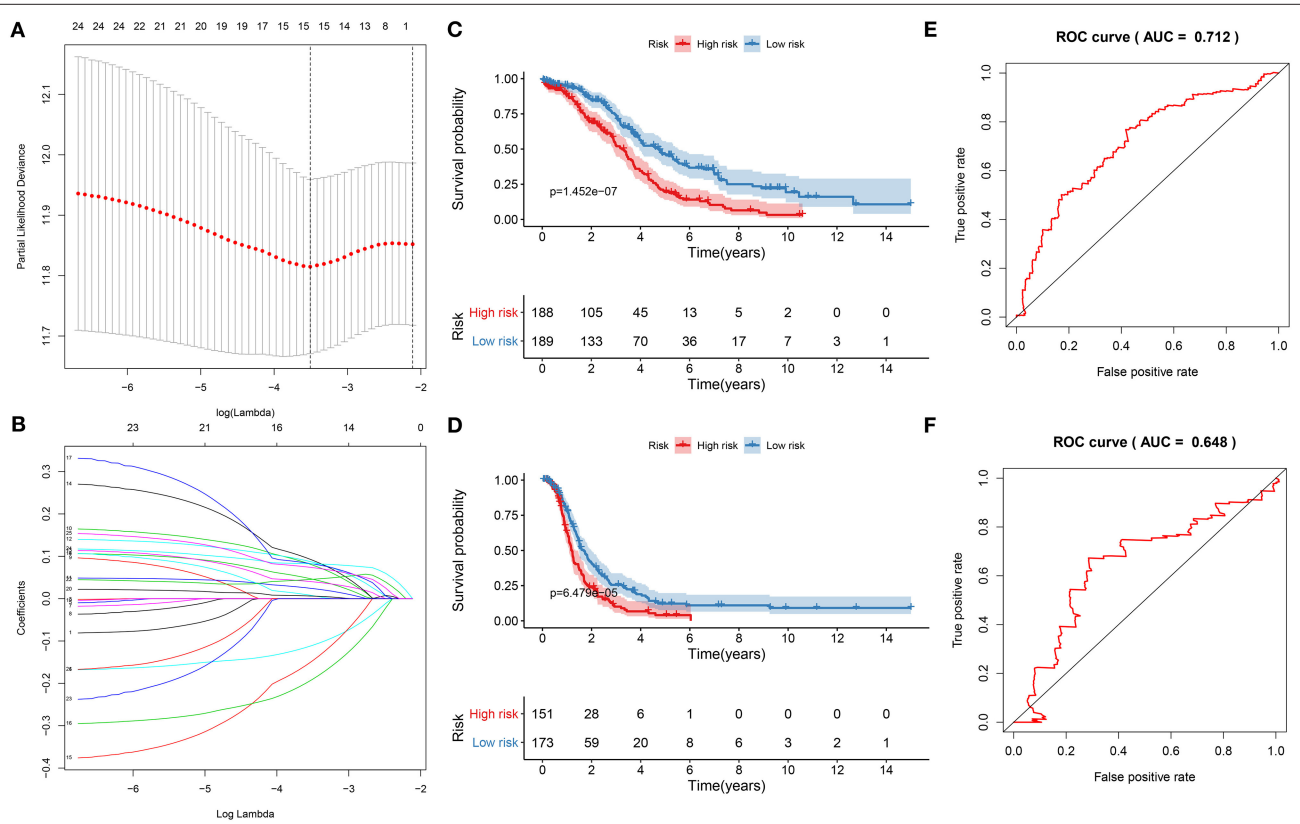

FIGURE 5 | Construction of a ferroptosis-related signature for prediction of prognosis in ovarian cancer. **(A)** LASSO regression with 10-fold cross-verification. **(B)** LASSO coefficient profiles of 25 ferroptosis-related mRNAs. Kaplan-Meier curves for **(C)** OS and **(D)** DFS between high and low risk groups. Time-dependent ROC curves for **(E)** OS and **(F)** DFS.

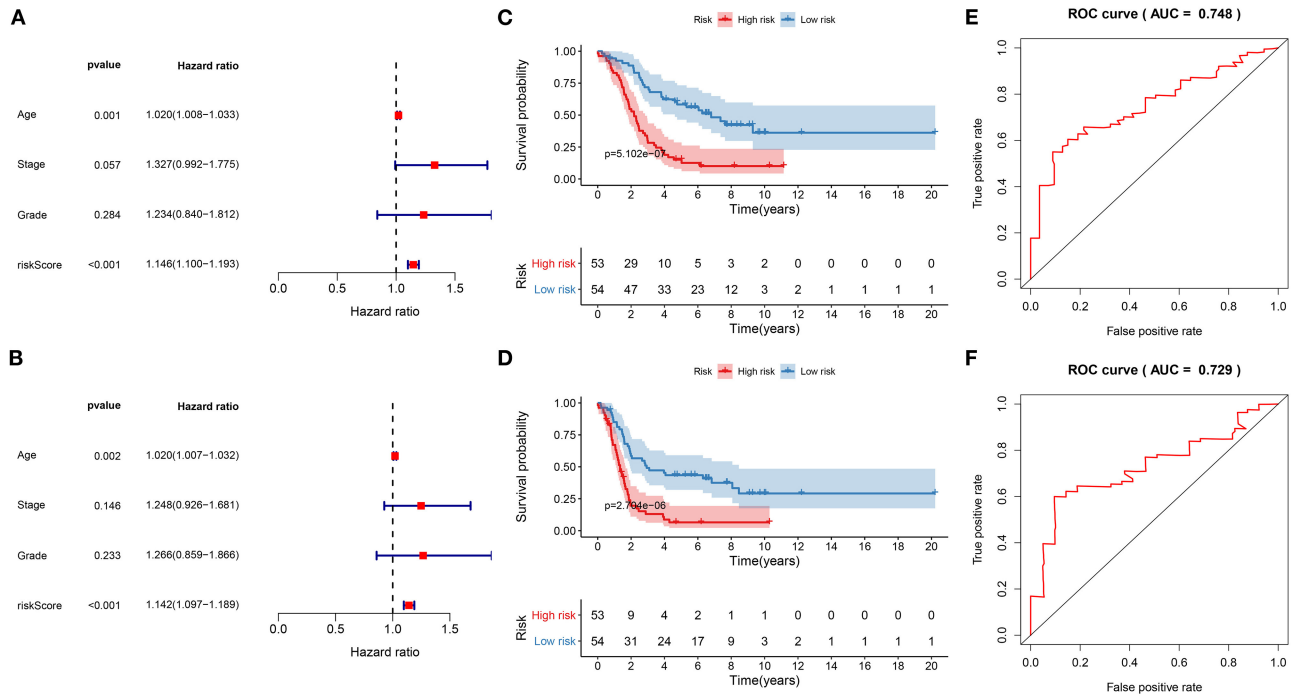

FIGURE 6 | Evaluation of the stability and reliability of the signature for prediction of prognosis in ovarian cancer. **(A)** Univariant and **(B)** multivariate cox regression analysis of age, stage, grade, and risk score in the training set. Kaplan-Meier curves for **(C)** OS and **(D)** DFS of risk score in the GSE26193 dataset. ROC curves for **(E)** OS and **(F)** DFS of risk score in the GSE26193 dataset.

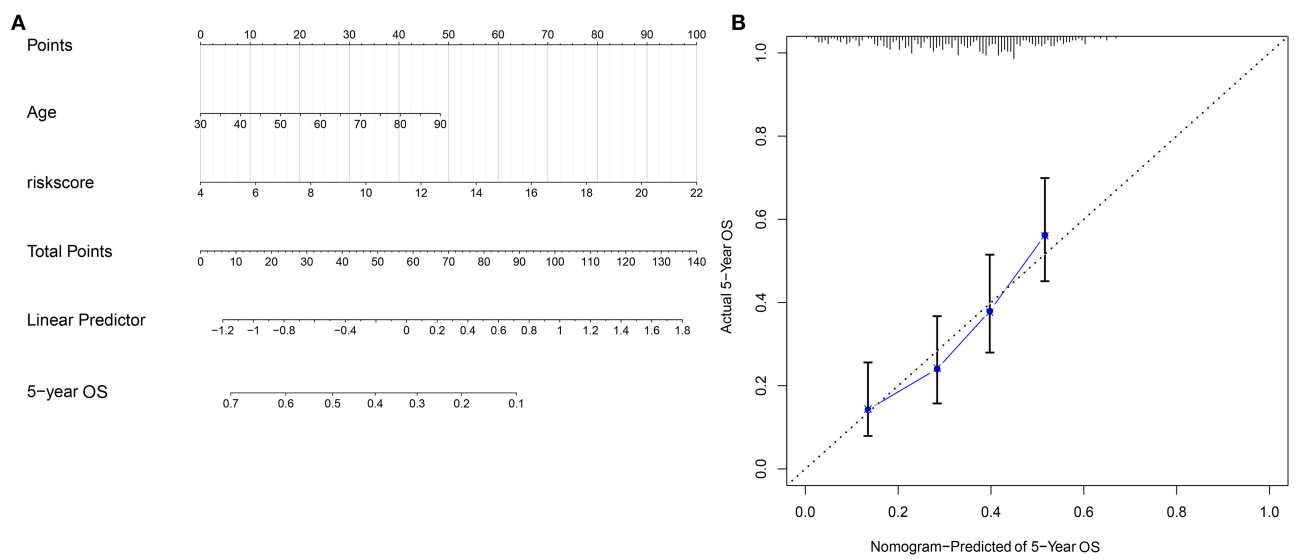

FIGURE 7 | Construction and evaluation of a nomogram combining the risk score and age. **(A)** A nomogram for prediction of 5-year OS probability. **(B)** Calibration plots for assessing the relationships between predicted 5-year overall survival and actual survival time.

expressed in the nuclear of tumor cells. Meanwhile, FAS, GABARAPL1, NFKB1, PEX3, PPP1R15A, IFNG, and MTMR14 were primarily distributed in cytoplasmic and membranous regions. IL24 was mainly distributed in cytoplasmic and membranous nuclear.

Validation of 15 Ferroptosis-Related mRNAs in Ovarian Cancer by RT-qPCR

These 15 ferroptosis-related mRNAs were verified in 20 paired ovarian cancer and normal tissues by RT-qPCR. Our

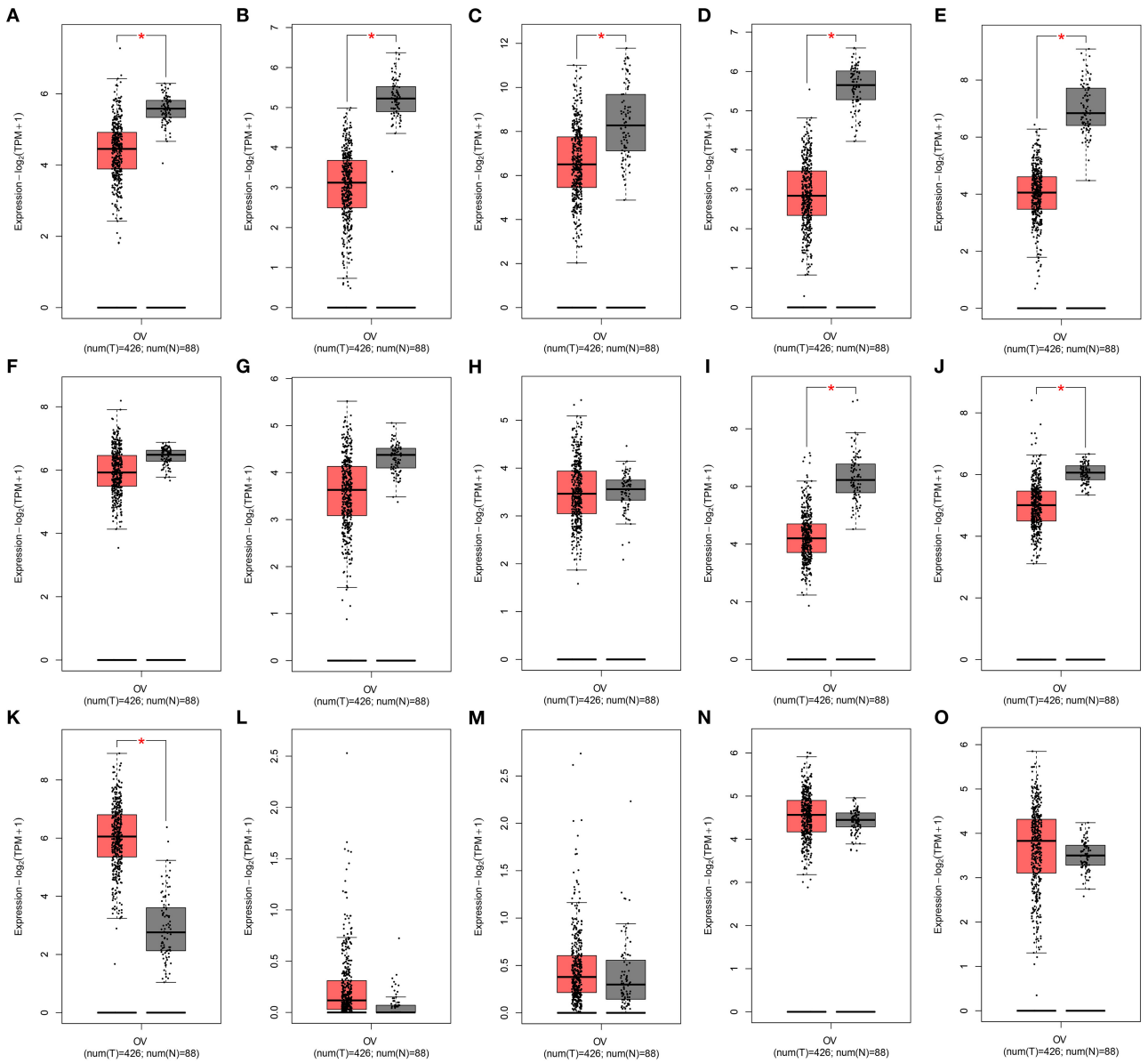

FIGURE 8 | Expression of the 15 ferroptosis-related mRNAs from the signature in an ovarian cancer cohort from the GEPIA database. Box plots for the expression of **(A)** CDKN1B; **(B)** FAS; **(C)** FOS; **(D)** FOXO1; **(E)** GABARAPL1; **(F)** HDAC1; **(G)** NFKB1; **(H)** PEX3; **(I)** PPP1R15A; **(J)** SIRT2; **(K)** CXCR4; **(L)** IFNG; **(M)** IL24; **(N)** MTMR14; **(O)** RB1 in ovarian cancer and normal tissues.

data confirmed the down-regulation of CDKN1B, FAS, FOS, FOXO1, GABARAPL1, HDAC1, NFKB1, PEX3, PPP1R15A, SIRT2, and CXCR4 in ovarian cancer than normal tissues (**Figures 10A–K**). Furthermore, IFNG, IL24, MTMR14, and RB1 were highly expressed in ovarian cancer than normal tissues (**Figures 10L–O**).

DISCUSSION

Ovarian cancer, with high heterogeneity, has various subtypes based on histological and molecular features (17). Herein, two tumor subtypes with distinct prognosis were characterized by ferroptosis-related signatures for ovarian cancer, which highlighted the diversity among ovarian cancer samples.

In this study, two molecular subtypes (C1 and C2) of ovarian cancer were defined through the mRNA expression profiles of ferroptosis-related mRNAs. Ovarian cancer samples are composed of cancer and stromal cells (18). There exists the tight crosstalk between cancer and stromal cells in tumor microenvironment (19). Targeting this crosstalk is a hopeful therapeutic approach (20). Our data demonstrated that C2 had a distinctly higher stromal score than C1. It has been found

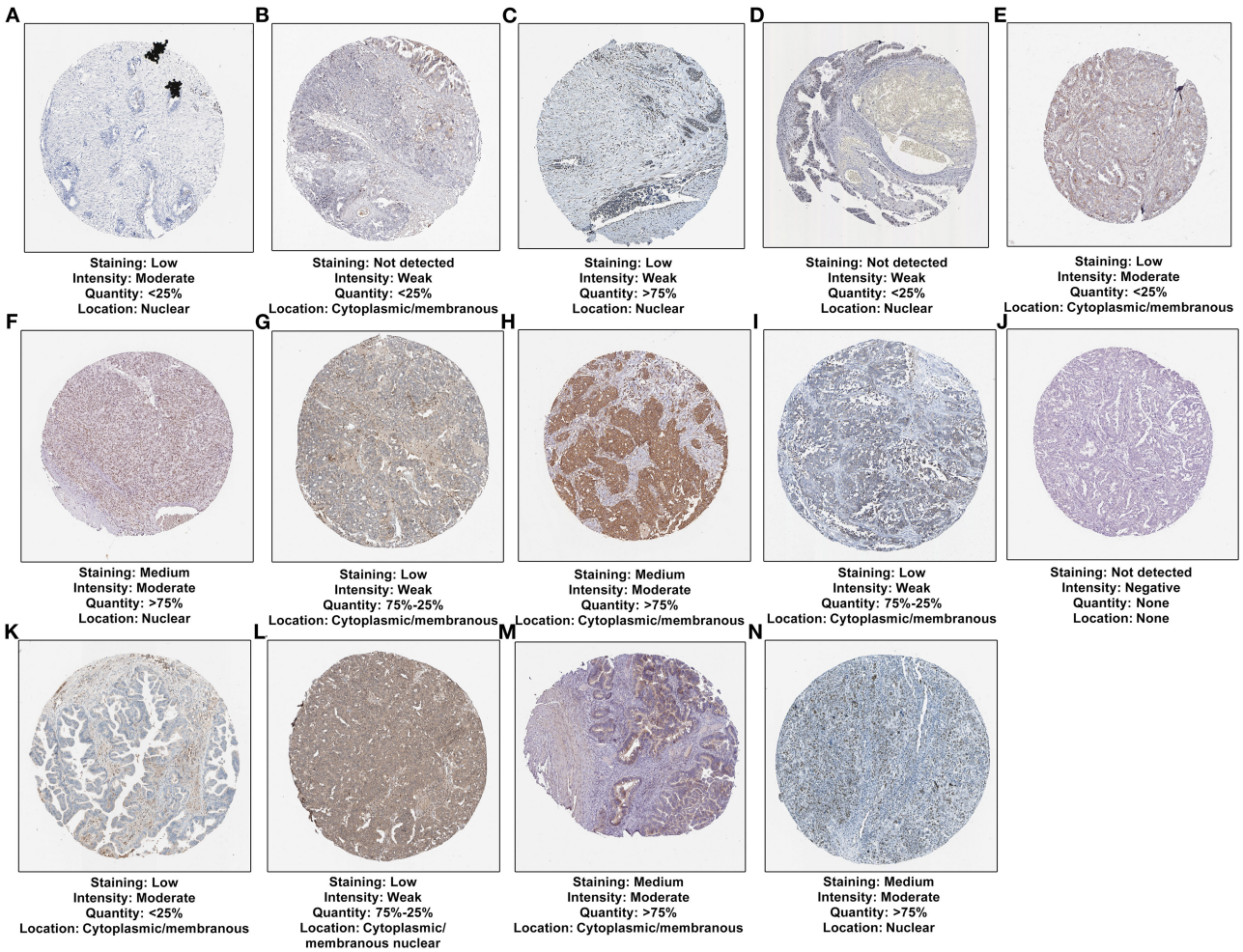

FIGURE 9 | Verification of the expression of 14 mRNAs from the risk score at the translation levels. **(A)** CDKN1B; **(B)** FAS; **(C)** FOS; **(D)** FOXO1; **(E)** GABARAPL1; **(F)** HDAC1; **(G)** NFKB1; **(H)** PEX3; **(I)** PPP1R15A; **(J)** SIRT2; **(K)** IFNG; **(L)** IL24; **(M)** MTMR14; **(N)** RB1.

that cancer-associated stroma contributes to poor outcomes for high-grade serous ovarian cancer (18). T cell dysfunction is a hallmark of cancers (21). Nevertheless, the mechanisms of dysfunction remain unclear. We found that C1 exhibited significantly higher infiltration levels of T helper and Treg cells than C2, indicating that ferroptosis might be related to T cell dysfunction. Previously, T cells can activate tumor ferroptosis in immunotherapies (9). Moreover, C1 had higher infiltration levels of DCs, macrophages, mast cells, neutrophils compared to C2. Polarization of tumor-associated macrophages is driven by autophagy-dependent ferroptosis (22). Furthermore, ferroptosis can be induced neutrophils, thereby promoting tumor necrosis in glioblastoma (23). Our results suggested that APC co-inhibition, parainflammation, and type II IFN response had higher levels in C1 compared to C2. Ferroptosis can be induced by interferon-γ in cancer cells (24). The immune checkpoints including CD274, PDCD1LG2, PDCD1, LAG3, TIGIT, CTLA4, and HAVCR2 exhibited higher levels in C1 compared to C2. Immunity therapy such as anti-PD-1 and ani-PD-L1 is representative of the tomorrow of cancer treatment. Consistently, induction of ferroptosis tumor cells at early stage may efficiently boost immunity response (25).

Exploitation of ferroptosis inducers offers a novel therapeutic approach for treating ovarian cancer. A few conventional drugs may induce ferroptosis in cancer cells such as Sulfasalazine, Artesunate, Temozolomide, and Cisplatin (26). Herein, we predicted the small molecular drugs targeting ferroptosis. For example, we found that mTOR (LY-294002 and sirolimus) and PI3K inhibitors (wortmannin) could be potential ferroptosis inducers. Consistently, a preclinical study has reported that PI3K-AKT-mTOR pathway inhibits ferroptosis and inhibition of PI3K and mTOR can activate ferroptosis in cancer cells (27). Combination of ferroptosis inducers and chemotherapeutic drugs exhibits remarkably synergistic effects on anti-cancer activities (28). Here, we found that ferroptosis-related molecular subtypes were markedly related to the sensitivity to A.443654, AZD.0530, AZD6482, AZD7762, AZD8055, BAY.61.3606, Bicalutamide, and CGP.60474. It appeared that patients in

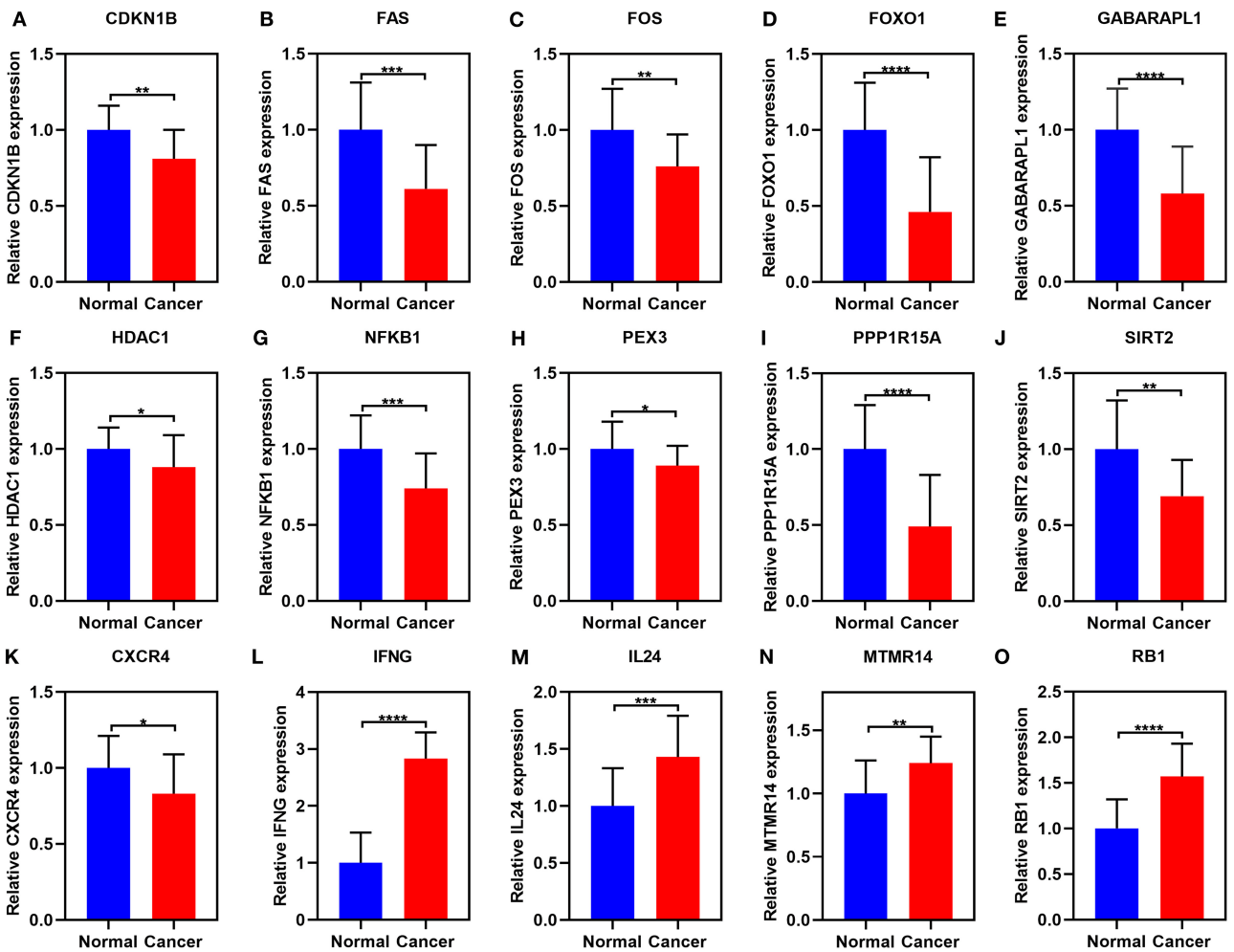

FIGURE 10 | RT-qPCR for the expression of the 15 ferroptosis-related mRNAs in ovarian cancer and normal tissues. **(A)** CDKN1B; **(B)** FAS; **(C)** FOS; **(D)** FOXO1; **(E)** GABARAPL1; **(F)** HDAC1; **(G)** NFKB1; **(H)** PEX3; **(I)** PPP1R15A; **(J)** SIRT2; **(K)** CXCR4; **(L)** IFNG; **(M)** IL24; **(N)** MTMR14; **(O)** RB1. $^{*}p < 0.05$; $^{**}p < 0.01$; $^{***}p < 0.001$; $^{****}p < 0.0001$.

C1 had higher sensitivity to these chemotherapeutic drugs. Among them, AZD6482 is an inhibitor of PI3K that is related to ferroptosis (29). AZD7762 can overcome cisplatin resistance in ovarian cancer (30). AZD8055, an inhibitor of mTORC1/2, can strengthen the sensitivity to MEK inhibitor Trametinib in ovarian cancer cells (31).

We constructed a 15-ferroptosis mRNA signature for predicting the prognosis of ovarian cancer, composed of CDKN1B, CXCR4, FAS, FOS, FOXO1, GABARAPL1, HDAC1, IFNG, IL24, MTMR14, NFKB1, PEX3, PPP1R15A, RB1, and SIRT2. All of them could be involved in the progression of ovarian cancer. For example, low CDKN1B expression is indicative of poor prognosis for ovarian cancer (32). CXCR4 is a critical determinant for tumor initiation, progression as well as metastasis of ovarian cancer (33). The intuitive and effective nomogram combining the signature and age was developed, which could be expediently employed for predicting patients' prognosis. These mRNAs could become potential therapeutic targets for ovarian cancer treatment.

Nevertheless, several limitations should be pointed out. Firstly, this was a retrospective study. The subtypes and signature models should be validated in a larger and multi-center ovarian cancer cohort. Secondly, the roles of ferroptosis-related mRNA in ovarian cancer required to be investigated in more experiments.

CONCLUSION

Collectively, this study characterized two ferroptosis-related molecular subtypes in ovarian cancer, with distinct prognosis, tumor microenvironment and sensitivity to chemotherapeutic drugs. We predicted several underlying small molecular drugs against ovarian cancer such as LY-294002, sirolimus and wortmannin. A 15-ferroptosis mRNA signature was constructed, which robustly predicted the outcomes. These mRNAs could be promising therapeutic

targets. Following combining this signature and age, we established an intuitive and effective nomogram, which could be applied for assisting precision treatment. Taken together, our findings indicated that inducing ferroptosis could be a promising therapeutic approach for ovarian cancer.

DATA AVAILABILITY STATEMENT

The datasets presented in this study can be found in online repositories. The names of the repository/repositories and accession number(s) can be found in the article/**Supplementary Material**.

ETHICS STATEMENT

The studies involving human participants were reviewed and approved by the Ethics Committee of Cangzhou Central Hospital (2019045). The patients/participants provided their written informed consent to participate in this study.

AUTHOR CONTRIBUTIONS

SZ conceived and designed the study. JZ conducted most of the experiments, data analysis, and wrote the manuscript. JX and PH participated in collecting data and helped to draft the manuscript. All authors reviewed and approved the manuscript.

SUPPLEMENTARY MATERIAL

The Supplementary Material for this article can be found online at: https://www.frontiersin.org/articles/10.3389/fmed.2021.644053/full#supplementary-material

Supplementary Table 1 | A list of ferroptosis-related mRNAs.

Supplementary Table 2 | 25 prognosis-related ferroptosis mRNAs in ovarian cancer.

REFERENCES

1. Ksiazek K. Where does cellular senescence belong in the pathophysiology of ovarian cancer? *Semin Cancer Biol.* (2020) 20:30260–1. doi: 10.1016/j.semcancer.2020.11.021
2. Yang WH, Huang Z, Wu J, Ding CC, Murphy SK, Chi JT. A TAZ-ANGPTL4-NOX2 axis regulates ferroptotic cell death and chemoresistance in epithelial ovarian cancer. *Mol Cancer Res.* (2020) 18:79–90. doi: 10.1158/1541-7786.Mcr-19-0691
3. Pan J, Hu Y, Sun S, Chen L, Schnaubelt M, Clark D, et al. Glycoproteomics-based signatures for tumor subtyping and clinical outcome prediction of high-grade serous ovarian cancer. *Nat Commun.* (2020) 11:6139. doi: 10.1038/s41467-020-19976-3
4. Kim O, Park EY, Kwon SY, Shin S, Emerson RE, Shin YH, et al. Targeting progesterone signaling prevents metastatic ovarian cancer. *Proc Natl Acad Sci USA.* (2020) 117:31993–2004. doi: 10.1073/pnas.2013595117
5. Zou Y, Henry WS, Ricq EL, Graham ET, Phadnis VV, Maretich P, et al. Plasticity of ether lipids promotes ferroptosis susceptibility and evasion. *Nature.* (2020) 585:603–8. doi: 10.1038/s41586-020-2732-8
6. Tesfay L, Paul BT, Konstorum A, Deng Z, Cox AO, Lee J, et al. Stearoyl-CoA desaturase 1 protects ovarian cancer cells from ferroptotic cell death. *Cancer Res.* (2019) 79:5355–66. doi: 10.1158/0008-5472.Can-19-0369
7. Drakes ML, Czerlanis CM, Stiff PJ. Immune checkpoint blockade in gynecologic cancers: state of affairs. *Cancers.* (2020) 12:3301. doi: 10.3390/cancers12113301
8. Friedmann Angeli JP, Krysko DV, Conrad M. Ferroptosis at the crossroads of cancer-acquired drug resistance and immune evasion. *Nat Rev Cancer.* (2019) 19:405–14. doi: 10.1038/s41568-019-0149-1
9. Wang W, Green M, Choi JE, Gijón M, Kennedy PD, Johnson JK, et al. CD8(+) T cells regulate tumour ferroptosis during cancer immunotherapy. *Nature.* (2019) 569:270–4. doi: 10.1038/s41586-019-1170-y
10. Wilkerson MD, Hayes DN. ConsensusClusterPlus: a class discovery tool with confidence assessments and item tracking. *Bioinformatics.* (2010) 26:1572–3. doi: 10.1093/bioinformatics/btq170
11. Lamb J, Crawford ED, Peck D, Modell JW, Blat IC, Wrobel MJ, et al. The connectivity map: using gene-expression signatures to connect small molecules, genes, and disease. *Science.* (2006) 313:1929–35. doi: 10.1126/science.1132939
12. Bindea G, Mlecnik B, Tosolini M, Kirilovsky A, Waldner M, Obenauf AC, et al. Spatiotemporal dynamics of intratumoral immune cells reveal the immune landscape in human cancer. *Immunity.* (2013) 39:782–95. doi: 10.1016/j.immuni.2013.10.003
13. Yang W, Soares J, Greninger P, Edelman EJ, Lightfoot H, Forbes S, et al. Genomics of drug sensitivity in cancer (GDSC): a resource for therapeutic biomarker discovery in cancer cells. *Nucleic Acids Res.* (2013) 41:D955–61. doi: 10.1093/nar/gks1111
14. Geeleher P, Cox N, Huang RS. pRRophetic: an R package for prediction of clinical chemotherapeutic response from tumor gene expression levels. *PLoS ONE.* (2014) 9:e107468. doi: 10.1371/journal.pone.0107468
15. Friedman J, Hastie T, Tibshirani R. Regularization paths for generalized linear models via coordinate descent. *J Stat Softw.* (2010) 33:1–22.
16. Tang R, Xu J, Zhang B, Liu J, Liang C, Hua J, et al. Ferroptosis, necroptosis, and pyroptosis in anticancer immunity. *J Hematol Oncol.* (2020) 13:110. doi: 10.1186/s13045-020-00946-7
17. Basuli D, Tesfay L, Deng Z, Paul B, Yamamoto Y, Ning G, et al. Iron addiction: a novel therapeutic target in ovarian cancer. *Oncogene.* (2017) 36:4089–99. doi: 10.1038/onc.2017.11
18. Zhang Q, Wang C, Cliby WA. Cancer-associated stroma significantly contributes to the mesenchymal subtype signature of serous ovarian cancer. *Gynecol Oncol.* (2019) 152:368–74. doi: 10.1016/j.ygyno.2018.11.014
19. De Nola R, Menga A, Castegna A, Loizzi V, Ranieri G, Cicinelli E, et al. The crowded crosstalk between cancer cells and stromal microenvironment in gynecological malignancies: biological pathways and therapeutic implication. *Int J Mol Sci.* (2019) 20:2401. doi: 10.3390/ijms20102401
20. Yang Z, Yang X, Xu S, Jin P, Li X, Wei X, et al. Reprogramming of stromal fibroblasts by SNAI2 contributes to tumor desmoplasia and ovarian cancer progression. *Mol Cancer.* (2017) 16:163. doi: 10.1186/s12943-017-0732-6
21. Kim K, Park S, Park SY, Kim G, Park SM, Cho JW, et al. Single-cell transcriptome analysis reveals TOX as a promoting factor for T cell exhaustion and a predictor for anti-PD-1 responses in human cancer. *Genome Med.* (2020) 12:22. doi: 10.1186/s13073-020-00722-9
22. Dai E, Han L, Liu J, Xie Y, Kroemer G, Klionsky DJ, et al. Autophagy-dependent ferroptosis drives tumor-associated macrophage polarization via release and uptake of oncogenic KRAS protein. *Autophagy.* (2020) 16:2069–83. doi: 10.1080/15548627.2020.1714209
23. Yee PP, Wei Y, Kim SY, Lu T, Chih SY, Lawson C, et al. Neutrophil-induced ferroptosis promotes tumor necrosis in glioblastoma progression. *Nat Commun.* (2020) 11:5424. doi: 10.1038/s41467-020-19193-y
24. Zitvogel L, Kroemer G. Interferon-γ induces cancer cell ferroptosis. *Cell Res.* (2019) 29:692–3. doi: 10.1038/s41422-019-0186-z
25. Efimova I, Catanzaro E, Van der Meeren L, Turubanova VD, Hammad H, Mishchenko TA, et al. Vaccination with early ferroptotic cancer cells induces efficient antitumor immunity. *J Immunother Cancer.* (2020) 8:2. doi: 10.1136/jitc-2020-001369

26. Mou Y, Wang J, Wu J, He D, Zhang C, Duan C, et al. Ferroptosis, a new form of cell death: opportunities and challenges in cancer. *J Hematol Oncol.* (2019) 12:34. doi: 10.1186/s13045-019-0720-y
27. Yi J, Zhu J, Wu J, Thompson CB, Jiang X. Oncogenic activation of PI3K-AKT-mTOR signaling suppresses ferroptosis via SREBP-mediated lipogenesis. *Proc Natl Acad Sci USA*. (2020) 117:31189–97. doi: 10.1073/pnas.2017152117
28. Guo J, Xu B, Han Q, Zhou H, Xia Y, Gong C, et al. Ferroptosis: a novel anti-tumor action for cisplatin. *Cancer Res Treat.* (2018) 50:445–60. doi: 10.4143/crt.2016.572
29. Xu PF, Yang JA, Liu JH, Yang X, Liao JM, Yuan FE, et al. PI3Kβ inhibitor AZD6482 exerts antiproliferative activity and induces apoptosis in human glioblastoma cells. *Oncol Rep*. (2019) 41:125–32. doi: 10.3892/or.2018.6845
30. Itamochi H, Nishimura M, Oumi N, Kato M, Oishi T, Shimada M, et al. Checkpoint kinase inhibitor AZD7762 overcomes cisplatin resistance in clear cell carcinoma of the ovary. *Int J Gynecol Cancer.* (2014) 24:61–9. doi: 10.1097/igc.0000000000000014
31. Pétigny-Lechartier C, Duboc C, Jebahi A, Louis MH, Abeilard E, Denoyelle C, et al. The mTORC1/2 inhibitor AZD8055 strengthens the efficiency of the MEK inhibitor trametinib to reduce the Mcl-1/[Bim and Puma] ratio and to sensitize ovarian carcinoma cells to ABT-737. *Mol Cancer Ther.* (2017) 16:102–15. doi: 10.1158/1535-7163.Mct-16-0342
32. Li X, Tang M. Exosomes released from M2 macrophages transfer miR-221-3p contributed to EOC progression through targeting CDKN1B. *Cancer Med.* (2020) 9:5976–88. doi: 10.1002/cam4.3252
33. Mao TL, Fan KF, Liu CL. Targeting the CXCR4/CXCL12 axis in treating epithelial ovarian cancer. *Gene Ther.* (2017) 24:621–9. doi: 10.1038/gt.2017.69

Conflict of Interest: The authors declare that the research was conducted in the absence of any commercial or financial relationships that could be construed as a potential conflict of interest.

Copyright © 2021 Zhang, Xi, Huang and Zeng. This is an open-access article distributed under the terms of the Creative Commons Attribution License (CC BY). The use, distribution or reproduction in other forums is permitted, provided the original author(s) and the copyright owner(s) are credited and that the original publication in this journal is cited, in accordance with accepted academic practice. No use, distribution or reproduction is permitted which does not comply with these terms.

frontiers in Medicine

ORIGINAL RESEARCH
published: 05 March 2021
doi: 10.3389/fmed.2021.642615

C3AR1 mRNA as a Potential Therapeutic Target Associates With Clinical Outcomes and Tumor Microenvironment in Osteosarcoma

Tiannan Zou[1,2,3], *Weibing Liu*[1], *Zeyu Wang*[1,3], *Jiayu Chen*[1,3], *Sheng Lu*[1,2,3], *Kun Huang*[1,3]* *and Weichao Li*[1,2,3]*

[1] Department of Orthopedic Surgery, The First People's Hospital of Yunnan Province, Affiliated Hospital of Kunming University of Science and Technology, Kunming, China, [2] Faculty of Medical Science, Kunming University of Science and Technology, Kunming, China, [3] Yunnan Key Laboratory of Digital Orthopaedics, Kunming, China

OPEN ACCESS

Edited by:
Fu Wang,
Xi'an Jiaotong University, China

Reviewed by:
Fengbiao Mao,
University of Michigan, United States
Yuwei Wang,
Macau University of Science and Technology, Macau
Chaoyun Pan,
Sun Yat-Sen University, China

***Correspondence:**
Kun Huang
hkkhgk@126.com
Weichao Li
liweichao0394@sina.com

Specialty section:
This article was submitted to Precision Medicine, a section of the journal Frontiers in Medicine

Received: *16 December 2020*
Accepted: *01 February 2021*
Published: *05 March 2021*

Citation:
Zou T, Liu W, Wang Z, Chen J, Lu S, Huang K and Li W (2021) C3AR1 mRNA as a Potential Therapeutic Target Associates With Clinical Outcomes and Tumor Microenvironment in Osteosarcoma. Front. Med. 8:642615. doi: 10.3389/fmed.2021.642615

Objective: Targeting cancer-specific messenger RNAs (mRNAs) may offer novel insights into therapeutic strategies in osteosarcoma. This study aimed to discover possible osteosarcoma-specific mRNA and probe its biological functions.

Methods: Based on mRNA-seq data from the TARGET database, stromal and immune scores were estimated for each osteosarcoma sample via the ESTIMATE algorithm. Stromal and immune mRNAs were obtained via integration of differentially expressed mRNAs between high and low stromal / immune score groups. Among hub and prognostic mRNAs, C3AR1 mRNA was focused and its prognostic value was assessed. The associations between C3AR1 mRNA and immune cells were analyzed via the CIBERSORT algorithm. Its expression was verified in osteosarcoma tissues and cells by RT-qPCR and western blot. The functions of C3AR1 were investigated by a series of experiments.

Results: Low stromal and immune scores were both indicative of unfavorable outcomes for osteosarcoma patients. Eighty-eight up-regulated and seven down-regulated stromal and immune mRNAs were identified. Among 30 hub mRNAs, low expression of C3AR1 mRNA indicated worse outcomes than its high expression. There was a lower mRNA expression of C3AR1 in metastatic than non-metastatic osteosarcoma. C3AR1 mRNA was closely correlated to various immune cells such as macrophages. C3AR1 was verified to be down-regulated in osteosarcoma tissues and cells. Its overexpression suppressed proliferation, migration and invasion and induced apoptosis in osteosarcoma cells.

Conclusion: C3AR1 mRNA could be a promising therapeutic target for osteosarcoma, linked with prognosis and tumor microenvironment.

Keywords: osteosarcoma, C3AR1, mRNA, therapeutic target, prognosis, tumor immune microenvironment

INTRODUCTION

Osteosarcoma, as a common malignant bone cancer, is prevailing in childhood and adolescence (1). It has a characteristic of immortal cell proliferation as well as high levels of mRNA translation (2). The main treatment approaches are composed of neoadjuvant chemotherapy, surgery as well as adjuvant chemotherapy (3). It remains unaltered for therapy and prognosis of osteosarcoma in the past 30 years. The 5-year survival rate is over 60% among all cases (4). Nevertheless, for advanced osteosarcoma, the effects of emerging therapies like targeted therapy and immunotherapy are unfavorable (4). Thus, it is of significance for exploiting novel therapies or available signatures to prolong the survival time of osteosarcoma patients.

Growing evidence has emphasized that mRNAs are feasible therapeutic targets in cancer therapy (5). Alterations in abundant cancer-specific mRNAs may activate oncogenes and inactivate tumor-suppressor genes, thereby facilitating tumor progression (5). The concept about RNA-targeted therapy was put forward in 1978. Since there are no risks of insertion mutagenesis, it is attractive to use mRNAs in place of DNAs as therapeutic substances (6). In comparison to protein or peptide delivery, mRNAs can extend the practicality of effective molecules (7). It is challenging to develop the effective therapy without adverse effects in cancers. Hence, it is of significance to understand the functional implications of cancer-specific mRNAs in osteosarcoma biology.

Tumor microenvironment is composed of immune and stromal cells. Stromal and immune mRNAs are critical factors for prognosis of osteosarcoma (4). Therefore, the comprehensive analysis of the correlation between immune-related gene signatures and overall survival may shed light on pathogenesis of osteosarcoma. Manipulating the tumor immune microenvironment may be a key part of various therapeutic applications for cancers (8). Nucleic acid-based approaches particularly mRNA is required and exploited for immunotherapies. *In vivo* research has offered attractive demonstrations concerning the feasibility of mRNA-based immunotherapy (9, 10). Herein, we identified a novel stromal and immune prognostic mRNA, which could be a promising therapeutic target in osteosarcoma.

MATERIALS AND METHODS

Data Acquisition and Preprocessing

mRNA-seq data and matched clinical information of osteosarcoma were downloaded from the TARGET database (https://ocg.cancer.gov/programs/target) on November 3, 2020. Genes that encode proteins were annotated using Homo sapiens gene annotation files from the Ensemble database (http://www.ensembl.org/index.html). Following removing samples without complete clinical information. Eighty-six osteosarcoma samples were obtained for this study. Sample information was merged with mRNA-seq.

Estimation of STromal and Immune Cells in MAlignant Tumor Tissues Using Expression Data

Stromal and immune levels were estimated for each osteosarcoma sample based on the mRNA-seq data using the ESTIMATE software (11). The stromal and immune cell scores were then calculated for each sample. All osteosarcoma samples were, respectively, separated into high and low stromal/immune cell score groups according to the median values. Kaplan-Meier curves were conducted for the survival time between groups and differences in survival probability were assessed via log-rank test using the Survminer package in R. The associations between stromal or immune cell scores and other clinicopathological characteristics including age, diagnosis, gender, race, primary tumor site and specific tumor site were estimated by Wilcoxon rank-sum test or Kruskal–Wallis test.

Differential Expression Analyses

To screen mRNAs related to stromal and immune scores, differential expression analyses were presented between high and low stromal or immune score groups. The criteria for differentially expressed mRNAs were as follows: $|\log 2$ fold change (FC)$| > 1$ and false discovery rate (FDR) < 0.01. These mRNAs were visualized into heatmaps. Then, up- and down-regulated stromal and immune mRNAs were separately obtained.

Functional Annotation Analyses

Gene Ontology (GO) and Kyoto Encyclopedia of Genes and Genomes (KEGG) functional annotation analyses were presented based on differentially expressed stromal and immune mRNAs via the Database for Annotation, Visualization, and Integrated Discovery (DAVID; http://www.david.niaid.nih.gov) (12). GO terms were composed of biological process (BP), cellular component (CC), as well as molecular function (MF).

Protein-Protein Interaction

Differentially expressed stromal and immune mRNAs were imported into the Search Tool for the Retrieval of Interacting Genes Database (STRING) database (http://string-db.org/) (13). A PPI network was visualized by the Cytoscape software (https://cytoscape.org/) (14). Hub mRNAs were identified according to degrees.

Univariate Cox Regression Analysis

Univariate cox regression analysis was presented to analyze the associations between differentially expressed stromal and immune mRNAs and prognosis among osteosarcoma.

CIBERSORT

The infiltration levels of 22 immune cells in osteosarcoma samples were estimated by the CIBERSORT algorithm

Abbreviations: mRNAs, messenger RNAs; ESTIMATE, Estimation of STromal and Immune cells in MAlignant Tumor tissues using Expression data; FC, fold change; FDR, false discovery rate; GO, Gene Ontology; KEGG, Kyoto Encyclopedia of Genes and Genomes; DAVID, Database for Annotation, Visualization, and Integrated Discovery; BP, biological process; CC, cellular component; MF, molecular function; PPI, protein-protein interaction; STRING, Search Tool for the Retrieval of Interacting Genes Database; GEPIA, Gene Expression Profiling Interactive Analysis.

(http://cibersort.stanford.edu/) (15). The differences in the infiltration levels of these immune cells were compared between osteosarcoma and normal samples via the Wilcoxon rank-sum test.

Osteosarcoma Tissues

Ten paired osteosarcoma and normal tissue specimens were collected from the Department of Orthopedic Surgery of The First People's Hospital of Yunnan Province (Kunming, China). This research followed the Declaration of Helsinki and gained the approval of the Ethics Committee of The First People's Hospital of Yunnan Province (2020048). All subjects provided written informed consent.

RT-qPCR

RNA extraction was achieved through TRIZOL reagent (Beyotime, Beijing, China). RNA was reverse transcribed into cDNA. qPCR was presented by SYBR Green Master kit (Roche, Switzerland). The primer sequences were as follows: C3AR1, 5′-CCCTACGGCAGGTTCCTATG-3′ (forward) and 5′-GACA GCGATCCAGGCTAATGG-3′ (reverse), GAPDH, 5′-ACAACT TTGGTATCGTGGAAGG-3′ (forward) and 5′-GCCATCACG

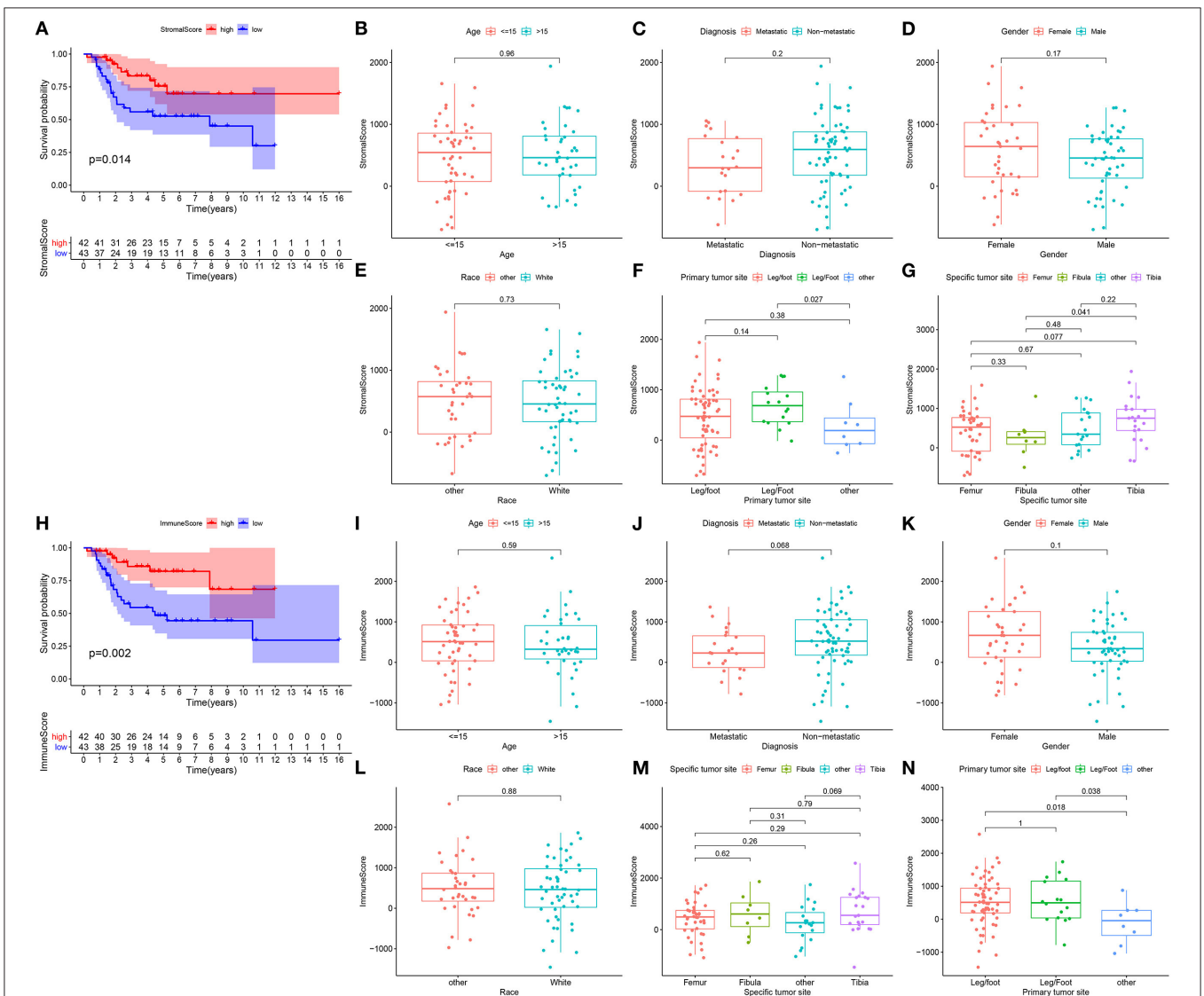

FIGURE 1 | Stromal and immune scores are correlated to prognosis and clinicopathological characteristics in osteosarcoma. **(A)** Kaplan-Meier of overall survival probability for high (red) and low (blue) stromal score osteosarcoma subgroups. **(B–G)** Box plots for the association between stromal score and clinicopathological characteristics including age **(B)**, metastasis **(C)**, gender **(D)**, race **(E)**, primary tumor site **(F)** and specific tumor site **(G)**. **(H)** Kaplan-Meier of overall survival probability for high (red) and low (blue) immune score groups. **(I–N)** Box plots for the association between immune score and clinicopathological characteristics including age **(I)**, metastasis **(J)**, gender **(K)**, race **(L)**, specific tumor site **(M)** and primary tumor site **(N)**.

CCACAGTTTC-3′ (reverse). C3AR1 expression was quantified with the $2^{-\Delta\Delta Ct}$ method.

Cell Culture and Transfection

Human osteosarcoma cell lines Saos-2 and U-2OS (ATCC, USA) and osteoblast hFOB 1.19 were cultured in RPMI-1640 medium plus 10% fetal bovine serum (FBS; Beyotime). Plasmid (Genepharma, Shanghai, China) and controls were utilized for overexpressing C3AR1. Saos-2 and U-2OS cells were transfected with 100 nM RNA oligonucleotides via Lipofectamine 2000 (Beyotime).

Western Blot

Total protein was extracted via RIPA buffer, which was evaluated by BCA kit (Beyotime). Samples were separated by SDS-PAGE and transferred onto PVDF membrane. Following being blocked, membrane was incubated by anti-C3AR1 (1:1,000; ab126250; Abcam, USA) or anti-GAPDH (1:1,000; ab8245) at 4°C overnight, followed by being probed with secondary antibody (1:5,000; ab7090). The protein bands were then visualized through ECL Plus substrate (Beyotime).

Clone Formation Assay

Transfected cells were grown in a 6-well plate (1×10^3/well) for 2 weeks. Following being washed by PBS, cells were fixed by paraformaldehyde and stained by 0.5% crystal violet. The images were observed under a microscope (Olympus, Japan).

Flow Cytometry

Cells were centrifuged at 2,000 g at 4°C. Then, supernatant samples were removed. Cells were suspended by binding buffer and incubated by Annexin V-FITC and propidium iodide. The apoptotic level was assessed via Annexin-V-FITC detection kits (Solarbio, Beijing, China) on flow cytometry.

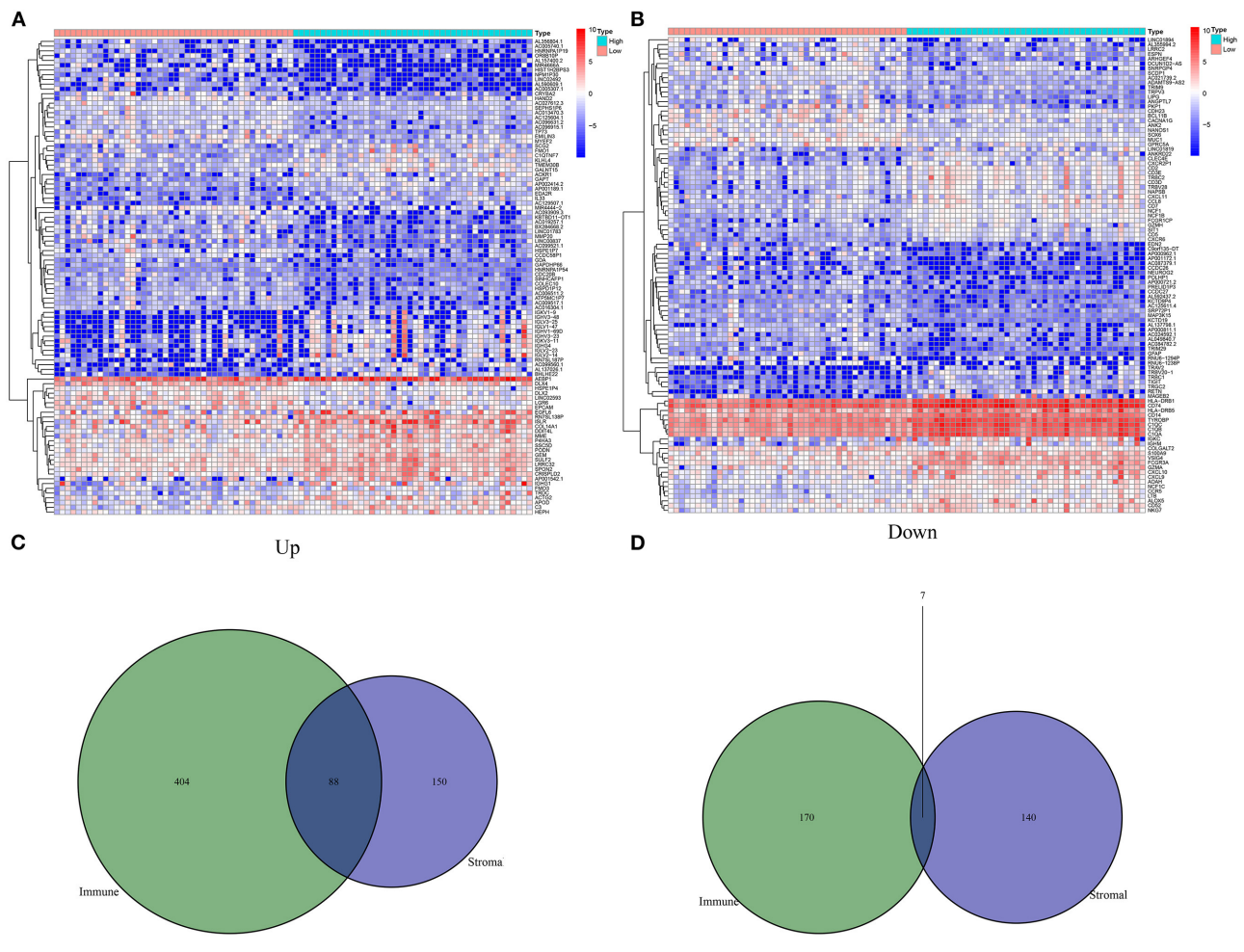

FIGURE 2 | Screening differentially expressed stromal and immune mRNAs in osteosarcoma. **(A)** Heat map for differentially expressed mRNAs between high and low stromal score groups. **(B)** Heat map for differentially expressed mRNAs between high and low immune score groups. **(C)** Venn diagram for up-regulated stromal and immune mRNAs. **(D)** Venn diagram for down-regulated stromal and immune mRNAs.

Scratch Assay

Transfected cells were planted into a 6-well plate for 24 h. A mark perpendicular to the bottom was drawn. Cells were incubated by serum-free medium. After 0, 24, and 48 h, images were investigated under a microscope (Olympus, Japan).

Transwell Assay for Invasion

Transfected cells were seeded onto the upper chamber. Matrigel was added to transwell inserts lasting 2 h. FBS were added to the lower chamber. After 24 h, non-invasive cells were removed through a cotton swab. Invasive cells were stained by crystal violet.

Statistical Analysis

All analysis was conducted by R language or GraphPad Prism software. The correlation between the levels of immune cells was analyzed by Spearson correlation analysis. Moreover, Spearson correlation analysis was presented whether C3AR1 mRNA expression exhibited associations with the levels of immune cells. $|r| \geq 0.8$ suggests an extremely strong correlation between the two variables; $0.6 \leq |r| < 0.8$ indicates strong correlation; $0.4 \leq |r| < 0.6$ indicates moderate correlation; $0.2 \leq |r| < 0.4$ represents a weak correlation; $|r| < 0.2$ shows extremely weak. For experiments, data were expressed as mean ± standard deviation. Comparisons between groups were analyzed by student's *t*-test or one-way analysis of variance. $P < 0.05$ was statistically significant.

RESULTS

Stromal and Immune Scores Closely Link With Clinical Outcomes and Clinicopathological Characteristics in Osteosarcoma

In this study, we estimated the stromal and immune scores for each osteosarcoma sample from the TARGET database via the ESTIMATE algorithm. As depicted in Kaplan-Meier curves, patients with low stromal scores experienced poorer survival time than those with high scores ($p = 0.014$; **Figure 1A**). The association between stromal scores and clinicopathological characteristics was probed in depth. No significant differences between stromal scores and age ($p = 0.96$; **Figure 1B**), metastasis ($p = 0.2$; **Figure 1C**), gender ($p = 0.17$; **Figure 1D**) and race ($p = 0.73$; **Figure 1E**) were detected between high and low stromal score patients. There was a distinct difference in stromal levels among primary tumor sites (**Figure 1F**). For specific tumor sites, stromal scores were markedly elevated in tibia than fibular ($p = 0.041$; **Figure 1G**). Meanwhile, we analyzed the clinical implications of immune scores in osteosarcoma. In **Figure 1H**, high immune scores indicated prolonged survival time than

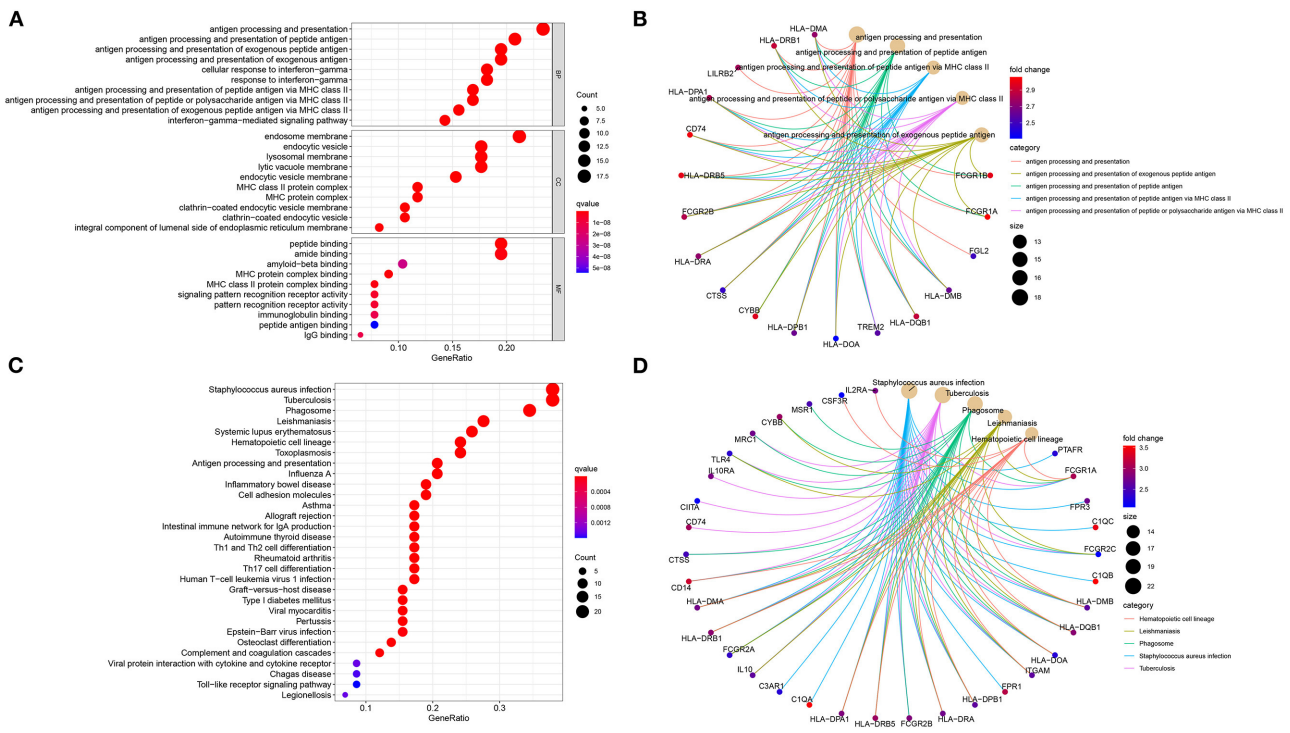

FIGURE 3 | Biological functions of stromal and immune mRNAs. **(A)** The top ten biological processes (BP) cellular components (CC) and molecular functions (MF), respectively. **(B)** The top five biological processes and enriched mRNAs. **(C)** Bubble chart for the top 30 signaling pathways. **(D)** The top five KEGG pathways and enriched mRNAs.

low immune scores ($p = 0.002$). There was no significance in age ($p = 0.59$; **Figure 1I**), metastasis ($p = 0.068$; **Figure 1J**), gender ($p = 0.1$; **Figure 1K**), race ($p = 0.88$; **Figure 1L**) and specific tumor sites (**Figure 1M**) between high and low immune score groups. Among different primary tumor sites, immune scores were statistically significant (**Figure 1N**). Above findings revealed the clinical implications of stromal and immune scores in osteosarcoma.

Differentially Expressed Stromal and Immune mRNAs in Osteosarcoma

With the cutoff of |log 2 FC| > 1 and FDR < 0.01, 385 differentially expressed stromal mRNAs were screened between high and low stromal score groups (**Figure 2A**). Meanwhile, 669 immune mRNAs were dysregulated between high and low immune score groups (**Figure 2B**). Because both stromal and immune score exhibited important clinical implications, we focused on the analysis of stromal and immune mRNAs. Following overlapping above two lists of mRNAs, we obtained 88 up-regulated stromal and immune mRNAs (**Figure 2C**). Additionally, 7 down-regulated stromal and immune mRNAs were acquired in osteosarcoma (**Figure 2D**). **Supplementary Table 2** listed all abnormally expressed stromal and immune mRNAs. These mRNAs could be linked with stromal and immune levels in osteosarcoma.

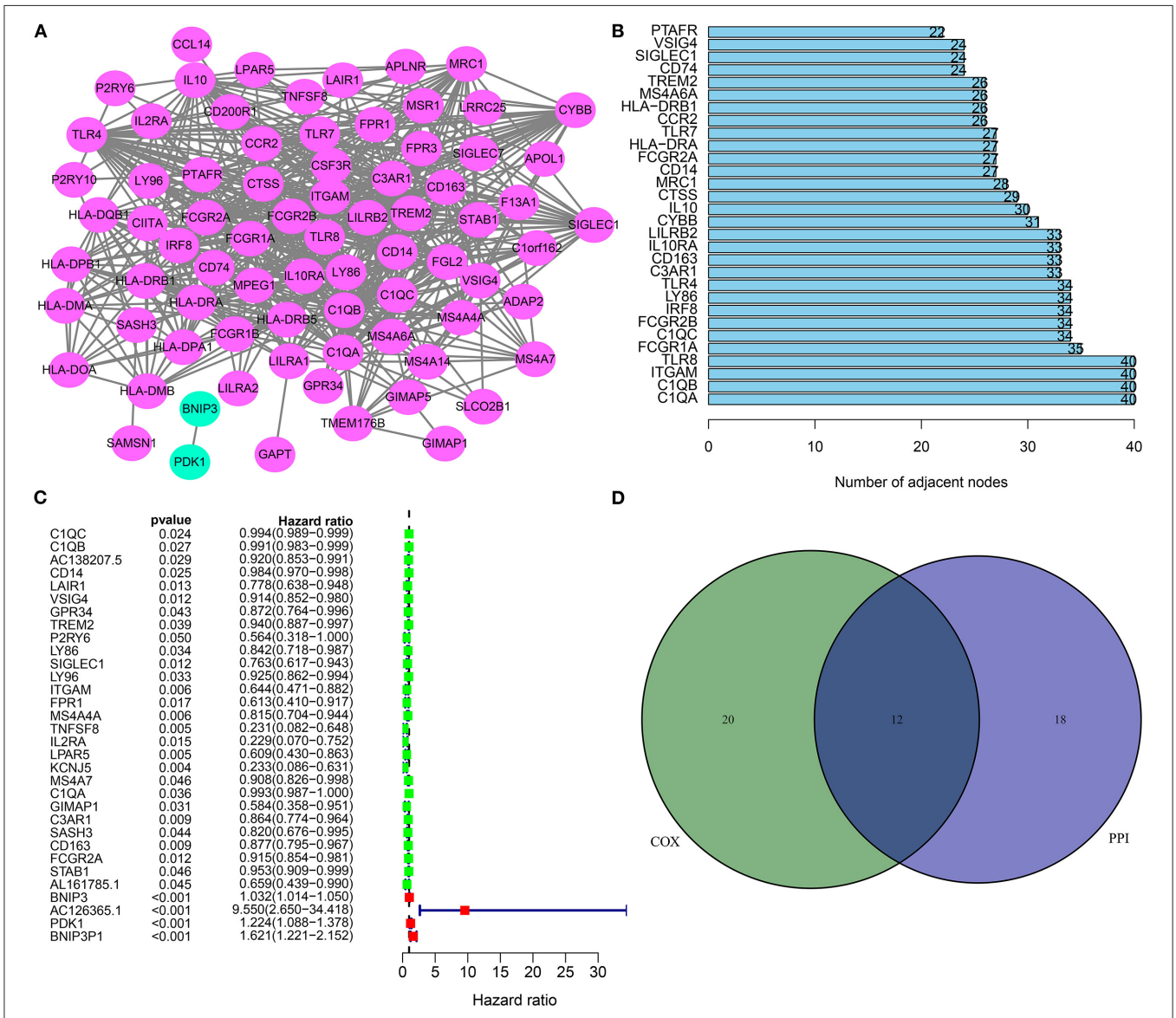

FIGURE 4 | Hub and prognosis-related mRNAs for osteosarcoma. **(A)** A PPI network based on differentially expressed stromal and immune mRNAs. **(B)** The 30 hub genes according to degrees. **(C)** Forest diagram for 32 prognosis-related stromal and immune mRNAs according to univariate cox regression analysis. **(D)** Venn diagram for 12 hub and prognosis-related stromal and immune mRNAs.

Biological Functions of Stromal and Immune mRNAs

The functional functions of stromal and immune mRNAs were probed in depth. GO enrichment analysis suggested that these mRNAs were distinctly enriched in antigen processing and presentation-related processes (**Figure 3A**). Furthermore, they were involved in MHC protein complex formation and had the MHC protein complex binding molecular function. **Figure 3B** showed the most enriched biological processes and corresponding mRNAs. As depicted in the KEGG enrichment analysis, immune-related pathways were distinctly enriched such as hematopoietic cell lineage, phagosome, antigen processing and presentation, Th1, Th2, and Th17 cell differentiations (**Figures 3C,D**). Hence, these mRNAs could participate in modulating immune pathways in osteosarcoma.

Hub and Prognostic mRNAs for Osteosarcoma

Based on these stromal and immune mRNAs, a PPI network was established, as shown in **Figure 4A**. There were 77 nodes in the network. Among them, 76 mRNAs were up-regulated in high stromal and immune score group. **Figure 4B** listed the top 30 mRNAs according to degrees, which were considered as hub mRNAs. Univariate cox regression analysis showed that 32 stromal and immune mRNAs had significant correlations to prognosis of osteosarcoma (**Figure 4C**). After integration of hub mRNAs and prognosis-related mRNAs, we obtained 12 hub and

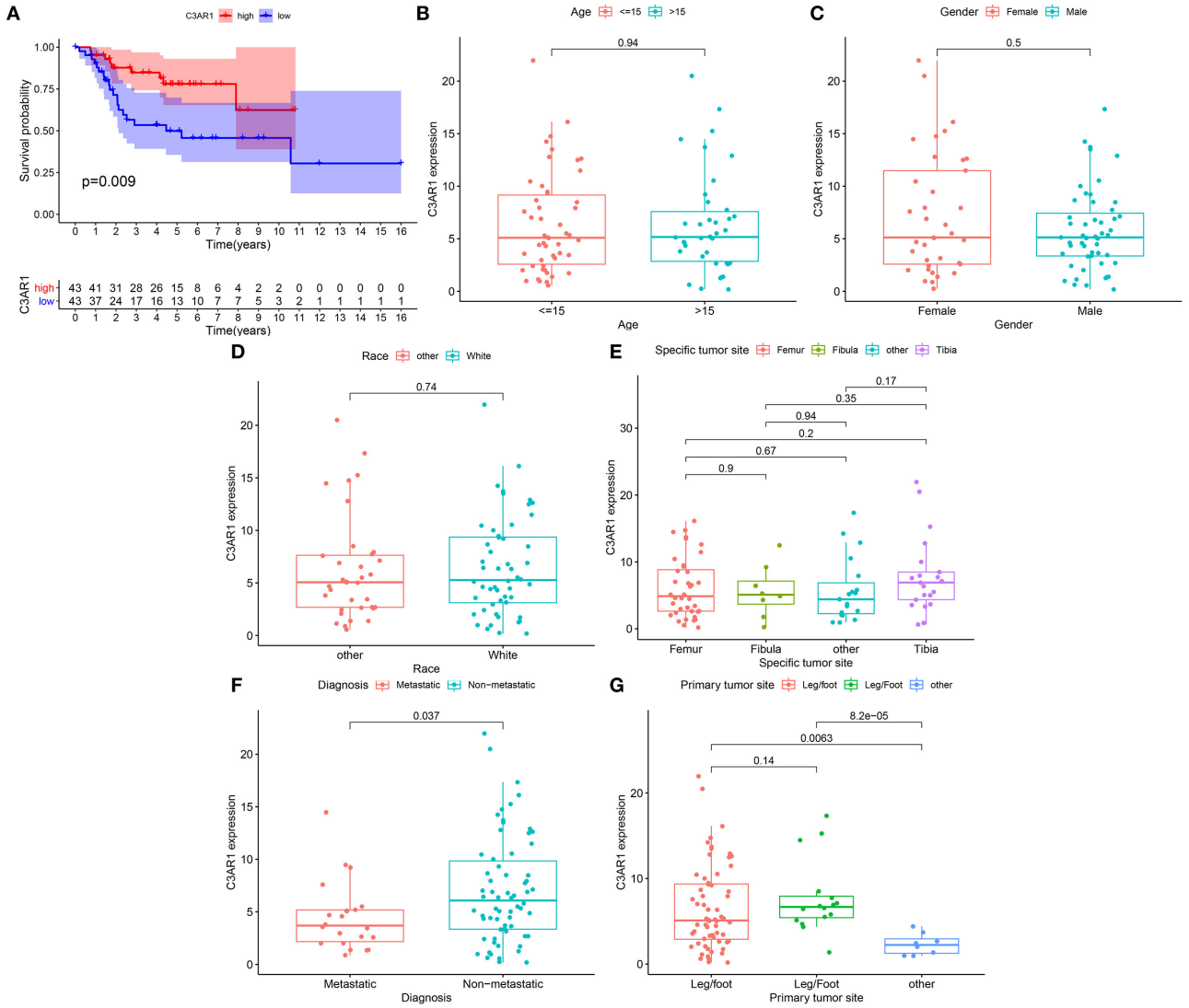

FIGURE 5 | Association between C3AR1 mRNA expression and prognosis and clinicopathological characteristics among osteosarcoma. **(A)** Kaplan-Meier of overall survival between high (red) and low (blue) C3AR1 mRNA expression osteosarcoma groups. **(B–G)** The association between C3AR1 mRNA expression and age **(B)**, gender **(C)**, race **(D)**, specific tumor site **(E)**, metastasis **(F)** and primary tumor sites **(G)**.

prognosis-related mRNAs (C1QA, C1QB, ITGAM, C1QC, LY86, C3AR1, CD163, CD14, FCGR2A, TREM2, SIGLEC1, and VSIG4) for osteosarcoma (**Figure 4D**), which could play key roles in osteosarcoma progression.

Low C3AR1 mRNA Expression Is Correlated to Poor Prognosis and Metastasis in Osteosarcoma

Our Kaplan-Meier curves showed that patients with high C3AR1 expression had prolonged survival time in comparison to those with its low expression ($p = 0.009$; **Figure 5A**). We analyzed the correlation between C3AR1 expression and clinicopathological characteristics among osteosarcoma patients. There was no significant correlation between C3AR1 expression and age (**Figure 5B**), gender (**Figure 5C**), race (**Figure 5D**), and specific tumor site (**Figure 5E**). C3AR1 expression was distinctly decreased in metastatic compared to non-metastatic osteosarcoma patients ($p = 0.037$; **Figure 5F**). Compared to others, there was a distinct difference in C3AR1 expression between primary tumor sites (**Figure 5G**). Thus, lowly expressed

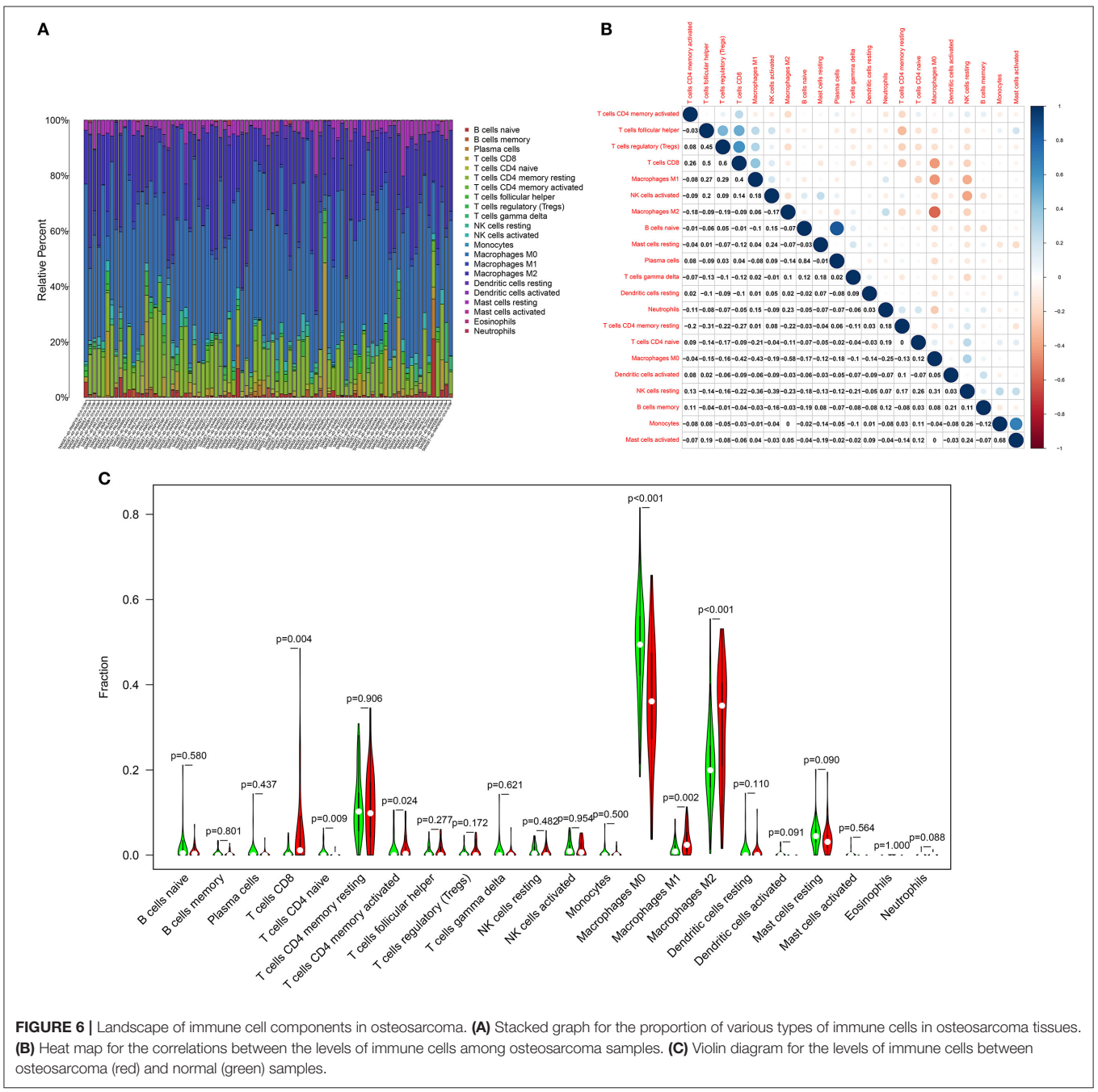

FIGURE 6 | Landscape of immune cell components in osteosarcoma. **(A)** Stacked graph for the proportion of various types of immune cells in osteosarcoma tissues. **(B)** Heat map for the correlations between the levels of immune cells among osteosarcoma samples. **(C)** Violin diagram for the levels of immune cells between osteosarcoma (red) and normal (green) samples.

C3AR1 mRNA could be correlated to poor prognosis and metastasis in osteosarcoma.

Landscape of Immune Cell Components in Osteosarcoma

The CIBERSORT algorithm was utilized for examining the relative proportions of immune cells in each osteosarcoma specimen. **Figure 6A** showed the heterogeneity in levels of B cells naïve, B cells memory, plasma cells, T cells CD8, T cells CD4 naïve, T cells CD4 memory resting, T cells CD4 memory activated, T cells follicular helper, T cells regulatory (Tregs), T cells gamma delta, NK cells resting, NK cells activated, monocytes, macrophages M0, macrophages M1, macrophages M2, dendritic cells resting, dendritic cells activated, mast cells resting, mast cells activated, eosinophils and neutrophils among osteosarcoma tissues. Positive and negative correlations between immune cells were observed, as shown in **Figure 6B**. There was a strong correlation between mast cells activated and monocytes ($r = 0.68$) in osteosarcoma. Plasma cells were extremely strongly correlated with B cells naïve ($r = 0.84$). Macrophages M0 had

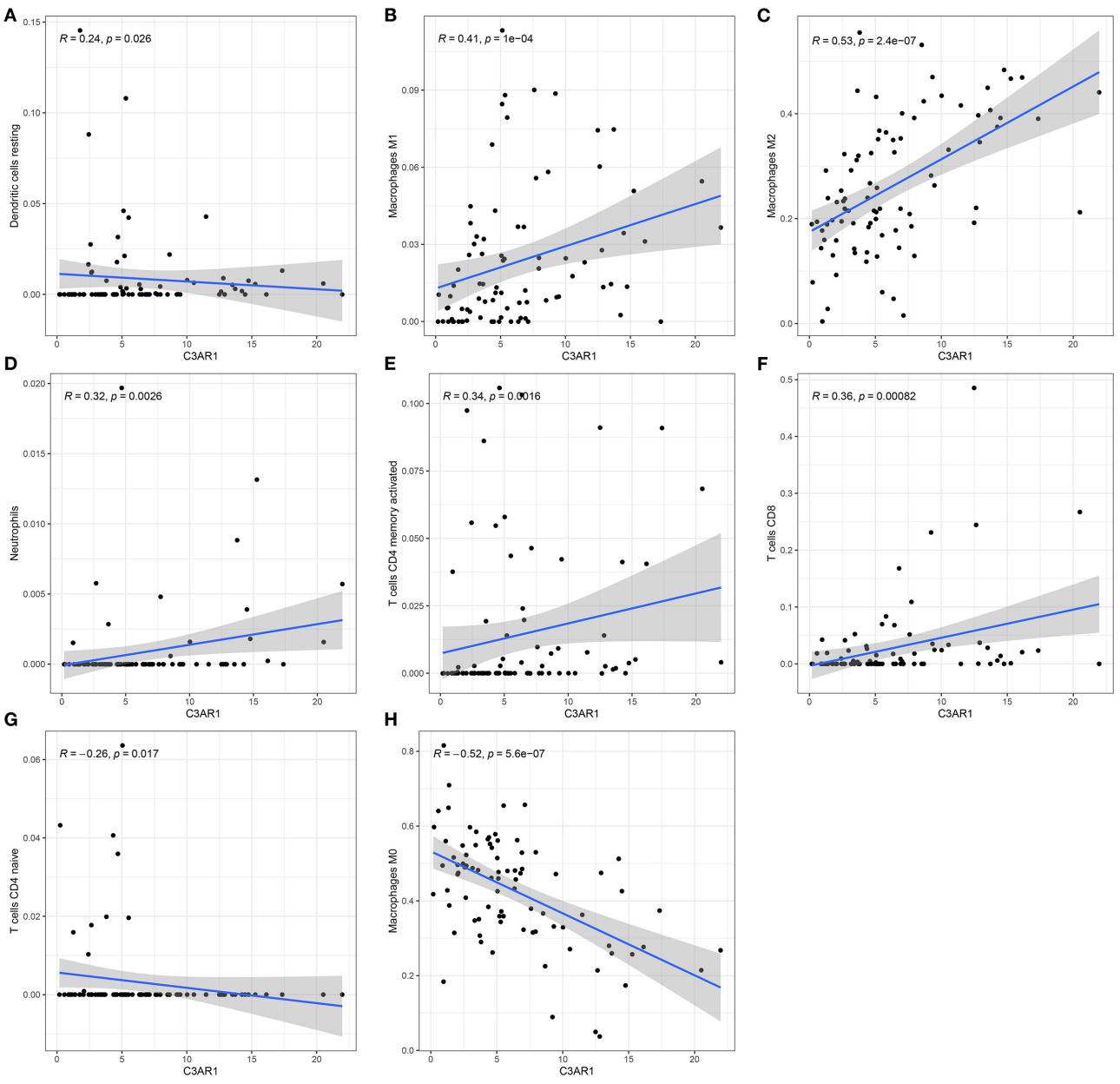

FIGURE 7 | C3AR1 mRNA expression associates with distinct kinds of immune cells in osteosarcoma. There were significant correlations between C3AR1 expression and **(A)** dendritic cells, **(B)** macrophages M1, **(C)** macrophages M2, **(D)** neutrophils, **(E)** T cells CD4 memory activated, **(F)** T cells CD8, **(G)** T cells CD4 naïve and **(H)** macrophages M0.

moderate and negative links with macrophages M2 ($r = -0.58$), macrophages M1 ($r = -0.43$), T cells CD8 ($r = -0.43$). T cells CD8 were positively and moderately linked with Tregs ($r = 0.6$) and T cells follicular helper ($r = 0.5$). Above correlation analysis between different kinds of immune cells revealed that there was the crosstalk between immune cells. We further analyzed the differences in immune cell levels between osteosarcoma and normal tissues. The data showed that the levels of T cells CD8 ($p = 0.004$), T cells CD4 memory activated ($p = 0.024$), macrophages M1 ($p = 0.002$) and macrophages M2 ($p < 0.001$) were markedly higher in osteosarcoma than normal tissues (**Figure 6C**). In contrast, T cells CD4 naïve ($p = 0.009$) and macrophages M0 ($p < 0.001$) had lowered levels in osteosarcoma compared to normal tissues.

C3AR1 mRNA Is Moderately Correlated With Tumor Immune Microenvironment in Osteosarcoma

The association between C3AR1 mRNA expression and immune cells was further analyzed. As a result, C3AR1 mRNA expression had a weak correlation with dendritic cells resting levels ($r = 0.24$, $p = 0.026$; **Figure 7A**). C3AR1 expression was moderately correlated to macrophages M1 ($r = 0.41$, $p = 1e\text{-}04$; **Figure 7B**) and macrophages M2 ($r = 0.53$, $p = 2.4e\text{-}07$; **Figure 7C**). Meanwhile, there were weak associations between C3AR1 expression and neutrophils ($r = 0.32$; $p = 0.0026$; **Figure 7D**), T cells CD4 memory activated ($r = 0.34$; $p = 0.0016$; **Figure 7E**), and T cells CD8 ($r = 0.36$; $p = 0.00082$; **Figure 7F**). A weak negative correlation between C3AR1 expression and T cells CD4 naïve levels was found among osteosarcoma samples ($r = -0.26$; $p = 0.0017$; **Figure 7G**). In **Figure 7H**, C3AR1 expression was moderately and negatively associated with macrophages M0 ($r = -0.52$; $p = 5.6e\text{-}07$). Collectively, C3AR1 expression may associate with tumor immune microenvironment in osteosarcoma.

Down-Regulation of C3AR1 in Osteosarcoma

C3AR1 was further verified in osteosarcoma tissues and cells. Our data confirmed that C3AR1 mRNA (**Figure 8A**) and protein (**Figures 8B,C**) were both lowered in cancer than normal tissue specimens (both $p < 0.0001$). Also, its down-regulation was detected in osteosarcoma cells (Saos-2 and U-2OS) compared to normal osteoblast hFOB 1.19 cells (**Figure 8D**; both $p < 0.0001$). To investigate the biological functions of C3AR1, it was successfully overexpressed in Saos-2 and U-2OS cells (**Figures 8E,F**; both $p < 0.0001$).

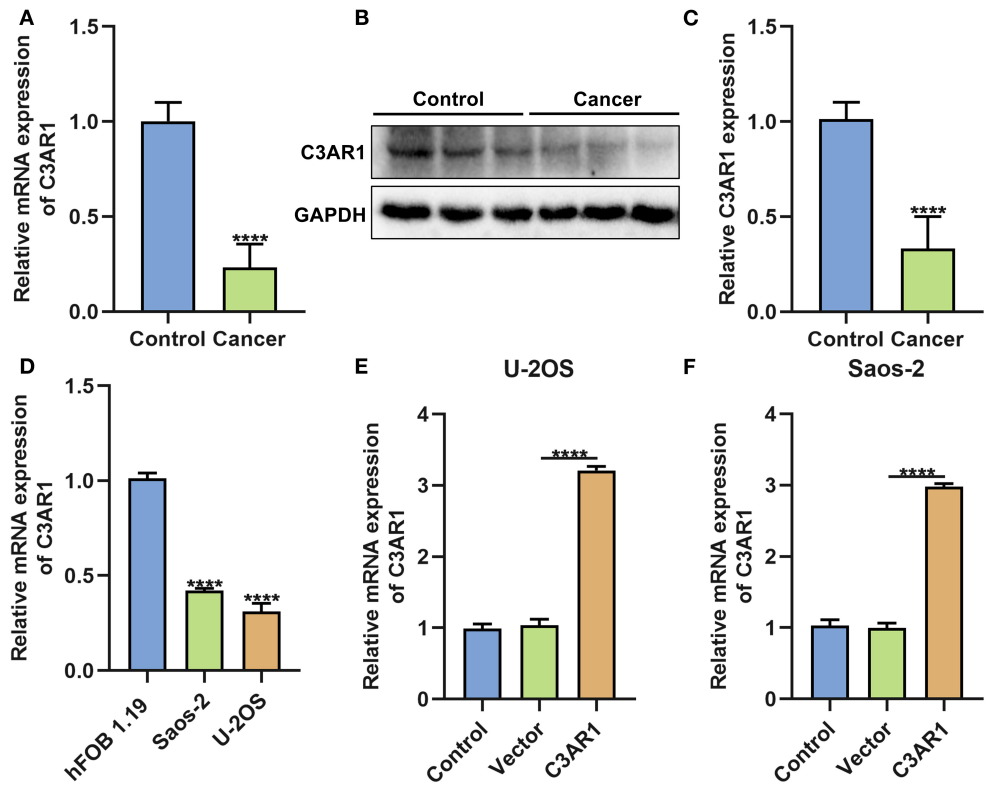

FIGURE 8 | C3AR1 down-regulation in osteosarcoma. **(A)** RT-qPCR and **(B,C)** western blot for C3AR1 expression in osteosarcoma and control tissue specimens. **(D)** RT-qPCR for C3AR1 expression in osteosarcoma cell lines Saos-2 and U-2OS and osteoblast hFOB 1.19. **(E,F)** RT-qPCR for C3AR1 expression in Saos-2 and U-2OS cells after overexpressing C3AR1. ****$p < 0.0001$.

C3AR1 Overexpression Suppresses Proliferation and Induces Apoptosis in Osteosarcoma Cells

After overexpressing C3AR1, proliferation and apoptosis of osteosarcoma cells were evaluated. We found that C3AR1 overexpression distinctly reduced number of colonies of Saos-2 ($p < 0.0001$) and U-2OS cells ($p < 0.01$; **Figures 9A–C**). Moreover, apoptotic levels were markedly lessened following overexpressing C3AR1 for Saos-2 ($p < 0.01$) and U-2OS cells ($p < 0.05$; **Figures 9D–F**).

C3AR1 Overexpression Inhibits Migration and Invasion of Osteosarcoma Cells

Migrated and invasive capacities of osteosarcoma cells were observed after overexpressing C3AR1. This study showed that wound distance was markedly wider in Saos-2 ($p < 0.05$) and U-2OS cells ($p < 0.01$) transfected with C3AR1 overexpression (**Figures 10A–D**). Furthermore, C3AR1 overexpression decreased the number of invasive Saos-2 ($p < 0.001$) and U-2OS cells ($p < 0.01$; **Figures 10E–G**).

DISCUSSION

This study revealed the clinical implications of stromal and immune scores in osteosarcoma. We identified 12 critical stromal and immune mRNAs that exhibited tight correlations with outcomes of osteosarcoma. Among them, C3AR1 mRNA was associated with prognosis, metastasis, and tumor immune microenvironment in osteosarcoma. Hence, C3AR1 mRNA might be a promising therapeutic target for osteosarcoma.

The ESTIMATE algorithm has been used for various cancers, suggesting that it is effective and robust based on the expression profiles. Utilizing this algorithm, Ke et al. identified novel immune-related genes such as LINC01564, LINC02208 and ODAM for testicular cancer (16). Wang et al. developed a stromal and immune score-related gene signature composed of SOX9, LRRC32, CECR1, and MS4A4A for gastric cancer (17). Zhou et al. screened prognostic genes related to the tumor

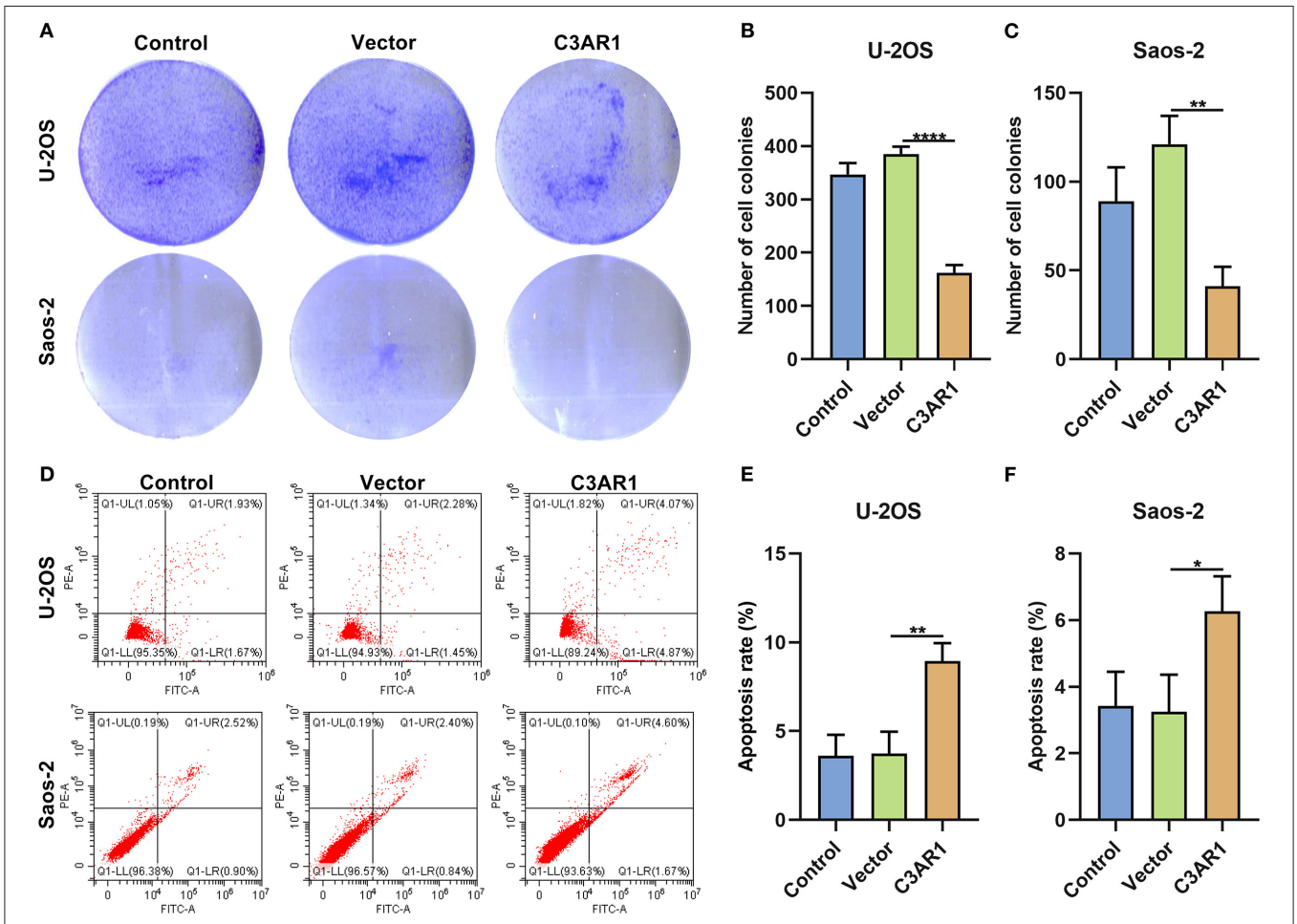

FIGURE 9 | C3AR1 overexpression suppresses proliferation and induces apoptosis in osteosarcoma cells. **(A–C)** Number of cell colonies of Saos-2 and U-2OS cells with C3AR1 overexpression. **(D–F)** Flow cytometry for apoptotic levels in Saos-2 and U-2OS cells with C3AR1 overexpression. *$p < 0.05$; **$p < 0.01$; ****$p < 0.0001$.

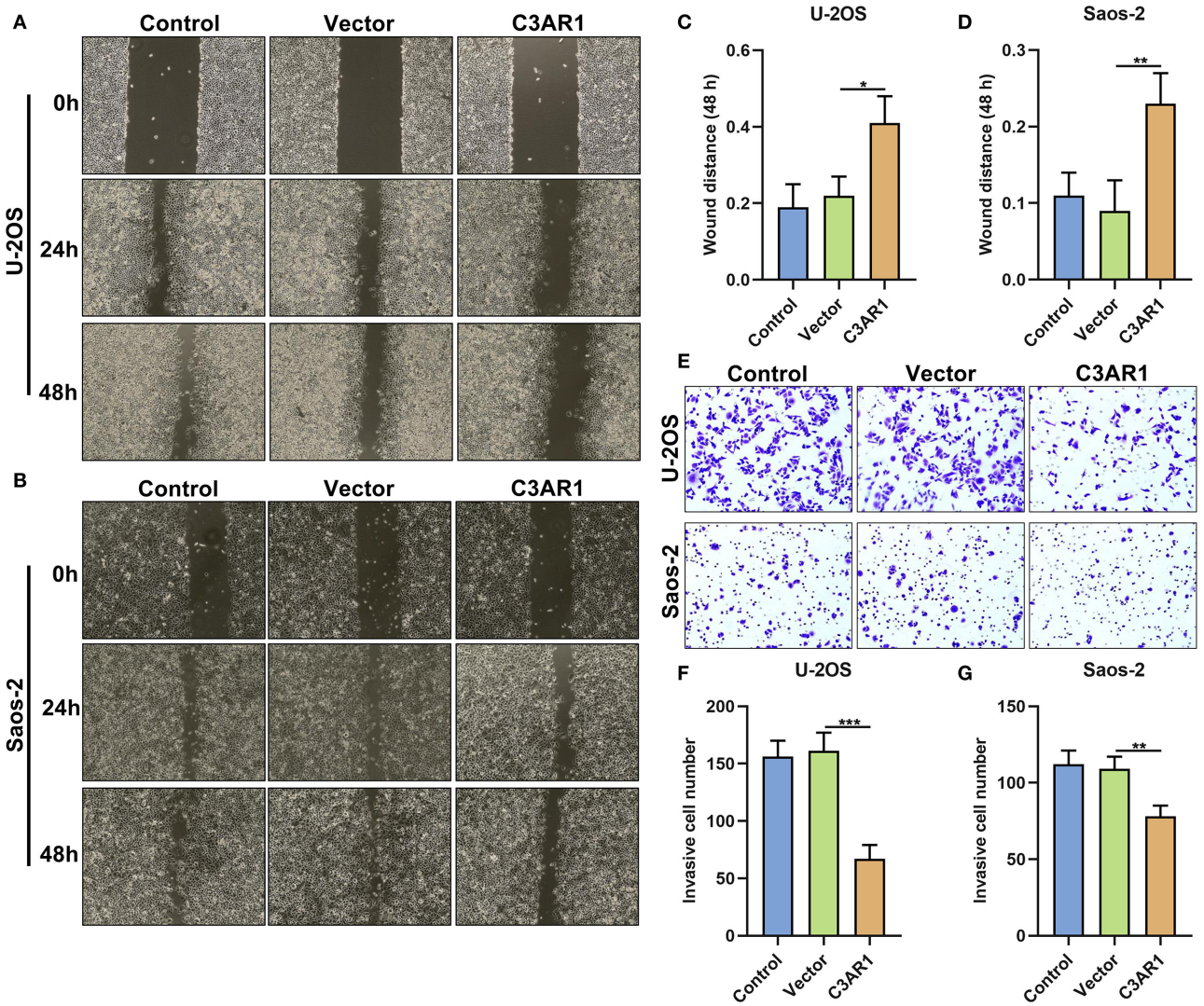

FIGURE 10 | C3AR1 overexpression reduces migration and invasion of osteosarcoma cells. **(A–D)** Assessment of wound distance of Saos-2 and U-2OS cells with C3AR1 overexpression. **(E–G)** Number of invasive Saos-2 and U-2OS cells with C3AR1 overexpression. *$p < 0.05$; **$p < 0.01$; ***$p < 0.001$.

microenvironment in stomach adenocarcinoma (18). Herein, we estimated stromal and immune levels based on the ESTIMATE algorithm. Our results showed that stromal and immune scores were both linked with outcomes for osteosarcoma patients. Consistent with a previous study, high stromal and immune scores were both indicative of prolonged survival time (18). These data demonstrated that tumor microenvironment exhibited a distinct correlation with prognosis of osteosarcoma.

Eighty-eight up- and seven down-regulated stromal and immune mRNAs were identified in osteosarcoma. They were mainly involved in several immune pathways such as antigen processing and presentation, MHC protein complex, Th1, Th2, and Th17 cell differentiation and the like. For instance, antigen presentation may be decreased in osteosarcoma than healthy bones (19). We established a PPI network based on these stromal and immune mRNAs. Thirty hub mRNAs were screened. Among them, 12 mRNAs were distinctly correlated to outcomes of osteosarcoma patients. We found that C3AR1 mRNA could be a predictive factor for prognosis of osteosarcoma patients. After validation, C3AR1 was down-regulated in osteosarcoma tissues and cells. As previous studies, C3AR1 mRNA overexpression in the early stages of acute myeloid leukemia could predict shorter survival time (20). Furthermore, it is involved in ductal carcinoma *in situ* progression (21). C3AR1 is a hub mRNA for multiple myeloma (22), colon cancer (23) and melanoma (24). C3AR1 may predict chemotherapy resistance and outcomes of soft tissue sarcomas (25). Metastatic osteosarcoma leads to poor clinical outcomes, especially lung metastases. The 5-year survival rates are <30% toward patients with osteosarcoma metastasized to lungs (26). Increasing evidence has highlighted that the

biological drivers of metastatic phenotype of osteosarcoma have a distinction from primary tumors (27). Our data suggested that C3AR1 mRNA was closely linked with metastatic progression. Its overexpression suppressed proliferation, migration and invasion and induced apoptosis of osteosarcoma cells. Collectively, C3AR1 mRNA could be a prognostic marker for prognosis and metastasis in osteosarcoma.

The CIBERSORT algorithm was utilized for detection of the relative proportions of immune cells in each osteosarcoma specimen. As a previous study, utilizing the CIBERSORT algorithm, macrophages could be primary infiltrating immune cells in osteosarcoma samples, especially in macrophages M0 and M2 (28). Our data demonstrated that there were positive and negative correlations between immune cells in osteosarcoma. There was a strong correlation between mast cells activated and monocytes, between plasma cells and B cells naïve, between macrophages M0 and macrophages M2/M1, between T cells CD8 and Tregs/T cells follicular helper, indicating that there was the crosstalk between immune cells in tumor microenvironment. Furthermore, we found that the levels of T cells CD8, T cells CD4 memory activated, macrophages M1 and macrophages M2 were markedly higher in osteosarcoma than normal tissues. Oppositely, T cells CD4 naïve and macrophages M0 had lowered levels in osteosarcoma compared to normal tissues. These findings indicated that immune cell infiltrates could be linked with osteosarcoma progression.

Previously, C3AR1 is closely associated with immune responses. For example, C3AR1 is associated with immune infiltration in sepsis (29). Inactivated C3AR1 could reverse an abnormal immune network in Alzheimer's disease (30). Endothelial C3AR1 regulates vascular inflammatory response in aging or neurodegenerative diseases (31). Our results showed that C3AR1 mRNA expression had a weak correlation with dendritic cells resting levels. Moreover, it was moderately correlated to macrophages M1 and macrophages M2. C3AR1 is a major effector for macrophages-regulated fibrosing steatohepatitis (32). Meanwhile, there were weak associations between C3AR1 expression and neutrophils, T cells CD4 memory activated, and T cells CD8. It has been found that C3AR1 may control the mobilization of neutrophils after spinal cord damage (33). Autocrine or paracrine C3AR1 correlates Toll-like receptor 2 stimulation with maturation of dendritic cells, thereby promoting the response of effector T cells (34). Inactivation of C3AR1 suppresses expansion and differentiation for alloreactive T cells CD8 (35). There was a weak negative correlation between C3AR1 expression and T cells CD4 naïve levels in osteosarcoma samples. C3AR1 expression was moderately and negatively associated with macrophages M0 levels. Hence, C3AR1 mRNA may be linked with tumor immune microenvironment in osteosarcoma.

Taken together, our study identified a novel stromal- and immune-related C3AR1 mRNA, which could be tightly correlated to outcomes of osteosarcoma patients. C3AR1 mRNA might be a feasible therapeutic target in osteosarcoma therapy.

CONCLUSION

This study showed that stromal and immune scores were distinctly correlated with prognosis of osteosarcoma. We further screened stromal and immune prognostic mRNAs. Among them, C3AR1 mRNA was focused, which was associated with outcomes and metastasis in osteosarcoma. Also, there was a closely correlation between C3AR1 mRNA and immune cells, indicating that C3AR1 mRNA could be involved in regulation of tumor immune microenvironment. Hence, C3AR1 mRNA could be an underlying therapeutic target for osteosarcoma.

DATA AVAILABILITY STATEMENT

The original contributions presented in the study are included in the article/**Supplementary Material**, further inquiries can be directed to the corresponding author/s.

ETHICS STATEMENT

The studies involving human participants were reviewed and approved by the Ethics Committee of The First People's Hospital of Yunnan Province (2020048). The patients/participants provided their written informed consent to participate in this study.

AUTHOR CONTRIBUTIONS

KH and WL conceived and designed the study. TZ and WL conducted most of the experiments and data analysis, and wrote the manuscript. ZW, JC, and SL participated in collecting data and helped to draft the manuscript. All authors contributed to the article and approved the submitted version.

FUNDING

This work was funded by The National Natural Science Foundation of China (81860240); The Basic Research Project of Yunnan Provincial Science and Technology (2018FB119); The Yunnan Provincial Science and Technology Department-Kunming Medical University Joint Special Project (2019FE001-123); The Talent Development Program of Yunnan Province (H-2018100).

SUPPLEMENTARY MATERIAL

The Supplementary Material for this article can be found online at: https://www.frontiersin.org/articles/10.3389/fmed.2021.642615/full#supplementary-material

Supplementary Table 1 | Clinical information of 86 osteosarcoma samples from the TARGET database.

Supplementary Table 2 | Differentially expressed stromal and immune mRNAs in osteosarcoma.

REFERENCES

1. Isakoff MS, Bielack SS, Meltzer P, Gorlick R. Osteosarcoma: current treatment and a collaborative pathway to success. *J Clin Oncol.* (2015) 33:3029–35. doi: 10.1200/JCO.2014.59.4895
2. Pal I, Safari M, Jovanovic M, Bates SE, Deng C. Targeting translation of mRNA as a therapeutic strategy in cancer. *Curr Hematol Malig Rep.* (2019) 14:219–27. doi: 10.1007/s11899-019-00530-y
3. Shankar GM, Clarke MJ, Ailon T, Rhines LD, Patel SR, Sahgal A, et al. The role of revision surgery and adjuvant therapy following subtotal resection of osteosarcoma of the spine: a systematic review with meta-analysis. *J Neurosurg Spine.* (2017) 27:97–104. doi: 10.3171/2016.12.SPINE16995
4. Wen C, Wang H, Wang H, Mo H, Zhong W, Tang J, et al. A three-gene signature based on tumour microenvironment predicts overall survival of osteosarcoma in adolescents and young adults. *Aging.* (2020) 13:619–45. doi: 10.18632/aging.202170
5. Desterro J, Bak-Gordon P, Carmo-Fonseca M. Targeting mRNA processing as an anticancer strategy. *Nat Rev Drug Discov.* (2020) 19:112–29. doi: 10.1038/s41573-019-0042-3
6. Dowdy SF. Overcoming cellular barriers for RNA therapeutics. *Nat Biotechnol.* (2017) 35:222–9. doi: 10.1038/nbt.3802
7. Barata P, Sood AK, Hong DS. RNA-targeted therapeutics in cancer clinical trials: current status and future directions. *Cancer Treat Rev.* (2016) 50:35–47. doi: 10.1016/j.ctrv.2016.08.004
8. Schlake T, Thess A, Thran M, Jordan I. mRNA as novel technology for passive immunotherapy. *Cell Mol Life Sci.* (2019) 76:301–28. doi: 10.1007/s00018-018-2935-4
9. An D, Schneller JL, Frassetto A, Liang S, Zhu X, Park JS, et al. Systemic messenger RNA therapy as a treatment for methylmalonic acidemia. *Cell Rep.* (2017) 21:3548–58. doi: 10.1016/j.celrep.2017.11.081
10. Prieve MG, Harvie P, Monahan SD, Roy D, Li AG, Blevins TL, et al. Targeted mRNA therapy for ornithine transcarbamylase deficiency. *Mol Ther.* (2018) 26:801–13. doi: 10.1016/j.ymthe.2017.12.024
11. Yoshihara K, Shahmoradgoli M, Martínez E, Vegesna R, Kim H, Torres-Garcia W, et al. Inferring tumour purity and stromal and immune cell admixture from expression data. *Nat Commun.* (2013) 4:2612. doi: 10.1038/ncomms3612
12. Dennis G Jr, Sherman BT, Hosack DA, Yang J, Gao W, Lane HC, et al. DAVID: database for annotation, visualization, and integrated discovery. *Genome Biol.* (2003) 4:P3. doi: 10.1186/gb-2003-4-5-p3
13. Szklarczyk D, Morris JH, Cook H, Kuhn M, Wyder S, Simonovic M, et al. The STRING database in 2017: quality-controlled protein-protein association networks, made broadly accessible. *Nucleic Acids Res.* (2017) 45:D362–d368. doi: 10.1093/nar/gkw937
14. Doncheva NT, Morris JH, Gorodkin J, Jensen LJ. Cytoscape StringApp: network analysis and visualization of proteomics data. *J Proteome Res.* (2019) 18:623–32. doi: 10.1021/acs.jproteome.8b00702
15. Newman AM, Liu CL, Green MR, Gentles AJ, Feng W, Xu Y, et al. Robust enumeration of cell subsets from tissue expression profiles. *Nat Methods.* (2015) 12:453–7. doi: 10.1038/nmeth.3337
16. Ke ZB, Wu YP, Huang P, Hou J, Chen YH, Dong RN, et al. Identification of novel genes in testicular cancer microenvironment based on ESTIMATE algorithm-derived immune scores. *J Cell Physiol.* (2021) 236:706–13. doi: 10.1002/jcp.29898
17. Wang H, Wu X, Chen Y. Stromal-immune score-based gene signature: a prognosis stratification tool in gastric cancer. *Front Oncol.* (2019) 9:1212. doi: 10.3389/fonc.2019.01212
18. Zhou L, Huang W, Yu HF, Feng YJ, Teng X. Exploring TCGA database for identification of potential prognostic genes in stomach adenocarcinoma. *Cancer Cell Int.* (2020) 20:264. doi: 10.1186/s12935-020-01351-3
19. Endo-Munoz L, Cumming A, Sommerville S, Dickinson I, Saunders NA. Osteosarcoma is characterised by reduced expression of markers of osteoclastogenesis and antigen presentation compared with normal bone. *Br J Cancer.* (2010) 103:73–81. doi: 10.1038/sj.bjc.6605723
20. Wu SY, Fan J, Hong D, Zhou Q, Zheng D, Wu D, et al. C3aR1 gene overexpressed at initial stage of acute myeloid leukemia-M2 predicting short-term survival. *Leuk Lymphoma.* (2015) 56:2200–2. doi: 10.3109/10428194.2014.986481
21. Song G, He L, Yang X, Yang Y, Cai X, Liu K, et al. Identification of aberrant gene expression during breast ductal carcinoma in situ progression to invasive ductal carcinoma. *J Int Med Res.* (2020) 48:300060518815364. doi: 10.1177/0300060518815364
22. Tian H. Identification of candidate genes for myeloma-induced osteocyte death based on microarray data. *J Orthop Surg Res.* (2016) 11:81. doi: 10.1186/s13018-016-0411-0
23. Xing S, Wang Y, Hu K, Wang F, Sun T, Li Q. WGCNA reveals key gene modules regulated by the combined treatment of colon cancer with PHY906 and CPT11. *Biosci Rep.* (2020) 40:BSR20200935. doi: 10.1042/BSR20200935
24. Xia Z, Shang H, Cholewa J, Wang Q, Ding X, Su Q, et al. The effect of exercise on gene expression and signaling in mouse melanoma tumors. *Med Sci Sports Exerc.* (2020) 52:1485–94. doi: 10.1249/MSS.0000000000002291
25. Zhang J, Chen M, Zhao Y, Xiong H, Sneh T, Fan Y, et al. Complement and coagulation cascades pathway correlates with chemosensitivity and overall survival in patients with soft tissue sarcoma. *Eur J Pharmacol.* (2020) 879:173121. doi: 10.1016/j.ejphar.2020.173121
26. Zhang K, Dong C, Chen M, Yang T, Wang X, Gao Y, et al. Extracellular vesicle-mediated delivery of miR-101 inhibits lung metastasis in osteosarcoma. *Theranostics.* (2020) 10:411–25. doi: 10.7150/thno.33482
27. Morrow JJ, Mendoza A, Koyen A, Lizardo MM, Ren L, Waybright TJ, et al. mTOR inhibition mitigates enhanced mRNA translation associated with the metastatic phenotype of osteosarcoma cells *in vivo*. *Clin Cancer Res.* (2016) 22:6129–41. doi: 10.1158/1078-0432.CCR-16-0326
28. Niu J, Yan T, Guo W, Wang W, Zhao Z, Ren T, et al. Identification of potential therapeutic targets and immune cell infiltration characteristics in osteosarcoma using bioinformatics strategy. *Front Oncol.* (2020) 10:1628. doi: 10.3389/fonc.2020.01628
29. Xu C, Xu J, Lu L, Tian W, Ma J, Wu M. Identification of key genes and novel immune infiltration-associated biomarkers of sepsis. *Innate Immun.* (2020) 26:666–82. doi: 10.1177/1753425920966380
30. Litvinchuk A, Wan YW, Swartzlander DB, Chen F, Cole A, Propson NE, et al. Complement C3aR inactivation attenuates tau pathology and reverses an immune network deregulated in tauopathy models and Alzheimer's disease. *Neuron.* (2018) 100:1337–53.e1335. doi: 10.1016/j.neuron.2018.10.031
31. Propson NE, Roy ER, Litvinchuk A, Köhl J, Zheng H. Endothelial C3a receptor mediates vascular inflammation and BBB permeability during aging. *J Clin Invest.* (2020) 131:e140966. doi: 10.1172/JCI140966
32. Han J, Zhang X, Lau JK, Fu K, Lau HC, Xu W, et al. Bone marrow-derived macrophage contributes to fibrosing steatohepatitis through activating hepatic stellate cells. *J Pathol.* (2019) 248:488–500. doi: 10.1002/path.5275
33. Brennan FH, Jogia T, Gillespie ER, Blomster LV, Li XX, Nowlan B, et al. Complement receptor C3aR1 controls neutrophil mobilization following spinal cord injury through physiological antagonism of CXCR2. *JCI Insight.* (2019) 4:e98254. doi: 10.1172/jci.insight.98254
34. Sheen JH, Strainic MG, Liu J, Zhang W, Yi Z, Medof ME, et al. TLR-induced murine dendritic cell (DC) activation requires DC-intrinsic complement. *J Immunol.* (2017) 199:278–91. doi: 10.4049/jimmunol.1700339
35. Mathern DR, Horwitz J, Heeger PS. Absence of recipient C3aR1 signaling limits expansion and differentiation of alloreactive CD8(+) T cell immunity and prolongs murine cardiac allograft survival. *Am J Transplant.* (2019) 19:1628–40. doi: 10.1111/ajt.15222

Conflict of Interest: The authors declare that the research was conducted in the absence of any commercial or financial relationships that could be construed as a potential conflict of interest.

Copyright © 2021 Zou, Liu, Wang, Chen, Lu, Huang and Li. This is an open-access article distributed under the terms of the Creative Commons Attribution License (CC BY). The use, distribution or reproduction in other forums is permitted, provided the original author(s) and the copyright owner(s) are credited and that the original publication in this journal is cited, in accordance with accepted academic practice. No use, distribution or reproduction is permitted which does not comply with these terms.

frontiers in Medicine

REVIEW
published: 18 March 2021
doi: 10.3389/fmed.2021.649383

Diagnostic and Prognostic Value of Circulating CircRNAs in Cancer

Mina Wang[1,2†], *Feiyu Xie*[1,3†], *Jiaran Lin*[1,4†], *Yihan Zhao*[5], *Qian Zhang*[1], *Zehuan Liao*[6,7*] and *Peng Wei*[1*]

[1] School of Traditional Chinese Medicine, Beijing University of Chinese Medicine, Beijing, China, [2] Department of Acupuncture and Moxibustion, Beijing Hospital of Traditional Chinese Medicine, Capital Medical University, Beijing Key Laboratory of Acupuncture Neuromodulation, Beijing, China, [3] Oncology Department, Wangjing Hospital of China Academy of Chinese Medical Sciences, Beijing, China, [4] Department of Nephrology and Endocrinology, Dongzhimen Hospital Affiliated to Beijing University of Chinese Medicine, Beijing, China, [5] National Clinical Research Center for Chinese Medicine Cardiology, Xiyuan Hospital, China Academy of Chinese Medical Sciences, Beijing, China, [6] School of Biological Sciences, Nanyang Technological University, Singapore, Singapore, [7] Department of Microbiology, Tumor, and Cell Biology (MTC), Karolinska Institutet, Biomedicum, Solnavägen, Sweden

Cancer has been regarded as one of the leading causes of mortality worldwide. Diagnostic and prognostic biomarkers with high sensitivity and specificity for cancer play a crucial role in preventing or treating cancer. Circular RNAs (circRNAs), which hold great potential for the management of cancer patients due to their abundance, stable property, and high specificity in serum, plasma, and other body fluids, can be used as non-invasive and blood-based biomarkers in cancer diagnosis and prognosis. There are four types of circRNAs including exonic circRNAs (ecircRNA), intronic circRNAs, exon-intron circRNAs (ElciRNA), and intergenic circRNAs. CircRNAs can act as miRNA sponges, affect protein translation, interplay with RNA binding proteins, regulate protein recruitment, and modulate protein scaffolding and assembly. Therefore, the multifunctionalities of circRNAs make them ideal for detecting and predicting cancer. Indeed, circRNAs manifest high sensitivity and specificity in more than ten types of cancer. This review aims to consolidate the types and functions of circRNAs, as well as discuss the diagnostic and prognostic value of circulating circRNAs in cancer.

Keywords: circRNA, circulation, cancer diagnosis, cancer prognosis, biomarker

OPEN ACCESS

Edited by:
Guo Chen,
Jinan University, China

Reviewed by:
Xue Gao,
University of Chicago, United States
Youwei Sun,
Emory University, United States

***Correspondence:**
Peng Wei
weipeng@bucm.edu.cn
Zehuan Liao
liao0058@e.ntu.edu.sg

[†]These authors have contributed equally to this work

Specialty section:
This article was submitted to Precision Medicine, a section of the journal Frontiers in Medicine

Received: *04 January 2021*
Accepted: *15 February 2021*
Published: *18 March 2021*

Citation:
Wang M, Xie F, Lin J, Zhao Y, Zhang Q, Liao Z and Wei P (2021) Diagnostic and Prognostic Value of Circulating CircRNAs in Cancer. Front. Med. 8:649383. doi: 10.3389/fmed.2021.649383

INTRODUCTION

Cancer, which was estimated to lead to 18.1 million new cases and 9.6 million deaths according to GLOBOCAN 2018, is regarded as one of the most detrimental disease to our society (1–6). Given the concealment and non-specificity of clinical manifestations, most cancer cases are diagnosed at advanced stages. Hence the best therapies are only suitable for limited number of patients, let alone frequent dug resistance and adverse events (7–10). Taking tissue biopsies and imaging examinations as well as using cancer biomarkers are some of the most widely used methods in cancer diagnosis. However, these methods have their own limitations. For example, although taking tissue biopsies is viewed as the gold standard of cancer diagnosis, there is a risk for patients with coagulation dysfunction or other concomitant diseases to take biopsies (11). Moreover, only tumors growing to certain size can be detected by imaging examination such as CT (12). Also, many cancer biomarkers are unable to possess both superior sensitivity and specificity simultaneously. Therefore, it is an urgent need to discover effective cancer biomarkers for people to prevent or to receive treatment at early stages of cancer.

With progress achieved in the field of non-coding RNA (ncRNA), circular RNAs (circRNAs), a unique type of ncRNA characterized by its loop structure, have emerged as playing a significant role in carcinogenesis, metastasis, recurrence and multidrug resistance (13). CircRNAs are formed through back-splicing process whereby a downstream 5′ splice donor site is ligated with an upstream 3′ splice acceptor site to form a single-strand covalently closed loop. Afterwards, the spliceosome removes all or part of introns and the remaining sequences are linked together (14). CircRNAs are of considerable diagnostic and prognostic value not only due to the convenience for detection but also the exhibition of tissue/developmental-stage-specific expression. CircRNAs are prone to be detected because of large quantity, for example, over 25,000 different circRNAs having been identified in human fibroblasts (15). In addition, alternative circularization caused by the competition between different flanking complementary introns increases the isoforms of circRNAs, thus contributing to the abundance of circRNAs (16). Besides, the covalently closed loop structure without 5′-3′ polarity or polyadenylated tail confers great stability upon circRNAs, preventing them from being degraded by RNase R, debranching enzyme or RNA exonuclease (17). As a result, the average half-life of circRNAs in cells is much longer than that of mRNA (messenger RNA). Furthermore, Rybak-Wolf et al. (18) analyzed thousands of neuronal human and mouse circRNAs, discovering that circRNAs are highly conserved in sequence. This phenomenon might result from the conservation of splicing regulatory elements, complementary flanking introns and few polymorphisms of miRNA target sites of circRNA sponges (19). Accoring to Memczak et al., (20) circRNAs are much higher expressed in peripheral whole blood compared with linear ncRNAs, and consequently circRNAs can be detected without using invasive methods. Last but not least, tissue/developmental-stage-specifc expression pattern is a distinguished feature of circRNAs, which means their expression levels are extremely diverse and variable based on cell types and development stage of tissues, respectively (21). With advantages elucidated above, circRNAs are practical biomarkers in cancer diagnosis and prognosis.

In this review, we will focus on sorting out the types and functions of circRNAs and the expression levels of circulating circRNAs systematically according to the latest research. Moreover, perspectives and challenges will be proposed to analyze the application prospect of circRNAs in cancer diagnosis and prognosis.

TYPES AND FUNCTIONS OF CircRNAs

In recent years, ncRNAs have been recognized as a new sensitive, non-invasive biomarker for diagnosis, prognosis and even prediction to therapeutic responses due to the high stability in body fluids (urine, plasma, exosomes, etc.) and the development of detection techniques (22), among which circRNAs are presumably more stable than most linear RNAs because they form a unique, circular, covalently closed continuous loop that is resistant to exonuclease-mediated degradation because it has no 5′ or 3′ ends (**Figure 1**).

Types of CircRNAs

CircRNAs are divided into four categories: exonic circRNAs (ecircRNA), intronic circRNAs, exon-intron circRNAs (EIciRNA), and intergenic circRNAs (23). Most circRNAs come from exons of protein coding genes via "back-splicing" (24), where a downstream splice donor site (5′ splice site) connects to an upstream acceptor splice site (3′ splice site). There are three possible models of ecircRNAs biogenesis: lariat-driven circularization, intron-pairing-driven circularization, and resplicing-driven circularization (25). Similarly formed like ecircRNAs, EIciRNAs are circularized with introns "retained" between exons, which predominantly localize in the nucleus and are associated with RNA polymerase II in human cells (26). CircRNAs from introns include circular intronic RNAs (ciRNAs), excised group I introns, excised group II introns, intron lariats, and excised tRNA introns (27). GU-rich sequences near the 5′ splice site and C-rich sequences near the branch point are sufficient for an intron to escape debranching and become a stable circRNA (28). Sequence analyses indicated that intergenic or intronic circRNAs generally showed only weak conservation, whereas coding exons serve additional, presumptively regulatory functions when expressed within circRNAs (29). Generally, knowledge about these circularized transcripts, and the specific mechanism regulating the biogenesis of circRNAs is still lacking.

Functions of CircRNAs

CircRNAs Act as miRNA Sponges

MicroRNAs (miRNAs) are important post-transcriptional regulators of gene expression that act by direct base pairing to target sites within untranslated regions of mRNAs. A few years ago, two independent studies discovered that endogenous circRNAs can work as miRNA sponges. This means that circRNAs bind to miRNAs and consequently repress their function (29, 30). For example, ciRS-7 (also termed as CDR1as), acting as a miR-7 sponge, contains more than 70 selectively conserved miRNA target sites, and is highly and widely associated with Argonaute (AGO) proteins in a miR-7-dependent manner (30). Expression of ciRS-7 inhibits miR-7 activity that leads to increase in expression of miR-7 targets such as UBE2A, EGFR, PI3K, etc. (30–33). The sex-determining region Y (SRY) gene produces a testis-specific circRNA known as cir-SRY. Studies have shown that cir-SRY serves as a miR-138 sponge and 16 putative target sites have been identified (30). Unlike the two circRNAs mentioned above that contain only one kind of miRNA binding site, circHIPK3 could bind to multiple miRNAs (9 miRNAs with 18 binding sites), suggesting that one circRNA might be associated with a variety of miRNAs. CircHIPK3 could regulate cell growth by sponging various miRNAs especially miR-124 in human cells (34).

Translating Proteins

Although circRNAs generally do not translate proteins due to the lack of 5′ cap structure for translation initiation, some circRNAs can be internally modified by m6A and start translating

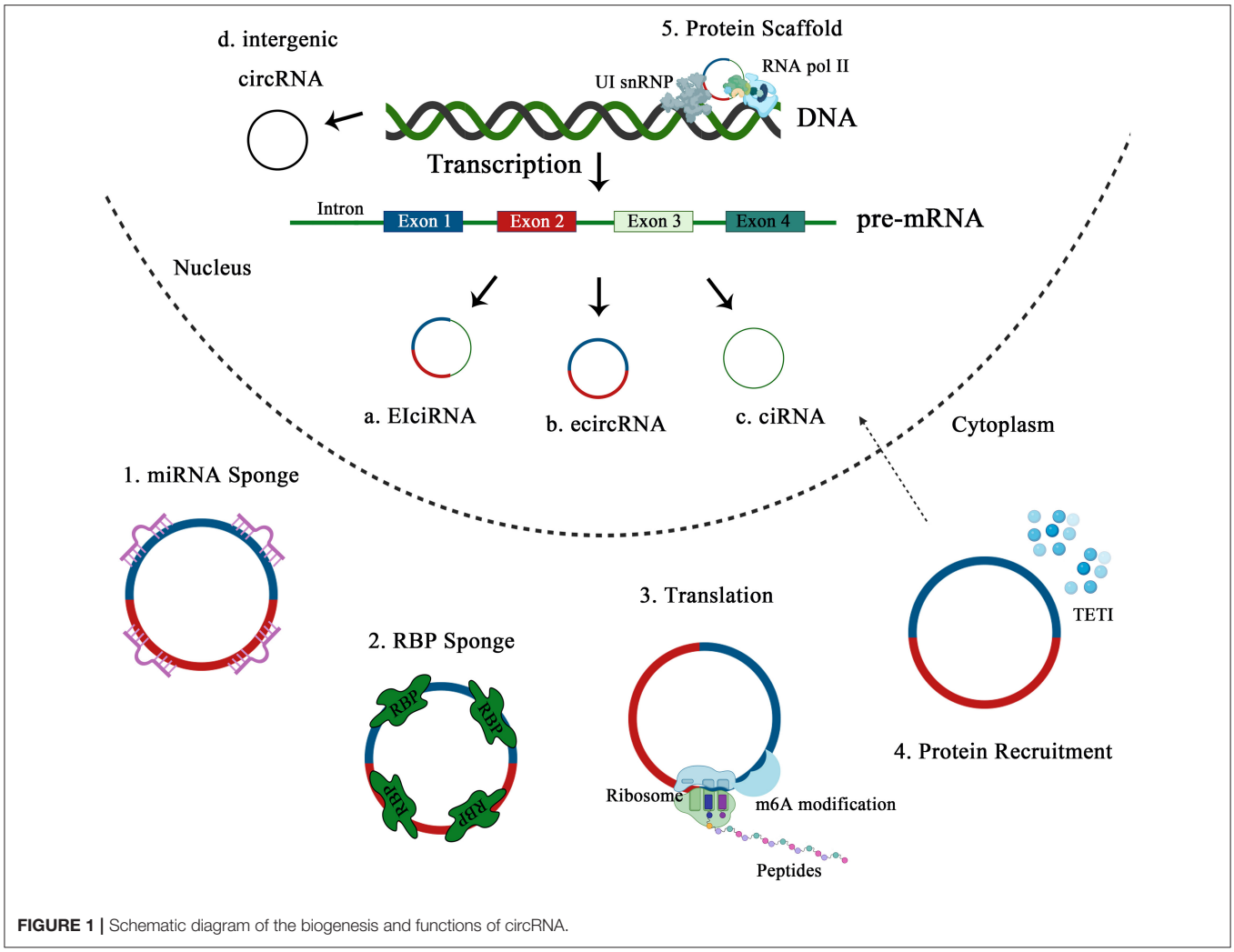

FIGURE 1 | Schematic diagram of the biogenesis and functions of circRNA.

small peptides (35). The small peptide can be bioactive such as a new 21-kDa protein encoded by circ-FBXW7, which is termed FBXW7-185aa. Upregulation of FBXW7-185aa in cancer cells could repress proliferation and cell cycle acceleration, while knockdown of FBXW7-185aa could lead to cancerous phenotypes *in vitro* and *in vivo*. CircPINTexon2 encodes PINT87aa which is decreased in glioma tissues and negatively impacts the clinical prognosis of glioma. Furthermore, PINT87aa could bind to the polymerase-associated factor 1 (PAF1) complex to prohibit the RNA elongation of multiple oncogenes (36). Circular SHPRH (circ-SHPRH) uses overlapping genetic codes to form a "UGA" stop codon, encoding a novel 17 kDa protein named after SHPRH-146aa. Both circ-SHPRH and SHPRH-146aa are amply expressed in normal human brains and decreased in glioblastoma. The overexpression of SHPRH-146aa in U251 and U373 glioblastoma cells weakens their malignant behavior and tumorigenicity *in vitro* and *in vivo* (37).

Interaction With RNA Binding Proteins

CircRNAs can also bind to RNA binding proteins (RBP) as protein sponges. Ashwal-Fluss et al. (38) observed that the splicing factor Muscleblind (MBL) strongly and specifically binds to circMbl, the circRNA generated from its own RNA. When the MBL protein is redundant, circMbl could sponge out the extra proteins by binding to it. Du et al. (39) reported that ectopic expression of circ-Foxo3 suppressed cell cycle progression by binding to the cell cycle proteins cyclin-dependent kinase 2 (also known as cell division protein kinase 2 or CDK2) and cyclin-dependent kinase inhibitor 1 (or p21), forming the structure of a ternary complex.

Protein Scaffolding and Assembly

In contrast to the protein sponge model, circRNAs also function as dynamic protein scaffolds enabling connection and assembly of proteins. Li et al. (26) revealed that EIciRNA could promote RNA Polymerase II-mediated parental gene transcription by acting as a linker of U1 snRNP and the pol II complex. Circ-Amotl1 has also been reported to serve as a protein scaffold by binding to AKT and PDK1 to form ternary complexes, hence promoting the nuclear translocation of pAKT (40).

Protein Recruitment

CircRNAs can also tether spliceosome for splicing or target chromatin modifiers to particular sites to modulate gene expression. For instance, FLI1 circular RNA termed with FECR1 could collaborate with the FLI1 promoter. FECR1 binds to the FLI1 promoter in cis and recruits Ten-Eleven Translocation methylcytosine dioxygenase 1 (TET1) demethylase, which may regulate metastasis of breast cancer cells by coordinating DNA methylation and demethylation (41).

CIRCULATING circRNAs IN DIFFERENT CANCERS

CirRNAs are abundant and stable molecules with high cell specificity presenting in serum, plasma and other body fluids, which can be used as non-invasive and blood-based biomarkers in cancer diagnosis and prognosis (42) (Refer to **Table 1**).

Nasopharyngeal Carcinoma

Nasopharyngeal carcinoma (NPC) as a highly invasive and metastatic head and neck malignant tumor, occurs commonly in Southern China and Southeast Asia. Plasma Epstein-Barr virus (EBV) DNA has been reported to be used for population screening (43), whereas several circRNAs have showed effect in diagnosis and prognosis of NPC. Shuai et al. (44) found that circRNA_000285 was significantly increased in the serum samples of patients with NPC, in comparison with that of healthy controls. Notably, the level of circRNA_000285 was upregulated by 3-fold in NPC patients with radiation resistance compared with those were radiation sensitive. Also, patients with high expression of circRNA_000285 had poorer overall survival rate than those with low expression. Besides, circMYC was highly expressed in patients with NPC as well, and the expression was significantly correlated with tumor size, lymphatic metastasis, tumor-node- metastasis stage (TNM stage), survival rate and disease recurrence. The AUC (area under the curve) value for differentiating radioresistant patients from radiosensitive patients was 0.945, with a sensitivity of 90.24% and a specificity of 94.51% (45). Wang et al. (46) observed a significant increase of hsa_circ_0066755 in the NPC patients' plasma with an AUC value of 0.904. Meanwhile, plasma hsa_circ_0066755 testing presented a comparable diagnostic accuracy to the magnetic resonance imaging (MRI) (46). Thus, circRNA_000285 and circMYC represent diagnostic and prognostic value for NPC, while hsa_circ_0066755 exhibits merely diagnostic characteristic.

Esophageal Cancer

Esophageal cancer is considered as one of the most aggressive and lethal malignant tumors with a poor 5-year survival rate due to inefficient diagnosis methods. There are two major type of esophageal cancer: esophageal adenocarcinoma (EAC) and esophageal squamous cell carcinoma (ESCC). Classical biomarkers include serum Squamous Cell Carcinoma Antigen (SCCA), Carbohydrate antigen-19-9 (CA19-9), and Carcinoma Embryonic Antigen (CEA). However, the lack of sensitivity and specificity limits them to be effectively used in the early detection of esophageal cancer. More and more evidence has indicated that dysregulation of circRNAs functions in the progression of various cancers, including esophageal cancer (80).

Recently, Hu et al. (2) found that the level of circGSK3β was significantly increased in the plasma of ESCC patients compared to that of healthy people. According to ROC (receiver operating characteristic) analysis, circGSK3β presented a sensitivity of 86.1%, a specificity of 58.1%, and an AUC of 0.782 in distinguishing ESCC patients from healthy people, indicating that plasma circGSK3β has significantly diagnostic value. Moreover, the AUC for circGSK3β in ESCC patients at early stages and healthy controls reached 0.793, with a sensitivity of 68.8% and a specificity of 81.3%. The diagnostic ability was verified in an independent validation cohort as well. The AUC of circGSK3β for ESCC/early stages of ESCC and healthy controls were 0.801 and 0.826, respectively. Additionally, the study has shown that the plasma level of circGSK3β was reduced in 75% of ESCC patients after surgery, while that of circGSK3β was increased in ESCC patients with recurrence/metastasis 10 months after surgery, suggesting the plasma level of circGSK3β has predictive values for clinical improvement. Besides, Huang et al. (81) demonstrated an upregulation of hsa_circ_0004771 in plasma was associated with a heavier tumor burden and a poor prognosis, causing a lower overall survival. The origin of hsa_circ_0004771 in plasma may be tumor-derived exosomes, and the ROC analysis revealed effective diagnostic performance of hsa_circ_0004771. Wang et al. discovered that plasma circ-SLC7A5 could serve as novel diagnostic biomarker for ESCC detection, with the area under the ROC curve of 0.772, and plasma circ-SLC7A5 expression was significantly up-regulated in ESCC patients, positively related to TNM stage and tend to have a poor overall survival (47). These findings have confirmed the significant diagnostic and prognostic value of circGSK3β, hsa_circ_0004771, and circ-SLC7A5 in esophageal cancer.

Lung Cancer

Lung cancer remains as the leading cause of cancer-related death worldwide, with more than 1.8 million new cases and nearly 1.6 million deaths estimated in 2012. Non-small-cell lung cancer (NSCLC) accounts for ∼80–85% of all cases, and small cell lung cancer (SCLC), accounts for about 15% (54). To date, the diagnosis for lung cancer include tumor-liberated proteins (e.g., CEA, NSE, TPA, chromogranin, CA125, CA19-9, and CYFRA21-1) and computed tomography (CT) (48). However, most patients are still diagnosed at advanced stages. Thus, having accurate and sensitive biomarkers is crucial for lung cancer diagnosis and prognosis.

Circulating circRNA emerges as a promising method for diagnosis and prognosis of lung cancer. Li et al. (49) compared the levels of serum FECR1 in SCLC patients with that in normal controls, they proved that FECR1 expression was higher in patients with SCLC, and much higher in those with distant metastasis. Notably, the level of serum FECR1 was strongly associated with chemotherapy response in SCLC patients, suggesting that serum FECR1 might be useful in detecting and tracking SCLC. As for NSCLC, the abundance of circFARSA in plasma has been reported to elevate in NSCLC patients, and the AUC was 0.710, which

TABLE 1 | Circulating circRNAs in different types of cancer.

Cancer type	Name of circRNAs	Changes	Functions	Sample	ROC curve	References
NPC	circRNA_000285	Upregulated	Diagnosis and prognosis	Serum	N/A	(34)
	circMYC	Upregulated	Diagnosis and prognosis	Plasma	AUC: 0.945 Sensitivity: 90.24% Specificity: 94.51%	(35)
	Has_circ_0066755	Upregulated	Diagnosis	Plasma	AUC: 0.904	(36)
ESCC	circGSK3β	Upregulated	Diagnosis and prognosis	Plasma	AUC: 0.782 Sensitivity: 86.1% Specificity: 58.1%	(38)
	circRNA_0004771	Upregulated	Diagnosis and prognosis	Plamsa	N/A	(39)
	circ-SLC7A5	Upregulated	Diagnosis and prognosis	Plasma	AUC: 0.772	(40)
SCLC	FECR1	Upregulated	Diagnosis and prognosis	Serum	N/A	(43)
NSCLC	circFARSA	Upregualted	Diagnosis	Plasma	AUC: 0.710	(44)
	F-circEA	Upregualted	Diagnosis and prognosis	Plasma	N/A	(45)
	hsa_circ_0005962	Upregualted	Diagnosis	Plasma	AUC: 0.730 Sensitivity: 71.9% Specificity: 72.2%	(46)
	hsa_circ_0086414	Downregulated	Diagnosis	Plasma	AUC: 0.780 Sensitivity: 77.1% Specificity: 66.7%	(46)
Breast cancer	hsa_circ_0001785	Upregualted	Diagnosis and prognosis	Plasma	AUC: 0.771 Sensitivity: 78.6% Specificity: 75.6%	(47)
Gastric cancer	hsa_circ_002059	Downregulated	Diagnosis and prognosis	Plasma	AUC: 0.730 Sensitivity: 81.0% Specificity: 62.0%	(48)
	hsa_circ_0000190	Downregulated	Diagnosis	Plasma	AUC: 0.060 Sensitivity: 41.4% Specificity: 87.5%	(49)
	hsa_circ_0000181	Upregulated	Diagnosis and prognosis	Plasma	AUC: 0.582 Sensitivity: 20.6% Specificity: 99.0%	(50)
	hsa_circ_0001649	Downregulated	Diagnosis	Serum	AUC: 0.834 Sensitivity: 71.1% Specificity: 81.6%	(51)
	hsa_circ_0000745	Downregulated	Diagnosis	Plasma	AUC: 0.683 Sensitivity: 85.5% Specificity: 45.0%	(52)
	circ-SFMBT2	Upregulated	Diagnosis	Plasma	AUC: 0.759 Sensitivity: 80.6% Specificity: 63.9%	(53)
	circ-ERBB2	Upregulated	Prognosis	Plasma	N/A	(54)
HCC	hsa_circ_0001445	Downregulated	Diagnosis	Plasma	AUC: 0.862 Sensitivity: 94.2% Specificity: 71.2%	(55)
	hsa_circ_104075	Upregulated	Diagnosis	Serum	AUC: 0.973 Sensitivity: 96.0% Specificity: 98.3%	(56)
	circ_0009582	Upregulated	Diagnosis	Plasma	AUC: 0.805	(57)
	circ_0037120	Upregulated	Diagnosis	Plasma	AUC: 0.835	(57)
	circ_0140117	Upregulated	Diagnosis	Plasma	AUC: 0.845	(57)
Pancreatic cancer	circ-LDLRAD3	Upregulated	Diagnosis and prognosis	Plasma	AUC: 0.670 Sensitivity: 57.4% Specificity: 70.5%	(58)
	circ-PDE8A	Upregulated	Prognosis	Plasma	N/A	(59)
	circ-IARS	Upregulated	Prognosis	Plasma	N/A	(60)
CRC	hsa_circ_0007534	Upregulated	Diagnosis and Prognosis	Plasma	AUC: 0.780 Sensitivity: 92.0% Specificity: 52.2%	(61)

(Continued)

TABLE 1 | Continued

Cancer type	Name of circRNAs	Changes	Functions	Sample	ROC curve	References
	hsa_circ_0001649	Upregulated	Diagnosis	Serum	N/A	(62)
	hsa_circ_0004585	Upregulated	Diagnosis	Peripheral blood	N/A	(63)
	circ-CCDC66, circ-ABCC1, circ-STIL	Downregulated	Diagnosis	Plasma	AUC: 0.780 Sensitivity: 64.4% Specificity: 85.2%	(64)
	circVAPA	Upregulated	Diagnosis and prognosis	Plasma	AUC: 0.724	(65)
	hsa_circ_0000370	Upregulated	Diagnosis and prognosis	Plasma	AUC: 0.815	(66)
	hsa_circ_0082182	Upregulated	Diagnosis and prognosis	Plasma	AUC: 0.737	(66)
	hsa_circ_0035445	Downregulated	Diagnosis and prognosis	Plasma	AUC: 0.703	(66)
	hsa_circ_0004771	Upregulated	Diagnosis	Serum	AUC: 0.880	(67)
	hsa_circ_0002320	Downregulated	Diagnosis and prognosis	Plasma	AUC: 0.823	(68)
Bladder cancer	hsa_circ_0003221	Upregulated	Prognosis	Whole blood	N/A	(69)
	circFARSA	Upregulated	Diagnosis and prognosis	Serum	N/A	(70)
	circSHKBP1	Upregulated	Diagnosis and Prognosis	Serum	AUC: 0.804	(70)
	circBANP	Upregulated	Prognosis	Serum	N/A	(70)
	hsa_circ_0000285	Downregulated	Prognosis	Serum	N/A	(71)
Endometrial cancer	hsa_circ_0109046	Upregulated	Prognosis	Serum	N/A	(72)
	hsa_circ_0002577	Upregulated	Prognosis	Serum	N/A	(72)
Cervical cancer	hsa_circ_0101996	Upregulated	Diagnosis	Whole blood	AUC: 0.906	(73)
	hsa_circ_0101119	Upregulated	Diagnosis	Whole blood	AUC: 0.887	(73)
	circFoxO3a	Downregulated	Prognosis	Serum	N/A	(74)
Leukemia	circBA9.3	Upregulated	Prognosis	Whole blood	N/A	(75)
	circHIPK3	Upregulated	Prognosis	Serum	N/A	(76)
Melanoma	hsa_circ_0001591	Upregulated	Prognosis	Serum	N/A	(77)
Osteosarcoma	hsa_circ_0081001	Upregulated	Diagnosis and prognosis	Serum	AUC: 0.898	(78)
	hsa_circ_0000885	Upregulated	Diagnosis and prognosis	Serum	AUC: 0.783	(79)

NPC, nasopharyngeal carcinoma; ESCC, esophageal squamous cell carcinoma; SCLC, small-cell lung cancer; NSCLC, non-small-cell-lung cancer; HCC, hepatocellular carcinoma; CRC, colorectal cancer; N/A, not available; AUC, area under the curve.

represents a potential diagnostic performance of circFARSA for NSCLC (50). Meanwhile, F-circEA specifically elevates in EML4-ALK fusion gene positive NSCLC patients' plasma, thus monitoring the EML4-ALK translocation and guiding the EML4-ALK-targeted NSCLC therapy. Also, F-circEA can independently promote cancer cell migration and invasion, leading to tumor progression. Taken together, F-circEA could be a "liquid biopsy" biomarker to diagnose NSCLC, as well as provide clinical implications for NSCLC therapy (51). In addition, Liu et al. (52) observed significant upregulations of hsa_circ_0005962 and downregulations of hsa_circ_0086414 in lung adenocarcinoma plasma and cells, and the plasma level of hsa_circ_0005962 was decreased in postoperative patients compared with preoperative patients. According to ROC analysis, the AUC of hsa_circ_0005962 was 0.730, with a sensitivity of 71.9% and specificity of 72.2%, and the AUC of hsa_circ_0086414 was 0.780, with a sensitivity and specificity of 77.1 and 66.7%, respectively. The best discriminatory ability was shown in the combination of the two circRNAs, with with an AUC of 0.810, sensitivity of 77.8% and specificity of 72.2%. Therefore, for lung cancer, FECR1 and F-circEA have the capability of both diagnosis and prognosis, whereas, circFARSA, hsa_circ_0005962 and hsa_circ_0086414 could serve as non-invasive diagnostic biomarkers.

Breast Cancer

Breast cancer is one of the most common malignant tumors for woman in the world. The neoplasm stage (when the disease is diagnosed) plays a key role in overall survival, with more than 95% of 5-year survival rate for early stage, but only 20% of that for distant metastasis patients. Although the diagnosis for breast cancer is developing, and conventional serum biomarkers like CEA, CA15-3, and CA125 have been used as ideal approaches for detecting breast cancer because of their low invasiveness (53, 82), high-efficiency and specific clinical molecules are still desired for the diagnosis and

prognosis of breast cancer. Yin et al. (83) selected three candidate circRNAs (hsa_circ_0001785, hsa_circ_0108942 and hsa_circ_0068033) out of 41 dysregulated circRNAs in the plasma of breast cancer patients, and hsa_circ_0001785 exhibited the highest diagnostic value with an AUC of 0.771, and a sensitivity of 78.6% and a specificity of 75.6%, indicating hsa_circ_0001785 could be a promising biomarker for breast cancer detection. They also compared the diagnostic efficiency of hsa_circ_0001785 with CEA and CA15-3 using plasma samples from 57 breast cancer patients, and hsa_circ_0001785 had the highest AUC value (0.784) compared with CEA (0.562) and CA15-3 (0.629). Notably, an even higher AUC value (0.839) was found in the combination of these three molecules. Moreover, the sensitivity and specificity of hsa_circ_0001785 (sensitivity: 76.4%, specificity: 70.0%) were significantly higher than that of CEA (sensitivity: 43.1%, specificity: 51.4%) and CA15-3 (sensitivity: 50.5%, specificity: 57.9%), and the combination of hsa_circ_0001785, CEA and CA15-3 showed the highest diagnostic efficiency with a sensitivity and a specificity of 75.8 and 90.4%, respectively. Besides, the plasma expression of hsa_circ_0001785 was significantly associated with histological grade ($P = 0.013$), TNM stage ($P = 0.008$) and distant metastasis ($P = 0.016$), which can predict the progression of breast cancer. Also, a lower plasma level of hsa_circ_0001785 was shown in postoperative patients compared with preoperative patients. Thus, the recurrence of postoperative cancer patients can be monitored by the plasma level of hsa_circ_0001785. The results of this study have confirmed the diagnostic and prognostic value of plasma hsa_circ_0001785 in breast cancer.

Gastric Cancer

Gastric cancer is the third leading cause of cancer-related death worldwide. CEA and CA19-9 are two non-invasive and highly practical circulating biomarkers that have been used clinically. However, they present low sensitivity and specificity for gastric cancer diagnosis (84). The levels of hsa_circ_002059 have been introduced to be lower in preoperative plasma samples than in postoperative plasma samples, and the AUC was 0.730, the sensitivity and specificity were 81.0 and 62.0%, respectively. Also, the low expression levels of hsa_circ_002059 were closely related to TNM stage and distal metastasis (55). Similarly, the plasma level of hsa_circ_0000190 was downregulated in the gastric cancer patients, with an AUC of 0.060, a sensitivity of 41.4%, and a specificity of 87.5%, when combining the use of tissue and plasma hsa_circ_0000190, the values of AUC, sensitivity and specificity were increased to 0.780, 71.2%, and 75.0%, respectively. However, it did not present any association with clinicopathological features such as age, gender, diameter, differentiation, lymphatic metastasis, distal metastasis, invasion, and TNM stage, but its level was higher in CEA positive patients (56). Same result was found in a study of hsa_circ_0000181 that CEA positive patients had higher plasma level of hsa_circ_0000181. Also, hsa_circ_0000181 was significantly decreased in gastric cancer plasma, and its reduced level was significantly associated differentiation. In addition, the AUC of hsa_circ_0000181 was 0.582, the specificity and sensitivity were 20.6 and 99.0%, respectively (57).

Besides, Li et al. (85) demonstrated that hsa_circ_0001649 may have a negative correlation with gastric cancer, since hsa_circ_0001649 expression in serum was significantly increased in the postoperative compared with the preoperative with an AUC of 0.834, a sensitivity of 71.1% and a specificity of 81.6%. Furthermore, a study of Huang et al. (86) has proven that the expression level of hsa_circ_0000745 in plasma was downregulated in gastric cancer patients, and its level correlated with TNM stage. The AUC of hsa_circ_0000745 in plasma was 0.683, and the sensitivity and specificity were 85.5 and 45.0%, respectively. While the combination of hsa_circ_0000745 and CEA represented increased values of AUC (0.775), sensitivity (80.0%), and specificity (63.3%). Apart from these down-regulated circRNAs, a circRNA named circ-SFMBT2 revealed an increased expression level in gastric cancer plasma samples compared with healthy people, suggesting it could be applied to detect gastric cancer (87). Moreover, high circERBB2 level in the plasma was correlated to poor prognosis for gastric cancer, with a low overall survival and a high rate of recurrence, which may associate with sponging some miRNAs and triggering tumor growth or metastasis. Notably, the increased plasma level of circERBB2 tended to be related to men (84). Since TNM stage, distal metastasis and differentiation are pivotal factors for evaluating the prognosis of gastric cancer, these seven molecules hsa_circ_0000190, hsa_circ_0001649, hsa_circ_0000745, and circ-SFMBT2 show a potential value as diagnostic biomarkers, circERBB2 could serve as a prognostic biomarker, and hsa_circ_002059 and hsa_circ_0000181 have promising performances in both diagnosis and prognosis of gastric cancer.

Hepatocellular Carcinoma

Liver cancer presented the sixth incidence and third mortality in malignancies worldwide in 2018. Hepatocellular carcinoma (HCC) is the most common form of liver cancer, accounting for 75–85% of all cases (1). HCC normally develops in patient with cirrhotic livers, which mainly result from hepatitis B virus (HBV)/ hepatitis C virus (HCV) infection or alcohol-related liver disease. For decades, the α-fetoprotein (AFP) (58), α-fetoprotein-L3 (AFP-L3) (59), and des-carboxy-prothrombin (DCP) (60) have been used for HCC diagnosis. Nevertheless, owing to their poor sensitivity and specificity, the current diagnostic methods are far from being satisfactory. Zhang et al. (88) assessed the diagnostic potential of plasma hsa_circ_0001445, using samples from 104 HCC patients, 57 cirrhosis patients, 44 HBV patients, and 52 healthy controls, and plasma hsa_circ_0001445 levels were significantly lower in HCC patients than other three groups. Compared with healthy controls, the AUC value of HCC patients was 0.862, with a specificity and a sensitivity of 94.2 and 71.2%, respectively. Moreover, the plasma hsa_circ_0001445 levels in HCC patients were associated with serum AFP levels, and the efficiency of the combination in distinguishing HCC patients from patients of cirrhosis (AUC = 0.743), from patients of HBV (AUC = 0.877), or from healthy controls (AUC = 0.970) was higher compared to using plasma hsa_circ_0001445 levels or serum AFP levels alone. Thus, the level of plasma hsa_circ_0001445 could be used

for HCC diagnosis. Furthermore, Zhang et al. (89) identified that hsa_circ_104075 was highly expression in HCC serum, and the AUC value of hsa_circ_104075 (0.973) was higher than that of lncRNA (DANCR: 0.851, HULC: 0.855, UCA1: 0.735), miRNA (miR-223: 0.818, miR-21: 0.782) and classical protein biomarkers (AFP: 0.750, AFP-L3: 0.766, DCP: 0.771), with a sensitivity of 96.0% and a specificity of 98.3%. In addition, three circRNAs including circ_0009582, circ_0037120, and circ_0140117 were confirmed to be upregulated in HCC patients' plasma. The AUC values of circ_0009582, circ_0037120, circ_0140117, combination of circRNAs, AFP, and combination of circRNAs and AFP were 0.805, 0.835, 0.845, 0.857, 0.803 and 0.955, respectively. The positive predictive value (PPV) and negative predictive value (NPV) were 95 and 95%, respectively when compared to healthy controls, while the PPV and NPV were 84 and 80%, respectively when distinguishing HCC from HBV infection, suggesting these three circRNAs are able to predict HCC from patients with HBV or healthy controls (90). The abovementioned circRNAs involving hsa_circ_0001445, hsa_circ_104075, circ_0009582, circ_0037120, and circ_0140117 have the capability of diagnosing HCC, whereas, they show no property in prognosing HCC.

Pancreatic Cancer

The estimated number of deaths due to pancreatic cancer was 432,000 in 2019 (61), with a 5-year survival rate of 9.3% (62). This is partly owing to the rapid invasion and early metastasis of pancreatic cancer as well as late diagnostic capabilities. The regular approaches applied clinically to detect pancreatic cancer include biopsy, CT and CA19-9 (63), and the discovery of biomarkers for the diagnosis of pancreatic cancer remains a major challenge. A study has verified that circ-LDLRAD3 was up-regulated in plasma of pancreatic cancer patients compared with healthy controls, and the level of plasma circ-LDLRAD3 was strongly related to CA19-9, N classification, venous invasion, and lymphatic invasion (64). The AUC value, sensitivity, and specificity of circ-LDLRAD3 were 0.670, 57.4%, and 70.5%, respectively, while the combination of circ-LDLRAD3 and CA19-9 increased the diagnostic value, with corresponding values for AUC, sensitivity, and specificity were 0.870, 80.3%, and 93.6%, respectively. Li et al. (65) analyzed the circ-PDE8A expression in plasma of pancreatic ductal adenocarcinoma (PDAC) patients and found that high expression of circ-PDE8A was associated with duodenal invasion, vascular invasion, T factor or TNM stage, as well as low survival rate. Moreover, high expression of circ-PDE8A acted as an independent risk for overall survival, suggesting circ-PDE8A expression was correlated with prognosis in PDAC.

Circ-IARS also has been reported to be an independent risk factor for pancreatic cancer, and it was presented an upregulation in plasma derived from patients with metastatic pancreatic cancer. Circ-IARS expression was positively associated with tumor vessel invasion, liver metastasis, and TNM stage and negatively associated with postoperative survival time (66). Besides, Seimiya et al. (67) suggested that circPDAC RNA might serve as a potential biomarker for PDAC, however, it was only examined in one serum of PDAC patient. Therefore, circ-PDE8A and Circ-IARS may be useful biomarkers for pancreatic cancer detection, circ-LDLRAD3 might be applied in the diagnosis and prognosis of pancreatic cancer.

Colorectal Cancer

Colorectal cancer (CRC) is one of the most frequent digestive tract cancers, and the second leading cause of cancer-related deaths worldwide (1). The regular approaches for detecting CRC include fecal occult blood testing, colonoscopy, stool DNA testing and conventional tumor biomarkers (e.g., CEA and CA19-9) (68, 91). Colonoscopy screening and subsequent pathological examinations are the criterion standard for the diagnosis of CRC, while due to the low adherence rates and reproducibility, the diagnosis of a lot of CRC patients has been delayed. The circRNAs have emerged as non-invasive biomarkers for CRC. Zhang et al. (69) found that hsa_circ_0007534 expression was significantly higher in CRC patients' plasma than in healthy controls, and the increased plasma level of hsa_circ_0007534 was associated with higher incidence of clinical classifications, metastatic phenotype, and poor differentiation in CRC patients. According to ROC analysis, compared with healthy controls, the AUC value was 0.780, the sensitivity was 92.0%, and specificity was 52.2%. According to Kaplan-Meier analysis, the high hsa_circ_0007534 expression group exhibited a significantly poorer prognosis than the low hsa_circ_0007534 expression group. Moreover, another circRNA called hsa_circ_0001649 was observed an upregulation expression in serum samples of CRC patients after surgery (70). The upregulation expression was also found in CRC patients peripheral blood of hsa_circ_0004585 (71). Furthermore, the plasma levels of three circRNAs (circ-CCDC66, circ-ABCC1, and circ-STIL) showed significantly reduction in CRC patients compared to in healthy volunteers. The AUC of the three-circRNA panel was 0.780, with 64.4% sensitivity and 85.2% specificity. The decreased plasma levels circ-CCDC66 and circ-ABCC1 were found to be associated with precursor lesions of CRC, including colon adenomas and adenomatous polyps, and circ-CCDC66 and circ-STIL expressions could be effectively applied in detecting early- stage CRC (92). Besides, Li et al. (72) evaluated the diagnostic and prognostic values of circVAPA for CRC, the results showed that circVAPA expression in the plasma was significantly increased in CRC patients compared to in healthy controls, with an AUC of 0.724, and circVAPA expression exhibited higher in stage III and IV patients than in stage I and II patients, indicating that the plasma level of circVAPA showed a positive trend with TNM stage progression.

In addition, a study has demonstrated that in CRC plasma, hsa_circ_0000370, and hsa_circ_0082182 were significantly upregulated, whereas hsa_circ_0035445 was downregulated (93). The AUC values of hsa_circ_0000370, hsa_circ_0082182, and hsa_circ_0035445 were 0.815, 0.737, and 0.703, respectively. The levels of hsa_circ_0000370 and hsa_circ_0082182 was closely related to lymph node metastasis, and the hsa_circ_0035445 expression was related to the TNM stage. Notably, hsa_circ_0000370 presented no significant difference between preoperative and postoperative stages, but hsa_circ_0082182 and hsa_circ_0035445 had a significant difference between these two stages. Pan et al. (73) verified

the level of serum hsa-circ-0004771 was increased in CRC patients compared to in healthy people and patients with benign intestinal diseases (BIDs), the AUC values were 0.590, 0.860 and 0.880 to discriminate BIDs, stage I/ II CRC patients and CRC patients from healthy people. Also, the expression of hsa-circ-0004771 was decreased in the serum of postoperative CRC patients. Besides, the level of plasma hsa_circ_0002320 was significantly downregulated in CRC patients, with an AUC of 0.823. Based on Kaplan-Meier analysis, the expression level of hsa_circ_0002320 was significantly connected with overall survival time: low level of hsa_circ_0002320 presented a poor overall survival time compared to CRC patients with high level of hsa_circ_0002320. Thus, hsa_circ_0002320 could be used for CRC diagnosis and prognosis (74). According to the studies of circRNAs in CRC, hsa_circ_0001649, hsa_circ_0004585, hsa-circ-0004771, circ-CCDC66, circ-ABCC1, and circ-STIL are non-invasive diagnostic biomarkers for CRC, and hsa_circ_0007534, hsa_circ_0000370, hsa_circ_0082182 hsa_circ_0035445, hsa_circ_0002320 and circVAPA can be applied for CRC diagnosis and prognosis.

Bladder Cancer

Bladder cancer is the most common occurring malignancy of urinary system, with an estimated 549,000 new cases and 200,000 deaths in 2018 (1). Cystoscopy and biopsy are used as the criterion standard for diagnosing bladder cancer and no reliable biomarker is available to replace these methods at present (94). However, owing to the invasiveness of cystoscopy and biopsy, patient compliance is poor. Therefore, promising non-invasive diagnostic and prognostic biomarkers for bladder cancer are urgently needed. Xu et al. (75) investigated the expression of hsa_circ_0003221 also called circPTK2 in the blood of patients with bladder cancer (75). The level of blood hsa_circ_0003221 was significantly high in the blood samples, with strong association with several clinicopathologic characteristics, involving poor differentiation, N2-N3 lymph node metastasis, and TNM stage. Another study has indicated that circFARSA, circSHKBP1, circBANP, and lncRNA urothelial carcinoma-associated 1 (UCA1) are correlated with the diagnosis and prognosis of bladder cancer (76). The expression of circFARSA, circSHKBP, and lncRNA UCA1 were significantly higher in the serum of bladder cancer patients than healthy people, but there was no significant difference of serum circBANP expression in bladder cancer patients compared with healthy people. The AUC value of circSHKBP1 and lncRNA UCA1 signature to discriminate patients with bladder cancer from controls was 0.804, and that of this signature was 0.870 with respect of low-grade tumors. Moreover, the expression of circFARSA, circSHKBP1, and circBANP increased in the recurrent bladder cancer patients in comparison with non-recurrent patients, the AUC of the combination of circFARSA and circBANP to distinguish tumor recurrence from those without was 0.737. Chi et al. (95) confirmed that sa_circ_0000285 was significantly reduced in bladder cancer serum in contrast to healthy controls, and it was related to tumor size, differentiation, lymph node metastasis, distant metastasis and TNM stage. Furthermore, hsa_circ_0000285 expression was lower in cisplatin-resistant bladder cancer patients when comparing with those who were cisplatin-sensitive, indicating its important role in bladder cancer chemo-sensitivity. Therefore, as for bladder cancer, hsa_circ_0003221, hsa_circ_0000285 and circBANP play crucial roles in the prognosis, and circFARSA, circSHKBP1 can be used in the both diagnosis and prognosis.

Endometrial Cancer

The prevalence of endometrial cancer has been increased that about 320,000 new cases and 76,000 deaths were estimated in 2012 (77). A study has aimed to explore the roles of serum circRNAs in endometrial cancer, and has elucidated that hsa_circ_0109046 and hsa_circ_0002577 were higher in the serum of patients with endometrial cancer than that that of healthy controls. Also, these two stable circRNAs could provide information about the development, metastasis and prognosis of endometrial cancer (96).

Cervical Cancer

Cervical cancer ranks as the fourth common malignant tumor in women, with an estimated 570,000 cases and 311,000 deaths in 2018 worldwide (1). Several invasive prognostic factors have been applied in clinical practice, such as International Federation of Gynecology and Obstetrics (FIGO) stage, lymph node metastasis, lymph-vascular space invasion (LVSI), and deep stromal infiltration (97). However, non-invasive approaches for detecting and predicting cervical cancer are needed. Wang et al. (78) identified that the expression of hsa_circ_0101996, hsa_circ_0104649, hsa_circ_0104443, and hsa_circ_0101119 in whole blood had similar trend compared with in tumor tissues. Among them, hsa_circ_01- 01996 and hsa_circ_0101119 were upregulated more than 4-fold in whole blood of cervical cancer patient in contrast to healthy controls. ROC analysis revealed that hsa_circ_0101996 and hsa_circ_0101119 could distinguish cervical cancer patients from healthy controls with AUC values of 0.906 and 0.887, respectively. Intriguingly, there was a markedly improved AUC value of 0.964 when combining hsa_circ_0101996 and hsa_circ_0101119, and the sensitivity and specificity reached to 94.3 and 87.3%, respectively. Tang et al. (79) validated that circFoxO3a expression was decreased in serum of cervical patients compared with healthy volunteers, and the low expression was associated with severe stromal invasion and positive lymph node metastasis. Meanwhile, the lower level of serum circFoxO3a led to poorer overall survival and recurrence-free survival, suggesting circFoxO3a is a non-invasive tool for predicting survival in cervical cancer patients. Based on these two studies, hsa_circ_0101996 and hsa_circ_0101119 are useful for diagnosing cervical cancer, while circFoxO3a affects the prognosis of cervical cancer.

Leukemia

Leukemia is a group of life-threatening malignant disorders of the blood and bone marrow, which lack of convenient methods to detect (98). Pan et al. (99) confirmed that circBA9.3 was associated with prognosis and tyrosine kinase inhibitors (TKIs) resistance in patients with chronic myeloid leukemia (CML). TKIs are effective therapy for CML patients, while

some patients who are not responsive to TKIs have elevated circBA9.3 expression in the blood. Moreover, the overexpression of circBA9.3 accelerates the proliferation and inhibits apoptosis of cancer cells. Besides, circHIPK3 was also upregulated in peripheral blood mononuclear cells (PBMC) and serum samples from CML compared with healthy controls, and high circHIPK3 predicted a poor outcome of CML patients and may be an independent prognostic factor for CML development. Knockdown of circHIPK3 prevented proliferation and triggered apoptosis of cancer cell (100), indicating circHIPK3 can participate in the prognosis of CML.

Melanoma

Melanoma originates from the basal layer of epidermis, and its morbidity keep increasing worldwide (101). A study has determined an upregulation of hsa_circ_0001591 in serum of patients with melanoma compared with normal controls. Moreover, high expression of hsa_circ_0001591 was correlated with inferior overall survival and disease-free survival in comparison with low expression group. The underlying mechanism may be related to the suppression of miR-431-5p (102).

Osteosarcoma

Osteosarcoma is the most frequent primary malignant bone tumor in children, adolescents and young adults (103). Alkaline phosphatase (ALP) and lactate dehydrogenase (LDH) remain as the most common serum biomarkers used for diagnosing osteosarcoma in spite of their unsatisfactory sensitivity and specificity (104). A study identified that a circRNA named hsa_circ_0081001 was significantly increased in the serum of osteosarcoma patients, and the expression of hsa_circ_0081001 was gradually increased in the benign bone tumor and osteosarcoma compared to the control group (105). The AUC value of hsa_circ_0081001 (0.898) was higher than that of ALP (0.673) and LDH (0.800). Further analysis suggested that high hsa_circ_0081001 expression was associated with chemoresistant, lung metastasis or recurrence of osteosarcoma, and the expression was remarkably reduced in the serum after preoperative chemotherapy of two cycles and after operation. The results confirmed that serum hsa_circ_0081001 is an independent diagnostic and prognostic factor for osteosarcoma patients. Similar findings were demonstrated in another study that a significant increase of serum hsa_circ_0000885 was detected in osteosarcoma patients, especially in patients with Enneking stage IIB and III osteosarcoma, compared with early-stage osteosarcoma (106). Moreover, the levels of serum hsa_circ_0000885 were significantly higher in patients with osteosarcoma than patients with benign bone tumors or healthy controls. The AUC value for distinguishing between patients with osteosarcoma from healthy individuals was 0.783, while it was 0.714 when comparing osteosarcoma with benign bone tumors. Also, the increased level of serum hsa_circ_0000885 promoted lung metastasis and narrowed overall survival and disease-free survival, and the serum levels of hsa_circ_0000885 markedly decreased after chemotherapy and surgery. Thus, hsa_circ_0000885 could serve as a promising diagnostic and prognostic biomarker for osteosarcoma.

PERSPECTIVES AND CHALLENGES

In comparison with linear RNAs, circRNAs have covalent circular structure without a 3′-end and 5′-end, which strengthens the characteristics of stability and abundance in circulating blood, especially in serum exosomes (107). Moreover, circRNAs are significantly upregulated or downregulated in various types of cancer with high AUC value, sensitivity, and specificity. Due to the biological functions of circRNAs and the non-invasive property of circulating circRNAs, relevant studies have verified that circulating circRNAs have the potential to act as promising biomarkers for diagnosing and prognosing different types of cancer. Nevertheless, there are several limitations when using circRNAs clinically to detect and predict cancer progression. A majority of circRNAs known to be dysregulated have been reported in only a single study with small scale of samples, and rare systematic validation studies with randomized trials based on these "verified" circRNAs with well-characterized and diverse patient samples have been conducted. Furthermore, a lack of standard naming system for circRNAs could cause confusion for further research. Also, since most circRNA sequences is shared with the miRNAs generated from the host gene, the identification, quantification, and validation, as well as overexpression and silencing strategies of circRNAs will be affected by specific back-splicing junction and become especially sensitive to biological and experimental artifacts (108). Besides, the underlying mechanisms have been scarcely reported in current studies. Therefore, studies based on larger samples and multiple centers should be conducted, and the "verified" circRNAs should be reconfirmed in more studies. Standard protocols including standard naming system, thorough validation, accurate quantification, careful confirmation, are urgently needed in order to compare findings from different studies. Additionally, we should investigate the role of circulating circRNAs in various types of cancer, whether they work as cancer promoting or suppressing agents, and how they work. A better understanding of the mechanisms of circulating circRNAs in cancer will promote the development of circRNA-based diagnostic tools and therapies for cancer. Although the study of circRNAs in cancer is still in its infancy, the current researches have validated the diagnostic and prognostic value of circulating circRNAs in different cancer types, and the importance given to circulating circRNAs as biomarkers for cancer diagnosis and prognosis has been increasing just over the last few years.

Apart from being effective biomarkers, economic benefit could be another important reason that emphasizes the value of circulating circRNAs. Since patients diagnosed with cancer are supposed to routinely monitor due to the risk of tumor recurrence and progression, the costs of cancer do tend to be high. According to the data from the Agency for Healthcare Research and Quality in the United States, there was a 98% increase from the agency projections in 2014 due to the

high expenditure of cancer care and treatment which may approximately cost the American taxpayer 173 billion dollars in 2020 (109, 110). A significant portion of these costs is associated with the poor diagnosis of cancer. Studies have confirmed that incremental costs are significantly higher for advanced-stage cancer than for early-stage cancer (111), and rough estimate for cost-savings from early-stage cancer is 26 billion dollars (112). Thus, cancer biomarkers with high sensitivity and specificity can significantly reduce the cost. Circulating circRNAs as a kind of non-invasive cancer biomarkers with high sensitivity and specificity in different cancer, have been proven to be clinically cost-effective and treatment-effective because they can distinguish low-risk patients from high-risk patients at an early tumor stage (113). Therefore, the clinical generalization of circulating circRNAs in the future may save substantial expenditure in cancer care and treatment.

CONCLUSION

Cancer remains as one of the leading causes of morbidity and mortality in the world, and circRNAs present a great capability to be promising biomarkers due to their high stability and conservation. Indeed, this discovery of the characteristics and biological functions of circRNAs has enabled a new understanding of the fundamental mechanisms of oncogenesis, and the relevant studies concerning circulating circRNAs has revealed exciting prospects for diagnosis and prognosis as cancer biomarkers. Although circulating circRNAs still lie in a new field with much to be explored, the source and function of circulating circRNAs should be investigated for better applying them in detecting and predicting cancer. As discussed in this review, there are still some challenges that should be overcome to further promote circulating circRNAs based biomarkers for clinical applications. By establishing this thorough review on circRNAs, we hope to provide valuable insights to how we can better tackle cancer in the future.

AUTHOR CONTRIBUTIONS

Conceptualization: ZL and PW. Writing: MW, FX, and JL. Figure and Table: YZ. Editing: MW, QZ, and ZL. Supervision: ZL and PW. Funding: PW. **Figure 1** was created using Biorender.com. All authors contributed to the article and approved the submitted version.

FUNDING

This work was funded by the National Natural Science Foundation of China (Grant No. 31800652), Young Scientist Program by Beijing University of Chinese Medicine (Grant No. BUCM-2019-QNKXJ-C014), and the Double First Class Construction Funds of Discipline of Integrated Traditional Chinese and Western Medicine of Beijing University of Chinese Medicine.

REFERENCES

1. Bray F, Ferlay J, Soerjomataram I, Siegel RL, Torre LA, Jemal A. Global cancer statistics 2018: GLOBOCAN estimates of incidence and mortality worldwide for 36 cancers in 185 countries. *CA Cancer J. Clin*. (2018) 68:394–424. doi: 10.3322/caac.21492
2. Liao Z, Tan ZW, Zhu P, Tan NS. Cancer-associated fibroblasts in tumor microenvironment–accomplices in tumor malignancy. *Cell. Immunol*. (2019) 343:103729. doi: 10.1016/j.cellimm.2017.12.003
3. Liao Z, Wong SW, Yeo HL, Zhao Y. Smart nanocarriers for cancer treatment: clinical impact and safety. *NanoImpact*. (2020) 20:100253. doi: 10.1016/j.impact.2020.100253
4. Yang Y, Yang T, Liu S, Cao Z, Zhao Y, Su X, et al. Concentrated ambient PM2. 5 exposure affects mice sperm quality and testosterone biosynthesis. *PeerJ*. (2019) 7:e8109. doi: 10.7717/peerj.8109
5. Wang M, Yang Y, Liao Z. Diabetes and cancer: epidemiological and biological links. *World J. Diabetes*. (2020) 11:227. doi: 10.4239/wjd.v11.i6.227
6. Gonzalez-Molina J, Gramolelli S, Liao Z, Carlson JW, Ojala PM, Lehti K. MMP14 in sarcoma: a regulator of tumor microenvironment communication in connective tissues. *Cells*. (2019) 8:991. doi: 10.3390/cells8090991
7. Milman N, Ginini L, Gil Z. Exosomes and their role in tumorigenesis and anticancer drug resistance. *Drug Resist. Updates*. (2019) 45:1–12. doi: 10.1016/j.drup.2019.07.003
8. Liao Z, Chua D, Tan NS. Reactive oxygen species: a volatile driver of field cancerization and metastasis. *Mol. Cancer*. (2019) 18:1–10. doi: 10.1186/s12943-019-0961-y
9. Wang M, Tan Y, Shi Y, Wang X, Liao Z, Wei P. Diabetes and sarcopenic obesity: pathogenesis, diagnosis, and treatments. *Front. Endocrinol*. (2020) 11:568. doi: 10.3389/fendo.2020.00568
10. Khan RMM, Chua ZJY, Tan JC, Yang Y, Liao Z, Zhao Y. From pre-diabetes to diabetes: diagnosis, treatments and translational research. *Medicina*. (2019) 55:546. doi: 10.3390/medicina55090546
11. Vaidyanathan R, Soon RH, Zhang P, Jiang K, Lim CT. Cancer diagnosis: from tumor to liquid biopsy and beyond. *Lab Chip*. (2019) 19:11–34. doi: 10.1039/C8LC00684A
12. Zaimy M, Saffarzadeh N, Mohammadi A, Pourghadamyari H, Izadi P, Sarli A, et al. New methods in the diagnosis of cancer and gene therapy of cancer based on nanoparticles. *Cancer Gene Therapy*. (2017) 24:233–43. doi: 10.1038/cgt.2017.16
13. Guarnerio J, Bezzi M, Jeong JC, Paffenholz SV, Berry K, Naldini MM, et al. Oncogenic role of fusion-circRNAs derived from cancer-associated chromosomal translocations. *Cell*. (2016) 165:289–302. doi: 10.1016/j.cell.2016.03.020
14. Li R, Jiang J, Shi H, Qian H, Zhang X, Xu W. CircRNA: a rising star in gastric cancer. *Cell. Mol. Life Sci*. (2020) 77:1661–80. doi: 10.1007/s00018-019-03345-5
15. Jeck WR, Sorrentino JA, Wang K, Slevin MK, Burd CE, Liu J, et al. Circular RNAs are abundant, conserved, and associated with ALU repeats. *RNA*. (2013) 19:141–57. doi: 10.1261/rna.035667.112
16. Zhang XO, Wang HB, Zhang Y, Lu X, Chen LL, Yang L. Complementary sequence-mediated exon circularization. *Cell*. (2014) 159:134–47. doi: 10.1016/j.cell.2014.09.001
17. Vicens Q, Westhof E. Biogenesis of circular RNAs. *Cell*. (2014) 159:13–4. doi: 10.1016/j.cell.2014.09.005
18. Rybak-Wolf A, Stottmeister C, GlaŽar P, Jens M, Pino N, Giusti S, et al. Circular RNAs in the mammalian brain are highly abundant, conserved, and dynamically expressed. *Mol. Cell*. (2015) 58:870–85. doi: 10.1016/j.molcel.2015.03.027
19. Thomas LF, Sætrom P. Circular RNAs are depleted of polymorphisms at microRNA binding sites. *Bioinformatics*. (2014) 30:2243–6. doi: 10.1093/bioinformatics/btu257
20. Memczak S, Papavasileiou P, Peters O, Rajewsky N. Identification and characterization of circular RNAs as a new class of putative biomarkers in human blood. *PLoS ONE*. (2015) 10:e0141214. doi: 10.1371/journal.pone.0141214

21. Kristensen LS, Andersen MS, Stagsted LVW, Ebbesen KK, Hansen TB, Kjems J. The biogenesis, biology and characterization of circular RNAs. *Nat. Rev. Genet*. (2019) 20:675–91. doi: 10.1038/s41576-019-0158-7
22. Martinez B, Peplow PV. MicroRNAs in blood and cerebrospinal fluid as diagnostic biomarkers of multiple sclerosis and to monitor disease progression. *Neural Regen. Res*. (2020) 15:606–19. doi: 10.4103/1673-5374.266905
23. Meng S, Zhou H, Feng Z, Xu Z, Tang Y, Li P, et al. CircRNA: functions and properties of a novel potential biomarker for cancer. *Mol. Cancer*. (2017) 16:1–8. doi: 10.1186/s12943-017-0663-2
24. Suzuki H, Zuo Y, Wang J, Zhang MQ, Malhotra A, Mayeda A. Characterization of RNase R-digested cellular RNA source that consists of lariat and circular RNAs from pre-mRNA splicing. *Nucleic Acids Res.* (2006) 34:e63. doi: 10.1093/nar/gkl151
25. Chen I, Chen CY, Chuang TJ. Biogenesis, identification, and function of exonic circular RNAs. *Wiley Interdiscipl. Rev*. (2015) 6:563–79. doi: 10.1002/wrna.1294
26. Li Z, Huang C, Bao C, Chen L, Lin M, Wang X, et al. Exon-intron circular RNAs regulate transcription in the nucleus. *Nat. Struct. Mol. Biol*. (2015) 22:256. doi: 10.1038/nsmb.2959
27. Lasda E, Parker R. Circular RNAs: diversity of form and function. *RNA*. (2014) 20:1829–42. doi: 10.1261/rna.047126.114
28. Wang F, Nazarali AJ, Ji S. Circular RNAs as potential biomarkers for cancer diagnosis and therapy. *Am. J. Cancer Res*. (2016) 6:1167.
29. Memczak S, Jens M, Elefsinioti A, Torti F, Krueger J, Rybak A, et al. Circular RNAs are a large class of animal RNAs with regulatory potency. *Nature*. (2013) 495:333–8. doi: 10.1038/nature11928
30. Hansen TB, Jensen TI, Clausen BH, Bramsen JB, Finsen B, Damgaard CK, et al. Natural RNA circles function as efficient microRNA sponges. *Nature*. (2013) 495:384–8. doi: 10.1038/nature11993
31. Kefas B, Godlewski J, Comeau L, Li Y, Abounader R, Hawkinson M, et al. microRNA-7 inhibits the epidermal growth factor receptor and the Akt pathway and is down-regulated in glioblastoma. *Cancer Res*. (2008) 68:3566–72. doi: 10.1158/0008-5472.CAN-07-6639
32. Pan H, Li T, Jiang Y, Pan C, Ding Y, Huang Z, et al. Overexpression of circular RNA ciRS-7 abrogates the tumor suppressive effect of miR-7 on gastric cancer via PTEN/PI3K/AKT signaling pathway. *J. Cell. Biochem*. (2018) 119:440–6. doi: 10.1002/jcb.26201
33. Lukiw W. Circular RNA (circRNA) in Alzheimer's disease (AD). *Front. Genet*. (2013) 4:307. doi: 10.3389/fgene.2013.00307
34. Zheng Q, Bao C, Guo W, Li S, Chen J, Chen B, et al. Circular RNA profiling reveals an abundant circHIPK3 that regulates cell growth by sponging multiple miRNAs. *Nat. Commun*. (2016) 7:1–13. doi: 10.1038/ncomms11215
35. Yang Y, Fan X, Mao M, Song X, Wu P, Zhang Y, et al. Extensive translation of circular RNAs driven by N 6-methyladenosine. *Cell Res*. (2017) 27:626–41. doi: 10.1038/cr.2017.31
36. Zhang M, Zhao K, Xu X, Yang Y, Yan S, Wei P, et al. A peptide encoded by circular form of LINC-PINT suppresses oncogenic transcriptional elongation in glioblastoma. *Nat. Commun*. (2018) 9:1–17. doi: 10.1038/s41467-018-06862-2
37. Zhang M, Huang N, Yang X, Luo J, Yan S, Xiao F, et al. A novel protein encoded by the circular form of the SHPRH gene suppresses glioma tumorigenesis. *Oncogene*. (2018) 37:1805–14. doi: 10.1038/s41388-017-0019-9
38. Ashwal-Fluss R, Meyer M, Pamudurti NR, Ivanov A, Bartok O, Hanan M, et al. circRNA biogenesis competes with pre-mRNA splicing. *Mol. Cell*. (2014) 56:55–66. doi: 10.1016/j.molcel.2014.08.019
39. Du WW, Yang W, Liu E, Yang Z, Dhaliwal P, Yang BB. Foxo3 circular RNA retards cell cycle progression via forming ternary complexes with p21 and CDK2. *Nucleic Acids Res*. (2016) 44:2846–58. doi: 10.1093/nar/gkw027
40. Zeng Y, Du WW, Wu Y, Yang Z, Awan FM, Li X, et al. A circular RNA binds to and activates AKT phosphorylation and nuclear localization reducing apoptosis and enhancing cardiac repair. *Theranostics*. (2017) 7:3842. doi: 10.7150/thno.19764
41. Chen N, Zhao G, Yan X, Lv Z, Yin H, Zhang S, et al. A novel FLI1 exonic circular RNA promotes metastasis in breast cancer by coordinately regulating TET1 and DNMT1. *Genome Biol*. (2018) 19:1–14. doi: 10.1186/s13059-018-1594-y
42. Anfossi S, Babayan A, Pantel K, Calin GA. Clinical utility of circulating non-coding RNAs - an update. *Nat. Rev. Clin. Oncol*. (2018) 15:541–63. doi: 10.1038/s41571-018-0035-x
43. Chen YP, Chan ATC, Le QT, Blanchard P, Sun Y, Ma J. Nasopharyngeal carcinoma. *Lancet*. (2019) 394:64–80. doi: 10.1016/S0140-6736(19)30956-0
44. Shuai M, Hong J, Huang D, Zhang X, Tian Y. Upregulation of circRNA_0000285 serves as a prognostic biomarker for nasopharyngeal carcinoma and is involved in radiosensitivity. *Oncol. Lett*. (2018) 16:6495–501. doi: 10.3892/ol.2018.9471
45. Luo Y, Ma J, Liu F, Guo J, Gui R. Diagnostic value of exosomal circMYC in radioresistant nasopharyngeal carcinoma. *Head Neck*. (2020) 42:3702–11. doi: 10.1002/hed.26441
46. Wang J, Kong J, Nie Z, Chen D, Qiang J, Gao W, et al. Circular RNA Hsa_circ_0066755 as an oncogene via sponging miR-651 and as a promising diagnostic biomarker for nasopharyngeal carcinoma. *Int. J. Med. Sci*. (2020) 17:1499–507. doi: 10.7150/ijms.47024
47. Wang Q, Liu H, Liu Z, Yang L, Zhou J, Cao X, et al. Circ-SLC7A5, a potential prognostic circulating biomarker for detection of ESCC. *Cancer Genet*. (2020) 240:33–9. doi: 10.1016/j.cancergen.2019.11.001
48. Collins LG, Haines C, Perkel R, Enck RE. Lung cancer: diagnosis and management. *Am. Fam. Physician*. (2007) 75:56–63. doi: 10.1186/1471-2296-8-1
49. Li L, Li W, Chen N, Zhao H, Xu G, Zhao Y, et al. FLI1 exonic circular RNAs as a novel oncogenic driver to promote tumor metastasis in small cell lung cancer. *Clin. Cancer Res*. (2019) 25:1302–17. doi: 10.1158/1078-0432.CCR-18-1447
50. Hang D, Zhou J, Qin N, Zhou W, Ma H, Jin G, et al. A novel plasma circular RNA circFARSA is a potential biomarker for non-small cell lung cancer. *Cancer Med*. (2018) 7:2783–91. doi: 10.1002/cam4.1514
51. Tan S, Gou Q, Pu W, Guo C, Yang Y, Wu K, et al. Circular RNA F-circEA produced from EML4-ALK fusion gene as a novel liquid biopsy biomarker for non-small cell lung cancer. *Cell Res*. (2018) 28:693–5. doi: 10.1038/s41422-018-0033-7
52. Liu X-X, Yang Y-E, Liu X, Zhang M-Y, Li R, Yin H-Y, et al. A two-circular RNA signature as a noninvasive diagnostic biomarker for lung adenocarcinoma. *J. Transl. Med*. (2019) 17:50. doi: 10.1186/s12967-019-1800-z
53. Wu SG, He ZY, Zhou J, Sun JY, Li FY, Lin Q, et al. Serum levels of CEA and CA15-3 in different molecular subtypes and prognostic value in Chinese breast cancer. *Breast*. (2014) 23:88–93. doi: 10.1016/j.breast.2013.11.003
54. Torre LA, Bray F, Siegel RL, Ferlay J, Lortet-Tieulent J, Jemal A. Global cancer statistics, 2012. *CA Cancer J. Clin*. (2015) 65:87–108. doi: 10.3322/caac.21262
55. Li P, Chen S, Chen H, Mo X, Li T, Shao Y, et al. Using circular RNA as a novel type of biomarker in the screening of gastric cancer. *Clin. Chim. Acta*. (2015) 444:132–6. doi: 10.1016/j.cca.2015.02.018
56. Chen S, Li T, Zhao Q, Xiao B, Guo J. Using circular RNA hsa_circ_0000190 as a new biomarker in the diagnosis of gastric cancer. *Clin. Chim. Acta*. (2017) 466:167–71. doi: 10.1016/j.cca.2017.01.025
57. Zhao Q, Chen S, Li T, Xiao B, Zhang X. Clinical values of circular RNA 0000181 in the screening of gastric cancer. *J. Clin. Lab Anal*. (2018) 32:e22333. doi: 10.1002/jcla.22333
58. Notarpaolo A, Layese R, Magistri P, Gambato M, Colledan M, Magini G, et al. Validation of the AFP model as a predictor of HCC recurrence in patients with viral hepatitis-related cirrhosis who had received a liver transplant for HCC. *J. Hepatol*. (2017) 66:552–9. doi: 10.1016/j.jhep.2016.10.038
59. Li J, Gao T, Gu S, Zhi J, Yang J, Li G. An electrochemical biosensor for the assay of alpha-fetoprotein-L3 with practical applications. *Biosens. Bioelectron*. (2017) 87:352–7. doi: 10.1016/j.bios.2016.08.071
60. Lok AS, Sterling RK, Everhart JE, Wright EC, Hoefs JC, Di Bisceglie AM, et al. Des-gamma-carboxy prothrombin and alpha-fetoprotein as biomarkers for the early detection of hepatocellular carcinoma. *Gastroenterology*. (2010) 138:493–502. doi: 10.1053/j.gastro.2009.10.031
61. Rawla P, Sunkara T, Gaduputi V. Epidemiology of pancreatic cancer: global trends, etiology and risk factors. *World J. Oncol*. (2019) 10:10–27. doi: 10.14740/wjon1166
62. Siegel RL, Miller KD, Jemal A. Cancer statistics, 2020. *CA Cancer J. Clin*. (2020) 70:7–30. doi: 10.3322/caac.21590

63. McGuigan A, Kelly P, Turkington RC, Jones C, Coleman HG, McCain RS. Pancreatic cancer: a review of clinical diagnosis, epidemiology, treatment and outcomes. *World J. Gastroenterol*. (2018) 24:4846–61. doi: 10.3748/wjg.v24.i43.4846
64. Yang F, Liu DY, Guo JT, Ge N, Zhu P, Liu X, et al. Circular RNA circ-LDLRAD3 as a biomarker in diagnosis of pancreatic cancer. *World J. Gastroenterol*. (2017) 23:8345–54. doi: 10.3748/wjg.v23.i47.8345
65. Li Z, Yanfang W, Li J, Jiang P, Peng T, Chen K, et al. Tumor-released exosomal circular RNA PDE8A promotes invasive growth via the miR-338/MACC1/MET pathway in pancreatic cancer. *Cancer Lett*. (2018) 432:237–50. doi: 10.1016/j.canlet.2018.04.035
66. Li J, Li Z, Jiang P, Peng M, Zhang X, Chen K, et al. Circular RNA IARS (circ-IARS) secreted by pancreatic cancer cells and located within exosomes regulates endothelial monolayer permeability to promote tumor metastasis. *J. Exp. Clin. Cancer Res*. (2018) 37:177. doi: 10.1186/s13046-018-0822-3
67. Seimiya T, Otsuka M, Iwata T, Tanaka E, Sekiba K, Shibata C, et al. Aberrant expression of a novel circular RNA in pancreatic cancer. *J. Hum. Genet*. (2020) 66:181–91. doi: 10.1038/s10038-020-00826-5
68. Cho WC. Epigenetic alteration of microRNAs in feces of colorectal cancer and its clinical significance. *Expert Rev. Mol. Diagn*. (2011) 11:691–4. doi: 10.1586/erm.11.57
69. Zhang W, Yang S, Liu Y, Wang Y, Lin T, Li Y, et al. Hsa_circ_0007534 as a blood-based marker for the diagnosis of colorectal cancer and its prognostic value. *Int. J. Clin. Exp. Pathol*. (2018) 11:1399–406.
70. Ji W, Qiu C, Wang M, Mao N, Wu S, Dai Y. Hsa_circ_0001649: a circular RNA and potential novel biomarker for colorectal cancer. *Biochem. Biophys. Res. Commun*. (2018) 497:122–6. doi: 10.1016/j.bbrc.2018.02.036
71. Tian J, Xi X, Wang J, Yu J, Huang Q, Ma R, et al. CircRNA hsa_circ_0004585 as a potential biomarker for colorectal cancer. *Cancer Manage. Res*. (2019) 11:5413–23. doi: 10.2147/CMAR.S199436
72. Li XN, Wang ZJ, Ye CX, Zhao BC, Huang XX, Yang L. Circular RNA circVAPA is up-regulated and exerts oncogenic properties by sponging miR-101 in colorectal cancer. *Biomed. Pharmacother*. (2019) 112:108611. doi: 10.1016/j.biopha.2019.108611
73. Pan B, Qin J, Liu X, He B, Wang X, Pan Y, et al. Identification of serum exosomal hsa-circ-0004771 as a novel diagnostic biomarker of colorectal cancer. *Front. Genet*. (2019) 10:1096. doi: 10.3389/fgene.2019.01096
74. Yang N, Xu B, Kong P, Han M, Li BH. Hsa_circ_0002320: a novel clinical biomarker for colorectal cancer prognosis. *Medicine*. (2020) 99:e21224. doi: 10.1097/MD.0000000000021224
75. Xu ZQ, Yang MG, Liu HJ, Su CQ. Circular RNA hsa_circ_0003221 (circPTK2) promotes the proliferation and migration of bladder cancer cells. *J. Cell Biochem*. (2018) 119:3317–25. doi: 10.1002/jcb.26492
76. Pan J, Xie X, Li H, Li Z, Ren C, Ming L. Detection of serum long non-coding RNA UCA1 and circular RNAs for the diagnosis of bladder cancer and prediction of recurrence. *Int. J. Clin. Exp. Pathol*. (2019) 12:2951–8.
77. Morice P, Leary A, Creutzberg C, Abu-Rustum N, Darai E. Endometrial cancer. *Lancet*. (2016) 387:1094–108. doi: 10.1016/S0140-6736(15)00130-0
78. Wang YM, Huang LM, Li DR, Shao JH, Xiong SL, Wang CM, et al. Hsa_circ_0101996 combined with hsa_circ_0101119 in peripheral whole blood can serve as the potential biomarkers for human cervical squamous cell carcinoma. *Int. J. Clin. Exp. Pathol*. (2017) 10:11924–31.
79. Tang X, Liu S, Ding Y, Guo C, Guo J, Hua K, et al. Serum circular FoxO3a serves as a novel prognostic biomarker in squamous cervical cancer. *Cancer Manage. Res*. (2020) 12:2531–40. doi: 10.2147/CMAR.S243329
80. Hirajima S, Komatsu S, Ichikawa D, Takeshita H, Konishi H, Shiozaki A, et al. Clinical impact of circulating miR-18a in plasma of patients with oesophageal squamous cell carcinoma. *Br. J. Cancer*. (2013) 108:1822–9. doi: 10.1038/bjc.2013.148
81. Huang E, Fu J, Yu Q, Xie P, Yang Z, Ji H, et al. CircRNA hsa_circ_0004771 promotes esophageal squamous cell cancer progression via miR-339-5p/CDC25A axis. *Epigenomics*. (2020) 12:587–603. doi: 10.2217/epi-2019-0404
82. Harris L, Fritsche H, Mennel R, Norton L, Ravdin P, Taube S, et al. American society of clinical oncology 2007 update of recommendations for the use of tumor markers in breast cancer. *J. Clin. Oncol*. (2007) 25:5287–312. doi: 10.1200/JCO.2007.14.2364
83. Yin WB, Yan MG, Fang X, Guo JJ, Xiong W, Zhang RP. Circulating circular RNA hsa_circ_0001785 acts as a diagnostic biomarker for breast cancer detection. *Clin. Chim. Acta*. (2018) 487:363–8. doi: 10.1016/j.cca.2017.10.011
84. Nanishi K, Konishi H, Shoda K, Arita T, Kosuga T, Komatsu S, et al. Circulating circERBB2 as a potential prognostic biomarker for gastric cancer: an investigative study. *Cancer Sci*. (2020) 111:4177–86. doi: 10.1111/cas.14645
85. Li WH, Song YC, Zhang H, Zhou ZJ, Xie X, Zeng QN, et al. Decreased expression of Hsa_circ_00001649 in gastric cancer and its clinical significance. *Dis. Markers*. (2017) 2017:4587698. doi: 10.1155/2017/4587698
86. Huang M, He YR, Liang LC, Huang Q, Zhu ZQ. Circular RNA hsa_circ_0000745 may serve as a diagnostic marker for gastric cancer. *World J. Gastroenterol*. (2017) 23:6330–8. doi: 10.3748/wjg.v23.i34.6330
87. Sun H, Xi P, Sun Z, Wang Q, Zhu B, Zhou J, et al. Circ-SFMBT2 promotes the proliferation of gastric cancer cells through sponging miR-182-5p to enhance CREB1 expression. *Cancer Manage. Res*. (2018) 10:5725–34. doi: 10.2147/CMAR.S172592
88. Zhang X, Zhou H, Jing W, Luo P, Qiu S, Liu X, et al. The circular RNA hsa_circ_0001445 regulates the proliferation and migration of hepatocellular carcinoma and may serve as a diagnostic biomarker. *Dis. Markers*. (2018) 2018:3073467. doi: 10.1155/2018/3073467
89. Zhang X, Xu Y, Qian Z, Zheng W, Wu Q, Chen Y, et al. circRNA_104075 stimulates YAP-dependent tumorigenesis through the regulation of HNF4a and may serve as a diagnostic marker in hepatocellular carcinoma. *Cell Death Dis*. (2018) 9:1091. doi: 10.1038/s41419-018-1132-6
90. Wu C, Deng L, Zhuo H, Chen X, Tan Z, Han S, et al. Circulating circRNA predicting the occurrence of hepatocellular carcinoma in patients with HBV infection. *J. Cell Mol. Med*. (2020) 24:10216–22. doi: 10.1111/jcmm.15635
91. Levin B, Brooks D, Smith RA, Stone A. Emerging technologies in screening for colorectal cancer: CT colonography, immunochemical fecal occult blood tests, and stool screening using molecular markers. *CA Cancer J. Clin*. (2003) 53:44–55. doi: 10.3322/canjclin.53.1.44
92. Lin J, Cai D, Li W, Yu T, Mao H, Jiang S, et al. Plasma circular RNA panel acts as a novel diagnostic biomarker for colorectal cancer. *Clin. Biochem*. (2019) 74:60–68. doi: 10.1016/j.clinbiochem.2019.10.012
93. Ye DX, Wang SS, Huang Y, Chi P. A 3-circular RNA signature as a noninvasive biomarker for diagnosis of colorectal cancer. *Cancer Cell Int*. (2019) 19:276. doi: 10.1186/s12935-019-0995-7
94. Ehdaie B, Atoria CL, Lowrance WT, Herr HW, Bochner BH, Donat SM, et al. Adherence to surveillance guidelines after radical cystectomy: a population-based analysis. *Urol. Oncol*. (2014) 32:779–84. doi: 10.1016/j.urolonc.2014.01.024
95. Chi BJ, Zhao DM, Liu L, Yin XZ, Wang FF, Bi S, et al. Downregulation of hsa_circ_0000285 serves as a prognostic biomarker for bladder cancer and is involved in cisplatin resistance. *Neoplasma*. (2019) 66:197–202. doi: 10.4149/neo_2018_180318N185
96. Xu H, Gong Z, Shen Y, Fang Y, Zhong S. Circular RNA expression in extracellular vesicles isolated from serum of patients with endometrial cancer. *Epigenomics*. (2018) 10:187–97. doi: 10.2217/epi-2017-0109
97. Leonardi S, Buttarelli M, De Stefano I, Ferrandina G, Petrillo M, Babini G, et al. The relevance of prelamin A and RAD51 as molecular biomarkers in cervical cancer. *Oncotarget*. (2017) 8:94247–58. doi: 10.18632/oncotarget.21686
98. Juliusson G, Hough R. Leukemia. *Prog. Tumor Res*. (2016) 43:87–100. doi: 10.1159/000447076
99. Pan Y, Lou J, Wang H, An N, Chen H, Zhang Q, et al. CircBA9.3 supports the survival of leukaemic cells by up-regulating c-ABL1 or BCR-ABL1 protein levels. *Blood Cells Mol. Dis*. (2018) 73:38–44. doi: 10.1016/j.bcmd.2018.09.002
100. Feng XQ, Nie SM, Huang JX, Li TL, Zhou JJ, Wang W, et al. Circular RNA circHIPK3 serves as a prognostic marker to promote chronic myeloid leukemia progression. *Neoplasma*. (2020) 67:171–7. doi: 10.4149/neo_2018_181129N908
101. Long GV, Hauschild A, Santinami M, Atkinson V, Mandalà M, Chiarion-Sileni V, et al. Adjuvant dabrafenib plus trametinib in stage III BRAF-mutated melanoma. *N. Engl. J. Med*. (2017) 377:1813–23. doi: 10.1056/NEJMoa1708539

102. Yin D, Wei G, Yang F, Sun X. Circular RNA has circ 0001591 promoted cell proliferation and metastasis of human melanoma via ROCK1/PI3K/AKT by targeting miR-431-5p. *Hum. Exp. Toxicol*. (2020) 40:310–24. doi: 10.1177/0960327120950014
103. Saraf AJ, Fenger JM, Roberts RD. Osteosarcoma: accelerating progress makes for a hopeful future. *Front. Oncol*. (2018) 8:4. doi: 10.3389/fonc.2018.00004
104. Marais LC, Bertie J, Rodseth R, Sartorius B, Ferreira N. Pre-treatment serum lactate dehydrogenase and alkaline phosphatase as predictors of metastases in extremity osteosarcoma. *J. Bone Oncol*. (2015) 4:80–4. doi: 10.1016/j.jbo.2015.09.002
105. Kun-Peng Z, Chun-Lin Z, Jian-Ping H, Lei Z. A novel circulating hsa_circ_0081001 act as a potential biomarker for diagnosis and prognosis of osteosarcoma. *Int. J. Biol. Sci*. (2018) 14:1513–20. doi: 10.7150/ijbs.27523
106. Zhu K, Niu L, Wang J, Wang Y, Zhou J, Wang F, et al. Circular RNA hsa_circ_0000885 levels are increased in tissue and serum samples from patients with osteosarcoma. *Med. Sci. Monit*. (2019) 25:1499–1505. doi: 10.12659/MSM.914899
107. Li Y, Zheng Q, Bao C, Li S, Guo W, Zhao J, et al. Circular RNA is enriched and stable in exosomes: a promising biomarker for cancer diagnosis. *Cell Res*. (2015) 25:981–4. doi: 10.1038/cr.2015.82
108. Jeck WR, Sharpless NE. Detecting and characterizing circular RNAs. *Nat. Biotechnol*. (2014) 32:453–61. doi: 10.1038/nbt.2890
109. Mariotto AB, Yabroff KR, Shao Y, Feuer EJ, Brown ML. Projections of the cost of cancer care in the United States: 2010-2020. *J. Natl. Cancer Inst*. (2011) 103:117–28. doi: 10.1093/jnci/djq495
110. Keehan SP, Cuckler GA, Poisal JA, Sisko AM, Smith SD, Madison AJ, et al. National health expenditure projections, 2019-28: expected rebound in prices drives rising spending growth. *Health Aff*. (2020) 39:704–14. doi: 10.1377/hlthaff.2020.00094
111. Blumen H, Fitch K, Polkus V. Comparison of treatment costs for breast cancer, by tumor stage and type of service. *Am. Health Drug Benefits*. (2016) 9:23–32.
112. Kakushadze Z, Raghubanshi R, Yu W. Estimating cost savings from early cancer diagnosis. *Data*. (2017) 2:30. doi: 10.3390/data2030030
113. Okholm TLH, Nielsen MM, Hamilton MP, Christensen LL, Vang S, Hedegaard J, et al. Circular RNA expression is abundant and correlated to aggressiveness in early-stage bladder cancer. *NPJ Genom. Med*. (2017) 2:36. doi: 10.1038/s41525-017-0038-z

Conflict of Interest: The authors declare that the research was conducted in the absence of any commercial or financial relationships that could be construed as a potential conflict of interest.

Copyright © 2021 Wang, Xie, Lin, Zhao, Zhang, Liao and Wei. This is an open-access article distributed under the terms of the Creative Commons Attribution License (CC BY). The use, distribution or reproduction in other forums is permitted, provided the original author(s) and the copyright owner(s) are credited and that the original publication in this journal is cited, in accordance with accepted academic practice. No use, distribution or reproduction is permitted which does not comply with these terms.

frontiers in Medicine

ORIGINAL RESEARCH
published: 31 March 2021
doi: 10.3389/fmed.2021.651904

Mutant Allele Frequency-Based Intra-Tumoral Genetic Heterogeneity Related to the Tumor Shrinkage Mode After Neoadjuvant Chemotherapy in Breast Cancer Patients

*Chun-hui Zheng[1,2], Zhao-yun Liu[3], Chen-xi Yuan[4], Xiao-yun Dong[5], Hai-mei Li[6], Jin-jin Wang[7], Zhao-peng Zhang[3], Hong-Ying Liu[5], Xiao-yan Ding[8], Wendy Wu[7], Rui-ru Wang[7] and Yong-sheng Wang[3]**

[1] Breast Cancer Center, Shandong Cancer Hospital, Cheeloo College of Medicine, Shandong University, Jinan, China, [2] Departments of Oncology Surgery, People's Hospital, Weifang, China, [3] Breast Cancer Center, Shandong Cancer Hospital and Institute, Shandong First Medical University, Shandong Academy of Medical Sciences, Jinan, China, [4] Department of Radiation Oncology, The Affiliated Yantai Yuhuangding Hospital of Qingdao University, Yantai, China, [5] Genetics Department in School of Bioscience and Technology, Weifang Medical University, Weifang, China, [6] Department of Molecular Biology in School of Bioscience and Technology, Weifang Medical University, Weifang, China, [7] Berry Oncology Corporation, Digital Fujian Park, Fuzhou, China, [8] Department of Laboratory Medicine, Key Laboratory of Clinical Laboratory Diagnostics in Universities of Shandong, Weifang Medical University, Weifang, China

OPEN ACCESS

Edited by:
Guo Chen,
Jinan University, China

Reviewed by:
Youwei Sun,
Emory University, United States
Xue Gao,
University of Chicago, United States

***Correspondence:**
Yong-sheng Wang
wangysh2008@aliyun.com

Specialty section:
This article was submitted to Precision Medicine, a section of the journal Frontiers in Medicine

Received: 11 January 2021
Accepted: 15 February 2021
Published: 31 March 2021

Citation:
Zheng C-h, Liu Z-y, Yuan C-x, Dong X-y, Li H-m, Wang J-j, Zhang Z-p, Liu H-Y, Ding X-y, Wu W, Wang R-r and Wang Y-s (2021) Mutant Allele Frequency-Based Intra-Tumoral Genetic Heterogeneity Related to the Tumor Shrinkage Mode After Neoadjuvant Chemotherapy in Breast Cancer Patients. Front. Med. 8:651904. doi: 10.3389/fmed.2021.651904

The shrinkage mode of tumor extent after neoadjuvant chemotherapy (NAC) is an important index to evaluate the odds of breast-conserving surgery. However, there is no sufficient measurement to predict the shrinkage mode after NAC. In this study, we analyzed 24 patients' formalin-fixed, paraffin-embedded samples before and after treatment and analyzed 456 cancer-related genes panel by using target next-generation sequencing. Meanwhile, the pathological shrinkage mode was reconstructed in three dimensions after surgery, and the genetic heterogeneity level was estimated by mutant-allele tumor heterogeneity (MATH). We measured the genetic intra-tumor heterogeneity and explored its correlation with the shrinkage mode after NAC. A total of 17 matched pair samples of primary tumor tissue and residual tumor tissue were successfully accessed. It was found that the most common mutated genes were TP53 and PIK3CA in both samples before and after NAC, and no recurrent mutations were significantly associated with the shrinkage mode. Besides, the MATH value of formalin-fixed, paraffin-embedded samples before and after NAC was analyzed by the area under the curve of the receiver operating characteristic, and it is feasible to classify patients into concentric shrinkage mode and non-concentric shrinkage mode in NAC based on the MATH threshold of 58. Our findings indicate that the MATH value was associated with the shrinkage mode of breast cancer in a non-linear model. Patients with the MATH value below the threshold of 58 before and after NAC displayed a concentric shrinkage mode. The area under the

curve was 0.89, with a sensitivity of 0.69 and specificity of 1. Our study might provide a promising application of intra-tumor heterogeneity that is measured by MATH to make a choice of surgery.

Keywords: breast cancer, next generation sequencing, gene heterogeneity, shrinkage mode, neoadjuvant chemotherapy

INTRODUCTION

Neoadjuvant chemotherapy (NAC) is prescribed increasingly in patients with advanced breast cancer (1). Previous studies have shown that NAC could facilitate breast conservation in locally advanced breast cancer, reducing volume resection in breast-conserving therapies (2, 3). In contrast, tumors downsized by NAC were reported to have a higher local recurrence after breast-conserving therapy than those who have not (4). Furthermore, large lumpectomy volumes were sacrificed in high response patients (5). There are two states of tumor shrink after NAC, concentric shrinkage mode (CSM) and non-concentric shrinkage mode (NCSM). Patients with CSM after NAC is considered to be ideal candidates for breast-conserving treatment (BCT). Simultaneously, NCSM can potentially lead to false-negative reporting of margins, which may increase the risk of locoregional recurrence (6). At the St. Gallen International Expert Consensus Conference on the Primary Therapy of Early Breast Cancer 2017, experts voted that different surgical strategies should be adopted for breast cancer based on shrinkage mode (7). It is a critical NAC therapeutic effect evaluation criterion to predict the patient will present CSM or NCSM after NAC; predictive measurements are urgently needed to inform the design of the surgical scheme and treatment strategy.

Indeed, the current method of estimating the shrinkage mode after NAC is still under research. Previous studies have reported that tumor response to NAC varied greatly by clinicopathologic variables [i.e., molecular subtype (8); clinical stage (9)]. Patients with triple-negative- and human epidermal growth factor receptor 2-positive tumors have a higher probability of achieving CSM (8). In contrast, there is still a lack of genetic composition studies to improve the stratification.

Recently, remarkable advances in oncogene investigations have made it possible to incorporate next-generation sequencing (NGS) technology into precise clinical care. Intra-tumoral genetic heterogeneity based on the NGS approach for monitoring the response to chemotherapies is currently underway. Tumors with high genetic heterogeneity were thought to contain more comprehensive resistant populations and distinct subpopulations leading to worse survival (10, 11). Thus, we speculated that the complex genetic composition might also influence the shrinkage mode after NAC. A better understanding of the genomics information of the shrinkage mode may suggest more clear classification methods for surgical strategy.

Several bioinformatics methods based on NGS have been proposed to explore tumor genetic heterogeneity (12–14). Mutant-allele tumor heterogeneity (MATH) was used to generally measure genetic heterogeneity, which is based on estimating allelic frequencies of the tumor and making it a measurable variable (15).

This study was designed to identify the pathological shrinkage modes after NAC for breast carcinomas using NGS genomic profiling. As these are clinical data regarding the response, the intra-tumor genetic heterogeneity may help to understand breast cancer biology and performing local-regional management.

METHODS

Patients and Samples

Between October 2016 and April 2018, 24 patients with primary invasive breast cancer confirmed by histopathology with clinical stages II and III were enrolled. Breast MRI was performed before NAC and a week before surgery. Patients diagnosed with the distant metastatic disease before surgery or not examined using MRI before NAC were excluded. All the patients received a full course of anthracycline and taxane-based chemotherapy regimens and underwent radical surgery. Trastuzumab treatment was delivered to human epidermal growth factor receptor 2-positive patients.

To define the tumor molecular subtypes, we identified the immunohistochemistry (IHC) expression of estrogen receptor, progesterone receptor, HER2 status, and proliferation index (Ki-67). Fluorescence *in situ* hybridization was conducted when HER2 expression was detected as grade 2 on IHC. One percent expression rate was used as the cutoff to define positive hormone receptors. HER2 receptor was considered to be positive when HER2 expression was detected as grade 3 on IHC or HER2 gene amplification on fluorescence *in situ* hybridization. The expression of Ki-67 over 20% was considered as high.

The retrospective study was approved by the Institute Review Board of Shandong Cancer Hospital (institute review board approval number: SDTHEC201802002). The informed consents were obtained from all patients.

Pathological Three-Dimensional Reconstruction

After a mastectomy, all specimens were cut into successive large slices and stained with hematoxylin–eosin staining. The residual tumor in the slice was outlined under the microscope, and a three-dimensional model was created under Photoshop 13.0 and 3D-DOCTOR 4.0 software (16).

Abbreviations: NAC, neoadjuvant chemotherapy; ITH, intra-tumor heterogeneity; MATH, mutant-allele tumor heterogeneity; ROC, receiver operating characteristic; CSM, concentric shrinkage mode; NCSM, non-concentric shrinkage mode; FFPE, formalin-fixed, paraffin-embedded; BCT, breast-conserving treatment; NGS, next-generation sequencing.

Clinical–Pathological Patterns

We divided shrinkage mode into two modes, CSM and NCSM (16).

MRI was performed at baseline before NAC; CSM means that the longest diameter retraction rate of the residual tumor was ≤2 cm and ≥50% compared with the longest diameter of the primary tumor before NAC and included four modes, pathologic complete response (PCR); isolated, concentric shrinkage without surrounding lesions; nodular, residual multinodular lesions; and clumps with scattered, concentric shrinkage with surrounding lesions. NCSM means that the longest diameter retraction rate of residual tumor after NAC was >2 cm and/or <50% compared with the longest diameter of the primary tumor before NAC and included two modes, isolated, concentric shrinkage with surrounding lesions; and clumps with scattered and diffuse, replaced lesions (diffuse in whole quadrants) (**Figure 1**) (16).

Tissue DNA Isolation and Purification

Genomic DNA was extracted from the FFPE samples using GeneRead DNA FFPE Kit (Qiagen, USA). The quality of purified DNA was assayed by gel electrophoresis and quantified by Qubit® 4.0 Fluorometer (Life Technologies, USA).

Library Construction and 456 Gene Panel Sequencing

The purified genomic DNA was first fragmented into DNA pieces around 200–300 bp using the enzymatic method (5× WGS Fragmentation Mix, Qiagen, USA). After end repairing, a tailing and T-adaptors ligating by polymerase chain reaction (PCR) reagents were performed in pre-library. The products were followed by exon capture. Captured fragments were subsequently purified and hybridized by 456 gene panels designed by Berry Oncology Corporation, including drug-target genes and hot-spot mutated genes related to cancer development. SNV, Indel, gene fusion, and copy number variation data were detected through 456 panels in 1,000× coverage. All results were annotated by COSMIC, TCGA, ClinVar, and in-house Berry Oncology database (Berry Oncology Corporation, **Supplementary Table 1**).

Bioinformatics Analysis of Mutations

FASTP (17) was used to trim adapters and to remove low-quality sequences to obtain clean reads. The clean reads aligned to Ensemble GRCh37/hg19 reference genome performed by BWA (18). PCR duplications were processed by gencore (19). SAMtools (20) was applied to detect single-nucleotide variations (SNVs), insertions, and deletions. HGVS variant description was annotated by ANNOVAR (21) software. We excluded SNVs with PopFreqMax > 0.05 and identified non-synonymous SNVs with VAF > 0.5% or with VAF > 0.1% in cancer hotspots for further analysis.

Statistical Analysis

Mroz et al. (15) introduced a measurement of heterogeneity termed as MATH. It is the ratio of scaled median absolute deviation (MAD) to median stated in percentage. To investigate the correlation between intra-tumoral genetic heterogeneity and the shrinkage mode after NAC, we used MATH value to assess intra-tumoral genetic heterogeneity.

The MATH value for tumors was based on the distribution of mutant-allele fractions among specific mutated loci, calculated as the percentage ratio of the width (MAD scaled by a constant factor so that the expected MAD of a sample from a normal distribution equals the standard deviation) to the center (median) of its distribution (15):

$$MATH = 100 * MAD/median.$$

The Fisher exact test was used for the comparison of MATH value between CSM and NCSM groups. $P < 0.05$ was considered statistically significant. MATH value was assessed using the area under the curve of the receiver operating characteristic (ROC). All statistical analyses were performed by SPSS 22.0 software.

RESULTS

We carried out high-coverage sequencing of 456 cancer-relevant genes on a group of 24 paired pre/post-NAC matched samples. Seven paired specimens (7/24, 29.1%) were excluded from the analysis because of insufficient amount/poor quality of DNA content. For 17 (17/24, 70.8%) patients, both primary tumor biopsy and residual tissues were successfully accessed and analyzed. Thirteen patients got CSM, and four patients got NCSM. Patient's characteristics are listed in **Table 1**.

Significantly Mutated Genes in the Paired Samples

After NAC, the 18 most commonly mutated genes in the pre-NAC tumors were observed in this breast cancer cohort, as summarized in **Figure 2**. We compared the gene mutation frequency before and after NAC. In all cases, the most frequently altered genes were TP53 altered in 11 cases (11/17, 70.6%) of pre-NAC and 8 cases (8/17, 52.9%) of post-NAC samples, *PIK3CA* altered in 6 (6/17, 35.3%) of pre-NAC and 8 (8/17,47.1%) of post-NAC samples, followed by *ACVR2A* (3/17, 17.6% vs. 1/17, 5.9%), and *BRCA2* (3/17, 17.6% vs. 2/17, 11.8%) (**Figure 2**, **Supplementary Table 2**). There was no significant difference in the frequency of gene mutation between the two groups.

We compared *TP53* and *PIK3CA* hot mutations frequency between pre-NAC and post-NAC in CSM and NCSM. It was found that *TP53* hot mutations frequency in CSM declined from 70% in pre-NAC to 30% in post-NAC, and those values in NSCM raised from 50 to 100%. *PIK3CA* hot mutations frequency in CSM was from 23% in pre-NAC, then climbed to 38%, and in NSCM from 50 to 75% (**Table 2**).

From all these samples, we identified 142 variants in 456 genes. One hundred thirteen mutations were detected in the pre-NAC group, and 70 gene (70/142, 49.3%) mutations were only found in the pre-NAC group (**Supplementary Table 2**). The mutation frequency of *NOTCH1* was 17.6% (3/17) in pre-NAC samples. Meanwhile, *CSF1R*, *JAK2*, *MAP3K1*, *MECOM*, *PAX5,* and *PTEN* were mutated in 11.8% (2/17) among

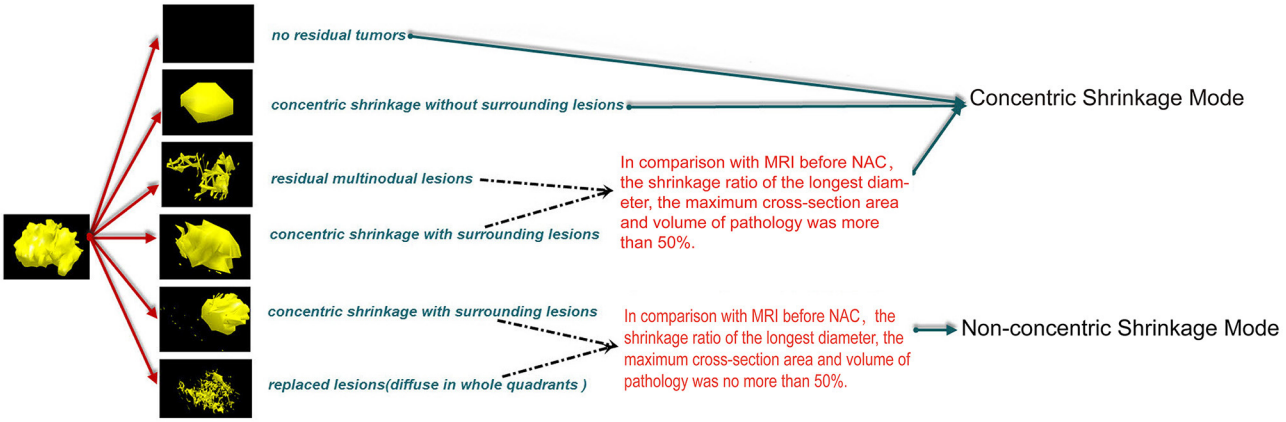

FIGURE 1 | CSM means that the longest diameter retraction rates of the residual tumor were ≤2 cm and ≥50% compared with the longest diameter of the primary tumor before NAC and included four modes, PCR, pathologic complete response; isolated, concentric shrinkage without surrounding lesions; nodular, residual multinodular lesions; clumps with scattered, concentric shrinkage with surrounding lesions. NCSM means that the longest diameter retraction rates of residual tumor after NAC were >2 cm and/or <50% compared with the longest diameter of the primary tumor before NAC and included two modes, isolated, concentric shrinkage with surrounding lesions; clumps with scattered and diffuse replaced lesions (diffuse in whole quadrants). CSM, concentric shrinkage mode; NAC, neo-adjuvant chemotherapy; PCR, pathologic complete response; NCSM, non-concentric shrinkage mode.

TABLE 1 | Patient and tumor characteristics.

Pre-NAC sample No	Post-NAC sample No	Pre-MATH value	Post-MATH value	Molecular subtype	Shrinkage mode
C1803725	C1803700	16.41	1.1	Luminal B/HER2 positive	CSM
C1803704	C1803772	79.74	128	Luminal B	NSCM
C1803878	C1803788	27.4	93.22	Triple-negative	CSM
C1803804	C1803818	92.47	15.3	Luminal B	CSM
C1803790	C1803821	59.7	102.7	Luminal A	NCSM
C1803787	C1803826	70.21	115.7	Her-2 positive	NCSM
C1803814	C1803829	93.11	0	Triple-negative	CSM
C1803796	C1803830	24.36	71	Luminal A	CSM
C1803799	C1803833	21.42	85.32	Luminal A	CSM
C1803870	C1803834	48.5	66.29	Luminal B/HER2 positive	CSM
C1803783	C1803840	136.3	130.1	Luminal B	NCSM
C1803813	C1803841	57.84	39.66	Luminal B/HER2 positive	CSM
C1803792	C1803854	36.1	24.68	Luminal B/HER2 positive	CSM
C1803817	C1803862	0	0	Her-2 positive	CSM
C1803805	C1803863	42.74	47.38	Her-2 positive	CSM
C1803791	C1803869	79.36	46.86	Luminal A	CSM
C1803876	C1803873	9.8	121.55	Her-2 positive	CSM

NAC, neo-adjuvant chemotherapy; MATH, mutant-allele tumor heterogeneity; CSM, concentric shrinkage mode; NCSM, non-concentric shrinkage mode.

pre-NAC samples, and the frequency of the remaining 63 genes was 5.9% (1/17) in pre-NAC samples. Also, these mutated genes vanished under the NAC. Concurrently, 29 gene (29/142, 20.4%) mutations were found in post-NAC samples. The frequency of these gene mutations was only 5.9% (1/17). These gene mutations were accompanied by chemotherapy, but the mutation frequency was low and scattered. There were 43 genes (43/142, 30.3%) mutated both in the pre-NAC and post-NAC samples (**Figure 3**, **Supplementary Table 2**).

Mutant-Allele Tumor Heterogeneity Score Before and After Treatment Was Associated With the Pathological Pattern After Neoadjuvant Chemotherapy

First, we analyzed the MATH value of 17 paired samples. The MATH value of the CSM group was significantly lower than that of the NCSM group (39.66 vs. 102.7, $P < 10–4$; **Figure 4**). We also compared the MATH value of the samples before NAC with the samples after NAC, and the mean value of MATH in the samples

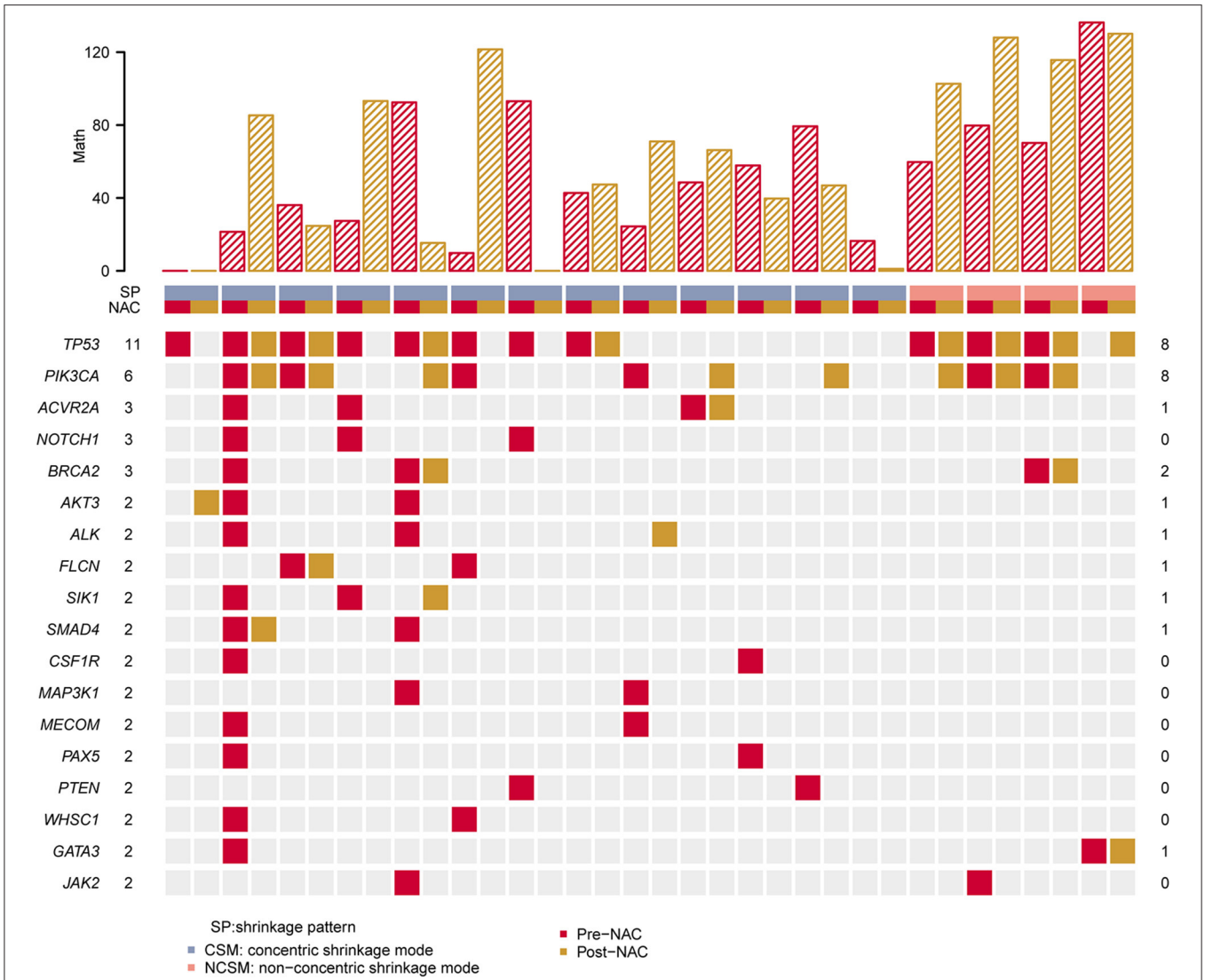

FIGURE 2 | Heat map showing somatic mutation profile of CSM and NCSM. Top is the number of each MATH value of different sample. Red represents mutations detected in pre-NAC samples, and yellow shows mutations in post-NAC samples. CSM, concentric shrinkage mode; NCSM, non-concentric shrinkage mode; NAC, neo-adjuvant chemotherapy.

TABLE 2 | Hot mutations frequency before and after NAC.

	TP53			PIK3CA		
	CSM (*N* = 13)	**NCSM (*N* = 4)**	***p***	**CSM (*N* = 13)**	**NCSM (*N* = 4)**	***p***
Pre-NAC	9 (70%)	2 (50%)	0.584	3 (23%)	2 (50%)	0.538
Post-NAC	4 (30%)	4 (100%)	0.029	5 (38%)	3 (75%)	0.294

TP53 hot mutations frequency in CSM was from 53% in Pre-NAC declined to 30% in Post-NAC, and in NSCM from 50% raised to 100%. PIK3CA hot mutations frequency in CSM was from 23% in Pre-NAC claimed to 38%, and in NSCM from 50% raised to 75%. CSM, concentric shrinkage mode; NCSM, non-concentric shrinkage mode; NAC, neo-adjuvant chemotherapy.

before NAC was higher than that in the samples after NAC (64.05 vs. 52.67). In the CSM group, the MATH value of 6 (6/13, 46%) patients increased after NAC, whereas it was decreased in the remaining 6 (6/13, 46%) patients. What is more, we found that the mutation number before and after treatment was always one; the MATH value before and after was the same. In the NCSM group, the MATH of 3 (3/4, 75%) patients was increased, whereas it was decreased in 1 (1/4, 25%) patient (**Figure 2**).

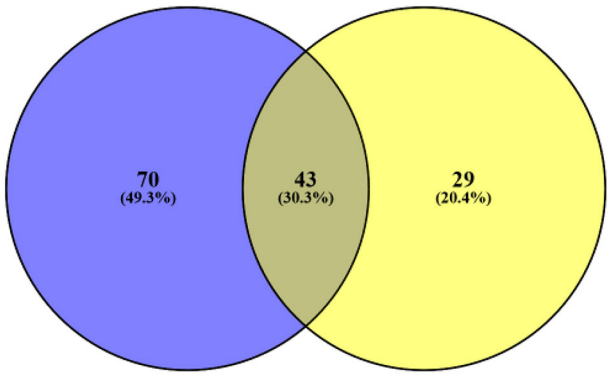

FIGURE 3 | Blue represents the number of gene mutations only detected in pre-NAC, yellow represents the number of gene mutations only detected in post-NAC. Also, middle represents 43 gene mutations both in pre- and post-NAC. NAC, neo-adjuvant chemotherapy.

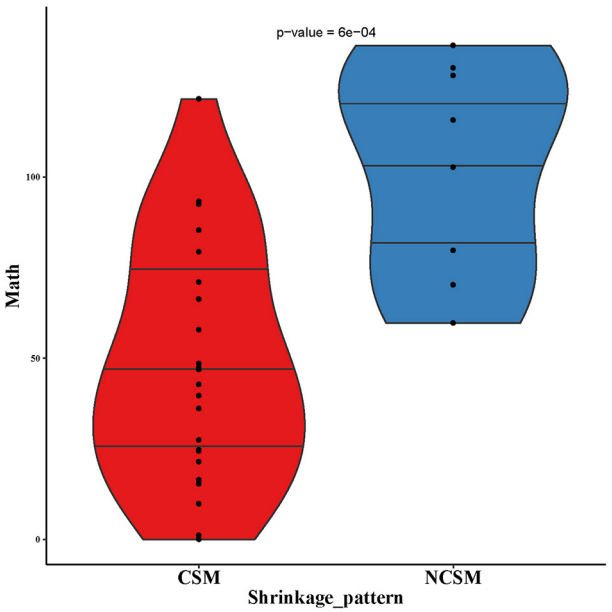

FIGURE 4 | MATH values of pre-NAC in samples of CSM and NCSM. NAC, neo-adjuvant chemotherapy; CSM, concentric shrinkage mode; NCSM, non-concentric shrinkage mode.

Second, based on the analysis of the ROC curve, the optimal threshold value of MATH was 58; the tumor would have CSM after NAC, no matter the tumor samples were before NAC or after NAC (**Figure 5**). ROC curve was used to analyze the MATH value and shrinkage mode, as shown in **Figure 6**. The area under the curve was 0.89, with a sensitivity of 0.69 and specificity of 1. The threshold value of 58 indicated a good accuracy to distinguish the two different shrinkage modes.

Characteristics of the Mutant-Allele Tumor Heterogeneity Value Before and After Neoadjuvant Chemotherapy in Patients With Different Molecular Typing

Considering the different MATH values of various molecular types of breast cancer at baseline levels, we assessed whether patients with different molecular typing met the threshold in the same way.

Three of four patients had one MATH value below the threshold of 58 (**Figure 5**), but the three of four patients' MATH values were increased during NAC. In the luminal B (luminal HER2-positive excluded) group, the MATH value in one of three patients was under the threshold of 58, and two of three patients declined their MATH value during NAC. In the Her2-positive group, seven of eight cases had MATH values under the threshold of 58 before NAC. In the triple-negative group, all of these patients achieved CSM, but 50% of the cases had MATH values raised after NAC. We analyzed the MATH value of the luminal B Her2-positive patients; all patients had MATH values under the threshold of 58 before NAC, and all of them achieved CSM. Obviously, if the patients had MATH values under 58, no matter what happened before or after NAC, they all would become CSM. However, not all patients with CSM would experience a reduction in MATH after NAC treatment.

DISCUSSION

In this study, we have detected the genomic landscape of a breast cancer cohort before and after NAC and constructed pathological three-dimensional shrinkage mode for postoperative samples. We associated the MATH value of samples before and after NAC with the shrinkage mode after NAC. Our findings extend the knowledge in the field of BCT after NAC in several ways.

First, our results may provide an effective way to select suitable patients for BCT under NAC. As we know, one issue currently under discussion during NAC is how to identify those patients who are suitable for BCT. Lack of effective measurements to select patients may lead to a decrease in BCT safety and rates. For one thing, BCT after NAC for unscreened patients may lead to an increase in local recurrence rate. A recent meta-analysis reported that NAC was associated with more frequent local recurrence than adjuvant chemotherapy: the 15-year local recurrence was 21.4% for classical treatment vs. 15.9% for neoadjuvant therapy (4). For another, considering the safety, some clinicians challenged the choice of BCT after NAC (22–24), which may be due to insufficient estimation of NCSM. Our analysis revealed that NGS of pre- and post-NAC samples might help to select patients who are suitable for BCT. However, our findings require confirmation in a larger dataset and multicenter research.

Second, our results suggested that genetic heterogeneity within a tumor may be the major factor determining the shrinkage mode after NAC. The factors affecting the shrinkage mode after NAC are currently limited to clinical parameters; genetic information was not available. Previous research by our group and others (8, 16) has investigated the association between

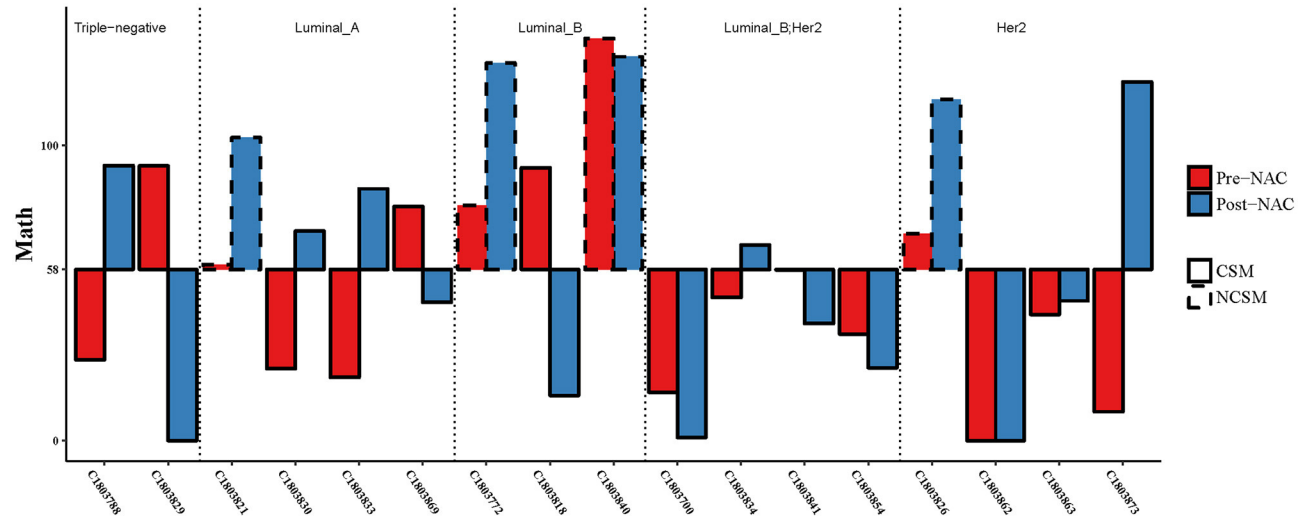

FIGURE 5 | Combining the MATH values of pre- and post-NAC, when the threshold was 58, CSM and NSCM can be separated. CSM, concentric shrinkage mode; NCSM, non-concentric shrinkage mode; NAC, neo-adjuvant chemotherapy.

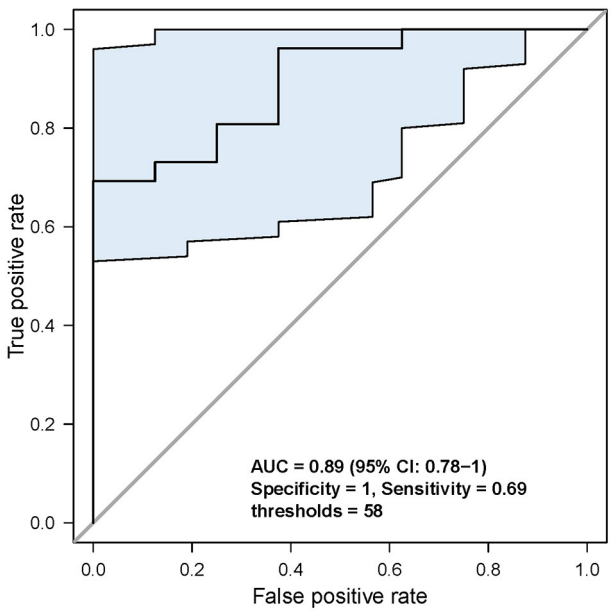

FIGURE 6 | Analysis of the specificity and sensitivity of the MATH value. When threshold was 58, sensitivity and specificity were the highest.

the shrinkage mode and tumor subtype, showing that patients with triple-negative and HER2-positive tumors have a higher probability of achieving the CSM. However, we found that the shrinkage mode differed within the same subgroups; it was insufficient to match the clinical needs. In this research, our results provided direct evidence that the breast cancer patients with high-MATH before and after NAC would show NCSM.

Our results also showed that breast cancer is a highly heterogeneous disease with few high recurrent genes. In accordance with previous reports (11, 25), most genes except *TP53* and *PIK3CA* in the samples before and after NAC occurred at a low frequency. We were not able to find specific tumor somatic mutations associated with the shrinkage mode after NAC. However, our results showed that patients with CSM had a greater reduction in the number of mutations after NAC. Previous reports (26, 27) have suggested that changes in mutations may be linked to the sensitivity of chemotherapeutic drugs. Drawing on the report mentioned earlier, we guessed the possible explanation. As known, tumors with higher heterogeneity contain more variety clones than homogeneous ones. The patients with low MATH values have a relatively uniform response and sensibility to NAC and are prone to CSM. For the patients with high-MATH value, the tumor contains more variety clones; a portion of their cancer cells are sensitive to NAC, whereas the rest are not. Therefore, cells containing mutations are eliminated, and few mutations emerge, the mutant alleles relatively reduce, the patients show CSM, and the MATH values decrease below the threshold. Conversely, for patients with NCSM, their cancer cells might be resistant to NAC, and without enough loss of mutations after NAC, the mutant alleles remain or are not sufficiently reduced.

These results also raised questions, whether the heterogeneity assessment of the primary tumor is sufficient to predict treatment outcome and whether the state after chemotherapy needs to be considered. In previous studies (15, 28), the heterogeneity of the primary tumor was assessed to study the correlation with treatment outcomes without considering the heterogeneity of the tumor after chemotherapy. In contrast, they did not produce the desired results. Similarly, in our study, patients with high MATH value primary tumor still achieved the desired results and even PCR, but the MATH value after NAC was consistent. Meanwhile, we also observed changes in the heterogeneity during NAC. Both pre- and post-NAC assessments of intratumoral

heterogeneity may be needed to risk stratification, a conjecture which is consistent with the previous report (27). Suffered from a shortage of sample size, the determination of threshold value was rather vague. Multiple thresholds apply to our findings. In our series of results, we selected 58 as the threshold, and all of them satisfied our findings. Larger sample size and multicenter cohort are needed to help to determine threshold values.

Noteworthy, multiple types of breast cancers differed in the assessment of MATH before and after NAC. Our results showed that 75% of luminal A patients had MATH value increased after NAC, 87.5% of Her2-positive patients were below the threshold before NAC, even all the luminal B patients were above the threshold before NAC. Combined with previous reports (29), we can conclude that molecular characteristics are related to heterogeneity. Consequently, If the conclusion was confirmed, considering the costs of serial sequencing assays that preclude its clinical implication, we pointed out that precise selection sequencing is based on molecular typing. For patients with luminal B, the NGS genetic test of post-NAC specimens was first considered. Conversely, for patients with luminal A or Her2-positive, primary tumor biopsy for NGS is the first choice.

Traditionally, the pattern of residual tumor is classified into CSM and NCSM based on morphological changes showed on MRI. Of note, we used a more precise definition of CSM, as we further characterize the shrinkage mode with concentric shrinkage. This method considered the morphology of surrounding lesions as well as the extent of the residual tumors. We defined the mode with the longest diameter retraction rate of the residual tumor $\leq$2 cm and $\geq$50% as CSM, which was also a good candidate for BCT and regarded as a good response to NAC. The definition seemed to be consistent with "limited multifocal regression" reported by Diane C (30). In their reports, they further subdivided multifocal regression into diffuse and limited multifocal shrinkage. Similarly, their results suggest that only the diffuse multifocal shrinkage is a risk factor that portends a worse outcome rather than a limited multifocal mode. Simultaneously, a study from the Netherlands by Briete Goorts et al. reported that patients with Pinder classification 50–90% were regarded as pathological responders (31).

Our study has some limitations. First, a small sample size may mislead the correct understanding of the result and affect the precise determination of thresholds value. Second, restricted cancer gene panel may affect the calculation of MATH results, as MATH values developed based on whole-exome sequencing (15). Furthermore, more accurate methods for determining heterogeneity, including changes in copy numbers, may enhance the study's persuasiveness.

CONCLUSIONS

NGS provides a way to show dynamics of genetic heterogeneity before and after NAC in breast cancer with different shrinkage modes, suggesting that MATH scores may correlate with pathological shrinkage mode after NAC, informing that NGS-based approaches may have the potential to be used to estimate the shrinkage mode and to enable the selection of the most appropriate patients for BCT during NAC. Specifically, our results showed that patients with CSM had a greater reduction in the number of mutations after NAC. Thus, we provide possible explanations for genetic heterogeneity associated with shrinkage mode. Finally, optimizing the choice of pre- or post-NAC samples can be selected based on individualized molecular typing. These findings might help to optimize the choice of surgical options. To enable the selection of cost-effective sequencing options and further determine the threshold, additional large clinical studies are needed.

DATA AVAILABILITY STATEMENT

The raw sequence data reported in this paper have been deposited in the Genome Sequence Archive in BIG Data Center, Beijing Institute of Genomics (BIG), Chinese Academy of Sciences, under accession number HRA000501 that can be accessed at http://bigd.big.ac.cn/gsa-human.

ETHICS STATEMENT

The retrospective study was approved by the Institute Review Board of Shandong Cancer Hospital (IRB Approval Number: SDTHEC201802002). The informed consents were obtained from all patients. The patients/participants provided their written informed consent to participate in this study. Written informed consent was obtained from the individual(s) for the publication of any potentially identifiable images or data included in this article.

AUTHOR CONTRIBUTIONS

Y-sW: conceptualization, methodology, project administration, supervision, writing-original draft, and writing-review and editing. C-hZ: conceptualization, analysis, methodology, writing–original draft, and writing–review and editing. J-jW, Z-pZ, WW, and R-rW: conceptualization, project administration, supervision, writing–original draft, and literature search. X-yDo, H-mL, X-yDi, and H-YL: analysis, writing–original draft, writing–review and editing, and literature search. Z-yL and C-xY: data curation, supervision, and investigation. All authors contributed to the article and approved the submitted version.

FUNDING

This work was supported by the Medical and Health Science Technology Development Program in Shandong Province (2019WS254) and the Natural Science Foundation of Shandong Province of China (Grant No. ZR2019BC095).

SUPPLEMENTARY MATERIAL

The Supplementary Material for this article can be found online at: https://www.frontiersin.org/articles/10.3389/fmed.2021.651904/full#supplementary-material

REFERENCES

1. Siegel RL, Miller KD, Jemal A. Cancer statistics, (2019). *CA Cancer J Clin.* (2019) 69:7–34. doi: 10.3322/caac.21551
2. Krug D, Loibl S. Neoadjuvant chemotherapy for early breast cancer. *Lancet Oncol.* (2018) 19:e129. doi: 10.1016/S1470-2045(18)30118-9
3. Paluch-Shimon S, Pagani O, Partridge AH, Abulkhair O, Cardoso MJ, Dent RA, et al. ESO-ESMO 3rd international consensus guidelines for breast cancer in young women (BCY3). *Breast.* (2017) 35:203–17. doi: 10.1016/j.breast.2017.07.017
4. Early Breast Cancer Trialists' Collaborative Group (EBCTCG). Long-term outcomes for neoadjuvant versus adjuvant chemotherapy in early breast cancer: meta-analysis of individual patient data from ten randomised trials. *Lancet Oncol.* (2018) 19:27–39. doi: 10.1016/S1470-2045(17)30777-5
5. Volders JH, Haloua MH, Krekel NM, Negenborn VL, Barbé E, Sietses C, et al. "the nationwide network and registry of histo- and cytopathology in the Netherlands (PALGA)". Neoadjuvant chemotherapy in breast-conserving surgery-consequences on margin status and excision volumes: a nationwide pathology study. *Eur J Surg Oncol.* (2016) 42:986–93. doi: 10.1016/j.ejso.2016.02.252
6. Criscitiello C, Golshan M, Barry WT, Viale G, Wong S, Santangelo M, et al. Impact of neoadjuvant chemotherapy and pathological complete response on eligibility for breast-conserving surgery in patients with early breast cancer: a meta-analysis. *Eur J Cancer.* (2018) 97:1–6. doi: 10.1016/j.ejca.2018.03.023
7. Curigliano G, Burstein HJ, Winer EP, Gnant M, Dubsky P, Loibl S, et al. De-escalating and escalating treatments for early-stage breast cancer: the St. Gallen international expert consensus conference on the primary therapy of early breast cancer 2017. *Ann Oncol.* (2017). 28:1700–12. doi: 10.1093/annonc/mdx308
8. Goorts B, van Nijnatten TJ, de Munck L, Moossdorff M, Heuts EM, de Boer M, et al. Clinical tumor stage is the most important predictor of pathological complete response rate after neoadjuvant chemotherapy in breast cancer patients. *Breast Cancer Res Treat.* (2017) 163:83–91. doi: 10.1007/s10549-017-4155-2
9. Ballesio L, Gigli S, Di Pastena F, Giraldi G, Manganaro L, Anastasi E, et al. Magnetic resonance imaging tumor regression shrinkage patterns after neoadjuvant chemotherapy in patients with locally advanced breast cancer: correlation with tumor biological subtypes and pathological response after therapy. *Tumour Biol.* (2017) 39:1010428317694540. doi: 10.1177/1010428317694540
10. Mroz EA, Tward AD, Hammon RJ, Ren Y, Rocco JW. Intra-tumor genetic heterogeneity and mortality in head and neck cancer: analysis of data from the cancer genome Atlas. *PLoS Med.* (2015) 12:e1001786. doi: 10.1371/journal.pmed.1001786
11. Pereira B, Chin SF, Rueda OM, Vollan HK, Provenzano E, Bardwell HA, et al. The somatic mutation profiles of 2,433 breast cancers refines their genomic and transcriptomic landscapes. *Nat Commun.* (2016) 7:11479. doi: 10.1038/ncomms11908
12. Gerlinger M, Rowan AJ, Horswell S, Math M, Larkin J, Endesfelder D, et al. Intratumor heterogeneity and branched evolution revealed by multiregion sequencing. *N Engl J Med.* (2012) 366:883–92. doi: 10.1056/NEJMoa1113205
13. Venteicher AS, Tirosh I, Hebert C, Yizhak K, Neftel C, Filbin MG, et al. Decoupling genetics, lineages, and microenvironment in IDH-mutant gliomas by single-cell RNA-seq. *Science.* (2017) 355:eaai8478. doi: 10.1126/science.aai8478
14. Niida A, Nagayama S, Miyano S, Mimori K. Understanding intratumor heterogeneity by combining genome analysis and mathematical modeling. *Cancer Sci.* (2018) 109:884–92. doi: 10.1111/cas.13510
15. Mroz EA, Tward AD, Pickering CR, Myers JN, Ferris RL, Rocco JW. High intratumor genetic heterogeneity is related to worse outcome in patients with head and neck squamous cell carcinoma. *Cancer.* (2013) 119:3034–42. doi: 10.1002/cncr.28150
16. Yang T, Zhang ZP, Sun XY, Liu G, Mu DB, Wang YS. [Shrinkage mode of the primary breast tumor after neoadjuvant chemotherapy analyzed with part-mount sub-serial sectioning and three-dimensional reconstruction technique]. *Zhonghua Zhong Liu Za Zhi.* (2016) 38:270–6. doi: 10.3760/cma.j.issn.0253-3766.2016.04.006
17. Chen S, Zhou Y, Chen Y, Gu J. fastp: an ultra-fast all-in-one FASTQ preprocessor. *Bioinformatics.* (2018) 34:i884–90. doi: 10.1093/bioinformatics/bty560
18. Li H, Durbin R. Fast and accurate short read alignment with burrows-wheeler transform. *Bioinformatics.* (2009) 25:1754–60. doi: 10.1093/bioinformatics/btp324
19. Chen S, Zhou Y, Chen Y, Huang T, Liao W, Xu Y, et al. Gencore: an efficient tool to generate consensus reads for error suppressing and duplicate removing of NGS data. *BMC Bioinformatics.* (2019) 20 (Suppl. 23):606. doi: 10.1186/s12859-019-3280-9
20. Li H, Handsaker B, Wysoker A, Fennell T, Ruan J, Homer N, et al. The sequence alignment/map format and SAMtools. *Bioinformatics.* (2009) 25:2078–9. doi: 10.1093/bioinformatics/btp352
21. Wang K, Li M, Hakonarson H. ANNOVAR: functional annotation of genetic variants from high-throughput sequencing data. *Nucleic Acids Res.* (2010) 38:e164. doi: 10.1093/nar/gkq603
22. Volders JH, Negenborn VL, Spronk PE, Krekel NMA, Schoonmade LJ, Meijer S, et al. Breast-conserving surgery following neoadjuvant therapy-a systematic review on surgical outcomes. *Breast Cancer Res Treat.* (2018) 168:1–12. doi: 10.1007/s10549-017-4598-5
23. Vaidya JS, Massarut S, Vaidya HJ, Alexander EC, Richards T, et al. Rethinking neoadjuvant chemotherapy for breast cancer. *BMJ.* (2018) 360:j5913. doi: 10.1136/bmj.j5913
24. Wadhwani N, Jatoi I. Overuse of neo-adjuvant chemotherapy for primary breast cancer. *Indian J Surg Oncol.* (2020) 11:12–4. doi: 10.1007/s13193-019-01002-8
25. Loibl S, Treue D, Budczies J, Weber K, Stenzinger A, Schmitt WD, et al. Mutational diversity and therapy response in breast cancer: a sequencing analysis in the neoadjuvant GeparSepto trial. *Clin Cancer Res.* (2019) 25:3986–95. doi: 10.1158/1078-0432.CCR-18-3258
26. Lips EH, Michaut M, Hoogstraat M, Mulder L, Besselink NJ, Koudijs MJ, et al. Next generation sequencing of triple negative breast cancer to find predictors for chemotherapy response. *Breast Cancer Res.* (2015) 17:134. doi: 10.1186/s13058-015-0642-8
27. Di Cosimo S, Appierto V, Silvestri M, Pruneri G, Vingiani A, Perrone F, et al. Targeted-Gene sequencing to catch triple negative breast cancer heterogeneity before and after neoadjuvant chemotherapy. *Cancers.* (2019) 11:1753. doi: 10.3390/cancers11111753
28. Pribluda A, de la Cruz CC, Jackson EL. Intratumoral heterogeneity: from diversity comes resistance. *Clin Cancer Res.* (2015) 21:2916–23. doi: 10.1158/1078-0432.CCR-14-1213
29. Ma D, Jiang YZ, Liu XY, Liu YR, Shao ZM. Clinical and molecular relevance of mutant-allele tumor heterogeneity in breast cancer. *Breast Cancer Res Treat.* (2017) 162:39–48. doi: 10.1007/s10549-017-4113-z
30. Ling DC, Sutera PA, Iarrobino NA, Diego EJ, Soran A, Johnson RR, et al. Is multifocal regression a risk factor for ipsilateral breast tumor recurrence in the modern era after neoadjuvant chemotherapy and breast conservation therapy? *Int J Radiat Oncol Biol Phys.* (2019) 104:869–76. doi: 10.1016/j.ijrobp.2019.03.012
31. Goorts B, Dreuning KMA, Houwers JB, Kooreman LFS, Boerma EG, Mann RM, et al. MRI-based response patterns during neoadjuvant chemotherapy can predict pathological (complete) response in patients with breast cancer. *Breast Cancer Res.* (2018) 20:34. doi: 10.1186/s13058-018-0950-x

Conflict of Interest: J-jW, WW, and R-rW were employed by the company Berry Oncology Corporation.

The remaining authors declare that the research was conducted in the absence of any commercial or financial relationships that could be construed as a potential conflict of interest.

Copyright © 2021 Zheng, Liu, Yuan, Dong, Li, Wang, Zhang, Liu, Ding, Wu, Wang and Wang. This is an open-access article distributed under the terms of the Creative Commons Attribution License (CC BY). The use, distribution or reproduction in other forums is permitted, provided the original author(s) and the copyright owner(s) are credited and that the original publication in this journal is cited, in accordance with accepted academic practice. No use, distribution or reproduction is permitted which does not comply with these terms.

frontiers in Medicine

ORIGINAL RESEARCH
published: 01 April 2021
doi: 10.3389/fmed.2021.649326

Three Immune-Related Prognostic mRNAs as Therapeutic Targets for Pancreatic Cancer

Cangang Zhang[1†], Yueji Zou[2†], Yanan Zhu[3], Yi Liu[4], Hui Feng[4], Fan Niu[4], Pengcheng He[4*] and Haibo Liu[4*]*

[1] Department of Pathogenic Microbiology and Immunology, School of Basic Medical Sciences, Xi'an Jiaotong University, Xi'an, China, [2] Department of Imaging, Penglai Traditional Chinese Medicine Hospital, Penglai, China, [3] Jiangsu ALF Biotechnology Co., Ltd., Nanjing, China, [4] Department of Hematology, The First Affiliated Hospital of Xi'an Jiaotong University, Xi'an, China

Objective: Pancreatic cancer is a highly lethal malignancy globally. This study aimed to probe and validate immune-related prognostic mRNAs as therapeutic targets for pancreatic cancer.

Methods: Gene transcriptome data of pancreatic cancer and normal pancreas were retrieved from TCGA-GTEx projects. Two thousand four hundred and ninety-eight immune-related genes were obtained from the IMMUPORT database. Abnormally expressed immune-related genes were then identified. Under univariate and multivariate cox models, a gene signature was constructed. Its predictive efficacy was assessed *via* ROCs. The interactions between the 21 genes were analyzed by Spearson analysis and PPI network. Using the GEPIA and The Human Protein Atlas databases, their expression and prognostic value were evaluated. The TIMER database was utilized to determine the relationships between MET, OAS1, and OASL mRNAs and immune infiltrates. Finally, their mRNA expression was externally verified in the GSE15471 and GSE62452 datasets.

Results: An immune-related 21-gene signature was developed for predicting patients' prognosis. Following verification, this signature exhibited the well predictive performance. There were physical and functional interactions between them. MET, OAS1, and OASL mRNAs were all up-regulated in pancreatic cancer and associated with unfavorable prognosis. They showed strong correlations with tumor progression. Furthermore, the three mRNAs were distinctly associated with immune infiltrates. Their up-regulation was confirmed in the two external datasets.

Conclusion: These findings identified three immune-related prognostic mRNAs MET, OAS1, and OASL, which may assist clinicians to choose targets for immunotherapy and make personalized treatment strategy for pancreatic cancer patients.

Keywords: pancreatic cancer, met, OAS1, OASL, therapeutic targets, prognosis

OPEN ACCESS

Edited by:
Fu Wang,
Xi'an Jiaotong University, China

Reviewed by:
Tian Li,
Independent researcher, Xi'an, China
Youwei Sun,
Emory University, United States

***Correspondence:**
Haibo Liu
haibo52099@sina.com
Pengcheng He
hepengcheng@xjtu.edu.cn
Fan Niu
niufan@xjtufh.edu.cn

[†]These authors have contributed equally to this work

Specialty section:
This article was submitted to Precision Medicine, a section of the journal Frontiers in Medicine

Received: *04 January 2021*
Accepted: *10 March 2021*
Published: *01 April 2021*

Citation:
Zhang C, Zou Y, Zhu Y, Liu Y, Feng H, Niu F, He P and Liu H (2021) Three Immune-Related Prognostic mRNAs as Therapeutic Targets for Pancreatic Cancer. Front. Med. 8:649326. doi: 10.3389/fmed.2021.649326

INTRODUCTION

Pancreatic cancer is a highly lethal disease with fairly high mortality globally (1). Annual mortality is nearly equal to incidence in many countries such as China (2). The 5-year survival is ∼7% (3). Its unfavorable prognosis is mainly attributed to local infiltration and distant metastases. Pancreatic ductal adenocarcinoma accounts for around 95% of all cases. Only 10% of cases are

due to genetic factors (4). Smoking, drinking, and obesity are common modifiable risk factors for this disease (5). Routine therapy methods like surgery offer dissatisfactory clinical outcomes. Only ∼20% could benefit from curative surgical resection (6). Recently, immunotherapy has become a promising adjunct treatment for pancreatic cancer (7). Nevertheless, most of pancreatic cancer patients are resistant to most therapies including immunotherapy because tumors may evade immune surveillance (8). Moreover, there is currently no targeted therapy against driver genes in pancreatic cancer. Thus, it is of necessity to develop novel strategies to build up treatment efficacy.

High-throughput sequencing may assist us to probe therapeutic targets for cancer therapies and understand the underlying mechanisms of the anti-cancer efficacy in depth (9). Pancreatic cancer is featured by distinct immune disorders. Components in immune system contribute to the initiation and development of pancreatic cancer (10). Integrated analysis of relationships between immune-related genes and clinical outcomes of pancreatic cancer is critical to explore novel prognostic markers as well as therapeutic targets. For example, Wu et al. found that three immune-related genes CKLF, ERAP2, and EREG showed distinct correlations with pancreatic cancer patients' survival (11). In this study, we identified three immune-related prognostic genes MET, OAS1, and OASL from the 21-gene signature. Following multiple dataset verification, these genes could be promising therapeutic targets as well as prognostic markers in pancreatic cancer.

MATERIALS AND METHODS

Downloaded Datasets

Gene transcriptome data of 165 normal pancreas samples from the Genotype-Tissue Expression (GTEx) project and 178 pancreatic cancer samples from The Cancer Genome Atlas (TCGA) database were downloaded based on the UCSC Xena browser (https://xenabrowser.net/datapages/). Clinical information of these pancreatic cancer patients including gender, pathologic T, N and histologic grade was retrieved from Genomic Data Commons (GDC). Those without available follow-up data were removed. **Table 1** listed the clinical features for each patient.

Two microarray datasets GSE15471 and GSE62452 were downloaded from the Gene Expression Omnibus (GEO) database (https://www.ncbi.nlm.nih.gov/gds/). Of which, the GSE15471 dataset included 39 pairs of pancreatic cancer and normal tissues. Meanwhile, the GSE62452 dataset contained 69 pancreatic cancer and adjacent normal tissue specimens (12).

Abbreviations: GTEx, Genotype-Tissue Expression; TCGA, The Cancer Genome Atlas; GDC, Genomic Data Commons; GEO, Gene Expression Omnibus; DEGs, differentially expressed genes; limma, Linear Models for Microarray Data; FC, fold change; FDR, false discovery rate; ROCs, Receiver Operating Characteristic curves; AUCs, Areas under the curves; GO, Gene ontology; BP, biological processes; MF, molecular functions; CC, cellular components; KEGG, Kyoto Encyclopedia of Genes and Genomes; PPI, Protein-protein interaction; STRING, Search Tool for the Retrieval of Interacting Genes Database; GEPIA, Gene Expression Profiling Interactive Analysis; OS, overall survival; DFS, disease-free survival; HR, hazard ratio; CI, confidence interval.

TABLE 1 | Clinical features of 178 pancreatic cancer patients from TCGA database.

Clinical features	Number
Gender	
Male	102
Female	83
Pathologic T	
T1	7
T2	24
T3	148
T4	4
Tx	1
Pathologic N	
N0	50
N1	126
N1b	4
Nx	4
Histologic grade	
G1	32
G2	97
G3	51
G4	2
Gx	3

Screening for Abnormally Expressed Immune-Related Genes

After merging gene matrix of GTEx and TCGA datasets based on the Ensembl IDs, differentially expressed genes (DEGs) between pancreatic cancer and normal pancreas specimens were screened *via* the Linear Models for Microarray Data (limma) package in R (13). The screening criteria were as follows: $|\log$ fold change (FC)$| > 2$ and false discovery rate (FDR) < 0.05. Two thousand four hundred and ninety-eight immune-related genes were obtained from the IMMUPORT database (https://www.immport.org/home). Following integration of DEGs and immune-related genes, abnormally expressed immune-related genes were identified for pancreatic cancer.

An Immune-Related Gene Signature Construction

For differentially expressed immune-related genes, univariate Cox regression analysis was conducted using TCGA dataset. Genes with $p < 0.001$ were considered related to pancreatic cancer prognosis. Then, candidate genes were screened *via* multivariate Cox regression analysis. Based on them, a risk score was established according to the following formula: risk score $= \beta_1 x_1 + \beta_2 x_2 + \ldots + \beta_i x_i$ (where βi indicates the coefficient of gene i, and x_i indicates the expression level of gene i). The risk score of each patient was calculated and all patients were separated into high- and low-risk groups in accordance with the median value. Kaplan–Meier survival analysis was conducted between high- and low-risk groups through the survival package in R. The Receiver Operating

Characteristic curves (ROCs) for overall survival were drawn utilizing the survivalROC package in R (14). Areas under the curves (AUCs) were calculated for detection of the efficacy to predict survival for the signature and other clinical features (age, gender, grade, pathologic T, pathologic N, and stage). Univariate and multivariate cox regression analyses were utilized to assess whether risk score could be independently predictive of patients' survival. Hazard ratio (HR), 95% confidence interval (CI) and p were calculated. HR > 1 indicated risk factors and HR < 1 indicated protective factors.

Functional Annotation Analysis

Gene ontology (GO) including biological processes (BP), molecular functions (MF) and cellular components (CC) and Kyoto Encyclopedia of Genes and Genomes (KEGG) functional annotation analyses of the survival-related genes were presented for exploring underlying biological functions *via* the clusterProfiler package in R (15). Terms with adjusted $p < 0.05$ were significantly enriched.

Protein-Protein Interaction (PPI) Analysis

The physical and functional interactions of proteins from the immune-related gene signature were analyzed *via* the Search Tool for the Retrieval of Interacting Genes Database (STRING) database (http://string-db.org/) (16). The degree of nodes was then calculated.

Gene Expression Profiling Interactive Analysis (GEPIA)

The expression of MET, OAS1, and OASL in pancreatic cancer and normal samples was confirmed using TCGA-GTEx projects *via* the online GEPIA database (http://gepia.cancer-pku.cn/index.html) (17). Furthermore, overall survival (OS) and disease-free survival (DFS) analyses were generated for high and low expression of MET, OAS1, or OASL groups among pancreatic cancer patients.

Immunohistochemistry and Immunofluorescence

Immunohistochemistry of MET, OAS1, and OASL proteins in pancreatic cancer and normal pancreas specimens was obtained from The Human Protein Atlas (https://www.proteinatlas.org/). Furthermore, their immunofluorescence images were also downloaded.

Immune Infiltration Analysis

The correlations between expression or copy number (arm-level deletion, diploid / normal, arm-level gain, and high amplification) of MET, OAS1, and OASL and the abundance of immune infiltrates composed of B cell, $CD4^+$ T cell, $CD8^+$ T cell, neutrophil, macrophage, and dendritic cell were assessed using the TIMER database (https://cistrome.shinyapps.io/timer/ (18)).

Statistical Analysis

All analyses were presented utilizing R version 3.5.2. Spearman correlation analysis was used to assess the associations between genes from the gene signature. The strengths of correlations were determined as follows: 0–0.39: weak; 0.40–0.59: moderate; 0.60–0.79: strong; 0.80–1.0: very strong. The differences in gene expression between two subgroups were calculated using the Wilcox test. $P < 0.05$ indicated statistical significance.

RESULTS

Construction of a Prognostic Immune-Related Gene Signature for Pancreatic Cancer

From TCGA-GTEx datasets, 1,737 DEGs with $|\log FC| > 2$ and FDR < 0.05 were identified for pancreatic cancer ($n = 178$) than normal pancreas specimens ($n = 165$), which were composed of 962 down- and 775 up-regulated genes listed in **Supplementary Table 1**. Among all DEGs, 229 were immune-related genes (**Figure 1A**; **Supplementary Table 2**). In **Figure 1B**, 50 abnormally expressed immune-related genes were significantly related to prognosis of pancreatic cancer. Using multivariate Cox regression analysis, 21 candidate genes were identified for constructing a prognostic immune-related gene signature (**Table 2**). The risk score was calculated for each patient by combining coefficient and expression level. One hundred and seventy-eight patients were separated into high- and low-risk groups in accordance with the median value. Those in the high-risk group exhibited an unfavorable prognosis ($p = 1.499e-14$; **Figure 1C**). To assess whether the risk score accurately and sensitively predicted patients' survival, ROCs were established. In **Figure 1D**, the AUC of the risk score for overall survival was 0.833, which was much higher than other clinicopathological factors, suggesting that the risk score possessed high accuracy in predicting survival.

The Immune-Related Gene Signature as an Independent Prognostic Factor for Pancreatic Cancer

One hundred and seventy-eight pancreatic cancer patients were ranked according to their risk scores (**Figure 2A**). As the risk scores elevated, the number of dead patients gradually increased (**Figure 2B**). **Figure 2C** depicted the expression patterns of these 21 genes in high and low-risk groups. As shown in univariate cox regression analysis, age [HR (95% CI): 1.027 (1.005–1.049), $p = 0.018$], N [HR (95% CI): 2.180 (1.283–3.706), $p = 0.004$] and risk score [HR (95% CI): 1.117 (1.078–1.157), $p < 0.001$] were risk factors for pancreatic cancer (**Figure 2D**). Multivariate cox regression analysis revealed that risk score was an independent predictive factor for prognosis of pancreatic cancer (**Figure 2E**).

Enrichment Analysis for Survival-Related Genes

We further probed biological functions of the survival-related genes. In **Figure 3A**, these genes were distinctly associated with regulation of migration of multiple cells such as epithelial and endothelial cells. Also, they could be involved in key cellular components like endoplasmic reticulum lumen and specific granule and possess different molecular functions such as receptor activity, cytokine binding and growth factor

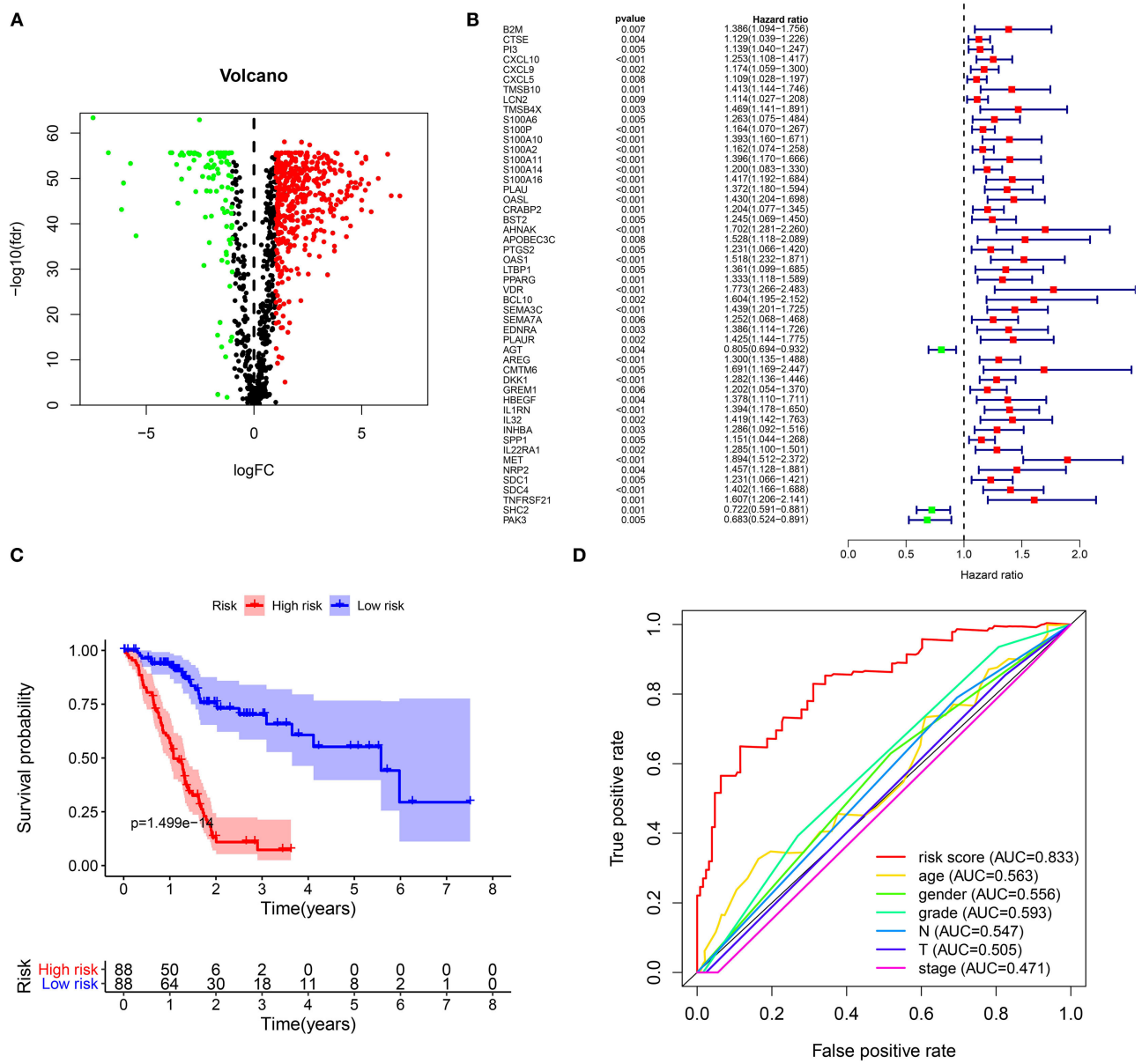

FIGURE 1 | Construction of a prognostic immune-related gene signature for pancreatic cancer. **(A)** Volcano diagram for 192 up- (red) and 37 down-regulated (green) immune-related genes in pancreatic cancer. **(B)** Forest plot for 50 abnormally expressed immune-related genes that were associated with patients' survival. **(C)** Kaplan-Meier curves for overall survival between high (red) and low-risk (blue) groups. **(D)** ROCs of risk score and other clinical prognostic factors for overall survival.

activity. As shown in KEGG enrichment analysis, these genes could participate in ErbB and proteoglycans in cancer pathways (**Figure 3B**).

Interactions Between Genes From the Immune-Related Gene Signature

In **Figure 4A**, genes from immune-related gene signature were all abnormally expressed in pancreatic cancer than normal samples (all $p < 0.001$). Except for IL22RA1 and PAK3, most of them were up-regulated in pancreatic cancer. We further calculated their correlations at the expression levels using Spearson analysis, as shown in **Figure 4B**. S100A16 was strongly correlated to PAK3 (r = −0.68), SDC4 (r = 0.64), PLAUR (r = 0.74), MET (r = 0.66), and TMSB10 (r = 0.6). PAK3 had strong correlations with PLAUR (r = −0.64) and TMSB10 (r = −0.61). SDC4 exhibited a strong association with MET (r = 0.7). OASL was very strongly associated with OAS1 (r = 0.81). PLAUR showed a strong relationship with TMSB10 (r = 0.69). The PPI network confirmed the closely interactions between them (**Figure 4C**). **Figure 4D** listed the

TABLE 2 | Multivariate cox regression analysis for 21 candidate genes in pancreatic cancer.

ID	Coefficients	Risk ratio	95% low	95% high	*P*
B2M	−0.84756	0.42846	0.269333	0.681603	0.000346
PI3	0.126991	1.135407	1.003735	1.284353	0.043462
CXCL9	0.484476	1.623325	1.293371	2.037454	2.93*E*−05
TMSB10	0.359616	1.43278	0.933127	2.199975	0.100254
LCN2	0.178297	1.19518	1.01854	1.402454	0.028882
S100A16	0.873443	2.395142	1.571083	3.651434	4.91*E*−05
OASL	0.511952	1.668545	1.105363	2.518668	0.014819
PTGS2	0.242464	1.274385	1.025728	1.583322	0.028572
OAS1	0.411634	1.509282	0.980257	2.323809	0.061566
LTBP1	0.566777	1.762578	1.172497	2.649628	0.006428
PLAUR	−1.28398	0.276934	0.146236	0.524442	8.11*E*−05
AGT	−0.36056	0.697283	0.545836	0.890749	0.003902
AREG	0.340822	1.406103	1.086432	1.819832	0.0096
CMTM6	−0.64978	0.522162	0.291347	0.935836	0.029056
HBEGF	0.51271	1.669811	1.177601	2.367752	0.004009
SPP1	0.21316	1.237583	1.050946	1.457366	0.010596
IL22RA1	0.170068	1.185385	0.937948	1.498097	0.154535
MET	0.82481	2.281447	1.443826	3.605005	0.00041
NRP2	−0.59908	0.549317	0.341531	0.88352	0.013485
SDC4	−0.62306	0.536299	0.36083	0.797097	0.002059
PAK3	0.669971	1.95418	1.058236	3.608666	0.032287

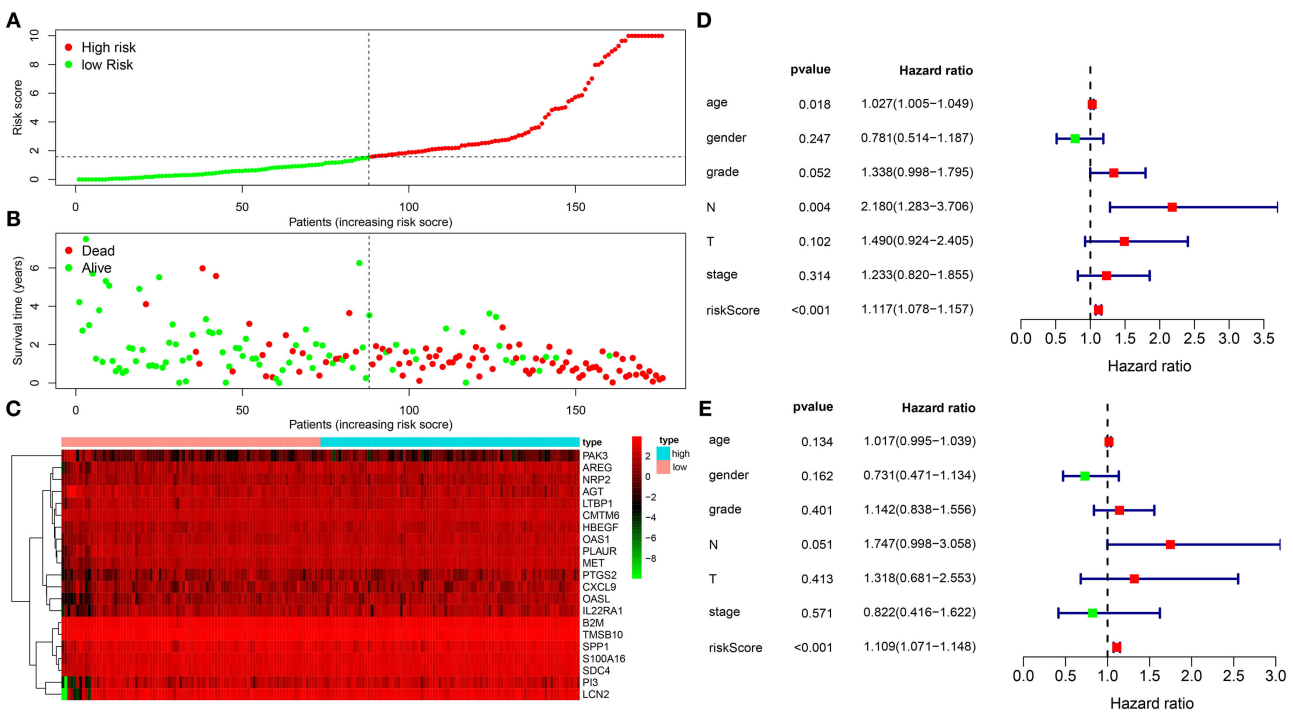

FIGURE 2 | The immune-related gene signature as an independent prognostic factor for pancreatic cancer. **(A)** Risk score ranking. **(B)** Distribution of survival status including dead (red) and alive (green) according to risk scores. **(C)** Heat map for the expression patterns of 21 genes in high and low risk groups. **(D)** Univariate and **(E)** multivariate cox regression analyses for risk score and other clinical indicators.

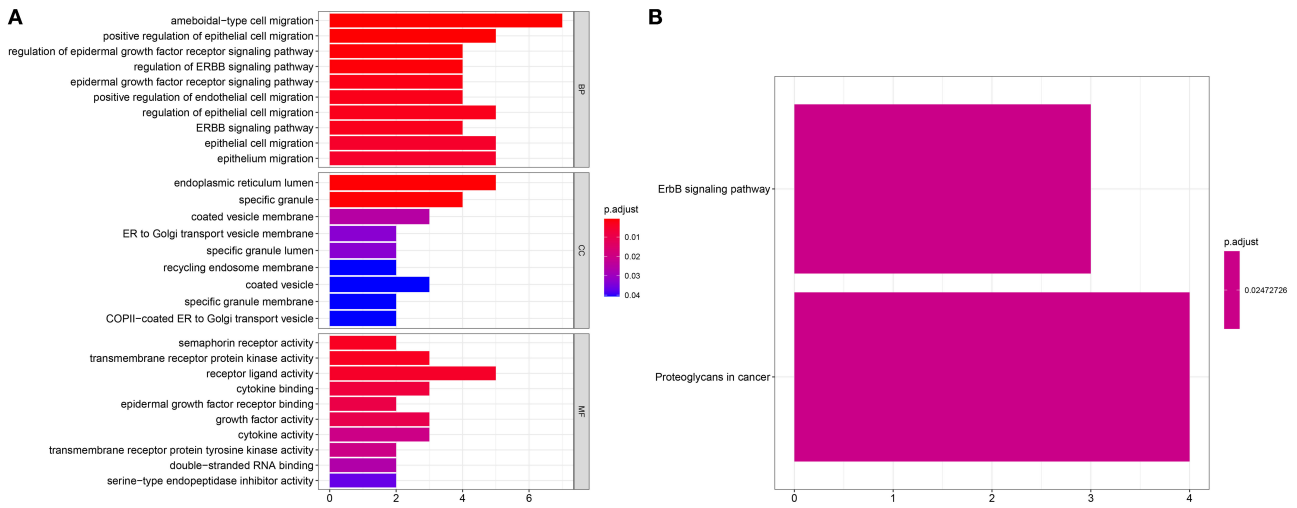

FIGURE 3 | Enrichment analysis for survival-related genes. Bar chart for **(A)** GO functional annotation analysis including biological process (BP), cellular component (CC), and molecular function (MF) and **(B)** KEGG pathway enrichment analysis.

degree of each node in the network. We found that SSP1 had the highest degree.

Up-Regulation of MET, OAS1, and OASL Is Associated With Poor Clinical Outcomes of Pancreatic Cancer

Among 21 genes from the immune-related signature, MET, OAS1, and OASL were significantly associated with prognosis of pancreatic cancer patients. Patients with high MET expression were indicative of shorter DFS (p = 0.00044; **Figure 5A**) and OS (p = 0.00023; **Figure 5B**) time than those with low expression. Furthermore, high OAS1 (p = 0.047; **Figure 5C**) and OASL (p = 0.0072; **Figure 5D**) expression was distinctly related to poorer OS. MET (**Figure 5E**), OAS1 (**Figure 5F**), and OASL (**Figure 5G**) were all up-regulated at the mRNA and protein levels. Immunofluorescence results demonstrated that MET (**Figure 5H**), OAS1 (**Figure 5I**), and OASL (**Figure 5J**) were mainly distributed in cytoplasm and nucleus. This study further assessed whether MET, OAS1, and OASL expression was in association with clinical features. The data showed that MET expression was significantly higher in G3-G4 (p = 0.005; **Figure 6A**) and T3-T4 (p = 0.012; **Figure 6B**). Furthermore, higher OAS1 expression was detected in N1 (p = 0.019; **Figure 6C**) and T3-T4 (p = 0.006; **Figure 6D**). There was higher OASL expression in >65 (p = 0.048; **Figure 6E**) or T3-T4 (p = 0.009; **Figure 6F**) patients. These findings indicated that MET, OAS1, and OASL might be related to pancreatic cancer progression.

MET, OAS1, and OASL Correlates With Immune Infiltrates

Utilizing the TIMER database, we analyzed the correlation of MET, OAS1, and OASL expression with immune infiltrates. Our data suggested that MET expression was significantly correlated to B cell (r = 0.177, p = 2.08e-02), CD8 + T cell (r = 0.35, p = 2.64e-06), CD4 + T cell (r = −0.259, p = 6.68e-04), neutrophil (r = 0.21, p = 5.79e-03), and dendritic cell (r = 0.261, p = 5.69e-04) in **Figure 7A**. OAS1 expression exhibited significant associations with neutrophil (r = 0.302, p = 5.89e-05) and dendritic cell (r = 0.185, p = 1.54e-02; **Figure 7B**). OASL expression showed a significant correlation with neutrophil (r = 0.189, p = 1.32e-02; **Figure 7C**). Moreover, copy number of MET, OAS1, and OASL was also correlated to immune infiltrates. In **Figure 7D**, there were significant associations between copy number of MET and B cell and CD4 + T cell. Copy number of OAS1 (**Figure 7E**) and OASL (**Figure 7F**) was distinctly correlated to B cell, CD4 + T cell, CD4 + T cell, and neutrophil.

Validation of MET, OAS1, and OASL Expression in External Datasets

The expression of MET, OAS1, and OASL in pancreatic cancer was verified in the GSE15471 and GSE62452 datasets. Consistently, MET was up-regulated in pancreatic cancer both in the GSE15471 (p = 1.002e-09; **Figure 8A**) and GSE62452 datasets (p = 2.792e-11; **Figure 8B**). Higher OAS1 expression was detected in pancreatic cancer than para-carcinoma tissues in the GSE15471 (p = 3.519e-07; **Figure 8C**) and GSE62452 datasets (p = 1.215e-11; **Figure 8D**). Meanwhile, OASL expression was markedly elevated in tumor specimens in the GSE15471 (p = 1.328e-05; **Figure 8E**) and GSE62452 datasets (p = 7.153e-10; **Figure 8F**).

DISCUSSION

This study constructed an immune-related gene signature for predicting clinical outcomes of pancreatic cancer patients. We identified three key genes (MET, OAS1, and OASL) that were all

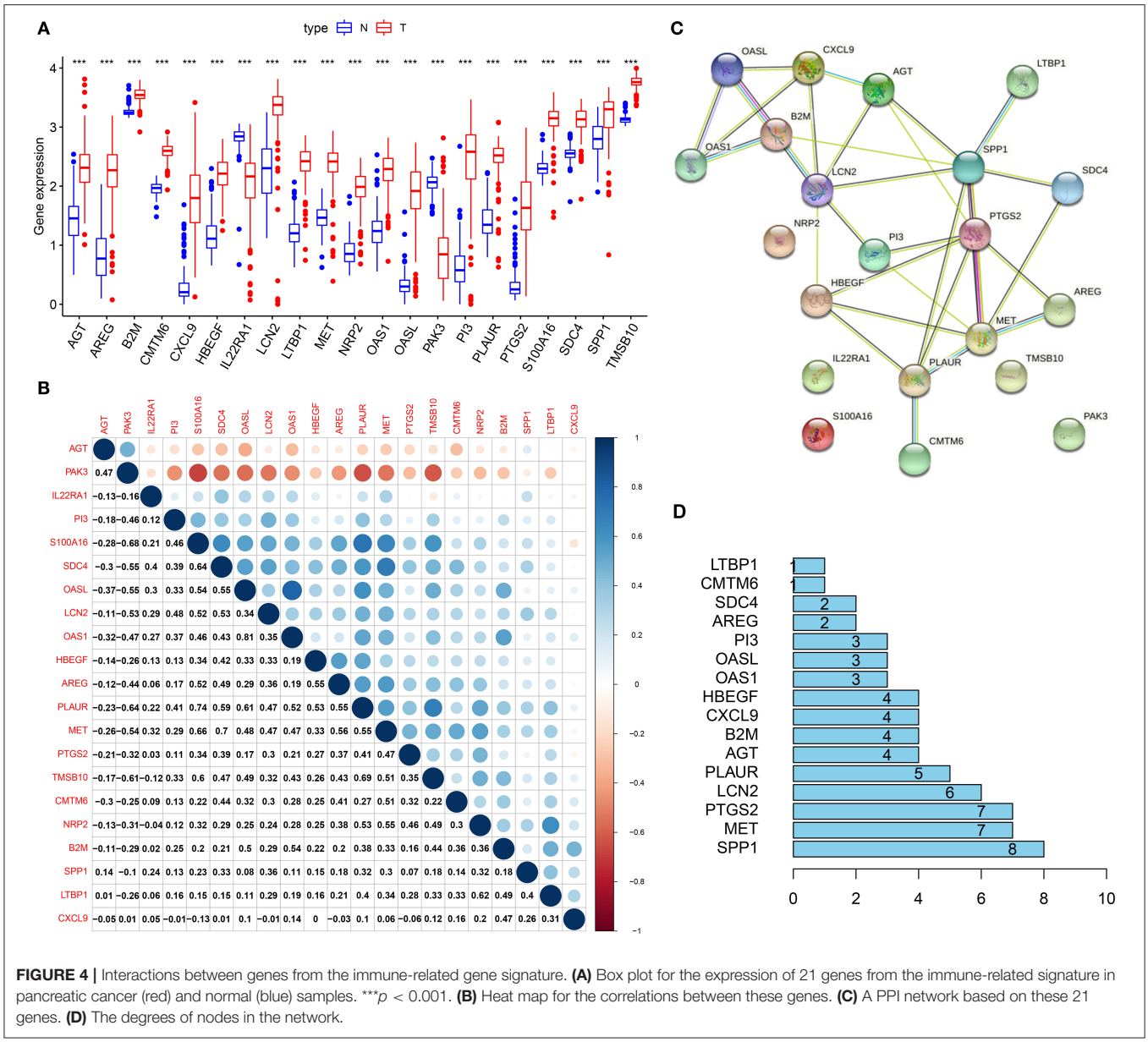

FIGURE 4 | Interactions between genes from the immune-related gene signature. **(A)** Box plot for the expression of 21 genes from the immune-related signature in pancreatic cancer (red) and normal (blue) samples. ***$p < 0.001$. **(B)** Heat map for the correlations between these genes. **(C)** A PPI network based on these 21 genes. **(D)** The degrees of nodes in the network.

up-regulated in pancreatic cancer and indicated an unfavorable prognosis. Following multiple dataset verification, the three genes might be promising therapeutic targets, which were worthy of further research.

Despite the TNM stage system as an efficient tool to detect tumor stage, there is discrepancy in prognosis based on TNM stage (19). Thus, the efficacy of TNM stage is limited. Gene-based markers have been widely explored for pancreatic cancer in recent years (20). Recently, several prognosis-related gene signatures have been established for pancreatic cancer (21–23). For example, Zhuang et al. developed a prognosis-related lncRNA signature for pancreatic cancer (24). Following comparing other clinical risk factors, the signature exhibited better predictability. Wu et al. constructed 9-gene signature for prediction of survival time of pancreatic cancer patients (25). There is still a lack of immune-related prognostic models. Herein, the immune-related 21-gene signature could accurately and sensitively predict survival time of pancreatic cancer patients. It performed better than other clinicopathological characteristics like age, gender, grade, N, T, and stage. This signature could be independently predictive of patients' prognosis.

The molecular mechanisms of highly aggressive behaviors remain unknown. We analyzed biological functions of survival-related genes. These genes could regulate migration of multiple cells such as epithelial and endothelial cells and were involved in key cellular components like endoplasmic reticulum lumen and specific granule and possess different molecular functions such as receptor activity, cytokine binding, and growth factor

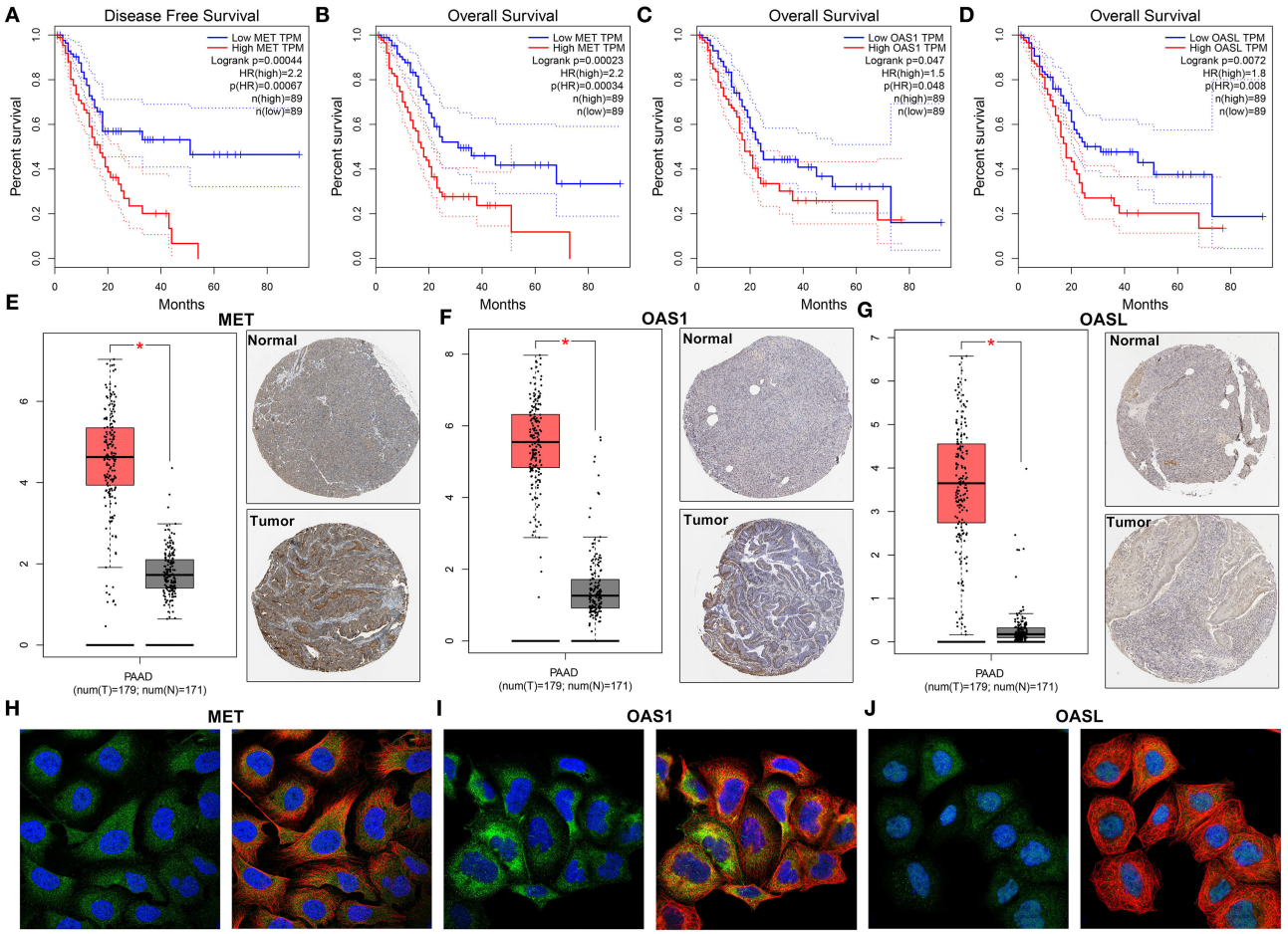

FIGURE 5 | MET, OAS1, and OASL are up-regulated in pancreatic cancer and associated with poor clinical outcomes. Kaplan-Meier curves for **(A)** DFS and **(B)** OS of MET, **(C)** OS of OAS1, and **(D)** OASL *via* the GEPIA. Up-regulation of **(E)** MET, **(F)** OAS1, and **(G)** OASL in pancreatic cancer specimens. The left picture shows the mRNA expression levels from the GEPIA and the right one shows the immunohistochemistry images from The Human Protein Atlas. Immunofluorescence images of **(H)** MET, **(I)** OAS1, and **(J)** OASL in cells. The nucleus was stained blue, the microtubules were stained red, and the MET OAS1 and OASL proteins were stained green. *$P<0.05$.

activity. These data were indicative that these genes were involved in tumor progression. For example, CCN1/Cyr61 secreted by pancreatic cancer cells may promote migration of endothelial cells (26). Nerve growth factors regulate CD133 functions, thereby promoting migration of pancreatic cancer cells (27). Targeting IL-1 and its receptor can prolong survival time in pancreatic cancer (28). We also found that these genes could participate in ErbB and proteoglycans in cancer pathways. It has been confirmed that dysregulated ErbB signaling promotes tumorigenesis for pancreatic cancer (29). Hence, these survival-related genes might participate in pancreatic tumor progression.

Our study revealed that there were physical and functional interactions between 21 genes from the immune-related gene signature. Among them, MET, OAS1, and OASL were verified to be markedly up-regulated in pancreatic cancer and associated with poor clinical outcomes of patients. Furthermore, MET expression was significantly correlated to infiltration of B cell, CD8 + T cell, CD4 + T cell, neutrophil, and dendritic cell. MET gene is located on chromosome 7q21-31. Changes in MET functions have been a hallmark of multiple cancers including pancreatic cancer (30). MET overexpression induces pancreatic cancer progression (31). Consistently, MET up-regulation was markedly correlated to tumor grade and T stage (32). Dysregulated MET functions correlate with aggressive phenotypes. Consistent with previous research, MET is involved in the crosstalk between tumor cells and tumor microenvironment (30). Thus, targeting MET has been considered as an adjuvant therapy in pancreatic cancer. OAS1 and OASL, $2^{'}$-$5^{'}$-oligoadenylate synthetases, are interferon-induced antiviral enzymes. We found that OAS1 expression exhibited significant associations with neutrophil and dendritic cell infiltration. OASL expression showed a significant correlation with neutrophil infiltration. Consistently, Zhang et al. also found that OAS1 and OASL were correlated to neutrophil cell infiltration in breast cancer (33). Thus,

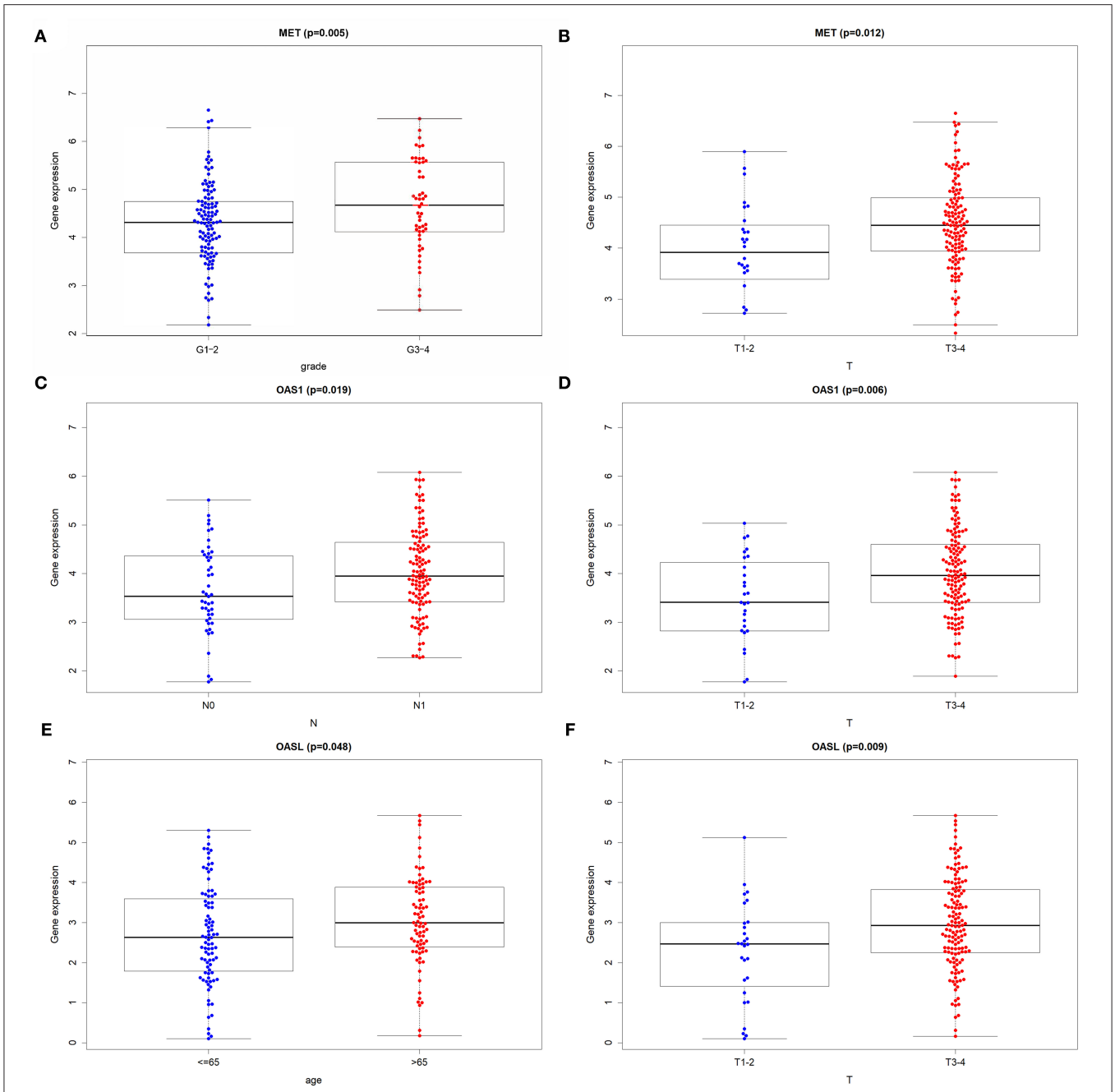

FIGURE 6 | Correlation of MET, OAS1, and OASL expression with clinical features. Box plots for correlation of **(A)** MET with grade and **(B)** pathologic T, correlation of **(C)** OAS1 with pathologic N and **(D)** pathologic T and correlation of **(E)** OASL with age and **(F)** pathologic T.

MET, OAS1, and OASL were distinctly correlated to tumor immune microenvironment.

Collectively, we identified three immune-related prognostic genes MET, OAS1, and OASL, which could be promising therapeutic targets as well as prognostic markers for pancreatic cancer. However, several limitations of this study should be pointed out. First, the biological functions of MET, OAS1, and OASL such as their interactions with immune cells in tumor microenvironment need to be explored *in vitro* experiments. Second, their prognostic values should be verified in prospective research.

CONCLUSION

In this study, we established an immune-related 21-gene signature for prediction of pancreatic cancer prognosis. This signature could be accurately and independently predictive of

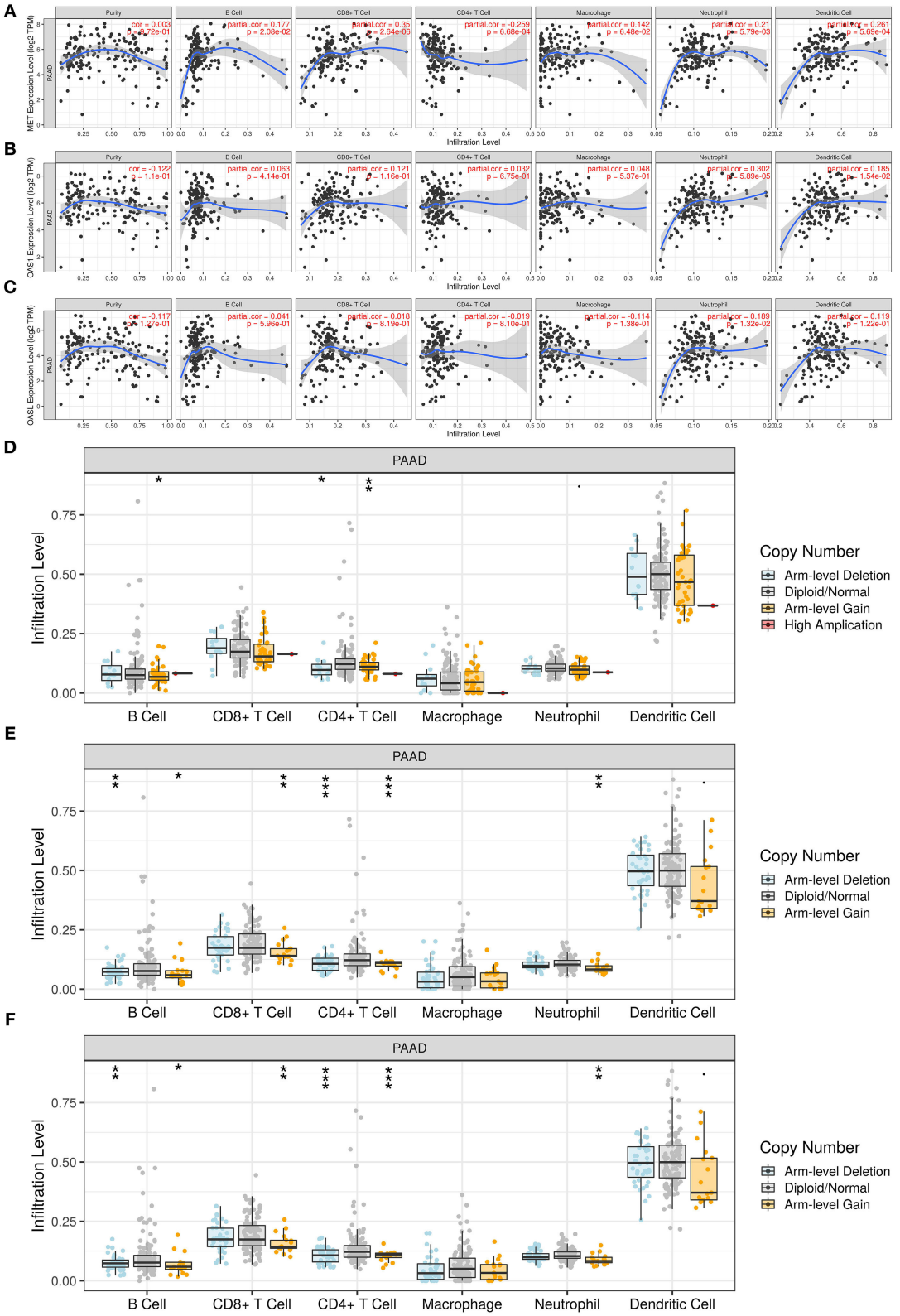

FIGURE 7 | Association of MET, OAS1, and OASL with immune infiltrates *via* the TIMER database. **(A–C)** Correlation of **(A)** MET, **(B)** OAS1, and **(C)** OASL expression with immune infiltrates. **(D–F)** Correlation of copy number of **(D)** MET, **(E)** OAS1, and **(F)** OASL with immune infiltrates. $^{*}p < 0.05$; $^{**}p < 0.01$; $^{***}p < 0.001$.

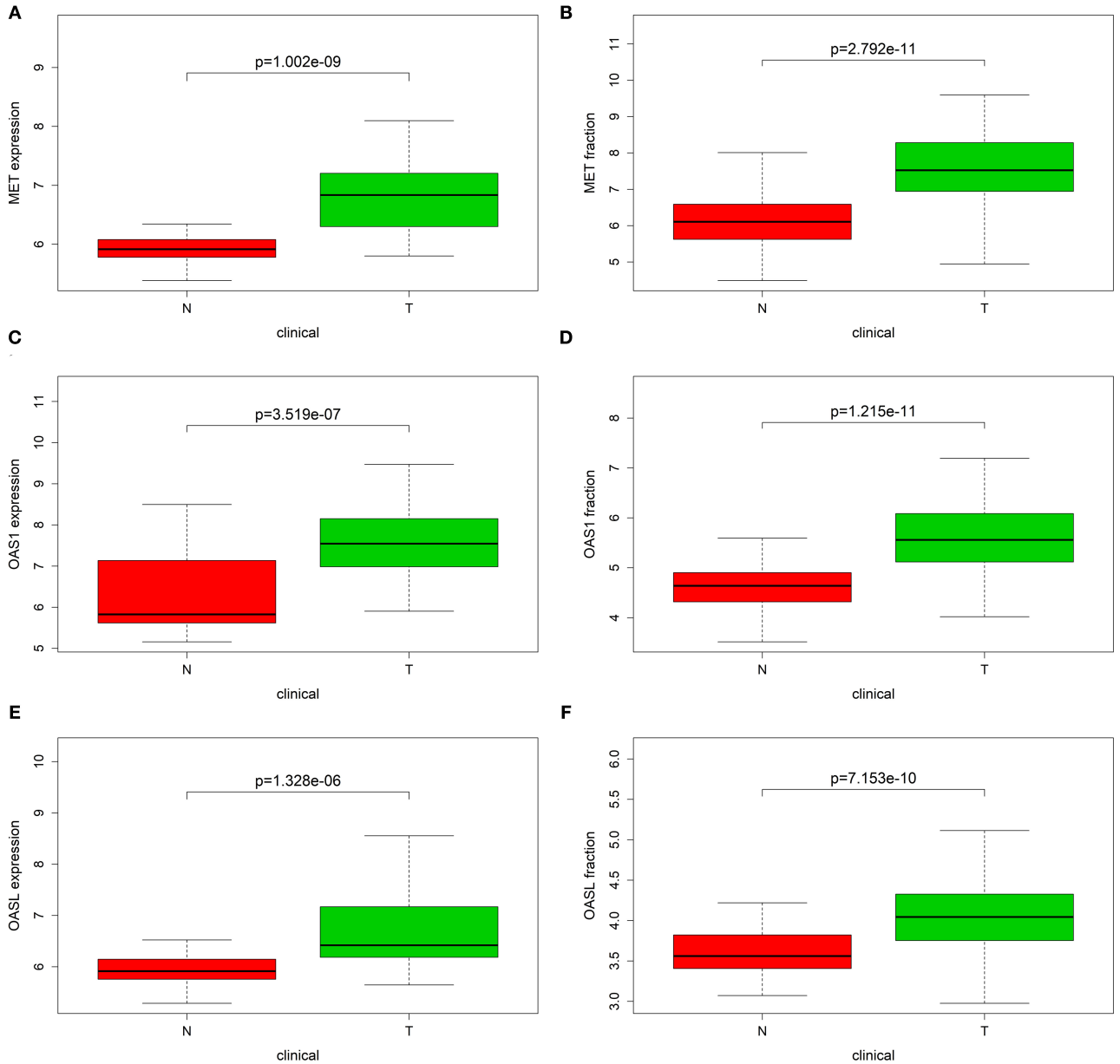

FIGURE 8 | Validation of MET, OAS1, and OASL expression in external datasets. Box plot showing the expression of **(A,B)** MET, **(C,D)** OAS1, and **(E,F)** OASL expression in tumor (T) and normal (N) tissue specimens in GSE15471 and GSE62452 datasets.

patients' survival. Among these genes, MET, OAS1, and OASL were validated to be up-regulated in pancreatic cancer and associated with unfavorable prognosis of patients. Also, there were closely interactions between them and immune infiltrates. Thus, MET, OAS1, and OASL could be potential therapeutic markers in pancreatic cancer.

DATA AVAILABILITY STATEMENT

The datasets generated for this study can be found in online repositories. The names of the repository/repositories and accession number(s) can be found in the article/**Supplementary Materials**.

AUTHOR CONTRIBUTIONS

HL conceived and designed the study. CZ, FN, and PH conducted most of the experiments, data analysis, and wrote the manuscript. YZo, YZh, YL, and HF participated in collecting data and helped to draft

the manuscript. All authors reviewed and approved the manuscript.

FUNDING

This work was funded by National Scientific and Technological Major Special Project for Significant Creation of New drugs (2020ZX09201020) and Key Research and Development Program of Shaanxi (2018ZDCXL-SF-01-02-01).

SUPPLEMENTARY MATERIAL

The Supplementary Material for this article can be found online at: https://www.frontiersin.org/articles/10.3389/fmed.2021.649326/full#supplementary-material

Supplementary Table 1 | One thousand seven hundred and thirty-seven abnormally expressed genes in pancreatic cancer.

Supplementary Table 2 | Two hundred and twenty-nine differentially expressed immune-related genes in pancreatic cancer.

REFERENCES

1. GBD 2017 Pancreatic Cancer Collaborators. The global, regional, and national burden of pancreatic cancer and its attributable risk factors in 195 countries and territories, 1990-2017: a systematic analysis for the Global Burden of Disease Study 2017. *Lancet Gastroenterol Hepatol*. (2019) 4:934–47. doi: 10.1016/S2468-1253(19)30347-4
2. Lin QJ, Yang F, Jin C, Fu DL. Current status and progress of pancreatic cancer in China. *World J Gastroenterol*. (2015) 21:7988–8003. doi: 10.3748/wjg.v21.i26.7988
3. Karamitopoulou E. Tumour microenvironment of pancreatic cancer: immune landscape is dictated by molecular and histopathological features. *Br J Cancer*. (2019) 121:5–14. doi: 10.1038/s41416-019-0479-5
4. Barone E, Corrado A, Gemignani F, Landi S. Environmental risk factors for pancreatic cancer: an update. *Arch Toxicol*. (2016) 90:2617–42. doi: 10.1007/s00204-016-1821-9
5. Midha S, Chawla S, Garg PK. Modifiable and non-modifiable risk factors for pancreatic cancer: a review. *Cancer Lett*. (2016) 381:269–77. doi: 10.1016/j.canlet.2016.07.022
6. Lai E, Puzzoni M, Ziranu P, Pretta A, Impera V, Mariani S, et al. New therapeutic targets in pancreatic cancer. *Cancer Treat Rev*. (2019) 81:101926. doi: 10.1016/j.ctrv.2019.101926
7. Banerjee K, Kumar S, Ross KA, Gautam S, Poelaert B, Nasser MW, et al. Emerging trends in the immunotherapy of pancreatic cancer. *Cancer Lett*. (2018) 417:35–46. doi: 10.1016/j.canlet.2017.12.012
8. Yamamoto K, Venida A, Yano J, Biancur DE, Kakiuchi M, Gupta S, et al. Autophagy promotes immune evasion of pancreatic cancer by degrading MHC-I. *Nature*. (2020) 581:100–5. doi: 10.1038/s41586-020-2229-5
9. Huang X, Tang T, Zhang G, Hong Z, Xu J, Yadav DK, et al. Genomic investigation of co-targeting tumor immune microenvironment and immune checkpoints in pan-cancer immunotherapy. *NPJ Precis Oncol*. (2020) 4:29. doi: 10.1038/s41698-020-00136-1
10. Sethi V, Vitiello GA, Saxena D, Miller G, Dudeja V. The role of the microbiome in immunologic development and its implication for pancreatic cancer immunotherapy. *Gastroenterology*. (2019) 156:2097–115.e2. doi: 10.1053/j.gastro.2018.12.045
11. Wu G, Deng Z, Jin Z, Wang J, Xu B, Zeng J, et al. Identification of prognostic immune-related genes in pancreatic adenocarcinoma and establishment of a prognostic nomogram: a bioinformatic study. *Biomed Res Int*. (2020) 2020:1346045. doi: 10.1155/2020/1346045
12. Yang S, He P, Wang J, Schetter A, Tang W, Funamizu N, et al. A novel MIF signaling pathway drives the malignant character of pancreatic cancer by targeting NR3C2. *Cancer Res*. (2016) 76:3838–50. doi: 10.1158/0008-5472.CAN-15-2841
13. Ritchie ME, Phipson B, Wu D, Hu Y, Law CW, Shi W, et al. limma powers differential expression analyses for RNA-sequencing and microarray studies. *Nucleic Acids Res*. (2015) 43:e47. doi: 10.1093/nar/gkv007
14. Heagerty PJ, Lumley T, Pepe MS. Time-dependent ROC curves for censored survival data and a diagnostic marker. *Biometrics*. (2000) 56:337–44. doi: 10.1111/j.0006-341X.2000.00337.x
15. Yu G, Wang LG, Han Y, He QY. clusterProfiler: an R package for comparing biological themes among gene clusters. *Omics*. (2012) 16:284–7. doi: 10.1089/omi.2011.0118
16. Szklarczyk D, Morris JH, Cook H, Kuhn M, Wyder S, Simonovic M, et al. The STRING database in 2017: quality-controlled protein-protein association networks, made broadly accessible. *Nucleic Acids Res*. (2017) 45(D1):D362–8. doi: 10.1093/nar/gkw937
17. Tang Z, Li C, Kang B, Gao G, Li C, Zhang Z. GEPIA: a web server for cancer and normal gene expression profiling and interactive analyses. *Nucleic Acids Res*. (2017) 45(W1):W98–102. doi: 10.1093/nar/gkx247
18. Li T, Fu J, Zeng Z, Cohen D, Li J, Chen Q, et al. TIMER2.0 for analysis of tumor-infiltrating immune cells. *Nucleic Acids Res*. (2020) 48(W1):W509–14. doi: 10.1093/nar/gkaa407
19. Huang R, Mao M, Lu Y, Yu Q, Liao L. A novel immune-related genes prognosis biomarker for melanoma: associated with tumor microenvironment. *Aging*. (2020) 12:6966–80. doi: 10.18632/aging.103054
20. Tang H, Jiang L, Stolzenberg-Solomon RZ, Arslan AA, Beane Freeman LE, Bracci PM, et al. Genome-wide gene-diabetes and gene-obesity interaction scan in 8,255 Cases and 11,900 controls from PanScan and PanC4 consortia. *Cancer Epidemiol Biomark Prev*. (2020) 29:1784–91. doi: 10.1158/1055-9965.EPI-20-0275
21. Qiu X, Hou QH, Shi QY, Jiang HX, Qin SY. Identification of hub prognosis-associated oxidative stress genes in pancreatic cancer using integrated bioinformatics analysis. *Front Genet*. (2020) 11:595361. doi: 10.3389/fgene.2020.595361
22. Wu M, Li X, Liu R, Yuan H, Liu W, Liu Z. Development and validation of a metastasis-related gene signature for predicting the overall survival in patients with pancreatic ductal adenocarcinoma. *J Cancer*. (2020) 11:6299–318. doi: 10.7150/jca.47629
23. Xu D, Wang Y, Liu X, Zhou K, Wu J, Chen J, et al. Development and clinical validation of a novel 9-gene prognostic model based on multi-omics in pancreatic adenocarcinoma. *Pharmacol Res*. (2020) 164:105370. doi: 10.1016/j.phrs.2020.105370
24. Zhuang H, Huang S, Zhou Z, Ma Z, Zhang Z, Zhang C, et al. A four prognosis-associated lncRNAs (PALnc) based risk score system reflects immune cell infiltration and predicts patient survival in pancreatic cancer. *Cancer Cell Int*. (2020) 20:493. doi: 10.1186/s12935-020-01588-y
25. Wu M, Li X, Zhang T, Liu Z, Zhao Y. Identification of a nine-gene signature and establishment of a prognostic nomogram predicting overall survival of pancreatic cancer. *Front Oncol*. (2019) 9:996. doi: 10.3389/fonc.2019.00996
26. Maity G, Mehta S, Haque I, Dhar K, Sarkar S, Banerjee SK, et al. Pancreatic tumor cell secreted CCN1/Cyr61 promotes endothelial cell migration and aberrant neovascularization. *Sci Rep*. (2014) 4:4995. doi: 10.1038/srep04995
27. Xin B, He X, Wang J, Cai J, Wei W, Zhang T, et al. Nerve growth factor regulates CD133 function to promote tumor cell migration and invasion via activating ERK1/2 signaling in pancreatic cancer. *Pancreatology*. (2016) 16:1005–14. doi: 10.1016/j.pan.2016.09.005
28. Brunetto E, De Monte L, Balzano G, Camisa B, Laino V, Riba M, et al. The IL-1/IL-1 receptor axis and tumor cell released inflammasome adaptor ASC are key regulators of TSLP secretion by cancer associated fibroblasts in pancreatic cancer. *J Immunother Cancer*. (2019) 7:45. doi: 10.1186/s40425-019-0521-4
29. Lin T, Ren Q, Zuo W, Jia R, Xie L, Lin R, et al. Valproic acid exhibits anti-tumor activity selectively against EGFR/ErbB2/ErbB3-coexpressing pancreatic cancer via induction of ErbB family members-targeting microRNAs. *J Exp Clin Cancer Res*. (2019) 38:150. doi: 10.1186/s13046-019-1160-9
30. Modica C, Tortarolo D, Comoglio PM, Basilico C, Vigna E. MET/HGF co-targeting in pancreatic cancer: a tool to provide insight into the

tumor/stroma crosstalk. *Int J Mol Sci*. (2018) 19:3920. doi: 10.3390/ijms19123920
31. Takiguchi S, Inoue K, Matsusue K, Furukawa M, Teramoto N, Iguchi H. Crizotinib, a MET inhibitor, prevents peritoneal dissemination in pancreatic cancer. *Int J Oncol*. (2017) 51:184–92. doi: 10.3892/ijo.2017.3992
32. Delitto D, Vertes-George E, Hughes SJ, Behrns KE, Trevino JG. c-Met signaling in the development of tumorigenesis and chemoresistance: potential applications in pancreatic cancer. *World J Gastroenterol*. (2014) 20:8458–70. doi: 10.3748/wjg.v20.i26.8458
33. Zhang Y, Yu C. Prognostic characterization of OAS1/OAS2/OAS3/OASL in breast cancer. *BMC Cancer*. (2020) 20:575. doi: 10.1186/s12885-020-07034-6

Conflict of Interest: YZh was employed by the company Jiangsu ALF Biotechnology Co., Ltd.

The remaining authors declare that the research was conducted in the absence of any commercial or financial relationships that could be construed as a potential conflict of interest.

The Handling Editor declared a shared affiliation, though no other collaboration, with one of the authors CZ.

Copyright © 2021 Zhang, Zou, Zhu, Liu, Feng, Niu, He and Liu. This is an open-access article distributed under the terms of the Creative Commons Attribution License (CC BY). The use, distribution or reproduction in other forums is permitted, provided the original author(s) and the copyright owner(s) are credited and that the original publication in this journal is cited, in accordance with accepted academic practice. No use, distribution or reproduction is permitted which does not comply with these terms.

frontiers in Medicine

ORIGINAL RESEARCH
published: 13 April 2021
doi: 10.3389/fmed.2021.637743

A Ferroptosis-Related Signature Robustly Predicts Clinical Outcomes and Associates With Immune Microenvironment for Thyroid Cancer

Mingqin Ge, Jie Niu, Ping Hu, Aihua Tong, Yan Dai, Fangjiang Xu and Fuyuan Li*

Department of Endocrinology, Linyi Central Hospital, Linyi, China

Objective: This study aimed to construct a prognostic ferroptosis-related signature for thyroid cancer and probe into the association with tumor immune microenvironment.

Methods: Based on the expression profiles of ferroptosis-related genes, a LASSO cox regression model was established for thyroid cancer. Kaplan-Meier survival analysis was presented between high and low risk groups. The predictive performance was assessed by ROC. The predictive independency was validated *via* multivariate cox regression analysis and stratified analysis. A nomogram was established and verified by calibration curves. The enriched signaling pathways were predicted *via* GSEA. The association between the signature and immune cell infiltration was analyzed by CIBERSORT. The ferroptosis-related genes were validated in thyroid cancer tissues by immunohistochemistry and RT-qPCR.

Results: A ferroptosis-related eight gene model was established for predicting the prognosis of thyroid cancer. Patients with high risk score indicated a poorer prognosis than those with low risk score (p = 1.186e-03). The AUCs for 1-, 2-, and 3-year survival were 0.887, 0.890, and 0.840, respectively. Following adjusting other prognostic factors, the model could independently predict the prognosis (p = 0.015, HR: 1.870, 95%CI: 1.132–3.090). A nomogram combining the signature and age was constructed. The nomogram-predicted probability of 1-, 3-, and 5-year survival approached the actual survival time. Several ferroptosis-related pathways were enriched in the high-risk group. The signature was distinctly associated with the immune cell infiltration. After validation, the eight genes were abnormally expressed between thyroid cancer and control tissues.

Conclusion: Our findings established a prognostic ferroptosis-related signature that was associated with the immune microenvironment for thyroid cancer.

Keywords: ferroptosis, gene signature, thyroid cancer, immune microenvironment, prognosis

OPEN ACCESS

Edited by:
Fu Wang,
Xi'an Jiaotong University, China

Reviewed by:
Fengbiao Mao,
University of Michigan, United States
Chaoyun Pan,
Sun Yat-Sen University, China

****Correspondence:***
Ping Hu
lyzxyyhp@163.com

Specialty section:
This article was submitted to Precision Medicine, a section of the journal Frontiers in Medicine

Received: *04 December 2020*
Accepted: *15 March 2021*
Published: *13 April 2021*

Citation:
Ge M, Niu J, Hu P, Tong A, Dai Y, Xu F and Li F (2021) A Ferroptosis-Related Signature Robustly Predicts Clinical Outcomes and Associates With Immune Microenvironment for Thyroid Cancer. Front. Med. 8:637743. doi: 10.3389/fmed.2021.637743

INTRODUCTION

Thyroid cancer is the most often diagnosed endocrine malignancy, accounting for 1% of all newly diagnosed cancers (1). In the past 30 years, the global incidence of thyroid cancer has markedly increased (2). The disease is expected to become the fourth major cancer worldwide (3). Surgery followed by radioactive iodine or observation is the main therapy for most of patients (2).

The application of high-throughput technology is increasing, which deepens the understanding about the molecular characteristics of thyroid cancer. Molecular markers have also become effective tools for predicting prognosis and identifying new therapeutic targets in thyroid cancer management.

Activated immune cells in the tumor microenvironment secrete pro-inflammatory cytokines and chemokines, which may promote the progression of thyroid cancer (4). Immunotherapy provides new possibilities for curing thyroid cancer. Recently, the crosstalk between ferroptosis and immune cells is involved in mediating response to the immunotherapy (5). Ferroptosis characterized by unique morphologies (decreased cell size, elevated mitochondrial membrane density) and bioenergy characteristics, is a novel form of regulated cell death with an iron-dependent manner (6). Glutathione depletion or glutathione peroxidase 4 inactivation may lead to the metabolic imbalance, thereby inducing ferroptosis of cancer cells (7). Ferroptosis has exhibited great potential in cancer therapy. FDA has approved small molecule inducers of ferroptosis to kill cancer cells such as Erastin, Sulphasalazine, Sorafenib and Statins (8). However, the exact mechanisms of ferroptosis and the association with the tumor immune microenvironment have not been uncovered. Recently, Liang et al. established a robust prognostic gene signature based on 10 ferroptosis-related genes for hepatocellular carcinoma (9). Furthermore, Wu et al. developed a ferroptosis-related five signature for predicting prognosis for clear cell renal cell carcinoma (10). Nevertheless, at present, there is still a lack of ferroptosis-related gene model for predicting the prognosis of patients with thyroid cancer. Hence, in this study, we established a prognostic ferroptosis-related signature, which could robustly predict the survival time of patients and was associated with the immune microenvironment for thyroid cancer.

MATERIALS AND METHODS

Thyroid Cancer Datasets

RNA sequencing (RNA-seq) transcriptome data of thyroid cancer were downloaded from The Cancer Genome Atlas (TCGA, http://cancergenome.nih.gov/) database on September 14, 2020. Using the Ensembl database (http://asia.ensembl.org/index.html), gene names were transformed from Ensembl ID into gene symbol matrix. The corresponding clinical information including age, gender, stage and TNM was also retrieved from TCGA database. Following removing samples without complete follow-up information, 510 thyroid cancer samples and 58 normal samples were included in this study. **Table 1** listed the clinical characteristics of these thyroid cancer patients. Sixty ferroptosis-related genes were obtained from the previous literature (9). The expression profiles of these ferroptosis-related genes were extracted from above samples (**Supplementary Table 1**). Differentially expressed ferroptosis-related genes were screened between thyroid cancer and normal samples utilizing the edgeR package in R with the threshold of adjusted $p < 0.05$ (11).

Abbreviations: RNA-seq, RNA sequencing; TCGA, The Cancer Genome Atlas; LASSO, least absolute shrinkage and selection operator; ROC, Receiver Operating Characteristic; PCA, Principal Component Analysis; GSEA, Gene Set Enrichment Analysis; FDR, false discovery rate; qRT-PCR, quantitative real-time PCR; HR, hazard ratio; CI, confidence interval; AUC, area under the curve.

Construction of a Least Absolute Shrinkage and Selection Operator Cox Model

Differentially expressed ferroptosis-related genes were used for construction of a LASSO Cox model. Prognosis-related genes were evaluated by univariate Cox regression analysis *via* the survival package in R. Genes with $p < 0.05$ were selected for LASSO Cox model analysis. A LASSO Cox model was then established through the Glmnet package in R (12). Variable selection was presented to get better performance parameters, followed by regularization so as to avoid overfitting. The regularization of LASSO was controlled by the parameter λ. The larger the λ, the greater the penalty for linear models with more variables. In this study, a 10-fold cross-validation was presented for each λ and the partial likelihood deviance values was determined. The optimal λ was selected to establish the model. The risk score for each sample was calculated according to $\beta_1 x_1 + \beta_2 x_2 + \ldots + \beta_p x_p$ (where β_p indicates the coefficients, and x_p indicates the gene expression levels). Based on the median value of risk scores, patients were separated into high- and low- risk groups. Kaplan-Meier overall survival (OS) analysis was presented, followed by log-rank test. The sensitivity and accuracy of the signature was validated by the Receiver Operating Characteristic (ROC) curve utilizing the SurvivalROC package in R. Principal Component Analysis (PCA) was presented for assessing the accuracy of the classification according to the high and low risk scores.

Univariate and Multivariate Cox Regression Analysis

Univariate cox regression analysis was presented for assessment of the prognostic values of the risk score and clinical features (age, gender, stage, T, N, and M). Afterwards, multivariate cox regression analysis was used to determine which prognostic factors could independently predict the survival of patients.

Nomogram Model Establishment

By combining the eight ferroptosis-related genes, a nomogram was established. Moreover, another nomogram was constructed by combining age and the risk score. The total point of each patient was calculated based on the nomogram. The nomogram-predicted probability of 1-, 3-, and 5-year survival time was contrast by the actual survival time, which was visualized by the calibration curves.

Stratified Survival Analysis

Patients were divided into different subgroups according to age (<65 and ≥65), gender (female and male) and stage (stage I-II

TABLE 1 | The clinical characteristics of thyroid cancer patients.

Characteristics		Number
Age		
	<65	436
	>65	71
Gender		
	Male	136
	Female	371
Stage		
	Stage I	285
	Stage II	52
	Stage III	113
	Stage IV	55
	Unknown	2
T		
	T1	144
	T2	167
	T3	171
	T4	23
	Tx	2
M		
	M0	283
	M1	9
	Mx	213
	Unknown	1

TABLE 2 | Primer sequences for qRT-PCR.

Primer	Sequence (5′-3′)
DPP4	ATTCCAAACAACACACAGT (forward)
	CTTCATAAACCCAGTCAGT (reverse)
GPX4	GTAAAACCGGACCAGAAGTACAAG (forward)
	CCCACCTGCTTCCCGAACTG (reverse)
GSS	CTGGAGCGGCTGAAGGACA (forward)
	AGCTCTGAGATGCACTGGACA (reverse)
AKR1C1	TGCAGAGGTTCCTAAAAGTAAAGCTTTA (forward)
	GGAAAATGAATAAGGTAGAGGTCAACATAA (reverse)
HMGCR	AGTTTGAAGAGGATGTTTTG (forward)
	TCCCTTACTTCATCCTGTGA (reverse)
TFRC	ACCATTGTCATATACCCGGTTCA (forward)
	CAATAGCCCAAGTAGCCAATCAT (reverse)
SQLE	TGGTTACATGATTCATGATC (forward)
	TACTGAACTCCCATCACAAC (reverse)
PGD	ATTCTCAAGTTCCAAGACACCG (forward)
	GTGGTAAAACAGGGCATGGGA (reverse)
GAPDH	CTGCCCAGAACATCATCC (forward)
	CTCAGATGCCTGCTTCAC (reverse)

and stage III-IV). Kaplan-Meier survival analysis followed by log-rank test was presented between high and low risk score groups in different subgroups.

Gene Set Enrichment Analysis

GSEA was performed between high and low risk score groups (13). The "c2.cp.kegg.v7.1.symbols" was utilized as the reference. Signaling pathways with nominal p-value < 0.05 and false discovery rate (FDR) <0.05 were significantly enriched.

Estimation of Immune Infiltration

The infiltration levels of 22 immune cells in thyroid cancer samples were assessed *via* CIBERSORT (http://cibersort.stanford.edu/) (14). The differences in the infiltration levels of immune cells were compared between high and low risk score groups *via* the Wilcoxon rank-sum-test.

Immunohistochemistry

Immunohistochemistry of DPP4, GPX4, GSS, AKR1C1, HMGCR, TFRC, SQLE, and PGD in thyroid cancer and normal tissues was obtained from The Human Protein Atlas database (https://www.proteinatlas.org/).

Patients and Specimens

Twenty thyroid cancer and 10 adjacent normal tissues were obtained from Linyi Central Hospital between 2019 and 2020. Thyroid cancer was confirmed by post-operative pathological examination. Before surgery, no patient underwent radiation therapy or thyrotropin suppression therapy. The study was approved by the Ethics Committee of Linyi Central Hospital and followed the Declaration of Helsinki (2019019). Each patient provided written informed consent. All the resected specimens were placed instantly into liquid nitrogen and stored at −80°C.

Quantitative Real-Time PCR

Total RNA was extracted from tissues or cells *via* TRIzol (Invitrogen, Carlsbad, California, USA), followed by reverse transcription into cDNA. PCR was carried out using the TB Green® Premix Ex Taq™ II kit (TAKARA, China). The reaction procedures were as follows: 40 cycles at 94°C lasting 15 s, 60°C lasting 10 s, and 72°C lasting 20 s. GAPDH served as an internal control. The relative expression levels were quantified with the $2^{-\Delta\Delta Ct}$ method. The primer sequences were listed in **Table 2**.

Cell Culture and Transfection

Human thyroid cancer cell lines TPC-1 and FTC-133 (American Type Culture Collection, ATCC) were cultured in Dulbecco's modified eagle medium (Gibco, USA) containing 10% FBS, 100 U/ml penicillin and 100 μg/ml streptomycin in a 5% CO_2 incubator at 37°C. The cells were seeded in 6-well plates (2×10^5/well). When the cell confluence reached 60%, transfection of siRNA-negative control (si-NC), si-AKR1C1#1 and si-AKR1C1#2 was carried out according to the Lipofectamine 2000 (Invitrogen, USA) instructions. After 48 h, the cells were harvested.

Flow Cytometry

The transfected cells were seeded in 6-well plates (2×10^4/well). After culturing for 48 h, the culture medium was discarded, and the cells were trypsinized and collected.

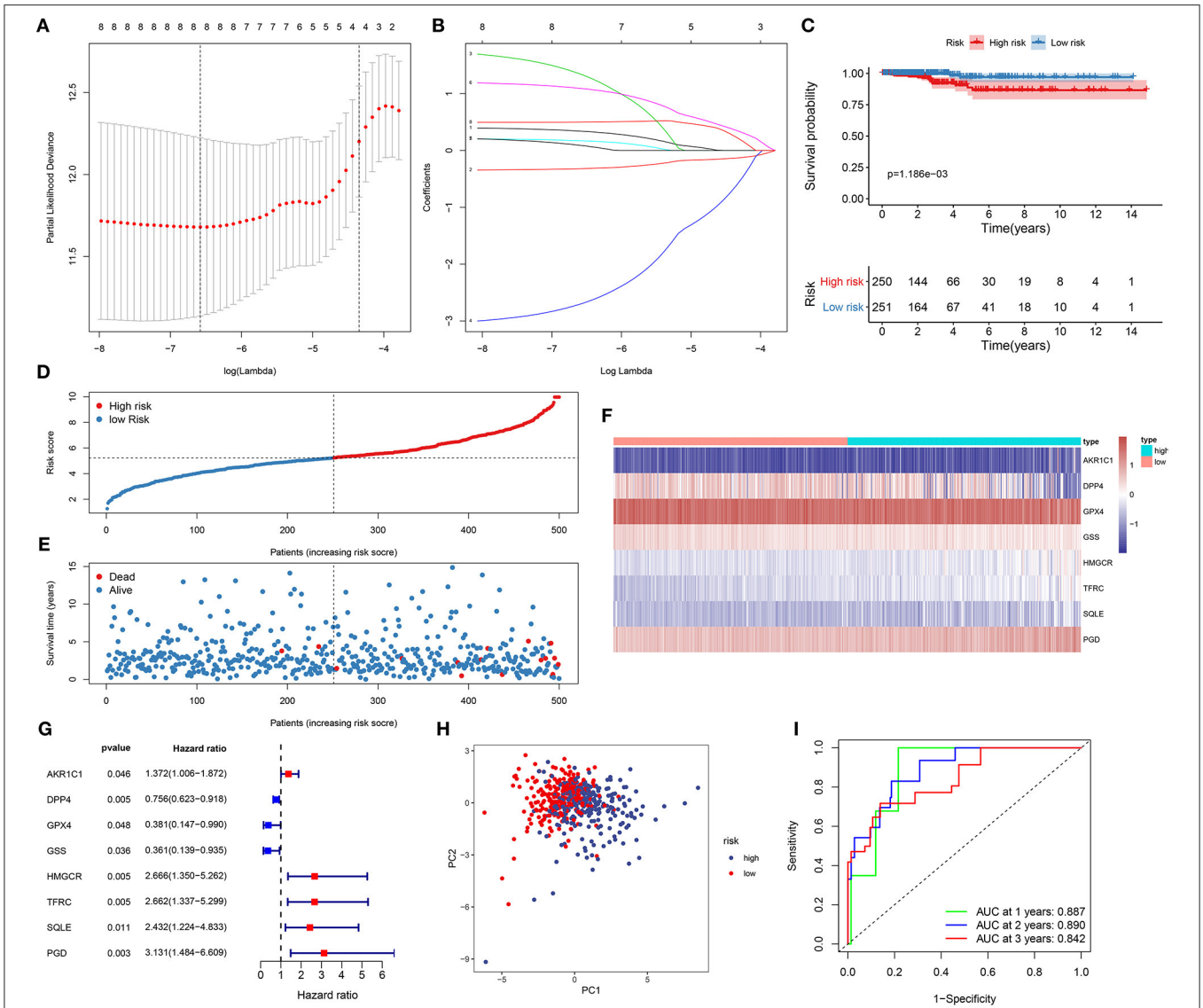

FIGURE 1 | Establishment of a ferroptosis-related eight-gene model for predicting the prognosis of thyroid cancer patients. **(A)** Selection of the optimal λ-value through the 10-fold cross-validation. **(B)** Fitting processes of LASSO Cox regression model. Each curve is indicative of the change trajectory of an independent variable coefficient. The ordinate is the value of the coefficient, the lower abscissa is log(λ), and the upper abscissa is the number of non-zero coefficients in the model. **(C)** Kaplan-Meier overall survival analysis for high (red) and low (blue) risk groups. **(D)** The ranking of the risk scores among all thyroid cancer samples. **(E)** The survival status including dead (red) and alive (blue) in high and low risk groups. **(F)** Heat map visualizing the expression levels of the eight ferroptosis-related genes in high (blue) and low (red) risk groups. **(G)** The prognostic values of the eight ferroptosis-related genes for thyroid cancer based on univariate cox regression analysis. **(H)** PCA for the high (blue) and low (red) risk thyroid cancer samples. **(I)** ROC for 1- (green), 2- (blue) and 3-year (red) survival time for high and low risk patients.

Following the instructions of Annexin V-FITC / PI kit, 200 μl binding buffer was added to resuspend cells, followed by 5 μl Annexin V-FITC and 5 μl PI. After incubating for 20 min in the dark, the apoptosis rate was detected by flow cytometry (BD, USA).

Wound Healing

The transfected cells were seeded into 24-well plates (5×10^4/well). The next day, a 200 μl pipette tip was utilized to draw a straight line perpendicular to the bottom of the cell culture plate. The width of scratches (×40) was investigated at 0 and 24 h under a microscope.

Transwell

Matrigel was diluted at 1:10 by serum-free medium, which was added to the upper layer of the transwell chamber (Corning, USA). The transfected cells diluted to 2×10^5/ml with serum-free medium were added to the upper layer of the chamber at 100 μl per well. Five hundred microliter of medium containing 10% FBS was added to the lower layer. After 24 h, the cells were fixed

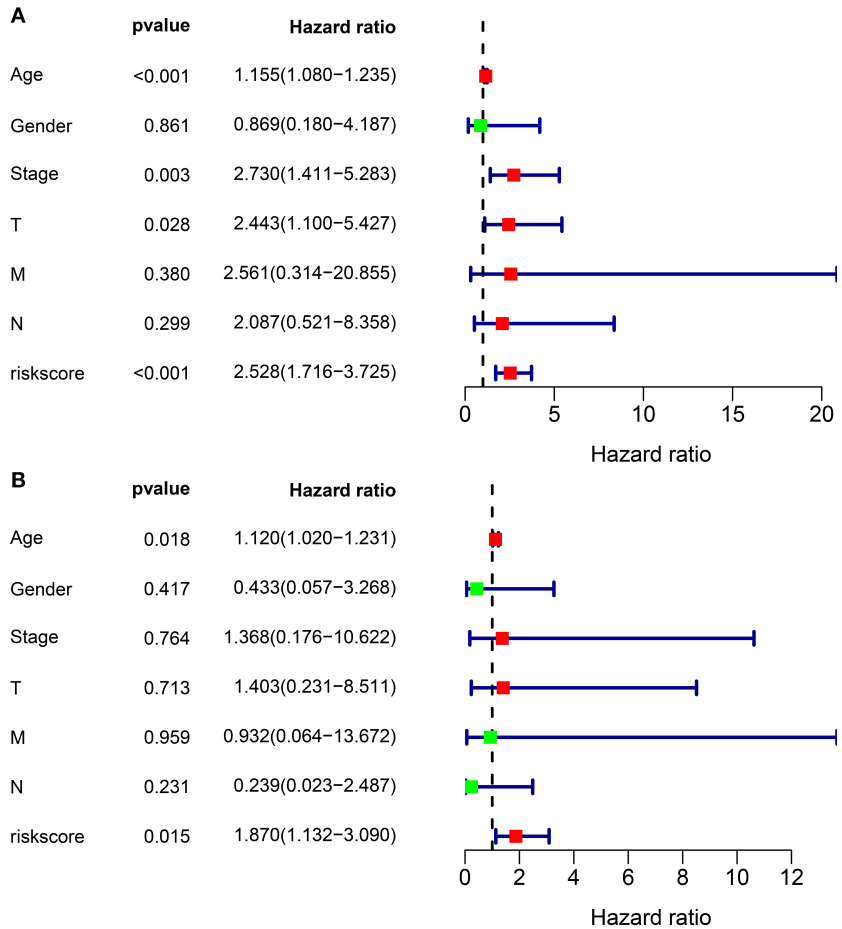

FIGURE 2 | The independency of the ferroptosis-related eight-gene model for predicting the clinical outcomes for thyroid cancer. **(A)** Univariate cox regression analysis for assessment of the prognostic values of different clinicopathological characteristics (age, gender, stage, T, N, M) and the risk score. **(B)** Evaluation of the independency of the risk score and other factors for predicting the prognosis of thyroid cancer using multivariate cox regression analysis.

with formaldehyde and stained with crystal violet. The number of invasive cells was counted.

Statistical Analysis

Statistical analysis was presented through R 3.6.3 and GraphPad 7.0. Data were presented as means ± standard deviation. Comparisons between two groups were analyzed by paired student's *t*-test or Wilcoxon rank-sum-test. Multiple comparisons were presented by one-way ANOVA. Difference with $p < 0.05$ was considered statistically significant.

RESULTS

Differentially Expressed Ferroptosis-Related Genes for Thyroid Cancer

A total of 60 ferroptosis-related genes were included in this study. Among them, 46 genes with adjusted $p < 0.05$ were differentially expressed between 510 thyroid cancer samples and 58 normal samples.

Establishment of a Prognostic Ferroptosis-Related Eight-Gene Model for Thyroid Cancer

Based on 46 differentially expressed ferroptosis-related genes, prognosis-related genes were selected for LASSO Cox regression analysis. When $\log \lambda = -6.6$, the model exhibited the optimal performance and the least number of independent variables (**Figure 1A**). As the values of λ increased, the LASSO coefficients of these variables were close to zero (**Figure 1B**). As a result, eight ferroptosis-related genes were utilized for the establishment of a prognostic model. The risk score for each sample was calculated as follows: (0.340143834733433) * AKR1C1 expression + (−0.319305763663027) * DPP4 expression + (1.3413362890122) * GPX4 + (−2.69880844893117) * GSS + (0.171053637326744) * HMGCR + (1.0923479137719) * TFRC + (0.0892997114590679) * SQLE + (0.499540011822522) * PGD. In line with the

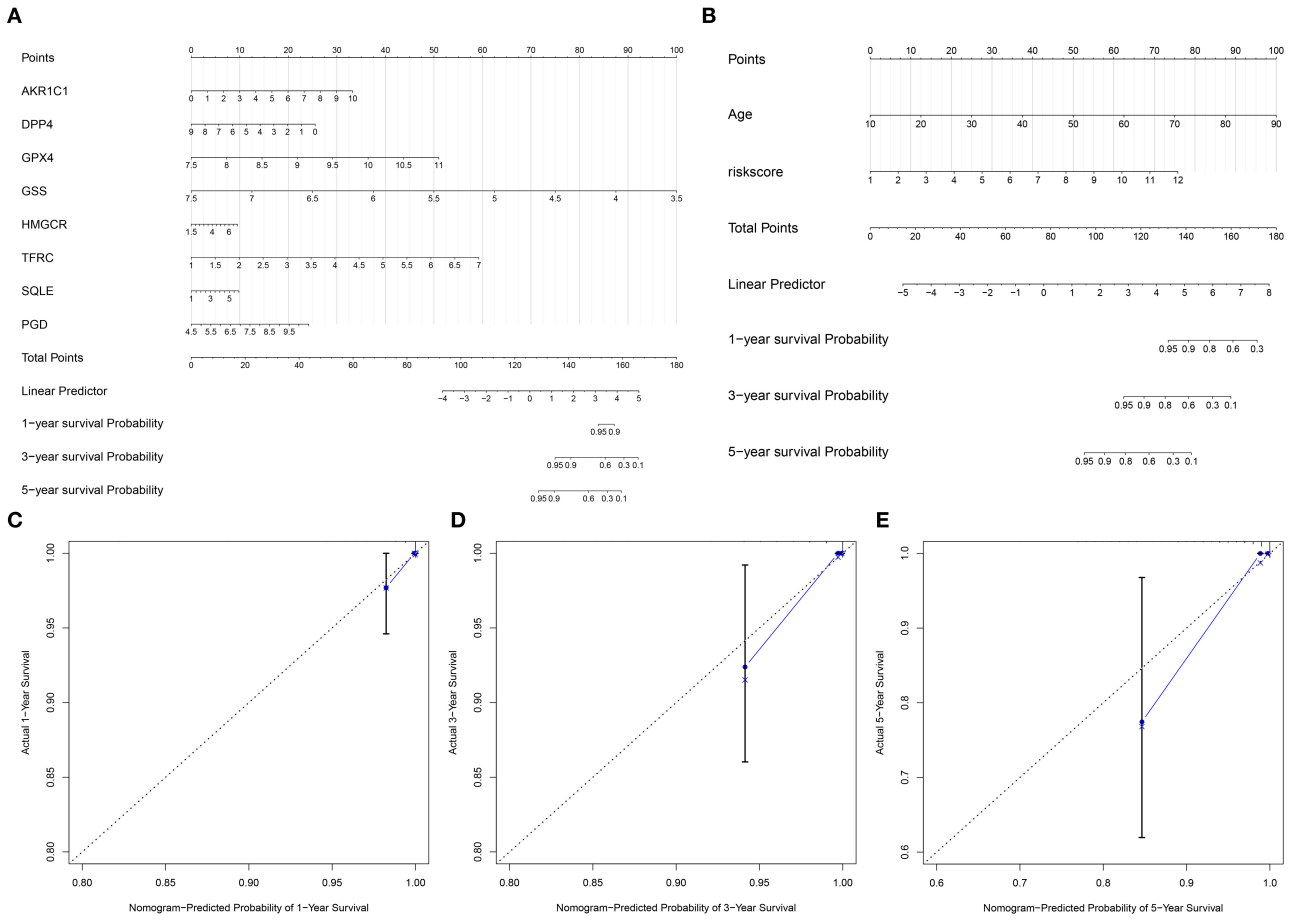

FIGURE 3 | Construction of nomogram models for thyroid cancer. **(A)** A nomogram combining the eight ferroptosis-related genes. **(B)** A nomogram combining the risk score and age. **(C–E)** Calibration curves comparing the nomogram-predicted **(C)** 1-, **(D)** 3-, and **(E)** 5-year survival and actual survival.

median value of all risk scores, 510 thyroid cancer patients were separated into high- and low-risk score groups. Kaplan-Meier curves showed that low risk patients could outlive high risk patients 21 ($p = 1.186 - 03$; **Figure 1C**). As the risk scores increased, the number of died patients was gradually increased (**Figures 1D,E**). Heat map visualized the expression patterns of the eight ferroptosis-related genes between high- and low-risk groups (**Figure 1F**). Univariate cox regression analysis demonstrated that DPP4 [hazard ratio (HR): 0.756, 95% confidence interval (CI): 0.623–0.918, $p = 0.004$], GPX4 (HR: 0.381, 95% CI: 0.147–0.990, $p = 0.048$) and GSS (HR: 0.361, 95% CI: 0.139–0.935, $p = 0.036$) were protective factors for thyroid cancer prognosis (**Figure 1G**). Meanwhile, AKR1C1 (HR: 1.372, 95% CI: 1.006–1.872, $p = 0.046$), HMGCR (HR: 2.666, 95% CI: 1.350–5.262, $p = 0.005$), TFRC (HR: 2.662, 95% CI: 1.337–5.299, $p = 0.005$), SQLE (HR: 2.432, 95% CI: 1.224–4.833, $p = 0.011$) and PGD (HR: 3.131, 95% CI: 1.484–6.609, $p = 0.003$) were risk factors for thyroid cancer prognosis (**Figure 1G**). PCA results confirmed the accuracy of the classification among the thyroid cancer samples (**Figure 1H**). To further validate the accuracy and sensitivity of the model, we constructed a ROC analysis. Our data confirmed that the model could accurately and sensitively predict the survival probability for 1- [area under the curve (AUC) = 0.887], 2- (AUC = 0.890), and 3-year (AUC = 0.842) survival time (**Figure 1I**). Collectively, this ferroptosis-related eight-gene model could be a robust prognostic model for thyroid cancer.

The Ferroptosis-Related Eight-Gene Model Was an Independent Factor for Predicting Prognosis of Thyroid Cancer

We further evaluated the performance of the ferroptosis-related eight-gene model for predicting the prognosis of thyroid cancer patients. Firstly, univariate cox regression analysis results showed that the risk score was a risk factor for thyroid cancer prognosis (HR: 2.528, 95% CI: 1.716–3.725, $p < 0.001$) in **Figure 2A**. Furthermore, age (HR: 1.155, 95% CI: 1.080–1.235, $p < 0.001$), stage (HR: 2.730, 95% CI: 1.411–5.283, $p = 0.003$), and T (HR: 2.443, 95% CI: 1.100–5.427, $p = 0.028$) were significantly associated with thyroid cancer prognosis (**Figure 2A**). Following multivariate cox regression analysis, the risk score was an

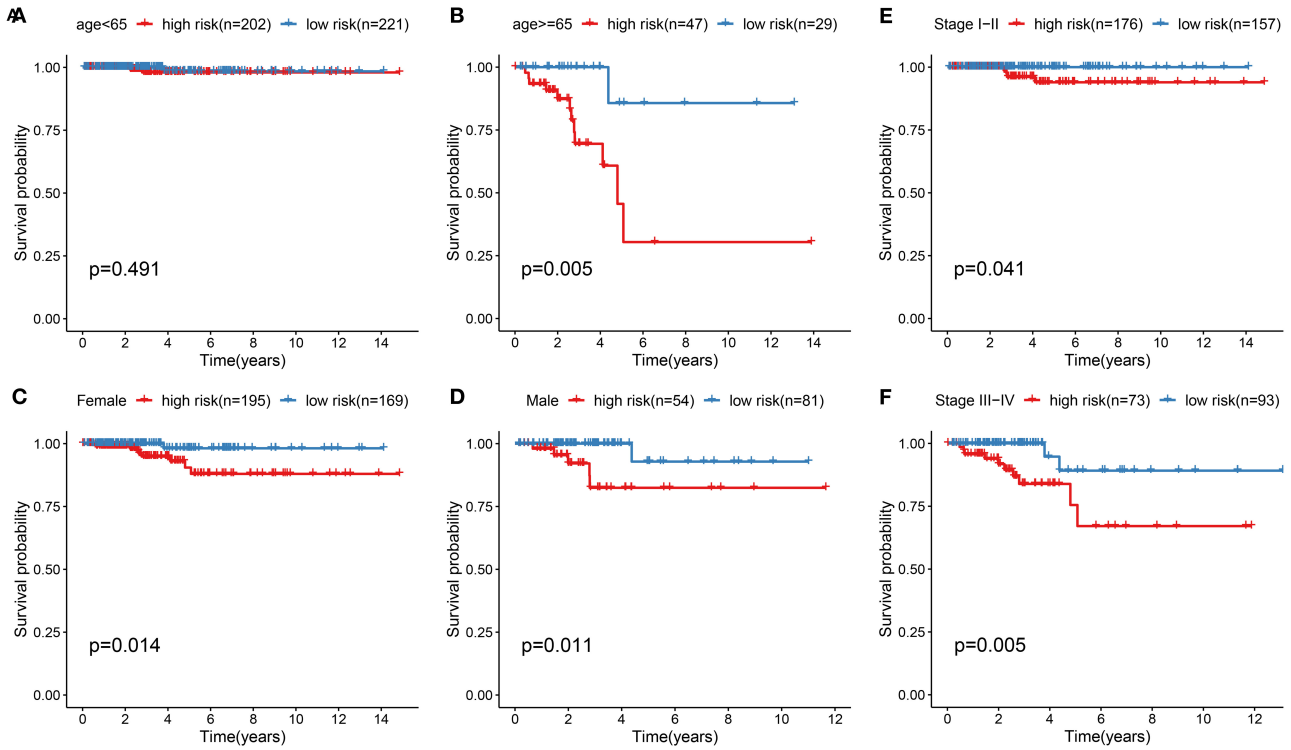

FIGURE 4 | Stratified analysis for the predictive efficacy of the ferroptosis-related model among thyroid cancer samples. **(A,B)** Kaplan-Meier curves for high and low risk group in the two subgroups of age < 65 and age ≥ 65. **(C,D)** Kaplan-Meier curves for high and low risk group in the two subgroups of female and male. **(E,F)** Kaplan-Meier curves for high and low risk group in the two subgroups of stage I-II and stage III-IV.

independent risk factor for thyroid cancer (HR: 1.870, 95% CI: 1.132–3.090, $p = 0.015$; **Figure 2B**). Except to the risk score, age independently predicted the prognosis of thyroid cancer (HR: 1.120, 95% CI: 1.020–1.231, $p = 0.018$). Collectively, the ferroptosis-related eight-gene model was an independent prognostic factor for thyroid cancer.

Construction of Nomogram Models for Thyroid Cancer

On the basis of the eight ferroptosis-related genes that could independently predict the prognosis of thyroid cancer, a nomogram was established for predicting 1-, 3-, and 5-year survival probability of thyroid cancer patients (**Figure 3A**). Furthermore, by combining the two independent prognostic factors (age and risk score), we constructed a nomogram model for thyroid cancer (**Figure 3B**). Calibration curves confirmed that the nomogram-predicted 1- (**Figure 3C**), 3- (**Figure 3D**), and 5- (**Figure 3E**) year survival probability approached the actual survival.

Stratified Analysis for the Predictive Efficacy of the Ferroptosis-Related Model

To assess whether the ferroptosis-related eight-gene model could sensitively predict the prognosis of thyroid cancer, stratified analysis was performed. For patients with age <65, there was no significant difference in the overall survival time between high and low risk groups (**Figure 4A**). For patients aged >65, high risk score was indicative of the shorter survival time compared to low risk score (**Figure 4B**; $p = 0.005$). Both for female (**Figure 4C**; $p = 0.014$) and male (**Figure 4D**; $p = 0.011$) patients, high risk score suggested a poorer prognosis in comparison to low risk score. In **Figure 4E**, patients at the stage I-II in the high-risk group exhibited the less optimistic prognosis than those in the low-risk group ($p = 0.041$). Similarly, high risk score indicated the poorer clinical outcomes for patients with stage III-IV than low risk score (**Figure 4F**; $p = 0.005$). Collectively, the model was a sensitive prognostic marker for thyroid cancer.

Potential Signaling Pathways for High-Risk Group

To uncover the potential signaling pathway in high- and low-risk groups, we presented GSEA. Our GSEA results showed that calcium signaling pathway (NES = 1.8147893 and $p < 0.0001$), MAPK signaling pathway (NES = 1.7950739 and $p = 0.0042643924$), mTOR signaling pathway (NES = 1.8197428 and $p < 0.0001$), pathways in cancer (NES = 1.7282541 and $p = 0.008281574$), PPAR signaling pathway (NES = 1.7024437 and $p = 0.008247423$), TGF-beta signaling pathway (NES = 1.8606039 and $p = 0.0020283975$), and WNT signaling pathway (NES = 1.8473499 and $p = 0.0020876827$) were significantly enriched in the high-risk group (**Figure 5**). However, no pathways with

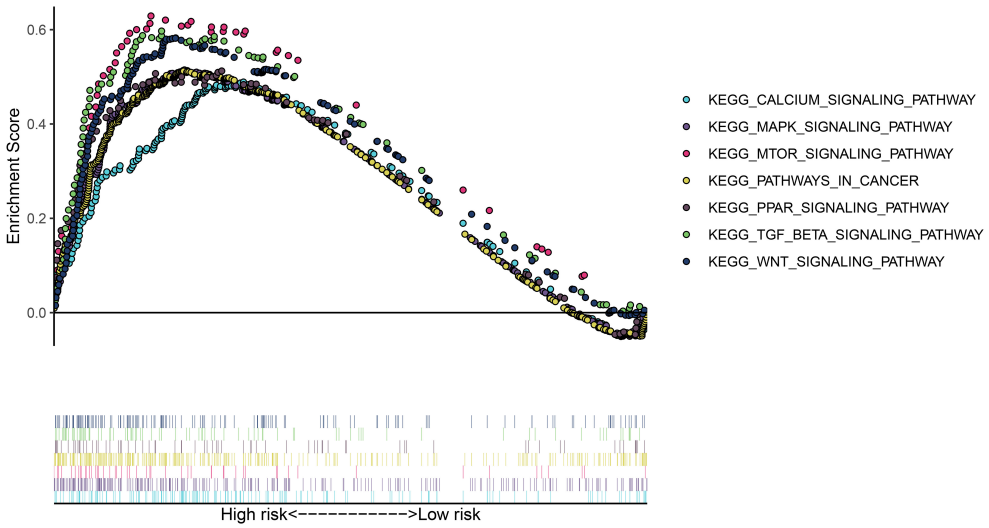

FIGURE 5 | GSEA revealed the signaling pathways enriched in the high-risk group.

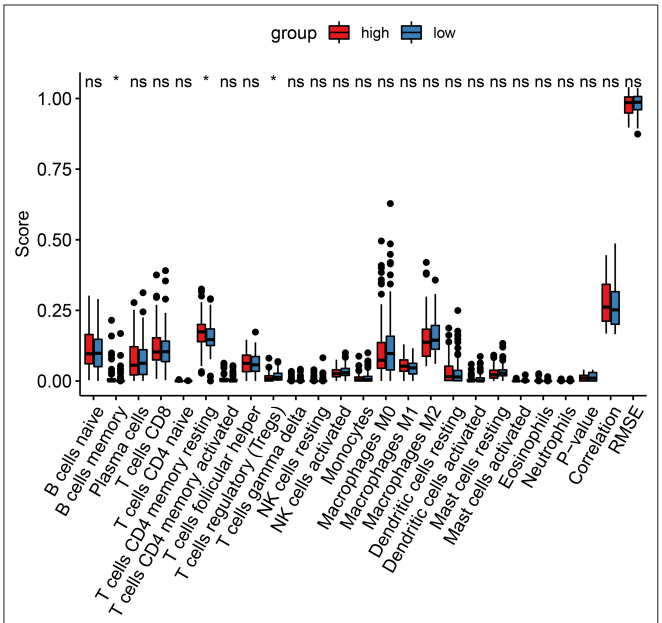

FIGURE 6 | CIBERSORT identifies the association between the ferroptosis-related model and immune cell infiltration in thyroid cancer. Red, the high-risk group and blue, low-risk group. Ns, not significant; *$p < 0.05$.

nominal p-value < 0.05 and FDR < 0.05 were found in the low-risk group, indicating that there were no pathways significantly enriched in the low-risk group.

The Ferroptosis-Related Model Is Associated With Immune Cell Infiltration in Thyroid Cancer

It has been reported that ferroptosis is involved in the tumor immune microenvironment. Hein, we assessed the correlation between the ferroptosis-related risk scores and immune cell infiltrations among thyroid cancer patients using the CIBERSORT. In **Figure 6**, the risk score was significantly associated with the infiltration levels of B cells memory ($p < 0.05$), T cells CD4 memory resting ($p < 0.05$), and T cells regulatory (Treg; $p < 0.05$). The high-risk samples exhibited a distinctly higher infiltration level of T cells CD4 memory resting compared to the low risk samples. Lower infiltration level of Tregs was detected in the high-risk group than the low risk group.

Validation of Eight Ferroptosis-Related Genes in Thyroid Cancer Tissues

We further validated the expression of the eight ferroptosis-related genes in thyroid cancer and control tissues. Immunohistochemistry results showed the expression and distribution of AKR1C1 (**Figure 7A**), DPP4 (**Figure 7B**), GPX4 (**Figure 7C**), GSS (**Figure 7D**), HMGCR (**Figure 7E**), TFRC (**Figure 7F**), SQLE (**Figure 7G**), and PGD (**Figure 7H**) in thyroid cancer and normal tissues. Furthermore, the mRNA expression levels of the eight ferroptosis-related genes were examined between thyroid cancer and normal tissues by RT-qPCR. Our data suggested that AKR1C1 ($p < 0.0001$; **Figure 8A**), DPP4 ($p < 0.0001$; **Figure 8B**), GPX4 ($p = 0.0001$; **Figure 8C**), GSS ($p < 0.0001$; **Figure 8D**), HMGCR ($p < 0.0001$; **Figure 8E**), TFRC ($p < 0.0001$; **Figure 8F**), SQLE ($p = 0.0004$; **Figure 8G**), and PGD ($p = 0.0005$; **Figure 8H**) were all significantly highly expressed in thyroid cancer tissues compared to normal tissues.

Silencing AKR1C1 Promotes Apoptosis and Suppresses Migration and Invasion in Thyroid Cancer Cells

Among the eight ferroptosis-related genes, we selected AKR1C1 to validate its function in thyroid cancer. AKR1C1 expression was distinctly silenced by si-AKR1C1 in TPC-1 and FTC-133 cells (**Figure 9A**). After silencing its expression, the apoptotic

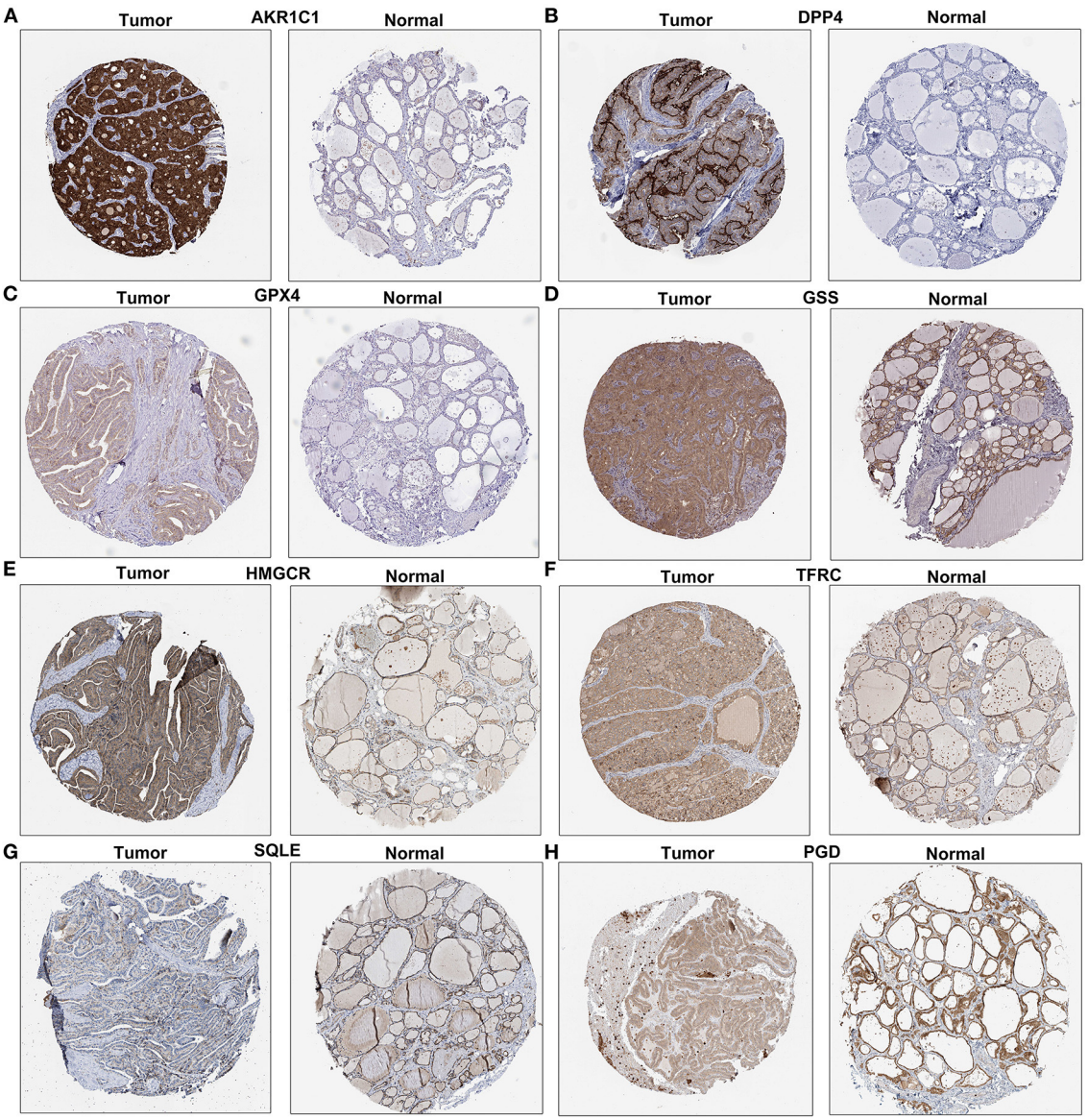

FIGURE 7 | Immunohistochemistry showing the expression of **(A)** AKR1C1, **(B)** DPP4, **(C)** GPX4, **(D)** GSS, **(E)** HMGCR, **(F)** TFRC, **(G)** SQLE, and **(H)** PGD in thyroid cancer and normal tissues. Scale bar: 200 μm.

levels were significantly promoted in TPC-1 and FTC-133 cells (**Figures 9B,C**). Also, we found that the migrated (**Figures 9D,E**) and invasive (**Figures 9F,G**) capacities were markedly restrained by AKR1C1 knockdown in TPC-1 and FTC-133 cells. These data demonstrated that AKR1C1 might participate in thyroid cancer progression.

DISCUSSION

Increasing evidence emphasizes the importance of ferroptosis on the cancer therapy. Nevertheless, it remains unclear whether ferroptosis may affect the clinical outcomes for thyroid cancer patients. Thus, elucidating the molecular mechanisms and signaling pathways of ferroptosis enables us to develop novel therapeutic targets for thyroid cancer. In this study, we developed a ferroptosis-related eight gene model, which can robustly predict the prognosis of thyroid cancer.

Herein, a ferroptosis-related eight gene model was constructed for predicting the prognosis of thyroid cancer *via* LASSO Cox regression analysis. For thyroid cancer patients, high risk score was indicative of poorer prognosis than low risk score. ROC confirmed that the signature could have accurate and sensitive predictive efficacy. Multivariate cox regression analysis demonstrated that the signature can independently predict the survival for thyroid cancer. Among them, DPP4, GPX4, and GSS were protective factors for thyroid cancer prognosis. Meanwhile, AKR1C1, HMGCR, TFRC, SQLE, and PGD were risk factors for thyroid cancer prognosis. As previous studies, DPP4 is highly expressed in thyroid cancer tissues, which has been considered

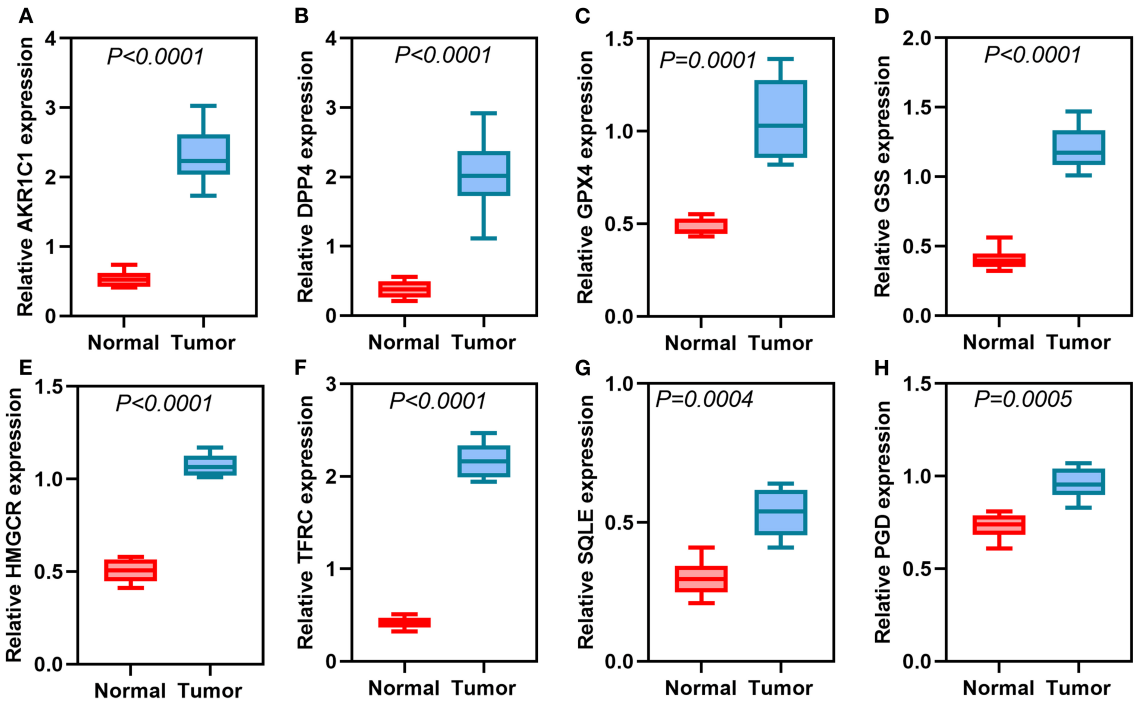

FIGURE 8 | RT-qPCR detecting the mRNA expression of **(A)** AKR1C1, **(B)** DPP4, **(C)** GPX4, **(D)** GSS, **(E)** HMGCR, **(F)** TFRC, **(G)** SQLE, and **(H)** PGD in thyroid cancer and normal tissues.

as a prognostic factor (15). It can induce proliferative, invasive, as well as migrated capacities for thyroid cancer (16). GPX4 is an important regulator of ferroptosis for cancer cells (17). Depletion of GPX4 may induce ferroptosis, which can sensitize cells to ferroptosis (18). AKR1C1 can activate STAT3, thereby promoting lung cancer metastasis (19). Furthermore, it mediates cisplatin-resistance for head and neck squamous cell carcinoma *via* STAT1/3 pathways (20). Targeting HMGCR may suppress the invasive ability of thyroid cancer cells (21). It has been reported that YAP can facilitate ferroptosis *via* up-regulation of a ferroptosis regulator TFRC in cancer cells (22). Moreover, TFRC induces epithelial ovarian cancer cell proliferation as well as metastases by up-regulating AXIN2 (23). SQLE has become a pharmaceutical target for various cancers. For example, it may drive non-alcoholic fatty liver disease-induced hepatocellular carcinoma (24). Additionally, SQLE expression can predict the fatality rate of prostate cancer (25). However, the functions of these eight ferroptosis-related genes remains to be clarified in thyroid cancer. Our immunohistochemistry and qRT-PCR confirmed that these eight genes were all activated in thyroid cancer. This study may offer novel clues for exploring the biological roles and clinical significance of these ferroptosis-related genes. Our multivariate cox regression analysis suggested that age at diagnosis was an independent risk factor for thyroid cancer. Consistently, age has been commonly applied as a risk factor for stratifying the prognosis of thyroid cancer (26). Among adults aged over 65 years old, the incidence of thyroid cancer is the highest (27). Our stratified analysis revealed that the ferroptosis-related eight gene model could accurately predict the clinical outcomes for patients with >65 years old. Moreover, regardless of whether it was a male or female patient, high risk score implied a worse prognosis. For patients with stage I-II or III-IV, high risk score was indicative of shorter survival time. Hence, the signature could accurately predict the clinical outcomes for thyroid cancer. In order to expand the clinical application of this model, we combined it with age to construct a nomogram that could be easy to calculate the expected survival rate for an individual patient. Calibration curves confirmed that the nomogram-predicted 1-, 3-, and 5-year survival time was close to the actual survival time. This suggested that the nomogram had the potential as a clinically predictive tool for thyroid cancer prognosis.

Various signaling pathways participate in regulating the process of ferroptosis. Herein, our data suggested that MAPK, mTOR, pathways in cancer, PPAR, TGF-beta, and WNT signaling pathways were enriched in the high-risk group. MAPK pathway can be activated in ferroptosis cells (28). In turn, blockage of MAPK pathway also protects cells from ferroptosis (29). The activation of MAPK pathways can lead to the occurrence and progression of thyroid cancer (30). Ferroptosis-induced ROS accumulation could inactivate MAPK pathway to kill thyroid cancer cells (30). Four targeted therapies (Sorafenib, Lenvatinib, Vandetanib, and Cabozantinib) have been approved for treating thyroid cancer patients resistant to standard therapy, which can have the effects *via* blockage of MAPK pathway (31). Hence, their capacity to prolong the survival time of patients remain to be limited because of poor efficacies and other molecular interventions such as ferroptosis (31). mTOR pathway

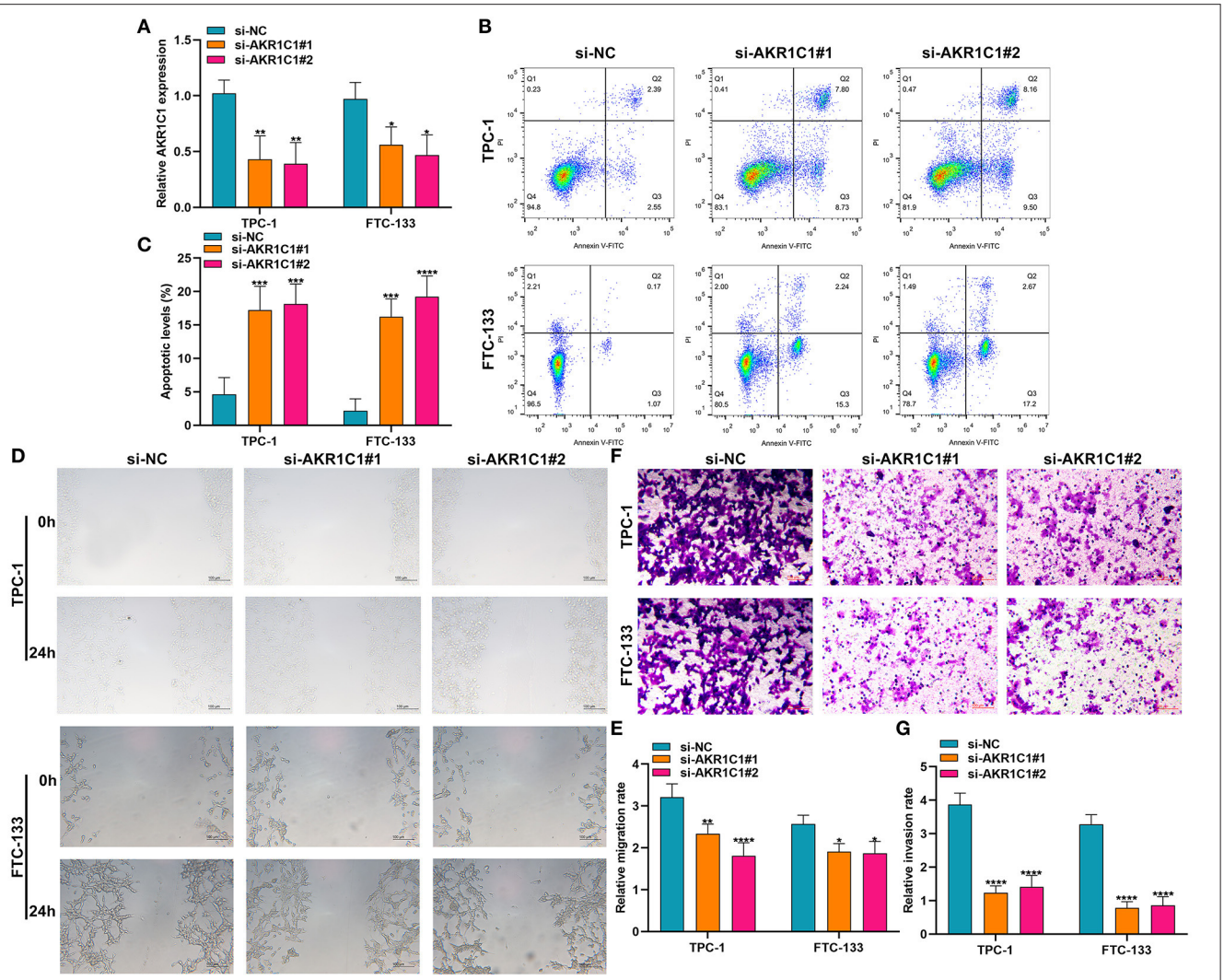

FIGURE 9 | The effects of AKR1C1 knockdown on apoptosis, migration, and invasion in thyroid cancer cells. **(A)** RT-qPCR for the mRNA expression of AKR1C1 in TPC-1 and FTC-133 cells transfected with si-AKR1C1. **(B,C)** Flow cytometry detecting the apoptosis of si-AKR1C1-transfected TPC-1 and FTC-133 cells. **(D,E)** Wound healing for the migration of TPC-1 and FTC-133 cells transfected with si-AKR1C1. **(F,G)** Transwell for the invasion of TPC-1 and FTC-133 cells transfected with si-AKR1C1. $^{*}p < 0.05$; $^{**}p < 0.01$; $^{***}p < 0.001$; $^{****}p < 0.0001$.

can mediate cellular proliferative capacities and the uptake of iodine for thyroid cells (32). Recently, mTOR pathway has been confirmed to be involved in mediating ferroptosis in different cancers such as colorectal cancer (33). Activation of mTOR transduction may protect cancer cells from oxidative stress and ferroptosis (34). PPARα promotes ferroptosis by mediating lipid remodeling in cancer cells (35). In WNT pathway, Frizzled-7 is sensitive to ferroptosis for platinum-tolerant ovarian cancer cells (36). Taken together, our results indicated that various pathways could be involved in ferroptosis for thyroid cancer. The roles of these pathways in ferroptosis should be assessed by more experiments.

Many thyroid cancer patients who are not accompanied by thyroiditis, immune infiltrations are found following surgery, suggesting that changes in the immune microenvironment is related to the progression of thyroid cancer (37). Our data demonstrated that the model was significantly associated with the infiltration of B cells memory, T cells CD4 memory resting and Tregs. Further analysis should be presented to probe into the associations between the ferroptosis-related model and the tumor microenvironment. A larger cohort should be required to verify the predictive values of the ferroptosis-related eight gene model for thyroid cancer.

CONCLUSION

Collectively, we constructed a ferroptosis-related eight gene model that exhibited a well predictive performance. The model had a significant association with the tumor immune microenvironment. The nomogram combining the model and age could provide new possibilities for individualized therapy of thyroid cancer patients. Hence, ferroptosis could be promising therapeutic targets.

DATA AVAILABILITY STATEMENT

The datasets presented in this study can be found in online repositories. The names of the repository/repositories and accession number(s) can be found in the article/**Supplementary Material**.

ETHICS STATEMENT

The studies involving human participants were reviewed and approved by the Ethics Committee of Linyi Central Hospital (2019019). The patients/participants provided their written informed consent to participate in this study.

AUTHOR CONTRIBUTIONS

PH conceived and designed the study. MG, JN, and AT conducted most of the experiments and data analysis, and wrote the manuscript. YD, FX, and FL participated in collecting data and helped to draft the manuscript. All authors reviewed and approved the manuscript.

SUPPLEMENTARY MATERIAL

The Supplementary Material for this article can be found online at: https://www.frontiersin.org/articles/10.3389/fmed.2021.637743/full#supplementary-material

Supplementary Table 1 | A list of 60 ferroptosis-related genes.

REFERENCES

1. Hernando J, Ros J, Arroyo A, Capdevila J. Clinical and translational challenges in thyroid cancer. *Curr Med Chem*. (2020) 27:4806–22. doi: 10.2174/0929867327666200214125712
2. Cabanillas ME, McFadden DG, Durante C. Thyroid cancer. *Lancet*. (2016) 388:2783–95. doi: 10.1016/S0140-6736(16)30172-6
3. Kim J, Gosnell JE, Roman SA. Geographic influences in the global rise of thyroid cancer. *Nat Rev Endocrinol*. (2020) 16:17–29. doi: 10.1038/s41574-019-0263-x
4. Varricchi G, Loffredo S, Marone G, Modestino L, Fallahi P, Ferrari SM, et al. The immune landscape of thyroid cancer in the context of immune checkpoint inhibition. *Int J Mol Sci*. (2019) 20:3934. doi: 10.3390/ijms20163934
5. Wang W, Green M, Choi JE, Gijón M, Kennedy PD, Johnson JK, et al. CD8(+) T cells regulate tumour ferroptosis during cancer immunotherapy. *Nature*. (2019) 569:270–4. doi: 10.1038/s41586-019-1170-y
6. Shen Z, Song J, Yung BC, Zhou Z, Wu A, Chen X. Emerging strategies of cancer therapy based on ferroptosis. *Adv Mater*. (2018) 30:e1704007. doi: 10.1002/adma.201704007
7. Lu B, Chen XB, Ying MD, He QJ, Cao J, Yang B. The role of ferroptosis in cancer development and treatment response. *Front Pharmacol*. (2017) 8:992. doi: 10.3389/fphar.2017.00992
8. Hassannia B, Vandenabeele P, Vanden Berghe T. Targeting ferroptosis to iron out cancer. *Cancer Cell*. (2019) 35:830–49. doi: 10.1016/j.ccell.2019.04.002
9. Liang JY, Wang DS, Lin HC, Chen XX, Yang H, Zheng Y, et al. A novel ferroptosis-related gene signature for overall survival prediction in patients with hepatocellular carcinoma. *Int J Biol Sci*. (2020) 16:2430–41. doi: 10.7150/ijbs.45050
10. Wu G, Wang Q, Xu Y, Li Q, Cheng L. A new survival model based on ferroptosis-related genes for prognostic prediction in clear cell renal cell carcinoma. *Aging (Albany NY)*. (2020) 12:14933–48. doi: 10.18632/aging.103553
11. Robinson MD, McCarthy DJ, Smyth GK. edgeR: a bioconductor package for differential expression analysis of digital gene expression data. *Bioinformatics*. (2010) 26:139–40. doi: 10.1093/bioinformatics/btp616
12. Friedman J, Hastie T, Tibshirani R. Regularization paths for generalized linear models *via* coordinate descent. *J Stat Softw*. (2010) 33:1–22. doi: 10.18637/jss.v033.i01
13. Subramanian A, Tamayo P, Mootha VK, Mukherjee S, Ebert BL, Gillette MA, et al. Gene set enrichment analysis: a knowledge-based approach for interpreting genome-wide expression profiles. *Proc Natl Acad Sci USA*. (2005) 102:15545–50. doi: 10.1073/pnas.0506580102
14. Newman AM, Liu CL, Green MR, Gentles AJ, Feng W, Xu Y, et al. Robust enumeration of cell subsets from tissue expression profiles. *Nat Methods*. (2015) 12:453–7. doi: 10.1038/nmeth.3337
15. Du J, Fu L, Ji F, Wang C, Liu S, Qiu X. FosB recruits KAT5 to potentiate the growth and metastasis of papillary thyroid cancer in a DPP4-dependent manner. *Life Sci*. (2020) 259:118374. doi: 10.1016/j.lfs.2020.118374
16. Wang Y, Han J, Lv Y, Zhang G. miR-29a inhibits proliferation, invasion, and migration of papillary thyroid cancer by targeting DPP4. *Onco Targets Ther*. (2019) 12:4225–33. doi: 10.2147/OTT.S201532
17. Yang WS, SriRamaratnam R, Welsch ME, Shimada K, Skouta R, Viswanathan VS, et al. Regulation of ferroptotic cancer cell death by GPX4. *Cell*. (2014) 156:317–31. doi: 10.1016/j.cell.2013.12.010
18. Chen GQ, Benthani FA, Wu J, Liang D, Bian ZX, Jiang X. Artemisinin compounds sensitize cancer cells to ferroptosis by regulating iron homeostasis. *Cell Death Differ*. (2020) 27:242–54. doi: 10.1038/s41418-019-0352-3
19. Zhu H, Chang LL, Yan FJ, Hu Y, Zeng CM, Zhou TY, et al. AKR1C1 activates STAT3 to promote the metastasis of non-small cell lung cancer. *Theranostics*. (2018) 8:676–92. doi: 10.7150/thno.21463
20. Chang WM, Chang YC, Yang YC, Lin SK, Chang PM, Hsiao M. AKR1C1 controls cisplatin-resistance in head and neck squamous cell carcinoma through cross-talk with the STAT1/3 signaling pathway. *J Exp Clin Cancer Res*. (2019) 38:245. doi: 10.1186/s13046-019-1256-2
21. Revilla G, Pons MP, Baila-Rueda L, García-León A, Santos D, Cenarro A, et al. Cholesterol and 27-hydroxycholesterol promote thyroid carcinoma aggressiveness. *Sci Rep*. (2019) 9:10260. doi: 10.1038/s41598-019-46727-2
22. Wu J, Minikes AM, Gao M, Bian H, Li Y, Stockwell BR, et al. Intercellular interaction dictates cancer cell ferroptosis *via* NF2-YAP signalling. *Nature*. (2019) 572:402–6. doi: 10.1038/s41586-019-1426-6
23. Huang Y, Huang J, Huang Y, Gan L, Long L, Pu A, et al. TFRC promotes epithelial ovarian cancer cell proliferation and metastasis *via* up-regulation of AXIN2 expression. *Am J Cancer Res*. (2020) 10:131–47.
24. Liu D, Wong CC, Fu L, Chen H, Zhao L, Li C, et al. Squalene epoxidase drives NAFLD-induced hepatocellular carcinoma and is a pharmaceutical target. *Sci Transl Med*. (2018) 10:aap9840. doi: 10.1126/scitranslmed.aap9840
25. Stopsack KH, Gerke TA, Sinnott JA, Penney KL, Tyekucheva S, Sesso HD, et al. Cholesterol metabolism and prostate cancer lethality. *Cancer Res*. (2016) 76:4785–90. doi: 10.1158/0008-5472.CAN-16-0903
26. Shen X, Zhu G, Liu R, Viola D, Elisei R, Puxeddu E, et al. Patient age-associated mortality risk is differentiated by BRAF V600E status in papillary thyroid cancer. *J Clin Oncol*. (2018) 36:438–45. doi: 10.1200/JCO.2017.74.5497
27. Haymart MR, Banerjee M, Reyes-Gastelum D, Caoili E, Norton EC. Thyroid ultrasound and the increase in diagnosis of low-risk thyroid cancer. *J Clin Endocrinol Metab*. (2019) 104:785–92. doi: 10.1210/jc.2018-01933
28. Nakamura T, Naguro I, Ichijo H. Iron homeostasis and iron-regulated ROS in cell death, senescence and human diseases. *Biochim Biophys Acta Gen Subj*. (2019) 1863:1398–409. doi: 10.1016/j.bbagen.2019.06.010
29. Poursaitidis I, Wang X, Crighton T, Labuschagne C, Mason D, Cramer SL, et al. Oncogene-selective sensitivity to synchronous cell death following modulation of the amino acid nutrient cystine. *Cell Rep*. (2017) 18:2547–56. doi: 10.1016/j.celrep.2017.02.054

30. Su X, Shen Z, Yang Q, Sui F, Pu J, Ma J, et al. Vitamin C kills thyroid cancer cells through ROS-dependent inhibition of MAPK/ERK and PI3K/AKT pathways *via* distinct mechanisms. *Theranostics*. (2019) 9:4461–73. doi: 10.7150/thno.35219
31. Naoum GE, Morkos M, Kim B, Arafat W. Novel targeted therapies and immunotherapy for advanced thyroid cancers. *Mol Cancer*. (2018) 17:51. doi: 10.1186/s12943-018-0786-0
32. Souza EC, Ferreira AC, Carvalho DP. The mTOR protein as a target in thyroid cancer. *Expert Opin Ther Targets*. (2011) 15:1099–112. doi: 10.1517/14728222.2011.594044
33. Zhang L, Liu W, Liu F, Wang Q, Song M, Yu Q, et al. IMCA induces ferroptosis mediated by SLC7A11 through the AMPK/mTOR pathway in colorectal cancer. *Oxid Med Cell Longev*. (2020) 2020:1675613. doi: 10.1155/2020/1675613
34. Yi J, Zhu J, Wu J, Thompson CB, Jiang X. Oncogenic activation of PI3K-AKT-mTOR signaling suppresses ferroptosis *via* SREBP-mediated lipogenesis. *Proc Natl Acad Sci USA*. (2020) 117:31189–97. doi: 10.1073/pnas.2017152117
35. Venkatesh D, O'Brien NA, Zandkarimi F, Tong DR, Stokes ME, Dunn DE, et al. MDM2 and MDMX promote ferroptosis by PPARα-mediated lipid remodeling. *Genes Dev*. (2020) 34:526–43. doi: 10.1101/gad.334219.119
36. Wang Y, Zhao G, Condello S, Huang H, Cardenas H, Tanner EJ, et al. Frizzled-7 identifies platinum tolerant ovarian cancer cells susceptible to ferroptosis. *Cancer Res*. (2020) 384–99. doi: 10.1101/2020.05.28.121590
37. Nicolson NG, Brown TC, Korah R, Carling T. Immune cell infiltrate-associated dysregulation of DNA repair machinery may predispose to papillary thyroid carcinogenesis. *Surgery*. (2020) 167:66–72. doi: 10.1016/j.surg.2019.02.024

Conflict of Interest: The authors declare that the research was conducted in the absence of any commercial or financial relationships that could be construed as a potential conflict of interest.

Copyright © 2021 Ge, Niu, Hu, Tong, Dai, Xu and Li. This is an open-access article distributed under the terms of the Creative Commons Attribution License (CC BY). The use, distribution or reproduction in other forums is permitted, provided the original author(s) and the copyright owner(s) are credited and that the original publication in this journal is cited, in accordance with accepted academic practice. No use, distribution or reproduction is permitted which does not comply with these terms.

frontiers in Medicine

ORIGINAL RESEARCH
published: 13 April 2021
doi: 10.3389/fmed.2021.649279

Targeting Antisense lncRNA PRKAG2-AS1, as a Therapeutic Target, Suppresses Malignant Behaviors of Hepatocellular Carcinoma Cells

*Yanjiao Ou, Yong Deng, Hong Wang, Qingyi Zhang, Huan Luo and Peng Hu**

Department of Hepatobiliary Surgery, The First Affiliated Hospital of Army Medical University, Chongqing, China

OPEN ACCESS

Edited by:
Fu Wang,
Xi'an Jiaotong University, China

Reviewed by:
Jingang Huang,
Sun Yat-sen Memorial Hospital, China
Ying Wang,
Jiangnan University, China
Jing Zhang,
Shanghai Jiao Tong University, China

****Correspondence:***
Peng Hu
pengboyfei@163.com

Specialty section:
This article was submitted to Precision Medicine, a section of the journal Frontiers in Medicine

Received: *04 January 2021*
Accepted: *08 March 2021*
Published: *13 April 2021*

Citation:
Ou Y, Deng Y, Wang H, Zhang Q, Luo H and Hu P (2021) Targeting Antisense lncRNA PRKAG2-AS1, as a Therapeutic Target, Suppresses Malignant Behaviors of Hepatocellular Carcinoma Cells. Front. Med. 8:649279. doi: 10.3389/fmed.2021.649279

Objective: Increasing evidence highlights antisense long non-coding RNAs (lncRNAs) as promising therapeutic targets for cancers. Herein, this study focused on the clinical implications and functions of a novel antisense lncRNA PRKAG2-AS1 in hepatocellular carcinoma (HCC).

Methods: PRKAG2-AS1 expression was examined in a cohort of 138 HCC patients by RT-qPCR. Overall survival (OS) and disease-free survival (DFS) analyses were presented based on PRKAG2-AS1 expression, followed by ROCs. After silencing PRKAG2-AS1, cell proliferation was assessed via CCK-8, colony formation and EdU staining assays. Migrated and invasive capacities were assessed by wound healing and transwell assays. The relationships between PRKAG2-AS1, miR-502-3p and BICD2 were validated by luciferase reporter, RIP and RNA pull-down assays. The expression and prognostic value of BICD2 were analyzed in TCGA database.

Results: PRKAG2-AS1 was up-regulated in HCC than normal tissue specimens. High PRKAG2-AS1 expression was indicative of poorer OS and DFS time. Area under the curves (AUCs) for OS and DFS were 0.8653 and 0.7891, suggesting the well predictive efficacy of PRKAG2-AS1 expression. Targeting PRKAG2-AS1 distinctly inhibited proliferation, migration, and invasion in HCC cells. PRKAG2-AS1 was mainly expressed in cytoplasm of HCC cells. PRKAG2-AS1 may directly bind to the sites of miR-502-3p. Up-regulation of BICD2 was found in HCC tissues and associated with unfavorable prognosis. BICD2 was confirmed to be a downstream target of miR-502-3p. PRKAG2-AS1 could regulate miR-502-3p/BICD2 axis.

Conclusion: Our findings identified a novel lncRNA PRKAG2-AS1 that was associated with clinical implications and malignant behaviors. Thus, PRKAG2-AS1 could become a promising therapeutic target.

Keywords: PRKAG2-AS1, hepatocellular carcinoma, therapeutic target, proliferation, migration, invasion

INTRODUCTION

Hepatocellular carcinoma (HCC) is the third leading cause of cancer-related deaths globally, occupying 75–80% among all liver cancer cases (1). The five-year survival rate is only 15–17% due to recurrence and metastasis (2). Surgical resection followed by transcatheter arterial chemoembolization is the main therapeutic method (3). In recent years, immune and targeted therapies have been widely given wide attention and exhibited favorable clinical outcomes (4, 5). However, only a small percentage of patients will benefit from the latest treatment strategies. Furthermore, molecular target therapy is currently still limited (6). Hence, exploration of novel therapeutic targets is still of significance.

It is well-acknowledged that dysregulated oncogenes or tumor suppressor genes are correlated to carcinogenesis and progression in HCC (7). In the human genome, ∼70% is non-coding RNAs (ncRNAs) that are classified into circRNAs, lncRNAs and small ncRNAs according to sequence lengths of transcripts (8). Numerous lncRNAs and circRNAs are indicative to participate in the tumorigenesis and development for HCC (9–11). For instance, an oncogenic antisense lncRNA MCM3AP-AS1 is positively correlated to undesirable clinical outcomes in HCC patients (12). Moreover, its overexpression accelerates tumor malignant growth in HCC. A novel antisense lncRNA PRKAG2-AS1 is overexpressed in colon adenocarcinoma (13), advanced prostate cancer (14) and esophageal squamous cell carcinoma (15). Moreover, its up-regulation could be indicative of unfavorable clinical outcomes of patients. However, the expression and clinical implications of PRKAG2-AS1 remain unclear in HCC. In this study, we identified that this lncRNA was a prognostic factor of HCC patients. Targeting PRKAG2-AS1 could suppress proliferation, migration, and invasion of HCC cells. Hence, it could become a promising therapeutic target.

MATERIALS AND METHODS

Microarray Dataset

From the Gene Expression Omnibus (GEO, http://www.ncbi.nlm.nih.gov/geo) database, microarray data of five pairs of HCC and adjacent normal tissue specimens were obtained in the GSE39678 dataset. Differential expression analysis between HCC and normal tissues was presented via the limma package in R (16). The screening criteria were set as false discovery rate (FDR) < 0.01 and $|\log2 \text{ fold change (FC)}| > 2$.

Clinical Specimens

Totally, 138 pairs of HCC and adjacent normal tissue specimens were gathered during liver resection at The First Affiliated Hospital of Army Medical University. All patients did not experience any treatment such as transcatheter arterial chemoembolization, immune therapy, or targeted therapy before surgery. Pathological diagnosis was done by two experienced pathologists. Clinical information including age, tumor size, tumor number, HBsAg, tumor differentiation, lymph node metastasis, and clinical stage was obtained for each patient. HCC stage was diagnosed according to the American Joint Committee on Cancer (AJCC) staging standards. All specimens were instantly frozen in liquid nitrogen, followed by being stored at −80°C. Each participant provided the written informed consent. This research met the standards of the Declaration of Helsinki, and was approved by the Ethics Committee of The First Affiliated Hospital of Army Medical University (2018077).

TABLE 1 | The primer sequences utilized in this study for RT-qPCR.

Names	Sequences (5′-3′)
PRKAG2-AS1: F	ACTCCAGTTCGAGAAGCCATGC
PRKAG2-AS1: R	CGGAGATCAGCGTTGCAACT
miR-502-3p: F	ACACTCCAGCTGGGAATGCACCTGGGCAAGG
miR-502-3p: R	CTCAACTGGTGTCGTGGA
BICD2: F	CGGAGCGCGAACAGAAGAA
BICD2: R	CAGCATCGTCACTGAACTTGA
GAPDH: F	CGCTCTCTGCTCCTCCTGTTC
GAPDH: R	ATCCGTTGACTCCGACCTTCAC
U6: F	CTCGCTTCGGCAGCACA
U6: R	AACGCTTCACGAATTTGCGT

Cell Culture

Human normal hepatocyte cell line LO2 and HCC cell lines Huh7, HepG2, HCCLM3, and PLC5 were purchased from the Cell Bank of Type Culture Collection of Chinese Academy of Sciences (Shanghai, China). They were grown in DMEM (Gibco, USA) plus 10% FBS in a humidified atmosphere with 5% CO_2 at 37°C.

Real-Time Quantitative Polymerase Chain Reaction (RT-qPCR)

Total RNA extraction from tissue specimens or cells was presented utilizing TRIzol reagent (Invitrogen, Carlsbad, California, USA), which was reverse-transcribed into cDNA through the PrimeScript RT reagent kit with gDNA Eraser (Invitrogen). RT-qPCR was performed via the ABI 7500 Fast RT-PCR platform. Using the $2^{-\Delta\Delta Ct}$ method, the relative expression levels of PRKAG2-AS1, miR-502-3p and BICD2 were determined based on the normalization by GAPDH or U6. **Table 1** listed the primer sequences.

Plasmids and Transfection

HCCLM3 and PLC5 cells were transfected by short-hairpin (shRNA) targeting PRKAG2-AS1 (GenePharma, Shanghai, China) as well as non-targeting negative control (NC) plasmids (sh-NC) via lentivectors. The shRNA sequences targeting PRKAG2-AS1 were as follows: sh-1, 5′-ACGAGAATATCA TTCAATCTT-3′; sh-2, 5′-TGGTAATGCAGCTTTTCAGTT-3′. miR-502-3p mimics and NC were purchased from Thermo Fisher Scientific (China) Co., Ltd. (Shanghai, China), which

Abbreviations: lncRNAs, long non-coding RNAs; HCC, hepatocellular carcinoma; OS, overall survival; DFS, disease-free survival; ncRNAs, non-coding RNAs; GEO, gene expression omnibus; FDR, false discovery rate; FC, fold change; RT-qPCR, real-time quantitative polymerase chain reaction; NC, negative control; CCK-8, cell counting kit-8; EdU, ethynyl deoxyuridine; RIP, RNA immunoprecipitation; ROCs, receiver operating characteristic curves; TCGA, the cancer genome atlas.

were transfected into HCC cells through Lipofectamine 2000 (12566014; Invitrogen, Carlsbad, California, USA) in line with the supplier's specification.

Cell Counting Kit-8 (CCK-8)

CCK-8 kit (CK04; Dojindo, Japan) was utilized for determination of proliferation of HCCLM3 and PLC5 cells. Briefly, cell suspension was seeded to 96-well plates (100 μL/well). The cells were pre-cultured until the cells grown adherently. Then, 10 μL CCK-8 solution was added to each well. Following being incubated for 2 h, absorbance values at 450 nm were determined with a microplate reader at 48, 72, and 96 h.

Colony Formation Assay

Forty-Eight hour following transfection, HCCLM3 and PLC5 cell suspension was inoculated in 6-well plates (1×10^3/well) with culture medium lasting 2 weeks. The supernatant was then discarded. Four percentage paraformaldehyde (158127; Sigma, USA) was utilized to fix cell clones lasting 30 min at room temperature. Afterwards, 0.5% crystal violet (Solarbio, Beijing, China) was used to stain the samples lasting 30 min.

Ethynyl Deoxyuridine (EdU) Incorporation Assay

Cell Proliferation EdU Image Kit (KTA2031; AmyJet Scientific, Wuhan, China) was used for examining the proliferative ability of transfected HCCLM3 and PLC5 cells. Cell suspensions were seeded onto 96-well plates (1×10^3/well). Then, 100 μL 50 μM EdU was added to each well and incubated for 2 h. Cells were fixed by 4% paraformaldehyde (50 μL) for 30 min at room temperature. To neutralize paraformaldehyde, 50 μL 2 mg/mL glycine was added to each well and cultured for 5 min. Afterwards, each well was incubated with 100 μL 0.5% TritonX-100 in PBS for 10 min in order to enhance the permeability of cell membranes. The samples were stained with DAPI dihydrochloride for 5 min. Finally, the images were acquired under a fluorescence microscope (Olympus, Japan).

Animal Experiment

Twelve BALB/c nude mice aged 4-6 weeks with a body weight of 18–22 g were randomly divided into sh-NC and sh-1 groups. 0.1 mL sh-NC- or sh-1-transfected HCCLM3 cell suspension (1×10^8/mL) was inoculated subcutaneously on the dorsal side of the right hind limb of nude mice. After 28 days, the nude mice were euthanized. The subcutaneous tumor was completely peeled off, and the tumor was weighed. This animal experiment gained the approval of the Animal Ethics Committee of The First Affiliated Hospital of Army Medical University (2018077).

Wound Healing

Migrated capacity of HCCLM3 and PLC5 cells was assessed via wound healing assay. Firstly, a marker pen was utilized to draw a straight line on the back of 6-well plates. The transfected cells were seeded in the 6-well plates and cultured until confluence was up to 70%. Then, two parallel lines were drawn with a 10 μl pipette tip perpendicular to the marking line. After washing away the scratched cells with PBS, the medium was added to each well. At 0 and 48 h, the images were photographed under an inverted microscope.

Transwell Assay

Transwell assay was carried out for assessment of invasive capacities of HCCLM3 and PLC5 cells. Briefly, Matrigel (Corning, Shanghai, China) that was diluted with serum-free DMEM was used to coat the upper chambers of transwell insert. 1×10^5 transfected HCCLM3 and PLC5 cells were seeded onto the upper chambers. Moreover, 600 μl DMEM was added to the lower chambers. Following 24 h, 4% paraformaldehyde was used to fix cells. Methanol was added to permeabilize cells. The cells in the upper chambers were then removed. The cells in the lower chambers were stained with 0.3% crystal violet dye. Under a light microscope (×200), the results were acquired and the number of invasive cells were counted.

Western Blot

Transfected HCCLM3 and PLC5 cells were lysed utilizing RIPA buffer (Beyotime, Shanghai, China). The quality of protein samples was assessed via BCA method. Then, the samples were separated by SDS–PAGE, followed by being transferred to PVDF membranes. The membranes were blocked with 5% skimmed milk powder blocking solution at room temperature for 2 h. Afterwards, the membranes were incubated with primary antibodies against E-cadherin (1:10000; ab40772, Abcam, USA) N-cadherin (1:1000; ab76057, Abcam), vimentin (1:1000; 741, Cell Signaling Technology, USA), BICD2 (1:1000; ab237616, Abcam), and GAPDH (1:1000; ab181602, Abcam) overnight at 4°C, followed by being incubated with HRP-conjugated secondary antibodies (1:1000; ab7097, Abcam) at room temperature lasting 2 h. Enhanced chemiluminescence kit (Beyotime) was used for visualizing the protein bands. The grayscale density was measured by ImageJ software.

Extraction of Nuclear and Cytoplasmic RNAs

Nuclear and cytoplasmic RNAs were isolated from HCCLM3 and PLC5 cells utilizing the PARIS kit (Invitrogen) in line with the supplier's specification. PRKAG2-AS1 expression was detected by RT-qPCR.

Luciferase Reporter Assay

Fragments of PRKAG2-AS1 that contained the predicted miR-502-3p binding sites were amplified using PCR, which were used for forming the reporter vector PRKAG2-AS1-wild-type (PRKAG2-AS1-wt). The putative binding sites of miR-502-3p in the PRKAG2-AS1 were mutated, called as PRKAG2-AS1-mutated-type (PRKAG2-AS1-MuT). Meanwhile, 3′-UTR of BICD2 was amplified using PCR and reporter vector BICD2-wt was constructed. BICD2-MuT was then formed. Then, miR-502-3p mimics or inhibitors were transfected into HCCLM3 and PLC5 cells via Lipofectamine 2000 reagent (Invitrogen). Finally, the luciferase activity was measured through the Dual-Luciferase Reporter Assay (GenePharma, Shanghai, China).

RNA Immunoprecipitation (RIP)

The relationships between PRKAG2-AS1, miR-502-3p and Ago2 were detected using RIP kits (Millipore, USA). The HCCLM3 and PLC5 cells were lysed with RIPA lysis buffer lasting 5 min. After being resuspended with RIP wash buffer, beads were incubated with 5 μg antibodies against Ago2 (1:50, ab156870; Abcam) and IgG (1:100, ab133470; Abcam) for binding. Then, following being

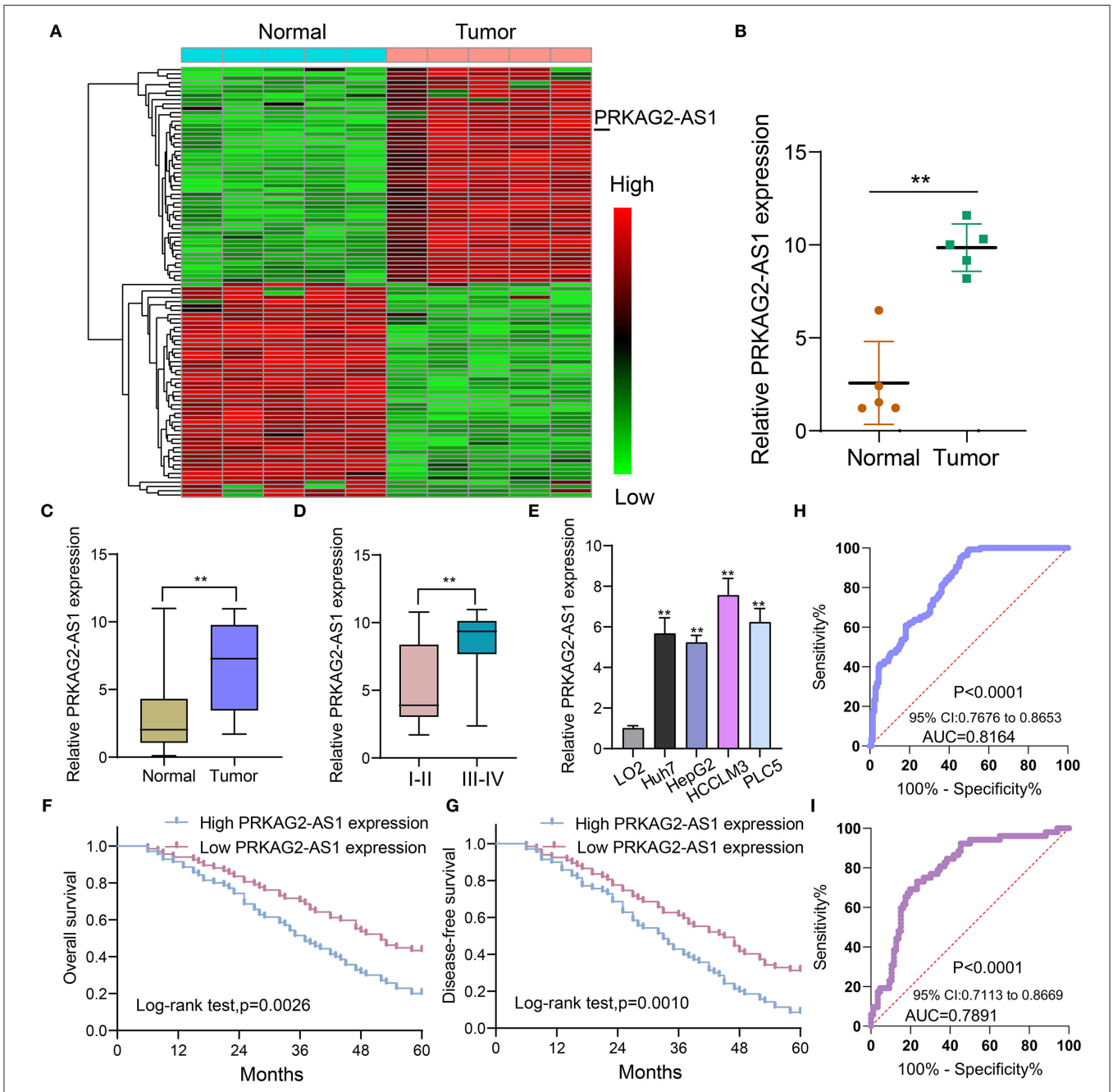

FIGURE 1 | Antisense lncRNA PRKAG2-AS1 is up-regulated both in HCC tissues and cells and could predict clinical outcomes of patients. **(A)** Heat map for dysregulated expressed lncRNAs between HCC and normal tissue specimens from the GEO database. Red: up-regulation and green: down-regulation. **(B)** According to microarray results, PRKAG2-AS1 expression was visualized between HCC and normal tissue specimens. **(C)** RT-qPCR confirming the up-regulation of PRKAG2-AS1 in HCC than normal tissue specimens in an HCC cohort ($n = 138$). **(D)** Violin diagram for the differences in PRKAG2-AS1 expression between stage I-II and III-IV HCC patients. **(E)** RT-qPCR examining PRKAG2-AS1 expression in normal liver cells (LO2) and four kinds of HCC cells (Huh7, HepG2, HCCLM3, and PLC5). **(F,G)** Kaplan-Meier curves for OS and DFS among HCC patients, assessed by log-rank test. **(H,I)** ROCs for OS and DFS based on PRKAG2-AS1 expression. $^{**}p < 0.01$.

TABLE 2 | Association of PRKAG2-AS1 expression with clinicopathological characteristics of HCC patients.

Parameters	Group	Total	PRKAG2-AS1 expression		*P*-value
			High	Low	
Gender	Male	79	38	41	0.476
	Female	59	32	27	
Age (years)	<60	71	33	38	0.304
	≥60	67	37	30	
Tumor size (cm)	<5	77	36	41	0.294
	≥5	61	34	27	
Tumor number	Solitary	64	31	33	0.617
	Multiple	74	39	35	
HBsAg	Positive	92	47	45	0.904
	Negative	46	23	23	
Tumor differentiation	Well/moderate	85	38	47	0.073
	Poor	53	32	21	
Lymph node metastasis	Absence	94	41	53	0.015
	Presence	44	29	15	
Clinical stage	I-II	86	36	50	0.007
	III-IV	52	34	18	

resuspended, the magnetic bead-antibody complexes were harvested on a magnetic base. The samples and inputs were digested using proteinase K. Extracted RNA was detected using RT-qPCR.

RNA Pull-Down

HCCLM3 and PLC5 cells were transfected with 50 nM biotinylated PRKAG2-AS1-wt and PRKAG2-AS1-MuT (GenePharma). Following 48 h, the harvested cells were lysed, which were incubated overnight at 4 °C with beads (Sigma, USA). At last, the bound RNAs were purified through Trizol reagent. The enrichment of miR-502-3p was measured via RT-qPCR.

Statistical Analysis

One hundred thirty-eight HCC patients were separated into high and low PRKAG2-AS1 expression groups in line with its median value. To evaluate the prognostic value of PRKAG2-AS1, Kaplan-Meier curves were depicted for overall survival (OS) and disease-free survival (DFS). The associations of PRKAG2-AS1 expression with clinicopathological characteristics were determined via Chi-square test. Receiver operating characteristic curves (ROCs) for OS and DFS were presented to assess whether PRKAG2-AS1 expression accurately and sensitively predicted the clinical outcomes. Multivariate analyses were presented to assess the association of PRKAG2-AS1 expression and clinicopathological characteristics with OS and DFS by Cox regression model. Form the Cancer Genome Atlas (TCGA), the expression and clinical implications of BICD2 were analyzed in HCC. $P < 0.05$ was considered statistically significant.

RESULTS

Antisense lncRNA PRKAG2-AS1, as a Prognostic Factor, Is Up-Regulated in HCC Tissues and Cells

Herein, we analyzed dysregulated lncRNAs between 5 pairs of HCC and normal tissue specimens from the GEO database (**Figure 1A**). Among all differentially expressed lncRNAs, a novel antisense lncRNA PRKAG2-AS1 caught our attention. It was significantly up-regulated in HCC than normal tissue specimens (**Figure 1B**). We further expanded the sample size to verify its expression. In a cohort of 138 HCC patients, its up-regulation was detected in HCC than normal tissue specimens, which was consistent with microarray consequences (**Figure 1C**). Moreover, we compared the differences in its expression between stage I–II and III–IV. As shown in **Figure 1D**, higher expression of PRKAG2-AS1 was found in stage III-IV than I-II, indicating that PRKAG2-AS1 might be correlated to HCC progression. We also examined PRKAG2-AS1 expression in different kinds of HCC cell lines. Compared to LO2 normal liver cells, its higher expression was detected in Huh7, HepG2, HCCLM3 and PLC5 HCC cell lines (**Figure 1E**). Association of PRKAG2-AS1 expression with clinicopathological characteristics of HCC patients was further analyzed in our cohort. In **Table 2**, PRKAG2-AS1 expression was distinctly correlated to lymph node metastasis ($p = 0.015$) and stage ($p = 0.007$). Also, patients with high PRKAG2-AS1 expression usually experienced shorter OS time ($p = 0.0026$; **Figure 1F**) and DFS time ($p = 0.0010$; **Figure 1G**). To further verify the predictive performance of PRKAG2-AS1 expression, we conducted ROCs for OS and DFS. The data suggested that the area under the curves (AUCs) for OS and DFS were 0.8164 (**Figure 1H**) and 0.7891 (**Figure 1I**), respectively. Multivariate analyses revealed that

TABLE 3 | Multivariate analyses for overall survival and disease-free survival by Cox regression model.

Variable	Overall survival			Disease-free survival		
	HR	95% CI	*P*	HR	95% CI	*P*
Gender	1.453	0.678–1.932	0.323	1.378	0.785–2.221	0.213
Age	1.132	0.564–1.893	0.233	1.324	0.656–2.341	0.159
Tumor size	1.455	0.832–2.438	0.132	1.665	0.986–2.513	0.091
Tumor number	1.376	0.683–1.982	0.345	1.469	0.773–2.158	0.243
HBsAg	0.867	0.472–1.475	0.562	0.943	0.656–1.883	0.676
Tumor differentiation	1.447	0.956–2.218	0.091	1.554	1.038–2.145	0.086
Lymph node metastasis	3.362	1.348-5.672	0.001	3.672	1.554-6.329	0.001
Clinical stage	2.867	1.286-4.879	0.012	3.018	1.345-5.334	0.007
PRKAG2-AS1 expression	2.955	1.211-4.675	0.015	3.118	1.345-5.122	0.009

PRKAG2-AS1 expression could independently predict OS (HR: 2.955; 95%CI: 1.211–4.675; $p = 0.015$) and DFS (HR: 3.118; 95%CI: 1.345–5.122; $p = 0.009$) for HCC patients (**Table 3**). Hence, PRKAG2-AS1 could be a robust prognostic factor for HCC.

Targeting PRKAG2-AS1 Suppresses Proliferative Ability of Hcc Cells

The roles of PRKAG2-AS1 on malignant behaviors of HCC cells were investigated in depth. Two shRNAs targeting PRKAG2-AS1 were transfected into HCCLM3 and PLC5 cells. RT-qPCR confirmed that PRKAG2-AS1 expression was stably silenced (**Figure 2A**). As shown in CCK-8 results, PRKAG2-AS1 knockdown distinctly slowed down the proliferation of HCCLM3 and PLC5 cells (**Figure 2B**). Moreover, clone formation assay demonstrated that, compared to sh-NC group, the number of clones of HCC cells was significantly lessened following silencing PRKAG2-AS1 (**Figure 2C**). EdU staining results also confirmed that the proliferative ability of HCCLM3 and PLC5 cells was markedly restrained by PRKAG2-AS1 knockdown in **Figure 2D**. Collectively, targeting PRKAG2-AS1 may suppress proliferation of HCC cells.

Silencing PRKAG2-AS1 Suppresses Tumor Growth

Nude mouse tumorigenicity assay was presented by inoculating HCCLM3 cells transfected with sh-NC or sh-1 targeting PRKAG2-AS1 (**Figure 3A**). After 28 days, we removed the tumors of two groups. In **Figure 3B**, tumor volume was distinctly decreased in sh-1 group than sh-NC group. The growth curves of tumor volume were depicted, as shown in **Figure 3C**. The tumor growth was distinctly suppressed by sh-1 targeting PRKAG2-AS1. We also measured the tumor weights of tumors in two groups. Lower tumor weights were detected after silencing PRKAG2-AS1 (**Figure 3D**).

Targeting PRKAG2-AS1 Inhibits Migration and Invasion of HCC Cells

The migrated and invasive capacities of HCC were further assessed following transfection with PRKAG2-AS1 shRNAs. In **Figure 4A**, compared to sh-NC group, wound distance was significantly wider in HCCLM3 and PLC5 cells with PRKAG2-AS1 knockdown. Furthermore, transwell assay was presented to evaluate the invasive ability of transfected HCC cells. The data showed that the number of invasive cells was distinctly decreased following transfection with PRKAG2-AS1 shRNAs (**Figure 4B**). Western blot was used for evaluation of the expression of epithelial-to-mesenchymal transition (EMT)-related proteins in HCC cells. In **Figure 4C**, E-cadherin expression was markedly increased in HCCLM3 and PLC5 cells with PRKAG2-AS1 knockdown. Meanwhile. N-cadherin and Vimentin expression was both decreased in the two HCC cells transfected with PRKAG2-AS1 shRNAs. Taken together, targeting PRKAG2-AS1 inhibited migration, invasion and EMT process of HCC cells.

LncRNA PRKAG2-AS1 Can Bind to miR-502-3p

We firstly detected the cellular distribution of PRKAG2-AS1 in HCCLM3 and PLC5 cells. In **Figure 5A**, PRKAG2-AS1 was mainly expressed in cytoplasm. Based on the DIANA-LncBase v2 database (http://www.microrna.gr/LncBase) (17), there was a binding region between PRKAG2-AS1 and miR-502-3p (**Figure 5B**). Luciferase reporter assay results confirmed that PRKAG2-AS1 directly bound to the predicted region of miR-502-3p. As shown in **Figure 5C**, when transfection with miR-502-3p mimics, the relative luciferase activity was distinctly decreased in HCC cells transfected with PRKAG2-AS1-WT not PRKAG2-AS1-MuT. The RIP results demonstrated the binding of PRKAG2-AS1 to Ago2 (**Figure 5D**). Moreover, RNA pull-down confirmed that more miR-502-3p was enriched in HCC cells with RKAG2-AS1-WT than those with PRKAG2-AS1-MuT (**Figure 5E**). After silencing PRKAG2-AS1, miR-502-3p expression was markedly decreased in two HCC cells (**Figure 5F**). Additionally, in HCC cells transfected with miR-502-3p inhibitors, PRKAG2-AS1 expression was distinctly elevated (**Figure 5G**). On the contrary, its expression was significantly reduced when transfection with miR-502-3p mimics. These findings revealed that PRKAG2-AS1 can bind to miR-502-3p.

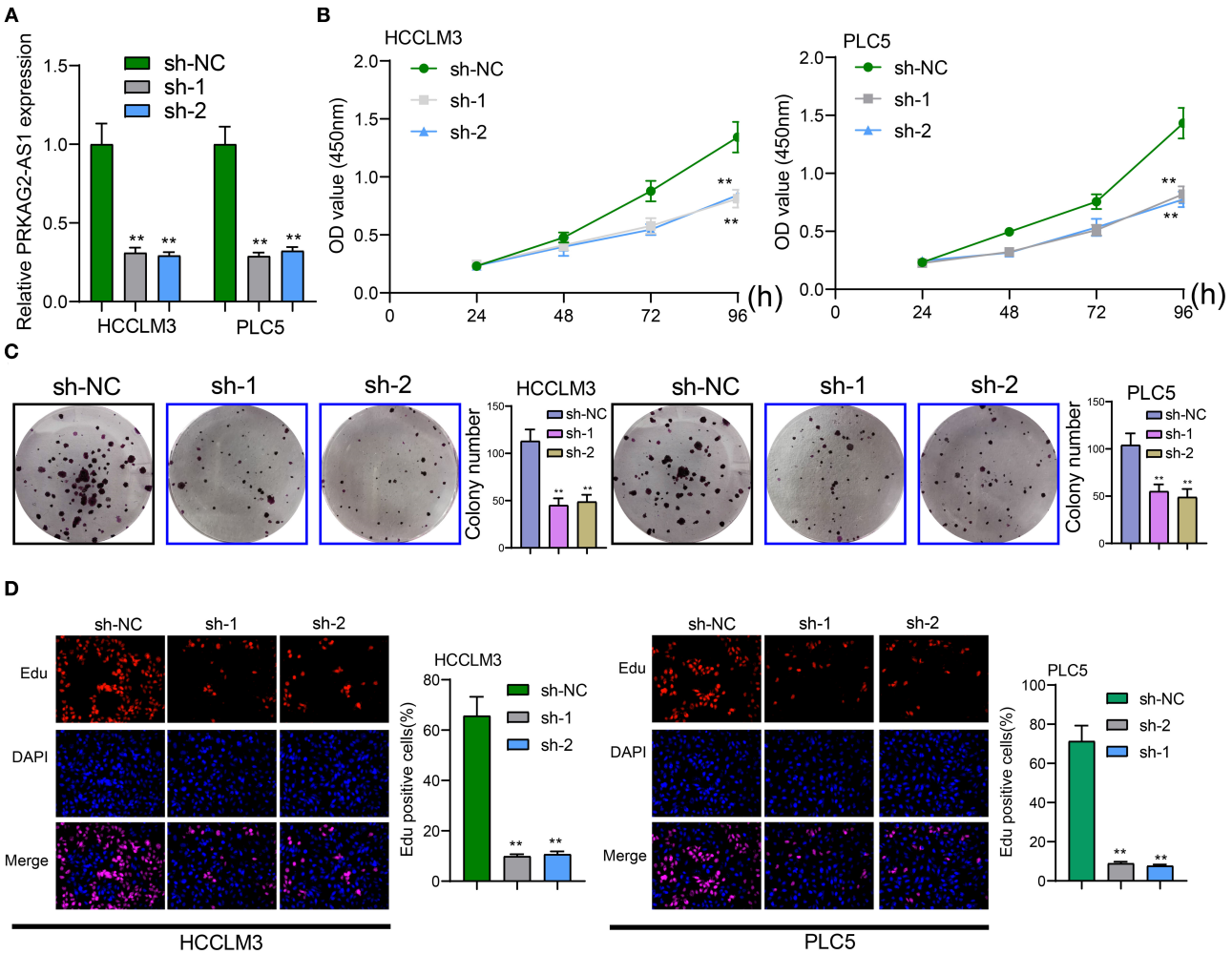

FIGURE 2 | Targeting PRKAG2-AS1 inhibits proliferative capacity of HCC cells. **(A)** RT-qPCR confirmed the successful suppression of PRKAG2-AS1 expression by two shRNAs. **(B)** CCK-8 for examining the relative cell viability of HCC cells after transfection with shRNAs for 48, 72, and 96 h. **(C)** The colony formation was evaluated for HCCLM3 and PLC5 cells with PRKAG2-AS1 knockdown. **(D)** Representative images of EdU staining for HCC cells with PRKAG2-AS1 knockdown. $^{**}p < 0.01$.

BICD2, as a Prognostic Factor for HCC, Is a Potential Target of miR-502-3p

From the starbase database (http://starbase.sysu.edu.cn/) (18), there was a binding site between miR-502-3p and BICD2 (**Figure 6A**), indicating that BICD2 could be a potential target of miR-502-3p. In TCGA database, we analyzed the clinical implications of BICD2 expression in HCC. In **Figure 6B**, BICD2 was significantly up-regulated in HCC than normal tissue specimens. Moreover, patients with nodal metastasis showed higher BICD2 expression compared to those without nodal metastasis (**Figure 6C**). As depicted in **Figure 6D**, there was a distinct difference in BICD2 expression among different stages. Patients with high BICD2 expression was indicative of poorer DFS ($p = 0.0026$) and OS ($p = 0.027$) in comparison to those with its low expression (**Figure 6E**). These data demonstrated that BICD2 was an underlying prognostic marker for HCC. The luciferase reporter assay results confirmed the direct relationship between BICD2 and miR-502-3p (**Figure 6F**). miR-502-3p mimics markedly reduced BICD2 expression in HCCLM3 and PLC5 cells (**Figure 6G**). Furthermore, PRKAG2-AS1 knockdown distinctly lowered BICD2 expression (**Figure 6H**). However, miR-502-3p inhibitors ameliorated the decrease in BICD2 expression in HCC cells. Thus, PRKAG2-AS1 could mediate miR-502-3p/BICD2 axis in HCC.

DISCUSSION

HCC is a commonly diagnosed malignancy of the digestive system (19–21). Its pathogenesis involves in complex multiple factors and steps (22). There is still no curative treatment targeting HCC (23). Hence, it is of clinical significance to probe promising therapeutic targets. Herein, this study identified a novel antisense lncRNA PRKAG2-AS1, which could robustly predict unfavorable prognosis. Targeting PRKAG2-AS1 could

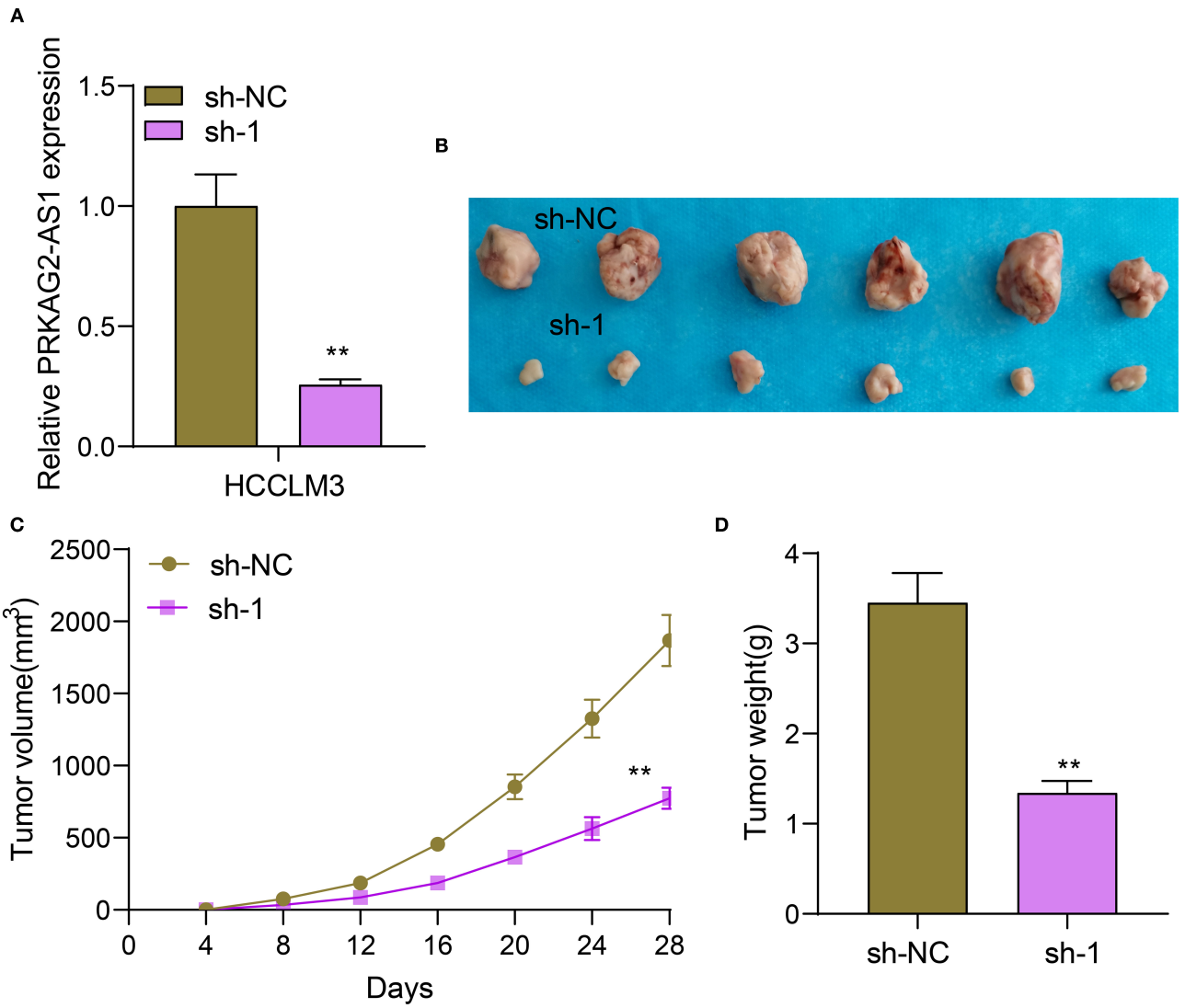

FIGURE 3 | Silencing PRKAG2-AS1 suppresses tumor growth. **(A)** RT-qPCR for the expression of PRKAG2-AS1 in HCCLM3 cells transfected with sh-NC and sh-1 targeting PRKAG2-AS1. **(B)** Tumor images from nude mice inoculated with HCCLM3 cells transfected with sh-NC and sh-1. **(C)** The tumor growth curves. **(D)** Measurement of the tumor weights. $^{**}p < 0.01$.

suppress malignant behaviors. In consequence, this novel could be a prospective therapeutic target for HCC.

Up-regulation of PRKAG2-AS1 was detected in HCC than normal tissue specimens. As previous studies, this lncRNA could be overexpressed in colon adenocarcinoma (13), advanced prostate cancer (14) and esophageal squamous cell carcinoma (15). Our data suggested that PRKAG2-AS1 up-regulation was suggestive of poor OS and DFS. As confirmed by ROCs, PRKAG2-AS1 expression accurately and sensitively predicted clinical outcomes of HCC patients. Also, its expression was markedly correlated to lymph node metastasis and stage. As validated by multivariate analyses, PRKAG2-AS1 expression could independently predict OS and DFS. Thus, PRKAG2-AS1 could be a promising prognostic factor for HCC. Previously, PRKAG2-AS1 has been identified as a prognostic marker for colon adenocarcinoma (13), advanced prostate cancer (14) and esophageal squamous cell carcinoma (15).

Our further analyses revealed that targeting PRKAG2-AS1 distinctly suppressed malignant biological behaviors including proliferation, migration, as well as invasion. Epithelial-to-mesenchymal transition (EMT) is involved in invasion and metastasis in various cancers (24). Numerous studies have verified its key role in HCC development. For example, Wang et al. found that lncRNA CASC2 may suppress EMT process of HCC cells via CASC2/miR-367/FBXW7 axis (25). Our data suggested that targeting PRKAG2-AS1

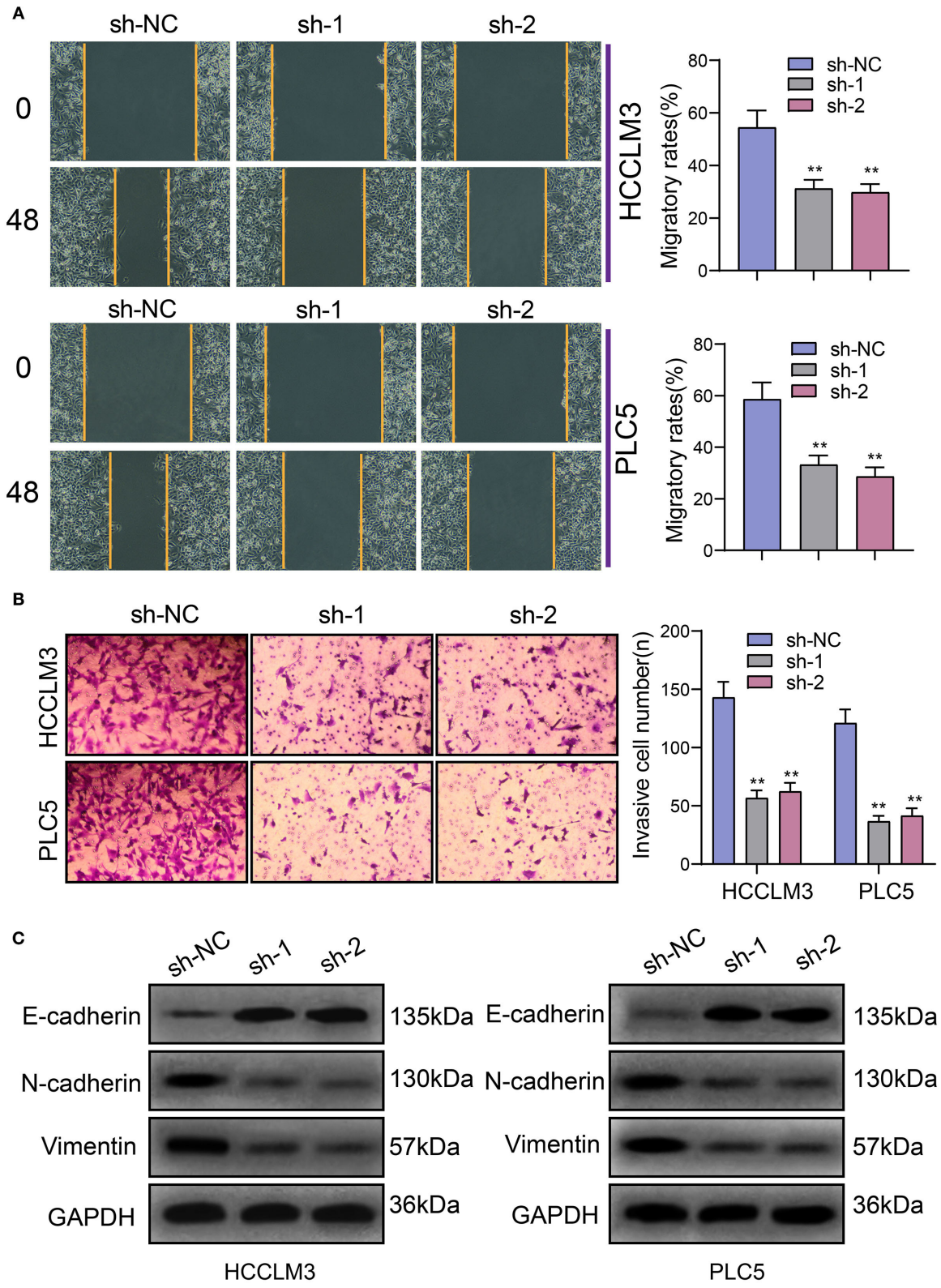

FIGURE 4 | Targeting PRKAG2-AS1 inhibits migration, invasion, and EMT process of HCC cells. **(A)** Wound healing assay for assessment of the migrated capacity of HCCLM3 and PLC5 cells transfected with PRKAG2-AS1 shRNAs. **(B)** Transwell assay for examining the number of invasive cells after PRKAG2-AS1 knockdown. **(C)** Western blot for measuring the expression of EMT-related proteins including E-cadherin, N-cadherin, and Vimentin in HCC cells transfected with PRKAG2-AS1 shRNAs or sh-NC. $^{**}p < 0.01$.

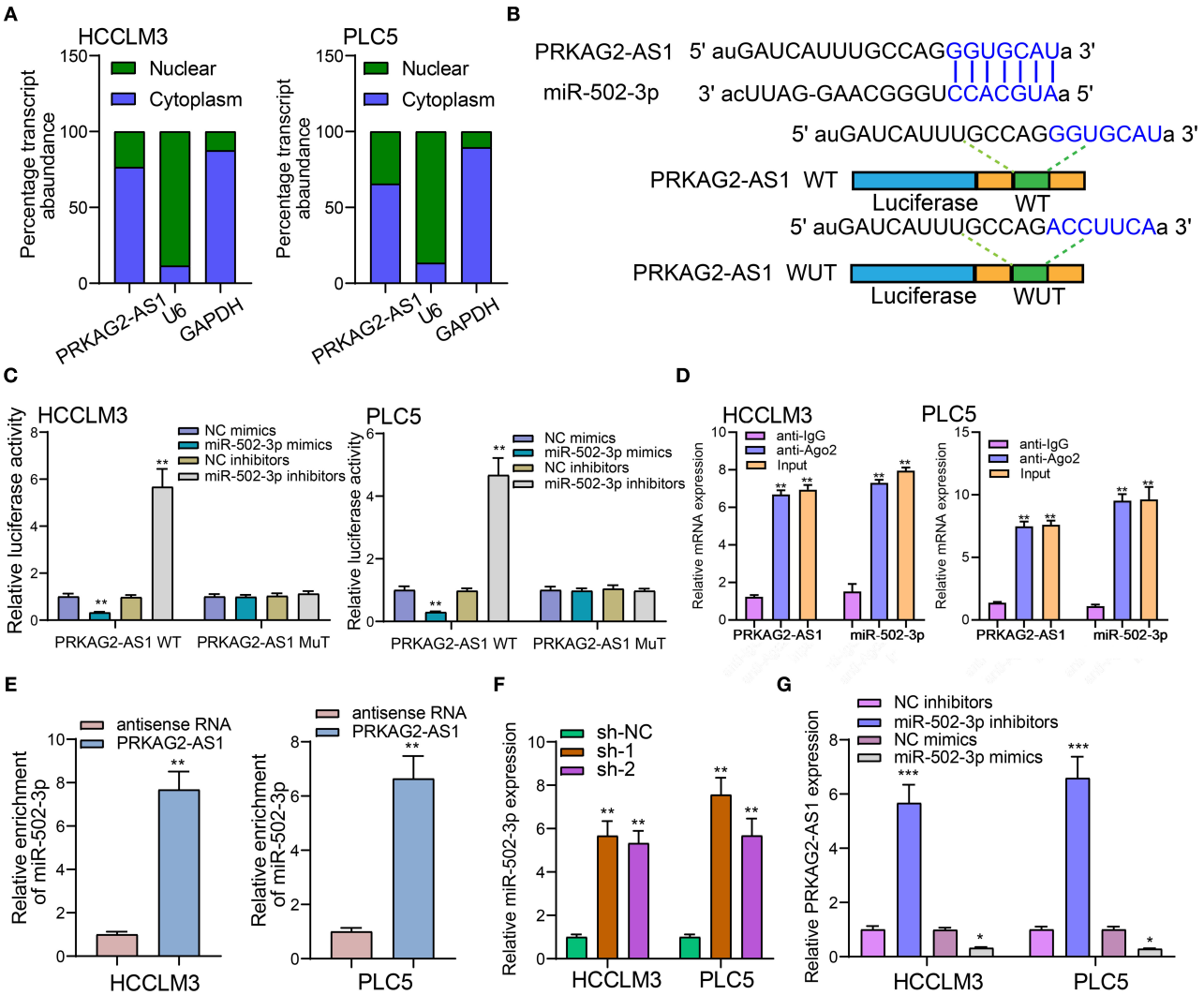

FIGURE 5 | LncRNA PRKAG2-AS1 can bind to miR-502-3p. **(A)** The cellular distribution of PRKAG2-AS1 expression. U6 as a control of nuclear and GAPDH as a control of cytoplasm. **(B)** The schematic diagram of the binding sites between PRKAG2-AS1 and miR-502-3p. **(C)** The luciferase reporter assay results confirming the direct binding relationship between PRKAG2-AS1 and miR-502-3p. **(D)** RIP results for the binding of PRKAG2-AS1 to Ago2. **(E)** RNA pull-down for the enrichment levels of miR-502-3p in HCC cells transfected with PRKAG2-AS1-WT and PRKAG2-AS1-MuT. **(F)** RT-qPCR for detection of miR-502-3p expression in HCC cells with PRKAG2-AS1 knockdown. **(G)** RT-qPCR examining PRKAG2-AS1 expression in HCC cells transfected with miR-502-3p mimics or inhibitors. $^{*}p < 0.05$; $^{**}p < 0.01$; $^{***}p < 0.001$.

elevated E-cadherin expression, while lowered N-cadherin and Vimentin expression in HCC cells, thereby inactivating EMT process. Numerous up-regulated lncRNAs have been found to facilitate malignant biological behaviors, such as lncRNA-BC200 (26), lncRNA FAL1 (27), lncRNA SNHG7 (28), and the like.

PRKAG2-AS1 was mainly distributed in the cytoplasm of HCC cells. After validation by luciferase reporter, RIP and RNA pull-down assays, PRKAG2-AS1 can directly bind to miR-502-3p. There were mutual regulatory relationships between the two. miR-502-3p down-regulation has been found in various cancers. For example, its down-regulation could facilitate proliferative and migrated capacities of gallbladder cancer cells (29). Low miR-502-3p expression accelerates proliferation as well as migration for gastric cancer cells via NRAS/MEK1/ERK1/2 axis (30). Here, our study identified that PRKAG2-AS1 was a sponge of miR-502-3p, thereby promoting HCC progression. By verification of luciferase reporter assay, BICD2 was a downstream target of miR-502-3p. It was up-regulated in HCC than normal tissues and was associated with nodal metastasis, stage, and clinical outcomes. Hence, BICD2 could be a promising prognostic marker for HCC. BICD2 suppressed by miR-340 is up-regulated in pancreatic cancer (31). It can also enhance vinorelbine-mediated mitotic arrest in non-small-cell lung cancer cells

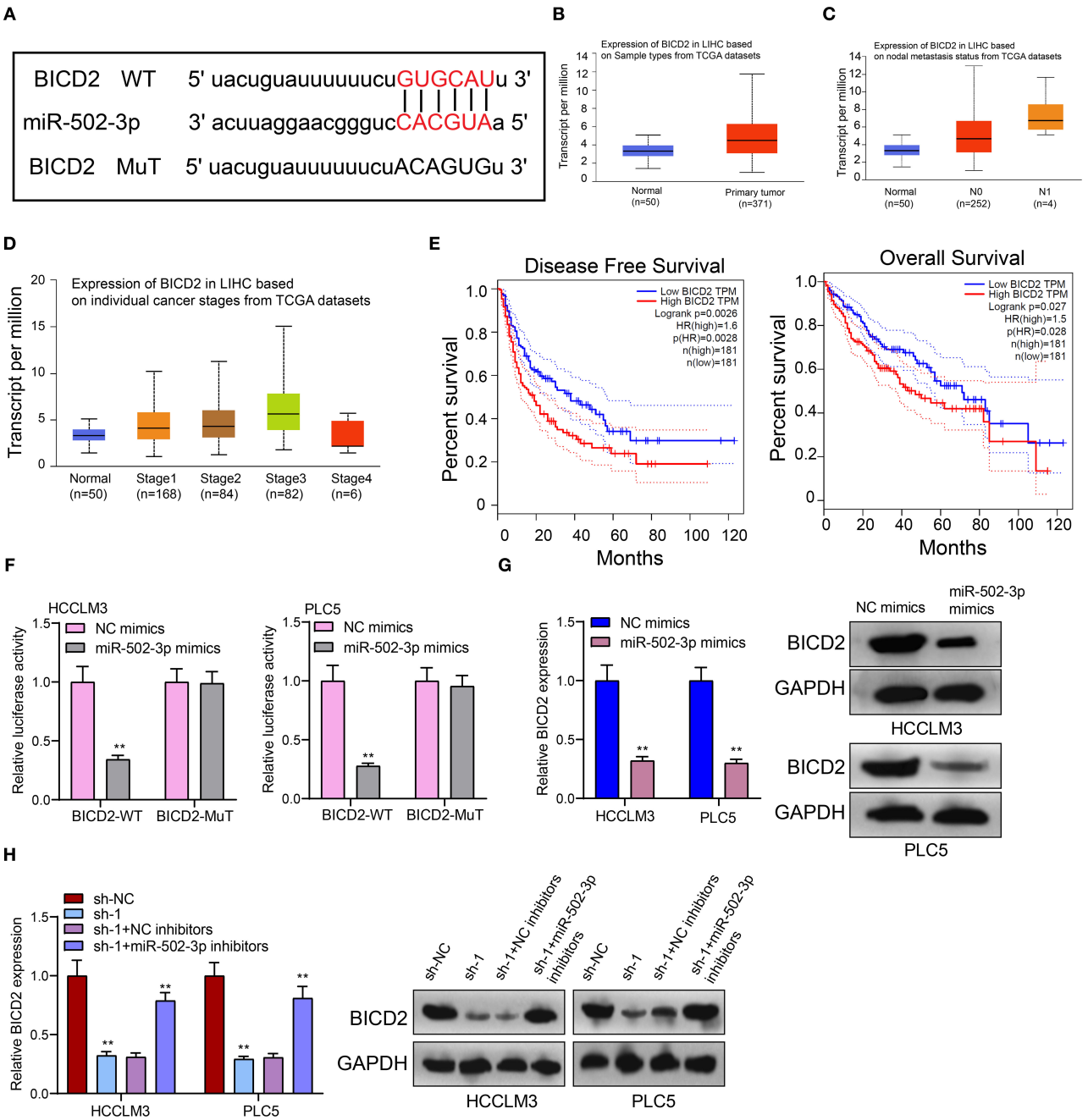

FIGURE 6 | BICD2 is a prognostic factor for HCC and is a potential target of miR-502-3p. **(A)** The schematic diagram of the binding sites between BICD2 and miR-502-3p. **(B)** Box plots for the expression of BICD2 in HCC and normal samples from TCGA database. **(C)** The differences in BICD2 expression in HCC patients with or without nodal metastasis. **(D)** The expression of BICD2 among different stages. **(E)** Kaplan-Meier curves for DFS and OS between high and low BICD2 expression among HCC patients. **(F)** The luciferase reporter assay for the direct relationship between BICD2 and miR-502-3p. **(G)** Western blot for BICD2 expression in HCC cells with miR-502-3p mimics or NC. **(H)** Western blot for BICD2 expression in HCC cells with PRKAG2-AS1 shRNA and/or miR-502-3p inhibitors. $^{**}p < 0.01$.

(32). miR-502-3p mimics could lower BICD2 expression. Furthermore, miR-502-3p inhibitors ameliorated the decrease in BICD2 expression induced by PRKAG2-AS1 knockdown. Therefore, PRKAG2-AS1 could mediate miR-502-3p / BICD2 axis in HCC.

CONCLUSION

Collectively, our study identified a novel antisense up-regulated lncRNA PRKAG2-AS1 for HCC. The up-regulation independently predicted worse clinical outcomes of patients.

Targeting PRKAG2-AS1 may restrain malignant behaviors. In terms of mechanism, PRKAG2-AS1 could mediate miR-502-3p / BICD2 axis, thereby facilitating the progression of HCC. Hence, PRKAG2-AS1 could be a possible therapeutic target for HCC.

DATA AVAILABILITY STATEMENT

The datasets presented in this study can be found in online repositories. The names of the repository/repositories and accession number(s) can be found in the article/**Supplementary Material**.

ETHICS STATEMENT

The studies involving human participants were reviewed and approved by The Ethics Committee of The First Affiliated Hospital of Army Medical University (2018077). The patients/participants provided their written informed consent to participate in this study.

AUTHOR CONTRIBUTIONS

PH conceived and designed the study. YO and YD conducted most of the experiments and data analysis, and wrote the manuscript. HW, QZ, and HL participated in collecting data and helped to draft the manuscript. All authors reviewed and approved the manuscript.

FUNDING

This work was funded by National Natural Science Foundation of China (81972760); Key Project of Chongqing (cstc2018jscx-mszdX0016).

SUPPLEMENTARY MATERIAL

The Supplementary Material for this article can be found online at: https://www.frontiersin.org/articles/10.3389/fmed.2021.649279/full#supplementary-material

REFERENCES

1. Bray F, Ferlay J, Soerjomataram I, Siegel RL, Torre LA, Jemal A. Global cancer statistics 2018: GLOBOCAN estimates of incidence and mortality worldwide for 36 cancers in 185 countries. *CA Cancer J. Clin*. (2018) 68:394–424. doi: 10.3322/caac.21492
2. Xu W, Li K, Song C, Wang X, Li Y, Xu B, et al. Knockdown of lncRNA LINC01234 suppresses the tumorigenesis of liver cancer via sponging miR-513a-5p. *Front. Oncol*. (2020) 10:571565. doi: 10.3389/fonc.2020.571565
3. Li C, Wang MD, Lu L, Wu H, Yu JJ, Zhang WG, et al. Preoperative transcatheter arterial chemoembolization for surgical resection of huge hepatocellular carcinoma (≥10 cm): a multicenter propensity matching analysis. *Hepatol. Int*. (2019) 13:736–47. doi: 10.1007/s12072-019-09981-0
4. Greten TF, Lai CW, Li G, Staveley-O'Carroll KF. Targeted and immune-based therapies for hepatocellular carcinoma. *Gastroenterology*. (2019) 156:510–24. doi: 10.1053/j.gastro.2018.09.051
5. Liu Z, Lin Y, Zhang J, Zhang Y, Li Y, Liu Z, et al. Molecular targeted and immune checkpoint therapy for advanced hepatocellular carcinoma. *J. Exp. Clin. Cancer. Res*. (2019) 38:447. doi: 10.1186/s13046-019-1412-8
6. Nakagawa H, Fujita M, Fujimoto A. Genome sequencing analysis of liver cancer for precision medicine. *Semin. Cancer Biol*. (2019) 55:120–7. doi: 10.1016/j.semcancer.2018.03.004
7. Khemlina G, Ikeda S, Kurzrock R. The biology of hepatocellular carcinoma: implications for genomic and immune therapies. *Mol. Cancer*. (2017) 16:149. doi: 10.1186/s12943-017-0712-x
8. Tsagakis I, Douka K, Birds I, Aspden JL. Long non-coding RNAs in development and disease: conservation to mechanisms. *J. Pathol*. (2020) 250:480–95. doi: 10.1002/path.5405
9. Lim LJ, Wong SYS, Huang F, Lim S, Chong SS, Ooi LL, et al. Roles and regulation of long noncoding RNAs in hepatocellular carcinoma. *Cancer Res*. (2019) 79:5131–9. doi: 10.1158/0008-5472.CAN-19-0255
10. Wei L, Wang X, Lv L, Liu J, Xing H, Song Y, et al. The emerging role of microRNAs and long noncoding RNAs in drug resistance of hepatocellular carcinoma. *Mol. Cancer*. (2019) 18:147. doi: 10.1186/s12943-019-1086-z
11. Xia Q, Li Z, Zheng J, Zhang X, Di Y, Ding J, et al. Identification of novel biomarkers for hepatocellular carcinoma using transcriptome analysis. *J. Cell Physiol*. (2019) 234:4851–63. doi: 10.1002/jcp.27283
12. Wang Y, Yang L, Chen T, Liu X, Guo Y, Zhu Q, et al. A novel lncRNA MCM3AP-AS1 promotes the growth of hepatocellular carcinoma by targeting miR-194-5p/FOXA1 axis. *Mol. Cancer*. (2019) 18:28. doi: 10.1186/s12943-019-0957-7
13. Yang H, Lin HC, Liu H, Gan D, Jin W, Cui C, et al. A 6 lncRNA-based risk score system for predicting the recurrence of colon adenocarcinoma patients. *Front. Oncol*. (2020) 10:81. doi: 10.3389/fonc.2020.00081
14. Takayama KI, Fujimura T, Suzuki Y, Inoue S. Identification of long non-coding RNAs in advanced prostate cancer associated with androgen receptor splicing factors. *Commun. Biol*. (2020) 3:393. doi: 10.1038/s42003-020-01120-y
15. Zhang C, Zhang Z, Zhang G, Xue L, Yang H, Luo Y, et al. A three-lncRNA signature of pretreatment biopsies predicts pathological response and outcome in esophageal squamous cell carcinoma with neoadjuvant chemoradiotherapy. *Clin. Transl. Med*. (2020) 10:e156. doi: 10.1002/ctm2.156
16. Ritchie ME, Phipson B, Wu D, Hu Y, Law CW, Shi W, et al. limma powers differential expression analyses for RNA-sequencing and microarray studies. *Nucleic Acids Res*. (2015) 43:e47. doi: 10.1093/nar/gkv007
17. Paraskevopoulou MD, Vlachos IS, Karagkouni D, Georgakilas G, Kanellos I, Vergoulis T, et al. DIANA-LncBase v2: indexing microRNA targets on non-coding transcripts. *Nucleic Acids Res*. (2016) 44:D231–8. doi: 10.1093/nar/gkv1270
18. Li JH, Liu S, Zhou H, Qu LH, Yang JH. starBase v2.0: decoding miRNA-ceRNA, miRNA-ncRNA and protein-RNA interaction networks from large-scale CLIP-Seq data. *Nucleic Acids Res*. (2014) 42:D92–7. doi: 10.1093/nar/gkt1248
19. Ferlay J, Colombet M, Soerjomataram I, Mathers C, Parkin DM, Piñeros M, et al. Estimating the global cancer incidence and mortality in 2018: GLOBOCAN sources and methods. *Int. J. Cancer*. (2019) 144:1941–53. doi: 10.1002/ijc.31937
20. Feng RM, Zong YN, Cao SM, Xu RH. Current cancer situation in China: good or bad news from the 2018 Global Cancer Statistics? *Cancer Commun*. (2019) 39:22. doi: 10.1186/s40880-019-0368-6
21. Anwanwan D, Singh SK, Singh S, Saikam V, Singh R. Challenges in liver cancer and possible treatment approaches. *Biochim. Biophys. Acta Rev. Cancer*. (2020) 1873:188314. doi: 10.1016/j.bbcan.2019.188314
22. Zhang Y, Zhou H. LncRNA BCAR4 promotes liver cancer progression by upregulating ANAPC11 expression through sponging miR-1261. *Int. J. Mol. Med*. (2020) 46:159–66. doi: 10.3892/ijmm.2020.4586
23. Orcutt ST, Anaya DA. Liver resection and surgical strategies for management of primary liver cancer. *Cancer Control*. (2018) 25:1073274817744621. doi: 10.1177/1073274817744621
24. Zhu X, Chen L, Liu L, Niu X. EMT-Mediated acquired EGFR-TKI resistance in NSCLC: mechanisms and strategies. *Front. Oncol*. (2019) 9:1044. doi: 10.3389/fonc.2019.01044

25. Wang Y, Liu Z, Yao B, Li Q, Wang L, Wang C, et al. Long non-coding RNA CASC2 suppresses epithelial-mesenchymal transition of hepatocellular carcinoma cells through CASC2/miR-367/FBXW7 axis. *Mol. Cancer*. (2017) 16:123. doi: 10.1186/s12943-017-0702-z
26. Tan N, Zhu B, Shu H, Tao YF, Wu JR, Fang M, et al. Effect of lncRNA-BC200 on proliferation and migration of liver cancer cells *in vitro* and *in vivo*. *Oncol. Rep*. (2020) 43:461–70. doi: 10.3892/or.2019.7447
27. Li B, Mao R, Liu C, Zhang W, Tang Y, Guo Z. LncRNA FAL1 promotes cell proliferation and migration by acting as a CeRNA of miR-1236 in hepatocellular carcinoma cells. *Life Sci*. (2018) 197:122–9. doi: 10.1016/j.lfs.2018.02.006
28. Shan Y, Ma J, Pan Y, Hu J, Liu B, Jia L. LncRNA SNHG7 sponges miR-216b to promote proliferation and liver metastasis of colorectal cancer through upregulating GALNT1. *Cell Death Dis*. (2018) 9:722. doi: 10.1038/s41419-018-0759-7
29. Hu YP, Jin YP, Wu XS, Yang Y, Li YS, Li HF, et al. LncRNA-HGBC stabilized by HuR promotes gallbladder cancer progression by regulating miR-502-3p/SET/AKT axis. *Mol. Cancer*. (2019) 18:167. doi: 10.1186/s12943-019-1097-9
30. Zhang J, Hou L, Liang R, Chen X, Zhang R, Chen W, et al. CircDLST promotes the tumorigenesis and metastasis of gastric cancer by sponging miR-502-5p and activating the NRAS/MEK1/ERK1/2 signaling. *Mol. Cancer*. (2019) 18:80. doi: 10.1186/s12943-019-1015-1
31. Zhou Y, Li Z, Ding Y, Zhang P, Wang J. MicroRNA-340 suppresses pancreatic cancer growth by targeting BICD2. *Pancreatology*. (2019). doi: 10.1016/j.pan.2019.05.453. [Epub ahead of print].
32. Li H, Sun L, Li H, Lv X, Semukunzi H, Li R, et al. DT-13 synergistically enhanced vinorelbine-mediated mitotic arrest through inhibition of FOXM1-BICD2 axis in non-small-cell lung cancer cells. *Cell Death Dis*. (2017) 8:e2810. doi: 10.1038/cddis.2017.218

Conflict of Interest: The authors declare that the research was conducted in the absence of any commercial or financial relationships that could be construed as a potential conflict of interest.

Copyright © 2021 Ou, Deng, Wang, Zhang, Luo and Hu. This is an open-access article distributed under the terms of the Creative Commons Attribution License (CC BY). The use, distribution or reproduction in other forums is permitted, provided the original author(s) and the copyright owner(s) are credited and that the original publication in this journal is cited, in accordance with accepted academic practice. No use, distribution or reproduction is permitted which does not comply with these terms.

frontiers in Medicine

ORIGINAL RESEARCH
published: 22 April 2021
doi: 10.3389/fmed.2021.663558

Long Non-coding RNA LINC00847 Induced by E2F1 Accelerates Non-small Cell Lung Cancer Progression Through Targeting miR-147a/IFITM1 Axis

Huan Li[1†], Yao-kai Chen[1†], Qiu Wan[2], An-qi Shi[2], Min Wang[2], Ping He[3] and Li-xin Tang[2]*

[1] Department of Infectious Diseases, Chongqing Public Health Medical Center, Chongqing, China, [2] Department of Respiratory Geriatrics and Otolaryngology, Chongqing Public Health Medical Center, Chongqing, China, [3] Department of Thoracic Surgery, Chongqing Southwest Hospital, Chongqing, China

OPEN ACCESS

Edited by:
Fu Wang,
Xi'an Jiaotong University, China

Reviewed by:
Jindong Shi,
Fudan University, China
Shailendra Kumar Gupta,
Columbia University Irving Medical Center, United States

***Correspondence:**
Li-xin Tang
lwfb@cqgwzx.com

[†] *These authors have contributed equally to this work*

Specialty section:
This article was submitted to Precision Medicine, a section of the journal Frontiers in Medicine

Received: *03 February 2021*
Accepted: *29 March 2021*
Published: *22 April 2021*

Citation:
Li H, Chen Y-k, Wan Q, Shi A-q, Wang M, He P and Tang L-x (2021) Long Non-coding RNA LINC00847 Induced by E2F1 Accelerates Non-small Cell Lung Cancer Progression Through Targeting miR-147a/IFITM1 Axis. Front. Med. 8:663558. doi: 10.3389/fmed.2021.663558

Background: Long non-coding RNAs (lncRNAs) can remarkably regulate human malignancies in terms of the development and the progression. Previously, lncRNA LINC00847 (LINC00847) has been reported to present dysregulation in several tumors. However, the expression and function of LINC00847 in non-small cell lung cancer (NSCLC) have not been investigated.

Methods: RT-qPCR was performed to determine the expressions of LINC00847 in collected tissue samples and cell lines. The clinical significance of LINC00847 was statistically analyzed. CCK-8 test, cell scratch test and trans-well test were used to evaluate the proliferation, invasion and migration abilities of NSCLC cells, respectively. The xenograft tumor model was constructed to confirm the effects of LINC00847 knockdown on NSCLC *in vivo*. Further, luciferase reporter assays and Western blot were performed to explore molecular mechanisms underlying the functions of LINC00847.

Results: Increased expressions of LINC00847 were observed in NSCLC samples as well as cell lines. Additionally, E2F1 could be capable of directly binding to the LINC00847 promoter region, followed by promoting its expression. Clinically, LINC00847 high-expression could lead to poor prognosis of NSCLC patients. Functionally, LINC00847 knockdown noticeably repressed NSCLC cell growth and metastasis. Mechanically, miR-147a/IFITM1 axis was a downstream target of LINC00847, and silencing of miR-147a could rescue the anti-cancer effects of LINC00847 knockdown on NSCLC cell behaviors.

Conclusion: Overall, up regulation of LINC00847 induced by E2F1 promoted the progression of NSCLC by modulating miR-147a/IFITM1 axis, representing a novel regulatory mechanism for NSCLC progression.

Keywords: LncRNA LINC00847, NSCLC, IFITM1, E2F1, biomarker

INTRODUCTION

Lung cancer can be seen as the major cause of cancer-related death globally, thereinto, non-small cell lung cancer (NSCLC) occupies about 85% (1–3). Over one-third of new NSCLC cases could be found in China, which was a heavy burden facing patients, their families, the society and the whole country (4). Despite the big progress in terms of the diagnosis and the therapy of NSCLC recently, it faces a poor 5-year overall survival (OS) because most patients are diagnosed at advanced stages with lymphatic metastasis, thereby limiting the successful treatment (5, 6). Therefore, identifying novel NSCLC biomarkers as well as better figuring out the potential molecular mechanisms of NSCLC can assist in improving NSCLC diagnosis and treatment.

Long non-coding RNAs (lncRNAs) refer to a cluster of evolutionarily conserved ncRNAs which are over 200 nucleotides long, with limited or without protein-coding capacity (7). The lncRNAs which have been found newly show tissue-specific expression patterns. Based on new evidence, lncRNAs have different functions in different biological activities, particularly in the development process of tumors (8, 9). It has been demonstrated that lncRNAs act as potential regulators in the expression of tumor-related genes, which suggested, together with their frequent dysregulation, that lncRNAs could effectively affect the diagnosis of tumors as well as be an effective therapeutic target (10, 11). For instance, lncRNA HOXA11-AS was highly expressed in lung cancer, and its overexpression facilitated the proliferation and metastasis of lung cancer cells via miR-148a-3p/DNMT1 axis (12). LncRNA LOXL1-AS1 knockdown hindered the ability of cell growth and invasion through increasing MYBL2 expression via sponging miRNA-423-5p (13). However, the expression and function of many lncRNAs have not been investigated.

LncRNA LINC00847 (LINC00847), located on 5q35.3, was a newly identified lncRNA. In recent years, the abnormal expressions of LINC00847 have been reported in several tumors, such as renal cell carcinoma, breast carcinoma and lung cancer (14–16). However, those results were based on the level of a small size of samples, and the functional assays of LINC00847 in tumors have not been performed. The study contributed to clinical evidences to prove LINC00847 as a kind of overexpressed lncRNA in NSCLC. Also, many *in vitro* assays were conducted to explore its tumor-related function.

MATERIALS AND METHODS

Patients and Specimens

We obtained paired NSCLC specimens together with adjacent non-neoplasm lung specimens from 70 patients receiving curative surgical removal in Chongqing Public Health Medical Center between July 2015 and December 2017. All patients provided written informed consent. The clinical diagnosis for all NSCLC patients was confirmed by two pathologists who make their own judgment independently. The clinic pathological data of all 70 patients were reviewed and collected from The Follow-up Department, and TNM stages of tumors were classified based on the eighth edition AJCC system. The resent study has obtained the approval of the Ethics Committee of Chongqing Public Health Medical.

Cell Culture, Cell Transfection and RNA Interference

We obtained human NSCLC cell lines (SK-MES-1, Calu-3, A549 and H460 cells) from the American Type Culture Collection (ATCC, Rockville, MD, USA). The normal human bronchial epithelial (NHBE) cells were provided by the Shanghai Institute of Cell Biology. All cells were grown in RPMI-1,640 medium, which contained 10% fetal bovine serum (FBS, Biocyto Technology, Daxuecheng, Guangzhou, China), 1.2% antibiotics (Boaosen, Haidian, Beijing, Chian) and 1% glutamate (Biocyto Technology) followed by incubation at 37°C.

SiRNAs targeting E2F1 (si-E2F1), LINC00847(si-LINC00847-1, si-LINC00847-#2), miR-147a mimics, miR-147a inhibitors came from GEkai Teconology (Xuhui, Shanghai, China). Experimenters cloned LINC00847 or E2F1 into pcDNA3.1 empty vector for the consistent expression of LINC00847 or E2F1, respectively. Lipofectamine 3,000 reagents (Fujun, Haidian, Beijing, China) assisted in transfecting cells following the kits' protocols.

RNA Isolation and RT-PCR Assays

Total RNA was extracted from specimen samples as well as above cells by TRIzol (Kehaojia, Hongshan, Wuhan, China) containing 0.2 ml chloroform (Hengdu, Pudong, Shanghai, China). Reverse transcription of RNA was performed to obtain cDNA templates by the use of Super M-MLV (Baitaike, PR6502, Pudong, Shanghai, China). For the determination of lncRNA, miRNA and mRNAs, qPCR was conducted using the SYBR Green PCR Kit on a BioRad Chromo4 PCR system (Biosystems, Foster City, CA, USA). GADPH or U6 served as an endogenous control. $2^{-\Delta\Delta Ct}$ method was applied to calculate the levels of the above factors. The primer was synthetized by Kairuiji Technology (Shijingshan, Beijing, China), and its sequences were presented in **Table 1**.

TABLE 1 | The primers used in this study for RT-PCR.

Genes	Sequences (5′ – 3′)
LINC00847: forward	TGACCATCAGAATGGCAGATA
LINC00847: reverse	GACCCTGACGCTGTCGATCAA
E2F1: forward	AGCGGCGCATCTATGACATC
E2F1: reverse	GTCAACCCCTCAAGCCGTC
miR-147a: forward	CCCCTATCACGATTAGCATTAA
miR-147a: reverse	CCCAAGCTTTTATGTGGTTGTT
IFITM1: forward	TCGCCTACTCCGTGAAGTCTA
IFITM1: reverse	TGTCACAGAGCCGAATACCAG
GAPDH: forward	TATAAATTGAGCCCGCAGCC
GAPDH: reverse	TACGACCAAATCCGTTGACTC
U6: forward	GCGCGTCGTGAAGCGTTC
U6: reverse	GTGCAGGGTCCGAGGT

Luciferase Reporter Assay

JASPAR was used to identify the E2F1-binding motif in LINC00847 promoter region. The divergent fragment sequences were synthesized by Jima Technology (Hangzhou, Zhejiang, China), followed by being inserted into pGL3-basic vector (Promega, Haidian, Beijing, China) and co-transfected with E2F1 plasmid into Calu-3 and A549 cells. The miR-147a sequence was also inserted into pGL3-basic vector and wild-type and mutant LINC00847 plasmid were used for co-transfection. Luciferase activities were measured 24 h later using the dual luciferase

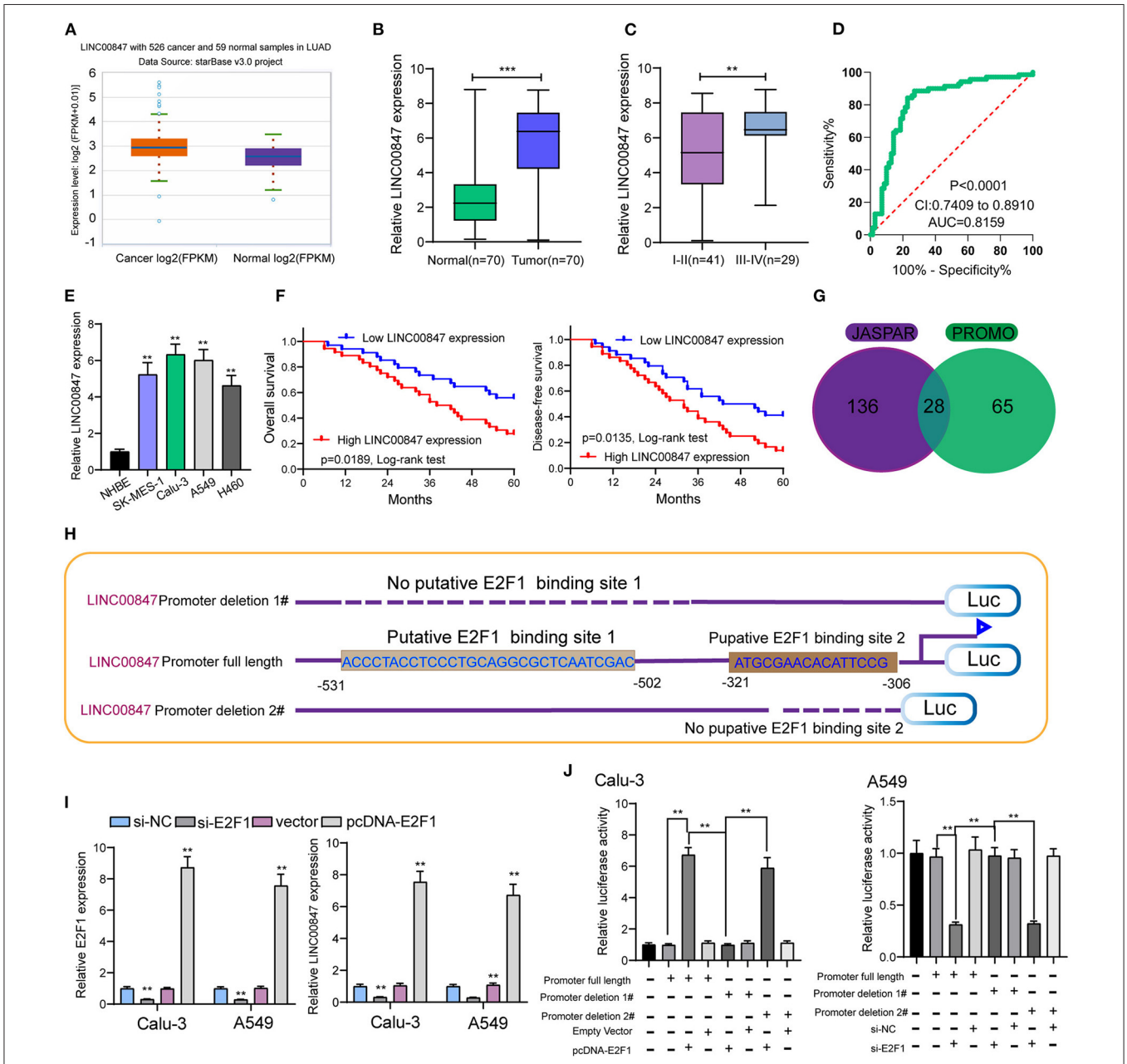

FIGURE 1 | LINC00847 expression was up regulated in NSCLC and induced by E2F1. **(A)** The expressing trend of LINC00847 in lung cancer and normal lung samples of TCGA datasets. **(B)** Relative expressions of LINC00847 in 70 NSCLC tissue samples and their paired non-cancerous specimen samples measured by RT-qPCR. **(C)** LINC00847 expression was higher in advanced NSCLC specimens. **(D)** ROC assays for the exploration of the diagnostic value of LINC00847 expression in NSCLC specimens. **(E)** RT-PCR for the determination of LINC00847 levels in four NSCLC cell lines and NHBE. **(F)** Kaplan-Meier curves for the overall survival and disease-free survival in patients with NSCLC. **(G)** 28 transcription factors were predicted for LINC00847 using JASPAR and PROMO databases. **(H)** Description of E2F1-binding sites in the promoter region of LINC00847 and the schematic of LINC00847 promoter deletion 1# and LINC00847 promoter deletion 2# luciferase reporter vectors. **(I)** The expression of LINC00847 after knockdown or overexpression of E2F1. **(J)** Relative luciferase activities as analyzed in Calu-3 and A549 cells co-transfected with the related vectors. $^{**}p < 0.01$.

reporter system (Promega, Madison, WI, USA). Renilla luciferase activity was used as a standardized control.

RNA Pull-Down Assays

A Magnetic RNA Protein Pull-Down Kit (Pierce, USA) was applied to the RNA pull-down assay following the manual.

Subcellular Fractionation

The PARIS Kit (Life Technologies, USA) was applied to the subcellular fractionation (separating nuclear from cytoplasmic) following the instruction of the producer.

Cell Proliferation Assays

CCK-8 assays as well as colony formation assays were carried out for determining the proliferative ability of tumor cells after the special treatments in different conditions. For CCK-8 assays, we seeded cells in 48-well plates (1,500 cells per well) which were maintained at 37°C for 4 days. CCK-8 reagent was added at the setting time after cell seeding. The viable cells were assessed by measuring the absorbance at 450 nm. For the colony formation assays, tumor cells (300 cells per well in a 24-well plate) were placed in a 6-well plate and cultured with RPMI 1,640 medium (GIBCO, Haidian, Beijing, China) for 14 days. The colony formation was visualized by crystal violet staining.

Colony Formation Assays

We seeded 3,000 cells on each well of a 6-well plate, and used individual siRNA oligonucleotides to transfect them. The medium was changed each 4 days. Two weeks later, methanol was employed to fix the colonies, which then received 15 min of staining treatment in 0.1 % crystal violet (Sigma, Pudong, Shanghai, China) in PBS. We captured the images of these colonies containing ≥50 cells and used ImageJ (V.1.8.0) software for counting.

Ethynyldeoxyuridine (EdU) Assays

Cell-Light EdU Apollo 567 *in vitro* Imaging Kit (Ribobio Technology, Guangzhou, China) served for the EdU assays following the instruction of the producer. Fluorescent microscopy (Nikon, Japan) assisted in measuring the percentage occupied by EdU-positive cells in the five random fields each well. The experiments were conducted repeatedly in triplicate.

In vivo Assay

To explore the potential function of LINC00847 on tumor growth, 5–6 week old female athymic nude mice (BALB/c Nude) were used for the xenograft model ($n = 6$ per group). A549 cells stably transfected with sh-control and sh-LINC00847-1 were dissociated using trypsin and washed twice with sterilized PBS. Then, 0.3 mL of PBS containing 3×10^6 cells was subcutaneously inoculated into the flank of mice. The tumor size was determined every 3–4 days after tumor formed (around 1–2 weeks). The tumor volumes were recorded every 4 days and calculated in accordance with a formula (length × width^2 × 0.5). The animal-related protocol was approved by the Animal Research Ethics Committee of Chongqing Public Health Medical Center.

Cell Wound Healing

Each well of a 6-well plate was added with approximately 4×10^5 cells, which were cultured until completely confluent. Then, in a gentle way, a 20-μl micropipette tip was used to scratch cells in the center of the well. At 0 and 48 h incubation, the NSCLC cell lines were photographed using the inverted microscope (Olympus, Japan) and the scratch area was assessed using Image J software.

Trans Well Assay

The trans well assay was conducted for the functional assays of LINC00847 using the 24-well trans wells precoated with the Matrigel (Solarbio, Hengfei Technology, Shanghai, China). Serum-free RPMI-1,640 assisted in seeding Calu-3 and A549 cells (5,000) into the upper chamber. The lower chamber was added with medium (which contained 10% FBS) as the chemical attractant. Then, a cotton swab was used to remove the cells that remained on membrane upper surface. Following 24 h of incubation, methanol was used to fix invaded cells. Then 1% crystal violet solution was used to stain the invaded cells. At last, a light microscope served for calculating invaded cells in five random view fields.

TABLE 2 | Correlation between LINC00847 expression and clinicopathological characteristics of NSCLC patients.

Variable	Number	LINC00847 expression		*p*
		High	Low	
Age (years)				0.229
< 55	36	16	20	
≥ 55	34	20	14	
Gender				0.663
Male	43	23	20	
Female	27	13	14	
Tumor size (cm)				0.134
< 3	41	18	23	
≥ 3	29	18	11	
Histology				0.650
Adeno	39	21	18	
Squamous	31	15	16	
Smoking history				0.967
Smokers	41	21	20	
Never smoke	29	15	14	
Clinical stages				0.047
I-II	41	17	24	
III-IV	29	19	10	
TNM stage				—
I(T1-2N0M0)	36	15	21	
II(T1-2N1M0)	5	2	3	
IIIA (T3N0M0;T1-3N2M0)	17	8	9	
IIIB(T1-4N3M0;T4N1M0)	9	8	1	
IV(T1-4N1-3M1)	3	3	0	
Lymph nodes metastasis				0.041
No	48	21	27	
Yes	22	15	7	

Western Blot Assays

Total protein from NSCLC cells was obtained by applying RIPA lysis buffer (Sigma, Hangzhou, Zhejiang China) with protease suppressor cocktail (Roche, Pudong, Shanghai, China). Polyacrylamide gel electrophoresis (10%) assisted in resolving 30μg protein, followed by PVDF membrane transferring (Millipore, Chida Technology, Xuhui, Shanghai, China) in ice bath. Next, the membranes were blocked for 2 h by 5% BSA diluted with TBST at 37 °C, which were further probed by using the primary antibodies for one night at 4 °C. Subsequently, PBST which contained anti-rabbit-horseradish peroxidase-conjugated secondary antibodies (Sangong, Hangzhou, Zhejiang, China) was used to incubate the membranes for 60 min at 37 °C. Densitometry was performed using ImageJ software. The primary antibodies were purchased from Haodi Technology (Shenzhen, Guangdong, China).

Statistical Analysis

SPSS 21.0 (SPSS Inc., Chicago, IL, USA) together with GraphPad Prism 8.0 software were applied for statistical calculation and graphing, respectively. Student's *t*-test was applied to compare the two groups. The chi-square test assisted in analyzing the clinical value possessed by LINC00847 in NSCLC patients. The Kaplan-Meier method was applied for analyzing the survival, and the Log-rank (Mantel-Cox) test served for determining the between-group differences in survivals. Univariate and multivariate analyses for the examination of the prognostic value of LINC00847 were based on the Cox regression model. A $p < 0.05$ exhibited statistical significance.

RESULTS

LINC00847 Expression Level Was Overexpressed in NSCLC Samples

For the exploration of the function of LINC00847 expression in NSCLC progression, we searched starbase 3.0(http://starbase.sysu.edu.cn/) which is an online tool and can be used to analyze TCGA datasets. As shown in **Figure 1A**, we observed that LINC00847 is an overexpressed lncRNA in NSCLC (**Figure 1A**). As demonstrated by RT-PCR results, higher LINC00847 levels were observed in NSCLC specimens than matched normal specimens ($p < 0.01$, **Figure 1B**). Also, the NSCLC specimens with advanced stages exhibited a higher level of LINC00847 (**Figure 1C**). According to the ROC assays, our group observed that high LINC00847 expression had an AUC value of 0.7951(95% CI: 0.7447–0.8456) for NSCLC (**Figure 1D**). Next, our group tested LINC00847 expression in NSCLC cell lines, finding that LINC00847 was more expressed in NSCLC cell lines (**Figure 1E**).

High-Expressions of LINC00847 Predicts Unfavorable Prognosis in NSCLC Patients

Given the fact that the distinct up regulation of LINC00847 was observed in NSCLC tissues, we wondered whether its levels may display an influence on the clinical progress of NSCLC patients. LINC00847 expression value was taken as a standard to divide enrolled patients into two groups, and chi-square test which indicated the up regulation of LINC00847 expressions showed an obvious relation to clinical stage ($p = 0.047$) and lymph nodes metastasis ($p = 0.041$, **Table 2**). Moreover, we further performed Kaplan-Meier analysis for confirming the prognostic value owned by LINC00847 in NSCLC patients. It was observed that the patients with high LINC00847 expression displayed evidently poorer OS ($p = 0.0189$) and disease-free survival (DFS) ($p < 0.0135$) relative to lower LINC00847 expressions (**Figure 1F**). Finally, as revealed by multivariate Cox regression analyses, LINC00847 expression may independently predict the OS and DFS of NSCLC patients (**Table 3**).

E2F1 Activates LINC00847 Transcription in NSCLC Cells

For figuring out the mechanism involved in LINC00847 overexpression in NSCLC cells, we analyzed the JASPAR tool for the determination of possible transcription factors binding to the LINC00847 promoter. As shown in **Figure 1G**, we found several transcription factors which may be the potential candidates, such as YY1, ZNF354C, ZNF263 and E2F1. We focused on E2F1 because several E2F1 binding sites displayed high scores and E2F1 have been demonstrated to be highly expressed in lung cancer and served as a tumor pro motor(**Figure 1H**) (17, 18). Then, the expression of LINC00847 was silenced or overexpressed and RT-PCR was performed, which suggested that the transfection of si-E2F1 could suppress the levels of both E2F1 and LINC00847 in A549 and calu-3 cells; by contrast,

TABLE 3 | Summary of multivariate Cox regression analyses of overall survival and disease-free survival duration.

Parameter	Overall survival			Disease-free survival		
	HR	95% CI	*p*	HR	95% CI	*p*
Age	0.893	0.463–1.773	0.232	1.241	0.664–2.311	0.188
Gender	1.215	0.667–2.152	0.188	1.452	0.783–1.987	0.267
Tumor size	1.427	0.782–2.441	0.139	1.118	0.673–2.231	0.109
Histology	1.576	0.875–2.774	0.119	1.334	0.678–2.213	0.342
Smoking history	1.334	0.673–1.893	0.231	0.986	0.674–1.783	0.134
Clinical stage	2.986	1.376–4.782	0.011	2.675	1.175–4.376	0.019
Lymph nodes metastasis	3.328	1.477–5.271	0.006	2.986	1.218–4.778	0.009
LINC00847 expression	2.896	1.476–5.221	0.009	2.562	1.217–4.562	0.018

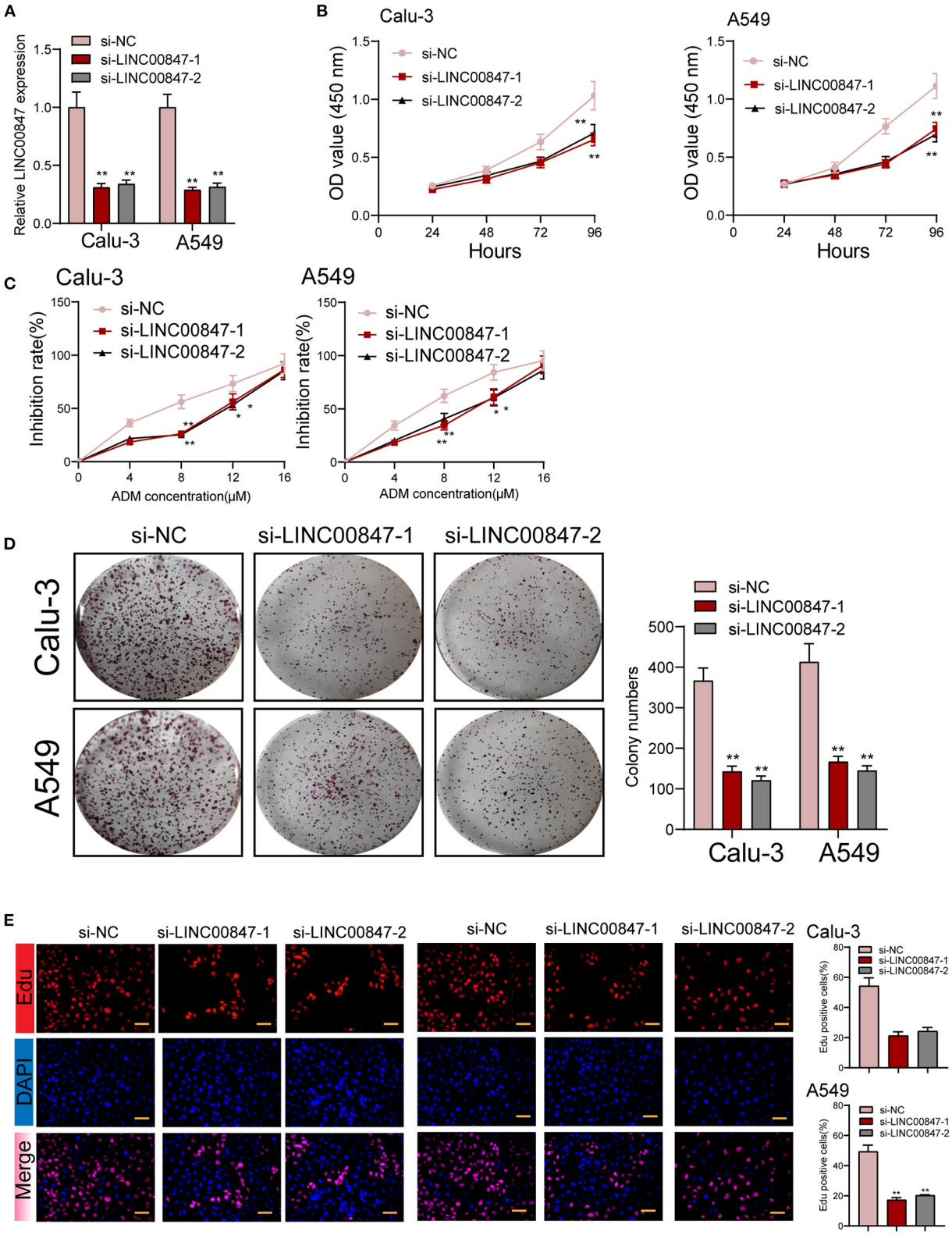

FIGURE 2 | The proliferation of NSCLC is promoted by LINC00847. **(A)** Relative expression of LINC00847 in NSCLC cells transfected with LINC00847 siRNA (si-LINC00847-1 or si-LINC00847-2) and scrambled siRNA. **(B)** CCK8 assay was used to detect cell viability. **(C)** Calu-3 and A549 cells were treated with ADM (0, 4,8,12,16μM) for 48 h. Inhibition rate increased with the increase of concentration of ADM. **(D)** LINC00847 knockdown remarkably impaired the ability of colony formation. **(E)** EDU assays for the determination of the cell proliferation changes after LINC00847 down-regulation in Calu-3 and A549 cells. $^{*}p < 0.05$, $^{**}p < 0.01$.

E2F1 overexpression showed a positive effect (**Figure 1I**). Dual luciferase reporter assays revealed that the promoter activity reduced remarkably due to LINC00847 promoter deletion 1# relative to the full-length promoter construct and LINC00847 promoter deletion 2# (**Figure 1J**). Our data revealed that E2F1 transcriptionally activated LINC00847 and promoted its levels in NSCLC cells.

Knockdown of LINC00847 in NSCLC Decreased Cell Growth

The frequent overexpression of LINC00847 and its effects on enhancing tumor metastasis in clinical progress encouraged us to further explore the possible biological function in the NSCLC behaviors. Using siRNA, LINC00847 expression was silenced in Calu-3 and A549 cells (**Figure 2A**). CCK8 assays suggested that cell growth was distinctly inhibited in both cell lines transfected with si-LINC00847 compared with si-NC (**Figure 2B**). The study also paid attention to exploring how LINC00847 affected the chemotherapy resistance exhibited by NSCLC cells, finding that ADM concentration increase led to increased inhibition rate, and LINC00847 knockdown weakened the inhibition effect imposed by ADM specific to NSCLC cells (**Figure 2C**). In addition, we also observed that colony-formation ability was decreased by LINC00847 knockdown in NSCLC cells (**Figure 2D**). In line with EDU staining, there were fewer EDU-positive cells in si-LINC00847-1 and si-LINC00847-2 group compared with the si-NC group (**Figure 2E**). Then, *in vivo* experiments were used to further explore the potential influence of LINC00847 inhibition on tumor growth. **Figure 3A** confirmed the transfection efficiency of sh-LINC00847. *In vivo* assays suggested that depletion of LINC00847 distinctly decreased tumor growth rate (**Figure 3B**). We also examine the levels of miR-147a and IFITM1 in these tumors, finding that miR-147a expression in tumors with sh-LINC00847 group was distinct higher than those with tumors with sh-NC group, while a significant decrease of IFITM1 expression was observed in tumors with sh-LINC00847 group compared with those with sh-NC group (**Figures 3C,D**). In addition, our group showed that the tumor volume and weight were apparently lessened in sh-LINC00847 group compared with control group (**Figures 3E,F**). Overall, our findings suggested that knockdown of LINC00847 suppressed NSCLC tumorigenesis *in vivo*.

Silencing LINC00847 Inhibits Invasion and Migration of NSCLC Cells

The wound-healing and trans well assays served for further examining the ability of cell metastasis. In line with **Figure 4A**, the migratory areas of si-LINC00847 in Calu-3 and A549 cells were distinctly smaller than those of si-NC. In addition, the

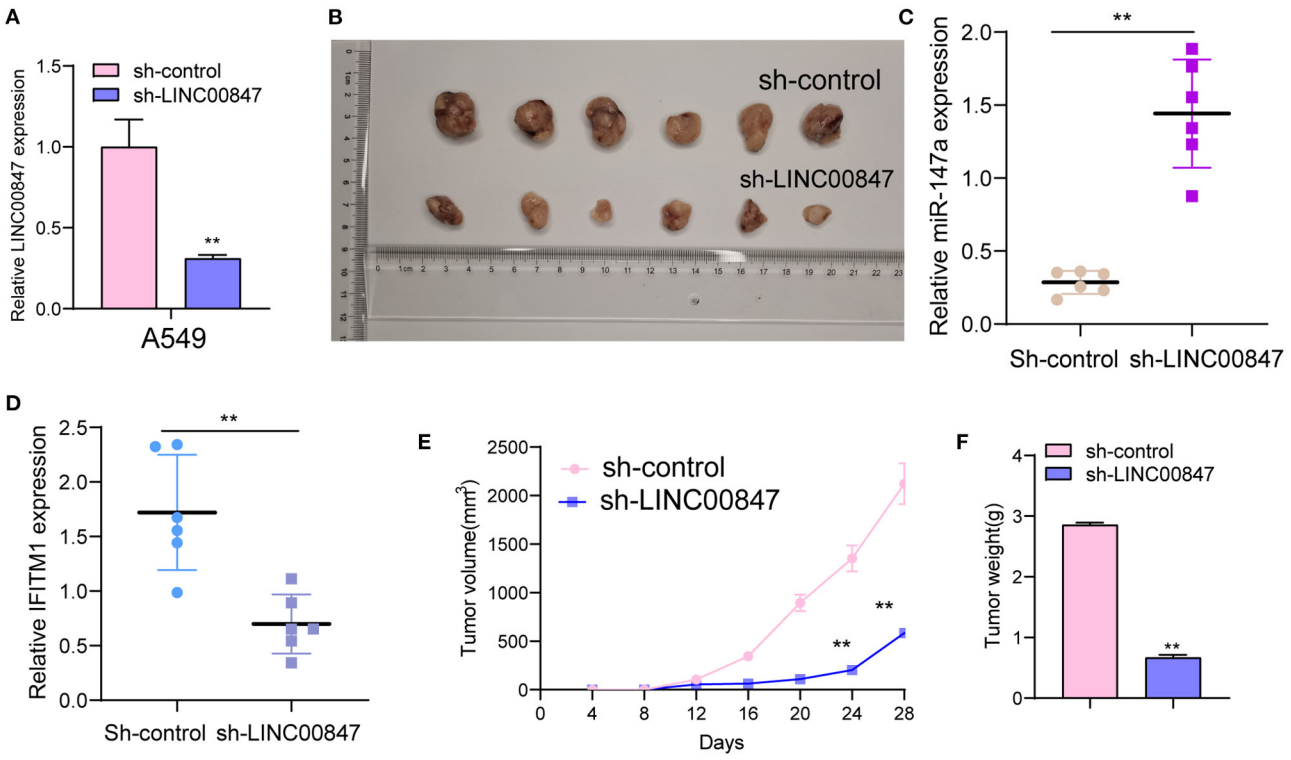

FIGURE 3 | LINC00847 promoted tumor growth *in vivo*. **(A)** The distinct knockdown of LINC00847 expression in A549 cells transfected with LINC00847 were demonstrated by RT-PCR. **(B)** Tumors derived from mice in two different groups were presented. **(C, D)** RT-PCR determined the expression of miR-147a and IFITM1 in tumors with sh-control and sh-LINC00847. **(E)** Tumor growth curves were shown every 7 days. **(F)** The subcutaneous tumor weights were detected at the 28th day after injection. $^{**}p < 0.01$.

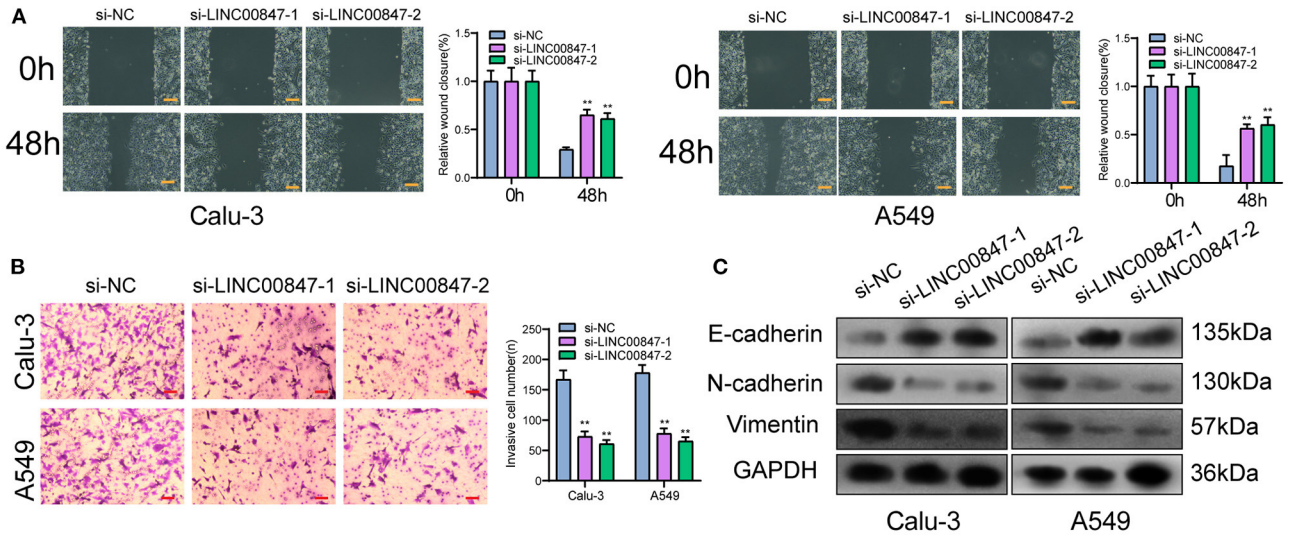

FIGURE 4 | LINC00847 dramatically influenced the invasion, migration and EMT progress of NSCLC cells. **(A)** Wound healing assays were used to detect cell invasion in LINC00847-knockdown-Calu-3 and A549 cells. **(B)** Trans well assays were carried out in Calu-3 and A549 cells after knockdown of LINC00847. **(C)** Western blot examined the levels of EMT-related factors after knockdown of LINC00847. $^{**}p < 0.01$.

results of trans well assays indicated that the si-LINC00847 group had a significantly decreased cell invasion ability relative to the si-NC group (**Figure 4B**). Besides, to explore the metastatic mechanism involved in LINC00847 function, we performed Western blot for detecting the activity exhibited by epithelial-mesenchymal transition (EMT)-related markers. As shown in **Figure 4C**, the suppression of LINC00847 distinctly reduced the N-cadherin and Vimentin levels as well as improved the E-cadherin levels in both Calu-3 and A549 cells. Our data revealed that LINC00847 may promote metastasis and EMT progress in NSCLC cells.

LINC00847 Directly Interacts With miR-147a and Represses Its Expression

Using the data of Lncatlas, it was discovered that LINC00847 was mainly expressed in the cytoplasm, suggesting this lncRNA may exhibit its tumor-promotive role via sponging miRNAs (**Figures 5A**,**B**) (19). Starbase 3.0 revealed that miR-147a contained a putative binding sites with LINC00847 (**Figure 5C**). Using subcellular fractionation, our group discovered that the nucleus and cytoplasm observed LINC00847 expressions (**Figures 5D–F**). The distinct down-regulation of miR-147a was also observed in NSCLC specimens (**Figure 5G**). NSCLC specimens with III-IV stages exhibited a lower level of miR-147a than those with I-II stages (**Figure 5H**). In four NSCLC cells, a significant decrease of miR-147a was observed compared with NHBE cells (**Figure 5I**). The diagnostic value of miR-147a was demonstrated by ROC assays (**Figure 5J**). Functional assays revealed that overexpression of miR-147a suppressed Calu-3 and A549 cell proliferation and invasion (**Figures 5K,L**). RNA-pull down demonstrated the association between LINC00847 and miR-147a (**Figure 5M**). More importantly, luciferase reporter assays provided evidence that miR-147a overexpression dramatically diminished the luciferase activity of LINC00847-Wt, but failed to change the relative luciferase activity possessed by LINC00847-Mut (**Figure 5N**). Besides, knockdown of LINC00847 resulted in the distinct promotion of miR-147a expression, while miR-147a overexpression suppressed the expression of LINC00847 (**Figures 5O,P**). Overall, our finding revealed that LINC00847 may exhibit its function in NSCLC progression via sponging miR-147a.

IFITM1 Acted as a Target of miR-147a and LINC00847 Regulated IFITM1 Expression Through miR-147a in NSCLC Cells

To explore the effects of miR-147a in the mechanisms and functions of LINC00847, we next sought to discover the downstream target of miR-147a using starbase algorithm, and found that IFITM1, a well-known oncogene in diverse cancer types, might be the possible target (**Figure 6A**). Then, the distinct overexpression of IFITM1 in NSCLC specimens and cells and its diagnostic value were also clinically demonstrated (**Figures 6B–E**). To confirm the binding between IFITM1 and miR-147a, luciferase activity assays were conducted. The results validated that co-transfection with wild-type1 (WT1) or wild-type2 (WT2) but not mutant-type1(MuT1) or mutant-type2 (MuT2) IFITM1 reporters led to significantly decreased luciferase activities in NSCLC cells, which demonstrated that miR-147a could directly target IFITM1 in NSCLC cells (**Figures 6F,G**). Furthermore, miR-147a overexpression suppressed the IFITM1 expressions at both mRNA and protein level (**Figure 6H**). Besides, the positive correlation between LINC00847 and IFITM1, and the negative correlation between LINC00847 and miR-147a

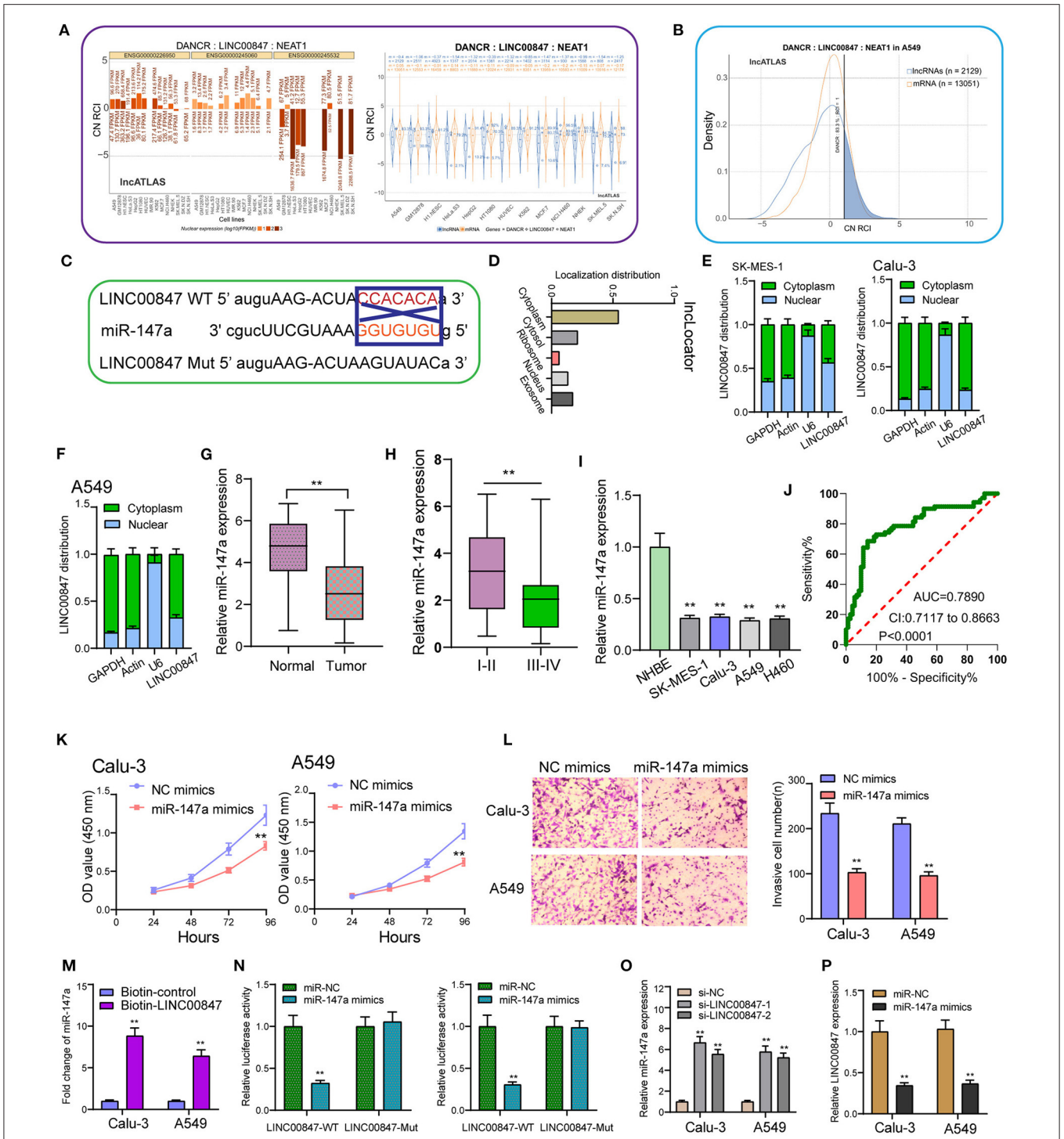

FIGURE 5 | miR-147a is predicted to interact with LINC00847. **(A)** The subcellular localization of LINC00847 in several types of tumor cells based on the data of LncATLAS. **(B)** Cytoplasmic/Nuclear Localization: RCI distribution in A549 cells. **(C)** The schematic diagram presents the complementary binding sites within LINC00847 and miR-147a. **(D)** Localization distribution of LINC00847 by analyzing lncLoctor. **(E, F)** Relative LINC00847 expression levels in nuclear and cytosolic fractions of SK-MES-1, Calu-3 and A549 cells. **(G)** RT-PCR for the determination of miR-147a expression in our cohort. **(H)** The levels of miR-147a in NSCLC with different stages. **(I)** The down-regulation of miR-147a was observed in NSCLC cells. **(J)** The diagnostic value of miR-147a was determined using ROC assays. **(K)** CCK-8 assays determined the proliferation ability of Calu-3 and A549 cells after transfection of miR-147a mimics. **(L)** Trans well-assay was used to detect cell invasion in miR-147a mimics transfected Calu-3 and A549 cells. **(M)** RNA-pull down experiments suggested the combination between miR-147a and LINC00847. **(N)** Luciferase reporter assay showed the activity within miR-147a and LINC00847 wild type or mutant. **(O)** The levels of miR-147a was increased in Calu-3 and A549 cells after the transfection of si-LINC00847-1 and si-LINC00847-2. **(P)** Overexpression of miR-147a inhibited the expression of LINC00847. $^{**}p < 0.01$.

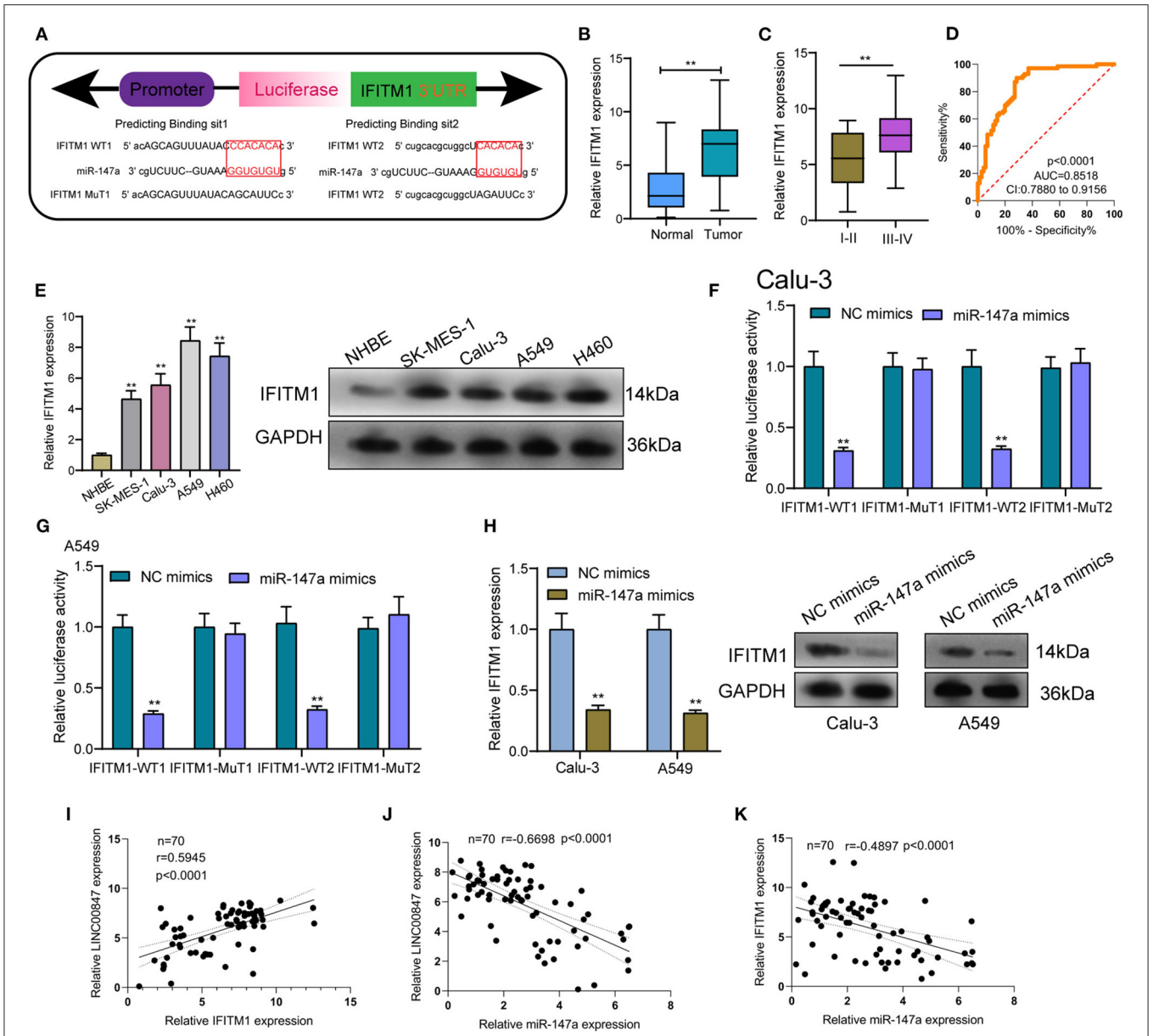

FIGURE 6 | IFITM1 is a direct target of miR-147a. **(A)** Seed sequences of miR-147a against the wild-type or mutant 3'-UTR of IFITM1. **(B)** Expression levels of IFITM1 in clinical specimens of NSCLC. **(C)**The levels of IFITM1 in NSCLC specimens with different stages. **(D)** The area under the ROC curve was 0.8518. **(E)** the protein level of IFITM1 was increased in four NSCLC cell lines. **(F, G)** Relative luciferase activity was detected by luciferase assays in Calu-3 and A549 cells. **(H)** IFITM1 levels were increased after overexpression of miR-147a. **(I–K)** The correlation among LINC00847, miR-147a and IFITM1 expressions in our cohort was determined by Spearman's correlation analysis. **p < 0.01.

and IFITM1 and LINC00847 were demonstrated in our cohort (**Figures 6I–K**). On the other hand, the results of rescue experiments revealed that LINC00847 knockdown resulted in the suppression of IFITM1 expression in Calu-3 and A549 cells, which was reversed because of the miR-147a knockdown (**Figure 7A**). According to a series of *in vitro* assays, in Calu-3 and A549 cells, miR-147a exhaustion weakened the proliferation and invasion suppression resulted from silencing LINC00847 (**Figures 7B–E**).

DISCUSSION

At present, the clinically common therapeutic method for lung cancer is chemotherapy, which, however, is only capable of prolonging the survival time of cancan patients but can not achieve the ultimate cure (20, 21). The identification of novel biomarkers for NSCLC patients is very important in the improvements of the clinical prognosis of patients. In this study, a novel NSCLC-related lncRNA, LINC00847 was identified,

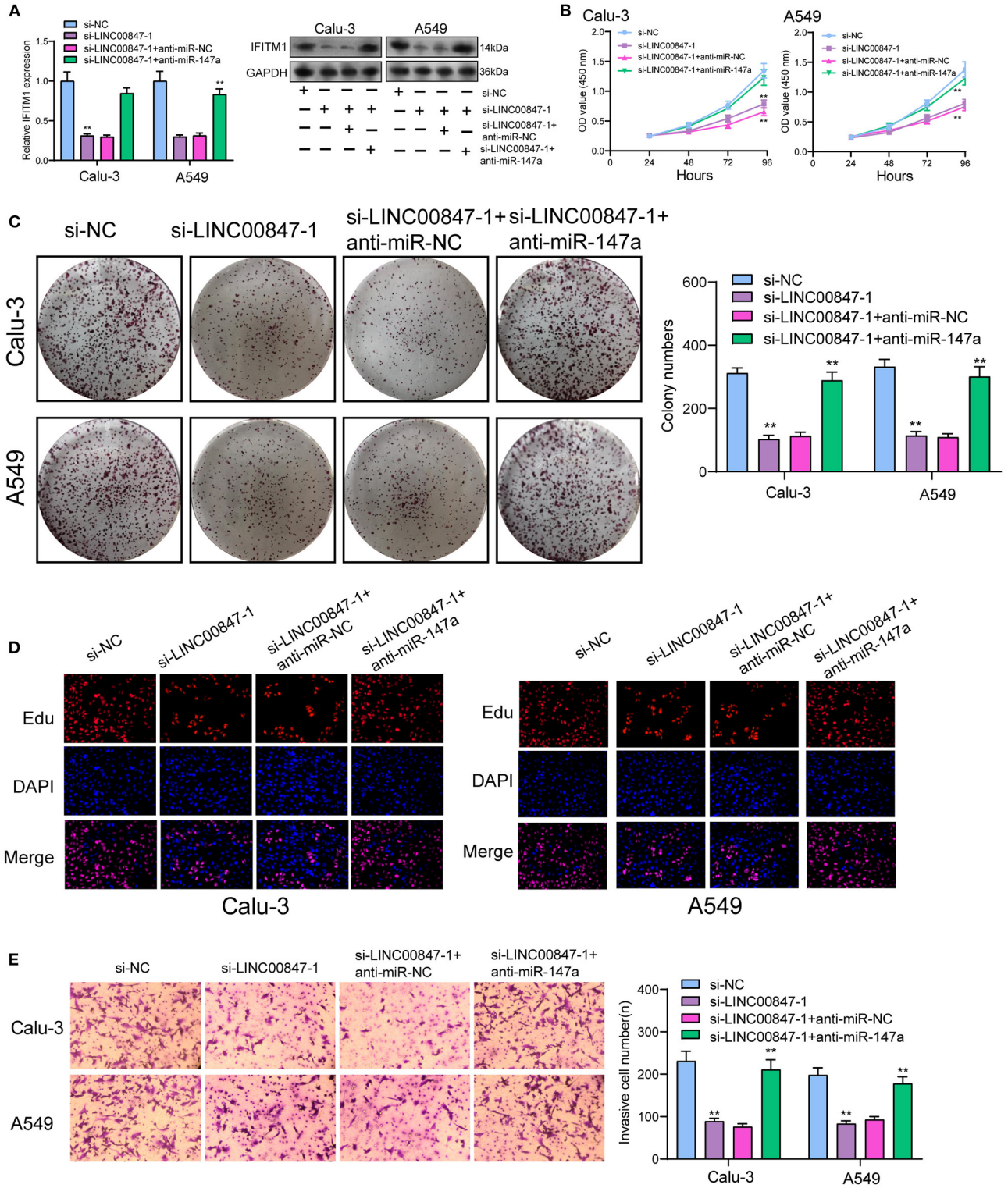

FIGURE 7 | LINC00847 promoted the progression of NSCLC via sponging miR-146a to increase IFITM1. **(A)** The expression of IFITM1 at mRNA and protein level in Calu-3 and A549 cells after transfected with si-LINC00847-1, si-LINC00847-1/anti-miR-NC or si-LINC00847-1/anti-miR-147a. **(B)** CCK-8, **(C)** colon formation and **(D)** EdU were performed to detect cell proliferation. **(E)**The cell invasive ability of Calu-3 and A549 cells were assessed using Trans well-assays. $^{**}p < 0.01$.

which showed overexpression in both NSCLC specimens and cell lines. Clinical studies also confirmed its diagnostic value in screening NSCLC specimens and provided evidence that high LINC00847 expression could lead to advanced clinical stages, distant metastasis and shorter OS and DFS. Our findings suggested LINC00847 being a new biomarker for the diagnosis and prognosis of NSCLC patients.

Although an increasing number of lncRNAs have been reported to exhibit a dysregulated level in different tumor specimens, the potential mechanisms remained largely unclear. Based on recent evidences, lncRNAs expression can be subjected to the transcription factors just like protein coding genes (22). In this study, we used JASPAR and PROMO to search the possible targets, finding that E2F1 may be a candidate with a high score. Then, we performed luciferase reporter assays, determining that E2F1 was capable of binding to the LINC00847 promoter region as well as inducing its transcription. The results of RT-PCR also confirmed the positive regulation between E2F1 and LINC00847. These essential data revealed that E2F1 activated LINC00847 translational expression to increase LINC00847 expression in NSCLC.

In recent years, growing studies have demonstrated the involvement of lncRNAs in the regulation of tumor growth and metastasis (23, 24). As LINC00847 was obviously overexpressed in NSCLC, we performed loss-of-function assays to explore its effects. As expected, we observed that LINC00847 knockdown weakened the proliferation, migration and invasion related to Calu-3 and A549 cells, suggesting it as a tumor pro motor in NSCLC. To explore the potential mechanisms by which LINC00847 promoted the progression of NSCLC, the localization in cancer cells was identified first because the function of LINC00847 was based on its subcellular localization. The results of biological information and subcellular fractionation confirmed the expression of LINC00847 in the cytoplasm as well as the nucleus, indicating cytosolic LINC00847 may act as a microRNA sponge. In addition, LINC00847 served as a ceRNA specific to miR-147a and sponged miR-147a. Previously, the tumor-suppressive roles of miR-147a in lung cancer and some other tumors have been demonstrated (25, 26). In functional exploration, we also observed that miR-147a presented a low expression in NSCLC and hindered NSCLC cell proliferation and invasion. As revealed, LINC00847 may serve as a tumor pro motor via sponging miR-147a.

Interferon-induced trans membrane protein 1 (IFITM1) acts as a member of the IFN-inducible trans membrane protein family and plays a functional role in the activity of cell adhesion signals and the anti-growth transduction (27). In recent years, growing studies have demonstrated that abnormal levels of IFITM1 affect the progression of several tumors types (28–30). In lung cancer, IFITM1 had the function of facilitating lung cancer cell proliferation and metastasis (31). In this study, bioinformatics analysis was used and identified IFITM1 as a potential target of miR-147a. Consistent with previous results, we also confirmed the distinct overexpression and the diagnostic value of IFITM1 in NSCLC. Further luciferase reporter assays demonstrated IFITM1 as a direct target of miR-147a. Besides, it was found that LINC00847 expression showed a positive relation to IFITM1 expression and a negative relation to miR-147a expression. In the rescue experiments, we observed that the down-regulation of miR-147a had the function of promoting NSCLC cells in terms of the proliferation and metastasis, that was hindered by LINC00847 knockdown. Overall, our findings suggested LINC00847 may exhibit its tumor-pro motive effects on the NSCLC progression by increasing IFITM1 expression via sponging miR-147a.

CONCLUSIONS

LINC00847 expression was found to be increased in NSCLC and was activated by E2F1. LINC00847 may facilitate NSCLC cell proliferation and metastasis via sponging miR-147a and elevating IFITM1. The findings in the study help us to more deeply understand how lncRNAs affect NSCLC progression, how lncRNAs serve as an effective therapeutic target as well as how lncRNAs predict NSCLC prognosis.

DATA AVAILABILITY STATEMENT

The raw data supporting the conclusions of this article will be made available by the authors, without undue reservation.

ETHICS STATEMENT

The studies involving human participants were reviewed and approved by Chongqing Public Health Medical Center. The patients/participants provided their written informed consent to participate in this study. The animal study was reviewed and approved by Chongqing Public Health Medical Center.

AUTHOR CONTRIBUTIONS

HL, L-xT, and MW wrote the main manuscript and analyzed the data. HL, Y-kC, QW, A-qS, and PH performed the experiments. HL, Y-kC, and L-xT designed the study. All authors read and approved the final manuscript. All authors contributed to the article and approved the submitted version.

REFERENCES

1. Thomas L, Doyle LA, Edelman MJ. Lung cancer in women: emerging differences in epidemiology, biology, and therapy. *Chest.* (2005) 128:370–81. doi: 10.1378/chest.128.1.370
2. Siegel RL, Miller KD, Jemal A. Cancer Statistics, 2017. *CA Cancer J Clin.* (2017) 67:7–30. doi: 10.3322/caac.21387
3. Hirsch FR, Scagliotti GV, Mulshine JL, Kwon R, Curran Jr WJ, Wu YL, et al. Lung cancer: current therapies and new targeted treatments. *Lancet.* (2017) 389:299–311. doi: 10.1016/S0140-6736(16)30958-8
4. Cao M, Chen W. Epidemiology of lung cancer in China. *Thor Cancer.* (2019) 10:3–7. doi: 10.1111/1759-7714.12916
5. Lakshmanan I, Ponnusamy MP, Macha MA, Haridas D, Majhi PD, Kaur S, et al. Mucins in lung cancer: diagnostic,

prognostic, and therapeutic implications. *J Thor Oncol.* (2015) 10:19–27. doi: 10.1097/JTO.0000000000000404
6. Duma N, Santana-Davila R, Molina JR. Non-small cell lung cancer: epidemiology, screening, diagnosis, and treatment. *Mayo Clin Proc.* (2019) 94:1623–40. doi: 10.1016/j.mayocp.2019.01.013
7. Kopp F, Mendell JT. Functional classification and experimental dissection of long noncoding RNAs. *Cell.* (2018) 172:393–407. doi: 10.1016/j.cell.2018.01.011
8. Qian X, Zhao J, Yeung PY, Zhang QC, Kwok CK. Revealing lncRNA structures and interactions by sequencing-based approaches. *Trends bio Sci.* (2019) 44:33–52. doi: 10.1016/j.tibs.2018.09.012
9. Atianand MK, Caffrey DR, Fitzgerald KA. Immunobiology of long noncoding RNAs. *Ann Rev Immunol.* (2017) 35:177–98. doi: 10.1146/annurev-immunol-041015-055459
10. Bhan A, Soleimani M, Mandal SS. Long noncoding RNA and cancer: a new paradigm. *Cancer Res.* (2017) 77:3965–81. doi: 10.1158/0008-5472.CAN-16-2634
11. Karreth FA, Pandolfi PP. ceRNA cross-talk in cancer: when ce-bling rivalries go awry. *Cancer Dis.* (2013) 3:1113–21. doi: 10.1158/2159-8290.CD-13-0202
12. Bai Y, Lang L, Zhao W, Niu R. Long non-coding RNA HOXA11-AS promotes non-small cell lung cancer tumorigenesis through microRNA-148a-3p/DNMT1 regulatory axis. *Onco Targets Therapy.* (2019) 12:11195–206. doi: 10.2147/OTT.S198367
13. Li W, Zhang B, Jia Y, Shi H, Wang H, Guo Q, et al. LncRNA LOXL1-AS1 regulates the tumorigenesis and development of lung adenocarcinoma through sponging miR-423-5p and targeting MYBL2. *Cancer Med.* (2020) 9:689–99. doi: 10.1002/cam4.2641
14. Safarpour-Dehkordi M, Doosti A, Jami MS. Integrative analysis of lncRNAs in kidney cancer to discover a new lncRNA (LINC00847) as a therapeutic target for staphylococcal enterotoxin tst gene. *Cell J.* (2020) 22(Suppl. 1):101–9. doi: 10.22074/cellj.2020.6996
15. Hu Y, Gu X, Duan Y, Shen Y, Xie X. Bioinformatics analysis of prognosis-related long non-coding RNAs in invasive breast carcinoma. *Oncol Letters.* (2020) 20:113–22. doi: 10.3892/ol.2020.11558
16. Yu H, Xu Q, Liu F, Ye X, Wang J, Meng X. Identification and validation of long noncoding RNA biomarkers in human non-small-cell lung carcinomas. *J Thor Oncol.* (2015) 10:645–54. doi: 10.1097/JTO.0000000000000470
17. Lv X, Lian Y, Liu Z, Xiao J, Zhang D, Yin X. Exosomal long non-coding RNA LINC00662 promotes non-small cell lung cancer progression by miR-320d/E2F1 axis. *Aging.* (2021) 13:6010–24. doi: 10.18632/aging.202522
18. Li H, Tong F, Meng R, Peng L, Wang J, Zhang R, et al. E2F1-mediated repression of WNT5A expression promotes brain metastasis dependent on the ERK1/2 pathway in EGFR-mutant non-small cell lung cancer. *Cell Mol Life Sci.* (2021) 78:2877–91. doi: 10.1007/s00018-020-03678-6
19. Qi X, Zhang DH, Wu N, Xiao JH, Wang X, Ma W. ceRNA in cancer: possible functions and clinical implications. *J Med Genet.* (2015) 52:710–8. doi: 10.1136/jmedgenet-2015-103334
20. Jacobsen MM, Silverstein SC, Quinn M, Waterston LB, Thomas CA, Benneyan JC, et al. Timeliness of access to lung cancer diagnosis and treatment: a scoping literature review. *Lung Cancer.* (2017) 112:156–64. doi: 10.1016/j.lungcan.2017.08.011
21. Quaratino S, Forssmann U, Marschner JP. New approaches in immunotherapy for the treatment of lung cancer. *Curr Top Microbiol Immunol.* (2017) 405:1–31. doi: 10.1007/82_2014_428
22. Long Y, Wang X, Youmans DT, Cech TR. How do lncRNAs regulate transcription? *Sci Adv.* (2017) 3:eaao2110. doi: 10.1126/sciadv.aao2110
23. Ferrè F, Colantoni A, Helmer-Citterich M. Revealing protein-lncRNA interaction. *Bri Bio.* (2016) 17:106–16. doi: 10.1093/bib/bbv031
24. Peng WX, Koirala P, Mo YY. LncRNA-mediated regulation of cell signaling in cancer. *Oncogene.* (2017) 36:5661–7. doi: 10.1038/onc.2017.184
25. Li F, Wang X, Yang L. MicroRNA-147 targets BDNF to inhibit cell proliferation, migration and invasion in non-small cell lung cancer. *Oncol Letters.* (2020) 20:1931–7. doi: 10.3892/ol.2020.11715
26. Sui CJ, Xu F, Shen WF, Dai BH, Lu JJ, Zhang MF, et al. MicroRNA-147 suppresses human hepatocellular carcinoma proliferation migration and chemosensitivity by inhibiting HOXC6. *Am J Cancer Res.* (2016) 6:2787–98.
27. Yánez DC, Ross S, Crompton T. The IFITM protein family in adaptive immunity. *Immunology.* (2020) 159:365–72. doi: 10.1111/imm.13163
28. Liang R, Li X, Zhu X. Deciphering the roles of IFITM1 in tumors. *Mol Diag Therapy.* (2020) 24:433–41. doi: 10.1007/s40291-020-00469-4
29. Yang J, Li L, Xi Y, Sun R, Wang H, Ren Y, et al. Combination of IFITM1 knockdown and radiotherapy inhibits the growth of oral cancer. *Cancer Sci.* (2018) 109:3115–28. doi: 10.1111/cas.13640
30. Zheng W, Zhao Z, Yi X, Zuo Q, Li H, Guo X, et al. Down-regulation of IFITM1 and its growth inhibitory role in cervical squamous cell carcinoma. *Cancer Cell Int.* (2017) 17:88. doi: 10.1186/s12935-017-0456-0
31. Yan J, Jiang Y, Lu J, Wu J, Zhang M. Inhibiting of proliferation, migration, and invasion in lung cancer induced by silencing interferon-induced transmembrane protein 1 (IFITM1). *Bio Med Res Int.* (2019) 2019. doi: 10.1155/2019/9085435

Conflict of Interest: The authors declare that the research was conducted in the absence of any commercial or financial relationships that could be construed as a potential conflict of interest.

Copyright © 2021 Li, Chen, Wan, Shi, Wang, He and Tang. This is an open-access article distributed under the terms of the Creative Commons Attribution License (CC BY). The use, distribution or reproduction in other forums is permitted, provided the original author(s) and the copyright owner(s) are credited and that the original publication in this journal is cited, in accordance with accepted academic practice. No use, distribution or reproduction is permitted which does not comply with these terms.

frontiers in Medicine

ORIGINAL RESEARCH
published: 27 April 2021
doi: 10.3389/fmed.2021.651473

hsa-miR-33-5p as a Therapeutic Target Promotes Apoptosis of Breast Cancer Cells *via* Selenoprotein T

Wei Zhuang[1†], *Jianhui Liu*[2†] *and Wenjin Li*[3*]

[1] Department of Laboratory, Jinan People's Hospital Affiliated to Shandong First Medical University, Jinan, China, [2] Department of Radiotherapy, Yantai Yuhuangding Hospital, Yantai, China, [3] Department of Breast, Linyi Cancer Hospital, Linyi, China

Objective: Increasing evidence suggests that microRNA (miRNA) participates in regulating tumor cell apoptosis. We aimed to observe the effect of hsa-miR-33-5p on the apoptosis of breast cancer cells and to explore its regulatory relationship with selenoprotein T (SelT).

Methods: RT-qPCR was used to examine the expression of hsa-miR-33-5p and SelT both in breast cancer tissues and cells. MCF-7 and MDA-MB-231 cells were transfected with hsa-miR-33-5p mimics or si-SelT. Then, a flow cytometry assay was carried out to examine the apoptosis of cells. Furthermore, SelT and apoptosis-related proteins including caspase-3, caspase-8, caspase-9, Bax, and Bcl-2 were detected *via* RT-qPCR and western blot. A luciferase reporter assay was utilized for assessing whether SelT was targeted by hsa-miR-33-5p.

Results: Downregulated hsa-miR-33-5p was found both in breast cancer tissues and cells. After its overexpression, MCF-7 cell apoptosis was significantly promoted. Furthermore, our data showed that miR-33-5p elevated apoptosis-related protein expression in MCF-7 cells. Contrary to hsa-miR-33-5p, SelT was upregulated both in breast cancer tissues and cells. SelT expression was significantly inhibited by hsa-miR-33-5p overexpression. The luciferase reporter assay confirmed that SelT was a direct target of hsa-miR-33-5p. SelT overexpression could ameliorate the increase in apoptosis induced by hsa-miR-33-5p mimics.

Conclusion: Our findings revealed that hsa-miR-33-5p, as a potential therapeutic target, could accelerate breast cancer cell apoptosis.

Keywords: breast cancer, hsa-miR-33-5p, Selenoprotein T, apoptosis, therapeutic target

OPEN ACCESS

Edited by:
Fu Wang,
Xi'an Jiaotong University, China

Reviewed by:
Chaoyun Pan,
Sun Yat-sen University, China
Bibo Tan,
Fourth Hospital of Hebei Medical University, China

***Correspondence:**
Wenjin Li
lyzllwj@sina.com

[†] *These authors have contributed equally to this work*

Specialty section:
This article was submitted to Precision Medicine, a section of the journal Frontiers in Medicine

Received: *09 January 2021*
Accepted: *15 March 2021*
Published: *27 April 2021*

Citation:
Zhuang W, Liu J and Li W (2021) hsa-miR-33-5p as a Therapeutic Target Promotes Apoptosis of Breast Cancer Cells via Selenoprotein T. Front. Med. 8:651473. doi: 10.3389/fmed.2021.651473

INTRODUCTION

Breast cancer is a commonly diagnosed malignancy worldwide (1). Despite considerable progress in early detection and diagnosis, breast cancer patients' prognosis has been only slightly improved (2, 3). Moreover, its incidence in developed countries is still high, while it is increasing in developing countries due to changes in lifestyle and life expectancy (4). Hence, it is of significance to explore novel and effective therapeutic targets for breast cancer.

miRNA is a small and evolutionarily conserved non-coding RNA, with about 18–25 nucleotides in its length (5, 6). It has been widely accepted that miRNAs can bind to the 3′ untranslated region (UTR) of target genes, thereby negatively regulating their expression and causing the degradation of target mRNAs (7–9). It has been discovered that miRNAs are involved in many critical cell processes by regulating target genes at a post-transcriptional level, including cell apoptosis (10–12). There is ample evidence that aberrantly expressed miRNAs could be associated with breast cancer progression (13–15). So far, miRNAs have become promising markers for breast cancer due to the fact that they can be easily detected in tumor biopsies or body fluids (16). Dysregulated miRNAs have been recognized as early indicators and pathogenic factors of breast cancer (7, 17, 18). Furthermore, miRNA expression can predict the prognosis and progression of breast cancer (19–21). Therefore, a deeper understanding of miRNAs may provide opportunities for novel treatment strategies for breast cancer.

Previous studies found that hsa-miR-33-5p could induce osteoblast differentiation through targeting Hmga2 (22). Apoptosis is an important cellular process that is controlled by a variety of factors, including miRNAs. Abnormal apoptosis exhibits a close relationship with breast cancer occurrence, yet the function of hsa-miR-33-5p in breast cancer cell apoptosis needs to be clarified. In this study, our results suggested that hsa-miR-33-5p expression was downregulated in breast cancer. More importantly, its overexpression could promote breast cancer cell apoptosis. By further analysis, SelT could be directly targeted by hsa-miR-33-5p. Thus, our study proposed that hsa-miR-33-5p, as an underlying therapeutic target, could facilitate breast cancer cell apoptosis by SelT.

MATERIALS AND METHODS

Tissue Specimens

Breast cancer tissues as well as corresponding normal tissue specimens were harvested from 20 patients with breast cancer from January 2018 to December 2019 in the Linyi Cancer Hospital. All tissues were instantly stored in liquid nitrogen. No patient received chemotherapy or radiation before surgery. All the patients provided written informed consent. The study was approved by the Ethics Committee of Linyi Cancer Hospital (LYZLYY-2018-012).

Bioinformatics Analysis

The MiRWalk 2.0 database (http://mirwalk.uni-hd.de/) was used to predict the targets of hsa-miR-33-5p, which provides predicted and validated miRNA–target interactions (23). Furthermore, the immunohistochemical results of apoptosis-related proteins including Bax, Bcl2, caspase-3/8/9, and SelT in breast cancer and normal samples were downloaded from the Human Protein Atlas website (https://www.proteinatlas.org/).

Abbreviations: miRNAs, microRNAs; SelT, selenoprotein T; UTR, untranslated region.

Cell Culture and Transfection

Human breast cancer MCF-7 and MDA-MB-231 cells and normal breast MCF10A cells were grown in 1640 medium (Invitrogen, CA, USA) with 10% FBS at 37°C and 5% CO_2 in a humid environment. hsa-miR-33-5p mimics, siRNAs against SelT, and corresponding controls were used for transfection into two cells *via* Lipofectamine 2000 (Invitrogen). At 48 h after transfection, the cells were collected for further analysis. The cultured cells were treated with H_2O_2 as a control.

Flow Cytometry

Cellular apoptotic levels were examined *via* the annexin V-FITC/PI apoptosis detection kit (Keygene, Nanjing, China). At 48 h after transfection, the cell resuspension (100 μl) was treated with annexin V-FITC/PI lasting for 15 min in the dark. The apoptotic rates were detected by flow cytometry.

RT-qPCR

Total RNA was extracted using TRIzol (Invitrogen), followed by reverse transcription into cDNAs. The RT-qPCR was carried out on the real-time PCR system. The primer sequences of hsa-miR-33-5p and SelT were as follows: hsa-miR-33-5p, 5′-GGAMCTWYACGVAGGTG-3′ (forward), 5′-TGAAM TGCACRGAGCTTGC-3′ (reverse); SelT, 5′-TTGCTGCTTCT GCTGGTG-3′ (forward), 5′-CGTGGCGTACTGCATCTT-3′(reverse); β-actin, 5′-CGAGAAGATGACCCAGATCATG-3′ (forward), 5′-GTGAAGCTGTAGCCGCGCTCGG-3′ (reverse). β-actin was used as a control. Then, their expression levels were determined with the $2^{-\Delta\Delta CT}$ method.

Western Blot

Protein was extracted *via* RIPA lysis buffers (Beyotime, China), which was assessed with a bicinchoninic acid protein assay kit (Beyotime). The sample was separated through sodium dodecyl sulfate polyacrylamide gel electrophoresis and transferred onto a PVDF membrane. Then, the membrane was blocked using 5% non-fat milk for 1 h, which was incubated overnight with primary antibodies at 4°C and secondary antibody (1:2,000; Abcam, USA) lasting 1 h at room temperature. The primary antibodies included anti-Bax (1:1,000; Abcam), anti-Bcl2 (1:1,000; Abcam), anti-cleaved-caspase-3 (1:1,000; Abcam), anti-pro-caspase-3 (1:1,000; Abcam), anti-cleaved-caspase-8 (1:1,000; Abcam), anti-pro-caspase-8 (1:1,000; Abcam), anti-cleaved-caspase-9 (1:1,000; Abcam), anti-pro-caspase-9 (1:1,000; Abcam), and anti-GAPDH (1:1,000; Abcam). GAPDH served as a control. Image Lab™ Software (Bio-Rad, China) was used to quantify the intensity of blots.

Luciferase Reporter Assay

The wild-type luciferase vector (wt-LucSelT) containing hsa-miR-33-5p response elements in the 3′UTR of SelT, or the mutant (mut-LucSelT) vector was constructed and transfected in RKO cells with hsa-miR-33-5p mimics or its control. Luciferase reporter assay systems (Promega, USA) were utilized to quantify the firefly and Renilla luciferase activity.

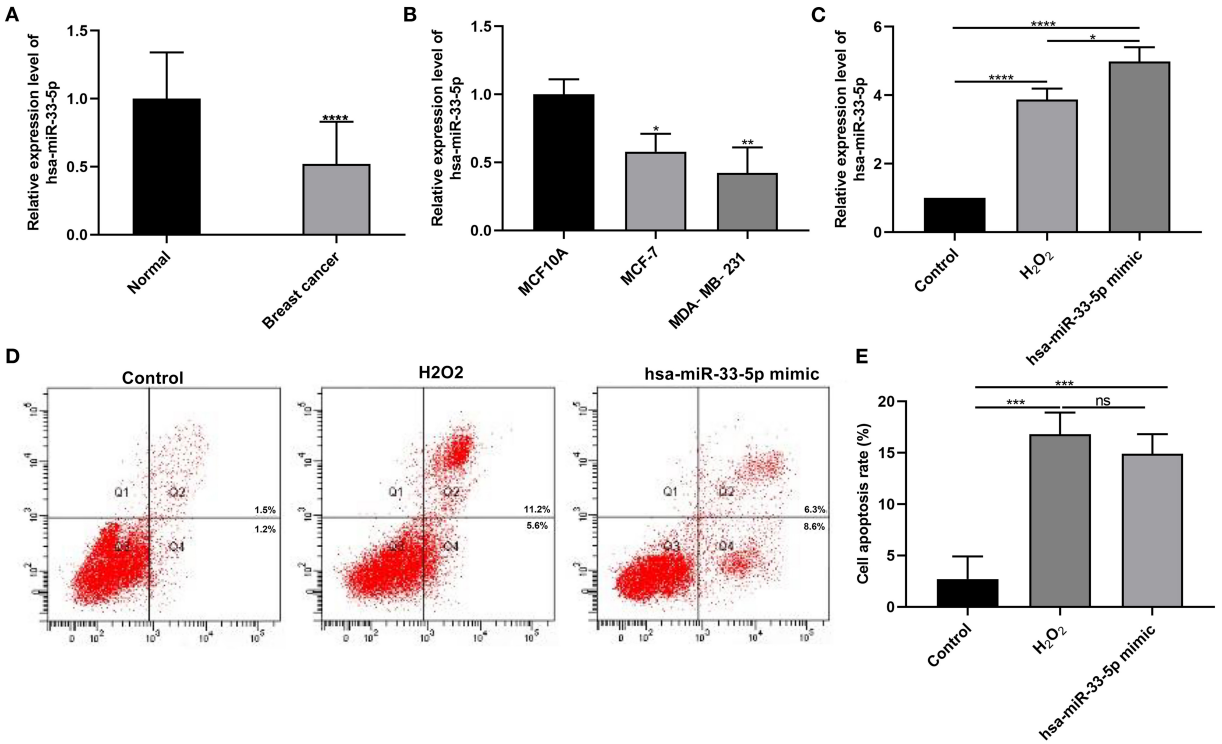

FIGURE 1 | hsa-miR-33-5p is downregulated in breast cancer, and its overexpression promotes the apoptosis of breast cancer cells. **(A,B)** RT-qPCR results showing downregulated hsa-miR-33-5p both in breast cancer tissues **(A)** and cells **(B)**. **(C)** RT-qPCR showing hsa-miR-33-5p expression in MCF-7 cells following transfection by hsa-miR-33-5p mimics. **(D,E)** Flow cytometry for the cell apoptosis in MCF-7 cells under transfection by hsa-miR-33-5p mimics. *$p < 0.05$; **$p < 0.01$; ***$p < 0.001$; ****$p < 0.0001$; ns, not significant.

Transferase-Mediated dUTP Nick End Labeling Staining

A transferase-mediated dUTP nick end labeling (TUNEL) kit (Atagenix, Wuhan, China) was used to assess the apoptotic levels. The sections were treated with TUNEL solution in the dark for 60 min. Afterwards, the samples were incubated with 0.05 μg/μl of 4′,6-diamidino-2-phenylindole solution for 10 min. Anti-fluorescence quenching mounting tablets were utilized for mounting. Images were investigated under a fluorescence microscope (Olympus, Japan).

Statistical Analyses

Statistical analyses were performed using GraphPad Prism 8.0. Data are expressed as mean ± standard deviation from at least three independent experiments. Comparison between different groups was analyzed using Student's *t* test or one-way analysis of variance. $P < 0.05$ was considered statistically significant.

RESULTS

hsa-miR-33-5p Is Downregulated in Breast Cancer and Its Overexpression Promotes the Apoptosis of Breast Cancer Cells

According to RT-qPCR results, hsa-miR-33-5p expression was lower in breast cancer than normal tissue specimens (**Figure 1A**; $p < 0.0001$). Furthermore, its lower expression was observed in MCF-7 as well as MDA-MB-231 cells more than MCF10A cells (both $p < 0.05$; **Figure 1B**). These results suggested that hsa-miR-33-5p was downregulated in breast cancer tissues as well as cells. As shown in **Figure 1C**, hsa-miR-33-5p mimics significantly overexpressed its expression compared to control ($p < 0.0001$). We also found that H_2O_2 significantly elevated hsa-miR-33-5p expression in MCF-7 cells (**Figure 1C**; $p < 0.0001$). hsa-miR-33-5p expression was significantly higher in MCF-7 cells following transfection by hsa-miR-33-5p overexpression than H_2O_2 treatment (**Figure 1C**; $p < 0.05$). The above-mentioned results suggested that hsa-miR-33-5p was successfully overexpressed. The flow cytometry results suggested that hsa-miR-33-5p overexpression could promote the apoptosis of MCF-7 cells (**Figures 1D,E**; $p < 0.001$). Furthermore, compared to control, H_2O_2 treatment also significantly induced cell apoptosis ($p < 0.001$). However, there was no significant difference in cell apoptosis between cells transfected with hsa-miR-33-5p mimics and H_2O_2 treatment.

hsa-miR-33-5p Significantly Mediates Apoptosis-Related Proteins in Breast Cancer Cells

Apoptosis is a key cellular process in breast cancer. We detected apoptosis-related proteins in tumor tissues. **Figure 2A**

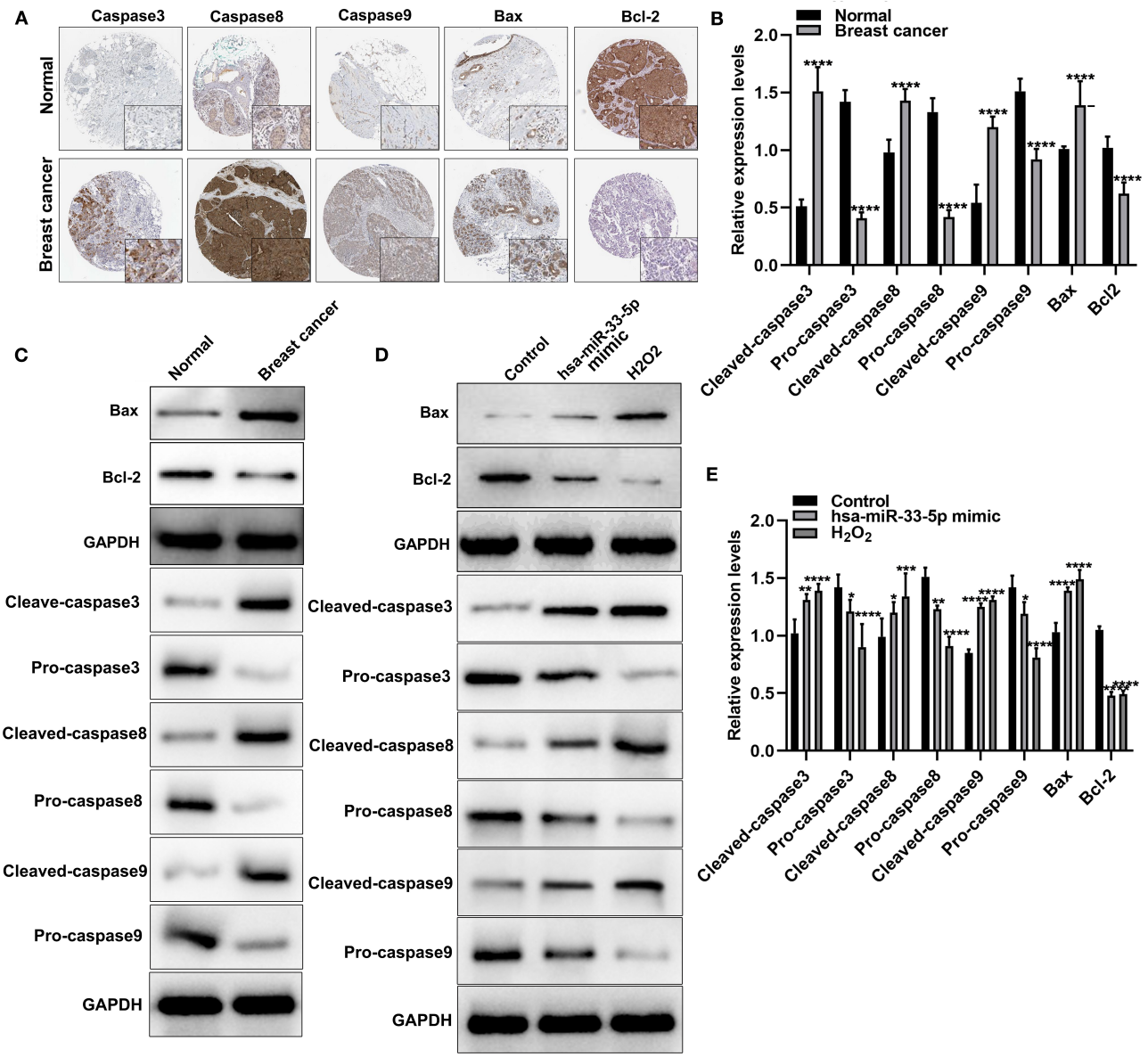

FIGURE 2 | hsa-miR-33-5p significantly mediates apoptosis-related proteins in breast carcinoma cells. **(A)** Immunohistochemistry for the expression and distribution of the apoptosis-related proteins including caspase-3/8/9, Bax, and Bcl-2 in breast cancer tissues and normal tissues. **(B,C)** Western blot for the expression of apoptosis-related proteins including cleaved caspase-3, pro-caspase-3, cleaved caspase-8, pro-caspase-8, cleaved caspase-9, pro-caspase-9, Bax, and Bcl-2 in breast cancer tissues and normal tissues. **(D,E)** Western blot for the expression of cleaved caspase-3, pro-caspase-3, cleaved caspase-8, pro-caspase-8, cleaved caspase-9, pro-caspase-9, Bax, and Bcl-2 in breast cancer cells transfected with hsa-miR-33-5p mimics. *$p < 0.05$; **$p < 0.01$; ***$p < 0.001$; ****$p < 0.0001$.

depicts the expression and distribution of these apoptosis-related proteins including caspase-3, caspase-8, caspase-9, Bax, and Bcl-2 in breast cancer tissues according to immunohistochemistry results. Furthermore, using western blot, we found that cleaved caspase-3, cleaved caspase-8, cleaved caspase-9, and Bax proteins were significantly overexpressed in breast cancer and normal tissues (all $p < 0.0001$; **Figures 2B,C**). Meanwhile, pro-caspase-3, pro-caspase-8, pro-caspase-9, and Bcl-2 protein (all $p < 0.0001$) exhibited significantly low expressions in breast cancer tissues (**Figures 2B,C**). hsa-miR-33-5p overexpression significantly elevated the expression of cleaved caspase-3 ($p < 0.01$), cleaved caspase-8 ($p < 0.05$), cleaved caspase-9 ($p < 0.0001$), and Bax ($p < 0.0001$) compared to control (**Figures 2D,E**). Moreover, pro-caspase-3 ($p < 0.05$), pro-caspase-8 ($p < 0.01$), pro-caspase-9 ($p < 0.05$), and Bcl-2 ($p < 0.0001$) expressions were distinctly lowered in MCF-7 cells after transfection by overexpressed hsa-miR-33-5p (**Figures 2D,E**). Similar results were investigated in MCF-7 cells exposed to H_2O_2. Thus, hsa-miR-33-5p could mediate apoptosis-related proteins in breast cancer cells.

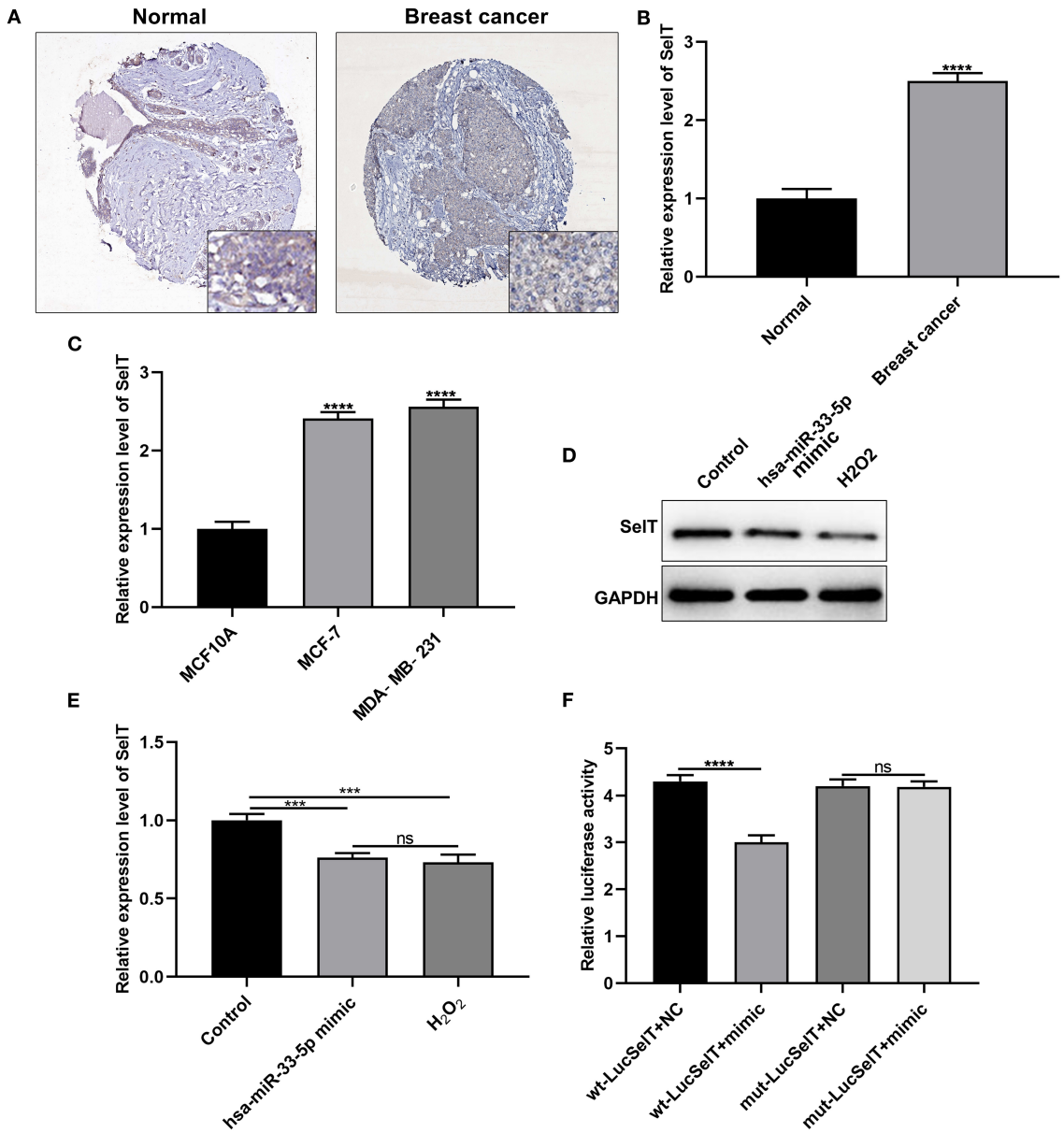

FIGURE 3 | SelT is upregulated in breast carcinoma and is an underlying target of hsa-miR-33-5p. **(A)** Immunohistochemistry for the expression of SelT in breast cancer and normal tissues. **(B,C)** RT-qPCR results showing upregulated SelT both in breast cancer tissues **(B)** and cells **(C)**. **(D,E)** Western blot results for the expression of SelT in breast cancer cells transfected with hsa-miR-33-5p mimics or treated with H_2O_2. **(F)** Luciferase reporter assay for hsa-miR-33-5p and SelT. ***$p < 0.001$; ****$p < 0.0001$; ns, not significant.

SelT Is Upregulated in Breast Carcinoma and Is a Target of hsa-miR-33-5p

As demonstrated by immunohistochemistry and RT-qPCR results, SelT expression had a significantly higher level in breast carcinoma than normal tissue samples (**Figures 3A,B**; $p < 0.0001$). Similarly, its upregulation was found in MCF-7 and MDA-MB-231 cells more than MCF10A cells (**Figure 3C**; $p < 0.001$). The above-mentioned results confirmed the upregulation of SelT in both breast cancer tissues and cells.

As predicted, SelT could be a target of hsa-miR-33-5p. As shown in **Figures 3D,E**, SelT was significantly suppressed in breast cancer cells following transfection by overexpressed hsa-miR-33-5p or H_2O_2 treatment at the protein level ($p < 0.001$). However, no statistical difference in SelT expression was observed between hsa-miR-33-5p overexpression and H_2O_2 treatment groups. The luciferase reporter assay results confirmed that SelT was directly targeted by hsa-miR-33-5p (**Figure 3F**).

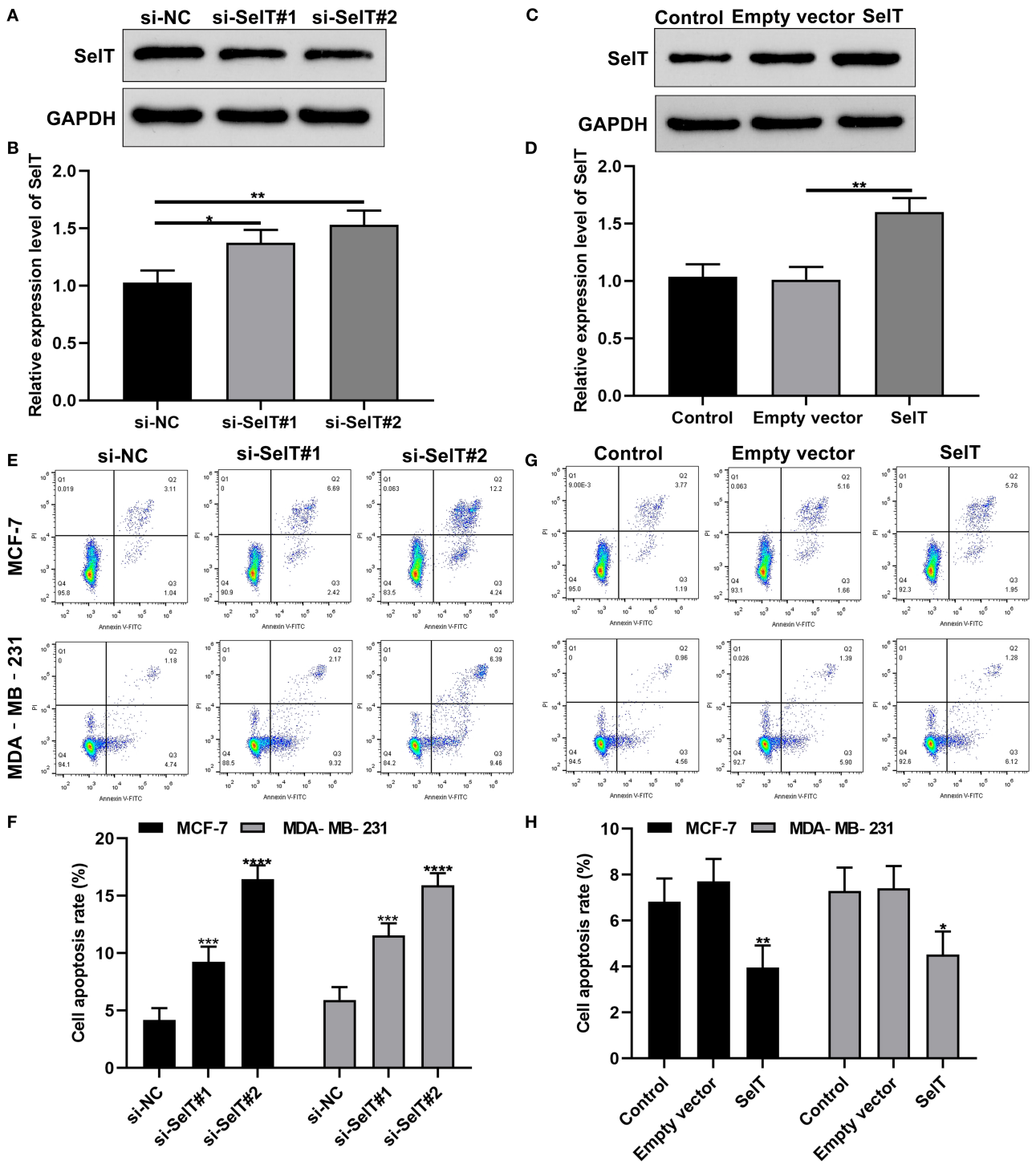

FIGURE 4 | Inhibition of SelT promotes the apoptosis of breast cancer cells. **(A,B)** Western blot for the expression of SelT in breast cancer cells transfected with si-SelT#1 and si-SelT#2. **(C,D)** Validation of SelT expression in breast cancer cells transfected with SelT by western blot. **(E,F)** Flow cytometry assay for apoptotic levels of MCF-7 as well as MDA-MB-231 cells transfected by si-SelT#1 and si-SelT#2. **(G,H)** Assessment of breast carcinoma cell apoptosis under SelT overexpression. $^{*}p < 0.05$; $^{**}p < 0.01$; $^{***}p < 0.001$; $^{****}p < 0.0001$.

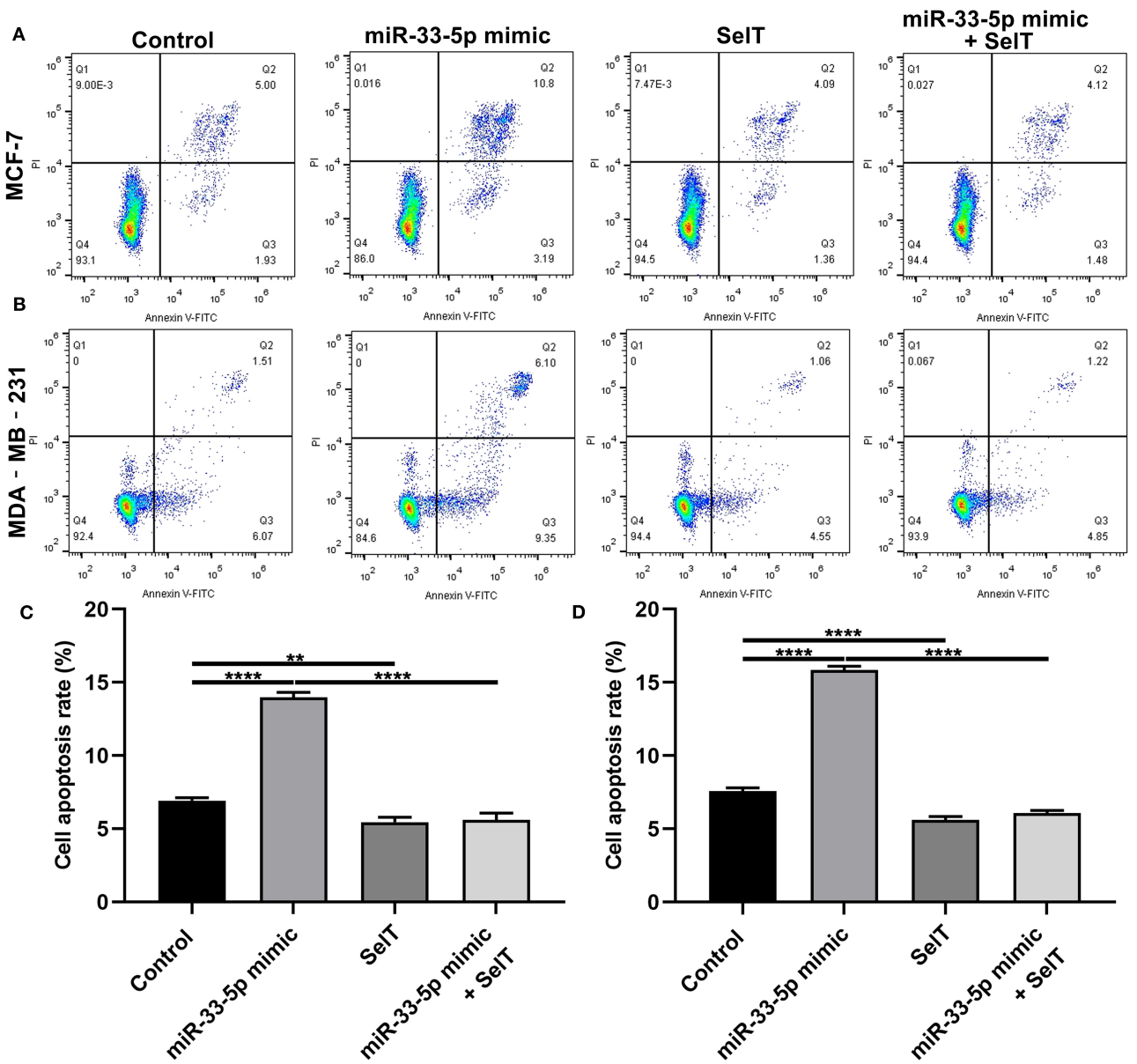

FIGURE 5 | hsa-miR-33-5p promotes the apoptosis of breast cancer cells *via* SelT. **(A,B)** Representative images of flow cytometry assay results. **(C)** MCF-7 as well as **(D)** MDA-MB-231 cell apoptosis was determined when transfected by hsa-miR-33-5p mimics and/or SelT. $^{**}p < 0.01$; $^{****}p < 0.0001$.

Inhibition of SelT Promotes the Apoptosis of Breast Cancer Cells

We further investigated whether SelT could promote the apoptosis of breast cancer cells. Two siRNAs targeting SelT were designed and transfected into breast cancer cells. As shown in **Figures 4A,B**, SelT expression was significantly suppressed by si-SelT#1 ($p < 0.05$) and si-SelT#2 ($p < 0.01$). Furthermore, SelT was successfully overexpressed in breast cancer cells (**Figures 4C,D**; $p < 0.01$). The flow cytometry data demonstrated that SelT knockdown markedly elevated the apoptotic levels of MCF-7 as well as MDA-MB-231 cells (**Figures 4E,F**). Meanwhile, SelT overexpression distinctly inhibited the apoptosis of MCF-7 as well as MDA-MB-231 cells (**Figures 4G,H**). The data demonstrated that inhibition of SelT may promote the apoptosis of breast cancer cells.

hsa-miR-33-5p Promotes the Apoptosis of Breast Cancer Cells *via* SelT

Our further analysis found that hsa-miR-33-5p mimics promoted the apoptosis of MCF-7 ($p < 0.0001$) and MDA-MB-231 cells ($p < 0.0001$), which was significantly ameliorated by SelT overexpression ($p < 0.0001$), as shown in **Figures 5A–D**. Furthermore, TUNEL staining results confirmed that SelT overexpression distinctly ameliorated the increase in apoptosis

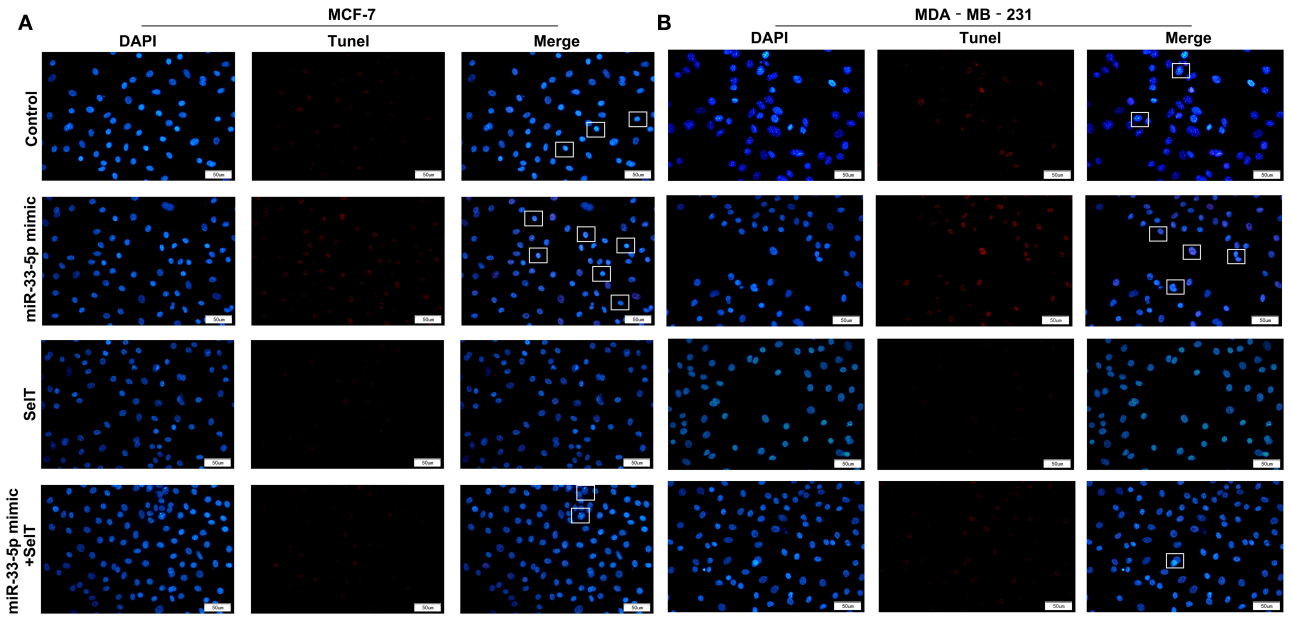

FIGURE 6 | TUNEL staining for **(A)** MCF-7 as well as **(B)** MDA-MB-231 cell apoptosis transfected by hsa-miR-33-5p mimics and/or SelT. Bar = 50 μm. Magnification, ×400.

induced by hsa-miR-33-5p mimics in MCF-7 (**Figure 6A**) and MDA-MB-231 (**Figure 6B**) cells. These data demonstrated that hsa-miR-33-5p may promote the apoptosis of breast cancer cells *via* SelT.

DISCUSSION

In these findings, we identified a novel miRNA, and found that hsa-miR-33-5p was downregulated in both breast cancer tissues and cells. Its overexpression significantly promoted the apoptosis of breast cancer cells. Furthermore, SelT was an underlying target of hsa-miR-33-5p in breast cancer. hsa-miR-33-5p could facilitate the apoptosis of breast cancer cells *via* SelT. Our findings deepened the understanding of molecular mechanisms in breast cancer progression and provided potential therapeutic targets.

Our findings demonstrated that hsa-miR-33-5p was dysregulated in breast cancer. So far, no studies have reported the expression and role of hsa-miR-33-5p in breast cancer. As previously reported, hsa-miR-33-5p could induce osteoblast differentiation through targeting Hmga2 (22, 24). Its knockdown could inhibit abdominal aortic aneurysm development through ABCA1 expression and activation of the PI3K/Akt pathway (25). Lowly expressed hsa-miR-33-5p is involved in inhibiting the apoptosis of murine dorsal root ganglion neurons (26). Furthermore, hsa-miR-33-5p is in association with mesangial cell apoptosis in diabetic nephropathy (27).

Resistance to apoptosis is one of the hallmarks of cancer (28). Apoptosis could maintain homeostasis *via* mediating senescent cell death (29). Tumor cells can resist apoptosis by upregulating anti-apoptotic proteins and/or reducing pro-apoptotic proteins (30). Apoptotic caspases mainly include initiator caspases (caspase-2/8/9/10) and executioner caspases (caspase-3/6/7) (31). Bax is an apoptotic protein, and Bcl2 is an important regulator of anti-apoptosis, both of which are involved in mitochondrial death signals (32). Thus, inducing apoptosis of tumor cells has a promising potential to eradicate cancer cells. In this study, we examined apoptosis-related proteins including caspase-3/8/9, Bax, and Bcl-2. We found that caspase-3/8/9 and Bax expressions were elevated in breast cancer tissues, while Bcl-2 expression was decreased in breast cancer tissues. These findings revealed that the apoptosis process could occur in breast cancer. As with previous findings, many miRNAs could participate in breast cancer cell apoptosis. For example, hsa-miR-106a (33), hsa-miR-205 (34), and hsa-miR-216a (35) could induce the apoptosis of breast carcinoma cells. We explored the regulatory effect of hsa-miR-33-5p in breast cancer. hsa-miR-33-5p overexpression was successfully induced in MCF-7 cells. Its overexpression significantly induced the apoptosis of breast carcinoma cells as shown in flow cytometry results. Oxidative stress is involved in the process of apoptosis. H_2O_2 is one of the major components of exogenous reactive oxygen species, which is considered to be a key factor in regulating tumor cell viability (36). Different cell types have different responses to H_2O_2-induced oxidative stress and cell viability both in a dose- and time-dependent manner (37). As previously described, in this study, H_2O_2 exposure significantly induced breast cancer cell apoptosis. Furthermore, H_2O_2 exposure promoted hsa-miR-33-5p expression in MCF-7 cells. hsa-miR-33-5p overexpression significantly elevated caspase-3, caspase-8, caspase-9, and Bax expressions, while Bcl-2 was significantly inhibited in MCF-7 cells with hsa-miR-33-5p overexpression. As expected, similar results were investigated in MCF-7 cells exposed with H_2O_2. The above-mentioned data confirmed that hsa-miR-33-5p expression can be induced by oxidative stress.

Upregulated SelT was found in both breast cancer tissues and cells. Its knockdown could promote the apoptosis of breast cancer cells. SelT is a recently characterized thioredoxin-like protein that is widely expressed during development (38). It is upregulated during neuroendocrine cell differentiation (39, 40). Furthermore, SelT expression is strictly regulated in time. In most adult tissues, the expression level of SelT is decreased (41, 42). Previous studies have found that SelT is dysregulated in a few cancers like gastric cancer (43) and bladder cancer (44). hsa-miR-33-5p could significantly inhibit the expression of SelT. As validated by the luciferase reporter assay, SelT was directly targeted by hsa-miR-33-5p. hsa-miR-33-5p could accelerate the apoptosis of breast cancer cells *via* SelT. Furthermore, the results showed that, when breast cancer cells were exposed to H_2O_2, SelT expression was significantly inhibited. SelT could regulate various biological processes, like apoptosis. It possesses oxidoreductase functions and is localized in the endoplasmic reticulum. A similar result has found that, when LO2 cells were exposed to H_2O_2, SelX expression was suppressed and cell apoptosis was induced (45). The above-mentioned findings were indicative of the fact that SelT may participate in oxidative stress response and apoptosis in breast cancer, which was consistent with a previous study (46).

In conclusion, we found that hsa-miR-33-5p could induce the apoptosis of breast cancer cells. Moreover, SelT was directly targeted by hsa-miR-33-5p in breast cancer. hsa-miR-33-5p may facilitate the apoptosis of breast cancer cells *via* SelT. In future studies, we will continue studying the regulatory relationships between hsa-miR-33-5p and SelT and their functions on breast carcinoma cell apoptosis in animal models.

CONCLUSION

In this study, downregulated hsa-miR-33-5p was investigated in breast cancer tissues and cells. Its overexpression could promote the apoptosis of breast cancer cells. Furthermore, SelT was targeted by hsa-miR-33-5p. These findings may offer novel therapeutic targets against breast carcinoma.

DATA AVAILABILITY STATEMENT

The datasets presented in this study can be found in online repositories. The names of the repository/repositories and accession number(s) can be found in the article/supplementary material.

ETHICS STATEMENT

The studies involving human participants were reviewed and approved by The study was approved by the Ethics Committee of Linyi Cancer Hospital (LYZLYY-2018-012). The patients/participants provided their written informed consent to participate in this study.

AUTHOR CONTRIBUTIONS

WL conceived and designed the study. WZ conducted most of the experiments and data analysis and wrote the manuscript. JL participated in collecting data and helped to draft the manuscript. All the authors reviewed and approved the manuscript.

REFERENCES

1. Bray F, Ferlay J, Soerjomataram I, Siegel RL, Torre LA, Jemal A. Global cancer statistics 2018: GLOBOCAN estimates of incidence and mortality worldwide for 36 cancers in 185 countries. *CA Cancer J Clin.* (2018) 68:394–424. doi: 10.3322/caac.21492
2. Mavaddat N, Michailidou K, Dennis J, Lush M, Fachal L, Lee A, et al. Polygenic risk scores for prediction of breast cancer and breast cancer subtypes. *Am J Hum Genet.* (2019) 104:21–34. doi: 10.1016/j.ajhg.2018.11.002
3. Siegel RL, Jemal A, Wender RC, Gansler T, Ma J, Brawley OW. An assessment of progress in cancer control. *CA Cancer J Clin.* (2018) 68:329–39. doi: 10.3322/caac.21460
4. Siegel RL, Miller KD, Jemal A. Cancer statistics, 2018. *CA Cancer J Clin.* (2018) 68:7–30. doi: 10.3322/caac.21442
5. Di Leva G, Garofalo M, Croce CM. MicroRNAs in cancer. *Annu Rev Pathol.* (2014) 9:287–314. doi: 10.1146/annurev-pathol-012513-104715
6. Rupaimoole R, Slack FJ. MicroRNA therapeutics: towards a new era for the management of cancer and other diseases. *Nat Rev Drug Discov.* (2017) 16:203–22. doi: 10.1038/nrd.2016.246
7. Fan CN, Ma L, Liu N. Systematic analysis of lncRNA-miRNA-mRNA competing endogenous RNA network identifies four-lncRNA signature as a prognostic biomarker for breast cancer. *J Transl Med.* (2018) 16:264. doi: 10.1186/s12967-018-1640-2
8. Pham VV, Zhang J, Liu L, Truong B, Xu T, Nguyen TT, et al. Identifying miRNA-mRNA regulatory relationships in breast cancer with invariant causal prediction. *BMC Bioinformatics.* (2019) 20:143. doi: 10.1186/s12859-019-2668-x
9. Wu Q, Guo L, Jiang F, Li L, Li Z, Chen F. Analysis of the miRNA-mRNA-lncRNA networks in ER+ and ER- breast cancer cell lines. *J Cell Mol Med.* (2015) 19:2874–87. doi: 10.1111/jcmm.12681
10. Breunig C, Pahl J, Kublbeck M, Miller M, Antonelli D, Erdem N, et al. MicroRNA-519a-3p mediates apoptosis resistance in breast cancer cells and their escape from recognition by natural killer cells. *Cell Death Dis.* (2017) 8:e2973. doi: 10.1038/cddis.2017.364
11. Sharma S, Nagpal N, Ghosh PC, Kulshreshtha R. P53-miR-191-SOX4 regulatory loop affects apoptosis in breast cancer. *Rna.* (2017) 23:1237–46. doi: 10.1261/rna.060657.117
12. Xue J, Chi Y, Chen Y, Huang S, Ye X, Niu J, et al. MiRNA-621 sensitizes breast cancer to chemotherapy by suppressing FBXO11 and enhancing p53 activity. *Oncogene.* (2016) 35:448–58. doi: 10.1038/onc.2015.96
13. Aggarwal V, Priyanka K, Tuli HS. Emergence of circulating MicroRNAs in breast cancer as diagnostic and therapeutic efficacy biomarkers. *Mol Diagn Ther.* (2020) 24:153–73. doi: 10.1007/s40291-020-00447-w
14. Huang R, Li J, Pan F, Zhang B, Yao Y. The activation of GPER inhibits cells proliferation, invasion and EMT of triple-negative breast cancer via CD151/miR-199a-3p bio-axis. *Am J Transl Res.* (2020) 12:32–44.
15. Kanchan RK, Siddiqui JA, Mahapatra S, Batra SK, Nasser MW. microRNAs Orchestrate pathophysiology of breast cancer brain metastasis: advances in therapy. *Mol Cancer.* (2020) 19:29. doi: 10.1186/s12943-020-1140-x
16. Bertoli G, Cava C, Castiglioni I. MicroRNAs: new biomarkers for diagnosis, prognosis, therapy prediction and therapeutic tools for breast cancer. *Theranostics.* (2015) 5:1122–43. doi: 10.7150/thno.11543
17. Aushev VN, Lee E, Zhu J, Gopalakrishnan K, Li Q, Teitelbaum SL, et al. Novel Predictors of breast cancer survival derived from miRNA activity analysis. *Clin Cancer Res.* (2018) 24:581–91. doi: 10.1158/1078-0432.Ccr-17-0996
18. Cai WL, Huang WD, Li B, Chen TR, Li ZX, Zhao CL, et al. microRNA-124 inhibits bone metastasis of breast cancer by repressing Interleukin-11. *Mol Cancer.* (2018) 17:9. doi: 10.1186/s12943-017-0746-0

19. Hamam R, Hamam D, Alsaleh KA, Kassem M, Zaher W, Alfayez M, et al. Circulating microRNAs in breast cancer: novel diagnostic and prognostic biomarkers. *Cell Death Dis.* (2017) 8:e3045. doi: 10.1038/cddis.2017.440
20. McGuire A, Brown JA, Kerin MJ. Metastatic breast cancer: the potential of miRNA for diagnosis and treatment monitoring. *Cancer Metastasis Rev.* (2015) 34:145–55. doi: 10.1007/s10555-015-9551-7
21. Nassar FJ, Nasr R, Talhouk R. MicroRNAs as biomarkers for early breast cancer diagnosis, prognosis and therapy prediction. *Pharmacol Ther.* (2017) 172:34–49. doi: 10.1016/j.pharmthera.2016.11.012
22. Wang H, Sun Z, Wang Y, Hu Z, Zhou H, Zhang L, et al. miR-33-5p, a novel mechano-sensitive microRNA promotes osteoblast differentiation by targeting Hmga2. *Sci Rep.* (2016) 6:23170. doi: 10.1038/srep23170
23. Dweep H, Gretz N. miRWalk2.0: a comprehensive atlas of microRNA-target interactions. *Nat Methods.* (2015) 12:697. doi: 10.1038/nmeth.3485
24. Wang H, Hu Z, Shi F, Dong J, Dang L, Wang Y, et al. Osteoblast-targeted delivery of miR-33-5p attenuates osteopenia development induced by mechanical unloading in mice. *Cell Death Dis.* (2018) 9:170. doi: 10.1038/s41419-017-0210-5
25. Zhao L, Huang J, Zhu Y, Han S, Qing K, Wang J, et al. miR-33-5p knockdown attenuates abdominal aortic aneurysm progression via promoting target adenosine triphosphate-binding cassette transporter A1 expression and activating the PI3K/Akt signaling pathway. *Perfusion.* (2020) 35:57–65. doi: 10.1177/0267659119850685
26. Zhang H, Wang K. Downregulation of MicroRNA-33-5p protected bupivacaine-induced apoptosis in murine dorsal root ganglion neurons through GDNF. *Neurotox Res.* (2019) 35:860–6. doi: 10.1007/s12640-018-9994-z
27. Tsai YC, Kuo PL, Hung WW, Wu LY, Wu PH, Chang WA, et al. Angpt2 induces mesangial cell apoptosis through the MicroRNA-33-5p-SOCS5 loop in diabetic nephropathy. *Mol Ther Nucleic Acids.* (2018) 13:543–55. doi: 10.1016/j.omtn.2018.10.003
28. Hanahan D, Weinberg RA. Hallmarks of cancer: the next generation. *Cell.* (2011) 144:646–74. doi: 10.1016/j.cell.2011.02.013
29. Basu SC, Boyle P, Ma R, Agarwal A, Basu M, Moskal JR, et al. Induction of apoptosis in metastatic breast cancer cells: XV. downregulation of DNA polymerase-alpha—helicase complex (Replisomes) and glyco-genes. *Adv Exp Med Biol.* (2018) 1112:199–221. doi: 10.1007/978-981-13-3065-0_15
30. Thapa B, Bahadur Kc R, Uludag H. Novel targets for sensitizing breast cancer cells to TRAIL-induced apoptosis with siRNA delivery. *Int J Cancer.* (2018) 142:597–606. doi: 10.1002/ijc.31079
31. Shi Y. Mechanisms of caspase activation and inhibition during apoptosis. *Mol Cell.* (2002) 9:459–70. doi: 10.1016/s1097-2765(02)00482-3
32. Mirzapur P, Khazaei MR, Moradi MT, Khazaei M. Apoptosis induction in human breast cancer cell lines by synergic effect of raloxifene and resveratrol through increasing proapoptotic genes. *Life Sci.* (2018) 205:45–53. doi: 10.1016/j.lfs.2018.04.035
33. You F, Luan H, Sun D, Cui T, Ding P, Tang H, et al. miRNA-106a Promotes breast cancer cell proliferation, clonogenicity, migration, and invasion through inhibiting apoptosis and chemosensitivity. *DNA Cell Biol.* (2019) 38:198–207. doi: 10.1089/dna.2018.4282
34. Hu Y, Qiu Y, Yague E, Ji W, Liu J, Zhang J. miRNA-205 targets VEGFA and FGF2 and regulates resistance to chemotherapeutics in breast cancer. *Cell Death Dis.* (2016) 7:e2291. doi: 10.1038/cddis.2016.194
35. Cui Y, Wang J, Liu S, Qu D, Jin H, Zhu L, et al. miR-216a promotes breast cancer cell apoptosis by targeting PKCalpha. *Fundam Clin Pharmacol.* (2019) 33:397–404. doi: 10.1111/fcp.12481
36. Orrenius S. Reactive oxygen species in mitochondria-mediated cell death. *Drug Metab Rev.* (2007) 39:443–55. doi: 10.1080/03602530701468516
37. Han Y-H, Zhang Z-W, Su J, Zhang B, Li S, Xu S-W. Effects of chicken selenoprotein W on H2O2-induced apoptosis in CHO-K1 cells. *Biol Trace Elem Res.* (2012) 147:395–402. doi: 10.1007/s12011-011-9311-7
38. Hamieh A, Cartier D, Abid H, Calas A, Burel C, Bucharles C, et al. Selenoprotein T is a novel OST subunit that regulates UPR signaling and hormone secretion. *EMBO Rep.* (2017) 18:1935–46. doi: 10.15252/embr.201643504
39. Boukhzar L, Hamieh A, Cartier D, Tanguy Y, Alsharif I, Castex M, et al. Selenoprotein T exerts an essential oxidoreductase activity that protects dopaminergic neurons in mouse models of parkinson's disease. *Antioxid Redox Signal.* (2016) 24:557–74. doi: 10.1089/ars.2015.6478
40. Grumolato L, Ghzili H, Montero-Hadjadje M, Gasman S, Lesage J, Tanguy Y, et al. Selenoprotein T is a PACAP-regulated gene involved in intracellular Ca2+ mobilization and neuroendocrine secretion. *Faseb J.* (2008) 22:1756–68. doi: 10.1096/fj.06-075820
41. Tanguy Y, Falluel-Morel A, Arthaud S, Boukhzar L, Manecka DL, Chagraoui A, et al. The PACAP-regulated gene selenoprotein T is highly induced in nervous, endocrine, and metabolic tissues during ontogenetic and regenerative processes. *Endocrinology.* (2011) 152:4322–35. doi: 10.1210/en.2011-1246
42. Prevost G, Arabo A, Jian L, Quelennec E, Cartier D, Hassan S, et al. The PACAP-regulated gene selenoprotein T is abundantly expressed in mouse and human beta-cells and its targeted inactivation impairs glucose tolerance. *Endocrinology.* (2013) 154:3796–806. doi: 10.1210/en.2013-1167
43. Lan X, Xing J, Gao H, Li S, Quan L, Jiang Y, et al. Decreased Expression of Selenoproteins as a poor prognosticator of gastric cancer in humans. *Biol Trace Elem Res.* (2017) 178:22–8. doi: 10.1007/s12011-016-0908-8
44. Reszka E. Selenoproteins in bladder cancer. *Clin Chim Acta.* (2012) 413:847–54. doi: 10.1016/j.cca.2012.01.041
45. Tang J, Cao L, Li Q, Wang L, Jia G, Liu G, et al. Selenoprotein X gene knockdown aggravated H2O2-induced apoptosis in liver LO2 cells. *Biol Trace Elem Res.* (2016) 173:71–8. doi: 10.1007/s12011-016-0653-z
46. Pan T, Liu T, Tan S, Wan N, Zhang Y, Li S. Lower Selenoprotein T expression and immune response in the immune organs of broilers with exudative diathesis due to selenium deficiency. *Biol Trace Elem Res.* (2017) 182:1–9. doi: 10.1007/s12011-017-1110-3

Conflict of Interest: The authors declare that the research was conducted in the absence of any commercial or financial relationships that could be construed as a potential conflict of interest.

Copyright © 2021 Zhuang, Liu and Li. This is an open-access article distributed under the terms of the Creative Commons Attribution License (CC BY). The use, distribution or reproduction in other forums is permitted, provided the original author(s) and the copyright owner(s) are credited and that the original publication in this journal is cited, in accordance with accepted academic practice. No use, distribution or reproduction is permitted which does not comply with these terms.

frontiers in Medicine

ORIGINAL RESEARCH
published: 12 May 2021
doi: 10.3389/fmed.2021.668787

LncRNA PITPNA-AS1 as a Potential Diagnostic Marker and Therapeutic Target Promotes Hepatocellular Carcinoma Progression via Modulating miR-448/ROCK1 Axis

Qing-fang Wang[1], *Qing-lin Wang*[2] *and Ming-bo Cao*[3]*

[1] Department of Clinical Laboratory, The First Affiliated Hospital of Zhengzhou University, Zhengzhou, China, [2] Department of Pharmacology, The First Affiliated Hospital of Zhengzhou University, Zhengzhou, China, [3] Department of Telemedicine Center, The First Affiliated Hospital of Zhengzhou University, Zhengzhou, China

Background: Long non-coding RNAs are critical to hepatocellular carcinoma (HCC) developments. LncRNA PITPNA antisense RNA 1 (PITPNA-AS1) is a new regulator in several tumors. However, the mechanism by which PITPNA-AS1 mediates the tumorigenesis of HCC remains unclear.

Methods: RT-qPCR was used to detect the level of PITPNA-AS1 in HCC specimens and cells. The biological functions of PITPNA-AS1 were explored by several functional experiments *in vivo* and *in vitro*. The binding relationship among PITPNA-AS1, miR-448 and ROCK1 were studied by Luciferase assay and pull-down assays.

Results: We found that PITPNA-AS1 expressions were distinctly upregulated in both HCC specimens and cell lines. High PITPNA-AS1 levels were an unfavorable biomarker for patients with HCC. Functionally, knockdown of PITPNA-AS1 suppressed the proliferation, migration and invasion of HCC cells. Mechanistically, PITPNA-AS1 functioned as competing endogenous RNA to increase ROCK1 expressions via sponging miR-448.

Conclusion: The newly identified PITPNA-AS/miR-448/ROCK1 axis promoted the oncogenicity of HCC cells. This novel axis is likely to be a promising HCC therapeutic aim.

Keywords: LncRNA PITPNA-AS1, miR-448, ROCK1, hepatocellular carcinoma, biomarker

OPEN ACCESS

Edited by:
Fu Wang,
Xi'an Jiaotong University, China

Reviewed by:
Dong Xu,
Huaihua First People's Hospital, China
Yang Hsiang Lin,
Linkou Chang Gung Memorial Hospital, Taiwan

***Correspondence:**
Ming-bo Cao
cmb66914@sina.com

Specialty section:
This article was submitted to Precision Medicine, a section of the journal Frontiers in Medicine

Received: *17 February 2021*
Accepted: *13 April 2021*
Published: *12 May 2021*

Citation:
Wang Q-f, Wang Q-l and Cao M-b (2021) LncRNA PITPNA-AS1 as a Potential Diagnostic Marker and Therapeutic Target Promotes Hepatocellular Carcinoma Progression via Modulating miR-448/ROCK1 Axis. Front. Med. 8:668787. doi: 10.3389/fmed.2021.668787

INTRODUCTION

Hepatocellular carcinoma (HCC) is a common malignancy worldwide and the second leading cause of cancer-related death (1). Several researches have indicated that HCC morbidity is primarily caused by environmental pollution, alcohol addiction, liver cirrhosis and hepatitis B/C virus infecting process (2). Even though effective surgical technique and diagnostic processes have resulted in the distinct improvements of clinical outcome of HCC patients, the long-term survivals are still unsatisfactory largely due to positive metastasis and the high recurrence (45–65% at 5 years) (3, 4). Thus, the molecular systems within HCC progression should be explored in depth for the improvements of diagnosis and clinical treatments of HCC.

Long non-coding RNAs (lncRNAs) are non-protein coding transcripts longer than 200 nucleotides (5). Many lncRNAs modulate gene expressions at several levels including transcription and posttranscriptional processing (6). More and more evidences have demonstrated the involvements of lncRNAs in a variety of disease states. According to a growing volume of literature, the dysregulation of lncRNAs was frequent in various tumors and involved in tumor progression (7, 8). Functional lncRNAs have been identified to serve as tumor promotors or anti-oncogenes, which suggests their potential used as novel tumor biomarkers and potential therapeutic targets (9). However, the expression and underlying mechanism of HCC associated with aberrant lncRNAs remain largely unclear.

When we analyzed TCGA datasets, we found an overexpressed lncRNA, PITPNA-AS1, within HCC. PITPNA-AS1, located on 17p13.3, exhibited a high level in several different types of tumors. In recent years, several researches reported the expression and tumor-related function of PITPNA-AS1 in several tumors, including HCC, lung tumor and colorectal tumor (10–12). However, the roles and related mechanisms of PITPNA-AS1 in the initiation and progressions of HCC were rarely reported.

MATERIALS AND METHODS

Cases and Samples

Ninety-three sets of HCC tissues and adjacent normal hepatic tissues were obtained from patients with HCC who underwent HCC resection at the First Affiliated Hospital of Zhengzhou University between July 2015 and November 2017. No chemotherapy and radiotherapy were performed before the surgery. By complying with the 2009 American Joint Committee for Cancer staging system, histological and pathological diagnostics for patients with HCC were determined. The present work received the approving process from Institute Research Medical Ethics Committee of the First Affiliated Hospital of Zhengzhou University. The respective case presented the consent in an informed manner prior to the research.

Cell Lines and Transfection

Liver normal cell lines L02 and HCC cell lines (including Hep3B, HepG2, SMMC-7721 as well as HCCLM3) of humans were provided by Shanghai Institute of Cell Biology (Shanghai, China). RPMI 1640 medium involving 10 % fetal bovine serum (Bieyu Technology, Nanjing, Jiangsu, China), 100 U/ml penicillin, and 100 mg/ml streptomycin was used to culture cells in humidified air with 5 % CO_2 at the temperature of 37°C.

Short hairpin RNA (shRNA) sequences aiming PITPNA-AS1 were designed by OriGene Company (Hiadian, Beijing, China). The shRNAs were inserted into lentiviral pHBLV/U6-Scramble-Luc-Puro01 vector (Biomart Technology, Haidian, Beijing, China), termed as sh-PITPNA-AS1-1 as well as sh-PITPNA-AS1-2; negative control was named sh-NC. MiR-448 mimics and miR-448 inhibitors together with their controls were provided by Ziqibo Technology (Xuhui, Shanghai, China). The present work adopted Lipofectamine 2000 (Invitrogen, Chengdu, Sichuan, China) for performing plasmid transfections based on the producer's protocol. Western blot assays or RT-qPCR was used to examine transfection efficiency.

TABLE 1 | Primers for qPCR assays.

Names	Sequence (5′-3′)
PITPNA-AS1: forward	GACCACACATTCACCCTCAT
PITPNA-AS1: reverse	CTTACTCACCGTTGCCACCCAC
miR-448: forward	TCGGCAGGTTGCATATGTAGGA
miR-448: reverse	CTCAACTGGTGTCGTGGA
ROCK1: forward	AACATGCTGCTGGATAAATCTGG
ROCK1: reverse	TGTATCACATCGTACCATGCCT
U6: forward	CTCGCTTCGGCAGCACA
U6: reverse	AACGCTTCACGAATTTGCGT
GAPDH: forward	GGAGCGAGATCCCTCCAAAAT
GAPDH: reverse	GGCTGTTGTCATACTTCTCATGG

Bioinformatics Analysis

"GEPIA" (http://gepia.cancer-pku.cn/) analyzed the expressing state and clinical significance pertaining to PITPNA-AS1 in HCC. The binding sites among PITPNA-AS1, miR-448 and ROCK1 received the prediction on starBase (http://starbase.sysu.edu.cn/index.php).

Quantitative Real-Time PCR Assay

Total RNA was extracted from tissues or cultured cells with TRIzol (Invitrogen). cDNA synthesis was performed with 2 μg of overall RNA, using the miScript II RT Tool (Qiagen) by complying with the directions of the producer. The expressing states pertaining to lncRNA and genes received the assessment based on one ABI7500 Real-Time PCR Process (Applied Biosystems) as well as the SYBR-Green PCR Master Mix Tool (Takala, Hangzhou, Zhejiang, China). The results received the normalization to expressing states pertaining to U6 or GAPDH. Comparative quantification was determined using the $2^{-\Delta\Delta Ct}$ methods. All primer sequences are summarized in **Table 1**.

Cell Counting Kit-8 (CCK-8) Assay

Cells proliferation was examined by the use of the cell proliferation reagent WST-8 (Absin, Pudong, Shanghai, China). Within 24-well plates based on 3×10^5 cells/well density, cells received the plating process. Next, within 10% CCK-8 under the dilution by using common culture medium, HCC cells received the incubation at 37°C to achieve color conversion. Based on Elx800 Reader, Absorbance (A) then received the recording process at 450 nm.

Colony Formation Assay

At a density of 100 cells/well within 6-well plates, HCC cells received the seeding process. When cells received the 2-weeks incubating process, they underwent the PBS-based cleaning process two times, followed by the methanol-based fixing process and the staining process based on crystal violet. Based on a microscope, the present study made a counting of the colonies covering >50 cells.

Wound Healing Assays

Indicated HCC cells were plated in 6-well plates and cultured at 37°C. Once cells were attached completely, they were scraped to form a wound in the middle of the plates. Washed with PBS three times, DMSO and 3c compound was added in duplicate. After final incubation, pictures were again taken under microscope.

Transwell Assays

Cells (5×10^4) received the suspending process within serum-free DMEM and then the addition into chambers (8 mm, BD Biosciences) under the coating of BD BioCoat Matrigel. When the incubating process was achieved, by employing one cotton tip, the cells onto the surface of the upper membrane received the removal. The RPMI 1640 medium involving 10% FBS received the addition into the bottom chamber. Cells under the migrating or invading process within the bottom chamber received the 0.1% crystal violet-based staining process. Cells were then counted under an optical microscope.

EdU Staining

Cells (5×10^4) were suspended in serum-free DMEM and added to chambers (8 mm, BD Biosciences) coated with BD BioCoat Matrigel. Subsequently, 5×10^4 cells underwent the 4% paraformaldehyde-based fixing process, 0.5% Troxin X-100 based incubating process, as well as 1 × Apollo® 488 fluorescent staining. For determining EdU-positive cells' percentage within 5 random fields in the respective well, this study employed fluorescent microscopy (Nikon, Japan).

Subcellular Fractionation

By employing a PARIS tool (AM1921, Invitrogen, Wosheng Biology, Hangzhou, Zhejiang, China) by complying with the guidelines of the producers, this study conducted the nuclear and cytosolic part separating process.

RNA Pull-Down Assays

After cells were quantitated, our group employed 1 ml of cell lysis buffer for 72 h treating of cells. Next, cells received the rotating process overnight at 4°C after adding 500 pM antisense oligos and 2 μl of RNase inhibitors (Keming Technology, Haidian, Beijing, China). Cell lysis buffer was applied to wash beads five times. Total RNAs were subjected to RT-PCR assays.

Luciferase Reporter Assays

pMiR-Reporter Vector and DNA oligonucleotide received the utilization for constructing the report vector of PITPNA-AS1 wild type/mutant (PITPNA-AS1-WT/MUT) and ROCK1 wild type/mutant (ROCK1-WT/MUT). Subsequently, the above two vectors received the co-transfecting process by using miR-448 mimics and negative control mimics (NC mimics), respectively, and then co-transfected into HCCLM3 and HepG2 cells. Forty-eight hours after transfection, the luciferase activity was detected under a dual-luciferase reporter assay system (Promega).

Xenograft Tumor Model

BALB/c female nude mice according to Vital River Company (Chaoyang, Beijing, China) were used for *in vivo* experiments. HepG2 cells under the stable transfection by employing sh-PITPNA-AS1-1 or sh-NC received the subcutaneous injection in nude mice's right flank ($n = 6$). Samples received the euthanizing process, and the xenografts underwent the dissecting and weighing process based on 28-days injecting process. Tumor volume received the calculation by (length × width^2)/2. The animal-related protocol was approved by the Animal Research Ethics Committee of the First Affiliated Hospital of Zhengzhou University.

Western Blot

Overall protein received the extraction based on the Total Protein Extraction Tool (Abnova, Aimeijie, Wuhan, Hubei, China). Based on the BCA approach, the contents pertaining to the protein samples received the determination, and 40 μg protein according to the respective sample underwent the treatment with 10% SDS-PAGE. Then the proteins received the transfer to Millipore 0.45 μM polyvinylidene difluoride (PVDF) membrane. When the samples received the incubating process by employing antibodies specific in terms of E-cadherin, N-cadherin, Vimentin, ROCK1 and GAPDH, the blots received the incubating process by employing anti-mouse or goat anti-rabbit secondary antibodies. All antibodies were purchased from Qiangyao Technology (Pudong, Shanghai, China). Signals were visualized using ECL Substrates (Pierce). GAPDH served as an endogenous control.

Statistical Analysis

The present study employed SPSS v. 20.0 software package (IBM Corp., Armonk, NY, USA) to statistically investigate the information acquired. The group differences were compared using the ANOVA test or student's *t*-test. The total surviving states pertaining to HCC cases received the assessment based on the Kaplan-Meier curve, and the distinction within total surviving states received the determination with the use of log-rank methods. Multivariate Cox regression was performed on each clinical covariate to examine its influence on patient survival. $P < 0.05$ was regarded as statistically significant.

RESULTS

Increased PITPNA-AS1 Expression in HCC Tissues

For screening functional lncRNAs in HCC progression, we analyzed TCGA datasets. We found a lncRNA, PITPNA-AS1 which was distinctly overexpressed in HCC specimens from TCGA datasets (**Figure 1A**). Advanced HCC specimens also showed higher levels of PITPNA-AS1 than those with early stages (**Figure 1B**). A pan-cancer analysis indicated the overexpressed trend of PITPNA-AS1 in many different types of tumors (**Figure 1C**). Based TCGA datasets, patients with high PITPNA-AS1 showed a shorter overall survival than those with low PITPNA-AS1 expression (**Figure 1D**). These results highlighted the involvements of PITPNA-AS1 in HCC progression. Then, we performed RT-PCR in our cohort and observed that PITPNA-AS1 expression in HCC specimens was distinctly higher than that

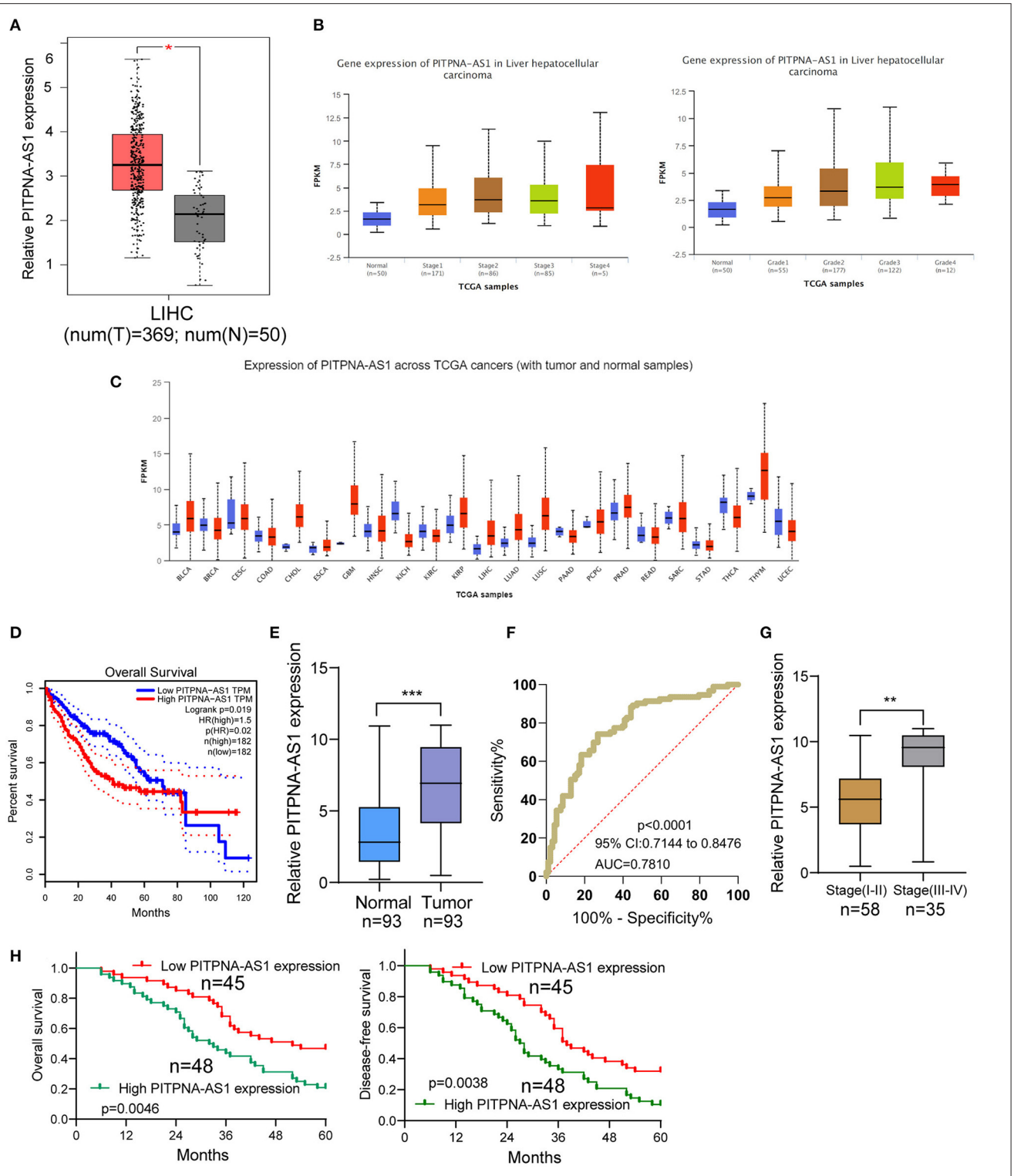

FIGURE 1 | PITPNA-AS1 is upregulated in HCC tissues and is associated with poor prognosis. **(A)** The distinct upregulation of PITPNA-AS1 expression in HCC specimens ($n = 369$) compared to non-tumor specimens ($n = 50$) from TCGA datasets. **(B)** The expressing pattern of PITPNA-AS1 in HCC specimens with different stages. **(C)** Based on TCGA datasets, Pan-cancer expressions of PITPNA-AS1 were shown. The red column represented the tumor samples and the blue column represented the normal samples. **(D)** Kaplan-Meier curves for survival time in HCC patients divided according to PITPNA-AS1 expression based on TCGA datasets. **(E)** RT-PCR for the determination of PITPNA-AS1 expression in 93 pairs of HCC specimens and non-tumor tissues. **(F)** ROC curves analysis for the HCC diagnostic capability of PITPNA-AS1 expression. **(G)** Higher levels of PITPNA-AS1 were observed in HCC specimens with advanced stages than those with early stages. **(H)** Kaplan-Meier curves for overall survival and disease-free survival in patients with HCC divided according to PITPNA-AS1 expression. $^{***}P < 0.001$, $^{**}P < 0.01$.

in the matched non-tumor specimens (**Figure 1E**). ROC assays confirmed the diagnostic value of high PITPNA-AS1 expression in distinguishing HCC specimens from normal tissues with an AUC = 0.7810 and $p < 0.001$ (**Figure 1F**). Higher levels of PITPNA-AS1 were observed in HCC specimens with stage (III-IV) than those with stage (I-II) (**Figure 1G**). Overall, our findings suggested PITPNA-AS1 as a possible functional lncRNA in HCC progression.

Prognostic Values of PITPNA-AS1 Expression in HCC Patients

Using the mean value of PITPNA-AS1 expression level (6.87) as the cut-off value, 93 samples were divided into two groups (high expression and low expression). We observed that high PITPNA-AS1 expression was associated with larger tumor size ($p = 0.004$), tumor differentiation ($p = 0.021$), positive lymph node metastasis ($p = 0.012$), and advanced clinical stage ($p = 0.011$) (**Table 2**). To explore whether the dysregulation of PITPNA-AS1 may influence the survivals of HCC patients, we performed Kaplan-Meier methods, finding that the 5-years overall survival ($p = 0.0046$) and disease-free survival ($p = 0.0038$) of high PITPNA-AS1 expression group were distinctly shorter than those of low PITPNA-AS1 expression group (**Figure 1H**). More importantly, Multivariate analysis revealed that high PITPNA-AS1 expression was an independent prognostic factor for both OS (HR = 3.241, 95% CI: 1.376–5.467, $P = 0.005$) and DFS (HR = 3.413, 95% CI: 1.457–5.774, $P = 0.002$, **Table 3**).

TABLE 2 | Relationship between PITPNA-AS1 expression and clinicopathological characteristics.

Parameters	Group	Total	PITPNA-AS1 expression		*p*-value
			High	Low	
Gender	Male	53	28	25	0.787
	Female	40	20	20	
Age (years)	<50	44	23	21	0.904
	≥50	49	25	24	
Tumor size (cm)	<4	52	20	32	0.004
	≥4	41	28	13	
Tumor differentiation	Well/Moderate	57	24	33	0.021
	Poor	36	24	12	
Lymph node metastasis	Absence	65	28	37	0.012
	Presence	28	20	8	
Clinical stage	I-II	58	24	34	0.011
	III-IV	35	24	11	

Silencing of PITPNA-AS1 Suppresses the Proliferating Process and Metastasizing Process Pertaining to HCC Cells

We examined the levels of PITPNA-AS1 within HCC cells and found that PITPNA-AS1 expression was upregulated in four HCC cells (**Figure 2A**). HepG2 and HCCLM3 cells with highest PITPNA-AS1 levels were chosen for further study. This study carried out RT-PCR for detecting the efficient property of the transfecting process pertaining to sh-PITPNA-AS1-1/-2/NC. According to the results, PITPNA-AS1 expression decreased distinctly when sh-PITPNA-AS1-1/-2 was transfected in HepG2 and HCCLM3 cells (**Figure 2B**). The growth curves obtained from CCK8 proliferation assay indicated that PITPNA-AS1 knockdown significantly inhibited cell proliferation and colony formation in HCC cells (**Figures 2C,D**). EdU assays were performed and the results showed that PITPNA-AS1 knockdown significantly reduced the number of Edu-positive cells compared with that among the control cells (**Figure 2E**). The results of *in vivo* assays also confirmed that volume and weight of tumors in the sh-PITPNA-AS1 (PITPNA-AS1 knockdown) group were significantly smaller than the control group (**Figures 2F–H**). To further explore whether the dysregulation of PITPNA-AS1 exhibited effects on metastasis abilities of HCC cells, Transwell tests and Wound healing tests were carried out. According to the result, knockdown of PITPNA-AS1 limited HCC cells from migrating and invading (**Figures 3A,B**). The present study employed for Western blotting detecting the expressions pertaining to proteins associated with EMT, and the information proved that the down-regulation of PITPNA-AS1 elevated E-cadherin expression and down-regulated Vimentin and N-cadherin expressions (**Figure 3C**).

TABLE 3 | Multivariate analyses of prognostic factors in HCC patients.

Variables	Overall survival			Disease-free survival		
	HR	95% CI	*p*-value	HR	95% CI	*p*-value
Gender	0.783	0.456–1.783	0.342	0.974	0.545–2.013	0.251
Age (years)	0.978	0.554–2.132	0.432	1.241	0.678–2.342	0.268
Tumor size	1.453	0.832–2.342	0.134	1.554	0.942–2.456	0.117
Tumor differentiation	3.113	1.342–4.443	0.014	3.241	1.432–4.765	0.008
Lymph node metastasis	3.344	1.452–6.773	0.001	3.563	1.677–7.347	0.001
Clinical stage	2.896	1.327–5.138	0.012	3.183	1.442–5.348	0.008
PITPNA–AS1 expression	3.241	1.376–5.467	0.005	3.413	1.457–5.774	0.002

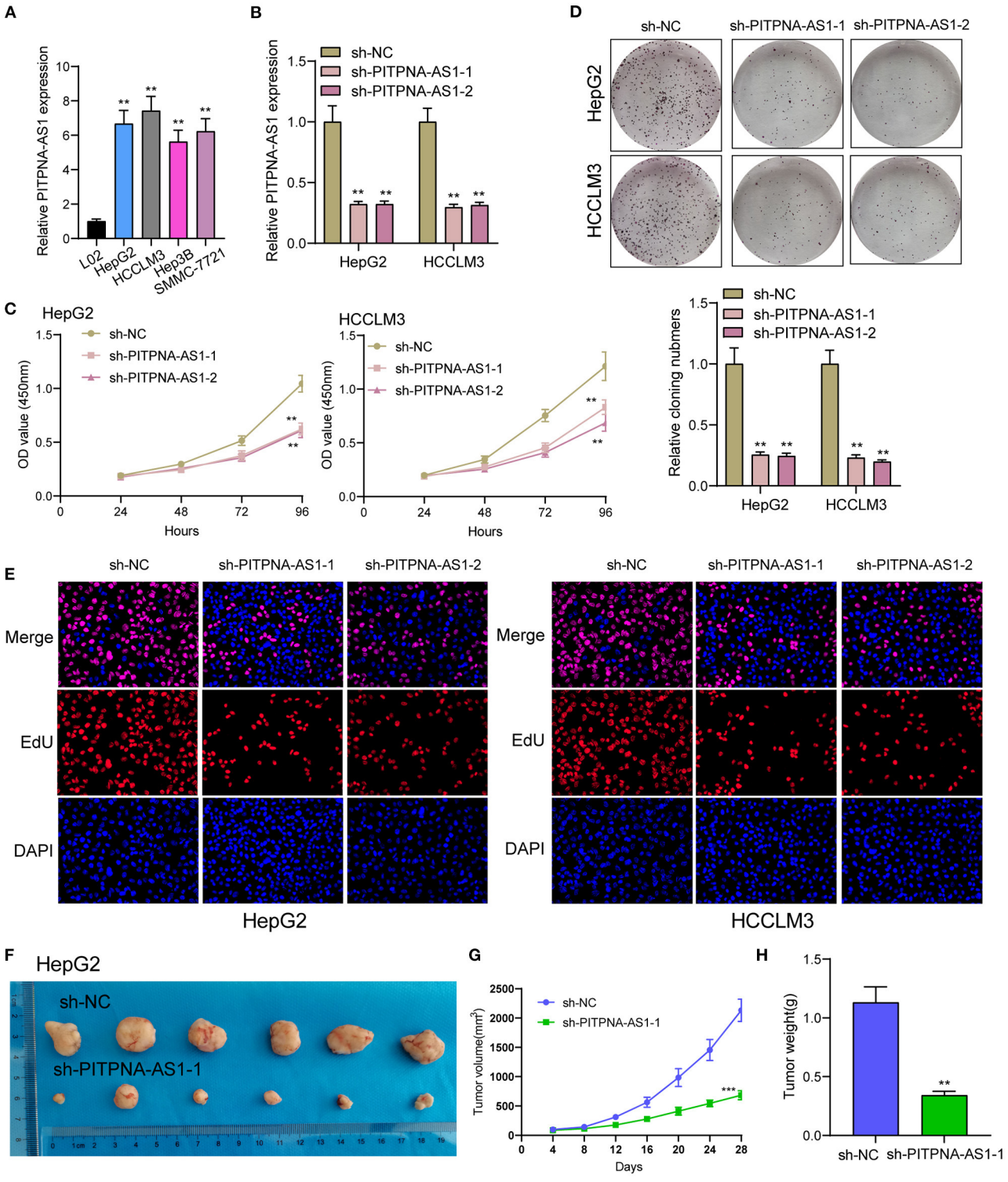

FIGURE 2 | PITPNA-AS1 promotes HCC cell proliferation *in vitro* and *in vivo*. **(A)** The expression in four HCC cells and LO2 cells was determined by RT-PCR. **(B)** RT-PCR confirmed the transfection efficiency of sh-PITPNA-AS1-1 and sh-PITPNA-AS1-2. **(C)** CCK-8 assays were performed to detect the proliferative abilities of the transfected HepG2 and HCCLM3 cells. **(D)** A colony-forming growth assay was performed to determine the proliferation of HepG2 and HCCLM3 cells after treatments. **(E)** EDU staining assays were applied to detect the proliferation of sh-PITPNA-AS1-1 and sh-PITPNA-AS1-2-transfected HCC cells. **(F)** Total number of tumors after removal from the mice. **(G)** Tumor growth curve. HepG2 cells were transfected with sh-NC or sh-PITPNA-AS1-1, and then injected into nude mice (n = 6), respectively. **(H)** Tumor weight were represented. ***$P < 0.001$, **$P < 0.01$.

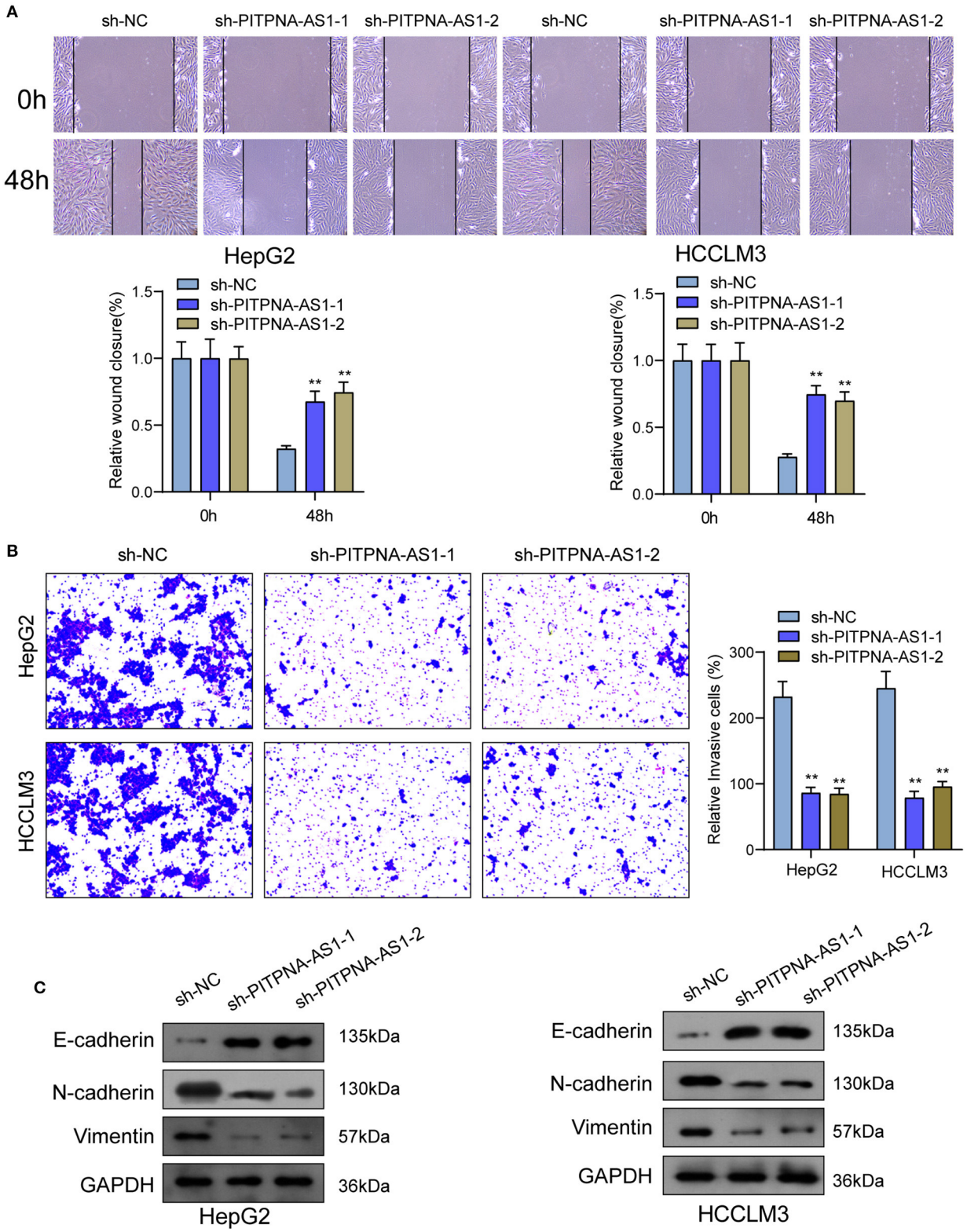

FIGURE 3 | PITPNA-AS1 knockdown inhibited cell migration and invasion of HCC cells. **(A)** The migration abilities of tumor cells were assessed by wound healing assays. **(B)** The number of invasion cell was detected by Transwell assays. **(C)** Western blotting was applied to detect the expression of EMT-related proteins in HepG2 and HCCLM3 cells. $^{**}P < 0.01$.

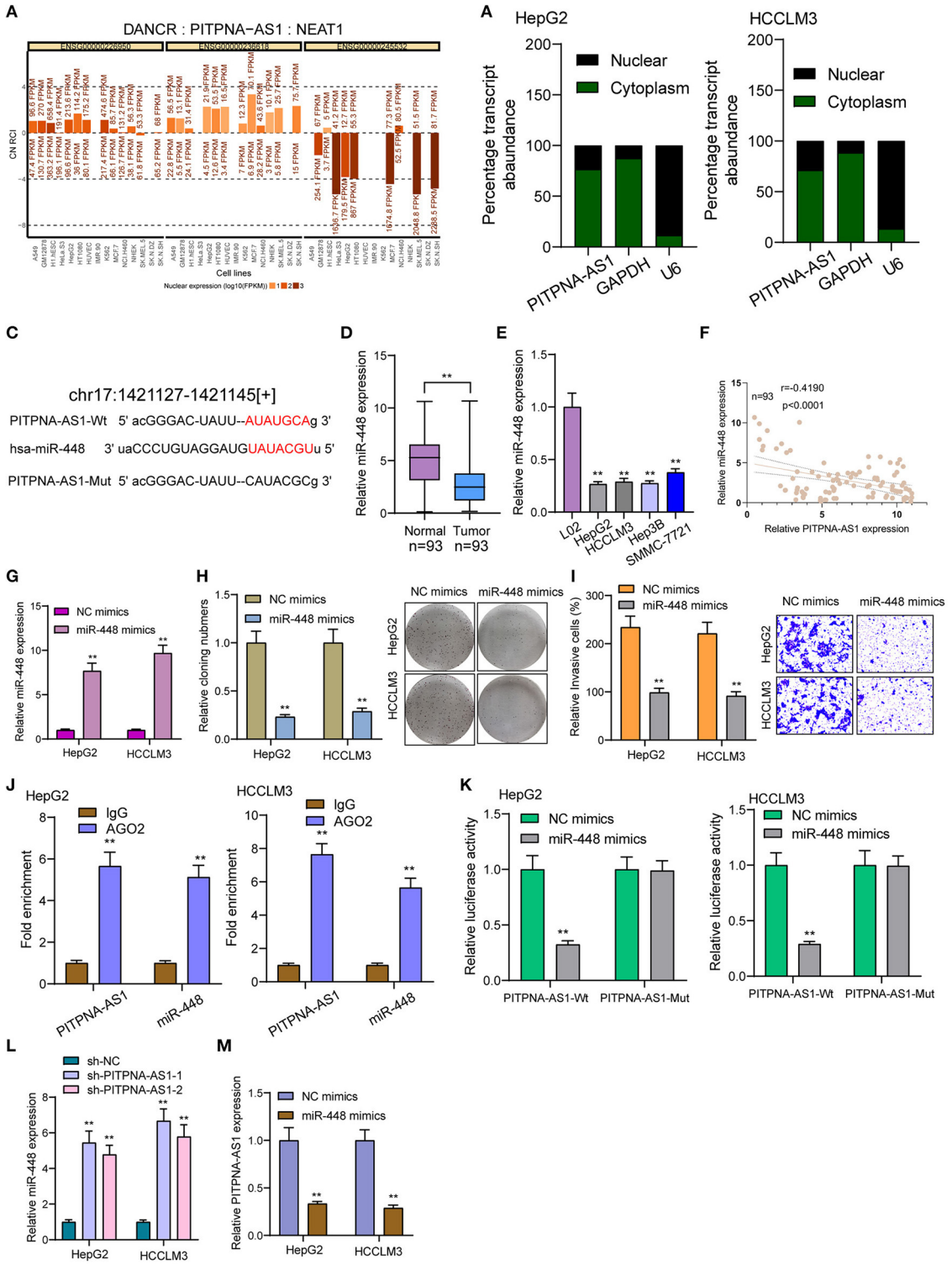

FIGURE 4 | PITPNA-AS1 functioned as a sponge of miR-448. **(A)** "lncATLAS" showed the subcellular localization of PITPNA-AS1 in a series of tumor cells. **(B)** Relative PITPNA-AS1 expression levels in nuclear and cytosolic fractions of HepG2 and HCCLM3 cells. **(C)** Schematic outlining the predicted binding sites between PITPNA-AS1 and miR-448. **(D,E)** RT-PCR determined the expression of miR-448 in HCC specimens and cell lines. **(F)** Correlation analysis between PITPNA-AS1 expression and miR-448 expression in 93 HCC specimens. **(G)** Knockdown of miR-448 in HepG2 and HCCLM3 cells after the transfection of mi-448 mimics. **(H)** Clone formation assay showed the clone number of HCC cells transfected with miR-448 mimics and NC mimics. **(I)** Transwell assays were used to determine the

(Continued)

FIGURE 4 | effects of mi-448 overexpression on HepG2 and HCCLM3 cells invasion. **(J)** RNA pull-down assays were performed for the determination of combination between miR-448 and PITPNA-AS1. **(K)** Luciferase reporter assay showed the activity within miR-448 and PITPNA-AS1 wild type or mutant. **(L)** miR-448 expression was deceased in HepG2 and HCCLM3 cells transfected with sh-PITPNA-AS1-1 or sh-PITPNA-AS1-2. **(M)** miR-448 overexpression resulted in the suppression of PITPNA-AS1 expression in HepG2 and HCCLM3 cells. $^{**}P < 0.01$.

PITPNA-AS1 Acted as ceRNA of miR-448 in HCC

By competitively binding microRNAs, cytoplasmic lncRNAs act as competing endogenous RNAs (ceRNAs) to exhibit their regulator functions. According to the lncATLAS website (http://lncatlas.crg.eu/), PITPNA-AS1 was primarily distributed in the cytoplasm (**Figure 4A**). Using subcellular fractionation, we also observed that a larger proportion of PITPNA-AS1 was in the cytoplasm (**Figure 4B**). Based on online prediction algorithm (starBase v2.0), miR-448 was estimated to involve a putative binding site with PITPNA-AS1 (**Figure 4C**). As revealed from the results of RT-PCR, miR-448 expression was distinctly down-regulated in both HCC specimens and cell lines (**Figures 4D,E**). Correlation analysis revealed that PITPNA-AS1 expression was negatively associated with miR-448 in 93 HCC tissues (**Figure 4F**). Then, we explored the function of miR-448 in HCC cells, and miR-448 overexpressing state was found to limit HCCLM3 and HepG2 cells from being proliferated and invaded (**Figures 4G–I**). RNA-pull down assays suggested the combination between miR-448 and PITPNA-AS1 in HCC cells (**Figure 4J**). According to Luciferase reporter assays, miR-448 mimics noticeably limited PITPNA-AS1-WT's luciferase activity, whereas it failed to alter PITPNA-AS1-MUT's relative luciferase activity (**Figure 4K**). Finally, we observed that knockdown of PITPNA-AS1 resulted in the distinct suppression of miR-448, while overexpression of miR-448 exhibited a contrary result (**Figures 4L,M**).

PITPNA-AS1 Upregulates ROCK1 Expression by miR-448

For determining the specific systems of miR-448 activity within HCC cells, this study carried out bioinformatics investigation for identifying the possible targets of miR-448. This study reported one miR-448 binding site inside ROCK1′s 3′-UTR (**Figure 5A**), as taken to carry out the following verifying process for its critical oncogenic roles in HCC. According to RT-PCR and Western blot tests, ROCK1 was overexpressed within HCC cells compared with LO2 cells (**Figure 5B**). According to functional tests, knockdown of ROCK1 noticeably inhibited HCC cells from being proliferated and invaded (**Figures 5C–E**). To verify the ROCK1 aiming based on miR-448, the present study carried out the luciferase activity test. As opposed to the control the cotransfection of miR-448 with WT-3′UTR in HepG2 and HCCLM3 cells limited luciferase activity noticeably, whereas Mut-3′UTR luciferase activity remained unchanged (**Figure 5F**). In addition, overexpression of miR-448 distinctly inhibited the expression of ROCK1 at both mRNA and protein levels (**Figure 5G**). To explore whether PITPNA-AS1 subsequently controls ROCK1 expression, we performed rescue experiments and observed that miR-448 knockdown reversed the suppression of PITPNA-AS1 knockdown on the expression of ROCK1 (**Figure 6A**). Moreover, a series of functional assays confirmed that miR-448 knockdown reversed the suppression of PITPNA-AS1 knockdown on the proliferation and invasion (**Figures 6B–D**). Taken together, PITPNA-AS1 aggravated the oncogenicity of HCC cells by regulating the miR-448/ROCK1 axis.

DISCUSSION

Recently, growing studies have suggested the potential of lncRNAs used as novel diagnostic and prognostic biomarkers for HCC, such as lncRNA p34822 and lncRNA SNHG1 (13, 14). These functional lncRNAs were shown to be positively associated with metastasis and relapses, which encouraged us to further identify novel biomarkers for HCC. In this study, we found that PITPNA-AS1 was distinctly overexpressed in HCC based on TCGA datasets and RT-PCR data from our cohort, which was consistent with previous findings by Sun et al. (11). We also observed that patients with high PITPNA-AS1 expression exhibited advanced clinical stages, positive metastasis and poor prognosis than those with low PITPNA-AS1 expression. Previously, the prognostic value of PITPNA-AS1 was also reported in colorectal cancer and cervical cancer (12, 15). Our study firstly provided clinical evidence that PITPNA-AS1 may be used as a novel biomarker. However, the sample size is relatively small, large clinical trials are needed to conduct.

Recently, PITPNA-AS1 was found for facilitating colorectal cancer cells' proliferation and metastasis through miRNA-129-5p/HMGB1 axis (12). In lung squamous cell carcinoma, PITPNA-AS1 was also observed to boost tumor cells' proliferating and migrating processes via recruiting TAF15 for stabilizing HMGB3 mRNA (10). Sun et al. also reported the oncogenic roles of PITPNA-AS1 within HCC (11). These findings suggested that the function of PITPNA-AS1 as a tumor promotor was a common event in different types of tumors. We also observed that knockdown of PITPNA-AS1 suppressed the proliferation, migration and invasion of HCC cells *in vitro* and *in vivo* studies. EMT, one primary system of tumor metastasizing process, results in the loss of cell-cell adhesion and promotes the ability to migrate and invade (16). Here, we confirmed the EMT progress was suppressed after the knockdown of PITPNA-AS1. Our findings, together with previous findings, suggested PITPNA-AS1 as an oncogene in HCC.

When the effect exerted by PITPNA-AS1 to be an oncogene in HCC was verified, the molecular systems influencing the changed malignant phenotypes received the exploration. It has been demonstrated that cytosolic lncRNAs are capable of modulating mRNA stable property and protein localizing

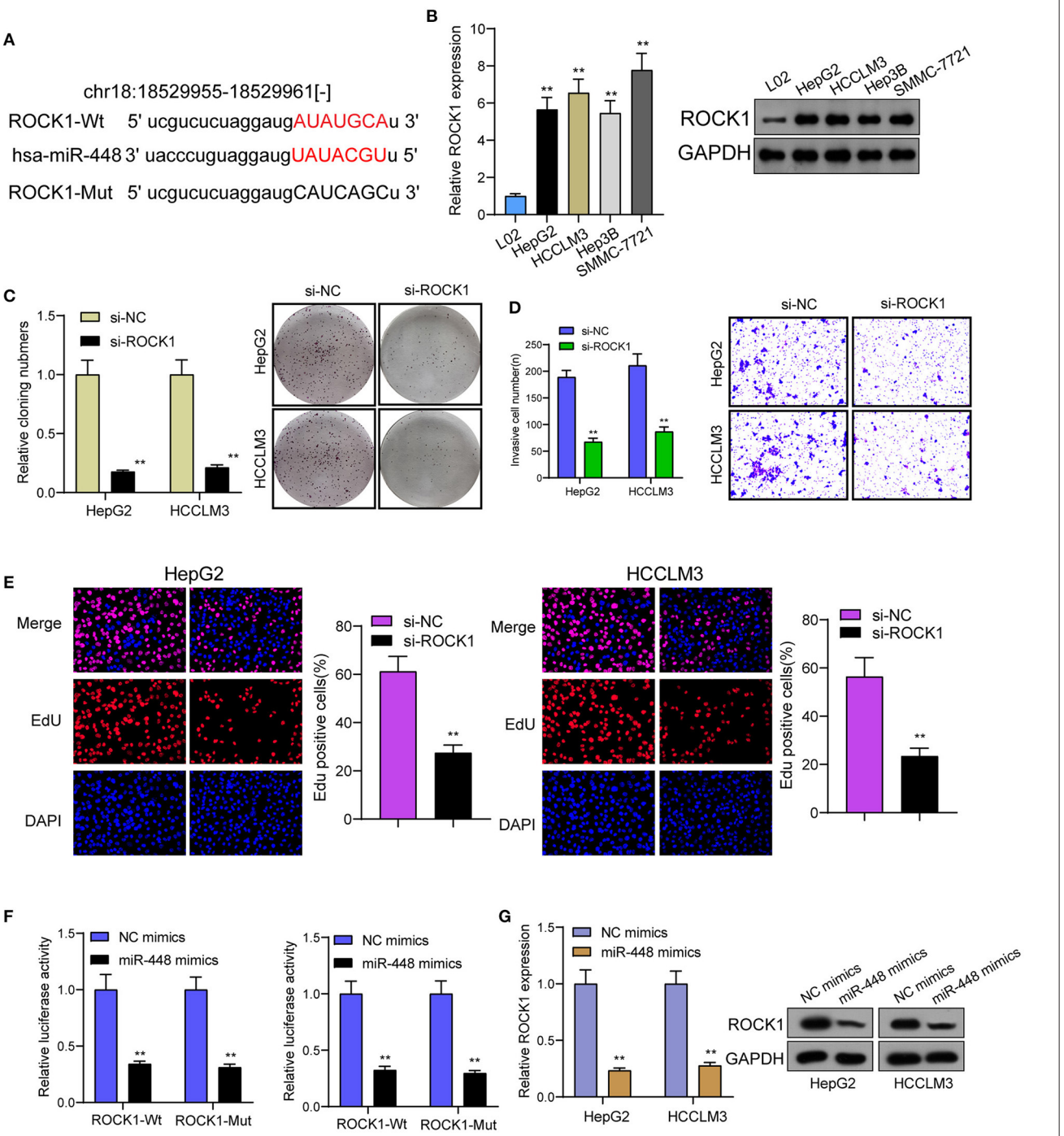

FIGURE 5 | miR-448 regulated ROCK1 expression in HCC cells. **(A)** The predicted miR-448 target site in the 3′UTRof ROCK1 mRNA and its mutated version. **(B)** ROCK1 levels in different HCC cell lines were measured by RT-PCR and western blot. **(C)** The cell proliferation in response to ROCK1 knockdown was examined using colony formation analysis. **(D)** Transwell assays were conducted to measure cell invasion. **(E)** EdU were performed to detect cell proliferation after knockdown of ROCK1. **(F)** miR-448 significantly suppressed the luciferase activity that carried wild-type ROCK1 but not the mutant ROCK1. **(G)** Overexpression of miR-448 suppressed the expression of ROCK1 in HepG2 and HCCLM3 cells. $^{**}P < 0.01$.

process, as well as becoming microRNA sponge (17, 18). PITPNA-AS1 was suggested to have the expression in the cytoplasm and the nucleus, and PITPNA-AS1 was observed in the cytoplasm with a higher rate, suggesting PITPNA-AS1 may serve as a ceRNA. Then, PITPNA-AS1 was evidenced to be a ceRNA for miR-448 inside the cytoplasm and

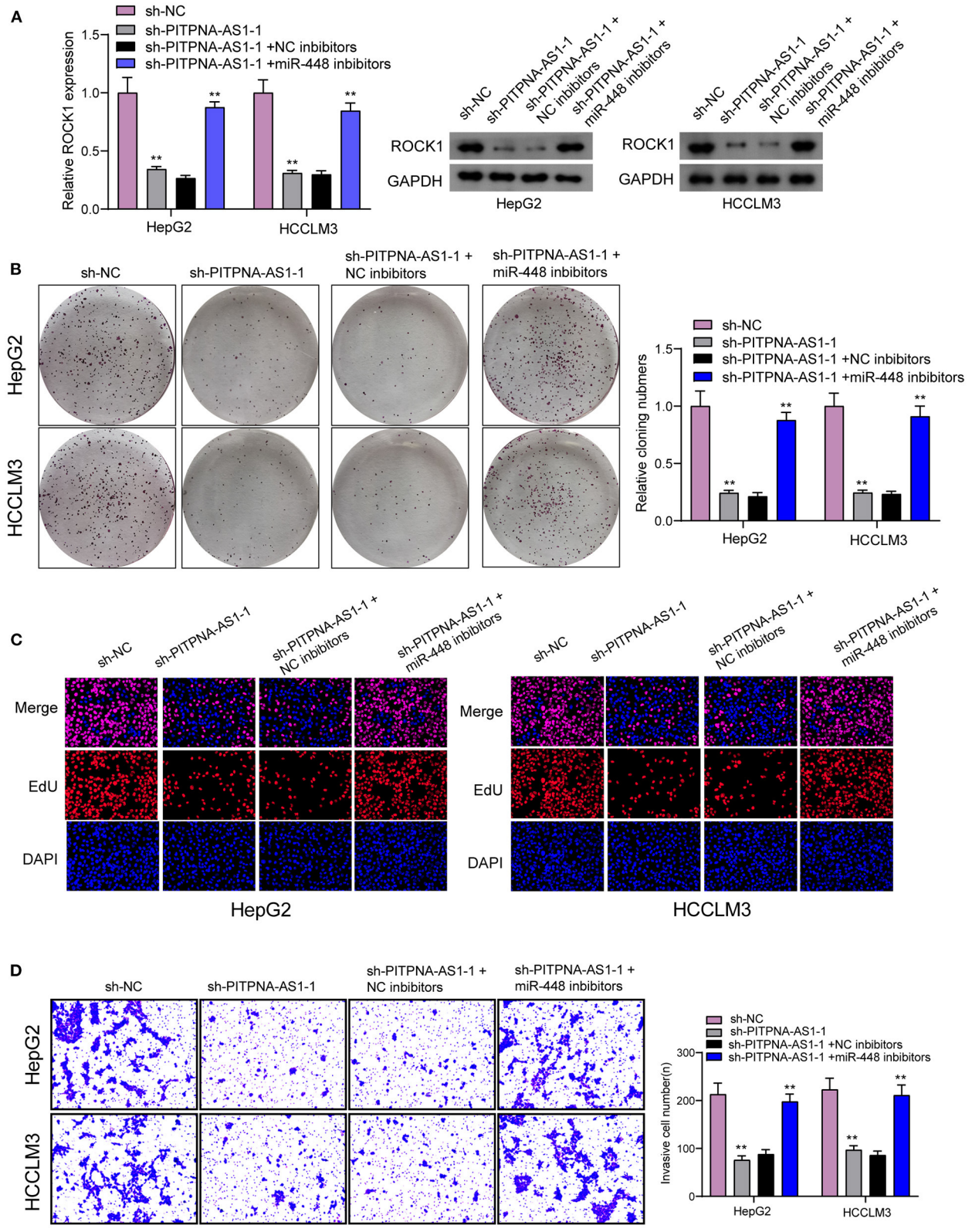

FIGURE 6 | PITPNA-AS1 promoted HCC progression via decreasing ROCK1 through sponging miR-448. **(A)** The expression of ROCK1 in HepG2 and HCCLM3 cells transfected with sh-NC, sh-PITPNA-AS1-1, sh-PITPNA-AS1-1+NC inhibitors or sh-PITPNA-AS1-1+ miR-448 inhibitors. **(B–D)** colony-forming growth assay, Edu assays and Transwell assays were used to examine the proliferation and invasion of HepG2 and HCCLM3 cells after the above transfection. $^{**}P < 0.01$.

suppressed miR-448 expressions. Previously, several studies have demonstrated that miR-448 was lowly expressed in several tumors, including HCC, and overexpression of miR-448 was observed to promote tumor metastasis of HCC (19, 20). We also observed the oncogenic roles of miR-448 in HCC, which was consistent with previous findings. Thus, these results suggested PITPNA-AS1 may exhibit its effects via sponging miR-448.

ROCK1, a vital downstream effecting element pertaining to the small GTPase RhoA, refers to one serine/threonine kinase, mediating a range of cellular responding processes (e.g., cell proliferating process, growing process, and apoptosis based on microtubule network organizing process and influences on the cytoskeleton) (21). ROCK1 served as an oncogene, with the involvement inside different progressions (e.g., cell migrating process, metastasis, as well as invading process) (22, 23). In HCC, it has been demonstrated that ROCK1 was overexpressed in HCC specimens and promoted the proliferation and metastasis of HCC cells (24–28). However, the potential mechanisms involved in ROCK1 function remained largely unclear. In this study, we found ROCK1 may be a target of miR-448. Previously, miR-448 was reported to directly target ROCK1, thus suppressing the progression of retinoblastoma (29). However, whether a similar function was observed in HCC remained unknown. We provided evidence that miR-448 targeted miR-448 and suppressed its expression. To further explore the association among PITPNA-AS1, miR-448 and ROCK1, we performed rescue experiments and found that knockdown of miR-448 reversed the suppression of PITPNA-AS1 down-regulation on the expression of ROCK1. In addition, a series of functional assays also showed that knockdown of miR-448 could reverse the inhibition of PITPNA-AS1 down-regulation on the proliferating process and metastasis of HCC cells. Therefore, PITPNA-AS1 promotes the progression of HCC via sponging miR-448 to decrease ROCK1 expression.

CONCLUSIONS

Our study first revealed that PITPNA-AS1 is upregulated in HCC, and its overexpression may be an unfavorable prognostic factor for patients with HCC. PITPNA-AS1 could promote HCC cell proliferation and metastasis through sponging miR-448 and releasing ROCK1. The results here elucidate HCC progression and pathogenesis, probably facilitating therapeutics and diagnostics in HCC under the direction by lncRNAs.

DATA AVAILABILITY STATEMENT

The raw data supporting the conclusions of this article will be made available by the authors, without undue reservation.

ETHICS STATEMENT

The studies involving human participants were reviewed and approved by the First Affiliated Hospital of Zhengzhou University. The patients/participants provided their written informed consent to participate in this study. The animal study was reviewed and approved by the First Affiliated Hospital of Zhengzhou University.

AUTHOR CONTRIBUTIONS

Q-fW and M-bC designed the study and wrote the manuscript. Q-fW and Q-lW conducted the experiments and data analysis. Q-lW provided technical support. All authors read and approve the final manuscript.

REFERENCES

1. Siegel RL, Miller KD, Jemal A. Cancer statistics. *CA*. (2018) 68:7–30. doi: 10.3322/caac.21442
2. El Jabbour T, Lagana SM, Lee H. Update on hepatocellular carcinoma: Pathologists' review. *World J Gastroenterol*. (2019) 25:1653–65. doi: 10.3748/wjg.v25.i14.1653
3. Gish RG. Hepatocellular carcinoma: overcoming challenges in disease management. *Clin Gastroenterol Hepat*. (2006) 4:252–61. doi: 10.1016/j.cgh.2006.01.001
4. Testino G, Leone S, Patussi V, Scafato E, Borro P. Hepatocellular carcinoma: diagnosis and proposal of treatment. *Min Med*. (2016) 107:413–26.
5. Jathar S, Kumar V, Srivastava J, Tripathi V. Technological developments in lncRNA biology. *Adv Exp Med Biol*. (2017) 1008:283–323. doi: 10.1007/978-981-10-5203-3_10
6. St Laurent G, Wahlestedt C, Kapranov P. The Landscape of long noncoding RNA classification. *TIG*. (2015) 31:239–51. doi: 10.1016/j.tig.2015.03.007
7. Bhan A, Soleimani M, Mandal SS. Long noncoding RNA and cancer: a new paradigm. *Cancer Res*. (2017) 77:3965–81. doi: 10.1158/0008-5472.CAN-16-2634
8. Peng WX, Koirala P, Mo YY. LncRNA-mediated regulation of cell signaling in cancer. *Oncogene*. (2017) 36:5661–7. doi: 10.1038/onc.2017.184
9. Chan JJ, Tay Y. Noncoding RNA:RNA Regulatory Networks in Cancer. *Int J Mol Sci*. 19:310. doi: 10.3390/ijms19051310
10. Ren P, Xing L, Hong X, Chang L, Zhang H. LncRNA PITPNA-AS1 boosts the proliferation and migration of lung squamous cell carcinoma cells by recruiting TAF15 to stabilize HMGB3 mRNA. *Cancer Med*. (2020) 9:7706–16. doi: 10.1002/cam4.3268
11. Sun J, Zhang Y, Li B, Dong Y, Sun C, Zhang F, et al. PITPNA-AS1 abrogates the inhibition of miR-876-5p on WNT5A to facilitate hepatocellular carcinoma progression. *Cell Death Dis*. (2019) 10:844. doi: 10.1038/s41419-019-2067-2
12. Yuan, C., and Yang, L. Long Non-Coding RNA PITPNA-AS1 accelerates the progression of colorectal cancer through miR-129-5p/HMGB1 Axis. *Cancer Manag Res*. (2020) 12:12497–507. doi: 10.2147/CMAR.S267844
13. Li W, Dong X, He C, Tan G, Li Z, Zhai B, et al. LncRNA SNHG1 contributes to sorafenib resistance by activating the Akt pathway and is positively regulated by miR-21 in hepatocellular carcinoma cells. *J Exp Clin Cancer Res*. (2019) 38:183. doi: 10.1186/s13046-019-1177-0
14. Park S, Lee J, Kim YH, Park J, Shin JW, Nam S. Clinical relevance and molecular phenotypes in gastric cancer, of TP53 mutations and gene expressions, in combination with other gene mutations. *Sci Rep*. (2016) 6:34822. doi: 10.1038/srep34822
15. Guo Q, Li L, Bo Q, Chen L, Sun L, Shi H. Long noncoding RNA PITPNA-AS1 promotes cervical cancer progression through regulating the cell cycle and apoptosis by targeting the miR-876-5p/c-MET axis. *Biomed Pharmacother*. (2020) 128:110072. doi: 10.1016/j.biopha.2020.110072
16. Pastushenko I, Blanpain C. EMT transition states during tumor progression and metastasis. *Trends Cell Biol*. (2019) 29:212–26. doi: 10.1016/j.tcb.2018.12.001

17. Qi X, Zhang DH, Wu N, Xiao JH, Wang X, Ma W. ceRNA in cancer: possible functions and clinical implications. *J Med Gen*. (2015) 52:710–8. doi: 10.1136/jmedgenet-2015-103334
18. Thomson DW, Dinger ME. Endogenous microRNA sponges: evidence and controversy. *Nat Rev Genet*. (2016) 17:272–83. doi: 10.1038/nrg.2016.20
19. Guo JC, Yang YJ, Zhang JQ, Guo M, Xiang L, Yu SF, et al. microRNA-448 inhibits stemness maintenance and self-renewal of hepatocellular carcinoma stem cells through the MAGEA6-mediated AMPK signaling pathway. *J Cell Phys*. (2019) 234:23461–74. doi: 10.1002/jcp.28915
20. Jin J, Wu Y, Zhou D, Sun Q, Wang W. miR-448 targets Rab2B and is pivotal in the suppression of pancreatic cancer. *Oncol Rep*. (2018) 40:1379–89. doi: 10.3892/or.2018.6562
21. Shimokawa H, Sunamura S, Satoh K. RhoA/Rho-Kinase in the Cardiovascular System. *Circul Res*. (2016) 118:352–66. doi: 10.1161/CIRCRESAHA.115.306532
22. Xin T, Lv W, Liu D, Jing Y, Hu F. ROCK1 knockdown inhibits non-small-cell lung cancer progression by activating the LATS2-JNK signaling pathway. *Aging (Albany NY)*. (2020) 12:12160–74. doi: 10.18632/aging.103386
23. Chen, J., Chen, J., Sun, B., Wu, J., and Du, C. ONECUT2 accelerates tumor proliferation through activating ROCK1 expression in gastric cancer. *Cancer Manag Res*. (2020) 12:6113–21. doi: 10.2147/CMAR.S256316
24. Guo D, Li Y, Chen Y, Zhang D, Wang X, Lu G, et al. DANCR promotes HCC progression and regulates EMT by sponging miR-27a-3p via ROCK1/LIMK1/COFILIN1 pathway. *Cell Prolif*. (2019) 52:e12628. doi: 10.1111/cpr.12628
25. Ma W, Sze KM, Chan LK, Lee JM, Wei LL, Wong CM, et al. RhoE/ROCK2 regulates chemoresistance through NF-κB/IL-6/STAT3 signaling in hepatocellular carcinoma. *Oncotarget*. (2016) 7:41445–59. doi: 10.18632/oncotarget.9441
26. Deng Q, Xie L, Li H. MiR-506 suppresses cell proliferation and tumor growth by targeting Rho-associated protein kinase 1 in hepatocellular carcinoma. *Biochem Biophys Res Commun*. (2015) 467:921–7. doi: 10.1016/j.bbrc.2015.10.043
27. Zhang T, Zhang L, Han D, Tursun K, Lu X. Circular RNA hsa_Circ_101141 as a competing endogenous RNA facilitates tumorigenesis of hepatocellular carcinoma by regulating miR-1297/ROCK1 pathway. *Cell Transpl*. (2020) 29:963689720948016. doi: 10.1177/0963689720948016
28. Wu H, Chen Y, Li B, Li C, Guo J, You J, et al. Targeting ROCK1/2 blocks cell division and induces mitotic catastrophe in hepatocellular carcinoma. *Biochem Pharm*. (2021) 184:114353. doi: 10.1016/j.bcp.2020.114353
29. Wu S, Ai N, Liu Q, Zhang J. MicroRNA-448 inhibits the progression of retinoblastoma by directly targeting ROCK1 and regulating PI3K/AKT signalling pathway. *Oncol Rep*. (2018) 39:2402–12. doi: 10.3892/or.2018.6302

Conflict of Interest: The authors declare that the research was conducted in the absence of any commercial or financial relationships that could be construed as a potential conflict of interest.

Copyright © 2021 Wang, Wang and Cao. This is an open-access article distributed under the terms of the Creative Commons Attribution License (CC BY). The use, distribution or reproduction in other forums is permitted, provided the original author(s) and the copyright owner(s) are credited and that the original publication in this journal is cited, in accordance with accepted academic practice. No use, distribution or reproduction is permitted which does not comply with these terms.

frontiers in Medicine

ORIGINAL RESEARCH
published: 24 May 2021
doi: 10.3389/fmed.2021.675842

Exosomal Circular RNA RNA-seq Profiling and the Carcinogenic Role of Exosomal circ-CYP24A1 in Cutaneous Squamous Cell Carcinoma

*Zheng Zhang, Hao Guo, Wenjia Yang and Jiuhong Li**

Department of Dermatology, Key Laboratory of Immunodermatology, The First Hospital of China Medical University, Shenyang, China

Objective: Aberrantly expressed exosomal circular RNAs (circRNAs) have been reported in various human cancers. Nevertheless, it remains elusive in cutaneous squamous cell carcinoma (cSCC). Herein, based on RNA-seq, we systematically uncovered the expression and implication of exosomal circRNAs in cSCC.

Methods: Plasma exosomes derived from cSCC and healthy subjects were characterized by nanoparticle tracking analysis (NTA), transmission electron microscopy (TEM), and western blot. Differentially expressed exosomal circular RNAs (circRNAs) were screened by RNA-seq analysis, which were validated by RT-qPCR. Among them, the biological structure of circ-CYP24A1 was validated by Sanger sequencing and RNase R digestion. Si-circ-CYP24A1 was transfected into exosomes, followed by incubation with A431 and SCL-1 cells. Then, viability, apoptosis, migration, and invasion were evaluated by CCK-8, TUNEL staining and migration assays.

Results: This study identified 25 up- and 76 down-regulated exosomal circRNAs in cSCC than healthy subjects. Among them, circulating circ-CYP24A1 was confirmed to be up-regulated in cSCC. Circ-CYP24A1 had a covalently closed circular structure and was not sensitive to RNase R digestion. After incubation with si-circ-CYP24A1-transfected exosomes, proliferation, migration, and invasion were lowered while apoptosis was enhanced in A431 and SCL-1 cells. Meanwhile, si-circ-CYP24A1-transfected exosomes significantly decreased the expression of downstream targets CDS2, MAVS, and SOGA in cSCC cells.

Conclusion: Collectively, our study identified that targeting exosomal circ-CYP24A1 could suppress cSCC progression by weakening tumor malignant behaviors, which might provide a promising therapeutic target and non-invasive diagnostic biomarker for cSCC.

Keywords: exosomes, circular RNA, cutaneous squamous cell carcinoma, circ-CYP24A1, progression

OPEN ACCESS

Edited by:
Fu Wang,
Xi'an Jiaotong University, China

Reviewed by:
Peisen Sun,
Shaanxi Normal University, China
Yanwei Luo,
Central South University, China

****Correspondence:***
Jiuhong Li
pfkljh@126.com

Specialty section:
This article was submitted to Precision Medicine, a section of the journal Frontiers in Medicine

Received: *04 March 2021*
Accepted: *29 April 2021*
Published: *24 May 2021*

Citation:
Zhang Z, Guo H, Yang W and Li J (2021) Exosomal Circular RNA RNA-seq Profiling and the Carcinogenic Role of Exosomal circ-CYP24A1 in Cutaneous Squamous Cell Carcinoma. Front. Med. 8:675842. doi: 10.3389/fmed.2021.675842

INTRODUCTION

Cutaneous squamous cell carcinoma (cSCC), a common malignant tumor, is representative of 20-50% all skin tumors, which shows a rapidly increased tendency in incidence globally (1). This malignancy has high risks of local recurrence, metastases as well as death (2). Although the outcomes of cSCC patients are acceptable, advanced cSCC is in relation to terrible morbidity as well as mortality (3). Most of cSCC subjects can be cured through complete surgical excision, but some will experience metastasis (4). The pathogenesis of cSCC has not yet been elucidated, so exploring the molecular mechanisms of its occurrence and progression may help prolong the survival time of patients.

Circular RNA (circRNA) is a non-coding RNA with a covalently closed circular structure without 5′ caps and 3′ poly tails (5). In recent years, it has gradually become a hot spot in molecular biology and clinical diagnostics. The expression of circRNAs in different species, tissues, and cells is different, with tissue specificity (6). Furthermore, circRNAs are not sensitive to nucleases and are more stable than linear RNAs, which make circRNAs have obvious advantages in the development and application of new clinical diagnostic markers (7). CircRNAs can also be used as molecular sponge of miRNAs to inhibit the activity of miRNAs, and has the function of regulating gene transcription and binding RNA binding proteins (8). The extensiveness, conservation, and tissue specificity all indicate that circRNAs are expected to become new tumor markers and potential targets, providing new directions for tumor diagnosis and targeted therapy (9). At present, there are few research reports on circRNAs in cSCC, and there is a lack of research on screening abnormally expressed circRNAs from an omics perspective.

Exosomes, extracellular vesicles secreted from eukaryotic cells (30–150 nm), are involved in cell-to-cell communication (10). Exosomes are key biological signal transmitters and carriers in pathological and physiological processes (11). Studies have shown that exosomes are released from cells through exocytosis, and then taken up by target cells, and can transfer biological signals between local or remote cells (12). Exosomes play wide roles in intercellular communication mainly through paracrine and autocrine processes, and actively act as biologically active molecules between different tissues and cells. Exosomes carry biologically active components derived from parent cells and are used as carriers for cell-to-cell communication (13). Their specific communication functions are closely related to the nature of the molecules they transport, and target cells can be modified while transferring these molecules. Recent research has verified the enrichment and stability of circRNAs in exosomes (14). Nevertheless, the clinical implications of exosomal circRNAs are still uncharted in cSCC. Here, this study systematically analyzed the expression patterns of exosomal circRNAs in cSCC by RNA-seq and validated the carcinogenic role of exosomal circ-CYP24A1 in cSCC, which extended the precise roles and mechanisms of exosomal circRNAs.

Abbreviations: cSCC, cutaneous squamous cell carcinoma; circRNA, circular RNA; NTA, nanoparticle tracking analysis; TEM, transmission electron microscopy; FC, fold change; GO, Gene Ontology; KEGG, Kyoto Encyclopedia of Genes and Genomes; si-NC, si-negative control; CCK-8, Cell Counting Kit-8; TUNEL, Terminal deoxynucleotidyl transferase (TdT) dUTP Nick-End Labeling.

MATERIALS AND METHODS

Patients and Specimens

A total of five cSCC patients and five healthy subjects were recruited from The First Hospital of China Medical University (Shenyang, China) between 2018 and 2019. We collected the clinical information of each subject including maximum tumor diameter, tumor thickness, preoperative serum SCC-Ag and serum SCC-Ag 1 month after surgery. Each participant signed the informed consent and this study gained the Ethics Committee of The First Hospital of China Medical University (2018010). 5 mL of peripheral venous blood samples were drawn from each participant, which were then stored at −4°C overnight. The samples were immediately centrifuged at 2,000 g for 5 min. The upper serum samples were taken and placed in a sterile EP tube at −80°C.

Isolation of Exosomes From Plasma and Medium

According to the specification of the exoEasy Maxi Kit (Qiagen), exosomes were isolated from plasma and cell culture medium. 1 volume of XBP buffer was added to 1 volume of samples. After mixing immediately, the sample/XBP buffer mixture was put at room temperature. The mixture was then added to the exoEasy spin column and centrifuged at 500 g for 1 min. After discarding the flow-through, the spin column was placed in the same collection tube. 10 mL XWP buffer was added to the tube and residual volume in the spin column was removed by centrifugation at 5,000 g for 5 min. All flow-through in the collection tube was discarded. The spin column was moved to a new collection tube. 400 μl XE buffer was added to the membrane and incubated for 1 min. Following centrifugation at 500 g for 5 min, the eluate was collected and re-added to the exoEasy spin column. Then, the eluate was incubated for 1 min and centrifuged at 5,000 g for 5 min. The eluate was harvested and transferred to a new collection tube.

Nanoparticle Tracking Analysis

The pellet of exosomes after centrifugation was dissolved in 1 mL PBS. The samples were vortexed to distribute as evenly as possible and diluted to 1×10^{12}/L exosomal suspension. 1 mL exosomal suspension was taken and placed it in a clean cuvette. A Malvern Panalytical particle size analyzer was used to detect the particle size distribution of exosomes.

Transmission Electron Microscopy

10 μg plasma exosomes were dropped on a dedicated copper net and fixed with 1% glutaraldehyde fixative for 10 min. Then, samples were rinsed with PBS buffer. After the negative staining with 2% phosphotungstic acid, the TEM (JEM-2100) was used to observe and take pictures under a voltage of 100 kV.

TABLE 1 | The primer sequences of RT-qPCR.

Targets	Sequences (5′-3′)
Circ-CYP24A1	TTTGCCAGCGATAATACG (forward)
	CCTGGTTTCATTAGTTTCTTT (reverse)
Circ-DNA2	GGCACCAGCATAGCCAGT (forward)
	CCAGGCGCTTTTCACAGT (reverse)
circ-SYNE2	TGCAAGAACTTTAATGACTGGT (forward)
	TTGCAGGTGGTGTTCAAGAA (reverse)
CYP24A1	AGTCTAATGTGGATTCTCT (forward)
	CGTAAGCCTCATAGATTC (reverse)
Circ-ALDH3A2	CTGTTGCTCACTTTCCTGGG (forward)
	TGACTTCCTGACTGTACACATTG (reverse)
Circ-LRBA	CCTTGCCCACCAACTTCA (forward)
	AGCCATTTTCCATGCAGC (reverse)
Circ-SENP2	ACAGCTGAATGGGAGTGATTG (forward)
	GTGGCAGCACAGAACCTTC (reverse)
Circ-HLA-B	ACTACAACCAGAGCGAGGAC (forward)
	GTAATCCTTGCCGTCGTAGG (reverse)
CDS2	TCTCTATCTAATAGGATTCTG (forward)
	TTACAACAATCAGCAATG (reverse)
MAVS	CTATAAGTATATCTGCCGCAATT (forward)
	AGTCGATCCTGGTCTCTT (reverse)
SOGA1	AAAGCATAAATCGGGCAACTC (forward)
	CTCCTCAATCTCGTCCTTCTC (reverse)
GAPDH	GGCCTCCAAGGAGTAAGACC (forward)
	AGGGGAGATTCAGTGTGGTG (reverse)

Western Blot

After resuspending plasma exosomes in a lysis buffer containing protease inhibitors, total protein was extracted for analysis. The extracted protein was added to polyacrylamide gel electrophoresis for separation and transferred to PVDF membranes. After blocking with 5% skim milk for 1 h, membranes were incubated with CD9 (1:2000; ab92726; Abcam), CD63 (1:2000; ab134045; Abcam), TSG101 (1:1000; ab125011; Abcam) overnight in a refrigerator at 4°C. After washing with PBS buffer, the secondary antibody was incubated for 1 h. The chemiluminescence method was utilized to develop color.

CircRNA RNA-Seq Analysis

In line with the QIAzol kit procedure, total exosomal RNAs were extracted from three pairs of cSCC patients and healthy subjects. After the purity and concentration test met the standards, Shanghai Yunxu Biotechnology Co., Ltd. applied RNA-seq technology to detect the circRNA expression profile of exosomes. Briefly, ribosomal RNAs were removed with NEBNext rRNA Depletion Kit (New England Biolabs, Inc., Massachusetts, USA) and circRNAs were enriched in extracted exosomal RNAs. After constructing the RNA library with NEBNext® Ultra™ II Directional RNA Library Prep Kit (New England Biolabs, Inc., Massachusetts, USA), libraries were controlled for quality and quantified through the BioAnalyzer 2100 system (Agilent Technologies, Inc., USA). Library sequencing was carried out on an illumina Hiseq instrument with 150 bp paired end reads. After sequencing by Illumina HiSeq 4000 sequencer, paired-end reads were harvested. Q30 was used for quality control. Cutadapt software (v1.9.3) was employed to trim the 3'end and delete the poor-quality reads (15). By STAR software (v2.5.1b), the obtained high-quality reads were compared with the reference genome (UCSC HG19) (16). The obtained circRNAs were identified through the DCC software (v0.4.4) that had high predictive accuracy and sensitivity (17). The edgeR software (v3.16.5) was applied for standardization for raw junction reads with TMM method, followed by log2 conversion (18). CircRNAs were annotated by the Circ2Trait (19) and CircBase databases. Differentially expressed circRNAs were screened between cSCC and healthy subjects with |fold change (FC)| $\geq$2 and p-value $\leq$ 0.05. Gene Ontology (GO) and Kyoto Encyclopedia of Genes and Genomes (KEGG) enrichment analyses were presented for differentially expressed circRNAs-associated genes *via* clusterProfiler package (20). Terms with p-value $\leq$ 0.05 were significantly enriched. RNA-seq data have been uploaded to the GEO database (accession number: GSE136113).

RT-qPCR

Total RNA was extracted from plasma and cells, which was reverse transcribed into cDNA via PrimerscriptTMRT reverse transcription kit. RT-qPCR was presented with SYBR Premix Ex Taq™ (Takara, Beijing, China). Primers were synthesized by Xiamen Antihela Biotechnology Co., Ltd. (Fujian, Xiamen, China), as listed in **Table 1**. The relative expression levels were determined with $2^{-\Delta\Delta CT}$ method.

Sanger Sequencing

2% agarose gel was prepared for this study. 2 g agar powder was poured into a glass bottle, and 100 mL 1X TAE solution was added to the bottle. Then, the bottle was repeatedly heated in a microwave oven and boiled until the agar powder was completely dissolved. The glass bottle was cooled to 60°C. Afterwards, 1 μl Red was added according to the instructions. The agarose gel liquid was poured into the tank and let it stand at room temperature until the gel was completely solidified for 40 min. The comb was then gently and slowly pull out. The gel was put into the electrophoresis tank in the correct way and 1XTAE buffer was added to it. PCR product and DNA maker were added to the sample tank. The voltage was set to 100 V, and the electrophoresis was about 30 min. After the electrophoresis was over, the gel was taken out. The gel imaging system was observed and the corresponding PCR band was cut out for Sanger sequencing.

Cell Culture and Transfection

A431 cells and SCL-1 cells were purchased from the American Type Culture Collection (ATCC). The cells were cultured in DMEM medium containing 10% fetal bovine serum, 100 U/mL streptomycin and penicillin at 37°C and 5% CO_2. The siRNAs were designed and synthesized by Hanheng Biological Technology Co., Ltd. (Shanghai, China). The siRNAs against circ-CYP24A1 were as follows: circ-CYP24A1, 5′-GAUAAUACGCCUCAGGGAATT-3′ (sense), 5′-UUCCCUGAGGCGUAUUAUCTT-3′ (antisense); si-negative

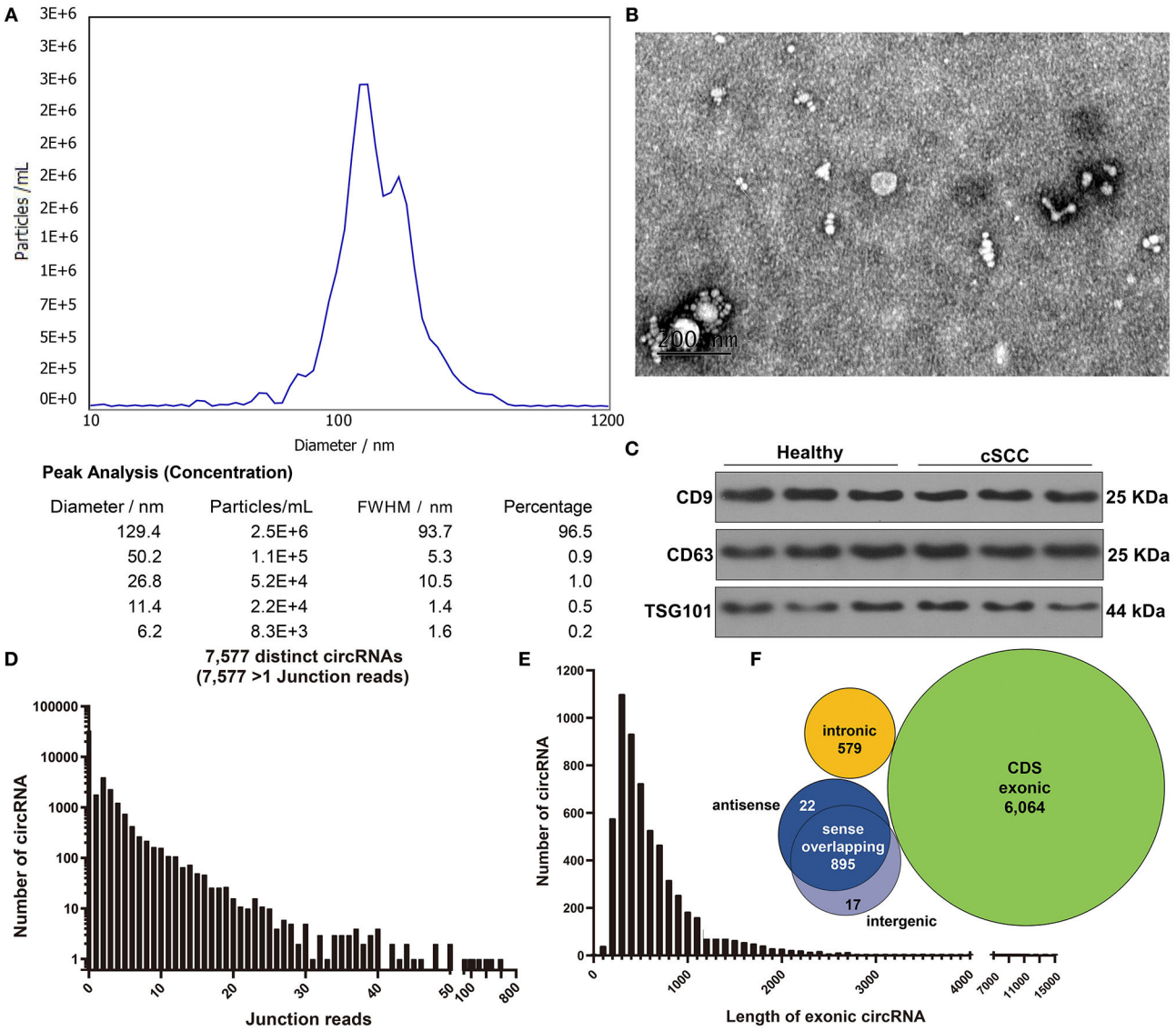

Diameter / nm	Particles/mL	FWHM / nm	Percentage
129.4	2.5E+6	93.7	96.5
50.2	1.1E+5	5.3	0.9
26.8	5.2E+4	10.5	1.0
11.4	2.2E+4	1.4	0.5
6.2	8.3E+3	1.6	0.2

FIGURE 1 | Characterization of exosomes from plasma of cSCC and healthy subjects. **(A)** NTA for detection of the particle size of isolated exosomes. **(B)** TEM for the appearance of exosomes. Bar = 200 nm. **(C)** Western blot for examining the expression of exosomal specific markers CD9 and CD63. **(D)** The junction reads of exosomal circRNAs. **(E)** The length of exonic circRNAs. **(F)** The genomic source of exosomal circRNAs.

control (si-NC), 5′- UUCUCCGAACGUGUCACGUTT-3′ (sense), 5′- ACGUGACACGUUCGGAGAATT-3′ (antisense). Exosomes were separated from the supernatant of cultured A431 cells and SCL-1 cells. Before harvesting the culture medium, A431 cells and SCL-1 cells were washed twice with PBS, and then cultured for 48 h. The supernatant was harvested and centrifuged at 2,000 g for 30 min at 4°C, 10,000 g for 30 min, and 100,000 g for 70 min. The exosomes were washed once with PBS, then ultracentrifuged again at 100,000 g for 70 min. After characterization of exosomes, the siRNAs were transfected into exosomes via Exosome Transfection Kit. Then, transfected exosomes were incubated with A431 cells or SCL-1 cells for 48 h. RT-qPCR was used for examining the expression of circ-CYP24A1.

RNase R Digestion

Total RNA was extracted from A431 and SCL-1 cells. They, samples were incubated with 6 units of RNase R for 15 min at 37°C. The expression of circ-CYP24A1 and CYP24A1 was detected through RT-qPCR.

Tracer Experiment

2 μg exosomes derived from A431 cells and SCL-1 cells were taken and resuspended in 1 mL Diluent C. 4 μL PKH67 was added to 1 mL Diluent C to prepare the dye. 1 mL of exosomes were mixed with 1 mL dye suspension for 5 min. 2 mL of serum was added to stop staining. The medium was changed with the complete medium containing PKH67-labeled exosomes. Then, cells were fixed with paraformaldehyde

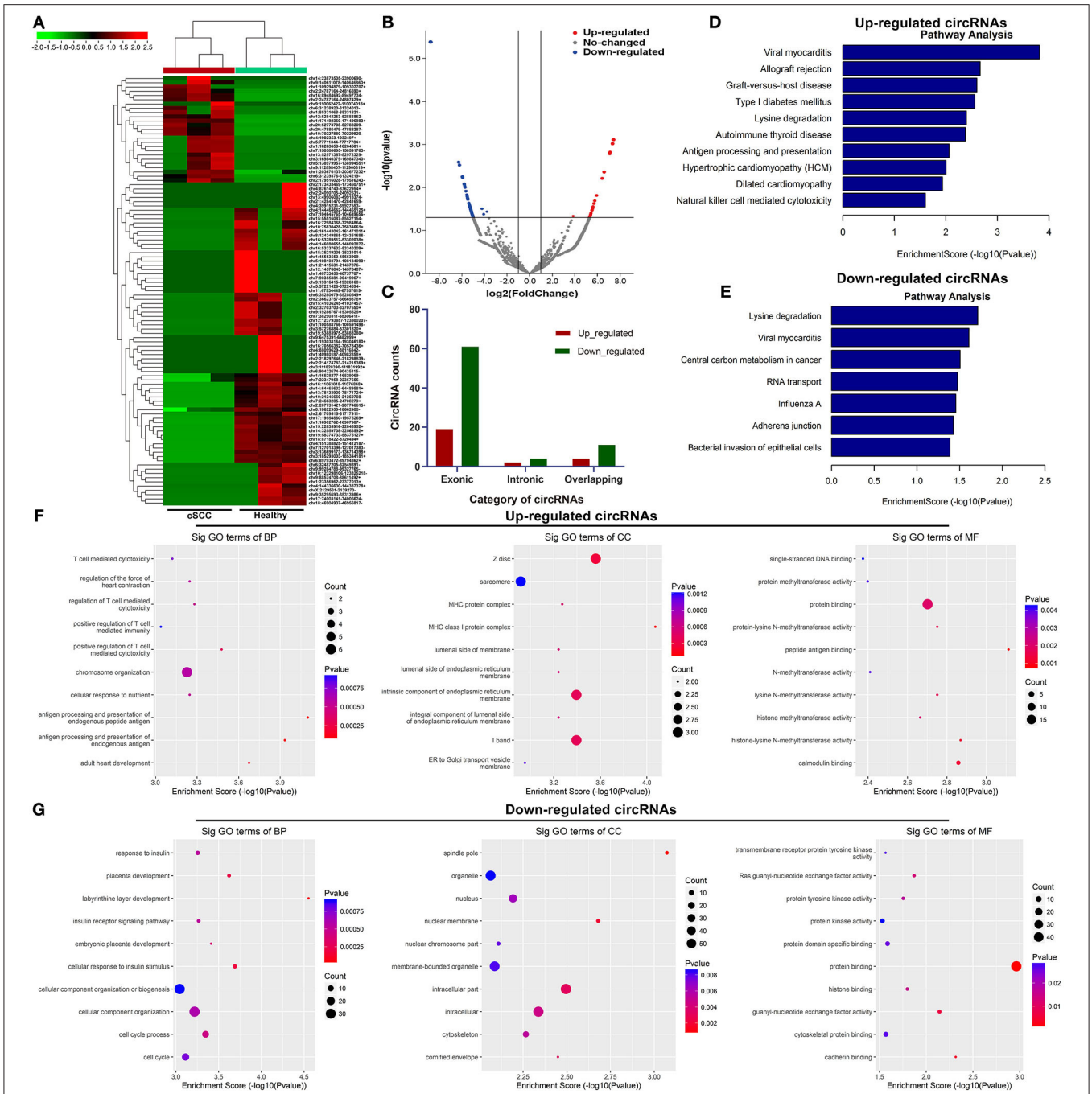

FIGURE 2 | Identification of exosomal circRNAs and their functions in cSCC. **(A)** Heatmap for the up- (red) and down-regulated (green) exosomal circRNAs between cSCC and healthy individuals. **(B)** Volcano plots of up- (red) and down-regulated (blue) circRNAs between cSCC and healthy individuals. **(C)** Category of differentially expressed circRNAs. **(D,E)** KEGG pathway enrichment results of up- and down-regulated circRNAs. **(F,G)** GO annotation results of up- and down-regulated circRNAs.

for 40 min. After staining A431 cells and SCL-1 cells with Hoechst for 10 min, they were washed twice with PBS. Then, 20 μL anti-fluorescence mounting solution was added to the slide for mounting. A laser confocal microscope was used to observe the interaction between exosomes and A431 cells and SCL-1 cells.

Cell Counting Kit-8assay

A431 cells and SCL-1 cells were inoculated into a 96-well plate (1,000 cells/well). After co-incubating the transfected exosomes, 100 μl CCK-8 (Dojindo, Kumamoto, Japan) was added. A microplate reader was utilized to detect the absorbance at 0, 24, 48, 72, and 96 h. Six multiple holes were set in each group.

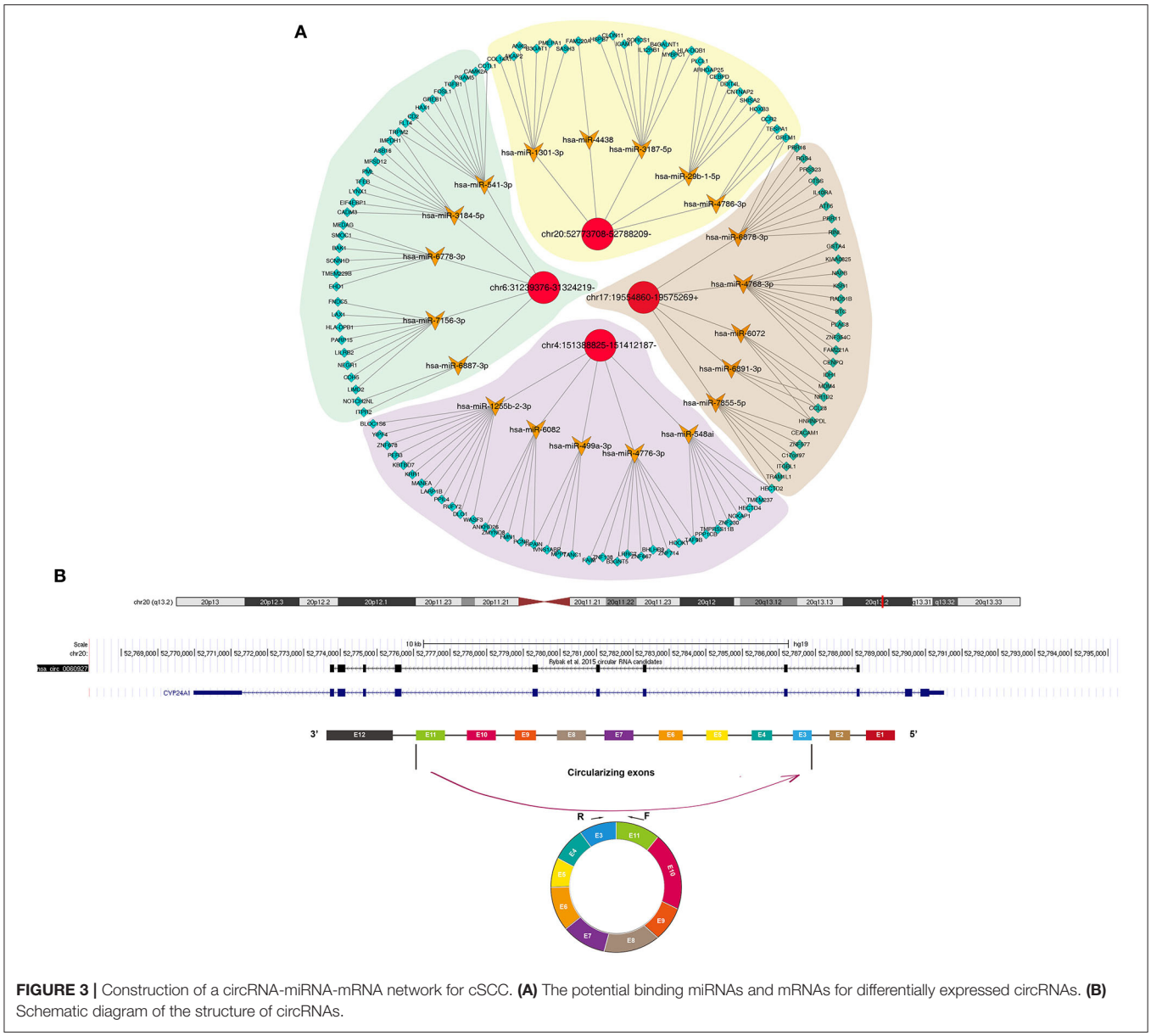

FIGURE 3 | Construction of a circRNA-miRNA-mRNA network for cSCC. **(A)** The potential binding miRNAs and mRNAs for differentially expressed circRNAs. **(B)** Schematic diagram of the structure of circRNAs.

Terminal Deoxynucleotidyl Transferase dUTP Nick-End Labeling Assay

A431 cells and SCL-1 cells were seeded into a 96-well plate (1,000 cells/well), which were co-incubated with the transfected exosomes for 48 h. The cells were fixed with 4% paraformaldehyde for 30 min. Then, the cells were incubated with TUNEL detection solution at 37°C for 60 min in the dark. After mounting with anti-fluorescence quenching mounting solution, images were acquired under a fluorescence microscope.

Transwell Assays

A431 cells and SCL-1 cells were cultured in a 24-well plant (5,000 cells/well). The cells were co-incubated with the transfected exosomes for 24 h. The cells were resuspended with serum-free DMEM medium. 10^4 cells were seeded onto the upper chamber of the Transwell. For invasion assay, the bottom of the upper chamber was pre-coated with Matrigel (Corning, USA). Meanwhile, 650 μL DMEM complete medium containing 10% FBS was added to the bottom chamber. There were three replicate wells in each group. After culturing for 24 h, the cells on the inner surface of the bottom of the chamber were wiped with a cotton swab. The cells were fixed with paraformaldehyde and stained with crystal violet.

Statistical Analyses

Statistical analyses were presented by R language and Graphpad Prism software. Correlation between circRNAs (circ-CYP24A1, circ-DNA2, and circ-ALDH3A2) and clinical features (including maximum tumor diameter, tumor

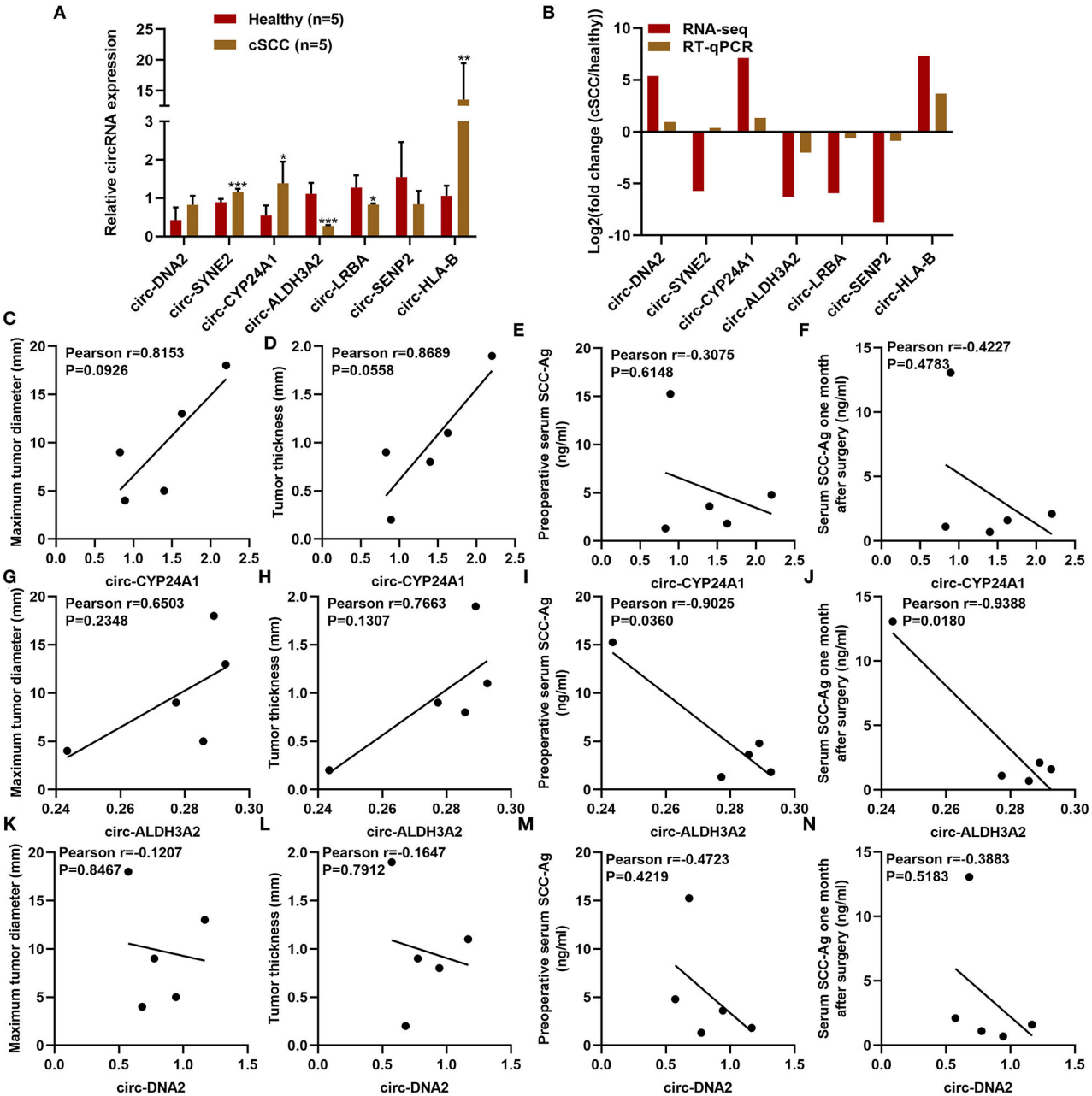

FIGURE 4 | Clinical characteristics of differentially expressed circRNAs in cSCC. **(A,B)** RT-qPCR for validation of the expression of plasma circ-DNA2, circ-SYNE2, circ-CYP24A1, circ-ALDH3A2, circ-LRBA, circ-SENP2, and circ-HLA-B in 5 paired cSCC and healthy individuals. **(C-N)** The correlations of plasma **(C-F)** circ-CYP24A1, **(G-J)** circ-ALDH3A2, and **(K-N)** circ-DNA2 levels with maximum tumor diameter, tumor thickness, pre-operative serum SCC-Ag and serum SCC-Ag 1 month after surgery. *P-value < 0.05; **p-value < 0.01; ***p-value < 0.001.

thickness, pre-operative serum SCC-Ag, and serum SCC-Ag 1 month after surgery) was evaluated by Pearson test. Each experiment was repeated three times and data were expressed as the mean ± standard deviation. Comparisons between groups were presented by student's t-test or one-way analysis of variance. P-value < 0.05 indicated statistical significance.

RESULTS

Characterization of Exosomes Derived From cSCC Patients' Plasma

Here, plasma samples from three paired cSCC patients and healthy individuals. Firstly, plasma exosomes were identified by employing NTA, TEM, and western blot. NTA results

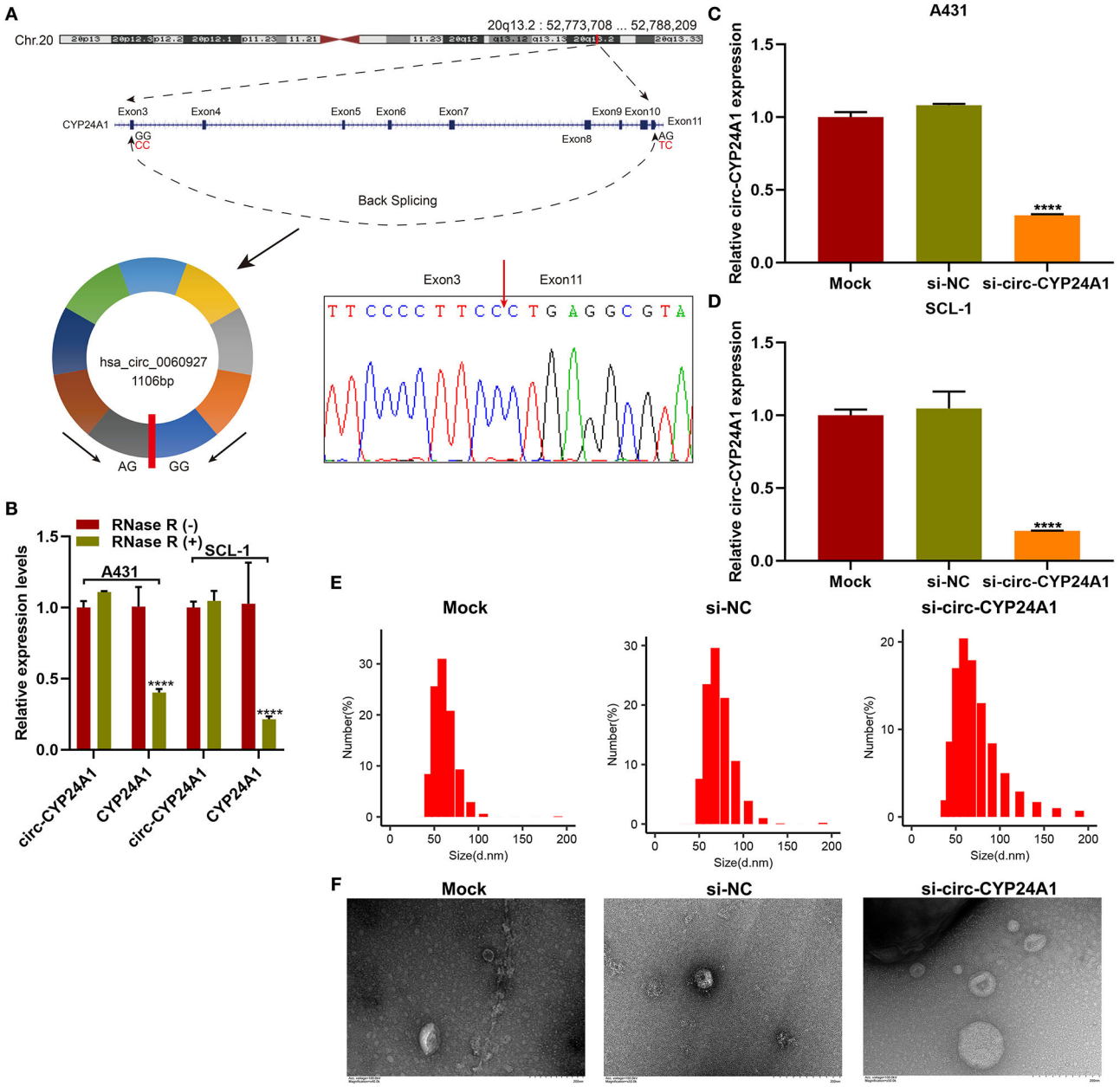

FIGURE 5 | Validation of the biological structure of circ-CYP24A1. **(A)** Sanger sequencing for the circ-CYP24A1 PCR products. **(B)** RT-qPCR for the expression of circ-CYP24A1 in A431 and SCL-1 cells under RNase R (-) or RNase R (+). **(C,D)** RT-qPCR confirming the expression of circ-CYP24A1 in A431 and SCL-1 cells incubated with si-circ-CYP24A1-transfected exosomes. **(E)** NTA for detecting the particle size of transfected exosomes. **(F)** TEM for the appearance of transfected exosomes. Bar = 200 nm. ****P-value < 0.0001.

showed the peak size of most exosomes (96.5%) was 129.4 nm (**Figure 1A**). TEM analysis demonstrated that exosomes that both came from cSCC and healthy individuals had a single layer membrane structure and the appearance of exosomes was round or elliptical vesicle-like structure with a diameter of 40-100 nm, which conformed to exosomal morphology (**Figure 1B**). Our western blot results confirmed that exosomal specific markers CD9 and CD63 had high abundance in plasma exosomes from cSCC and healthy individuals (**Figure 1C**). RNA-seq technique was employed to obtain exosomal circRNAs. After image recognition and base recognition, the original reads were harvested from the Illumina HiSeq sequencer. We applied cutadapt software to obtain high-quality clean reads. By STAR software, we compared clean reads to UCSC hg19. **Figure 1D** showed the junction reads of identified circRNAs. A total of 7,577 exosomal circRNAs were detected by DCC software. We divided the circRNAs into both ends on exonic, intronic, intergenic and antisense circRNAs according to the

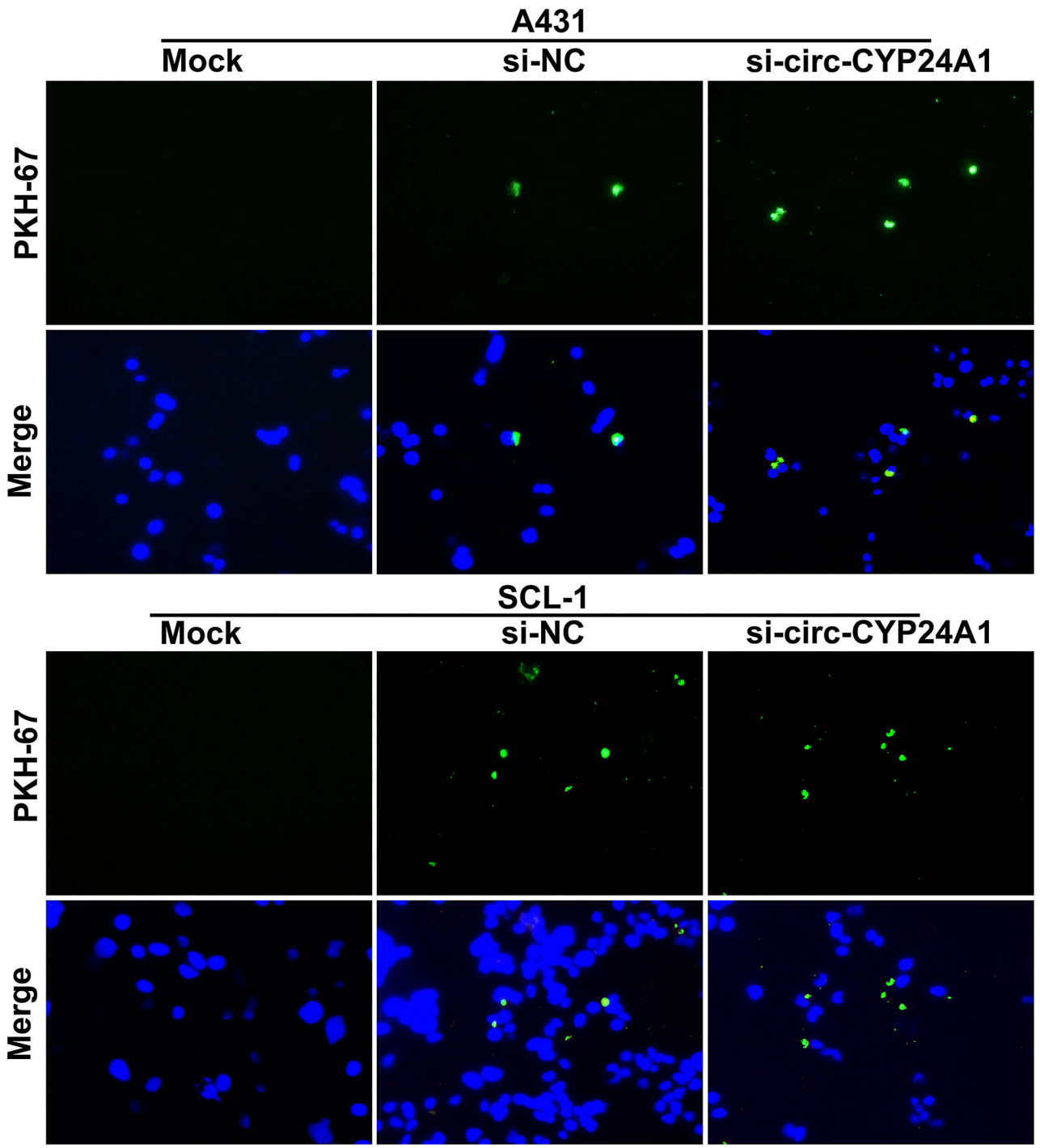

FIGURE 6 | A tracer experiment for observing the uptake of exosomes carrying circ-CYP24A1 by A431 and SCL-1 cells.

alignment position of the two ends of the circRNAs. The length of both ends on exonic circRNAs was counted, as shown in **Figure 1E**. As expected, most exosomal circRNAs were composed of both ends on exons, followed by intergenic and antisense (**Figure 1F**).

Identification of Exosomal CircRNAs and Their Functions in cSCC

Based on the standardized number of reads, logCPM value of each circRNA was calculated in each sample. We screened the differentially expressed exosomal circRNAs between cSCC and

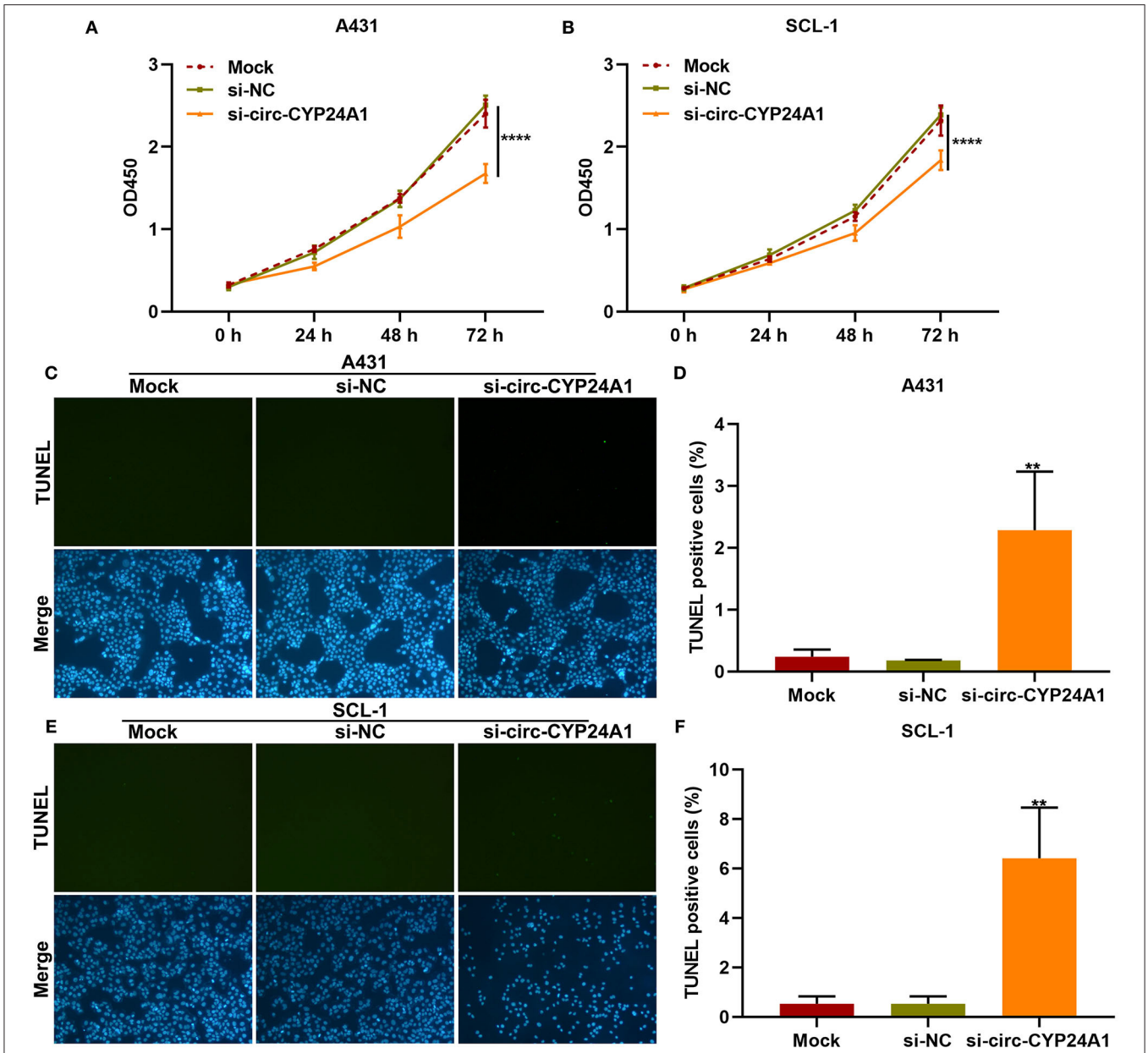

FIGURE 7 | The effects of exosomal circ-CYP24A1 knockdown on proliferation and apoptosis of cSCC cells. **(A,B)** CCK-8 for the cell viability of A431 and SCL-1 cells incubated with si-circ-CYP24A1-transfected exosomes. **(C-F)** TUNEL staining for assessing the apoptosis of **(C,D)** A431 and **(E,F)** SCL-1 cells incubated with si-circ-CYP24A1-transfected exosomes. $^{**}P$-value < 0.01; $^{****}p$-value < 0.0001.

healthy samples. 25 circRNAs were up-regulated and 76 were down-regulated in cSCC compared to healthy subjects with the threshold of $|FC| \geq 2$ and p-value ≤ 0.05 (**Figures 2A,B**; **Supplementary Table 1**). Most of them were exonic circRNAs (**Figure 2C**). We further annotated the host genes of these differentially expressed circRNAs to predict their functions. As a result, up-regulated circRNAs were mainly enriched in immune-related pathways like antigen processing and presentation and natural killer cell mediated cytotoxicity (**Figure 2D**) while down-regulated circRNAs were significantly related to central carbon metabolism in cancer, RNA transport and bacterial invasion of epithelial cells (**Figure 2E**). GO enrichment analysis also revealed that up-regulated circRNAs were primarily enriched in T cell mediated cytotoxicity or immunity and MHC protein complex (**Figure 2F**), while down-regulated circRNAs had distinct relationships with cellular component organization and cell cycle (**Figure 2G**).

Construction of a circRNA-miRNA-mRNA Network for cSCC

Increasing evidence highlights the roles of circRNAs as miRNA sponges. Here, we predicted the binding miRNAs

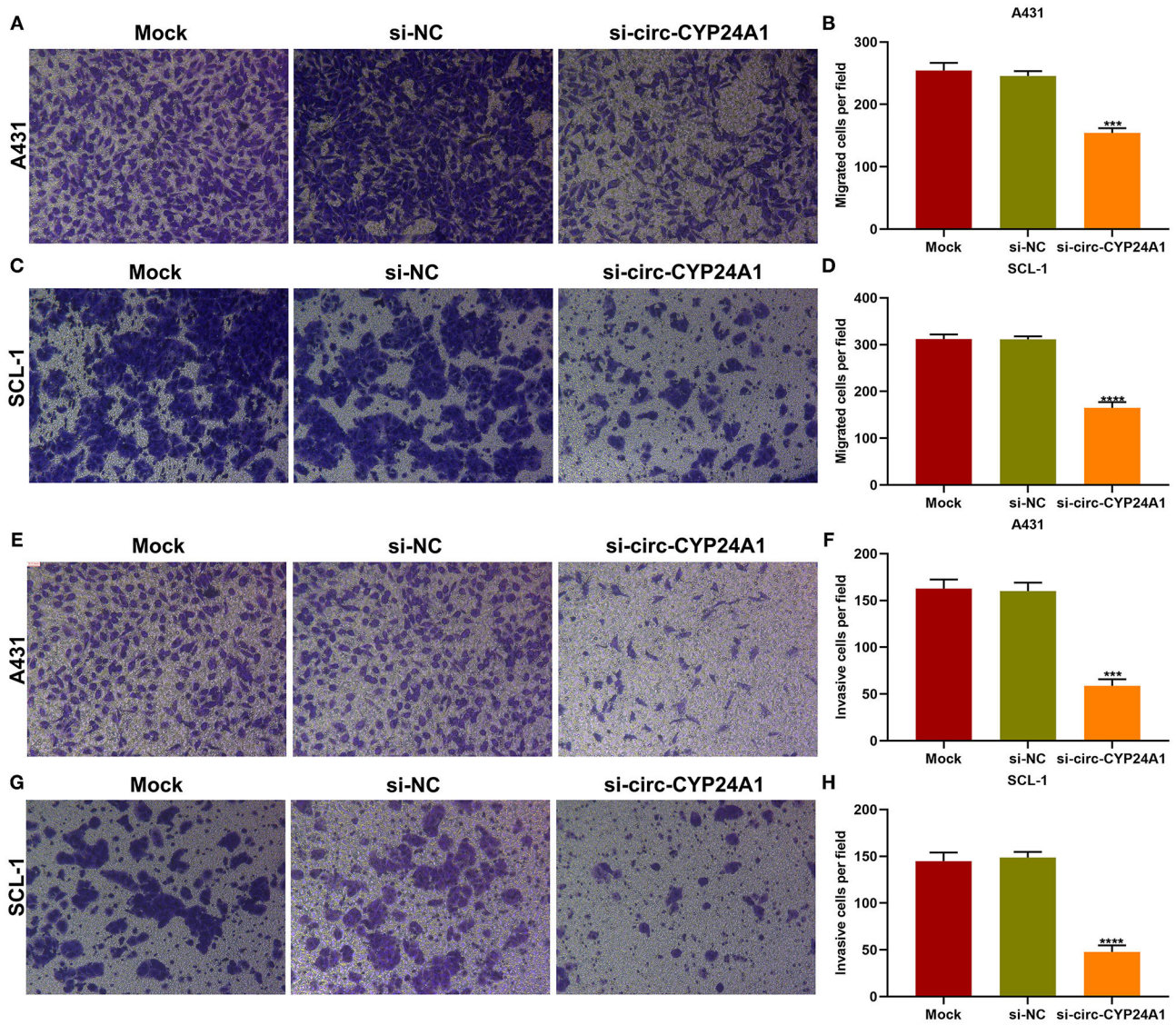

FIGURE 8 | The roles of exosomal circ-CYP24A1 on migrated and invasive abilities of cSCC cells. **(A-D)** The number of migrated **(A,B)** A431 cells and **(C,D)** SCL-1 cells under incubation with si-circ-CYP24A1-transfected exosomes. **(E-H)** The number of invasive **(E,F)** A431 cells and **(G,H)** SCL-1 cells when incubated with si-circ-CYP24A1-transfected exosomes. ***P-value < 0.001; ****p-value < 0.0001.

of differentially expressed circRNAs through circbank database (http://www.circbank.cn/) and target mRNAs of these miRNAs by Targetscan database (http://www.targetscan.org). The potential binding miRNAs and mRNAs were detected for differentially expressed circRNAs, as shown in **Figure 3A**. Furthermore, we visualized the structure of circRNAs (**Figure 3B**).

Clinical Characteristics of Differentially Expressed circRNAs in cSCC

RT-qPCR was used for validation of the expression of differentially expressed circRNAs including circ-DNA2, circ-SYNE2, circ-CYP24A1, circ-ALDH3A2, circ-LRBA, circ-SENP2, and circ-HLA-B in plasma samples from 5 paired cSCC and healthy individuals. Our results confirmed that plasma circ-SYNE2, circ-CYP24A1, circ-ALDH3A2, and circ-HLA-B were all significantly up-regulated in cSCC than healthy individuals while plasma circ-ALDH3A2 and circ-LRBA were both significantly down-regulated in cSCC compared to healthy subjects (**Figures 4A,B**). The clinical features of plasma circ-CYP24A1, circ-ALDH3A2, and circ-DNA2 were further assessed. We found that plasma circ-CYP24A1 (**Figures 4C–F**), circ-ALDH3A2 (**Figures 4G–J**) and circ-DNA2 (**Figures 4K–N**) levels displayed correlations to maximum tumor diameter, tumor thickness, preoperative serum SCC-Ag and serum SCC-Ag 1 month after surgery.

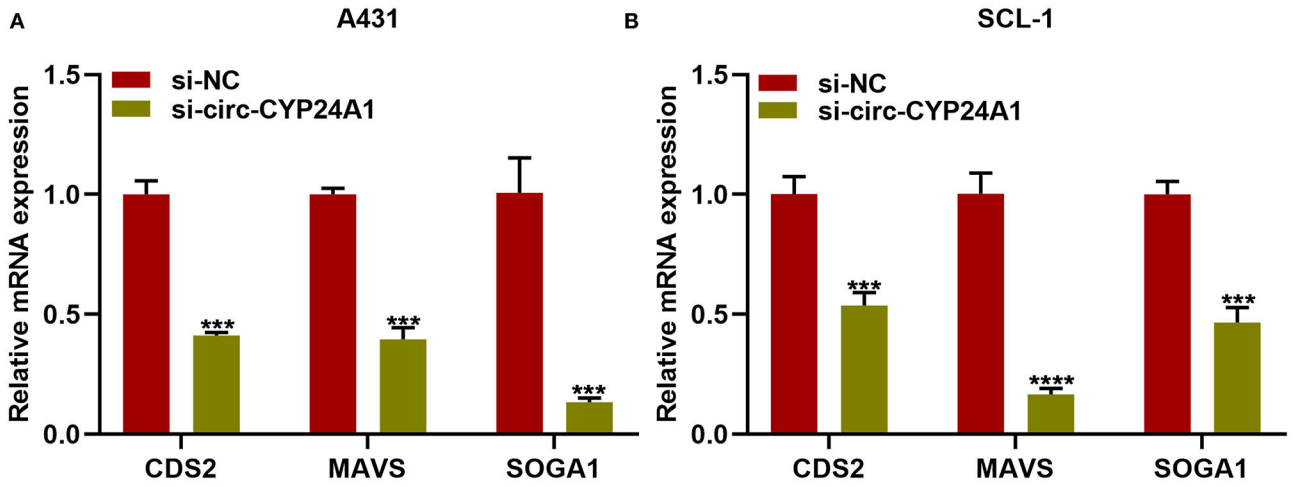

FIGURE 9 | Exosomal circ-CYP24A1 knockdown lowers CDS2, MAVS and SOGA1 expression in cSCC cells. **(A,B)** RT-qPCR for the mRNA expression of CDS2, MAVS and SOGA1 in **(A)** A431 cells and **(B)** SCL-1 cells incubated with si-circ-CYP24A1-transfected exosomes. ***P-value < 0.001; ****p-value < 0.0001.

Validation of the Biological Structure of Exosomal Circ-CYP24A1

Our sanger sequencing results confirmed that circ-CYP24A1 possessed a covalently closed circular structure (**Figure 5A**). Furthermore, circ-CYP24A1 was not sensitive to RNase R digestion, while linear CYP24A1 was mostly digested (**Figure 5B**). To investigate the biological functions of exosomal circ-CYP24A1 in cSCC, A431 and SCL-1 cells were incubated with si-circ-CYP24A1-transfected exosomes. RT-qPCR results confirmed that circ-CYP24A1 was significantly lowered both in A431 cells (**Figure 5C**) and SCL-1 cells (**Figure 5D**). The exosomes transfected with si-circ-CYP24A1 were characterized by NTA (**Figure 5E**) and TEM (**Figure 5F**).

Crosstalk Between Exosomes and cSCC Cells

To verify whether the exosomes carrying circ-CYP24A1 can be taken up by cSCC cells, this study used PKH67-labeled exosomes and co-cultured with A431 cells and SCL-1 cells. Under a laser confocal microscope, we found that exosomes carrying circ-CYP24A1 were taken up by A431 cells and SCL-1 cells (**Figure 6**), confirming the crosstalk between exosomes and cSCC cells.

Exosomal Circ-CYP24A1 Knockdown Restrains Proliferation and Induces Apoptosis of cSCC Cells

We further observed whether exosomal circ-CYP24A1 affected the proliferation and apoptosis of cSCC cells. Our CCK-8 results showed that exosomes transfected with si-circ-CYP24A1 distinctly lowered the cell viability of A431 cells (**Figure 7A**) and SCL-1 cells (**Figure 7B**). As shown in TUNEL staining results, the apoptosis was markedly enhanced by exosomes transfected with si-circ-CYP24A1 in A431 cells (**Figures 7C,D**) and SCL-1 cells (**Figures 7E,F**). Thus, exosomal circ-CYP24A1 knockdown may restrain proliferation and induce apoptosis of cSCC cells.

Exosomal Circ-CYP24A1 Knockdown Restrains Migration and Invasion of cSCC Cells

Migration and invasion of A431 and SCL-1 cells incubated with si-circ-CYP24A1-transfected exosomes were evaluated by transwell assays. As a result, the number of migrated A431 cells (**Figures 8A,B**) and SCL-1 cells (**Figures 8C,D**) was significantly lessened after incubation with si-circ-CYP24A1-transfected exosomes. Moreover, we found that si-circ-CYP24A1-transfected exosomes markedly decreased the number of invasive A431 cells (**Figures 8E,F**) and SCL-1 cells (**Figures 8G,H**). These data demonstrated that exosomal circ-CYP24A1 knockdown may suppress migration as well as invasion of cSCC cells.

Exosomal Circ-CYP24A1 Knockdown Lowers CDS2, MAVS and SOGA1 Expression in cSCC Cells

Our bioinformatics analysis predicted that CDS2, MAVS and SOGA1 were downstream mRNAs. Here, we further verified the relationships of exosomal circ-CYP24A1 with CDS2, MAVS and SOGA1. After incubation with si-circ-CYP24A1-transfected exosomes, RT-qPCR confirmed that the mRNA expression of CDS2, MAVS and SOGA1 was distinctly decreased in A431 cells (**Figure 9A**) and SCL-1 cells (**Figure 9B**). Above results indicated that CDS2, MAVS and SOGA1 could be potential targets of circ-CYP24A1 in cSCC.

DISCUSSION

This study constructed RNA-seq expression profiles of exosomal circRNAs in cSCC and verified the tumorigenic roles of exosomal circ-CYP24A1 in cSCC via regulating malignant biological behaviors.

CircRNA has a covalently closed loop structure without 5′ caps and 3′ poly tails. Several aberrantly expressed circRNAs have

been reported. Circ-001937 is highly expressed in cSCC tissues (21). Its knockdown restrains proliferation as well as induces apoptosis through miRNA-597-3p/FOSL2 axis in cSCC (21). Circ-0070934 may facilitate proliferative and invasive capacities of cSCC cells through sponging miR-1238 and miR-1247-5p (22). Circ-0070934 promotes cSCC progression through miR-1236-3p/HOXB7 regulatory axis (23). Circ-0001821 up-regulation has been detected in cSCC tissues and induces proliferation as well as migration of cSCC cells (24). Circ-SEC24A is overexpressed in cSCC tissues and its silencing lowers proliferation, migration, invasion, and glycolysis as well as induces apoptosis in cSCC cells (25). Circ-0001360 is down-regulated in cSCC tissue specimens and up-regulating circ-0001360 may accelerate cSCC development (26). CircRNAs are enriched and stable in exosomes (27). There is distinct differentiation in exosomal circRNAs between patients and healthy individuals (28). Exosomal circRNAs have been considered as diagnosed markers for specific diseases (29). Nevertheless, the implications of exosomal circRNAs remain elusive in cSCC. Here, the differential expression of exosomal circRNAs was analyzed between 3 pairs of cSCC patients and healthy individuals by RNA-seq. 25 exosomal circRNAs were up-regulated and 76 were down-regulated in cSCC, which deserved in-depth exploration.

Exosomal circRNAs provide added evidence toward conventional diagnostic approaches, which are applied to restrain the malignant progression of malignant tumors (30). For instance, tumor-derived exosomal circ-PACRGL acts as the carcinogenic function in colorectal cancer progress and metastasis (31). Here, we verified a novel circ-CYP24A1 that was dysregulated in cSCC. Abnormal proliferation is a key factor in neoplastic transformation (32). Exosomal circ-CYP24A1 knockdown distinctly lowered the proliferative ability as well as elevated the apoptotic levels in cSCC cells. Despite the benign clinical behaviors, cSCC exhibits locally invasive and metastatic properties (33). Our data demonstrated that targeting exosomal circ-CYP24A1 may limit migrated and invasive capacities of cSCC cells. However, the clinical significance of exosomal circ-CYP24A1 will be validated in larger cSCC cohorts.

CONCLUSION

Taken together, we systematically analyzed the exosomal circRNAs in cSCC and identified the carcinogenesis of exosomal circ-CYP24A1 in cSCC, which may provide a mechanistic insight into the roles of exosomal circRNAs in cSCC development and promising markers toward cSCC therapy.

DATA AVAILABILITY STATEMENT

The datasets presented in this study can be found in online repositories. The names of the repository/repositories and accession number(s) can be found below: https://www.ncbi.nlm.nih.gov/geo/query/acc.cgi?acc=GSE136113.

ETHICS STATEMENT

The studies involving human participants were reviewed and approved by the study was approved by the Ethics Committee of The First Hospital of China Medical University (2018010). The patients/participants provided their written informed consent to participate in this study. Each participant signed the informed consent.

AUTHOR CONTRIBUTIONS

JL conceived and designed the study. ZZ conducted most of the experiments, data analysis, and wrote the manuscript. HG and WY participated in collecting data and helped to draft the manuscript. All authors reviewed and approved the manuscript.

SUPPLEMENTARY MATERIAL

The Supplementary Material for this article can be found online at: https://www.frontiersin.org/articles/10.3389/fmed.2021.675842/full#supplementary-material

Supplementary Table 1 | 25 up-regulated circRNAs and 76 down-regulated circRNAs in cSCC compared to healthy subjects.

REFERENCES

1. Que SKT, Zwald FO, Schmults CD. Cutaneous squamous cell carcinoma: Incidence, risk factors, diagnosis, and staging. *J Am Acad Dermatol.* (2018) 78:237-47. doi: 10.1016/j.jaad.2017.08.059
2. Bander TS, Nehal KS, Lee EH. Cutaneous squamous cell carcinoma: updates in staging and management. *Dermatol Clin.* (2019) 37:241-51. doi: 10.1016/j.det.2019.03.009
3. Soura E, Gagari E, Stratigos A. Advanced cutaneous squamous cell carcinoma: how is it defined and what new therapeutic approaches are available? *Curr Opin Oncol.* (2019) 31:461-8. doi: 10.1097/CCO.0000000000000566
4. Mulvaney PM, Schmults CD. Molecular prediction of metastasis in cutaneous squamous cell carcinoma. *Curr Opin Oncol.* (2020) 32:129-36. doi: 10.1097/CCO.0000000000000609
5. Vo JN, Cieslik M, Zhang Y, Shukla S, Xiao L, Zhang Y, et al. The landscape of circular RNA in cancer. *Cell.* (2019) 176:869-81.e13. doi: 10.1016/j.cell.2018.12.021
6. Kristensen LS, Andersen MS, Stagsted LVW, Ebbesen KK, Hansen TB, Kjems J. The biogenesis, biology and characterization of circular RNAs. *Nat Rev Genet.* (2019) 20:675-91. doi: 10.1038/s41576-019-0158-7
7. Ruan H, Xiang Y, Ko J, Li S, Jing Y, Zhu X, et al. Comprehensive characterization of circular RNAs in ∼ 1000 human cancer cell lines. *Genome Med.* (2019) 11:55. doi: 10.1186/s13073-019-0663-5
8. Zhao X, Cai Y, Xu J. Circular RNAs: biogenesis, mechanism, and function in human cancers. *Int J Mol Sci.* (2019) 20:3926. doi: 10.3390/ijms20163926
9. Li Z, Ruan Y, Zhang H, Shen Y, Li T, Xiao B. Tumor-suppressive circular RNAs: mechanisms underlying their suppression of tumor occurrence and use as therapeutic targets. *Cancer Sci.* (2019) 110:3630-8. doi: 10.1111/cas.14211
10. Dai J, Su Y, Zhong S, Cong L, Liu B, Yang J, et al. Exosomes: key players in cancer and potential therapeutic strategy. *Signal Transduct Target Ther.* (2020) 5:145. doi: 10.1038/s41392-020-00261-0
11. Zhang L, Yu D. Exosomes in cancer development, metastasis, and immunity. *Biochim Biophys Acta Rev Cancer.* (2019) 1871:455-68. doi: 10.1016/j.bbcan.2019.04.004

12. Xie M, Yu T, Jing X, Ma L, Fan Y, Yang F, et al. Exosomal circSHKBP1 promotes gastric cancer progression *via* regulating the miR-582-3p/HUR/VEGF axis and suppressing HSP90 degradation. *Mol Cancer.* (2020) 19:112. doi: 10.1186/s12943-020-01208-3
13. Bai H, Lei K, Huang F, Jiang Z, Zhou X. Exo-circRNAs: a new paradigm for anticancer therapy. *Mol Cancer.* (2019) 18:56. doi: 10.1186/s12943-019-0986-2
14. Wang Y, Liu J, Ma J, Sun T, Zhou Q, Wang W, et al. Exosomal circRNAs: biogenesis, effect and application in human diseases. *Mol Cancer.* (2019) 18:116. doi: 10.1186/s12943-019-1041-z
15. Kechin A, Boyarskikh U, Kel A, Filipenko M. cutPrimers: a new tool for accurate cutting of primers from reads of targeted next generation sequencing. *J Comput Biol.* (2017) 24:1138-43. doi: 10.1089/cmb.2017.0096
16. Dobin A, Davis CA, Schlesinger F, Drenkow J, Zaleski C, Jha S, et al. STAR: ultrafast universal RNA-seq aligner. *Bioinformatics.* (2013) 29:15-21. doi: 10.1093/bioinformatics/bts635
17. Cheng J, Metge F, Dieterich C. Specific identification and quantification of circular RNAs from sequencing data. *Bioinformatics.* (2016) 32:1094-6. doi: 10.1093/bioinformatics/btv656
18. Robinson MD, McCarthy DJ, Smyth GK. edgeR: a Bioconductor package for differential expression analysis of digital gene expression data. *Bioinformatics.* (2010) 26:139-40. doi: 10.1093/bioinformatics/btp616
19. Ghosal S, Das S, Sen R, Basak P, Chakrabarti J. Circ2Traits: a comprehensive database for circular RNA potentially associated with disease and traits. *Front Genet.* (2013) 4:283. doi: 10.3389/fgene.2013.00283
20. Yu G, Wang LG, Han Y, He QY. clusterProfiler: an R package for comparing biological themes among gene clusters. *Omics.* (2012) 16:284-7. doi: 10.1089/omi.2011.0118
21. Gao L, Jin HJ, Zhang D, Lin Q. Silencing circRNA_001937 may inhibit cutaneous squamous cell carcinoma proliferation and induce apoptosis by preventing the sponging of the miRNA-597-3p/FOSL2 pathway. *Int J Mol Med.* (2020) 46:1653-60. doi: 10.3892/ijmm.2020.4723
22. An X, Liu X, Ma G, Li C. Upregulated circular RNA circ_0070934 facilitates cutaneous squamous cell carcinoma cell growth and invasion by sponging miR-1238 and miR-1247-5p. *Biochem Biophys Res Commun.* (2019) 513:380-5. doi: 10.1016/j.bbrc.2019.04.017
23. Zhang DW, Wu HY, Zhu CR, Wu DD. CircRNA hsa_circ_0070934 functions as a competitive endogenous RNA to regulate HOXB7 expression by sponging miR-1236-3p in cutaneous squamous cell carcinoma. *Int J Oncol.* (2020) 57:478-87. doi: 10.3892/ijo.2020.5066
24. Chen S, Ding J, Wang Y, Lu T, Wang L, Gao X, et al. RNA-Seq profiling of circular RNAs and the oncogenic role of circPVT1 in cutaneous squamous cell carcinoma. *Onco Targets Ther.* (2020) 13:6777-88. doi: 10.2147/OTT.S252233
25. Lu X, Gan Q, Gan C. Circular RNA circSEC24A promotes cutaneous squamous cell carcinoma progression by regulating miR-1193/MAP3K9 axis. *Onco Targets Ther.* (2021) 14:653-66. doi: 10.2147/OTT.S275691
26. Chen P, Li C, Huang H, Liang L, Zhang J, Li Q, et al. Circular RNA profiles and the potential involvement of down-expression of hsa_circ_0001360 in cutaneous squamous cell carcinogenesis. *FEBS Open Bio.* (2021) 11:1209-22. doi: 10.1002/2211-5463.13114
27. Mashouri L, Yousefi H, Aref AR, Ahadi AM, Molaei F, Alahari SK. Exosomes: composition, biogenesis, and mechanisms in cancer metastasis and drug resistance. *Mol Cancer.* (2019) 18:75. doi: 10.1186/s12943-019-0991-5
28. Wang M, Yu F, Li P, Wang K. Emerging function and clinical significance of exosomal circRNAs in cancer. *Mol Ther Nucleic Acids.* (2020) 21:367-83. doi: 10.1016/j.omtn.2020.06.008
29. Tai YL, Chen KC, Hsieh JT, Shen TL. Exosomes in cancer development and clinical applications. *Cancer Sci.* (2018) 109:2364-74. doi: 10.1111/cas.13697
30. McAndrews KM, Kalluri R. Mechanisms associated with biogenesis of exosomes in cancer. *Mol Cancer.* (2019) 18:52. doi: 10.1186/s12943-019-0963-9
31. Shang A, Gu C, Wang W, Wang X, Sun J, Zeng B, et al. Exosomal circPACRGL promotes progression of colorectal cancer via the miR-142-3p/miR-506-3p-TGF-β1 axis. *Mol Cancer.* (2020) 19:117. doi: 10.1186/s12943-020-01235-0
32. Castel P, Rauen KA, McCormick F. The duality of human oncoproteins: drivers of cancer and congenital disorders. *Nat Rev Cancer.* (2020) 20:383-97. doi: 10.1038/s41568-020-0256-z
33. Corchado-Cobos R, García-Sancha N, González-Sarmiento R, Pérez-Losada J, Cañueto J. Cutaneous squamous cell carcinoma: from biology to therapy. *Int J Mol Sci.* (2020) 21:2956. doi: 10.3390/ijms21082956

Conflict of Interest: The authors declare that the research was conducted in the absence of any commercial or financial relationships that could be construed as a potential conflict of interest.

Copyright © 2021 Zhang, Guo, Yang and Li. This is an open-access article distributed under the terms of the Creative Commons Attribution License (CC BY). The use, distribution or reproduction in other forums is permitted, provided the original author(s) and the copyright owner(s) are credited and that the original publication in this journal is cited, in accordance with accepted academic practice. No use, distribution or reproduction is permitted which does not comply with these terms.

frontiers in Medicine

ORIGINAL RESEARCH
published: 24 May 2021
doi: 10.3389/fmed.2021.654635

Multi-Omics Integrative Analysis Uncovers Molecular Subtypes and mRNAs as Therapeutic Targets for Liver Cancer

*Yi Shen, Wei Xiong, Qi Gu, Qin Zhang, Jia Yue, Changsong Liu and Duan Wang**

Department of Cardiovascular Medicine, The Third Affiliated Hospital of Chongqing Medical University, Chongqing, China

Objective: This study aimed to systematically analyze molecular subtypes and therapeutic targets of liver cancer using integrated multi-omics analysis.

Methods: DNA copy number variations (CNVs), simple nucleotide variations (SNVs), methylation, transcriptome as well as corresponding clinical information for liver carcinoma were retrieved from The Cancer Genome Atlas (TCGA). Multi-omics analysis was performed to identify molecular subtypes of liver cancer via integrating CNV, methylation as well as transcriptome data. Immune scores of two molecular subtypes were estimated using tumor immune estimation resource (TIMER) tool. Key mRNAs were screened and prognosis analysis was performed, which were validated using RT-qPCR. Furthermore, mutation spectra were analyzed in the different subtypes.

Results: Two molecular subtypes (iC1 and iC2) were conducted for liver cancer. Compared with the iC2 subtype, the iC1 subtype had a worse prognosis and a higher immune score. Two key mRNAs (ANXA2 and CHAF1B) were significantly related to liver cancer patients' prognosis, which were both up-regulated in liver cancer tissues in comparison to normal tissues. Seventeen genes with $p < 0.01$ differed significantly for SNV loci between iC1 and iC2 subtypes.

Conclusion: Our integrated multi-omics analyses provided new insights into the molecular subtypes of liver cancer, helping to identify novel mRNAs as therapeutic targets and uncover the mechanisms of liver cancer.

Keywords: liver cancer, multi-omics, molecular subtype, ANXA2, CHAF1B, mRNA, therapeutic target

OPEN ACCESS

Edited by:
Fu Wang,
Xi'an Jiaotong University, China

Reviewed by:
Cheng Zhang,
Fourth Affiliated Hospital of China Medical University, China
Wei-Dong Li,
Tianjin Medical University, China

****Correspondence:***
Duan Wang
650150@cqmu.edu.cn

Specialty section:
This article was submitted to Precision Medicine, a section of the journal Frontiers in Medicine

Received: *17 January 2021*
Accepted: *06 April 2021*
Published: *24 May 2021*

Citation:
Shen Y, Xiong W, Gu Q, Zhang Q, Yue J, Liu C and Wang D (2021) Multi-Omics Integrative Analysis Uncovers Molecular Subtypes and mRNAs as Therapeutic Targets for Liver Cancer. Front. Med. 8:654635. doi: 10.3389/fmed.2021.654635

INTRODUCTION

Liver cancer is the fifth largest malignant tumor and the second leading cause of cancer-related deaths worldwide (1, 2). It was estimated that 42,220 new cases and 30,200 death cases occurred in the United States in 2018 (3). The mortality of liver cancer accounts for about 6% of death cases of cancers in men and 3% of death cases in women (3). Most patients have advanced liver cancer when first diagnosed. As we all know, several potential risk factors contribute to the occurrence and development of liver cancer, including chronic hepatitis B/C virus infection, alcoholism and aflatoxin exposure (4). Under the exposure of these risk factors, genetics and epigenetic changes may be gradually accumulated, thereby leading to activation of oncogenes and inactivation of tumor suppressor genes, which in turn will lead to the occurrence of liver cancer (5, 6).

Furthermore, cancers have association with an increased risk of coronary heart disease in time of the first 6 months following diagnoses (7). Despite the considerable progress over the past few decades, the prognosis of patients with liver cancer is still poor (5-year survival rate<20%) due to the high recurrence rate (8). Although extensive research has been conducted on the mechanisms of liver cancer occurrence and development, its etiology and carcinogenesis remain unclear. Considering the high morbidity and mortality of liver cancer, identification of effective markers and exploration of their potential roles have important clinical significance for early diagnosis, prevention, and control of liver cancer.

Growing multi-omics studies have confirmed that genomic and epigenomic imbalances can affect the occurrence and development of liver cancer. TCGA project provides genomic, epigenomic, transcriptomics, and proteomics of 32 human cancers. A number of data portals such as UCSC Cancer Genomics Browser (https://genome-cancer.ucsc.edu/) have been developed (9). As a key regulator of genomic and epigenomic abnormalities, CNV is significantly correlated with individual genetic variations and human genetic diversities, which may change gene expression via modulating mRNA expression and affecting transcription. Several CNVs have been found to be closely related to liver cancer. For example, Jagged1 copy number amplification indicates poor prognosis in patients with liver cancer (10). In-depth research on CNV may help understand the mechanisms and probe susceptible targets for liver cancer. Studies have shown that epigenetic changes such as DNA methylation, contribute to the development of liver cancer (11, 12). DNA methylation has been considered as a useful biomarker for early diagnosis of liver cancer. During carcinogenesis, abnormal DNA methylation is mainly manifested by focal methylation around the promoters of specific genes, and global methylation in non-promoter regions (13, 14). Hypermethylation of the promoter region is a crucial process that can lead to epigenetic silencing of tumor suppressor genes (15, 16). Moreover, abnormal DNA methylation of non-promoter elements is in association with intratumor heterogeneity (17).

Herein CNV, DNA methylation, as well as mRNA levels were detected in a variety of liver cancer samples. Copy number variation-correlated (CNVcor) as well as methylation-correlated (METcor) genes were identified to distinguish molecular subtypes of liver cancer. Furthermore, specific biomarkers were proposed to drive the classification of these subtypes.

MATERIALS AND METHODS

Data Collection

HTSeq—counts and HTSeq—FPKM gene expression RNA-seq, Illumina Human Methylation 450K, and SNV data (mutect2) were downloaded from the TCGA-liver hepatocellular carcinoma (LIHC) dataset ($n = 363$) using the Genetic Disease Control (GDC) Data Portal (https://portal.gdc.cancer.gov/). The hub is last updated on 2019-08-28. Masked Copy Number Segment data were also obtained from the GDC dataset. Furthermore, clinical information of all samples including age, gender, survival status, pathologic TNM, tumor stage and overall survival time was retrieved from the TCGA data portal, listed in **Table 1**.

TABLE 1 | Clinical characteristic information for the LIHC cohort (overall=363).

Characteristics	Groups	Number
Age (median [IQR])		61.00 [52.00, 69.00]
Gender (%)	Female	118 (32.5)
	Male	245 (67.5)
Race (%)	American Indian or Alaska native	1 (0.3)
	Asian	154 (42.4)
	Black or African American	17 (4.7)
	White	181 (49.9)
HBV/HCV infection status (%)	Yes	151 (41.6)
	No	212 (58.4)
Status (%)	Dead	233 (64.2)
	Alive	130 (35.8)
Pathologic T (%)	T1	179 (49.6)
	T2	91 (25.2)
	T3	77 (21.3)
	T4	13 (3.6)
	TX	1 (0.3)
Pathologic N (%)	N0	248 (68.5)
	N1	3 (0.8)
	NX	111 (30.7)
Pathologic M (%)	M0	262 (72.2)
	M1	3 (0.8)
	MX	98 (27.0)
Tumor stage (%)	I	169 (49.9)
	II	84 (24.8)
	III	82 (24.2)
	IV	4 (1.2)

Data Preprocessing

By applying GISTIC2.0, this study calculated the genetic copy number changes for each sample (18). The methylation data preprocessing was as follows. Methylation sites that were undetectable in over 70% of specimens were removed. The KNN was then utilized for filling in missing values. Furthermore, we removed the following methylation data: (1) the methylation data of the SNP sites, (2) the methylation site data on the sex chromosome, and (3) the multi-aligned methylation site data. Methylated sites in the 200 bp range upstream or downstream from gene transcription start were retained in this study. For mRNA expression profiles, this study filtered out mRNAs with FPKM value < 0.1 across 50% specimens.

Abbreviations: CNV, copy number variation; SNV, simple nucleotide variation; TIMER, tumor immune estimation resource; CNVcor, Copy number variation-correlated; METcor, methylation-correlated.

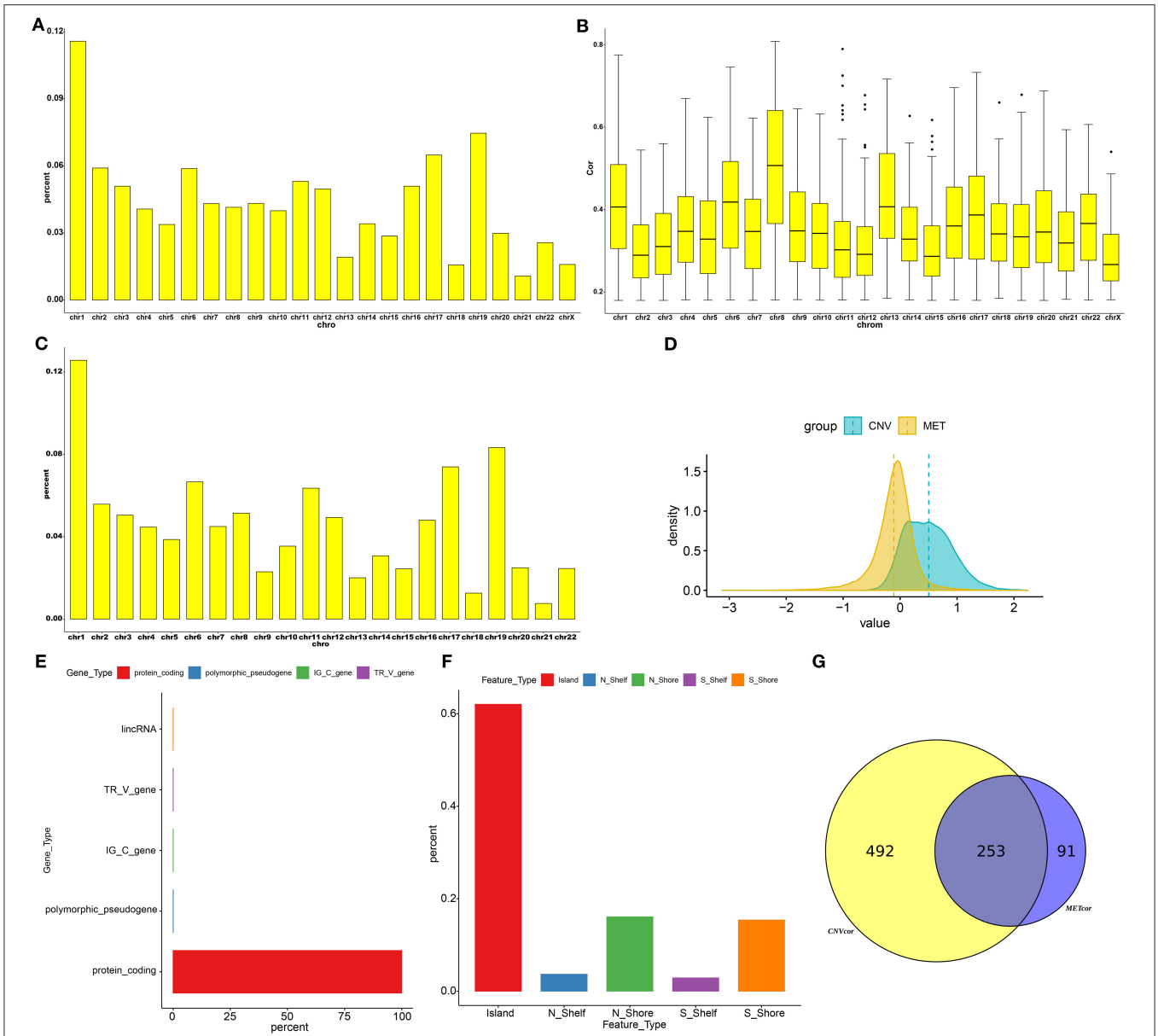

FIGURE 1 | Screening CNVCor and METCor genes in liver cancer. Chromosomal distributions **(A)** and correlations **(B)** of CNVcor genes. Horizontal axis indicates chromosomes; ordinate axis represents the proportion or the correlation coefficients of CNVcor genes. The middle line of the box plot is the median of the data, which represents the average level of the sample data. The upper and lower limits of the box plot are the upper quartile and the lower quartile of the data. Black dots represent outliers. **(C)** Chromosomal distribution of METcor genes. Y-axis represents the proportion of METcor genes. **(D)** Distribution of z-values for CNVcor genes and METcor genes. Horizontal axis is z value correlation, and ordinate axis is the density distributions corresponding to z values. **(E)** The proportion of each METcor gene type. **(F)** The proportion of each methylation locus. **(G)** Venn diagram showing overlapping survival-related CNVcor genes and METcor genes.

Correlation Analysis

The correlation coefficient of CNV data or methylation data with gene expression was calculated, which was then transformed to z-value based on ln [(1 + r)/(1 − r)]. Under the screening criterion of $p < 0.01$, CNVcor and METcor genes were obtained with the test of correlation coefficient.

Integrative Analysis of CNV, Methylation and mRNA Expression Data

Multi-omics clustering analysis was conducted by integrating CNV, methylation as well as mRNA expression profiles using the non-negative matrix factorization (NMF) package in R (19). Lambda values were used to determine optimal weights for CNV, methylation, and mRNA expression data sets.

TABLE 2 | Fisher significance test of CNVCor and METCor gene frequencies on chromosomes.

Chromosomes	All genes	METcor genes	CNVcor genes	METcor FisherP	METcor FDR	CNVcor FisherP	CNVcor FDR
chr1	2059	777	1055	1.92E-04	0.001056215	0.011311298	0.045345148
chr10	734	219	364	0.418195975	0.460015573	0.290234004	0.35473045
chr11	1318	393	484	0.267306507	0.322891157	1.95E-05	4.28E-04
chr12	1030	305	453	0.278860544	0.322891157	0.390088389	0.451681293
chr13	323	124	175	0.084400506	0.142831625	0.098603748	0.216928245
chr14	820	190	311	6.67E-05	4.89E-04	0.003285193	0.018068562
chr15	613	151	261	0.004556993	0.011139317	0.284006963	0.35473045
chr16	865	297	464	0.278179575	0.322891157	0.012366858	0.045345148
chr17	1187	457	591	0.001112523	0.00407925	0.156199369	0.286365511
chr18	271	78	143	0.450440412	0.471889955	0.220911045	0.35473045
chr19	1461	515	680	0.060434835	0.110797198	0.904106072	0.904106072
chr2	1296	345	538	0.003469529	0.010615833	0.040472584	0.111299606
chr20	540	154	272	0.242389855	0.322891157	0.267280512	0.35473045
chr21	233	47	98	0.003860303	0.010615833	0.475549326	0.523104258
chr22	489	152	234	0.815424881	0.815424881	0.685593908	0.718241237
chr3	1072	312	464	0.175300624	0.257107583	0.247938803	0.35473045
chr4	747	276	371	0.044594131	0.089188261	0.279538529	0.35473045
chr5	870	239	308	0.044592458	0.089188261	6.12E-05	6.73E-04
chr6	1043	412	536	4.37E-04	0.001922587	0.055334401	0.13526187
chr7	969	278	393	0.135649877	0.213164093	0.031565197	0.099204905
chr8	670	318	378	2.69E-08	2.96E-07	0.002640408	0.018068562
chr9	774	142	394	3.04E-10	6.68E-09	0.13166299	0.263325981

Immune Infiltration Estimation

Immune infiltrates across liver cancer were from the Tumor Immune Estimation Resource (TIMER) website (https://cistrome.shinyapps.io/timer/) (20, 21). The infiltration levels of six immune cells composed of B cells, CD4+ T cells, CD8+ T cells, neutrophils, macrophages, and dendritic cells were estimated.

Gene Set Variation Analysis (GSVA)

The GSVA algorithm was applied for evaluating the enriched signaling pathways between subtypes based on gene expression profiles (22). The pathway enrichment score of each sample was determined and the differences between subtypes were analyzed by employing the limma package in R (23).

RT-qPCR

Total RNA was extracted from 20 pairs of liver cancer tissues and normal tissues using Trizol reagent (Invitrogen, USA), which was reverse transcribed cDNA. All patients provided written informed consent. This study was approved by the Ethics Committee of The Third Affiliated Hospital of Chongqing Medical University (2019063). SYBR fluorescence quantitative PCR kit (Takara, Japan) was utilized to perform PCR. ANXA2: 5′-GTGGTGGAGATGACTGAAGCC-3′ (forward) and 5′-CCACGGGGACTGTTATTCG-3′ (reverse); CHAF1B: 5′-CCTGGAAAAGCCACTCTTGCTG-3′ (forward) and 5′- ACA GAAGCACGGAATCCTCCGA-3′(reverse); GAPDH: 5′-TGA CTTCAACAGCGACACCCA-3′ (forward) and 5′-CACCCT GTTGCTGTAGCCAAA-3′ (reverse). GAPDH served as a reference control. Relative ANXA2 and CHAF1B expression was determined with the $2^{-\Delta\Delta Ct}$.

Western Blot

RIPA lysis buffer (Beijing Biotech Biotechnology Company, China) was used to extract total protein from tissue specimens. The protein concentration was determined with BCA assay kit (BioTek, USA). Twenty micro gram total protein was separated by 10% sodium dodecyl sulfate-polyacrylamide (SDS-PAGE) (Beyotime, Shanghai, China), and transferred to PVDF membrane (Millipore, USA). The PVDF membrane was blocked with 10% skimmed milk powder for 1 h at room temperature and incubated with the primary antibodies against ANXA2 (1/10000; ab178677; Abcam, USA), CHAF1B (1/10000; ab109442; Abcam, USA) and β-actin (1/5000; ab179467; Abcam, USA) overnight at 4°C. The membrane was washed 3 times with TBST and incubated with secondary antibody (1/3000, ab6789; Abcam, USA) for 2 h at room temperature. The membrane was visualized with an enhanced chemiluminescence solution (Thermo Fisher, USA).

Statistical Analysis

All analyses were carried out using R packages and Graphpad Prism software. ANXA2 and CHAF1B expression was validated in liver cancer and normal tissues using the gene expression data from the International Cancer Genome Consortium (ICGC; http://icgc.org/). Each experiment was repeated three times. Data

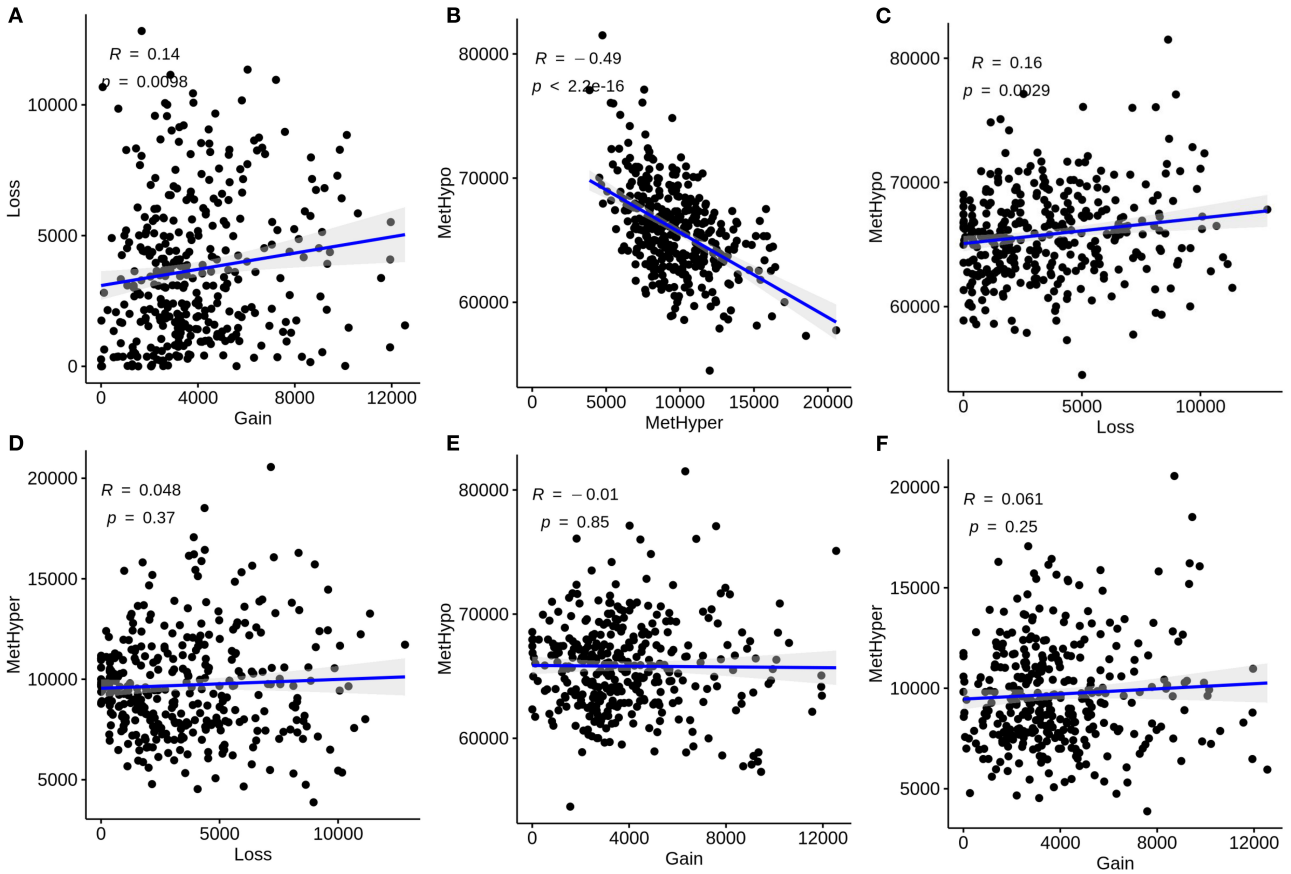

FIGURE 2 | Correlation between CNVs and methylations in liver carcinoma. **(A)** Correlations of CNV gain with loss. **(B)** Correlations of MetHypo with MetHyper. **(C)** Correlations of CNV loss with MetHypo. **(D)** Correlations between CNV loss and MetHyper. **(E)** Correlations of CNV gain with MetHyper. **(F)** Correlations of CNV gain with MetHyper. X axis represents CNV or methylation scores and y axis represents CNV or methylation scores.

were presented as the mean ± standard deviation. Student's t test was applied for comparisons between two groups. $P < 0.05$ indicated statistical significance.

RESULTS

Screening CNVCor/METCor Genes in Liver Cancer

Totally, 9161 CNVCor genes were identified ($p < 0.01$; **Supplementary Table 1**). As depicted in the distribution of CNVCor genes on chromosomes, CNVCor genes most frequently occurred on chr1 (FDR<0.05; **Figure 1A** and **Table 2**). The box plots showed the distribution in pearson correlation coefficients of CNVCor genes on chromosomes (**Figure 1B**). 16037 methylation sites corresponding 6181 genes were identified under the screening criteria of $p < 0.01$ (**Supplementary Table 2**). As shown in **Figure 1C** and **Table 2**, METcor genes were prone to appear on chr1. In the correlation z-value distribution, the correlation between CNVcor gene and its expression leaned to the right, while the correlation between METcor gene and its expression leaned to the left, indicating positive associations between CNVs and gene expressions, while negative associations between methylations and gene expressions (**Figure 1D**). METcor genes mainly contained protein-coding genes (**Figure 1E**). Furthermore, methylation loci were mainly situated in the island, S shore, N shore, S shelf as well as N shelf regions (**Figure 1F**). According to the median expression value of CNVCor/METCor genes, the samples were divided into high- and low- groups. Kaplan-Meier survival analysis was then performed. CNVCor genes and METCor genes with $p < 0.01$ were identified as survival-related CNVCor ($n = 745$)/METCor genes ($n = 344$). Two-hundred and fifty-three overlapping CNVcor genes and METcor genes were in significant association with survival of liver cancer (**Figure 1G**), which were used for further analysis.

Correlations Between CNVs and Methylations in Liver Cancer

We further analyzed the correlations between CNVs and methylations in liver cancer. CNVs were divided into three

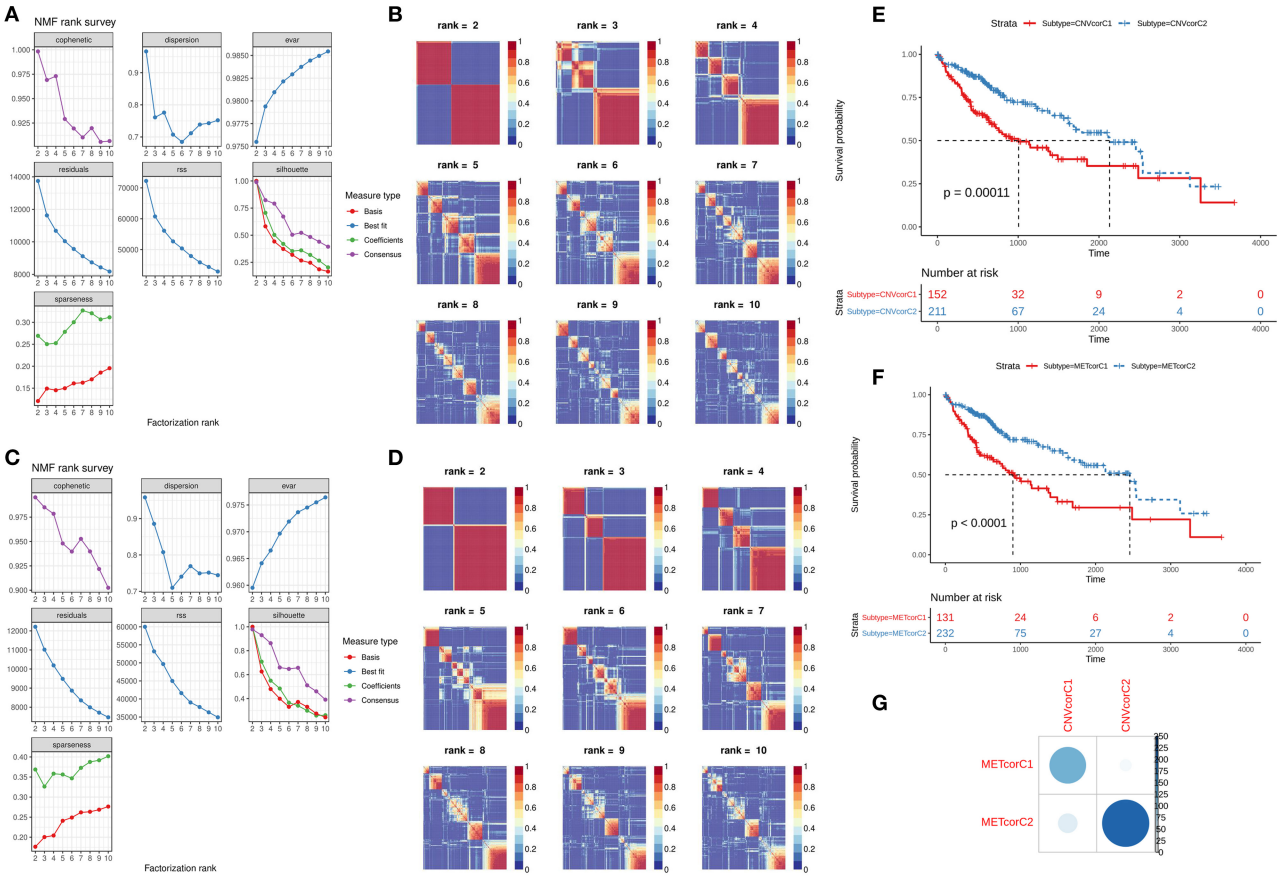

FIGURE 3 | Identification of molecular subtypes according to CNVcor and METcor genes. **(A,B)** NMF cluster analysis based on CNVcor genes. **(C,D)** NMF cluster analysis based on METcor genes. Kaplan-Meier curve analysis of CNVcor gene clusters **(E)** and METcor gene clusters **(F)**. **(G)** Overlap between CNVcor and METcor gene clusters. The color shade indicates the number of overlapping specimens.

classifications: loss, normal, as well as gain according to−0.3-0.3. We classified methylations into hypomethylation (MetHypo), normal and hypermethylation (MetHyper) based on the cutoffs of 0.2 and 0.8. The correlations among loss, gain, MetHypo and MetHyper were analyzed. The results showed that CNV gain was positively correlated to CNV loss (R = 0.14, p = 0.0098; **Figure 2A**). Furthermore, a strong negative correlation between MetHypo and MetHyper was found in **Figure 2B** (R = −0.49; p < 2.2e-16). Intriguingly, we found that CNV loss was positively correlated with MetHypo (R = 0.16, p = 0.0029; **Figure 2C**). However, there were no distinct correlations between CNV loss and MetHyper (**Figure 2D**), between CNV gain and MetHyper (**Figure 2E**), between CNV gain and MetHyper (**Figure 2F**).

Identification of CNVcor and METcor Gene Molecular Subtypes

NMF method was used for clustering analysis according to CNVcor and METcor genes. The optimal number of clustering was 2 for CNVcor genes (**Figures 3A,B**) and METcor genes (**Figures 3C,D**). Both the CNVcor genes (p = 0.00011) and METcor genes (p < 0.0001) in the two molecular subtypes were in significant association with overall survival of patients with liver cancer (**Figures 3E,F**). We further compared the differences between CNVcor and METcor gene molecular subtypes. There were high proportions of overlapping samples between CNVcor and METcor gene molecular subtypes (**Figure 3G**).

Construction of Two Multi-Omics Molecular Subtypes for Liver Cancer After Integration of CNV, DNA Methylation and mRNA Expression

Based on the CNV data related to the CNVcor genes, the methylation site data related to the METcor genes, and the transcriptome data of the CNVcor and METcor genes, multi-omics clustering analysis was performed using iCluster. The iCluster clustering results showed that the optimal clustering results were 2 groups. iCluster clustering heat maps depicted the distributions of CNVs of CNVcor

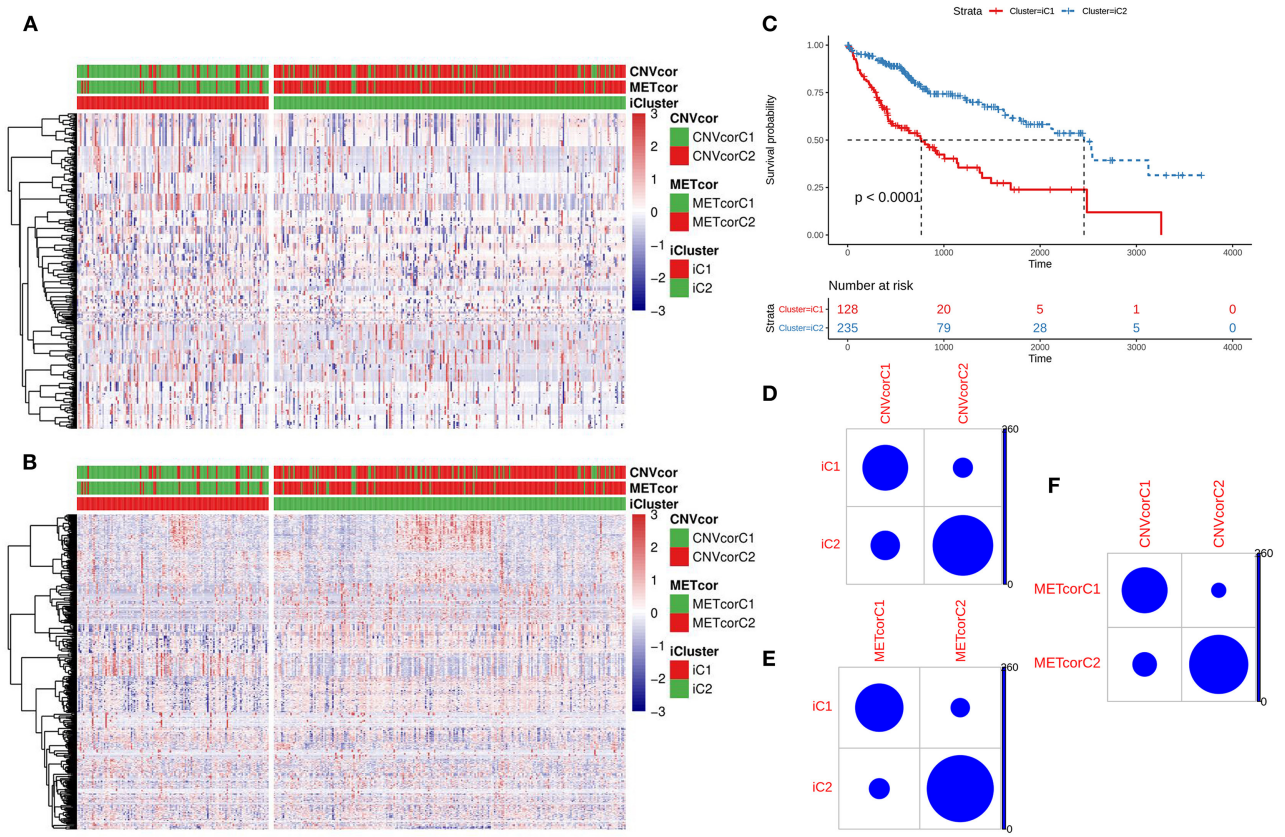

FIGURE 4 | Multi-omics clustering analysis of CNV, DNA methylation and mRNA expression. **(A)** iCluster clustering heat map showing the CNV distribution of CNVcor genes. **(B)** iCluster clustering heat map showing the methylation site distribution of METcor genes. **(C)** Kaplan-Meier survival analysis results for two subtypes. **(D)** Intersection of NMF and iCluster CNVcor gene sets. **(E)** Overlap between NMF METcor gene subsets and iCluster METcor subsets. **(F)** Overlap between iCluster METcor gene subsets and iCluster CNVcor gene subsets.

genes (**Figure 4A**) and of methylation sites of METcor genes (**Figure 4B**) in two iClusters, respectively. There was significantly difference in overall survival between iC1 and iC2 ($p < 0.0001$; **Figure 4C**). There were high proportions of overlapping samples between NMF CNVcor and iCluster CNVcor gene clustering subsets (**Figure 4D**), between NMF METcor and iCluster METcor gene clustering subsets (**Figure 4E**), between iCluster CNVcor and iCluster METcor gene subsets (**Figure 4F**).

Differences in Immune Infiltrations Between Two Multi-Omics Molecular Subtypes for Liver Cancer

All genes were clustered into two iClusters. Correlations between genes and immune infiltrations were estimated using TIMER. Intriguingly, we found that the immune scores of iC1 subtype in B cells ($p = 3e\text{-}06$; **Figure 5A**), CD4+ T cells ($p = 0.0003$; **Figure 5B**), CD8+ T cells ($p = 4.9e\text{-}07$; **Figure 5C**), dendritic cells ($p = 3.2e\text{-}09$; **Figure 5D**), macrophages ($p = 2.1e\text{-}10$; **Figure 5E**) and neutrophils (3.3e-10; **Figure 5F**) were all significantly higher that of iC2 subtype. Heatmaps depicted that there was significant difference in six immune cell scores between two iClusters (**Figure 5G**).

Molecular Features of Gene Subtypes in Liver Cancer

We analyzed differences in CNVs (adjusted $p < 0.01$), methylation (adjusted $p < 0.01$) and mRNA expression ($|FC|>1.5$ and $FDR<0.05$) between iC1 and iC2 subtypes. Venn diagram showed two genes (including ANXA2 and CHAF1B) differed in CNVs, methylation and mRNA expression between iC1 and iC2 subtypes (**Figure 6A**). A high proportion of ANXA2 gain in iC2 subtype and its loss in iC1 subtype was found in **Figure 6B**. Hypomethylated ANXA2 more frequently occurred in iC1 and iC2 subtypes (**Figure 6C**). Box plots depicted that ANXA2 was significantly up-regulated in iC1 subtype than iC2 subtype ($p < 2.22e\text{-}16$; **Figure 6D**). High ANXA2 expression significantly indicated a poorer prognosis of liver cancer ($p = 0.019$; **Figure 6E**). There was a higher proportion of CHAF1B gain and a lower proportion of its loss in iC2 compared

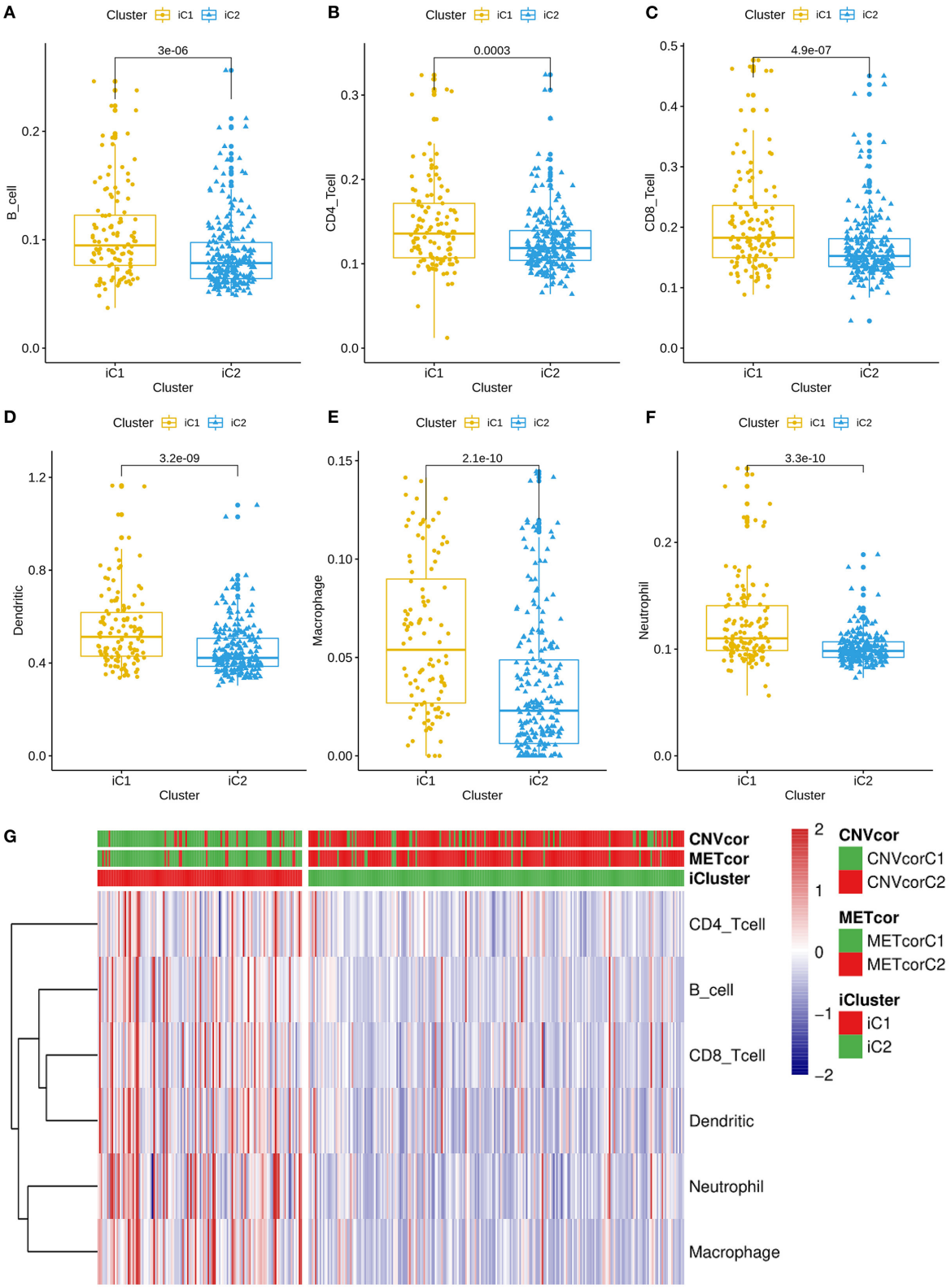

FIGURE 5 | Differences in immune infiltrations between two multi-omics molecular subtypes for liver cancer. Differences in contents of B cells **(A)**, CD4+ T cells **(B)**, CD8+ T cells **(C)**, dendritic cells **(D)**, macrophages **(E),** and neutrophils **(F)** between iC1 and iC2 subtypes. **(G)** Heatmap for six immune cell scores among all samples.

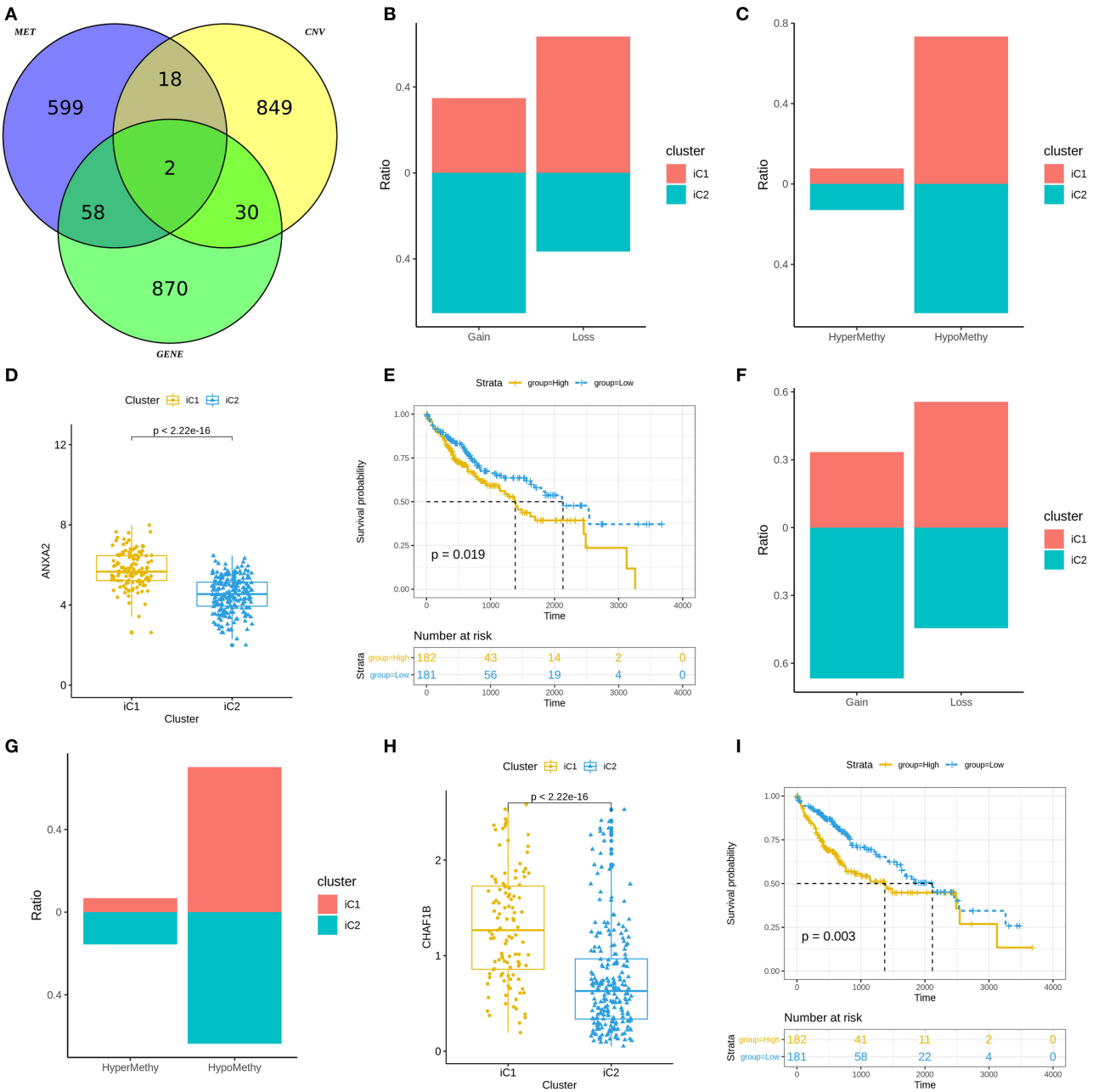

FIGURE 6 | Molecular features of gene subtypes in liver cancer. **(A)** Venn diagram showing differences in CNVs, methylation and mRNA expression between iC1 and iC2 subtypes. **(B)** Proportions of ANXA2 gain and loss in iC1 and iC2 subtypes. **(C)** Proportions of ANXA2 hypermethylation and hypomethylation. **(D)** Box plots showing the differences in ANXA2 expression between iC1 and iC2 subtypes. **(E)** Kaplan-Meier survival curves for ANXA2 expression. **(F)** Proportions of CHAF1B gain and loss in iC1 and iC2 subtypes. **(G)** The proportion of CHAF1B hypermethylation and hypomethylation. **(H)** Box plots showing the differences in CHAF1B expression between iC1 and iC2 subtypes. **(I)** Kaplan-Meier survival analysis results for CHAF1B expression.

to iC1 subtype (**Figure 6F**). CHAF1B hypermethylation more frequently occurred in iC2 subtype (**Figure 6G**). Higher CHAF1B expression was found in iC2 compared to iC1 subtype ($p < 2.22e\text{-}16$; **Figure 6H**). Its high expression was significantly associated with shorter survival time of patients with liver cancer ($p = 0.003$; **Figure 6I**).

Differences in SNVs and Pathways Between Two Multi-Omics Molecular Subtypes for Liver Cancer

Fisher-exact tests were applied for comparing the differences in SNV locus mutation between two subtypes. Seventeen significant mutated sites with adjusted $p < 0.01$ were screened, as shown

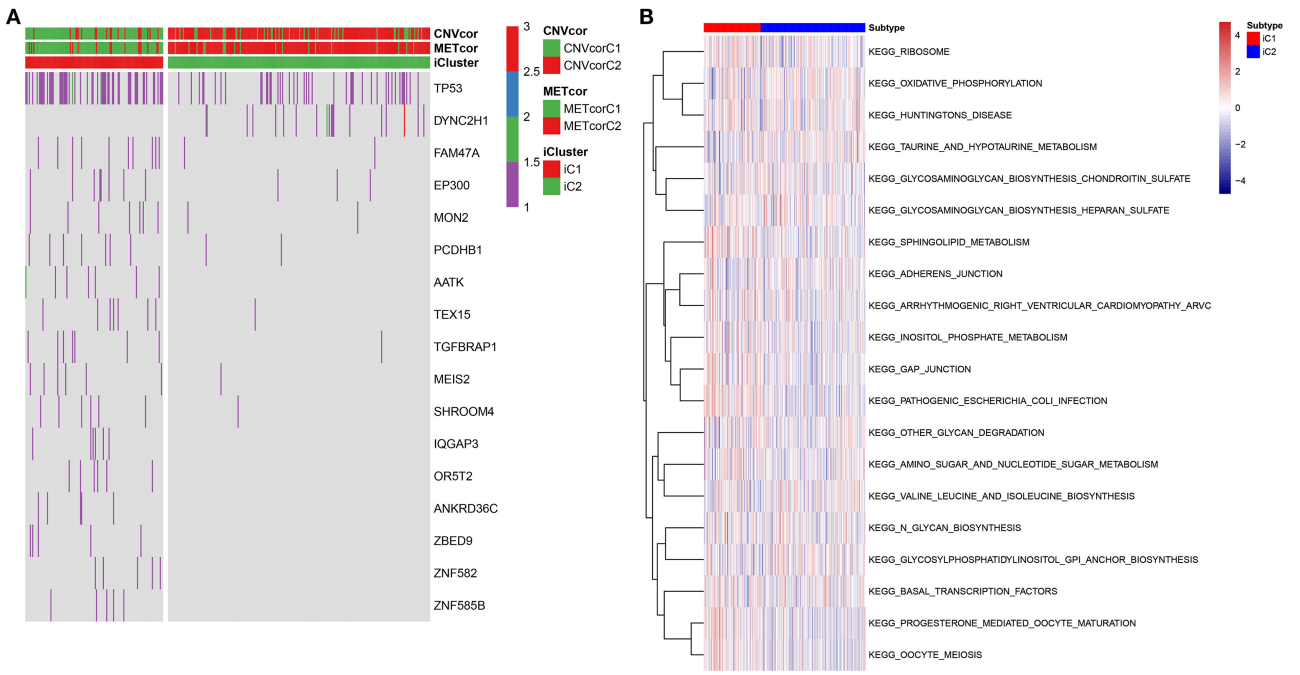

FIGURE 7 | Genetic mutations and enriched pathways in two multi-omics molecular subtypes for liver cancer. **(A)** Differences in genes with single-nucleotide variant (SNV) in iC1 and iC2 multi-omics molecular subtype for liver cancer. Different colors express different numbers of mutations in a gene. **(B)** Differences in enriched signaling pathways between subtypes by GSVA method.

TABLE 3 | The top ten most significant associations between ANXA2 expression and SNVs.

Genes	snvGenes	SNVs	CorrP	Corr
ANXA2	ACAN	p.V2481V	0.00315	0.157184
ANXA2	ADCYAP1R1	p.G46V	0.00315	0.157184
ANXA2	ANAPC1	p.L1872*	0.00315	0.157184
ANXA2	ARFGEF1	p.V494A	0.00315	0.157184
ANXA2	ARHGAP26	p.K475*	0.00315	0.157184
ANXA2	ATP6V0D2	p.M300I	0.00315	0.157184
ANXA2	BRF1	p.Y294C	0.00315	0.157184
ANXA2	C11orf87	p.P168Q	0.00315	0.157184
ANXA2	C2CD4C	p.D129D	0.00315	0.157184
ANXA2	CDH11	p.R50H	0.00315	0.157184

TABLE 4 | The top ten most significant associations between CHAF1B expression and SNVs.

Gene name	snvGene	SNV	Corr	CorrP
CHAF1B	TP53	p.R249S	0.219796	3.30E-05
CHAF1B	ESYT2	p.R569H	0.210288	7.20E-05
CHAF1B	ABCC3	p.T267K	0.158038	0.002988
CHAF1B	ADGRE1	p.C742Y	0.158038	0.002988
CHAF1B	ADGRL4	p.V295A	0.158038	0.002988
CHAF1B	ADH4	p.F182V	0.158038	0.002988
CHAF1B	AKAP10	p.D573Y	0.158038	0.002988
CHAF1B	ALB	p.L609Nfs*33	0.158038	0.002988
CHAF1B	ARHGEF11	p.K1355*	0.158038	0.002988
CHAF1B	ATG2B	p.H211R	0.158038	0.002988

in **Figure 7A**. We found that iC1 subtype had higher frequency mutations than iC2 subtype. We further assessed the correlation between each SNV locus and expression of ANXA2 and CHAF1B. **Tables 3**, **4** show the top ten SNV loci for ANXA2 and CHAF1B, respectively. Our findings indicated that these SNV loci might affect expression of ANXA2 and CHAF1B. To explore the differences in biological functions between iC1 and iC2 subtypes, GSVA method was applied. As a result, there were distinct differences in metabolism pathways between subtypes such as taurine and hypotaurine metabolism, sphingolipid metabolism, inositol phosphate metabolism, amido sugar and nucleotide sugar metabolism (**Figure 7B**).

Validation of ANXA2 and CHAF1B in Liver Cancer Tissues

In the ICGC database, our data confirmed that ANXA2 and CHAF1B were both up-regulated in liver cancer in comparison to normal tissues (**Figures 8A,B**). Twenty paired liver cancer and normal tissue specimens were harvested in this study. Using RT-qPCR, we validated the mRNA

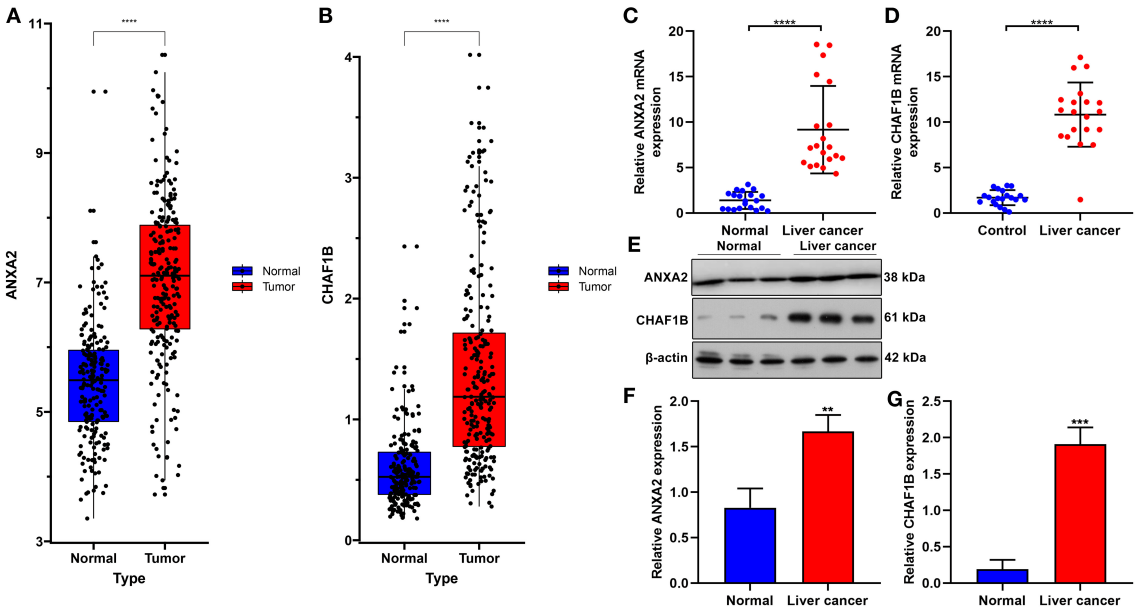

FIGURE 8 | Validation of ANXA2 and CHAF1B mRNAs in liver cancer tissues. **(A,B)** Box plots for ANXA2 and CHAF1B expressions in liver cancer and normal tissues from the ICGC database. **(C,D)** RT-qPCR and **(E–G)** western blot for ANXA2 and CHAF1B expressions in 20 paired liver cancer and normal tissue specimens. $^{**}P < 0.01$; $^{***}P < 0.001$; $^{****}P < 0.0001$.

expression of ANXA2 and CHAF1B in liver cancer. The results showed that ANXA2 (**Figure 8C**) and CHAF1B (**Figure 8D**) were highly expressed in liver cancer compared to normal specimens, which were consistent with bioinformatics analysis results. Consistently, higher ANXA2 (**Figure 8E**) and CHAF1B (**Figures 8F,G**) expressions were found in liver cancer specimens by western blot.

DISCUSSION

Liver cancer is an aggressive malignant tumor and one of the leading causes of tumor-related deaths (24, 25). Unfortunately, traditional TNM staging can only stratify patients on the basis of clinical manifestations. Despite advances in treatment strategies, effective molecular targets have not been successfully validated. Hence, there is an urgent need to understand the molecular mechanisms and explore therapeutic targets of liver cancer to improve patients' prognosis. With the advances in sequencing technology, it is accessible to obtain large amounts of high-throughput genome sequencing data. Comprehensive analyses about multi-omics data may help conduct accurate management against liver cancer (26–28). Thus, in this study, we integrated multi-omics data from 363 patients with liver cancer to establish two molecular subtypes (iC1 and iC2). Compared with the iC2 subtype, the iC1 subtypes had a worse prognosis. These data emphasize the clinical significance concerning multi-omics analyses of CNVs and methylations in liver cancer. We further characterized the immune cell populations of these two liver cancer subtypes. The scores of the six immune cells of the iC1 subtype were significantly higher than those of the iC2 subtype. In addition, mutation profiles showed that the mutation level of iC1 subtype was markedly higher than that of iC2 subtype, which might lead to poor prognosis of iC1 subtype. Some recent studies have shown that genomics, epigenomics, and transcriptomics play a vital role in tumorigenesis and can predict patients' prognosis (29, 30). Thus, multi-omics studies can help determine tumor heterogeneity, candidate therapeutic targets, and new mechanisms for cancers (22).

By integration of gene expression, CNV gain/loss and hypomethylation/hypermethylation, we identified two prognostic molecular targets, ANXA2 and CHAF1B. Due to the establishment and collection of three data sets and corresponding clinical follow-up information by different organizations, only two overlapping genes in the three data sets may be induced due to internal heterogeneity as well as diversity. These two mRNAs were validated in three independent data sets, suggesting that these genes have universal prognostic significance. Both genes were highly expressed in the iC1 subtype compared to the iC2 subtype. More importantly, their high expression indicated a poorer prognosis. Correlation analysis showed that the mutation site of SNV was significantly correlated with ANXA2 and CHAF1B gene expression. Therefore, assessing the gene expression may be helpful in the diagnoses of early liver cancer. Consistent with previous studies, ANXA2 has been found to be highly expressed in hepatocellular carcinoma (HCC) tissues compared to adjacent normal tissues, furthermore, its high expression is in association

with an aggressive phenotype in HCC (31). Highly expressed ANXA2 could induce HCC chemotaxis and metastasis (32), while its knockdown could suppress invasion and migration of liver cancer cells (33). ANXA2 has good diagnostic potential for patients with HBV-related HCC (34). ANXA2 is also involved in the pathogenesis of cardiovascular diseases. For example, both rs11633032 and rs17191344 SNPs can reduce ANXA2 gene expression. Its down-regulation is related to an increased risk of coronary heart disease (35). Also, ANXA2 modulates pulmonary arterial smooth muscle cell proliferation for hepatopulmonary syndrome (36). For CHAF1B, it has been reported that it can promote liver cancer cell migration (37). Thus, in-depth mechanism of these two mRNAs in liver cancer will be probed in further research.

However, several limitations of our study should be pointed out. First, our conclusions were based on retrospective cohorts, and prospective research will be performed to verify these findings. Second, this integrated multi-omics analysis was only based on genomics, epigenomics, and transcriptomics not including proteomics and metabolomics because there were no proteomics and metabolomics data in TCGA database. Third, although our RT-qPCR and western blot results confirmed that ANXA2 and CHAF1B were highly expressed in liver cancer tissues compared to normal specimens, biological functions and mechanisms of ANXA2 and CHAF1B in liver cancer should be further validated.

CONCLUSION

In conclusion, we investigated the possible pathogenesis of liver cancer through multi-omics analysis based on genomics, epigenomics, and transcriptomics. Our results suggested that DNA CNV and methylation may play important roles in liver cancer. Furthermore, we identified two clinically relevant molecular subtypes as well as two key biomarkers for liver cancer. These novel mechanisms and clinical classifications may help develop accurate diagnosis and treatments for patients with liver cancer.

DATA AVAILABILITY STATEMENT

The datasets presented in this study can be found in online repositories. The names of the repository/repositories and accession number(s) can be found in the article/**Supplementary Material**.

ETHICS STATEMENT

The studies involving human participants were reviewed and approved by the Ethics Committee of The Third Affiliated Hospital of Chongqing Medical University (2019063). The patients/participants provided their written informed consent to participate in this study.

AUTHOR CONTRIBUTIONS

DW conceived and designed the study. YS, WX, and QG conducted most of the experiments and data analysis, and wrote the manuscript. QZ, JY, and CL participated in collecting data and helped to draft the manuscript. All authors reviewed and approved the manuscript.

SUPPLEMENTARY MATERIAL

The Supplementary Material for this article can be found online at: https://www.frontiersin.org/articles/10.3389/fmed.2021.654635/full#supplementary-material

Supplementary Table 1 | 9161 CNVCor genes for liver cancer.

Supplementary Table 2 | 6181 METCor genes for liver cancer.

REFERENCES

1. EASL Clinical Practice Guidelines: management of hepatocellular carcinoma. *J Hepatol.* (2018) 69:182–236. doi: 10.1016/j.jhep.2018.03.019
2. Akinyemiju T, Abera S, Ahmed M, Alam N, Alemayohu MA, Allen C, et al. The burden of primary liver cancer and underlying etiologies from 1990 to 2015 at the global, regional, and national level: results from the global burden of disease study 2015. *JAMA Oncol.* (2017) 3:1683–91. doi: 10.1001/jamaoncol.2017.3055
3. Siegel RL, Miller KD, Jemal A. Cancer statistics, 2018. *CA Cancer J Clin.* (2018) 68:7–30. doi: 10.3322/caac.21442
4. Yang JD, Roberts LR. Hepatocellular carcinoma: a global view. *Nat Rev Gastroenterol Hepatol.* (2010) 7:448–58. doi: 10.1038/nrgastro.2010.100
5. Hamdane N, Juhling F, Crouchet E, El Saghire H, Thumann C, Oudot MA, et al. HCV-induced epigenetic changes associated with liver cancer risk persist after sustained virologic response. *Gastroenterology.* (2019) 156:2313–29. doi: 10.1053/j.gastro.2019.02.038
6. Perez S, Kaspi A, Domovitz T, Davidovich A, Lavi-Itzkovitz A, Meirson T, et al. Hepatitis C virus leaves an epigenetic signature post cure of infection by direct-acting antivirals. *PLoS Genet.* (2019) 15:e1008181. doi: 10.1371/journal.pgen.1008181
7. Zöller B, Ji J, Sundquist J, Sundquist K. Risk of coronary heart disease in patients with cancer: a nationwide follow-up study from Sweden. *Eur J Cancer.* (2012) 48:121–8. doi: 10.1016/j.ejca.2011.09.015
8. Meniconi RL, Komatsu S, Perdigao F, Boelle PY, Soubrane O, Scatton O. Recurrent hepatocellular carcinoma: a Western strategy that emphasizes the impact of pathologic profile of the first resection. *Surgery.* (2015) 157:454–62. doi: 10.1016/j.surg.2014.10.011
9. Goldman M, Craft B, Swatloski T, Cline M, Morozova O, Diekhans M, et al. The UCSC cancer genomics browser: update 2015. *Nucleic Acids Res.* (2015) 43:D812–7. doi: 10.1093/nar/gku1073
10. Kawaguchi K, Honda M, Yamashita T, Okada H, Shirasaki T, Nishikawa M, et al. Jagged1 DNA copy number variation is associated with poor outcome in liver cancer. *Am J Pathol.* (2016) 186:2055–67. doi: 10.1016/j.ajpath.2016.04.011
11. Hou Y, Guo H, Cao C, Li X, Hu B, Zhu P, et al. Single-cell triple omics sequencing reveals genetic, epigenetic, and transcriptomic heterogeneity in hepatocellular carcinomas. *Cell Res.* (2016) 26:304–19. doi: 10.1038/cr.2016.23
12. Lin DC, Mayakonda A, Dinh HQ, Huang P, Lin L, Liu X, et al. Genomic and epigenomic heterogeneity of hepatocellular carcinoma. *Cancer Res.* (2017) 77:2255–65. doi: 10.1158/0008-5472.CAN-16-2822
13. Baylin SB, Esteller M, Rountree MR, Bachman KE, Schuebel K, Herman JG. Aberrant patterns of DNA methylation, chromatin

formation and gene expression in cancer. *Hum Mol Genet.* (2001) 10:687–92. doi: 10.1093/hmg/10.7.687
14. Lee ST, Wiemels JL. Genome-wide CpG island methylation and intergenic demethylation propensities vary among different tumor sites. *Nucleic Acids Res.* (2016) 44:1105–17. doi: 10.1093/nar/gkv1038
15. Esteller M. Epigenetic gene silencing in cancer: the DNA hypermethylome. *Hum Mol Genet.* (2007) 16 Spec No 1:R50–9. doi: 10.1093/hmg/ddm018
16. Berdasco M, Esteller M. Aberrant epigenetic landscape in cancer: how cellular identity goes awry. *Dev Cell.* (2010) 19:698–711. doi: 10.1016/j.devcel.2010.10.005
17. Hansen KD, Timp W, Bravo HC, Sabunciyan S, Langmead B, McDonald OG, et al. Increased methylation variation in epigenetic domains across cancer types. *Nat Genet.* (2011) 43:768–75. doi: 10.1038/ng.865
18. Mermel CH, Schumacher SE, Hill B, Meyerson ML, Beroukhim R, Getz G. GISTIC2.0 facilitates sensitive and confident localization of the targets of focal somatic copy-number alteration in human cancers. *Genome Biol.* (2011) 12:R41. doi: 10.1186/gb-2011-12-4-r41
19. Gaujoux R, Seoighe C. A flexible R package for nonnegative matrix factorization. *BMC Bioinformatics.* (2010) 11:367. doi: 10.1186/1471-2105-11-367
20. Li B, Severson E, Pignon JC, Zhao H, Li T, Novak J, et al. Comprehensive analyses of tumor immunity: implications for cancer immunotherapy. *Genome Biol.* (2016) 17:174. doi: 10.1186/s13059-016-1028-7
21. Li T, Fan J, Wang B, Traugh N, Chen Q, Liu JS, et al. TIMER: A web server for comprehensive analysis of tumor-infiltrating immune cells. *Cancer Res.* (2017) 77:e108–10. doi: 10.1158/0008-5472.CAN-17-0307
22. Hänzelmann S, Castelo R, Guinney J. GSVA: gene set variation analysis for microarray and RNA-seq data. *BMC Bioinformatics.* (2013) 14:7. doi: 10.1186/1471-2105-14-7
23. Ritchie ME, Phipson B, Wu D, Hu Y, Law CW, Shi W, et al. limma powers differential expression analyses for RNA-sequencing and microarray studies. *Nucleic Acids Res.* (2015) 43:e47. doi: 10.1093/nar/gkv007
24. Chaudhary K, Poirion OB, Lu L, Garmire LX. Deep learning-based multi-omics integration robustly predicts survival in liver cancer. *Clin Cancer Res.* (2018) 24:1248–59. doi: 10.1158/1078-0432.CCR-17-0853
25. Woo HG, Choi JH, Yoon S, Jee BA, Cho EJ, Lee JH, et al. Integrative analysis of genomic and epigenomic regulation of the transcriptome in liver cancer. *Nat Commun.* (2017) 8:839. doi: 10.1038/s41467-017-00991-w
26. Loffler MW, Mohr C, Bichmann L, Freudenmann LK, Walzer M, Schroeder CM, et al. Multi-omics discovery of exome-derived neoantigens in hepatocellular carcinoma. *Genome Med.* (2019) 11:28. doi: 10.1186/s13073-019-0636-8
27. Xie Q, Fan F, Wei W, Liu Y, Xu Z, Zhai L, et al. Multi-omics analyses reveal metabolic alterations regulated by hepatitis B virus core protein in hepatocellular carcinoma cells. *Sci Rep.* (2017) 7:41089. doi: 10.1038/srep41089
28. Yoo BC, Kim KH, Woo SM, Myung JK. Clinical multi-omics strategies for the effective cancer management. *J Proteomics.* (2018) 188:97–106. doi: 10.1016/j.jprot.2017.08.010
29. Kong L, Liu P, Zheng M, Xue B, Liang K, Tan X. Multi-omics analysis based on integrated genomics, epigenomics and transcriptomics in pancreatic cancer. *Epigenomics.* (2020) 12:507–24. doi: 10.2217/epi-2019-0374
30. Zheng M, Hu Y, Gou R, Wang J, Nie X, Li X, et al. Integrated multi-omics analysis of genomics, epigenomics, and transcriptomics in ovarian carcinoma. *Aging (Albany NY).* (2019) 11:4198–215. doi: 10.18632/aging.102047
31. Wang QS, Shi LL, Sun F, Zhang YF, Chen RW, Yang SL, et al. High Expression of ANXA2 pseudogene ANXA2P2 promotes an aggressive phenotype in hepatocellular carcinoma. *Dis Markers.* (2019) 2019:9267046. doi: 10.1155/2019/9267046
32. Li H, Wang Y, Lu Y, Li F. Annexin A2 interacting with ELMO1 regulates HCC chemotaxis and metastasis. *Life Sci.* (2019) 222:168–74. doi: 10.1016/j.lfs.2019.03.003
33. Zhang HJ, Yao DF, Yao M, Huang H, Wang L, Yan MJ, et al. Annexin A2 silencing inhibits invasion, migration, and tumorigenic potential of hepatoma cells. *World J Gastroenterol.* (2013) 19:3792–801. doi: 10.3748/wjg.v19.i24.3792
34. Zhang HJ, Yao DF, Yao M, Huang H, Wu W, Yan MJ, et al. Expression characteristics and diagnostic value of annexin A2 in hepatocellular carcinoma. *World J Gastroenterol.* (2012) 18:5897–904. doi: 10.3748/wjg.v18.i41.5897
35. Fairoozy RH, Cooper J, White J, Giambartolomei C, Folkersen L, Wannamethee SG, et al. Identifying low density lipoprotein cholesterol associated variants in the Annexin A2 (ANXA2) gene. *Atherosclerosis.* (2017) 261:60–8. doi: 10.1016/j.atherosclerosis.2017.04.010
36. Liao L, Zheng B, Yi B, Liu C, Chen L, Zeng Z, et al. Annexin A2-modulated proliferation of pulmonary arterial smooth muscle cells depends on caveolae and caveolin-1 in hepatopulmonary syndrome. *Exp Cell Res.* (2017) 359:266–74. doi: 10.1016/j.yexcr.2017.07.020
37. Peng X, Fu H, Yin J, Zhao Q. CHAF1B knockdown blocks migration in a hepatocellular carcinoma model. *Oncol Rep.* (2018) 40:405–13. doi: 10.3892/or.2018.6437

Conflict of Interest: The authors declare that the research was conducted in the absence of any commercial or financial relationships that could be construed as a potential conflict of interest.

Copyright © 2021 Shen, Xiong, Gu, Zhang, Yue, Liu and Wang. This is an open-access article distributed under the terms of the Creative Commons Attribution License (CC BY). The use, distribution or reproduction in other forums is permitted, provided the original author(s) and the copyright owner(s) are credited and that the original publication in this journal is cited, in accordance with accepted academic practice. No use, distribution or reproduction is permitted which does not comply with these terms.

frontiers in Medicine

ORIGINAL RESEARCH
published: 24 May 2021
doi: 10.3389/fmed.2021.651600

Long Non-coding RNA EBLN3P Regulates UHMK1 Expression by Sponging miR-323a-3p and Promotes Colorectal Cancer Progression

Xiang-hao Xu[1,2†], *Wen Song*[3†], *Jun-hua Li*[3], *Ze-qi Huang*[3], *Ya-fang Liu*[3], *Qiang Bao*[4*] and *Zhi-wen Shen*[3*]

[1] Guangdong Provincial Key Laboratory of Malignant Tumor Epigenetics and Gene Regulation, Sun Yat-sen Memorial Hospital, Sun Yat-sen University, Guangzhou, China, [2] Breast Tumor Center, Sun Yat-sen Memorial Hospital, Sun Yat-sen University, Guangzhou, China, [3] Department of Anesthesiology, Sun Yat-sen Memorial Hospital, Sun Yat-sen University, Guangzhou, China, [4] Department of Intensive Care Unit, Sun Yat-sen Memorial Hospital, Sun Yat-sen University, Guangzhou, China

OPEN ACCESS

Edited by:
Fu Wang,
Xi'an Jiaotong University, China

Reviewed by:
Shukui Wang,
Nanjing Medical University, China
Bangshun He,
Nanjing Medical University, China

***Correspondence:**
Qiang Bao
baoqiang3@mail.sysu.edu.cn
Zhi-wen Shen
shenzhw3@mail.sysu.edu.cn

†*These authors have contributed equally to this work*

Specialty section:
This article was submitted to Precision Medicine, a section of the journal Frontiers in Medicine

Received: *10 January 2021*
Accepted: *15 March 2021*
Published: *24 May 2021*

Citation:
Xu X-h, Song W, Li J-h, Huang Z-q, Liu Y-f, Bao Q and Shen Z-w (2021) Long Non-coding RNA EBLN3P Regulates UHMK1 Expression by Sponging miR-323a-3p and Promotes Colorectal Cancer Progression. Front. Med. 8:651600. doi: 10.3389/fmed.2021.651600

Background: Growing studies have demonstrated that long non-coding RNA (lncRNA) can act as crucial roles during the progression of various tumors, including colorectal carcinoma (CRC). We aimed to determine lncRNA endogenous bornavirus-like nucleoprotein (EBLN3P) expression in CRC and examine its influence on tumor behaviors of CRC cells.

Materials and Methods: Quantitative real-time polymerase chain reaction was used to determine the expression levels of EBLN3P and miR-323a-3p in CRC tissues and cell lines. Cell viability, migration, invasion, and apoptosis were assessed by Cell Counting Kit 8, colony formation, Transwell assay, wound healing assays, and flow cytometry. Bioinformatics and dual-luciferase assays were used to investigate the interaction between EBLN3P and miR-323a-3p, as well as between miR-323a-3p and U2AF homology motif kinase 1 (UHMK1). Western blot was applied for detecting the expressions of the related proteins.

Results: EBLN3P was highly expressed in CRC, and its high expression was distinctly associated with increased tumor size, histology/differentiation and advanced TNM stage, and poor clinical outcome of CRC patients. EBLN3P silencing significantly inhibited the proliferation and metastasis and induced the apoptosis of CRC cells. Mechanistically, overexpression of EBLN3P exhibited tumorigenic effects through downregulating the inhibitory effects of miR-323a-3p on UHMK1 expression. The correlation analysis confirmed the positive or negative association among EBLN3P, miR-323a-3p, and UHMK1.

Conclusion: EBLN3P promoted the development of CRC *via* targeting miR-323a-3p/UHMK1, which provided a new idea for treating CRC.

Keywords: LncRNA EBLN3P, MiR-323a-3p, UHMK1, biomarker, colorectal carcinoma, metastasis

INTRODUCTION

Colorectal carcinoma (CRC) refers to the third most prevalent carcinoma carried by males, as well as a major cause of cancer death rate worldwide, particularly in developed countries (1). A more serious scene exhibits in China, where the mortality and incidence for CRC rank second among all types of tumors (2). Despite the distinct advancements with efforts for many years in diagnosis methods and combined treatments including surgical resection and adjuvant therapies, CRC cases' 5-year surviving ratio remains at approximately 15% (3, 4). Survival probability can be distinctly improved by the use of the early detection (5). Thus, an in-depth insight into the molecularly related systems of CRC progression is urgently needed to facilitate the prevention and treatments of CRC cases.

Long non-coding RNAs (lncRNAs, with the length of >200 nucleotides) refer to one new non-coding RNA molecule family exhibiting restricted or no ability to code protein (6). There is growing evidence that lncRNAs may control epigenetic modification and chromatin remodeling to be involved in a large range of cellular processes, including growth, migratory ability, tumor differentiation, and stem cell pluripotency (7). More and more researches have revealed that lncRNAs may be novel tumor markers and therapeutic targets and exhibit antioncogenic or tumor-promotive effects in many human tumors, including CRC (8, 9). Hence, it is critical to better understand the CRC progression to explore novel tumor-related lncRNAs and to investigate their biological effects.

U2AF homology motif kinase 1 (UHMK1) is a ubiquitously expressed nuclear serine (Ser, S)/threonine (Thr, T) kinase (10). Although the biological function of UHMK1 remains largely unclear, its dysregulated expression in tumor specimens and potential regulatory effects on tumor progression have been frequently reported (11, 12). In CRC, UHMK1 overexpression and its oncogenic roles have been demonstrated (13). However, the potential mechanisms involved in its dysregulation were rarely reported.

LncRNA endogenous bornavirus-like nucleoprotein (EBLN3P) was a recently identified lncRNA, suggested to impact liver carcinoma's progressing state (14). Nevertheless, its expressing state and function in other tumors have not been investigated. In this study, we first reported its increased levels in CRC cases and further explored its tumor-related function *via in vitro* assays.

MATERIALS AND METHODS

Tissue Collection

Ninety-five paired CRC tissue samples in this study received the collection from July 2014 to June 2016 in Sun Yat-sen Memorial Hospital, Sun Yat-sen University. No locally or systemically related treating processes were conducted in 95 cases prior to the surgery. Two experienced pathologists demonstrated all tumor and non-tumor specimens carefully. All samples received the snap-freezing and storing processes inside liquid nitrogen when resected for subsequent reverse transcriptase–polymerase chain reaction (RT-PCR) assays. Clinical and pathological characteristics were also collected for each patient. This study gained the approval from the ethics committee of Sun Yat-sen Memorial Hospital, Sun Yat-sen University. All cases included in this study provided informed consent in a written form.

Bioinformatics Analysis

The binding sites among EBLN3P, miR-323a-3p, and UHMK1 received the prediction on starBase (http://starbase.sysu.edu.cn/index.php). "GEPIA" analyzed UHMK1 expression and its clinical significance (http://gepia.cancer-pku.cn/). *Potential miRNA binding to EBLN3P*. miRNA–EBLN3P interaction was predicted by miRanda (http://www.miranda.org/), RegRNA2(http://regrna2.mbc.nctu.edu.tw/), and starBase 2.0 (http://starbase.sysu.edu.cn/).

Cell Lines and Cell Transfection

The Chinese Academy of Sciences (Shanghai, China) provided colonic epithelial cell line NCM460 of humans and CRC cell lines HCT116, SW480, LoVo, and HT29 cells. The culture medium for all cells was 90% Roswell Park Memorial Institute (RPMI) 1640. Cells were maintained in 5% CO_2 and at 37°C.

Short hairpin RNA (shRNA) sequences targeting EBLN3P were designed by Yiyan Technology (Shenzhen, Guangdong, China). The shRNAs were inserted into lentiviral pHBLV/U6-Scramble-Luc-Puro^{01} vector (GenePharma, Pudong, Shanghai, China), named sh-1 and sh-2, and negative control was named sh-NC. MiR-323a-3p inhibitors were synthesized by Weizhen Biology (Jinan, Shandong, China). miR-323a-3p mimic was synthesized by Ribo Co., Ltd. (Guangdong, China). Plasmid transfections were performed with Lipofectamine 2000 (Invitrogen, Hangzhou, Zhejiang, China) in accordance with the producer's protocol. The efficiency of the transfecting process received the detection based on RT–quantitative PCR (qPCR).

RNA Extracting Process and RT-qPCR

Overall RNA received the extraction according to tumor samples and cells with the use of Trizol reagent (Invitrogen, Nanjing, Jiangsu, China), based on the manufacturer's instructions. After purification, cDNA was synthesized from 10 μg total RNAs applying the Prime Script RT Master Mix (Takara, Nanjing, Jiangsu, China). This study conducted PCR in a real

TABLE 1 | The primers used in this study for RT-PCR.

Names	Sequences (5′-3′)
EBLN3P: F	GTGTTGTCCCGGAAGTGCCTTCTC
EBLN3P: R	TTGAAGGTTTGCCTTCTCTGAATAG
miR-323a-3p: F	TCTAGAGGTGGTCCGTGGC
miR-323a-3p: R	CTCAACTGGTGTCGTGGA
UHMK1: F	ACGCTGTCTGTTGCTTGAACT
UHMK1: R	GGCACAATGCTGTATCATCCAC
GAPDH: F	GGAGCGAGATCCCTCCAAAAT
GAPDH: R	GGCTGTTGTCATACTTCTCATGG
U6: F	ATTGGAACGATACAGAGAAGATT
U6: R	GGAACGCTTCACGAATTTG

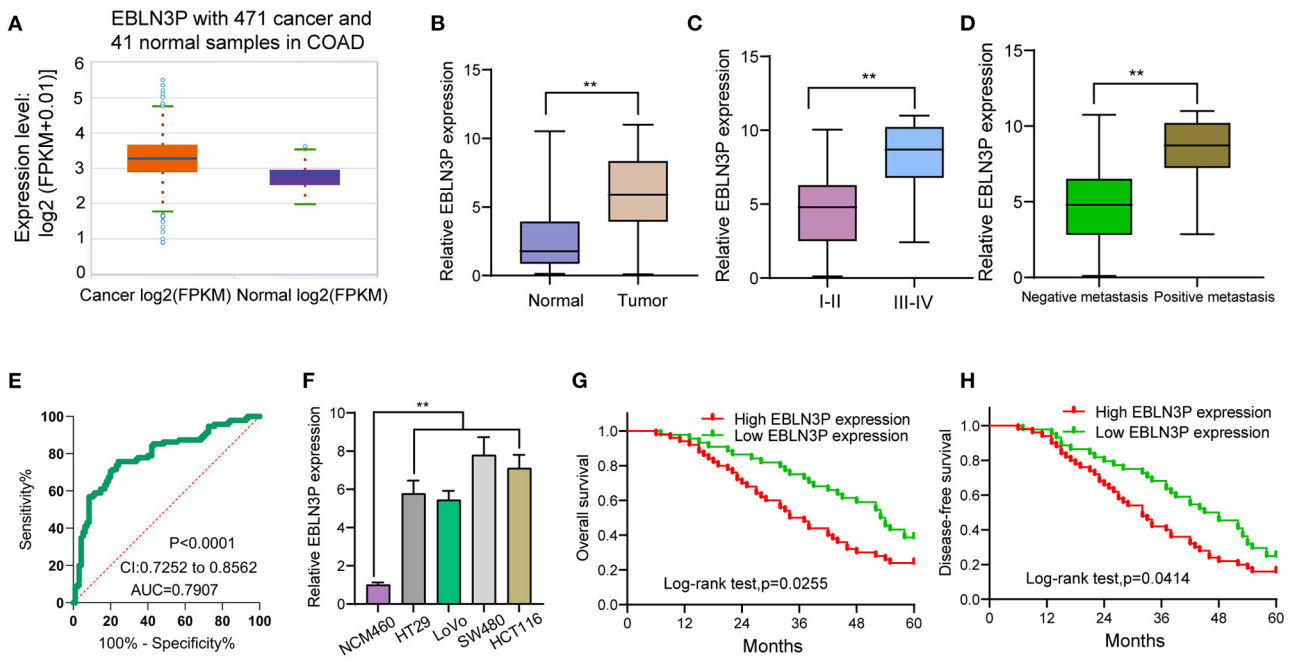

FIGURE 1 | Increased expression of EBLN3P in CRC and its clinical significance. **(A)** The expression of EBLN3P in 471 CRC specimens and 41 non-tumor specimens from TCGA datasets. **(B)** The levels of EBLN3P in 95 pairs of primary CRC tissues and the matched non-tumor specimens by RT-PCR. **(C,D)** Higher levels of EBLN3P were observed in specimens with advanced stages and positive metastasis than those with early stages and negative metastasis. **(E)** ROC assays for the diagnostic value of EBLN3P expression in CRC specimens. **(F)** RT-PCR for the levels of EBLN3P in four CRC cell lines (HT29, LoVo, SW480, and HCT116) and human colonic epithelial cell lines NCM46 cells. **(G,H)** The survival assays of 95 CRC patients according to the mean expression of EBLN3P in 95 CRC specimens. $^{**}p < 0.01$.

time based on the standard SYBR-Green PCR kit protocol on ABI 7600 (Applied Biosystems, Shenzhen, Guangdong, China). The relatively expressing state pertaining to miRNAs or EBLN3P received the calculation with the $2^{-\Delta\Delta Ct}$ methods and normalized to U6 and GAPDH, separately. **Table 1** lists the primer sequences employed in this study. The qRT-PCR reactions were performed in triplicate.

Cell Proliferation Assays

Cell proliferating process received the measurement based on Cell Counting Kit 8 (CCK-8, Dojindo, Haidian, Beijing, China) by complying with the producer's instructions. Briefly, a total of 3.0×10^3 cells received the seeding process inside 96-well plates' respective well. The kit was used to measure cell viability at 24, 48, and 72 h when the cells were seeded. The absorbance at 450 nm at each time point was recorded, followed by plotting of the cell proliferation curves.

Colony Formation Assay

Cells receiving the plating process on six-well plates at 1×10^3 cells per underwent the 10-day culturing process. Next, colonies received the 10-min fixing process by using 10% formaldehyde, as well as the 10-min staining process by using 1.0% crystal violet.

Flow Cytometry

A double-staining approach based on the Vybrant Apoptosis Teat Kit#2 (Puluosai Biology, Haidian, Beijing, China) was applied to measure apoptosis. When the infecting stage was achieved, cells received the processing based on the technical manual. Five hundred microliters of 1× annexin-binding buffer (Puluosai Biology, Haidian, Beijing, China) received the addition, and the cells that received the staining process underwent analysis based on FACSCalibur flow cytometer (no. 342973, BD Biosciences, Pudong, Shanghai) by the use of CellQuest software.

Subcellular Fractionation

The subcellular-related fractionating process for EBLN3P received the measuring process based on PARIS Tool (Life Technologies, Haidian, Beijing, China) based on technical manual, including nuclear and cytoplasmic fraction.

Wound Healing Assay

CRC cells (4×10^5 cells/well) received the seeding process inside six-well plates and the culturing process until confluence was reached. This study used a 20-μL pipette tip for drawing one scratch in the cell monolayer. Plates received the washing process one time by using fresh medium when they have achieved the 48-h culturing process for removing non-adherent cells. When the washing process was achieved, the images of the plates were captured.

Transwell Invasion Assays

The cell invasion was carried out by the use of one 24-well Transwell chamber (Corning, Hangzhou, Zhejiang, China).

Cells received the plating process in the upper chamber under the precoating process with 2% Matrigel (BD Biosciences, Hangzhou, Zhejiang, China). The lower chambers received the loading process by using 500 μl Dulbecco modified eagle medium supplemented by 20% fetal bovine serum. One hundred percent methanol was used to fix the invaded cells, which further received the 20-min staining process with 0.1% crystal violet. A microscope was used to count the number of invaded cells.

Animal Study

BALB/c female nude mice from Shanghai GemPharmatech (Jiangbei, Nanjing, China) were applied for *in vivo* experiments. SW480 cells stably transfected with sh-NC and sh-EBLN3P-1 at a density of 4×10^6 were injected into nude mice ($n = 6$). Every 4 days, the tumor volumes were recorded. A formula (length × width^2 × 0.5) was used to calculate the volumes. Twenty-eight days later, tumors were excised from killed mice and weighed for further analysis. The animal-related protocol was approved by the Animal Research Ethics Committee of Sun Yat-sen Memorial Hospital, Sun Yat-sen University.

Luciferase Reporter Assay

EBLN3P fragment was supplemented by the assessed miR-323a-3p binding site; the binding site's wide-type or mutant putative sequences received the subcloning process in one pmirGLO dual-luciferase vector (Bafeier Biology, Shijingshan, Beijing, China) for forming the pmiRGLO-EBLN3P mutant (EBLN3P-mut) or reporter vector pmiRGLO- EBLN3P wild type (EBLN3P-wt). EBLN3P-wt or EBLN3P-mut received the cotransfecting process by using negative control (miRNC) or miR-323a-3p mimics inside SW480 and HCT116 cells based on Lipofectamine 2000. Similarly, the reporter vector pmiRGLO-UHMK1–wild type (UHMK1-wt) or pmiRGLO-UHMK1–mutant (UHMK1-mut) received the synthesizing process. At 48 h when the transfecting process was achieved, the corresponding activities of luciferase received the measuring process.

RNA Pull-Down Assays

RNA pull-down assays were carried out by complying with RNA Pull-Down Tool's guidelines (Pierce, Shenzhen, Guangdong, China). In brief, EBLN3P and EBLN3P antisense (negative control) received the cloning process inside pcDNA 3.1 vector, followed by transcription by the use of T7 RNA polymerase (Promega, Pudong, Shanghai, China). The mentioned RNAs received the labeling process based on biotin. After washing, this study carried out RT-PCR for measuring the coprecipitated RNAs.

Western Blot Analysis

Cells were lysed with RIPA lysis buffer (E-BC-R327, Elabscinece, Pudong, Shanghai, China) for total protein extraction. Equal amounts of proteins (50 μg) were separated by 10% sodium dodecyl sulfate–polyacrylamide gel electrophoresis (Yita Technology, Haidian, Beijing, China) and transferred onto a polyvinylidene fluoride membrane (Biomart, Haidian, Beijing, China). The membrane was incubated with 5% non-fat milk for 1 h at room temperature, followed by incubation with corresponding primary antibodies against cleaved caspase-3, caspase-3, cleaved caspase-9, caspase-9, N-cadherin, vimentin, E-cadherin, or GAPDH overnight at 4°C. The membrane was then washed three times with phosphate-buffered saline, followed by incubation with horseradish peroxidase–conjugated secondary antibody at room temperature for 1 h. All antibodies were purchased from Aviva Biology (Daxing, Beijing, China). An enhanced chemiluminescence kit (Abcam) was used to detect the Western blot bands.

TABLE 2 | Correlation between EBLN3P expression and clinicopathological features of CRC.

Clinicopathological features	No. of cases	EBLN3P expression		*P*-value
		High	Low	
Age				0.931
≤60 years	49	26	23	
>60 years	46	24	22	
Gender				0.706
Male	51	30	31	
Female	44	20	24	
Tumor size				0.032
≤5 cm	46	19	27	
>5 cm	49	31	18	
Histology/differentiation				0.013
Well + moderate	55	23	32	
Poor	40	27	13	
TNM stage				0.010
I–II	59	25	34	
III–IV	36	25	11	
Distant metastasis				0.029
Yes	68	31	37	
No	27	19	8	

Statistical Analysis

Based on SPSS 18.0 (SPSS Inc., Chicago, IL, USA), the authors conducted the statistics-related analyzing processes. By performing individual two-tailed Student *t* testing process, the data received the analysis. This study adopted receiver operating characteristic (ROC) curve for analyzing the efficacy of EBLN3P in the diagnosis of CRC specimens from non-tumor specimens. This study conducted the χ^2 testing process for assessing the relationship of EBLN3P expressing states with clinicopathologically related characteristics. The authors obtained surviving curves of disease-free survival (DFS) and overall survival (OS) using Kaplan–Meier estimates. In addition, the authors determined the differences between groups based on the log-rank testing process. Prognostic significance pertaining to each variable received the analysis using the Cox regression model. $p < 0.05$ exhibited statistical significance.

TABLE 3 | Multivariate analyses for disease-free survival and overall survival by Cox regression model.

Variable	Overall survival			Disease-free survival		
	HR	95% CI	*P*	HR	95% CI	*P*
Age	0.893	0.456–1.783	0.231	1.132	0.567–2.034	0.134
Gender	1.231	0.567–2.055	0.346	1.445	0.756–2.214	0.214
Tumor size	1.542	0.783–2.341	0.087	1.491	0.858–2.441	0.094
Histology/differentiation	2.984	1.238–4.868	0.015	3.018	1.472–5.229	0.008
TNM stage	3.258	1.458–5.672	0.001	3.587	1.558–6.582	0.001
Distant metastasis	3.135	1.243–5.252	0.011	3.324	1.343–5.677	0.007
EBLN3P expression	2.863	1.372–4.675	0.008	3.152	1.347–5.183	0.004

RESULTS

EBLN3P Displayed a Significant Up-Regulation in CRC Cases

First, we performed RT-PCR to examine the expression of EBLN3P in 95 CRC patients. According to the results, EBLN3P expression was distinctly increased in CRC specimens compared with matched non-tumor tissues (**Figure 1A**). We also observed higher levels of EBLN3P in CRC specimens with advanced stages and positive metastasis than those with early stages and negative metastasis (**Figures 1B,C**). Using TCGA dataset, we also observed an increased expression of EBLN3P in CRC samples (**Figure 1D**). According to the ROC assays, our group observed that high EBLN3P expression had 0.7907 AUC [95% confidence interval (CI) = 0.7252–0.8562] in terms of CRC (**Figure 1E**). Then, the level of EBLN3P was checked in CRC cell lines and NCM460. In **Figure 1F**, EBLN3P overexpressed in four cell lines compared with NCM460. Overall, the research presented here suggested EBLN3P as a novel modulator in CRC progression.

High-Expression Level of EBLN3P Predicts Weak Prognostic Process Inside CRC Cases

To explore the clinical significance of EBLN3P expression in CRC patients, 95 patient samples were divided into low group (<5.83) and high groups (>5.83) according to the mean expression of EBLN3P (5.83). As shown in **Table 2**, we observed that high EBLN3P expression was associated with tumor size ($p = 0.032$), histology/differentiation ($p = 0.013$), TNM stage ($p = 0.010$), and distant metastasis ($p = 0.029$). To further study the clinical value of EBLN3P in CRC cases, we analyzed survival data of all 95 CRC cases using a Kaplan–Meier survival analysis. We observed that the OS (**Figure 1G**, $p = 0.0255$) and DFS (**Figure 1H**, $p = 0.0414$) of cases with high EBLN3P expression were distinctly shorter than those of cases with low BLN3P expression. More importantly, in a multivariate Cox model, we found that EBLN3P expression was an independent poor prognostic factor for both OS [hazard ratio (HR) = 2.863, 95% CI = 1.372–4.675, $p = 0.008$; **Table 2**] and DFS (HR = 3.152, 95% CI = 1.347–5.183, $p = 0.004$; **Table 3**) in CRC.

EBLN3P Knockdown Suppressed the Proliferation of CRC Cell Lines

The distinct overexpression of EBLN3P in CRC prompted us to evaluate the biological roles of EBLN3P in CRC cells. The specific lentiviral vector expressing EBLN3P shRNAs was transected to SW480 and HCT116 to decrease the expression of EBLN3P. A distinctly decreased expression of EBLN3P in SW480 and HCT116 cells transfected with sh-1 and sh-2 was demonstrated using RT-PCR (**Figure 2A**). CCK-8 experiments revealed that the proliferation rate of SW480 and HCT116 cells transfected with sh-1 or sh-2 was significantly decreased compared with negative control (sh-NC) (**Figure 2B**). Colony formation assays indicated that the cells transfected with sh-1 or sh-2 exhibited a weakened capacity for colony formation compared with the control group in SW480 and HCT116 cells (**Figure 2C**). Flow cytometry indicated that knockdown of EBLN3P promoted apoptosis of SW480 and HCT116 cells (**Figure 2D**). Moreover, we examined the influence of EBLN3P on the expression of caspase-3 and caspase-9, and the results of Western blot revealed that knockdown of EBLN3P distinctly resulted in the suppression of the expression of caspase-3 and caspase-9, while it promoted the expression of cleaved caspase-3 and cleaved caspase-9 (**Figure 2E**). On the other hand, we also performed *in vivo* assays to explore the influence of EBLN3P knockdown on tumor growth. As shown in **Figure 3A**, we observed that the tumor growth speed was slower on nude mice after subcutaneous injection with sh-EBLN3P-1 than control group (**Figure 3A**). Besides, we found that the tumor volume and weight were apparently lessened in sh-EBLN3P-1 group compared with control group (**Figures 3B,C**).

EBLN3P Knockdown Suppressed the Metastasis of CRC Cell Lines

To further explore whether EBLN3P has a functional effect on tumor metastasis ability, we performed a scratch-wound healing assay and observed that compared with SW480 and HCT116 cells transfected with sh-NC, those transfected with sh-1 or sh-2 showed a significantly increased migration 24 h after transfection (**Figure 4A**). In addition, Transwell assays suggested

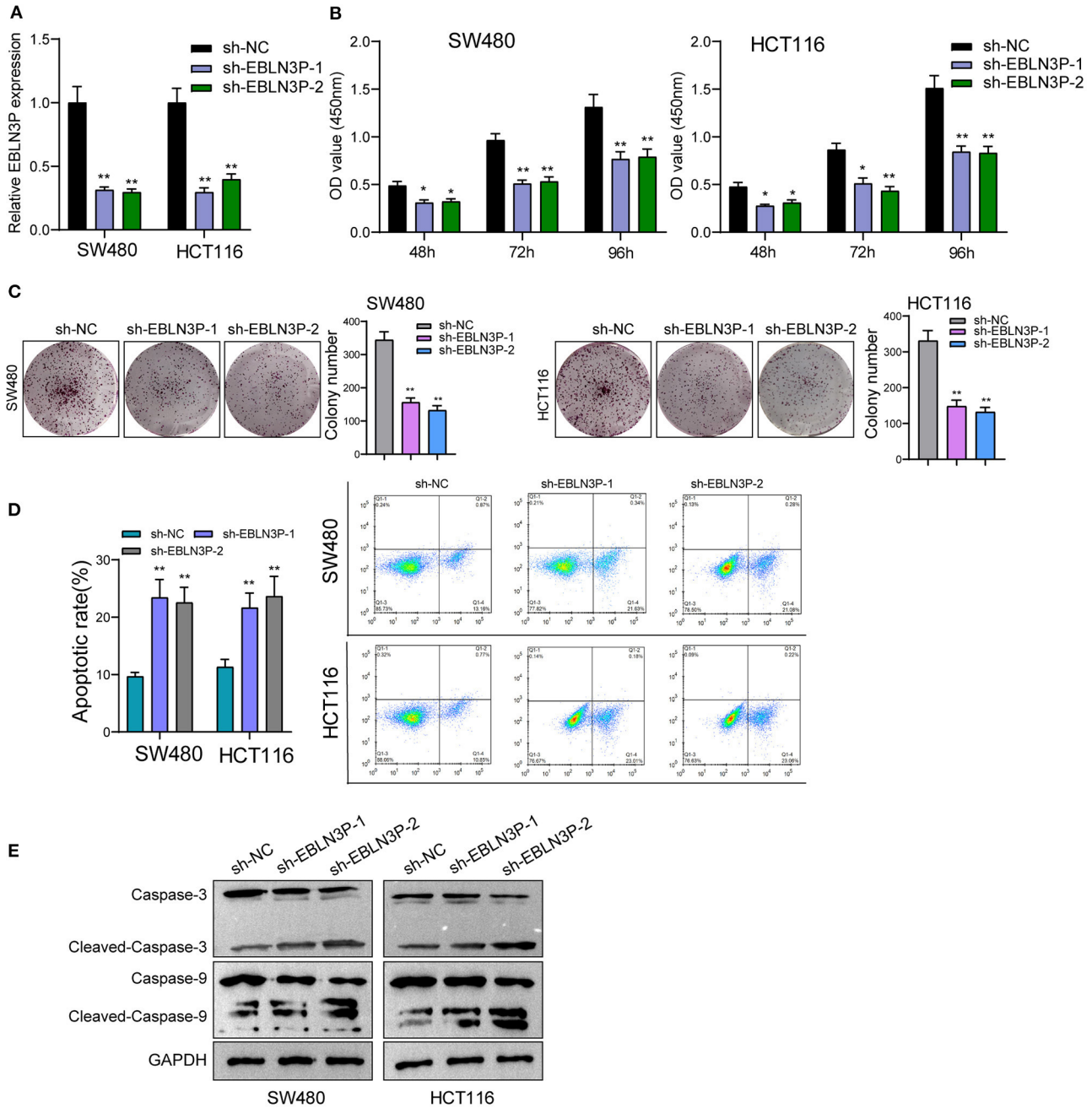

FIGURE 2 | Knockdown of EBLN3P suppressed the proliferation of SW480 and HCT116 cells. **(A)** RT-PCR for the expression of EBLN3P in SW480 and HCT116 cells transfected with sh-EBLN3P-1, EBLN3P-2, or sh-NC. **(B)** CCK-8 assays determined the cell ability in SW480 and HCT116 cells transfected with sh-EBLN3P-1, EBLN3P-2 or sh-NC. **(C)** Clone formation capacity of SW480 and HCT116 cells was assessed by the clone formation assays. **(D)** Apoptotic rate of CRC cells was shown after the transfection. **(E)** Western blot for the expression of cleaved caspase-3, caspase-3, cleaved caspase-9, and caspase-9 in SW480 and HCT116 cells transfected with sh-EBLN3P-1, EBLN3P-2, or sh-NC. $^{*}p < 0.05$; $^{**}p < 0.01$.

that EBLN3P knockdown notably enhanced the invasion of SW480 and HCT116 cells (**Figure 4B**). It has been demonstrated that epithelial–mesenchymal transition (EMT) is one of the important indicators for tumor metastasis (15). For the detection of EMT-related proteins, Western blot was performed. As shown in **Figure 4C**, we observed that EBLN3P knockdown induced a pronounced decrease in N-cadherin and vimentin expression and an increase in E-cadherin expression. Collectively, we concluded that EBLN3P was involved in CRC metastasis, and functioned as an oncogenic lncRNA.

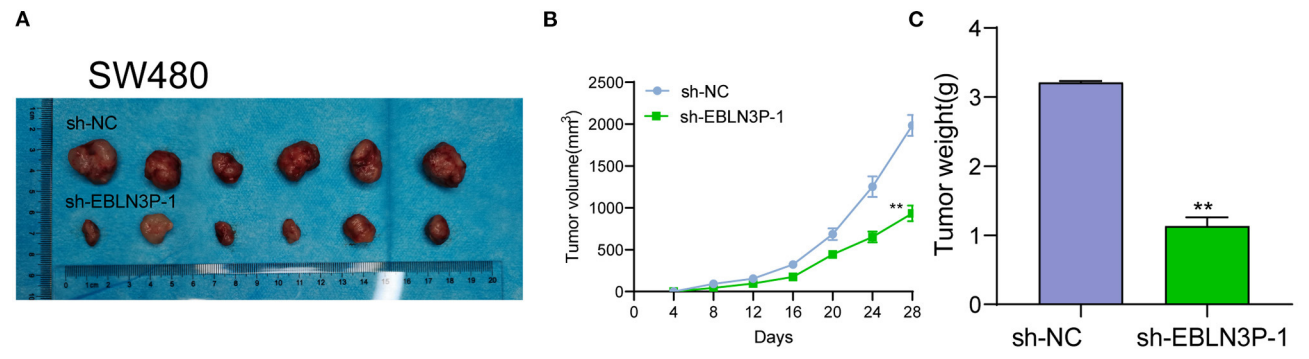

FIGURE 3 | EBLN3P promotes CRC tumor growth *in vivo*. **(A)** Representative images of the subcutaneous tumors formed by EBLN3P-knockdown and control SW480 cells. **(B)** Tumor volumes were detected every 7 days. **(C)** The subcutaneous tumor weights were detected at the 28th day after injection. $^{**}p < 0.01$.

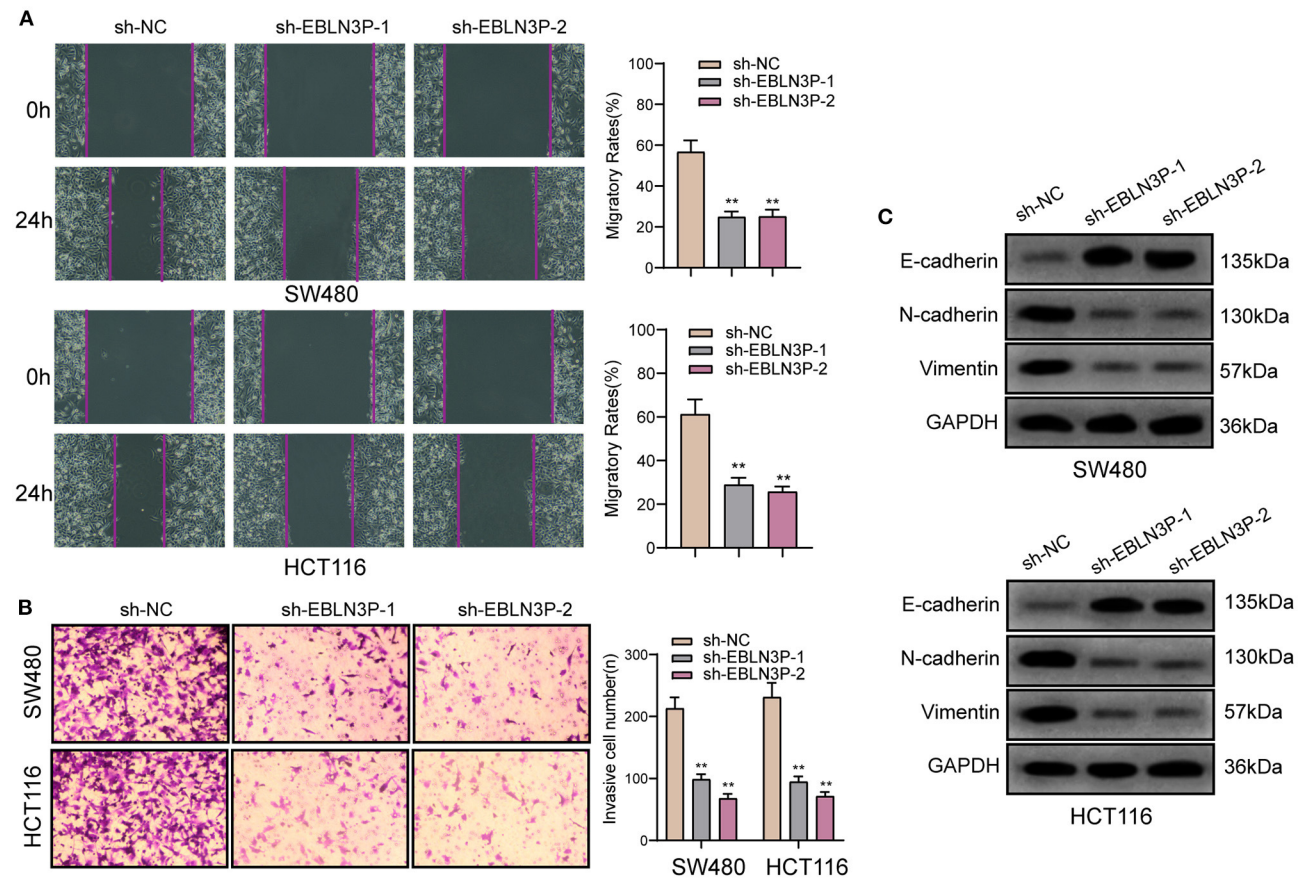

FIGURE 4 | The antioncogenic roles of EBLN3P knockdown on the migration of invasion of SW480 and HCT116 cells. **(A)** Scratch assay following EBLN3P knockdown. **(B)** Transwell assays following EBLN3P knockdown. **(C)** Western blot assays for the expression of EMT markers. $^{**}p < 0.01$.

EBLN3P Acted as miR-323a-3p Sponge in CRC Cells

It has been known to us that lncRNAs exhibit their effects according to subcellular distribution (16). To determine the cellular location of EBLN3P, SW480 and HCT116 cells were isolated into nuclear and cytoplasmic fractions. Then, we observed that EBLN3P was mainly expressed in the cytoplasm (**Figure 5A**). To test this hypothesis, we used three bioinformatics databases (miRanda, RegRNA2, and starBase v2.0) for the prediction of the possible interaction between miRNAs and EBLN3P. Our group observed that EBLN3P contained multiple miRNA binding sites (**Figure 5B**). Then, we chose the top

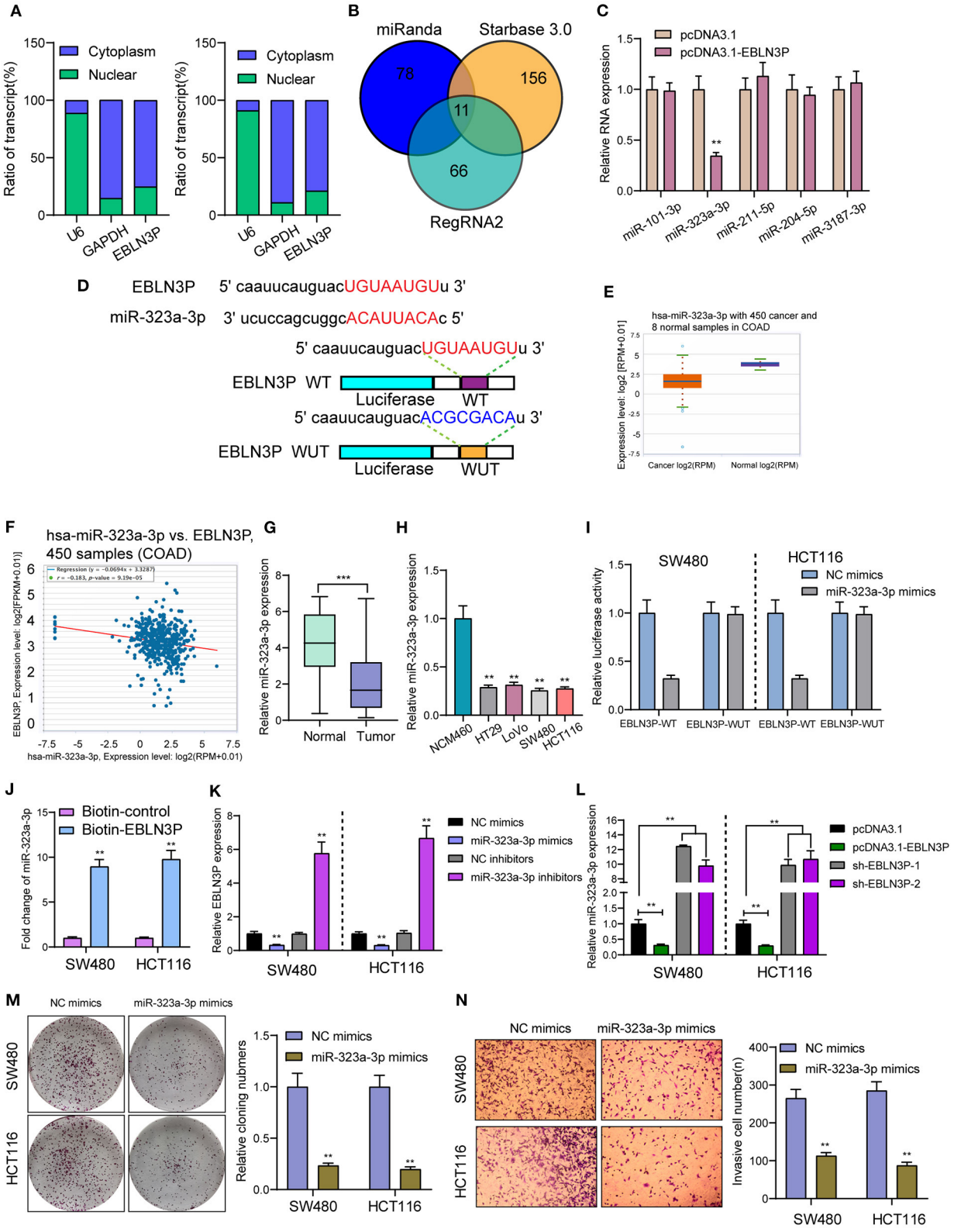

FIGURE 5 | EBLN3P acts as a sponge for miR-323-3p in the cytoplasm. **(A)** Relative EBLN3P expression levels in nuclear and cytosolic fractions of SW480 and HCT116 cells. **(B)** Potential miRNA binding to EBLN3P. miRNA–EBLN3P interaction was predicted by miRanda, RegRNA2 and starBase 2.0, of which 11 were

(Continued)

FIGURE 5 | overlapped. **(C)** RT-PCR confirmed miR-323-3p expression was decreased in SW480 cells after overexpression of EBLN3P. **(D)** Schematic outline of the predicted binding sites for miR-323-3p on EBLN3P and the mutation pattern of EBLN3P. **(E)** The expression of miR-323-3p in 450 CRC specimens and 8 non-tumor tissues based on TCGA datasets. **(F)** The correlation between EBLN3P and miR-323-3p expression analyzed in 450 CRC samples. **(G)** Increased expression of miR-323-3p in normal specimens compared to matched CRC specimens from our cohort. **(H)** RT-PCR for the levels of miR-323-3p in four CRC cell lines (HT29, LoVo, SW480, and HCT116) and human colonic epithelial cell lines NCM46 cells. **(I)** Luciferase activity assay revealed that miR-323-3p significantly decreased the luciferase detection of EBLN3P-Wt, but not EBLN3P-mut in SW480 and HCT116 cells. **(J)** RNA pull-down verifying miR-323-3p binding to EBLN3P. **(K)** The expression of EBLN3P in SW480 and HCT116 cells after overexpression or knockdown of miR-323-3p. **(L)** The expression of miR-323-3p in SW480 and HCT116 cells after overexpression or knockdown of EBLN3P. **(M,N)** Colony formation assays and Transwell assays for the functional exploration of miR-323-3p. $^{**}p < 0.01$, $^{***}p < 0.01$.

five miRNAs (miR-101-3p, miR-323-3p, miR-211-5p, miR-204-5p, and miR-3187-3p) in starBase v2.0 for further RT-PCR experiments and found that overexpression of EBLN3P suppressed the expression of miR-323a-3p, whereas the levels of miR-101-3p miR-211-5p, miR-204-5p, and miR-3187-3p remained unchanged (**Figure 5C**). Then, we chose miR-323a-3p for subsequent experiments. The combined sequences between EBLN3P and miR-323a-3p are shown in **Figure 5D**. Previously, miR-323a-3p has been demonstrated to suppress the proliferation and metastasis of CRC cells (17). Using TCGA datasets, we observed a lower level of miR-323a-3p in CRC specimens compared to normal tissues (**Figure 5E**). A negative association between miR-323a-3p expression and EBLN3P expression was also observed in 450 CRC samples (**Figure 5F**). In addition, the results of RT-PCR also showed that miR-323a-3p was lowly expressed in CRC specimens from our cases and for CRC cell lines (**Figures 5G,H**). Luciferase reporter assay showed that upregulation of miR-323a-3p could decrease EBLN3P-WT activity, but it had no effect on EBLN3P-MUT in both SW480 and HCT116 cells (**Figure 5I**). Further RNA pull-down also confirmed miR-323a-3p may target EBLN3P (**Figure 5J**). Moreover, overexpression of miR-323a-3p was found to suppress EBLN3P expression, whereas miR-323a-3p downregulation displayed an opposite result (**Figure 5K**). Similarly, the transfection of EBLN3P suppressed the expression of miR-323a-3p, whereas EBLN3P knockdown displayed an opposite result (**Figure 5L**). Moreover, we performed Transwell invasion assays and colony formation assays to determine the function of miR-323a-3p in CRC cells, finding that overexpression of miR-323a-3p distinctly suppressed the proliferation and invasion of SW480 and HCT116 cells (**Figures 5M,N**). Our findings suggest EBLN3P acted as miR-323a-3p sponge in CRC cells.

EBLN3P Increased UHMK1 Expression *via* Sponging miR-323a-3p

This study employed miRanDa (www.microrna.org) and TargetScan 6.2 (www.targetscan.org) for assessing the probable miR-323a-3p target. The authors reported UHMK1–3′-UTR to cover the complementary sequence for miR-323a-3p (**Figure 6A**). UHMK1 expression was distinctly increased in CRC specimens in comparison with non-tumor tissues by analyzing TCGA datasets (**Figure 6B**). The negative association between miR-323a-3p and UHMK1 and the positive association between EBLN3P and UHMK1 was demonstrated according to the data of TCGA datasets (**Figures 6C,D**). We also examined the levels of mRNA UHMK1 in CRC cell lines, confirming it was overexpressed (**Figure 6E**). As revealed from the outcomes of the Luciferase reporter test, upregulation of miR-323a-3p could decrease UHMK1-WT activity, but it had no effect on UHMK1-MUT in both SW480 and HCT116 cells (**Figure 6F**). RT-PCR further suggested that miR-323a-3p overexpression resulted in the suppression of EBLN3P and UHMK1 expression, while miR-323a-3p knockdown resulted in the promotion of EBLN3P and UHMK1 expression (**Figures 6G,H**). We also observed that knockdown of UHMK1 suppressed the proliferation and invasion of CRC cells (**Figures 6I,J**). Finally, we performed rescue experiments, finding that overexpression of EBLN3P reversed the suppression of miR-323a-3p mimics on the expression of UHMK1 (**Figure 7A**). In addition, in a series of functional experiments, we observed that the transfection of miR-323a-3p mimics reversed the distinct suppression of the transfection of pcDNA3.1-EBLN3P on the proliferation and invasion of SW480 and HCT116 cells (**Figures 7B–D**). Thus, our findings suggest EBLN3P may promote CRC progression *via* regulating miR-323a-3p/UHMK1 axis.

DISCUSSION

In our nation, CRC's incidence and death rate merely fall behind those of lung and liver carcinoma, which rise yearly, particularly among younger generations (18). Early diagnosis is very important to improve the clinical prognosis of CRC cases. Although many methods exist for the diagnosis of CRC, the sensitive diagnostic methods are limited (19). In recent years, growing studies have revealed the potential of lncRNAs used as novel diagnostic and prognostic biomarkers for CRC cases (20, 21). In this study, we identified a novel CRC-related lncRNA, EBLN3P which was demonstrated to be overexpressed in 95 CRC cases and cell lines. We also showed its diagnostic value in screening CRC specimens from normal tissues using ROC assays. Clinical assays revealed that high EBLN3P expression was associated with tumor size, Histology/differentiation, TNM stage and poor prognosis. Our findings suggest EBLN3P as a novel biomarker for CRC cases.

In recent years, growing studies have revealed that lncRNAs serve as regulators in CRC progression (22). For instance, lncRNA SNHG7, an overexpressed factor in CRC specimens, was found to promote the proliferation and metastasis of tumor cells *via* upregulating GALNT1 (23). LncRNA SLCO4A1-AS1 was highly expressed in CRC cells, and both *in vitro* and *in vivo* assays revealed that its knockdown suppressed the growth and migration of CRC cells *via* Wnt pathway (24). LncRNA-ZFAS1, whose upregulation was induced by SP1, was shown to

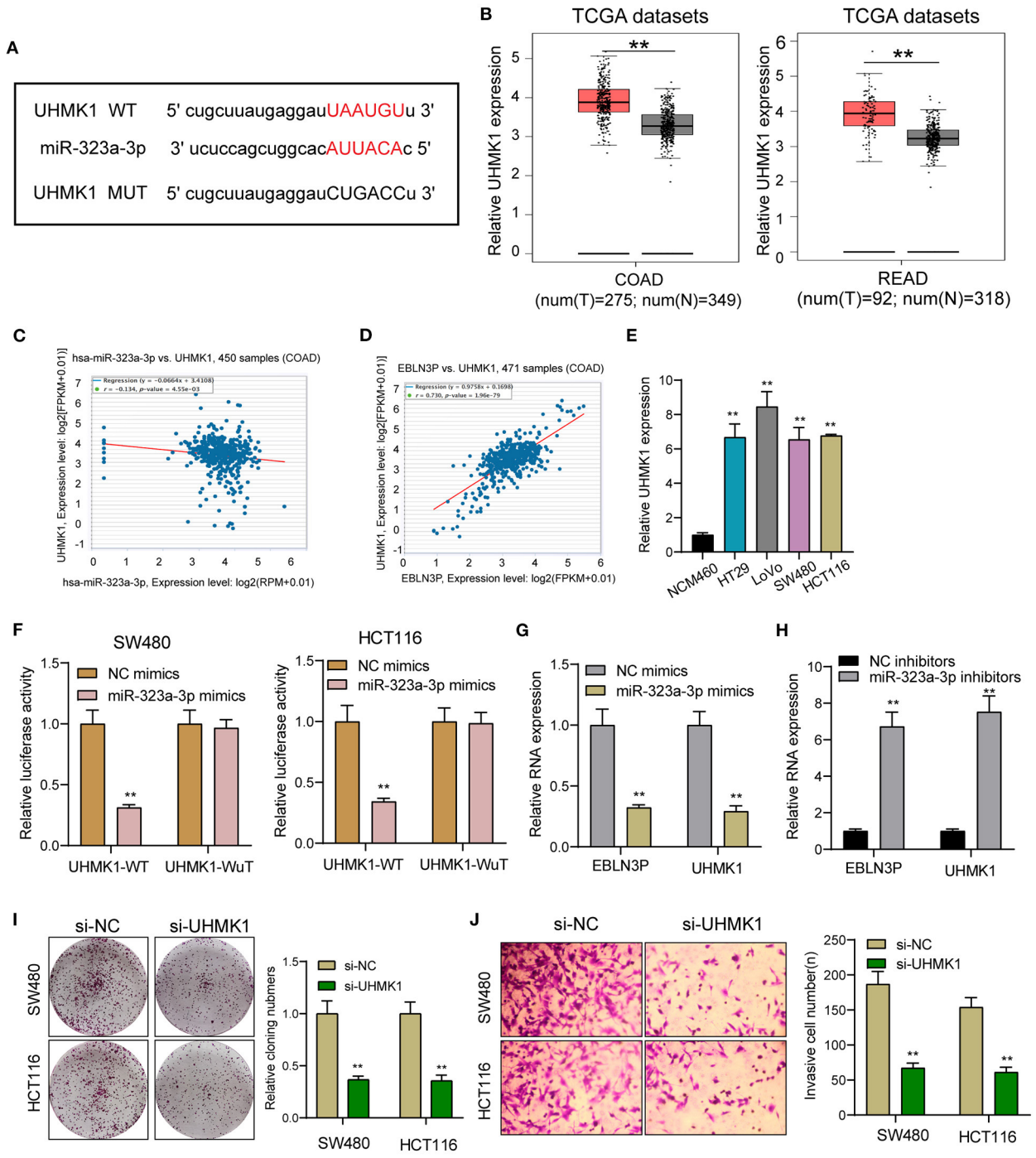

FIGURE 6 | UHMK1 expression was a potential target of miR-323a-3p. **(A)** Sequence alignment of human miR-323-3p with 3′-UTR of UHMK1 mRNA predicted by TargetScan. **(B)** UHMK1 expression in 275 CRC specimens and 349 non-tumor specimens according to the data of TCGA datasets. **(C)** The correlation between UHMK1 and miR-323-3p expression analyzed in 450 CRC samples. **(D)** The correlation between UHMK1 and EBLN3P expression analyzed in 471 CRC samples. **(E)** Decreased UHMK1 mRNA expression was observed in four CRC cells compared to NCM460 cells. **(F)** The luciferase activity of the wild-type UHMK1 3′-UTR (Wt) and mutant UHMK1 3′-UTR (Mut) cotransfected with miR-323-3p mimics or NC mimics was measured. **(G)** The levels of EBLN3P and UHMK1 in CRC cells transfected with miR-323-3p mimics or NC mimics by RT-PCR. **(H)** The levels of EBLN3P and UHMK1 in CRC cells transfected with miR-323-3p mimics or NC inhibitors by RT-PCR. **(I,J)** Colony formation assays and Transwell assays for the functional exploration of UHMK1 knockdown. $^{**}p < 0.01$.

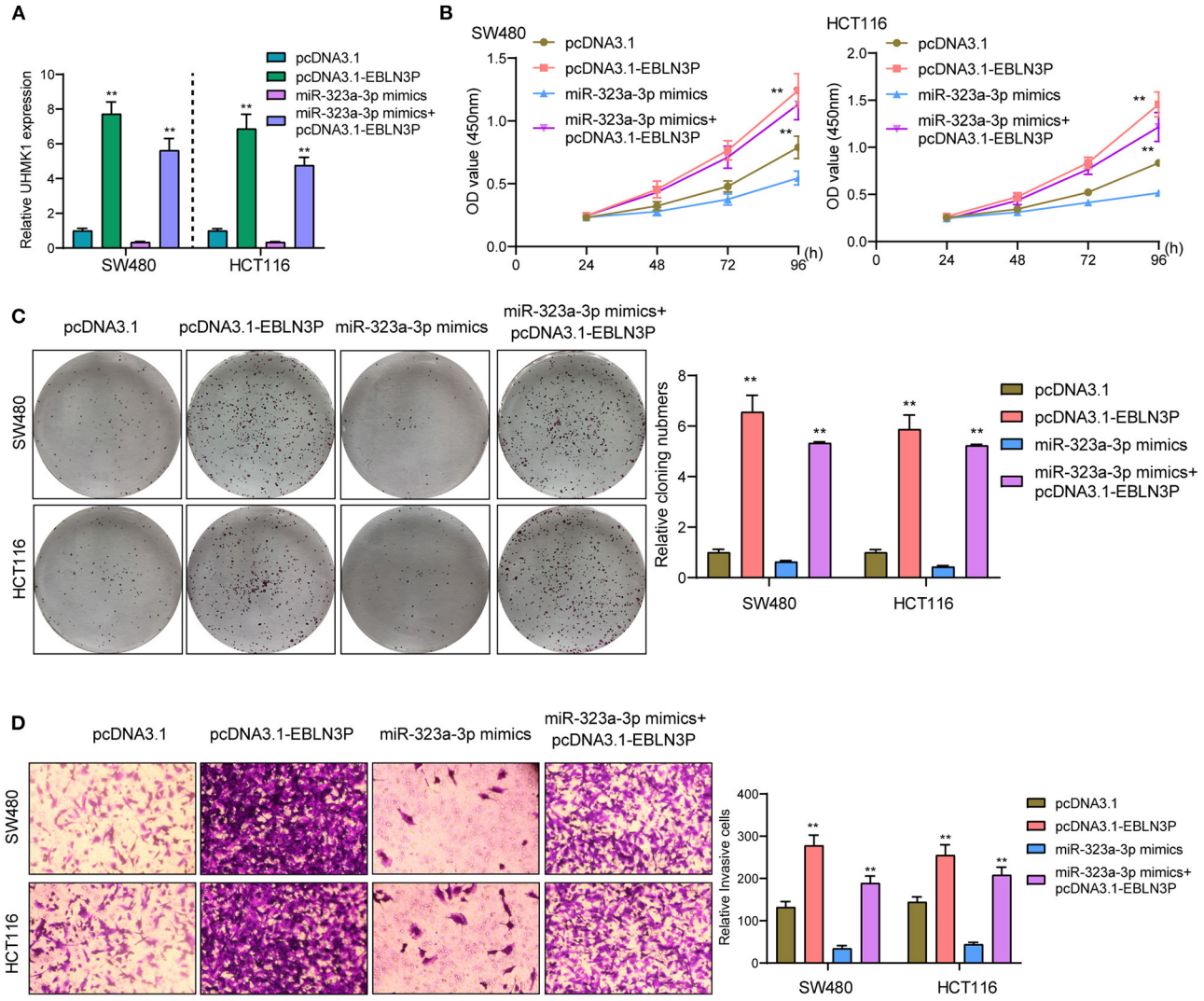

FIGURE 7 | EBLN3P promoted CRC progression *via* modulating miR-323-3p/ UHMK1 axis. **(A)** RT-PCR determined the expression of UHMK1 in SW480 and HCT116 cells transfected with pcDNA3.1, pcDNA3.1-EBLN3P, miR-323-3p mimics, or miR-323-3p mimics + pcDNA3.1–EBLN3P. **(B–D)** The ability of SW480 and HCT116 cells transfected with the above factors on the proliferation and invasion was determined using CCK-8, colony formation assays, and Transwell assays. $^{**}p < 0.01$.

accelerate the proliferation and invasion of CRC cells through the miRNA-150-5p/VEGFA axis (25). The findings suggest lncRNAs as novel players in CRC progression. Previously, Hang et al. first reported that EBLN3P was overexpressed in liver cancer. Then, they performed functional assays, which revealed that forced EBLN3P expression resulted in the promotion of the proliferation and metastasis of liver cancer cells *via* alteration of miRNA-144-3p/DOCK4 signal (14). However, to our best knowledge, the expression and function of EBLN3P in other tumor types remained largely unclear. In this study, we also performed *in vitro* experiments, finding that knockdown of EBLN3P suppressed the proliferation, migration, and invasion of SW480 and HCT116 and promoted apoptosis, suggesting EBLN3P as a tumor promoter in CRC progression. Our findings were consistent with the oncogenic roles of EBLN3P in liver cancer. To explore the related mechanisms, we performed Western blot to determine the effects of EBLN3P on EMT pathways, confirming that EBLN3P knockdown suppressed the activity of EMT pathways, which could explain the reason that EBLN3P could contribute to the abilities of metastaticity.

For the in-depth exploration of the basic molecular systems allowing EBLN3P to regulate downstream effectors inside CRC, this study first reported its site in carcinoma cells, given that lncRNA functions are dependent on its subcellular localization (26). Cytosolic lncRNAs are capable of modulating mRNA stability and protein localization and act as microRNA sponge (27). In this study, we observed that EBLN3P was mainly expressed both in the cytoplasm. Bioinformatics analyses

predicted miR-323a-3p targeting sites on EBLN3P. Luciferase reporter assay, binding site mutation analysis, and qPCR further verified that EBLN3P is a genuine target of miR-323a-3p. We also observed that miR-323a-3p expression was distinctly upregulated in SW480 and HCT116 cells, and the levels of EBLN3P were regulated by the transfection of miR-323a-3p mimics or miR-323a-3p inhibitors. Previously, a decreased expression of miR-323a-3p has been reported, and its overexpression suppressed the proliferation and metastasis of CRC cells, (17) which was consistent with our findings. Thus, together with previous findings, EBLN3P may display its oncogenic roles *via* sponging miR-323a-3p.

UHMK1 refers to one nuclear serine/threonine kinase exhibiting a U2AF homology motif and receiving phosphorylating process. Originally, this study found it regulating the stathmin's function (28). In recent years, UHMK1 dysregulating process or mutating process was suggested as one high-penetrant element inside various tumors of humans (e.g., gastric cancer as well as CRC) (12, 13). Here, UHMK1 exhibited a significant expressing state inside CRC. As confirmed by bioinformatics analysis and luciferase reporting element test, UHMK1 acts as miR-323a-3p's direct target. According to the correlation study, UHMK1 expressing state displayed a negative relationship to miR-323a-3p, while positively associated with EBLN3P in 471 CRC samples from TGCA datasets. Furthermore, we also found that the transfection of miR-323a-3p mimics reversed the distinct suppression of the transfection of pcDNA3.1-EBLN3P on the proliferation and invasion of SW480 and HCT116 cells. Thus, our findings suggest EBLN3P may promote CRC progression by increasing UHMK1 expression *via* sponging miR-323a-3p.

Although our study showed that EBLN3P acts as an oncogene in CRC, there are several limitations that exist in this study such as limited clinical specimens, the function of EBLN3P/miR-323a-3p/UHMK1 axis in CRC *in vivo*, and the association of EBLN3P and other potential miRNAs. Moreover, the specific role of EBLN3P-mediated regulatory mechanism in CRC needs further investigation.

CONCLUSION

In summary, an EBLN3P-miR-323a-3p-UHMK1 regulating axis inside CRC pathogenic mechanism received the identification here. EBLN3P is an oncogenic lncRNA facilitating CRC tumor formation through the way of being one ceRNA regulating UHMK1's expressing state *via* sponging miR-323a-3p. Here, miR-323a-3p is proven as one probable therapeutic aim for managing CRC.

DATA AVAILABILITY STATEMENT

The original contributions presented in the study are included in the article/supplementary files, further inquiries can be directed to the corresponding author/s.

ETHICS STATEMENT

The studies involving human participants were reviewed and approved by Sun Yat-sen Memorial Hospital, Sun Yat-sen University. The patients/participants provided their written informed consent to participate in this study. The animal study was reviewed and approved by Sun Yat-sen Memorial Hospital, Sun Yat-sen University.

AUTHOR CONTRIBUTIONS

X-hX, QB, and Z-wS conceived and designed the experiments. X-hX, WS, and J-hL performed the experiments. Z-qH and Y-fL analyzed the data. X-hX and QB wrote the paper. All authors read and approved the final manuscript.

REFERENCES

1. Siegel R, Desantis C, Jemal A. Colorectal cancer statistics, 2014. *CA Cancer J Clin.* (2014) 64:104–117. doi: 10.3322/caac.21220
2. Pan R, Zhu M, Yu C, Lv J, Guo Y, Bian Z, et al. Cancer incidence and mortality: a cohort study in China, 2008–2013. *Int J Cancer.* (2017) 141:1315–23. doi: 10.1002/ijc.30825
3. Silva A, Faria G, Araújo A, Monteiro MP. Impact of adiposity on staging and prognosis of colorectal cancer. *Crit Rev Oncol Hematol.* (2020) 145:102857. doi: 10.1016/j.critrevonc.2019.102857
4. Lech G, Słotwiński R, Słodkowski M, Krasnodebski IW. Colorectal cancer tumour markers and biomarkers: Recent therapeutic advances. *World J Gastroenterol.* (2016) 22:1745–55. doi: 10.3748/wjg.v22.i5.1745
5. Yiu AJ, Yiu CY. Biomarkers in colorectal cancer. *Anticancer Res.* (2016) 36:1093–102. doi: 10.1002/sim.7149
6. Bhan A, Soleimani M, Mandal SS. Long noncoding RNA and cancer: a new paradigm. *Cancer Res.* (2017) 77:3965–81. doi: 10.1158/0008-5472.CAN-16-2634
7. Charles Richard JL, Eichhorn PJA. Platforms for investigating LncRNA functions. *SLAS Technol.* (2018) 23:493–506. doi: 10.1177/2472630318780639
8. Chan JJ, Tay Y. Noncoding RNA: RNA regulatory networks in cancer. *Int J Mol Sci.* (2018) 19:1310. doi: 10.3390/ijms19051310
9. Chandra Gupta S, Nandan Tripathi Y. Potential of long non-coding RNAs in cancer patients: from biomarkers to therapeutic targets. *Int J Cancer.* (2017) 140:1955–67. doi: 10.1002/ijc.30546
10. Francone VP, Ifrim MF, Rajagopal C, Leddy CJ, Wang Y, Carson JH, et al. Signaling from the secretory granule to the nucleus: Uhmk1 and PAM. *Mol Endocrinol.* (2010) 24:1543–58. doi: 10.1210/me.2009-0381
11. Wang H, Zhan M, Yang R, Shi Y, Liu Q, Wang J. Elevated expression of NFE2L3 predicts the poor prognosis of pancreatic cancer patients. *Cell Cycle.* (2018) 17:2164–74. doi: 10.1080/15384101.2018.1520558
12. Feng X, Ma D, Zhao J, Song Y, Zhu Y, Zhou Q, et al. UHMK1 promotes gastric cancer progression through reprogramming nucleotide metabolism. *EMBO J.* (2020) 39:e102541. doi: 10.15252/embj.2019102541
13. Chowdhury A, Katoh H, Hatanaka A, Iwanari H, Nakamura N, Hamakubo T, et al. Multiple regulatory mechanisms of the biological function of NRF3 (NFE2L3) control cancer cell proliferation. *Sci Rep.* (2017) 7:12494. doi: 10.1038/s41598-017-12675-y
14. Li H, Wang M, Zhou H, Lu S, Zhang B. Long Noncoding RNA EBLN3P Promotes the Progression of Liver Cancer via Alteration of

microRNA-144-3p/DOCK4 Signal. *Cancer Manage Res.* (2020) 12:9339–49. doi: 10.2147/CMAR.S261976
15. Gonzalez DM, Medici D. Signaling mechanisms of the epithelial-mesenchymal transition. *Sci Signal.* (2014) 7:re8. doi: 10.1126/scisignal.2005189
16. Weidle UH, Birzele F, Kollmorgen G, Ruger R. Long Non-coding RNAs and their role in metastasis. *Cancer Genomics Proteomics.* (2017) 14:143–60. doi: 10.21873/cgp.20027
17. Bjeije H, Soltani BM, Behmanesh M, Zali MR. YWHAE long non-coding RNA competes with miR-323a-3p and miR-532-5p through activating K-Ras/Erk1/2 and PI3K/Akt signaling pathways in HCT116 cells. *Human Mol Genet.* (2019) 28:3219–31. doi: 10.1093/hmg/ddz146
18. Zhu J, Tan Z, Hollis-Hansen K, Zhang Y, Yu C, Li Y. Epidemiological trends in colorectal cancer in china: an ecological study. *Dig Dis Sci.* (2017) 62:235–43. doi: 10.1007/s10620-016-4362-4
19. Schreuders EH, Ruco A, Rabeneck L, Schoen RE, Sung JJY, Young GP, et al. Colorectal cancer screening: a global overview of existing programmes. *Gut.* (2015) 64:1637–49. doi: 10.1136/gutjnl-2014-309086
20. Okugawa Y, Grady WM, Goel A. Epigenetic alterations in colorectal cancer: emerging biomarkers. *Gastroenterology.* (2015) 149:1204–25.e1212. doi: 10.1053/j.gastro.2015.07.011
21. Wang L, Cho KB, Li Y, Tao G, Xie Z, Guo B. Long noncoding RNA (lncRNA)-mediated competing endogenous RNA networks provide novel potential biomarkers and therapeutic targets for colorectal cancer. *Int J Mol Sci.* (2019) 20:5758. doi: 10.3390/ijms20225758
22. Javed Z, Khan K, Sadia H, Raza S, Salehi B, Sharifi-Rad J, et al. LncRNA & Wnt signaling in colorectal cancer. *Cancer Cell Int.* (2020) 20:326. doi: 10.1186/s12935-020-01412-7
23. Shan Y, Ma J, Pan Y, Hu J, Liu B, Jia L. LncRNA SNHG7 sponges miR-216b to promote proliferation and liver metastasis of colorectal cancer through upregulating GALNT1. *Cell Death Dis.* (2018) 9:722. doi: 10.1038/s41419-018-0759-7
24. Yu J, Han Z, Sun Z, Wang Y, Zheng M, Song C. LncRNA SLCO4A1-AS1 facilitates growth and metastasis of colorectal cancer through β-catenin-dependent Wnt pathway. *J Exp Clin Cancer Res.* (2018) 37:222. doi: 10.1186/s13046-018-0896-y
25. Chen X, Zeng K, Xu M, Hu X, Liu X, Xu T, et al. SP1-induced lncRNA-ZFAS1 contributes to colorectal cancer progression via the miR-150-5p/VEGFA axis. *Cell Death Dis.* (2018) 9:982. doi: 10.1038/s41419-018-0962-6
26. Quinn JJ, Chang HY. Unique features of long non-coding RNA biogenesis and function. *Nat Rev Genet.* (2016) 17:47–62. doi: 10.1038/nrg.2015.10
27. Salmena L, Poliseno L, Tay Y, Kats L, Pandolfi PP. A ceRNA hypothesis: the Rosetta Stone of a hidden RNA language? *Cell.* (2011) 146:353–8. doi: 10.1016/j.cell.2011.07.014
28. Choi HJ, Park H, Zhang L, Kim JH, Kim YA, Yang J-Y, et al. Genome-wide association study in East Asians suggests UHMK1 as a novel bone mineral density susceptibility gene. *Bone.* (2016) 91:113–21. doi: 10.1016/j.bone.2016.07.008

Conflict of Interest: The authors declare that the research was conducted in the absence of any commercial or financial relationships that could be construed as a potential conflict of interest.

Copyright © 2021 Xu, Song, Li, Huang, Liu, Bao and Shen. This is an open-access article distributed under the terms of the Creative Commons Attribution License (CC BY). The use, distribution or reproduction in other forums is permitted, provided the original author(s) and the copyright owner(s) are credited and that the original publication in this journal is cited, in accordance with accepted academic practice. No use, distribution or reproduction is permitted which does not comply with these terms.

frontiers in Medicine

ORIGINAL RESEARCH
published: 26 May 2021
doi: 10.3389/fmed.2021.670188

MicroRNA-1-3p Suppresses Malignant Phenotypes of Ameloblastoma Through Down-Regulating Lysosomal Associated Membrane Protein 2-Mediated Autophagy

Xing Niu[1,2†], Biying Huang[2†], Xue Qiao[3], Jinwen Liu[2], Lijie Chen[1,2] and Ming Zhong[1,2]*

[1] Department of Stomatology, Xiang'an Hospital of Xiamen University, Xiamen, China, [2] Department of Oral Histopathology, Liaoning Province Key Laboratory of Oral Disease, School and Hospital of Stomatology, China Medical University, Shenyang, China, [3] Department of Central Laboratory, Liaoning Province Key Laboratory of Oral Disease, School and Hospital of Stomatology, China Medical University, Shenyang, China

OPEN ACCESS

Edited by:
Fu Wang,
Xi'an Jiaotong University, China

Reviewed by:
Bo Liu,
Sichuan University, China
Jiqin Lian,
Third Military Medical University, China

***Correspondence:**
Ming Zhong
zhongming_oral@aliyun.com

[†] These authors have contributed equally to this work

Specialty section:
This article was submitted to Precision Medicine, a section of the journal Frontiers in Medicine

Received: 20 February 2021
Accepted: 26 April 2021
Published: 26 May 2021

Citation:
Niu X, Huang B, Qiao X, Liu J, Chen L and Zhong M (2021) MicroRNA-1-3p Suppresses Malignant Phenotypes of Ameloblastoma Through Down-Regulating Lysosomal Associated Membrane Protein 2-Mediated Autophagy. Front. Med. 8:670188. doi: 10.3389/fmed.2021.670188

Objective: Several clinical trials have suggested that autophagy inhibition is a promising approach for cancer therapy. However, the implications of autophagy in ameloblastoma (AB) remain undiscovered. This study investigated the dysregulated autophagy and its regulatory mechanisms in AB.

Methods: The expression and distribution of autophagy-related proteins including B-cell lymphoma-2-interacting protein-1 (Beclin1), microtubule-associated protein 1 light chain 3 (LC3) II/I and lysosomal associated membrane protein 2 (LAMP2) were detected in AB and normal oral mucosa (NOM) tissues by immunohistochemistry and western blot analyses. Under transmission electron microscopy, the autophagy of AB was observed. LAMP2 was a potential target mRNA of miR-1-3p. Quantitative Real-time PCR (qRT-PCR) analysis was utilized for examining LAMP2 and miR-1-3p in AB tissues as well as AM-1 cells. The correlation between LAMP2 and miR-1-3p was analyzed in AB. After transfection with miR-1-3p mimic or inhibitor, LAMP2 expression, proliferation, migration, and invasion were separately detected in AM-1 cells. Rescue assays were finally presented.

Results: Our results showed that Beclin1 was lowly expressed as well as LC3II/I and LAMP2 were highly expressed in AB. Autophagosomes were observed in AB. MiR-1-3p was lowly expressed in AB, which exhibited negative correlations to LAMP2 expression. MiR-1-3p up-regulation significantly lowered LAMP2 expression in AM-1 cells. Furthermore, miR-1-3p overexpression restrained proliferative, migrated, and invasive capacities of AM-1 cells, which were ameliorated by LAMP2 overexpression.

Conclusion: Our findings demonstrated that miR-1-3p suppressed malignant phenotypes of AB through down-regulating LAMP2-mediated autophagy, which could become an underlying target for AB therapy.

Keywords: ameloblastoma, miR-1-3p, Beclin1, LAMP2, LC3, autophagy, malignant phenotypes

INTRODUCTION

Ameloblastoma (AB), a common odontogenic epithelial neoplasm, exhibits locally invasive and aggressive behaviors (1). More than 80% of AB cases occur in the mandible (2). It has up to 90% risk of recurrence following conservative treatment (3). Although radical surgery can distinctly cut down the high recurrence risk, patients usually meet facial deformities (4). Unfortunately, the etiology of AB remains still unclear. Thus, it is of importance to research the molecular mechanisms of AB.

Autophagy is a stress response of eukaryotic cells to external pressure or stimulation such as starvation, hypoxia and toxicity (5). In the process of tumor development, autophagy may restrain the progression of tumors, but once the tumor is formed, autophagy may facilitate survival and growth of tumor cells (6). A previous study has found that LC-3 and p62 were highly expressed in primary AB-derived epithelial cells (7). Therefore, research on autophagy in odontogenic tumors is of great significance for understanding tumor occurrence and development. During autophagosome formation, microtubule-associated protein 1 light chain 3 (LC3) can be transformed from LC3-I to LC3-II, and LC3-II binds to the newly formed autophagosome membrane until the final autophagosome fuses with the lysosome (8). Therefore, LC3-II has become a marker of intracellular autophagy. Lysosomal associated membrane protein 2 (LAMP2) is a member of the membrane glycoprotein family, which protects the lysosomal membrane from hydrolysis by acidic hydrolases, and regulates membrane fusion of lysosomes with other organelles during autophagy (9). Additionally, B-cell lymphoma-2-interacting protein-1 (Beclin1) exerts a critical role in a critical step of the autophagic process. However, there are few studies on the expressions and clinical implications of autophagy-related proteins in AB.

MicroRNAs (miRNAs), with 21–22 nucleotides in length, may mediate gene silencing at post-transcriptional levels (10, 11). In various tumors, abnormal expression of miRNAs is involved in various biological processes (12). The ability to regulate miRNA expression and activity *in vivo* by its mimic or inhibitor offers a direction for developing innovative treatment strategies against cancers. MiRNA-based therapies may provide higher stability as well as protection from nucleases (12). Several miRNA-targeted therapies against cancers have entered clinical trials such as miR-34 (12). However, it is a challenge about how to select the optimal candidate miRNAs for each disease. Many studies have demonstrated that miRNAs can play regulatory roles in the processes of autophagy by mediating target genes (13–15). Among them, miR-1-3p is down-regulated in a variety of human tumors. For instance, overexpressed miR-1-3p restrains autophagy via targeting ATG3 in non-small cell lung cancer (16). Nevertheless, its expression and role in AB remain unclear.

Herein, our research investigated abnormally expressed autophagy-related proteins and analyzed their clinical implications. Our findings suggested that autophagy imbalance could be involved in the progression of AB. Furthermore, LAMP2 might become a potential target mRNA of miR-1-3p in AB.

MATERIALS AND METHODS

Tumor Specimens

From 2014 to 2017, 12 paired AB and normal oral mucosa (NOM) fresh specimens were gathered from the oral and maxillofacial surgery of School and Hospital of Stomatology, China Medical University (Shenyang, China), which were then immediately stored at −80°C. Paraffin-embedded 104 AB tissues and 20 NOM tissues were retrieved from the Department of Oral Histopathology, School and Hospital of Stomatology, China Medical University between 2015 and 2016. This research strictly followed the Declaration of Helsinki. Each patient signed written informed consent. Our research gained the approval of the Ethics Committee of School and Hospital of Stomatology, China Medical University (2016-12).

Immunohistochemistry

Paraffin-embedded tissue sections were cut to 100 μm thick, dried, deparaffinized and rehydrated following standard protocols. The sections were incubated with primary antibodies against Beclin1 (1:500; ab622557; Abcam, Cambridge, MA, USA), LC3 (1:2,000; ab51520; Abcam) and LAMP2 (1:1,000; ab25631; Abcam) at 4°C overnight. Then, the sections were incubated with secondary antibodies for 30 min at room temperature. The sections were stained by diaminobenzidine (DAB; Thermo Fisher Scientific, Waltham, MA, USA). Nuclei were lightly stained with hematoxylin. For negative control, the sections were treated as above but PBS (Hyclone, South Logan, UT, USA) instead of primary antibodies.

For each section, three fields were randomly selected (×200). The expression scores of Beclin1, LC3, and LAMP2 were on the grounds of staining intensity (no coloring: 0 point; light yellow: 1 point; brown yellow: 2 points; sepia: 3 points) and percentage of positive tumor cells (0–5%: 0 point; 6–25%: 1 point; 26–50%: 2 points; >50%: 3 points) (17). The final score was determined by staining intensity score × percentage of positive tumor cells (>4 scores: positive and 0–3 scores: negative).

Western Blot

Tissues were lysed using 300 μl RIPA plus 3 μl protease inhibitor PMSF (Beyotime, Beijing, China) on the ice. After centrifugation for 5 min at 12,000 × g, the supernatant was stored at −20°C. The protein concentration was determined using a BCA protein assay kit (Beyotime). Total proteins in the supernatant were subjected to separation in 10% SDS-PAGE, followed by transference onto PVDF membranes (Millipore, USA). The membranes were blocked with 5% skim milk powder lasting 1 h at room temperature. Afterwards, the membrane was incubated by primary antibodies at 4°C overnight, and incubated with corresponding HRP-conjugated secondary antibodies (1:2,000;

Abbreviations: AB, ameloblastoma; NOM, normal oral mucosa; LAMP2, lysosomal associated membrane protein 2; Beclin1, B-cell lymphoma-2-interacting protein-1; LC3, microtubule-associated protein 1 light chain 3; miRNA, microRNA; qRT-PCR, quantitative Real-time PCR; CCK-8, cell counting kit-8; EMT, epithelial-mesenchymal transition.

TABLE 1 | The primer information for qRT-PCR.

Target genes	Primer sequences (5'-3')
LAMP2	5'-GTGAGTTGTATTGGGGTTGATGTTA-3' (forward)
	5'-CAATGATACTTGTCTGCTGGCTAC-3' (reverse)
β-actin	5'-TGGCACCCAGCACAATGAA-3' (forward)
	5'-CTAAGTCATAGTCCGCCTAGAAGCA-3' (reverse)
miR-1-3p	5'-CCACGATGGAATGTAAAGAAGT-3' (forward)
	5'-CAGAGCAGGGTCCGAGGTA-3' (reverse)
ATG3	5'-ACTGATGCTGGCGGTGAAGATG-3' (forward)
	5'-GTGCTCAACTGTTAAAGGCTGCC-3' (reverse)
U6	5'-ATTGGAACGATACAGAGAAGATT-3'(forward)
	5'-GGAACGCTTCACGAATTTG-3' (reverse)

Abcam) for 50 min at room temperature in the dark. The primary antibodies included anti-Beclin1 (1:2,000; ab622557; Abcam), anti-LC3 (1:1,000; ab51520; Abcam), anti-LAMP2 (1:500; ab25631; Abcam) and anti-GAPDH (1:8,000; ab9485; Abcam). GAPDH was used as an internal control. The protein blot was visualized using Odyssey CLx.

Quantitative Real-Time PCR

Total RNAs were extracted from tissues or cells with Trizol (Takara, Tokyo, Japan). For detection of miR-1-3p expression, cDNA was synthesized using TaqMan miRNA reverse transcription kit and specific primer of miR-1-3p. qRT-PCR was carried out on Hairpin-itTM Real-Time PCR Quantitation Kit. To detect the LAMP2 expression, cDNA synthesis was carried out using the SuperScript III. qRT-PCR quantification was performed using the SYBR Select Master Mix kit (Takara). β-actin and U6 served as internal controls of LAMP2 or miR-1-3p, respectively. The primer sequences of LAMP2, ATG3, β-actin, miR-1-3p, and U6 are shown in **Table 1**. LAMP2 and miR-1-3p expression was determined using $2^{-\Delta\Delta CT}$ method.

Transmission Electron Microscope

The tissues were washed using 0.1 cacodylate buffer (pH = 7.4), which were then fixed with PBS solution plus 3% glutaraldehyde as well as 2% paraformaldehyde. Standard protocols were presented for the rest of the process. The sections were stained with uranyl acetate and lead citrate. Images were captured under a transmission electron microscope.

Cell Culture

Human immortalized AM-1 cell line that was gifted by Iwate Medical University (Japan) were cultured in Keratinocyte-SFM (Gibco, Invitrogen, USA). Human immortalized epidermal HaCat cell line that was purchased from Hunan Fenghui Biotechnology Co., Ltd. (Hunan, China) was cultured in DMEM (Hyclone, USA) containing 10% FBS at 37°C, 5% CO_2.

Transfection

MiR-1-3p mimic, inhibitor and corresponding miR-negative control (miR-NC) as well as LAMP2 and control pcDNA3.1 were purchased from GenePharma (Shanghai, China). The sequences were as follows: miR-1-3p mimics: 5'-UGGAAUGUAAAGAAGUAUGUAU-3'; miR-1-3p inhibitors: 5'-AUACAUACUUCUUUACAUUCCA-3'; miR-NC: 5'-UUCUCCGAACGUGUCACGUTT-3' or 5'-CAGUACUUUUGUGUAGUACAA-3'. AM-1 cells were seeded onto a 6-well plate for 24 h. Hundred nanometer mimic, inhibitor, or miR-NC as well as 3 μg plasmid were separately transfected into cells via Lipofectamine 2,000 reagent (Invitrogen, Carlsbad, CA, USA). Following transfection for 48 h, cells were harvested.

Dual Luciferase Reporter Assay

The full or mutant fragments containing the predicted miR-1-3p binding sites in LAMP2 3'-UTR were cloned into the firefly luciferase gene in GP-miRGLO vector (Promega, Fitchburg, WI, USA). Afterwards, AM-1 cells were co-transfected miR-1-3p mimics or miR-NC with LAMP2 3'-UTR wild type (WT) or mutation (MUT). After 24 h, relative luciferase activity was determined through the Dual-Luciferase Reporter assay system (Promega).

Cell Counting Kit-8

AM-1 cells were inoculated into a 96-well plate (1×10^3 cells/well). After transfection with miR-1-3p mimic, miR-1-3p inhibitor and miR-NC or treatment with 3 mmol/L autophagy inhibitor 3-MA, cells were measured at 0, 24, 48, 72, and 96 h using CCK-8 kit (Dojindo, Kumamoto, Japan). The absorbance value at 450 nm was determined with a microplate reader.

Colony Formation Assay

AM-1 cells were inoculated in a 10 cm dish (1×10^3 cells/dish). Under culturing for 14 days, cells were fixed with methanol lasting 20 min, followed by staining with 0.1% crystal violet.

Flow Cytometry for Apoptosis

AM-1 cells were inoculated onto a 6-well plate (4×10^4 cells/well). Then, cells were centrifuged at 1,500 rpm for 5 min. Following washing with PBS for three times, cells were treated by 5 μL Annexin V-FITC as well as 5 μL PI lasting 10 min at room temperature away from light. Cell apoptosis was detected through flow cytometry.

Transwell Assay

AM-1 cells (4×10^4 cells/well) were inoculated onto the upper chamber in serum-free media with or without Matrigel. The lower chamber was added with culture medium. Under incubation lasting 24 h, migrated or invasive cells to the lower chamber were immobilized using 4% paraformaldehyde as well as stained using hematoxylin and eosin.

Statistical Analyses

Statistical analyses were carried out utilizing Graphpad prism 7.0 and SPSS 17.0. Data are expressed as the mean ± standard error of mean (SEM). All assays were repeated three times. Comparisons between groups were presented with student's *t*-test or one-way analysis of variance. Chi square test was used for comparing the associations between clinical parameters and expression of proteins. The correlation between miR-1-3p and

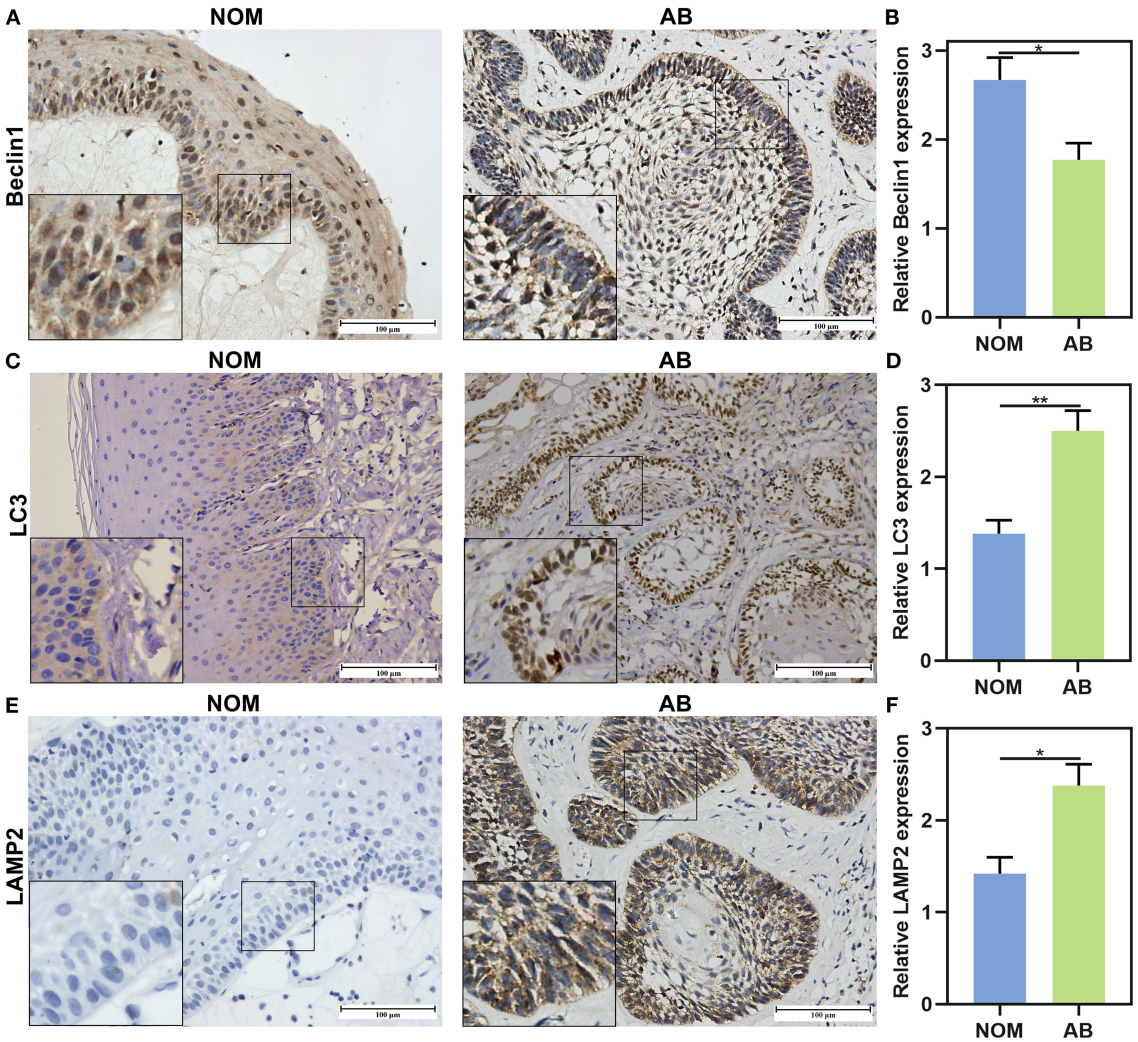

FIGURE 1 | The expression and distribution of Beclin1, LC3, and LAMP2 in AB and NOM tissues by immunohistochemistry. **(A)** Beclin1 is positively expressed in the nucleus of epithelial cells in NOM tissues and is positively expressed in the cytoplasm of epithelial cells in AB tissues. **(B)** Quantitative analysis results showing a lower expression level of Beclin1 in AB tissues than in NOM tissues. **(C)** LC3 is negatively expressed in NOM and is positively expressed in the nuclei of epithelial cells in AB tissues. **(D)** Quantitative analysis showing a higher expression level of LC3 in AB tissues than in NOM tissues. **(E)** LAMP2 is negatively expressed in NOM and is positively expressed in the cytoplasm and cell membrane of epithelial cells in AB tissues. **(F)** Quantitative analysis for a higher expression level of LAMP2 in AB tissues than in NOM tissues. Bar: 100 μm. Magnification: 200×. *$P < 0.05$; **$P < 0.01$.

LAMP2 was evaluated via Spearman analysis. P <0.05 was indicative of statistical significance.

RESULTS

The Expression and Distribution of Beclin1, LC3, and LAMP2 in AB and NOM Tissues

This study included 104 AB tissues and 20 NOM tissues. The expression and distribution of autophagy markers including Beclin1, LC3, and LAMP2 were assessed through immunohistochemistry. As shown in our results, Beclin1 was positively expressed in the nucleus of epithelial cells in NOM tissues (**Figure 1A**). Meanwhile, Beclin1 was positively expressed in the cytoplasm of epithelial cells in AB tissues. Quantitative analysis results confirmed that the expression of Beclin1 in NOM tissues was 1.51 times higher compared to that in AB tissues ($P < 0.05$; **Figure 1B**). The positive rate of Beclin1 expression in 104 cases of AB was 50% (52/104), which was significantly lower than that in NOM tissues (95%, 19/20). The correlations between Beclin1 expression and clinical pathological features were analyzed in AB. In **Table 2**, no significant difference was found between Beclin1 expression and age, gender, location, pathological classification, and recurrence of AB patients. In **Figure 1C**, LC3 was negatively expressed in NOM and the positive expression of LC3 was found in the nuclei of epithelial

cells in AB tissues. LC3 expression in AB tissues was 1.82 times that of NOM tissues ($P < 0.01$; **Figure 1D**). The positive expression rate of LC3 in 104 cases of AB was 76.92% (80/104), which displayed a distinct higher level compared to that in NOM specimens (10%, 2/20). But no significant difference was detected between the expression of LC3 and age, gender, and recurrence of AB patients (**Table 3**). Intriguingly, we found that the positive expression rate of LC3 in the mandible of AB was significantly increased compared to that in the maxillary. Furthermore, the positive rate of LC3 in solid/multicystic AB exhibited a higher level in comparison to that in other types. In **Figure 1E**, LAMP2 was negatively expressed in NOM tissues while LAMP2 was primarily distributed in the cytoplasm and cell membrane of epithelial cells of AB. After quantification, LAMP2 expression in AB tissues was 1.68 times higher compared to that in NOM tissues ($P < 0.05$; **Figure 1F**). The positive expression rate of LAMP2 in 104 cases of AB was 63.46% (66/104), which was prominently more than that in NOM tissues (5%, 1/20; $P < 0.05$). In **Table 4**, LAMP2 expression in the mandible of AB was significantly higher than that in the maxillary, indicating that LAMP2 expression might be related to AB location. These findings indicated the dysregulated autophagy in AB.

Dysregulation of Autophagy in AB Tissues

After immunohistochemistry, we further the expression levels of autophagy-related proteins including Beclin1, LC3II/I and LAMP2 in AB and NOM tissues by western blot. Consistent with immunohistochemistry results, western blot analysis demonstrated that Beclin1 expression in AB tissues was distinctly lower compared to that in NOM specimens ($P < 0.05$; **Figures 2A,B**). Furthermore, LC3II/I in AB tissues was significantly higher in comparison to that in NOM specimens ($P < 0.01$; **Figures 2C,D**). As expected, overexpressed LAMP2 was detected in AB tissues in comparison to NOM specimens ($P < 0.05$; **Figures 2E,F**). Ultrastructure of autophagosomes was investigated in AB tissues under a transmission electron microscopy (**Figure 3**). Above findings demonstrated the autophagy activation in AB.

LAMP2 Is a Target mRNA of miR-1-3p in AB

Previous studies have highlighted the roles of miR-1-3p in cancers. Bioinformatics analysis showed that miR-1-3p could bind to 3'UTR of LAMP2 mRNA among three autophagy-related proteins. We firstly analyzed the expression levels of miR-1-3p and LAMP2 in AB tissues by qRT-PCR. As a result, miR-1-3p was distinctly lowly expressed in AB than NOM tissues ($P < 0.001$; **Figure 4A**). On the contrary, LAMP2 mRNA in AB tissues displayed a higher level in comparison to NOM tissues ($P < 0.01$; **Figure 4B**). Spearman correlation analysis results suggested that miR-1-3p expression was negatively correlated with LAMP2 expression in AB tissues ($r = -0.8881$, $P = 0.0003$; **Figure 4C**). These data were indicative that LAMP2 might be a target mRNA of miR-1-3p in AB. MiR-1-3p expression was further detected in AM-1 and HaCat cells. Our results showed the down-regulation of miR-1-3p in AM-1 cells compared to HaCat cells ($P < 0.01$; **Figure 4D**). In **Figure 4E**, miR-1-3p was mainly expressed in extracellular, mitochondrion, nucleus, and cytosol. LAMP2 mRNA was significantly up-regulated in AM-1 cells compared to HaCat cells ($P < 0.01$; **Figure 4F**). MiRNAs mediate the silencing of target genes at the post-transcriptional level by binding to the 3'-untranslated region (3'-UTR) of mRNAs. By the miRanda database (http://www.miranda.org/), we found that LAMP2 was a potential target of miR-1-3p (**Figure 4G**). Luciferase assay confirmed that miR-1-3p may bind to LAMP2, and inhibited LAMP2 luciferase activity in AM-1 cells ($P < 0.0001$; **Figure 4G**). However, no inhibitory effect was found after mutation of this binding motif. To confirm whether miR-1-3p affected LAMP2 expression, miR-1-3p mimic or inhibitor was transfected into AM-1 cells. In **Figure 4H**, it was successfully overexpressed by miR-1-3p mimic transfection ($P < 0.0001$) while it was silenced after transfection with miR-1-3p inhibitor ($P < 0.05$). As expected, LAMP2 protein expression was decreased by miR-1-3p mimic ($P < 0.001$) and increased by its inhibitor ($P < 0.01$; **Figure 4I**). Similarly, miR-1-3p mimic significantly lowered the expression of LAMP2 mRNA in AM-1 cells ($P < 0.01$; **Figure 4J**). Meanwhile, LAMP2 expression was distinctly up-regulated when transfected by miR-1-3p inhibitor ($P < 0.001$). A previous study reported that ATG3 was a potential target of miR-1 in NSCLC cells (16). However, our data showed that miR-1-3p mimic or inhibitor did not significantly alter ATG3 expression in AM-1 cells (**Figure 4K**).

miR-1-3p Restrains Proliferation and Facilitates Apoptosis in AB Cells

Firstly, we observed the roles of autophagy on malignant phenotypes of AB. After AM-1 cells were treated with 3 mmol/L autophagy inhibitor 3-MA for 0, 24, 48, 72, and 96 h, cell viability was measured. As a result, 3-MA treatment distinctly suppressed cell proliferation ($p < 0.05$; **Figure 5A**), indicating that inhibiting autophagy could weaken malignant progression of AB. Then, the functions of miR-1-3p on AB progression were investigated in depth. As a result, its overexpression lowered the cell viability of AM-1 cells ($P < 0.0001$). Meanwhile, the cell viability of AM-1 cells was increased by its knockdown ($P < 0.0001$; **Figure 5B**). Clone formation ability was further evaluated. In **Figures 5C,D**, miR-1-3p mimic significantly decreased the number of clones ($P < 0.01$) and the opposite results were observed when transfected by miR-1-3p inhibitor ($P < 0.001$). Furthermore, AM-1 cells displayed elevated apoptotic levels following transfection by miR-1-3p mimic ($P < 0.001$; **Figures 5E,F**). However, its inhibitor decreased the apoptosis of AM-1 cells ($P < 0.01$). Collectively, miR-1-3p may restrain proliferation as well as facilitate apoptosis in AM-1 cells.

miR-1-3p Reduces Migrated and Invasive Capacities in AB Cells

This study further evaluated migration and invasion of AB cells by transwell assays. As a result, the number of migrated AM-1 cells was markedly reduced by miR-1-3p

TABLE 2 | The association of Beclin1 expression with clinical pathological characteristics of AB.

Clinical pathological characteristics		Cases	Beclin1 expression (*n*, %)	χ^2	*P*
Age	>50	31	17 (54.84)	0.414	0.520
	≤50	73	35 (47.95)		
Sex	Male	60	27 (45.00)	1.418	0.234
	Female	44	25 (56.82)		
Location	Mandible	84	43 (51.19)	0.248	0.619
	Maxillary	20	9 (45.00)		
Classification	Solid/multicystic	83	39 (46.99)	1.492	0.506
	Unicystic	12	13 (61.90)		
	Peripheral	6			
	Desmoplastic	3			
Recurrence	Yes	10	4 (40.00)	0.443	0.506
	No	94	48 (51.06)		

TABLE 3 | The association of LC3 expression with clinical pathological characteristics of AB.

Clinical pathological characteristics		Cases	LC3 expression (*n*, %)	χ^2	*P*
Age	>50	31	23 (74.19)	0.185	0.667
	≤50	73	57 (78.08)		
Sex	Male	60	46 (76.67)	0.005	0.942
	Female	44	34 (77.27)		
Location	Mandible	84	70 (83.33)	8.321	0.004**
	Maxillary	20	10 (50.00)		
Classification	Solid/multicystic	83	68 (81.93)	4.487	0.034*
	Unicystic	12	12 (57.14)		
	Peripheral	6			
	Desmoplastic	3			
Recurrence	Yes	10	8 (80.00)	<0.001	1.000
	No	94	72 (76.60)		

*$P < 0.05$; **$P < 0.01$.

TABLE 4 | The association of LAMP2 expression with clinical pathological characteristics of AB.

Clinical pathological characteristics		Cases	LAMP2 expression (*n*, %)	χ^2	*P*
Age	>50	31	16 (51.61)	2.674	0.102
	≤50	73	50 (68.49)		
Sex	Male	60	36 (60.00)	0.733	0.392
	Female	44	30 (68.18)		
Location	Mandible	84	60 (71.43)	11.957	0.001***
	Maxillary	20	6 (30.00)		
Classification	Solid/multicystic	83	52 (62.65)	0.117	0.733
	Unicystic	12	14 (66.67)		
	Peripheral	6			
	Desmoplastic	3			
Recurrence	Yes	10	6 (80.00)	<0.001	1.000
	No	94	60 (63.83)		

***$P < 0.001$.

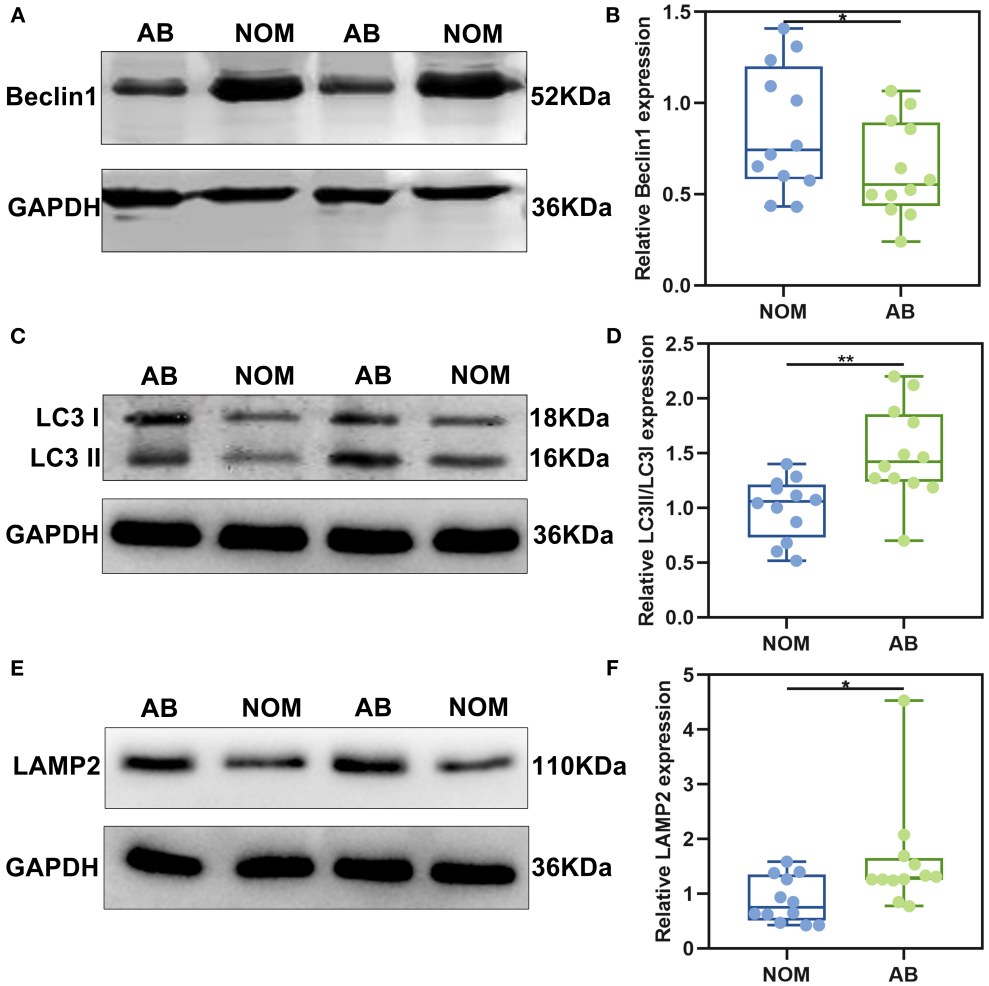

FIGURE 2 | The expression of autophagy-related proteins Beclin1, LC3II/I, and LAMP2 in AB and NOM tissues by western blot. **(A,B)** Beclin1; **(C,D)** LC3II/I; **(E,F)** LAMP2. *$P < 0.05$; **$P < 0.01$.

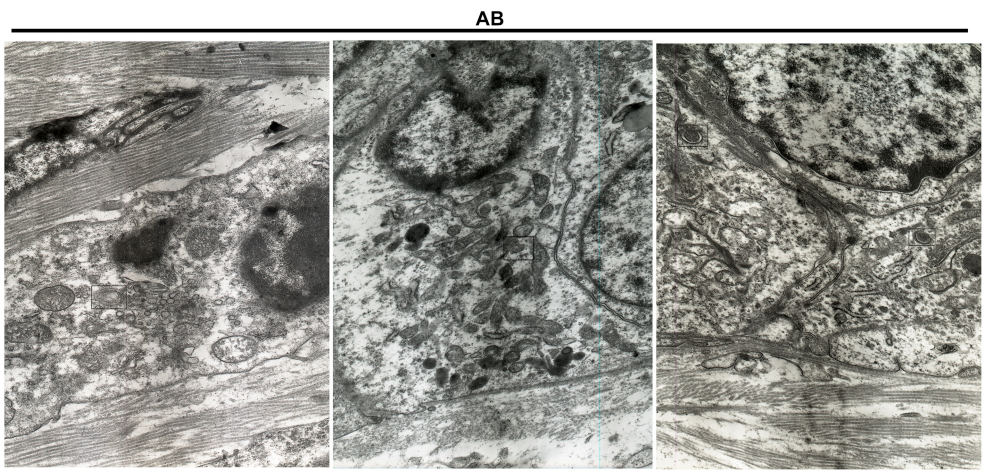

FIGURE 3 | Transmission electron microscopy for the structure of autophagosomes in AB. The autophagosomes are marked.

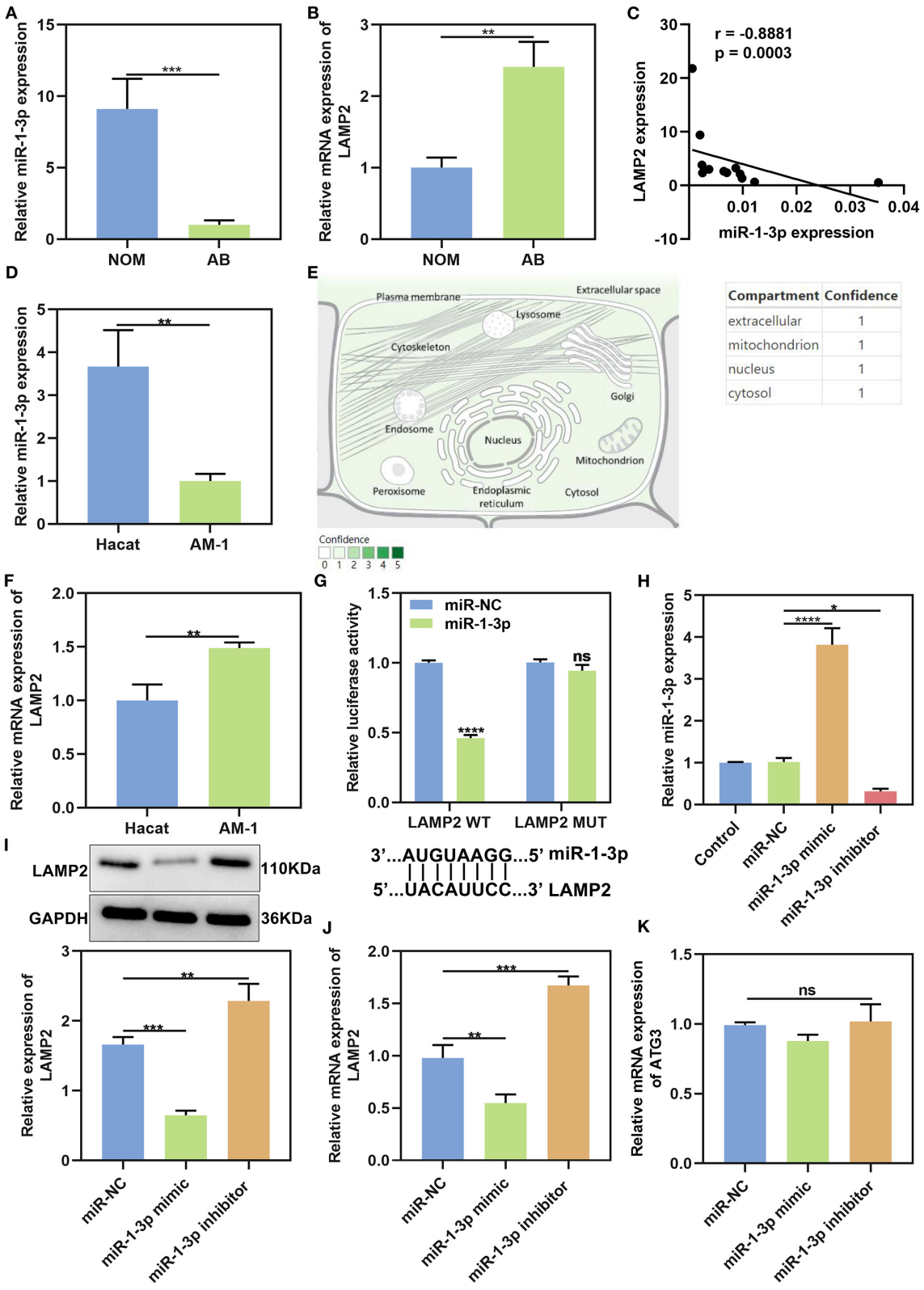

FIGURE 4 | MiR-1-3p suppresses LAMP2 expression in AB. **(A,B)** qRT-PCR for the expression of miR-1-3p and LAMP2 in NOM and AB tissues. **(C)** Spearman correlation analysis of miR-1-3p expression and LAMP2 expression in AB tissues ($r = -0.8881$, $P = 0.0003$). **(D)** qRT-PCR for the expression of miR-1-3p in AM-1

(Continued)

FIGURE 4 | cells and HaCat cells. **(E)** The distribution of miR-1-3p in cells. **(F)** qRT-PCR for the expression of LAMP2 in AM-1 cells and HaCat cells. **(G)** Assessment of relative luciferase activity in AM-1 cells after transfection with miR-1-3p mimic or miR-NC and schematic representation of the predicted miR-1-3p target sites within the 3'-UTR of LAMP2. **(H)** Assessment of the expression of miR-1-3p in AM-1 cells transfected with its mimic or inhibitor. **(I)** Western blot for LAMP2 expression in AM-1 cells transfected with miR-1-3p mimic or inhibitor. **(J)** qRT-PCR for detecting LAMP2 expression in AM-1 cells under transfection with miR-1-3p mimic or inhibitor. **(K)** qRT-PCR for examining ATG3 expression in AM-1 cells transfected with miR-1-3p mimic or inhibitor. *$P < 0.05$; **$P < 0.01$; ***$P < 0.001$; ****$P < 0.0001$; ns, not significant.

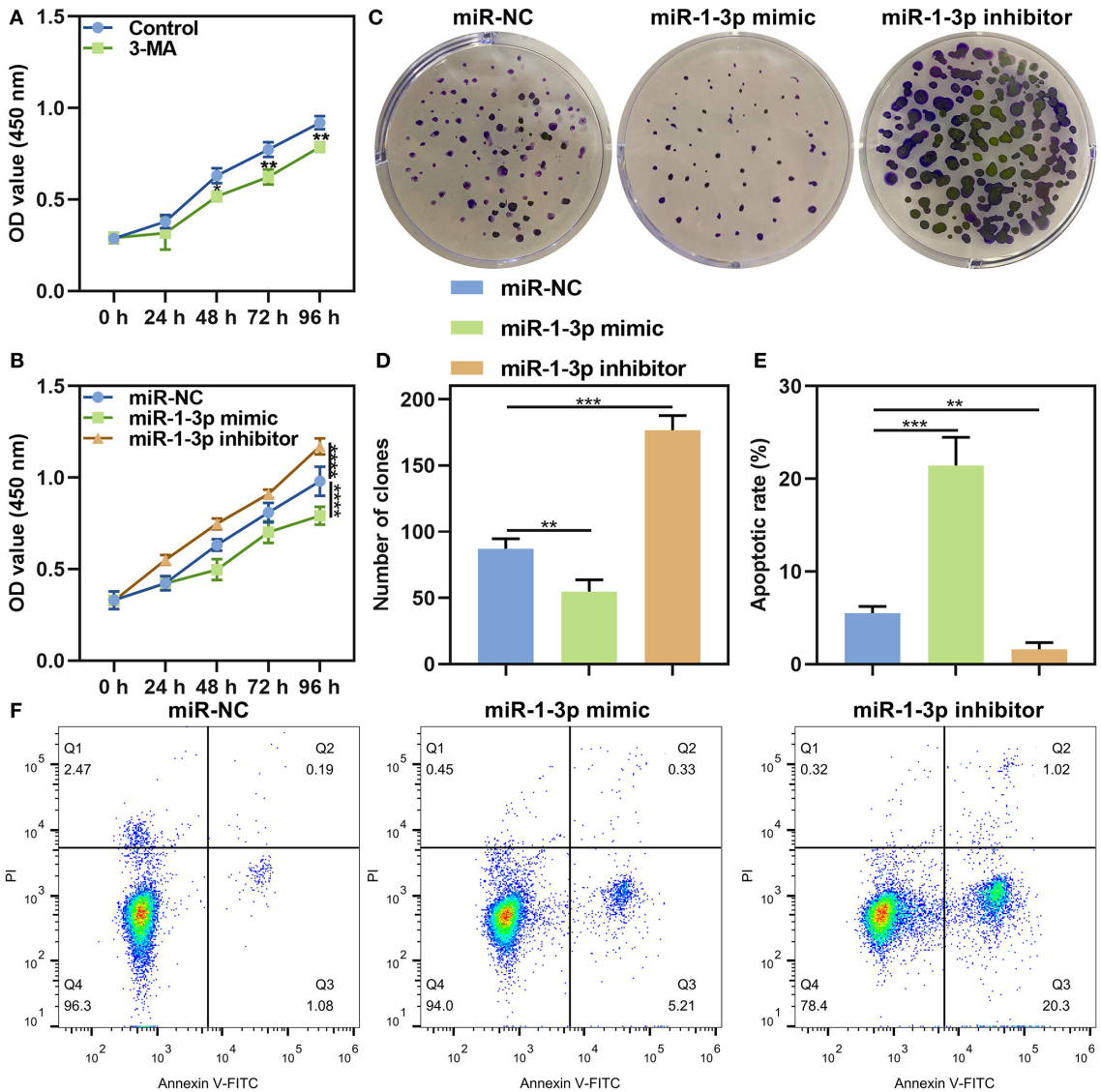

FIGURE 5 | The roles of miR-1-3p on proliferation and apoptosis in AM-1 cells. **(A)** CCK-8 for cell viability of AM-1 cells treated with autophagy inhibitor 3-MA at 0, 24, 48, 72, and 96 h. **(B)** CCK-8 for cell viability of AM-1 cells transfected with miR-1-3p mimic or inhibitor at 0, 24, 48, 72, and 96 h. **(C,D)** The number of colonies of AM-1 cells with miR-1-3p mimic or inhibitor transfection. **(E,F)** Flow cytometry for detecting apoptosis of transfected AM-1 cells. *$P < 0.05$; **$P < 0.01$; ***$P < 0.001$; ****$P < 0.0001$.

mimic ($P < 0.001$), which was increased after transfection by its inhibitor ($P < 0.001$; **Figures 6A,B**). Furthermore, its knockdown restrained invasive capacities of AM-1 cells ($P < 0.01$) and the opposite consequences were investigated after overexpressing miR-1-3p ($P < 0.001$; **Figures 6C,D**).

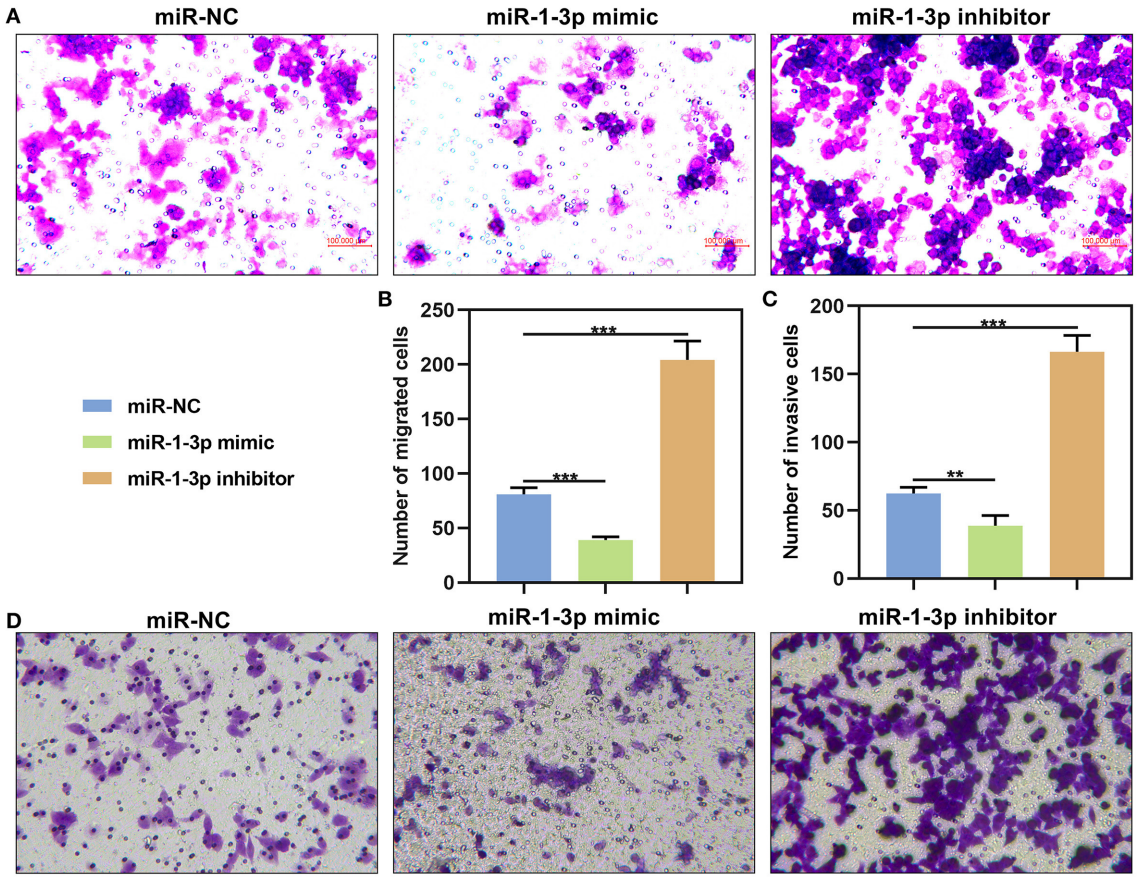

FIGURE 6 | The effects of miR-1-3p on migration and invasion of in AM-1 cells. **(A,B)** Evaluation of the number of migrated AM-1 cells transfected with miR-1-3p mimic or inhibitor. **(C,D)** Detection of the number of invasive AM-1 cells after transfection. $^{**}P < 0.01$; $^{***}P < 0.001$.

miR-1-3p Suppresses Malignant Phenotypes of AB Cells by Down-Regulating LAMP2

LAMP2 was significantly overexpressed in AM-1 cells under transfection with pcDNA3.1 LAMP2 ($P < 0.001$; **Figure 7A**). The up-regulation significantly increased the number of clones of AM-1 cells ($P < 0.0001$; **Figures 7B,C**). Furthermore, the decrease in the number of clones induced by miR-1-3p overexpression was markedly ameliorated by LAMP2 upreg ulation ($P < 0.01$). We also found that LAMP2 overexpression distinctly enhanced migrated ($P < 0.0001$; **Figures 7D,E**) and invasive ($P < 0.0001$; **Figures 7F,G**) abilities of AM-1 cells. Meanwhile, its up-regulation ameliorated the reduction in migrated ($P < 0.0001$) and invasive ($P < 0.0001$) abilities of AM-1 cells induced by miR-1-3p mimic. Above findings were indicative that miR-1-3p suppressed malignant phenotypes of AB cells by down-regulating LAMP2.

DISCUSSION

Here, our research analyzed the dysregulated expression and clinical implications of autophagy-related proteins including Beclin1, LC3II/I, and LAMP2 in AB. Also, we found that LAMP2 might be a potential target mRNA of miR-1-3p in AB. This miRNA may suppress malignant phenotypes of AB cells by down-regulating LAMP2.

Studies have shown that epithelial cells of AB have stronger autophagy activity than mesenchymal cells, human odontogenic cells, and maxillary mesenchymal stem cells, indicating that autophagy may promote the cell viability of residual AB epithelial cells in the hypoxic tumor microenvironment that is in relation to local invasion of AB (7). Consistently, our data showed that inhibiting autophagy significantly weakened cell proliferation of AM-1 cells. BRAF mutation often occurs in AB and is associated with recurrence of AB (18, 19). It has been found that BRAF oncogene induces the expression of key autophagy markers including LC3 and Beclin1, suggesting that the recurrence of AB might be due to the activation of autophagy of residual AB cells after surgery (20). However, in this study, we found that there was no correlation between LC3 or Beclin1 expression and AB recurrence, which requires in-depth research.

Epithelial-mesenchymal transition (EMT) is a key process in the invasion as well as metastases of AB (21). Adherent epithelial cells into highly active mesenchymal cells are the early stage of tumor invasion and metastasis. For example, in liver cancer,

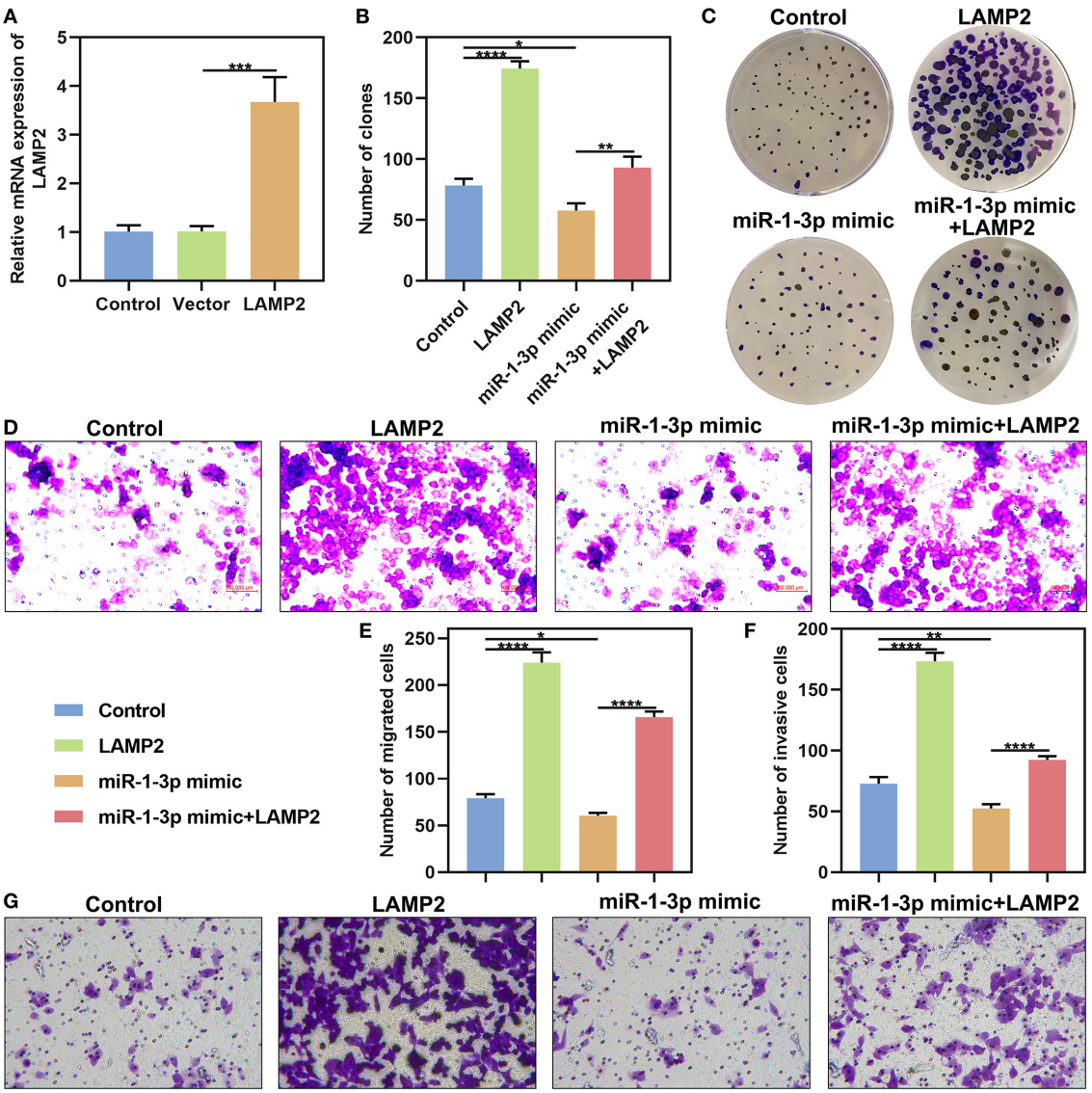

FIGURE 7 | miR-1-3p suppresses colony formation, migration and invasion of AM-1 cells by down-regulating LAMP2. **(A)** qRT-PCR for evaluating the expression of LAMP2 in AM-1 cells with pcDNA3.1 LAMP2 plasmid transfection. **(B,C)** The number of colonies for AM-1 cells transfected with LAMP2 and/or miR-1-3p mimic. **(D–G)** The number of **(D,E)** migrated and **(F,G)** invasive AM-1 cells under transfection with LAMP2 and/or miR-1-3p mimic. *$P < 0.05$; **$P < 0.01$; ***$P < 0.001$; ****$P < 0.0001$.

starvation-induced autophagy promotes the expression of EMT-related molecular markers through the transforming growth factor β (TGF-β)/Smad3 signaling pathway, thereby enhancing the invasive ability of hepatoma cells (22). In bladder cancer, it has been also demonstrated that autophagy can activate TGF-β/Smad signaling pathway-mediated EMT to promote tumor cell invasion and metastasis (23). At present, it has been found that EMT-related transcription factors Slug, Snail and TGF-β are up-regulated and E-cadherin expression is down-regulated in AB tissues, suggesting EMT may be involved in the development of AB (24). In this study, western blot analysis results showed that in AB tissues, Beclin1 expression was down-regulated, while LC3 and LAMP2 were both up-regulated, indicating that autophagy was activated in AB. Combining previous studies, autophagy might increase the invasive ability of AB cells via promoting EMT process.

As shown in immunohistochemistry, the positive expression rate of LC3 and LAMP2 in the mandible of AB was significantly elevated compared to that in the maxilla. Because the incidence rate of AB in the mandible is significantly higher than that in the maxilla. Moreover, there is no report on the relationships between AB location and tumor biological behaviors. It is difficult to prove that the expression levels of LAMP2 and LC3 are in association with AB location (25). We speculate that in the

mandible, blood supply is more singular, the bone is denser, and the tumor cells are more prone to hypoxia or energy deficiency compared to the maxilla, however, autophagy can supply energy for tumor cell proliferation. In this study, the cases of the AB occurring in the maxilla was small and the differences between the positive expression rates of LC3 and LAMP2 and AB location still need to be further validated in a larger cohort. In addition, the positive expression rate of LC3 in solid/polycystic AB was significantly higher than other classifications. It has been found that the recurrence rate of solid/polycystic AB is significantly higher than other classifications, suggesting that elevated levels of autophagy in solid/polycystic AB may be associated with tumor recurrence (26).

Currently, the molecular biology research on AB focuses on finding biomarkers. Combining with our previous human miRNA expression microarray results (six pairs of AB vs. NOM), among the down-regulated miRNAs, miR-1-3p in AB exhibited a down-regulated pattern than NOM tissues (27). Studies have demonstrated that it is down-regulated in a variety of tumors, which plays a role in inhibiting tumor cell proliferation as well as invasion (26, 28). Intriguingly, it can also influence the biological behavior of tumors by targeting and regulating autophagy-related molecules. In NSCLC, miRNA-1 binds to ATG3 to inhibit ATG3-mediated autophagy, thereby improving the cisplatin resistance of NSCLC cells (16). Through bioinformatics analysis, miR-1-3p might be an upstream regulatory molecule of LAMP2. The negative correlation between the expression of miR-1-3p and LAMP2 was found in AB. We found that there were miR-1-3p target sites within the 3′-UTR of LAMP2. Dual luciferase report confirmed that miR-1-3p could mediate LAMP2 expression by binding to the 3′-UTR of LAMP2. After validation, in AB cells, miR-1-3p up-regulation significantly suppressed LAMP2 expression at the mRNA and protein levels. Also, miR-1-3p restrained proliferation, migration and invasion of AB cells through down-regulating LAMP2. Several animal trials have reported the use of miR-1-3p as a target for cancer intervention or treatment. For instance, miR-1-3p may inhibit xenograft tumor growth of lung adenocarcinoma (29). MiR-1-3p up-regulation restrains hepatocellular carcinoma growth in mouse xenograft model (30). MiR-1-3p may overcome gefitinib resistance of lung cancer in tumor xenografts (31). In the formation and progression of tumors, lysosomes can increase the invasiveness of tumor cells by altering localization, volume, and composition, and releasing lysosomal enzymes (32, 33). LAMP2 mediates the fusion of autophagosomes and lysosomes during autophagy and plays an important role in autophagosome maturation (34). In colon cancer, LAMP2 is differentially expressed and has specific diagnostic value in the early stage of colon cancer as a molecular marker (35). In breast cancer, high expression of LAMP2 is also detected, and its high expression is significantly associated with tumor progression (36). In our research, LAMP2 was significantly up-regulated in AB tissues as well as epithelial-derived AM-1 cells, indicating that there could be an increase in autophagy activation in AB. LAMP2 up-regulation promoted colony formation, migrated and invasive abilities of AB cells. Our further study showed that LAMP2 was significantly negatively correlated with miR-1-3p in AB, suggesting that miR-1-3p may regulate autophagy by inhibiting LAMP2 expression at post-transcriptional levels in AB, thereby participating in AB progression.

CONCLUSION

In our study, we examined the abnormal expression of autophagy-related proteins including LAMP2, Beclin1, and LC3, suggesting the activation of autophagy in AB. Further study showed that LAMP2 might be a potential target mRNA of miR-1-3p in AB. MiR-1-3p silenced LAMP2 expression by binding to the 3'-UTR of LAMP2, thereby suppressing malignant phenotypes of AB. Thus, our research may provide a novel insight into the mechanisms of AB.

DATA AVAILABILITY STATEMENT

The original contributions presented in the study are included in the article/supplementary material, further inquiries can be directed to the corresponding author/s.

ETHICS STATEMENT

The studies involving human participants were reviewed and approved by the Ethics Committee of School and Hospital of Stomatology, China Medical University (2016-12). The patients/participants provided their written informed consent to participate in this study.

AUTHOR CONTRIBUTIONS

MZ conceived and designed the study. XN and BH conducted most of the experiments and data analysis, and wrote the manuscript. XQ, JL, and LC participated in collecting data and helped to draft the manuscript. All authors contributed to the article and approved the submitted version.

FUNDING

This work was funded by National Natural Science Foundation of China (81072197, 81470758).

REFERENCES

1. Siar CH, Ng KH. Epithelial-to-mesenchymal transition in ameloblastoma: focus on morphologically evident mesenchymal phenotypic transition. *Pathology*. (2019) 51:494–501. doi: 10.1016/j.pathol.2019.04.004
2. Guan P, Wong SF, Lim JQ, Ng CCY, Soong PL, Sim CQX, et al. Mutational signatures in mandibular ameloblastoma correlate with smoking. *J Dental Res*. (2019) 98:652–8. doi: 10.1177/0022034519837248
3. Wang GN, Zhong M, Chen Y, Ji J, Gao XQ, Wang TF. Expression of WNT1 in ameloblastoma and its significance. *Oncol Lett*. (2018) 16:1507–12. doi: 10.3892/ol.2018.8820

4. Hendra FN, Natsir Kalla DS, Van Cann EM, de Vet HCW, Helder MN, Forouzanfar T. Radical vs. conservative treatment of intraosseous ameloblastoma: systematic review and meta-analysis. *Oral Dis.* (2018) 25:1683–96. doi: 10.1111/odi.13014
5. Onorati AV, Dyczynski M, Ojha R, Amaravadi RK. Targeting autophagy in cancer. *Cancer.* (2018) 124:3307–18. doi: 10.1002/cncr.31335
6. Poillet-Perez L, Xie X, Zhan L, Yang Y, Sharp DW, Hu ZS, et al. Autophagy maintains tumour growth through circulating arginine. *Nature.* (2018) 563:569–73. doi: 10.1038/s41586-018-0697-7
7. Sharp RC, Effiom OA, Dhingra A, Odukoya O, Olawuyi A, Arotiba GT, et al. Enhanced basal autophagy supports ameloblastoma-derived cell survival and reactivation. *Arch Oral Biol.* (2019) 98:61–7. doi: 10.1016/j.archoralbio.2018.11.013
8. Xin X, Wu M, Meng Q, Wang C, Lu Y, Yang Y, et al. Long noncoding RNA HULC accelerates liver cancer by inhibiting PTEN via autophagy cooperation to miR15a. *Mol Cancer.* (2018) 17:94. doi: 10.1186/s12943-018-0843-8
9. Pajares M, Rojo AI, Arias E, Diaz-Carretero A, Cuervo AM, Cuadrado A. Transcription factor NFE2L2/NRF2 modulates chaperone-mediated autophagy through the regulation of LAMP2A. *Autophagy.* (2018) 14:1310–22. doi: 10.1080/15548627.2018.1474992
10. Hayes J, Peruzzi PP, Lawler S. MicroRNAs in cancer: biomarkers, functions and therapy. *Trends Mol Med.* (2014) 20:460–9. doi: 10.1016/j.molmed.2014.06.005
11. Lu TX, Rothenberg ME. MicroRNA. *J Allergy Clin Immunol.* (2018) 141:1202–7. doi: 10.1016/j.jaci.2017.08.034
12. Rupaimoole R, Slack FJ. MicroRNA therapeutics: towards a new era for the management of cancer and other diseases. *Nat Rev Drug Discov.* (2017) 16:203–22. doi: 10.1038/nrd.2016.246
13. Sun L, Hu L, Cogdell D, Lu L, Gao C, Tian W, et al. MIR506 induces autophagy-related cell death in pancreatic cancer cells by targeting the STAT3 pathway. *Autophagy.* (2017) 13:703–14. doi: 10.1080/15548627.2017.1280217
14. Zhang X, Li Z, Xuan Z, Xu P, Wang W, Chen Z, et al. Novel role of miR-133a-3p in repressing gastric cancer growth and metastasis via blocking autophagy-mediated glutaminolysis. *J Exp Clin Cancer Res.* (2018) 37:320. doi: 10.1186/s13046-018-0993-y
15. Zhu H, Gan X, Jiang X, Diao S, Wu H, Hu J. ALKBH5 inhibited autophagy of epithelial ovarian cancer through miR-7 and BCL-2. *J Exp Clin Cancer Res.* (2019) 38:163. doi: 10.1186/s13046-019-1159-2
16. Hua L, Zhu G, Wei J. MicroRNA-1 overexpression increases chemosensitivity of non-small cell lung cancer cells by inhibiting autophagy related 3-mediated autophagy. *Cell Biol Int.* (2018) 42:1240–9. doi: 10.1002/cbin.10995
17. Kim JY, Kim J, Bazarsad S, Cha IH, Cho SW, Kim J. Bcl-2 is a prognostic marker and its silencing inhibits recurrence in ameloblastomas. *Oral Dis.* (2019) 25:1158–68. doi: 10.1111/odi.13070
18. Cha YH, Cho ES, Kang HE, Ko J, Nam W, Kim HJ, et al. Frequent oncogenic BRAF V600E mutation in odontogenic keratocyst. *Oral Oncol.* (2017) 74:62–7. doi: 10.1016/j.oraloncology.2017.09.016
19. Kurppa KJ, Caton J, Morgan PR, Ristimaki A, Ruhin B, Kellokoski J, et al. High frequency of BRAF V600E mutations in ameloblastoma. *J Pathol.* (2014) 232:492–8. doi: 10.1002/path.4317
20. Fregnani ER, Perez DE, Paes de Almeida O, Fonseca FP, Soares FA, Castro-Junior G, et al. BRAF-V600E expression correlates with ameloblastoma aggressiveness. *Histopathology.* (2017) 70:473–84. doi: 10.1111/his.13095
21. Jiang C, Zhang Q, Shanti RM, Shi S, Chang TH, Carrasco L, et al. Mesenchymal stromal cell-derived interleukin-6 promotes epithelial-mesenchymal transition and acquisition of epithelial stem-like cell properties in ameloblastoma epithelial cells. *Stem Cells.* (2017) 35:2083–94. doi: 10.1002/stem.2666
22. Huang F, Wang BR, Wang YG. Role of autophagy in tumorigenesis, metastasis, targeted therapy and drug resistance of hepatocellular carcinoma. *World J Gastroenterol.* (2018) 24:4643–51. doi: 10.3748/wjg.v24.i41.4643
23. Tong H, Yin H, Hossain MA, Wang Y, Wu F, Dong X, et al. Starvation-induced autophagy promotes the invasion and migration of human bladder cancer cells via TGF-beta1/Smad3-mediated epithelial-mesenchymal transition activation. *J Cell Biochem.* (2019) 120:5118–27. doi: 10.1002/jcb.27788
24. Kurioka K, Wato M, Iseki T, Tanaka A, Morita S. Differential expression of the epithelial mesenchymal transition factors snail, slug, twist, TGF-beta, and E-cadherin in ameloblastoma. *Med Mol Morphol.* (2017) 50:68–75. doi: 10.1007/s00795-016-0149-0
25. Patsa S, Jadav RB, Halder GC, Ray JG, Datta S, Deb T. Demographic and histopathological variation of ameloblastoma: a hospital-based study. *J Oral Maxillofac Pathol.* (2016) 20:230–3. doi: 10.4103/0973-029X.185937
26. Antonoglou GN, Sandor GK. Recurrence rates of intraosseous ameloblastomas of the jaws: a systematic review of conservative versus aggressive treatment approaches and meta-analysis of non-randomized studies. *J Craniomaxillo Fac Surg.* (2015) 43:149–57. doi: 10.1016/j.jcms.2014.10.027
27. Chen L, Wang G, Qiao X, Wang X, Liu J, Niu X, et al. Downregulated miR-524-5p participates in the tumor microenvironment of ameloblastoma by targeting the interleukin-33 (IL-33)/suppression of tumorigenicity 2 (ST2) axis. *Med Sci Monit.* (2020) 26:e921863. doi: 10.12659/MSM.921863
28. Wu L, Wang T, He D, Li X, Jiang Y. miR-1 inhibits the proliferation of breast cancer stem cells by targeting EVI-1. *Onco Targets Ther.* (2018) 11:8773–81. doi: 10.2147/OTT.S188836
29. Li T, Wang X, Jing L, Li Y. MiR-1-3p inhibits lung adenocarcinoma cell tumorigenesis via targeting protein regulator of cytokinesis 1. *Front Oncol.* (2019) 9:120. doi: 10.3389/fonc.2019.00120
30. Zhang H, Zhang Z, Gao L, Qiao Z, Yu M, Yu B, et al. miR-1-3p suppresses proliferation of hepatocellular carcinoma through targeting SOX9. *Onco Targets Ther.* (2019) 12:2149–57. doi: 10.2147/OTT.S197326
31. Jiao D, Chen J, Li Y, Tang X, Wang J, Xu W, et al. miR-1-3p and miR-206 sensitizes HGF-induced gefitinib-resistant human lung cancer cells through inhibition of c-Met signalling and EMT. *J Cell Mol Med.* (2018) 22:3526–36. doi: 10.1111/jcmm.13629
32. Ngabire D, Kim GD. Autophagy and inflammatory response in the tumor microenvironment. *Int J Mol Sci.* (2017) 18:2016. doi: 10.3390/ijms18092016
33. Pu J, Guardia CM, Keren-Kaplan T, Bonifacino JS. Mechanisms and functions of lysosome positioning. *J Cell Sci.* (2016) 129:4329–39. doi: 10.1242/jcs.196287
34. Hubert V, Peschel A, Langer B, Groger M, Rees A, Kain R. LAMP-2 is required for incorporating syntaxin-17 into autophagosomes and for their fusion with lysosomes. *Biol Open.* (2016) 5:1516–29. doi: 10.1242/bio.018648
35. Janikowska G, Janikowski T, Pyka-Pajak A, Mazurek U, Janikowski M, Gonciarz M, et al. Potential biomarkers for the early diagnosis of colorectal adenocarcinoma - transcriptomic analysis of four clinical stages. *Cancer Biomark.* (2018) 22:89–99. doi: 10.3233/CBM-170984
36. Damaghi M, Tafreshi NK, Lloyd MC, Sprung R, Estrella V, Wojtkowiak JW, et al. Chronic acidosis in the tumour microenvironment selects for overexpression of LAMP2 in the plasma membrane. *Nat Commun.* (2015) 6:8752. doi: 10.1038/ncomms9752

Conflict of Interest: The authors declare that the research was conducted in the absence of any commercial or financial relationships that could be construed as a potential conflict of interest.

Copyright © 2021 Niu, Huang, Qiao, Liu, Chen and Zhong. This is an open-access article distributed under the terms of the Creative Commons Attribution License (CC BY). The use, distribution or reproduction in other forums is permitted, provided the original author(s) and the copyright owner(s) are credited and that the original publication in this journal is cited, in accordance with accepted academic practice. No use, distribution or reproduction is permitted which does not comply with these terms.

frontiers in Medicine

ORIGINAL RESEARCH
published: 22 June 2021
doi: 10.3389/fmed.2021.680378

Long Non-coding RNA SNHG12, a New Therapeutic Target, Regulates miR-199a-5p/Klotho to Promote the Growth and Metastasis of Intrahepatic Cholangiocarcinoma Cells

*Hong-Guo Yang[1,2], Tian-peng Wang[2], Sheng-an Hu[2], Chao-zhou Hu[2], Cheng-hang Jiang[2] and Qiang He[3]**

[1] Department of Hepatobiliary & Pancreatic Surgery, Tongde Hospital of Zhejiang Province, Hangzhou, China, [2] Department of Emergency, Zhejiang Provincial People's Hospital, Hangzhou, China, [3] Department of General Surgery, Zhejiang Provincial People's Hospital, Haining Hospital, Haining, China

OPEN ACCESS

Edited by:
Fu Wang,
Xi'an Jiaotong University, China

Reviewed by:
Ke He,
Guangdong Second Provincial General Hospital, China
Hong Jin,
Karolinska Institutet (KI), Sweden

***Correspondence:**
Qiang He
heqianglk1771@tom.com

Specialty section:
This article was submitted to Precision Medicine, a section of the journal Frontiers in Medicine

Received: *14 March 2021*
Accepted: *20 May 2021*
Published: *22 June 2021*

Citation:
Yang H-G, Wang T-p, Hu S-a, Hu C-z, Jiang C-h and He Q (2021) Long Non-coding RNA SNHG12, a New Therapeutic Target, Regulates miR-199a-5p/Klotho to Promote the Growth and Metastasis of Intrahepatic Cholangiocarcinoma Cells. Front. Med. 8:680378. doi: 10.3389/fmed.2021.680378

Background: Small nucleolar RNA host gene 12 (SNHG12) is a newly identified long non-coding RNA (lncRNA) whose involvements have been explored in several cancers. Our study aimed to explore the functions of SNHG12 on intrahepatic cholangiocarcinoma (ICC) progression and its interaction with miR-199a-5p and Klotho.

Methods: RT-PCR was performed to examine the expressions of SNHG12, miR-199a-5p and Klotho in ICC cells. Cell counting kit-8 (CCK-8), colony formation assays and transwell assays were applied to analyze the proliferation, migration and invasion of ICC cells. Luciferase assays, RIP assays and RNA pull-down assays were carried out to demonstrate the direct binding relationships among SNHG12, miR-199a-5p and Klotho. The xenograft nude models were applied to test the effects of SNHG12 on ICC tumor growth.

Results: The expression of SNHG12 and Klotho was distinctly increased in ICC cells, while miR-199a-5p expressions were decreased. Functionally, the silence of SNHG12 inhibited the proliferation and metastasis of ICC cells, while miR-199a-5p overexpression exhibited an opposite result. Mechanistically, Knockdown of SNHG12 significantly suppressed the expressions of miR-199a-5p by sponging it, and then increased Klotho expression. The final *in vivo* experiments suggested that the silence of SNHG12 distinctly inhibited tumor growth.

Conclusion: Our findings indicated that SNHG12 inhibited cell proliferation and metastasis process of ICC cells through modulating the miR-199a-5p/Klotho axis and it is expected to become a potential therapeutic target for ICC.

Keywords: lncRNA SNHG12, intrahepatic cholangiocarcinoma, miR-199a-5p, Klotho, metastasis

INTRODUCTION

Intrahepatic cholangiocarcinoma (ICC) is a heterogeneous group of malignancies that occur at any location along the biliary tree (1, 2). In the last 20 years, it has been reported that the incidence and mortality of ICC is increasing in China (3). So far, one of the most effective treatments remains surgical removal for ICC patients (4). However, for these patients with advanced stages, operative treatments provide limited chances (5). It is necessary to develop novel adjuvant therapies for the improved prognosis of ICC patients. However, the poor understanding of the mechanisms underlying the development and progression of ICC restricts the developments of novel approaches. Thus, it is necessary to establish molecular modulators influencing developments and progression of ICC, which will promote the developments of efficient therapies.

Long non-coding RNA (LncRNA) is defined as an endogenous RNA with molecules > 200 nt in length (6). Unlike other non-coding RNAs including miRNAs, the potential involvements of lncRNAs in human illnesses remains largely uncovered. More and more studies have indicated that lncRNAs were involved in the life activity via modulating the expression of various genes through complex mechanisms (7, 8). Their regulatory effects on chromatin remodeling, gene transcription and intercellular signaling were also reported in several studies (9, 10). In addition, in tumor biology, the vital roles of lncRNAs were also demonstrated by a growing volume of literature (11). The dysregulation of lncRNAs has been confirmed to display tumor-promotive or suppressive roles in various types of tumors (12, 13). Nevertheless, to date, the functional roles of lncRNAs in the progression of ICC are unclear.

Small nucleolar RNA host gene 12 (SNHG12), located at the p35.3 region on chromosome 1, is a newly identified tumor-related lncRNA (14). In recent years, its dysregulated expression was frequently reported in several types of tumors (15–17). In some specific tumors, the oncogenic roles of SNHG12 were also reported *in vitro* and *in vivo* experiments, such as renal cell carcinoma and cervical cancer (18, 19). However, the expressions and functions of SNHG12 in ICC were rarely reported.

MATERIALS AND METHODS

Cell Lines and Transfection

Control cell line (BEC) and ICC cell lines (CCLP1, TFK-1, HuCCT1 and RBE) was obtained from the Institute of Cell Research, Chinese Academy of Sciences (Shanghai, China). All cells were cultured in DMEM medium (Procell, Yipu Technology, Wuhan, Hubei, China). The culture media were all supplemented with 10% fetal bovine serum (MedChemExpress, Pudong, Shanhai, China), 50 U/ml of penicillin and 50 mg/ml of streptomycin (Invitrogen, Shenzhen, Guangdong, China). In a humidified incubator with 5% CO2 at 37°C, all cells were maintained.

CCLP1 and TFK-1 cells were transfected with sh-SNHG12-1, sh-SNHG12-1 and sh-NC, miR-199a-5p mimics and miR-NC, miR-199a-5p inhibitors and NC inhibitors, pcDNA3.1/SNHG12 and pcDNA3.1, or pcDNA3.1/Klotho and pcDNA3.1 (all, Genepharma, Shanghai, China). Lipofectamine 2000 (Invitrogen, Shenzheng, Guangdong, China) was used for the transfection.

TABLE 1 | The primers used in this study for RT-PCR.

Genes	Sequences (5′-3′)
SNHG12: forward	TCTGGTGATCGAGGACTTCC
SNHG12: reverse	ACCTCCTCAGTATCACACACT
miR-199a-5p: forward	GCCAAGCCCAGTGTTCAGAC
miR-199a-5p: reverse	GTGCAGGGTCCGAGGTATTC
Klotho: forward	TGAGGACGACCAGCTGAGGGT
Klotho: reverse	CATGGATGCCTTGGGCTCAAA
GAPDH: forward	AAAAGCATCACCCGGAGGAGAA
GAPDH: reverse	AAGGAAATGAATGGGCAGCCG
U6: forward	TGCGGGTGCTCGCTTCGGCAGC
U6: reverse	CCAGTGCAGGGTCCGAGGT

RNA Isolation and Quantitative Real-Time PCR

According to the manufacturers' instructions, TRIzol (Invitrogen, Yita Biology, Daxing, Beijing, China) was applied to extract total RNAs from ICC cells. Using the Reverse Transcriptase (Transgene, Beijing, China), the complementary DNA (cDNA) preparation was carried out based on the standard procedures. Then, RT-PCR assays were conducted on ABI 7600 using SYBR Premix ExTaq II kit (Takara, Haidian, Beijing, China). After RT-PCR data were corrected, the $2^{-\Delta\Delta Ct}$ methods were used to calculate them. GAPDH acted as the endogenous control to normalize the data. **Table 1** showed the primer sequences. The PCR was performed in triplicate.

Cell Viability Assays

Cellular viabilities were monitored using Cell Counting Kit-8 assays(LaiFuSai Technology, Nanjing, Jiangsu, China). The TFK-1 and CCLP1 cells after the transfection were grown in 96-well plates. Based on the manufacturer's protocol, cellular viabilities were assessed every 24 h. The densities of every group were examined at 450 nm.

For colony formation assays, TFK-1 and CCLP1 cells were trypsinized after the transfection. Approximately 600 cells were plated in each well of 6-well plates and maintained for 14 days to form colonies. Subsequently, the colonies were fixed with methanol (Jizhihua Company, Pudong, Shanghai, China) and stained with 0.1% crystal violet (Baoman Biology, Yangpu, Shanghai, China). For each assay, three independent experiments were carried out.

Cell Invasion and Migration

TFK-1 and CCLP1 cells in migration and invasion ability were examined applying the transwell assays. For migration assays, 5×10^4 cells were seeded into the upper chamber of a transwell insert (pore size, 8 μm) in RPMI-1640 medium. The lower chamber was covered using the above medium containing 8% FBS. For invasion assays, on the lower surface of the chamber, the matrix

gel was covered. In addition, the rest of experiment steps were in line with the migrated assays. After incubation for 24 h, the TFK-1 and CCLP1 cells which have finished migration and invasion were fixed with crystal violet. Finally, under a microscope, the cells were captured and counted.

Subcellular Fraction

According to the protocol of PARIS™ Kit (Invitrogen, Haidian, Beijing, China), the cytoplasmic and nuclear fractions of TFK-1 and CCLP1 cells were isolated. RT-PCR was applied to examine the isolated RNAs.

RNA-BINDING PROTEIN IMMUNOPRECIPITATION ASSAY

Following the manufacturer's directory, the Magna RIP RNA-Binding Protein Immunoprecipitation Kit (Millipore, Nanjing, Jiangsu, China) was applied to perform the RIP assays. Briefly, TFK-1 and CCLP1 cells at 75–85% confluency gathered and lysed using RIP lysis buffer. 150 μl of the extracts of TFK-1 and CCLP1 cells were then incubated with RIP buffer which contained magnetic beads conjugated to negative control normal mouse IgG or human anti-Ago2 antibody. Then, to digest the protein, Proteinase K was used to incubate the collected samples for 24 h. After collecting the immunoprecipitated RNAs, RT-PCR assays were applied to examine the purified RNAs.

RNA Pull-Down Assays

The bio-miR-199a-5p or bio-NC probes were dissolved in washing and binding buffer, followed by the incubation using Dynabeads M-290 Streptavidin (Solaibao Biology, Haidian, Beijing, China) at 25°C for 15 min. After generating probe-coated beads, the probe-coated beads were applied to incubate cell lysates of TFK-1 and CCLP1. Then, the RNA complexes were collected for further examination of the relative enrichment of RNAs by the use of RT-PCR.

Luciferase Reporter Assays

StarBase and TargetScan were used to predict the putative binding sites between SNHG12 and miRNA-199a-5p, miRNA-199a-5p and Klotho. The sequences of wild type SNHG12 (SNHG12-WT), mutant type SNHG12 (SNHG12-MuT), wild type 3′-UTR of Klotho (WT-Klotho), and mutant type 3′-UTR of Klotho (MUT-Klotho) containing the putative binding site with miR-199a-5p were amplified and cloned into the pmirGLO vector (Promega). Then, by the use of Lipofectamine 2000 (Invitrogen, Shenzhen, Guangdong, China), luciferase reporter vectors were co-transfected with miR-NC or miR-199a-5p mimics into TFK-1 and CCLP1 cells. A dual-luciferase reporter assay system examined the luciferase activity.

Animal Experiments

All BALB/c nude mice aged 6–7 weeks and weighing 20–22 g were used for *in vivo* assays. The animal studies were performed after we received the approval from Zhejiang Provincial People's Hospital. About 5.0×10^6 CCLP1 cells in the log phase were inoculated into the right flank of every nude mouse by subcutaneous injection. Sh-NC and sh-SNHG12-1 groups include six mice. The size of tumor was determined every 4 days. After 28 days, all mice were sacrificed. After their tumors were excised, the tumor weight was examined. Moreover, the tumor volumes were calculated using the formula: length × width$^2 \times 0.5$.

Statistical Analysis

All statistical analyses were performed using SPSS 17.0 (SPSS, Chicago, USA). The significance of difference between groups was analyzed by two-tailed Student's *t*-test one-way analysis or two-way analysis of variance. A two-sided *p*-value of <0.05 was considered to be statistically significant.

RESULTS

The Distinct Upregulation of SNHG12 in ICC Cells and Its Oncogenic Roles

To identify the functional lncRNA in ICC progression, we searched TCGA datasets and focused on SNHG12 which was distinctly overexpressed in ICC specimens ($n = 36$) compared with non-tumor specimens ($n = 9$) (**Figure 1A**). Then, RT-PCR assays also showed that SNHG12 expression was distinctly increased in four ICC cell lines compared with BEC cells (**Figure 1B**). Then, to explore the function of SNHG12 in the ability of ICC cells, we down-regulated SNHG12 expression in CCLP1 and TFK-1 cells using sh-SNHG12-1 and sh-SNHG12-2, which was confirmed by RT-PCR (**Figure 1C**). CCK8 and clone formation assays revealed that silence of SNHG12 observably suppressed the viability of CCLP1 and TFK-1 cells (**Figures 1D,E**). Transwell experiments indicated that knockdown of SNHG12 distinctly suppressed the metastasis ability of CCLP1 and TFK-1 cells (**Figures 1F,G**). On the contrary, we observed that overexpression of SNHG12 promoted the proliferation, migration and invasion of CCLP1 and TFK-1 cells (**Figures 2A–E**).

MiR-199a-5p Suppressed the Proliferation and Metastasis of ICC Cells

It has been demonstrated that many cytoplasmic lncRNAs act as ceRNAs by competitively binding miRNAs. By the use of subcellular fractionation, our group showed that SNHG12 was expressed both in the cytoplasm and nucleus, and a larger proportion of SNHG12 was observed in the cytoplasm (**Figure 3A**). Using StarBase v2.0 software (screening conditions: pan-cancer number: 5, medium, clip data), several miRNAs were predicted to have a high probability of binding to SNHG12 (**Figure 3B**). Among the 5 miRNAs, miR-199a-5p has been demonstrated to serve as an anti-oncogene in some cancers (20, 21). Thus, we chose it for further study. RT-PCR assays indicated that miR-199a-5p expressions were distinctly decreased in ICC cells (**Figure 3C**). Further qRT-PCR showed that miRNA-199a-5p mimics effectively overexpressed miR-199a-5p in CCLP1 and TFK-1 cells compared to miR-NC group (**Figure 3D**). Gain-of-function experiments indicated that overexpression of miR-199a-5p distinctly suppressed the proliferation, migration and invasion of CCLP1 and TFK-1 cells (**Figures 3E–H**).

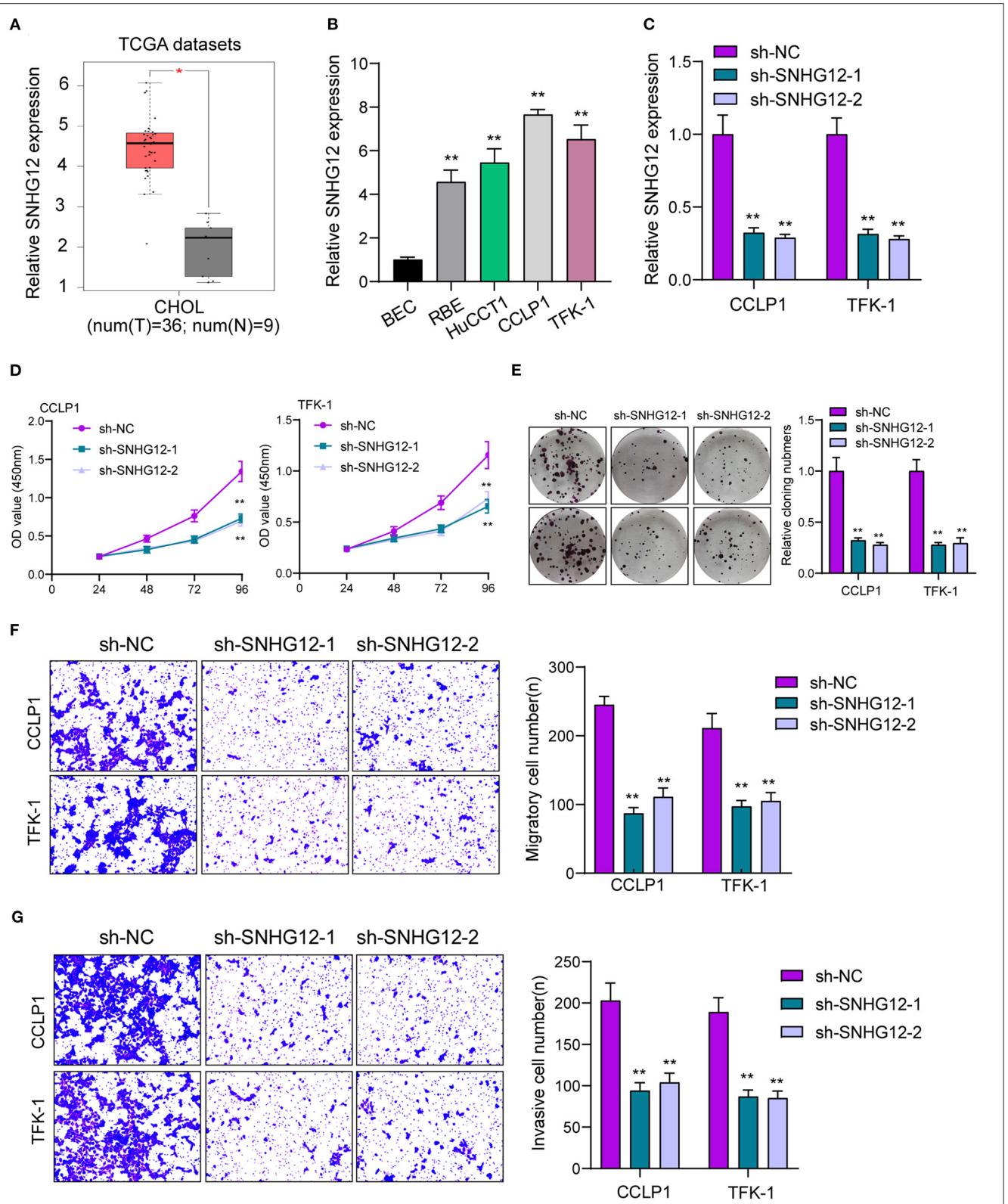

FIGURE 1 | Increased SNHG12 expression and its oncogenic roles in ICC cells. **(A)** Higher levels of SNHG12 were observed in ICC specimens than normal specimens by amazing TCGA datasets. **(B)** RT-PCR determined the expressions of SNHG12 in ICC cells and BEC cells. **(C)** SNHG12 expression was examined in TFK-1 and CCLP1 cells transfected with sh-NC, sh-SNHG12-1 or sh-SNHG12-2. **(D)** Cell proliferation analysis. TFK-1 and CCLP1 cells were detected for 24, 48 and 72 h after transfection. **(E)** Proliferation of TFK-1 and CCLP1 cells transfected with sh-SNHG12-1 or sh-SNHG12-2 as determined by colony formation assays. **(F,G)** Transwell assays were used to detect cellular invasion and migration in SNHG12-knockdown TFK-1 and CCLP1 cells. $^{*}p < 0.05$, $^{**}p < 0.01$.

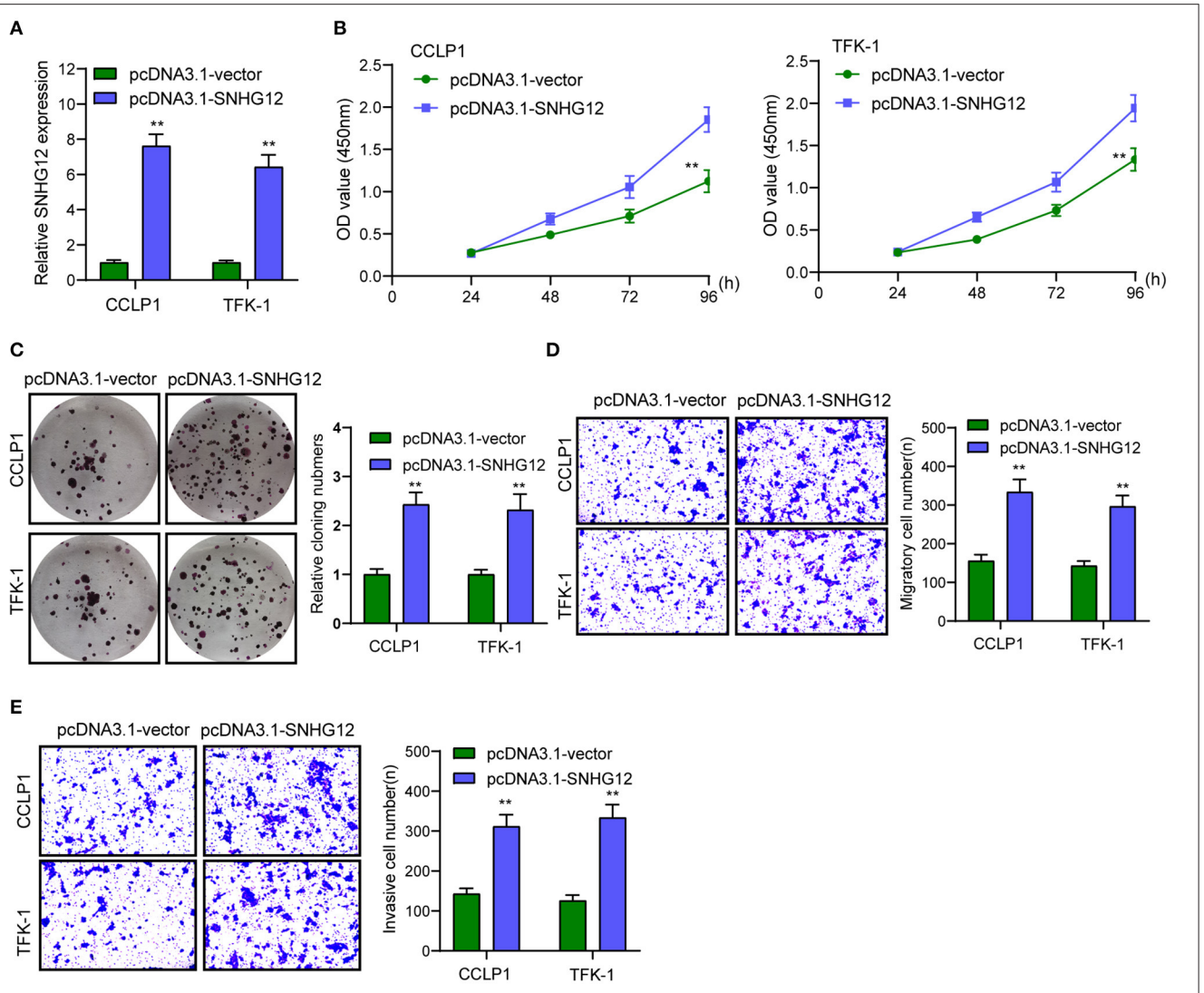

FIGURE 2 | Overexpression of SNHG12 promoted the proliferation and metastasis of TFK-1 and CCLP1 cells. **(A)** RT-PCR assay was used to detect SNHG12 level in SNHG12 overexpression plasmids transfected TFK-1 and CCLP1 cells. **(B,C)** Overexpression of SNHG12 distinctly promoted the proliferation of TFK-1 and CCLP1 cells. **(D,E)** Transwell assay indicated the migrated and invaded cell number in TFK-1 and CCLP1 cells cells. $^{**}p < 0.01$.

SNHG12 Promotes ICC progression via Sponging miR-199a-5p

To explore whether a ceRNA mechanism between SNHG12 and miR-199a-5p existed, we conduced RIP assays and found that SNHG12 and miRNA-199a-5p coexisted in CCLP1 and TFK-1 cells (**Figure 4A**). StarBase v2.0 showed miR-199a-5p contained a putative binding site with SNHG12 (**Figure 4B**). Luciferase reporter assays indicated that miR-199a-5p mimics distinctly decreased the luciferase activity of SNHG12-WT, while the relative luciferase activity of SNHG12-MUT remained unchanged (**Figure 4C**). Functional assays revealed that miR-199a-5p inhibition reversed the suppressor effects of SNHG12 knockdown on the proliferation, migration and invasion of CCLP1 and TFK-1 cells (**Figures 4D–G**).

Increased Expression of Klotho in ICC via a ceRNA Mechanism With SNHG12

To demonstrate the ceRNA network, our group was required to discover the target genes of miR-199a-5p. Using starbase 2.0, Klotho may be a potential one. We examined the expressions of Klotho in ICC cells using RT-PCR and observed Klotho was distinctly increased (**Figure 5A**). Then we explore whether the dysregulation of SNHG12 may exhibit an effect on the expression of Klotho. The results of RT-PCR suggested that knockdown of SNHG12 suppressed Klotho, while overexpression of SNHG12 exhibited a reverse effect (**Figure 5B**). Moreover, RIP assays demonstrated that SNHG12, miR-199a-5p and Klotho coexisted in CCLP1 and TFK-1 cells (**Figure 5C**). Pull-down assays also demonstrated that biotinylated miR-199a-5p could pull down SNHG12 and Klotho in CCLP1 and

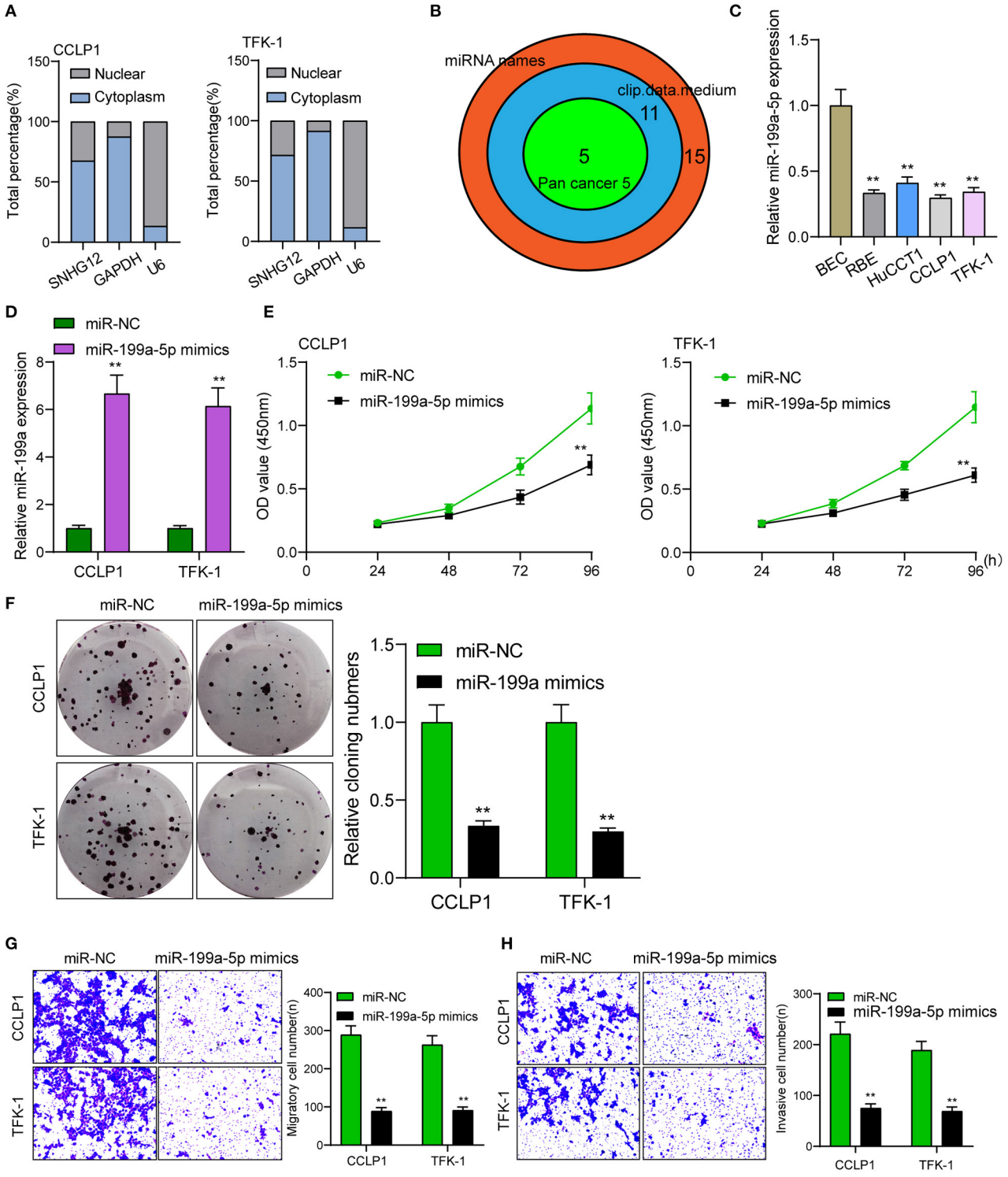

FIGURE 3 | miR-199a-5p overexpression promoted the proliferation and metastasis of TFK-1 and CCLP1 cells. **(A)** Relative SNHG12 levels in nuclear and cytosolic fractions of TFK-1 and CCLP1 cells. **(B)** Bioinformatics analysis to select relevant miRNAs. **(C)** The histogram of miR-199a-5p expressions in four ICC cells and BEC cells. **(D)** RT-PCR examined the expressions of miRNA-199a-5p in TFK-1 and CCLP1 cells transfected with miR-NC or miR-199a-5p mimics. **(E)** CCK-8 assays revealed that OD values of TFK-1 and CCLP1 cells were distinctly declined when transfected with miR-199a-5p mimics. **(F)** Cell clone number was distinctly decreased when transfected with miR-199a-5p mimics. **(G,H)** Transwell assays of migration and invasion of TFK-1 and CCLP1 cells after treatment with miR-199a-5p mimics or miR-NC. $^{**}p < 0.01$.

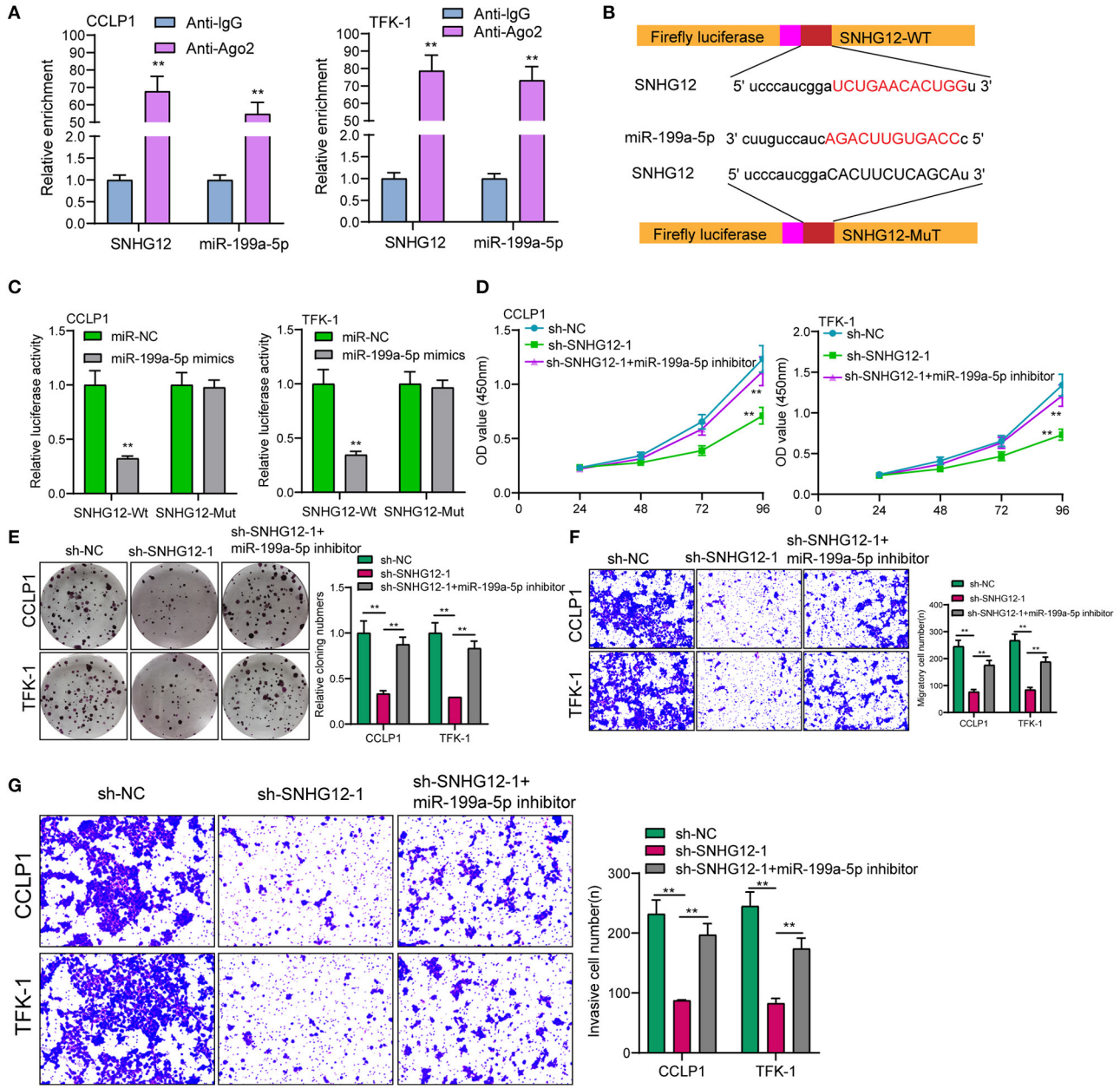

FIGURE 4 | Knockdown of miR-199a-5p reversed the distinct suppression of SNHG12 knockdown on the ICC progression. **(A)** RIP assay to confirm the coexistence of SNHG12 and miR-199a-5p in TFK-1 and CCLP1 cells. **(B)** Schematic outlining the predicted binding sites between miR-199a-5p and SNHG12. **(C)** miR-199a-5p mimics markedly reduced luciferase activity in SNHG12-wild not in SNHG12-Mut in TFK-1 and CCLP1 cells. **(D–G)** Rescue experiments were used to determine the efficacy of miR-199a-5p knockdown on SNHG12 down-regulation via CCK-8, colony formation assay and transwell assays. $^{**}p < 0.01$.

TFK-1 cells (**Figure 5D**). Besides, luciferase reporter assays demonstrated the predicted binding sites between miR-199a-5p and Klotho (**Figures 5E,F**). In addition, we performed rescue experiments with overexpressed Klotho, finding that overexpression of Klotho reversed the distinct suppression of SNHG12 knockdown on the proliferation, migration and invasion of CCLP1 and TFK-1 cells (**Figures 6A–D**). Finally, Xenografts model was applied for the determination of oncogenic roles of SNHG12 *in vivo*. As presented in **Figure 6E**, the tumor growth speed was slower on nude mice after subcutaneous injection with sh-SNHG12-1 than sh-NC group. Moreover, our group showed that the tumor volume and weight were distinctly lessened in sh-SNHG12-1 group compared with sh-NC group (**Figures 6F,G**).

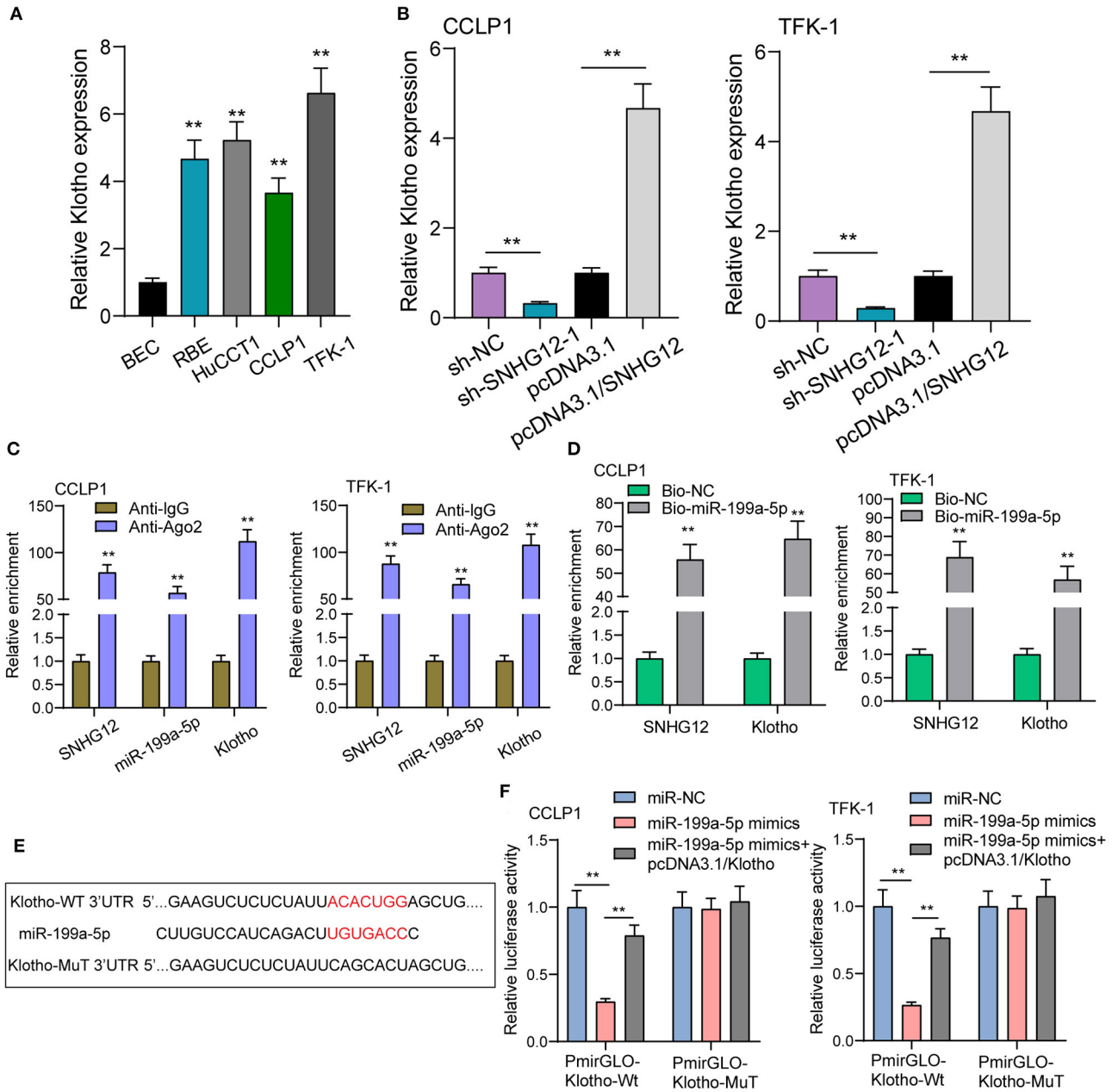

FIGURE 5 | Klotho is a target gene of miR-199a-5p. **(A)** Four ICC cells exhibited an increased expression of Klotho compare with BEC cells using RT-PCR. **(B)** RT-PCR for the expression of Klotho in TFK-1 and CCLP1 cells transfected with sh-NC, sh-SNHG12-1, pcDNA3.1 or pcDNA3.1/SNHG12. **(C)** RIP assays to verify the coexistence of three molecules. **(D)** RNA pull-down assay to test enrichment of SNHG12 and Klotho pulled down by miR-199a-5p. **(E)** Schematic representation of the predicted target site for miR-199a-5p in SNHG12. **(F)** Luciferase reporter assay in TFK-1 and CCLP1 cells, co-transfected with the reporter plasmid and the indicated miRs. $^{**}p < 0.01$.

DISCUSSION

In recent years, several studies have reported the potential effects of SNHG12 on several tumors. For instance, Liu et al. reported that SNHG12 was highly expressed in renal cell carcinoma and its overexpression via the transfection of pcDNA3.1/SNHG12 promoted the proliferation and invasion of renal cell carcinoma cells via increasing CDCA3 expression (18). In cervical cancer, SNHG12 was shown to exhibit a high level, and its knockdown was observed to modulate the radiosensitivity of cervical cancer via upregulating CDK1 expression through sponging miR-148a (19). The similar effects of SNHG12 acting as a tumor promotor were also observed in other tumors, such as esophageal squamous cell carcinoma cells and prostate cancer (22, 23). These

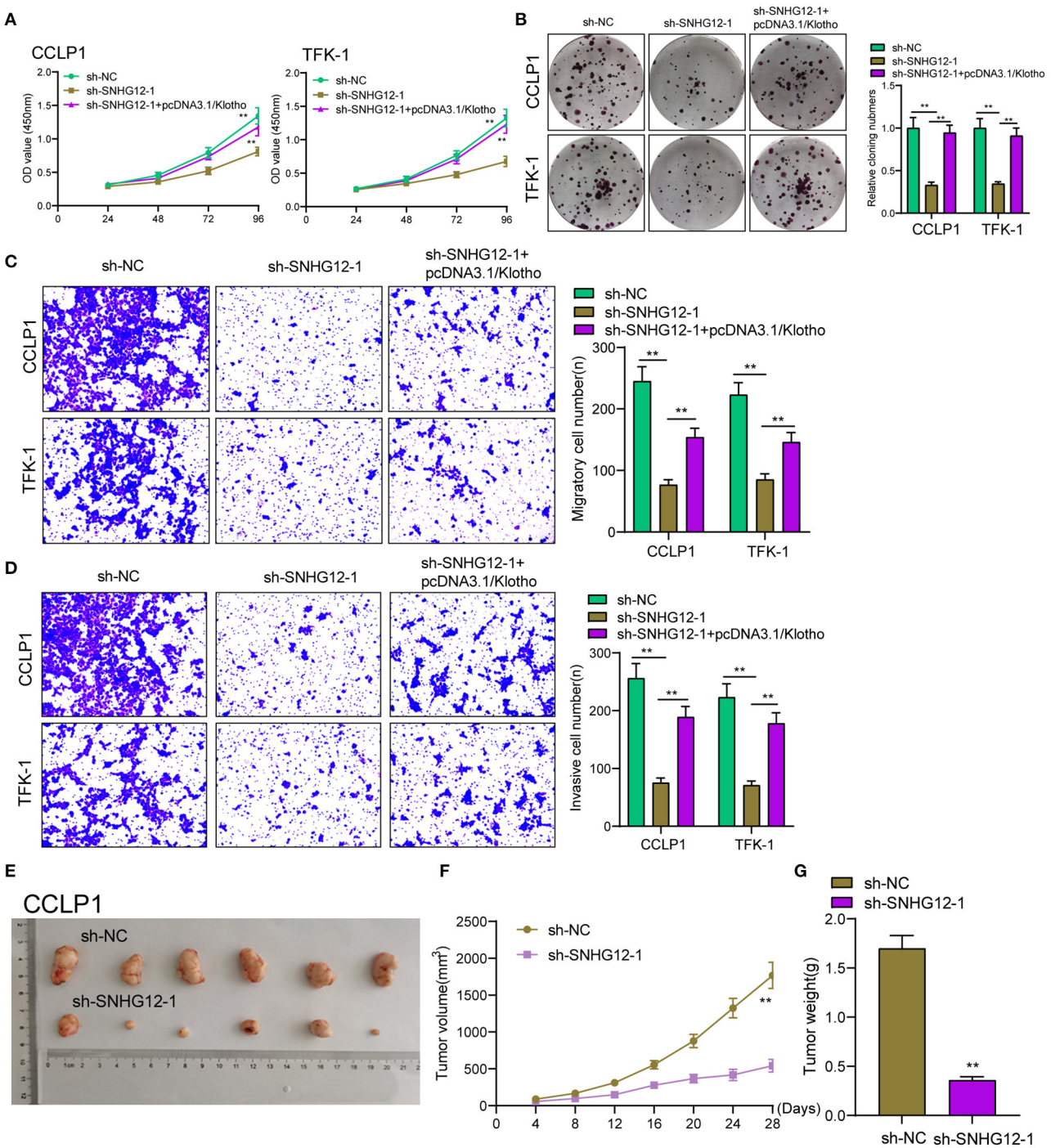

FIGURE 6 | The upregulation of Klotho reversed functional depletion caused by SNHG12 knockdown. **(A)** CCK-8 assays were applied to determine the proliferation of TFK-1 and CCLP1 cells cotransfected with sh-NC, sh-SNHG12-1 or sh-SNHG12-1 +pcDNA3.1/Klotho. **(B)** Colony formation assays were used to detect the proliferation of TFK-1 and CCLP1 cells cotransfected with sh-NC, sh-SNHG12-1 or sh-SNHG12-1 +pcDNA3.1/Klotho. **(C–E)** Transwell assays were applied to determine the migration and invasion of TFK-1 and CCLP1 cells cotransfected with sh-NC, sh-SNHG12-1 or sh-SNHG12-1 +pcDNA3.1/Klotho. **(E)** Tumors derived from mice in two different groups were presented. **(F,G)** Tumor volume and weight in the xenograft mice from the SNHG12-knockdown group and the control group. $^{**}p < 0.01$.

findings highlighted the important effects of SNHG12 in tumor progression. In this study, we searched TCGA datasets, finding that SNHG12 was an overexpressed lncRNA in ICC, which was also confirmed in four cell lines using RT-PCR. Then, we firstly provided evidence that knockdown of SNHG12 distinctly suppressed the proliferative and metastatic ability of ICC cells, while overexpression of SNHG12 exhibited an opposite effect. Our findings filled in the gaps in the fields of the potential effects of SNHG12 on ICC progression.

Then, we explored the potential mechanisms involved in the oncogenic roles of SNHG12 on ICC progression. It has been demonstrated that many cytoplasmic lncRNAs act as competing endogenous RNAs (ceRNAs) via binding miRNAs (24). In ICC, several lncRNAs such as lncRNA MT1JP and lncRNA AGAP2-AS1 have been shown to exhibit their tumor-related effects via sponging miRNAs to modulate the expression of various genes involved in tumor progression (25, 26). Previously, SNHG12 was also reported to act as a ceRNA in several tumors, such as cervical cancer and oral squamous cell carcinoma (19, 27). These findings encouraged us to explore the ceRNA mechanisms about SNHG12. Using Bioinformatics analysis, we screened five miRNAs. Importantly, among the five candidates, miR-199a-5p has been shown to suppress the proliferation and metastasis of hepatocellular carcinoma cells (21). Thus miR-199a-5p was used for further experiments. We found overexpression of miR-199a-5p suppressed the proliferation and metastasis of CCLP1 and TFK-1 cells. In mechanistic studies, we observed the coexistence of miR-199a-5p and SNHG12 in ICC cells and the binding sites between them. More importantly, rescue experiments confirmed that knockdown of miR-199a-5p reversed the anti-oncogenic roles of SNHG12 knockdown. These findings suggested SNHG12 may exhibit its tumor promotor effects via sponging miR-199a-5p.

To explore the possible mechanisms of miRNAs, establishing their functional targets counts a great deal. Thus, we searched internet databases, finding that klotho may be a potential target of miR-199a-5p. Klotho gene, encoding a 130-kDa transmembrane protein, is located on chromosome 13q12 (28). It has been demonstrated that Klotho is frequently expressed in the distal tubule of the renal, and less frequently in some other human specimens (29). In recent years, many studies have reported Klotho as an oncogene in several tumors, including hepatocellular carcinoma (30, 31). In this study, we also provided evidence that Klotho expression was increased in ICC cells. We firstly provided evidence which demonstrated the location and binding situation of SNHG12, miR-199a-5p and Klotho, demonstrating the ceRNA mechanism. Rescue experiments also confirmed Klotho overexpression saved functional attenuation caused by down-regulation of SNHG12. Finally, *in vivo* assays also demonstrated SNHG12 served as a tumor promotor in ICC.

CONCLUSION

Our findings demonstrated that SNHG12 facilitated the growth and metastasis of ICC cells by sponging miR-199a-5p and regulating Klotho expression, and provided a potential marker and therapeutic target for ICC patients.

DATA AVAILABILITY STATEMENT

The raw data supporting the conclusions of this article will be made available by the authors, without undue reservation.

ETHICS STATEMENT

The animal study was reviewed and approved by Zhejiang Provincial People's Hospital Animal Care Committee.

AUTHOR CONTRIBUTIONS

QH and H-GY designed and supervised the study. H-GY, QH, T-pW, and S-aH performed most experiments and wrote the manuscript. C-zH and C-hJ helped to perform parts of the experiments. QH and T-pW analyzed the data and revised the article. All authors contributed to the article and approved the submitted version.

FUNDING

This study was supported by grants from Medical Scientific Research Foundation of Zhejiang Province (No. 2017KY659) and Project of Administration of Traditional Chinese Medicine of Zhejiang Province (No. 2021ZB023).

REFERENCES

1. Mavros MN, Economopoulos KP, Alexiou VG, Pawlik TM. Treatment and prognosis for patients with intrahepatic cholangiocarcinoma: systematic review and meta-analysis. *JAMA Surg.* (2014) 149:565–74. doi: 10.1001/jamasurg.2013.5137
2. Razumilava N, Gores GJ. Cholangiocarcinoma. *Lancet.* (2014) 383:2168–79. doi: 10.1016/S0140-6736(13)61903-0
3. Zhang H, Yang T, Wu M, Shen F. Intrahepatic cholangiocarcinoma: epidemiology, risk factors, diagnosis and surgical management. *Cancer Lett.* (2016) 379:198–205. doi: 10.1016/j.canlet.2015.09.008
4. Massarweh NN, El-Serag HB. Epidemiology of hepatocellular carcinoma and intrahepatic cholangiocarcinoma. *Cancer Control.* (2017) 24:1073274817729245. doi: 10.1177/1073274817729245
5. Rizvi S, Khan SA, Hallemeier CL, Kelley RK, Gores GJ. Cholangiocarcinoma - evolving concepts and therapeutic strategies. *Nature reviews Clinical oncology.* (2018) 15:95–111. doi: 10.1038/nrclinonc.2017.157
6. Kopp F, Mendell JT. Functional classification and experimental dissection of long noncoding RNAs. *Cell.* (2018) 172:393–407. doi: 10.1016/j.cell.2018.01.011
7. Ulitsky I, Bartel DP. lincRNAs: genomics, evolution, and mechanisms. *Cell.* (2013) 154:26–46. doi: 10.1016/j.cell.2013.06.020
8. Zhao Z, Sun W, Guo Z, Zhang J, Yu H, Liu B. Mechanisms of lncRNA/microRNA interactions in angiogenesis. *Life Sci.* (2020) 254:116900. doi: 10.1016/j.lfs.2019.116900
9. Qian X, Zhao J, Yeung PY, Zhang QC, Kwok CK. Revealing lncRNA structures and interactions by sequencing-based approaches. *Trends Biochem Sci.* (2019) 44:33–52. doi: 10.1016/j.tibs.2018.09.012

10. St Laurent G, Wahlestedt C, Kapranov P. The landscape of long noncoding RNA classification. *Trends Genet.* (2015) 31:239–51. doi: 10.1016/j.tig.2015.03.007
11. Peng WX, Koirala P, Mo YY. LncRNA-mediated regulation of cell signaling in cancer. *Oncogene.* (2017) 36:5661–67. doi: 10.1038/onc.2017.184
12. Bhan A, Soleimani M, Mandal SS. Long noncoding RNA and cancer: a new paradigm. *Cancer Res.* (2017) 77:3965–81. doi: 10.1158/0008-5472.CAN-16-2634
13. Chan JJ, Tay Y. Noncoding RNA:RNA regulatory networks in cancer. *Int J Mol Sci.* (2018) 19:1310. doi: 10.3390/ijms19051310
14. Zhu TG, Xiao X, Wei Q, Yue M, Zhang LX. Revealing potential long non-coding RNA biomarkers in lung adenocarcinoma using long non-coding RNA-mediated competitive endogenous RNA network. *Brazilian journal of medical and biological research = Revista brasileira de pesquisas medicas e biologicas.* (2017) 50:e6297. doi: 10.1590/1414-431x20176297
15. Liu X, Zheng J, Xue Y, Qu C, Chen J, Wang Z, et al. Inhibition of TDP43-Mediated SNHG12-miR-195-SOX5 feedback loop impeded malignant biological behaviors of glioma cells. *Mol Ther Nucleic Acids.* (2018) 10:142–58. doi: 10.1016/j.omtn.2017.12.001
16. Zhang H, Lu W. LncRNA SNHG12 regulates gastric cancer progression by acting as a molecular sponge of miR-320. *Mol Med Rep.* (2018) 17:2743–9. doi: 10.3892/mmr.2017.8143
17. Zhou S, Yu L, Xiong M, Dai G. LncRNA SNHG12 promotes tumorigenesis and metastasis in osteosarcoma by upregulating Notch2 by sponging miR-195-5p. *Biochem Biophys Res Commun.* (2018) 495:1822–32. doi: 10.1016/j.bbrc.2017.12.047
18. Liu Y, Cheng G, Huang Z, Bao L, Liu J, Wang C, et al. Long noncoding RNA SNHG12 promotes tumour progression and sunitinib resistance by upregulating CDCA3 in renal cell carcinoma. *Cell Death Dis.* (2020) 11:515. doi: 10.1038/s41419-020-2713-8
19. Wang C, Shao S, Deng L, Wang S, Zhang Y. LncRNA SNHG12 regulates the radiosensitivity of cervical cancer through the miR-148a/CDK1 pathway. *Cancer Cell Int.* (2020) 20:554. doi: 10.1186/s12935-020-01654-5
20. Ahmadi A, Khansarinejad B, Hosseinkhani S, Ghanei M, Mowla SJ. miR-199a-5p and miR-495 target GRP78 within UPR pathway of lung cancer. *Gene.* (2017) 620:15–22. doi: 10.1016/j.gene.2017.03.032
21. Huang GH, Shan H, Li D, Zhou B, Pang PF. MiR-199a-5p suppresses tumorigenesis by targeting clathrin heavy chain in hepatocellular carcinoma. *Cell Biochem Funct.* (2017) 35:98–104. doi: 10.1002/cbf.3252
22. Cheng G, Song Z, Liu Y, Xiao H, Ruan H, Cao Q, et al. Long noncoding RNA SNHG12 indicates the prognosis of prostate cancer and accelerates tumorigenesis via sponging miR-133b. *J Cell Physiol.* (2020) 235:1235–46. doi: 10.1002/jcp.29039
23. Wu D, He X, Wang W, Hu X, Wang K, Wang M. Long noncoding RNA SNHG12 induces proliferation, migration, epithelial-mesenchymal transition, and stemness of esophageal squamous cell carcinoma cells via post-transcriptional regulation of BMI1 and CTNNB1. *Mol Oncol.* (2020) 14:2332–51. doi: 10.1002/1878-0261.12683
24. Qi X, Zhang DH, Wu N, Xiao JH, Wang X, Ma W. ceRNA in cancer: possible functions and clinical implications. *J Med Genet.* (2015) 52:710–8. doi: 10.1136/jmedgenet-2015-103334
25. Ji H, Wang J, Lu B, Li J, Zhou J, Wang L, et al. SP1 induced long non-coding RNA AGAP2-AS1 promotes cholangiocarcinoma proliferation via silencing of CDKN1A. *Mol Med.* (2021) 27:10. doi: 10.1186/s10020-020-00222-x
26. Zhao W, Zhao J, Guo X, Feng Y, Zhang B, Tian L. LncRNA MT1JP plays a protective role in intrahepatic cholangiocarcinoma by regulating miR-18a-5p/FBP1 axis. *BMC Cancer.* (2021) 21:142. doi: 10.1186/s12885-021-07838-0
27. Yin Y, Tan Y, Yao Y, Lu N, Zhang F. SNHG12/miR-326/E2F1 feedback loop facilitates the progression of oral squamous cell carcinoma. *Oral Dis.* (2020) 26:1631–9. doi: 10.1111/odi.13458
28. Cheikhi A, Barchowsky A, Sahu A, Shinde SN, Pius A, Clemens ZJ, et al. Klotho: an elephant in aging research. *J Gerontol A Biol Sci Med Sci.* (2019) 74:1031–42. doi: 10.1093/gerona/glz061
29. Kuro OM. The Klotho proteins in health and disease. *Nat Rev Nephrol.* (2019) 15:27–44. doi: 10.1038/s41581-018-0078-3
30. Mencke R, Olauson H, Hillebrands JL. Effects of Klotho on fibrosis and cancer: A renal focus on mechanisms and therapeutic strategies. *Adv Drug Deliv Rev.* (2017) 121:85–100. doi: 10.1016/j.addr.2017.07.009
31. Tang X, Wang Y, Fan Z, Ji G, Wang M, Lin J, et al. Klotho: a tumor suppressor and modulator of the Wnt/β-catenin pathway in human hepatocellular carcinoma. *Lab Invest.* (2016) 96:197–205. doi: 10.1038/labinvest.2015.86

Conflict of Interest: The authors declare that the research was conducted in the absence of any commercial or financial relationships that could be construed as a potential conflict of interest.

Copyright © 2021 Yang, Wang, Hu, Hu, Jiang and He. This is an open-access article distributed under the terms of the Creative Commons Attribution License (CC BY). The use, distribution or reproduction in other forums is permitted, provided the original author(s) and the copyright owner(s) are credited and that the original publication in this journal is cited, in accordance with accepted academic practice. No use, distribution or reproduction is permitted which does not comply with these terms.

frontiers in Medicine

ORIGINAL RESEARCH
published: 24 June 2021
doi: 10.3389/fmed.2021.667525

FABP5, a Novel Immune-Related mRNA Prognostic Marker and a Target of Immunotherapy for Multiple Myeloma

Haipeng Jia[1†], Xiaofen Zhang[1†], Xinxin Liu[1†], Ruifang Qiao[2], Yan Liu[1], Sulong Lv[1], Hongbo Zhu[1], Jie Wang[1], Qiuhong Kong[1], Hong Zhang[1] and Zhirong Zhang[1]*

[1] Department of Hematology, The Second Affiliated Hospital of Shandong First Medical University, Taian, China, [2] Respiratory Intensive Care Unit, Taian City Central Hospital, Taian, China

OPEN ACCESS

Edited by:
Fu Wang,
Xi'an Jiaotong University, China

Reviewed by:
Manh-Cuong Vo,
Chonnam National University Hwasun Hospital, South Korea
Youwei Sun,
Emory University, United States

***Correspondence:**
Zhirong Zhang
zhangzhirong@sdfmu.edu.cn

[†] These authors have contributed equally to this work

Specialty section:
This article was submitted to Precision Medicine, a section of the journal Frontiers in Medicine

Received: 13 February 2021
Accepted: 29 April 2021
Published: 24 June 2021

Citation:
Jia H, Zhang X, Liu X, Qiao R, Liu Y, Lv S, Zhu H, Wang J, Kong Q, Zhang H and Zhang Z (2021) FABP5, a Novel Immune-Related mRNA Prognostic Marker and a Target of Immunotherapy for Multiple Myeloma. Front. Med. 8:667525. doi: 10.3389/fmed.2021.667525

Objective: Multiple myeloma is an incurable hematological malignancy. It is imperative to identify immune markers for early diagnosis and therapy. Here, this study analyzed immune-related mRNAs and assessed their prognostic value and therapeutic potential.

Methods: Abnormally expressed immune-related mRNAs were screened between multiple myeloma and normal bone marrow specimens in the GSE47552 and GSE6477 datasets. Their biological functions were then explored. Survival analysis was presented for assessing prognosis-related mRNAs. CIBERSORT was utilized for identifying 22 immune cell compositions of each bone marrow specimen. Correlation between FABP5 mRNA and immune cells was then analyzed in multiple myeloma.

Results: Thirty-one immune-related mRNAs were abnormally expressed in multiple myeloma, which were primarily enriched in B cells-related biological processes and pathways. Following validation, FABP5 mRNA was a key risk factor of multiple myeloma. Patients with its up-regulation usually experienced unfavorable outcomes. There were distinct differences in the infiltration levels of B cells naïve, B cells memory, plasma cells, T cells CD4 naïve, resting memory CD4 T cells, activated memory CD4 T cells, Tregs, resting NK cells, M0 macrophages, M1 macrophages, M2 macrophages, and neutrophils between multiple myeloma and normal samples. FABP5 mRNA had correlations to B cells memory, B cells naïve, dendritic cells activated, macrophages M0, macrophages M1, macrophages M2, neutrophils, activated NK cells, resting memory CD4 T cells, CD8 T cells and Tregs.

Conclusion: Collectively, our data showed that FABP5 mRNA was related to immune microenvironment, which could be a target of immunotherapy and prognostic marker for multiple myeloma.

Keywords: multiple myeloma, FABP5, immunotherapy, prognosis, therapeutic target, immune microenvironment

INTRODUCTION

Multiple myeloma is a heterogenous and incurable neoplasm of plasma cells, accounting for 1% of malignancies and around 10% of all hematological malignancies (1). Stem cell transplantation, proteasome inhibitors and immunosuppressive agents are the main therapeutic strategies, which have prolonged survival time of multiple myeloma subjects (2). Multiple myeloma is a multi-step disease, initially characterized by asymptomatic monoclonal gammopathy (MGUS). MGUS accounts for 1% of the adult population, and ∼1% of MGUS patients turn into malignant multiple myeloma every year (3). Despite the remarkable clinical outcomes, nearly all subjects experience recurrence. Hence, it still requires novel therapeutic approaches.

The survival, growth as well as proliferation of myeloma cells depend upon the bone marrow microenvironment (4, 5). The microenvironment contains a variety of cell types, including hematopoietic cells (B cells, T cells, natural killer cells, bone marrow-derived suppressor cells, and osteoclasts) and non-hematopoietic cells (marrow stromal cells, osteoblasts, and endothelial cells) (6). These cells secrete various factors, thereby promoting the migrative as well as proliferative behaviors of multiple myeloma cells (7–9). Multiple myeloma progress closely associates with abnormal innate and adaptive immune systems (10). There is evidence that the residual immune cell dysfunction in the tumor microenvironment can lead to the suppression of the host's anti-tumor immune function (11–13). In the normal microenvironment, effector cells can produce a powerful anti-tumor response. Nevertheless, tumor cells often protect themselves from the host immune system by inhibiting the anti-tumor immunity of their surrounding microenvironment. The sophisticated interplays between immune microenvironment and this disease may affect the clinical responses to immuno-oncology therapies such as thalidomide, lenalidomide (14) as well as pomalidomide (15). Early studies have mainly established the role of the bone marrow microenvironment in the pathological process of multiple myeloma, but the immune components of the microenvironment have not received enough attention. The immune response is a dynamic and complex process. It is of importance for understanding the main factors that contribute to the immunosuppressive environment in multiple myeloma (16). Herein, we focused on abnormally expressed immune-related mRNAs in multiple myeloma. Among them, high expression of FABP5 mRNA displayed poor outcomes of subjects. FABP5 is a member of the FABP family, which is overexpressed in several cancers such as prostate cancer (17). Increasing evidence has demonstrated that FABP5 is involved in tumor progression (18). Nevertheless, the biological roles of FABP5 remain indistinct in multiple myeloma. Our further analysis demonstrated that FABP5 dysregulation was in relationship with immune microenvironment of multiple myeloma, indicating that FABP5 was an underlying immunotherapeutic target for multiple myeloma.

Abbreviations: GEO, Gene Expression Omnibus; ImmPort, Immunology Database and Analysis Portal; GO, Gene Ontology; KEGG, Kyoto Encyclopedia of Genes and Genomes; BP, biological process; MF, molecular function; CC, cellular component; HR, hazard ratio; CI, confidence interval; CIBERSORT, Cell-type Identification By Estimating Relative Subsets of RNA Transcripts; Tregs, T cells regulatory.

MATERIALS AND METHODS

Data Preparation

From the Gene Expression Omnibus (GEO) database (https://www.ncbi.nlm.nih.gov/gds/), microarray data of bone marrow specimens from 5 normal and 41 multiple myeloma subjects were retrieved from the GSE47552 dataset on the GPL6244 platform. Furthermore, microarray expression profiling of 15 normal and 103 multiple myeloma bone marrow samples was obtained from the GSE6477 dataset on the GPL96 platform. The gene expression profiles from the GSE47552 and GSE6477 datasets were utilized for differential expression analysis. Probe IDs were transformed to gene symbols, followed by log2 transformation. The GSE4452 dataset contained complete follow-up information of 65 multiple myeloma subjects. Moreover, the GSE4204 dataset comprised survival information of 538 multiple myeloma patients. The GSE4452 and GSE4204 datasets were used for survival analysis.

Immune-related mRNAs

Two thousand four hundred and ninety-eight immune-related mRNAs were obtained from the Immunology Database and Analysis Portal (ImmPort) database (https://www.immport.org/home) (19). **Supplementary Table 1** listed the list of immune-related mRNAs.

Differential Expression Analyses

The differences in immune-related mRNAs between multiple myeloma and normal bone marrow specimens from the GSE47552 and GSE6477 datasets were analyzed through "limma" package (20). These mRNAs with false discovery rate (FDR) < 0.05 and $|\log2\text{fold change}| > 1$ displayed differential expression. Abnormally expressed immune-related mRNAs were intersected between the GSE47552 and GSE6477 datasets.

Functional Annotation Analyses

Gene Ontology (GO) as well as Kyoto Encyclopedia of Genes and Genomes (KEGG) functional annotation analyses for abnormally expressed immune-related mRNAs were carried out *via* "clusterProfiler" package (21). GO terms contained biological process (BP), molecular function (MF), and cellular component (CC). Terms with FDR < 0.05 were significantly enriched. The enrichment results of the top 10 terms were depicted by "ggplot2" package.

Survival Analysis

Univariate cox regression analyses were presented for assessment of which mRNAs displayed significant relationships to outcomes of multiple myeloma in the GSE4204 dataset through "survival" package. Hazard ratio (HR), 95% confidence interval (CI) as well as *p*-value were separately determined. The mRNAs with

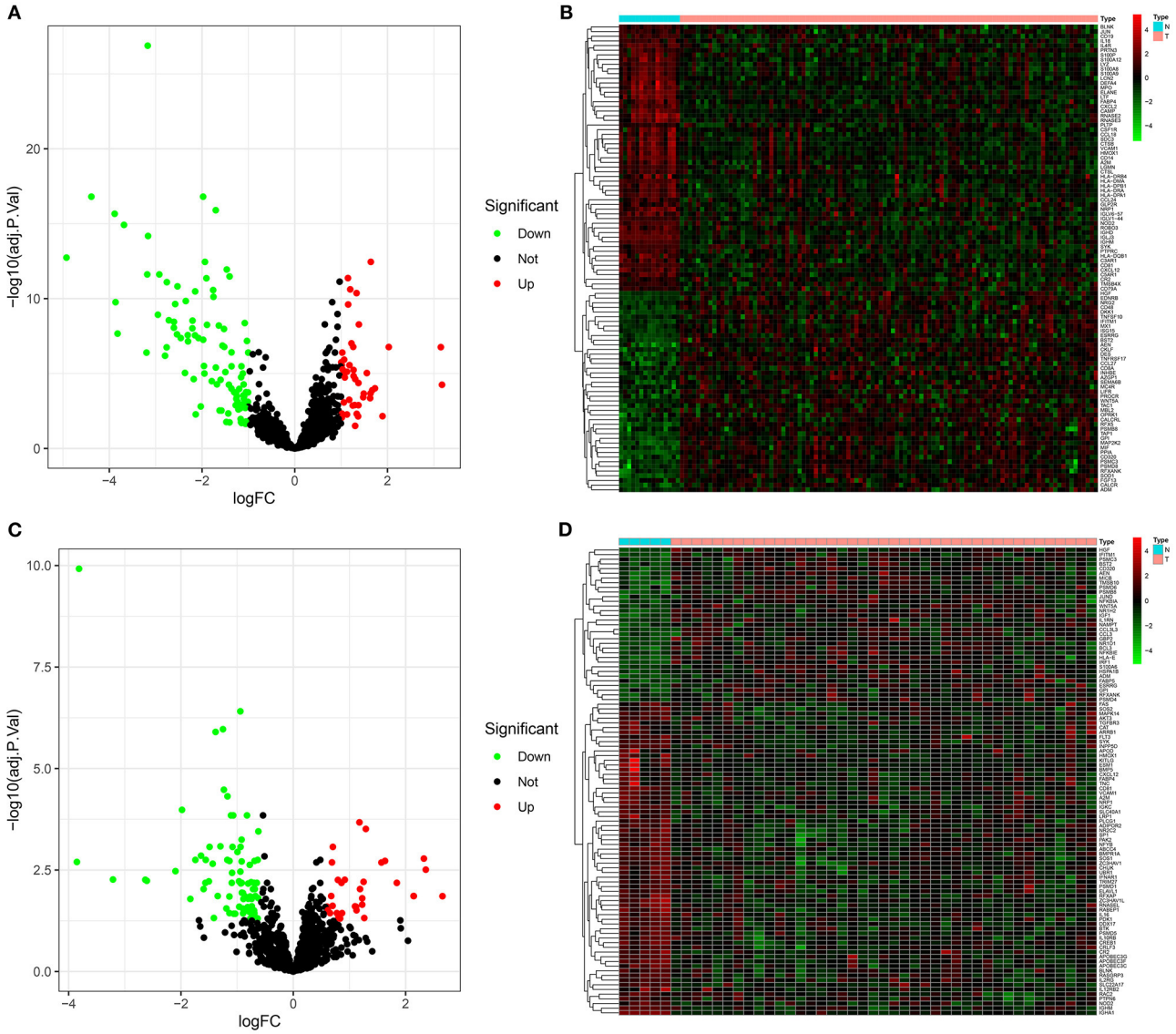

FIGURE 1 | Abnormally expressed immune-related mRNAs between multiple myeloma and normal bone marrow specimens. **(A)** Volcano plots for up-regulated (red) and down-regulated (green) immune-related mRNAs in multiple myeloma than normal specimens in the GSE6477 dataset. **(B)** Hierarchical clustering analyses for differential expression patterns of immune-related mRNAs in multiple myeloma and normal samples in the GSE6477 dataset. N indicates normal samples and T indicates multiple myeloma samples. **(C)** Volcano plots for highly (red) and lowly (green) expressed immune-related mRNAs in multiple myeloma than normal specimens in the GSE47552 dataset. **(D)** Heat map for abnormal expression patterns of immune-related mRNAs in multiple myeloma and normal samples in the GSE47552 dataset.

$p < 0.05$ were survival-related mRNAs. The mRNAs with HR > 1 were protective factors, while those with HR < 1 were risk factors. Then, patients in the GSE4204 dataset were separated into high and low expression subgroups in line with the median value of each survival-related mRNA. Kaplan-Meier curves between two subgroups were conducted. Log-rank test was utilized for evaluating whether there were differences in overall survival between subgroups. The prognostic implications of survival-related mRNAs were verified in the GSE4452 dataset.

Cell-Type Identification by Estimating Relative Subsets of RNA Transcripts (CIBERSORT)

Twenty-two immune cell compositions of bone marrow specimens were characterized based on the mRNA expression profiling from the GSE4204 dataset through the CIBERSORT algorithm (http://cibersort.stanford.edu/) (22). The perm was set at 1000. Specimens with $p < 0.05$ were retained for the analyses. These immune cells contained B cells naïve, B cells memory, plasma cells, CD8 T cells, T cells CD4,

TABLE 1 | The top 10 up- and down-regulated mRNAs for multiple myeloma in the GSE6477 dataset.

ID	logFC	Average Expression	*t*	*P*-value	FDR	B
EDNRB	3.17564	9.427753	4.73802	5.98E-06	5.62E-05	3.309497
DKK1	3.150724	9.880272	6.177481	9.22E-09	1.73E-07	9.570701
CD320	2.027545	8.59685	6.184919	8.90E-09	1.70E-07	9.605457
AZGP1	1.892662	7.210442	3.212207	0.001691	0.006999	−2.021902
INHBE	1.729437	6.682186	4.588078	1.11E-05	9.68E-05	2.718796
HGF	1.670569	8.019395	4.501167	1.58E-05	0.00013	2.382487
AEN	1.64025	9.420039	9.046557	3.19E-15	3.53E-13	24.13246
ISG15	1.633916	10.83147	4.363766	2.72E-05	0.000213	1.860149
ADM	1.625863	10.82119	4.152458	6.19E-05	0.00044	1.079927
ESRRG	1.554311	7.725752	5.205616	8.10E-07	9.27E-06	5.232271
RNASE3	−3.16441	7.972736	−9.838842	4.17E-17	6.60E-15	28.39332
RNASE2	−3.171877	8.870617	−15.60233	1.19E-30	1.32E-27	59.00869
CD14	−3.18157	6.364479	−8.654979	2.66E-14	2.43E-12	22.0487
HLA-DRA	−3.197716	8.593233	−5.971892	2.45E-08	4.00E-07	8.618598
LTF	−3.683454	6.394645	−10.17587	6.52E-18	1.20E-15	30.21743
LYZ	−3.821531	7.269164	−6.663122	8.59E-10	2.17E-08	11.88284
IGHM	−3.865049	11.58396	−7.703542	4.21E-12	1.73E-10	17.08209
ELANE	−3.88425	5.808598	−10.51921	9.80E-19	2.17E-16	32.07939
IGLJ3	−4.386589	10.19574	−11.08725	4.26E-20	1.57E-17	35.16217
IGHD	−4.923749	10.40866	−9.207839	1.32E-15	1.83E-13	24.99565

naïve T cells, CD4 memory resting, T cells CD4 memory activated, T cells follicular helper, T cells regulatory (Tregs), T cells gamma delta, NK cells resting, activated NK cells, monocytes, macrophages M0, macrophages M1, macrophages M2, dendritic cells resting, dendritic cells activated, mast cells resting, mast cells activated, eosinophils, and neutrophils. Correlation analyses were carried out between different immune cell compositions in each sample. The differences in fractions of 22 immune cells between normal and multiple myeloma bone marrow specimens were assessed through Mann-Whitney *U*-test. Correlations between FABP5 expression and immune cell fractions were determined among bone marrow samples by Pearson correlation analysis.

Statistical Analyses

R language (https://www.r-project.org/) and corresponding packages were carried out for statistical analyses.

RESULTS

Abnormal Expression of Immune-Related mRNAs in Multiple Myeloma

In the GSE6477 dataset, 139 immune-related mRNAs displayed abnormal expression between multiple myeloma and normal bone marrow specimens (**Supplementary Table 2**). Among them, 96 mRNAs showed down-regulation and 43 mRNAs exhibited up-regulation in multiple myeloma than normal bone marrow specimens (**Figure 1A**). The expression patterns of these mRNAs possessed conspicuous differences between multiple myeloma and normal subgroups (**Figure 1B**). **Table 1** listed the top 10 up- and down-regulated mRNAs in multiple myeloma. In the GSE47552 dataset, there were 33 up-regulated and 81 down-regulated immune-related mRNAs (**Figure 1C**). **Supplementary Table 3** listed the detailed information of 114 immune-related mRNAs. These mRNAs were distinguished multiple myeloma from normal bone marrow specimens (**Figure 1D**). **Table 2** displayed the top 10 up- and down-regulated mRNAs for multiple myeloma. Thus, immune-related mRNAs may participate in multiple myeloma progress.

Abnormal Expression of Immune-Related mRNAs Is Involved in B Cell-Related Pathways

Following intersection of abnormally expressed immune-related mRNAs in the GSE6477 and GSE47552 datasets, 31 common mRNAs were obtained, including CD81, PSMB8, CR2, ABCC4, ADM, IGHM, SYK, IFITM1, RASGRP3, IGKC, CXCL12, VCAM1, ESRRG, AEN, SLC22A17, NRP1, A2M, NOD2, BLNK, CD320, HGF, CCL8, BST2, RFXANK, HMOX1, PSMC3, FABP5, GPI, FABP4, WNT5A, and CD19 (**Figure 2A**). The biological functions that they were involved in were analyzed in depth. These mRNAs primarily participated in B cell-related biological processes such as B cell activation, regulation of immune effector process, immune response-activating cell surface receptor signaling pathway, immune response-activating signal transduction, leukocyte proliferation, antigen receptor-mediated signaling pathway, humoral immune response, regulation of B cell activation, B cell receptor signaling pathway, and regulation

TABLE 2 | The top 10 up- and down-regulated mRNAs for multiple myeloma in the GSE47552 dataset.

ID	logFC	Average Expression	*t*	*P*-value	FDR	B
CCL3	2.656638	8.795874	3.56051	0.000872	0.013934	−0.89655
IFITM1	2.359537	9.723628	4.272571	9.57E-05	0.003099	1.171609
ADM	2.325244	8.837015	4.62326	3.06E-05	0.001651	2.249141
HGF	2.145919	6.485812	3.566572	0.000856	0.013856	−0.879762
CCL3L3	2.141869	9.028911	3.576213	0.000832	0.013819	−0.853034
GBP2	1.843693	5.860666	3.907079	0.000304	0.006551	0.087163
IGF1	1.633367	7.666151	4.504304	4.52E-05	0.001888	1.880063
IRF1	1.569844	9.045278	4.42257	5.90E-05	0.002064	1.628528
PSMB8	1.291786	7.809183	5.30784	3.09E-06	0.000307	4.428956
WNT5A	1.263791	5.512224	2.879846	0.006015	0.048083	−2.669174
BMPR1A	−1.642355	5.335115	−4.698554	2.39E-05	0.001405	2.48447
PDK1	−1.743202	9.479215	−4.553513	3.85E-05	0.001781	2.032324
SLC40A1	−1.832581	7.009903	−3.460474	0.001172	0.016285	−1.171216
CD81	−1.981184	7.328404	−5.804343	5.63E-07	0.000104	6.050917
RASGRP3	−2.097604	7.852103	−4.238532	0.000107	0.003372	1.068818
VCAM1	−2.607187	6.369076	−4.016176	0.000216	0.005826	0.40622
CXCL12	−2.634773	7.51967	−4.051305	0.000193	0.0055	0.509833
IGKC	−3.210252	9.68074	−4.067062	0.000184	0.005416	0.556443
IGHA1	−3.814438	7.833927	−10.45918	9.24E-14	1.20E-10	20.88334
IGHM	−3.852736	9.121807	−4.457749	5.26E-05	0.002004	1.736577

of production of molecular mediator of immune response (**Figure 2B**). They were mainly involved in regulating the cellular components of external side of plasma membrane, secretory granule lumen, cytoplasmic vesicle lumen, vesicle lumen, blood microparticle, immunoglobulin complex, proteasome complex, platelet alpha granule lumen, endopeptidase complex, and immunoglobulin complex, circulating and the like. Moreover, they possessed the molecular functions of receptor ligand activity, signaling receptor activator activity, integrin binding, growth factor activity, glycosaminoglycan binding, cytokine activity, G protein-coupled receptor binding, long-chain fatty acid transporter activity, peptidoglycan binding, and chemoattractant activity and the like. The pathways enriched by these common mRNAs were analyzed. In **Figure 2C**, they principally participated in B cell receptor signaling pathway, Epstein-Barr virus infection, NF-kappa B signaling pathway, primary immunodeficiency, malaria, hepatocellular carcinoma, tuberculosis, axon guidance, proteasome, PPAR signaling pathway, complement and coagulation cascades, hematopoietic cell lineage, viral protein interaction with cytokine and cytokine receptor, TNF signaling pathway and leukocyte transendothelial migration.

FABP5 mRNA as an Immune-Related Prognostic Marker of Multiple Myeloma

As depicted by univariate cox regression analyses, among 31 common dysregulated immune-related mRNAs, AEN (HR: 1.35132218004432, 95% CI: 1.00336950593063–1.81993933788734, *p*-value: 0.0474670415899411), CD320 (HR: 1.2666572113788, 95% CI: 1.06872217896594–1.50125123508741, *p*-value: 0.0063988822159732), FABP5 (HR: 1.44824784649006, 95% CI: 1.25386429924306–1.67276620454803, *p*-value: 4.74125786831674e-07), and GPI (HR: 1.45171072863824, 95% CI: 1.06338050769041–1.98185317899107, *p*-value: 0.0189309122327046) were risk factors of multiple myeloma subjects in the GSE4204 dataset (**Figure 3A**). Meanwhile, CXCL12 (HR: 0.730888940033441, 95% CI: 0.568482755798023–0.939691903078592, *p*-value: 0.0144802428352221), IGKC (HR: 0.82233697739277, 95% CI: 0.704030330155922–0.960524107303318, *p*-value: 0.0135803713395964), NOD2 (HR: 0.842773450385212, 95% CI: 0.719652065331376–0.986959008235654, *p*-value: 0.0337646407355474), VCAM1 (HR: 0.761232879031875, 95% CI: 0.6455778262167–0.897607496086219, *p*-value: 0.00117564947725508) and WNT5A (HR: 0.891231234461453, 95% CI: 0.800514277560811–0.992228540507633, *p*-value: 0.035517571353358) were protective factors of multiple myeloma. In the GSE4204 dataset, our Kaplan-Meier survival analyses demonstrated that low expression of CXCL12 (*p*-value: 0.009800177; **Figure 3B**) and WNT5A (*p*-value: 0.012647237; **Figure 3C**) displayed more unfavorable outcomes for multiple myeloma patients. Meanwhile, subjects with high FABP5 (*p*-value: 5.22E-05; **Figure 3D**) and PSMB8 (*p*-value: 0.040988621; **Figure 3E**) expression often experienced shorter survival time. In the GSE4452 dataset, we found that subjects with high CD320 (*p*-value: 0.100794819; **Figure 3F**), FABP5 (*p*-value: 0.002496168; **Figure 3G**) and GPI (*p*-value: 0.087747724; **Figure 3H**) were indicative of poorer outcomes compared to those with their low expression. Combining above data,

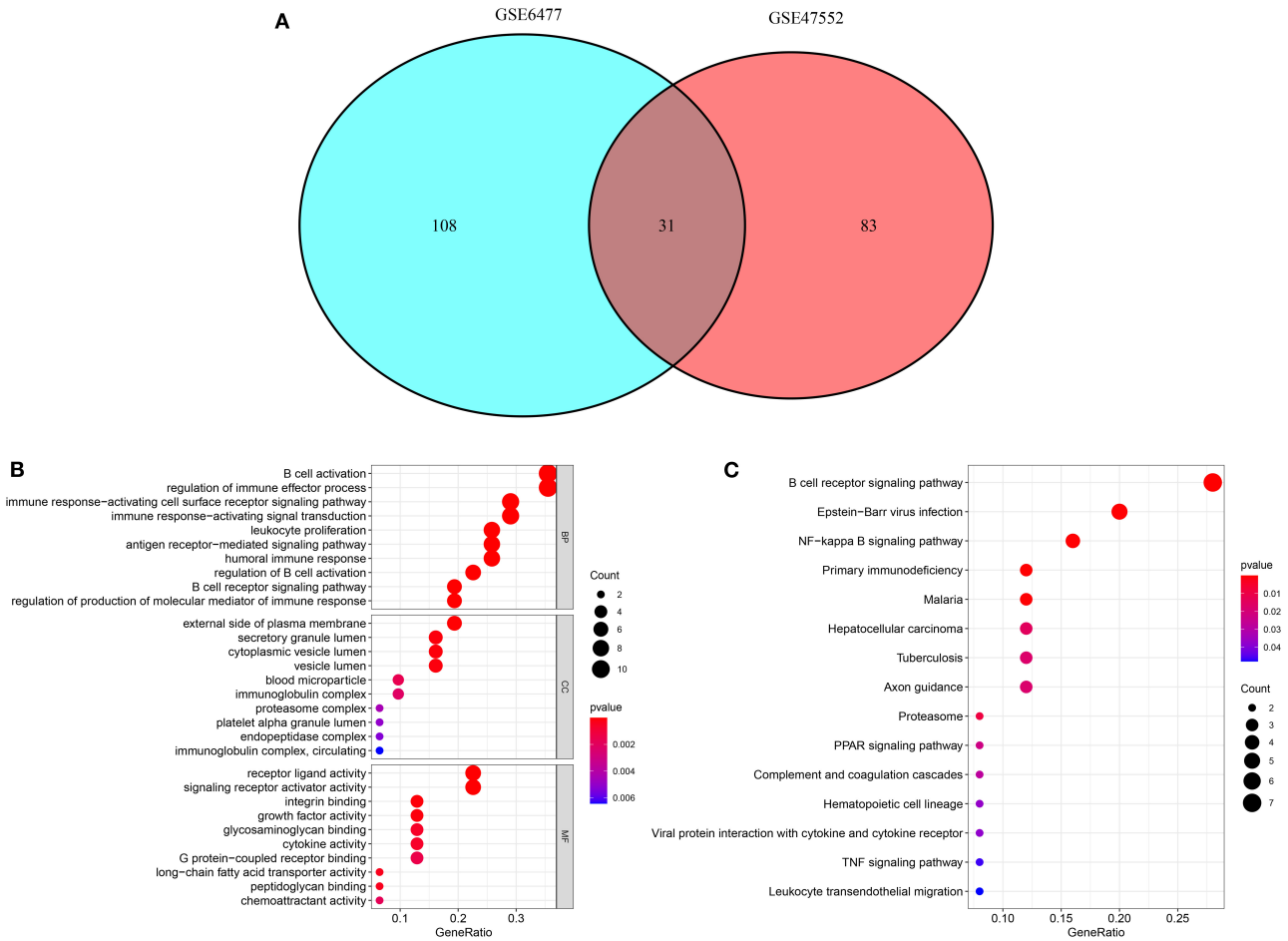

FIGURE 2 | Functional annotation analyses for dysregulated immune-related mRNAs. **(A)** Venn diagram for common dysregulated immune-related mRNAs in the GSE6477 and GSE47552 datasets. **(B)** The top 10 GO results enriched by common mRNAs, composed of biological process (BP), cellular component (CC), and molecular function (MF) terms. **(C)** KEGG pathways involved in common mRNAs. The size of the bubble is proportional to the count of enriched genes. The more the color tends to red, the smaller the *p*-value.

FABP5 mRNA was a key immune-related prognostic marker for multiple myeloma.

Tumor Immune Cells in Multiple Myeloma Bone Marrow Specimens

CIBERSORT was employed to identify the mixture of B cells naïve, B cells memory, plasma cells, CD8 T cells, T cells CD4, naïve T cells, CD4 memory resting, T cells CD4 memory activated, T cells follicular helper, Tregs, T cells gamma delta, NK cells resting, activated NK cells, monocytes, macrophages M0, macrophages M1, macrophages M2, dendritic cells resting, dendritic cells activated, mast cells resting, mast cells activated, eosinophils and neutrophils in multiple myeloma bone marrow specimens (**Figure 4A**). Correlations between the proportions of 22 immune cells in each multiple myeloma bone marrow sample were further analyzed. In **Figure 4B**, plasma cells displayed a strongly negative correlation to B cells memory ($r = -0.84$). Monocytes possessed a positive relationship with NK cells resting ($r = 0.41$).

Abnormal Expression of Immune Cells in Multiple Myeloma Bone Marrow

We compared the infiltrations of immune cells in multiple myeloma and normal bone marrow specimens in the GSE6477 dataset. Data showed that there were significant differences in the infiltration levels of B cells naïve ($p < 0.001$), B cells memory ($p < 0.001$), plasma cells ($p < 0.001$), T cells CD4 naïve ($p = 0.028$), resting memory CD4 T cells ($p = 0.012$), activated memory CD4 T cells ($p = 0.016$), Tregs ($p < 0.001$), resting NK cells ($p = 0.007$), M0 macrophages ($p = 0.002$), M1 macrophages ($p < 0.001$), M2 macrophages ($p = 0.004$), and neutrophils ($p < 0.001$) between multiple myeloma and normal bone marrow specimens (**Figure 5**).

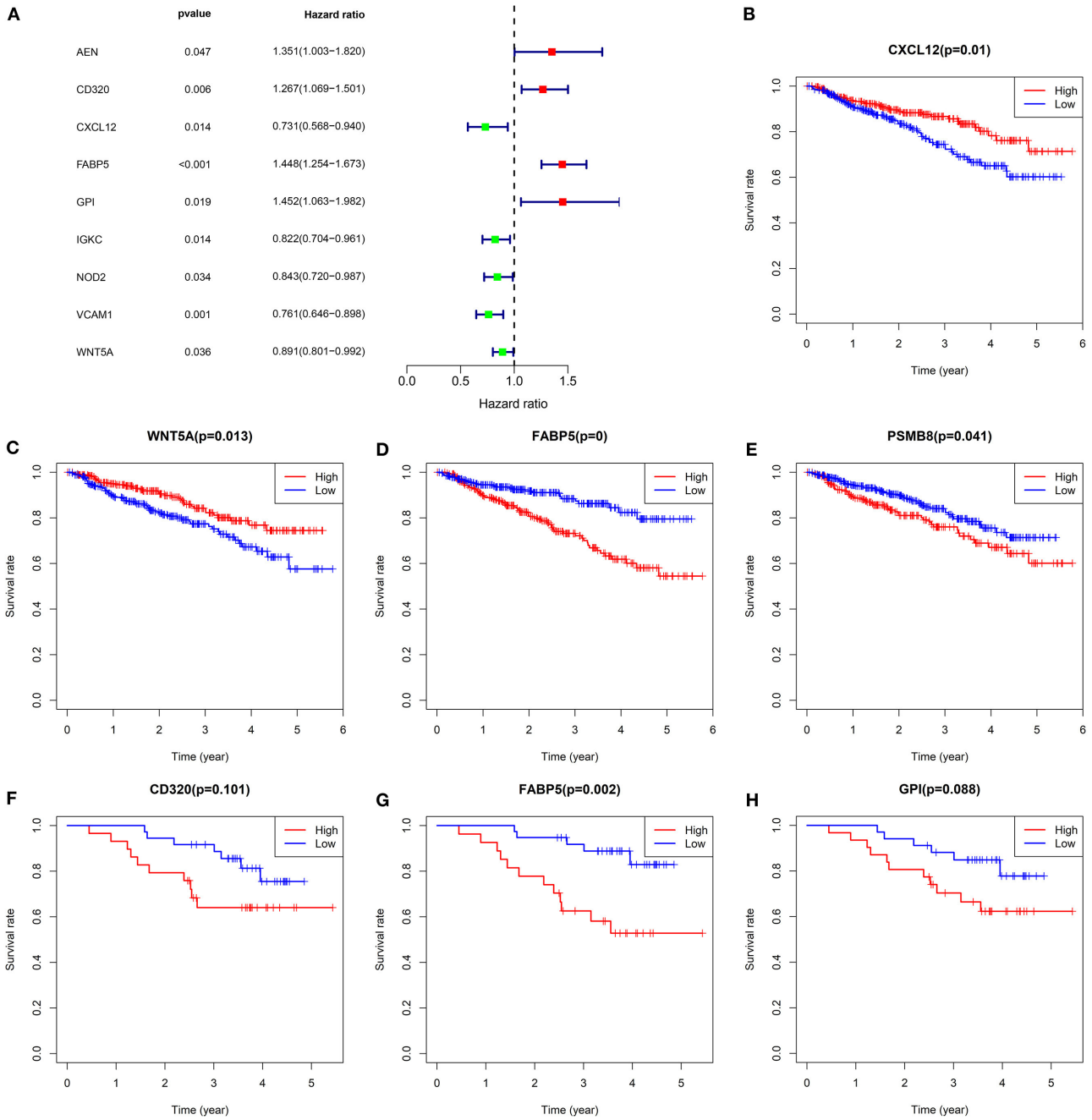

FIGURE 3 | Survival analysis for common dysregulated immune-related mRNAs in multiple myeloma. **(A)** Forest plots for univariate cox regression analysis of common dysregulated immune-related mRNAs in the GSE4204 dataset. Kaplan-Meier survival curves of **(B)** CXCL12, **(C)** WNT5A, **(D)** FABP5, and **(E)** PSMB8 expression among multiple myeloma subjects in the GSE4204 dataset. Kaplan-Meier survival curves of **(F)** CD320, **(G)** FABP5, and **(H)** GPI expression among subjects in the GSE4452 dataset. *P*-values for log-rank test. Red indicates high expression group while blue indicates low expression group.

FABP5 mRNA Exhibits Correlations to Immune Microenvironment of Multiple Myeloma

The relationships between FABP5 mRNA expression and infiltrations of immune cells were assessed in multiple myeloma bone marrow specimens. In **Figure 6A**, FABP5 mRNA displayed a negative association with infiltration of B cells memory ($r = -0.16$, $p = 3e\text{-}04$). A positive correlation between FABP5 mRNA and B cells naïve was detected in multiple myeloma bone marrow specimens ($r = 0.11$, $p = 0.015$; **Figure 6B**). FABP5 mRNA was

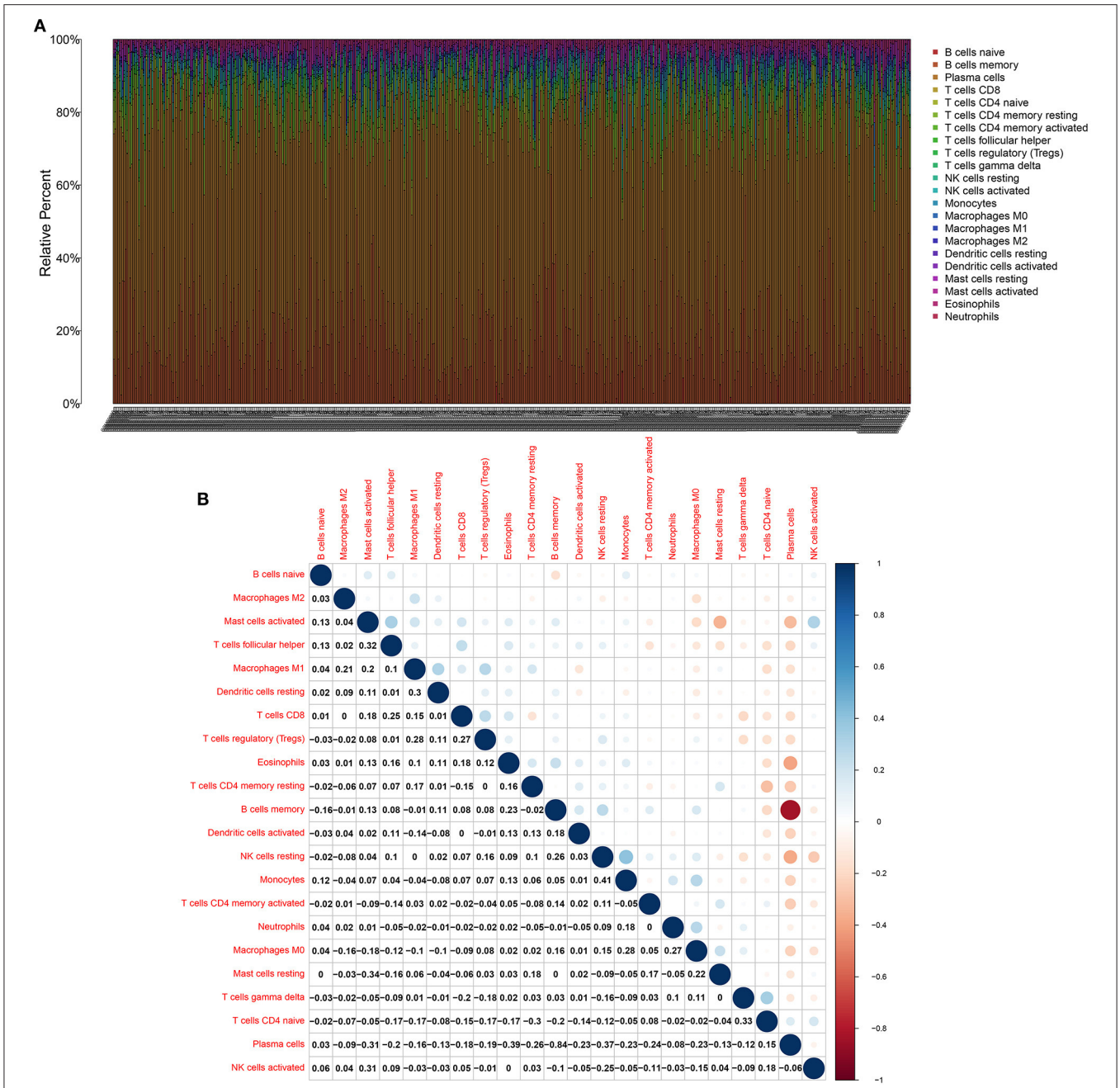

FIGURE 4 | CIBERSORT identifies tumor immune cells in multiple myeloma bone marrow specimens. **(A)** Stacked bar chart for the proportions of 22 kinds of immune cells in each multiple myeloma bone marrow samples. Each type of immune cell is identified by a unique color. **(B)** The correlation between the proportions of immune cells in multiple myeloma bone marrow specimens. Blue indicates negative correlation and red indicates positive correlation. The larger the correlation coefficient, the bigger the bubble.

negatively correlated to levels of dendritic cells activated ($r = -0.098$, $p = 0.023$; **Figure 6C**) and macrophages M0 ($r = -0.11$, $p = 0.0091$; **Figure 6D**). Furthermore, FABP5 mRNA exhibited positive correlations to infiltrations of macrophages M1 ($r = 0.09$, $p = 0.036$; **Figure 6E**), macrophages M2 ($r = 0.093$, $p = 0.03$; **Figure 6F**), neutrophils ($r = 0.15$, $p = 6e\text{-}04$; **Figure 6G**), activated NK cells ($r = 0.095$, $p = 0.028$; **Figure 6H**) and resting memory CD4 T cells ($r = 0.18$, $p = 3.4e\text{-}05$; **Figure 6I**). We also found that there were negative associations between FABP5 mRNA and infiltrations of CD8 T cells ($r = -0.14$, $p = 0.0016$; **Figure 6J**) and Tregs ($r = -0.1$, $p = 0.016$; **Figure 6K**). Both in the GSE6477 (**Figure 7A**) and GSE47552 (**Figure 7B**) datasets, FABP5 mRNA was up-regulated in multiple myeloma compared to normal bone marrow specimens ($p = 0.042$ and 0.002). There

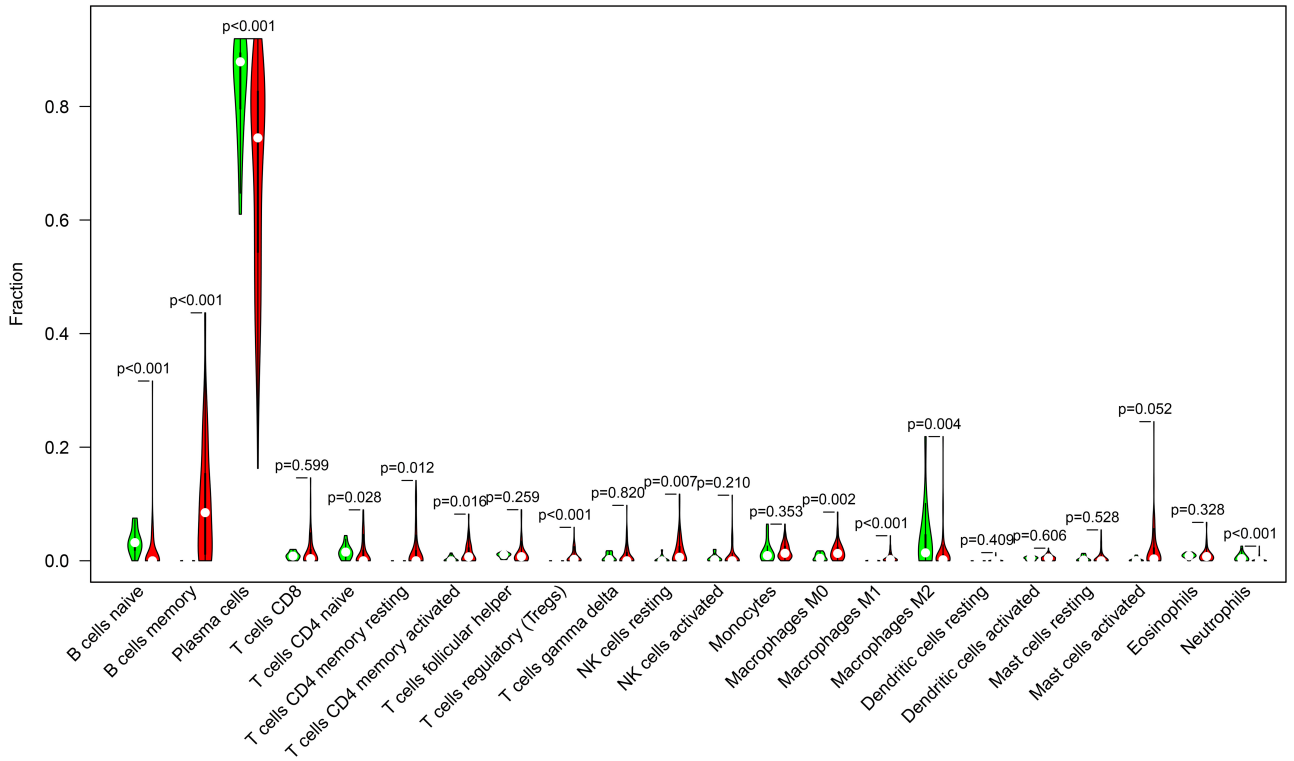

FIGURE 5 | Violin diagram for abnormal expression of immune cells in multiple myeloma (red) and normal (green) bone marrow specimens in the GSE6477 dataset.

were higher levels of B cells naïve ($p = 0.014$), T cells CD4 memory resting ($p < 0.001$), macrophages M2 ($p = 0.010$) and neutrophils ($p = 0.009$) as well as lower levels of B cells memory ($p = 0.004$) and T cells CD8 ($p = 0.002$) in the high FABP5 expression group compared to its low expression group (**Figure 7C**).

DISCUSSION

Multiple myeloma is an aggressive and incurable hematological malignancy, manifested by the malignant proliferation of abnormal plasma cells (23). Despite the advancement of treatment strategies, more therapeutic targets are still required for multiple myeloma. Here, we identified FABP5 as a novel immune-related mRNA as well as a prognostic marker for this malignancy.

Through integrative analyses of the GSE6477 and GSE47552 datasets, this study screened 31 common dysregulated immune-related mRNAs in multiple myeloma. These mRNAs were primarily enriched in B cell-related biological functions such as B cell activation, B cell receptor signaling pathway, plasma membrane. These data were indicative that they participated in the pathogenesis of multiple myeloma. Different patients' outcomes vary greatly. Thus, the establishment of a precise prognostic evaluation system to identify patients with different risks, especially for high-risk patients, is essential for clinicians to formulate overall treatment strategies, and can provide an important reference for patients and their families to understand the disease and achieve better management. Among all dysregulated immune-related mRNAs, AEN, CD320, FABP5, and GPI were risk factors for multiple myeloma, while CXCL12, IGKC, NOD2, VCAM1, and WNT5A were protective factors for multiple myeloma. Among them, CXCL12 up-regulation could be induced by HIF-2α in multiple myeloma plasma cells, thereby reducing migration as well as adhesion to mesenchymal stromal cells (24). CXCL12 is a target for reversing cellular adhesion-induced drug resistance against multiple myeloma (25). NOD2/CARD15 variant is correlated to the sensitivity of multiple myeloma bone marrow cells to bortezomib (26). Sialyltransferase inhibitor may suppress relationships between E-selectin, VCAM1, and MADCAM1, thereby prolonging survival time of multiple myeloma patients (27). WNT5A is an abundant growth factor upon myeloma bone marrow specimens (28). After multiple dataset verification, FABP5 was a key prognostic factor for multiple myeloma. Subjects with FABP5 up-regulation were indicative of more unfavorable outcomes. Hence, it was a risk factor of this disease. Nevertheless, the malignant roles of FABP5 mRNA remain undefined in multiple myeloma. Liu et al. reported that FABP5 was a stage-related prognostic factor of this malignancy (29). Its roles have been expounded in other malignancies. For instance, FABP5 is a critical driving factor of metastatic prostate carcinoma (30). Furthermore, it may promote lymph node metastases for cervical carcinoma *via* reprogramming fatty

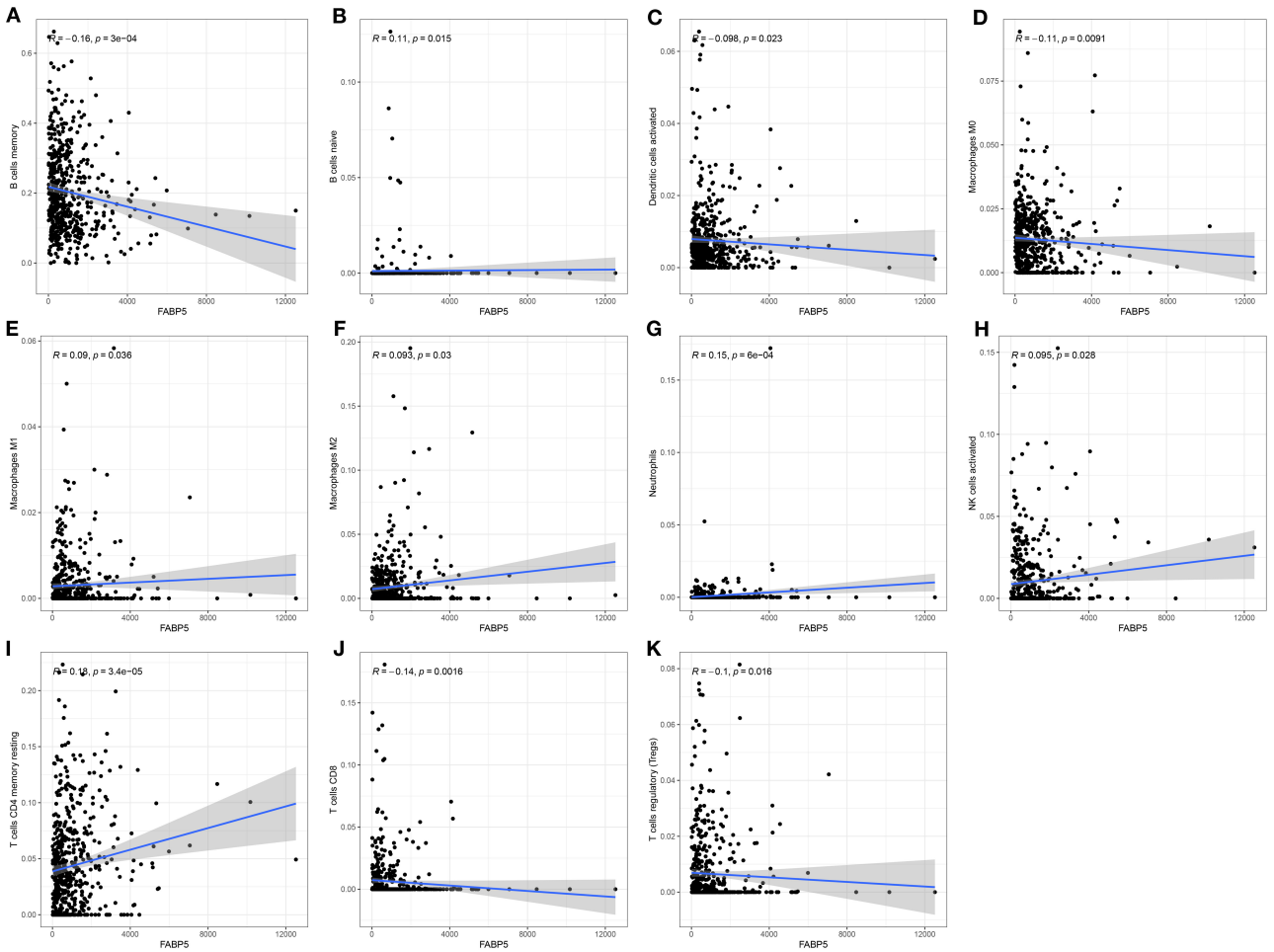

FIGURE 6 | Associations between FABP5 mRNA and infiltrations of immune cells in multiple myeloma bone marrow specimens. **(A)** B cells memory; **(B)** B cells naïve; **(C)** dendritic cells activated; **(D)** macrophages M0; **(E)** macrophages M1; **(F)** macrophages M2; **(G)** neutrophils; **(H)** activated NK cells; **(I)** resting memory CD4 T cells; **(J)** CD8 T cells; **(K)** Tregs.

acid metabolisms (17). Up-regulated FABP5 induced by fatty acid actuates hepatocellular carcinoma progress (31). FABP5 may elevate PI3K/AKT-mediated proliferation of renal carcinoma cells (18). Combining previous research, FABP5 mRNA might be a potential immunotherapeutic target of multiple myeloma. However, it remains unclear about which immunotherapy (dendritic cell vaccine, CAR T cells, or CAR NK cells) is good for targeting FABP5. Furthermore, whether FAPB5 targeted treatment causes any toxicity in patients with multiple myeloma requires further analysis. Thus, in our future studies, we will validate the therapeutic effects of FABP5 mRNA therapy in multiple myeloma by experiments.

There was a strongly negative correlation of plasma cells and B cells memory in multiple myeloma bone marrow specimens, indicating that there was interplay between plasma cells and B cells memory. There were distinct differences in the infiltration levels of B cells naïve, B cells memory, plasma cells, T cells CD4 naïve, resting memory CD4 T cells, activated memory CD4 T cells, Tregs, resting NK cells, M0 macrophages, M1 macrophages, M2 macrophages, and neutrophils between multiple myeloma and normal samples. Macrophages are innate immune cells that play a role in the host's own defense and maintenance of tissue homeostasis. Macrophages maintain the growth of myeloma cells through cell-to-cell contact-dependent behaviors and non-contact-mediated mechanisms in the bone marrow compartment, while enhancing the protective effect of mesenchymal stem cells on tumor cells (32). As an important part of the bone marrow microenvironment, through the connection between macrophages and tumor cell activation signal pathways, they can inhibit the protease pathway and block drug-induced apoptosis (33). Similar to solid tumors, multiple myeloma cells regulate immune molecules in the bone marrow microenvironment to adapt them to the growth of myeloma itself (34). The main immunosuppressive mechanisms during tumor progression include regulation of the expansion of immune cells, dysfunction of antigen presenting cells and suppression of immune effector cells (like effector T cells, NK cells) (35). Our data were indicative that FABP5 mRNA displayed

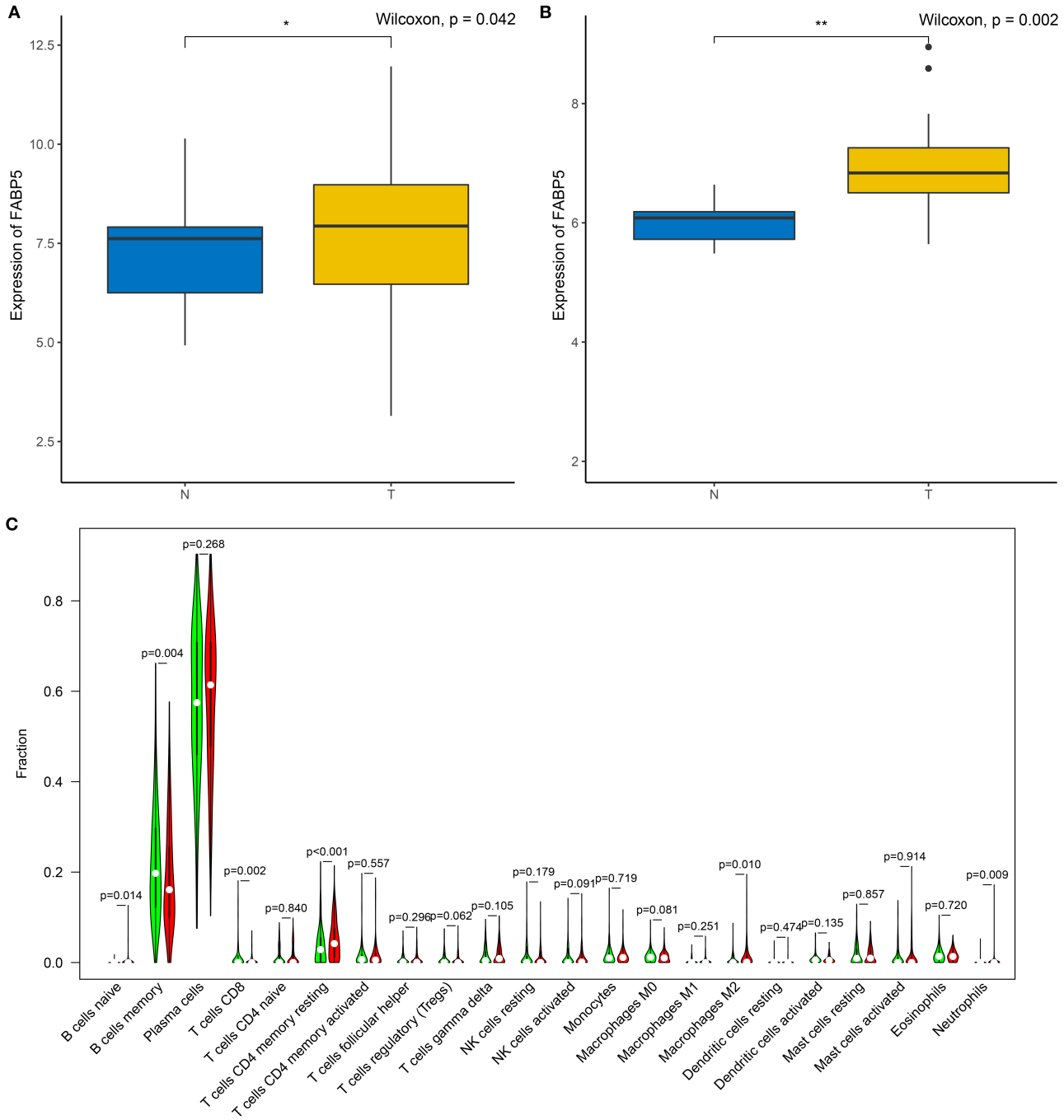

FIGURE 7 | Association between FABP5 mRNA and immune microenvironment of multiple myeloma. **(A,B)** Expression of FABP5 mRNA in multiple myeloma and normal bone marrow specimens in the **(A)** GSE6477 and **(B)** GSE47552 datasets. **(C)** Infiltration levels of immune cells between high and low FABP5 expression groups. Red: high FABP5 expression group; green: low expression group. $^{*}P < 0.05$; $^{**}P < 0.01$.

correlations to B cells memory, B cells naïve, dendritic cells activated, macrophages M0, macrophages M1, macrophages M2, neutrophils, activated NK cells, resting memory CD4 T cells, CD8 T cells and Tregs, suggesting the relationships of FABP5 mRNA with immune microenvironment of multiple myeloma.

However, the prognostic value of FABP5 mRNA will be confirmed in a multicenter multiple myeloma cohort. Moreover, more experiments should be verified the functions of FABP5 in multiple myeloma progress and immune microenvironment.

CONCLUSION

This study screened 31 abnormally expressed immune-related mRNAs for multiple myeloma. These mRNAs were primarily involved in B cell-related pathways. After verification in multiple datasets, patients with FABP5 mRNA usually unfavorable outcomes. There was crosstalk between immune cells in multiple myeloma bone marrow specimens. FABP5 mRNA displayed significant correlations to infiltrations of immune cells. Taken together, FABP5 mRNA could be a promising therapeutic target as well as prognostic marker in multiple myeloma.

DATA AVAILABILITY STATEMENT

The datasets presented in this study can be found in online repositories. The names of the repository/repositories and accession number(s) can be found in the article/**Supplementary Materials**.

AUTHOR CONTRIBUTIONS

ZZ conceived and designed the study. HJ, XZ, XL, RQ, and YL conducted most of the experiments, data analysis, and wrote the manuscript. SL, HZhu, JW, QK, and HZha participated in collecting data and helped to draft the manuscript. All authors reviewed and approved the manuscript.

SUPPLEMENTARY MATERIAL

The Supplementary Material for this article can be found online at: https://www.frontiersin.org/articles/10.3389/fmed.2021.667525/full#supplementary-material

Supplementary Table 1 | A list of 2,498 immune-related mRNAs.

Supplementary Table 2 | One hundred and thirty-nine abnormally expressed immune-related mRNAs for multiple myeloma in the GSE6477 dataset.

Supplementary Table 3 | One hundred and thirty-nine abnormally expressed immune-related mRNAs for multiple myeloma in the GSE47552 dataset.

REFERENCES

1. Luo SQ, Xiong DH, Li J, Li G, Wang Y, Zhang JM, et al. C1orf35 contributes to tumorigenesis by activating c-MYC transcription in multiple myeloma. *Oncogene*. (2020) 39:3354–66. doi: 10.1038/s41388-020-1222-7
2. Jung SH, Lee HJ, Vo MC, Kim HJ, Lee JJ. Immunotherapy for the treatment of multiple myeloma. *Crit Rev Oncol Hematol*. (2017) 111:87–93. doi: 10.1016/j.critrevonc.2017.01.011
3. Kuehl WM, Bergsagel PL. Multiple myeloma: evolving genetic events and host interactions. *Nat Rev Cancer*. (2002) 2:175–87. doi: 10.1038/nrc746
4. Hou J, Wei R, Qian J, Wang R, Fan Z, Gu C, et al. The impact of the bone marrow microenvironment on multiple myeloma (review). *Oncol Rep*. (2019) 42:1272–282. doi: 10.3892/or.2019.7261
5. Ho M, Chen T, Liu J, Dowling P, Hideshima T, Zhang L, et al. Targeting histone deacetylase 3 (HDAC3) in the bone marrow microenvironment inhibits multiple myeloma proliferation by modulating exosomes and IL-6 trans-signaling. *Leukemia*. (2020) 34:196–209. doi: 10.1038/s41375-019-0493-x
6. Ryu D, Kim SJ, Hong Y, Jo A, Kim N, Kim HJ, et al. Alterations in the transcriptional programs of myeloma cells and the microenvironment during extramedullary progression affect proliferation and immune evasion. *Clin Cancer Res*. (2020) 26:935–44. doi: 10.1158/1078-0432.CCR-19-0694
7. Umezu T, Imanishi S, Yoshizawa S, Kawana C, Ohyashiki JH, Ohyashiki K. Induction of multiple myeloma bone marrow stromal cell apoptosis by inhibiting extracellular vesicle miR-10a secretion. *Blood Adv*. (2019) 3:3228–40. doi: 10.1182/bloodadvances.2019000403
8. Kawano Y, Zavidij O, Park J, Moschetta M, Kokubun K, Mouhieddine TH, et al. Blocking IFNAR1 inhibits multiple myeloma-driven Treg expansion and immunosuppression. *J Clin Invest*. (2018) 128:2487–99. doi: 10.1172/JCI88169
9. Chen T, Moscvin M, Bianchi G. Exosomes in the pathogenesis and treatment of multiple myeloma in the context of the bone marrow microenvironment. *Front Oncol*. (2020) 10:608815. doi: 10.3389/fonc.2020.608815
10. Venken K, Favreau M, Gaublomme D, Menu E, Vanderkerken K, Elewaut D. Checkpoint inhibition in the treatment of multiple myeloma: a way to boost innate-like T cell anti-tumor function? *Mol Immunol*. (2018) 101:521–6. doi: 10.1016/j.molimm.2018.08.019
11. Bailur JK, McCachren SS, Doxie DB, Shrestha M, Pendleton K, Nooka AK, et al. Early alterations in stem-like/resident T cells, innate and myeloid cells in the bone marrow in preneoplastic gammopathy. *JCI Insight*. (2019) 5:e127807. doi: 10.1172/jci.insight.127807
12. Bilotta MT, Abruzzese MP, Molfetta R, Scarno G, Fionda C, Zingoni A, et al. Activation of liver X receptor up-regulates the expression of the NKG2D ligands MICA and MICB in multiple myeloma through different molecular mechanisms. *FASEB J*. (2019) 33:9489–504. doi: 10.1096/fj.201900319R
13. Martín-Antonio B, Suñe G, Najjar A, Perez-Amill L, Antoñana-Vildosola A, Castella M, et al. Extracellular NK histones promote immune cell anti-tumor activity by inducing cell clusters through binding to CD138 receptor. *J Immunother Cancer*. (2019) 7:259. doi: 10.1186/s40425-019-0739-1
14. Vo MC, Anh-NguyenThi T, Lee HJ, Nguyen-Pham TN, Jaya Lakshmi T, Jung SH, et al. Lenalidomide enhances the function of dendritic cells generated from patients with multiple myeloma. *Exp Hematol*. (2017) 46:48–55. doi: 10.1016/j.exphem.2016.11.004
15. Chu TH, Vo MC, Park HS, Lakshmi TJ, Jung SH, Kim HJ, et al. Potent anti-myeloma efficacy of dendritic cell therapy in combination with pomalidomide and programmed death-ligand 1 blockade in a preclinical model of multiple myeloma. *Cancer Immunol Immunother*. (2021) 70:31–45. doi: 10.1007/s00262-020-02654-0
16. Vo MC, Yang S, Jung SH, Chu TH, Lee HJ, Lakshmi TJ, et al. Synergistic antimyeloma activity of dendritic cells and pomalidomide in a murine myeloma model. *Front Immunol*. (2018) 9:1798. doi: 10.3389/fimmu.2018.01798
17. Zhang C, Liao Y, Liu P, Du Q, Liang Y, Ooi S, et al. FABP5 promotes lymph node metastasis in cervical cancer by reprogramming fatty acid metabolism. *Theranostics*. (2020) 10:6561–80. doi: 10.7150/thno.44868
18. Lv Q, Wang G, Zhang Y, Han X, Li H, Le W, et al. FABP5 regulates the proliferation of clear cell renal cell carcinoma cells via the PI3K/AKT signaling pathway. *Int J Oncol*. (2019) 54:1221–32. doi: 10.3892/ijo.2019.4721
19. Bhattacharya S, Andorf S, Gomes L, Dunn P, Schaefer H, Pontius J, et al. ImmPort: disseminating data to the public for the future of immunology. *Immunol Res*. (2014) 58:234–9. doi: 10.1007/s12026-014-8516-1
20. Ritchie ME, Phipson B, Wu D, Hu Y, Law CW, Shi W, et al. limma powers differential expression analyses for RNA-sequencing and microarray studies. *Nucleic Acids Res*. (2015) 43:e47. doi: 10.1093/nar/gkv007
21. Yu G, Wang LG, Han Y, He QY. clusterProfiler: an R package for comparing biological themes among gene clusters. *Omics*. (2012) 16:284–7. doi: 10.1089/omi.2011.0118
22. Newman AM, Liu CL, Green MR, Gentles AJ, Feng W, Xu Y, et al. Robust enumeration of cell subsets from tissue expression profiles. *Nat Methods*. (2015) 12:453–7. doi: 10.1038/nmeth.3337
23. Teramachi J, Tenshin H, Hiasa M, Oda A, Bat-Erdene A, Harada T, et al. TAK1 is a pivotal therapeutic target for tumor progression and bone destruction in myeloma. *Haematologica*. (2020) 106:1401–13. doi: 10.3324/haematol.2019.234476
24. Vandyke K, Zeissig MN, Hewett DR, Martin SK, Mrozik KM, Cheong CM, et al. HIF-2α promotes dissemination of plasma cells in multiple myeloma by regulating CXCL12/CXCR4 and CCR1. *Cancer Res*. (2017) 77:5452–63. doi: 10.1158/0008-5472.CAN-17-0115

25. Waldschmidt JM, Simon A, Wider D, Müller SJ, Follo M, Ihorst G, et al. CXCL12 and CXCR7 are relevant targets to reverse cell adhesion-mediated drug resistance in multiple myeloma. *Br J Haematol*. (2017) 179:36–49. doi: 10.1111/bjh.14807
26. Zmorzyński S, Popek-Marciniec S, Styk W, Wojcierowska-Litwin M, Korszeń-Pilecka I, Szudy-Szczyrek A, et al. The impact of the NOD2/CARD15 variant (3020insC) and PSMA6 polymorphism (-8C>G) on the development and outcome of multiple myeloma. *Biomed Res Int*. (2020) 2020:7629456. doi: 10.1155/2020/7629456
27. Natoni A, Farrell ML, Harris S, Falank C, Kirkham-McCarthy L, Macauley MS, et al. Sialyltransferase inhibition leads to inhibition of tumor cell interactions with E-selectin, VCAM1, and MADCAM1, and improves survival in a human multiple myeloma mouse model. *Haematologica*. (2020) 105:457–67. doi: 10.3324/haematol.2018.212266
28. Frenquelli M, Caridi N, Antonini E, Storti F, Viganò V, Gaviraghi M, et al. The WNT receptor ROR2 drives the interaction of multiple myeloma cells with the microenvironment through AKT activation. *Leukemia*. (2020) 34:257–70. doi: 10.1038/s41375-019-0486-9
29. Liu XP, Yin XH, Meng XY, Yan XH, Wang F, He L. Development and validation of a 9-gene prognostic signature in patients with multiple myeloma. *Front Oncol*. (2018) 8:615. doi: 10.3389/fonc.2018.00615
30. Carbonetti G, Wilpshaar T, Kroonen J, Studholme K, Converso C, d'Oelsnitz S, et al. FABP5 coordinates lipid signaling that promotes prostate cancer metastasis. *Sci Rep*. (2019) 9:18944. doi: 10.1038/s41598-019-55418-x
31. Seo J, Jeong DW, Park JW, Lee KW, Fukuda J, Chun YS. Fatty-acid-induced FABP5/HIF-1 reprograms lipid metabolism and enhances the proliferation of liver cancer cells. *Commun Biol*. (2020) 3:638. doi: 10.1038/s42003-020-01367-5
32. Chen H, Li M, Sanchez E, Soof CM, Bujarski S, Ng N, et al. JAK1/2 pathway inhibition suppresses M2 polarization and overcomes resistance of myeloma to lenalidomide by reducing TRIB1, MUC1, CD44, CXCL12, and CXCR4 expression. *Br J Haematol*. (2020) 188:283–94. doi: 10.1111/bjh.16158
33. De Beule N, De Veirman K, Maes K, De Bruyne E, Menu E, Breckpot K, et al. Tumour-associated macrophage-mediated survival of myeloma cells through STAT3 activation. *J Pathol*. (2017) 241:534–46. doi: 10.1002/path.4860
34. Liu Z, Liu H, He J, Lin P, Tong Q, Yang J. Myeloma cells shift osteoblastogenesis to adipogenesis by inhibiting the ubiquitin ligase MURF1 in mesenchymal stem cells. *Sci Signal*. (2020) 13:eaay8203. doi: 10.1126/scisignal.aay8203
35. André T, Najar M, Stamatopoulos B, Pieters K, Pradier O, Bron D, et al. Immune impairments in multiple myeloma bone marrow mesenchymal stromal cells. *Cancer Immunol Immunother*. (2015) 64:213–24. doi: 10.1007/s00262-014-1623-y

Conflict of Interest: The authors declare that the research was conducted in the absence of any commercial or financial relationships that could be construed as a potential conflict of interest.

Copyright © 2021 Jia, Zhang, Liu, Qiao, Liu, Lv, Zhu, Wang, Kong, Zhang and Zhang. This is an open-access article distributed under the terms of the Creative Commons Attribution License (CC BY). The use, distribution or reproduction in other forums is permitted, provided the original author(s) and the copyright owner(s) are credited and that the original publication in this journal is cited, in accordance with accepted academic practice. No use, distribution or reproduction is permitted which does not comply with these terms.

frontiers in Medicine

ORIGINAL RESEARCH
published: 15 July 2021
doi: 10.3389/fmed.2021.670141

A Novel RNA-Binding Protein Signature to Predict Clinical Outcomes and Guide Clinical Therapy in Gastric Cancer

Zhigang Qiu[1], *Haitao Jiang*[2], *Kun Ju*[3] *and Xichun Liu*[1]*

[1] *Department of Gastrointestinal Surgery, The Affiliated Hospital of Qingdao University, Qingdao, China,* [2] *Department of Oncology, Qingdao Municipal Hospital, Qingdao, China,* [3] *Department of Emergency, The Affiliated Hospital of Qingdao University, Qingdao, China*

Objective: This study aimed to develop an RNA-binding protein (RBP)-based signature for risk stratification and guiding clinical therapy in gastric cancer.

Methods: Based on survival-related RBPs, an RBP-based signature was established by LASSO regression analysis in TCGA dataset. Kaplan–Meier curves were drawn between high- and low-risk groups. The predictive efficacy of this signature was assessed via ROCs at 1-, 3-, and 5-year survival. Its generalizability was verified in an external dataset. Following adjustment with other clinicopathological characteristics, the independency of survival prediction was evaluated via multivariate Cox regression and subgroup analyses. GSEA was utilized in identifying activated pathways in two groups. Stromal score, immune score, tumor purity, and infiltration levels of 22 immune cells were determined in each sample via the ESTIMATE and CIBERSORT algorithms. The sensitivity to chemotherapy drugs was assessed through the GDSC database.

Results: Data showed that patients with high risk exhibited unfavorable clinical outcomes than those with low risk. This signature possessed good performance in predicting 1-, 3-, and 5-year survival and can be independently predictive of patients' survival. Calcium, ECM receptor interaction, and focal adhesion were highly enriched in high-risk samples. High-risk samples presented increased stromal and immune scores and reduced tumor purity. Moreover, this signature presented close relationships with immune infiltrations. Low-risk specimens were more sensitive to sorafenib, gefitinib, vinorelbine, and gemcitabine than high-risk specimens.

Conclusion: This RBP-based signature may be a promising tool for predicting clinical outcomes and guiding clinical therapy in gastric cancer.

Keywords: gastric cancer, RNA binding protein, signature, immune microenvironment, chemosensitivity, nomogram

OPEN ACCESS

Edited by:
Fu Wang,
Xi'an Jiaotong University, China

Reviewed by:
Manh-Cuong Vo,
Chonnam National University Hwasun Hospital, South Korea
Shukui Wang,
Nanjing Medical University, China

***Correspondence:**
Xichun Liu
liuxichun628@163.com

Specialty section:
This article was submitted to Precision Medicine, a section of the journal Frontiers in Medicine

Received: *20 February 2021*
Accepted: *10 May 2021*
Published: *15 July 2021*

Citation:
Qiu Z, Jiang H, Ju K and Liu X (2021) A Novel RNA-Binding Protein Signature to Predict Clinical Outcomes and Guide Clinical Therapy in Gastric Cancer. Front. Med. 8:670141. doi: 10.3389/fmed.2021.670141

INTRODUCTION

Gastric cancer ranks fifth in incidence and third mortality among global cancers (1, 2). Patients are diagnosed in histology following endoscopic biopsy and staged by computed tomography, endoscopic ultrasound, positron emission tomography, or laparoscopy (3). This cancer is a highly heterogeneous disease at the molecular and phenotypic levels. Subjects diagnosed by the same TNM stage and treated by similar therapeutic regimens present varied prognoses, emphasizing that TNM stage by itself cannot provide complete prognostic information (4). Endoscopic surgery is a primary therapeutic method for early subjects. Nevertheless, most patients are diagnosed at an advanced stage, who have missed the optimal time for surgery. Despite adjuvant chemotherapy, immunotherapy, and targeted therapy, advanced subjects' median survival time is <1 year (5). Hence, innovative strategies are required for boosting risk stratification as well as predictive accuracy of clinical outcomes.

RNA-binding proteins (RBPs), a type of protein, may be interacted with a variety of RNAs. At present, 1,542 human RBP genes have been found, which participate in posttranscriptional modulation such as RNA splicing, polyadenylation, editing, modification, and translation (6–8). Aberrant expression of RBPs may induce progress of various malignancies, including gastric cancer (9, 10). RBPs have been detected to widely express in tumor cells, thereby affecting the translation of mRNAs into proteins and carcinogenesis processes (11). Increasing evidence has highlighted clinicopathologic implication of immune microenvironment in survival outcomes and therapeutic efficacy in gastric cancer (12). Recent findings have found that RBPs may affect immune microenvironment across different cancer types (13). For example, RBP SORBS2 inhibits metastatic colonization of ovarian cancer through enhancing stability of tumor-suppressive immunomodulatory transcripts (13). In-depth understanding of the roles of RBPs will offer innovative ideas for immunotherapy of gastric cancer. Previously, Huang et al. (14) proposed a 6-RBP signature that predicted the survival of hepatocellular carcinoma with high accuracy. Li et al. (15) developed a 9-RBP signature with accurate predictive efficacy for lung squamous cell carcinoma patients' prognosis. However, there is still lack of gene signature based on RBPs for gastric cancer. Furthermore, the relationships between RBPs and immune microenvironment are required for further analysis. Here, this work developed and verified an RBP-based model that exhibited a good performance in predicting patients' survival and was significantly associated with immune microenvironment using public datasets.

Abbreviations: RBP, RNA-binding protein; TCGA, the cancer genome atlas; GEO, gene expression omnibus; LASSO, least absolute shrinkage and selection operator; ROC, receiver operating characteristic curve; AUC, area under the curve; HR, hazard ratio; CI, confidence interval; GSEA, gene set enrichment analysis; ESTIMATE, estimation of STromal and immune cells in MAlignant tumour tissues using expression data; CIBERSORT, Cell type identification by estimating relative subsets of RNA transcripts; GDSC, genomics of drug sensitivity in cancer; IC_{50}, half maximal inhibitory concentration.

MATERIALS AND METHODS

Gastric Cancer Datasets Acquiring and Preprocessing

Transcriptome FPKM RNA-seq profiles of gastric cancer were retrieved from the Cancer Genome Atlas (TCGA; https://tcga-data.nci.nih.gov/tcga/). Meanwhile, clinical information, including age, gender, grade, stage, TNM, and overall survival, was acquired by the UCSC Xena (https://xena.ucsc.edu/). The details are listed in **Supplementary Table 1**. After excluding samples with survival time of 0, 350 cases of gastric cancer specimens were retained as a training set. FPKM values were converted to TPM values for normalization (16). In the Gene Expression Omnibus (GEO; https://www.ncbi.nlm.nih.gov/gds/) repository, the GSE84437 dataset was obtained on the GPL6947 platform (17). A total of 431 samples with survival time >0 were utilized as a validation set. The clinical information is shown in **Supplementary Table 2**. Based on a previous published study, 1,542 RBPs were retrieved (**Supplementary Table 3**) (18).

Establishment and Validation of a Prognostic RNA-Binding Protein Gene Signature

Univariate Cox regression analyses were employed for analyzing associations between RBPs and clinical outcomes of gastric cancer. Prognosis-related RBPs with $p < 0.05$ were retained. Then, least absolute shrinkage and selection operator (LASSO) regression analyses were adopted to acquire key prognostic RBPs (19). The risk scores of subjects were determined following the formula: risk score $= \Sigma$ expression level of $gene_i$ * β_i. β represents the regression coefficient of $gene_i$. Then, the median value was utilized as the cutoff value. Subjects were separated into high- and low-risk subgroups. Utilizing Kaplan–Meier curves, survival probability between the two groups was compared by log-rank test. Receiver operating characteristic curves (ROCs) for 1-, 3-, and 5-year survival were conducted via the ROC package in R. Area under the curve (AUC) was then determined. With the same cutoff value, predictive efficacy of the RBP gene signature was validated in the verification set.

Protein–Protein Interaction Analysis

Functional associations between prognosis-related RBPs were predicted by the STRING online database (http://www.bork.embl-heidelberg.de/STRING/) (20).

Univariate and Multivariate Cox Regression Analyses

To analyze the relationships between clinical factors (age, gender, grade, stage, TNM, and risk score) and survival, univariate Cox regression analyses were carried out in the training and verification sets, separately. The independency of survival prediction of clinical factors was evaluated via multivariate Cox regression analyses. Hazard ratio

TABLE 1 | Univariate Cox regression analyses of survival-related RBPs in gastric cancer.

RBPs	HR	HR.95L	HR.95H	*P*	RBPs	HR	HR.95L	HR.95H	*P*
DAZAP1	0.6867	0.4886	0.9651	0.0304	TRIM25	0.6839	0.5358	0.873	0.0023
MSI2	0.7234	0.5639	0.9279	0.0108	ZFP36	1.2598	1.0622	1.4943	0.008
RBMS1	1.3013	1.0761	1.5735	0.0066	PURG	2.2696	1.11	4.6405	0.0247
RBMS3	1.248	1.0654	1.4619	0.0061	TSEN54	0.7761	0.6073	0.9919	0.0429
METTL2B	0.6348	0.4591	0.8777	0.006	EZH2	0.8015	0.6591	0.9746	0.0266
AKAP8	0.6722	0.4699	0.9618	0.0298	QKI	1.3028	1.0735	1.5811	0.0074
REPIN1	0.7522	0.6048	0.9356	0.0105	ISY1	0.658	0.4371	0.9905	0.0449
DZIP1	1.2199	1.0257	1.4509	0.0246	PPAN	0.735	0.5451	0.9911	0.0436
DYNLL1	1.5709	1.0392	2.3746	0.0322	RAVER1	0.7913	0.6337	0.9881	0.0389
GLE1	0.7245	0.5553	0.9452	0.0175	ENOX1	1.2325	1.0315	1.4726	0.0214
BOLL	1.8406	1.1722	2.8899	0.008	RNASE11	24.976	1.6554	376.83	0.0201
FBXO17	1.1401	1.0076	1.2899	0.0374	TRMT1	0.7019	0.5141	0.9584	0.0259
PWP2	1.3298	1.0832	1.6325	0.0065	RNASE13	13.306	2.5541	69.315	0.0021
MRPL4	0.7253	0.5586	0.9419	0.016	FTO	1.3563	1.0175	1.808	0.0377
QTRT1	0.7165	0.5246	0.9785	0.036	FAM98C	0.7202	0.5215	0.9947	0.0464
GTPBP3	0.7488	0.5634	0.9952	0.0463	PCF11	0.7254	0.5332	0.9869	0.041
SMAD5	1.3215	1.0084	1.7319	0.0433	TTF2	0.7462	0.5723	0.9731	0.0307
ADARB1	1.2343	1.011	1.5069	0.0387	TLR7	1.2283	1.0284	1.4669	0.0232
POLRMT	0.7285	0.5607	0.9466	0.0178	PABPC5	1.5082	1.0935	2.0801	0.0123
LENG9	0.8052	0.6575	0.9862	0.0362	RBM15	0.7482	0.5637	0.9932	0.0448
RNASE9	8.1851	1.8494	36.225	0.0056	NR0B1	3.9608	1.7366	9.0333	0.0011
REXO1	0.7606	0.5846	0.9895	0.0415	RPS4Y2	1.8092	1.1338	2.8869	0.0129
NXF5	8.1997	1.7738	37.904	0.0071	ADAT3	0.7003	0.5595	0.8764	0.0019
PEG10	1.1012	1.018	1.1912	0.0162	BICC1	1.208	1.0468	1.3941	0.0097
RNASE1	1.2357	1.0853	1.407	0.0014	SURF6	0.7307	0.5512	0.9685	0.0291
RNASE2	1.2156	1.0392	1.4219	0.0147	RPS23	1.3576	1.0036	1.8364	0.0473
RNASE3	1.3758	1.112	1.7022	0.0033	IFIT1	1.1369	1.005	1.2862	0.0414
HEXIM2	0.713	0.5087	0.9995	0.0497	NOVA1	1.2027	1.0229	1.4141	0.0255
LARP6	1.2314	1.0523	1.441	0.0094	EIF1AD	0.6806	0.4697	0.9862	0.042

RBPs, RNA-binding proteins; HR, hazard ratio; HR.95L, lower 95% confidence interval; HR.95H, higher 95% confidence interval.

(HR), 95% confidence interval (CI), and p values were calculated, respectively.

Subgroup Analyses

Patients were separated into different subgroups on the basis of different clinicopathological characteristics, including age (>65 and ≤65), gender (female and male), grade (grades 1–2 and grade 3), stage (stages I–II and stages III–IV), T (T1–2 and T3–4), N (N0 and N1–3), and M (M0 and M1). Kaplan–Meier curves followed by log-rank test were presented between high- and low-risk subjects in above subgroups.

Pathway Enrichment Analysis

The gene set enrichment analysis (GSEA) 4.0.3 software was utilized in identifying activated signaling pathways in high- and low-risk subgroups (21, 22). This study retrieved the hallmark gene set (h.all.v6.0.symbol.gmt) from the Molecular Signatures Database as a reference gene set. Enriched pathways were screened according to nominal p <0.05 and adjusted $p < 0.05$.

Estimation of Stromal Score, Immune Score, and Tumor Purity

Stromal score, immune score, and tumor purity for each specimen were evaluated via the Estimation of STromal and Immune cells in MAlignant Tumour tissues using Expression data (ESTIMATE) algorithm (23). The differences in stromal score, immune score, and tumor purity between the two subgroups were compared through the Wilcoxon rank-sum test. Kaplan–Meier curves were conducted for estimating survival differences between different subgroups, as follows: high vs. low stromal score, high vs. low immune score, and high and low tumor purity.

Assessment of Immune Cell Infiltration

The infiltration levels of 22 immune cell types were quantified in gastric cancer specimens utilizing the Cell type Identification by Estimating Relative Subsets of RNA Transcripts (CIBERSORT)

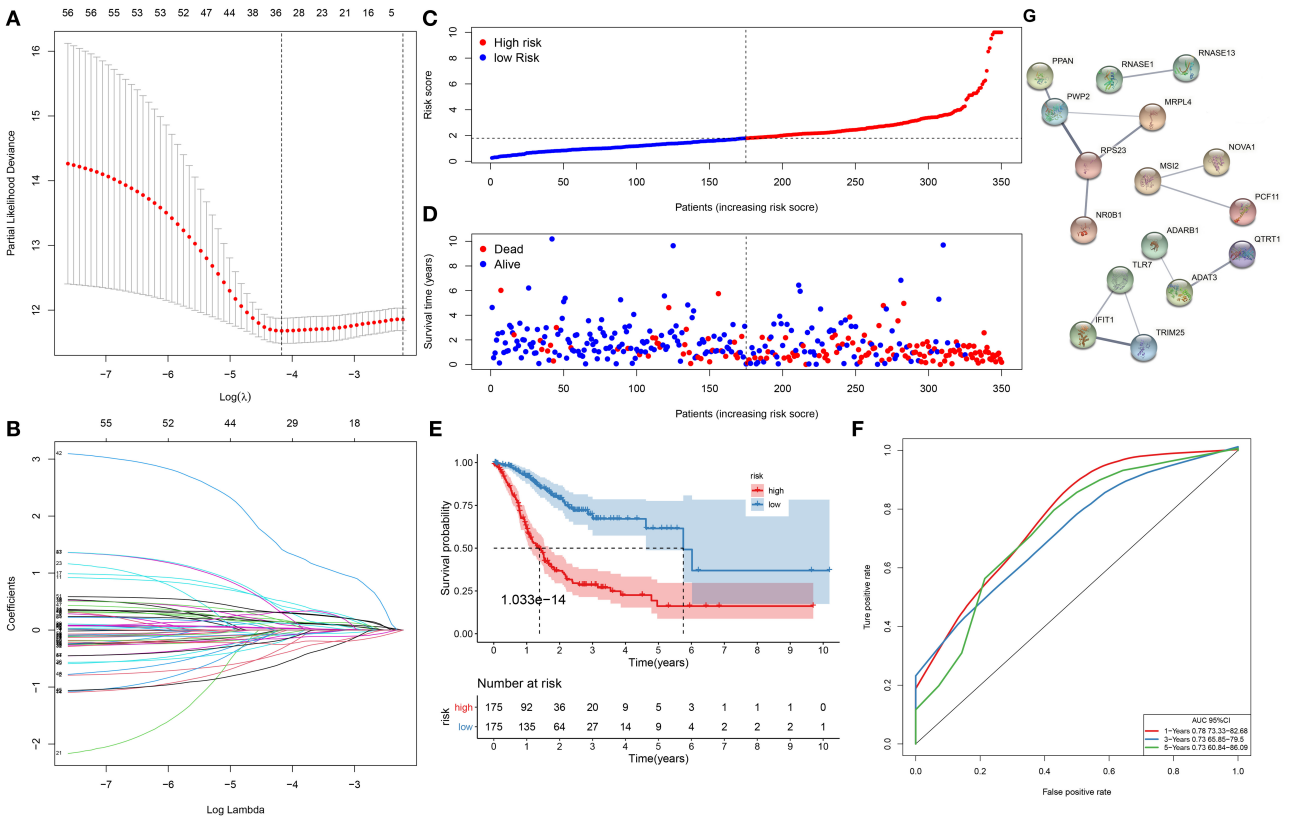

FIGURE 1 | A gene signature for predicting the survival of gastric cancer patients. **(A)** The optimal parameter (λ) is where the vertical dotted line is. **(B)** Regression coefficients for RNA-binding proteins (RBPs) when determining the optimal parameter (λ). Each curve represents the change in trajectory of coefficients for each independent variable, and the ordinate indicates the coefficient values. **(C)** The distribution of risk scores for all subjects. The vertical dotted line corresponds to the median value of risk scores. **(D)** Survival status for all subjects ranked by risk scores. **(E)** Kaplan–Meier curves of overall survival between high- and low-risk subjects. **(F)** Receiver operating characteristic curves (ROCs) of 1-, 3-, and 5-year survival. **(G)** A protein–protein interaction (PPI) network based on the 33 key RBP genes.

algorithm as well as the LM22 gene sets containing 547 markers (24). The comparison of immune cell types between the high- and low-risk groups was carried out through the Wilcoxon rank-sum test.

Estimation of Immune Checkpoint Expression

The expression levels of 47 immune checkpoints were estimated in gastric cancer samples. Their expression was compared in the high- and low-risk groups by the Wilcoxon rank-sum test.

Drug Sensitivity Assessment

The sensitivity to different chemotherapy drugs for each sample was estimated through the Genomics of Drug Sensitivity in Cancer (GDSC; https://www.cancerrxgene.org/) database (25). The calculation of half maximal inhibitory concentration (IC_{50}) was achieved through the pRRophetic package in R (26).

Construction a Prognostic Nomogram Model

A nomogram model construction was achieved by the rms package as well as the survival package in R. This nomogram contained independent prognostic factors. Calibration curves were then depicted for evaluation of the predictive potency for 1-, 3-, and 5-year clinical outcomes of this nomogram.

Statistical Analyses

All analyses were achieved by available packages in R language 3.4.1 (http://www.R-project.org). Comparisons between the two groups were performed by the Wilcoxon rank-sum test or Student' *t*-test. Values of $p < 0.05$ indicated statistical significance.

RESULTS

Construction of a Prognostic Signature for Gastric Cancer

Herein, 350 gastric cancer specimens were employed as the training set. Totally, 58 RBPs exhibited significant associations with survival of gastric cancer patients (**Table 1**). To avoid data overfitting, coexpressed RBPs were eliminated through LASSO regression analyses (**Figures 1A,B**). Consequently, 33 key RBPs were retained for establishment of a prognostic signature. We determined the risk scores of all subjects. **Table 2** listed the

TABLE 2 | The coefficients of 33 key RBPs in the gene signature.

Gene	Coef	Gene	Coef	Gene	Coef
MSI2	−0.41056215	RNASE3	0.148036367	PCF11	−0.586573788
METTL2B	−0.105183273	HEXIM2	−0.068963889	TTF2	−0.001441001
DYNLL1	0.181641481	TRIM25	−0.151111951	TLR7	0.013281286
BOLL	0.511182302	ZFP36	0.118338975	PABPC5	−0.00140872
PWP2	0.311152879	PURG	−0.02930587	NR0B1	0.319435254
MRPL4	−0.322619794	TSEN54	0.161142621	RPS4Y2	0.301449471
QTRT1	−0.062291791	ISY1	−0.196715792	ADAT3	−0.255476366
SMAD5	0.420293951	PPAN	0.301063239	BICC1	−0.002450685
ADARB1	0.096350867	RNASE13	1.413824833	RPS23	0.121943685
PEG10	0.025434693	FTO	0.364676671	IFIT1	0.036295595
RNASE1	0.147258292	FAM98C	−0.099287095	NOVA1	−0.173519708

Coef, coefficients.

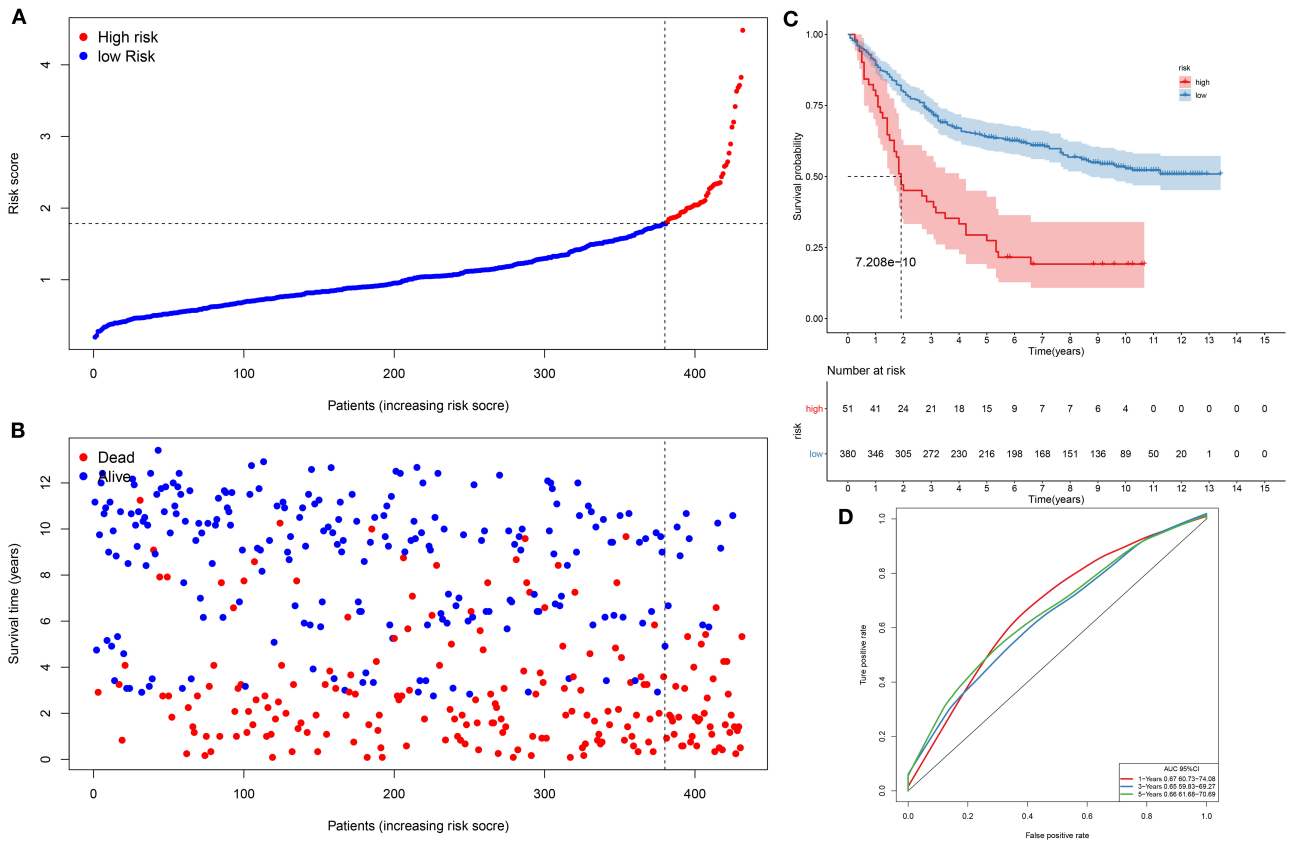

FIGURE 2 | Assessment of this prognostic signature in the verification dataset. **(A)** The ranking of risk scores, and **(B)** the distribution of survival status among gastric cancer samples. The vertical dotted line corresponds to the cutoff of risk scores. **(C)** Kaplan–Meier curves of clinical outcomes concerning high- and low-risk subjects. **(D)** ROCs of 1-, 3-, and 5-year survival.

regression coefficients of these key RBPs. Then, these subjects were separated into high- and low-risk groups (**Figure 1C**). In **Figure 1D**, the number of dead patients in the high-risk group was significantly higher than that in the low-risk group. The difference in survival between groups was compared in depth. **Figure 1E** displayed that subjects with high risk often experienced more unfavorable survival time than those with low risk (p = 1.033e−14). Following confirmation by ROCs, the AUCs for 1-, 3-, and 5-year clinical outcomes were separately 0.779, 0.759, and 0.788 (**Figure 1F**). These data were indicative

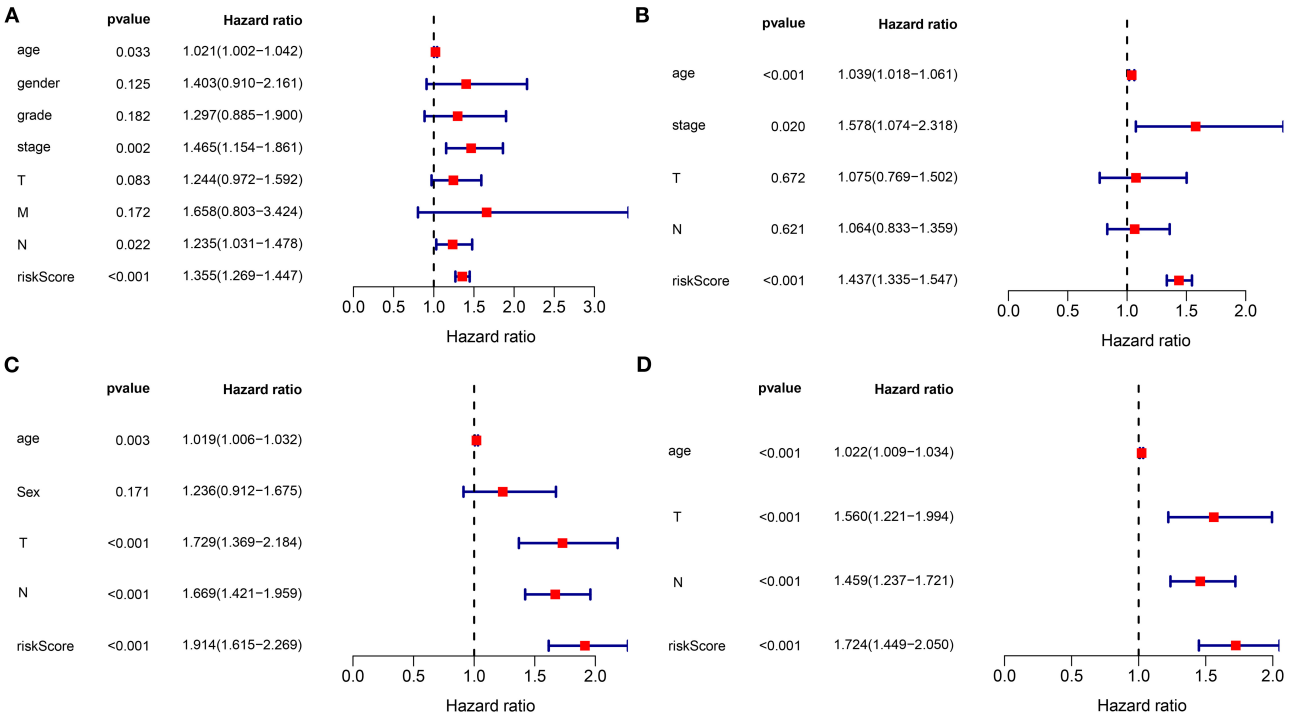

FIGURE 3 | The signature as an independent risk factor of gastric cancer. **(A)** Univariate and **(B)** multivariate Cox regression analyses of age, gender, grade, stage, TNM, as well as signature for gastric cancer in the training set. **(C)** Univariate and **(D)** multivariate Cox regression analyses for age, sex, T, N, and risk score for gastric cancer in the verification set.

of the predictive potential of the signature. To observe the interactions between 33 key RBPs, we constructed a PPI network. In **Figure 1G**, 14 key RBPs had mutual regulation.

Verification of the Prognostic Signature in an External Dataset

We further evaluated the generalizability of the signature in the GSE84437 dataset. With the same cutoff value, subjects were separated into high- and low-risk subgroups (**Figure 2A**). Compared with the low-risk group, there were more patients with dead status in the high-risk group (**Figure 2B**). Those with high risk presented worse survival time than those with low risk (p = 7.208e−10; **Figure 2C**). The AUCs of 1-, 3-, and 5-year clinical outcomes were separately 0.647, 0.645, and 0.669, which was suggestive that this signature might be used in predicting the patients' survival (**Figure 2D**).

The Signature as an Independent Prognostic Factor for Gastric Cancer

In the training set, our univariate Cox regression analyses were indicative that risk score presented a significant correlation with gastric cancer prognosis [$p < 0.001$; HR (95% CI): 1.355 (1.269–1.447)] in **Figure 3A**. Moreover, age ($p = 0.033$; HR (95%CI): 1.021 (1.002–1.042)], stage ($p = 0.002$; HR (95% CI): 1.465 (1.154–1.861)], and N [$p = 0.022$; HR (95%CI): 1.235 (1.031–1.478)] were also correlated to gastric cancer prognoses. Above were risk factors of gastric cancer. Following multivariate Cox regression analyses, age [$p < 0.001$; HR (95% CI): 1.039 (1.018–1.061)], stage [$p = 0.020$; HR (95% CI): 1.578 (1.074–2.318], and this gene signature [$p < 0.001$; HR (95% CI): 1.437 (1.335–1.547)] independently predicted the patients' survival (**Figure 3B**). We further verified the independency of the signature in predicting prognosis in an external dataset. Data showed that age [$p = 0.003$; HR (95% CI): 1.019 (1.006–1.032)], T [$p < 0.001$; HR (95% CI): 1.729 (1.369–2.184)], N ($p < 0.001$; HR (95% CI): 1.669 (1.421–1.959)], and this gene signature [$p < 0.001$; HR (95% CI): 1.914 (1.615–2.269)] were risk factors of gastric cancer (**Figure 3C**). By confirmation of multivariate Cox regression analyses, age [$p < 0.001$; HR (95% CI): 1.022 (1.009–1.034)], T [$p < 0.001$; HR (95% CI): 1.560 (1.221–1.994)], N [$p < 0.001$; HR (95% CI): 1.459 (1.237–1.721)], and this gene signature [$p < 0.001$; HR (95% CI): 1.724 (1.449–2.050)] were independently predictive of clinical outcomes (**Figure 3D**). Collectively, this signature was an independent risk factor of gastric cancer.

Subgroup Analysis of the Signature in Predicting Gastric Cancer Patients' Survival

Subgroup analysis was presented to assess whether the signature was accurately predictive of patients' clinical outcomes in the training set. Data indicated that subjects with high risk were indicative of more unfavorable survival in comparison with those with low risk in different subgroups according to age (>65 and ≤65; **Figures 4A,B**), gender (female and male; **Figures 4C,D**),

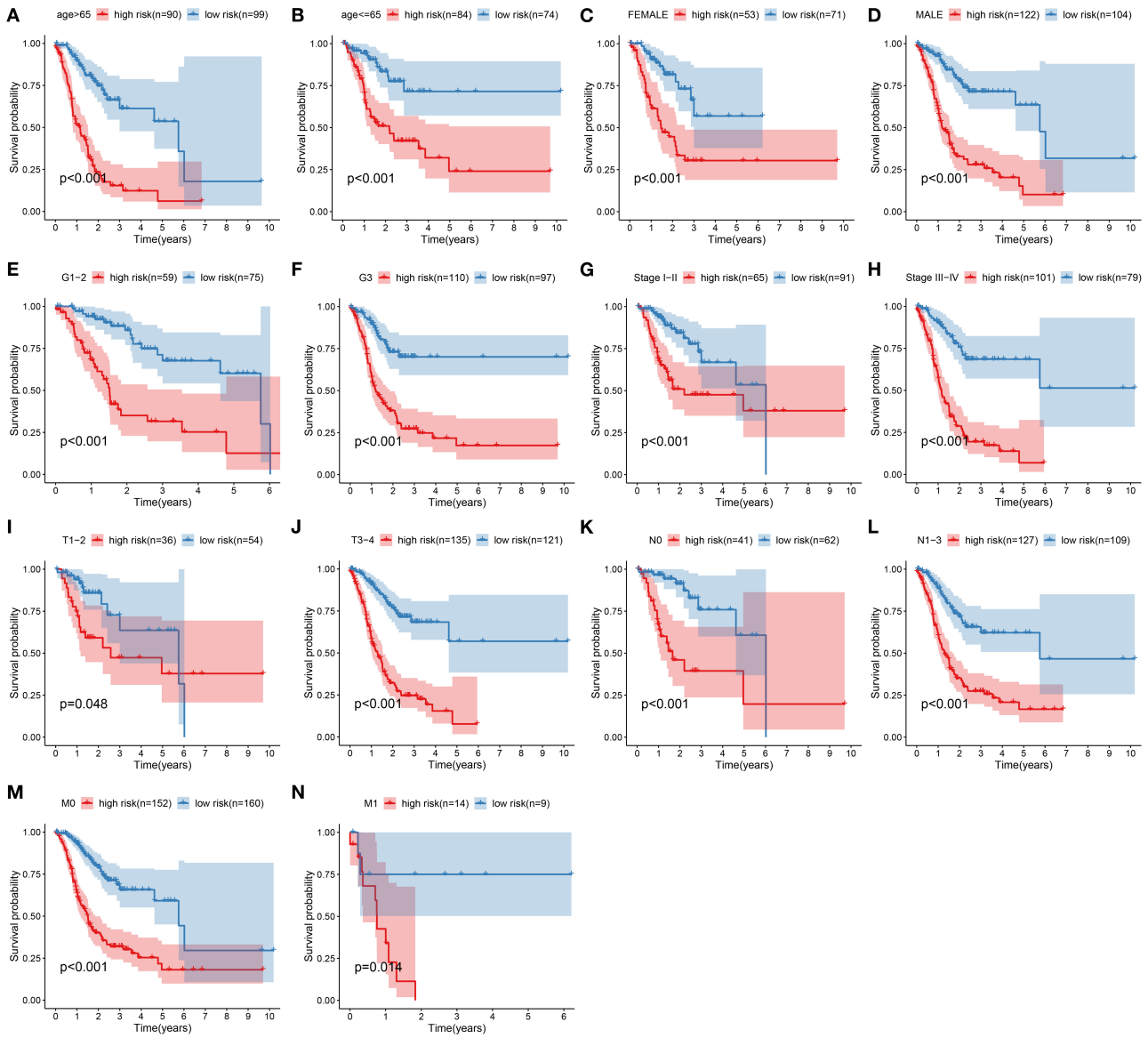

FIGURE 4 | Subgroup analysis of the signature in predicting gastric cancer patients' survival. Kaplan–Meier curves for high- and low-risk subjects in different subgroups including **(A)** age >65, **(B)** age ≤65; **(C)** female, **(D)** male; **(E)** grades 1–2, **(F)** grade 3; **(G)** stages I–II, **(H)** stages III–IV; **(I)** T1–2, **(J)** T3–4; **(K)** N0, **(L)** N1–3; **(M)** M0, **(N)** M1.

grade (G1–2 and G3; **Figures 4E,F**), stage (stages I–II and III–IV; **Figures 4G,H**), T (T1–2 and T3–4; **Figures 4I,J**), N (N0 and N1–3; **Figures 4K,L**), as well as M (M0 and M1; **Figures 4M,N**).

Signaling Pathways Involved in High- and Low-Risk Subgroups

This study evaluated the signaling pathways enriched by high- and low-risk samples via the GSEA in depth. Data indicated that calcium signaling pathway, ECM receptor interaction, and focal adhesion were highly enriched in high-risk samples (**Figure 5A**). In **Figure 5B**, base excision repair, cell cycle, DNA replication, mismatch repair, P53 signaling pathway, as well as spliceosome were highly enriched in low-risk specimens.

Association Between This Signature and Tumor Microenvironment

This study next probed the association between this signature and tumor microenvironment in the training set. In **Figure 6A**, high-risk specimens presented an increased stromal score ($p = 6.9e{-}11$) and immune score ($p = 0.0029$) than low-risk subjects. Meanwhile, high-risk subjects displayed distinctly lowered tumor purity in comparison with those with low risk ($p = 4.2e{-}07$).

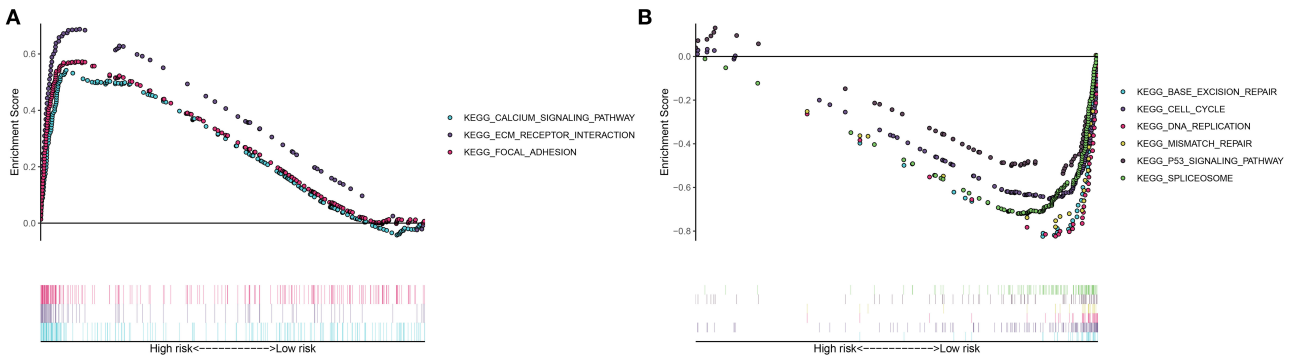

FIGURE 5 | Gene set enrichment analysis (GSEA) for signaling pathways involved in high- and low-risk groups. **(A)** Highly enriched pathways in high-risk gastric cancer samples. **(B)** Highly enriched pathways in low-risk specimens.

Prognostic values of stromal score, immune score, and tumor purity were then evaluated in gastric cancer. As a result, high stromal score was distinctly related to poorer prognosis than low stromal score ($p = 0.014$; **Figure 6B**). No significant difference in survival was found between high- and low-immune score groups ($p = 0.126$; **Figure 6C**). Moreover, high tumor purity was distinctly associated with prolonged survival duration ($p = 0.045$; **Figure 6D**). We further assessed whether the signature was in association with immune cell infiltrations in gastric cancer tissues from TCGA dataset. Data were indicative that subjects with high risk exhibited increased infiltration levels of T-cell CD4 memory resting ($p < 0.01$), monocytes ($p < 0.05$), macrophages M2 ($p < 0.01$), and mast cells resting ($p < 0.05$) in **Figure 6E**. Moreover, high-risk subjects had reduced infiltration levels of T-cell CD4 memory activated as well as T-cell follicular helper (both $p < 0.01$) than those with low risk. Furthermore, we found that high risk was characterized by increased expression of immune checkpoints including BTLA ($p < 0.01$), BTNL2 ($p < 0.05$), CD200 ($p < 0.001$), CD200R1 ($p < 0.05$), CD27 ($p < 0.05$), CD276 ($p < 0.05$), CD28 ($p < 0.01$), CD40 ($p < 0.01$), CD40LG ($p < 0.01$), CD44 CD40 ($p < 0.05$), CD48 ($p < 0.01$), CD40 ($p < 0.01$), CD86 ($p < 0.001$), HAVCR2 ($p < 0.01$), LAIR1 ($p < 0.01$), NRP1 ($p < 0.001$), PDCD1LG2 ($p < 0.001$), TMIGD2 ($p < 0.05$), TNFSF14 ($p < 0.05$), TNFSF18 ($p < 0.001$), TNFSF4 ($p < 0.001$), and VSIR ($p < 0.05$; **Figure 6F**).

Correlation Between This Signature and Drug Sensitivity

We further evaluated the sensitivity to chemotherapy drugs between high- and low-risk groups. Our data were indicative of increased IC_{50} values of sorafenib ($p = 5.23–05$; **Figure 7A**), gefitinib ($p = 0.011$; **Figure 7B**), vinorelbine ($p = 0.006$; **Figure 7C**), and gemcitabine ($p = 0.011$; **Figure 7D**) in specimens with high risk than those with low risk. Hence, low-risk specimens were more sensitive to sorafenib, gefitinib, vinorelbine, and gemcitabine than high-risk specimens.

Establishment of a Nomogram Integrating Age, Stage, and Risk Score

To personally predict the prognosis of each subject, a nomogram was established via integrating age, stage, and gene signature, which could be predictive of 1-, 3-, and 5-year survival probability (**Figure 8A**). Through confirmation of these calibration curves, 1-, 3-, and 5-year clinical outcomes by this nomogram exhibited high consistency with actual clinical outcomes for gastric cancer subjects in the training set (**Figures 8B–D**).

DISCUSSION

This study developed an RBP-based signature in the prediction of gastric cancer patients' survival. Subjects with high risk presented an unacceptable clinical outcome. Following verification, this signature was independently predictive of prognosis of patients. Moreover, it was distinctly related to immune microenvironment and sensitivity to chemotherapy drugs. Hence, this RBP-based signature may be a promising tool for predicting clinical outcomes and guiding clinical therapy in gastric cancer.

The molecular heterogeneity features between high- and low-risk patients were further analyzed. We found that calcium signaling pathway, ECM receptor interaction, and focal adhesion were highly activated in high-risk samples. Previously, calcium facilitates gastric carcinoma progress through calcium-sensing receptor as well as TRPV4 (27). Furthermore, VPAC1 and TRPV4 channels may accelerate gastric cancer progress by relying on calcium (28). The ECM receptor contributes to carcinogenesis, progress, and unfavorable survival in gastric cancer (29). Focal adhesion-related proteins are independently predictive of pessimistic clinical outcomes in gastric cancer (30). Meanwhile, activation of base excision repair, cell cycle, DNA replication, mismatch repair, P53 signaling pathway, as well as spliceosome was detected in low-risk specimens. The clinical implications of DNA repair like base excision repair and mismatch repair have been confirmed in gastric cancer (31). Deregulation of p53 pathway induces malignant biological properties for gastric cancer cells (32).

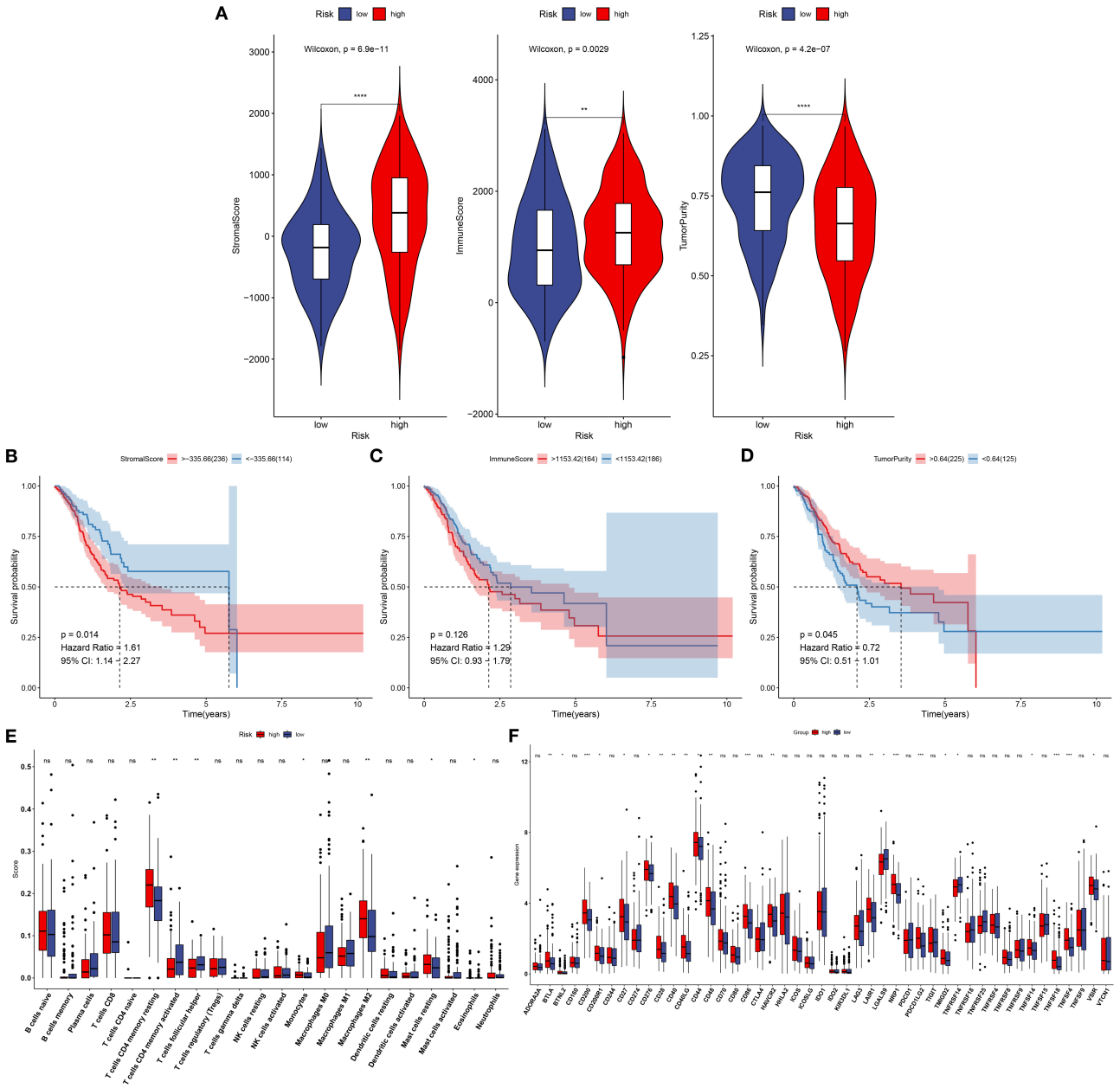

FIGURE 6 | Association between this signature and tumor microenvironment in the training set. **(A)** Violin plots for stromal score, immune score, and tumor purity of high- and low-risk specimens via the ESTIMATE. **(B)** Kaplan–Meier curves of high- and low-stromal score groups. **(C)** Kaplan–Meier curves of high- and low-immune score groups. **(D)** Kaplan–Meier curves of high- and low-tumor purity groups. **(E)** Box plots for infiltration levels of immune cells in high- and low-risk samples through the CIBERSORT. **(F)** Box plots for expression of immune checkpoints in high- and low-risk samples. Ns, not significant. *$p < 0.05$; **$p < 0.01$; ***$p < 0.001$; ****$p < 0.0001$.

Immune cell ingredients contribute to gastric cancer initiation and progression. Moreover, immune escape exerts a critical role in tumorigenesis. Immune infiltration levels distinctly affect patients' survival. Tumor immune microenvironment that contains stromal and immune cells exhibits an association with immunotherapy response (5). Immune cells are correlated with tumor invasion and metastases. Stromal cells present close relationships with tumor growth, progression, response to chemotherapy, as well as recurrence. This study demonstrated that high-risk subjects had increased immune and stromal scores than those with low risk. Consistently, Mao et al. (33) found that subjects with high stromal scores presented unfavorable clinical outcomes. At present, novel immunotherapies like anti-PD-1 and anti-PD-L1 have been applied in gastric cancer. Nevertheless, only a minority of subjects benefit from immunotherapies. The compositions in the immune

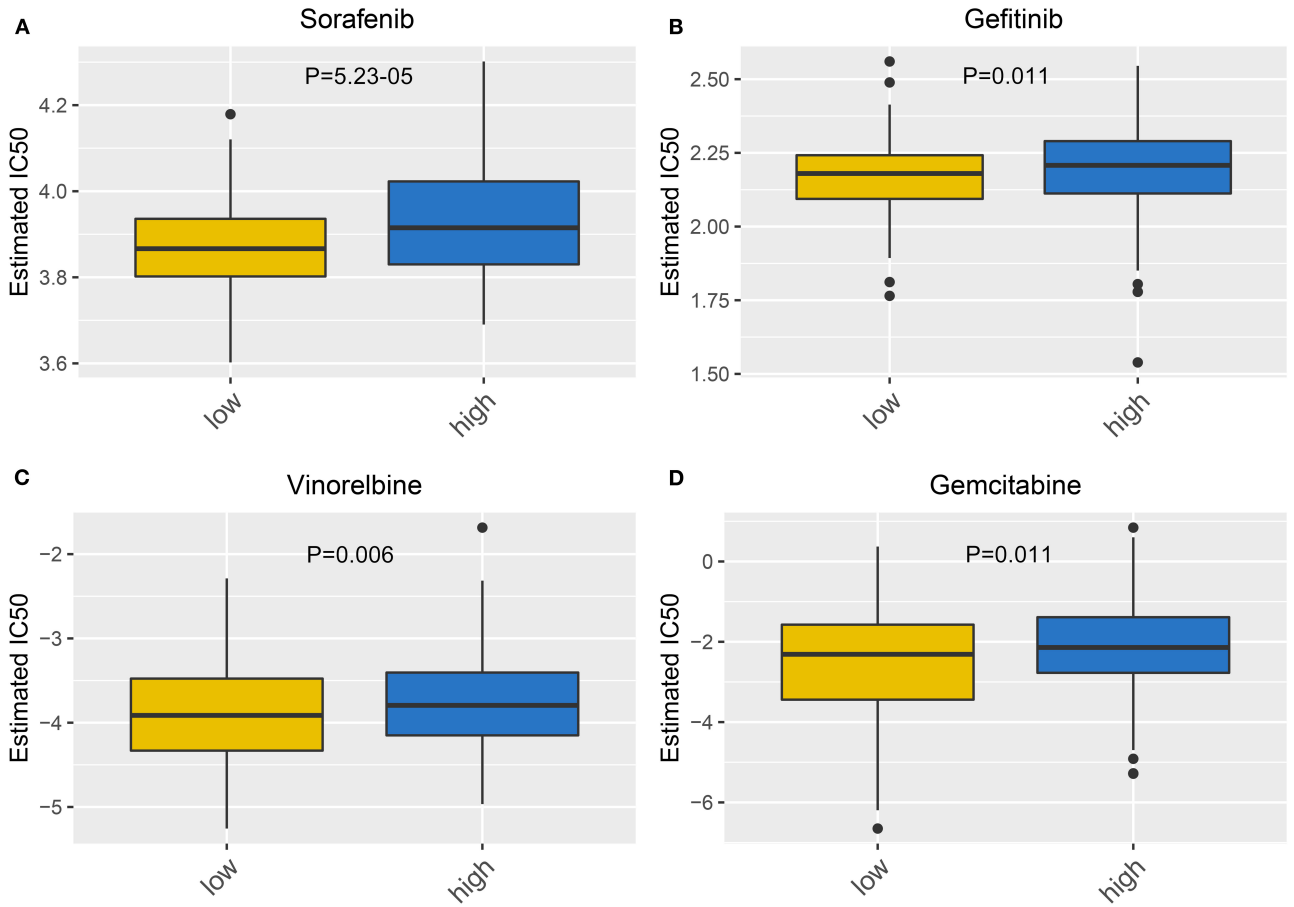

FIGURE 7 | Correlation between this signature and drug sensitivity. Box plots for estimated IC_{50} of **(A)** sorafenib, **(B)** gefitinib, **(C)** vinorelbine, and **(D)** gemcitabine between high- and low-risk gastric cancer specimens.

microenvironment are key determinants for prognoses and response to immunotherapies (34). Herein, this study comprehensively analyzed the correlations between immune cell infiltrations and this signature via the CIBERSORT algorithm. High-risk subjects presented increased infiltration levels of T-cell CD4 memory resting, monocytes, macrophage M2, and mast cells resting, and had reduced infiltration levels of T-cell CD4 memory activated as well as T-cell follicular helper than those with low risk. Moreover, we found that high risk was characterized by increased expression of immune checkpoints including BTLA that was expressed in B and T lymphocytes, BTNL2 that was expressed in antigen-processing and presentation cells, CD200 that was mainly expressed in B and T lymphocytes, CD200R1 that was expressed in myeloid lineage cells, CD27 that was expressed in T cells, CD276 that was expressed in cancer cells, CD28 that was expressed in T cells, CD40 that was expressed in antigen-presenting cells, CD40LG that was expressed in T cells, CD44 that was expressed in T cells, CD48 that was expressed in lymphocytes and dendritic cells, CD86 that was expressed in antigen-presenting cells, HAVCR2 that was expressed in T cells, LAIR1 that was expressed in natural killer cells, T cells, and B cells, NRP1 that was expressed in cancer cells, PDCD1LG2 that was expressed in T cells and dendritic cells, TMIGD2 that was expressed in T cells, TNFSF14 that was expressed in T cells, TNFSF18 that was expressed in T cells, TNFSF4 that was expressed in T cells, and VSIR that was expressed in T cells. These data were indicative of this signature being closely related to immunotherapy.

For advanced subjects, surgical resection followed by auxiliary chemotherapy is a major therapeutic strategy. In recent years, a few clinical trials of postoperative chemotherapy have been launched in gastric cancer (35–37). Miserably, response to chemotherapy is relatively low on account of tumor heterogeneity (38). Our data indicated that subjects with low risk were more sensitive to sorafenib, gefitinib, vinorelbine, and gemcitabine than those with high risk. This RBP-based signature seems to be considered as a classification tool for making individualized therapeutic decisions. Furthermore, a nomogram was then developed

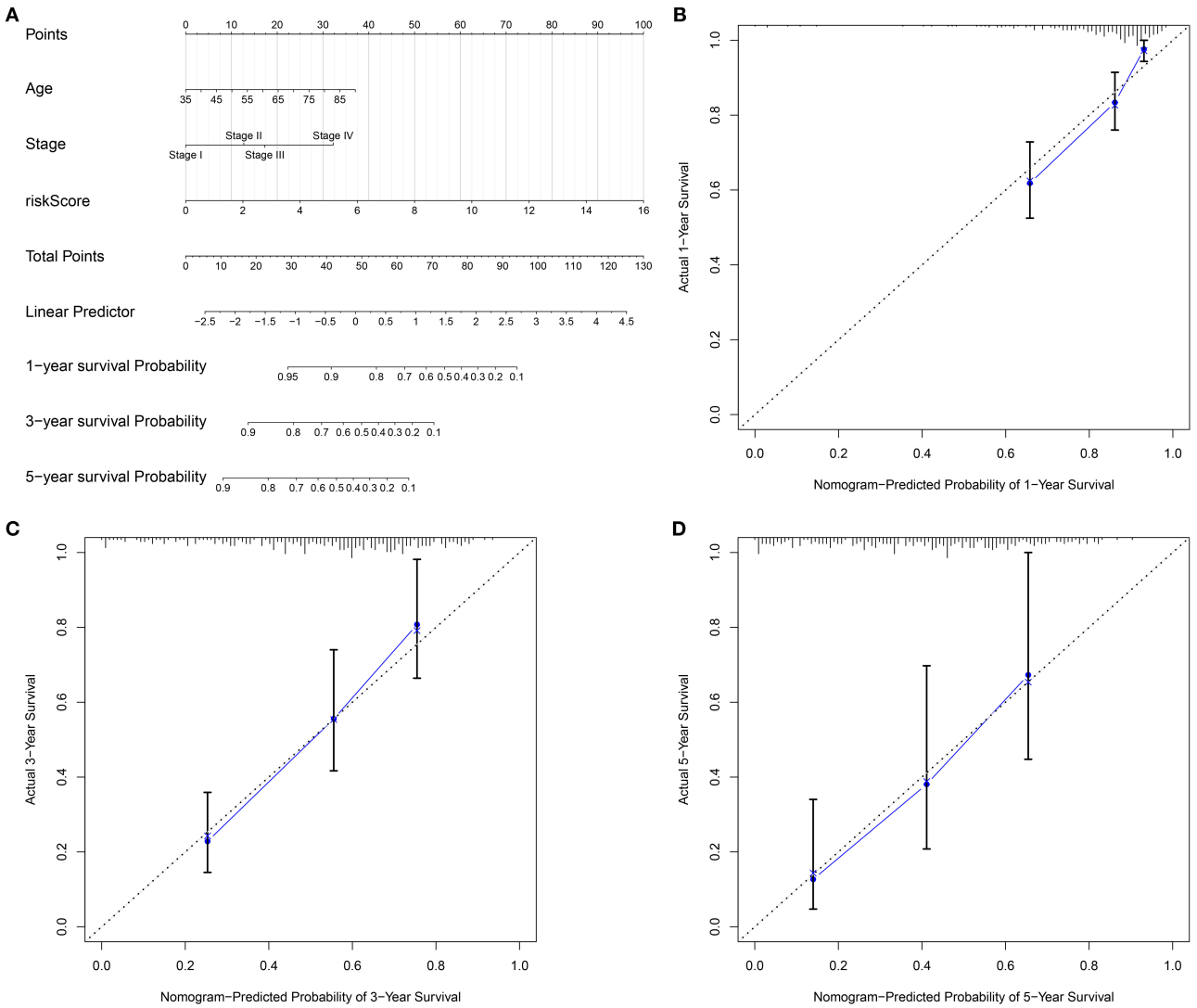

FIGURE 8 | Establishment of a nomogram for gastric cancer in the training set. **(A)** A nomogram integrating age, stage, as well as signature in prediction of 1-, 3-, and 5-year outcomes in gastric cancer. The calibration curves for the relationships between **(B)** 1-, **(C)** 3-, and **(D)** 5-year survival predicted by this nomogram and actual clinical outcomes.

for individualized clinical outcome prediction. This model also showed good predictive performance for 1-, 3-, and 5-year survival.

A few disadvantages of this study need to be pointed out. First, this was a retrospective study according to public datasets. In our future studies, we will present prospective multicenter clinical trials for validation of this RBP signature in predicting gastric cancer patients' survival. Second, activated signal pathways in high- and low-risk subgroups should be verified in further basic experiments. In future research, the molecular mechanisms of RBPs will be observed in gastric cancer. Furthermore, we will further validate the relationships of RBPs with immune microenvironment of gastric cancer, which could be used for guiding immunotherapy in clinical practice.

CONCLUSION

This study developed and externally verified an independent RBP-based signature in the prediction of gastric cancer patients' survival. This signature was closely related to tumor microenvironment and chemosensitivity, assisting in the expanding of the applications of immunotherapy and chemotherapy. A nomogram integrating this signature, age, and stage could offer individualized prediction of prognosis. Thus, this RBP

signature may represent a prognostic stratification tool for gastric cancer.

DATA AVAILABILITY STATEMENT

The datasets presented in this study can be found in online repositories. The names of the repository/repositories and accession number(s) can be found in the article/**Supplementary Material**.

AUTHOR CONTRIBUTIONS

XL conceived and designed the study. ZQ conducted most of the experiments and data analysis, and wrote the manuscript. HJ and KJ participated in collecting the data and helped draft the manuscript. All authors reviewed and approved the manuscript.

SUPPLEMENTARY MATERIAL

The Supplementary Material for this article can be found online at: https://www.frontiersin.org/articles/10.3389/fmed.2021.670141/full#supplementary-material

Supplementary Table 1 | Clinical information of gastric cancer patients from TCGA database.

Supplementary Table 2 | The clinical information of gastric cancer patients in the GSE84437 dataset.

Supplementary Table 3 | A list of 1542 RBPs.

REFERENCES

1. de Martel C, Georges D, Bray F, Ferlay J, Clifford GM. Global burden of cancer attributable to infections in 2018: a worldwide incidence analysis. *Lancet Glob Health.* (2020) 8:e180–90. doi: 10.1016/S2214-109X(19)30488-7
2. Ferlay J, Colombet M, Soerjomataram I, Mathers C, Parkin DM, Piñeros M, et al. Estimating the global cancer incidence and mortality in 2018: GLOBOCAN sources and methods. *Int J Cancer.* (2019) 144:1941–53. doi: 10.1002/ijc.31937
3. Smyth EC, Nilsson M, Grabsch HI, van Grieken NC, Lordick F. Gastric cancer. *Lancet.* (2020) 396:635–48. doi: 10.1016/S0140-6736(20)31288-5
4. Zeng D, Zhou R, Yu Y, Luo Y, Zhang J, Sun H, et al. Gene expression profiles for a prognostic immunoscore in gastric cancer. *Br J Surg.* (2018) 105:1338–48. doi: 10.1002/bjs.10871
5. Zhou YJ, Zhu GQ, Lu XF, Zheng KI, Wang QW, Chen JN, et al. Identification and validation of tumour microenvironment-based immune molecular subgroups for gastric cancer: immunotherapeutic implications. *Cancer Immunol Immunother.* (2020) 69:1057–69. doi: 10.1007/s00262-020-02525-8
6. Pereira B, Billaud M, Almeida R. RNA-binding proteins in cancer: old players and new actors. *Trends Cancer.* (2017) 3:506–28. doi: 10.1016/j.trecan.2017.05.003
7. Ule J, Blencowe BJ. Alternative splicing regulatory networks: functions, mechanisms, and evolution. *Mol Cell.* (2019) 76:329–45. doi: 10.1016/j.molcel.2019.09.017
8. Schultz CW, Preet R, Dhir T, Dixon DA, Brody JR. Understanding and targeting the disease-related RNA binding protein human antigen R (HuR). *Wiley Interdiscip Rev RNA.* (2020) 11:e1581. doi: 10.1002/wrna.1581
9. Yang F, Hu A, Li D, Wang J, Guo Y, Liu Y, et al. Circ-HuR suppresses HuR expression and gastric cancer progression by inhibiting CNBP transactivation. *Mol Cancer.* (2019) 18:158. doi: 10.1186/s12943-019-1094-z
10. Yue B, Song C, Yang L, Cui R, Cheng X, Zhang Z, et al. METTL3-mediated N6-methyladenosine modification is critical for epithelial-mesenchymal transition and metastasis of gastric cancer. *Mol Cancer.* (2019) 18:142. doi: 10.1186/s12943-019-1065-4
11. Wang L, Zhou N, Qu J, Jiang M, Zhang X. Identification of an RNA binding protein-related gene signature in hepatocellular carcinoma patients. *Mol Med.* (2020) 26:125. doi: 10.1186/s10020-020-00252-5
12. Zeng D, Li M, Zhou R, Zhang J, Sun H, Shi M, et al. Tumor microenvironment characterization in gastric cancer identifies prognostic and immunotherapeutically relevant gene signatures. *Cancer Immunol Res.* (2019) 7:737–50. doi: 10.1158/2326-6066.CIR-18-0436
13. Zhang B, Babu KR, Lim CY, Kwok ZH, Li J, Zhou S, et al. A comprehensive expression landscape of RNA-binding proteins (RBPs) across 16 human cancer types. *RNA Biol.* (2020) 17:211–26. doi: 10.1080/15476286.2019.1673657
14. Huang Y, Chen S, Qin W, Wang Y, Li L, Li Q, et al. A Novel RNA binding protein-related prognostic signature for hepatocellular carcinoma. *Front Oncol.* (2020) 10:580513. doi: 10.3389/fonc.2020.580513
15. Li W, Li X, Gao LN, You CG. Integrated analysis of the functions and prognostic values of RNA binding proteins in lung squamous cell carcinoma. *Front Genet.* (2020) 11:185. doi: 10.3389/fgene.2020.00185
16. Li B, Ruotti V, Stewart RM, Thomson JA, Dewey CN. RNA-Seq gene expression estimation with read mapping uncertainty. *Bioinformatics.* (2010) 26:493–500. doi: 10.1093/bioinformatics/btp692
17. Yoon SJ, Park J, Shin Y, Choi Y, Park SW, Kang SG, et al. Deconvolution of diffuse gastric cancer and the suppression of CD34 on the BALB/c nude mice model. *BMC Cancer.* (2020) 20:314. doi: 10.1186/s12885-020-06814-4
18. Gerstberger S, Hafner M, Tuschl T. A census of human RNA-binding proteins. *Nat Rev Genet.* (2014) 15:829–45. doi: 10.1038/nrg3813
19. Sauerbrei W, Boulesteix AL, Binder H. Stability investigations of multivariable regression models derived from low- and high-dimensional data. *J Biopharm Stat.* (2011) 21:1206–31. doi: 10.1080/10543406.2011.629890
20. von Mering C, Huynen M, Jaeggi D, Schmidt S, Bork P, Snel B. STRING: a database of predicted functional associations between proteins. *Nucleic Acids Res.* (2003) 31:258–61. doi: 10.1093/nar/gkg034
21. Mootha VK, Lindgren CM, Eriksson KF, Subramanian A, Sihag S, Lehar J, et al. PGC-1alpha-responsive genes involved in oxidative phosphorylation are coordinately downregulated in human diabetes. *Nat Genet.* (2003) 34:267–73. doi: 10.1038/ng1180
22. Subramanian A, Tamayo P, Mootha VK, Mukherjee S, Ebert BL, Gillette MA, et al. Gene set enrichment analysis: a knowledge-based approach for interpreting genome-wide expression profiles. *Proc Natl Acad Sci USA.* (2005) 102:15545–50. doi: 10.1073/pnas.0506580102
23. Yoshihara K, Shahmoradgoli M, Martínez E, Vegesna R, Kim H, Torres-Garcia W, et al. Inferring tumour purity and stromal and immune cell admixture from expression data. *Nat Commun.* (2013) 4:2612. doi: 10.1038/ncomms3612
24. Newman AM, Liu CL, Green MR, Gentles AJ, Feng W, Xu Y, et al. Robust enumeration of cell subsets from tissue expression profiles. *Nat Methods.* (2015) 12:453–7. doi: 10.1038/nmeth.3337
25. Yang W, Soares J, Greninger P, Edelman EJ, Lightfoot H, Forbes S, et al. Genomics of Drug Sensitivity in Cancer (GDSC): a resource for therapeutic biomarker discovery in cancer cells. *Nucleic Acids Res.* (2013) 41(Database issue):D955–61. doi: 10.1093/nar/gks1111
26. Geeleher P, Cox N, Huang RS. pRRophetic: an R package for prediction of clinical chemotherapeutic response from tumor gene expression levels. *PLoS ONE.* (2014) 9:e107468. doi: 10.1371/journal.pone.0107468
27. Xie R, Xu J, Xiao Y, Wu J, Wan H, Tang B, et al. Calcium promotes human gastric cancer via a novel coupling of calcium-sensing receptor and TRPV4 channel. *Cancer Res.* (2017) 77:6499–512. doi: 10.1158/0008-5472.CAN-17-0360
28. Tang B, Wu J, Zhu MX, Sun X, Liu J, Xie R, et al. VPAC1 couples with TRPV4 channel to promote calcium-dependent gastric cancer progression via a novel autocrine mechanism. *Oncogene.* (2019) 38:3946–61. doi: 10.1038/s41388-019-0709-6

29. Yang X, Chen L, Mao Y, Hu Z, He M. Progressive and prognostic performance of an extracellular matrix-receptor interaction signature in gastric cancer. *Dis Markers.* (2020) 2020:8816070. doi: 10.1155/2020/8816070
30. Park JH, Lee BL, Yoon J, Kim J, Kim MA, Yang HK, et al. Focal adhesion kinase (FAK) gene amplification and its clinical implications in gastric cancer. *Hum Pathol.* (2010) 41:1664–73. doi: 10.1016/j.humpath.2010.06.004
31. Yousaf S, Khan AU, Akram Z, Kayani MA, Nadeem I, Begum B, et al. Expression deregulation of DNA repair pathway genes in gastric cancer. *Cancer Genet.* (2019) 237:39–50. doi: 10.1016/j.cancergen.2019.06.002
32. Shin YJ, Kim Y, Wen X, Cho NY, Lee S, Kim WH, et al. Prognostic implications and interaction of L1 methylation and p53 expression statuses in advanced gastric cancer. *Clin Epigenetics.* (2019) 11:77. doi: 10.1186/s13148-019-0661-x
33. Mao M, Yu Q, Huang R, Lu Y, Wang Z, Liao L. Stromal score as a prognostic factor in primary gastric cancer and close association with tumor immune microenvironment. *Cancer Med.* (2020) 9:4980–90. doi: 10.1002/cam4.2801
34. Das S, Camphausen K, Shankavaram U. Cancer-specific immune prognostic signature in solid tumors and its relation to immune checkpoint therapies. *Cancers (Basel).* (2020) 12:2476. doi: 10.3390/cancers12092476
35. Fuchs CS, Niedzwiecki D, Mamon HJ, Tepper JE, Ye X, Swanson RS, et al. Adjuvant chemoradiotherapy with epirubicin, cisplatin, and fluorouracil compared with adjuvant chemoradiotherapy with fluorouracil and leucovorin after curative resection of gastric cancer: results from CALGB 80101 (Alliance). *J Clin Oncol.* (2017) 35:3671–7. doi: 10.1200/JCO.2017.74.2130
36. Oppedijk V, van der Gaast A, van Lanschot JJ, van Hagen P, van Os R, van Rij CM, et al. Patterns of recurrence after surgery alone versus preoperative chemoradiotherapy and surgery in the CROSS trials. *J Clin Oncol.* (2014) 32:385–91. doi: 10.1200/JCO.2013.51.2186
37. Shapiro J, van Lanschot JJB, Hulshof M, van Hagen P, van Berge Henegouwen MI, Wijnhoven BPL, et al. Neoadjuvant chemoradiotherapy plus surgery versus surgery alone for oesophageal or junctional cancer (CROSS): long-term results of a randomised controlled trial. *Lancet Oncol.* (2015) 16:1090–8. doi: 10.1016/S1470-2045(15)00040-6
38. Duan S, Wang P, Liu F, Huang H, An W, Pan S, et al. Novel immune-risk score of gastric cancer: a molecular prediction model combining the value of immune-risk status and chemosensitivity. *Cancer Med.* (2019) 8:2675–85. doi: 10.1002/cam4.2077

Conflict of Interest: The authors declare that the research was conducted in the absence of any commercial or financial relationships that could be construed as a potential conflict of interest.

Copyright © 2021 Qiu, Jiang, Ju and Liu. This is an open-access article distributed under the terms of the Creative Commons Attribution License (CC BY). The use, distribution or reproduction in other forums is permitted, provided the original author(s) and the copyright owner(s) are credited and that the original publication in this journal is cited, in accordance with accepted academic practice. No use, distribution or reproduction is permitted which does not comply with these terms.

frontiers in Medicine

ORIGINAL RESEARCH
published: 09 August 2021
doi: 10.3389/fmed.2021.667543

m^{6}A RNA Methylation Regulator YTHDF1 Correlated With Immune Microenvironment Predicts Clinical Outcomes and Therapeutic Efficacy in Breast Cancer

Ying Hu†, Qinwen Pan†, Minghao Wang, Xiang Ai, Yuzhao Yan, Yuan Tian, Yuting Jing, Peng Tang and Jun Jiang**

Department of Breast Surgery, First Affiliated Hospital of Army Military Medical University, Chongqing, China

OPEN ACCESS

Edited by:
Fu Wang,
Xi'an Jiaotong University, China

Reviewed by:
Huabing Li,
Shanghai Jiao Tong University School of Medicine, China
Robert Sebra,
Icahn School of Medicine at Mount Sinai, United States

***Correspondence:**
Peng Tang
tp1232000@sina.com
Jun Jiang
a_jiangjun001@163.com

†These authors have contributed equally to this work

Specialty section:
This article was submitted to Precision Medicine, a section of the journal Frontiers in Medicine

Received: *13 February 2021*
Accepted: *01 June 2021*
Published: *09 August 2021*

Citation:
Hu Y, Pan Q, Wang M, Ai X, Yan Y, Tian Y, Jing Y, Tang P and Jiang J (2021) m^{6}A RNA Methylation Regulator YTHDF1 Correlated With Immune Microenvironment Predicts Clinical Outcomes and Therapeutic Efficacy in Breast Cancer. Front. Med. 8:667543. doi: 10.3389/fmed.2021.667543

Objective: Increasing evidence highlights the roles of N^6-methyladenosine (m^{6}A) and its regulators in oncogenesis. Herein, this study observed the associations of m^{6}A regulators with breast cancer.

Methods: RNA-seq profiles of breast cancer were retrieved from the Cancer Genome Atlas (TCGA) database. The expression of m^{6}A regulators was analyzed in tumor and normal tissues. Their expression correlations were analyzed by Spearson test. Overall survival (OS) analysis of these regulators was then presented. Gene set enrichment analysis (GSEA) was performed in high and low YTHDF1 expression groups. The correlations of YTHDF1 expression with immune cells and tumor mutation burden (TMB) were calculated in breast cancer samples. Somatic variation was assessed in high and low YTHDF1 expression groups.

Results: Most of m^{6}A regulators were abnormally expressed in breast cancer compared to normal tissues. At the mRNA levels, there were closely relationships between them. Among them, YTHDF1 up-regulation was significantly related to undesirable prognosis ($p = 0.025$). GSEA results showed that high YTHDF1 expression was associated with cancer-related pathways. Furthermore, YTHDF1 expression was significantly correlated with T cells CD4 memory activated, NK cells activated, monocytes, and macrophages. There were higher TMB scores in YTHDF1 up-regulation group than its down-regulation group. Missense mutation and non-sense mutation were the most frequent mutation types.

Conclusion: Our findings suggested that dysregulated m^{6}A regulator YTHDF1 was predictive of survival outcomes as well as response to immunotherapy of breast cancer, and were closely related to immune microenvironment.

Keywords: N6-methyladenosine, regulators, breast cancer, immune microenvironment, immunotherapy, somatic mutation

INTRODUCTION

The incidence of breast cancer continues to rise globally (1). It represents the most mortal among the female population (2). This malignancy is heterogeneous on clinical, molecular behaviors as well as response to therapies (3). This management is multidisciplinary, including locoregional (surgery or radiotherapy) as well as systemic therapies (4). At present, advanced breast cancer with distant metastasis is incurable. Bone, lung, liver, and brain are common metastatic sites (5). Individualized therapy is future therapeutic goal for breast cancer. Thus, it is vital to elucidate the mechanisms of breast cancer initiation as well as progression.

m^6A is the most abundant modification in eukaryotic mRNAs, occupying 0.1–0.4% of the total adenine residues (6). The m^6A modification takes on varied biological functions (7) like RNA splicing, RNA stabilities, nuclear export as well as translation (8). This process is involved in three kinds of m^6A regulators, called as "writers," "erasers," and "readers," containing "writers" (METTL3, METTL14, WTAP, RBM15, KIAA1429, ZC3H13), "readers" (YTHDC1, YTHDC2, YTHDF1, YTHDF2, HNRNP), as well as "erasers" (FTO, ALKBH5). "Writers" are responsible for catalyzing the formation of m^6A. "Readers" are charge of decoding m^6A methylation as well as producing functional signals. "Erasers" can remove the methyl code from targeted mRNAs. The m^6A modification participates in carcinogenesis through regulating RNA production as well as metabolism. For instance, Niu et al. (9) demonstrated that FTO promoted breast tumor progress by inhibition of BNIP3. As in the study of Cai et al. (10), METTL3 up-regulation accelerates breast cancer cellular proliferation. Recent studies have emphasized the key implications of immune microenvironment in breast cancer progression as well as response to immunotherapy (11). Zhang et al. (12) reported that m^6A modification was involved in tumor immune microenvironment formation. ALKBH5 m^6A reader could regulate the response to anti-PD-1 immunotherapy through inhibiting the accumulation of tumor-infiltrating immune cells (13). Hence, evaluation of m^6A regulators in individual breast cancer may enhance our understanding about characteristics of tumor immune microenvironment as well as improve the therapeutic efficacy of immunotherapies. In this study, we evaluated the expression patterns of m^6A regulators and their correlations with survival outcomes, immune microenvironment, response to immunotherapy as well as somatic mutation in breast cancer.

MATERIALS AND METHODS

Data Sourcse

From TCGA database (http://cancergenome.nih.gov/), this study collected RNA-seq profiles of breast cancer subjects on January 15, 2021. Meanwhile, the matched clinical information was also retrieved. After removing samples with survival time of 0, 902 samples including Basal, Her2, LumA, and LumB subtypes were retained for further analysis (**Table 1**). The microarray expression profiling of 17 normal breast tissues and 104 breast cancer tissues were retrieved from the GSE42568 dataset of the Gene Expression Omnibus (GEO; https://www.ncbi.nlm.nih.gov/gds/) repository. Also, expression profiles and follow-up information of 266 breast cancer patients were retrieved from the GSE21653 dataset.

TABLE 1 | Clinicopathological characteristics of breast cancer patients in this study.

Characteristics	Groups	Number
Age	<65	641
	≥65	261
T	T1	232
	T2	534
	T3	103
	T4	33
N	N0	443
	N1	301
	N2	102
	N3	56
M	M0	886
	M1	16
Stage	Stage I	156
	Stage II	528
	Stage III	202
	Stage IV	16

m^6A Regulators

Totally, this study gathered 13 m^6A regulators including five writers (METTL3, METTL14, WTAP, RBM15, ZC3H13, KIAA1429), five readers (YTHDC1, YTHDC2, YTHDF1, YTHDF2, HNRNPC), two erasers (FTO, ALKBH5). The expressions of these m^6A regulators were assessed in breast cancer and normal tissue samples by Wilcoxon test. *P*-value was corrected with Bonferroni method. Spearson correlation analysis was presented between these regulators at the mRNA levels. $|r| > 0.5$ indicated a significant correlation.

Survival Analysis

Samples with survival status of zero were removed. Overall survival (OS) is defined as the time from the date of diagnosis to death due to any cause. The patients were classified into high and low expression of each m^6A regulator groups based on the median value of its expression. OS analyses were carried out between groups through univariate cox regression analysis. For each regulator, this study calculated *p*-value, hazard ratio (HR) as well as 95% confidence interval (CI). Regulators with *p*-value <0.05 and HR >1 were risk factors of breast cancer prognosis. Meanwhile, those with *p*-value <0.05 and HR <1 were protective factors.

Abbreviations: m^6A, N^6-methyladenosine; TCGA, The Cancer Genome Atlas; OS, overall survival; GSEA, gene set enrichment analysis; TMB, tumor mutation burden; HR, hazard ratio; CI, confidence interval; NES, normalized enrichment score; FDR, false discovery rate; DEGs, differentially expressed genes; GO, Gene Ontology; KEGG, Kyoto Encyclopedia of Genes and Genomes; CMap, Connectivity Map.

GSEA

Enrichment analysis was presented with GSEA software (14). Here, breast cancer subjects were separated into high and low YTHDF1 expression groups based on the media value of YTHDF1. Thousand gene set permutations were presented for each analysis. The expression level of YTHDF1 was considered a phenotype. According to the normalized enrichment score (NES), normalized *p*-value and false discovery rate (FDR), the enrichment pathways of each phenotype were classified. The absolute value of NES $\geq$1.0, normalized *p*-value $\leq$0.05 and FDR $\leq$ 0.25 were confirmed as meaningful gene sets.

Cell Culture and Transfection

Human breast cancer cells MCF-7 (ATCC, USA) were grown in DMEM (Thermo, USA) containing 10% FBS in an incubator with 5% CO_2 at 37°C. MCF-7 cells were seeded in 6-well plates. The culture medium was changed 1 day before transfection, and when the cells reached 70–90% of the growth density, the cells were transfected with synthetic siRNAs (si-YTHDF1; GenePharma, Suzhou, China) through the Lipofectamine™2000 Transfection Kit (Invitrogen, USA). Simultaneously, non-interfering siRNA was transfected as a negative control. The transfection process strictly followed the instructions of the kit, and the cells transfected for 48 h were collected for next research.

Western Blot

Transfected cells were lysed on ice with cell lysate to extract total protein. The BCA method was used for protein quantification. The proteins were separated by SDS-PAGE gel electrophoresis, and transferred to PVDF membranes at a constant voltage of 80 V. After blocking with 5% skimmed milk powder TBST at room temperature for 2 h, the membranes were incubated with YTHDF1 (1/500; ab230330; Abcam), Axin2 (1:1000; ab32197; Abcam), c-myc (1:5000; ab152146; Abcam), β-catenin (1:10000; ab81305; Abcam), cyclin D1 (1:10000; ab134175; Abcam), and β-actin (1:5000; ab179467; Abcam) overnight at 4°C. After washing, the membranes were incubated with secondary antibodies at room temperature for 1 h. The color was developed by chemiluminescence, and the gel imaging system was used to analyze images. The gray value of the bands was measured.

Somatic Variation

Somatic variant data of breast cancer that were stored in the mutation annotation format (MAF) were obtained from TCGA database. According to VarScan2 variant aggregation as well as masking data, somatic variation analyses were presented through "maftools" package (15). TMB score was determined for each patient as follows: (total mutation/total covered bases).

CIBERSORT

The CIBERSORT algorithm was employed for estimating the fractions of 22 phenotypes of immune cells in each specimen based on gene expression profiles (16). LM22 leukocyte gene signature matrix was utilized in conjunction. Specimens with *p*-value $<$ 0.05 were retained. For each specimen, the sum of the estimated fractions of immune cells was equal to 1. The enriched scores of each immune cell were compared in high and low YTHDF1 expression groups by Wilcoxon test.

TMB

TMB is defined as the total number of somatic mutations per Mb base in the coding region of an exon, which is an emerging biomarker for judging the efficacy of tumor immunotherapy (17). The greater the TMB score, the better the therapy efficacy. TMB is calculated as the total number of somatic mutations/the size of the target area, and the unit is mutations/Mb. The somatic mutation data were in MAF format. In this study, the somatic mutation data processed by vanscan software were downloaded from TCGA. The "maftools" package was applied to calculate the TMB score of each sample. The difference in TMB scores between high and low YTHDF1 expression groups was assessed by Wilcoxon test.

Differential Expression Analysis

Differentially expressed genes (DEGs) were screened between high and low YTHDF1 expression groups *via* the limma package. The screening thresholds were as follows: |log2 fold change (FC)| $>$ 1 and adjusted *p*-value $<$0.05.

Functional Enrichment Analysis

The "clusterProfiler" package was applied to present Gene Ontology (GO) and Kyoto Encyclopedia of Genes and Genomes (KEGG) pathways enrichment analysis based on YTHDF1-related DEGs (18). Terms with adjusted *p*-value $<$ 0.05 were significantly enriched.

Connectivity Map

CMap database (https://clue.io/) was employed for exploring candidate chemical compounds against breast cancer (19). Based on a list of DEGs, this study searched for the compounds through this database. The CMap connectivity score (range: −1 to 1) was indicative of the specificity degree related to the DEGs. The connectivity score of a compound tended to −1, suggesting that it negatively correlated with the DEGs. On the contrary, the connectivity score of a compound closer to 1 implied that it exhibited positive correlations with the DEGs. Here, the compounds with |connectivity score| $\geq$90 were candidate chemical agents.

Scratch Test

The cells were seeded in a 6-well plate and placed in a CO_2 cell incubator. After the cells were overgrown, a sterile toothpick was used to make a vertical mark of uniform thickness in each hole. After taking pictures of the initial state of the scratches at 0 h under an inverted microscope, the samples were put back into the incubator. After 24 h, the scratch state was photographed again. ImageJ software was used to calculate the scratch area. Relative migration rate = (0 h scratch area-24 h scratch area)/0 h scratch area.

Transwell

The cells were added to the Matrigel-coated Transwell chamber (1×10^5 cells/well). A medium containing 10% FBS was added to the well in the lower layer of each chamber. After culturing for

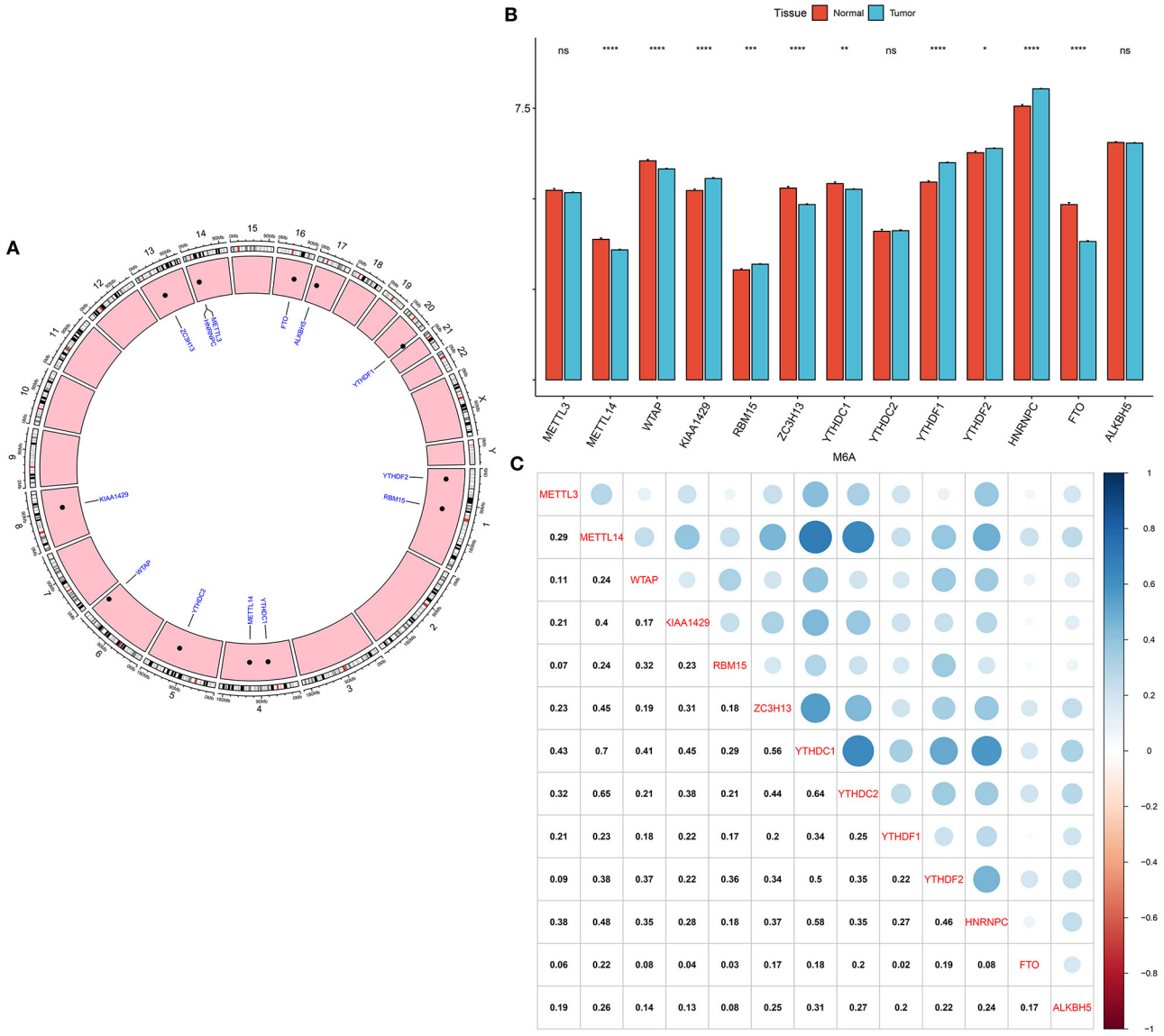

FIGURE 1 | Expression patterns and correlations of 13 m^{6}A regulators in breast cancer from TCGA database. **(A)** Genomic locations of the regulators. **(B)** Bar diagram for the expression of regulators in breast cancer and normal tissues. **(C)** Assessment of correlations between 13 m^{6}A regulators at the mRNA levels. Ns, not significant; *$p < 0.05$; **$p < 0.01$; ****$p < 0.0001$.

24 h, the chamber was removed. After staining with crystal violet, a cotton swab was used to gently wipe away the non-invasive cells in the upper chamber. The invasive cells were observed under an inverted microscope. Then, ImageJ software was applied to calculate the number of invasive cells.

Statistical Analysis

All statistical analysis was carried out through the packages of R software (http://www.r-project.org/) or Graphpad Prism. Student's *t*-test, Wilcoxon test or ANOVA test was applied for comparisons between groups. $P < 0.05$ indicated statistical significance.

RESULTS

Expression Patterns and Correlations of 13 m^{6}A Regulators in Breast Cancer

Genomic locations for 13 m^{6}A regulatory genes were displayed in **Figure 1A**, as follows: METTL3 (chr14: 21498133-21511342), METTL14 (chr4: 118685392-118715433), WTAP (chr6: 159725585-159756319), KIAA1429 (chr8: 94487689-94553529), RBM15 (chr1: 110338506-110346681), ZC3H13 (chr13: 45954465-46052759), YTHDC1 (chr4: 68310387-68350090), YTHDC2 (chr5: 113513694-113595285), YTHDF1 (chr20: 63195429-63216139), YTHDF2 (chr1: 28736621-28769775),

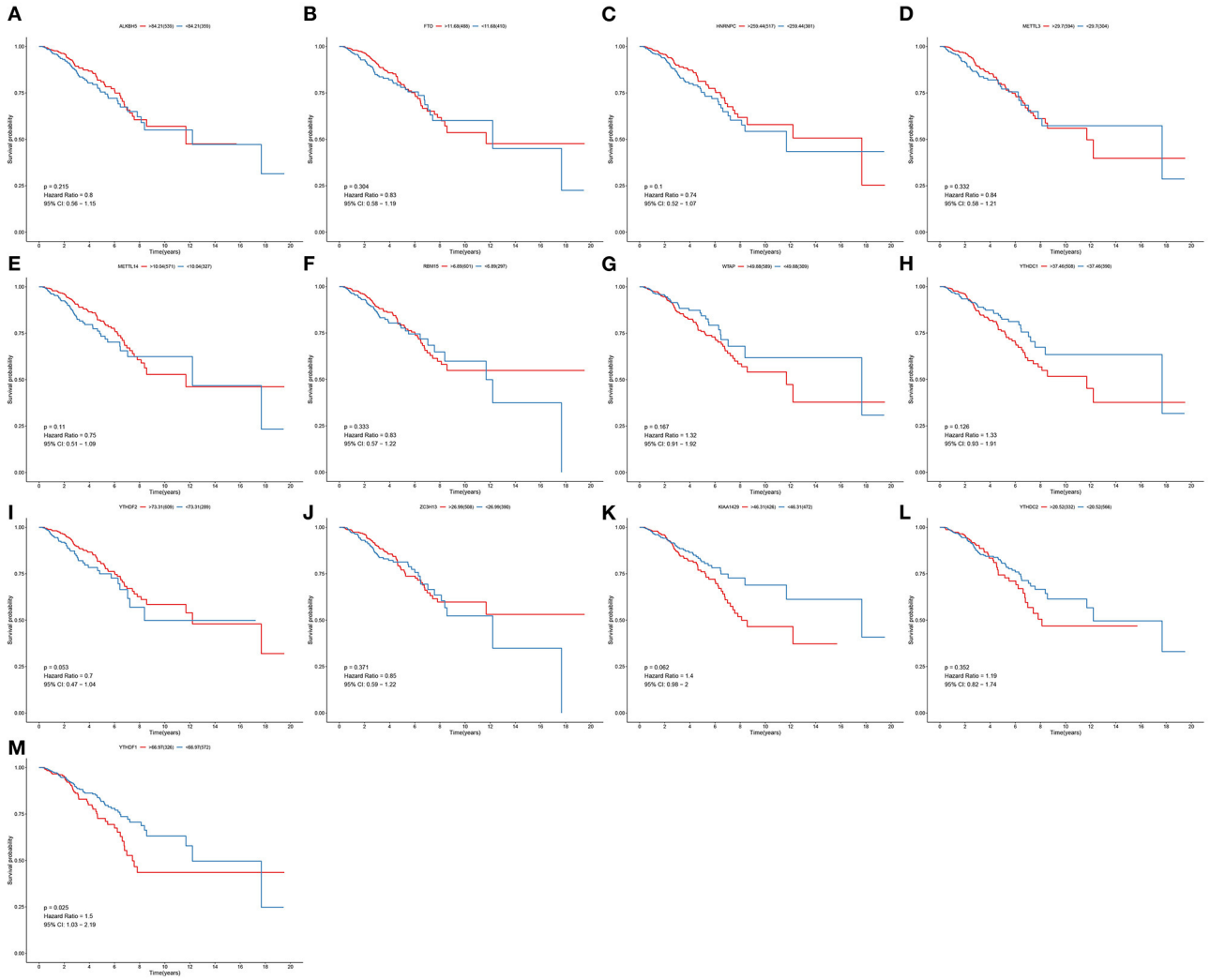

FIGURE 2 | Correlation between 13 m^{6}A regulators and breast cancer patients' survival. OS of **(A)** ALKBH5; **(B)** FTO; **(C)** HNRNPC; **(D)** METTL3; **(E)** METTL14; **(F)** RBM15; **(G)** WTAP; **(H)** YTHDC1; **(I)** YTHDF2; **(J)** ZC3H13; **(K)** KIAA1429; **(L)** YTHDC2; **(M)** YTHDF1 expression for breast cancer patients.

HNRNPC (chr14: 21209136-21269494), FTO (chr16: 53701692-54158512) and ALKBH5 (chr17: 18183078-18209954). The expression of these regulators was compared in breast cancer and normal tissues. We found that METTL14 (adjusted p-value = 9.10e-08), WTAP (adjusted p-value = 2.86e-07), KIAA1429 (adjusted p-value = 2.33e-06), RBM15 (adjusted p-value = 1.52e-03), ZC3H13 (adjusted p-value = 5.56e-12), YTHDC1 (adjusted p-value = 1.68e-03), YTHDF1 (adjusted p-value = 4.72e-27), YTHDF2 (adjusted p-value = 4.72e-02), HNRNPC (adjusted p-value = 1.60e-24), and FTO (adjusted p-value = 2.62e-33) were significantly abnormally expressed in breast cancer compared to normal tissues (**Figure 1B**). However, no significant differences in METTL3, YTHDC2, and ALKBH5 expression were found between tumor and normal samples. The correlations between 13 m^{6}A regulators were assessed at the mRNA levels among breast cancer specimens. Our data showed that METTL14 had a strong correlation to YTHDC1 ($r = 0.7$) and YTHDC2 ($r = 0.65$), as displayed in **Figure 1C**. Meanwhile, YTHDC1 was strongly associated with YTHDF1 ($r = 0.64$), and moderately correlated to HNRNPC ($r = 0.58$).

YTHDF1 Expression Is Correlated to Breast Cancer Patients' Survival

To determine the clinical implications of 13 m^{6}A regulatory mRNAs in breast cancer, this study observed the correlations between the expression of 13 m^{6}A regulatory mRNAs and patients' clinical outcomes. Our results showed that the expression of ALKBH5, FTO, HNRNPC, METTL3, METTL14, RBM15, WTAP, YTHDC1, YTHDF2, ZC3H13, KIAA1429, and YTHDC2 were all not associated with patients' survival (**Figures 2A–L**). Only YTHDF1 expression exhibited a significant correlation to subjects' prognosis (**Figure 2M**). Its expression was a risk factor for breast cancer ($p = 0.025$; HR: 1.5; 95% CI: 1.03–2.19). Subjects with high YTHDF1 expression often

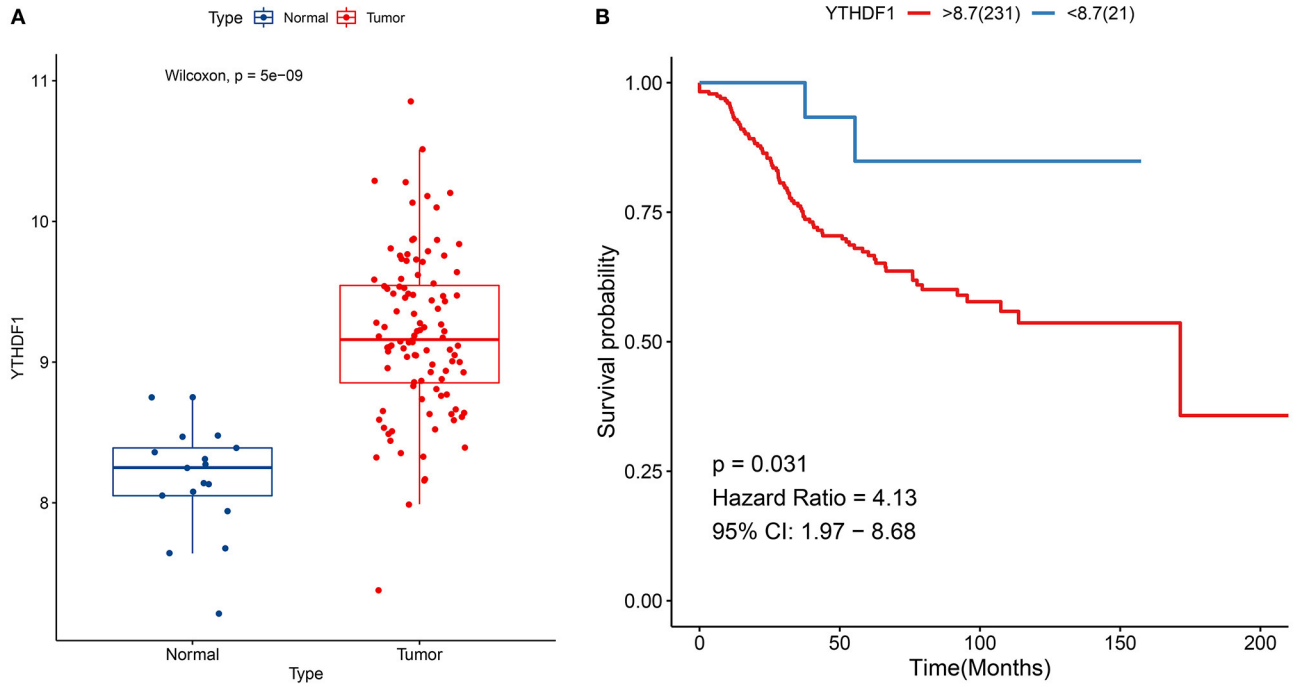

FIGURE 3 | Verification of expression and prognosis of YTHDF1 in breast cancer. **(A)** Box plots for YTHDF1 expression in the GSE42568 dataset. **(B)** Survival analysis of breast cancer with high and low YTHDF1 expression in the GSE21653 dataset.

experienced undesirable survival outcomes than those with its low expression.

Verification of Expression and Prognosis of YTHDF1 in Breast Cancer

YTHDF1 up-regulation was confirmed in breast cancer in the GSE42568 dataset ($p = 5e\text{-}09$; **Figure 3A**). Also, its up-regulation was in relation to unfavorable survival outcomes of subjects in the GSE21653 dataset ($p = 0.031$; **Figure 3B**).

Enriched Pathways in High and Low YTHDF1 Expression Groups

Then, we evaluated the enriched signaling pathways in high and low YTHDF1 expression groups. We found that cell cycle, ERBB signaling pathway, oocyte meiosis, pathways in cancer, spliceosome, ubiquitin mediated proteolysis, and WNT signaling pathway were distinctly enriched in high YTHDF1 expression group (**Figure 4A**). Meanwhile, ribosome was significantly enriched in low YTHDF1 expression group (**Figure 4B**). To verify whether YTHDF1 altered WNT pathway activation, YTHDF1 was successfully silenced by siRNA in MCF-7 cells (**Figures 4C,D**). Our data showed that YTHDF1 knockdown distinctly lowered the expression of Axin2, c-myc, β-catenin, and cyclin D1 in MCF-7 cells, confirming that YTHDF1 participated in the activation of WNT pathway in breast cancer (**Figures 4E–H**).

Correlation Between YTHDF1 Expression and Tumor Immune Microenvironment and Response to Immunotherapy

m^6A modification is closely related to tumor microenvironment cell infiltration in individual tumors (12). Here, we assessed the correlation between YTHDF1 expression and tumor immune microenvironment in breast cancer. Samples with high YTHDF1 expression distinctly exhibited higher infiltration scores of T cells CD4 memory activated and macrophages M1 those with its low expression (**Figure 5A**; **Table 2**). Lower infiltration levels of NK cells activated and monocytes were found in subjects with high YTHDF1 expression compared to those with its low expression. Despite the revolutionization of immune checkpoint blockade (ICB) therapy, most patients cannot benefit from ICB therapy (13). We found that high YTHDF1 expression was significantly correlated to higher TMB score, indicating that patients with its up-regulation had a better effect on immunotherapy (**Figure 5B**). Thus, YTHDF1 expression might be used for predicting the response to immunotherapy.

Somatic Mutations in High and Low YTHDF1 Breast Cancer

Somatic mutations were evaluated in high and low YTHDF1 breast cancer samples from TCGA database. Among 986 samples, 260 (26.37%) occurred somatic mutations in high YTHDF1 expression group. Here, we displayed the top 20 genes according to mutation frequency. As shown in **Figure 6A**,

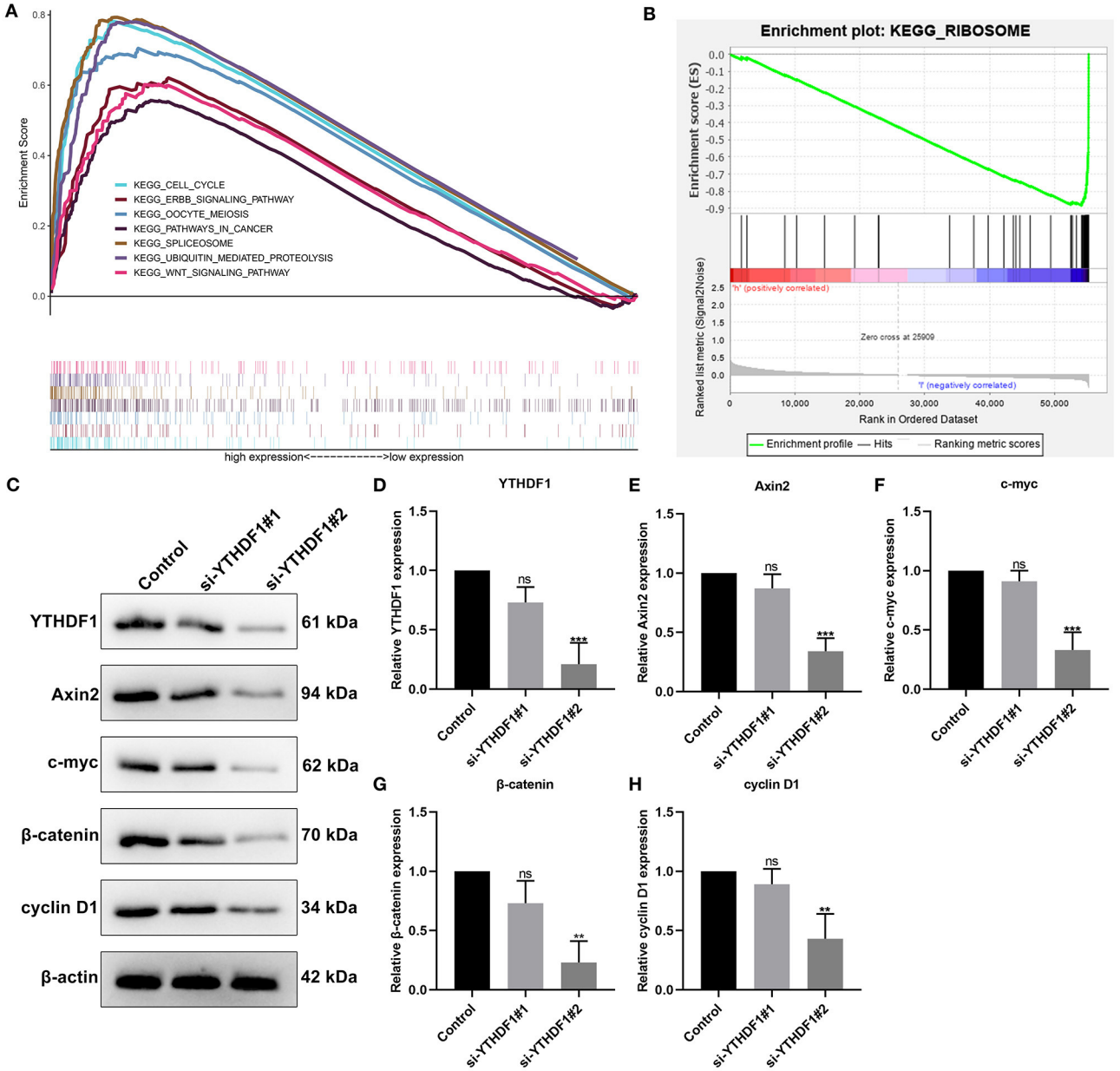

FIGURE 4 | Enriched pathways in high and low YTHDF1 expression groups. **(A)** Enriched pathways in high expression group. **(B)** An enriched pathway in low expression group. **(C)** Western blot for detecting the expressions of **(D)** YTHDF1, **(E)** Axin2, **(F)** c-myc, **(G)** β-catenin and **(H)** cyclin D1 in MCF-7 cells transfected with si-YTHDF1. Ns, not significant; $^{**}p < 0.01$; $^{***}p < 0.001$.

TP53 (12%) had the most frequently mutated gene, followed by PIK3CA (10%), TTN (5%), CDH1 (3%), and GATA3 (3%). Four hundred and forty samples occurred somatic mutations in low YTHDF1 expression group (**Figure 6B**). Consistent with high expression group, TP53 (16%), PIK3CA (17%), TTN (9%), CDH1 (8%), and GATA3 (7%) were the top five mutated genes. Both in high and low YTHDF1 expression groups, missense mutation was the most common mutation type.

Expression Patterns of YTHDF1 in Pan-Cancer

We comprehensively analyzed the expression of YTHDF1 in pan-cancer and corresponding normal tissues. Up-regulation of YTHDF1 was found in bladder cancer, breast cancer, cholangiocarcinoma, colon adenocarcinoma, esophageal carcinoma, glioblastoma multiforme, head and neck squamous cell carcinoma, kidney renal papillary cell carcinoma, liver hepatocellular carcinoma, lung adenocarcinoma, lung squamous

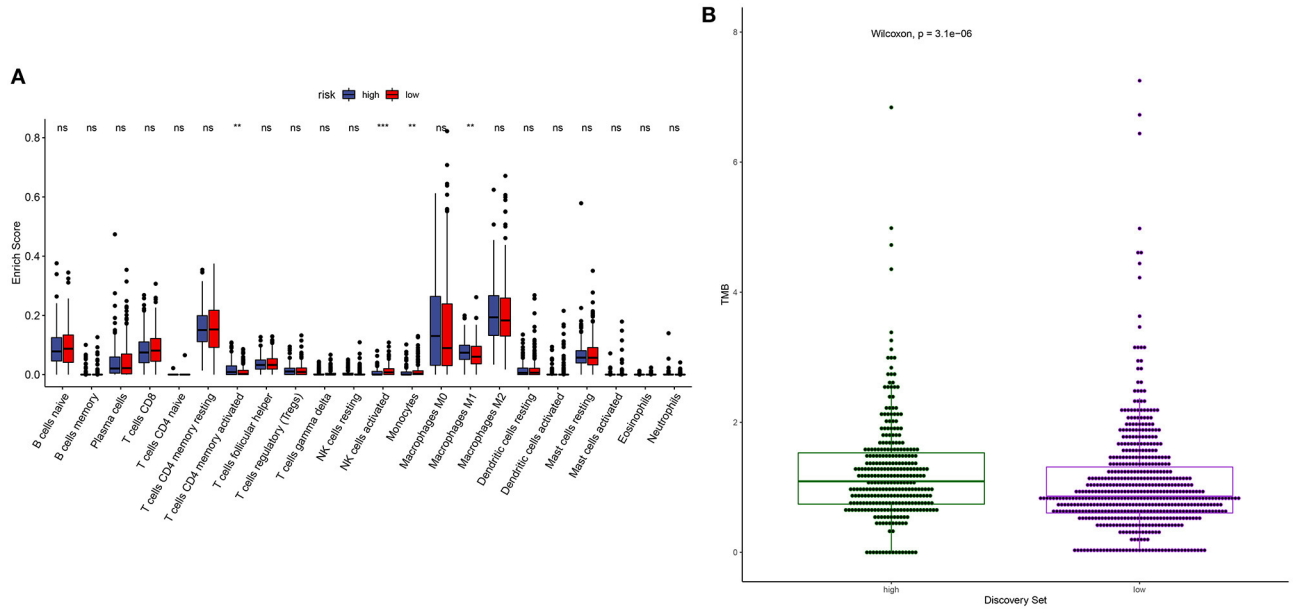

FIGURE 5 | Correlation between YTHDF1 expression and tumor immune microenvironment and response to immunotherapy. **(A)** Box plots for the association between YTHDF1 expression and infiltration levels of immune cells in breast cancer. **(B)** Box plots for the association between YTHDF1 expression and TMB score.

TABLE 2 | The correlations between YTHDF1 expression and tumor-infiltrating immune cells in breast cancer.

Immune cells	Correlation	*P*-value
B cells naive	0.040366409	0.386168381
B cells memory	−0.078822212	0.090245572
Plasma cells	−0.037586715	0.41974218
T cells CD8	−0.104667997	0.024304051
T cells CD4 naive	−0.004561896	0.922015306
T cells CD4 memory resting	0.081294778	0.080564543
T cells CD4 memory activated	0.120824713	0.009258723
T cells follicular helper	−0.057847282	0.214088643
T cells regulatory (Tregs)	−0.029972053	0.520014582
T cells gamma delta	−0.039701947	0.394041569
NK cells resting	0.044877857	0.33528083
NK cells activated	−0.218149178	$2.15E-06$
Monocytes	−0.129149449	0.005383934
Macrophages M0	0.031822789	0.49456461
Macrophages M1	0.14172183	0.002237962
Macrophages M2	0.017414151	0.708507533
Dendritic cells resting	−0.028485518	0.540933145
Dendritic cells activated	−0.014160222	0.761216826
Mast cells resting	0.084489829	0.069318397
Mast cells activated	−0.006961211	0.881250387
Eosinophils	−0.056387909	0.225892694
Neutrophils	0.074504463	0.109368677

cell carcinoma, pheochromocytoma and paraganglioma, prostate adenocarcinoma, rectum adenocarcinoma, stomach adenocarcinoma, and uterine corpus endometrial carcinoma compared to corresponding normal tissues (**Figure 7**). However, YTHDF1 was lowly expressed in thyroid carcinoma than normal samples.

Enrichment Analysis of YTHDF1-Related DEGs in Breast Cancer

Sixteen up-regulated and down-regulated genes were identified between high and low YTHDF1 expression breast cancer samples (**Table 3**). Their biological functions were then discovered through GO and KEGG enrichment analyses. We found that up-regulated genes were only enriched in columnar/cuboidal epithelial cell differentiation (**Figure 8A**). Down-regulated genes were significantly involved in RNA metabolism-related biological processes, such as cAMP-mediated signaling, cyclic-nucleotide-mediated signaling, and adenylate cyclase-modulating G protein-coupled receptor signaling pathway (**Figure 8B**). Furthermore, they had the molecular functions of G protein-coupled receptor binding and neuropeptide receptor binding. KEGG pathway enrichment analysis revealed that up-regulated genes significantly participated in GABAergic synapse (**Figure 8C**). In **Figure 8D**, neuroactive ligand-receptor interaction and renin secretion were distinctly enriched by down-regulated genes.

Candidate Therapeutic Agents Against Breast Cancer Based on YTHDF1-Related DEGs

Candidate therapeutic agents were discovered based on YTHDF1-related DEGs (**Table 4**). We found that indoprofen, nabumetone, nimesulide, and phenacetin shared the MoA of Cyclooxygenase inhibitor. Digitoxigenin, helveticoside, ouabain shared the MoA of ATPase inhibitor.

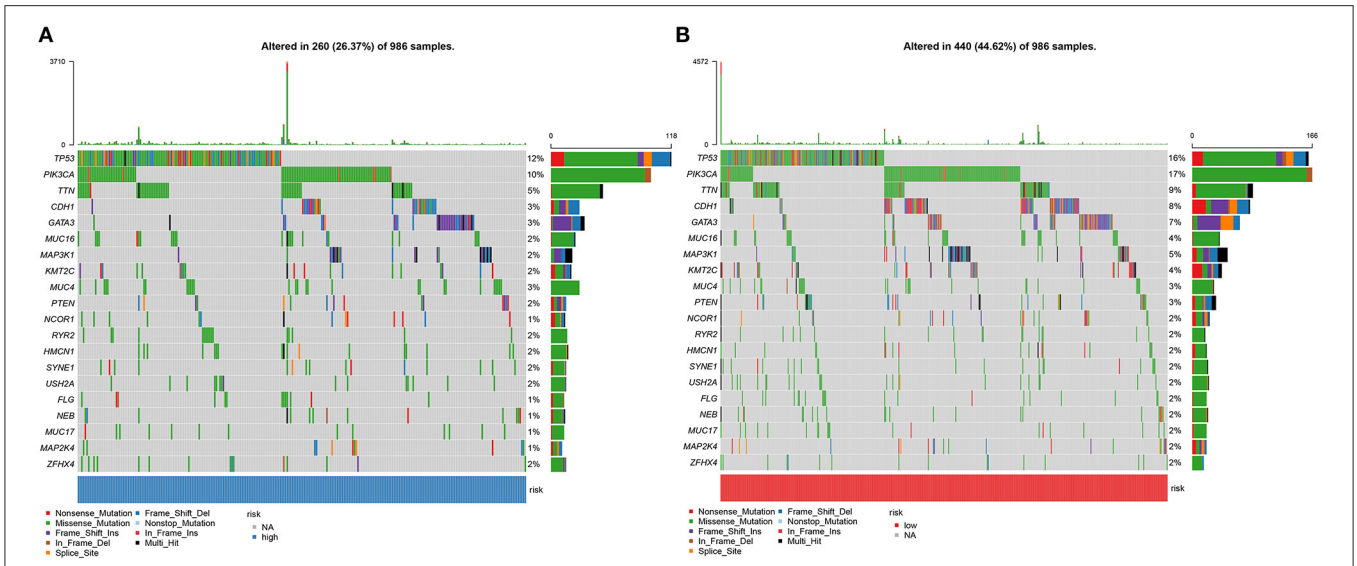

FIGURE 6 | Somatic mutations in high and low YTHDF1 breast cancer. **(A)** The top 20 genes according to mutation frequency in high YTHDF1 expression groups. **(B)** The top 20 genes according to mutation frequency in low expression groups. Each mutation type is identified by a unique color.

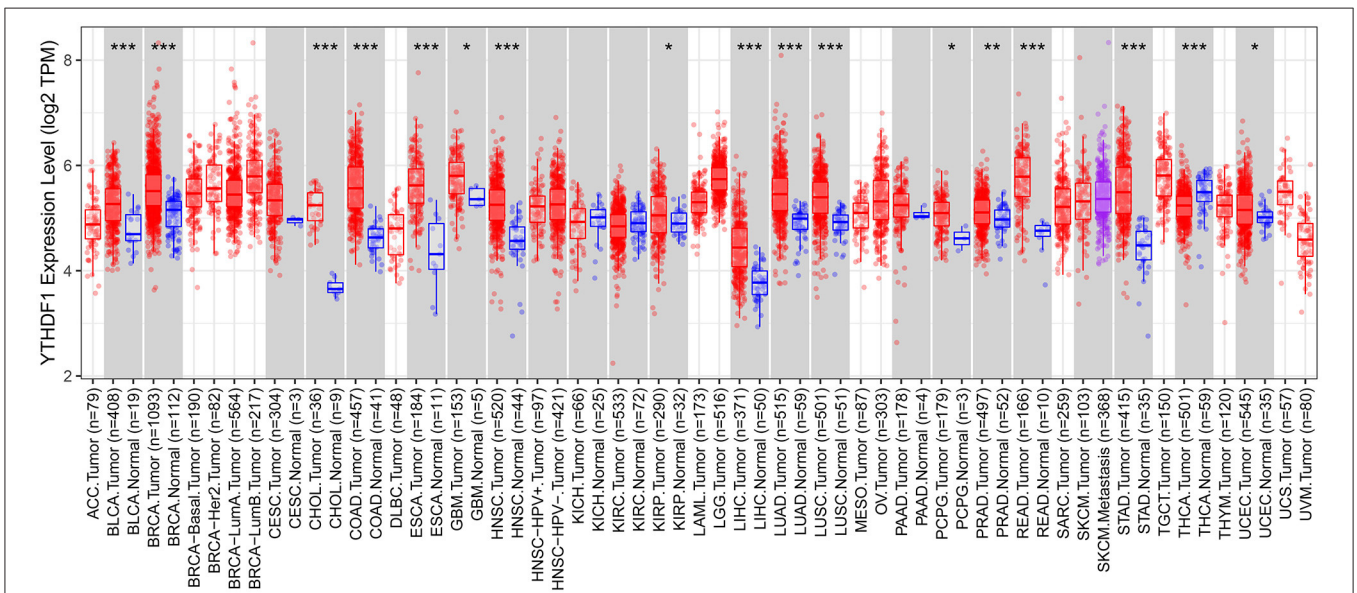

FIGURE 7 | Expression patterns of YTHDF1 in pan-cancer and matched normal tissues. Red indicates tumor specimens and blue indicates normal tissues. Each dot represents one sample. *$P < 0.05$; **$p < 0.01$; ***$p < 0.001$.

Alclometasone, mometasone, and piretanide shared the MoA of Glucocorticoid receptor agonist (**Figure 9**). These compounds could become candidate therapeutic agents against breast cancer.

YTHDF1 Knockdown Restrains Migrated and Invasive Abilities of Breast Cancer

Following YTHDF1 knockdown, migrated as well as invasive abilities of breast cancer were investigated in breast cancer. The scratch test demonstrated that silencing YTHDF1 markedly lowered the migrated levels of MCF-7 cells (**Figures 10A,B**). Moreover, the number of invasive cells was decreased by YTHDF1 knockdown (**Figures 10C,D**).

DISCUSSION

In this study, we characterized the expression patterns of m^6A regulators and their implications on survival outcomes, immune microenvironment, response to immunotherapy as well as somatic mutations in breast cancer. Our data highlighted the

TABLE 3 | DEGs between high and low YTHDF1 expression in breast cancer.

Gene	Low	High	Log2FC	*P*-value	FDR
UCP1	0.613741	0.24966	−1.29766	0.000168	0.000431
AC005150.1	0.381289	0.827139	1.117244	4.01E-06	1.38E-05
NDST4	0.153095	0.371715	1.279765	1.01E-06	3.83E-06
LIN28A	0.17983	0.396404	1.140337	5.25E-05	0.000149
SLITRK1	0.120873	0.280966	1.216906	0.000304	0.000742
RHOXF1P1	0.202294	0.553388	1.451838	1.21E-11	9.52E-11
CACNG6	0.383047	0.822432	1.102376	2.79E-05	8.30E-05
SLC4A10	0.249078	0.552009	1.148093	1.74E-06	6.37E-06
TEX19	0.188221	0.450787	1.260016	1.01E-14	1.22E-13
SBK2	0.213431	0.516452	1.274862	7.62E-08	3.46E-07
LINC00844	0.403406	0.198363	−1.02409	2.10E-06	7.57E-06
DPYSL5	0.224008	0.510557	1.188521	0.000552	0.001283
AC025423.3	0.490366	0.98134	1.000895	7.28E-08	3.31E-07
ADGRD2	0.308757	0.142028	−1.12029	0.006414	0.011896
CSMD3	0.101368	0.292825	1.530431	1.46E-09	8.52E-09
AL355075.4	0.287489	0.113742	−1.33774	0.021636	0.035462

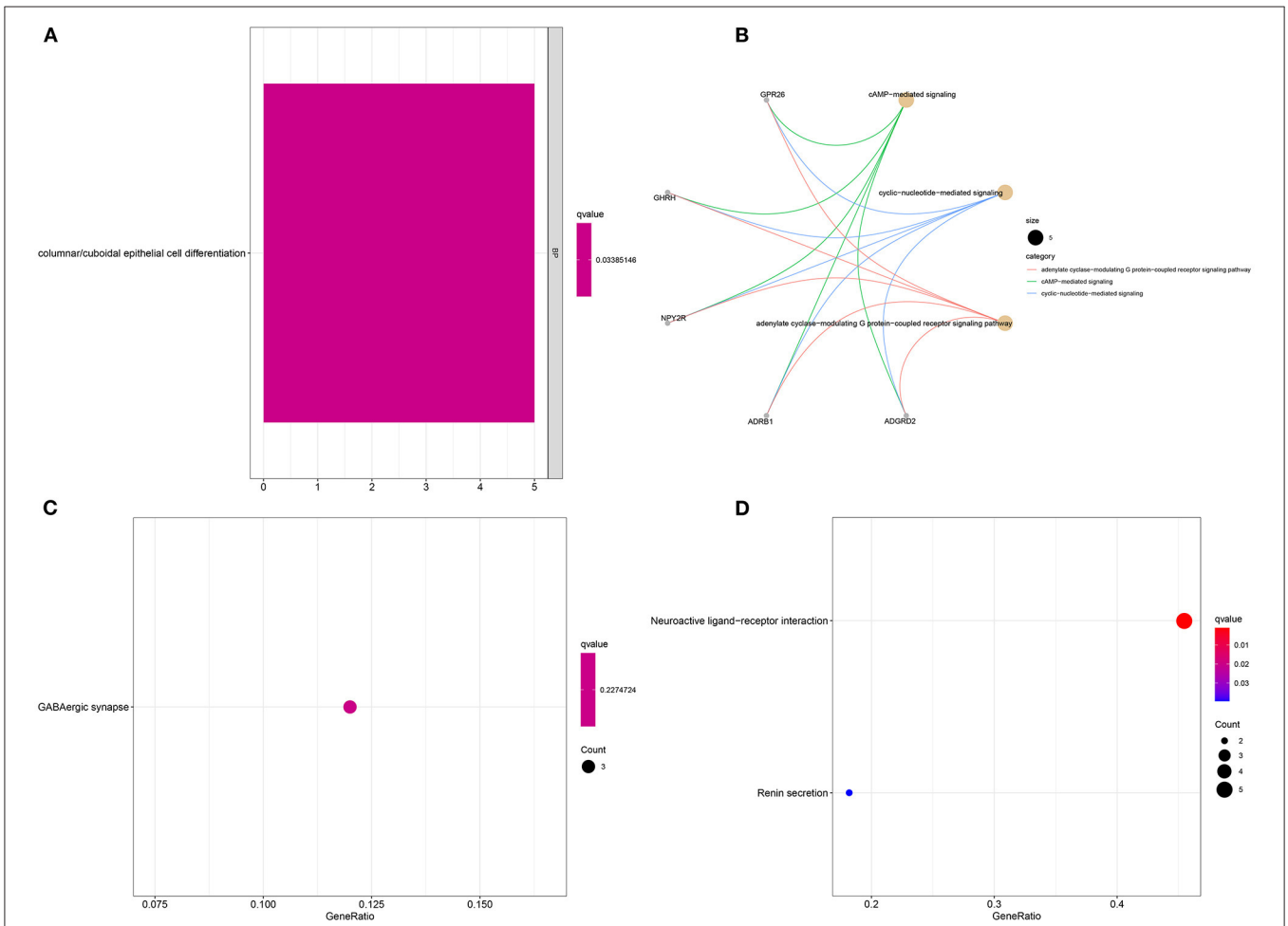

FIGURE 8 | Enrichment analysis of YTHDF1-related DEGs in breast cancer. GO enrichment results by **(A)** up-regulated and **(B)** down-regulated genes. KEGG pathway enrichment results by **(C)** up-regulated, and **(D)** down-regulated genes.

TABLE 4 | Candidate therapeutic agents against breast cancer.

Rank	CMap name	Mean	*N*	Enrichment	*P*	Specificity	Percent non-null
1	Harmalol	−0.82	3	−0.943	0.00028	0	100
2	Flucloxacillin	−0.362	4	−0.808	0.00265	0.0063	50
3	Lasalocid	−0.418	4	−0.807	0.00271	0.037	50
4	Tiletamine	−0.339	4	−0.794	0.00358	0.0057	50
5	Carteolol	−0.26	4	−0.777	0.00511	0.0177	50
6	Ethosuximide	0.371	4	0.767	0.00569	0.0145	50
7	Finasteride	−0.349	6	−0.635	0.00693	0.1402	50
8	Scriptaid	0.507	3	0.818	0.01192	0.1389	66
9	Clemastine	−0.467	3	−0.808	0.01418	0.0504	66
10	Mycophenolic acid	−0.542	3	−0.793	0.01797	0.0974	66
11	Prestwick-857	−0.54	4	−0.696	0.01804	0.0382	75
12	Coralyne	−0.571	4	−0.692	0.0193	0.0067	75
13	Amphotericin B	−0.598	4	−0.687	0.02065	0.0385	75
14	Caffeic acid	0.455	3	0.78	0.02143	0.0208	66
15	Clebopride	−0.582	4	−0.675	0.02487	0.0132	75
16	Nabumetone	0.335	4	0.665	0.02839	0.0325	50
17	Alimemazine	−0.534	4	−0.661	0.0298	0.0272	75
18	(-)-Atenolol	0.376	4	0.658	0.03165	0.0147	50
19	Colecalciferol	0.191	4	0.646	0.03804	0.0469	50
20	Piretanide	−0.392	4	−0.643	0.03909	0.0833	50
21	Zardaverine	0.327	4	0.635	0.04327	0.0725	50
22	Dimenhydrinate	−0.195	4	−0.634	0.04368	0.0432	50
23	Bumetanide	−0.424	4	−0.629	0.04629	0.1622	50

key roles of m^6A modification and their regulators in tumor progression and prognosis.

We found that most of m^6A regulators including METTL14, WTAP, KIAA1429, RBM15, ZC3H13, YTHDC1, YTHDF1, YTHDF2, HNRNPC, and FTO were dysregulated in breast cancer than normal tissues. METTL14 displayed a strong correlation to YTHDC1 and YTHDC2 while YTHDC1 was strongly correlated to YTHDF1 and moderately correlated to HNRNPC. Among them, m^6A reader YTHDF1 aberration is correlated to undesirable survival outcomes in breast cancer subjects, which exhibited the consistency with the research from Anita et al. (20). The carcinogenic roles of YTHDF1 have been confirmed in previous research. For example, Liu et al. (21) reported that YTHDF1 facilitated ovarian carcinoma progress through controlling EIF3C translation. Bai et al. (22) reported that YTHDF1 accelerated tumorigenicity in colorectal carcinoma. Shi et al. (23) found that YTHDF1 correlated to hypoxia adaptation may contribute to non-small cell lung cancer development. Pi et al. (24) also demonstrated that YTHDF1 promoted gastric carcinogenesis through elevating translation of FZD7. Our pan-cancer analysis revealed that YTHDF1 was up-regulated in most types of cancer. Thus, YTHDF1 could be an oncogene. Our experiments confirmed that silencing YTHDF1 suppressed migrated and invasive capacities of breast cancer cells. The GSEA results demonstrated that high YTHDF1 expression was distinctly correlated to cell cycle, ERBB signaling pathway, oocyte meiosis, pathways in cancer, spliceosome, ubiquitin mediated proteolysis, and WNT signaling pathway. Meanwhile, ribosome was significantly enriched in low YTHDF1 expression group. It has been reported that YTHDF1 could regulate cell cycle progression in hepatocellular carcinoma (25). Recent research has reported that YTHDF1 mediates Wnt pathway activation in intestinal stemness (26). These findings were indicative that YTHDF1 up-regulation could participate in carcinogenesis.

Tumor immune microenvironment affects initiation as well as progress in breast cancer (27). Tumor-infiltrating immune cells are correlated to survival outcomes. Here, we found that YTHDF1 expression was distinctly related to T cells CD4 memory activated, macrophages M1, NK cells activated, and monocytes in breast cancer tissues. Vaccines against dendritic cells have exhibited prolonged survival time in breast cancer patients (28). Tumor-associated macrophages may modulate the efficacy of anti-PD-1/PD-L1 therapy in breast cancer (29). Our data were indicative that YTHDF1 might modulate the immune microenvironment of breast cancer, thereby, affecting tumor progression as well as immunotherapy efficacy. For immunotherapy, the higher the TMB of cancer cells, the increased new antigens may be produced. The higher the immunogenicity of the antigen, the stronger the T cell response, and anti-tumor response, which is more suitable for immunotherapy. Immune-checkpoint inhibitors (ICIs) are novel therapeutic strategies against breast cancer. Nevertheless, only some subjects respond to PD-1 or PD-L1 therapy. As widely accepted, breast cancer patients with high TMB can benefit

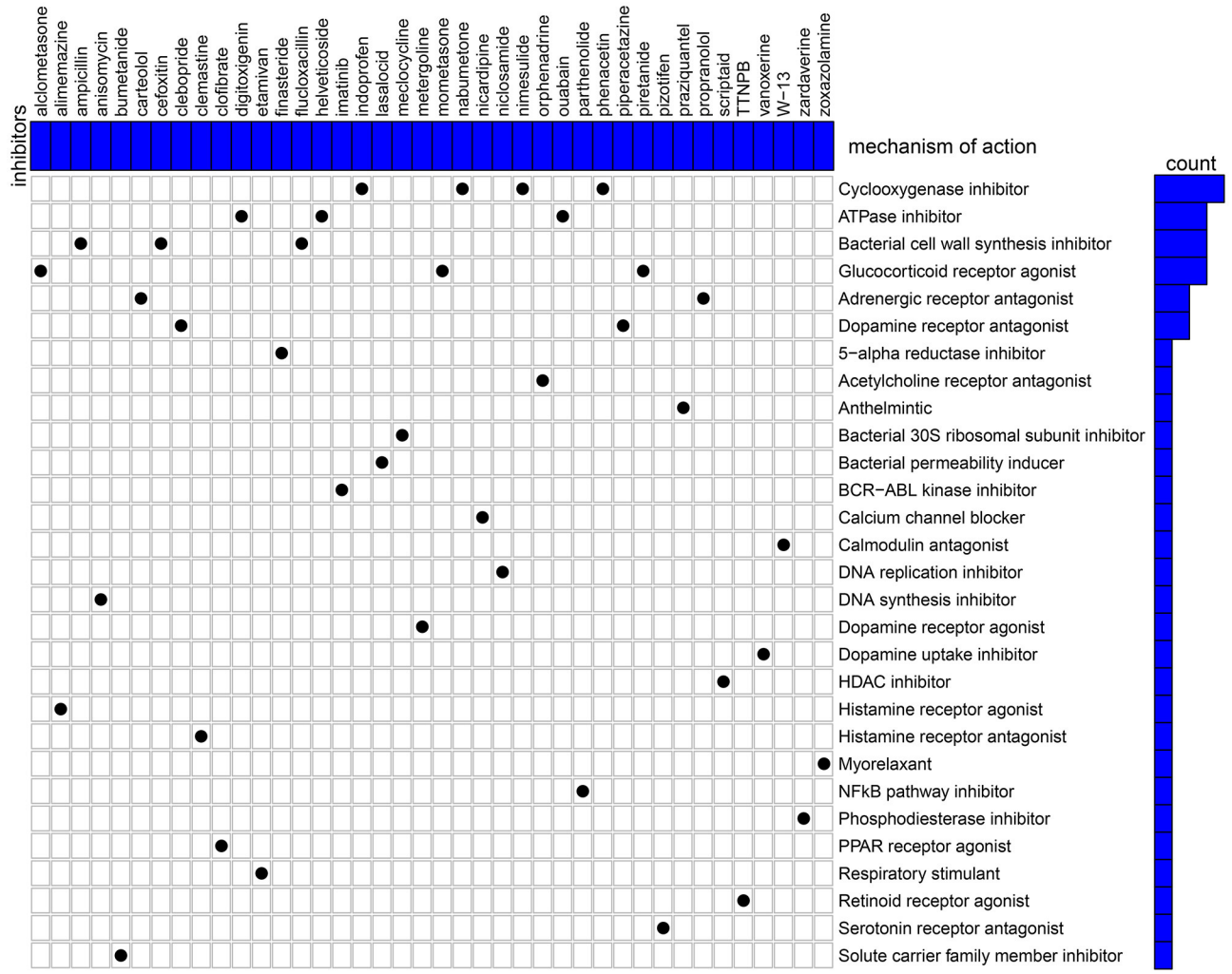

FIGURE 9 | CMap identifies the candidate therapeutic agents related to the DEGs between high and low YTHDF1 expression breast cancer samples. Heatmap shows each inhibitor (perturbagen) and its shared mechanism of action (row).

from immunotherapy (30). Here, we found that TMB score was significantly higher in high YTHDF1 expression group compared to its low expression group, indicating that subjects with high YTHDF1 expression were more likely to benefit from immunotherapy.

The occurrence of tumors is the result of the accumulation of somatic mutations (31). In fact, there are basically non-synonymous mutations in the development of tumors. Because the mutation will increase immunogenicity, but in order to avoid being detected and eliminated by the immune system, tumors often increase immune checkpoints (32). The driver gene mutations can lead to tumors, so that a large number of somatic mutations can produce new antigens, which can activate $CD8^+$ cytotoxic T cells, thereby, exerting T cell-mediated anti-tumor effects (33). Therefore, when the number of gene mutations accumulates, more new antigens will be produced, which will be more likely to be recognized by the immune system. Among the 986 breast cancer patients, 26.37% samples in high YTHDF1 expression group and 44.62% samples in low expression group occurred genetic mutations, indicating that the frequency of mutations in breast cancer patients was very high. Among them, missense mutation and non-sense mutation were most frequently. Both in high and low expression of YTHDF1 groups, the five most common mutant genes were TP53, PIK3CA, TTN, CDH1, and GATA3, indicating that these mutated genes contributed to the progression of breast cancer.

Except for breast cancer, up-regulation of YTHDF1 was found in various cancers, indicating that YTHDF1 could be an oncogene. To explore underlying molecular mechanisms of YTHDF1 in breast cancer, we screened DEGs between high and low YTHDF1 expression groups. Our results showed that DEGs were mainly involved in RNA metabolism processes, such as cAMP-mediated signaling, cyclic-nucleotide-mediated signaling, adenylate cyclase-modulating G protein-coupled receptor

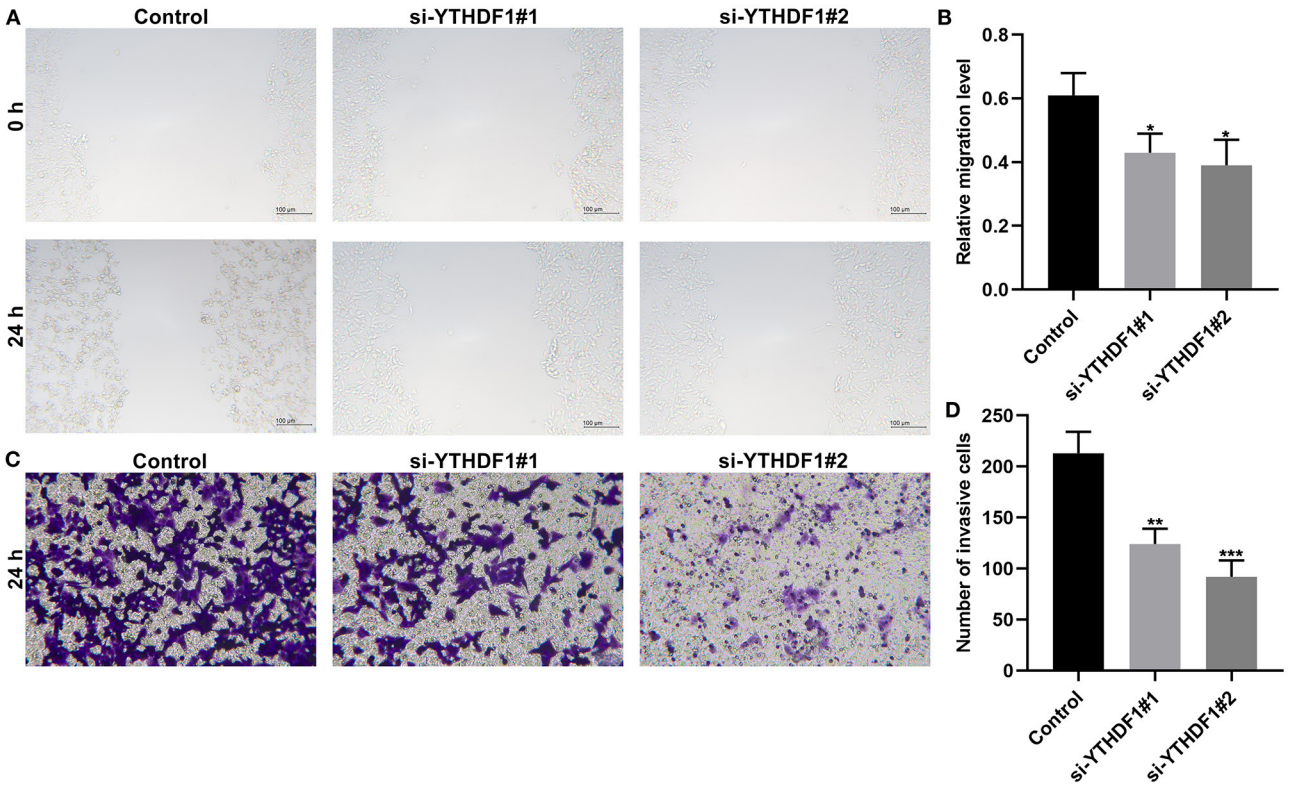

FIGURE 10 | YTHDF1 knockdown restrains migrated and invasive abilities of in MCF-7 cells transfected with si-YTHDF1. **(A,B)** Scratch test for the relative migrated levels of transfected MCF-7 cells. **(C,D)** Transwell for the number of invasive MCF-7 cells. $^{*}P < 0.05$; $^{**}p < 0.01$; $^{***}p < 0.001$.

signaling pathway, second-messenger-mediated signaling as well as adenylate cyclase-activating G protein-coupled receptor signaling pathway. These findings indicated that YTHDF1 promoted tumor progression mainly by m^{6}A modification. This study also screened several small molecular inhibitors such as cyclooxygenase inhibitor (indoprofen, nabumetone, nimesulide, and phenacetin), ATPase inhibitor (digitoxigenin, helveticoside, ouabain), glucocorticoid receptor agonist (alclometasone, mometasone, and piretanide), which might be candidate therapeutic agents against breast cancer. More experiments should be carried out to investigate the therapeutic effects of these small molecular inhibitors in breast cancer cells.

CONCLUSION

Collectively, this study characterized the dysregulated expression patterns of m^{6}A regulators in breast cancer. Among them, YTHDF1 overexpression was distinctly indicative of undesirable survival outcomes. Moreover, YTHDF1 up-regulation exhibited a significant association with cancer-related pathways such as cell cycle, pathways in cancer and Wnt signaling pathway. YTHDF1 expression was significantly correlated to tumor-infiltrating immune cells, indicating that it might contribute to the complexity and diversity of immune microenvironment. Furthermore, subjects with YTHDF1 up-regulation were more likely to benefit from immunotherapy. Several underlying small molecular compounds against breast cancer were discovered based on YTHDF1-related DEGs. In conclusion, our data suggested the implications of m^{6}A regulators in survival outcomes, immune microenvironment as well as response to immunotherapy in breast cancer.

DATA AVAILABILITY STATEMENT

The datasets presented in this study can be found in online repositories. The names of the repository/repositories and accession number(s) can be found in the article/supplementary material.

AUTHOR CONTRIBUTIONS

JJ and PT conceived and designed the study. YH, QP, and MW conducted most of the experiments and data analysis and wrote the manuscript. XA, YY, YT, and YJ participated in collecting data and helped to draft the manuscript. All authors reviewed and approved the manuscript.

FUNDING

This work was funded by Chongqing Basic Research and Frontier Exploration Project (cstc2018jcyjAX0379).

REFERENCES

1. Britt KL, Cuzick J, Phillips KA. Key steps for effective breast cancer prevention. *Nat Rev Cancer.* (2020) 20:417–36. doi: 10.1038/s41568-020-0266-x
2. de Bessa Garcia SA, Araújo M, Pereira T, Mouta J, Freitas R. HOX genes function in breast cancer development. *Biochim Biophys Acta Rev Cancer.* (2020) 1873:188358. doi: 10.1016/j.bbcan.2020.188358
3. Wagner J, Rapsomaniki MA, Chevrier S, Anzeneder T, Langwieder C, Dykgers A, et al. A single-cell atlas of the tumor and immune ecosystem of human breast cancer. *Cell.* (2019) 177:1330–45.e18. doi: 10.1016/j.cell.2019.03.005
4. Li N, Deng Y, Zhou L, Tian T, Yang S, Wu Y, et al. Global burden of breast cancer and attributable risk factors in 195 countries and territories, from 1990 to 2017: results from the Global Burden of Disease Study 2017. *J Hematol Oncol.* (2019) 12:140. doi: 10.1186/s13045-019-0828-0
5. Liang Y, Zhang H, Song X, Yang Q. Metastatic heterogeneity of breast cancer: molecular mechanism and potential therapeutic targets. *Semin Cancer Biol.* (2020) 60:14–27. doi: 10.1016/j.semcancer.2019.08.012
6. Chen XY, Zhang J, Zhu JS. The role of m(6)A RNA methylation in human cancer. *Mol Cancer.* (2019) 18:103. doi: 10.1186/s12943-019-1033-z
7. Li Y, Gu J, Xu F, Zhu Q, Chen Y, Ge D, et al. Molecular characterization, biological function, tumor microenvironment association and clinical significance of m6A regulators in lung adenocarcinoma. *Brief Bioinform.* (2020). doi: 10.1093/bib/bbaa225
8. Niu X, Xu J, Liu J, Chen L, Qiao X, Zhong M. Landscape of N(6)-methyladenosine modification patterns in human ameloblastoma. *Front Oncol.* (2020) 10:556497. doi: 10.3389/fonc.2020.556497
9. Niu Y, Lin Z, Wan A, Chen H, Liang H, Sun L, et al. RNA N6-methyladenosine demethylase FTO promotes breast tumor progression through inhibiting BNIP3. *Mol Cancer.* (2019) 18:46. doi: 10.1186/s12943-019-1004-4
10. Cai X, Wang X, Cao C, Gao Y, Zhang S, Yang Z, et al. HBXIP-elevated methyltransferase METTL3 promotes the progression of breast cancer *via* inhibiting tumor suppressor let-7g. *Cancer Lett.* (2018) 415:11–9. doi: 10.1016/j.canlet.2017.11.018
11. Azizi E, Carr AJ, Plitas G, Cornish AE, Konopacki C, Prabhakaran S, et al. Single-cell map of diverse immune phenotypes in the breast tumor microenvironment. *Cell.* (2018) 174:1293–308.e36. doi: 10.1016/j.cell.2018.05.060
12. Zhang B, Wu Q, Li B, Wang D, Wang L, Zhou YL. m(6)A regulator-mediated methylation modification patterns and tumor microenvironment infiltration characterization in gastric cancer. *Mol Cancer.* (2020) 19:53. doi: 10.1186/s12943-020-01170-0
13. Li N, Kang Y, Wang L, Huff S, Tang R, Hui H, et al. ALKBH5 regulates anti-PD-1 therapy response by modulating lactate and suppressive immune cell accumulation in tumor microenvironment. *Proc Natl Acad Sci U S A.* (2020) 117:20159–70. doi: 10.1073/pnas.1918986117
14. Subramanian A, Tamayo P, Mootha VK, Mukherjee S, Ebert BL, Gillette MA, et al. Gene set enrichment analysis: a knowledge-based approach for interpreting genome-wide expression profiles. *Proc Natl Acad Sci U S A.* (2005) 102:15545–50. doi: 10.1073/pnas.0506580102
15. Mayakonda A, Lin DC, Assenov Y, Plass C, Koeffler HP. Maftools: efficient and comprehensive analysis of somatic variants in cancer. *Genome Res.* (2018) 28:1747–56. doi: 10.1101/gr.239244.118
16. Newman AM, Liu CL, Green MR, Gentles AJ, Feng W, Xu Y, et al. Robust enumeration of cell subsets from tissue expression profiles. *Nat Methods.* (2015) 12:453–7. doi: 10.1038/nmeth.3337
17. Ravaioli S, Limarzi F, Tumedei MM, Palleschi M, Maltoni R, Bravaccini S. Are we ready to use TMB in breast cancer clinical practice? *Cancer Immunol Immunother.* (2020) 69:1943–5. doi: 10.1007/s00262-020-02682-w
18. Yu G, Wang LG, Han Y, He QY. clusterProfiler: an R package for comparing biological themes among gene clusters. *Omics.* (2012) 16:284–7. doi: 10.1089/omi.2011.0118
19. Subramanian A, Narayan R, Corsello SM, Peck DD, Natoli TE, Lu X, et al. A next generation connectivity map: L1000 platform and the first 1,000,000 profiles. *Cell.* (2017) 171:1437–52.e17. doi: 10.1016/j.cell.2017.10.049
20. Anita R, Paramasivam A, Priyadharsini JV, Chitra S. The m6A readers YTHDF1 and YTHDF3 aberrations associated with metastasis and predict poor prognosis in breast cancer patients. *Am J Cancer Res.* (2020) 10:2546–54.
21. Liu T, Wei Q, Jin J, Luo Q, Liu Y, Yang Y, et al. The m6A reader YTHDF1 promotes ovarian cancer progression *via* augmenting EIF3C translation. *Nucleic Acids Res.* (2020) 48:3816–31. doi: 10.1093/nar/gkaa048
22. Bai Y, Yang C, Wu R, Huang L, Song S, Li W, et al. YTHDF1 regulates tumorigenicity and cancer stem cell-like activity in human colorectal carcinoma. *Front Oncol.* (2019) 9:332. doi: 10.3389/fonc.2019.00332
23. Shi Y, Fan S, Wu M, Zuo Z, Li X, Jiang L, et al. YTHDF1 links hypoxia adaptation and non-small cell lung cancer progression. *Nat Commun.* (2019) 10:4892. doi: 10.1038/s41467-019-12801-6
24. Pi J, Wang W, Ji M, Wang X, Wei X, Jin J, et al. YTHDF1 promotes gastric carcinogenesis by controlling translation of FZD7. *Cancer Res.* (2020) 81:2651–65. doi: 10.1158/0008-5472.CAN-20-0066
25. Zhao X, Chen Y, Mao Q, Jiang X, Jiang W, Chen J, et al. Overexpression of YTHDF1 is associated with poor prognosis in patients with hepatocellular carcinoma. *Cancer Biomark.* (2018) 21:859–68. doi: 10.3233/CBM-170791
26. Han B, Yan S, Wei S, Xiang J, Liu K, Chen Z, et al. YTHDF1-mediated translation amplifies Wnt-driven intestinal stemness. *EMBO Rep.* (2020) 21:e49229. doi: 10.15252/embr.201949229
27. Tekpli X, Lien T, Røssevold AH, Nebdal D, Borgen E, Ohnstad HO, et al. An independent poor-prognosis subtype of breast cancer defined by a distinct tumor immune microenvironment. *Nat Commun.* (2019) 10:5499. doi: 10.1038/s41467-019-13329-5
28. Basu A, Ramamoorthi G, Jia Y, Faughn J, Wiener D, Awshah S, et al. Immunotherapy in breast cancer: current status and future directions. *Adv Cancer Res.* (2019) 143:295–349. doi: 10.1016/bs.acr.2019.03.006
29. Santoni M, Romagnoli E, Saladino T, Foghini L, Guarino S, Capponi M, et al. Triple negative breast cancer: key role of tumor-associated macrophages in regulating the activity of anti-PD-1/PD-L1 agents. *Biochim Biophys Acta Rev Cancer.* (2018) 1869:78–84. doi: 10.1016/j.bbcan.2017.10.007
30. Barroso-Sousa R, Jain E, Cohen O, Kim D, Buendia-Buendia J, Winer E, et al. Prevalence and mutational determinants of high tumor mutation burden in breast cancer. *Ann Oncol.* (2020) 31:387–94. doi: 10.1016/j.annonc.2019.11.010
31. Zhang Y, Xiong S, Liu B, Pant V, Celii F, Chau G, et al. Somatic Trp53 mutations differentially drive breast cancer and evolution of metastases. *Nat Commun.* (2018) 9:3953. doi: 10.1038/s41467-018-06146-9
32. Zacharakis N, Chinnasamy H, Black M, Xu H, Lu YC, Zheng Z, et al. Immune recognition of somatic mutations leading to complete durable regression in metastatic breast cancer. *Nat Med.* (2018) 24:724–30. doi: 10.1038/s41591-018-0040-8
33. Kraya AA, Maxwell KN, Wubbenhorst B, Wenz BM, Pluta J, Rech AJ, et al. Genomic signatures predict the immunogenicity of BRCA-deficient breast cancer. *Clin Cancer Res.* (2019) 25:4363–74. doi: 10.1158/1078-0432.CCR-18-0468

Conflict of Interest: The authors declare that the research was conducted in the absence of any commercial or financial relationships that could be construed as a potential conflict of interest.

Publisher's Note: All claims expressed in this article are solely those of the authors and do not necessarily represent those of their affiliated organizations, or those of the publisher, the editors and the reviewers. Any product that may be evaluated in this article, or claim that may be made by its manufacturer, is not guaranteed or endorsed by the publisher.

Copyright © 2021 Hu, Pan, Wang, Ai, Yan, Tian, Jing, Tang and Jiang. This is an open-access article distributed under the terms of the Creative Commons Attribution License (CC BY). The use, distribution or reproduction in other forums is permitted, provided the original author(s) and the copyright owner(s) are credited and that the original publication in this journal is cited, in accordance with accepted academic practice. No use, distribution or reproduction is permitted which does not comply with these terms.

frontiers in Medicine

ORIGINAL RESEARCH
published: 11 August 2021
doi: 10.3389/fmed.2021.658926

Isoflurane Suppresses Proliferation, Migration, and Invasion and Facilitates Apoptosis in Colorectal Cancer Cells Through Targeting miR-216

*Zhe Cai, Liangyuan Suo and Zeqing Huang**

Department of Anesthesiology, Cancer Hospital of China Medical University, Liaoning Cancer Hospital & Institute, Shenyang, China

Objective: Surgery is the first line treatment of colorectal cancer (CRC). Anesthetic isoflurane may improve outcomes of cancer surgery. Herein, we investigated the effects of isoflurane on malignant behaviors of CRC cells and its underlying therapeutic target.

Methods: SW620 and HCT116 CRC cells were exposed to a series of concentrations of isoflurane. CCK-8 assay was utilized for determination of the optimal concentration of isoflurane. Under treatment with isoflurane, proliferation, migration, and invasion were separately assessed via clone formation and transwell assays. Apoptotic levels were observed via flow cytometry and expression of Bax, Bcl-2, and Caspase3 proteins was quantified through western blot. MiR-216 expression was detected in isoflurane-induced SW620 and HCT116 cells by RT-qPCR. Following transfection with miR-216 mimic, malignant biological behaviors were examined in isoflurane-treated SW620 and HCT116 cells.

Results: 40 μM isoflurane distinctly restrained proliferative, migrated, and invasive capacities and elevated apoptotic levels in SW620 and HCT116 cells. Up-regulation of miR-216 was found in CRC cells. Its expression was suppressed by isoflurane. MiR-216 mimic ameliorated the reduction in proliferation, migration, and invasion and the increase in apoptosis for 40 μM isoflurane-induced SW620 and HCT116 cells.

Conclusion: Isoflurane, a promising drug of CRC, may suppress malignant biological behaviors of tumor cells. Furthermore, miR-216 is an underlying target of isoflurane. Thus, isoflurane could be adopted for CRC treatment.

Keywords: isoflurane, colorectal cancer, miR-216, proliferation, apoptosis, migration, invasion

OPEN ACCESS

Edited by:
Fu Wang,
Xi'an Jiaotong University, China

Reviewed by:
Weiwei Liu,
Chinese Academy of Agricultural Sciences (CAAS), China
Chunlin Ou,
Central South University, China

****Correspondence:***
Zeqing Huang
huangzeqing@cancerhosp-ln-cmu.com

Specialty section:
This article was submitted to Precision Medicine, a section of the journal Frontiers in Medicine

Received: *26 January 2021*
Accepted: *04 June 2021*
Published: *11 August 2021*

Citation:
Cai Z, Suo L and Huang Z (2021) Isoflurane Suppresses Proliferation, Migration, and Invasion and Facilitates Apoptosis in Colorectal Cancer Cells Through Targeting miR-216. Front. Med. 8:658926. doi: 10.3389/fmed.2021.658926

INTRODUCTION

Colorectal cancer (CRC) becomes the third most common malignant tumor as well as the second major cause of cancer-related deaths (1). It was estimated that there were 1,800,977 diagnosed cases and 861,663 death cases globally in 2018 (2). It has been under expectation that death toll will rise in colon and rectal carcinoma by 60 and 71.5% until 2035 (3). The incidence of CRC tends to be

younger (4). Though the 5-year survival rate is up to 90% among subjects diagnosed as stage I, this decrease is mildly >10% among those diagnosed as stage IV (5). Distant metastases contribute to unfavorable outcomes of CRC patients. CRC therapies often contain surgery, chemotherapy as well as targeted therapy. However, the therapeutic strategies against CRC remain dissatisfactory. Exploring new drugs and targets is indispensable.

Because CRC patients present a wide range of drug resistance and side effects for various chemotherapy drugs, it is of necessity for screening high-efficient and low-toxic anti-tumor drugs and finding effective therapeutic targets (6). Isoflurane is an inhaled anesthetic widely applied in surgery. Experimental and clinical research has confirmed the varying effects of anesthetics including isoflurane on cancer outcomes (7). Studies have shown that isoflurane is involved in various biological processes like proliferative, apoptotic, invasive, and metastatic capacities for multifarious malignant tumor cells including CRC (8–10). For instance, volatile anesthetic decreases invasive ability of CRC cells via down-regulating MMP-9 (11). Nevertheless, this effect of isoflurane on malignant behaviors of CRC cells and molecular mechanism remains ambiguous.

The progress of CRC is under the coordinated regulation of multiple genes, forming a long-term and complex regulation process (12). Various miRNAs are involved in mediating this disease (13). Identifying individual gene expression differences in CRC is a prerequisite for individualized therapy strategy (14). Recent studies have disclosed various specific miRNAs in tumor tissue specimens and serum from CRC subjects (15–17). Given that miRNAs have disease and tissue specific expression and huge regulatory potential on tumor malignant biological behaviors, miRNAs have aroused widespread concern. Previous studies have reported the roles of miR-216 in several cancers. For instance, miR-216 mediates proliferation, invasion, and cell cycle of gastric cancer cells (18). Furthermore, miR-216 is involved in tumorigenesis of cervical cancer cells (19). Specifically, circulating miR-216 is a predictor of the chemosensitivity for CRC subjects (20). Nevertheless, biological functions including cell proliferation, migration, and invasion of miR-216 in CRC require further exploration. Here, this study found that isoflurane may distinctly suppress proliferative, migrated, and invasive behaviors as well as elevate apoptotic levels of CRC cells partly through targeting miR-216.

MATERIALS AND METHODS

Cell Culture

Human normal colorectal mucosal cells NCM460 and two CRC cell lines SW620 and HCT116 (Cell Resource Center, Shanghai Institute of Biological Sciences, China). Because SW620 and HCT116 cells have been widely applied to study the molecular mechanism and potential drugs of CRC, we chose the two cells in this study. The cells were maintained in RPMI-1640 medium (Gibco, USA) plus 10% FBS in an incubator with 5% CO_2 at 37°C.

Abbreviations: CRC, colorectal cancer; qRT-PCR, quantitative real-time polymerase chain reaction; NC, negative control; CCK-8, cell counting kit-8; ns, no significance.

Quantitative Real-Time Polymerase Chain Reaction (qRT-PCR)

When taking RNA from CRC cells, the culture medium was discarded and rinsed twice. One milliliter of TRIzol reagent (Invitrogen, USA) was added to each well of the six-well plate. Using a pipette to repeatedly aspirate, samples were placed at room temperature to fully dissolve. Then the lysed cell solution was transferred to a centrifuge tube and 0.2 ml chloroform was added to the solution for 10 s. After leaving it at room temperature for 5 min, the cells were centrifuged at 10,000 g at 4°C for 15 min. The upper aqueous phase was transferred to a new RNase-free centrifuge tube. 0.5 ml isopropanol was added and then place it at room temperature for 10 min. Under centrifugation at 10,000 g at 4°C for 5 min, the supernatant was discarded. Cells were treated with 1 ml 75% ethanol made up of DEPC, and centrifuged at 10,000 g at 4°C for 5 min. After discarding the supernatant, 20 μl RNase-free water was added to dissolve the RNA precipitate. Using an ultraviolet spectrophotometer, the absorbance of RNA at OD260 and OD280 was detected. The ratio of OD260/OD280 was utilized for measuring RNA purity. qRT-PCR was used to detect the expression of miR-216. Poly (A) tailing reaction and reverse transcription reaction system were as follows: 5 μl 2×miRNA reaction buffer mix, 1 μl 0.1% BSA, 1 μl miRNA PrimeScript RT enzyme mix, 2.5 μl RNase-free H_2O and 0.5 μl total RNA. The reaction system of qRT-PCR was as follows: 20 μl SYBR Premix Ex Taq TMII, 3.2 μl upstream primer, 3.2 μl downstream primer, 4 μl cDNA template. miR-216: 5′-GCCGGCGCCCGAGCTCTGGCTC-3′ (forward), 5′-CATTATTACTTTTGGTACGCG-3′ (reverse), U6: 5′-CTCGCTTCGGCAGCACA-3′ (forward), 5′-AACGCTTCACGAATTTGCGT-3′ (reverse). The qRT-PCR reaction was carried out on the LightCycler 480II qRT-PCR instrument (Roche, Switzerland). The reaction conditions were 95°C for 30 s; at 95°C for 5 s of 40 cycles; at 60°C for 20 s. MiR-216 expression was quantified with the $2^{-\Delta\Delta Ct}$ method.

Transfection

CRC cells that were in a good growth state and in the logarithmic growth phase were digested with trypsin and inoculated in a 6-well plate. Transfection was presented when the cell density reached 50–60% after 24 h of culture. Fifty nanomolar of miR-216 mimic and negative control (NC; Gene Pharma, China) were transfected into CRC cells. According to the product instruction manual, miRNA mimic and lipofectamine 2000 (Invitrogen, USA) were diluted with Opti-MEM (Invitrogen, USA), which were added to the culture well. After culturing for 4 h, the medium was discarded and the medium containing 10% FBS was replaced to continue the culture. Forty-eight hours after transfection, the cells were collected for qRT-PCR.

Cell Counting Kit-8 (CCK-8)

CRC cells were seeded into 96-well culture plates (3×10^3 cells per well). They were treated with 0, 5, 10, 20, 40, 80, 160, and 320 μM isoflurane. After culturing for 48 h, each well

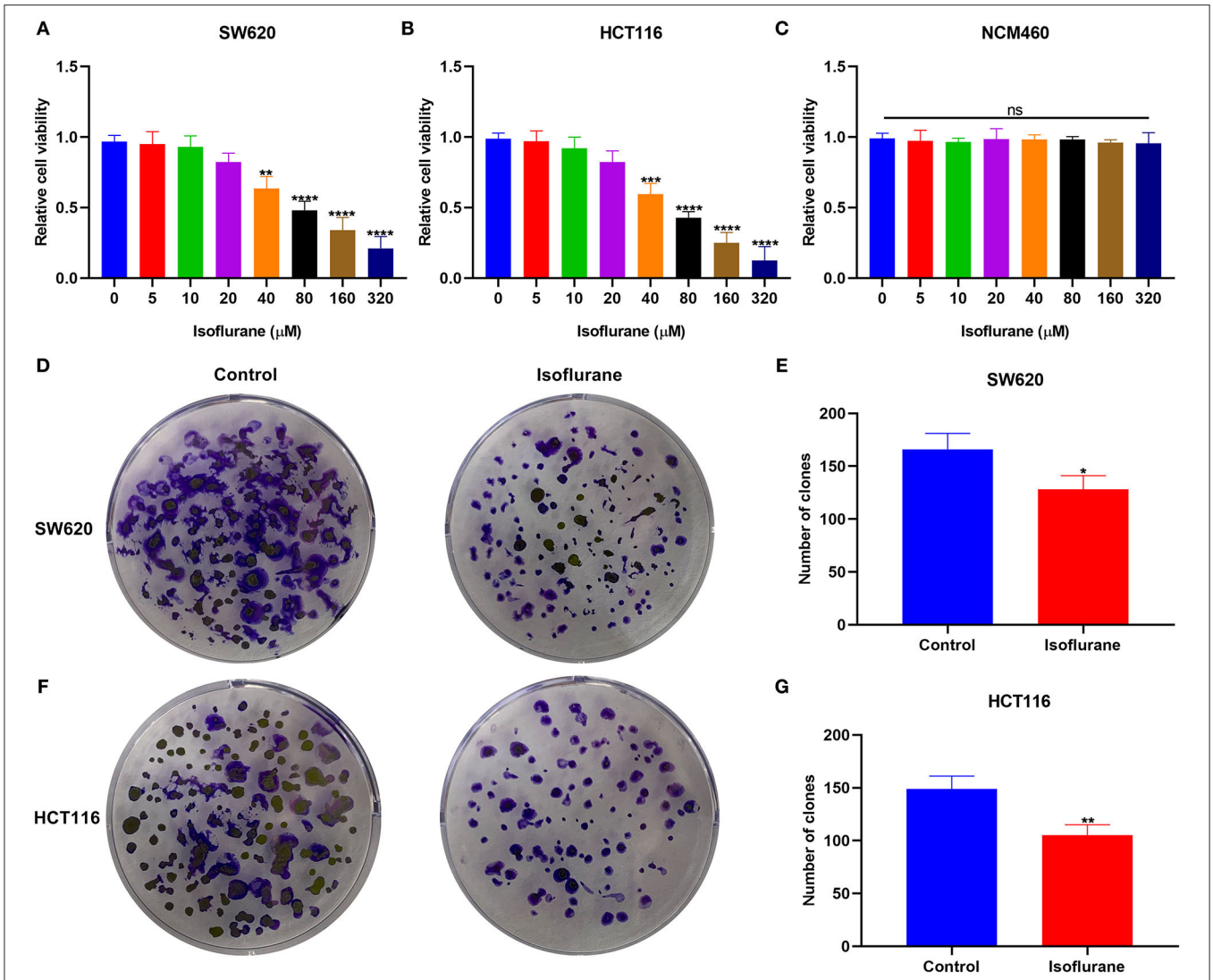

FIGURE 1 | The inhibitory effects of isoflurane on CRC cell proliferation. The cell viability of **(A)** SW620, **(B)** HCT116, and **(C)** NCM460 cells treated by 0, 5, 10, 20, 40, 80, 160, and 320 μM isoflurane. The number of clones of **(D,E)** SW620 and **(F,G)** HCT116 cells under treatment with 40 μM isoflurane. Ns, no significance; $^{*}p < 0.05$; $^{**}p < 0.01$; $^{***}p < 0.001$; $^{****}p < 0.0001$.

was replaced with a new medium. Ten microliters of CCK-8 solution (Dojindo, Japan) was added to each well, and continued incubating for 1 h. The microplate reader (Thermo, USA) was utilized to detect the absorbance value of each well at 450 nm wavelength.

Clone Formation Assay

1×10^4 CRC cells were seeded in 6-well plates. The cells were transfected with miRNA NC and miRNA mimic, respectively. After 48 h, cells were digested with 0.25% trypsin. They were seeded in a 6-well plate (400 cells/well) and cultured for 14 days. The cell culture medium was discarded. The cells were stained with crystal violet at room temperature for 15 min, and slowly washed twice with running water to wash away the dyeing solution. The number of colonies was counted.

Flow Cytometry

The transfected cells were digested with trypsin digestion solution without EDTA. The cell suspension was centrifuged at 1,000 g for 5 min. After discarding the supernatant, the cells were suspended in PBS and centrifuged again. The supernatant was then discarded. One hundred and ninety-five microliters of Annexin V-FITC (Beyotime, Hangzhou, China) binding solution was added to resuspend the cells, followed by 5 μl Annexin V-FITC and 10 μl PI (Beyotime, Hangzhou, China) staining solution. Flow cytometry was utilized to detect cell apoptosis.

Western Blot

After 48 h of cell transfection, the culture medium in the 6-well plate was discarded. One hundred and fifty microliters of RIPA lysis buffer was added to each well. The cells were pipetted with

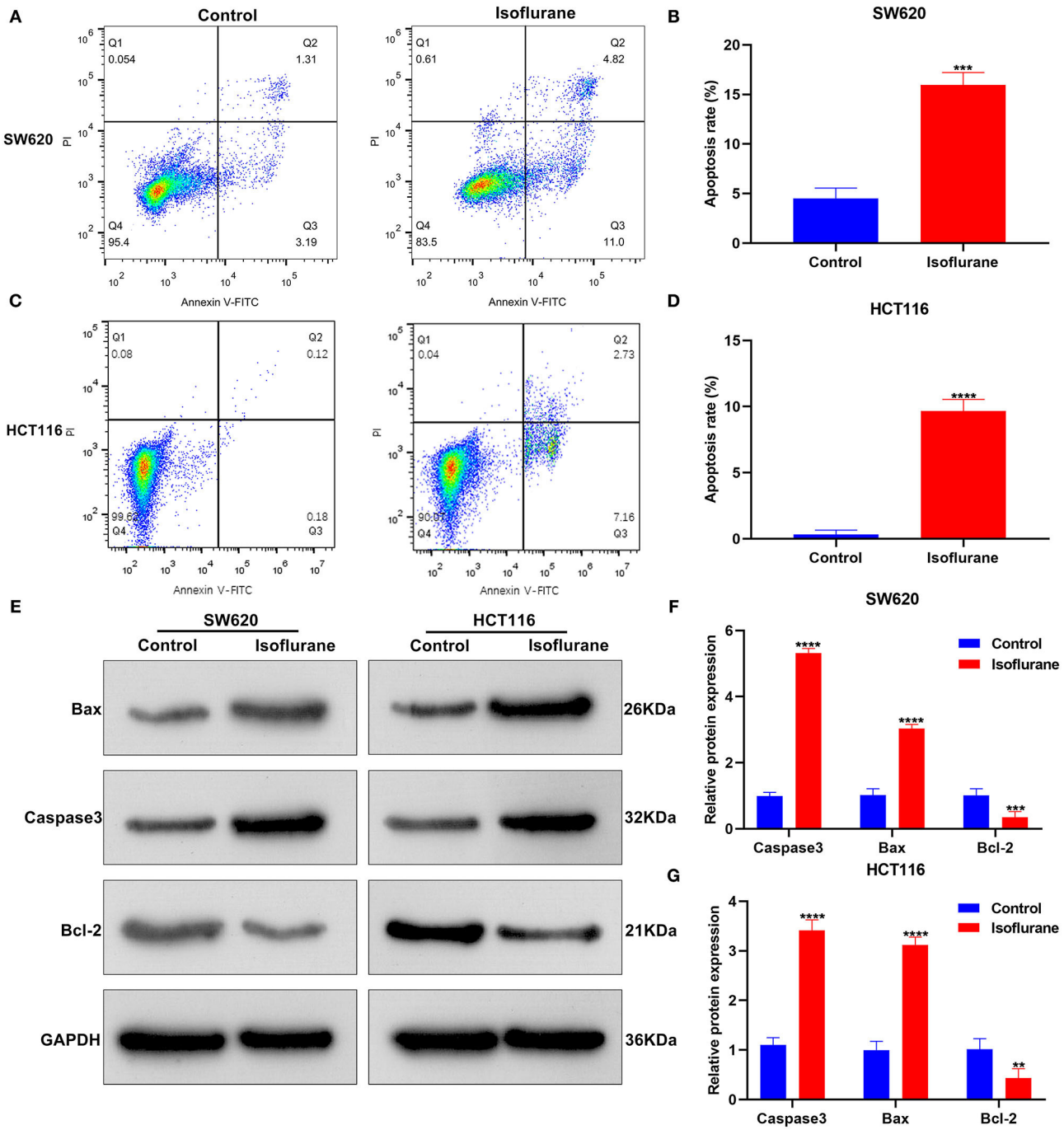

FIGURE 2 | The promotional effects of isoflurane on CRC cell apoptosis. Apoptosis rates of **(A,B)** SW620 and **(C,D)** HCT116 cells under treatment with 40 μM isoflurane. **(E–G)** Expression of Caspase3, Bax and Bcl-2 proteins in SW620 and HCT116 cells following exposure to 40 μM isoflurane. $^{**}p < 0.01$; $^{***}p < 0.001$; $^{****}p < 0.0001$.

a 200 μl pipette. After the cells were fully lysed, the lysate was centrifuged at 14,000 g for 5 min. The protein concentration was determined by the BCA method. The protein sample was mixed with the protein loading buffer in proportion and denatured it in boiling water for 5 min. According to the measured protein concentration, the sample load per well was 20 μg. The protein sample was separated by SDS-PAGE and transferred to PVDF membrane. The membrane was blocked with skim milk at room temperature for 1 h. After rinsing the membrane with 1 × TBST for 5 min × 3 times, the membrane was incubated with primary

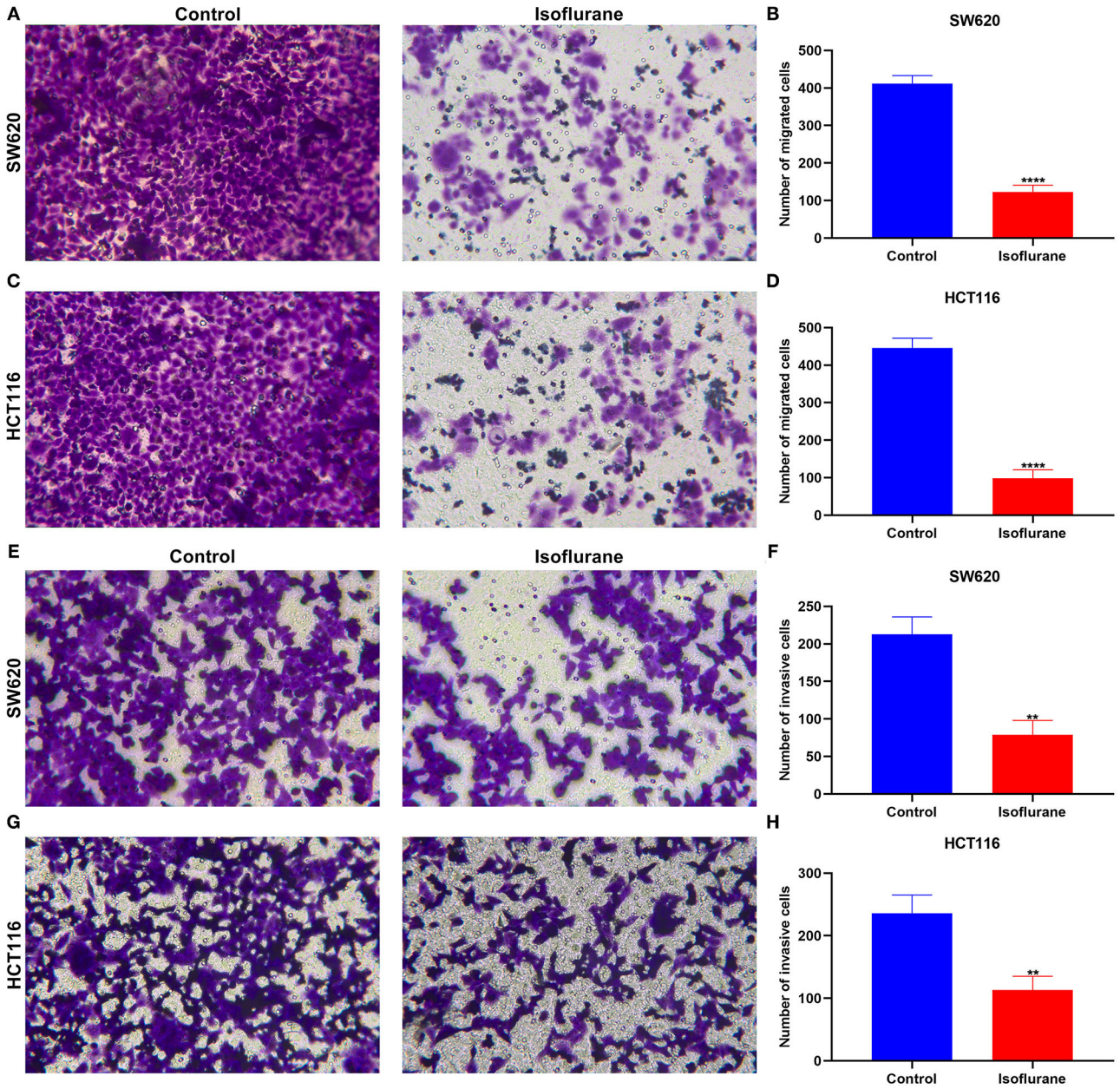

FIGURE 3 | The suppressed role of isoflurane on migrated and invasive capacities of CRC cells. The number of migrated **(A,B)** SW620 and **(C,D)** HCT116 cells following 40 μM isoflurane treatment. The number of invasive **(E,F)** SW620 and **(G,H)** HCT116 cells exposed to 40 μM isoflurane. $^{**}p < 0.01$; $^{****}p < 0.0001$.

antibody against Bax (1:1,000; ab270742; Abcam, USA), Bcl-2 (1:1,000; ab196495; Abcam, USA), Caspase3 (1:1,000; ab90437; Abcam, USA) and GAPDH (1:1,000; ab181602; Abcam, USA) overnight at 4°C. The membrane was placed on a 1 × TBST horizontal shaker and rinsed for 10 min × 3 times. HRP-labeled secondary antibody (ab7090; Abcam, USA) was diluted to 1:2,000 with 5% blocking solution and incubated it on a shaker at room temperature for 1 h. After rinsing again, the membrane was incubated with ECL reagent (Beyotime, Hangzhou, China). Image J analyzed the optical density value of the target band.

Transwell

Transwell assays were utilized for detecting migration and invasion. For migration assay, transwell chamber (Corning Costar, USA) was coated without Matrigel. For invasion assay, transwell chamber was coated with Matrigel (BD, USA). 3 × 10^5 CRC cells were seed onto the upper chamber. The lower chamber was incubated with 600 μl RPMI-1640 medium plus 20% FBS at 37°C. Using a cotton swab, cells that did not migrate or invade the upper chamber were removed. The cells in the lower chamber were fixed with methanol for 10 min and stained

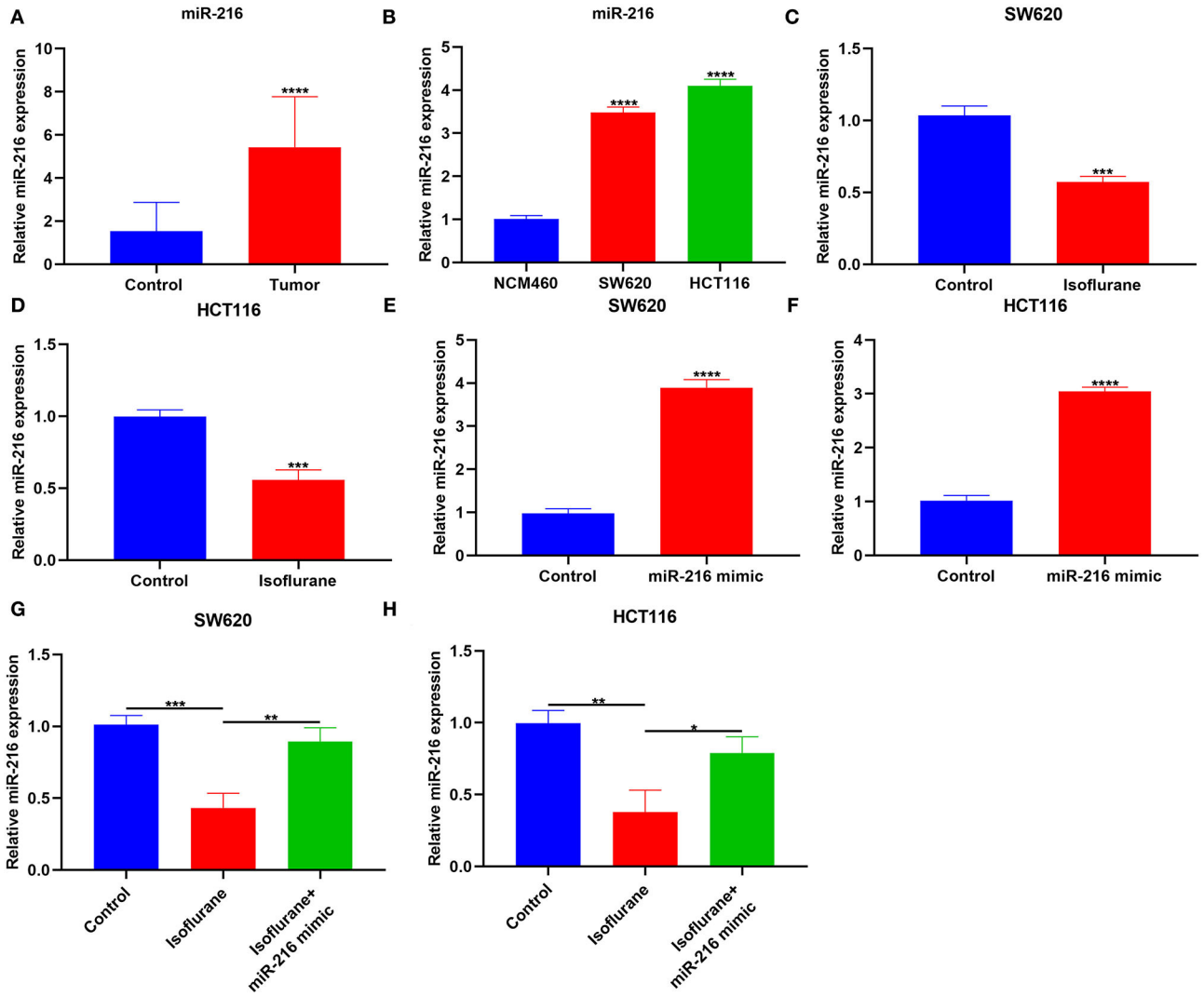

FIGURE 4 | The inhibitory function of isoflurane on miR-216 expression in CRC cells. **(A)** RT-qPCR for miR-216 expression in CRC and control tissue specimens. **(B)** miR-216 expression in NCM460, SW620, and HCT116 cells. **(C,D)** MiR-216 expression in **(B)** SW620 and **(C)** HCT116 cells exposed to 40 μM isoflurane. MiR-216 expression in **(E)** SW620 and **(F)** HCT116 cells transfected by miR-216 mimic. MiR-216 expression in **(G)** SW620 and **(H)** HCT116 cells following treatment with 40 μM isoflurane and/or miR-216 mimic. *$p < 0.05$; **$p < 0.01$; ***$p < 0.001$; ****$p < 0.0001$.

with crystal violet (Beyotime, Hangzhou, China) solution for 5 min.

Sample Collection

Totally, 30 CRC tissues and matched adjacent normal tissues were harvested from the Cancer Hospital of China Medical University (China). All of them did not experience chemotherapy/radiotherapy before surgery. Specimens were confirmed by two pathologists as CRC. This research was in line with the Declaration of Helsinki. This study acquired the approval of the ethics committee of the Cancer Hospital of China Medical University (2020021). Each participant signed a written informed consent. MiR-216 expression was detected in CRC and control tissues by qRT-PCR.

Statistical Analysis

Statistical analyses were presented through SPSS 21.0 software (SPSS Inc., Chicago, IL, USA). Data were expressed as the mean ± standard deviation. Comparisons between groups were analyzed by student's *t*-test or one-way ANOVA followed by Tukey's *post-hoc* test. $P < 0.05$ was indicative of statistical significance.

RESULTS

Isoflurane Restrains CRC Cell Proliferation

To determine the optimal concentration of isoflurane on CRC cells, SW620 and HCT116 CRC cells were treated with 0, 5, 10, 20, 40, 80, 160, and 320 μM isoflurane. CCK-8 results

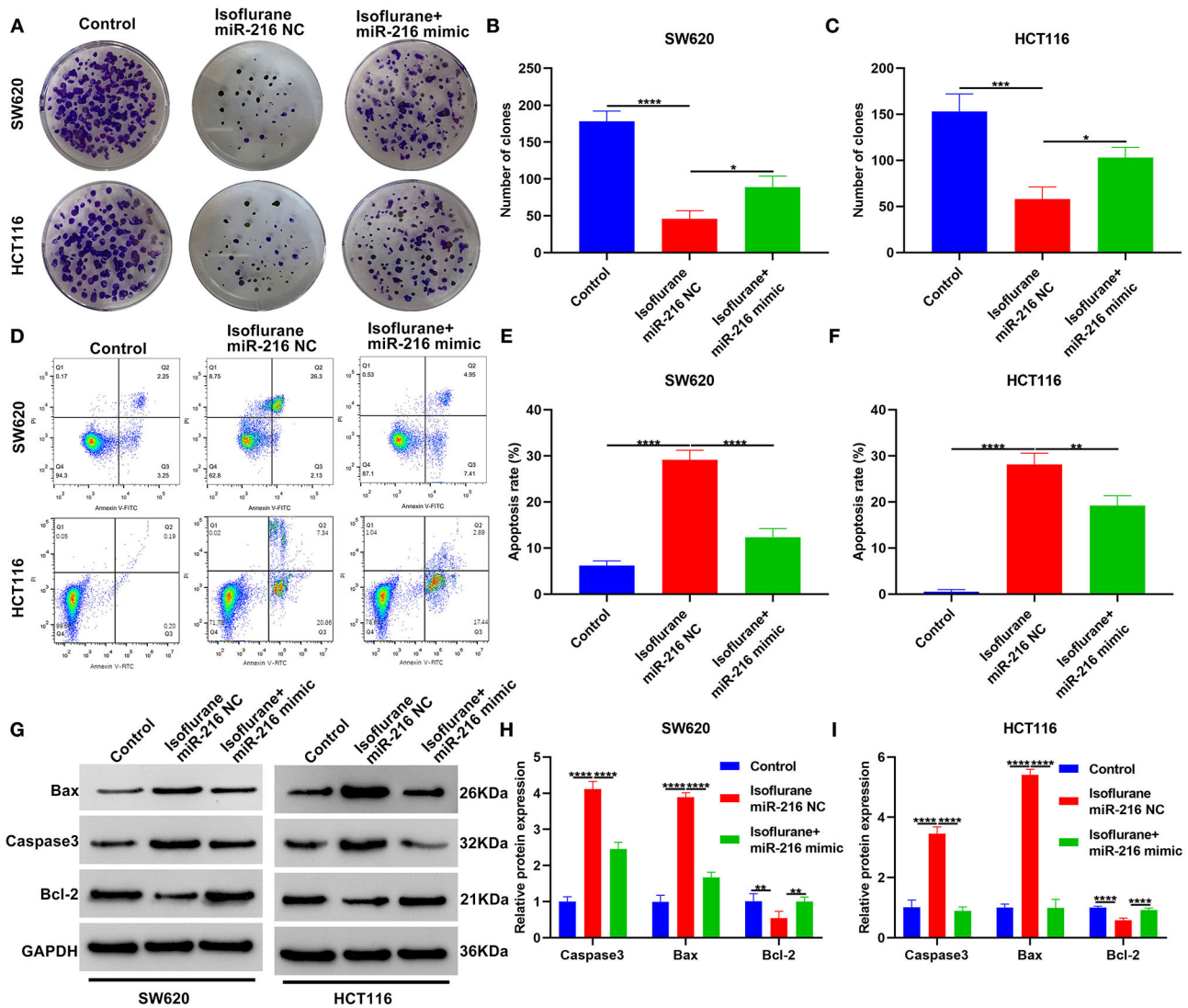

FIGURE 5 | Isoflurane restrains proliferation and facilitates apoptosis in CRC cells partly through miR-216. **(A–C)** The number of clones of SW620 and HCT116 cells treated with isoflurane and/or miR-216 mimic. **(D–F)** Apoptotic rate of SW620 and HCT116 cells under treatment with isoflurane and/or miR-216 mimic. **(G–I)** Expression of Caspase3, Bax and Caspase3 and Bax proteins in SW620 and HCT116 cells following treatment with isoflurane and/or miR-216 mimic. $^{*}p < 0.05$; $^{**}p < 0.01$; $^{***}p < 0.001$; $^{****}p < 0.0001$.

revealed that cell viability was inversely proportional to isoflurane concentrations in SW620 and HCT116 cells (**Figures 1A,B**). Compared to controls, when the concentration of isoflurane was 40 μM, cell viability was distinctly reduced in SW620 ($^{*}p < 0.01$) and HCT116 cells ($^{***}p < 0.001$). Thus, 40 μM isoflurane was determined as the optimal concentration for next assays. More importantly, a series of concentrations of isoflurane did not affect the viability of normal colorectal mucosal cells NCM460 (**Figure 1C**). When SW620 cells were treated with 40 μM isoflurane, the number of clones showed a distinct shrinkage than controls ($^{*}p < 0.05$; **Figures 1D,E**). This reduction was confirmed in another CRC cell line HCT116. As shown in **Figures 1F,G**, 40 μM isoflurane distinctly shrunk the number of HCT116 cell clones ($^{**}p < 0.01$).

Isoflurane Induces CRC Cell Apoptosis

We assessed the influence of isoflurane on CRC cell apoptosis. When SW620 cells were exposed to 40 μM isoflurane, flow cytometry data signified that apoptotic rate was significantly increased than controls ($^{***}p < 0.001$; **Figures 2A,B**). The similar findings were detected in HCT116 cells. In **Figures 2C,D**, 40 μM isoflurane displayed a promotional effect on HCT116 cell apoptosis ($^{****}p < 0.0001$). Apoptosis-related markers Caspase3, Bax, and Bcl-2 were tested in 40 μM isoflurane-induced SW620 and HCT116 cells. Data were indicative of the increase in Caspase3 (both $^{****}p < 0.0001$) and Bax (both $^{****}p < 0.0001$) expression as well as the decrease in Bcl-2 ($^{***}p < 0.001$ and $^{**}p < 0.01$) expression in SW620 and HCT116 cells under exposure to 40 μM isoflurane (**Figures 2E–G**).

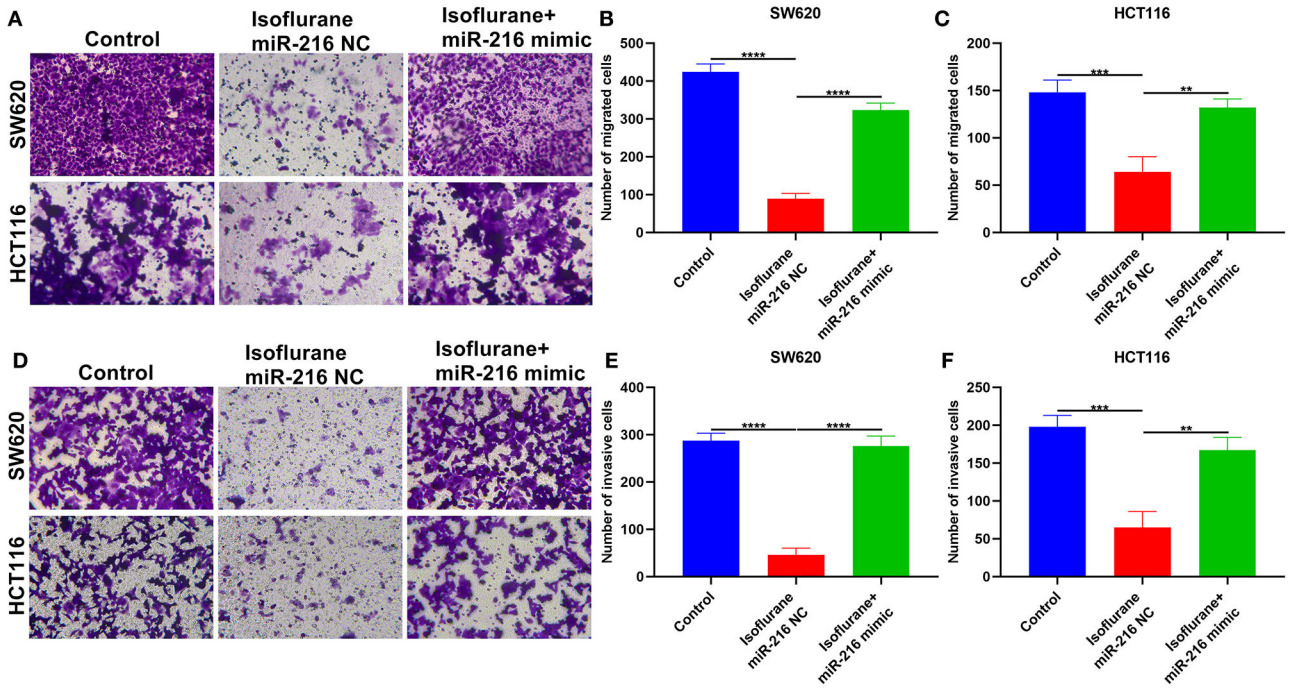

FIGURE 6 | Isoflurane weakens migration and invasion of CRC cells partly through miR-216. **(A–C)** The number of migrated SW620 and HCT116 cells under exposure to isoflurane and/or miR-216 mimic. **(D–F)** The number of invasive SW620 and HCT116 cells following treatment with isoflurane and/or miR-216 mimic. $^{**}p < 0.01$; $^{***}p < 0.001$; $^{****}p < 0.0001$.

Isoflurane Exerts a Suppressive Role on Migrated and Invasive Capacities of CRC Cells

Migrated and invasive capacities of CRC cells were evaluated under exposure to 40 μM isoflurane. In comparison to controls, the number of migrated SW620 cells was distinctly lessened when treated with 40 μM isoflurane ($^{****}p < 0.0001$; **Figures 3A,B**). Similarly, 40 μM isoflurane exhibited a suppressive role on HCT116 cell migration ($^{****}p < 0.0001$; **Figures 3C,D**). Meanwhile, the number of invasive SW620 cells was markedly shrunk under exposure to 40 μM isoflurane ($^{**}p < 0.01$; **Figures 3E,F**). The suppressive function of isoflurane on HCT116 cell invasion was found in **Figures 3G,H** ($^{**}p < 0.01$).

Isoflurane Decreases miR-216 Expression in CRC Cells

This study collected 30 paired CRC and control tissues. Our data showed that miR-216 displayed higher expression in CRC compared to control specimens ($^{****}p < 0.0001$; **Figure 4A**). Furthermore, miR-216 displayed an increased expression in SW620 and HCT116 cells compared to NCM460 cells (both $^{****}p < 0.0001$; **Figure 4B**). Under exposure to 40 μM isoflurane, miR-216 expression had reduced levels in SW620 and HCT116 cells than controls (both $^{***}p < 0.001$; **Figures 4C,D**). To further confirm whether miR-216 was a target of isoflurane, miR-216 expression was markedly overexpressed by its mimic in SW620 and HCT116 cells (both $^{****}p < 0.0001$; **Figures 4E,F**). Our data were indicative that the decrease in miR-216 expression induced by isoflurane was distinctly ameliorated by co-transfection of miR-216 mimic in SW620 ($^{**}p < 0.01$) and HCT116 cells ($^{*}p < 0.05$; **Figures 4G,H**). These data were indicative of miR-216 as a target of isoflurane in CRC cells.

Isoflurane Restrains Proliferation and Facilitates Apoptosis in CRC Cells Partly Through miR-216

This study investigated whether isoflurane exerted inhibitory effects on malignant behaviors of CRC cells via suppression of miR-216. We found that miR-216 mimic markedly ameliorated the inhibitory function of isoflurane on SW620 and HCT116 cell proliferation (both $^{*}p < 0.05$; **Figures 5A–C**). Apoptotic levels were assessed via flow cytometry. Data demonstrated that the increase in apoptotic levels of 40 μM isoflurane-induced SW620 ($^{****}p < 0.0001$) and HCT116 cells ($^{**}p < 0.01$) was markedly weakened by miR-216 mimic (**Figures 5D–F**). In **Figures 5G–I**, the increase in Caspase3 and Bax proteins and the decrease in Bcl-2 protein was markedly ameliorated by miR-216 mimic (all $^{****}p < 0.0001$). Above data suggested that isoflurane restrained proliferation and facilitated apoptosis in CRC cells partly through miR-216.

Isoflurane Weakens Migration and Invasion of CRC Cells Partly Through miR-216

This study further investigated whether isoflurane exposure could affect migration and invasion of CRC cells via miR-216. Data showed that the decrease in the number of migrated

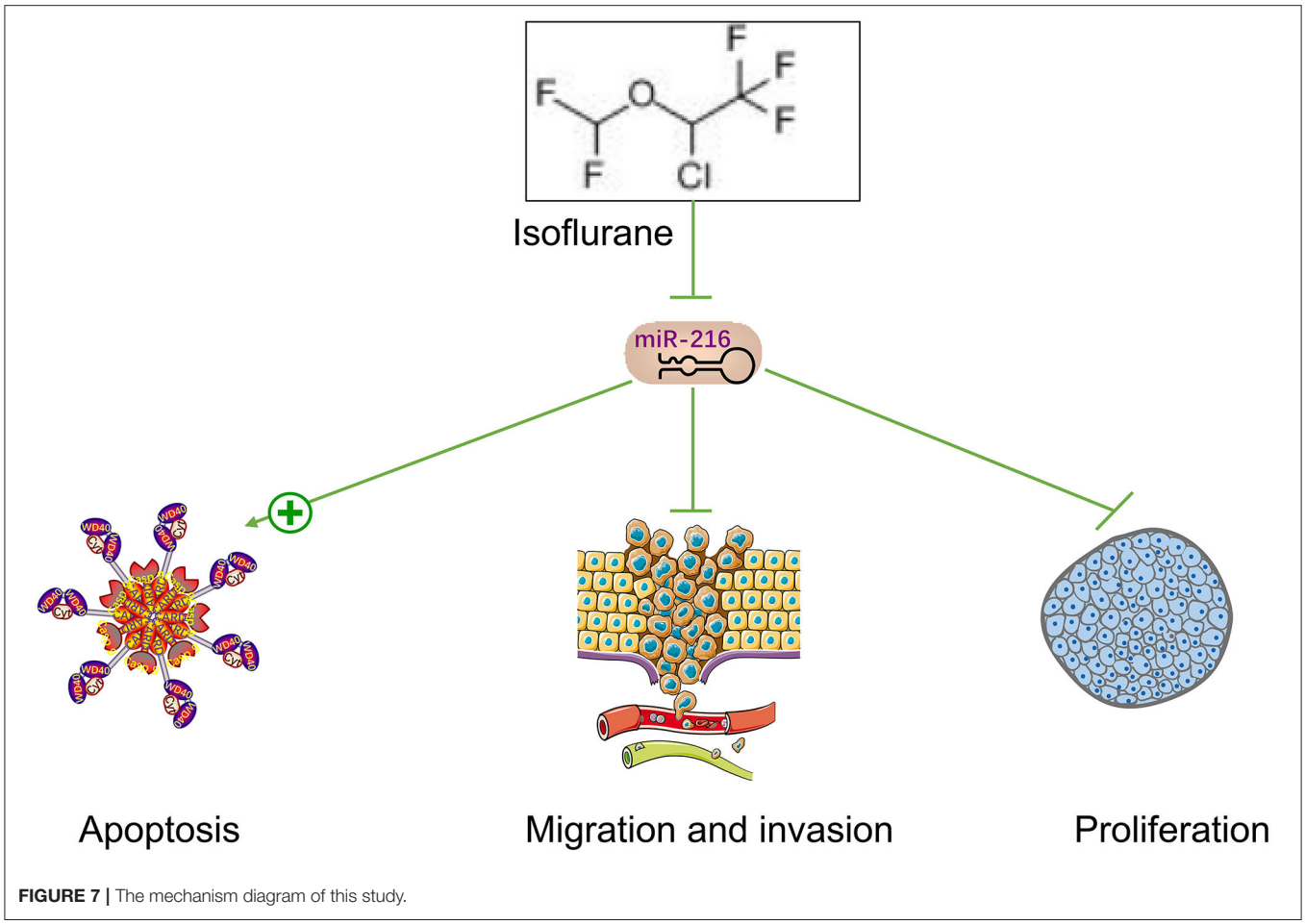

FIGURE 7 | The mechanism diagram of this study.

SW620 (****$p < 0.0001$) and HCT116 (**$p < 0.01$) cells exhibited an improvement by co-treatment with miR-216 mimic (**Figures 6A–C**). Furthermore, miR-216 mimic markedly improved the decrease in the number of invasive SW620 (****$p < 0.0001$) and HCT116 (**$p < 0.01$) cells (**Figures 6D–F**). Collectively, isoflurane weakened migrated and invasive abilities of CRC cells partly through suppression of miR-216. **Figure 7** depicted the schematic diagram of this study.

DISCUSSION

CRC is a common malignant tumor of the digestive tract, and its occurrence is related to heredity, environment, and lifestyle (21–23). At present, most conventional treatment methods are surgery, radiotherapy, chemotherapy, etc. (24–26). However, postoperative recurrence and metastasis, insensitivity to radiotherapy, and resistance to chemotherapy often occur, and the clinical efficacy is not ideal. Therefore, finding safe and effective treatment methods and new drugs has become a research focus in recent years. This study proposed that isoflurane was an underlying drug agent. Forty micromolar of isoflurane restrained proliferative, migrated, and invasive behaviors as well as elevated apoptotic levels in SW620 and HCT116 CRC cells. MiR-216, as a target of isoflurane, was lowly expressed in CRC cells. The up-regulation lessened the therapeutic effects of isoflurane on CRC. Hence, isoflurane exerted the inhibitory functions on malignant behaviors of CRC through miR-216.

The cell proliferation and apoptosis disorders are the main causes of tumors (27). The main mechanism of action of anti-tumor drugs is to inhibit tumor cell proliferation and induce apoptosis. This study showed that isoflurane displayed the inhibitory effects on CRC cell proliferation in a concentration-dependent manner but did not affect normal colorectal mucosal cells. Invasion and metastases are the most basic biological characteristics of malignancies. CRC has a strong ability of invasion as well as migration. Controlling distant metastases in the liver, lungs, and kidneys is the difficulty and key point in treating CRC. The current treatment methods are still difficult for patients with metastatic CRC. Thus, it is of significance concerning developing effective targeted intervention methods against CRC cell invasion and migration. Here, isoflurane restrained migrated as well as invasive abilities of CRC cells. Hence, isoflurane may be a promising drug against CRC. Recently, Lu et al. found that isoflurane did facilitate invasion as well as metastases of bladder carcinoma cells via HIF-1α/β-catenin/Notch1 axis (9). Zhang et al. reported the enhancement of isoflurane on proliferative ability of squamous

cervical carcinoma cells via mTOR-dependent pathway (28). As shown in research by Guo et al., isoflurane displayed the stimulative role on glucose metabolism of ovarian carcinoma cells by up-regulating miR-21 (29).

MiRNAs have been proven as key roles on the biology of CRC. Dysregulated miRNAs are involved in CRC progress by accommodating the expressions of specific target genes. Due to their high stability, miRNAs are also considered valuable biomarkers. Our data were indicative of the up-regulation of miR-216 in CRC cells. miR-216 expression is varying in different tumor specimens. Xiao et al. found that miR-216 motivated proliferative as well as invasive behaviors in bladder carcinoma cells through PIK3R2-regulated PI3K/Akt pathway (30). Chen et al. reported the regulatory functions of miR-216b on cellular proliferation, invasion as well as cell cycle through cyclin T2 in gastric carcinoma cells (18). The study from Zhang et al. confirmed miR-216b expression as an accurate marker of acute myeloid leukemia recurrence (31). Li et al. confirmed the down-regulation of miR-216b in glioma and its overexpression restrained tumor cellular growth as well as migration through activating AEG-1 (32). MiRNAs display closely correlations to CRC tumor growth as well as metastases (33–35). Herein, miR-216 was a target of isoflurane in CRC. Up-regulated miR-216 ameliorated the decrease in proliferation, migration, and invasion and increase in apoptotic levels in isoflurane-induced CRC cells. These data were indicative of the suppressive roles of isoflurane on CRC cellular malignant behaviors partly through miR-216. However, several limitations of this study should be pointed out. First, the possible mechanism that miR-216 is an underlying target of isoflurane requires further exploration. Second, clinical implication of miR-216 should be validated in a large CRC cohort. Third, the inhibitory effect of isoflurane on CRC will be observed *in vivo*.

CONCLUSION

Taken together, isoflurane, as a promising drug agent, distinctly restrained proliferative, migrated, and invasive behaviors as well as elevated apoptotic levels in CRC cells. MiR-216 up-regulation was discovered in CRC cells. MiR-216 was an effective target of isoflurane. MiR-216 overexpression may markedly lessen the therapeutic efficacy of isoflurane on CRC cellular malignant behaviors. These data were indicative of the therapeutic potential of isoflurane on CRC. Isoflurane exerted the inhibitory effects on CRC partly through miR-216. More assays require to confirm the therapeutic functions of isoflurane.

DATA AVAILABILITY STATEMENT

The original contributions presented in the study are included in the article/supplementary material, further inquiries can be directed to the corresponding author/s.

ETHICS STATEMENT

The studies involving human participants were reviewed and approved by This study acquired the approval of the ethics committee of the Cancer Hospital of China Medical University (2020021). The patients/participants provided their written informed consent to participate in this study.

AUTHOR CONTRIBUTIONS

ZH conceived and designed the study. ZC conducted most of the experiments, data analysis, and wrote the manuscript. LS participated in collecting data and helped to draft the manuscript. All authors reviewed and approved the manuscript.

REFERENCES

1. Keum N, Giovannucci E. Global burden of colorectal cancer: emerging trends, risk factors and prevention strategies. *Nat Rev Gastroenterol Hepatol.* (2019) 16:713–32. doi: 10.1038/s41575-019-0189-8
2. Safiri S, Sepanlou SG, Ikuta KS, Bisignano C, Salimzadeh H, Delavari A, et al. The global, regional, and national burden of colorectal cancer and its attributable risk factors in 195 countries and territories, 1990-2017: a systematic analysis for the Global Burden of Disease Study 2017. *Lancet Gastroenterol Hepatol.* (2019) 4:913−33. doi: 10.1016/S2468-1253(19)30345-0
3. Araghi M, Soerjomataram I, Jenkins M, Brierley J, Morris E, Bray F, et al. Global trends in colorectal cancer mortality: projections to the year 2035. *Int J Cancer.* (2019) 144:2992–3000. doi: 10.1002/ijc.32055
4. Siegel RL, Torre LA, Soerjomataram I, Hayes RB, Bray F, Weber TK, et al. Global patterns and trends in colorectal cancer incidence in young adults. *Gut.* (2019) 68:2179–85. doi: 10.1136/gutjnl-2019-319511
5. Angius A, Uva P, Pira G, Muroni MR, Sotgiu G, Saderi L, et al. Integrated analysis of miRNA and mRNA endorses a twenty miRNAs signature for colorectal carcinoma. *Int J Mol Sci.* (2019) 20:4067. doi: 10.3390/ijms20164067
6. Sasaki N, Clevers H. Studying cellular heterogeneity and drug sensitivity in colorectal cancer using organoid technology. *Curr Opin Genet Dev.* (2018) 52:117–22. doi: 10.1016/j.gde.2018.09.001
7. Makito K, Matsui H, Fushimi K, Yasunaga H. Volatile versus total intravenous anesthesia for cancer prognosis in patients having digestive cancer surgery. *Anesthesiology.* (2020) 133:764–73. doi: 10.1097/ALN.0000000000003440
8. Huang H, Benzonana LL, Zhao H, Watts HR, Perry NJ, Bevan C, et al. Prostate cancer cell malignancy via modulation of HIF-1α pathway with isoflurane and propofol alone and in combination. *Br J Cancer.* (2014) 111:1338–49. doi: 10.1038/bjc.2014.426
9. Lu N, Piao MH, Feng CS, Yuan Y. Isoflurane promotes epithelial-to-mesenchymal transition and metastasis of bladder cancer cells through HIF-1α-β-catenin/Notch1 pathways. *Life Sci.* (2020) 258:118154. doi: 10.1016/j.lfs.2020.118154
10. Zhu M, Li M, Zhou Y, Dangelmajer S, Kahlert UD, Xie R, et al. Isoflurane enhances the malignant potential of glioblastoma stem cells by promoting their viability, mobility *in vitro* and migratory capacity *in vivo*. *Br J Anaesth.* (2016) 116:870–7. doi: 10.1093/bja/aew124
11. Müller-Edenborn B, Roth-Z'graggen B, Bartnicka K, Borgeat A, Hoos A, Borsig L, et al. Volatile anesthetics reduce invasion of colorectal cancer cells through down-regulation of matrix metalloproteinase-9. *Anesthesiology.* (2012) 117:293–301. doi: 10.1097/ALN.0b013e3182605df1
12. Kastrinos F, Samadder NJ, Burt RW. Use of family history and genetic testing to determine risk of colorectal cancer. *Gastroenterology.* (2020) 158:389–403. doi: 10.1053/j.gastro.2019.11.029
13. Sur DG, Colceriu M, Sur G, Aldea C, Silaghi C, Samasca G, et al. MiRNAs roles in the diagnosis, prognosis and treatment of colorectal cancer. *Expert Rev Proteomics.* (2019) 16:851–6. doi: 10.1080/14789450.2019.1659732
14. To KK, Tong CW, Wu M, Cho WC. MicroRNAs in the prognosis and therapy of colorectal cancer: from bench to bedside. *World J Gastroenterol.* (2018) 24:2949–73. doi: 10.3748/wjg.v24.i27.2949

15. Hu JL, Wang W, Lan XL, Zeng ZC, Liang YS, Yan YR, et al. CAFs secreted exosomes promote metastasis and chemotherapy resistance by enhancing cell stemness and epithelial-mesenchymal transition in colorectal cancer. *Mol Cancer.* (2019) 18:91. doi: 10.1186/s12943-019-1019-x
16. Sun L, Liu X, Pan B, Hu X, Zhu Y, Su Y, et al. Serum exosomal miR-122 as a potential diagnostic and prognostic biomarker of colorectal cancer with liver metastasis. *J Cancer.* (2020) 11:630–7. doi: 10.7150/jca.33022
17. Zou G, Wang R, Wang M. Clinical response and prognostic significance of serum miR-497 expression in colorectal cancer. *Cancer Biomark.* (2019) 25:11–8. doi: 10.3233/CBM-181902
18. Chen X, Zhang L, Song Q, Chen Z. MicroRNA-216b regulates cell proliferation, invasion and cycle progression via interaction with cyclin T2 in gastric cancer. *Anticancer Drugs.* (2020) 31:623–31. doi: 10.1097/CAD.0000000000000915
19. Zhu H, Zeng Y, Zhou CC, Ye W. SNHG16/miR-216-5p/ZEB1 signal pathway contributes to the tumorigenesis of cervical cancer cells. *Arch Biochem Biophys.* (2018) 637:1–8. doi: 10.1016/j.abb.2017.11.003
20. Zhang J, Zhang K, Bi M, Jiao X, Zhang D, Dong Q. Circulating microRNA expressions in colorectal cancer as predictors of response to chemotherapy. *Anticancer Drugs.* (2014) 25:346–52. doi: 10.1097/CAD.0000000000000049
21. Jung G, Hernández-Illán E, Moreira L, Balaguer F, Goel A. Epigenetics of colorectal cancer: biomarker and therapeutic potential. *Nat Rev Gastroenterol Hepatol.* (2020) 17:111–30. doi: 10.1038/s41575-019-0230-y
22. Morse MA, Hochster H, Benson A. Perspectives on treatment of metastatic colorectal cancer with immune checkpoint inhibitor therapy. *Oncologist.* (2020) 25:33–45. doi: 10.1634/theoncologist.2019-0176
23. Song M, Chan AT, Sun J. Influence of the gut microbiome, diet, and environment on risk of colorectal cancer. *Gastroenterology.* (2020) 158:322–40. doi: 10.1053/j.gastro.2019.06.048
24. Al Bandar MH, Kim NK. Current status and future perspectives on treatment of liver metastasis in colorectal cancer (Review). *Oncol Rep.* (2017) 37:2553–64. doi: 10.3892/or.2017.5531
25. Breugom AJ, Swets M, Bosset JF, Collette L, Sainato A, Cionini L, et al. Adjuvant chemotherapy after preoperative (chemo)radiotherapy and surgery for patients with rectal cancer: a systematic review and meta-analysis of individual patient data. *Lancet Oncol.* (2015) 16:200–7. doi: 10.1016/S1470-2045(14)71199-4
26. Papamichael D, Hernandez P, Mistry R, Xenophontos E, Kakani C. Adjuvant chemotherapy in patients with colorectal cancer. Is there a role in the older adult? *Eur J Surg Oncol.* (2020) 46:363–8. doi: 10.1016/j.ejso.2020.01.002
27. Watson AJ. An overview of apoptosis and the prevention of colorectal cancer. *Crit Rev Oncol Hematol.* (2006) 57:107–21. doi: 10.1016/j.critrevonc.2005.06.005
28. Zhang W, Xue F, Xie S, Chen C, Li J, Zhu X. Isoflurane promotes proliferation of squamous cervical cancer cells through mTOR-histone deacetylase 6 pathway. *Mol Cell Biochem.* (2020) 476:45–55. doi: 10.1007/s11010-020-03884-7
29. Guo NL, Zhang JX, Wu JP, Xu YH. Isoflurane promotes glucose metabolism through up-regulation of miR-21 and suppresses mitochondrial oxidative phosphorylation in ovarian cancer cells. *Biosci Rep.* (2017) 37:BSR20170818. doi: 10.1042/BSR20170818
30. Xiao J, Lin HY, Zhu YY, Zhu YP, Chen LW. MiR-126 regulates proliferation and invasion in the bladder cancer BLS cell line by targeting the PIK3R2-mediated PI3K/Akt signaling pathway. *Onco Targets Ther.* (2016) 9:5181–93. doi: 10.2147/OTT.S105198
31. Zhang TJ, Wu DH, Zhou JD, Li XX, Zhang W, Guo H, et al. Overexpression of miR-216b: Prognostic and predictive value in acute myeloid leukemia. *J Cell Physiol.* (2018) 233:3274–81. doi: 10.1002/jcp.26171
32. Li Q, Wang M, Wang N, Wang J, Qi L, Mao P. Downregulation of microRNA-216b contributes to glioma cell growth and migration by promoting AEG-1-mediated signaling. *Biomed Pharmacother.* (2018) 104:420–6. doi: 10.1016/j.biopha.2018.05.048
33. Lan J, Sun L, Xu F, Liu L, Hu F, Song D, et al. M2 Macrophage-derived exosomes promote cell migration and invasion in colon cancer. *Cancer Res.* (2019) 79:146–58. doi: 10.1158/0008-5472.CAN-18-0014
34. Wang D, Wang X, Si M, Yang J, Sun S, Wu H, et al. Exosome-encapsulated miRNAs contribute to CXCL12/CXCR4-induced liver metastasis of colorectal cancer by enhancing M2 polarization of macrophages. *Cancer Lett.* (2020) 474:36–52. doi: 10.1016/j.canlet.2020.01.005
35. Wei C, Yang C, Wang S, Shi D, Zhang C, Lin X, et al. Crosstalk between cancer cells and tumor associated macrophages is required for mesenchymal circulating tumor cell-mediated colorectal cancer metastasis. *Mol Cancer.* (2019) 18:64. doi: 10.1186/s12943-019-0976-4

Conflict of Interest: The authors declare that the research was conducted in the absence of any commercial or financial relationships that could be construed as a potential conflict of interest.

Publisher's Note: All claims expressed in this article are solely those of the authors and do not necessarily represent those of their affiliated organizations, or those of the publisher, the editors and the reviewers. Any product that may be evaluated in this article, or claim that may be made by its manufacturer, is not guaranteed or endorsed by the publisher.

Copyright © 2021 Cai, Suo and Huang. This is an open-access article distributed under the terms of the Creative Commons Attribution License (CC BY). The use, distribution or reproduction in other forums is permitted, provided the original author(s) and the copyright owner(s) are credited and that the original publication in this journal is cited, in accordance with accepted academic practice. No use, distribution or reproduction is permitted which does not comply with these terms.

frontiers in Medicine

ORIGINAL RESEARCH
published: 13 September 2021
doi: 10.3389/fmed.2021.702638

Molecular Characteristics, Clinical Implication, and Cancer Immunity Interactions of Pyroptosis-Related Genes in Breast Cancer

Dandan Xu[1], *Zhipeng Ji*[2] *and Ling Qiang*[3]*

[1] *Internal Medicine II, The Third Affiliated Hospital of Shandong First Medical University (Affiliated Hospital of Shandong Academy of Medical Sciences), Jinan, China,* [2] *Department of Gastrointestinal Surgery, The Second Hospital, Cheeloo College of Medicine, Shandong University, Jinan, China,* [3] *Department of Medical Oncology, Shandong Cancer Hospital and Institute, Shandong First Medical University and Shandong Academy of Medical Sciences, Jinan, China*

Objective: Pyroptosis represents an emerging inflammatory form of programmed cell death. Herein, specific functions and clinical implications of pyroptosis-related genes were systematically characterized in breast cancer.

Methods: Expression, somatic mutation and copy number variation of 33 pyroptosis-related genes were assessed in breast cancer from TCGA dataset. Their interactions, biological functions and prognostic values were then observed. By stepwise Cox regression analysis, a pyroptosis-related gene signature was generated. The predictive efficacy in survival was examined by survival analyses, ROCs, univariate and multivariate analyses and subgroup analyses. Associations between risk score (RS) and cancer immunity cycle, *HLA*, immune cell infiltrations, and immune checkpoints were analyzed.

Results: Most of pyroptosis-related genes were abnormally expressed in breast cancer. *CASP8, NLRC4, NLRP3, NLRP2, PLCG1, NLRP1, NLRP7, SCAF11, GSDMC*, and *NOD1* occurred somatic mutations as well as most of them had high frequency of CNV. There were closely interactions between them. These genes were distinctly enriched in immune-related processes. A three-gene signature was generated, containing *IL-18, GSDMC*, and *TIRAP*. High RS predicted poorer overall survival, progression, and recurrence. After verification, this RS was an independent and sensitive predictive index. This RS was negatively correlated to cancer immunity cycle. Also, low RS was characterized by high *HLA*, immune cell infiltrations and immune checkpoints. A nomogram including age and RS was generated for accurately predicting 5-, 8-, and 10-year survival probabilities.

Conclusion: Pyroptosis-related genes exert key roles in cancer immunity and might be applied as a prognostic factor of breast cancer.

Keywords: breast cancer, pyroptosis, signature, prognosis, immune, nomogram

OPEN ACCESS

Edited by:
Fu Wang,
Xi'an Jiaotong University, China

Reviewed by:
Chunlin Ou,
Central South University, China
Lijie Chen,
ShengJing Hospital of China Medical University, China

***Correspondence:**
Ling Qiang
doctorqql@126.com

Specialty section:
This article was submitted to Precision Medicine, a section of the journal Frontiers in Medicine

Received: *29 April 2021*
Accepted: *17 August 2021*
Published: *13 September 2021*

Citation:
Xu D, Ji Z and Qiang L (2021) Molecular Characteristics, Clinical Implication, and Cancer Immunity Interactions of Pyroptosis-Related Genes in Breast Cancer. Front. Med. 8:702638. doi: 10.3389/fmed.2021.702638

INTRODUCTION

Breast cancer represents a frequently diagnosed malignancy among women globally, with a high mortality (1). This malignancy affects 1/20 globally and 1/8 in high-income countries (2). Females with high risk of developing breast cancer are a heterogeneous population (3). Further research requires to improve prognostic models to stratify high-risk patients. The biology in breast cancer progress is complex in which genetic and environmental elements are involved (4). Conventional breast cancer classification primarily replies on clinicopathologic characteristics and routine markers, not capturing various clinical courses of individual patient (5). In-depth understanding of the molecular mechanisms could lead to improvement in patients' prognoses.

Varied factors are in relation to carcinogenesis, such as activations of proto- and antioncogenes, immune microenvironment as well as chronic inflammation (6, 7). Pyroptosis represents a form of programmed cell death, which may induce the cleavage of *gasdermin D* along with activation of immune and inflammatory response (8). Activated pyroptosis induces the release of the inflammatory factors *IL-1* and *IL-18*, thereby promoting breast cancer initiation. It is featured by cell swelling as well as bubble-like protrusions. Interactions between pyroptosis and cancers are complex due to varied influence of pyroptosis on cancers in distinct tissue specimens as well as genetic background (9). Increasing evidences highlight the roles of pyroptosis in carcinogenesis (10). Previously, increased *GSDMB* expression is related to poor survival and high metastases of breast cancer (11). Furthermore, recent research has demonstrated the crosstalk between pyroptosis and anti-cancer immunity (12). Research has displayed that chemotherapy drugs, miRNAs, etc., may trigger cancer pyroptosis, which inhibits malignant development of cancers (13). Based on pyroptosis regulators, a seven-gene signature has been generated for predicting ovarian cancer prognoses (14). However, no studies have reported prognostic implications of pyroptosis-related gene signature in breast cancer.

Herein, we analyzed molecular characteristics and clinical implication of pyroptosis-related genes as well as their interactions with cancer immunity in breast cancer.

MATERIALS AND METHODS

Data Acquisition

RNA-seq profiling (FPKM values) of breast cancer was retrieved from the Cancer Genome Atlas (TCGA; https://cancergenome.nih.gov/) database. After removing samples without complete clinical information, 1,082 breast cancer samples were included in our study (**Supplementary Table 1**). Meanwhile, RNA-seq profiles of 113 adjacent normal tissues were also obtained from TCGA database. Then, FPKM values were converted to TPM values according to the following formula: TPMi = FPKMi*1000000/(FPKM0 + ... + FPKMm), where i represents gene i and m represents the total number of all genes. Somatic mutation and copy number variation (CNV) data were also retrieved from TCGA database.

Pyroptosis-Related Genes

We collected 33 pyroptosis-related genes from the published literature, including *GPX4, NLRP7, NLRP2, CASP6, CASP3, TNF, IL1B, IL18, CASP8, NLRP6, IL6, GSDMA, GSDMC, PYCARD, CASP5, AIM2, NOD2, NLRC4, NLRP3, CASP4, CASP1, PRKACA, ELANE, TIRAP, SCAF11, PJVK, CASP9, NOD1, PLCG1, NLRP1, GSDME, GSDMD,* and *GSDMB* (8, 15–17). The location of pyroptosis-related genes on the chromosome was plotted via Rcircos package (18). The mRNA expression of pyroptosis-related genes was compared between breast cancer and normal samples with unpaired student' s *t*-test. Their somatic mutations were analyzed using maftools package (19). Frequencies of genetic amplification and deletion were also summarized. Spearman correlation test was adopted for evaluation of the associations between pyroptosis-related genes across breast cancer samples.

Protein-Protein Interaction (PPI) and Gene Ontology (GO) Annotation Analysis

Thirty pyroptosis-related genes were uploaded onto the STRING database (https://string-db.org) and their interaction pairs were obtained (20). A PPI network of pyroptosis-related genes was visualized with Cytoscape (https://cytoscape.org/) (21). The gene set of 33 pyroptosis-related genes was analyzed via clusterProfiler package (22). Biological process, cellular component and molecular function of these pyroptosis-related genes were analyzed. Terms with adjusted $p < 0.05$ were significantly enriched.

Development of a Prognostic Model

To screen which pyroptosis-related genes were related to breast cancer prognoses, univariate analyses were carried out. Genes with $p < 0.05$ were included for conducting a stepwise Cox regression model. Risk score (RS) was calculated by linearly combining regression coefficients multiplied with expression values. Based on the median of RS, patients were stratified into two groups. Overall survival was compared between groups by Kaplan-Meier curves and log-rank tests. Expression patterns of genes in this model were visualized into heatmap. Area under the curve (AUC) of the receiver operating characteristic (ROC) curve was conducted for assessing the predictive efficacy of this model.

Univariate and Multivariate Cox Regression Analyses

Univariate analyses were applied for estimating the associations between prognoses and age, T, N, M, stage, and RS. Furthermore, multivariate analyses were presented for observing whether these factors were independently predictive of prognoses of breast

Abbreviations: ICIs, immune checkpoint inhibitors; TCGA, the Cancer Genome Atlas; CNV, copy number variation; PPI, protein-protein interaction; GO, Gene ontology; RS, risk score; ROC, receiver operating characteristic; HR, hazard ratio; CI, confidence interval; DFI, disease-free interval; DFS, disease-free survival; DSS, disease-specific survival; PFI, progression -free interval; ssGSEA, single sample gene set enrichment analysis; GSEA, Gene set enrichment analysis; KEGG, Kyoto Encyclopedia of Genes and Genomes.

cancer. Hazard ratio (HR), 95% confidence interval (CI), and *p*-values were separately determined.

Subgroup Analysis

To investigate the sensitivity of RS in predicting prognoses, patients were stratified into subgroups according to clinical characteristics, including age ≥65 and age <65, M0 and M1, N0 and N1–3, stage I-II and stage III-IV, T1-2 and T3-4 subgroups. OS was compared in high and low RS patients in each subgroup. *P*-values were determined with log-rank tests.

Assessment of Activated Pathways, HLA, Immune Cell Infiltration, and Immune Checkpoints

Enrichment scores of several cancer-related pathways were estimated by single sample gene set enrichment analysis (ssGSEA) algorithm (23), including IFN-Gamma signature, APM signal, base excision repair, cell cycle, DNA replication, Fanconi anemia pathway, homologous recombination, microRNAs in cancer, mismatch repair, nucleotide excision repair, oocyte meiosis, p53 signaling pathway, progesterone-mediated oocyte maturation, proteasome, pyrimidine metabolism, spliceosome, systemic lupus erythematosus, viral carcinogenesis. The gene sets of above pathways were listed in **Supplementary Table 2**. Associations between RS and enrichment scores of pathways were then analyzed with Spearman correlation test. Wilcoxon test was applied for estimating the differences in expression of HLA signatures and immune checkpoints between high- and low-risk groups. Also, infiltration levels of 28 immune cells were inferred by ssGSEA algorithm and were compared between groups. Adjusted $p\text{-}value < 0.05$ indicated the significant difference between high- and low-risk groups.

Estimation of Cancer Immunity Cycle

Each step of cancer immunity cycle (24) was inferred with ssGSEA algorithm, as follows: step1: release of cancer cell antigens (IL10, TGFB1, HMGB1, ANXA1, CALR, CXCL10, PDIA3, HSPA1A, HSPA1B, HSPA2, HSPA8, HSPA4, HSPA14, HSPA5, HSPA6, HSPA9, HSPA13, HSPA7, HSPA8, HSPA12A, HSPA12B, HSP90AA1, HSP90AB1, HSP90B1, IFNA2, IFNA1, IFNA13, IFNA6, IFNA21, IFNA4, IFNA8, IFNA5, IFNA7, IFNA14, IFNA16, IFNA10, IFNA17, IFNB1, IFNE, IFNW1), step2: cancer antigen presentation (TNF, IL1A, IL1B, IFNA2, IFNA1, IFNA13, IFNA6, IFNA21, IFNA4, IFNA8, IFNA5, IFNA7, IFNA14, IFNA16, IFNA10, IFNA17, CD40LG, CD40, NT5C, HMGB1, TLR1, TLR2, TLR3, TLR4, TLR5, TLR6, TLR7, TLR8, TLR9, TLR10, HLAA, B2M, TAP1, IL10, IL4, IL13), step3: priming and activation (CD3D, CD3E, CD3G, CD247, CD28, TNFRSF9, TNFSF9, TNFRSF4, TNFSF4, CD27, CD70, TNFRSF14, TNFSF14, CD40, CD40LG, TNFRSF18, TNFSF18, TNFRSF25, TNFSF15, TNFRSF8, TNFSF8, HAVCR1, TIMD4, SLAMF7, SLAMF6, SLAMF1, SLAMF9, SLAMF8, CD2, CD48, CD58, CD226, ICOS, ICOSLG, KLRK1, MICA, MICB, RAET1E, RAET1G, CRTAM, CADM1, CTLA4, PDCD1, PDCD1LG2, CD274, CD160, TNFRSF14, BTLA, VSIR, LAIR1, HAVCR1, HAVCR2, LGALS9, TIMD4, CD244, CD48, TIGIT, NECTIN3, LAG3, IL2, IL12A, IL12B), step4 T cell recruiting (CXCR5, CCR7, CXCL9, CCL3, CCL4, CCL5, CCL19, CCL21, CX3CL1, CXCL13), step4: CD8 T cell recruiting (CCR5, CXCR3, CXCL10, CXCL9, CCL20, CXCL11, CX3CL1, CXCL16), step4: Th1 cell recruiting (CXCR3, CXCL10, CXCL9, CXCL11), step4: dendritic cell recruiting (CCR7, CCL3, CCL4, CCL5, CCL21), step4: Th22 cell recruiting (CCR6, CCL20), step4: macrophage recruiting (CSF1, CCL2, CCL3, CCL4, CCL5), step4: monocyte recruiting (CCL2, CCL7, CX3CL1), step4: neutrophil recruiting (CXCL1, CXCL2, CXCL3, CXCL8, CXCL6, CXCL5), step4: NK cell recruiting (CXCR3, CXCL10, CXCL9, CCL3, CCL4, CCL5, CXCL11, CX3CL1), step4: eosinophil cell recruiting (CCL11, CCL24, CCL26), step4: basophil recruiting (CCL24, CCL26), step4: Th17 cell recruiting (CCR6, CCL20, CXCL12, CXCR4), step4: B cell recruiting (CXCR5, CXCL13), step4: Th2 cell recruiting (CCL1, CCL17, CCL22), step4: Treg cell recruiting (CCR4, CCR10, CCL1, CCL17, CCL22, CCL28), step4: MDSC recruiting (CXCR2, CXCL5), step5: infiltration of immune cells into tumors (STAT1, IRF5, KLF2, ITGB2, ICAM1, EZH2, DNMT1, VEGFA, EDNRB), step6: recognition of cancer cells by T cells (CD28, ICOS, ICOSLG, TNFRSF9, TNFSF9, CD27, CD70, TNFRSF4, TNFSF4, TNFSF14, CD40, CD40LG, HLAA, B2M, TAP1, BIRC5, MDM2, MAGEA4, TP53, PDCD1, PDCD1LG2, CD274, CTLA4, BTLA, VTCN1), step7: killing of cancer cells (IFNG, GZMB, PRF1, PDCD1, SMC3, VTCN1, HAVCR2, MICA, MICB, BTLA, VSIR, LAG3, IDO1, IDO2, ARG1, ARG2, NOS1, NOS2, NOS3, TGFB1, IL10, CCL28, CXCL12, CCL2, CXCL8). Correlation between RS and cancer immunity cycle was assessed.

Gene Set Enrichment Analysis (GSEA)

GSEA method was employed for identifying enriched Kyoto Encyclopedia of Genes and Genomes (KEGG) in high and low RS groups based on transcriptomic data (25). Terms with nominal enrichment score >2 and false discovery rates <0.05 were significantly enriched.

Nomogram Construction

Independent prognostic factors were incorporated for constructing a prognostic nomogram in predicting 5-, 8-, and 10-year survival duration with stepwise Cox regression analyses. Calibration plots were plotted for comparing nomogram-predicted and observed 5-, 8-, and 10-year survival.

Cell Culture

Human normal breast cells (MCF-10A) and breast cancer cells (MDA-MB-231 and HCC70) were retrieved from Shanghai Cell Bank of Chinese Academy of Sciences (China), which were maintained in DMEM plus 10% FBS (Gibco, USA) and 1% penicillin–streptomycin. All cells were incubated at 37°C under the condition of 5% CO_2.

Western Blot

MCF-10A, MDA-MB-231, and HCC70 cells were lysed by cell lysates (Beyotime, Beijing, China). Total protein was electrophoresed in 10% polyacrylamide gels. Afterwards, the protein was transferred onto PVDF membrane and blocked with 5% skimmed milk for 2 h at 37 °C. The membrane was incubated

by primary antibodies against GSDMC (1:1000; #PA5-101660; Invitrogen, USA), IL-18 (1:1,000; #PA5-19131; Invitrogen, USA), TIRAP (1:1,000; #PA5-88657; Invitrogen, USA), and GAPDH (1:1,000; #ab8245; Abcam, USA) at 4°C overnight, followed by incubation with secondary antibodies (1:2,000; #ab7090; Abcam, USA). Protein bands were acquired through ECL kit (Beyotime, Beijing, China).

Immunofluorescence

MCF-10A, MDA-MB-231, and HCC70 cells were fixed by 10% formaldehyde for 40 min, followed by being blocked by 5% BSA blocking buffer for 1 h at room temperature. Afterwards, the cells were incubated with GSDMC (1:100; #PA5-101660; Invitrogen, USA), IL-18 (1:100; #PA5-19131; Invitrogen, USA), and TIRAP (1:100; #PA5-88657; Invitrogen, USA) overnight at 4°C. Then, the cells were incubated with secondary antibodies (1:200; ab150077 or ab150080; Abcam, USA) for 30 min at 37°C. The cells were stained by DAPI (Solarbio, Beijing, China) and images were acquired under a fluorescence microscope (Olympus, Japan).

Statistical Analysis

Data were analyzed with the R (version 3.6.1) and R Bioconductor packages. Comparisons between two groups were evaluated with student' *t*-test or Wilcoxon test. Differences in disease-free interval (DFI), disease-free survival (DFS), disease-specific survival (DSS) and progression-free interval (PFI) were compared in high and low RS groups with Kaplan-Meier curves and log-rank tests. $P < 0.05$ indicated statistical significance.

RESULTS

Landscape of Expression and Mutation of Pyroptosis-Related Genes in Breast Cancer

In this study, 33 pyroptosis-related genes were dissected in breast cancer. **Figure 1A** displayed the location of these pyroptosis-related genes on chromosomes, as follows: *CASP9* (chr1: 15490832–15526534), *AIM2* (chr1: 159062484–159147096), *NLRP3* (chr1: 247416156–247449108), *NLRC4* (chr2: 32224453–32265854), *IL1B* (chr2: 112829751–112836903), *CASP8* (chr2: 201233443–201287711), *CASP6* (chr4: 109688622–109703583), *CASP3* (chr4: 184627696–184649509), *TNF* (chr6: 31575567–31578336), *IL6* (chr7: 22725884–22732002), *NOD1* (chr7: 3042452–30478784), *GSDMC* (chr8: 129748196–129786888), *GSDMD* (chr8: 143553207–143563062), *NLRP6* (chr11: 278365–285359), *CASP4* (chr11: 104942866–104969436), *CASP5* (chr11: 104994235–105023168), *CASP1* (chr11: 105025443–105035250), *CASP1* (chr11: 105025443–105035250), *IL18* (chr11: 112143251–112164117), *TIRAP* (chr11: 126283065–126298845), *SCAF11* (chr12: 45919131–45992120), *PYCARD* (chr16: 31201485–31203450), *NOD2* (chr16: 50693603–50733077), *NLRP1* (chr17: 5499427–5619424), *GSDMB* (chr17: 39904595–39919854), *GSDMA* (chr17: 39962973–39977766), *PLCG1* (chr20: 41136960–41196801), *ELANE* (chr19: 851014–856247), *GPX4* (chr19: 1103926–1106791), *PRKACA* (chr19: 14091688–14118084), *NLRP7* (chr19: 54923509–54966312), *NLRP2* (chr19: 54953130 – 55001142), *PJVK* (chr2: 179316163–179326117), and *GSDME* (chr7: 24737972–24809244). Expression of above pyroptosis-related genes was compared between breast cancer and normal tissues. Heatmap showed that *GPX4* ($p = 8.02e\text{-}03$), *NLRP7* ($p = 3.33e\text{-}02$), *CASP6* ($p = 1.04e\text{-}24$), *CASP3* ($p = 5.74e\text{-}31$), *IL1B* ($p = 4.99e\text{-}03$), *IL18* ($p = 3.39e\text{-}19$), *CASP8* ($p = 1.77e\text{-}02$), *NLRP6* ($p = 8.97e\text{-}04$), *IL6* ($p = 4.01e\text{-}33$), *GSDMC* ($p = 4.99e\text{-}03$), *PYCARD* ($p = 2.50e\text{-}29$), *AIM2* ($p = 7.36e\text{-}10$), *NOD2* ($p = 1.34e\text{-}21$), *NLRP3* ($p = 7.26e\text{-}15$), and *CASP4* ($p = 1.89e\text{-}18$) possessed aberrant expression patterns in breast cancer than normal tissue samples (**Figure 1B**). Furthermore, genetic mutations of the pyroptosis-related genes were assessed in depth. In **Figure 1C**, *CASP8* (2%), *NLRC4* (1%), *NLRP3* (1%), *NLRP2* (1%), *PLCG1* (1%), *NLRP1* (1%), *NLRP7* (1%), *SCAF11* (1%), *GSDMC* (1%), and *NOD1* (1%) occurred genetic mutations in breast cancer. Also, most of pyroptosis-related genes had high frequencies of CNVs in breast cancer (**Figure 1D**). We further ascertained whether the above genetic mutations affected the expression of pyroptosis-related genes in breast cancer. We observed that CNV could be a dominating factor leading to perturbations on the expression of pyroptosis-related genes. In comparison to normal breast tissues, pyroptosis-related genes with amplificated CNV had distinctly higher expression in breast cancer tissues (such as *GSDMC, GSDMD,* and *AIM2*), and vice versa (such as *CASP4, CASP1,* and *ELANE*).

Interactions Between Pyroptosis-Related Genes and Their Biological Implications

Spearman test was utilized for evaluating correlations between 33 pyroptosis-related genes in breast cancer from TCGA dataset. In **Figure 2A**, there were tight interactions between them, such as *CASP4* and *CASP1*. A PPI network was than constructed based on 33 pyroptosis-related genes (**Figure 2B**). Among all nodes, *CASP1* had the highest degree. Furthermore, biological implications of 33 pyroptosis-related genes were evaluated by clusterProfiler package. Our data showed that these pyroptosis-related genes were mainly involved in regulating *IL-1β* production and secretion biological processes (**Figure 2C**). Furthermore, they participated in cytosolic, inflammasome and membrane cellular components as well as apoptotic process.

Generation of a Pyroptosis-Related Gene Signature for Breast Cancer Prognoses

Clinical implications of pyroptosis-related genes were assessed in breast cancer. As shown in univariate cox regression analyses, *IL-18, GSDMC,* and *TIRAP* were significantly associated with survival outcomes of breast cancer. Among them, *IL-18* [$p = 0.015$, HR(95%CI): 0.832(0.717–0.965)] was a protective factor as well as *GSDMC* [$p = 0.044$, HR(95%CI): 1.120(1.003–1.251)] and *TIRAP* [$p = 0.025$, HR(95%CI): 1.336(1.037–1.722)] were risk factors for breast cancer prognoses (**Figure 3A**). According to their coefficients and expression levels, we calculated risk score (RS) for each patient (**Table 1**). Then, we evaluated association between RS and survival outcomes. In **Figure 3B**, patients with high RS exhibited poorer OS than those with low RS ($p =$

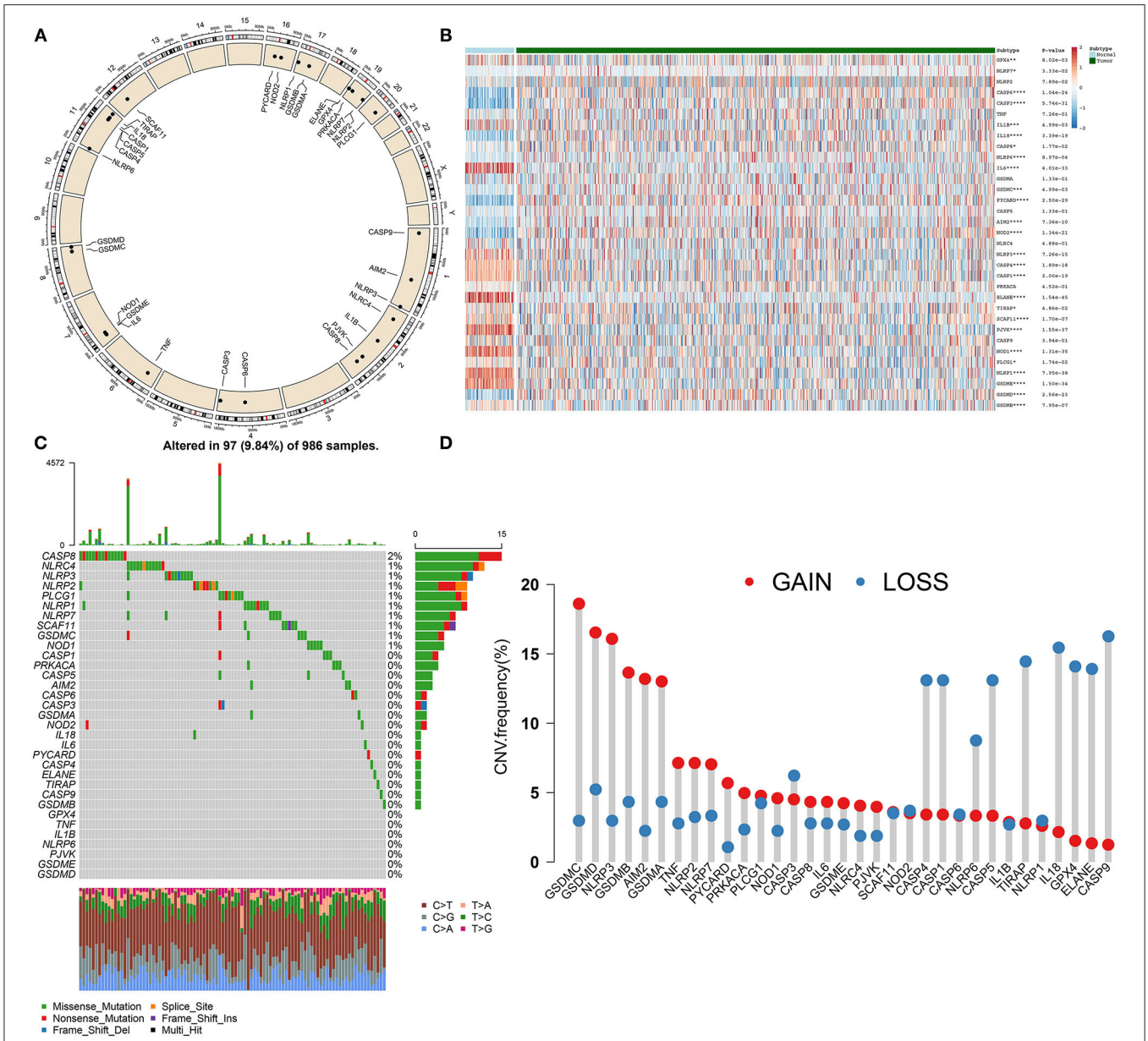

FIGURE 1 | Landscape of expression and genetic mutations of pyroptosis-related genes in breast cancer. **(A)** Circus plots of chromosome distributions of pyroptosis-related genes. **(B)** Heatmap of expression patterns of pyroptosis-related genes in normal and breast cancer tissues. *$p < 0.05$; **$p < 0.01$; ***$p < 0.001$; ****$p < 0.0001$. **(C)** Waterfall chart of somatic mutations of pyroptosis-related genes. **(D)** Frequencies of gain and loss for pyroptosis-related genes.

7.124e-05). Furthermore, we observed expression patterns of *IL-18*, *GSDMC*, and *TIRAP* in high and low RS samples. As a result, *IL-18* was down-regulated as well as *GSDMC* and *TIRAP* were up-regulated in high RS group compared with low RS group (**Figure 3C**). We also showed their expression in different clinical features including stage, age, T, N, and M. Time-dependent ROC curves were plotted for verifying the predictive performance. In **Figure 3D**, AUC was 0.652, indicating that RS possessed high accuracy and sensitivity in predicting prognoses of breast cancer.

Independency of the Pyroptosis-Related Gene Signature in Predicting Breast Cancer Prognoses

Correlation between clinical features and prognoses of breast cancer was analyzed via univariate analyses. In **Figure 4A**, age [$p < 0.001$, HR(95%CI): 1.030(1.018–1.043)], stage [$p < 0.001$, HR(95%CI): 2.167(1.733–2.709)], T [$p < 0.001$, HR(95%CI): 1.458(1. 198–1.774)], *N* [$p < 0.001$, HR(95%CI): 1.611(1.359–1.910)], M [$p < 0.001$, HR(95%CI): 4.765(2.847–7.976)], and RS

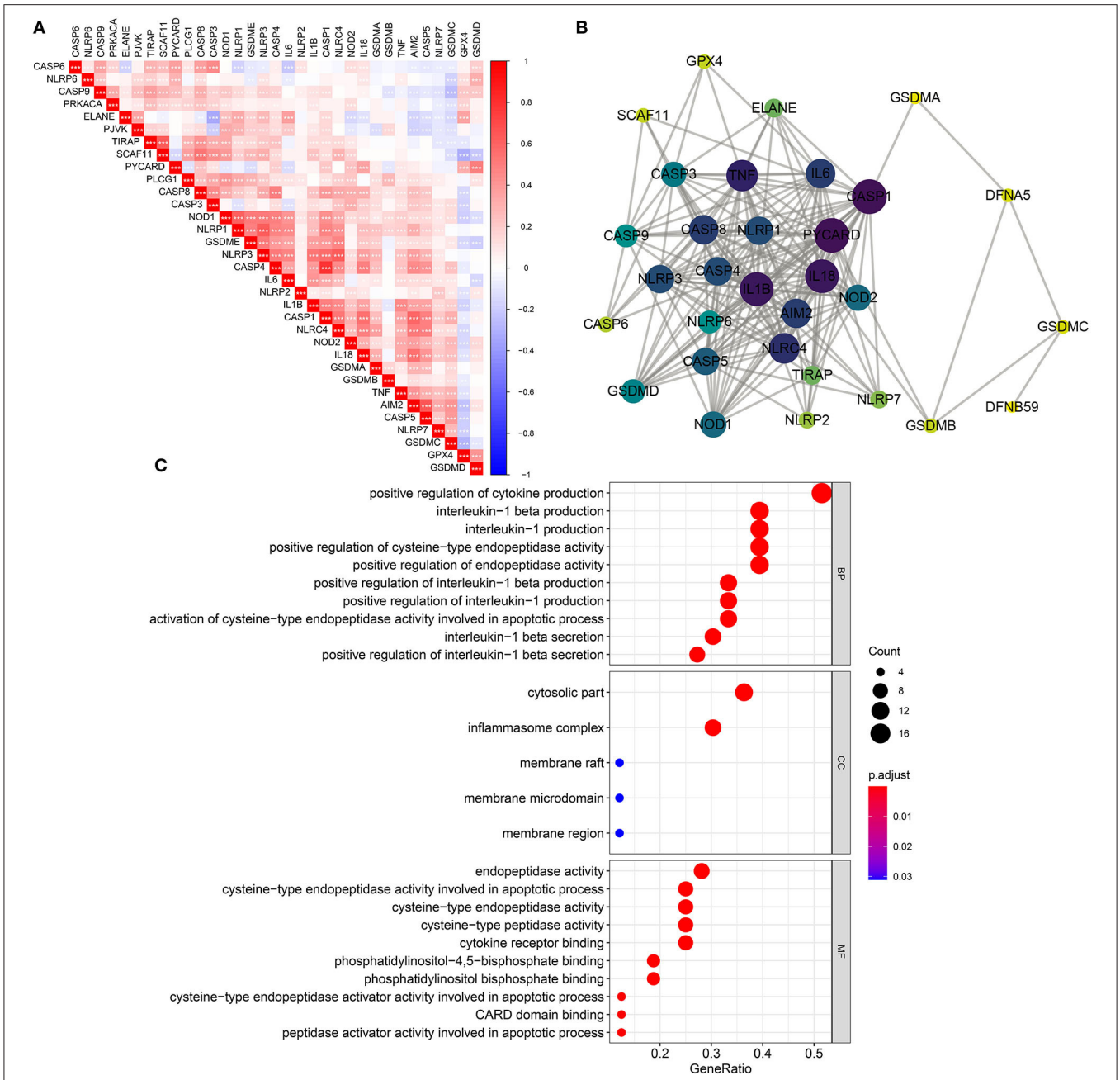

FIGURE 2 | Biological functions and interactions of pyroptosis-related genes in breast cancer. **(A)** Correlations between pyroptosis-related genes. *$p < 0.05$; **$p < 0.01$; ***$p < 0.001$. The darker the color, the stronger the correlation. **(B)** A PPI network of pyroptosis-related genes. The larger the circle, the greater the degree. **(C)** Biological process (BP), cellular component (CC), and molecular function (MF) enrichment analyses results of pyroptosis-related genes.

[$p < 0.001$, HR(95%CI): 2.258(1.623–3.142)] were all risk factors of breast cancer prognoses. To investigate the independency in predicting prognoses, multivariate cox regression analyses were carried out. As a result, age [$p < 0.001$, HR(95%CI): 1.030(1.016–1.045)] and RS [$p < 0.001$, HR(95%CI): 2.086(1.395–3.119)] were independent risk factors (**Figure 4B**). Subgroup analyses were also presented for analyzing predictive sensitivity of RS. Here, all patients were stratified into different groups. Our data revealed that high RS was indicative of poorer survival outcomes in comparison to low RS in age ≥65 ($p = 0.03692$; **Figure 4C**) and <65 ($p = 0.00067$; **Figure 4D**), M0 ($p = 0.00046$; **Figure 4E**) and M1 ($p = 0.70537$; **Figure 4F**), N0 ($p = 0.27403$; **Figure 4G**) and N1-3 ($p = 0.00097$; **Figure 4H**), stage I-II ($p = 0.00467$; **Figure 4I**) and stage III-IV ($p = 0.00358$; **Figure 4J**), T1-2 ($p = 0.00222$; **Figure 4K**) and T3-4 ($p = 0.00213$; **Figure 4L**) subgroups.

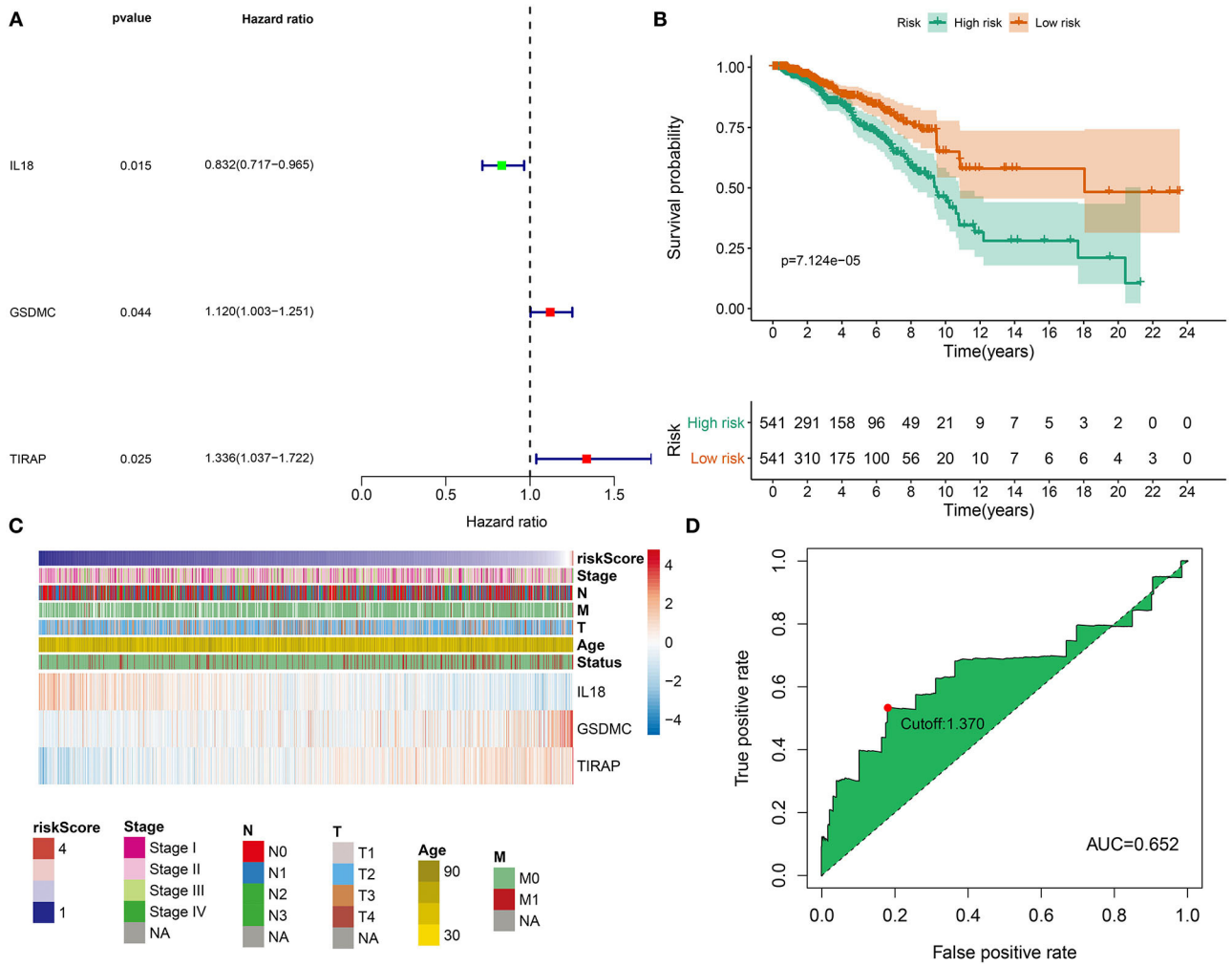

FIGURE 3 | Development of a pyroptosis-related gene signature for breast cancer prognoses. **(A)** Univariate analyses were utilized for screening prognoses-related pyroptosis genes and a pyroptosis-related gene signature was established. **(B)** OS probabilities in high- and low-risk patients, followed by log-rank tests. **(C)** Distributions of *IL18, GSDMC*, and *TIRAP* expression in risk scores and different clinical features. **(D)** ROC curves were plotted for examining the predictive efficacy of this signature.

TABLE 1 | Regression coefficients of genes in the prognostic model.

Genes	Coefficients	HR	HR.95L	HR.95H	*P*
IL18	−0.25528	0.774702	0.662455	0.905969	0.001391
GSDMC	0.171771	1.187405	1.061616	1.328099	0.002643
TIRAP	0.374042	1.453599	1.122064	1.883091	0.004627

The Pyroptosis-Related Gene Signature Predicts Progression and Metastasis of Breast Cancer

This study further investigated whether the pyroptosis-related gene signature might be predictive of progression and metastasis of breast cancer. Our results demonstrated that patients with high RS displayed worse DFI ($p = 8.586e\text{-}02$; **Figure 5A**), DFS ($p = 1.228e\text{-}02$; **Figure 5B**), DSS ($p = 5.637e\text{-}03$; **Figure 5C**) and PFI ($p = 2.963e\text{-}03$; **Figure 5D**) in comparison to those with low RS.

Association Between the Pyroptosis-Related Gene Signature and Immunogenicity

We further assessed whether the pyroptosis-related gene signature affected cancer immunity cycle. As a result, we found that the risk score almost negatively participated in each step of cancer immunity cycle, including release of cancer cell antigens, cancer antigen presentation, priming and activation, T cell recruiting, Th1 cell recruiting, dendritic cell recruiting, Th22 cell recruiting, macrophage recruiting, monocyte recruiting, neutrophil recruiting, NK cell recruiting, eosinophil cell recruiting, basophil recruiting, Th17 cell recruiting, B cell recruiting, Th2 cell recruiting, Treg cell recruiting, infiltration of

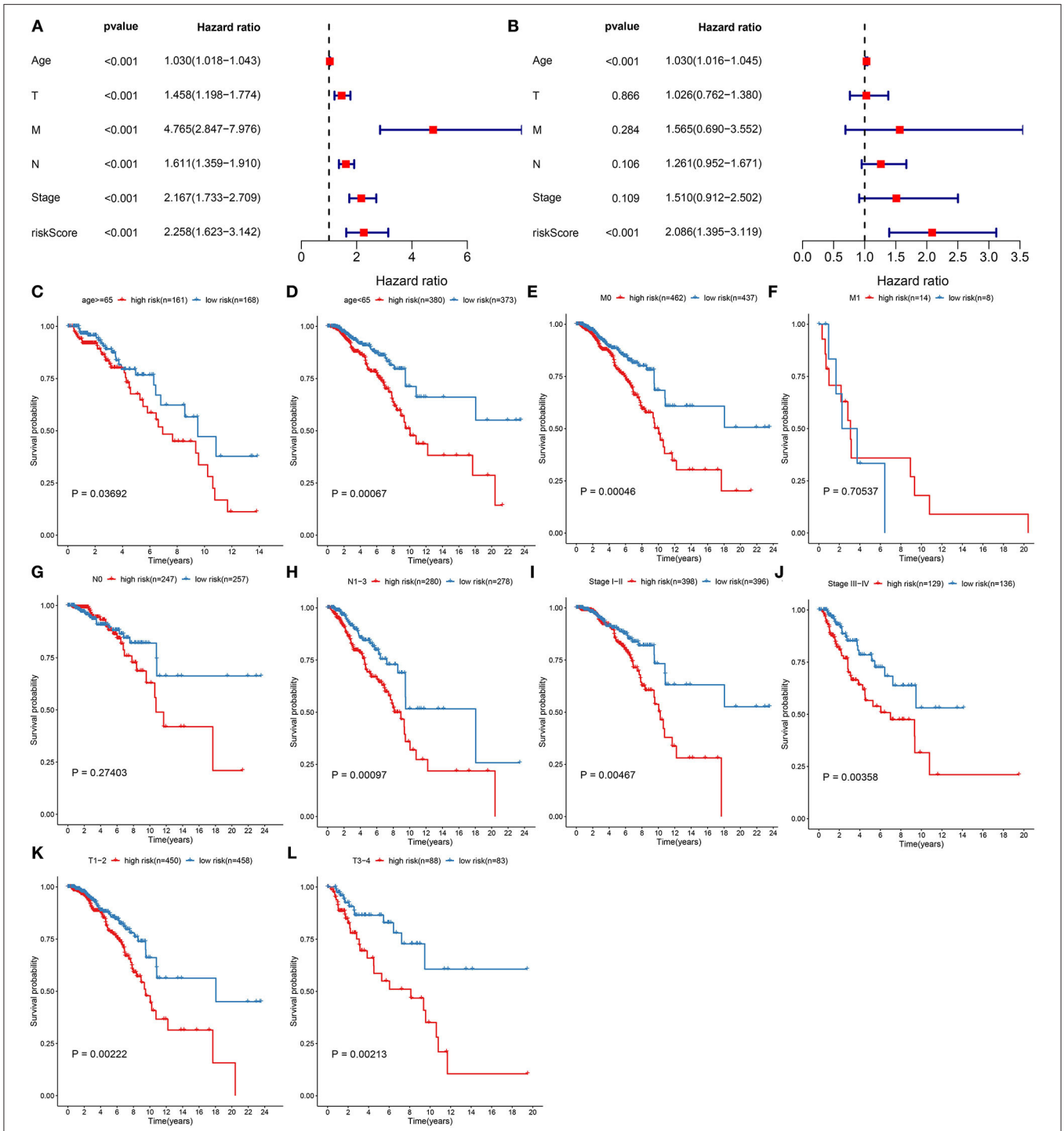

FIGURE 4 | Assessment of predictive independency of the pyroptosis-related gene signature in breast cancer prognoses. **(A)** Univariate and **(B)** multivariate analyses for estimating risk scores and age, T, N, M, and stage. Subgroup analysis for investigating the differences in OS probabilities between high- and low-risk samples in **(C)** age ≥65, **(D)** age <65, **(E)** M0, **(F)** M1, **(G)** N0, **(H)** N1-3, **(I)** stage I-II, **(J)** stage III-IV, **(K)** T1-2, **(L)** T3-4 subgroups.

immune cells into tumors, recognition of cancer cells by T cells, and killing of cancer cells (**Figure 6A**). Also, RS was distinctly related to the activation of IFN-gamma signature, APM signal, cell cycle, Fanconi anemia pathway, homologous recombination, microRNAs in cancer, oocyte meiosis, P53 signaling pathway, proteasome, spliceosome, and viral carcinogenesis (**Figure 6A**). The low RS breast cancer samples were characterized by increased expression of human lymphocyte antigen (HLA), as

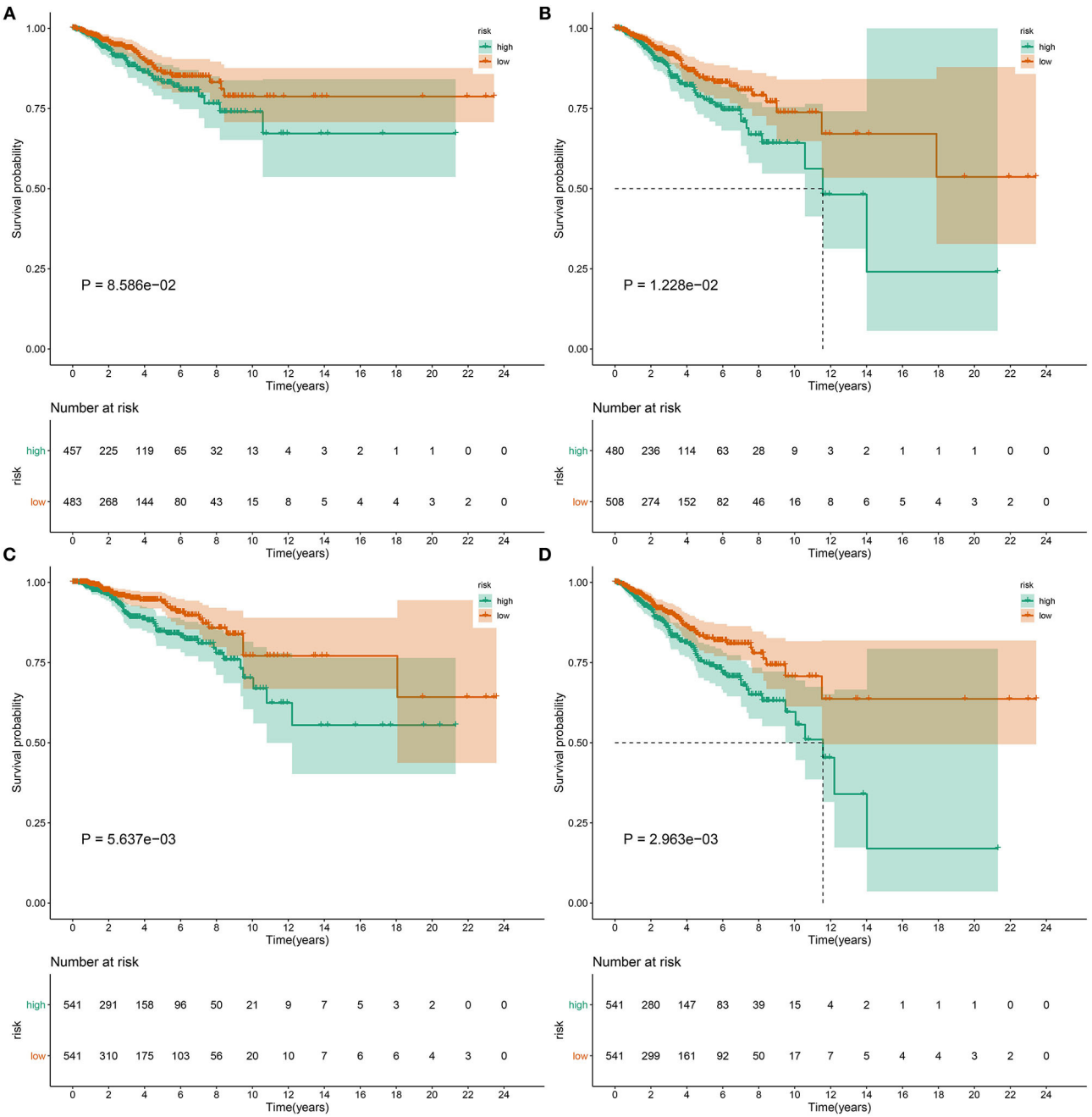

FIGURE 5 | The pyroptosis-related gene signature could predict progression and metastases of breast cancer. Differences in **(A)** DFI, **(B)** DFS, **(C)** DSS, and **(D)** PFI were compared in high- and low-risk samples by Kaplan-Meier curves and log-rank tests.

follows: *HLA-E, HLA-DPB2, HLA-C, HLA-J, HLA-DQB1, HLA-DQB2, HLA-DQA2, HLA-DQA1, HLA-A, HLA-DMA, HLA-DOB, HLA-DRB1, HLA-H, HLA-B, HLA-DRB5, HLA-DOA, HLA-DPB1, HLA-DRA, HLA-DRB6, HLA-L, HLA-F, HLA-G, HLA-DMB*, and *HLA-DPA1* (**Figure 6B**). Also, higher infiltration levels of nearly all immune cells were detected in the low RS group than the high RS group, including activated B cell, activated CD4 T cell, activated CD8 T cell, central memory CD4 T cell, effector memory CD4 T cell, effector memory CD8 T cell, gamma delta T cell, immature B cell, memory B cell, regulatory T cell, T follicular helper cell, type 1 T helper cell, type 17 T helper cell, type 2 T helper cell, activated dendritic cell, CD56bright natural killer cell, CD56dim natural killer cell, eosinophil, immature dendritic cell, macrophage, mast cell, MDSC, monocyte, natural killer cell, natural killer T cell, and neutrophil (**Figure 6C**). Moreover, we compared the expression

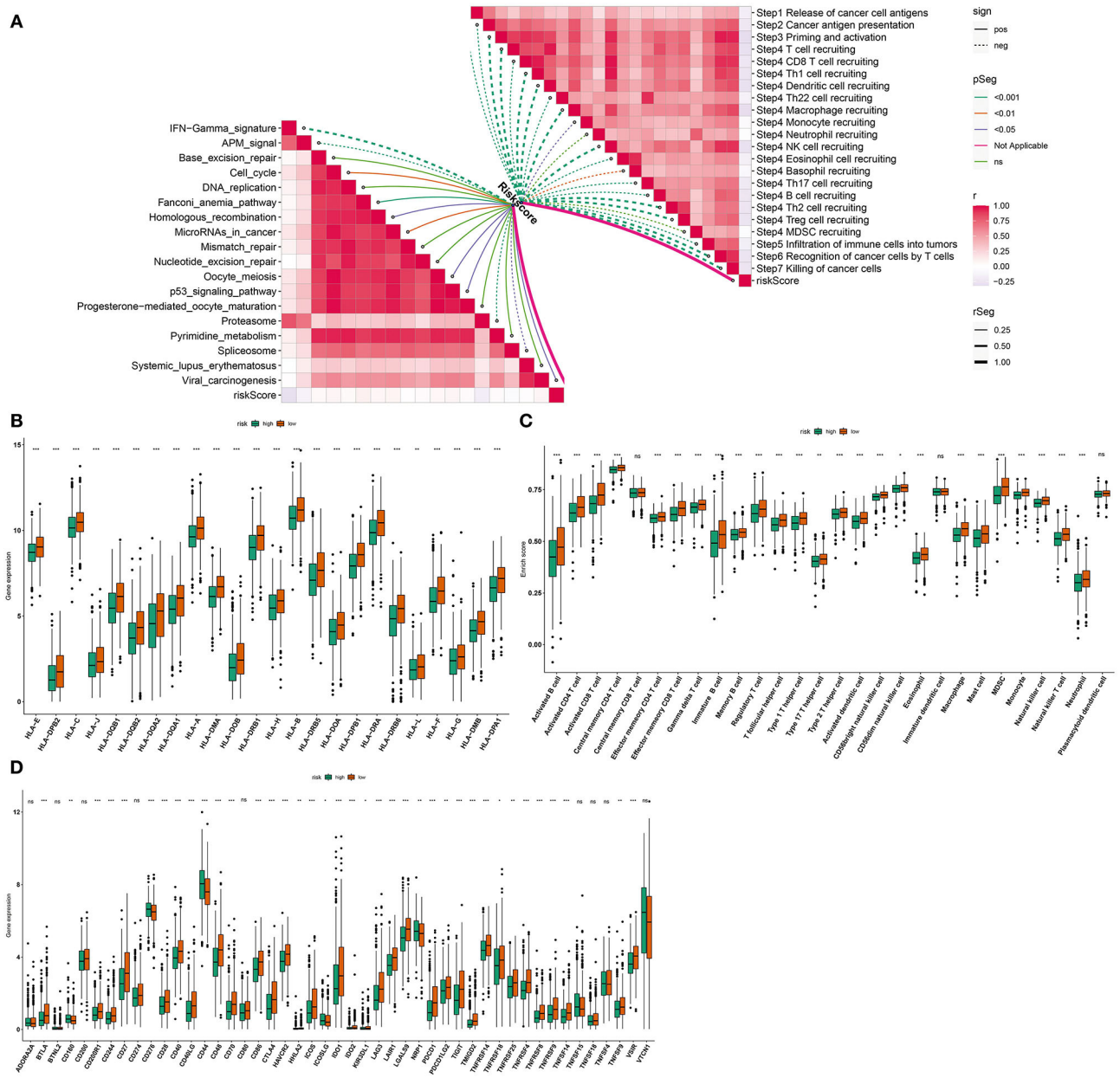

FIGURE 6 | Associations between the pyroptosis-related gene signature and immunogenicity of breast cancer. **(A)** Correlations between risk score and cancer immunity cycle and pathways. Dotted line indicates negative correlation and solid line indicates positive correlation. The darker the color, the stronger the correlation. **(B)** Box plots were plotted for HLA expression in high- and low-risk samples. **(C)** Box plots were depicted to show infiltration levels of immune cells in high- and low-risk samples. **(D)** Box plots were utilized for visualizing expression of immune checkpoints in high- and low-risk samples. Ns: not significant; $*p < 0.05$; $**p < 0.01$; $***p < 0.001$ that were derived from adjusted *p*-values.

of immune checkpoints between high and low RS groups. In **Figure 6D**, higher expression of *BTLA*, *CD200R1*, *CD244*, *CD27*, *CD28*, *CD40*, *CD40LG*, *CD48*, *CD70*, *CD86*, *CTLA4*, *HAVCR2*, *HHLA2*, *ICOS*, *IDO1*, *IDO2*, *KIR3DL1*, *LAG3*, *LAIR1*, *LGALS9*, *PDCD1*, *PDCD1LG2*, *TIGIT*, *TMIGD2*, *TNFRSF14*, *TNFRSF18*, *TNFRSF25*, *TNFRSF4*, *TNFRSF8*, *TNFRSF9*, *TNFSF14*, *TNFSF9*, and *VSIR* was found in the low RS group. Meanwhile, the high RS group was characterized by increased expression of *CD160*, *CD276*, *CD44*, *ICOSLG*, and *NRP1*. Above data suggested that RS was related to suppressive immunity in breast cancer.

Pathways Involved in the Pyroptosis-Related Gene Signature

GSEA was employed for exploring pathways involved in the pyroptosis-related gene signature. In **Figures 7A–F**, high RS was distinctly associated with cell cycle (NES = 1.85 and FDR =

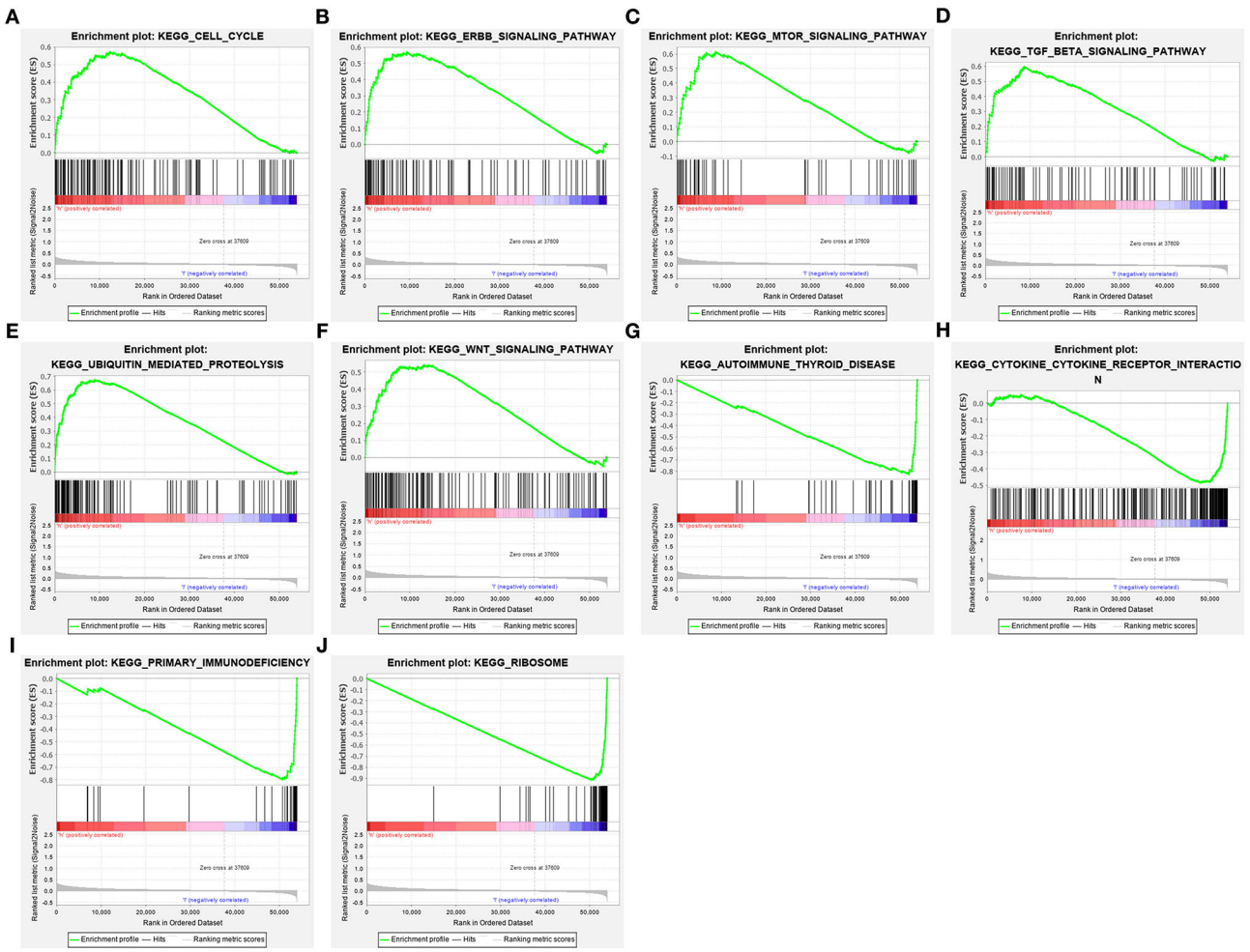

FIGURE 7 | Activated pathways involved in the pyroptosis-related gene signature by GSEA. **(A)** Cell cycle, **(B)** ERBB signaling pathway, **(C)** mTOR signaling pathway, **(D)** TGF-beta signaling pathway, **(E)** ubiquitin mediated proteolysis and **(F)** WNT signaling pathway were activated in high-risk samples. **(G)** Autoimmune thyroid disease, **(H)** cytokine-cytokine receptor interaction, **(I)** primary immunodeficiency, and **(J)** ribosome were activated in low-risk samples.

0.019), ERBB signaling pathway (NES = 2.06 and FDR = 0.005), mTOR signaling pathway (NES = 2.06 and FDR = 0.004), TGF-beta signaling pathway (NES = 2.06 and FDR = 0.005), ubiquitin mediated proteolysis (NES = 2.22 and FDR = 0.002) and WNT signaling pathway (NES = 2.09 and FDR = 0.005). Meanwhile, low RS was in relation to autoimmune thyroid disease (NES = −2.24 and FDR = 0.001), cytokine-cytokine receptor interaction (NES = −1.74 and FDR = 0.035), primary immunodeficiency (NES = −1.95 and FDR = 0.007), and ribosome (NES = −2.13 and FDR = 0.003; **Figures 7G–J**).

Development of a Prognostic Nomogram for Breast Cancer

Our multivariate analyses demonstrated that age and the pyroptosis-related gene signature were independent risk factors of breast cancer, which were used for developing a prognostic nomogram. In **Figure 8A**, this nomogram could predict 5-, 8- and 10-year survival probabilities. The predictive performance was evaluated by calibration plots. There were high consistencies in nomogram-predicted and actual 5-, 8- and 10-year survival (**Figures 8B–D**). Our data suggested that the nomogram exhibited the well predictive efficacy in 5-, 8- and 10-year survival probabilities.

Validation of the Expression of Genes in the Pyroptosis-Related Gene Signature

We further validated the expression of *IL-18, GSDMC*, and *TIRAP* in the pyroptosis-related gene signature *in vitro*. As depicted in western blotting, *IL-18, GSDMC,* and *TIRAP* expression was all markedly up-regulated in breast cancer cells MDA-MB-231 and HCC70 compared with normal breast cells MCF-10A (**Figures 9A–D**). Immunofluorescence also confirmed the significant up-regulation of *IL-18, GSDMC* and *TIRAP* expression in MDA-MB-231 and HCC70 cells than MCF-10A cells (**Figures 9E–G**).

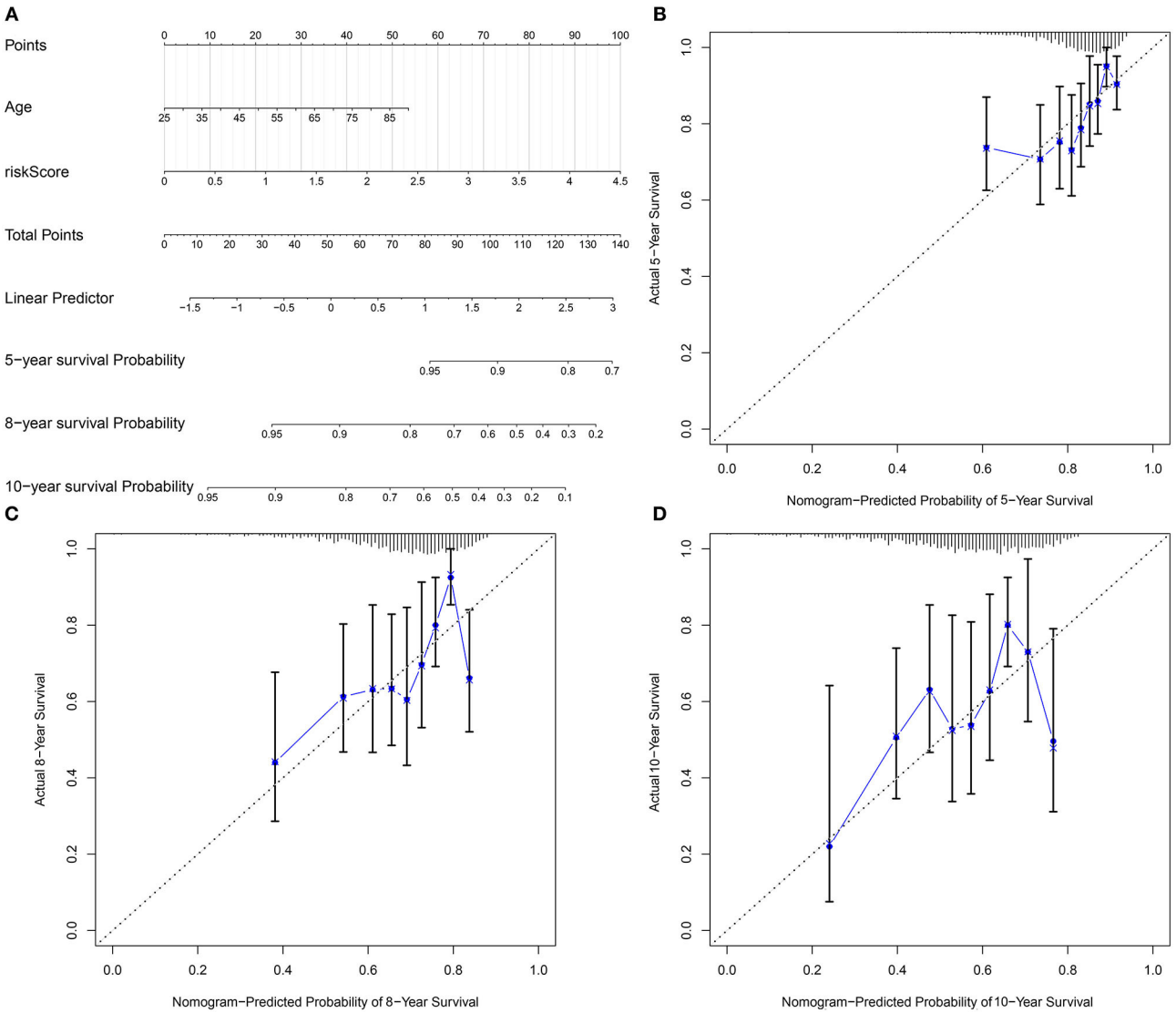

FIGURE 8 | Development of a nomogram for estimating 5-, 8-, and 10-year survival probabilities of breast cancer patients. **(A)** A nomogram incorporating age and risk score was a predictor of 5-, 8-, and 10-year survival probabilities. **(B–D)** Calibrate plots was applied for investigating the deviation in nomogram-predicted and actual 5-, 8-, and 10-year survival probabilities.

DISCUSSION

Programmed cell fate nearly focuses on apoptosis and necroptosis. It is of importance to find an alternative option when these cell deaths are compromised (26). Pyroptotic death represents a form of programmed cell death, which is induced by inflammasomes (27). Inducing apoptosis of cancer cells has been applied for eliminating malignant cells (28). Nevertheless, due to escaping apoptosis, induction of pyroptosis may be especially critical in treating antiapoptotic cancers. Immunotherapies show remarkable efficacy in treating breast cancer. Nevertheless, therapeutic effects are still limited (29). Pyroptosis offers an opportunity for alleviating immunosuppression as well as promoting an immune response in treating breast cancer (30). Here, we characterized expression, genetic mutations, and clinical implications of pyroptosis-related genes in breast cancer.

Among pyroptosis-related genes, *GPX4, NLRP7, CASP6, CASP3, IL1B, IL18, CASP8, NLRP6, IL6, GSDMC, PYCARD, AIM2, NOD2, NLRP3*, and *CASP4* were aberrantly expressed in breast cancer. Furthermore, *CASP8* (2%), *NLRC4* (1%), NLRP3 (1%), *NLRP2* (1%), *PLCG1* (1%), *NLRP1* (1%), *NLRP7* (1%), *SCAF11* (1%), *GSDMC* (1%), and *NOD1* (1%) occurred somatic mutations as well as most of them had high frequencies of CNV in breast cancer. Our spearman test and PPI network both revealed the tight interactions between pyroptosis-related genes. In the PPI network, *CASP1* had the highest degree. Consistently, *CASP1* is a prognostic factor as well as therapeutic target in breast cancer (31). As shown in GO enrichment analyses,

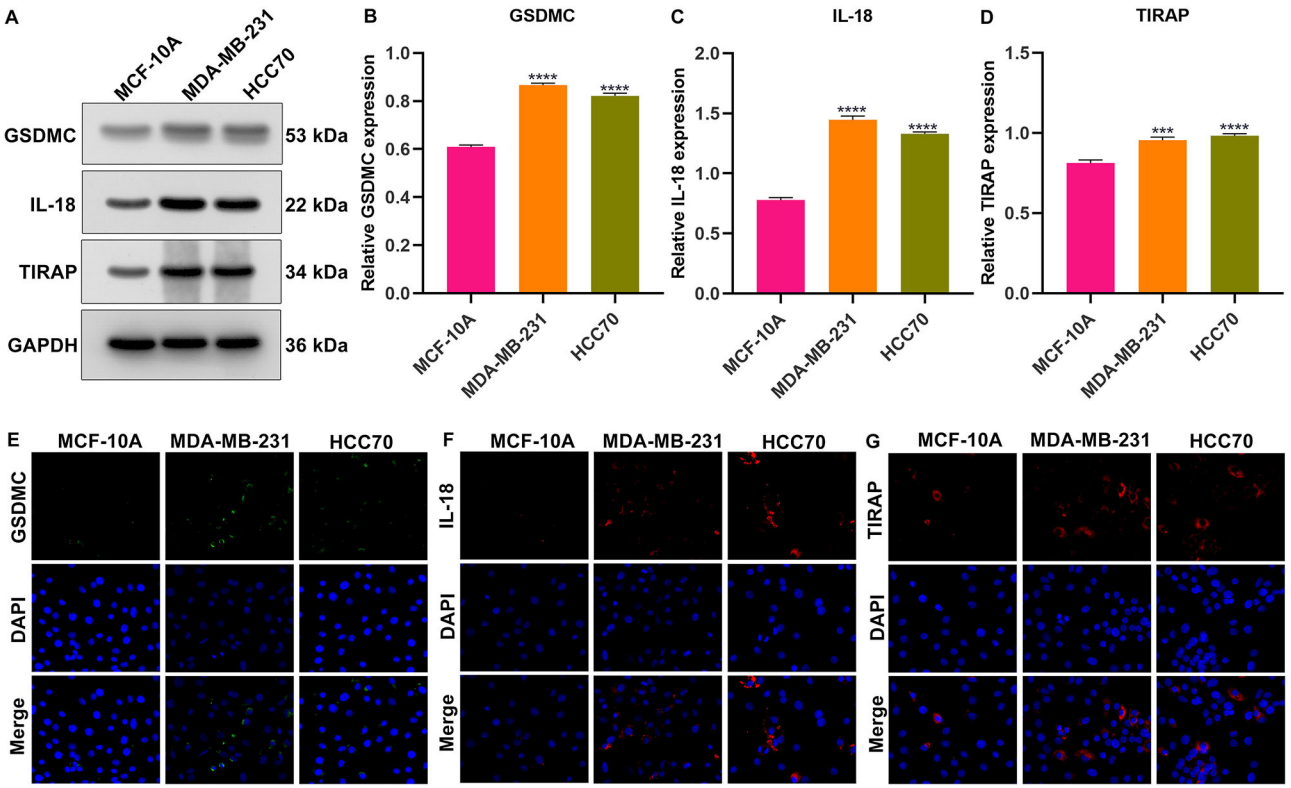

FIGURE 9 | Validation of the expression of *GSDMC, IL-18*, and *TIRAP* in normal breast cells (MCF-10A) and breast cancer cells (MDA-MB-231 and HCC70). **(A–D)** Western blot detecting the expression of GSDMC, IL-18, and TIRAP in MCF-10A, MDA-MB-231, and HCC70 cells. ***$p < 0.001$; ****$p < 0.0001$. **(E–G)** Immunofluorescence of the expression of GSDMC, IL-18, and TIRAP in MCF-10A, MDA-MB-231, and HCC70 cells. Scale bar, 5 μm; magnification 200 ×.

pyroptosis-related genes were primarily involved in mediating *IL-1β* production and secretion biological processes as well as cytosolic, inflammasome and membrane cellular components and apoptotic process, indicating the key biological implications of pyroptosis in tumorigenesis. We generated a pyroptosis-related gene signature, containing *IL-18, GSDMC*, and *TIRAP*. High RS was indicative of undesirable OS, recurrence, and progression of breast cancer. AUC = 0.652 demonstrated the well predictive efficacy. Multivariate analyses and subgroup analyses suggested that this RS was an independent risk factor of breast cancer prognoses. Previously, a pyroptosis-related gene signature was generated for prediction of ovarian cancer prognoses (14). Our univariate cox regression analyses showed that *IL-18* was a protective factor as well as *GSDMC* and *TIRAP* were risk factors for breast cancer prognoses. *IL-18*, a proinflammatory cytokine, modulates inflammation, and immune response. As confirmed by previous studies, mesenchymal stem cells expressing *IL-18* suppresses breast cancer proliferation and metastasis, suggesting the antitumor activities of *IL-18* (32, 33). *GSDMC* is specifically cleaved by *caspase-8* through *TNFα* to generate *GSDMC* N-terminal domain, thereby forming pores on the cell membrane as well as inducing pyroptosis. High expression of *GSDMC* is in relation to undesirable survival of cancer patients (34). Furthermore, there is evidence shows that *TIRAP* is a risk factor of cancer prognosis (35).

Immunotherapies especially immune checkpoint inhibitors (ICIs) may produce durable therapeutic effects. Nevertheless, only one third of patients respond to ICIs. Breast cancer is often considered as a cold tumor, with lowly frequent mutation, decreased immune cell infiltration, and suppressive immune microenvironment (36). Inducing cell deaths other than apoptosis has been considered as novel cancer therapeutic strategies due to innate resistance to apoptosis (37). Combination of inducing pyroptosis and ICIs could display synergistically increased anti-cancer activity (28, 38, 39). However, most evidences of interaction between immunity and pyroptosis are derived from animal and cellular model. Here, pyroptosis-related gene signature was negatively correlated to almost all steps of cancer immunity cycle (40). Also, we found that low RS was characterized by high HLA, immune cell infiltrations and immune checkpoints. This suggested that pyroptosis exerted an impact on immuno-oncology.

In-depth exploring pyroptosis mechanisms, up- and downstream pathways may offer novel insights into breast cancer therapy. Our GSEA results suggested that high RS was in relation to carcinogenic pathways including cell cycle, ERBB signaling pathway, mTOR signaling pathway, TGF-beta signaling pathway,

ubiquitin mediated proteolysis and WNT signaling pathway. Also, low RS was significantly related to immune-related pathways including autoimmune thyroid disease, cytokine-cytokine receptor interaction, primary immunodeficiency, and ribosome. These data indicated the interactions of pyroptosis-relevant RS with above pathways in breast cancer progression. Epidemiologic studies have confirmed that age is a risk factor of breast cancer (41). Personalized medicine is based on individual evaluation of risk. By including two independent risk factors age and this RS, we generated a nomogram for prediction of 5-, 8-, and 10-year survival probabilities. The predictive accuracy was confirmed by comparing observed survival duration.

There are several limitations in our study. Firstly, due to the limited clinical features of patients, we cannot carry out subgroup analyses by stratifying more factors. Secondly, the pyroptosis-relevant RS was constructed and verified based on retrospective cohorts. In conclusion, our findings revealed that pyroptosis induction might be a novel strategy for breast cancer immunotherapy, characterized by high compatibility and extensive clinical applicability. In future studies, prognostic implications of pyroptosis will be observed in a larger breast cancer cohort. Also, interactions of pyroptosis with cancer immunity will be further verified in cellular and animal models.

CONCLUSION

Collectively, our data characterized expression patterns and mutations of pyroptosis-related genes. A three-gene regression model including *IL18, GSDMC*, and *TIRAP* was regarded as an independent risk factor of breast cancer prognoses. The RS was distinctly cancer immunity cycle, HLA immune cell infiltration and immune checkpoints in breast cancer. Our data suggested that pyroptosis combining with immunotherapies might be a potential therapeutic strategy.

DATA AVAILABILITY STATEMENT

The original contributions presented in the study are included in the article/**Supplementary Material**, further inquiries can be directed to the corresponding author.

AUTHOR CONTRIBUTIONS

LQ conceived and designed the study. DX conducted most of the experiments and data analysis, and wrote the manuscript. ZJ participated in collecting data and helped to draft the manuscript. All authors reviewed and approved the manuscript.

SUPPLEMENTARY MATERIAL

The Supplementary Material for this article can be found online at: https://www.frontiersin.org/articles/10.3389/fmed.2021.702638/full#supplementary-material

Supplementary Table 1 | Clinical information of 1,082 breast cancer patients.

Supplementary Table 2 | The gene sets of cancer-related pathways.

REFERENCES

1. Liang Y, Zhang H, Song X, Yang Q. Metastatic heterogeneity of breast cancer: molecular mechanism and potential therapeutic targets. *Semin Cancer Biol.* (2020) 60:14–27. doi: 10.1016/j.semcancer.2019.08.012
2. Britt KL, Cuzick J, Phillips KA. Key steps for effective breast cancer prevention. *Nat Rev Cancer.* (2020) 20:417–36. doi: 10.1038/s41568-020-0266-x
3. Thorat MA, Balasubramanian R. Breast cancer prevention in high-risk women. *Best Pract Res Clin Obstet Gynaecol.* (2020) 65:18–31. doi: 10.1016/j.bpobgyn.2019.11.006
4. Barzaman K, Karami J, Zarei Z, Hosseinzadeh A, Kazemi MH, Moradi-Kalbolandi S, et al. Breast cancer: biology, biomarkers, and treatments. *Int Immunopharmacol.* (2020) 84:106535. doi: 10.1016/j.intimp.2020.106535
5. Tsang JYS, Tse GM. Molecular classification of breast cancer. *Adv Anat Pathol.* (2020) 27:27–35. doi: 10.1097/PAP.0000000000000232
6. Zhang L, Pan J, Chen W, Jiang J, Huang J. Chronic stress-induced immune dysregulation in cancer: implications for initiation, progression, metastasis, and treatment. *Am J Cancer Res.* (2020) 10:1294–307.
7. Deshmukh SK, Srivastava SK, Poosarla T, Dyess DL, Holliday NP, Singh AP, et al. Inflammation, immunosuppressive microenvironment and breast cancer: opportunities for cancer prevention and therapy. *Ann Transl Med.* (2019) 7:593. doi: 10.21037/atm.2019.09.68
8. Xia X, Wang X, Cheng Z, Qin W, Lei L, Jiang J, et al. The role of pyroptosis in cancer: pro-cancer or pro-"host"? *Cell Death Dis.* (2019) 10:650. doi: 10.1038/s41419-019-1883-8
9. Xue Y, Enosi Tuipulotu D, Tan WH, Kay C, Man SM. Emerging activators and regulators of inflammasomes and pyroptosis. *Trends Immunol.* (2019) 40:1035–52. doi: 10.1016/j.it.2019.09.005
10. Broz P, Pelegrín P, Shao F. The gasdermins, a protein family executing cell death and inflammation. *Nat Rev Immunol.* (2020) 20:143–57. doi: 10.1038/s41577-019-0228-2
11. Molina-Crespo Á, Cadete A, Sarrio D, Gámez-Chiachio M, Martinez L, Chao K, et al. Intracellular delivery of an antibody targeting gasdermin-B reduces HER2 breast cancer aggressiveness. *Clin Cancer Res.* (2019) 25:4846–58. doi: 10.1158/1078-0432.CCR-18-2381
12. Kay C, Wang R, Kirkby M, Man SM. Molecular mechanisms activating the NAIP-NLRC4 inflammasome: Implications in infectious disease, autoinflammation, and cancer. *Immunol Rev.* (2020) 297:67–82. doi: 10.1111/imr.12906
13. Tian C, Yang Y, Bai B, Wang S, Liu M, Sun RC, et al. Potential of exosomes as diagnostic biomarkers and therapeutic carriers for doxorubicin-induced cardiotoxicity. *Int J Biol Sci.* (2021) 17:1328–38. doi: 10.7150/ijbs.58786
14. Ye Y, Dai Q, Qi H. A novel defined pyroptosis-related gene signature for predicting the prognosis of ovarian cancer. *Cell Death Discov.* (2021) 7:71. doi: 10.1038/s41420-021-00451-x
15. Latz E, Xiao TS, Stutz A. Activation and regulation of the inflammasomes. *Nat Rev Immunol.* (2013) 13:397–411. doi: 10.1038/nri3452
16. Wang B, Yin Q. AIM2 inflammasome activation and regulation: A structural perspective. *J Struct Biol.* (2017) 200:279–82. doi: 10.1016/j.jsb.2017.08.001
17. Karki R, Kanneganti TD. Diverging inflammasome signals in tumorigenesis and potential targeting. *Nat Rev Cancer.* (2019) 19:197–214. doi: 10.1038/s41568-019-0123-y
18. Zhang H, Meltzer P, Davis S. RCircos: an R package for Circos 2D track plots. *BMC Bioinformatics.* (2013) 14:244. doi: 10.1186/1471-2105-14-244
19. Mayakonda A, Lin DC, Assenov Y, Plass C, Koeffler HP. Maftools: efficient and comprehensive analysis of somatic variants in cancer. *Genome Res.* (2018) 28:1747–56. doi: 10.1101/gr.239244.118

20. Szklarczyk D, Franceschini A, Wyder S, Forslund K, Heller D, Huerta-Cepas J, et al. STRING v10: protein-protein interaction networks, integrated over the tree of life. *Nucleic Acids Res.* (2015) 43:D447–52. doi: 10.1093/nar/gku1003
21. Doncheva NT, Morris JH, Gorodkin J, Jensen LJ. Cytoscape StringApp: network analysis and visualization of proteomics data. *J Proteome Res.* (2019) 18:623–32. doi: 10.1021/acs.jproteome.8b00702
22. Yu G, Wang LG, Han Y, He QY. clusterProfiler: an R package for comparing biological themes among gene clusters. *Omics.* (2012) 16:284–7. doi: 10.1089/omi.2011.0118
23. Hänzelmann S, Castelo R, Guinney J. GSVA: gene set variation analysis for microarray and RNA-seq data. *BMC Bioinformatics.* (2013) 14:7. doi: 10.1186/1471-2105-14-7
24. Chen DS, Mellman I. Oncology meets immunology: the cancer-immunity cycle. *Immunity.* (2013) 39:1–10. doi: 10.1016/j.immuni.2013.07.012
25. Subramanian A, Tamayo P, Mootha VK, Mukherjee S, Ebert BL, Gillette MA, et al. Gene set enrichment analysis: a knowledge-based approach for interpreting genome-wide expression profiles. *Proc Natl Acad Sci USA.* (2005) 102:15545–50. doi: 10.1073/pnas.0506580102
26. Taabazuing CY, Okondo MC, Bachovchin DA. Pyroptosis and apoptosis pathways engage in bidirectional crosstalk in monocytes and macrophages. *Cell Chem Biol.* (2017) 24:507–14. doi: 10.1016/j.chembiol.2017.03.009
27. Zheng Z, Bian Y, Zhang Y, Ren G, Li G. Metformin activates AMPK/SIRT1/NF-κB pathway and induces mitochondrial dysfunction to drive caspase3/GSDME-mediated cancer cell pyroptosis. *Cell Cycle.* (2020) 19:1089–104. doi: 10.1080/15384101.2020.1743911
28. Erkes DA, Cai W, Sanchez IM, Purwin TJ, Rogers C, Field CO, et al. Mutant BRAF and MEK inhibitors regulate the tumor immune microenvironment via pyroptosis. *Cancer Discov.* (2020) 10:254–69. doi: 10.1158/2159-8290.CD-19-0672
29. Faria SS, Costantini S, de Lima VCC, de Andrade VP, Rialland M, Cedric R, et al. NLRP3 inflammasome-mediated cytokine production and pyroptosis cell death in breast cancer. *J Biomed Sci.* (2021) 28:26. doi: 10.1186/s12929-021-00724-8
30. Zhao P, Wang M, Chen M, Chen Z, Peng X, Zhou F, et al. Programming cell pyroptosis with biomimetic nanoparticles for solid tumor immunotherapy. *Biomaterials.* (2020) 254:120142. doi: 10.1016/j.biomaterials.2020.120142
31. Hong W, Gu Y, Guan R, Xie D, Zhou H, Yu M. Pan-cancer analysis of the CASP gene family in relation to survival, tumor-infiltrating immune cells and therapeutic targets. *Genomics.* (2020) 112:4304–15. doi: 10.1016/j.ygeno.2020.07.026
32. Liu X, Hu J, Li Y, Cao W, Wang Y, Ma Z, et al. Mesenchymal stem cells expressing interleukin-18 inhibit breast cancer in a mouse model. *Oncol Lett.* (2018) 15:6265–74. doi: 10.3892/ol.2018.8166
33. Liu X, Hu J, Sun S, Li F, Cao W, Wang YU, et al. Mesenchymal stem cells expressing interleukin-18 suppress breast cancer cells *in vitro*. *Exp Ther Med.* (2015) 9:1192–200. doi: 10.3892/etm.2015.2286
34. Hou J, Zhao R, Xia W, Chang CW, You Y, Hsu JM, et al. PD-L1-mediated gasdermin C expression switches apoptosis to pyroptosis in cancer cells and facilitates tumour necrosis. *Nat Cell Biol.* (2020) 22:1264–75. doi: 10.1038/s41556-020-0575-z
35. Bagratuni T, Terpos E, Eleutherakis-Papaiakovou E, Kalapanida D, Gavriatopoulou M, Migkou M, et al. TLR4/TIRAP polymorphisms are associated with progression and survival of patients with symptomatic myeloma. *Br J Haematol.* (2016) 172:44–7. doi: 10.1111/bjh.13786
36. Jang BS, Han W, Kim IA. Tumor mutation burden, immune checkpoint crosstalk and radiosensitivity in single-cell RNA sequencing data of breast cancer. *Radiother Oncol.* (2020) 142:202–9. doi: 10.1016/j.radonc.2019.11.003
37. Tang R, Xu J, Zhang B, Liu J, Liang C, Hua J, et al. Ferroptosis, necroptosis, and pyroptosis in anticancer immunity. *J Hematol Oncol.* (2020) 13:110. doi: 10.1186/s13045-020-00946-7
38. Liang F, Zhang F, Zhang L, Wei W. The advances in pyroptosis initiated by inflammasome in inflammatory and immune diseases. *Inflamm Res.* (2020) 69:159–66. doi: 10.1007/s00011-020-01315-3
39. Wang Q, Wang Y, Ding J, Wang C, Zhou X, Gao W, et al. A bioorthogonal system reveals antitumour immune function of pyroptosis. *Nature.* (2020) 579:421–6. doi: 10.1038/s41586-020-2079-1
40. Cao J, Yan Q. Cancer Epigenetics, tumor immunity, and immunotherapy. *Trends Cancer.* (2020) 6:580–92. doi: 10.1016/j.trecan.2020.02.003
41. Coughlin SS. Epidemiology of breast cancer in women. *Adv Exp Med Biol.* (2019) 1152:9–29. doi: 10.1007/978-3-030-20301-6_2

Conflict of Interest: The authors declare that the research was conducted in the absence of any commercial or financial relationships that could be construed as a potential conflict of interest.

Publisher's Note: All claims expressed in this article are solely those of the authors and do not necessarily represent those of their affiliated organizations, or those of the publisher, the editors and the reviewers. Any product that may be evaluated in this article, or claim that may be made by its manufacturer, is not guaranteed or endorsed by the publisher.

Copyright © 2021 Xu, Ji and Qiang. This is an open-access article distributed under the terms of the Creative Commons Attribution License (CC BY). The use, distribution or reproduction in other forums is permitted, provided the original author(s) and the copyright owner(s) are credited and that the original publication in this journal is cited, in accordance with accepted academic practice. No use, distribution or reproduction is permitted which does not comply with these terms.

Advantages of publishing in Frontiers

OPEN ACCESS
Articles are free to read for greatest visibility and readership

FAST PUBLICATION
Around 90 days from submission to decision

HIGH QUALITY PEER-REVIEW
Rigorous, collaborative, and constructive peer-review

TRANSPARENT PEER-REVIEW
Editors and reviewers acknowledged by name on published articles

Frontiers
Avenue du Tribunal-Fédéral 34
1005 Lausanne | Switzerland

Visit us: www.frontiersin.org
Contact us: frontiersin.org/about/contact

REPRODUCIBILITY OF RESEARCH
Support open data and methods to enhance research reproducibility

DIGITAL PUBLISHING
Articles designed for optimal readership across devices

FOLLOW US
@frontiersin

IMPACT METRICS
Advanced article metrics track visibility across digital media

EXTENSIVE PROMOTION
Marketing and promotion of impactful research

LOOP RESEARCH NETWORK
Our network increases your article's readership